(Unclassified)

PRELIMINARY DESIGN AND EXPERIMENTAL INVESTIGATION OF THE FDL-5A UNMANNED HIGH L/D SPACECRAFT

Part III - Aerodynamics

C. F. Ehrlich, J. J. Rising, R. S. Peyton and C. M. Onspaugh

(U) FOREWORD

(U) This is the final report of work performed under Contract No. AF33(615)-5241, "Preliminary Design of Two Volumetrically Efficient High L/D Unmanned Flight Test Vehicles". This report was prepared under Project 1366, "Aerodynamics and Flight Mechanics", Task 136616, "Synthesis of Hypersonic Vehicles".

(U) The work was sponsored by the Aerospace Vehicle Branch, Flight Mechanics Division, Air Force Flight Dynamics Laboratory. The research investigation was performed under the direction of the Air Force Project Engineer Mr. Thomas R. Sieron. Mr. C. J. Cosenza and Mr. A. C. Draper of AFFDL provided overall technical guidance.

(U) The work was accomplished by the Lockheed-California Company, Burbank, California and the report is also identified as LR 21204.

(U) This is Part III of a five part report:

Part I	Summary
Part II	Parametric Configuration Development and Evolution
Part III	Aerodynamics
Part IV	Aerothermodynamics
Part V	Vehicle Design

(U) This manuscript was released by the authors for publication in January 1968.

(U) The contributions of Mr. J. F. Holliday to this report are gratefully acknowledged.

(U) This technical report has been reviewed and is approved.

Philip P. Antonatos
Chief, Flight Mechanics Division
Air Force Flight Dynamics Laboratory

(U) ABSTRACT

(U) The aerodynamic wind tunnel test program for the FDL-5 configuration is described in this Part III. The description includes the models, test facilities, data reduction and presentation, and the test schedules. A complete presentation of the aerodynamic test data are provided. The data include six component force and moment data, pressure data, and photographic data for the Mach number range between 1.5 to 20. Correlations between the data and appropriate theories are presented. The overall aerodynamic characteristics of the FDL-5 configuration are defined.

This report is subject to special export controls and each transmittal to foreign governments or foreign nationals may be made only with prior approval of the Air Force Flight Dynamics Laboratory (FDMS), Wright-Patterson Air Force Base, Ohio 45433.

TABLE OF CONTENTS

TABLE OF CONTENTS (Concluded)

LIST OF ILLUSTRATIONS

LIST OF ILLUSTRATIONS (Continued)

LIST OF ILLUSTRATIONS (Continued)

LIST OF ILLUSTRATIONS (Continued)

LIST OF ILLUSTRATIONS (Continued)

LIST OF ILLUSTRATIONS (Concluded)

LIST OF TABLES

SECTION 1

(U) INTRODUCTION AND SUMMARY

(U) The purpose of the aerodynamic analyses in this study was to configure a research vehicle which has high internal volume, has high lift-to-drag ratio at hypersonic speeds, can land horizontally, and is suitably stable and controllable over the entire reentry velocity spectrum. Interdisciplinary influences on the aerodynamic configuration were integrated and accounted for in the design.

(U) The aerodynamic study program consisted of two phases. The first phase was devoted to analytical and parametric tradeoff studies leading to the development of the wind tunnel test configuration and incorporating the interrelated influences of the various technical disciplines. The second phase was devoted to the preliminary design and experimental study of that configuration. The activities of the first phase, including the parametric analyses and basic configuration development of the FDL-5 configuration, are presented in Part II of this report. The aerodynamic studies, analytical and experimental, are reported in Parts III, IV and V.

(U) This volume describes the aerodynamic experimental program, and the results obtained for the FDL-5 test configuration, Figure 1. Three models were fabricated for the aerodynamic test series: 20-inch steel force and pressure models, and a 14.6-inch lightweight fiber glass model. The steel models were tested in the Arnold Engineering Development Center (AEDC), von Karman Facility (VKF) wind tunnels A, B, and C at M = 1.5 to 10.0; while the fiber glass model was tested in the AEDC VKF Tunnel F at M = 19.

(U) The test data were obtained at conditions approximating full scale Reynolds numbers. This duplication was achieved for Mach numbers above 5; at M = 5 and below, transition was induced to ensure turbulent flow over the models. The variation of Reynolds number with Mach number is presented in Figure 2 for the two reference trajectories selected for the study. The conditions at which the tests were performed are superimposed on Figure 2.

(U) The nominal pitch and yaw ranges were 0 - 25 and 0 - 10 degrees, respectively. At M = 10, the angle of attack range was extended to 45 degrees for the force model by use of an offset sting. Six-component force data were recorded to define aerodynamic effects of configuration build-up; elevon, flap, and aileron deflection; and Reynolds number variation.

(U) Pressure distribution data were obtained at M = 1.5 to define the local load distribution during maximum load conditions which occur during boost. Additional pressure data were recorded at M = 2.0 to 19; the M = 10 and 19 data are presented and discussed in Part IV of this report.

(U) Flow visualization photographs (vapor screen, oil flow, and schlieren) were also obtained; representative photographs are presented in this volume.

(C) The data indicate that the FDL-5 configuration is stable and controllable at all normal flight attitudes over the test Mach range (M = 1.5 to 19). Hypersonic L/D_{max} (trimmed), extrapolated to the full-scale nominal design conditions (h - 200,000 ft; V_∞ = 20,000 fps), is 2.84 at α = 11 degrees. Elevon control is sufficient to achieve stable trim at L/D_{max} down to about M = 10 for a reference CG at 62% to 65% of the vehicle length. At lower speeds, stable trim requires the use of an upper body flap to augment the elevon controls. The configuration is laterally and directionally stable at all flight attitudes over the Mach range tested.

(U) The test data correlate well with analytical predictions in most cases. In general, the best correlation was achieved using tangent-cone theory on compression surfaces and Prandtl-Meyer theory on expansion surfaces to determine local pressure coefficients; these pressures were integrated to obtain forces and moments for the body alone. These calculations were performed with an IBM 360 Arbitrary Body Computer Program. To these body loads, centerline fin loads and axial force skin friction (laminar and/or turbulent) were added.

(U) The test data, estimated elevon effectiveness and hinge moments, and predicted dynamic stability characteristics are crossplotted with Mach number and angle of attack. Skin friction forces have been included to provide full-scale axial force and L/D values; they include allowance for boundary layer transition according to established criteria. These data may be used for machine simulation of flight at speeds from M = 1.5 to 20 along an entry trajectory.

(U) The following sections in this volume present the details of the test program, results achieved, and data/theory correlations made. The discussions are supported by extensive test data plots.

SECTION 2

(U) TEST PROGRAM

2.1 (U) DESCRIPTION OF MODELS

(U) The models used in the aerodynamic test program are described in the following paragraphs. Models used to obtain Aerothermodynamic data are described in Part IV. The configuration notation is defined in Table 1.

2.1.1 (U) Force Model - Tunnels A, B, C

(U) The force model which was tested in Tunnels A, B, and C is made of ARMCO 17-4PH stainless steel, heat treated to 1200°F. It is a 0.05051 scale model of the FDL-5 configuration, (Figure 3). The model has a removable vertical fin on the body centerline and removable trailing edge elevons which were capable of deflection range of ±10, 0, -20 and -30 degrees. Off blocks were fabricated for testing the model with the fin and elevons removed. The overall model length, excluding the elevons, is 20.551 inches. The model weight for the basic configuration with fin and elevons installed is about 25 pounds. A steel pin locked the model to an adapter which was bolted to the AEDC -17 six-component balance-water jacket unit. The model was designed by the Lockheed Fluid Dynamics Laboratory and was fabricated by H & N Minicraft, Covina, California.

2.1.2 (U) Force Model - Tunnel F

(U) The Tunnel F force model is a 0.03687 scale model of the FDL-5 configuration (Figure 4), with an integral vertical fin on the body centerline and removable trailing edge elevons. Three copies of the model were fabricated to permit a dual model installation for testing, and to provide a spare model in case of model damage. The models are made of fiber glass; they were formed by making a female mold from a male master and building up layers of resin-impregnated fiber glass in the two-piece mold. The model shell consists of three layers of 0.007-inch fiber glass cloth bonded with RP 1710A laminating resin and finished on the outer surface with RP 1721A surface coat. The internal structure of the models consists of 0.125-inch thick balsa stringers or longerons and cross braces, two magnesium bulkheads, and a magnesium balance sleeve for the AEDC 1.00-inch diameter balance. The elevons are made of magnesium and are attached to recessed magnesium pads bonded to the model with epoxy cement. Magnesium elevon brackets were made to provide elevon settings and deflection angles of 0, ±10, -20 and -30 degrees. The overall model length, excluding elevons, is 15.002 inches. The model weight is approximately 160 grams for two of the models and 130 grams for the third model. The models were designed and fabricated by Micro Craft, Inc., Tullahoma, Tennessee.

2.1.3 (U) Pressure Model-Tunnels A, C

(U) The pressure model is a 0.0501 scale model of the FDL-5 configuration with an integral vertical fin on the body centerline and removable trailing edge elevons, Figure 5. The elevon mounts are designed to take the elevons from the 0.0501 scale steel force model. The pressure model was tested with the elevons in the undeflected position only. The model is made of ARMCO 17-4PH stainless steel, heat treated to 1200°F and is hollow. It is made in two pieces with a left and right half which are bolted together. The split line is offset slightly to the left of the model centerline to permit the installation of pressure orifices directly along the centerline. Only the right side of the model is instrumented. The vertical fin is solid steel but provisions are made for the installation of seven pressure taps. The model contains a total of 99 pressure orifices. The quarter-hard, seamless, stainless steel tubing has an outside diameter of 0.093 in. and a wall thickness of 0.014 in. The internal tubes are sealed into the model orifices with 1700°F silver solder. A 1.51-inch diameter sting of ARMCO 17-4 PH stainless steel is provided to mount the model in the tunnel. The model was designed by the Lockheed Fluid Dynamics Laboratory and was fabricated by H & N Minicraft, Covina, California.

2.2 (U) TEST FACILITIES

(U) The Test Facilities used in the aerodynamic test program are described in the following paragraphs.

2.2.1 (U) Tunnel A

(U) The VKF tunnel A, Figure 6, is a 40-inch x 40-inch, continuous closed-circuit, variable density supersonic wind tunnel with a Mach number capability of 1.5 to 6.0. Five stages of compression are available in the main compressor system and can provide a wide range of stagnation pressures from 1.5 psia to 200 psia. Stagnation temperatures vary from a minimum of 70°F at M = 1.5 to a maximum of 310°F at M = 6.0. Continuous-curvature nozzle contours are obtained by means of flexible top and bottom walls mounted on automatic electrically-driven screw jacks. The side walls of the nozzle are plane and parallel. The Reynolds number capability of the tunnel varies from a range of 0.41×10^6/ft to 9.0×10^6/ft at M = 1.5 to a range of 0.69×10^6/ft to 4.3×10^6/ft at M = 6.0. The model support system permits an angle-of-attack range of -5 to +15 degrees in the horizontal plane with a straight sting installation. The angle-of-attack range was increased by the use of a bent sting adapter. Remotely controlled roll actuators were used to obtain combined angles of attack and sideslip for yaw data. The steel force model installed in the tunnel as shown in Figure 7.

(U) On-line data reduction and test monitoring information is provided by a Control Data 1604-B computer. A double-pass schlieren system with a 35-inch

diameter optical path is available for observation of flow fields through any of three test section windows. Vapor screen photographs can be obtained by injecting steam into the tunnel circuit and photographing the model in conjunction with a laser beam.

2.2.2 (U) Tunnel B

(U) The AEDC VKF Tunnel B (Figure 8) is a 50-inch diameter, continuous, closed-circuit, variable density wind tunnel capable of operating at Mach numbers 6.0 and 8.0 The Reynolds number capability for the tunnel permits testing at Mach 6.0 at Reynolds numbers up to about 5.3 x 10^6/ft and at Mach number 8.0 at Reynolds numbers up to 3.8 x 10^6/ft. The test section is equipped with six fused quartz windows of optical quality with a viewing area about 17.25 inches in diameter for each window. The models are supported from the rear by a sting which is fitted to a hydraulically actuated vertical sector. The center of model rotation can be shifted so that the region of interest on the model remains within the viewing area of the windows. The model support sector is equipped with a remotely controlled, water-cooled roll sting with ±180 degrees of rotation. The model support is retracted into a tank below the test section for model installation and configuration changes. Model injection is accomplished in a minimum time of about two seconds with a maximum acceleration or deceleration of one g. Straight and bent water-cooled stings are available in Tunnel B, including a series of split bent stings with prebends ranging from 3 degrees to 48 degrees. The split stings can be interchanged without disconnecting the model instrumentation and permit the model to be pitched to a maximum angle of attack of about 60 degrees. Tunnel B shares the control data 1604-B computer with Tunnel A.

(U) Tunnel B utilizes a propane-fired heater to provide the 900°F stagnation temperature required to prevent liquefaction in the main airstream. The entire tunnel throat, nozzle, test section, model support section, and diffuser are cooled by integral, external water jackets.

2.2.3 (U) Tunnel C

(U) The VKF Tunnel C (Figure 9) is a continuous, closed-circuit tunnel with a 50-inch diameter axisymmetric nozzle. It can operate at either Mach 10 or Mach 12. The operating capability of the tunnel covers a stagnation pressure range of 200 to 2400 psia with stagnation temperatures up to 1940°F to prevent liquefaction. The Reynolds number capability at Mach 10 extends from 0.3 x 10^6/ft to 2.4 x 10^6/ft. The model support system permits an angle-of-attack range of ±15 degrees with a straight sting installation (see Figure 10). The angle-of-attack range was increased by the use of bent sting installations. A remote control roll pod permits the model to be rolled ±180 degrees during a run. Yaw runs with the model at some fixed angle of attack may be made with a combination pitch-roll variation of model attitude. The model support is retracted into the test section tank for model installation or modification. The models are cooled by a jet of cold air after retraction from the test section. Model injection time is about 2 seconds. A maximum of 99 pressures can be measured on a model using the Wiancko FM-type pressure transducers and

associated oscillators. The Wiancko FM pressure system uses temperature-controlled transducers which have an accuracy of ±0.07 percent of range and a required readout time of one second.

2.2.4 (U) Tunnel F

(U) The VKF tunnel F (Figure 11) is a 100-inch-diameter, arc-driven hypervelocity tunnel. The useful run time with the recently enlarged dump tank is about 100 milliseconds. The nominal test core diameter is 40 inches with time and space variations of pitot pressures of about ±10%. The standard shot conditions for the normal test section installation in Tunnel F provide Mach numbers of 19 and 20 with a Reynolds number range of 0.04×10^6/ft to 0.80×10^6/ft. Stagnation pressures range from 4000 psia to 28,000 psia. A special upstream installation of the model permits testing at Mach numbers of 14 and 15 with a Reynolds number range of 0.80×10^6/ft to 1.70×10^6/ft. A dual sting arrangement was used for these tests so that two models could be installed simultaneously to provide data for two different model attitudes during each run as seen in Figure 12. Tunnel F data are recorded on multichannel oscillographs for monitoring test runs and are also digitized for final computing and data reduction using the CDC1604-B computer.

2.3 (U) DATA REDUCTION

(U) The procedures followed in reducing the test data from the aerodynamic tests are described in the following paragraphs.

2.3.1 (U) Force Data

(U) All data from the force tests in Tunnels A, B, C, and F are referenced to body axes. The coefficients of lift and drag were also computed. The moment coefficients are referenced to a moment reference point located longitudinally at 62 percent of the model reference chord, and vertically .0567 percent above the horizontal reference line. The force and moment data are presented in terms of the following dimensionless coefficients (sign conventions are defined in Figure 13).

NORMAL FORCE COEFFICIENT	$C_N = F_N/q_\infty S$
AXIAL FORCE COEFFICIENT (TOTAL)	$C_A = F_A/q_\infty S$
BASE AXIAL FORCE COEFFICIENT	$C_{A_B} = A_B(P_B - P_\infty)/q_\infty S$
PITCHING MOMENT COEFFICIENT	$C_m = M_m/q_\infty Sc$
LIFT COEFFICIENT	$C_L = C_N \cos \alpha - C_A \sin \alpha$

DRAG COEFFICIENT	$C_D = C_A \cos \alpha + C_N \sin \alpha$
SIDE FORCE COEFFICIENT	$C_Y = F_y/q_\infty S$
YAWING MOMENT COEFFICIENT	$C_n = M_n/q_\infty Sb$
ROLLING MOMENT COEFFICIENT	$C_\ell = M/q_\infty Sb$

where:

F_n = Normal Force, lb

F_A = Axial Force, lb

M_m = Pitching Moment, in.-lb

F_L = Lift Force, lb

F_D = Drag Force, lb

F_Y = Side Force, lb

M_n = Yawing Moment, in.-lb

M_l = Rolling Moment, in.-lb

and:

A_B = Model Base Area, $in.^2$

b = Model Reference Span, in.

c = Model Reference Chord, in.

P = Free-Stream Static Pressure

q_∞ = Free-Stream Dynamic Pressure

S = Model Reference Area (Planform Area), $in.^2$

2.3.2 (U) Model Attitude

(U) α = Angle of attack of model horizontal reference line (body centerline along flat lower surface of aft body), degrees.

β = Angle of sideslip of model horizontal reference line.

The following reference dimensions are used for the data reduction:

Reference Dimension	0.05051 Scale	0.03687 Scale
b = Span, Lower Surface at Model Base	5.788 in.	4.225 in.
c = Chord, Reference Body Length	20.00 in.	14.60 in.
S = Body Planform Area	66.4945 $in.^2$	35.4283 $in.^2$
A_B = Base Area, including Balance Bore	10.286 $in.^2$	5.4807 $in.^2$

Model base pressures were measured and the base drag was calculated and tabulated but not applied; therefore the L/D ratios presented in this report are based upon total measured drag values.

2.3.3 (U) Pressure Data

(U) The pressure data from Tunnels A, C, and F were reduced to pressure ratios and coefficients using the following relationships:

Pressure Ratio P/P_∞

Pressure Coefficient $C_p = (P - P_\infty)/q_\infty$

Where:

P = Local pressure on model, psia

P_∞ = Free-stream Static Pressure, psia

q_∞ = Free-stream dynamic pressure, psia

2.4 (U) DATA PRECISION

(U) Data precision for the force and pressure data is discussed in the following paragraphs.

2.4.1 (U) Force Data - (Tunnels A, B, and C)

(U) The possible uncertainties in the force data were determined by ARO personnel on the basis of combined static loadings of the VKF strain-gage balance. Combined balance static loadings were applied to simulate the model loading range anticipated during the test. The uncertainties listed below correspond to the differences between the applied loads and the values calculated by the final data reduction equations and apply to the data from tunnels A, B, and C.

Balance Component	Design Load	Maximum Static Loads	Uncertainties
Normal force, lb	200	200	±0.9
Axial force, lb	50	10	±0.05 to ±0.2*
Pitching moment, in.-lb	680	300	±0.8
Yawing moment, in.-lb	680	60	±0.7
Rolling moment, in.-lb	100	60	±0.2
Side force, lb	200	40	±0.4

*The axial force undertainty range corresponds to a range of combined normal force from 0 to 200 lb

2.4.2 (U) Force Data - (Tunnel F)

(U) The accuracy of the results obtained from Tunnel F is, primarily, a function of the uncertainty of the direct measurements and the test section flow properties. The average magnitudes of these uncertainties are as follows:

Normal force coefficient (C_N)	±7 percent
Axial force coefficient (C_A)	±7 percent
Center of pressure (CP)	±1.5 percent
Free stream Mach number (M_∞)	±2 percent
Free stream Reynolds number (R_∞)	±15 percent

The uncertainties indicated for free stream Mach number and Reynolds number are based on specific values obtained for a particular data point and do not, therefore, indicate departures from quoted nominal values.

2.4.3 (U) Pressure Data - (Tunnels A and C)

(U) Model pressures were measured with the pressure systems provided in tunnels A and C. The Tunnel A system used 15-psid transducers. referenced to a near vacuum, calibrated for ranges of 1, 5, and 15 psia. From repeat calibrations, measurement of a given pressure is estimated to be precise within ±0.25 percent of full scale of the range being used. Tunnel C model pressures were measured with 1- and 15-psid transducers, referenced to a near vacuum. These tranducers were switched in and out of the system automatically to allow measuring to the best precision. From repeat calibrations, the estimated measurement precision was ±0.001 psia or ±0.5 percent, whichever was greater.

2.5 (U) DATA PRESENTATION

(U) CALCOMP Plotting Method. The final force and pressure data were obtained from ARO, Inc. in tabulated form and on magnetic tape in binary code decimal form. The data were plotted semi-automatically on a CALCOMP plotter for inclusion in this report. The CALCOMP plotter is a digital incremental plotter Model 565, manufactured by California Computer Products, Inc., Anaheim, California. It is a high speed, two-axis plotter designed for plotting one variable as a function of another. The instrument responds to digital incremental signals from any suitable source. The plot is produced by the movement of a pen over the surface of the chart paper. The Y axis plot is produced by lateral movement of the pen carriage, and the X-axis plot by rotary motion of the chart drum. Provision for Z-axis modulation is also incorporated through the use of a pen solenoid which permits the pen to be lifted or lowered to the plotting surface in response to electrical input signals. The plotter employs a bi-directional rotary step motor on both X and Y drives. Each step causes the drum or pen carriage to move 0.01-inch in either a positive or a negative direction. The motors are capable of operating at a rate

of up to 300 steps per second. Resolution is ±.01-inch (1 step) on either axis over the entire 120-foot roll of paper. A paper feed and takeup mechanism is provided which accepts chart paper rolls 12 inches wide by 120 feet long. The feed and takeup mechanism is bi-directional. The paper is driven by sprocket teeth on the drum which engages the sprocket holes on both edges of the paper, thus maintaining accurate registration between the recording pen and the paper.

TABLE 1

(U) MODEL CONFIGURATION SYMBOLS

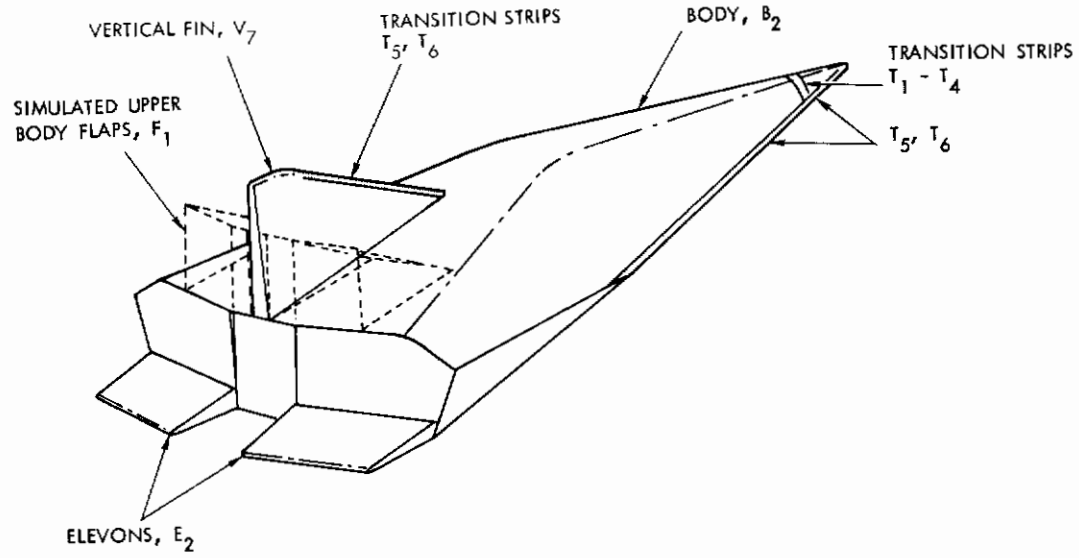

B_2	Basic FDL-5A body. Leading edge sweep = 81 deg.
E_2	FDL-5A trailing elevons. Deflection range, S_E = +10 deg to -30 deg. Minus deflection indicates trailing edge of elevon up.
F_1	Wedge blocks on aft upper body along either side of vertical fin. Simulated upper body flaps. Superscript, -30, indicates 30 degree wedge blocks. Equivalent to a 30 degree flap deflection, trailing edge up.
T_1	One-quarter-inch wide band of No. 40 carborundum transition grit around nose one inch aft of model stagnation point.
T_2	No. 100 carborundum grit. Same location as T_1.
T_3	No. 54 carborundum grit. Same location as T_1.
T_4	No. 20 carborundum grit. Same location as T_1.
T_5	One-quarter-inch wide band of No. 54 carborundum grit around nose, one inch aft of model stagnation point and 0.10-inch strips of No. 100 grit along the model and vertical fin leading edges.
T_6	No. 40 and No. 60 grit in the same location as the No. 54 and No. 100 grit, respectively, of T_5.
V_7	FDL-5A vertical fin along body centerline

SECTION 3
(U) TEST RESULTS

(U) This section presents the results of the aerodynamic wind tunnel test program conducted at the Arnold Engineering Development Center (AEDC) for the FDL-5 test configuration. Six-component force, moment, and pressure data, and flow visualization photographs for the various Mach numbers tested are shown and discussed.

(U) The force and moment data have been organized to show the effects on longitudinal aerodynamic characteristics of: (1) configuration build-up, (2) symmetrical elevon deflection, (3) upper surface flap deflection, (4) asymmetrical elevon deflection (aileron deflection), (5) Reynolds number variation, (6) forced transition, and (7) data repeatability. The lateral-directional forces and moments presented show the effects in yaw of configuration build-up and the effects in pitch of aileron control. The pitch data are presented for the angle of attack range -5 to 24 degrees; limited angle of attack data extended to 47 degrees are presented for M = 10. Combined pitch and yaw data are presented for sideslip angles from -2 to 8 degrees for various angles of attack in the range 0 to 20 degrees. At M = 19 the yaw data were recorded only for sideslip angles of 4 and 8 degrees.

(U) For ease of reference to the large body of force and moment data presented within this section, the data have been catalogued by:

- Mach number.
- Type of data for a given Mach number.

The latter category includes:

- Configuration buildup
- Elevon effects
- Aileron effects
- Flap effects
- Forced transition effects
- Repeatability

- Reynolds number effects
- Data at extended angles of attack

(U) Table 2 lists the data presented for the various Mach number cases; it provides a convenient outline for locating data of a particular type. The figures of this section, which are listed by number in Table 2, are arranged by Mach number and type of data. Also shown, are the nominal test conditions for each Mach number at which most of the data were obtained. Throughout the text of this section reference is made only to selected representative data plots. The remainder of the plots are provided for complete data presentation.

(U) Pressure test data are presented to define the external distribution of local loading in pitch at M = 1.5 to 10. M = 1.5 is approximately the Mach number for maximum loading on a typical launch vehicle VTO boost trajectory. An outline of the figures describing the pressure test data is also included in Table 2. The pressure data is catalogued by centerline and body station location for each Mach number.

(U) Vapor screen, surface oil flow, and schlieren photographs were obtained during the test program. These photographs were made to provide qualitative data about the flow field on and around the vehicle to assist the interpretation of the test data. Representative sample photographs presented include vapor screens at M = 1.5, 5.0, and 8.0; schlierens at M = 8.0 and 19.0; and oil flow at M = 10.0.

3.1 (U) DISCUSSION OF FORCE TEST DATA

(U) The six-component force data obtained during the tests at Mach numbers of 1.5 to 19 are discussed in the following paragraphs. Reference is made to selected, representative data plots.

3.1.1 (U) Axial Force Characteristics and Contributions

(U) The axial force (C_A) characteristics of the FDL-5 are produced primarily by the forebody and base contributions of the basic body; however, the centerline vertical fin and the trailing edge elevons do provide significant contributions to the total axial force. The data presented herein include the experimental base pressure.

3.1.1.1 (U) Forebody Axial Force. (C) The axial force of the forebody is strongly dependent on angle of attack and Mach number. At the lower supersonic Mach numbers the forebody axial force initially decreases over a range of increasing angle of attack and then starts increasing. For the initial range of angle of attack, the reduced pressures around the leading edges (sometimes referred to as leading edge suction) and on the lee side of the body predominate over the increased windward pressures forcing the reduction

TABLE 2

(U) TYPES OF DATA PRESENTED, SHOWING THE VARIOUS CASES AND THE INCLUDED FIGURE NUMBERS OF THE PLOTS IN SECTION 3

FORCE DATA	Type	M = 1.5	M = 2.0	M 2.5	M = 3.5	M = 5.0	M = 8.0	M = 10.0	M = 19.0
Configuration Buildup	Pitch	15 to 22	57 to 63	102 to 108	150 to 156	187 to 193	208 to 214	241 to 247	295 to 302
	Yaw	23 to 34	64 to 66	109 to 120	157 to 168	194 to 196	215 to 229	248 to 259	303 to 305
Elevons	Pitch	35 to 41	67 to 73	121 to 127			230 to 236	260 to 266	306 to 313
Combined flaps and elevons					169 to 175	197 to 203			
Flaps	Pitch	42 to 48	74 to 80	128 to 134					
Ailerons			81 to 90					271 to 280	
Forced transition		49 to 52	98 to 101	142 to 145	183 to 186	204 to 207			
Repeatability	Pitch	53 to 56		146 to 149			237 to 240	288 to 291	295 to 305*
	Yaw							292 to 294	
Reynolds number	Pitch		91 to 97	135 to 141	176 to 182			281 to 287	314 to 320
Extended angle of attack								267 to 270	
PRESSURE DATA									
Lower surface centerline		325	338	351	364	377		390	
X/L		326 to 330	339 to 343	352 to 356	365 to 369	378 to 382		391 to 395	
Upper surface centerline		331	344	357	370	383		396	
X/L		332 to 337	345 to 350	358 to 363	371 to 376	384 to 389		397 to 402	
NOMINAL TEST CONDITIONS:									
Reynolds number ($\times 10^{-6}$/ft)		2.4	2.4	2.4	2.4	2.4	2.35	2.1	.640**
Total Pressure (psia)		8.2	9.8	12.6	21.3	48.5	505	1725	18,000**
Total temperature (°F)		100	100	100	100	100	840	1440	4,220**

*Repeated data points are included in the Configuration Buildup curves.
**Values cited are "typical" since actual test conditions vary from run to run.

in axial force seen in Figure 14. This is most apparent in the neighborhood of α = 18 degrees. As angle of attack increases beyond this range, the windward pressures start to predominate and the axial force begins increasing. (This effect combined with the base axial force increase with angle of attack produces the oscillatory variation with angle of attack of the total axial force as shown in Figure 15). As Mach number increases the initial axial force decrease with angle of attack grows weaker until at M = 5 the data (Figure 187) show only an increase in axial force as angle of attack increases. In the hypersonic regime, the variation, with angle of attack, of the forebody axial force contribution due to pressure is not a strong function of Mach number; however, the variation with angle of attack of the friction contribution increases as Mach number increases (see Figure 296).

3.1.1.2 (U) Base Axial Force. (C) Base axial force C_{A_B} is primarily Mach number dependent; however, in the low supersonic Mach number range the data also show a dependence on angle of attack. Figure 14 shows that at M = 1.5 about 66% of the total axial force at α = 0 is contributed by the base. The axial force due to base drag increases 45% through 20 degree angle of attack. The tendency for base axial force to increase with angle of attack is shown to disappear as Mach number increases in a summary plot, Figure 16. For test Mach numbers greater than M = 2.5, the base axial force is essentially constant through the angle of attack range 0 to 24 degrees. As Mach number increases the base contribution to axial force decreases approximately as $1/M^2$.

3.1.1.3 (U) Centerline Fin. (C) The centerline vertical fin (V_7) contributes to the total frontal area encountered by the flow, thereby increasing the forebody and base contributions to axial force. The increment of axial force due to the addition of V_7 is most apparent in the lower supersonic Mach number range, as seen in Figure 15, where the base contribution is highest, and also where the shielding effects of the body are lowest. For the test Mach numbers greater than 5 the axial force contribution of V_7 is hardly noticeable, as seen in Figure 241, for example.

3.1.1.4 (U) Undeflected Elevons. (C) Although the addition of undeflected trailing edge elevons, E_2, does not contribute to the frontal area of the configuration, the axial force is increased, apparently due to an influence on the body base pressure. This influence is strongest at the lower Mach numbers since the base pressures are higher at these speeds and is somewhat dependent of angle of attack as seen in Figure 57. The increment of axial force due to the addition of undeflected elevons is about 8% of the total axial force at M = 1.5 and decreases to negligible values for M $\geq$ 2.49 (Figure 102).

(C) Negative as well as positive deflection of the trailing edge elevons influences axial force. Positive deflection of the elevons contributes to the vehicle frontal area, thereby significantly increasing axial force; while negative deflection, which does not contribute to the frontal area, produces secondary influence on axial force at all but the lowest supersonic Mach numbers. The changes in base pressure environment induced by negative elevon

deflection do produce discernible changes in the data at the lower Mach numbers; except for an obvious dependence on angle of attack, specific trends again are difficult to observe.

3.1.1.5 (U) Upper Surface Flaps. (C) Axial force is also strongly affected by deflection of the flaps located on the aft upper surface boattail of the body. The boattail and lee side shielding of these surfaces render them less effective in drag as Mach number and angle of attack increases as seen by comparing the flap deflection increments in Figures 42 and 197.

3.1.1.6 (U) Reynolds Number. (C) The most interesting effects to be noted from the axial force data for various Reynolds numbers occur at angle of attack in the supersonic Mach number range. For example, at M = 2.5 (Figure 135) at angles of attack greater than 15 degrees, there is an increase in axial force corresponding to an increase in Reynolds number. This behavior is apparently due to a Reynolds number influence on vortex formation. At hypersonic Mach numbers, M = 14 to 19, Reynolds number has a striking effect on axial force at α = 10 degrees. Figure 314 shows the variation of axial force with angle of attack for the nominal test Reynolds number of 0.672×10^6/ft. Included in the plot are the α = 10 degrees data for $0.114 \times 10^6 \leq$ Re/ft $\leq 2.090 \times 10^6$. The substantial C_A increase due to increased skin friction and viscous interaction are evident. The data for the highest Re/ft are at M = 14. Mach number effects are not large in this speed range.

3.1.1.7 (U) Forced Transition. (C) Comparison of supersonic axial force data from Tunnel A for the model with and without forced transition (induced by applying grit to the nose and leading edges) indicate that at α = 0 forced transition produces only a very slight increase in axial force, while at angle of attack the axial force increment is much more pronounced (see Figures 133 and 204).

3.1.1.8 (U) Repeatability. (C) The axial force data recorded for the various Mach numbers are, in general, smooth and show good repeatability except for a few notable discrepancies. The axial force repeatability data at M = 2.5 (Figure 146) show an unusually large deviation. The configuration build-up data for M = 5 (Figure 187) show a questionably large increment due to the addition of the undeflected elevons. Considerable data scatter is present in all of the M = 10 longitudinal data (Figure 241). Also, at M = 19, the data (Figure 295) show an unexplainable difference in axial force variation with angle of attack due to the addition of undeflected elevons.

3.1.2 (U) Normal Force Characteristics and Contributions

(C) The primary normal force characteristics of the model configuration are produced by the basic body; the addition of the centerline vertical fin and undeflected elevons change the normal force characteristics of the body only slightly.

3.1.2.1 (U) Body. (C) The important characteristic to be noted from the test data for the body is the initial slope of the normal force variation with angle of attack. The slope steadily decreases as Mach number increases. At

M = 19 (Figure 297) the initial C_{N_α} is 54% less than the value at M = 1.5 (Figure 17). Throughout the Mach number range tested the normal force is approximately linear through 8 degree angle of attack. At the lower Mach numbers, the low pressure region on the aft upper surface of the body produces a positive increment of normal force at zero degrees angle of attack. The influence of the boattail decreases as Mach number increases and the normal force at α = 0 decreases to a slightly negative value in the hypersonic Mach number range. This variation is clearly evident by comparing the pressure data, for example, compare the upper surface pressures for $S/S_{max} \geq 0.444$ @ X/L = 0.96 for M = 1.5 and 10.0 (Figures 237 and 302, respectively).

3.1.2.2 (U) Vertical Fin. (C) The influence of the vertical fin is hardly distinguishable; however, a very slight decrease in normal force can be detected at M = 1.5 (Figure 17).

3.1.2.3 (U) Undeflected Elevons. (C) The undeflected elevons at α = 0 add a small positive increment of normal force due mainly to the low pressure region on the base side of the elevons; as Mach number increases the base pressure coefficient approaches zero and this increment disappears (e.g.: see Figures 17 and 209). The normal force increment produced by addition of the elevons increases with angle of attack due to the increased pressures on the windward side of the elevons.

3.1.2.4 (U) Upper Surface Flaps. (C) At lower supersonic Mach numbers, the upper surface flaps produce negative C_N increments, as seen in Figure 43, since the flap intercepts the leading edge vortices evident in Figure 405e. In the hypersonic regime the flaps are in the flow shadow (Figure 406e) and are not effective at normal flight attitudes.

3.1.2.5 (U) Reynolds Number. (C) The data taken over the Mach number range 3.5 to 10.0 for the various Reynolds number conditions indicate that, in the angle of attack range 0 to 24 degrees, normal force is essentially independent of an order of magnitude variation of Reynolds number (0.7×10^6 to 10×10^6). However, for M = 1.5 to 2.5 (Figure 92) there is a slight decrease in normal force at angle of attack due to increased Reynolds number. This again is probably due to a vortex effect as discussed in paragraph 3.1.1. At Mach 19, insufficient data were taken to completely evaluate the influence of Reynolds number on normal force; the limited data which were taken at 10 degrees angle of attack (Figure 315) show that there is a slight variation in normal force for Reynolds number variation about the nominal value of 0.672×10^6/ft.

3.1.2.6 (U) Forced Transition. (C) Comparison of supersonic data with and without transition grit applied to the body nose and leading edges shows no significant changes in normal force due to forced boundary layer transition.

3.1.3 (U) Pitching Moment and Longitudinal Stability

(C) The pitching moment characteristics of the test configuration are produced primarily by the body and trailing edge elevons. The longitudinal stability of the basic configuration and the effect of the fin and elevons are discussed in the following paragraphs.

3.1.3.1 (U) Basic Configuration. (C) The pitching moment variation, with angle of attack, of the complete configuration with undeflected elevons is everywhere stable or neutrally stable; however, at the lower Mach numbers there is a force couple generated at zero-lift which produces a significant negative C_{m_o}. This increment is produced by the aft upper surfaces, and by the low pressure region on the base side of the elevons. The upper surface reduced pressures are evident in Figure 337. As Mach number increases, the pressure coefficients in these regions increase and the C_{m_o} disappears. The combined effectiveness of the elevons and flaps is sufficient to trim C_{m_o} (Figure 44) but a considerable penalty to L/D results (Figure 48).

(C) At the lower Mach numbers (M - 1.5 to 2.5), the stability of the configuration with elevons undeflected decreases as angle of attack increases since forebody lift is increased due to the leading edge vortices. At M = 1.5, for example, (Figure 19) the static margin at α = 0 degree is about 10% and for angles of attack greater than 18 degrees the configuration is neutrally stable. This trend is reversed at the higher Mach numbers since vortex action is not present. At M = 19 (Figure 299) the stability of the configuration is initially neutral and increases to 7% static margin at α = 20 degrees. For an intermediate Mach number case, the static margin at M = 3.5 is about 5% (Figure 153) and remains essentially constant for the angle-of-attack range tested.

3.1.3.2 (U) Vertical Tail. (C) The vertical tail contributes only a very small positive increment of pitching moment at the lower Mach numbers which does not significantly alter the variation of C_m with angle of attack for the basic body; this increment is due primarily to the moment of the fin base drag and is evident in Figure 18.

3.1.3.3 (U) Undeflected Elevons. (C) The undeflected elevons contribute a sizeable negative increment due to the low pressure region on the base side of the elevons. The contribution of the elevons is stabilizing at all Mach numbers.

(C) In the low supersonic Mach number range (M = 1.5 to 2.5) elevon deflection does not significantly influence longitudinal stability (Figure 38); however, deflection of the upper surface flaps provides a stabilizing influence at angle of attack (Figure 45); i.e., the static margin with flaps deflected tends to remain fairly constant, whereas with flaps undeflected the stability margin decreases with increasing angle of attack. In the hypersonic flow regime, positive deflection of the elevons tends to increase longitudinal stability while negative deflections are destabilizing as shown in Figures 309 and 310.

(C) It is important to note the control power capability of the elevons and flaps from the pitching moment data. The elevons produce moderately effective nose-up moment increments at the lower Mach numbers (Figure 38), but combined with the trimming effectiveness of the upper surface flaps, the potential control power capability is adequate (Figure 45). As Mach number increases the positive pitching moment increments produced by the flaps and elevons steadily decrease (Figure 200). The control capability of the configuration is reduced for Mach numbers greater than about 5. At M = 19, the flaps are

ineffective and the elevons produce relatively small positive pitching moment increments at angle of attack (Figure 309).

3.1.3.4 (U) Reynolds Number. (C) The deviations in pitching moment characteristics due to variation in Reynolds number are closely related to the corresponding normal force variations. As in the case of normal force, the pitching moment characteristics in the angle of attack range 0 to 24 degrees and the Mach number range 3.5 to 10 are essentially independent of an order of magnitude variation of Reynolds number about the value 4×10^6. At Mach numbers less than 2.5 (Figure 95), an increase in Reynolds number produces increased pitch-up at high angles of attack; at low angles of attack the stability is not strongly influenced.

3.1.3.5 (U) Forced Transition. (C) As in the case of normal force, forcing boundary layer transition does not affect the supersonic pitching moment data (Figure 100).

3.1.4 (U) Lift/Drag Ratio

3.1.4.1 (U) Configuration Build-up. (C) Configuration build-up effects on L/D are most significant in the supersonic Mach number range; at higher speeds, the small incremental changes experienced are negligible. The addition of the vertical fin produces a small negative L/D increment at low angles of attack, which becomes even less apparent at L/D_{max} (Figure 108). The addition of undeflected elevons produces positive increments in both lift and drag. In most cases these compensate in L/D, however, in some instances the ratio of incremental lift to incremental drag is less than that for the body resulting in an overall L/D reduction. An example of this occurs at M = 2 in the angle of attack range 6 to 20 degrees (Figure 63).

3.1.4.2 (U) Elevons and Flaps. (C) The elevon and flap deflections required to trim the vehicle at low supersonic Mach numbers produce strong penalties in L/D. This is due to the negative C_{m_o} characteristic of the configuration at these speeds which was discussed earlier. At Mach numbers 1.5, 2.0, and 2.5 combined flap and elevon deflections of -30 and -20 degrees, respectively, decrease L/D_{max} approximately 20% (Figure 80).

3.1.4.3 (U) Reynolds Number and Viscous Effects. (C) Reynolds number variation at supersonic speeds does not change the L/D characteristics significantly (Figure 97), but the tests at decreased Reynolds numbers at M = 10 and 19 result in sharp L/D reductions. The M = 10 test data (Figure 287) show that as the Reynolds number is reduced from 2.1×10^6 to 0.4×10^6 per foot, maximum L/D is reduced about 17%. At M = 19 (Figure 320), as the Reynolds number is reduced from 2.09×10^6 to 0.114×10^6 per foot, there is about a 56% reduction in maximum L/D due primarily to the increased axial force discussed previously.

(C) The correlation of maximum L/D with $\bar{v}$ shown in Figure 322 (where $\bar{v}^* = M_\infty \sqrt{C^*} / \sqrt{R_{e_L}}$) data from Tunnels B, C, and F. These data were developed

assuming T_w/T_r = .773 for Tunnels B and C. This ratio was developed from model wall temperatures measured on a similar steel model with a cooled internal balance in Tunnel B (Ref. 1). Rarefaction parameter values were calculated from the Tunnel F reduced data assuming T_w = 540°R. The inviscid value ($\bar{v}^*$ = 0) was determined from theory. The correlation defines a consistent trend showing an increase in L/D_{max} as $\bar{v}^*$ decreases; however, the Tunnels B and C correlations shown are fortuitous since some transition may be present in violation of the assumption of laminar flow for the correlation. At the nominal design condition, V_∞ = 20,000 fps, h = 2 x 10^5 ft, $\bar{v}^*$ is 0.0106 and the L/D_{max} indicated is 2.84.

(C) Variation of maximum L/D with Mach number for the configuration with elevons undeflected is shown in Figure 321. With the exception of the M = 20 point, the data points are taken directly from the test data for a model length Reynolds number of approximately 4 x 10^6. The value at M = 20 is obtained from Figure 3-309. The L/D ratio increases from a value of 2.05 at M = 1.5 to 3.45 at M = 10. Beyond M = 10 the increase in altitude associated with a normal entry flight path causes the L/D_{max} to decrease to 2.84 at M = 20 due to the increasing viscous effects. Potential increases in low speed L/D_{max} which may be achieved through aft end and elevon modification are also indicated on Figure 321.

3.1.5 (U) Extended Angle of Attack

(C) The nominal angle of attack range of the test data was extended at M = 10 to about 47 degrees. The longitudinal data obtained are shown in Figures 267 through 270 and present no unusual trends. A center of gravity location of 65% is required to achieve trim at α = 30 degrees.

3.1.6 (U) Side Force

(C) At M = 1.5 and α = 0 (Figure 23), the vertical fin provides about 36% of the side force coefficient slope (C_{Y_β}) of the complete configuration, and at M = 10 (Figure 248) the contribution is less than 10%. Configuration build-up data for the vertical fin (V_7) were not recorded at M = 19 since the model was built with an integral fin. The data for Mach numbers up to 10 show that the body side force coefficient slope increases gradually with Mach number. At M = 10 the body produces about 20% more side force than at M = 1.5.

(C) The slope of the side force variation with yaw angle decreases at the higher angles of attack due primarily to the reduced effectiveness of the vertical fin. This is shown in Figures 157 to 160 for M = 3.49. The data show that there is little effect due to the fin at α = 15 degrees.

(C) It is interesting to note that in several cases the addition of the vertical fin produces a β = 0 off-set of the side force data as seen in Figures 23 to 26 for example. This off-set is more in evidence at angle of attack greater than at α = 0. This effect is apparently due to model asymmetry, flow angularity, or both.

(C) Due to the decreased effectiveness of the vertical tail, the side force variation with yaw angle decreases as Mach number increases to M = 10. This trend is contradicted by the M = 19 data (Figure 303), which show a 40% increase in $|C_{Y_\beta}|$ over the value at M = 10 (Figure 248).

(C) Aside from the variance at M = 19, the side force data appear generally good. There is, however, an unaccounted discontinuity in the side force data at M = 10 and α = 10 degrees (Figure 250).

3.1.7 (U) Lateral-Directional Stability

(C) The directional stability of the body alone generally increases with Mach number and angle of attack. At the low supersonic Mach numbers the body alone is directionally unstable at low angles of attack becoming stable at the higher angles (Figure 27 to 30). At hypersonic speeds, the body alone is directionally stable at $\beta = 0$ for the complete angle of attack range tested (Figures 350 to 355); this verifies the concept of compression sharing employed in this configuration. At high angles of attack nonlinearity of the yawing moment variation with β shows a decrease in directional stability of the body for yaw angles greater than 4 degrees (compare Figures 3-102 and 3-150, for example).

(C) The addition of the vertical fin is sufficient to make the complete configuration directionally stable for the ranges of Mach number, angle of attack, and sideslip angle tested. The decreased effectiveness of the vertical fin as Mach number increases from 1.5 to 10 and as angle of attack increases from 0 to 20 degrees reduces the directional stability of the configuration. At hypersonic Mach numbers and high angles of attack, where the vertical fin is ineffective, the directional stability is not a strong function of Mach number and is relatively constant with angle of attack. This characteristic at angle of attack was one of the basic design concepts upon which the development of the FDL-5 configuration was based as described in Volume II of this report.

(C) As in the case of directional stability, the vertical fin contributes to roll stability only at low Mach numbers and low angles of attack. The vertical fin does not contribute significantly to roll stability for Mach number greater than 5 or for angles of attack greater than 15 degrees.

(C) The complete configuration is roll stable at all normal flight attitudes throughout the Mach number range. The data show that the configuration is stable at angles of attack above 5 degrees for all Mach numbers tested. At the low supersonic Mach numbers the configuration is also roll stable at low angles of attack due to the increased effectiveness of the vertical fin.

3.2 (U) PRESSURE DISTRIBUTION DATA

(C) The pressure distribution data obtained during the tests at Mach 1.5 are discussed in the following paragraphs. The sensor arrangement for the model is shown in Figure 323 and the spanwise locations defined in the following sketches.

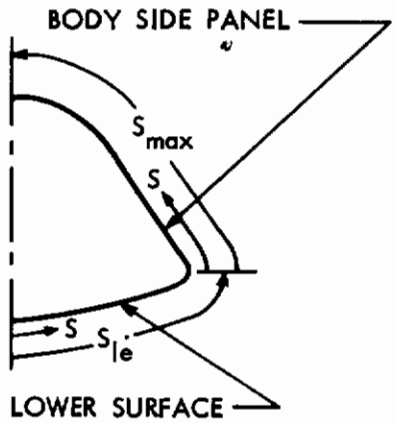

X/L ≤ 0.66

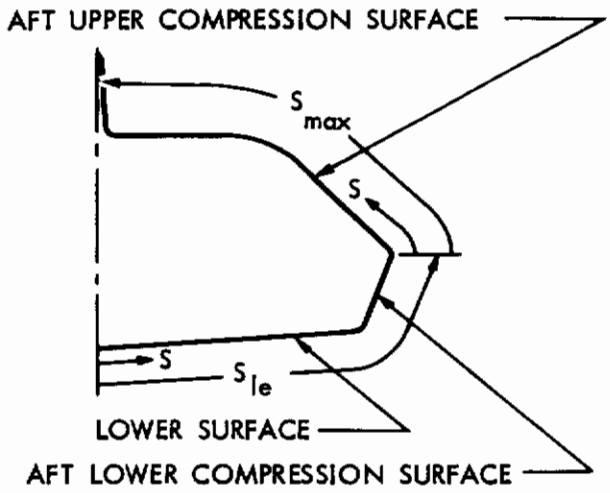

X/L ≥ 0.66

(U) The bulk of the discussion is based on the M = 1.5 data since it is at approximately this speed that the maximum load condition occurs as revealed in the cross plots of measured pressures at representative vehicle locations (Figures 324 a,b). The pressure data for Mach 1.5 and also for Mach numbers 2 to 10 are presented in plotted form in Figures 325 to 402. The M = 10 and M = 20 data are discussed in Volume IV of this report.

3.2.1 (U) Centerline Data

3.2.1.1 (C) Lower Surface. (C) The pressure data (at M = 1.5; β = 0 degrees) along the bottom centerline of the configuration (Figure 325) show a reduction in pressure as flow expands from the forward ramp onto the aft surface (at X/L ≈ 0.61) and a pressure recovery as the flow approaches the body trailing edge. The flow expands to a minimum pressure at X/L = 0.68 where recompression commences. Angle of attack variation produces essentially constant increments of pressure all along the bottom centerline. Tangent-cone theory generally underpredicts the pressures at α = 0 and overpredicts the pressures at α = 20 degrees.

3.2.1.2 (U) Upper Surface. (C) The pressure data along the upper surface centerline (Figure 331) show the pressure decreases as flow expands onto the upper surface boattail and increases on the fin leading edge. Flow expansion is first seen at X/L = 0.61 and reaches a minimum at X/L = 0.76, just forward of the fin leading edge (X/L = 0.78). The data on the fin (0.81 ≤ X/L ≤ 1.0) show a sharp compression and a pressure decay moving aft along the fin leading edge. (The pressure tap at X/L = 0.81 was inoperative.)

3.2.2 (U) Spanwise Data

3.2.2.1 (U) Lower Surface. (C) The spanwise pressure data show a nearly constant distribution of pressure at low angles of attack with a decreasing pressure gradient in the spanwise direction due to crossflow about the leading

edges as angle of attack is increased. At angle of attack the pressure gradient shows a smooth spanwise distribution at stations forward of X/L = 0.76. Negative pressure gradient is apparent across most of the span (Figures 326 to 328). The aft bottom surface (Figures 329 and 330) is flatter and the reduced pressures due to crossflow are not apparent until just inboard of the lower side compression surfaces. Upwash around the leading edges at angle of attack results in a sudden decrease in pressure on the lower side compression surfaces.

3.2.2.2 (U) Upper Surface. (C) At zero degree angle of attack, the spanwise distribution of pressure on the upper surface forward of X/L = 0.76 is essentially constant, while at X/L = 0.76 and for stations farther aft there is a strong spanwise variation of pressure due to afterbody boattailing (Figures 332 to 337). At X/L = 0.76 the data show the boattail effect for about half the inboard span, and for stations farther aft boattailing influences a wider range of span. The data for stations on the boattail (Figures 335 to 337) show that moving inboard (S/S_{max} = 0 towards 1) the pressures decrease to a minimum approximately at the juncture of the upper side compression surface and the flat upper surface and then increase moving toward the centerline fin. The positive pressure coefficients at S/S_{max} = 1 for X/L = 0.86 and 0.96 are on the vertical fin leading edge.

(C) The spanwise variations of upper surface pressures are considerably changed at angle of attack. Pressures along the side surfaces are more strongly decreased than pressures along the top surface due to the formation of leading edge vortices; this moves the minimum pressure location toward the leading edge to a point about midway along the lateral surfaces. These pressure reductions on the forebody sides with angle of attack due to the vortex buildup are particularly evident in Figure 334 . As the model attitude increases, the vortex strength becomes stronger and the leading edge suction forces become more pronounced. For example, at α = 8 degrees, the pressure data indicate that the flow is separated near the leading edge and reattaches at about S/S_{max} = 0.3. This corresponds to the separation seen in the vapor screen photograph, Figure 410b.

3.2.3 (U) Body Flow Field

(C) The leading edge vortex is a dominant feature of the body flow field at angle of attack. It owes its existence to the subsonic leading edge conditions present at low speeds. As the Mach number increases, the leading edges become essentially supersonic and the vortex disappears. Evidence of these changing flow fields is shown in Figure 403 which shows change in upper surface spanwise pressure distribution at the 50 percent chord length for Mach numbers 1.5 to 10.0. The reduced pressures on the side panel at M = 1.5 and the reduction of vortex strength with increasing Mach number are clearly evident.

3.2.4 (U) Higher Mach Number Data

(C) The M = 2.0 through 10.0 pressure data are presented in Figures 338 through 402 for reference to show equivalent data in the higher supersonic

and hypersonic regimes. The M = 10.0 data are also presented in Volume IV where they are discussed and correlated with analytical data.

3.3 (U) FLOW VISUALIZATION

(U) During the test program, flow visualization was accomplished through vapor screen photographs, oil flow photographs and schlieren photographs. The phenomena observed during the tests are discussed in the following paragraphs.

3.3.1 (U) Vapor Screen Photographs

(U) The vapor screen photographs are presented in Figures 404, 405 and 408. These photographs display the flow field about the model at various longitudinal body stations for Mach numbers 1.5, 5.0, and 8.0, respectively. Two procedures were used to generate vapor in the tunnel. In Tunnel A (M = 1.5 and 5.0), steam was introduced in the tunnel flow settling chamber upstream of the throat until the vapor in the test section was dense enough for photography. In Tunnel B, the test section vapor was produced by reducing the temperature of the air supply and allowing the residual water vapor to condense due to expansion through the throat. The illuminating light screen was generated by a narrow laser beam swept up and down across the flow in a plane normal to the tunnel centerline; the flow was then photographed with a time exposure to eliminate an image of a discrete light beam.

(U) This flow visualization process is relatively new and not too frequently used; however, certain flow field phenomena are revealed which would not otherwise be apparent except through extensive flow field surveys. The division between the light and dark portions is not clearly understood; however it is suspected that the division is related to an isotherm which causes the condensate to re-vaporize and become invisible to the light screen. There is also certain to be some connection of the isotherm with boundary layer thickness. Vortex phenomena may also be made visible because of the increased energy level in the vortex which would induce revaporization.

(C) At M = 1.5, a flow separation and vortex emanating from the body leading edge is apparent in each picture. The vortex moves up the upper compression surface and crosses the base over the flat aft body slope. It is not visible in any of the M = 5.0 photographs, Figure 405. Indeed, the entire aft upper surface appears to be in separated flow. The resulting effects on body pressures are shown in Figure 406. This separation, of course, would account for the decreasing effectiveness of the upper body flaps as Mach number increases from 1.5 to 5.0, as shown in Figure 407.

(U) Vortices caused by flow separation from the forebody shoulder are clearly shown in Figures 404 and 405. A "double-bubble" effect is apparent at both Mach numbers which may be caused by a secondary vortex system.

(U) At M = 5.0, the photographs show the shock wave system quite clearly. Figures 405a through e show the bow shock. Figure 405e shows the complex

shock system existing at the vehicle base. Three shocks are clearly identifiable: one, the outer shock is the continuation of the bow shock; two, the inner shock is generated by the centerline fin; and three, the middle shock is generated by the aft compression surfaces.

(U) At M = 8.0, another "double-bubble" phenomena appears which may or may not be related to that previously discussed. In Figure 407, the bubble is clearly defined on the lower surface at α = 0 degrees and on the upper surface at α = 5 degrees, the latter most clearly in Figure 407h. The bow shock is also clearly seen. This effect has also been noted in Tunnel C at M = 10.0 on a blunted flat plate delta wing at α = 0 degrees. Similarities appear in the oil flow pictures shown in Figures 408k and b. The bubble in Figure 407b seems to be related to the centerline streak in Figure 408k as well as the dark layer in the α = 0 degree schlieren in Figure 409. Similarly, the upper bubble (Figure 408e) appears related to the separation lines and secondary vortex streaks appearing in Figure 408b on the upper forebody.

3.3.2 (U) Oil Flow Photographs

(U) The oil flow photographs, of Figure 408, show the top, side, and bottom of the pressure model in Tunnel C at M = 10.0. The surface flow patterns were made visible by painting the model with a solution of titanium dioxide in silicon oil and injecting the model in the tunnel flow. After a suitable length of time, the model was withdrawn and photographs taken of the top, side, and bottom surfaces. New coatings were applied for each angle of attack. The pressure orifices on the model form traces in the fluid which help identify local flow direction.

(U) The top and side views, Figures 408a through j show that the flow is, as would be expected, in the direction of reduced pressure. At α = 0 degree with the upper forebody in compressive conical flow, the streamlines are generally parallel to the longitudinal axis curving upwards at the aft end toward the separated flow regime on the upper aft surface. This pattern is most clearly depicted in Figure 408a. At α = 6 degrees, the upper surface flow pattern for the higher angles of attack is well established, being characterized by an accumulation of fluid at the separation line on the shoulder. Secondary flow separations are visible at α = 12 degrees, Figure 408e, on the forebody and at α = 8 degrees adjacent to the fin in Figure 408c.

(U) The lower surface flow over the forebody is directed toward the centerline at α = 0 degree which may account for the "bubble" noted in Figures 407b to d. This centerline flow, which may be a vortex system, becomes much more complex on the lower boattail as additional separations are induced. At higher angles of attack (e.g., α = 12 degrees, Figure 408e) the lower forebody flow becomes conical; the boattail flow direction remains inboard partly due to the higher pressures on the lower side compression surface.

3.3.3 (U) Schlieren Photographs

(U) A typical set of schlieren photographs is presented in Figure 410. These pictures were taken in Tunnel B at M = 8.0 over the angle of attack range zero to 25.5 degrees. The fore and aft window photos have been combined to facilitate visualization. The Schlieren system used was a conventional single-pass system using a spark light source of about one-microsecond duration.

(U) Figure 410 shows the elevons mounted at zero deflection. Windward deflections show no evidence of separation propagating forward except for the trivial case of α = -4 degrees. Large negative deflections (TE up) showed complete separation at low angles of attack and reattached flow at large angles of attack (about 10 - 15 degrees depending on the elevon deflection).

(U) Figure 411 is a representative schlieren from the Tunnel F force test series which utilized the dual sting installation.

(U) The top model attitude is α = 4 degrees, β = 0 degree while the lower model attitude is α = 0 degree, β = 4 degrees (M = 18.1). Evidence of the lower surface "bubble" is again present as in Figure 410 (at α = 0 degree). The shock system for the lower (yawed) model also shows the strong shock produced by the compression surfaces.

SECTION 4

(U) CORRELATION OF TEST DATA WITH THEORY

4.1 (U) FORCE AND MOMENT DATA

(U) Estimated six-component static force and moment coefficients are compared with test data in the following subsections. The force and moment coefficients are presented for Mach numbers ranging from 1.5 to 19. The longitudinal aerodynamic coefficients (C_A, C_N, C_m) are illustrated for angles of attack from -4 to 24 degrees. The lateral-directional coefficients (C_Y, C_n, C_ℓ) are shown for angles of sideslip up to 10 degrees. Four analytical methods of estimation are illustrated by the predicted coefficients; each method employs a different technique for estimating the pressure force and moment contributions of the fuselage forebody. Other incremental force and moment contributions (friction drag, base drag, vertical tail lateral-directional coefficients, etc.) have been determined by identical techniques for each of the four methods. Therefore any difference between the coefficients predicted by the four methods is due entirely to the estimated fuselage forebody pressure force and moment increments.

4.1.1 (U) Prediction Methods

(U) The aerodynamic coefficients of the FDL-5 configuration have been predicted by estimating the separate force and moment contributions due to: (1) pressures acting on the fuselage forebody, the blunt nose cap, the fuselage base, and the vertical tail; and (2) friction forces acting on the wetted area (excluding the base area) of the entire configuration.

4.1.1.1 (U) Fuselage Forebody. (U) Three different analytical techniques have been used to determine the pressure force and moment contribution of the fuselage forebody. Method 1 uses the tangent-cone technique to predict the forebody force and moment coefficients. This method assumes that the pressure acting on a local surface is a function of the free stream Mach number and the local surface deflection angle. The pressure acting on a compression surface, then, is assumed to be identical to the pressure experienced on a right circular cone at zero yaw having a semi-vertex angle equal to the deflection angle of the local surface. Pressures acting on an expansion surface are assumed to be equal to the ambient pressure. The forces and moments acting on the body are determined by the integration of the local pressures over the entire surface of the body. A detailed description of the equations used in the calculation is presented in Reference 2.

(U) Method 2 employs the tangent-cone/Prandtl-Meyer technique to determine the forebody force and moment coefficients. Pressures acting on compression surfaces are determined by the tangent-cone technique of Method 1. The pressure acting on an expansion surface is taken equal to the pressure experienced by a two-dimensional surface having the same expansion angle as the angle of the local surface relative to the freestream velocity vector. The equations approximating the Prandtl-Meyer pressure coefficients are presented in Reference 3. The force and moment coefficients are again determined by integrating the local pressures over the surface of the entire forebody as in Method 1.

(U) Method 3 applies Newtonian flow theory to the fuselage forebody. The computer program used to perform the calculations is described in Reference 4.

4.1.1.2 (U) Nose Cap. (U) The axial force contribution due to pressures acting on the blunt nose cap was assessed with modified Newtonian flow theory. The applicable charts are presented in Reference 5.

4.1.1.3 (U) Fuselage Base. (U) The axial force contribution due to pressure acting on the fuselage base was approximated by $-1/M^2$.

4.1.1.4 (U) Vertical Fin. (U) The estimation of the force and moment contributions of the vertical tail was based on the local flow field properties in the region of the vertical tail. These flow field properties (local Mach number and local dynamic pressure) were determined by assuming that the flow acting on the portion of the vertical tail above the maximum fuselage height has expanded two-dimensionally through an angle equal to α. The flow acting on the portion of the vertical tail shielded by the fuselage was assumed to have expanded so that it was parallel to the upper fuselage afterbody. The axial force contribution due to pressures acting on the blunt leading edge of the vertical tail was estimated with the modified Newtonian flow theory of Reference 5. The axial force due to pressures acting on the sides of the vertical tail was assessed with the oblique shock data of Reference 6. The side force contribution of the vertical tail was estimated with the two-dimensional shock-expansion data of Reference 6. The yawing and rolling moment contributions of the vertical tail were obtained by applying the estimated side force at fthe 50 percent mean aerodynamic chord location of the vertical tail.

4.1.1.5 (U) Skin Friction. (U) Skin friction calculations were based on the Blasius incompressible equations for laminar and turbulent flow and Eckert's reference temperature method. The effects of viscous interaction were included in the M = 19 Tunnel F axial force estimates. The methods for laminar flow described in References 7 to 10 are included in the Arbitrary Body Computer Program.

(U) The equations for turbulent skin friction were not included in the machine program; therefore, for cases where there was transition (either forced or natural) from laminar to turbulent flow, skin friction was hand calculated

by a procedure using estimated average values for the local flow properties. The average (inviscid) pressure level over the body was calculated using the tangent-cont theory computing routine. This pressure was used to define an "equivalent cone" for which the corresponding average density, temperature, and dynamic pressure were obtained for use in the skin friction equations.

(C) A comparison of the "equivalent cone" method and machine-computed friction (local friction integrated over the body surface) is presented in Figure 422. These values were computed at M = 19 test conditions for wholly laminar flow. The figure illustrates the close correlation of the two approaches for these conditions.

(C) At Mach 10, heat transfer data show transition to occur on the vehicle centerline at 0.85L. A correlation of flight test data for transition location obtained from Reference 11 shows transition for the M = 10 test to occur in the range 0.47L to 1.12L. Heat transfer data were not measured for the M = 8 test; therefore, in the absence of better criteria, transition was assumed to occur at 0.85L.

(U) For cases where transition occurred (i.e., at Mach 10 and lower), friction was hand computed using the "equivalent cone" method for both the laminar and turbulent regimes.

4.1.2 (U) Discussion of Correlated Data

4.1.2.1 (U) Axial Force. (C) Methods 1, 2, and 3 were used to predict the axial force coefficients. Examination of Figures 413 through 416 shows that all three methods overpredict the axial force at Mach 5. It is possible that the skin friction drag was overestimated at this Mach number. It was assumed that the boundary layer trip used in the tests was effective, yielding a fully turbulent boundary layer over the model. If the boundary layer over the model. If the boundary layer was not tripped, a mixed laminar-turbulent boundary layer would have existed, producing lower friction drag than estimated. At Mach numbers 8 to 19, the axial force coefficient near zero angle of attack was accurately predicted by Method 2. All three methods overpredict the axial force in the 16 to 24 degree angle of attack range. Method 3 (Newtonian theory) estimates are in the closest agreement with the test data at these angles of attack.

4.1.2.2 (U) Normal Force. (C) Methods 1, 2, and 3 have been used to estimate the normal force coefficients for Mach numbers 5 and greater. Inspection of Figures 417 through 420 reveals that the Method 2 predictions at Mach numbers 5, 8 and 19 are in good agreement with the test data for angles of attack up to 12 degrees; the test points approach the Method 1 predictions near 20 degrees angle of attack at these Mach numbers. All of the methods underpredict the normal force coefficients at Mach 10. The Newtonian flow theory of Method 3 underpredicts the normal force coefficients at Mach numbers 5 and 8. The Method 3 normal force predictions improve with increasing Mach number, however, and are in good agreement with the test data at Mach 19.

4.1.2.3 (U) Pitching Moment. (C) Estimates of the pitching moment coefficient C_m, for a center of gravity at 65% L, at Mach numbers 5 through 19 were determined by Methods 1, 2, and 3. Method 2 yields the best agreement between estimated and measured data in this speed range, as evidenced by Figures 421 through 424. The Newtonian and tangent cone predictions of Methods 1 and 3 are in poorer agreement with the test data since both of these methods exclude the negative pitching moment increment contributed by the upper aft segment of the fuselage.

4.1.2.4 (U) Side Force. (C) Side force coefficients C_Y, for Mach numbers 5 and greater have been estimated with Methods 1, 2 and 3. Examination of the estimated and experimental data in Figures 425 through 436 indicates that the predictions of Methods 1 and 2, which are almost identical, are in good agreement with the test data. The Newtonian theory of Method 3 slightly underestimates the magnitude of the side force coefficients.

4.1.2.5 (U) Yawing Moment. (C) Yawing moments, C_n, for Mach numbers 5 through 19 have been estimated by Methods 1, 2, and 3. Comparison of these estimates with the test data in Figures 437 through 448 shows that the estimated data are in good agreement with the test data. The Mach 19 estimated data do not agree well with the test data. The test data indicate that C_{n_β} at Mach 19 and zero angle of attack is twice the corresponding value at Mach 10.

4.1.2.6 (U) Rolling Moment. (C) The rolling moment coefficients, C_l, of the model have been estimated by Methods 1, 2 and 3 for Mach 5 through 19. Comparison of the estimated and measured rolling moment coefficients in Figures 449 through 460 indicates that the predicted data do not consistently agree with the test data. All three methods predict about the same rolling moment values for the fuselage for Mach numbers 5 and greater, and are in reasonable agreement with the test data at zero angle of attack. All three methods consistently underpredict the magnitude of the fuselage rolling moment (it is negative) in the 10 to 20 degree angle of attack range, however. The estimated vertical tail rolling moment contributions are in agreement with the test data, and are neither consistently greater nor smaller than the measured vertical tail increments. Apparently the prediction methods do not correctly estimate the span loading of the fuselage. These methods are based on the assumption that the pressures acting on any surface element at a given Mach number are dependent only upon the angle between the surface element and the freestream velocity vector. They do not account for interference from surrounding surface elements or crossflow around the fuselage leading edge. Pressure measurements taken at Mach 10 indicate the existence of significant interference between surface elements. For example, for variable yaw angle and angles of attack of 10 and 20 degrees, pressures higher than predicted are observed on the lower surface of the fuselage adjacent to the windward compression sharing surface. These high pressures, which are apparently induced by the compression sharing surface, are strongest at the outboard span 1 location and decay toward values predicted by tangent cone theory at the fuselage centerline. Pressures induced in this manner would tend to increase the magnitude of the fuselage rolling moment due to sideslip at the higher angles of attack, and could possibly account for the discrepancy between the estimated and predicted rolling moment coefficients.

SECTION 5

(U) SUMMARY FDL-5 AERODYNAMIC CHARACTERISTICS

(U) In this section, the aerodynamic characteristics of the FDL-5 test configuration are summarized and presented as functions of Mach number. The axial force skin friction increments reflect the high and low design trajectories specified at the initiation of the study. The data may be used, then, to provide the aerodynamic characteristics along these entry trajectories or may be used for intermediate trajectories if suitably scaled. The following paragraphs describe the development and presentation of the summary curves.

5.1 (U) AXIAL FORCE

(U) The FDL-5 axial force characteristics due to pressure are shown in Figures 461 and 462. These figures present the Mach number variations of the forebody and base axial force increments for various angles of attack in the range 0 to 24 degrees. Note that the data are for the complete configuration with elevons undeflected.

(U) The viscous contributions to axial force of a 35-ft vehicle were calculated for the two trajectories shown in Figures 463 and 464. Boundary layer transition location was based upon criteria obtained from Reference 11. A correlation of flight test data presented by this reference shows transition to occur in the range

$$\left.\frac{Re_\theta}{M}\right|_{local} = 140 \text{ to } 220$$

where Re_θ is Reynolds number based on boundary layer momentum thickness. The value

$$\left.\frac{Re_\theta}{M}\right|_{local} = 150$$

was selected to conservatively estimate transition location for the FDL-5. For the high and low altitude reference trajectories, Figures 563 and 464 show the movement, as Mach number varies, of transition location for an FDL-5 configuration with a reference length of 35 feet.

(U) Skin friction axial force coefficients were calculated by the "equivalent cone" method described in Section 4. These calculations were based upon radiation equilibrium wall temperature estimates in the laminar and turbulent flow regions. Figure 465 presents the variations of skin friction axial force coefficient for a 35-ft FDL-5 at the high and low altitude reference conditions.

5.2 (U) NORMAL FORCE AND PITCHING MOMENT

(U) For the test Mach numbers from 1.5 to 10, force and moment data were obtained at a common free stream Reynolds number of approximately 4×10^6 based on model reference length. At Mach 19, variations of the force and moment data with angle of attack were obtained at a model Reynolds number of 0.8×10^6. In order to determine a smooth variation of normal force and pitching moment with Mach number, the wind tunnel data taken at a model Reynolds number of 4×10^6 were used to define the normal force and pitching moment variations over the Mach number range 1.5 to 10. These data defined smooth variations except at Mach 10 where there was an apparent discontinuity. Examination of the Mach 10 data indicated that there is about a one degree offset in the angle of attack for zero lift so that angles of attack measured during the test were about a degree too low. Accounting for this offset, the M = 10 data fall in line with data for the rest of the Mach number range. These data were extended through M = 19 using the Tunnel F data taken at a model Reynolds number of 0.8×10^6.

(U) Figures 5-15 and 5-16 present the Mach number variations of normal force and pitching moment coefficients for the FDL-5 at angles of attack from 0 to 24 degrees. These data are for the complete configuration with elevons undeflected.

5.3 (U) LIFT/DRAG RATIO

(C) The variations with Mach number of the full scale vehicle lift/drag ratio for the high and low altitude reference trajectories are presented in Figure 468. 468. It is of interest to note the L/D at M = 20 for the low altitude or maximum cross range trajectory; this trajectory is nearly a maximum L/D trajectory throughout the Mach number range. Figure 464 shows that for an altitude of 175,000 feet and α = 12 degrees, the flow is laminar over the 35-foot reference length. The L/D corresponding to this point is 2.92. The low values of L/D for the high altitude reference result from the high angles of attack required for this minimum downrange trajectory.

5.4 (U) LATERAL-DIRECTIONAL STABILITY

(U) As in the case for normal force and pitching moment, the lateral-directional stability characteristics were obtained from data taken at a model length Reynolds number of approximately 4×10^6 at Mach numbers 1.5 to 10 and for a model length Reynolds of 0.8×10^6 at M = 19. Only the initial yawing and rolling moment characteristics were determined by reading the slopes at $\beta = 0$ for the various angles of attack. These data were smoothed on plots versus angle of attack prior to cross-plotting versus Mach number.

5.5 (U) ELEVON EFFECTIVENESS

(U) The elevon effectiveness curves, Figures 471 to 487, have been cross-plotted from those of Section 4.2. The resulting curves were then modified to reflect the actual increments derived from the FDL-5 test data. Most of this refairing resulted from the M = 20 test data since the original estimates at this speed were based on purely theoretical, inviscid predictions. The curves for δ_e = +10 degrees are unchanged 1) since no test data were obtained for this deflection, and 2) since estimates of positive deflection increments have proven to be more reliable than for negative deflections at other Mach numbers.

5.6 (U) DYNAMIC STABILITY DERIVATIVES

(U) Estimates were made of the FDL-5 longitudinal, lateral, and rotary dynamic stability derivatives using analytical methods and test data presented in References 12 and 13. The nominal values of these derivatives and estimated upper and lower limits are presented in Figures 488 through 496. These limits were established by considering the degree of the uncertainty of the data and the analytical procedures used in estimating the derivatives. Although these derivatives were originally estimated for the fixed-geometry F-3 vehicle, they are also valid for the present FDL-5 vehicles, since the available analytical techniques are insensitive to variations between these vehicle configurations.

(U) The techniques that were utilized to estimate the stability derivatives were developed primarily for more conventional aircraft. As a result, confidence levels of the nominal values are not high, as reflected by the large variation in the upper and lower boundaries of the aerodynamic derivatives. A much higher confidence level was attained in the derivation of the subsonic longitudinal derivatives because the computational procedures were based primarily on experimental data obtained from References 12 and 14.

(U) The stability and response of the vehicle to control inputs has been determined for the various aerodynamic stability derivatives and their respective upper and lower boundaries that are presented in Figures 488 through 496. These derivatives and the vehicle physical constants were inserted into an existing digital computer program which determined the coefficients and roots of the S-domain transfer functions as the derivatives were varied between the previously established upper and lower limits. The locus of the root is automatically plotted in the S-plane as the derivative is varied. The S-plane plots were used for conventional root locus stability analysis. The transfer functions were used in mechanizing an analog simulation including the effects of control deflections and gusts. The parametric variations through the boundary range of the individual stability derivative inputs did establish the region of desirable stability boundaries. On the following figures the cross-hatched portions show the unstable regions of vehicle response due to variation of any particular derivative. Stable vehicle handling response was demonstrated for all the stability derivatives within the band of recommended upper and lower limits except as indicated in Figures 488, 489, 491, 493 and 495.

(C) The importance of roll rate on lateral directional stability is indicated in Figure 493 and is the only region where the nominal value of the derivative as estimated by present techniques was shown to be unstable. As noted, the yawing moment coefficient due to roll rate (C_{n_p}) is especially sensitive. The values of C_{n_p} greater than 0.7 per radian induce the phugoid mode to become unstable and values less than -0.6 per radian cause instability in short period oscillation.

SECTION 6

(U) CONCLUSIONS

(U) The following conclusions result from the aerodynamic analyses and testing of the FDL-5 configuration:

1. (C) The configuration is stable in all three axes over the Mach range from 1.5 to 20 and angle of attack range from 5 to 30 degrees with a center of gravity location from 62 to 65 percent of the reference length.

2. (C) No deflection of the elevons into the airstream is required for trim over the range of angle of attack from 5 to 30 degrees.

3. (C) Upper body flaps are required for trim at Mach numbers less than 8. Above 8 the upper body flaps are ineffective.

4. (C) Trimmed hypersonic L/D_{max}, extrapolated to reference conditions (200,000-ft altitude, 20,000 fps, 35-ft length), is 2.84 at 11 degrees angle of attack. Maximum trimmed L/D_{max} during entry is 3.3 at Mach 12.

5. (C) Subsonic trimmed L/D_{max} is estimated to range from 3.1 to 4.5 depending on details of revised upper aft surface and base fairing, and final elevon geometry.

6. (U) Test data correlate well with analytical predictions using tangent-cone theory on compression surfaces and Prandtl-Meyer theory on expansion surfaces. Axial and normal face coefficients, L/D, and moment coefficients can be accurately predicted at high supersonic and hypersonic speeds. Accuracy decreases below Mach 5.

7. (U) Semiautomatic machine data plotting from facility furnished magnetic tape is highly efficient and desirable for processing large amounts of test data.

8. (U) Flow field visualization methods, though largely undeveloped, are a significant aid in data analysis.

9. (C) Modifications to the aft upper surface, base, and elevon geometry will be required for subsonic and transonic flight. Modification of these surfaces of the FDL-5 system are not expected to affect hypersonic performance, provided the parametric bounds defined in this report are not violated.

REFERENCES

1. Lockheed-California Company, Summary Results of Wind Tunnel Tests of the AMR F-5 Configuration at Mach Numbers of 2.5, 3.5, 6.0, and 8.0 (U), C. P. Valery and C. M. Onspaugh, LR 20112, June 1966 (C)

2. E. F. Blick, Similarity Rule Estimation Methods for Cones, AIAA Journal, 1963.

3. NASA, The Correlation of Oblique Shock Parameters for Ratios of Specific Heats from 1 to 5/3 with Application to Real Gas Flows, M. H. Bertram and B. S. Cook, NASA TR-R-171, December 1963.

4. Lockheed-California Company, Computerized Newtonian Flow Analysis for Arbitrary Bodies in Hypersonic Flow, H. H. W. Drosdat and J. F. Holliday, LR 20169, November.

5. F. S. Malvestuto, et al, Study to Determine Aerodynamic Characteristics on Hypersonic Re-Entry Configurations, Part II - Analytical Phase, WADD TR 61-56, May 1961.

6. Ames Research Staff, Equations, Tables and Charts for Compressible Flow, NACA Report 1135, 1953.

7. T. R. Sieron and Conrad Martinez, Jr., Effects and Analysis of Mach Number and Reynolds Number of Laminar Skin Friction at Hypersonic Speeds, AFFDL-TR-65-5, April 1965.

8. Lockheed-California Company, Hypersonic Configuration Interference, LR 18442, November 1965.

9. E. R. G. Eckert, Survey on Heat Transfer at High Speeds, WADC Technical Report 54-70, April 1954.

10. Lockheed-California Company, A Simplified Method for Determining the Skin Friction Coefficients of Planar Surfaces at Hypersonic Speeds, LTM 50847, May 1, 1966.

11. L. L. Pagel, et al, ASSET, Correlative Analysis of Heat Transfer Data, Vol. IV, AFFDL-TR-65-31, April 1966.

REFERENCES (Continued)

12. B. J. Griffith and P. C. Shelton, Static Stability and Drag Characteristics of Five AFFDL High Lift-to-Drag Configurations at Mach 19, AEDC-TR-65-23, February 1965.

13. John Wiley and Sons, Inc., Dynamics of Flight, B. D. Etkin, 1959.

UNCITED REFERENCES

1. Lockheed-California Company, Summary Results of Wind Tunnel Tests of the AMR F-5 Configuration at a Mach Number of .26, C. P. Valery and C. M. Onspaugh, LR 20113, November 1966 (C)

2. Rand Corp., The Laminar Boundary on a Cone in a Supersonic Air Stream at Zero Angle of Attack, W. Hantzsche and H. Wendt, Translation RAT-6, 1947.

3. E. R. Van Driest, Turbulent Boundary Layer on a Cone in a Supersonic Flow at Zero Angle of Attack, J.A.S., January 1952.

4. Ministry of Aviation, Measurements of the Direct Pitching Oscillation Derivatives for Three Chopped Delta and Three Arrowhead Planforms at Subsonic and Transonic Speeds, R & M No. 3397, August 1962.

(REVERSE SIDE IS BLANK)

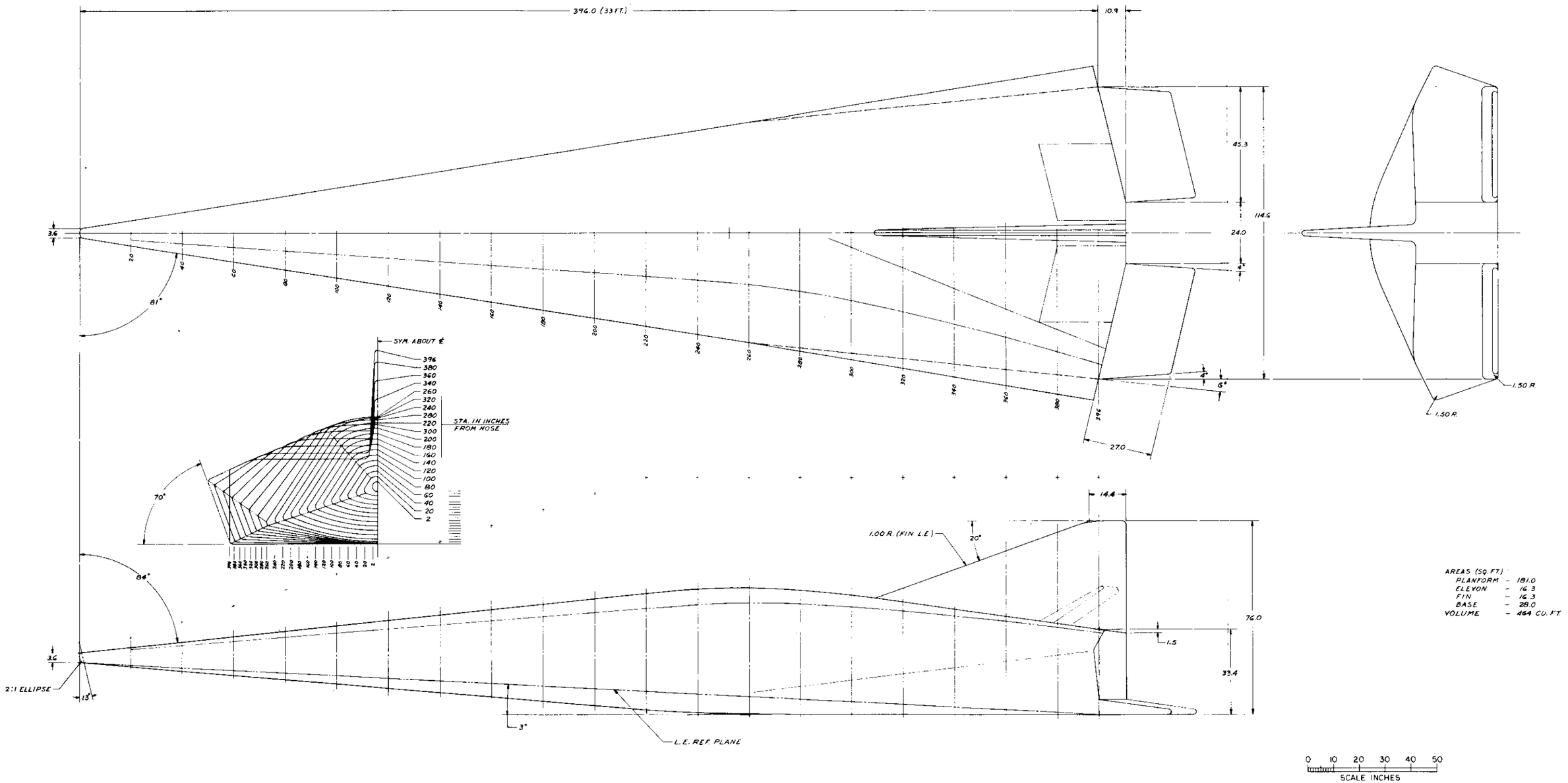

FIGURE 1 (U) FDL-5 TEST CONFIGURATION

(REVERSE SIDE IS BLANK)

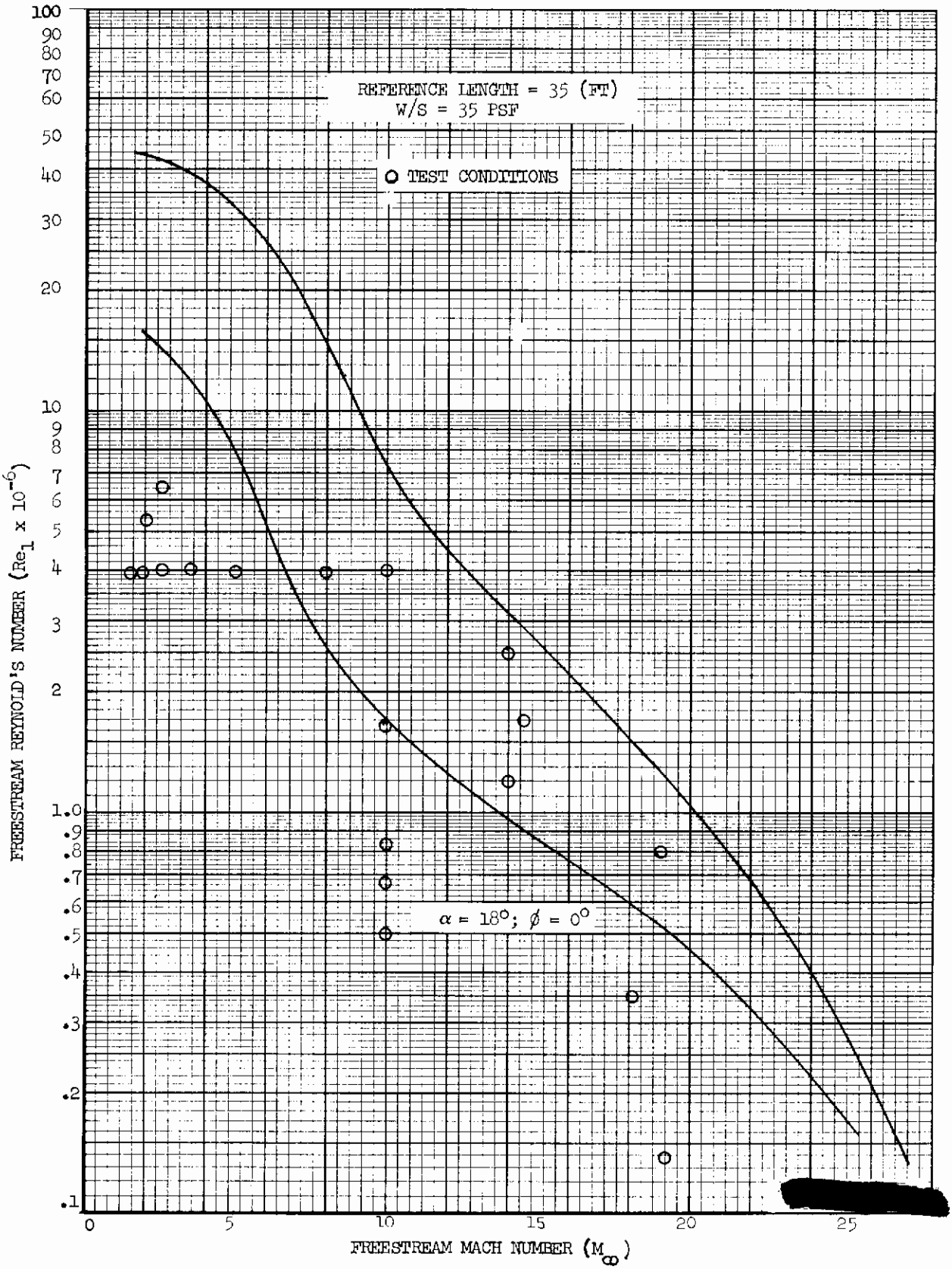

FIGURE 2 (U) AMR REFERENCE TRAJECTORIES

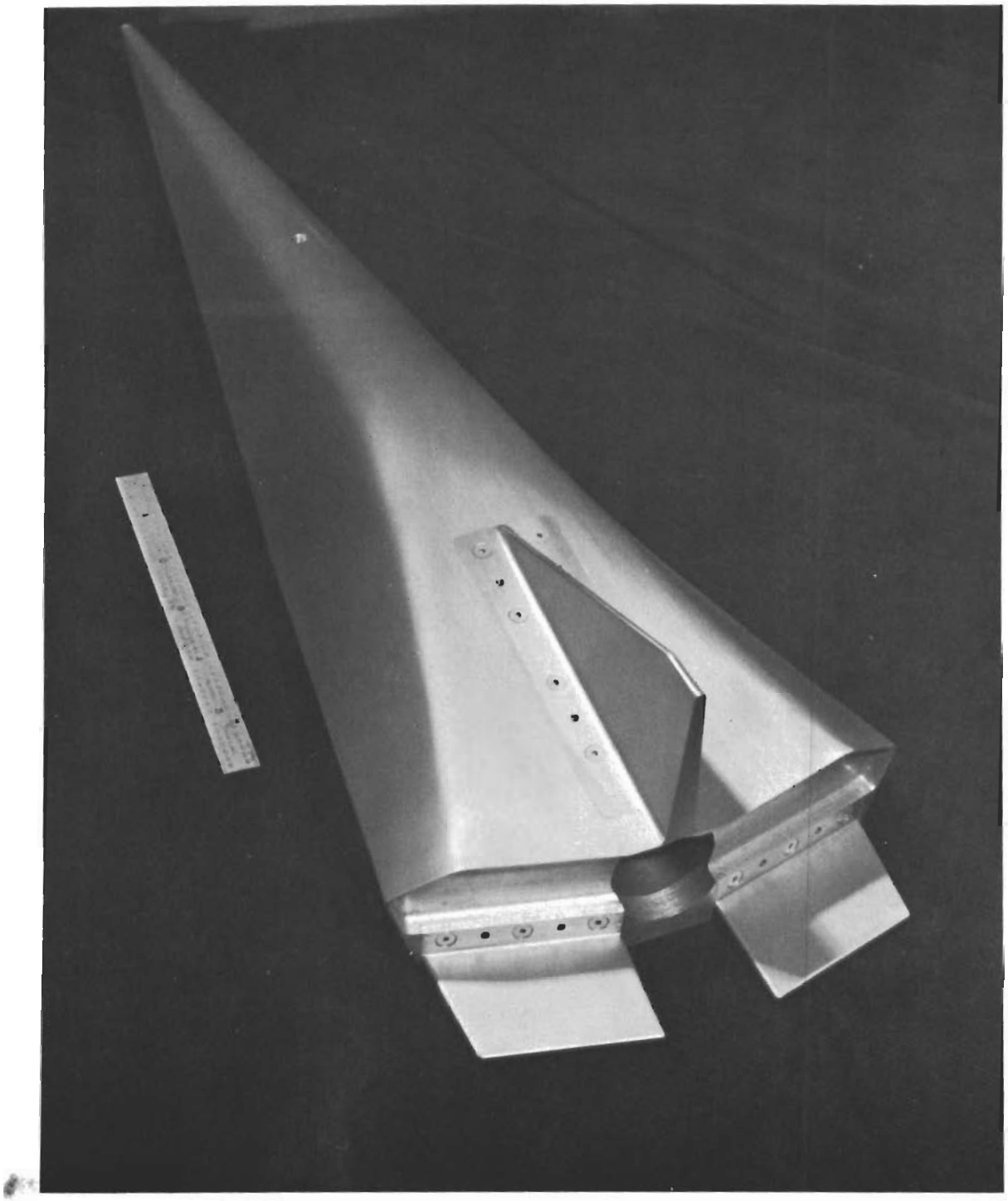

UNCLASSIFIED

FIGURE 3 (U) 20-INCH STEEL FORCE MODEL FOR AEDC TUNNELS A, B, AND C

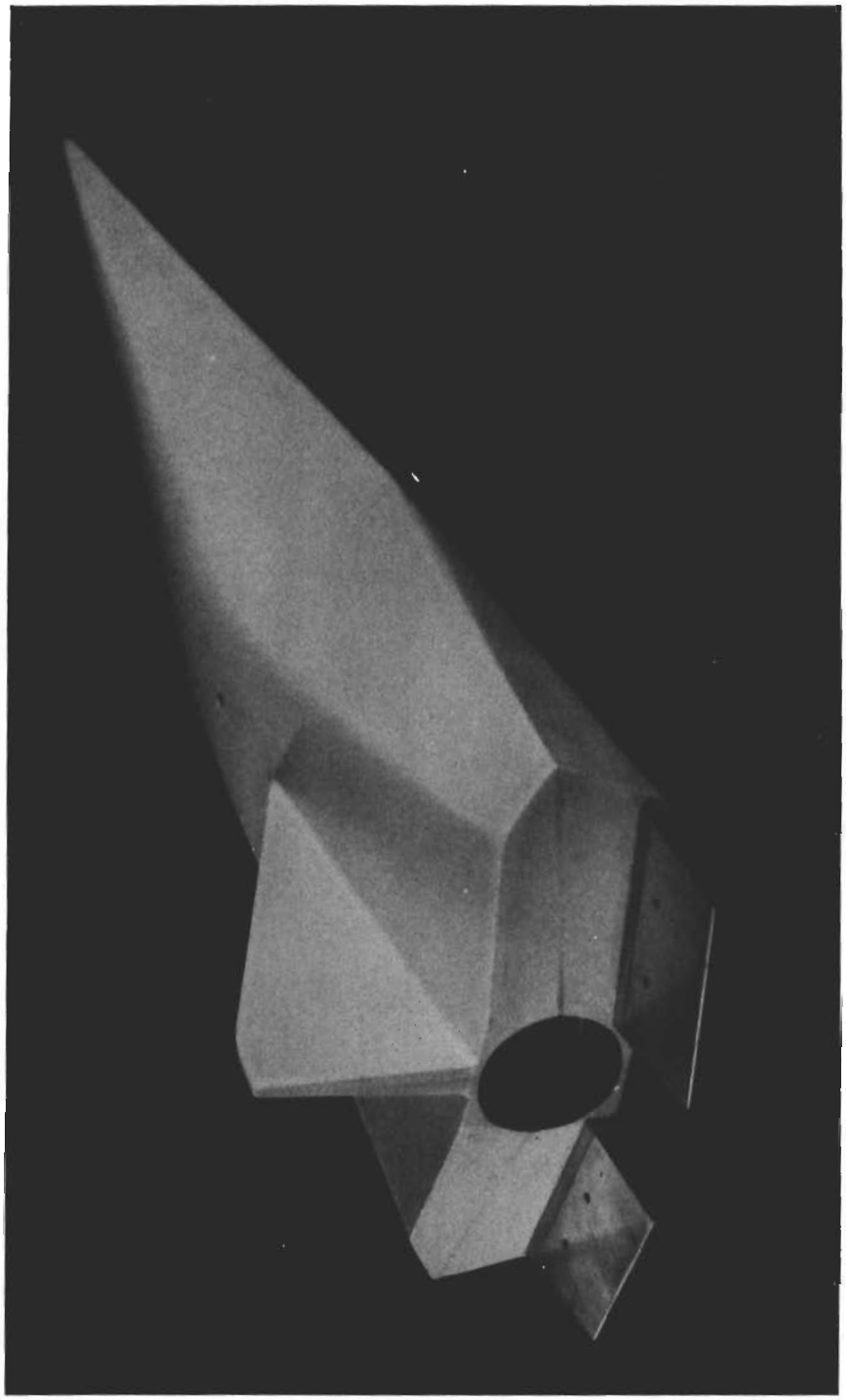

UNCLASSIFIED

FIGURE 4 (U) 15-INCH FIBERGLASS FORCE MODEL FOR AEDC TUNNEL F

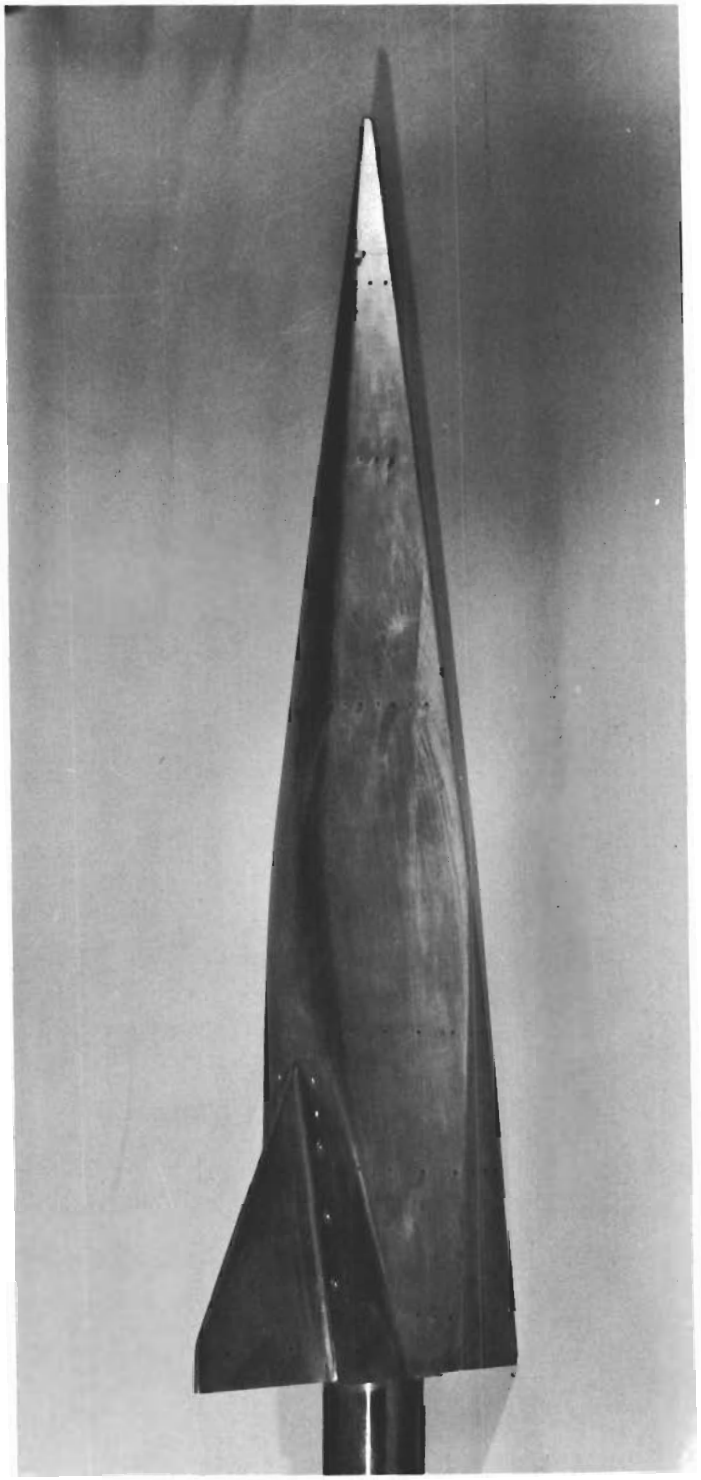

UNCLASSIFIED

FIGURE 5 (U) 20-INCH PRESSURE MODEL FOR TUNNEL C

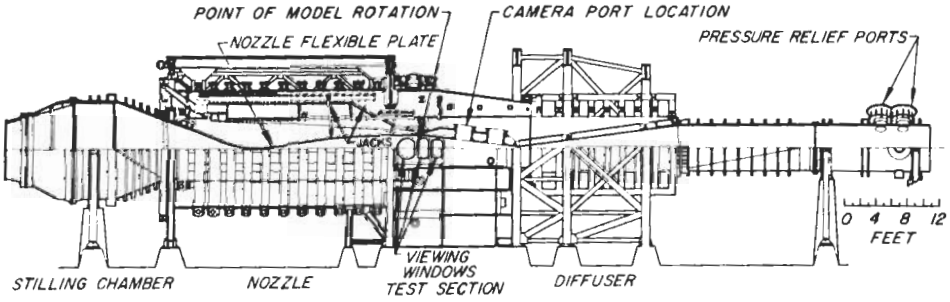

Assembly

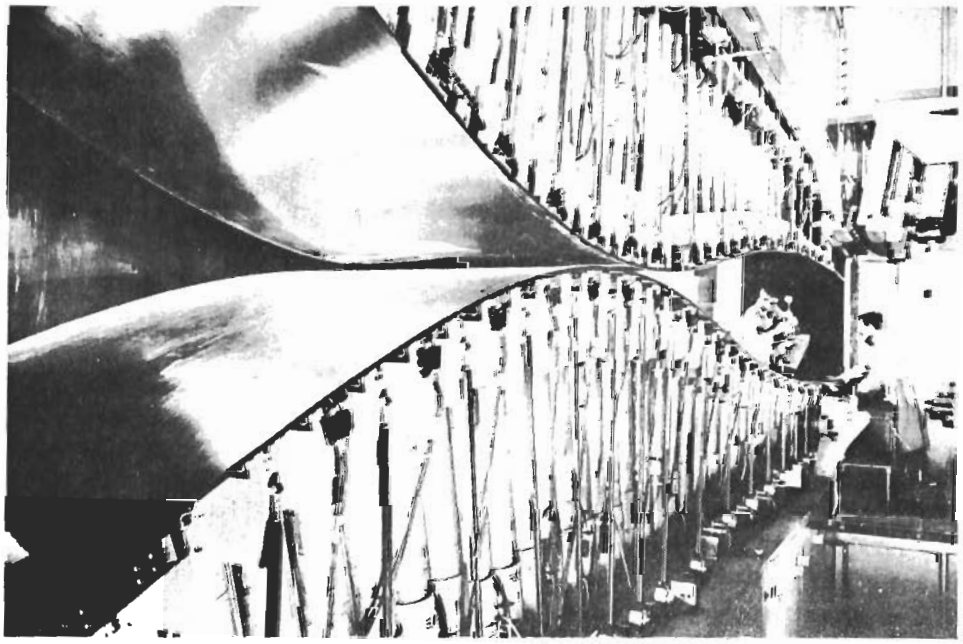

Nozzle and Test Section

UNCLASSIFIED

FIGURE 6 (U) THE AEDC VKF WIND TUNNEL A

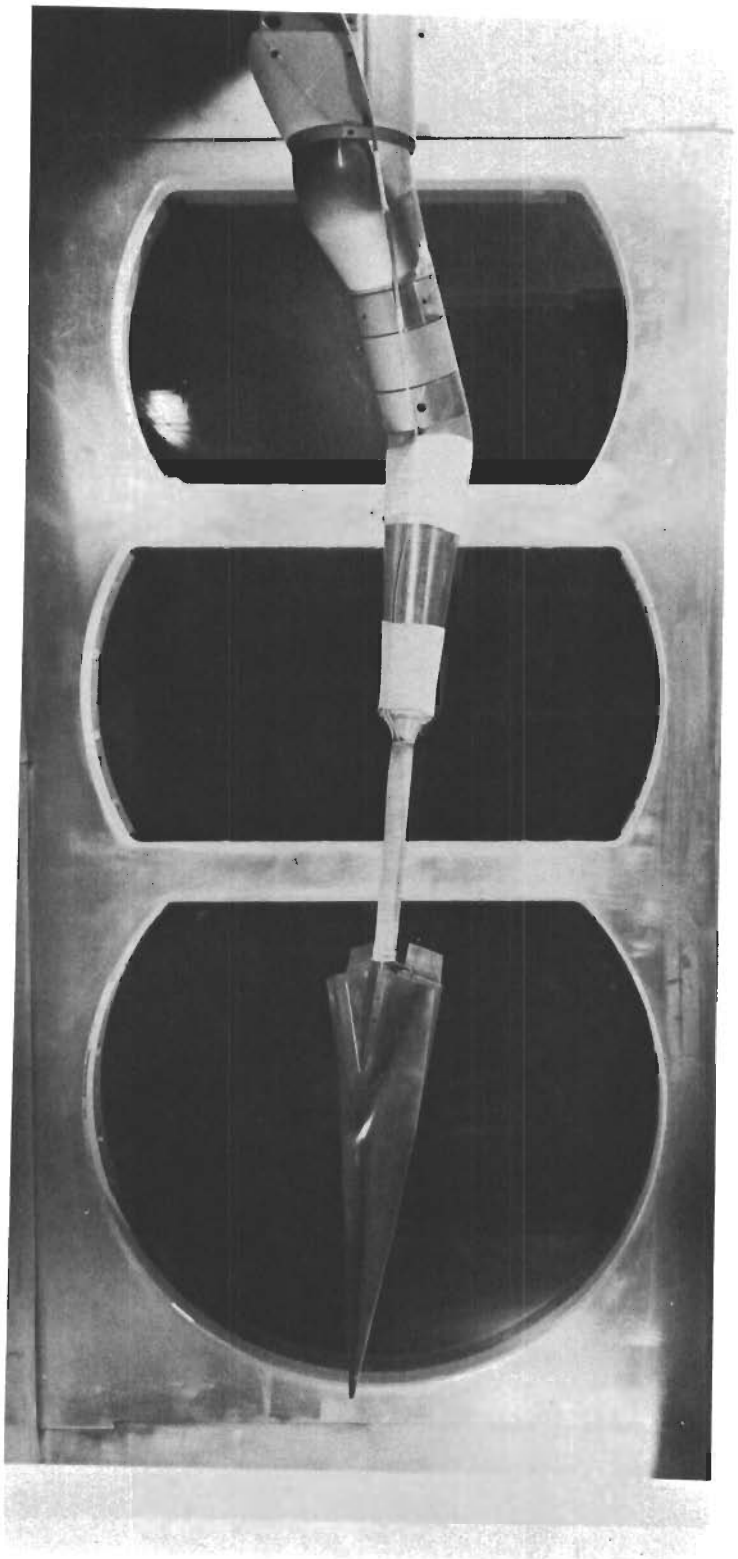

UNCLASSIFIED

FIGURE 7 (U) 20-INCH STEEL FORCE MODEL INSTALLED IN AEDC TUNNEL A

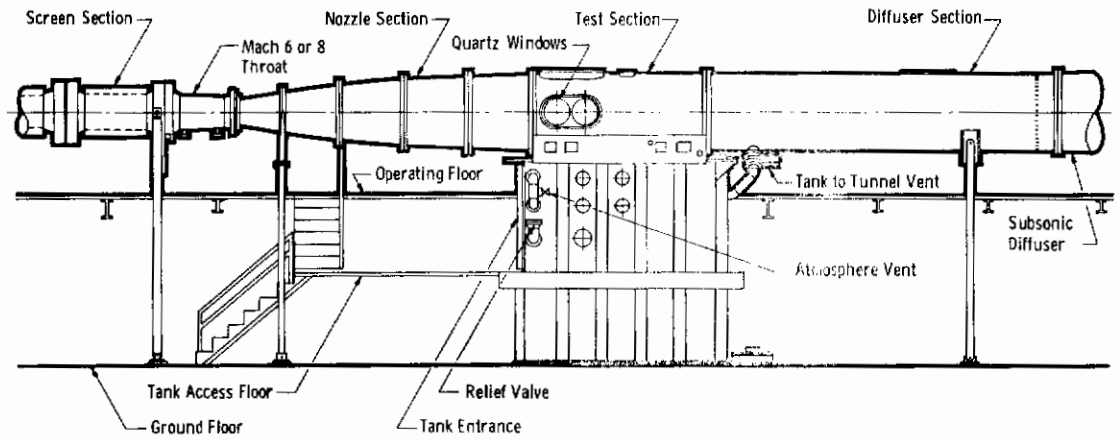

a. Tunnel Assembly

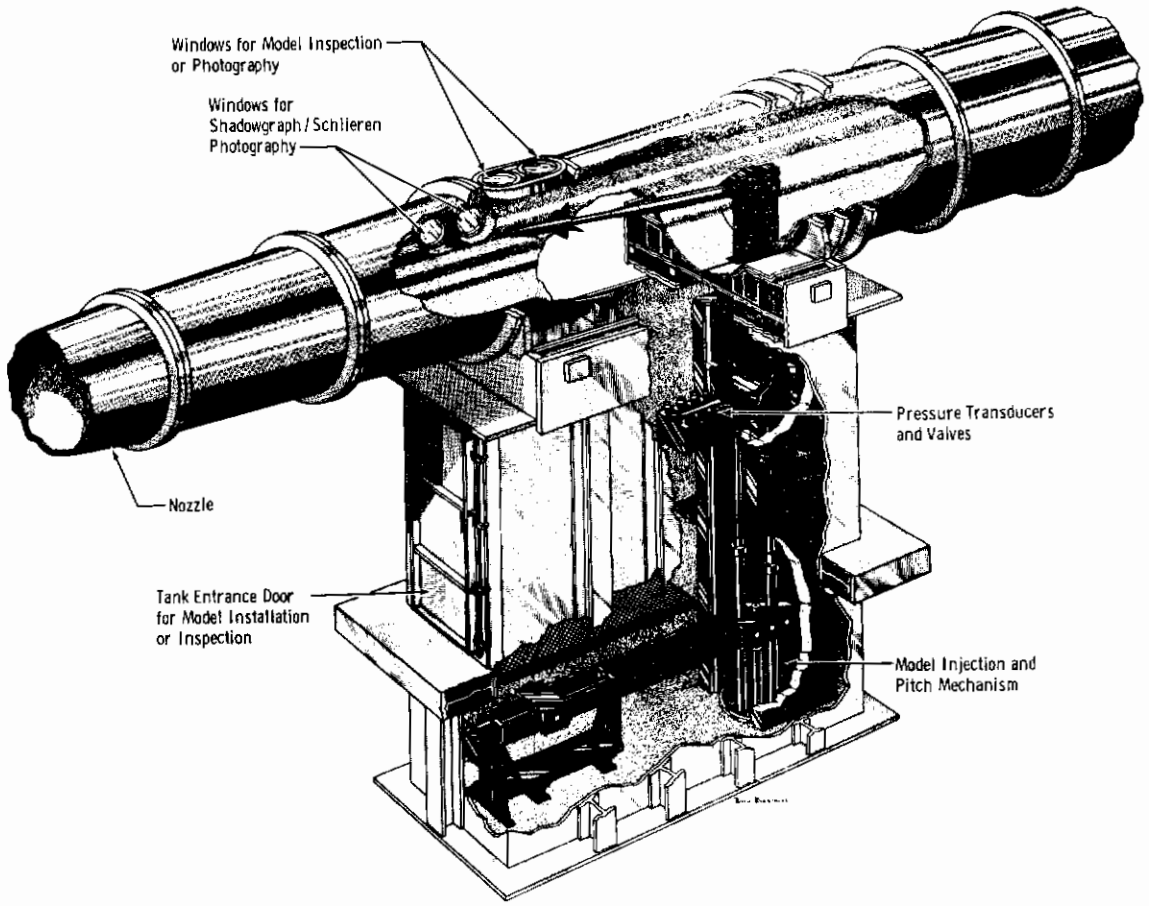

b. Tunnel Test Section

UNCLASSIFIED

FIGURE 8 (U) THE AEDC VKF TUNNEL B

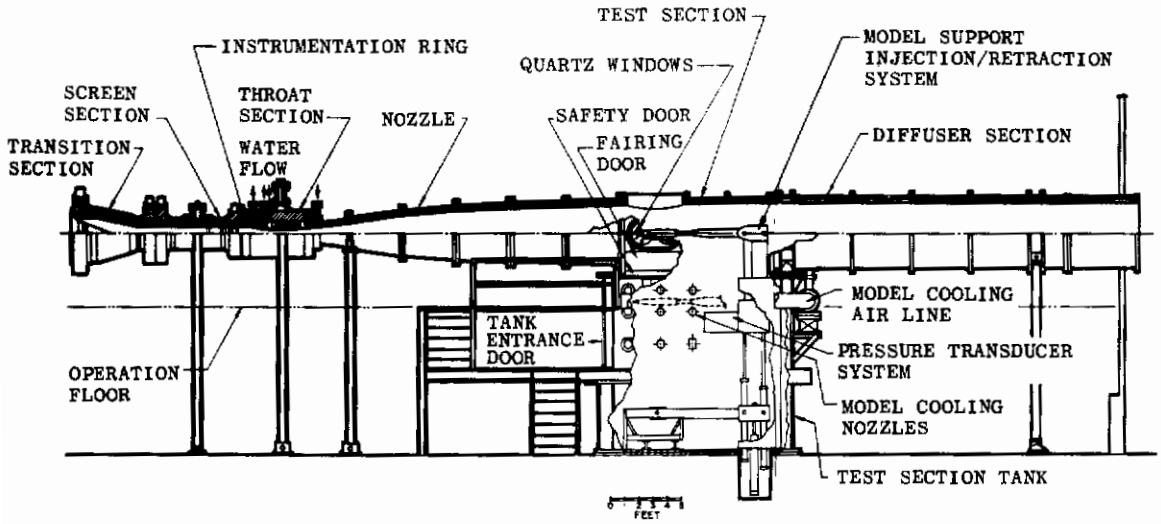

a. Tunnel Assembly

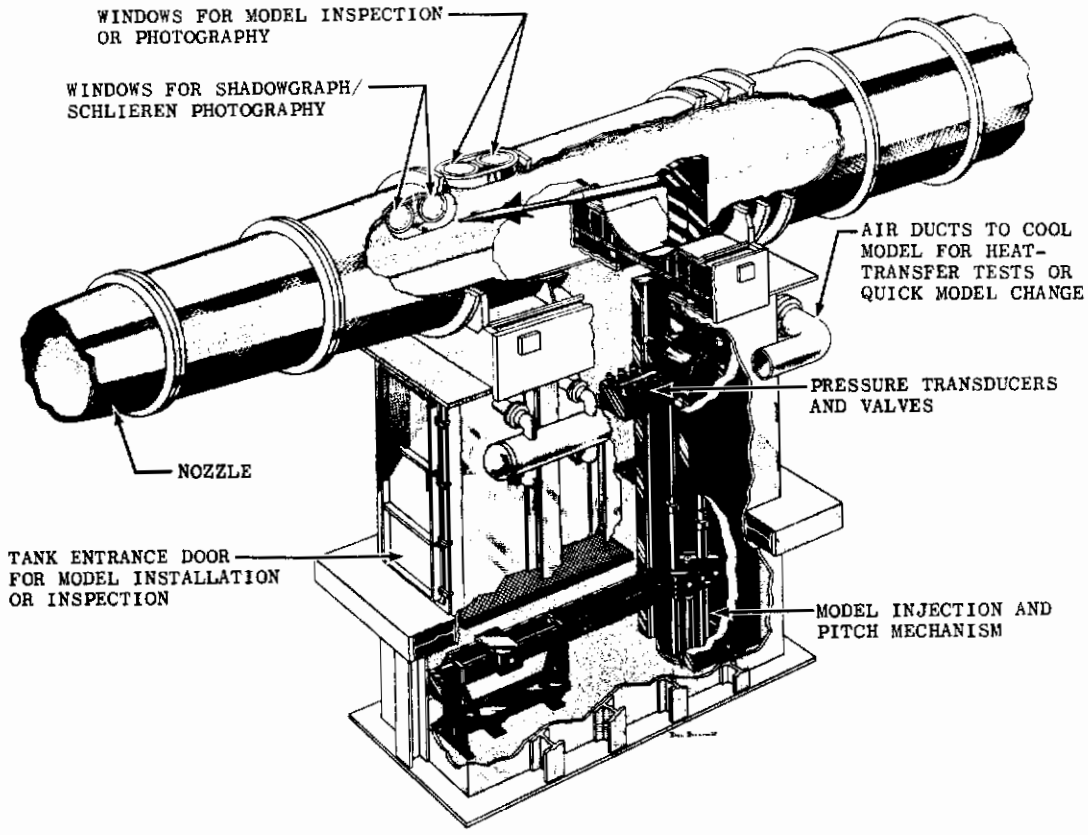

UNCLASSIFIED

b. Tunnel Test Section

FIGURE 9 (U) THE AEDC VKF TUNNEL C

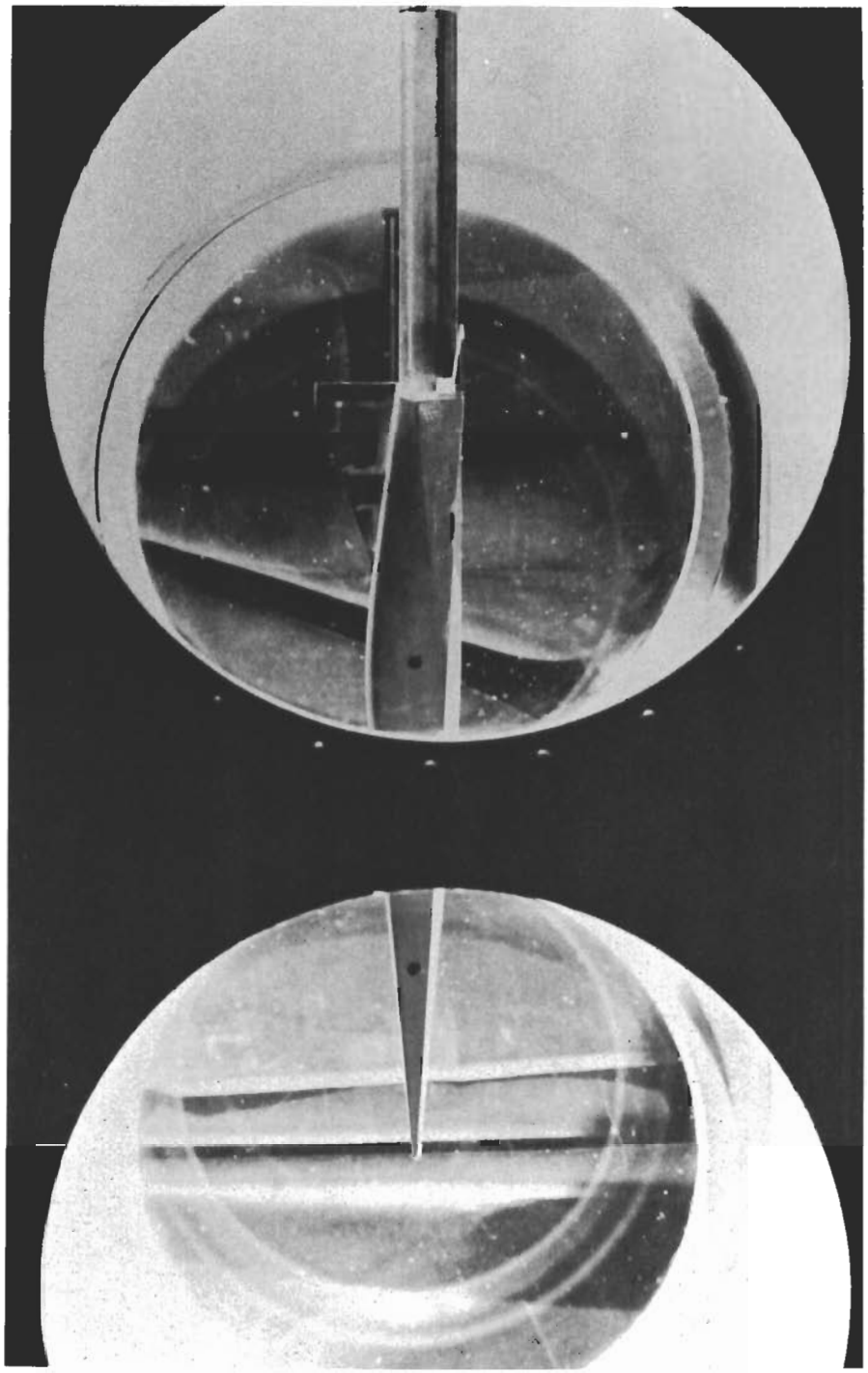

UNCLASSIFIED

FIGURE 10 (U) 20-INCH STEEL FORCE MODEL INSTALLED IN AEDC TUNNEL C

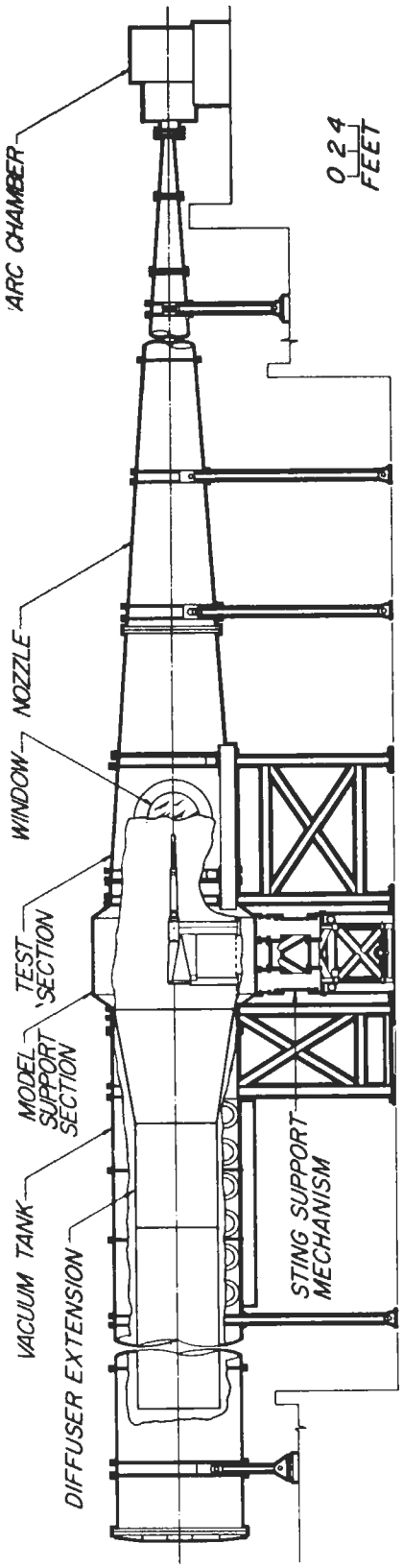

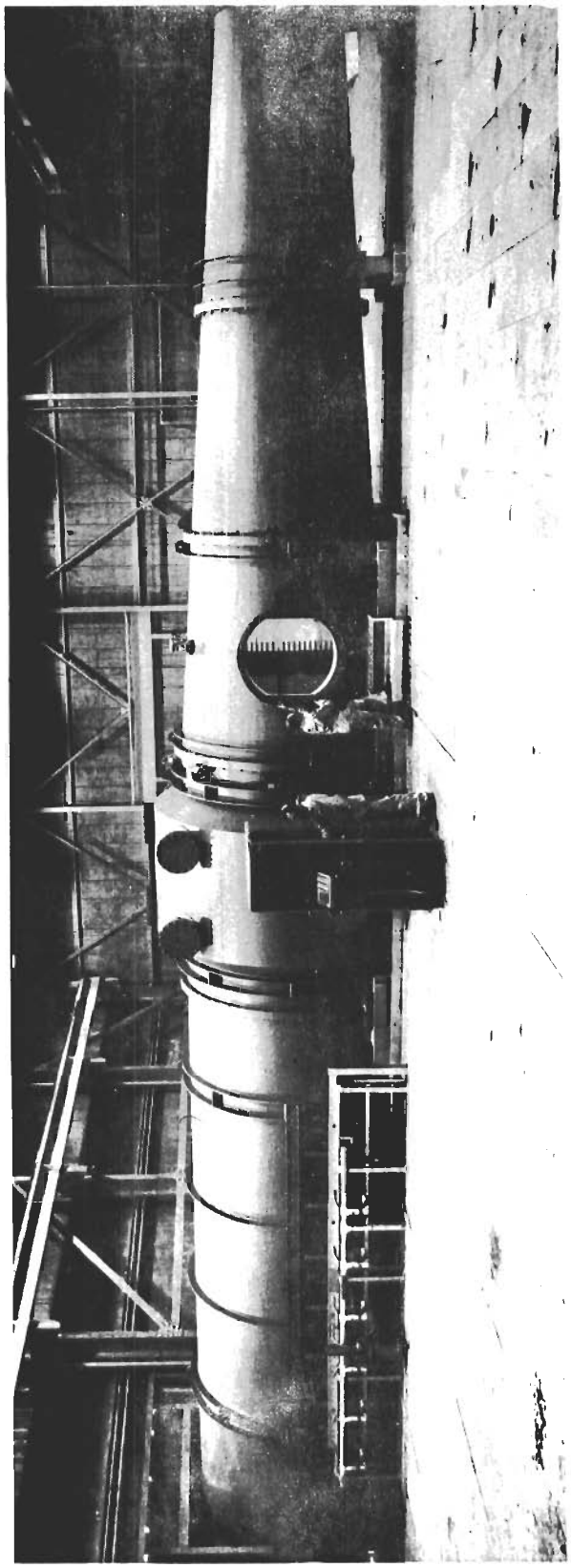

UNCLASSIFIED

FIGURE 11 (U) THE AEDC VKF 100-INCH TUNNEL F

UNCLASSIFIED

FIGURE 12 (U) 15-INCH FIBERGLASS MODEL DUAL INSTALLATION IN TUNNEL F

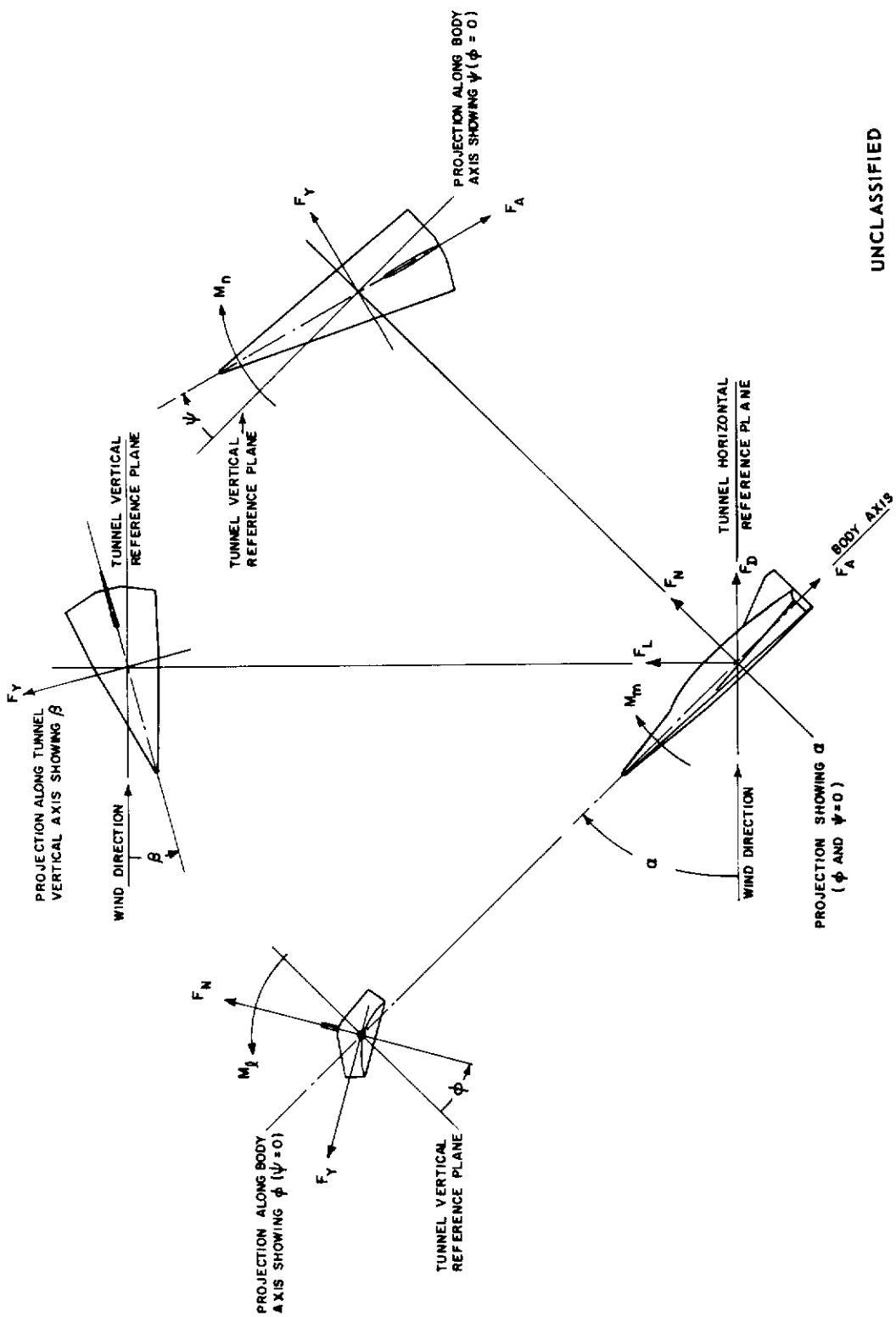

UNCLASSIFIED

FIGURE 13 (U) SIGN CONVENTIONS FOR FORCE AND MOMENT DATA

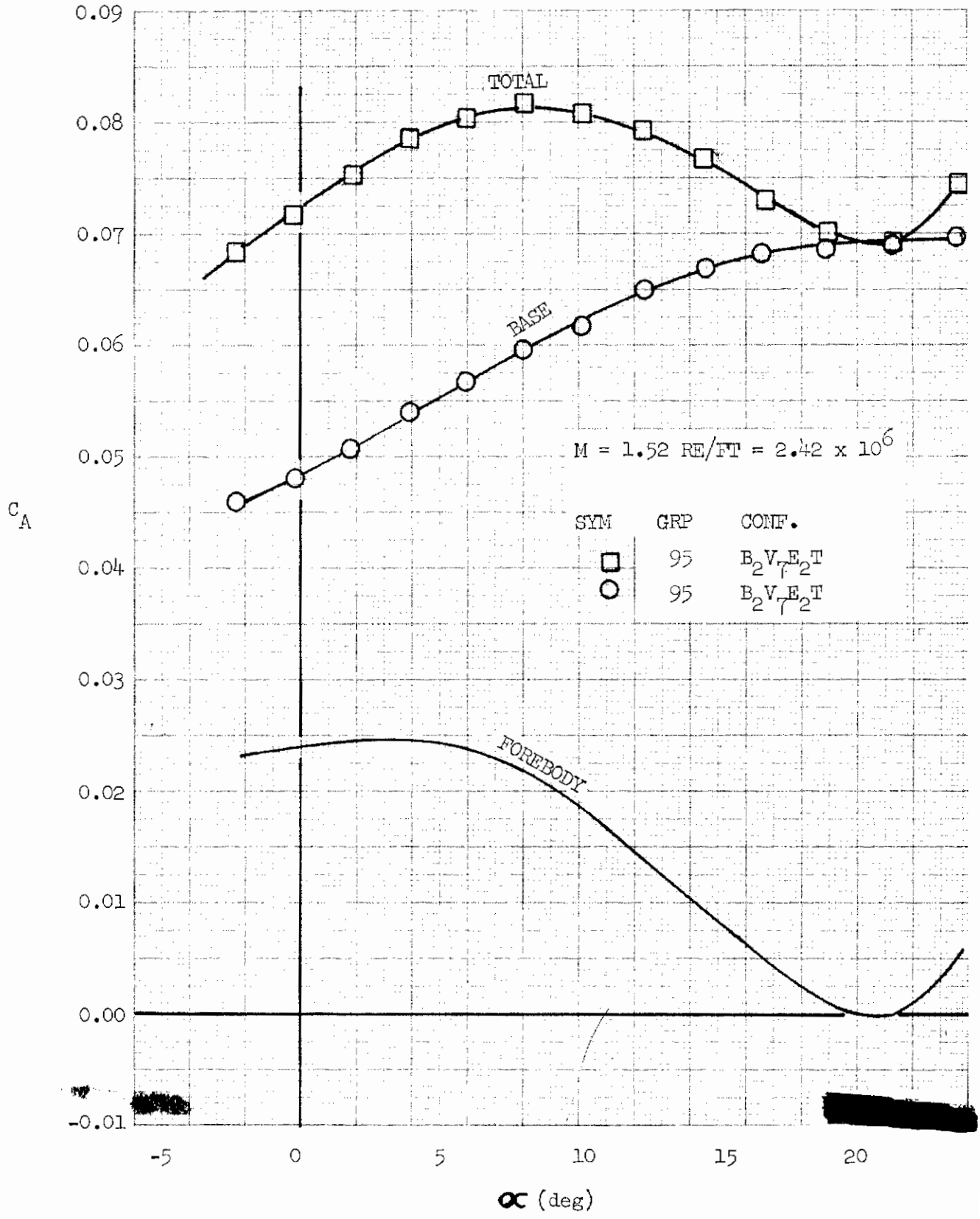

FIGURE 14 (U) AXIAL FORCE BUILDUP - AXIAL FORCE COEFFICIENT VARIATION WITH ANGLE OF ATTACK (M = 1.52)

LOCKHEED CALIFORNIA COMPANY

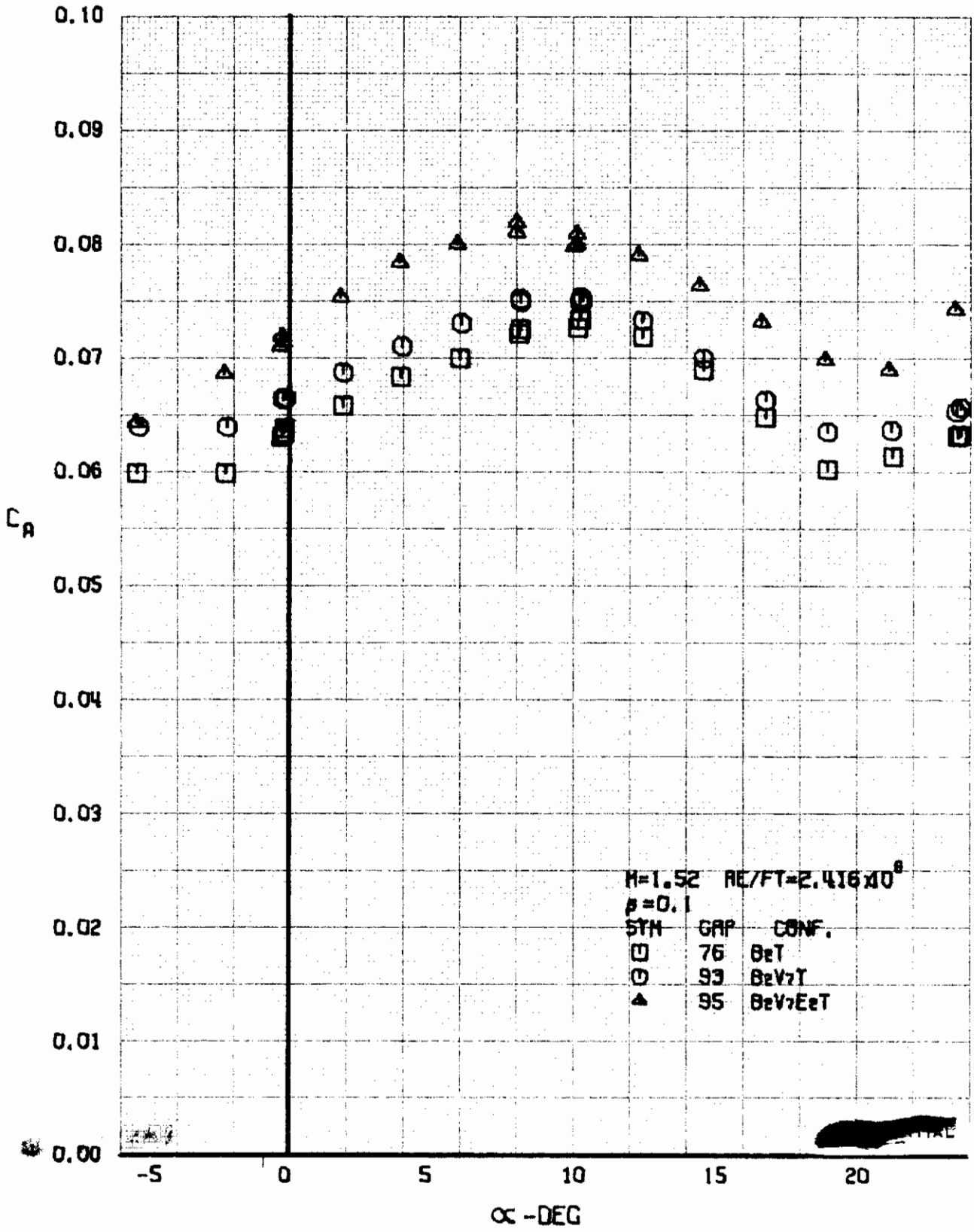

FIGURE 15 (U) CONFIGURATION BUILDUP
- AXIAL FORCE COEFFICIENT VARIATION WITH ANGLE OF ATTACK (M=1.52)

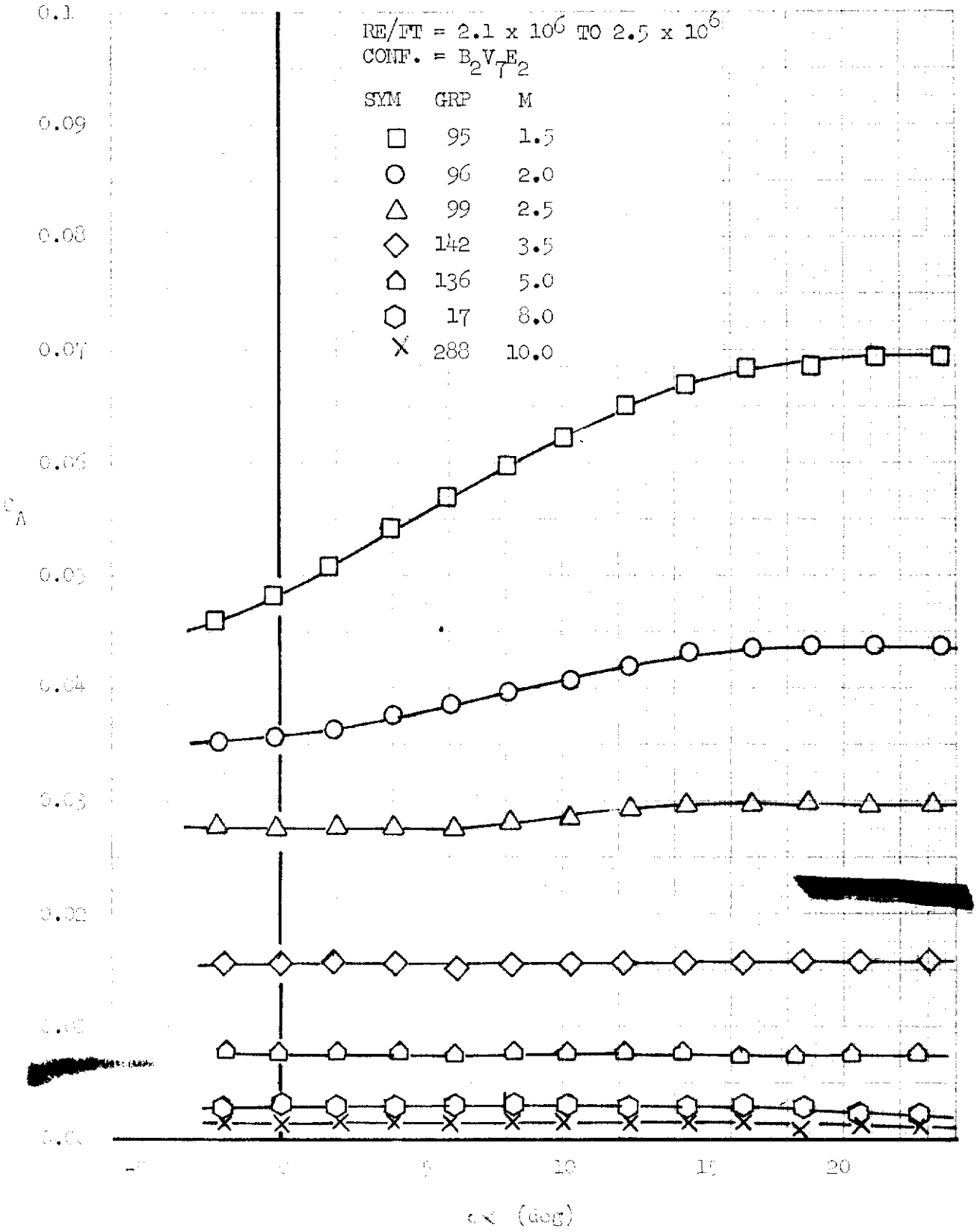

FIGURE 16 (U) BASE AXIAL FORCE - AXIAL FORCE COEFFICIENT VARIATION WITH ANGLE OF ATTACK

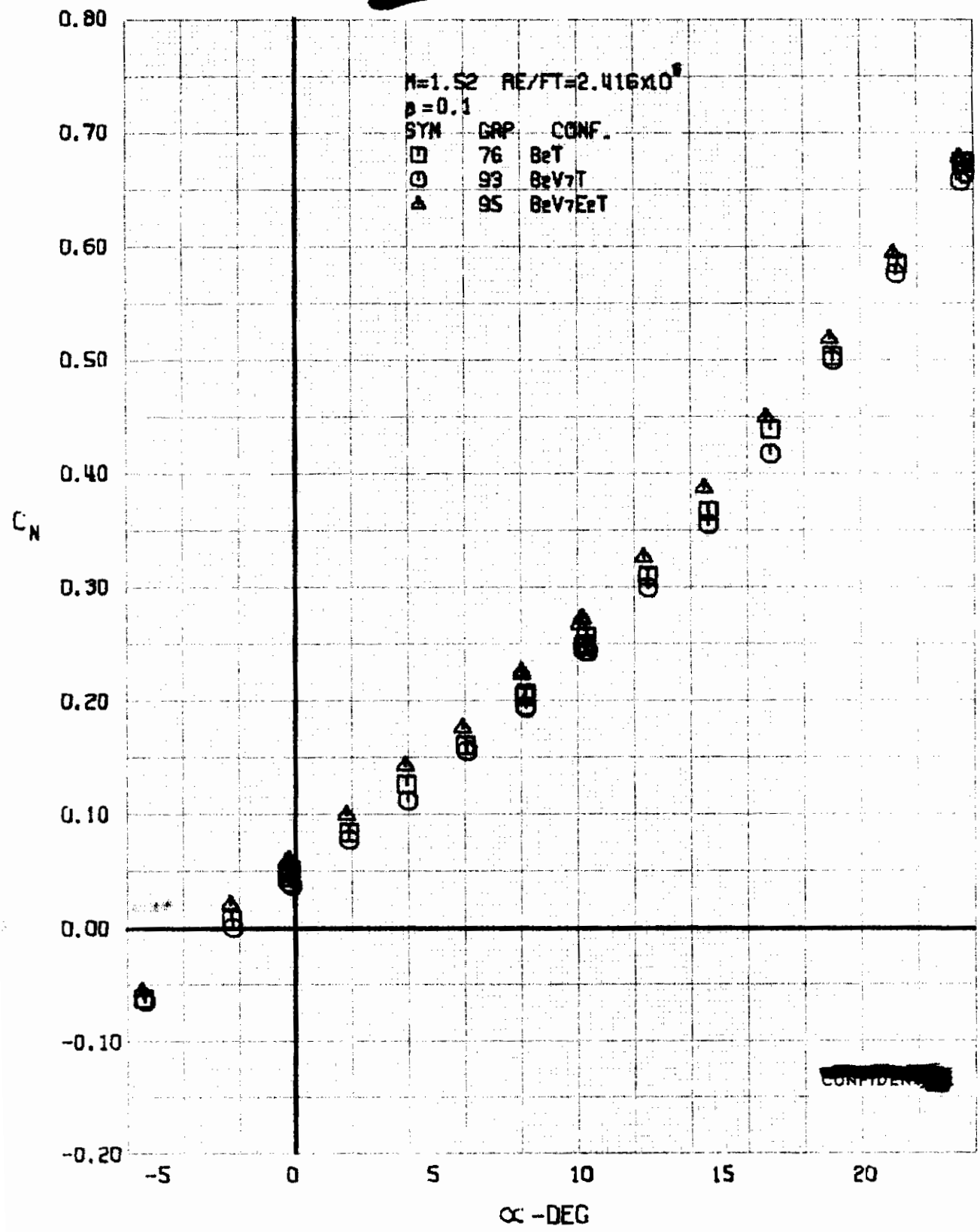

FIGURE 17 (U) CONFIGURATION BUILDUP
- NORMAL FORCE COEFFICIENT VARIATION WITH ANGLE OF ATTACK (M=1.52)

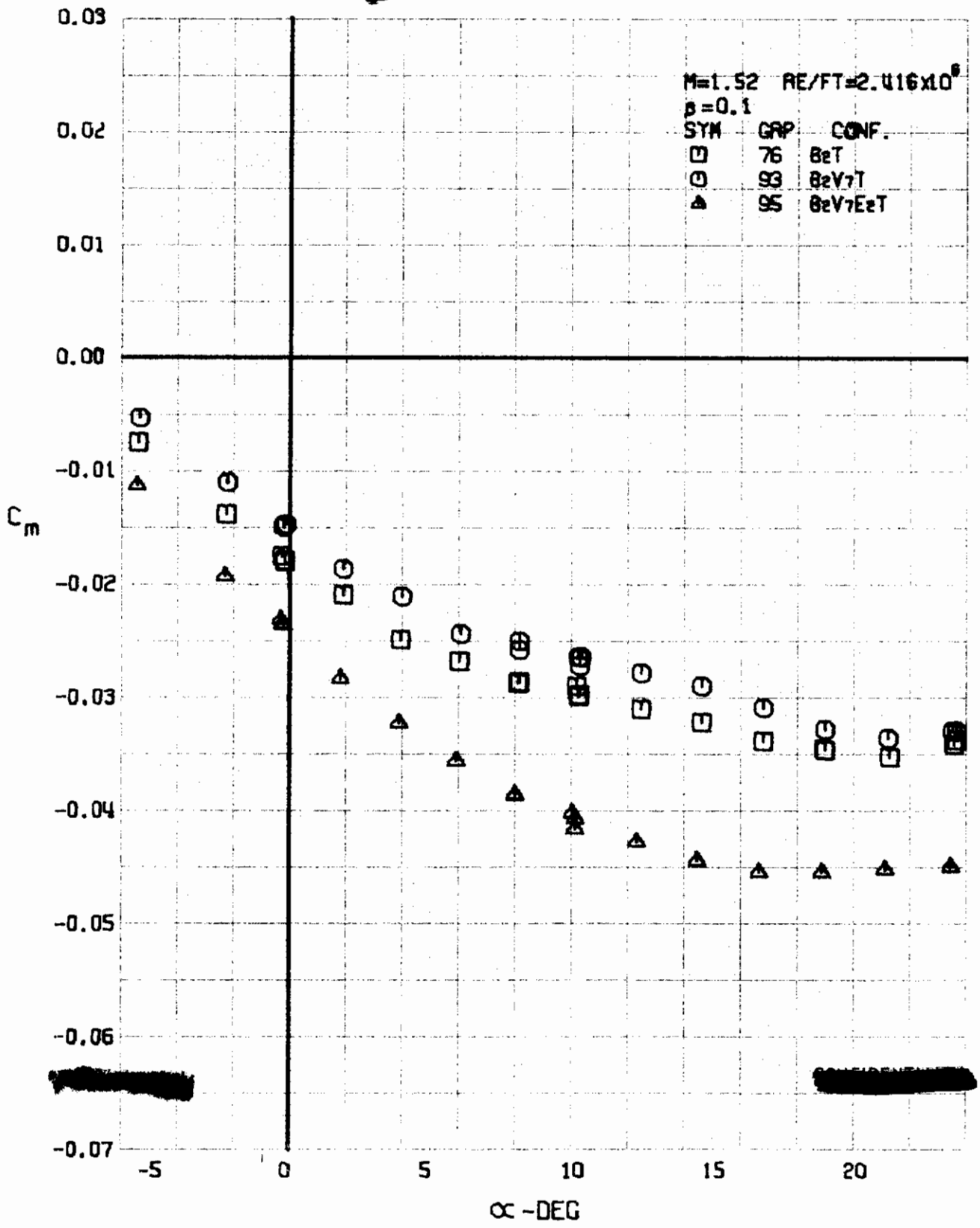

FIGURE 18 (U) CONFIGURATION BUILDUP
- PITCHING MOMENT COEFFICIENT VARIATION WITH ANGLE OF ATTACK (M=1.52)

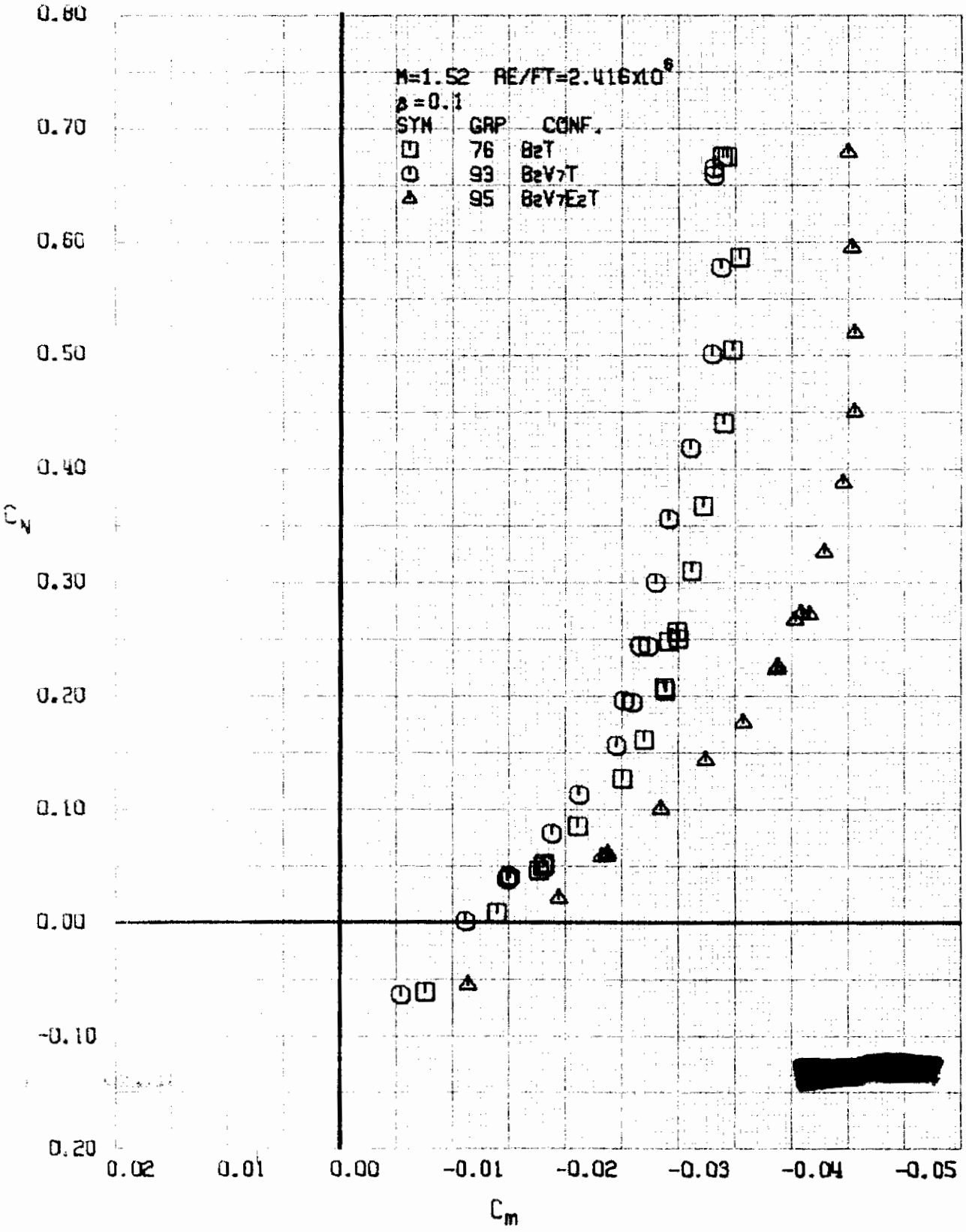

FIGURE 19 (U) CONFIGURATION BUILDUP
- LONGITUDINAL STABILITY VARIATION (M=1.52)

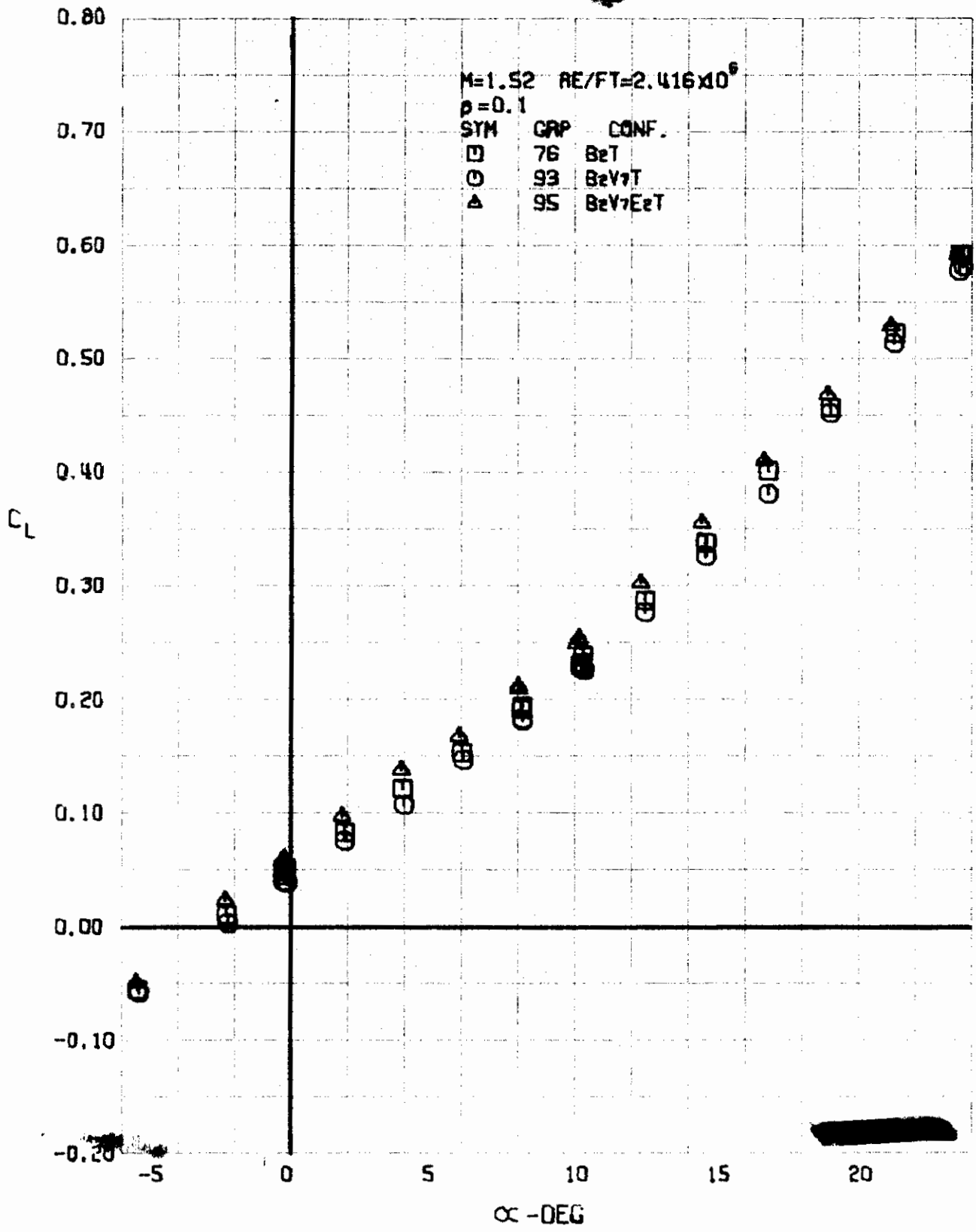

FIGURE 20 (U) CONFIGURATION BUILDUP
- LIFT COEFFICIENT VARIATION WITH ANGLE OF ATTACK (M=1.52)

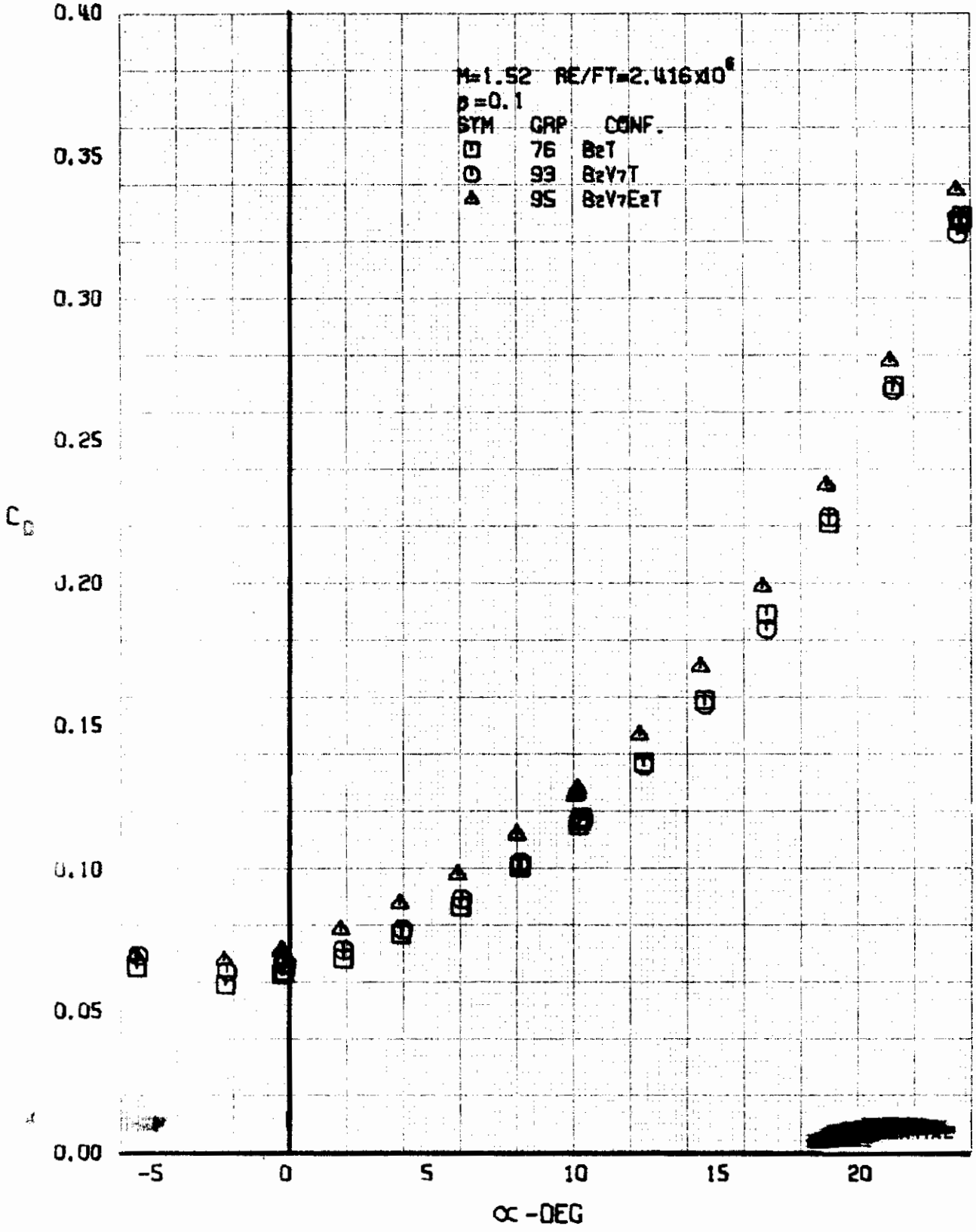

FIGURE 21 (U) CONFIGURATION BUILDUP
- DRAG COEFFICIENT VARIATION WITH ANGLE OF ATTACK (M=1.52)

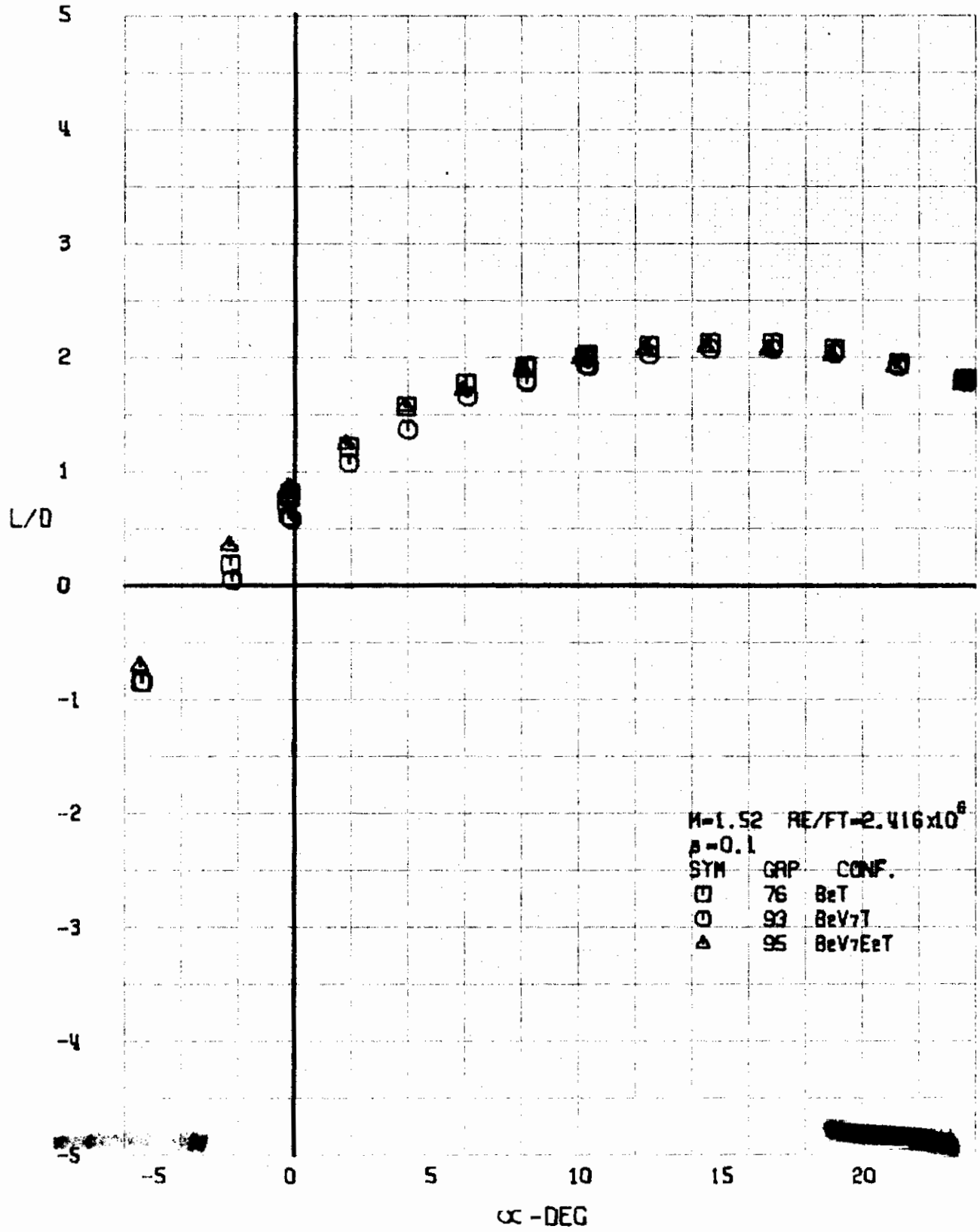

FIGURE 22 (U) CONFIGURATION BUILDUP
- LIFT-DRAG RATIO VARIATION WITH ANGLE OF ATTACK (M=1.52)

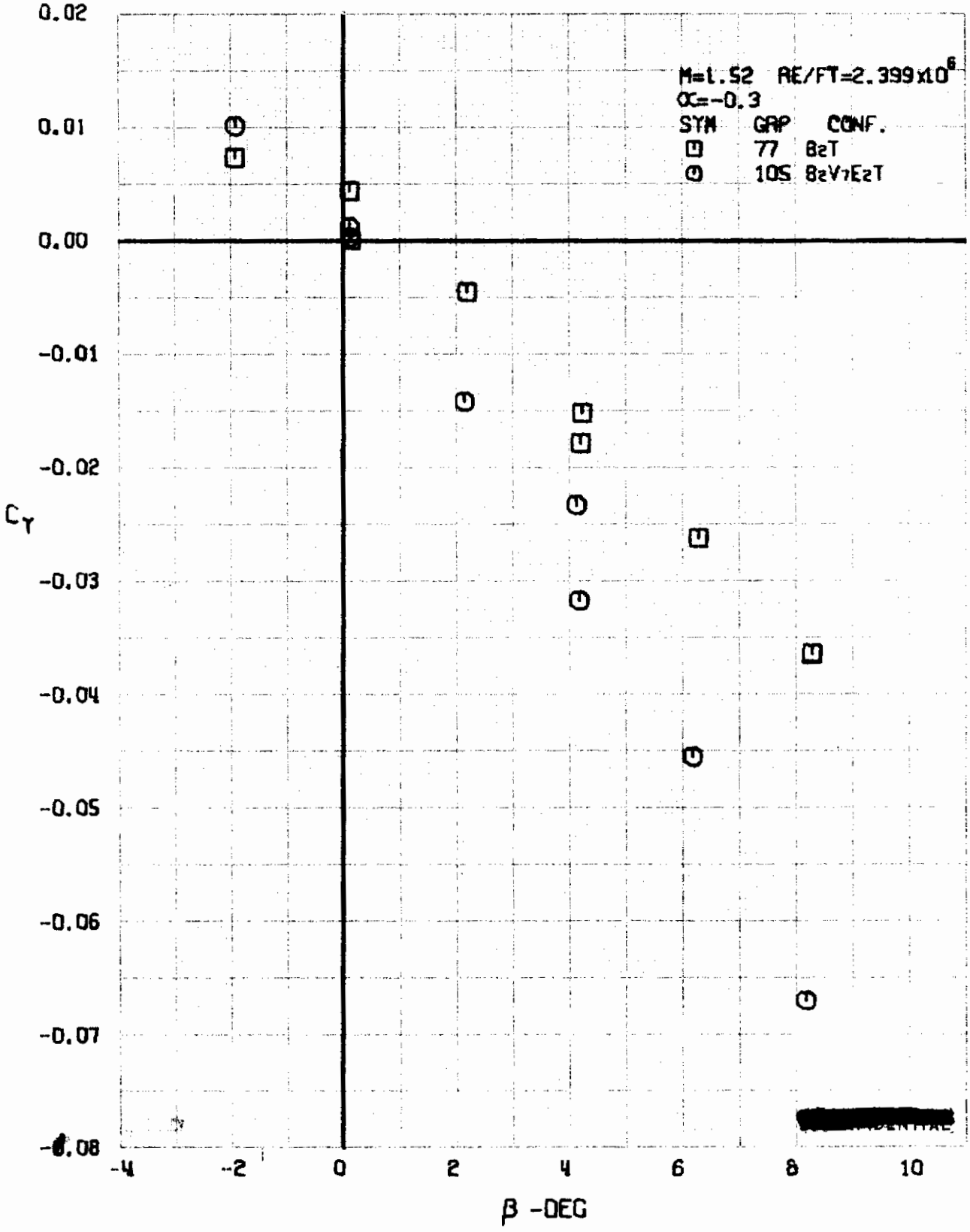

FIGURE 23 (U) CONFIGURATION BUILDUP
- SIDE FORCE COEFFICIENT VARIATION WITH ANGLE OF YAW (M= 1.52)

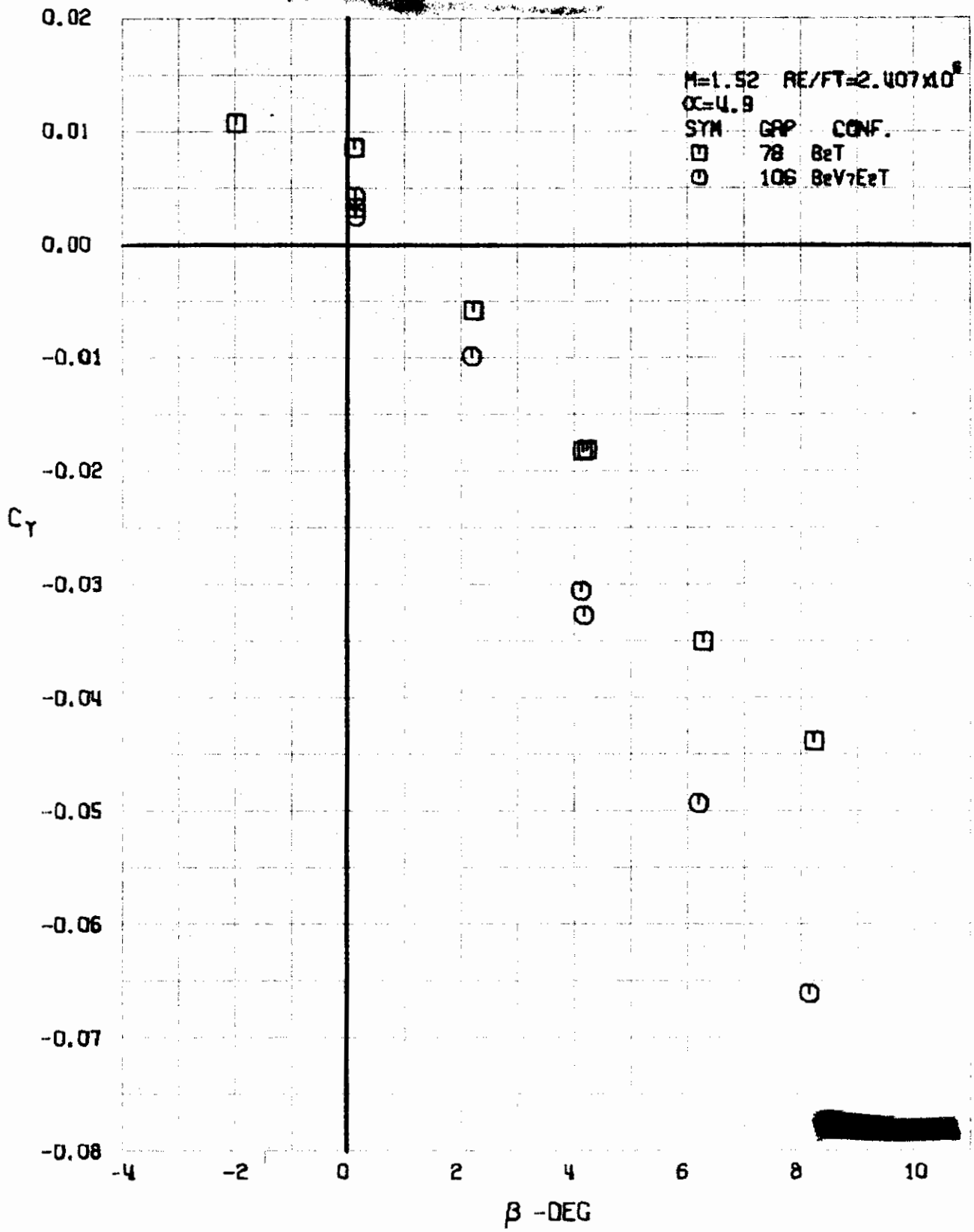

FIGURE 24 (U) CONFIGURATION BUILDUP
- SIDE FORCE COEFFICIENT VARIATION WITH ANGLE OF YAW (M= 1.52)

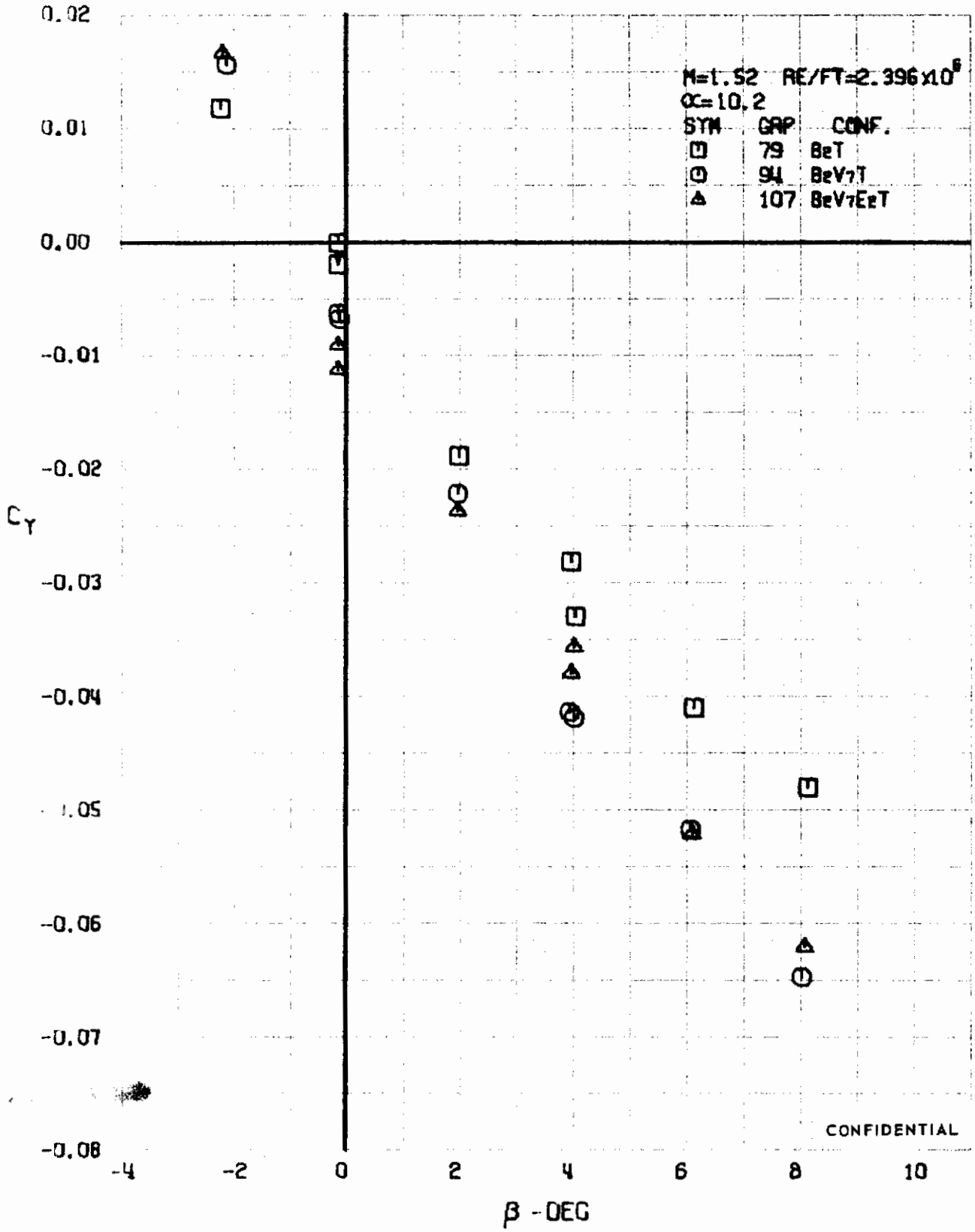

FIGURE 25 (U) CONFIGURATION BUILDUP
- SIDE FORCE COEFFICIENT VARIATION WITH ANGLE OF YAW (M=1.52)

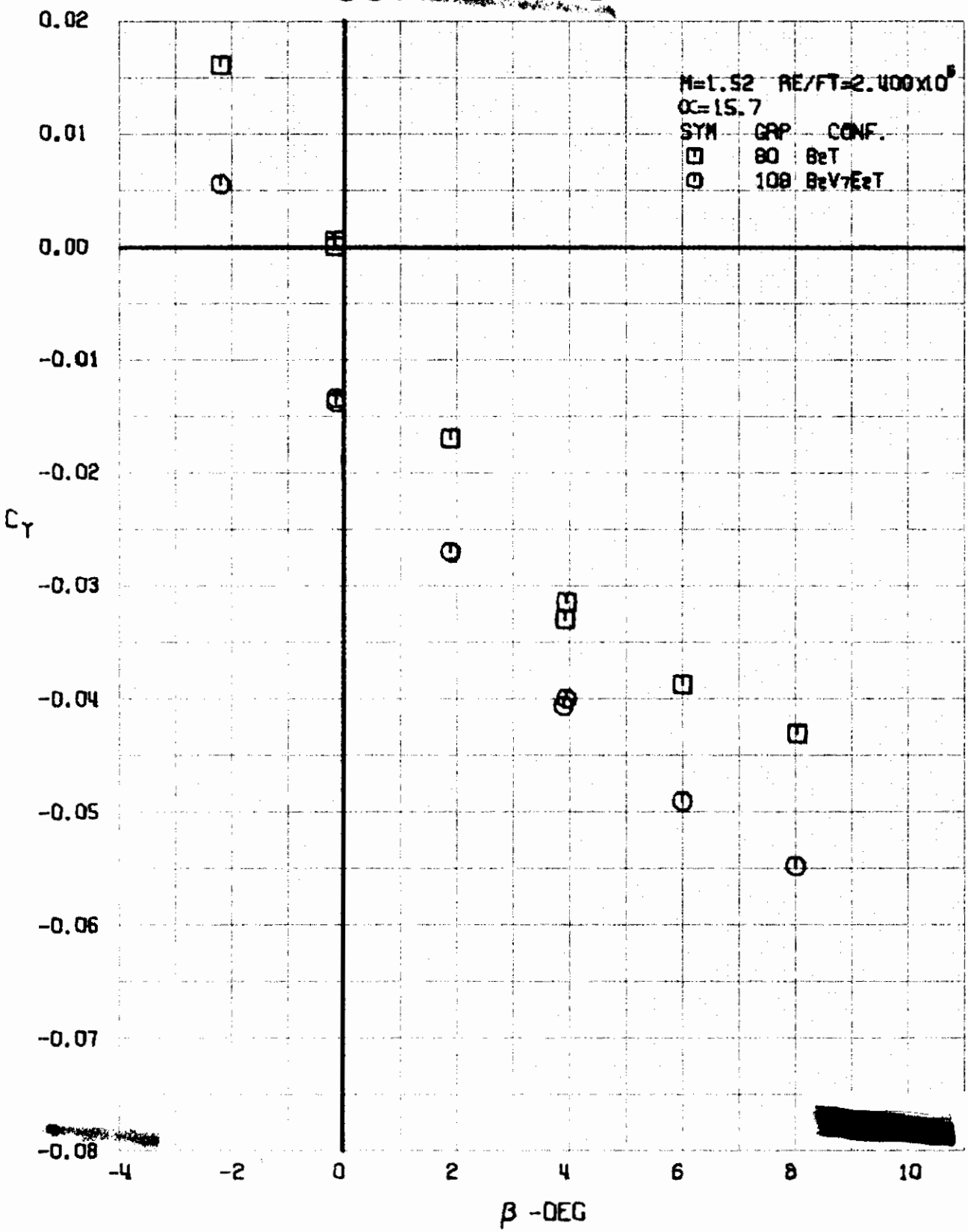

FIGURE 26 (U) CONFIGURATION BUILDUP
- SIDE FORCE COEFFICIENT VARIATION WITH ANGLE OF YAW (M= 1.52)

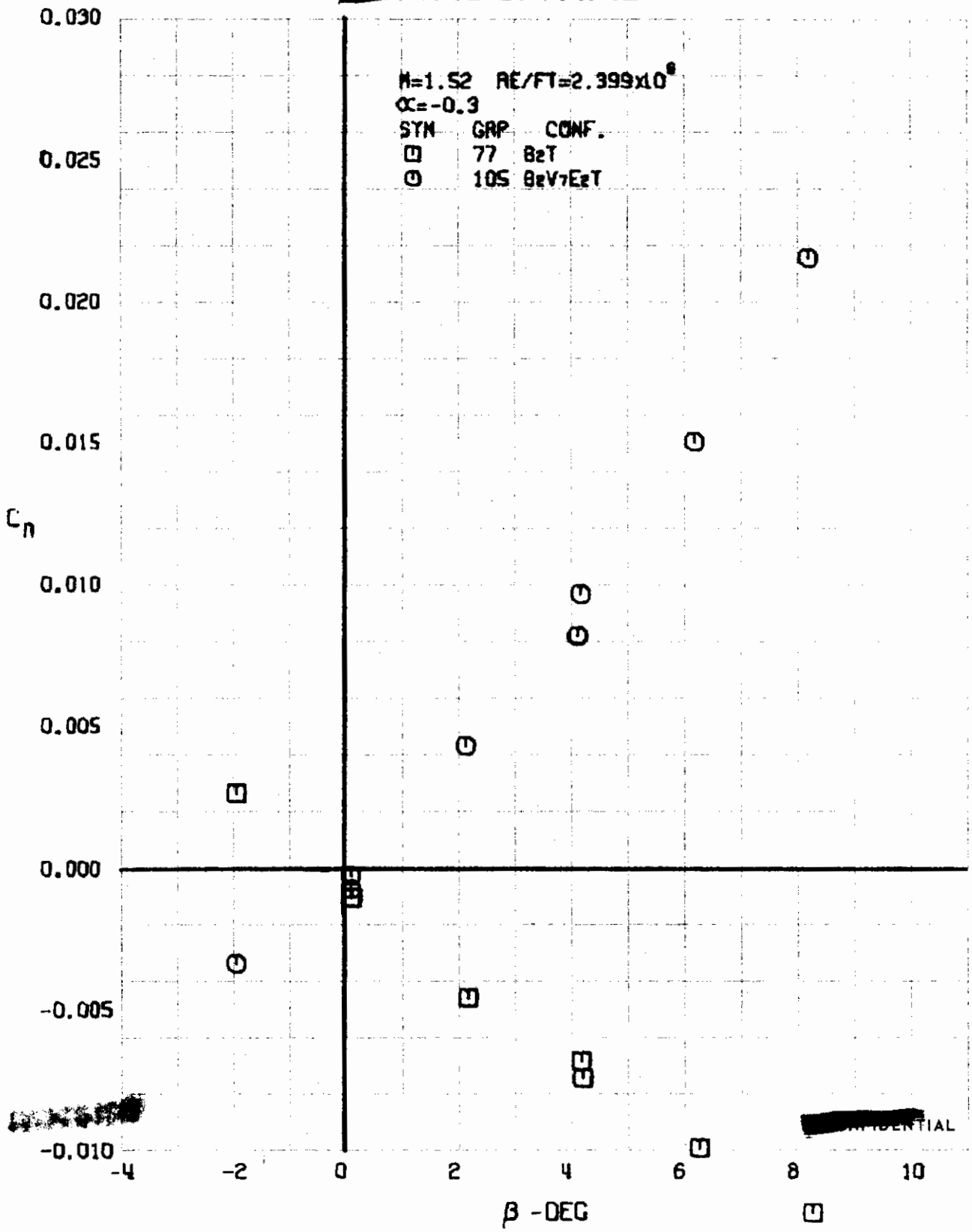

FIGURE 27 (U) CONFIGURATION BUILDUP
- YAWING MOMENT COEFFICIENT VARIATION WITH ANGLE OF YAW (M=1.52)

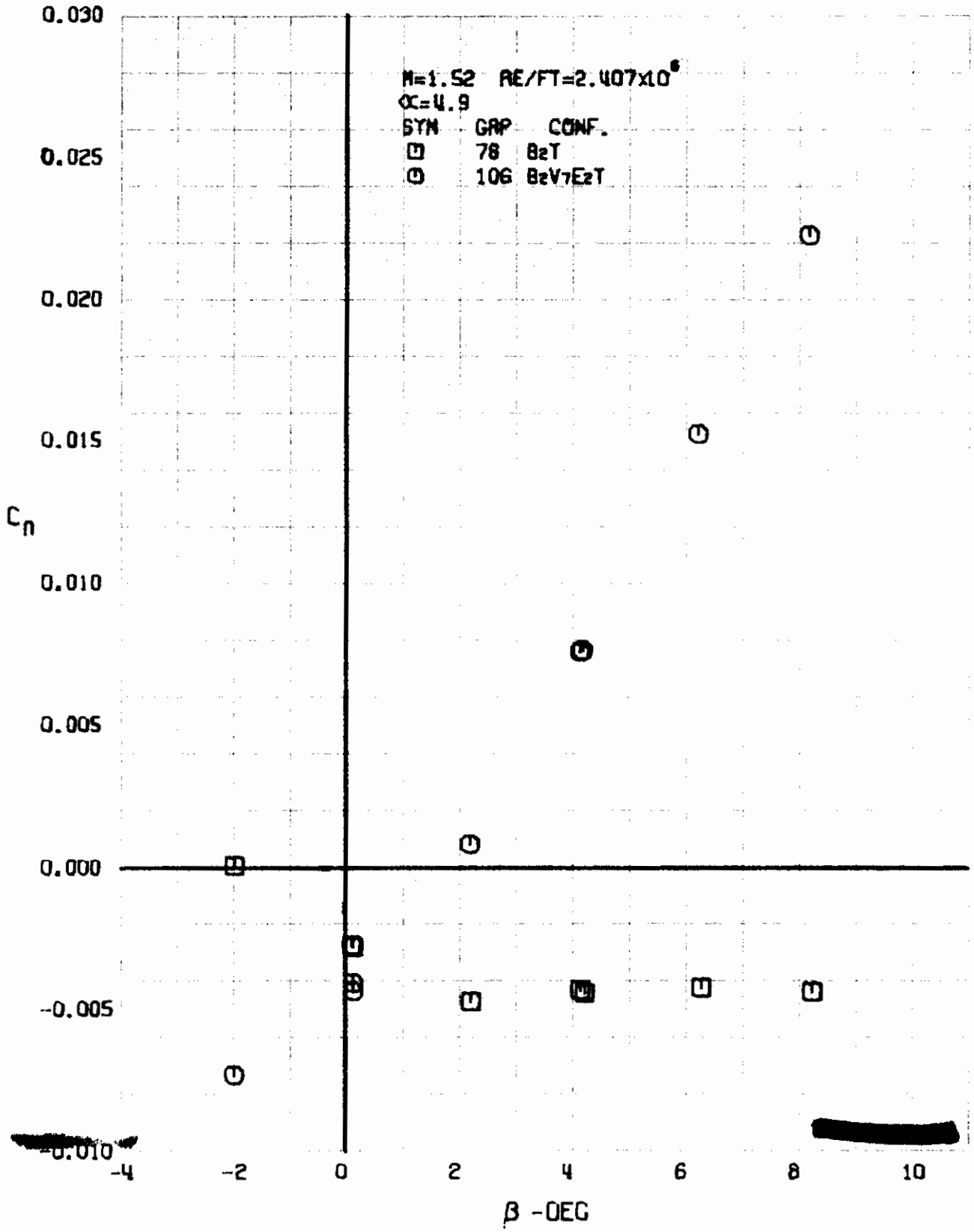

FIGURE 28 (U) CONFIGURATION BUILDUP
- YAWING MOMENT COEFFICIENT VARIATION WITH ANGLE OF YAW (M=1.52)

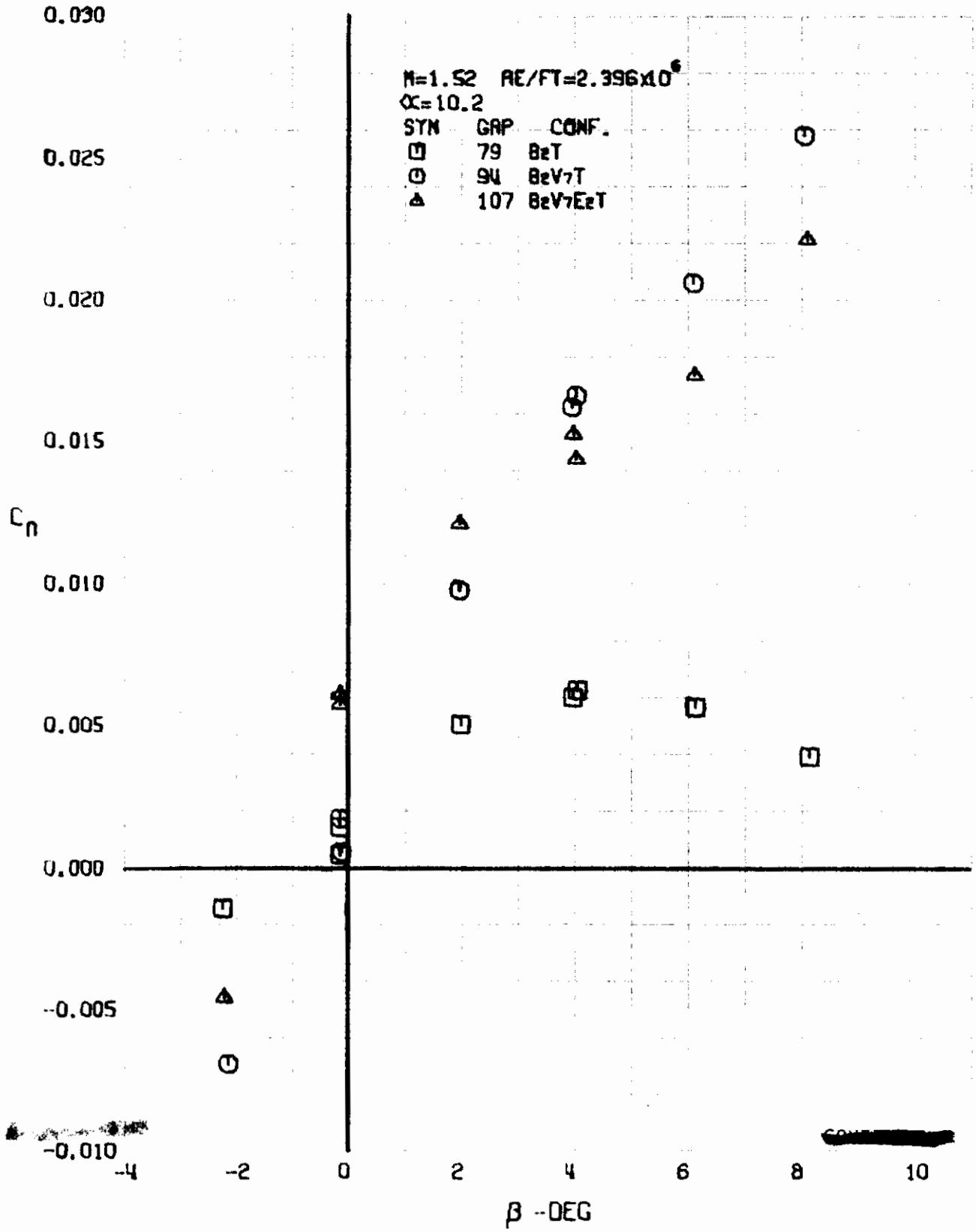

FIGURE 29 (U) CONFIGURATION BUILDUP
- YAWING MOMENT COEFFICIENT VARIATION WITH ANGLE OF YAW (M=1.52)

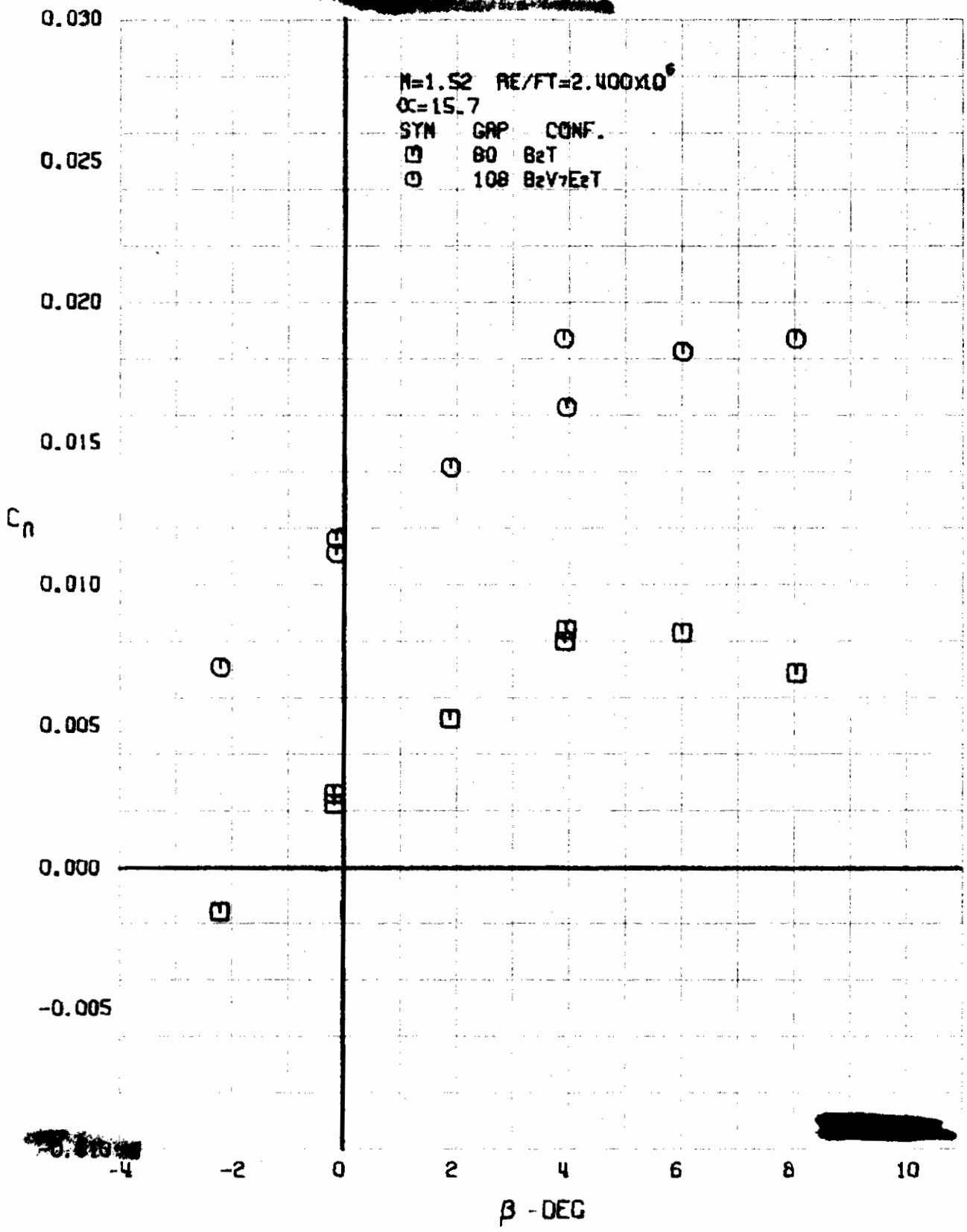

FIGURE 30 (U) CONFIGURATION BUILDUP
- YAWING MOMENT COEFFICIENT VARIATION WITH ANGLE OF YAW (M=1.52)

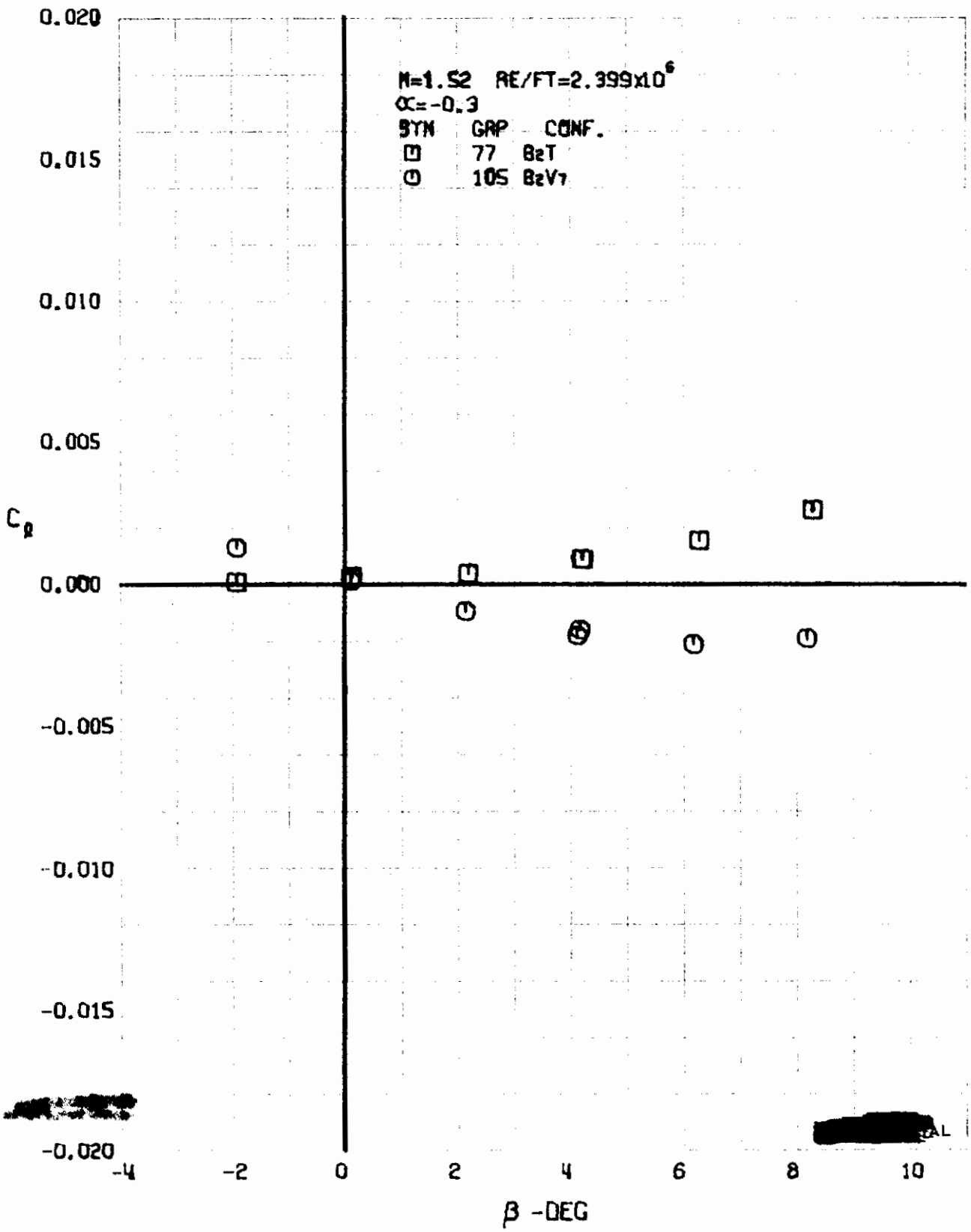

FIGURE 31 (U) CONFIGURATION BUILDUP
- ROLLING MOMENT COEFFICIENT VARIATION WITH ANGLE OF YAW (M=1.52)

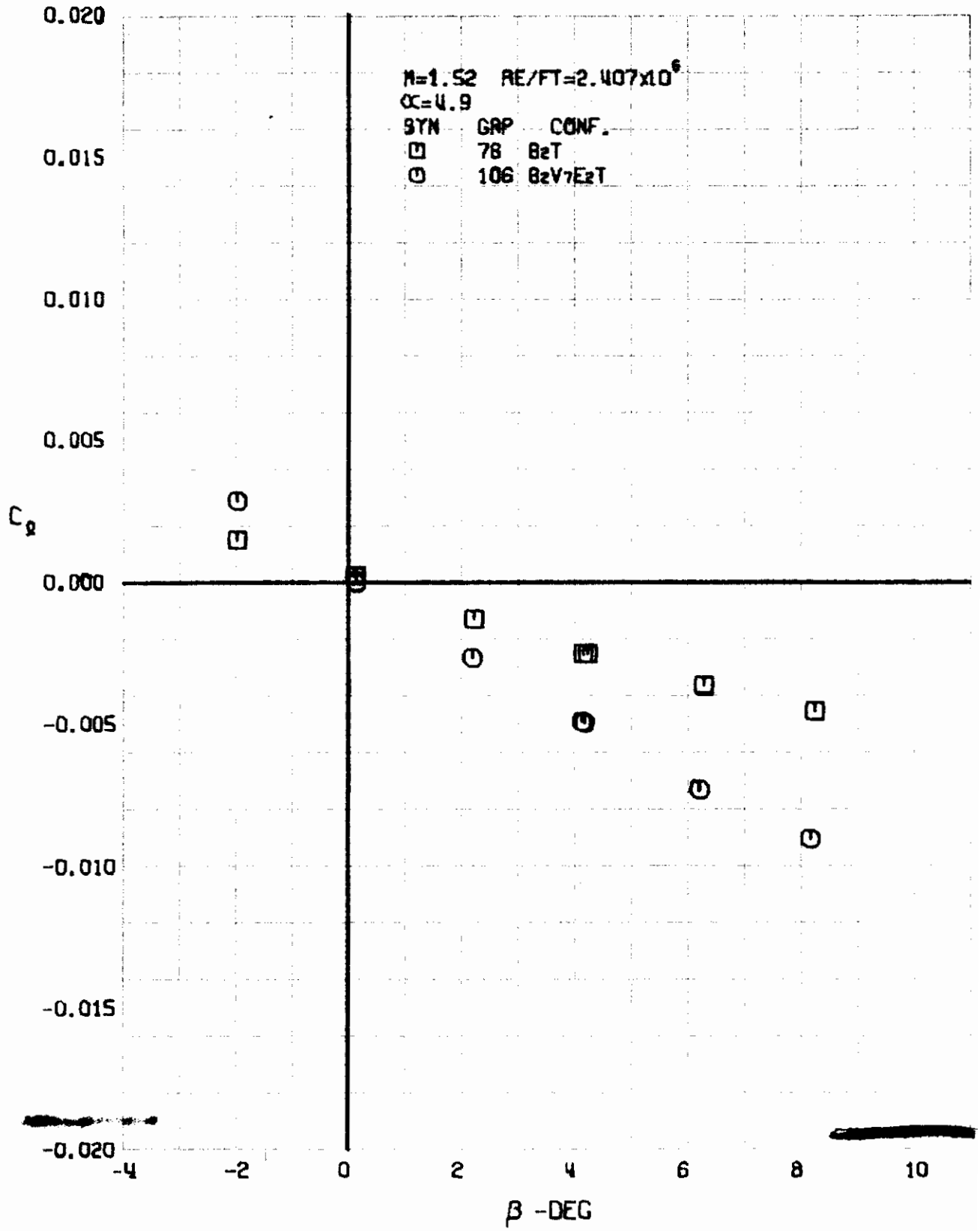

FIGURE 32 (U) CONFIGURATION BUILDUP
- ROLLING MOMENT COEFFICIENT VARIATION WITH ANGLE OF YAW (M=1.52)

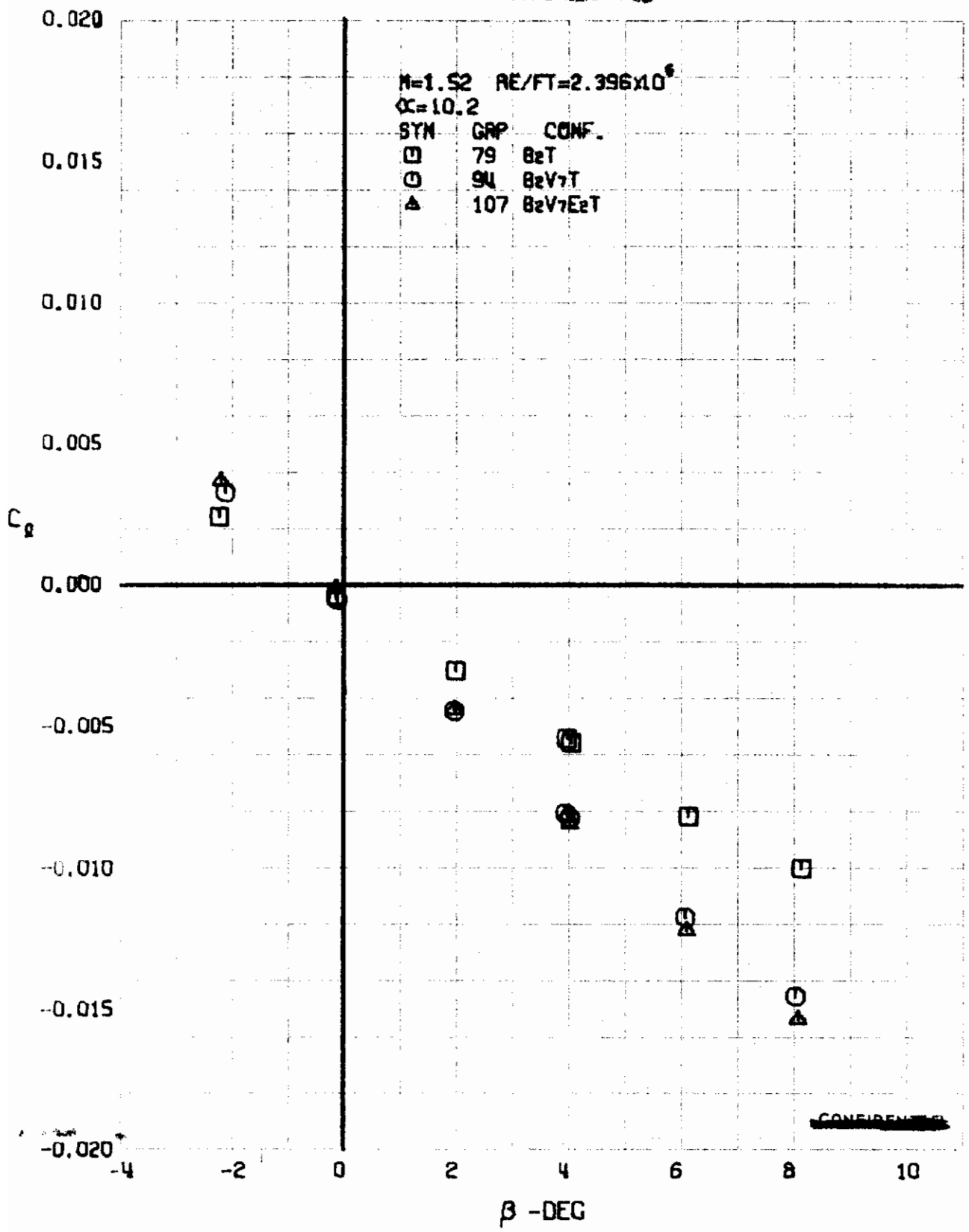

FIGURE 33 (U) CONFIGURATION BUILDUP
- ROLLING MOMENT COEFFICIENT VARIATION WITH ANGLE OF YAW (M=1.52)

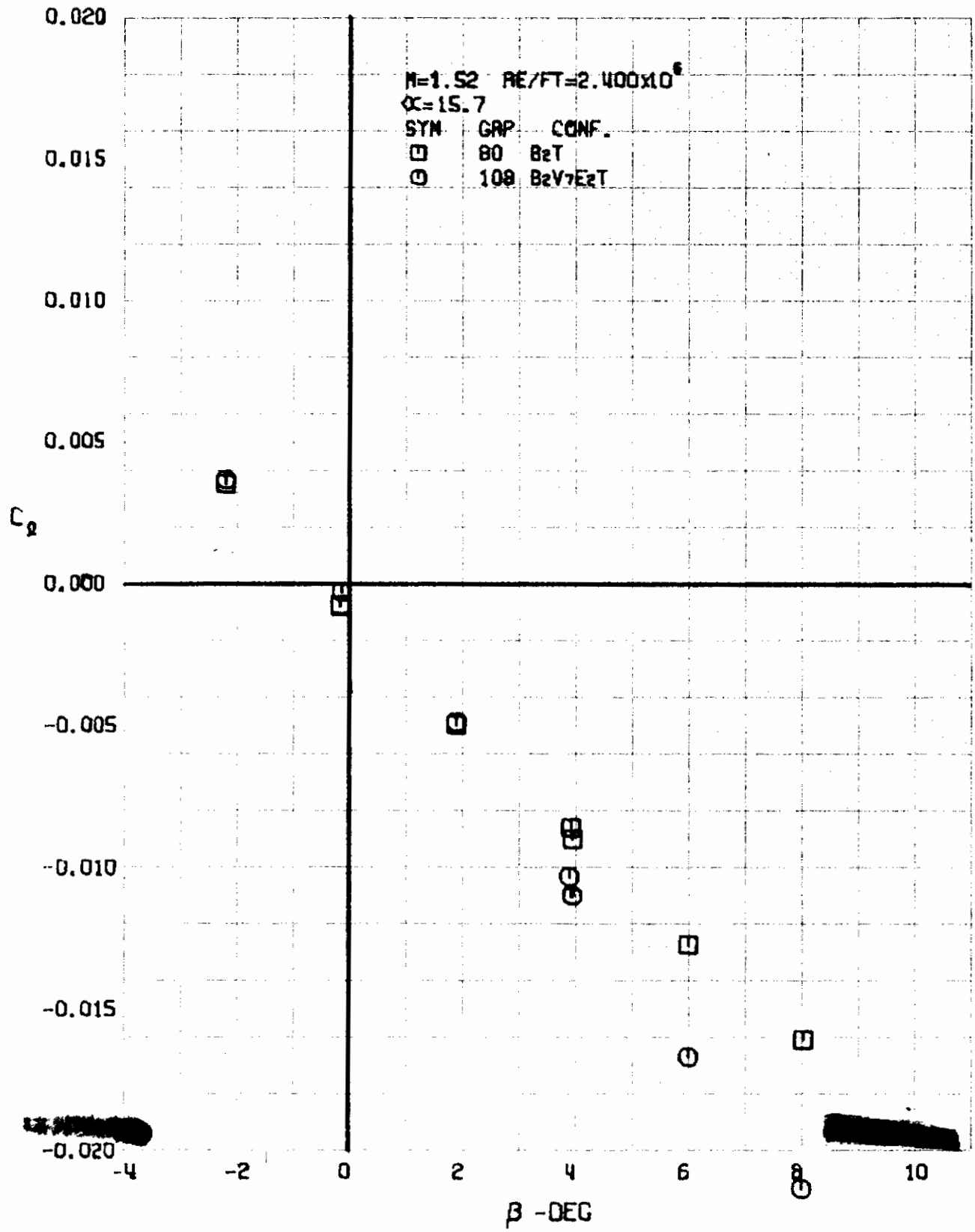

FIGURE 34 (U) CONFIGURATION BUILDUP
- ROLLING MOMENT COEFFICIENT VARIATION WITH ANGLE OF YAW (M=1.52)

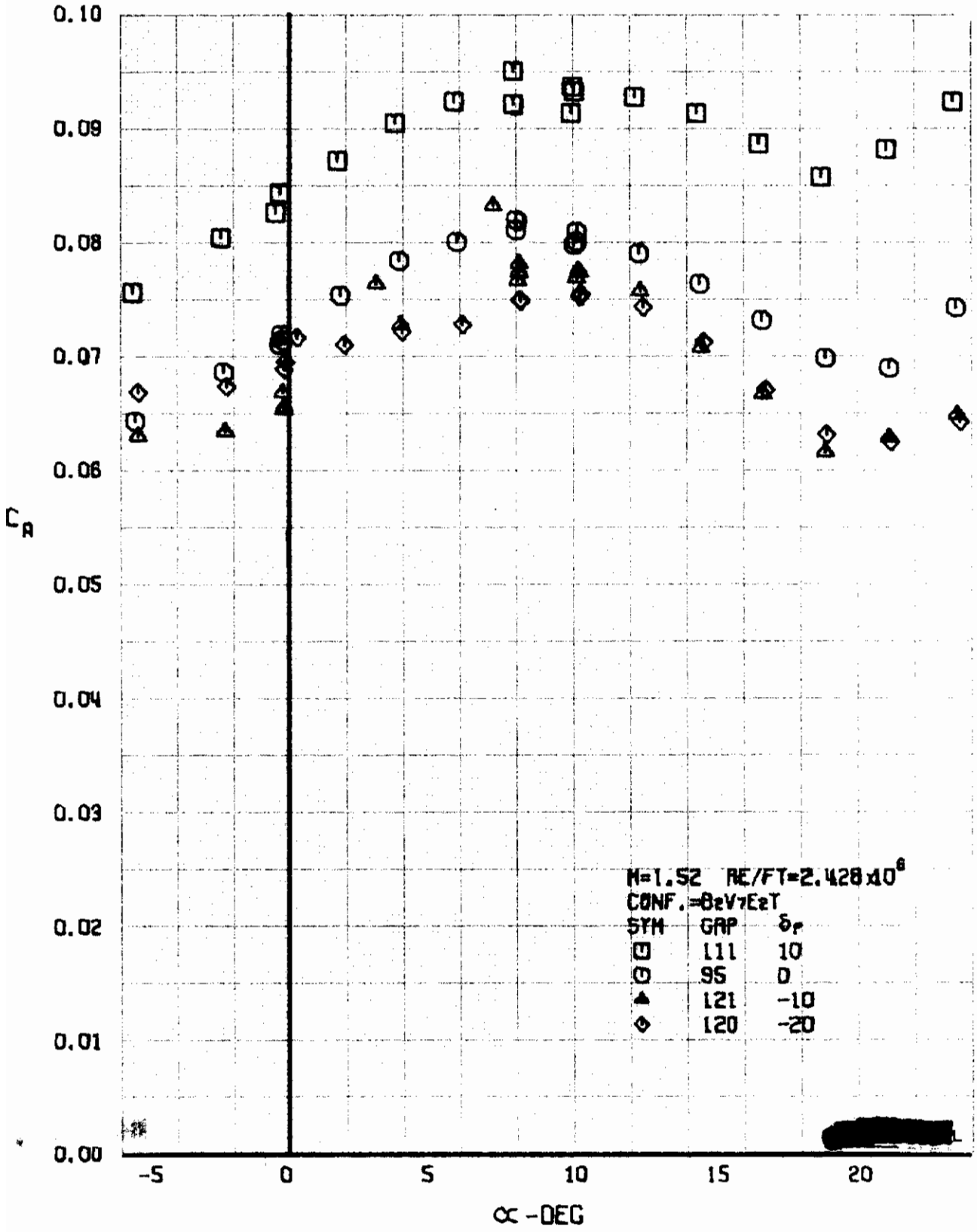

Figure 39 (U) ELEVON EFFECTS
- AXIAL FORCE COEFFICIENT VARIATION WITH ANGLE OF ATTACK (M=1.52)

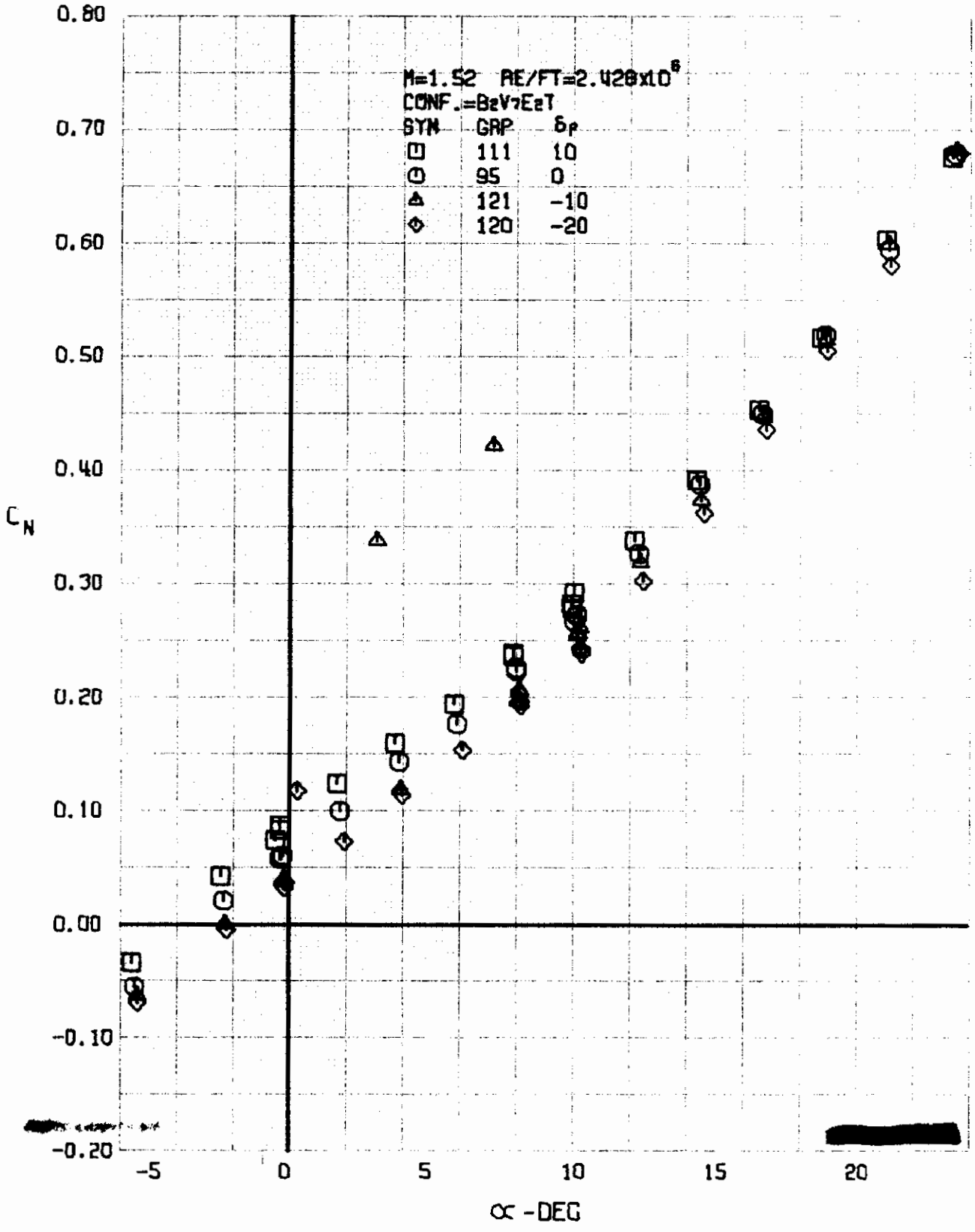

FIGURE 36 (U) ELEVON EFFECTS
- NORMAL FORCE COEFFICIENT VARIATION WITH ANGLE OF ATTACK (M= 1.52)

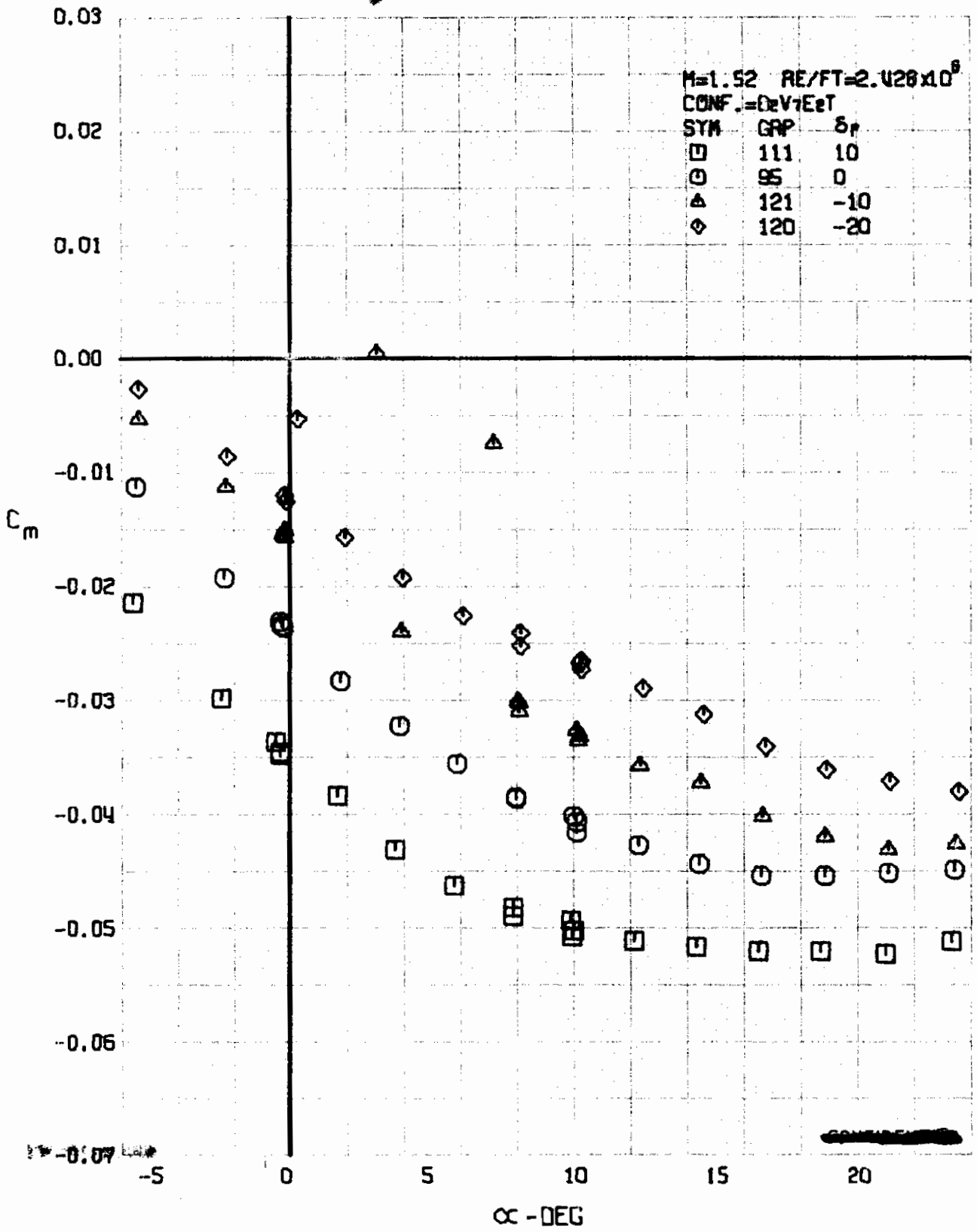

FIGURE 37 (U) ELEVON EFFECTS
- PITCHING MOMENT COEFFICIENT VARIATION WITH ANGLE OF ATTACK (M=1.52)

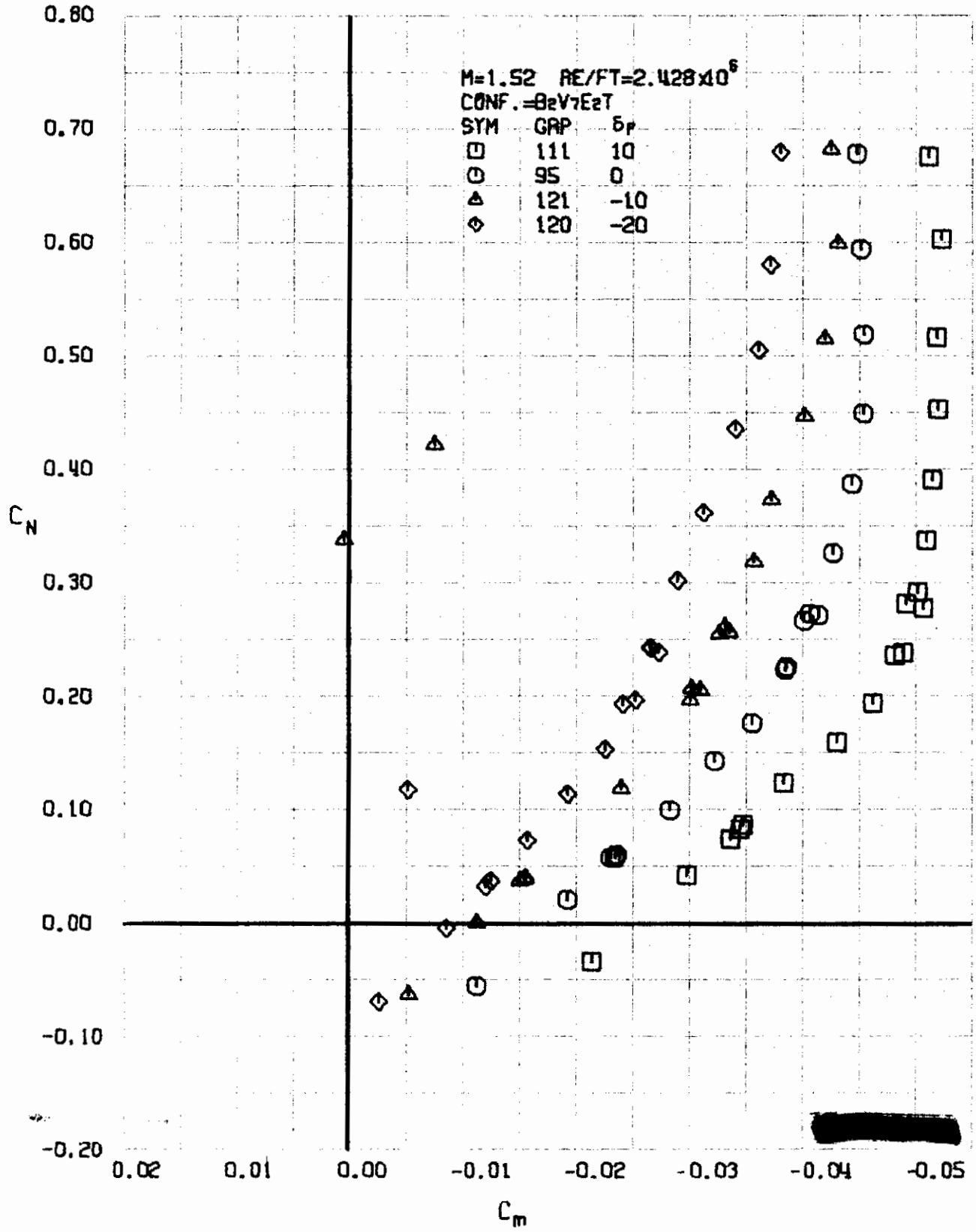

FIGURE 38 (U) ELEVON EFFECTS
- LONGITUDINAL STABILITY VARIATION (M=1.52)

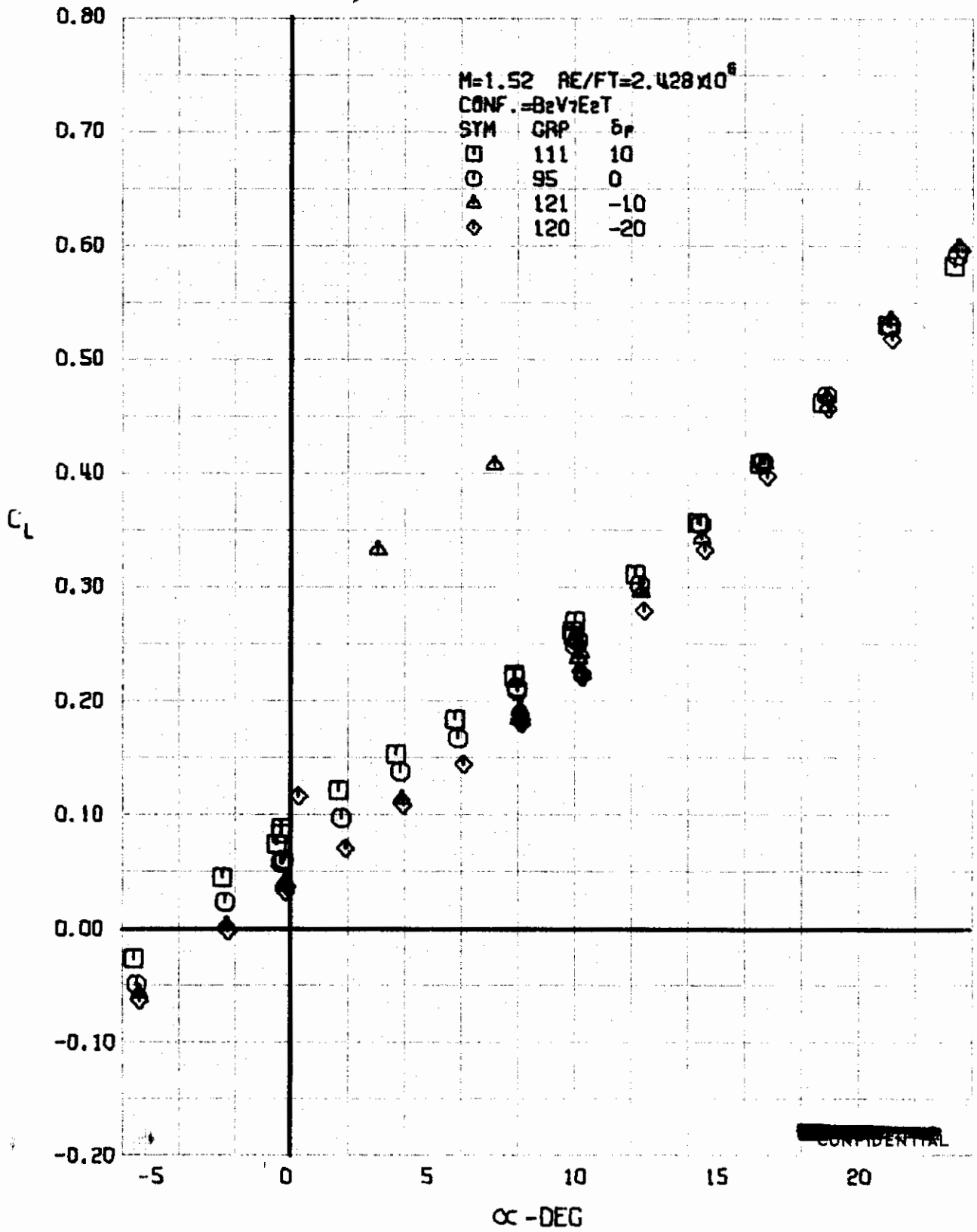

FIGURE 39 (U) ELEVON EFFECTS
- LIFT COEFFICIENT VARIATION WITH ANGLE OF ATTACK (M=1.52)

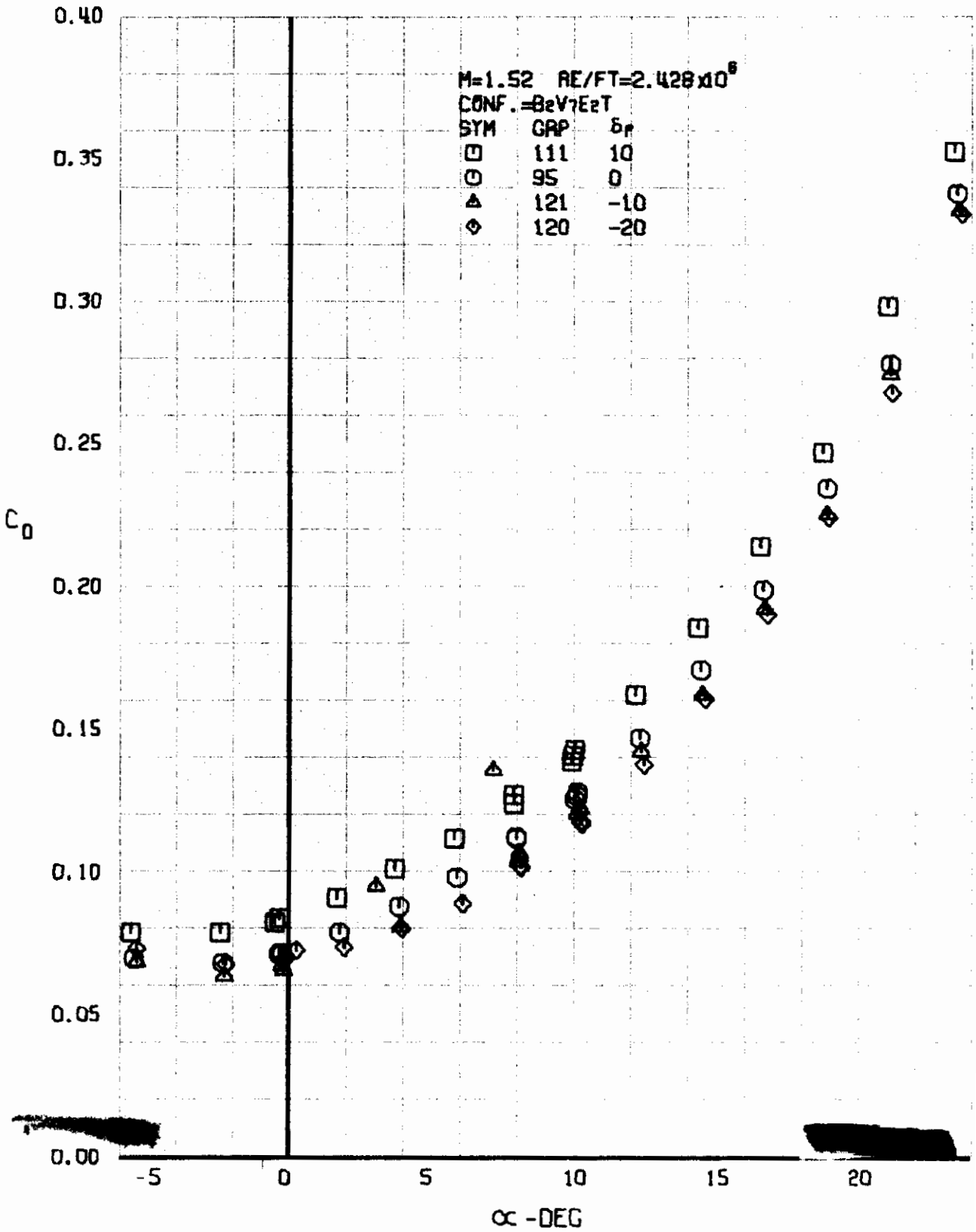

FIGURE 40 (U) ELEVON EFFECTS
- DRAG COEFFICIENT VARIATION WITH ANGLE OF ATTACK (M=1.52)

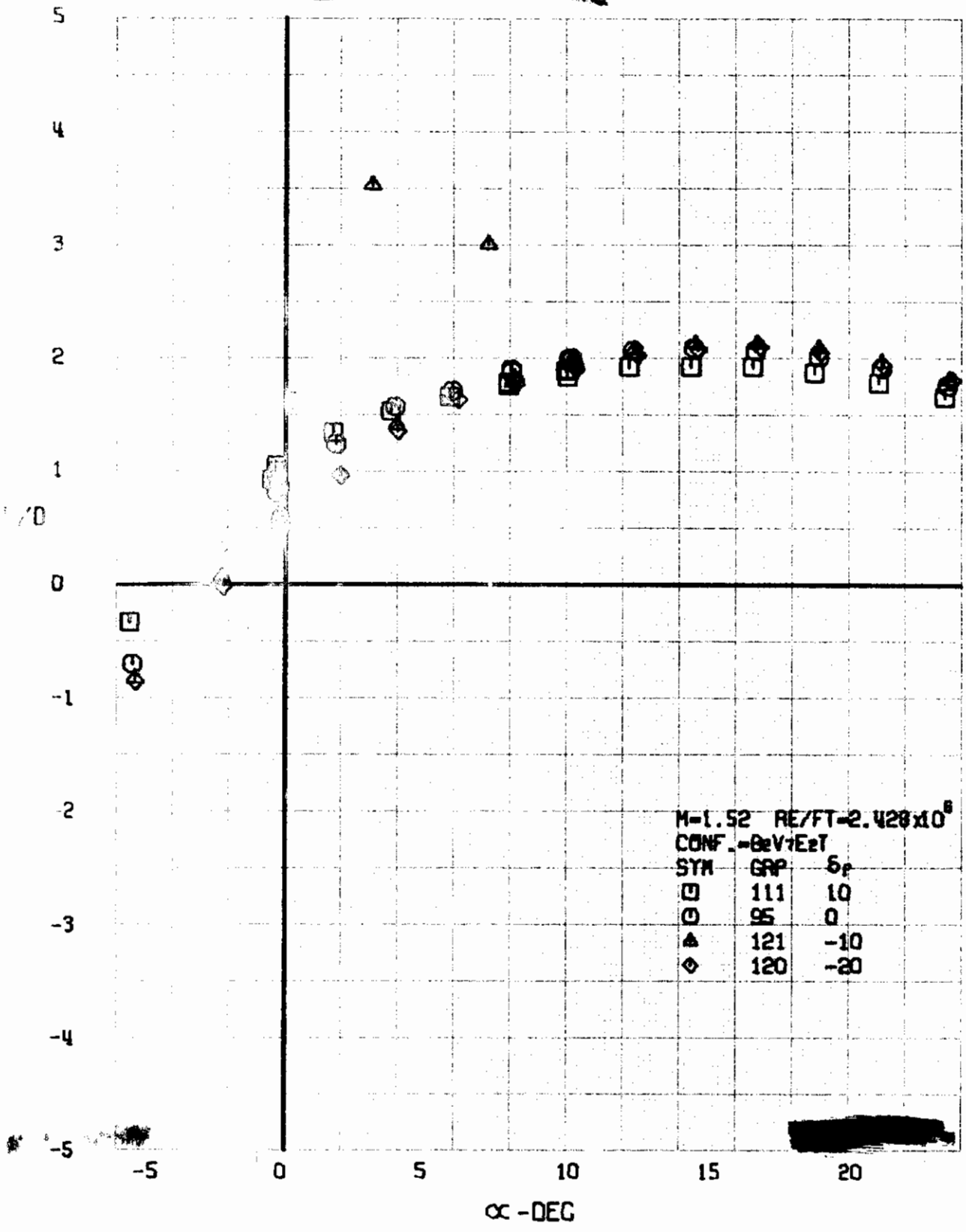

FIGURE 41 (U) ELEVON EFFECTS
- LIFT-DRAG RATIO VARIATION WITH ANGLE OF ATTACK (M=1.52)

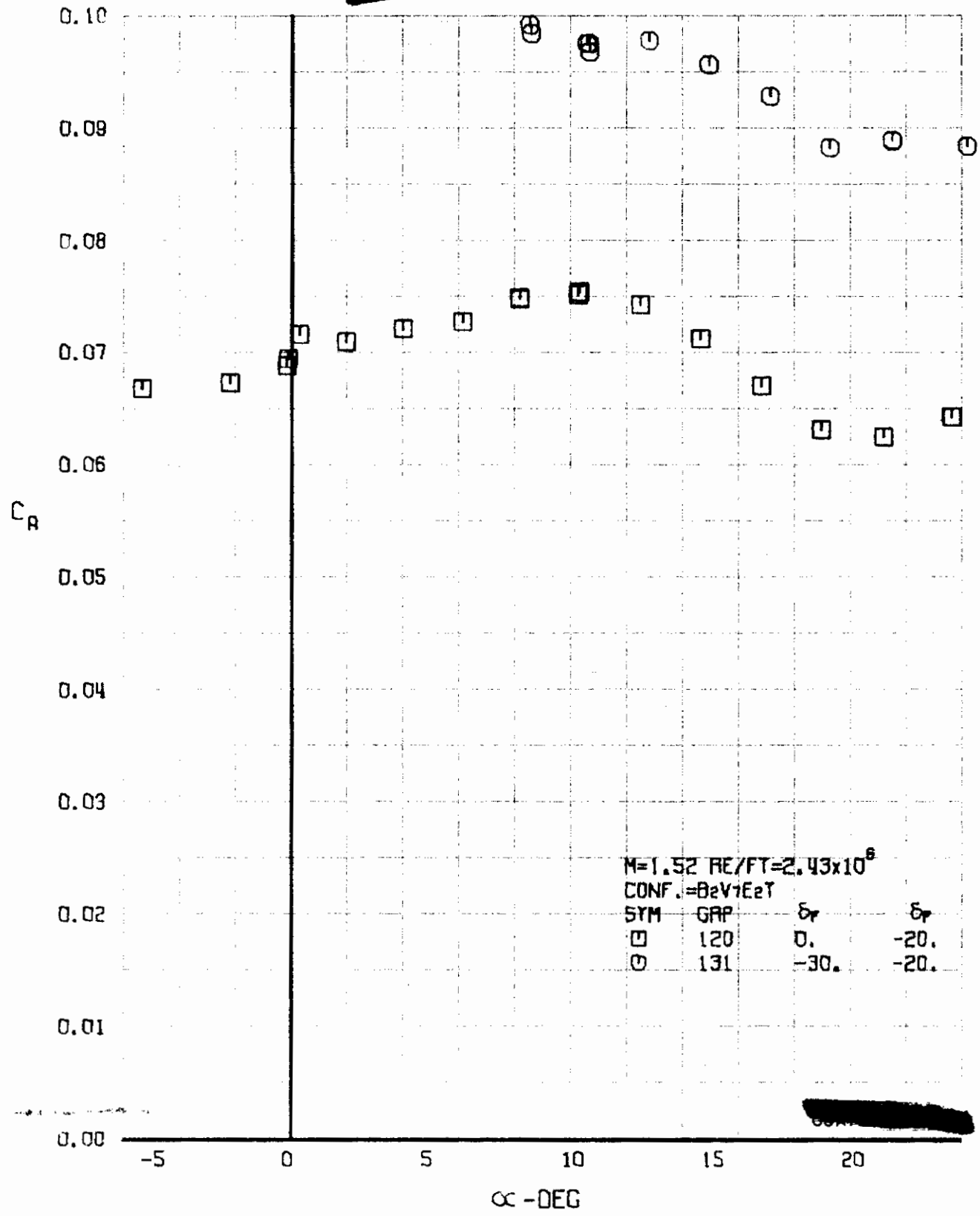

FIGURE 42 (U) FLAP EFFECTS
- AXIAL FORCE COEFFICIENT VARIATION WITH ANGLE OF ATTACK (M=1.52)

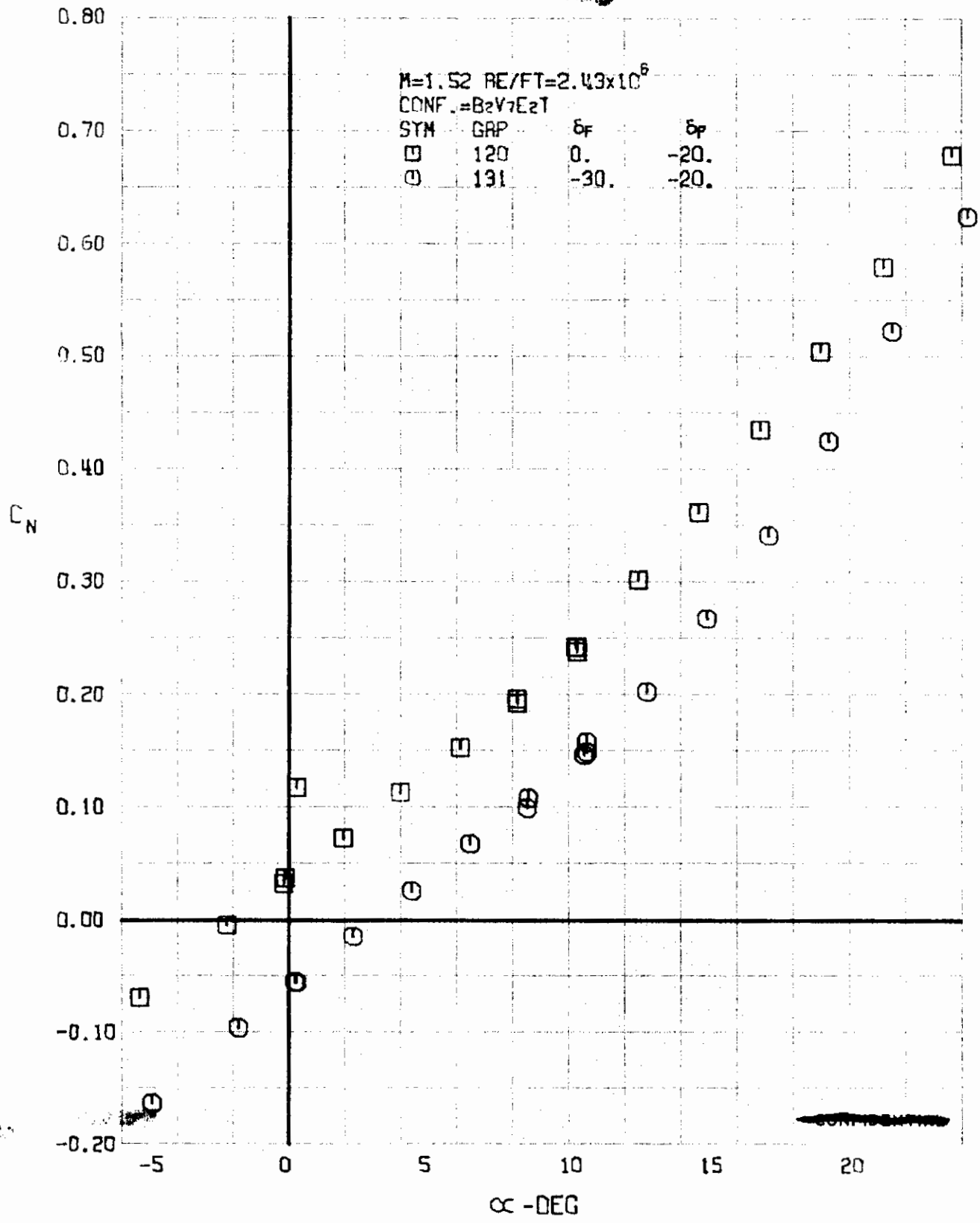

FIGURE 43 (U) FLAP EFFECTS
- NORMAL FORCE COEFFICIENT VARIATION WITH ANGLE OF ATTACK (M=1.52)

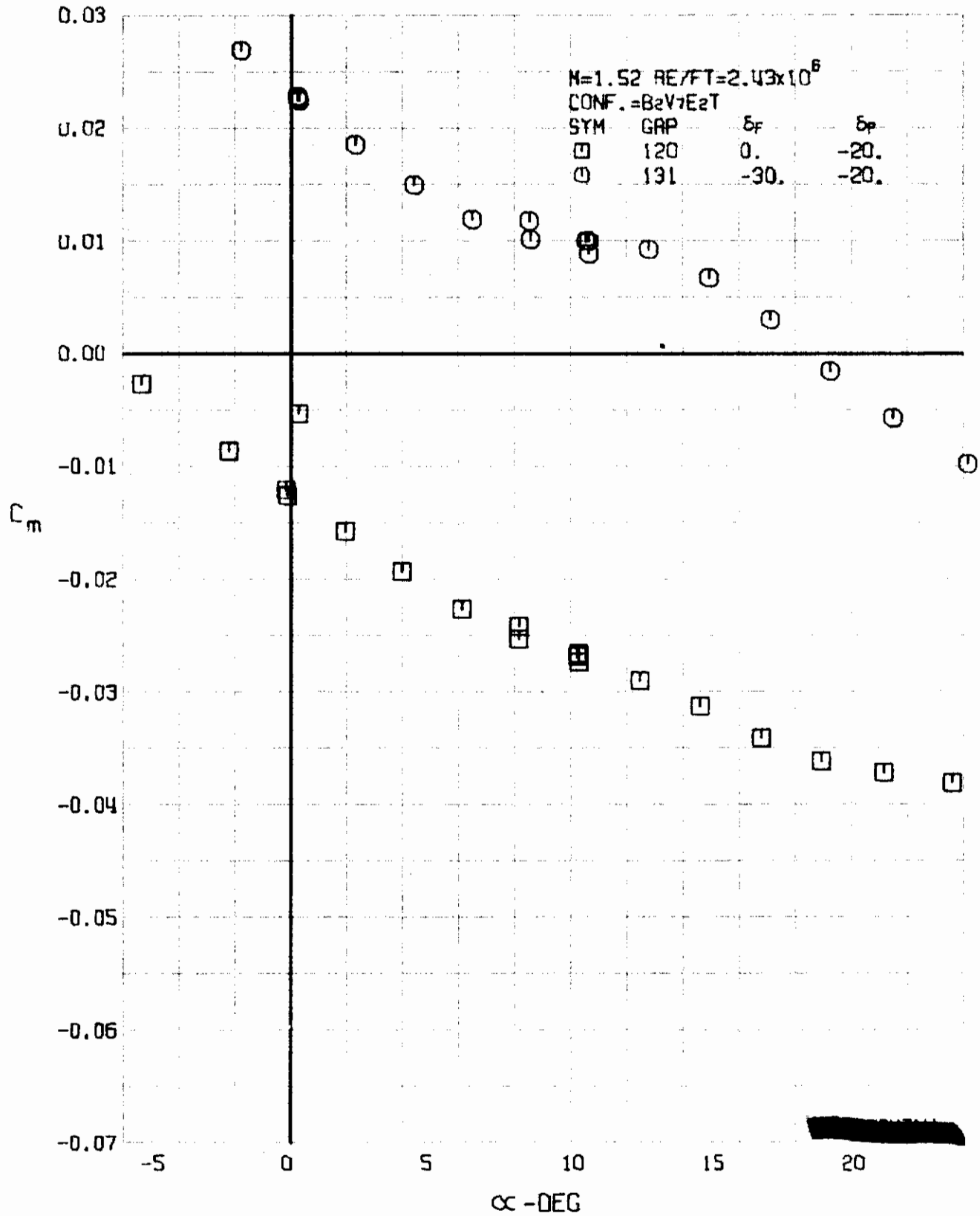

FIGURE 41 (U) FLAP EFFECTS
- PITCHING MOMENT COEFFICIENT VARIATION WITH ANGLE OF ATTACK (M=1.52)

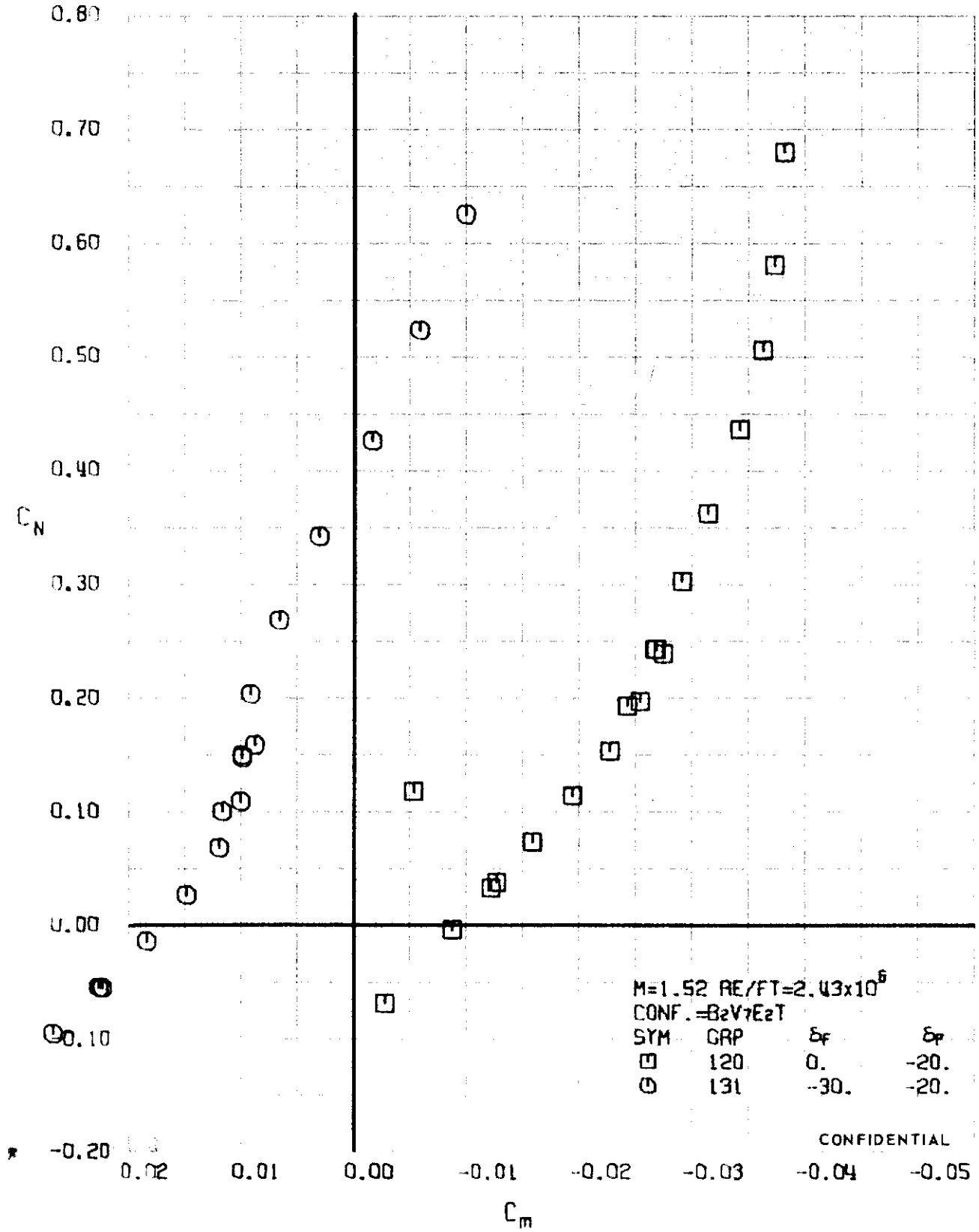

FIGURE 45 (U) FLAP EFFECTS
- LONGITUDINAL STABILITY VARIATION (M=1.52)

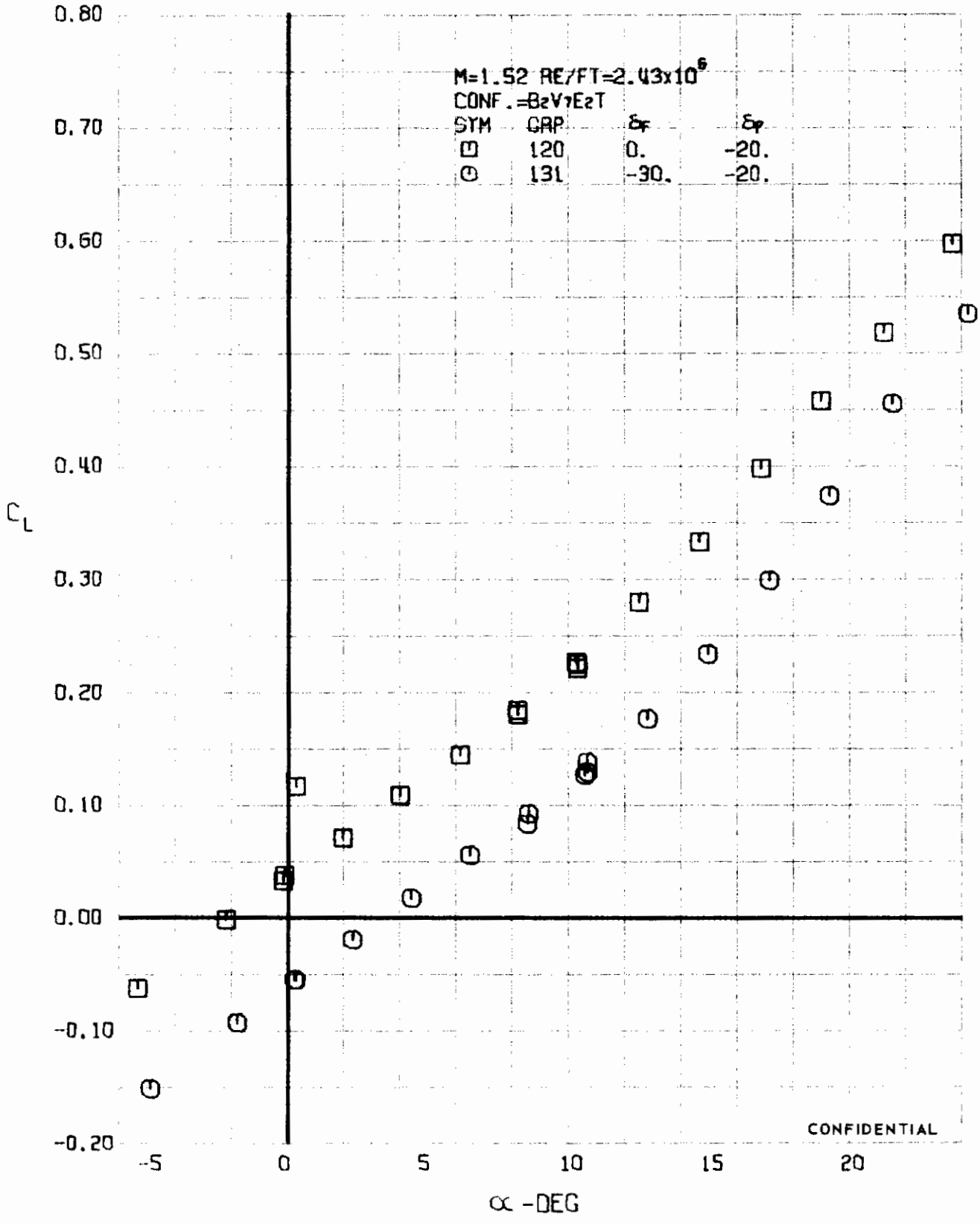

FIGURE 46 (U) FLAP EFFECTS
- LIFT COEFFICIENT VARIATION WITH ANGLE OF ATTACK (M=1.52)

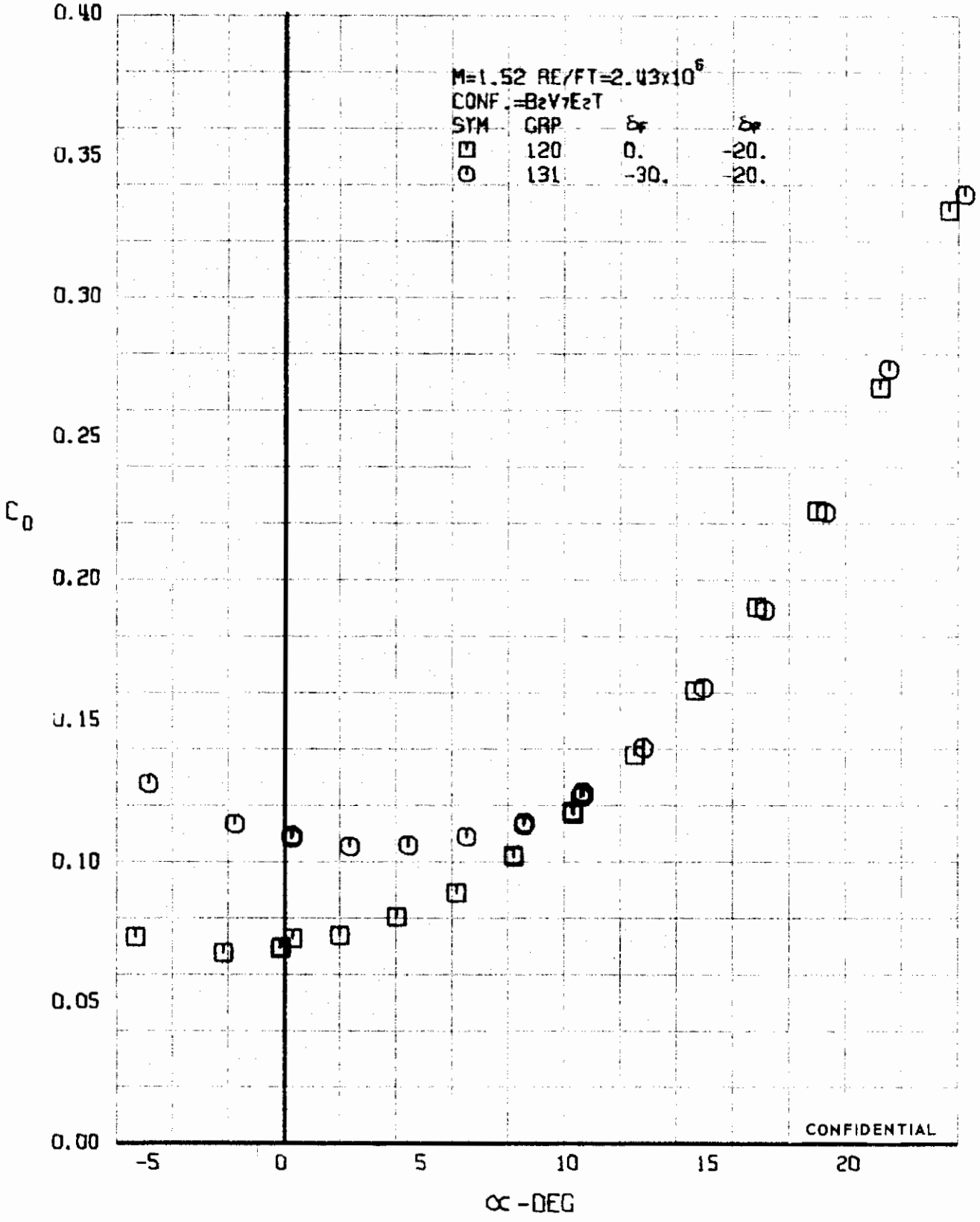

FIGURE 47 (U) FLAP EFFECTS
- DRAG COEFFICIENT VARIATION WITH ANGLE OF ATTACK (M=1.52)

[redacted]

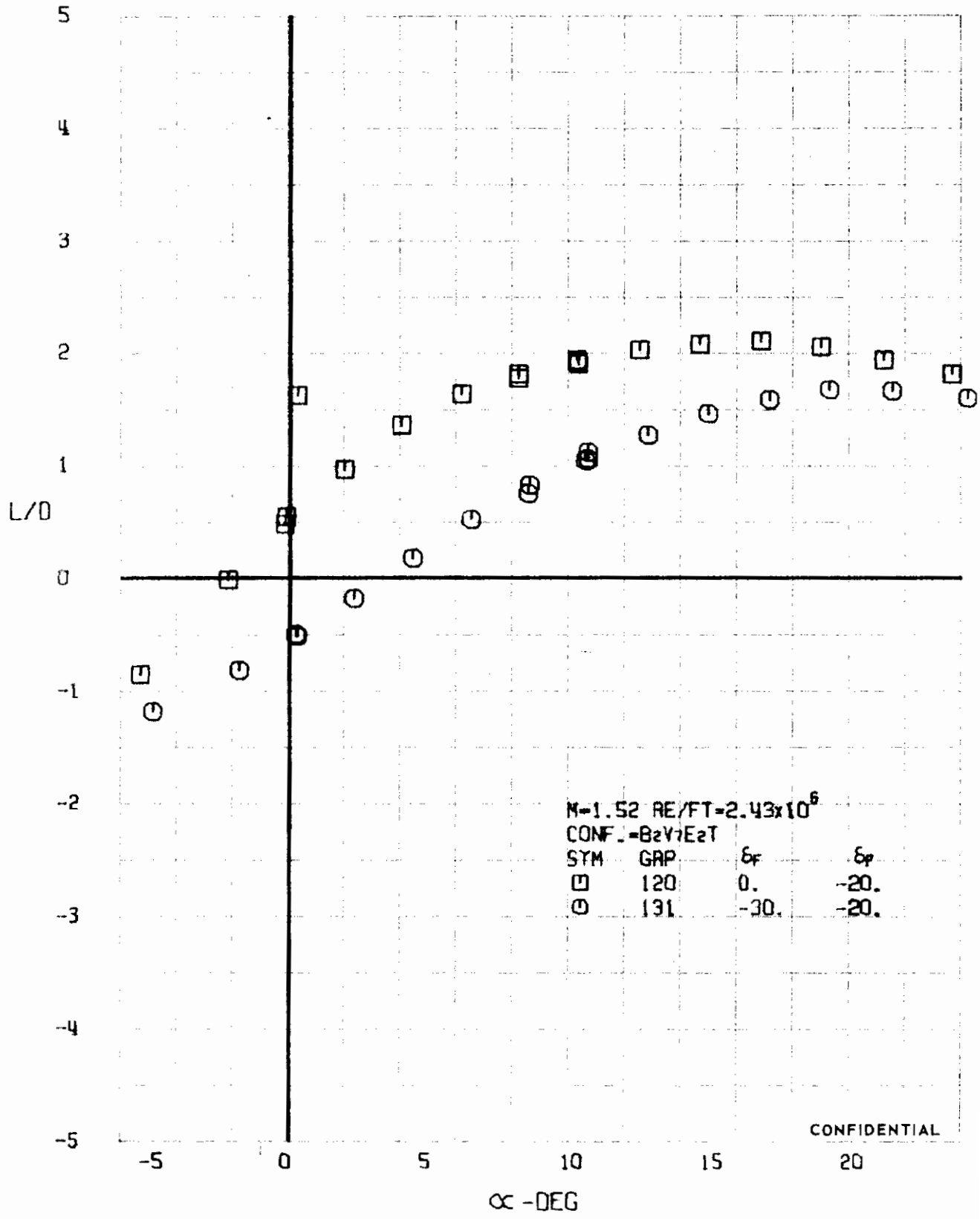

FIGURE 4 (U) FLAP EFFECTS
- LIFT-DRAG RATIO VARIATION WITH ANGLE OF ATTACK (M=1.52)

[redacted]

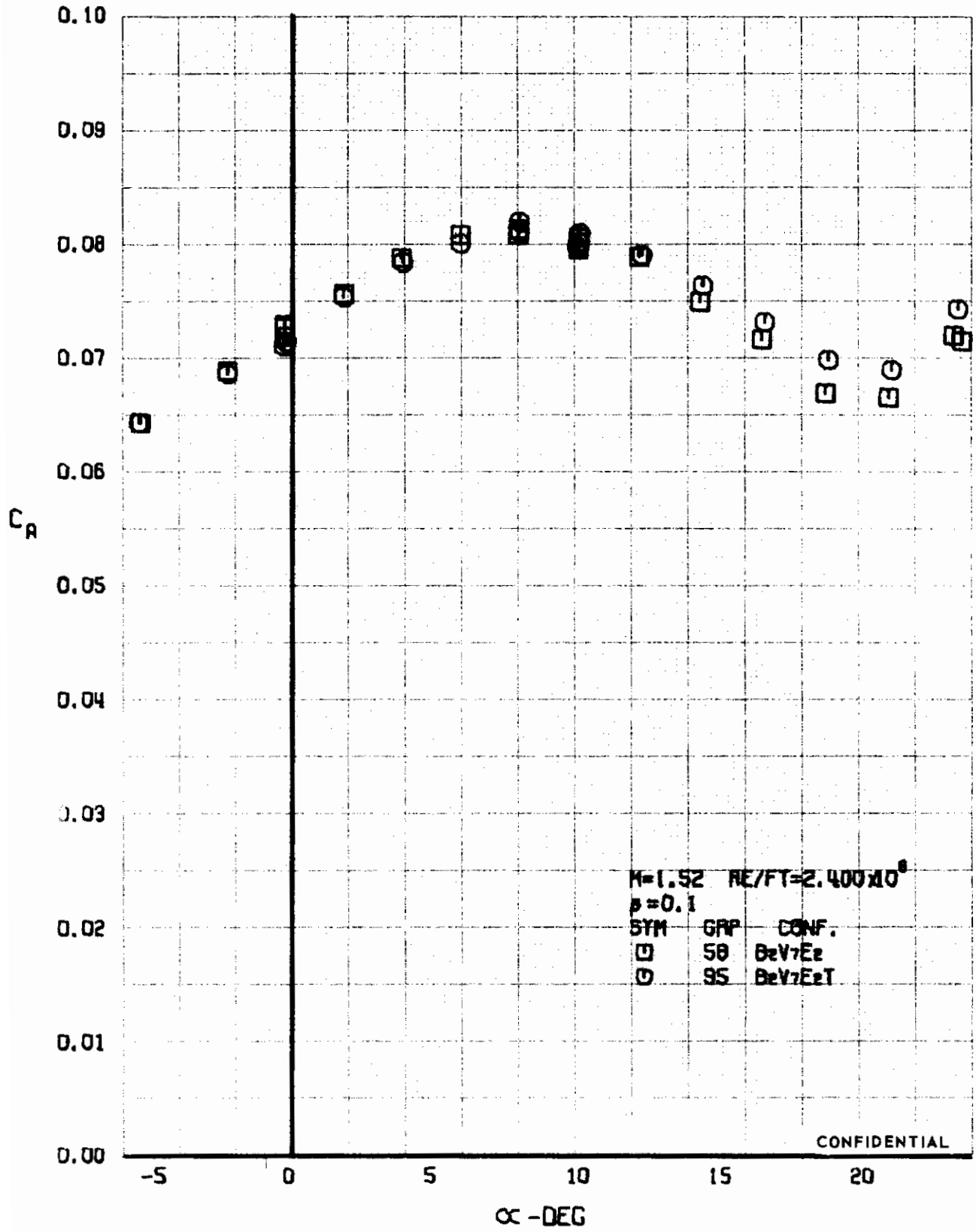

FIGURE 49 (U) FORCED TRANSITION EFFECTS
- AXIAL FORCE COEFFICIENT VARIATION WITH ANGLE OF ATTACK (M=1.52)

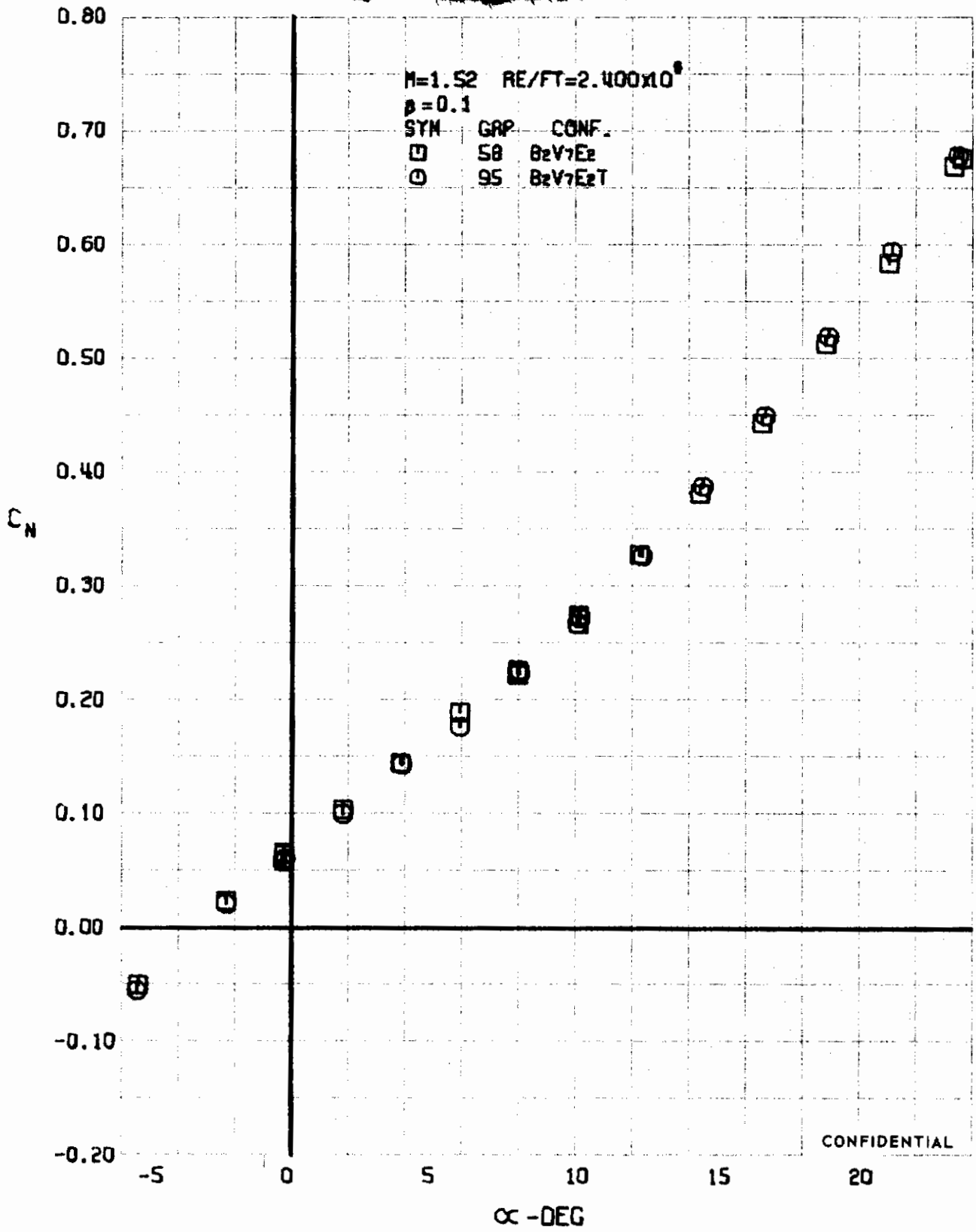

FIGURE 50 (U) FORCED TRANSITION EFFECTS
- NORMAL FORCE COEFFICIENT VARIATION WITH ANGLE OF ATTACK (M=1.52)

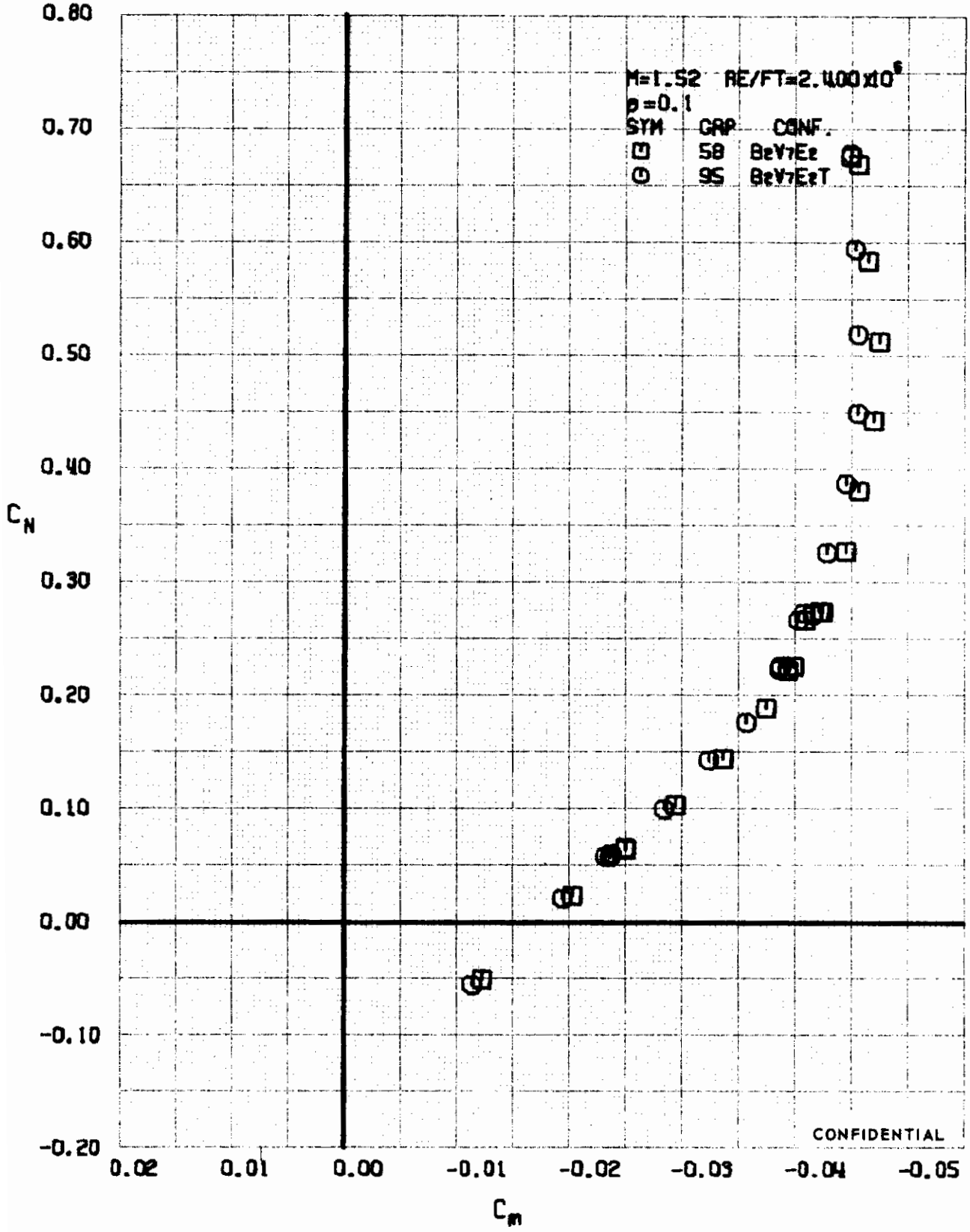

FIGURE 51 (U) FORCED TRANSITION EFFECTS
- LONGITUDINAL STABILITY VARIATION (M= 1.52)

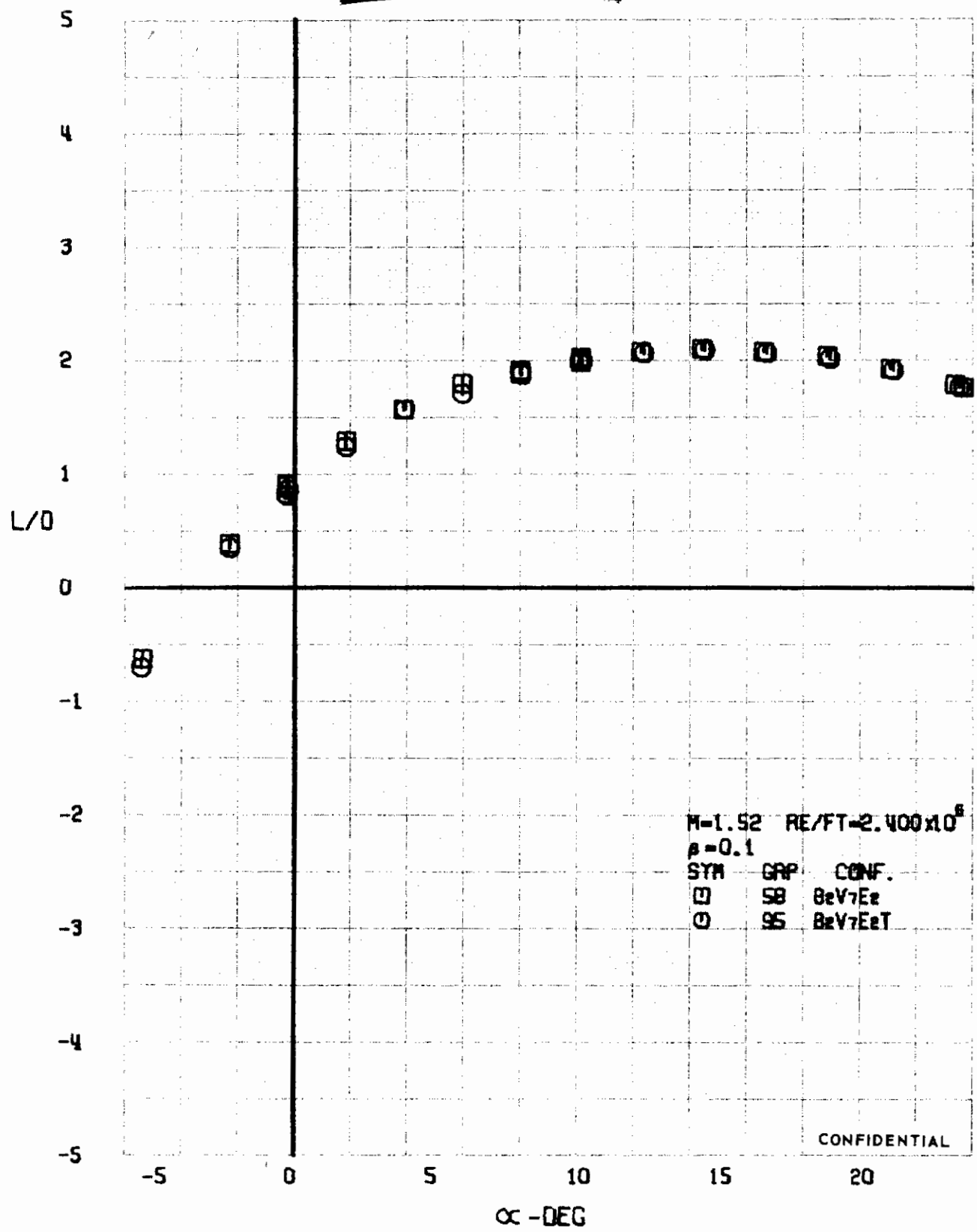

FIGURE 52 (U) FORCED TRANSITION EFFECTS
- LIFT-DRAG RATIO VARIATION WITH ANGLE OF ATTACK (M=1.52)

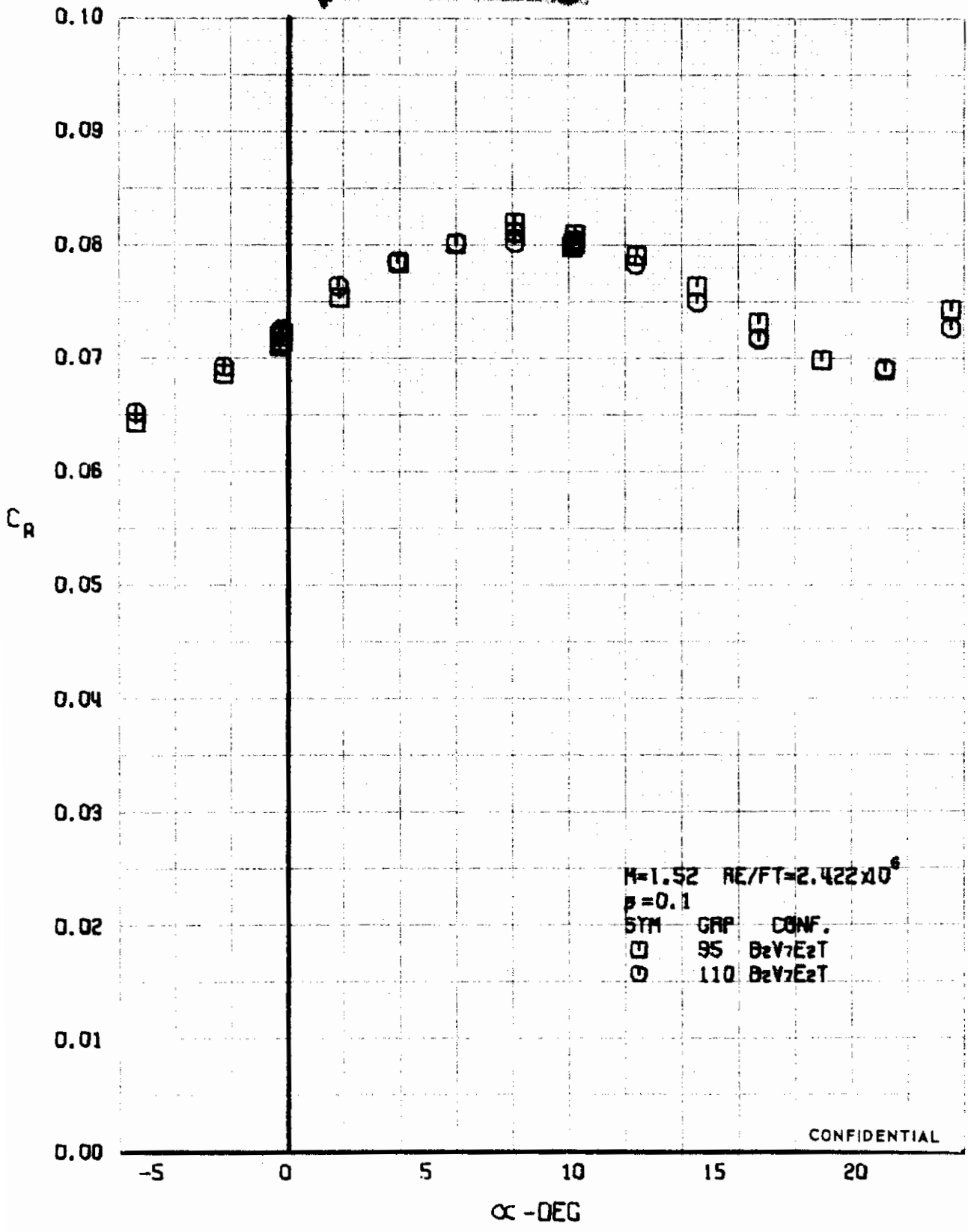

FIGURE 53 (U) REPEATABILITY
- AXIAL FORCE COEFFICIENT VARIATION WITH ANGLE OF ATTACK (M=1.52)

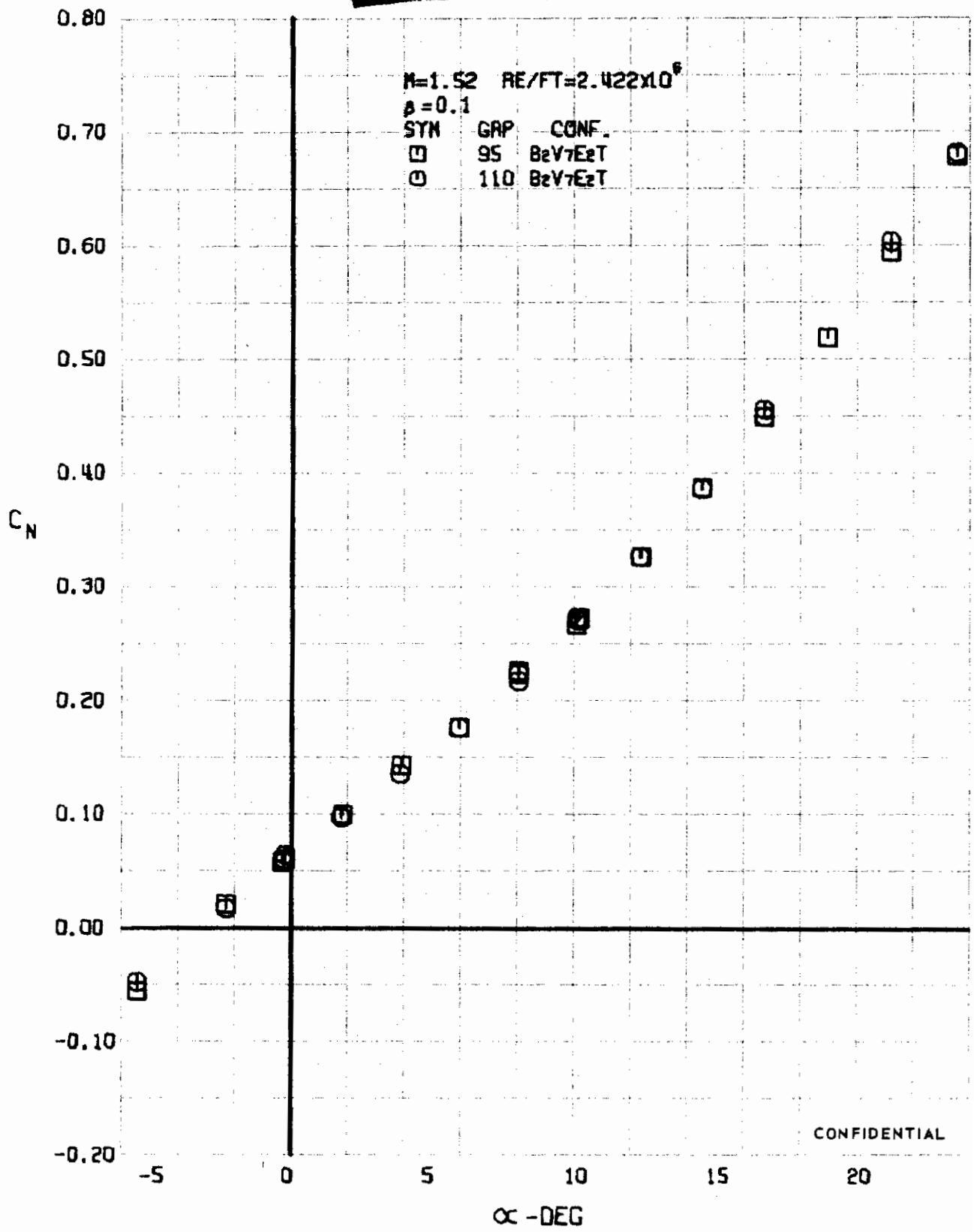

FIGURE 54 (U) REPEATABILITY
- NORMAL FORCE COEFFICIENT VARIATION WITH ANGLE OF ATTACK (M=1.52)

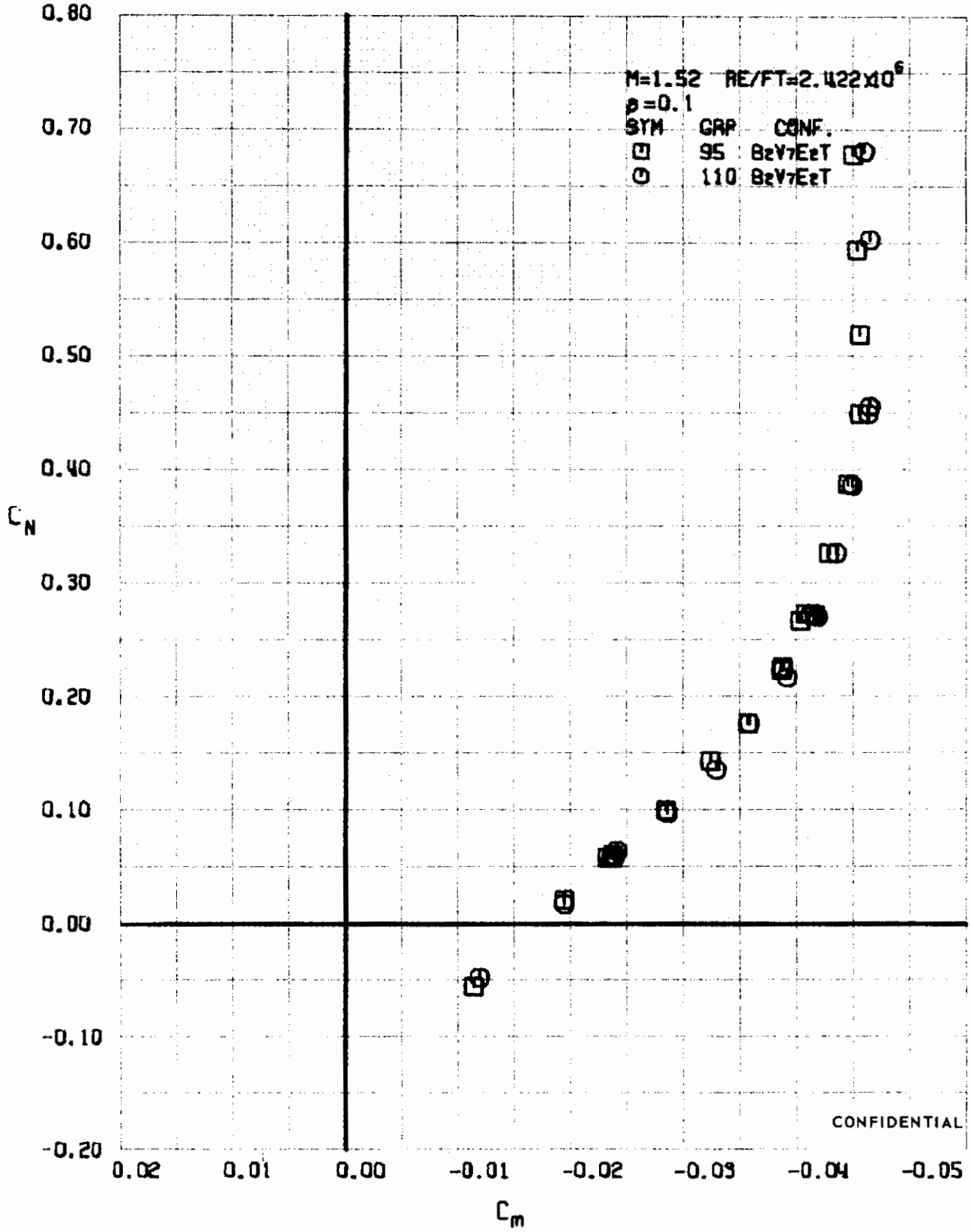

FIGURE 55 (U) REPEATABILITY
- LONGITUDINAL STABILITY VARIATION (M=1.52)

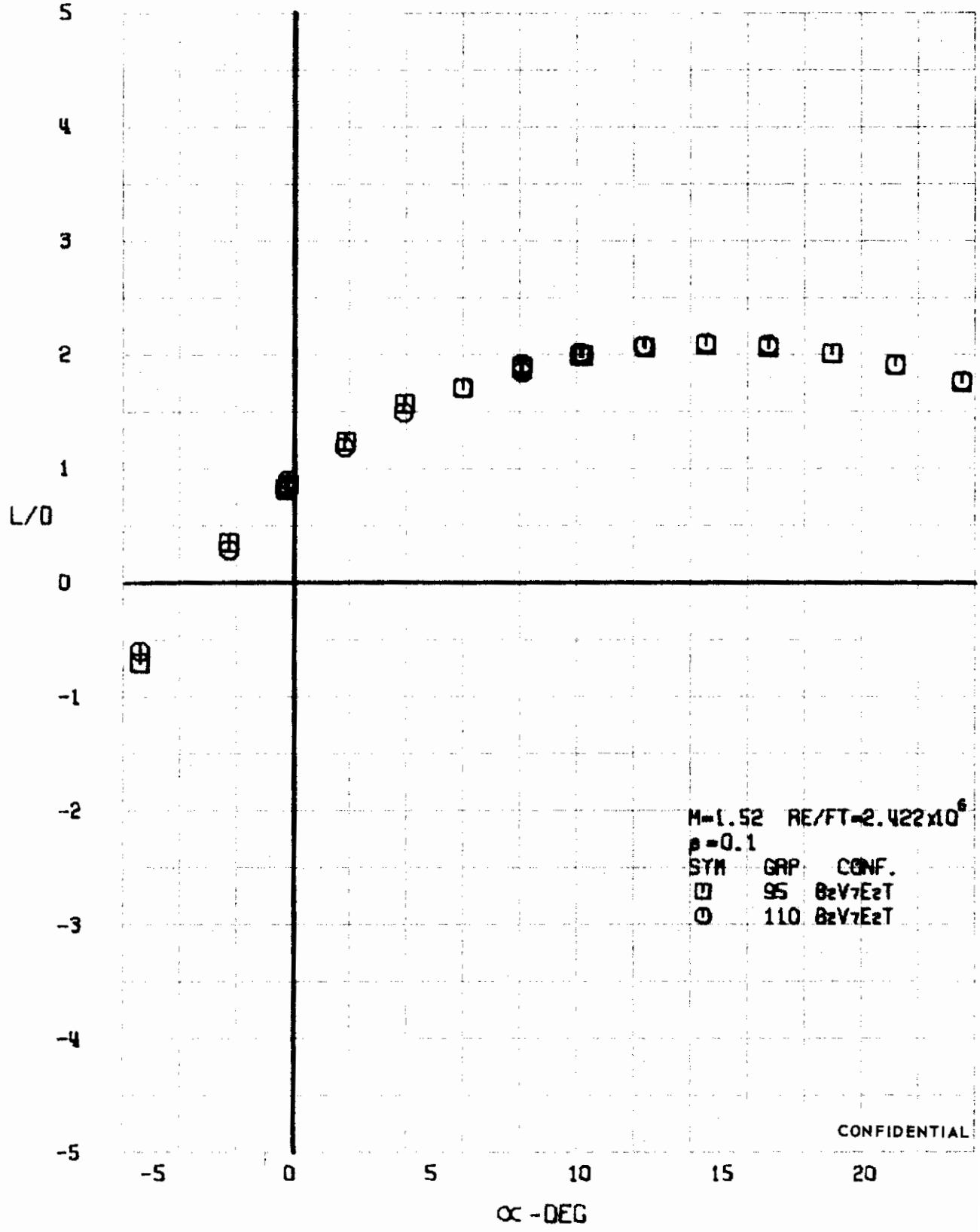

FIGURE 56 (U) REPEATABILITY
- LIFT-DRAG RATIO VARIATION WITH ANGLE OF ATTACK (M=1.52)

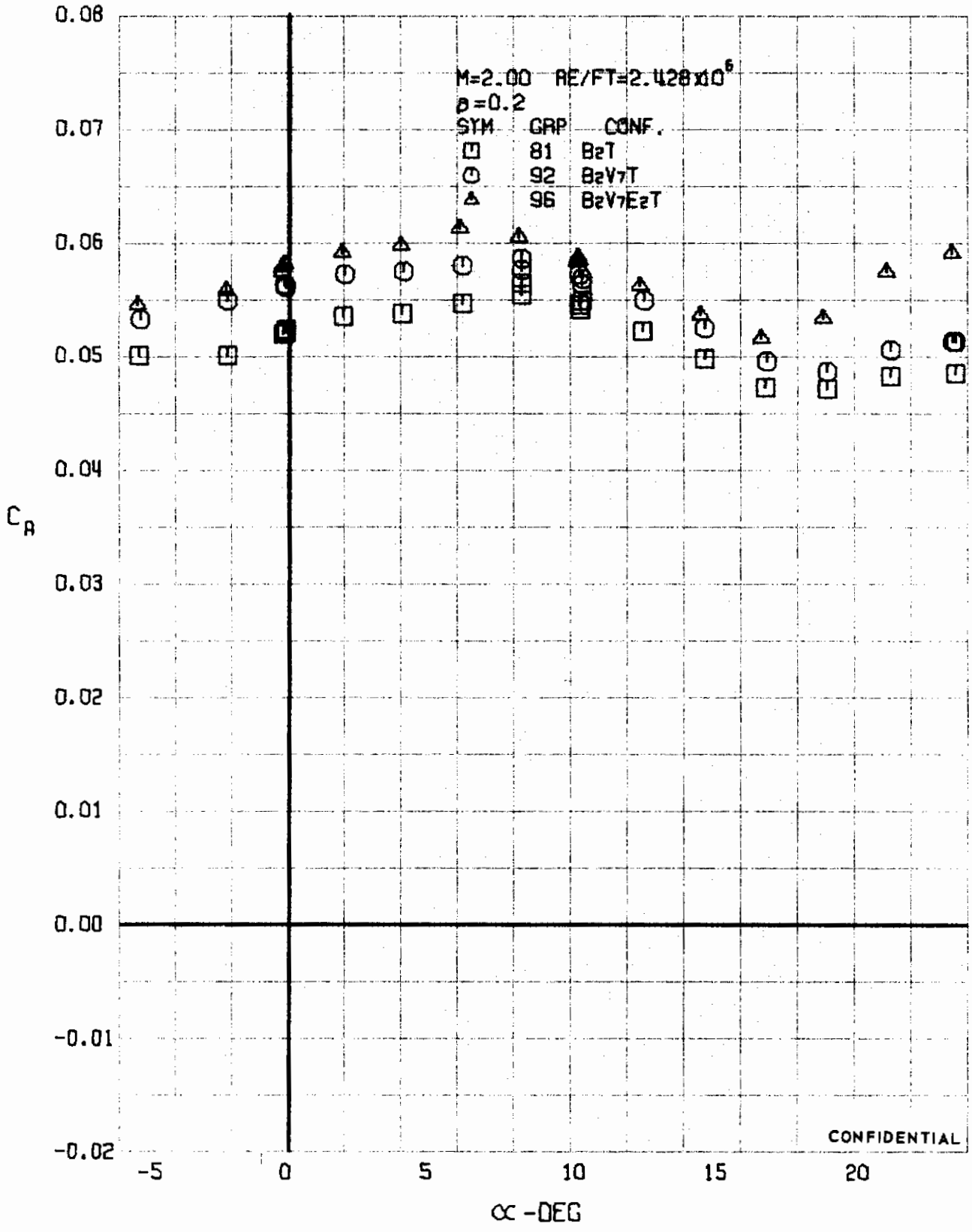

FIGURE 57 (U) CONFIGURATION BUILDUP
- AXIAL FORCE COEFFICIENT VARIATION WITH ANGLE OF ATTACK (M=2.00)

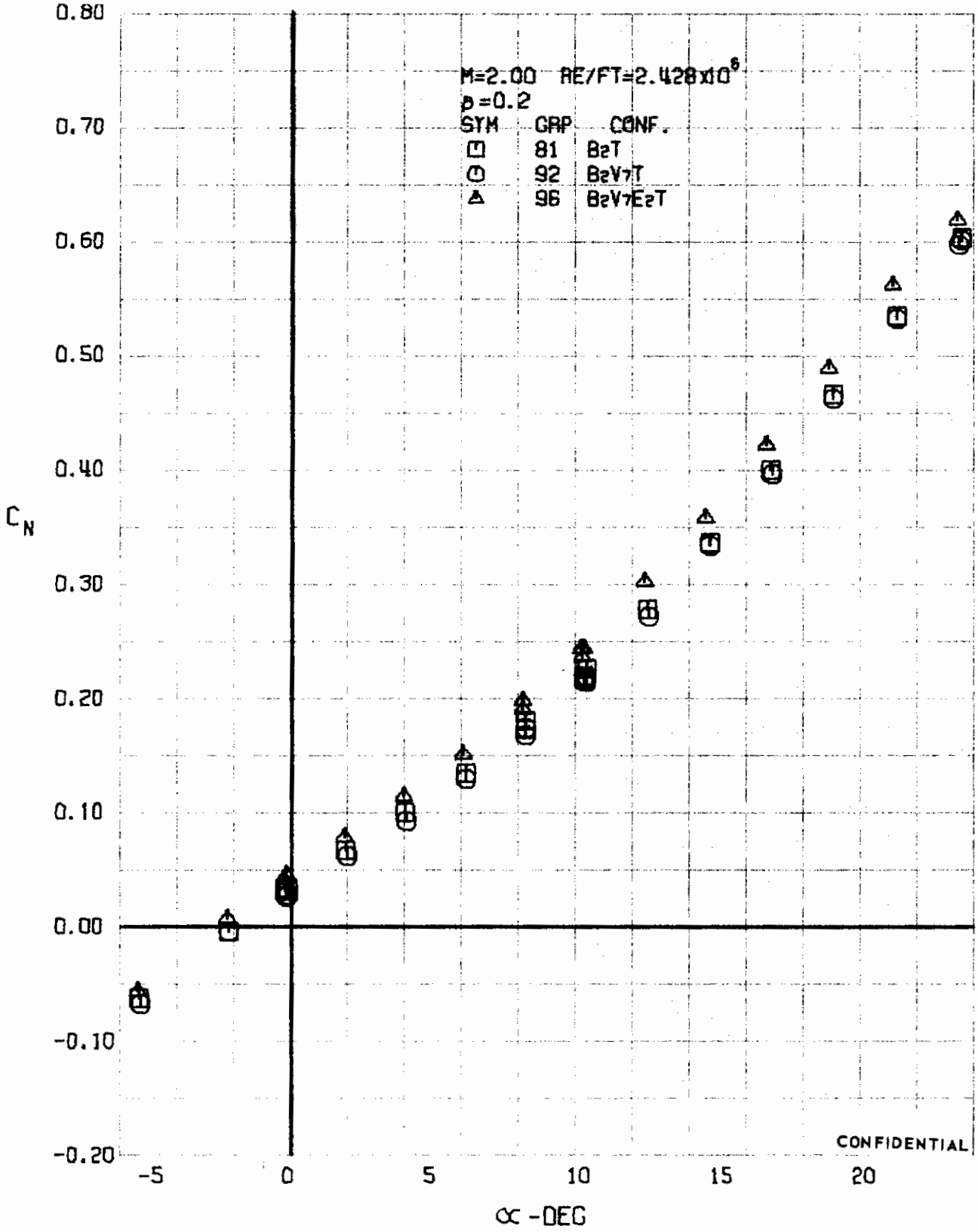

FIGURE 58 (U) CONFIGURATION BUILDUP
- NORMAL FORCE COEFFICIENT VARIATION WITH ANGLE OF ATTACK (M=2.00)

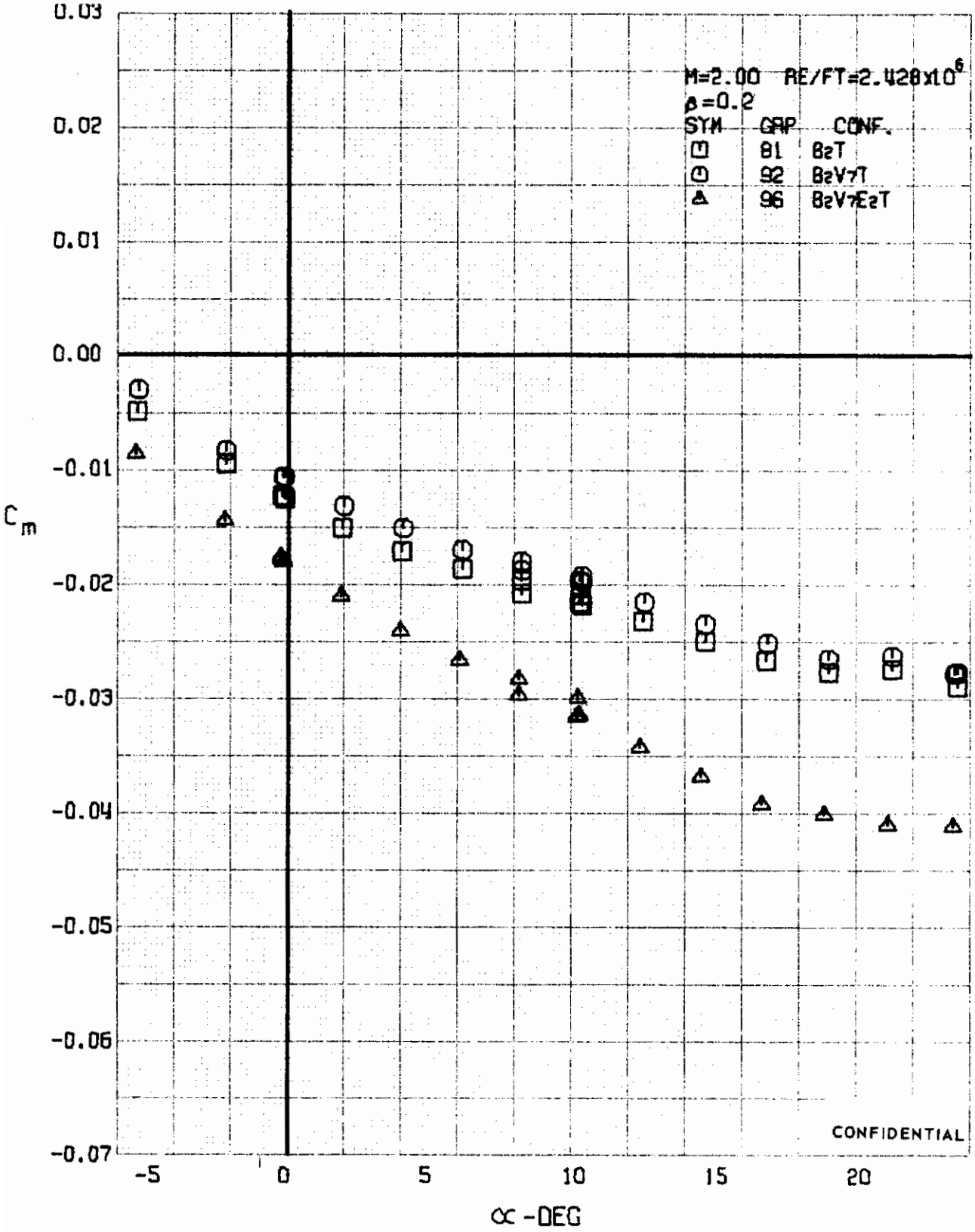

FIGURE 59 (U) CONFIGURATION BUILDUP
- PITCHING MOMENT COEFFICIENT VARIATION WITH ANGLE OF ATTACK (M=2.00)

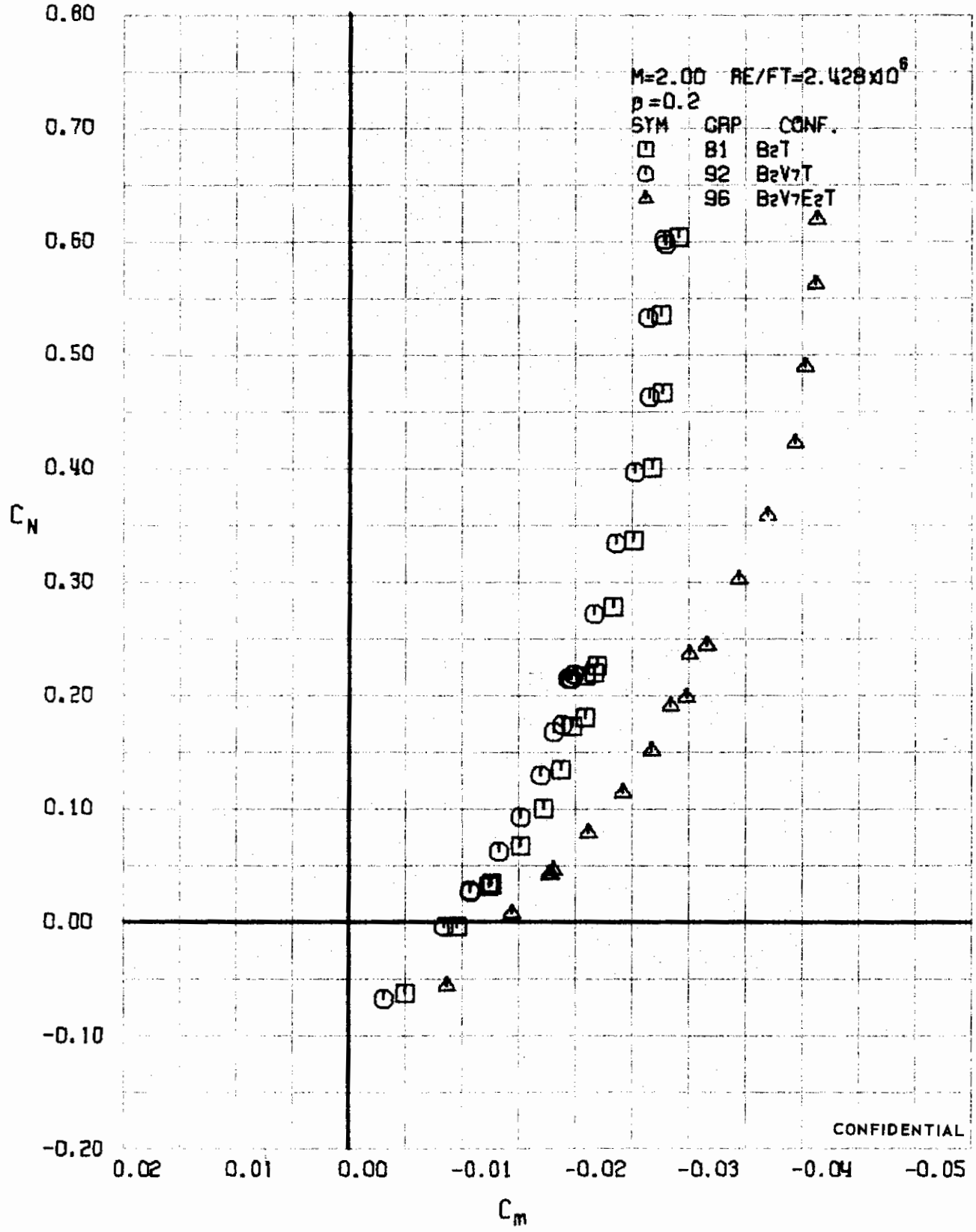

FIGURE 60 (U) CONFIGURATION BUILDUP
- LONGITUDINAL STABILITY VARIATION (M=2.00)

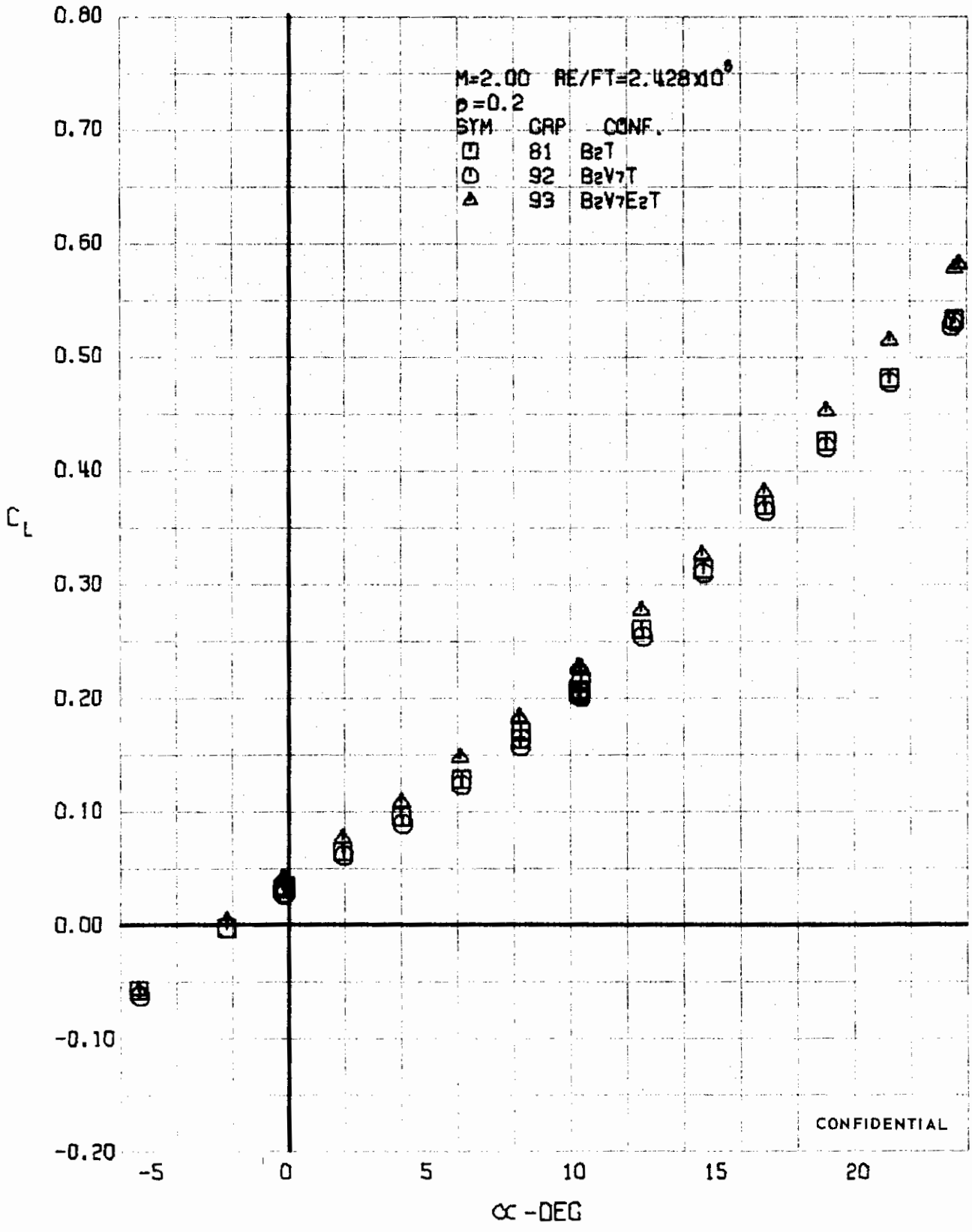

FIGURE 61 (U) CONFIGURATION BUILDUP
- LIFT COEFFICIENT VARIATION WITH ANGLE OF ATTACK (M=2.00)

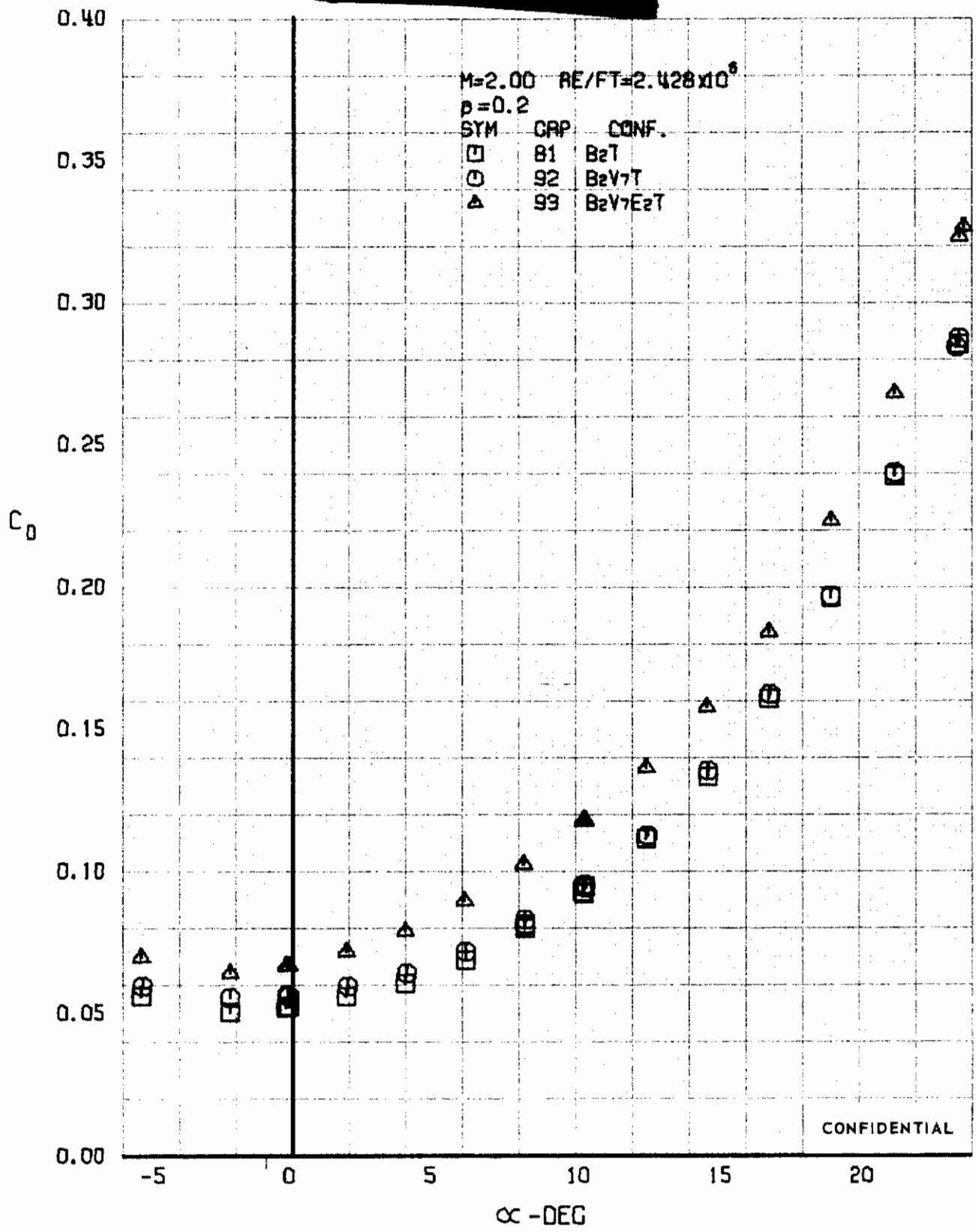

FIGURE 62 (U) CONFIGURATION BUILDUP
- DRAG COEFFICIENT VARIATION WITH ANGLE OF ATTACK (M=2.00)

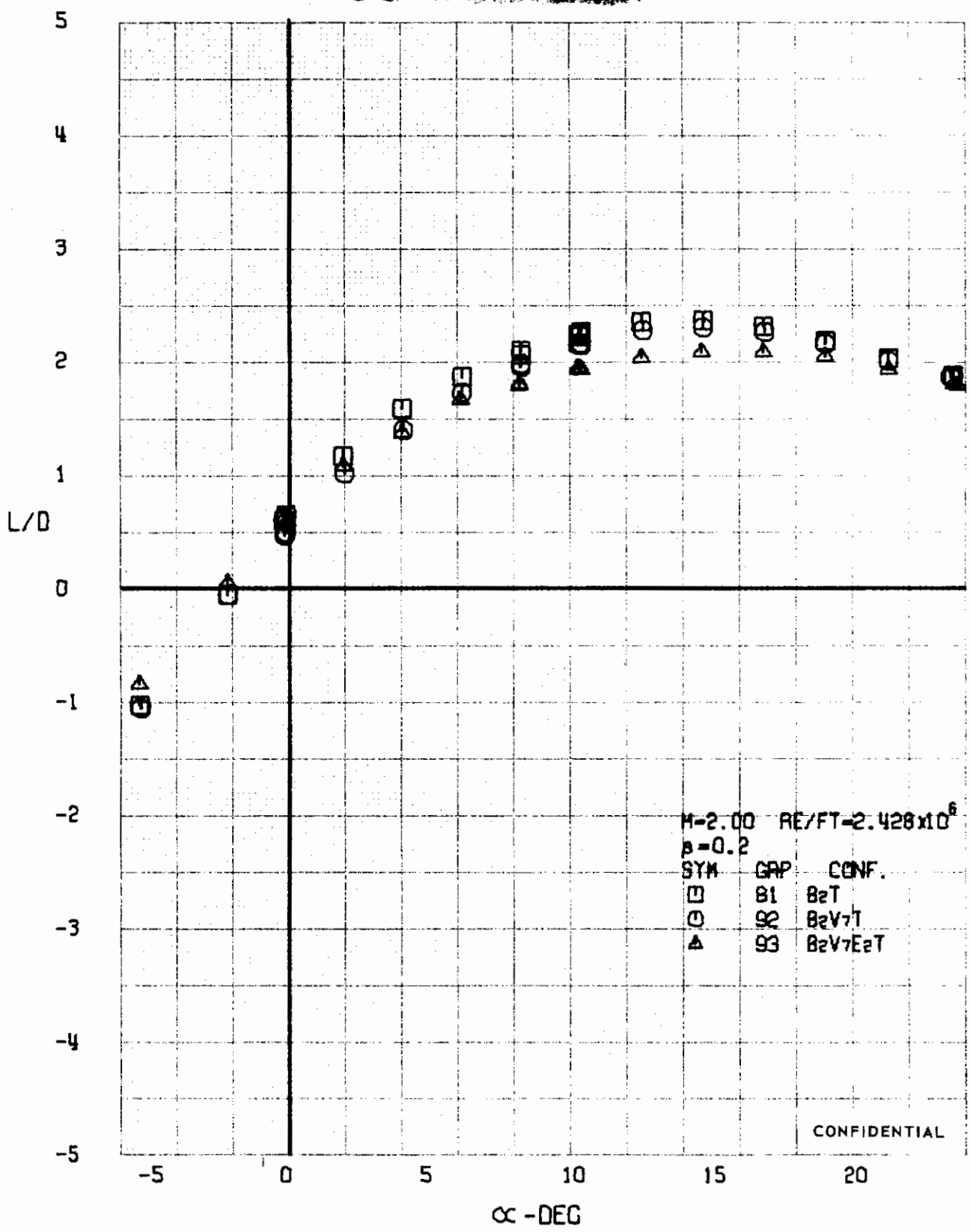

FIGURE 63 (U) CONFIGURATION BUILDUP
- LIFT-DRAG RATIO VARIATION WITH ANGLE OF ATTACK (M=2.00)

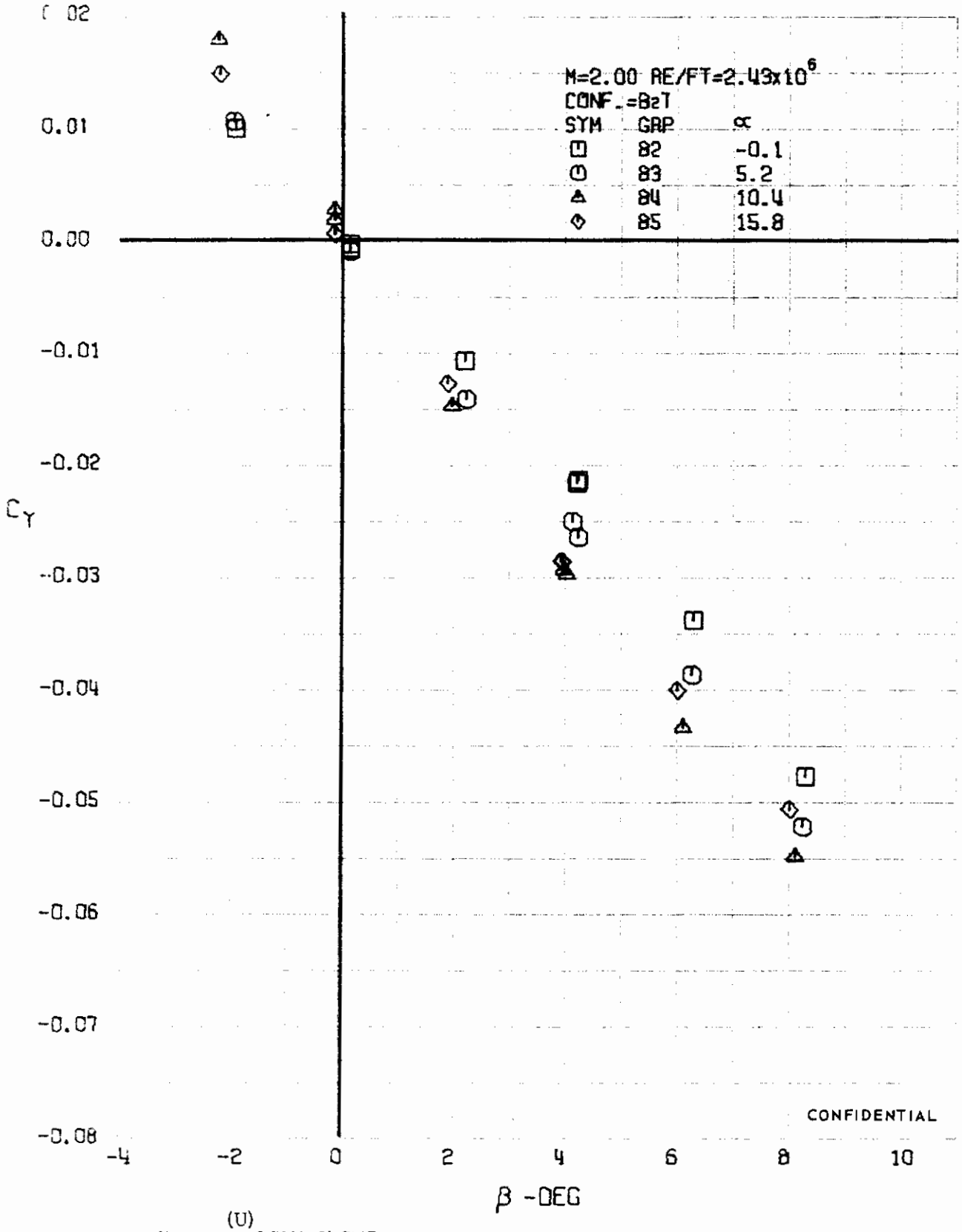

(U)

FIGURE 64 BODY ALONE
- SIDE FORCE COEFFICIENT VARIATION WITH ANGLE OF YAW (M=2.00)

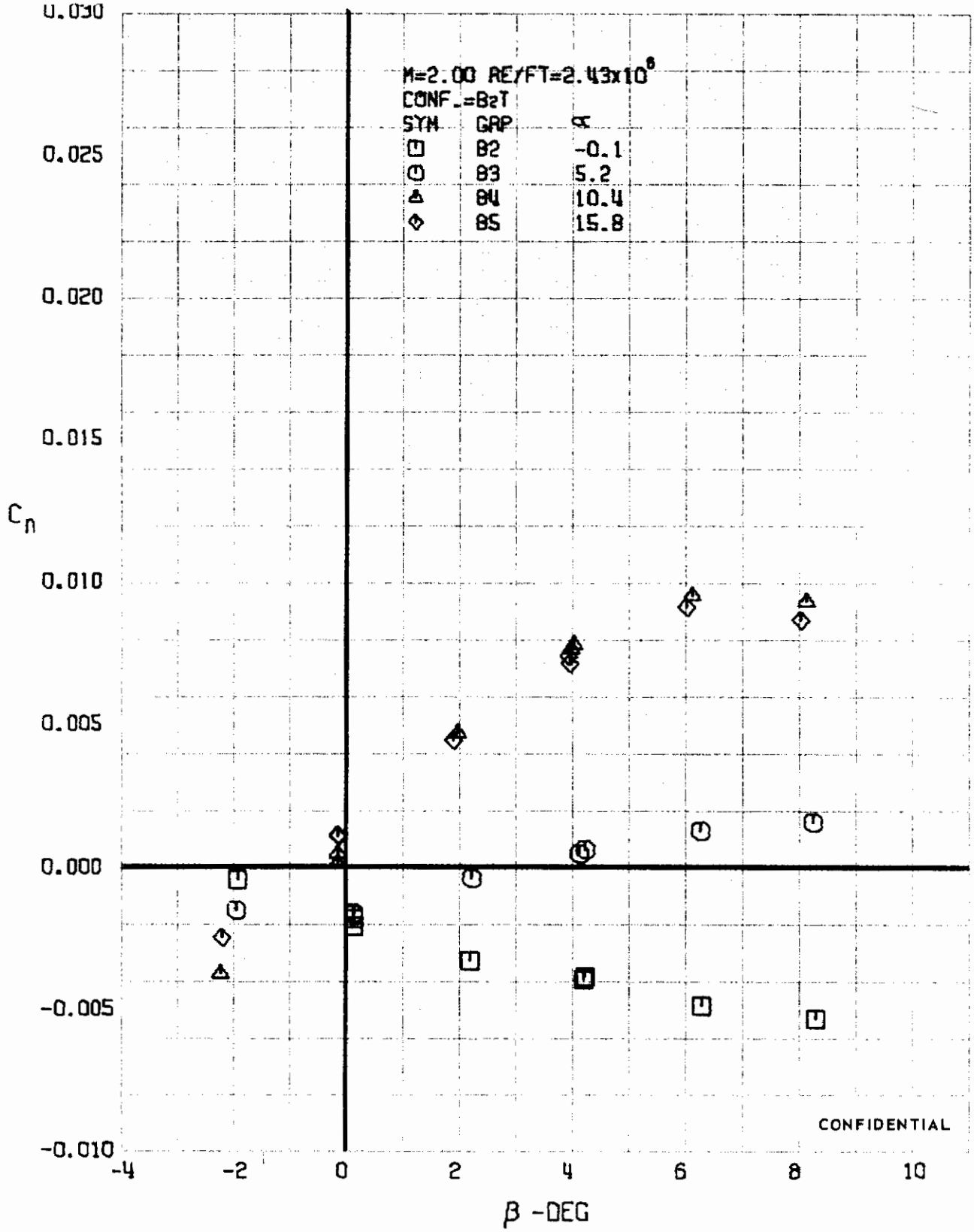

FIGURE 65 (U) BODY ALONE
- YAWING MOMENT COEFFICIENT VARIATION WITH ANGLE OF YAW (M=2.00)

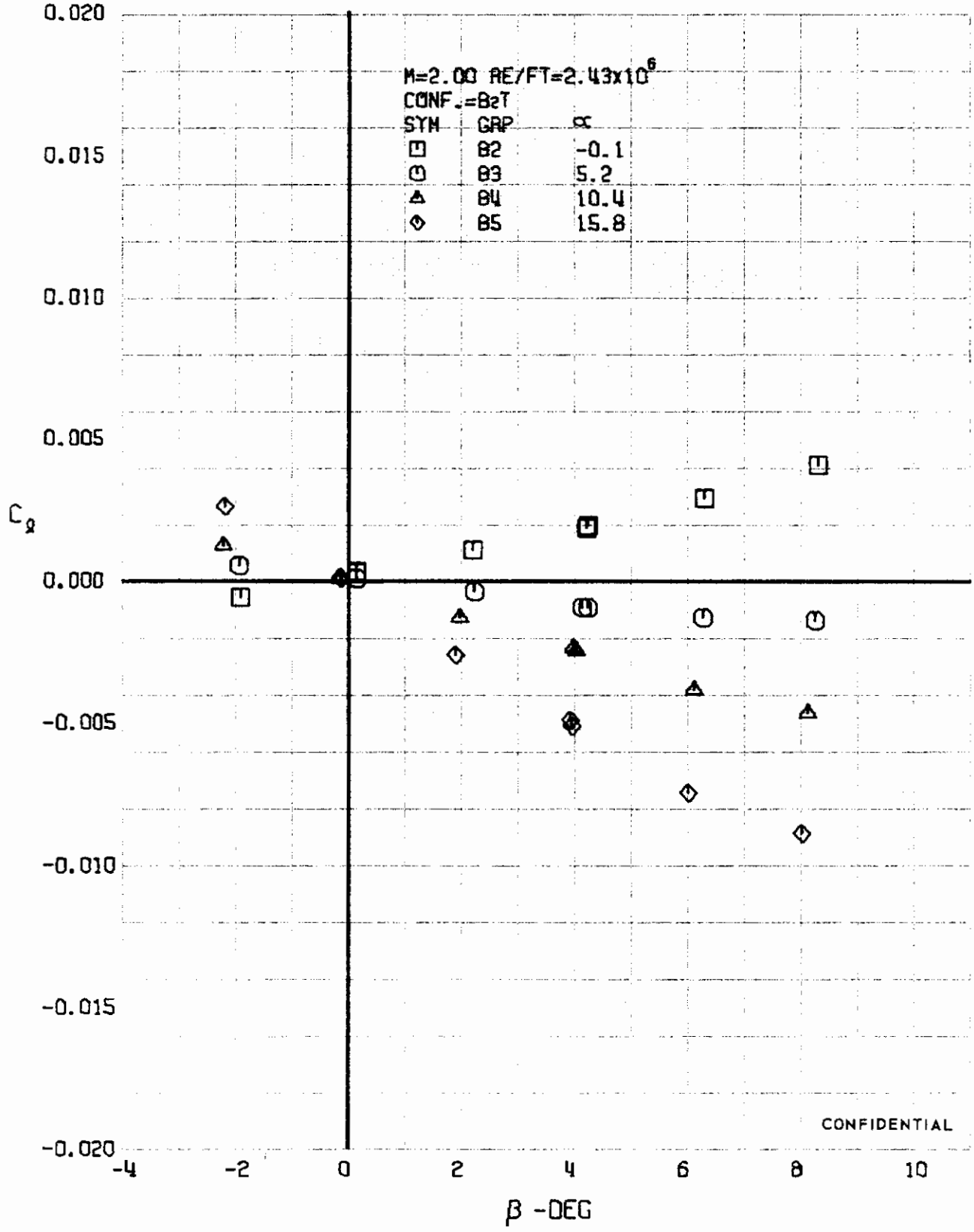

FIGURE 66 (U) BODY ALONE
- ROLLING MOMENT COEFFICIENT VARIATION WITH ANGLE OF YAW (M=2.00)

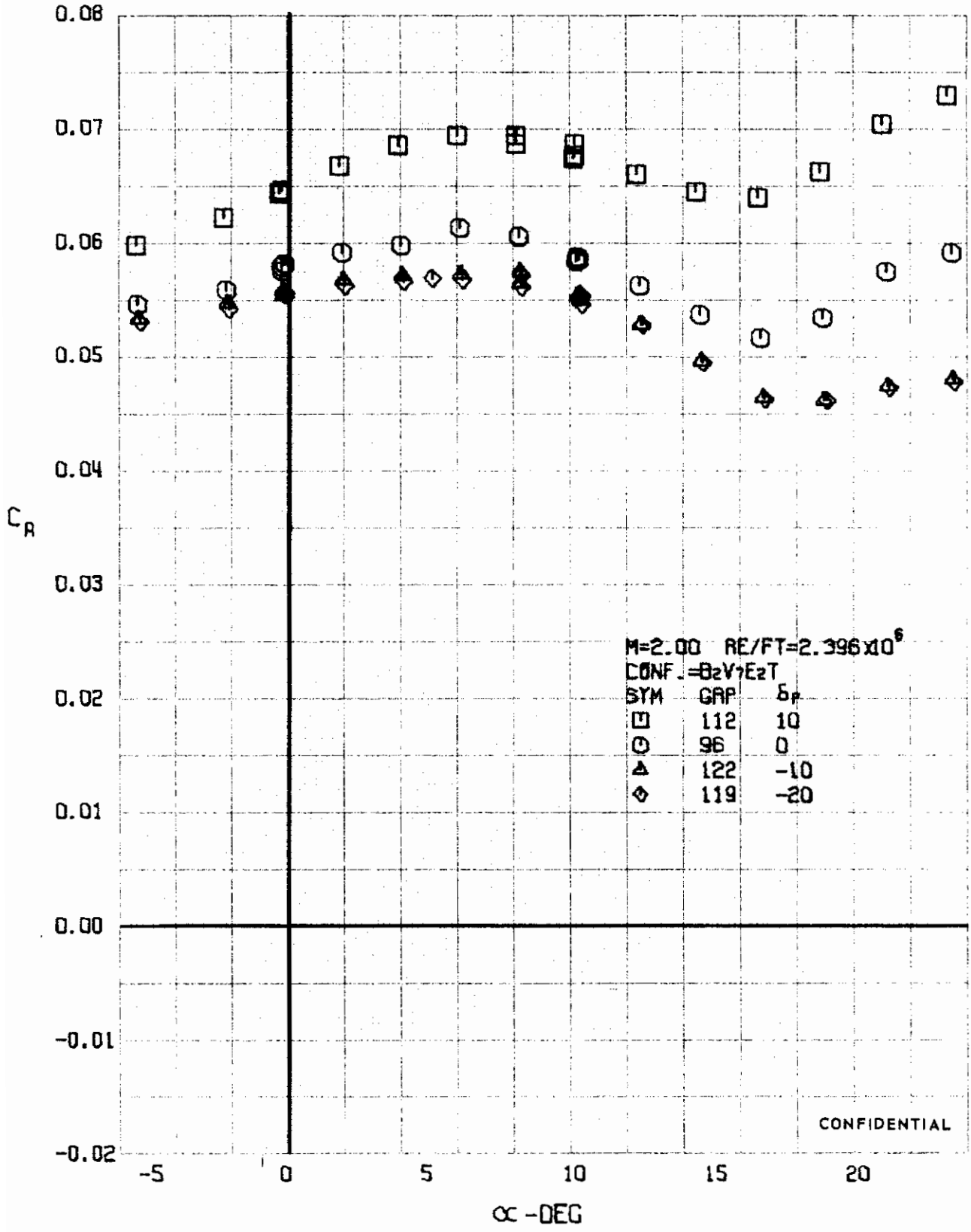

FIGURE 67 (U) ELEVON EFFECTS
- AXIAL FORCE COEFFICIENT VARIATION WITH ANGLE OF ATTACK (M=2.00)

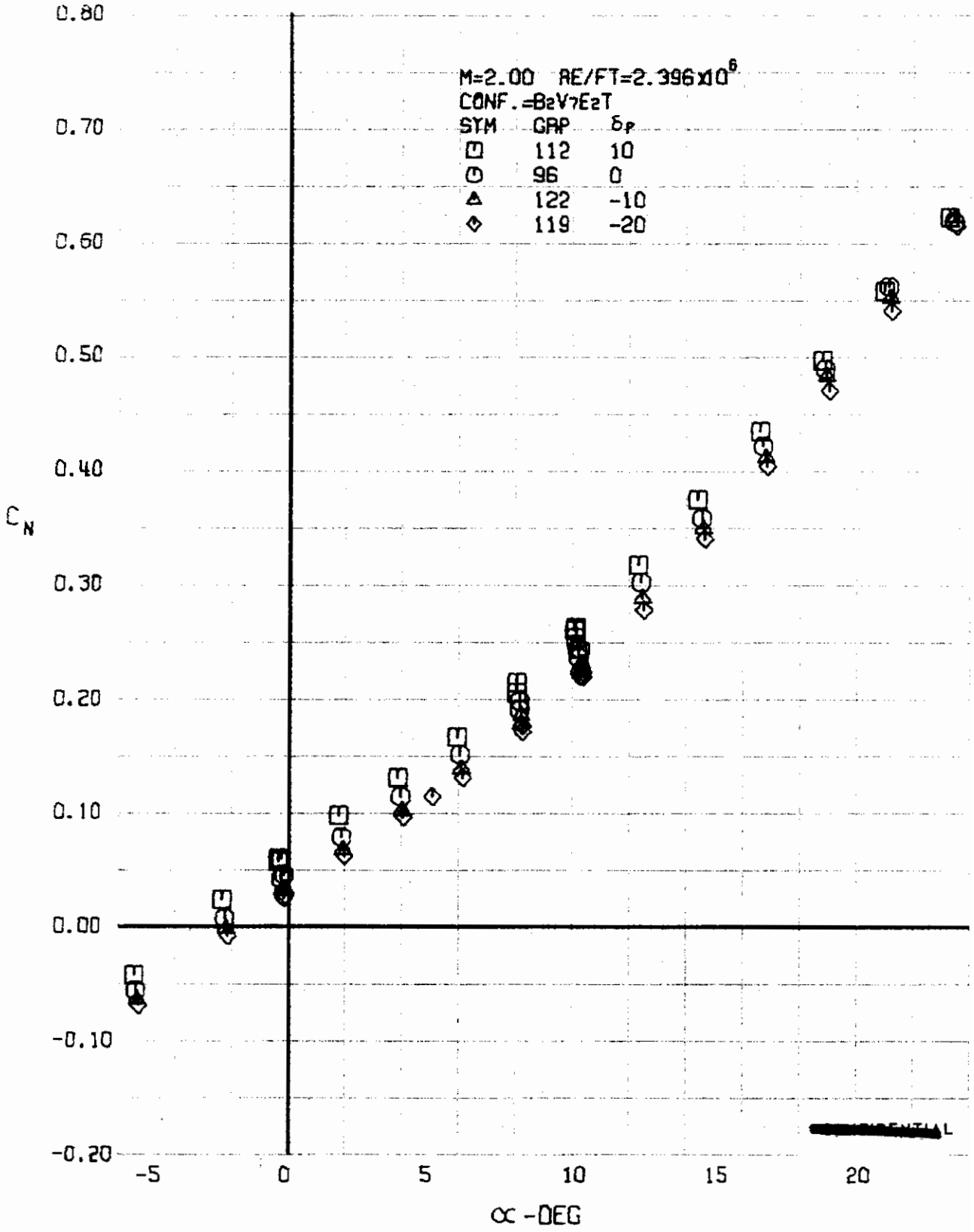

FIGURE 68 (U) ELEVON EFFECTS
- NORMAL FORCE COEFFICIENT VARIATION WITH ANGLE OF ATTACK (M=2.00)

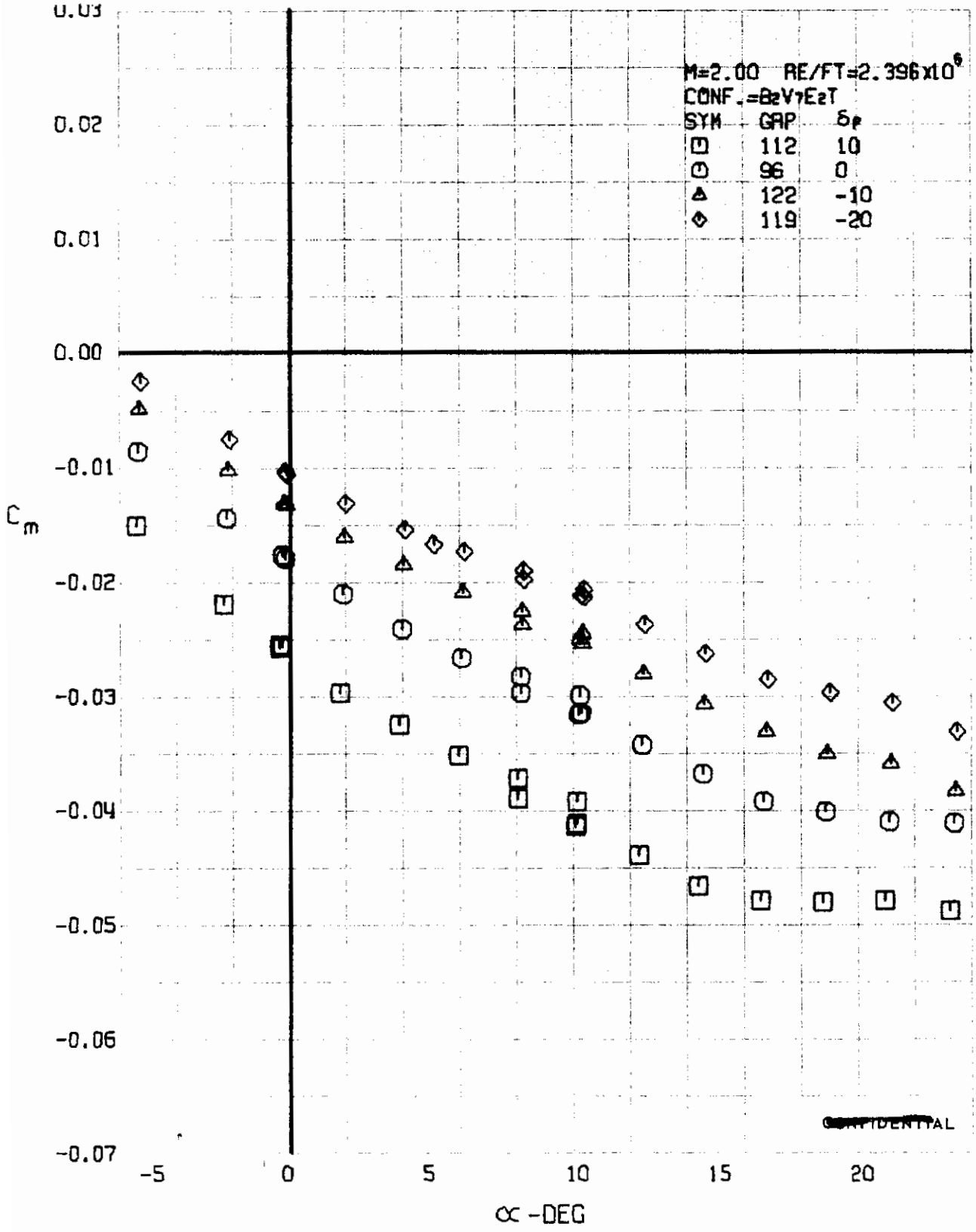

FIGURE 69 (U) ELEVON EFFECTS
- PITCHING MOMENT COEFFICIENT VARIATION WITH ANGLE OF ATTACK (M=2.00)

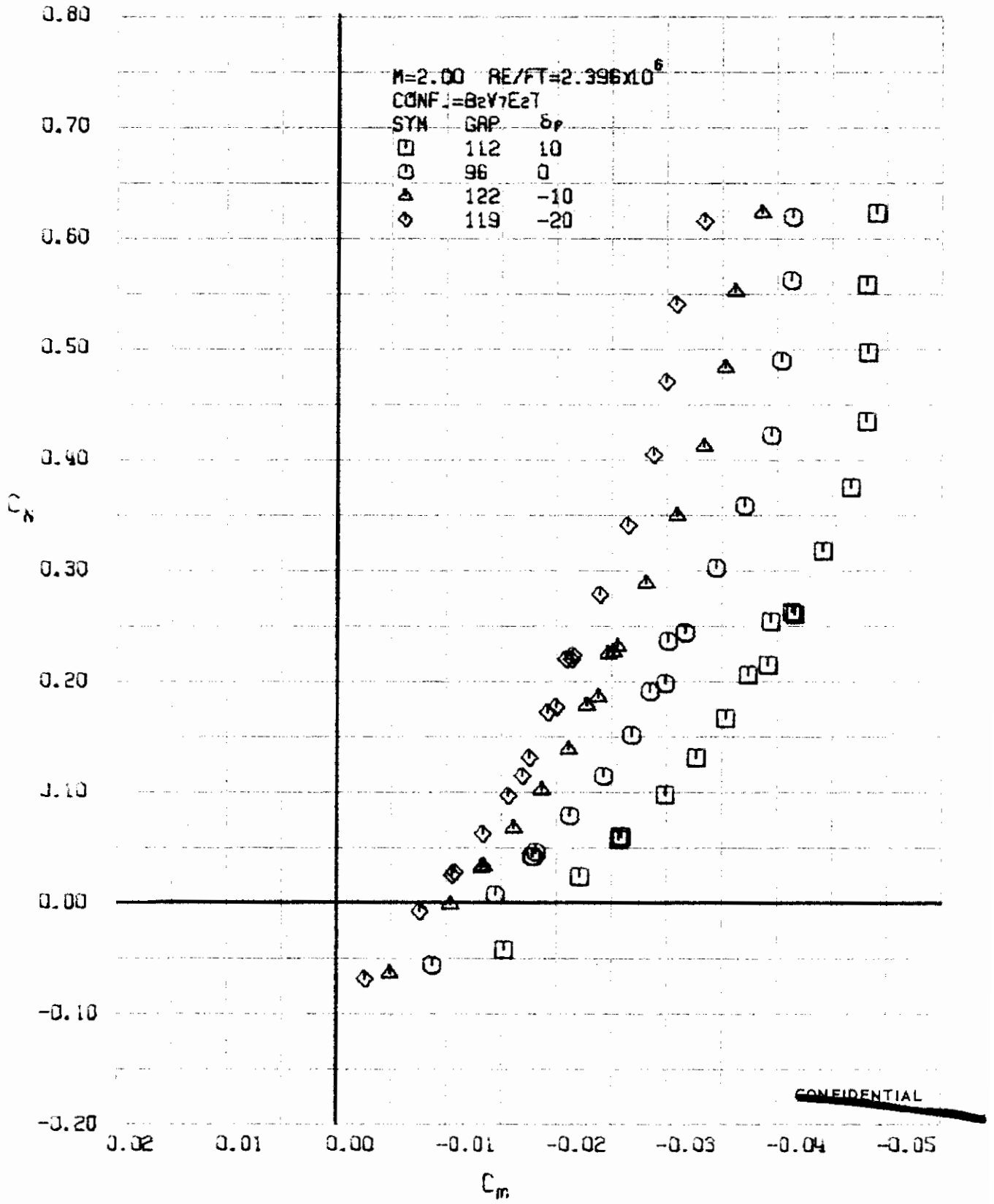

FIGURE 70 (U) ELEVON EFFECTS
- LONGITUDINAL STABILITY VARIATION (M=2.00)

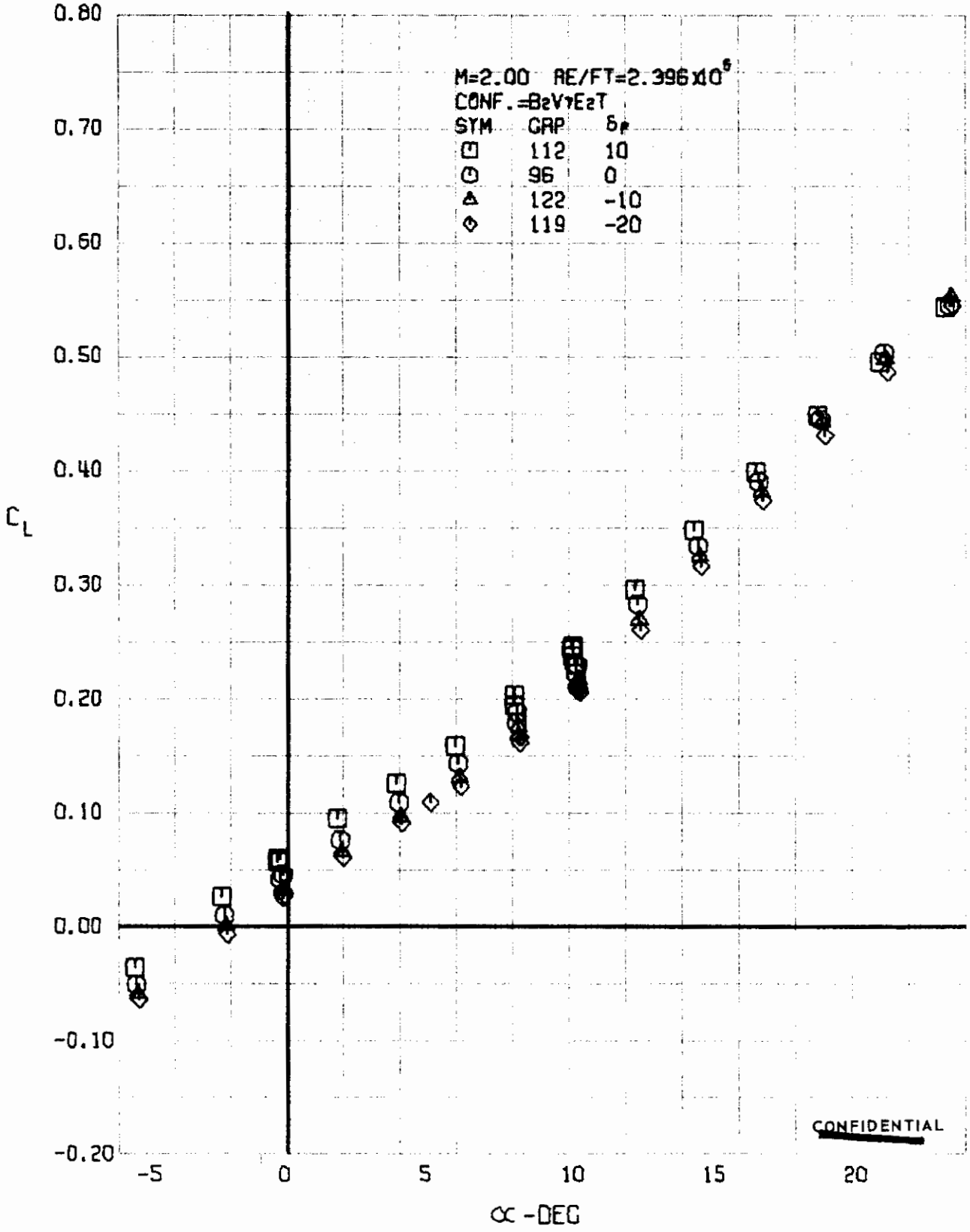

FIGURE 72 (U) ELEVON EFFECTS
- LIFT COEFFICIENT VARIATION WITH ANGLE OF ATTACK (M=2.00)

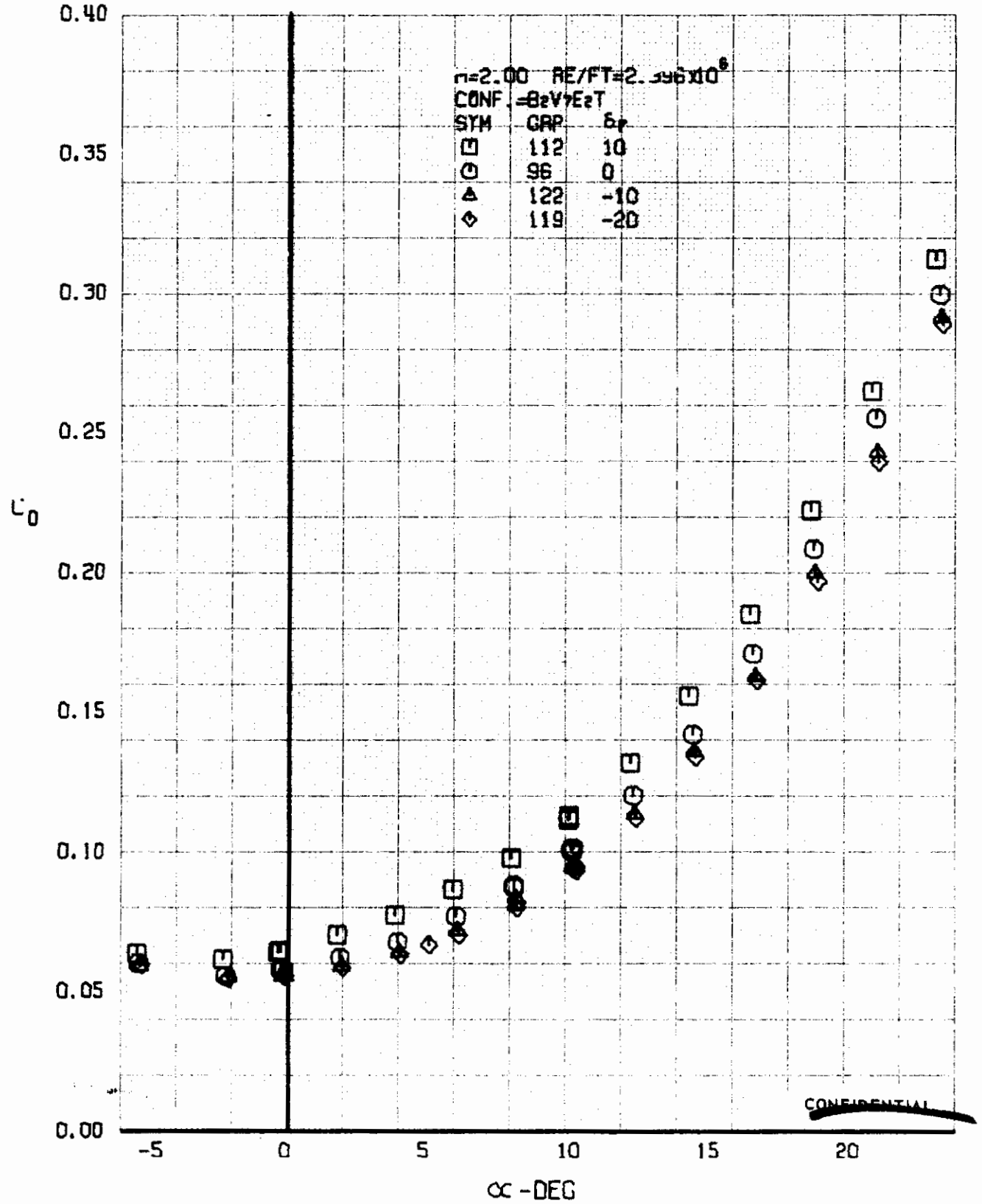

FIGURE 72 (U) ELEVON EFFECTS
- DRAG COEFFICIENT VARIATION WITH ANGLE OF ATTACK (M=2.00)

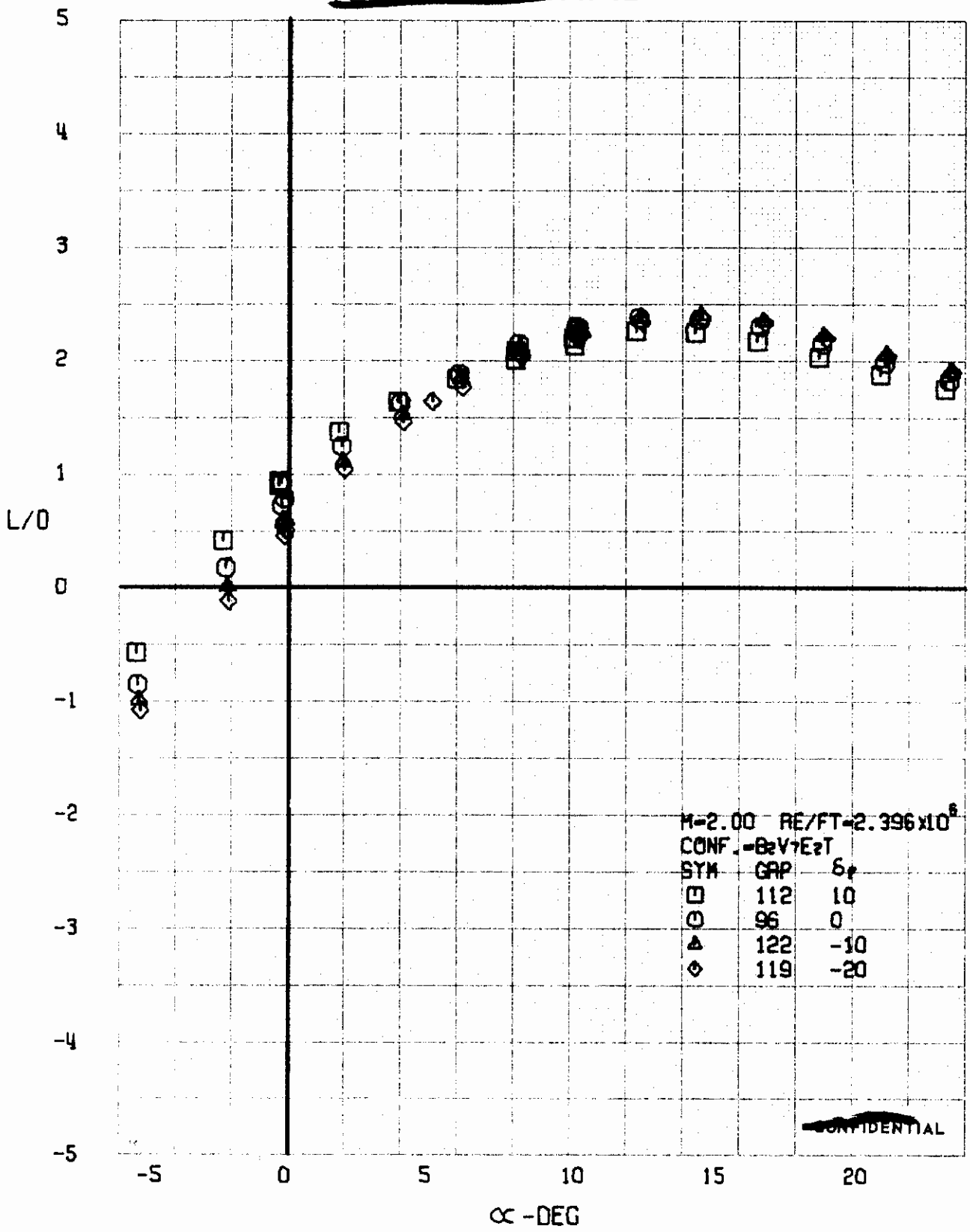

FIGURE 73 (U) ELEVON EFFECTS
- LIFT-DRAG RATIO VARIATION WITH ANGLE OF ATTACK (M=2.00)

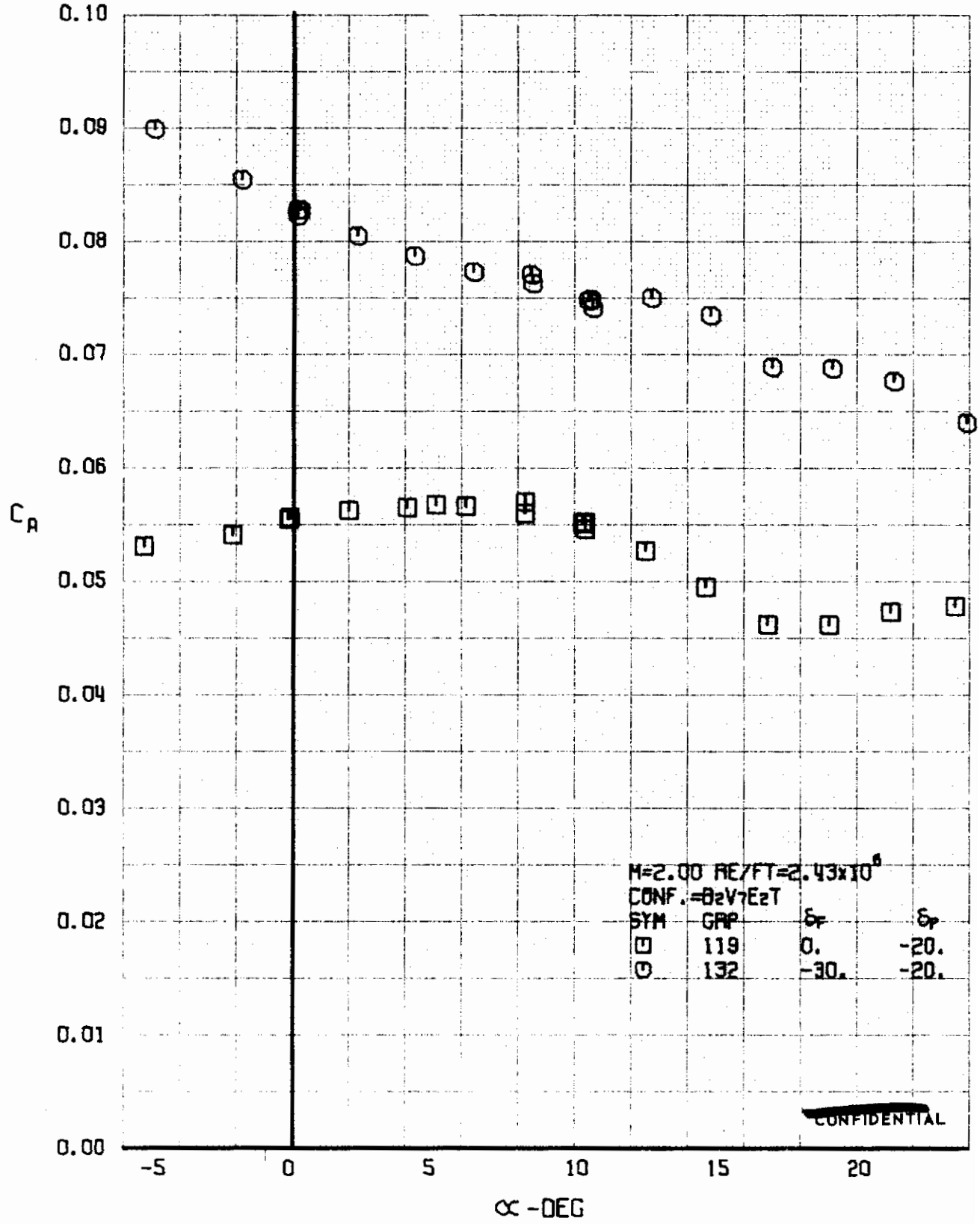

FIGURE 74 (U) FLAP EFFECTS
- AXIAL FORCE COEFFICIENT VARIATION WITH ANGLE OF ATTACK (M=2.00)

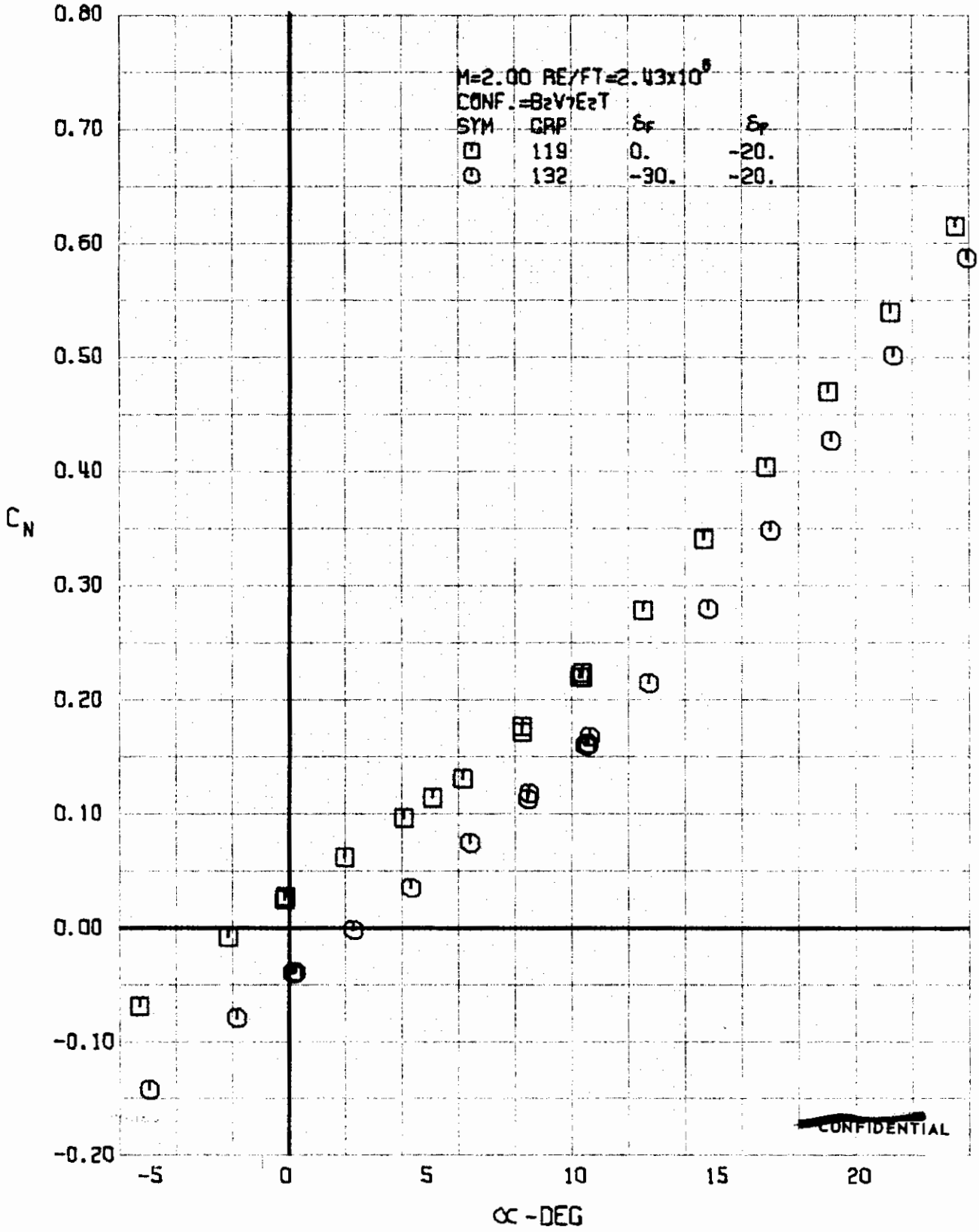

FIGURE 75 (U) FLAP EFFECTS
- NORMAL FORCE COEFFICIENT VARIATION WITH ANGLE OF ATTACK (M=2.00)

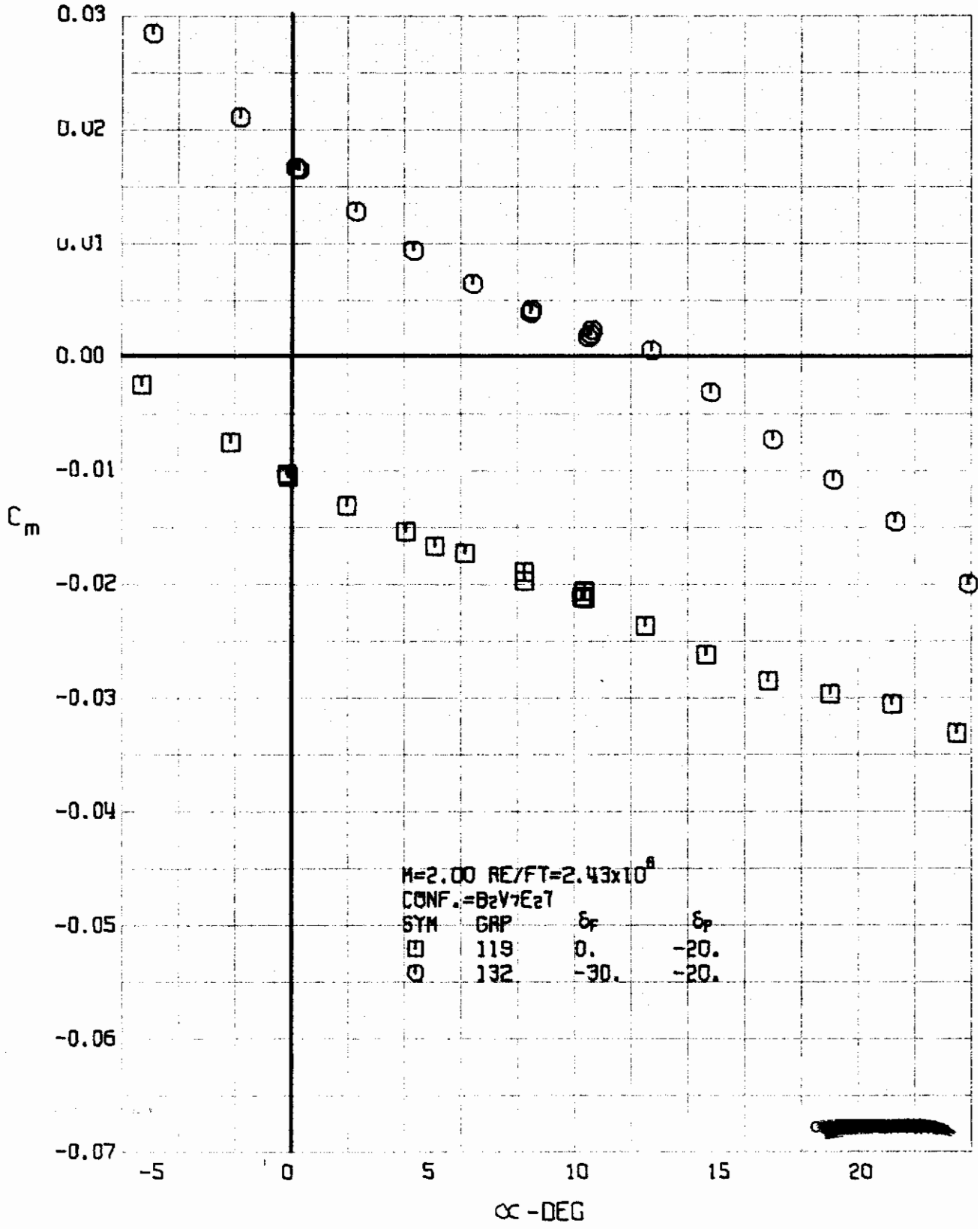

FIGURE 76 (U) FLAP EFFECTS
- PITCHING MOMENT COEFFICIENT VARIATION WITH ANGLE OF ATTACK (M=2.00)

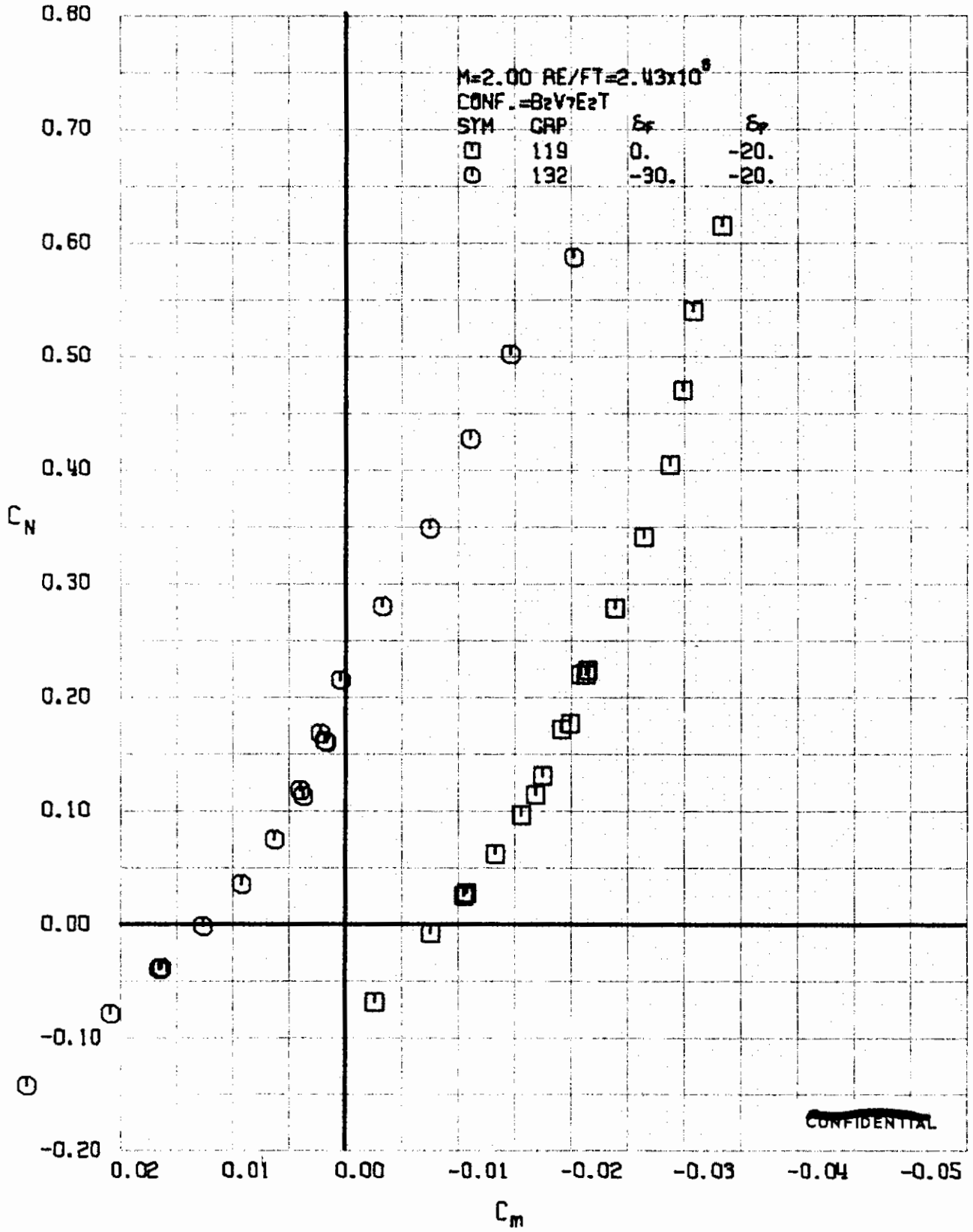

FIGURE 77 (U) FLAP EFFECTS
- LONGITUDINAL STABILITY VARIATION (M=2.00)

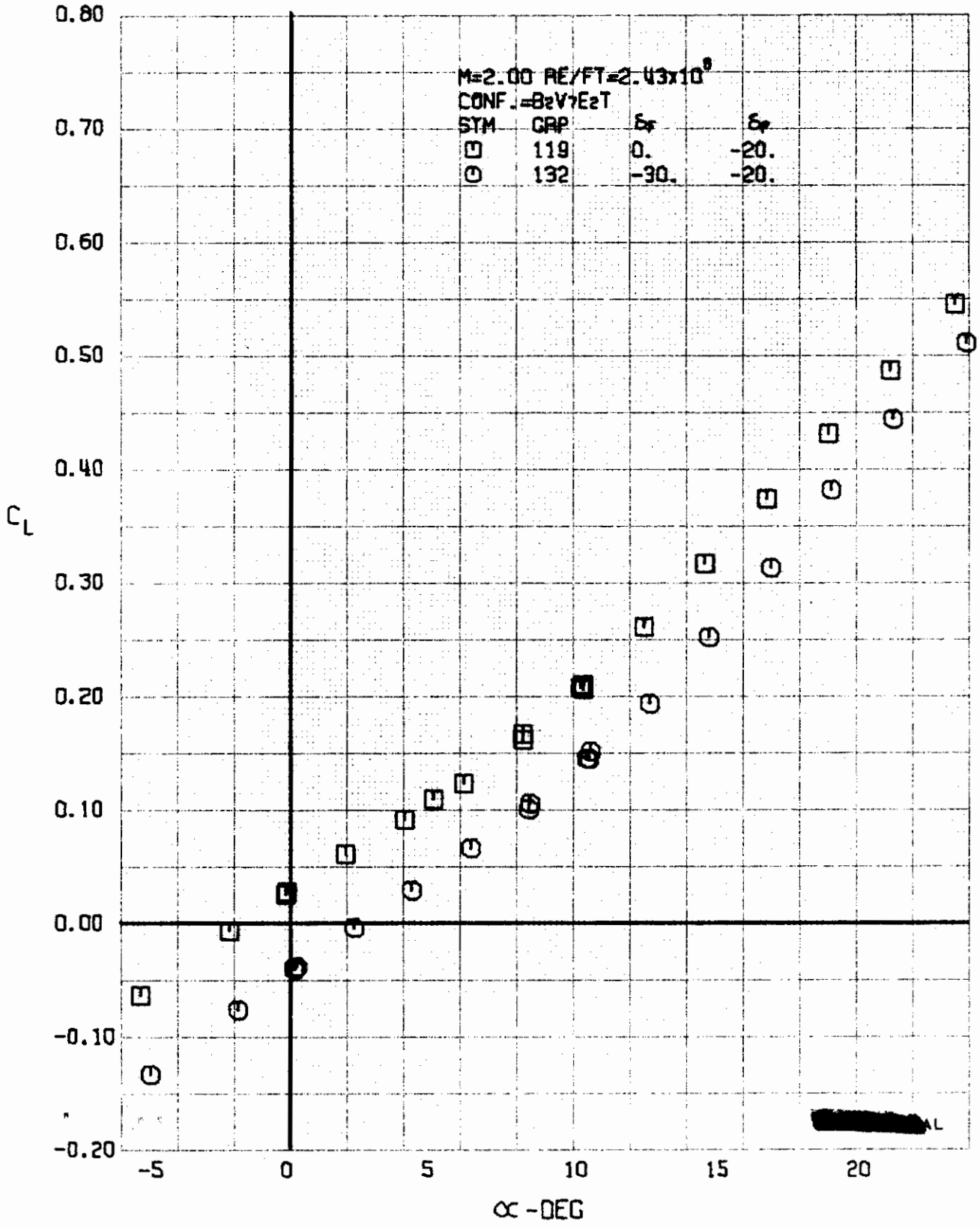

FIGURE 78 (U) FLAP EFFECTS
- LIFT COEFFICIENT VARIATION WITH ANGLE OF ATTACK (M=2.00)

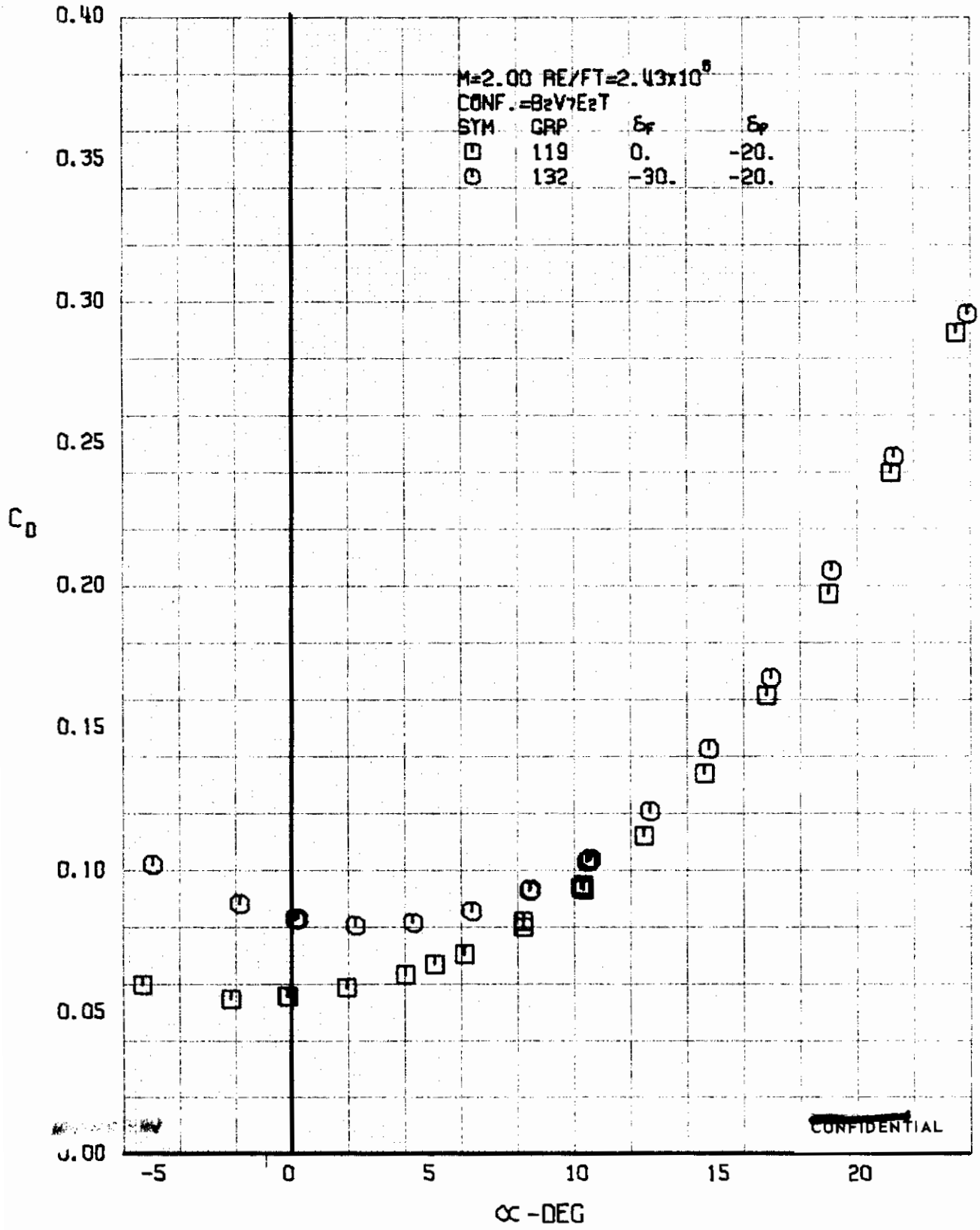

FIGURE 79 (U) FLAP EFFECTS
- DRAG COEFFICIENT VARIATION WITH ANGLE OF ATTACK (M=2.00)

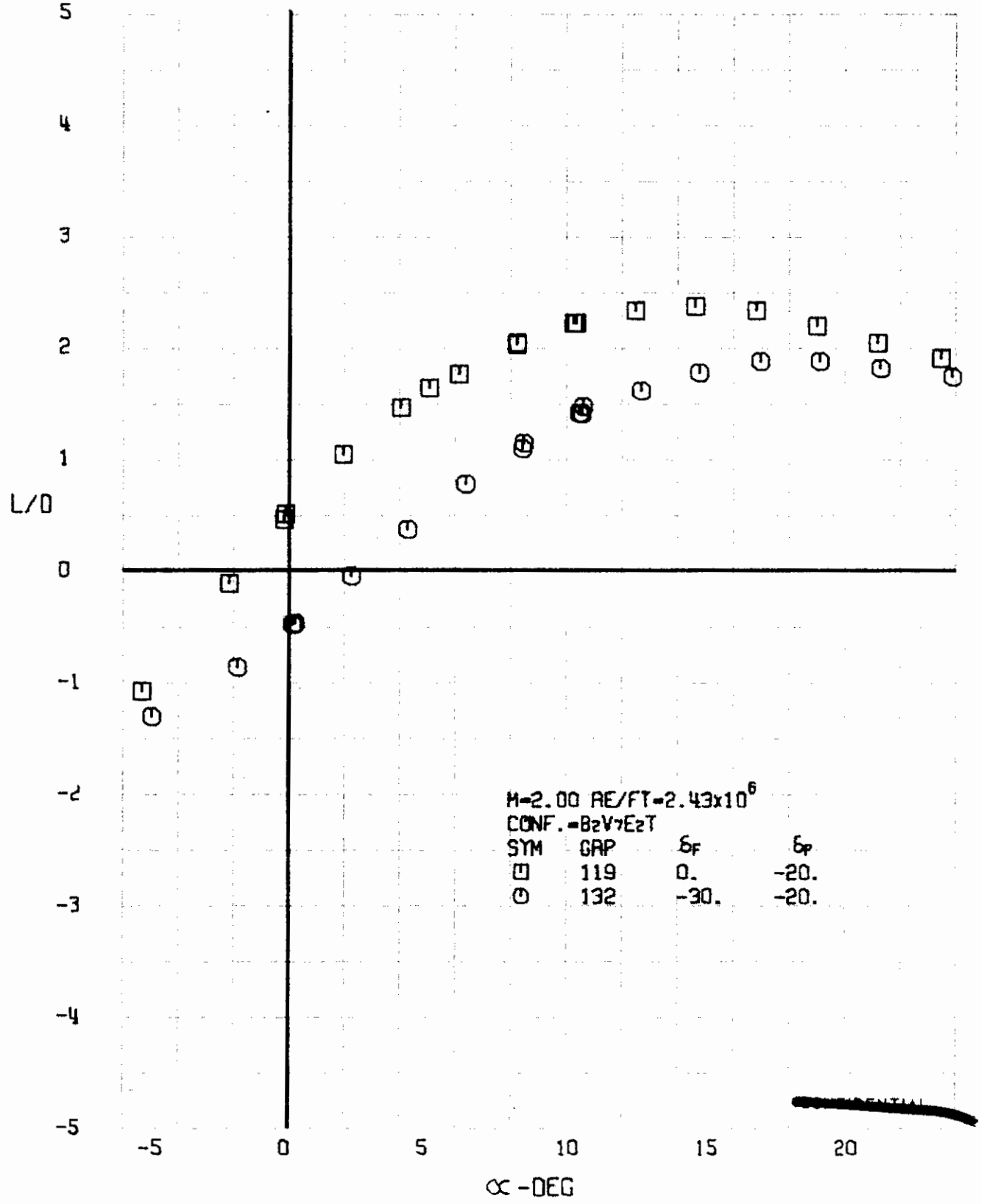

FIGURE 80 (U) FLAP EFFECTS
- LIFT-DRAG RATIO VARIATION WITH ANGLE OF ATTACK (M=2.00)

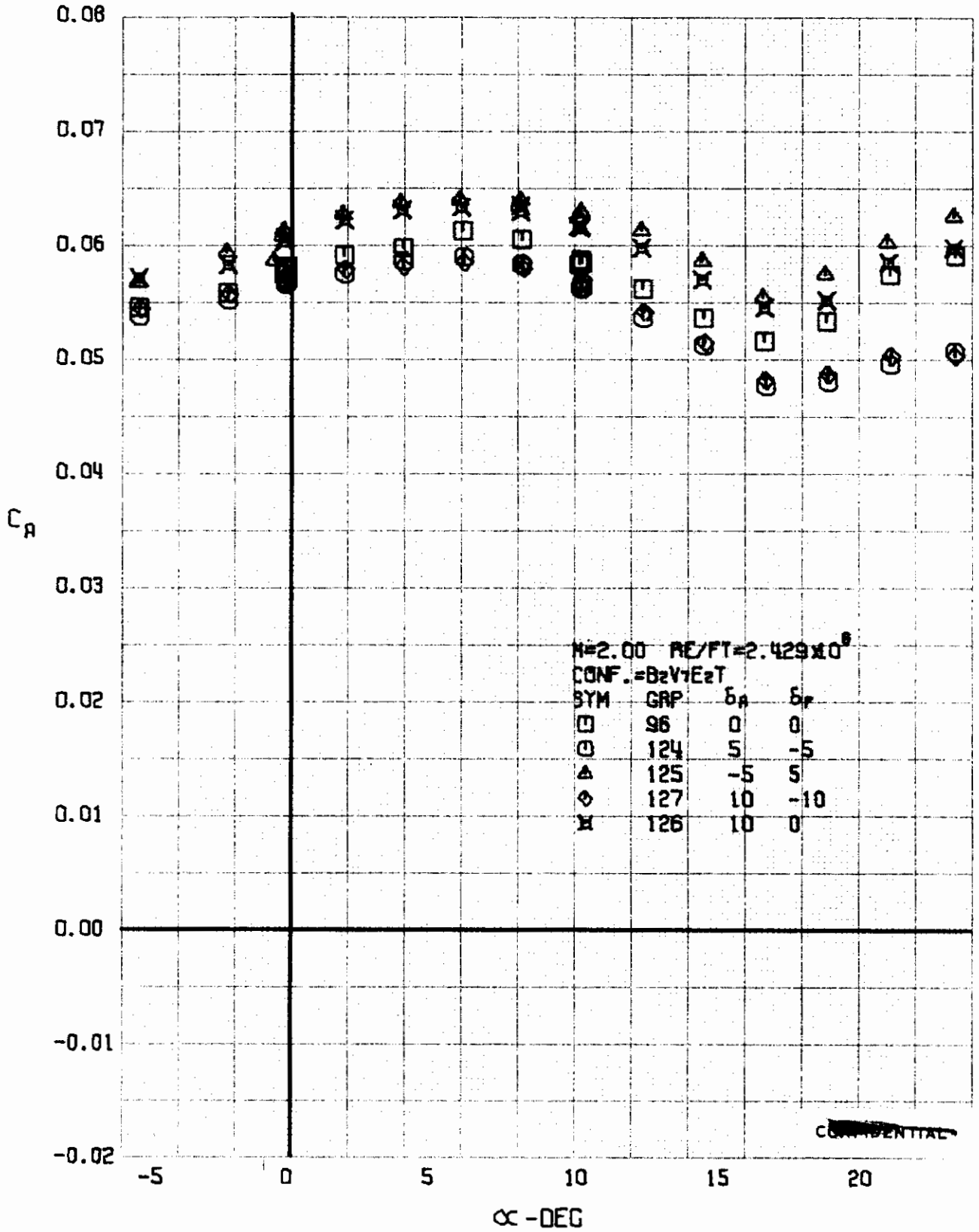

FIGURE 81 (U) AILERON EFFECTS
- AXIAL FORCE COEFFICIENT VARIATION WITH ANGLE OF ATTACK (M=2.00)

CONFIDENTIAL

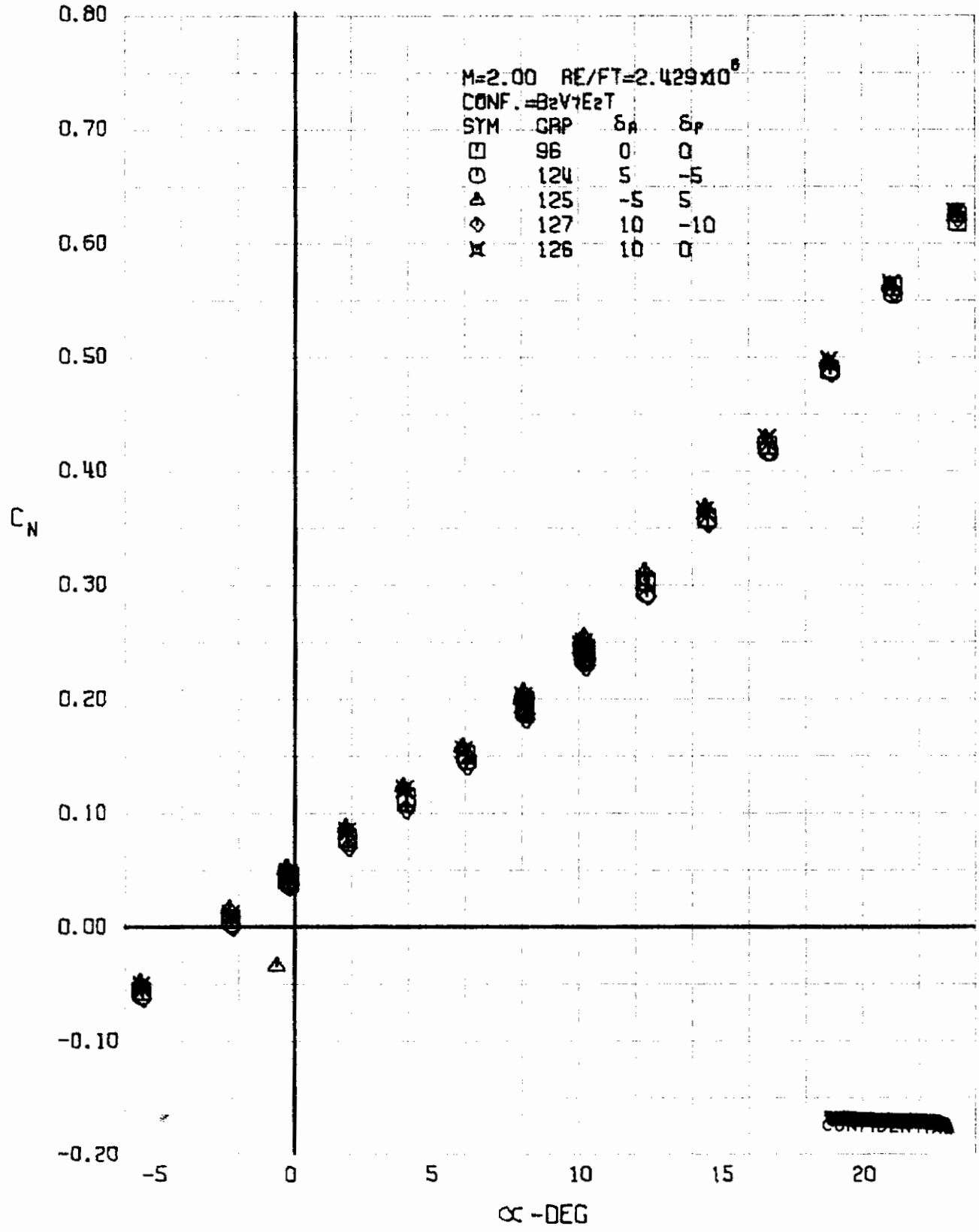

FIGURE 82 (U) AILERON EFFECTS
- NORMAL FORCE COEFFICIENT VARIATION WITH ANGLE OF ATTACK (M=2.00)

CONFIDENTIAL

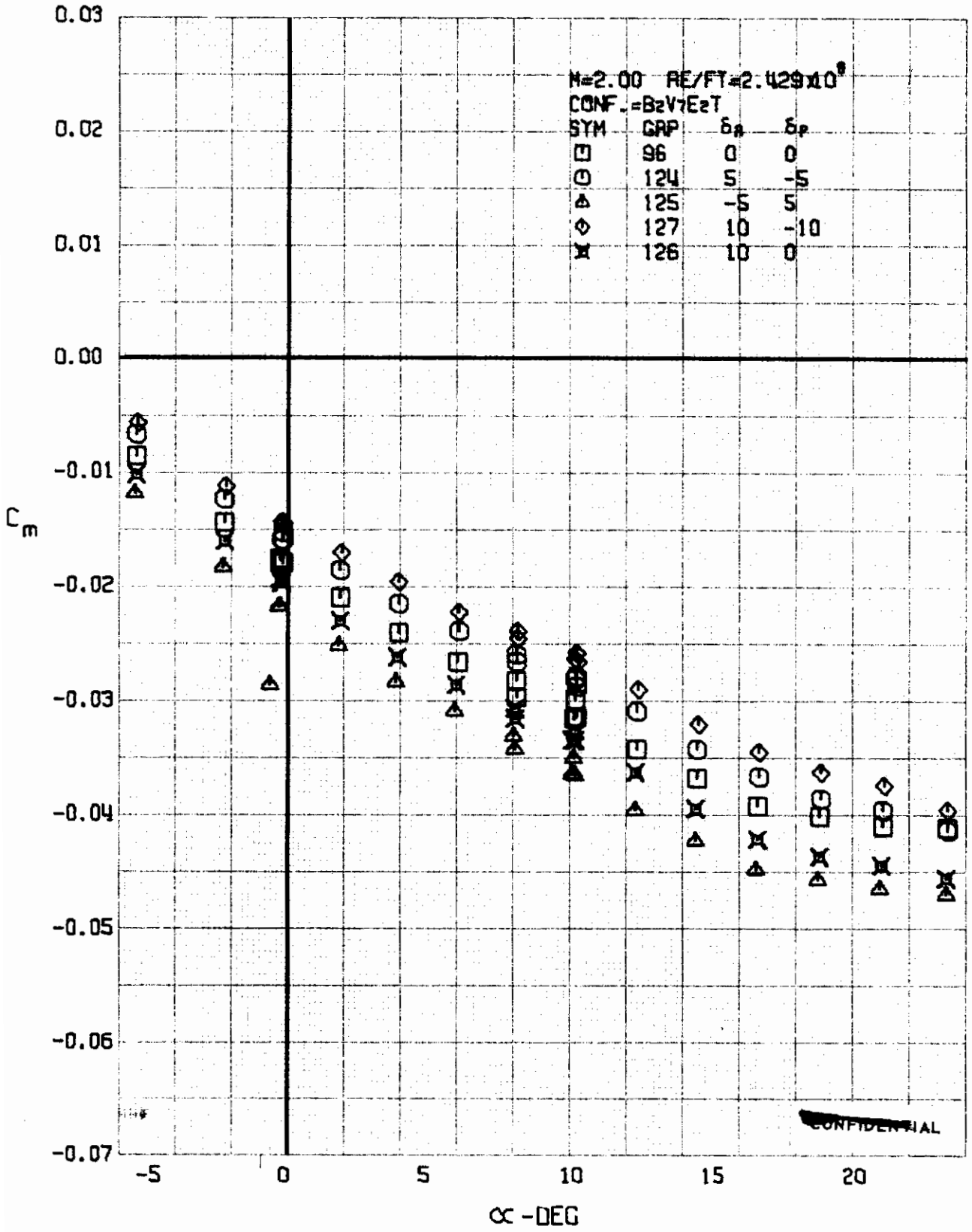

FIGURE 83 (U) AILERON EFFECTS
- PITCHING MOMENT COEFFICIENT VARIATION WITH ANGLE OF ATTACK (M=2.00)

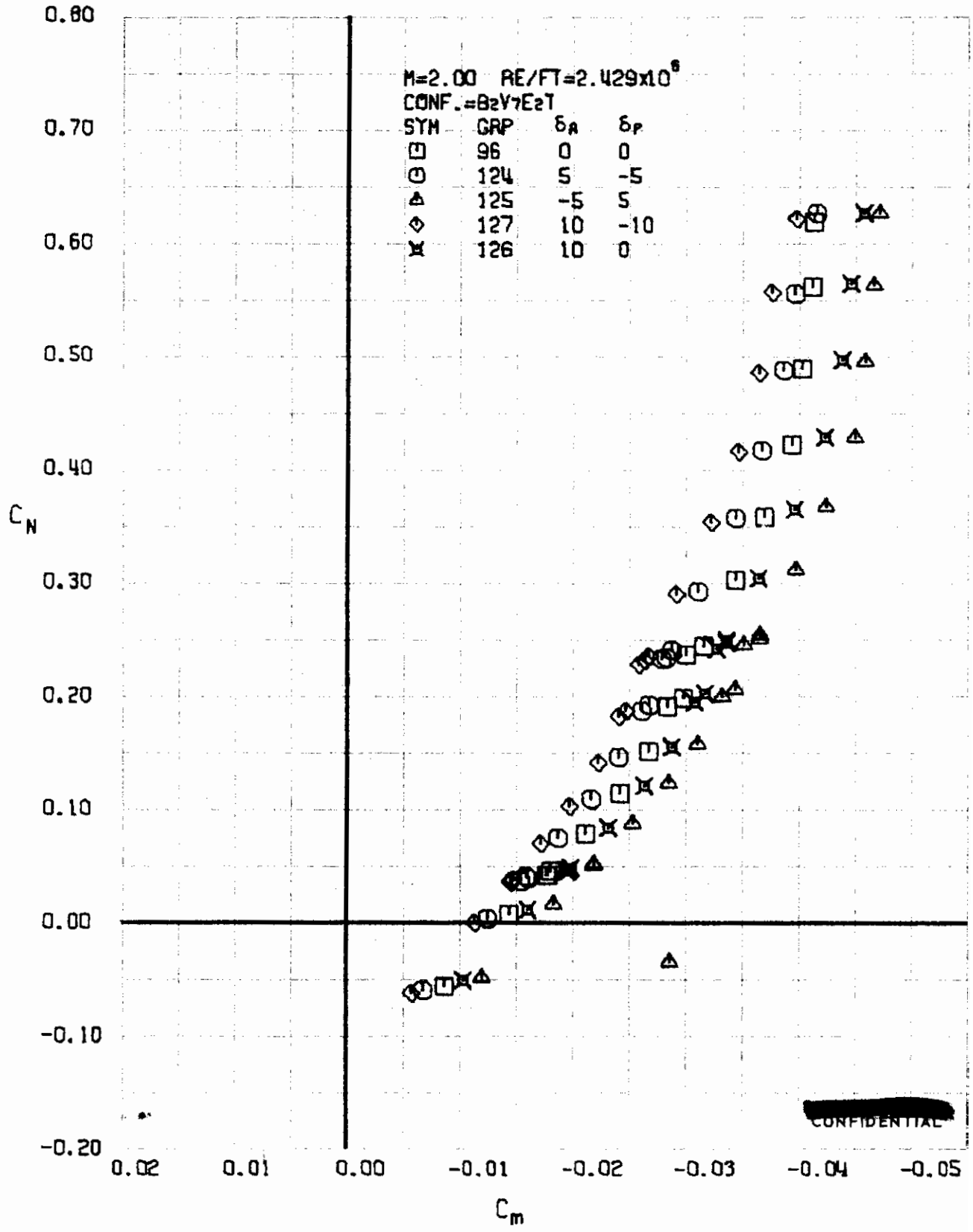

FIGURE 84 (U) AILERON EFFECTS - LONGITUDINAL STABILITY VARIATION (M=2.00)

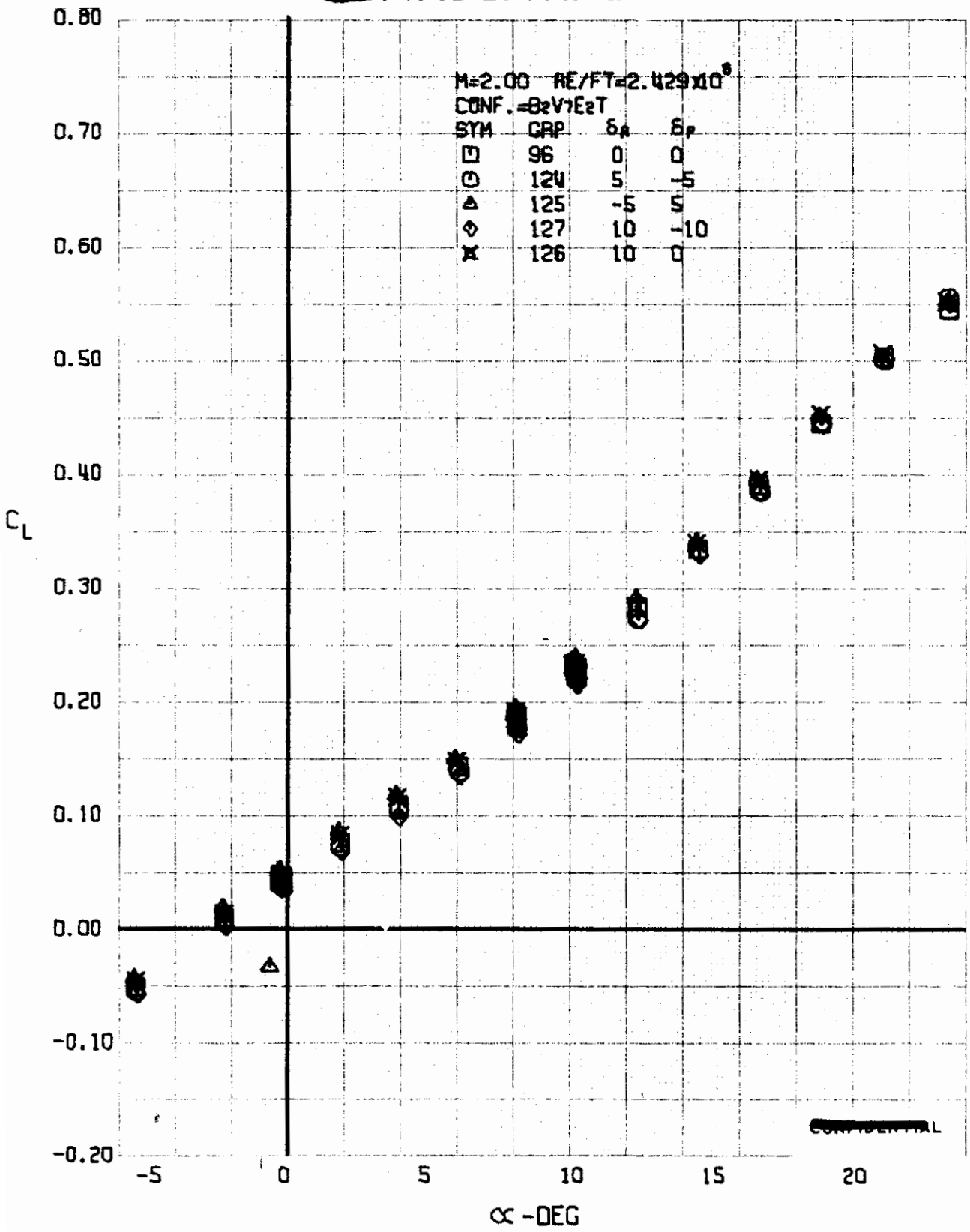

FIGURE 85 (U) AILERON EFFECTS
- LIFT COEFFICIENT VARIATION WITH ANGLE OF ATTACK (M=2.00)

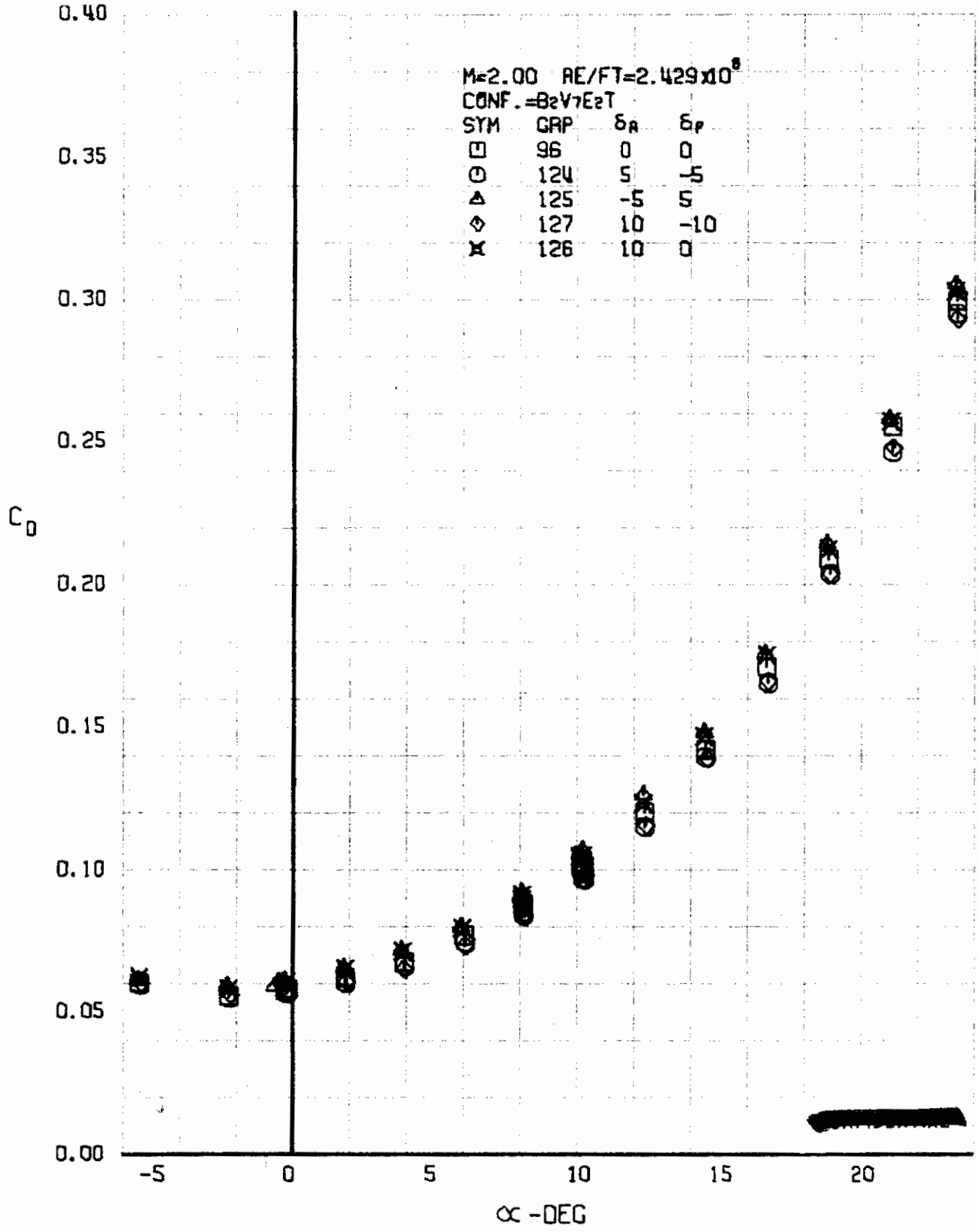

FIGURE 86 (U) AILERON EFFECTS
- DRAG COEFFICIENT VARIATION WITH ANGLE OF ATTACK (M=2.00)

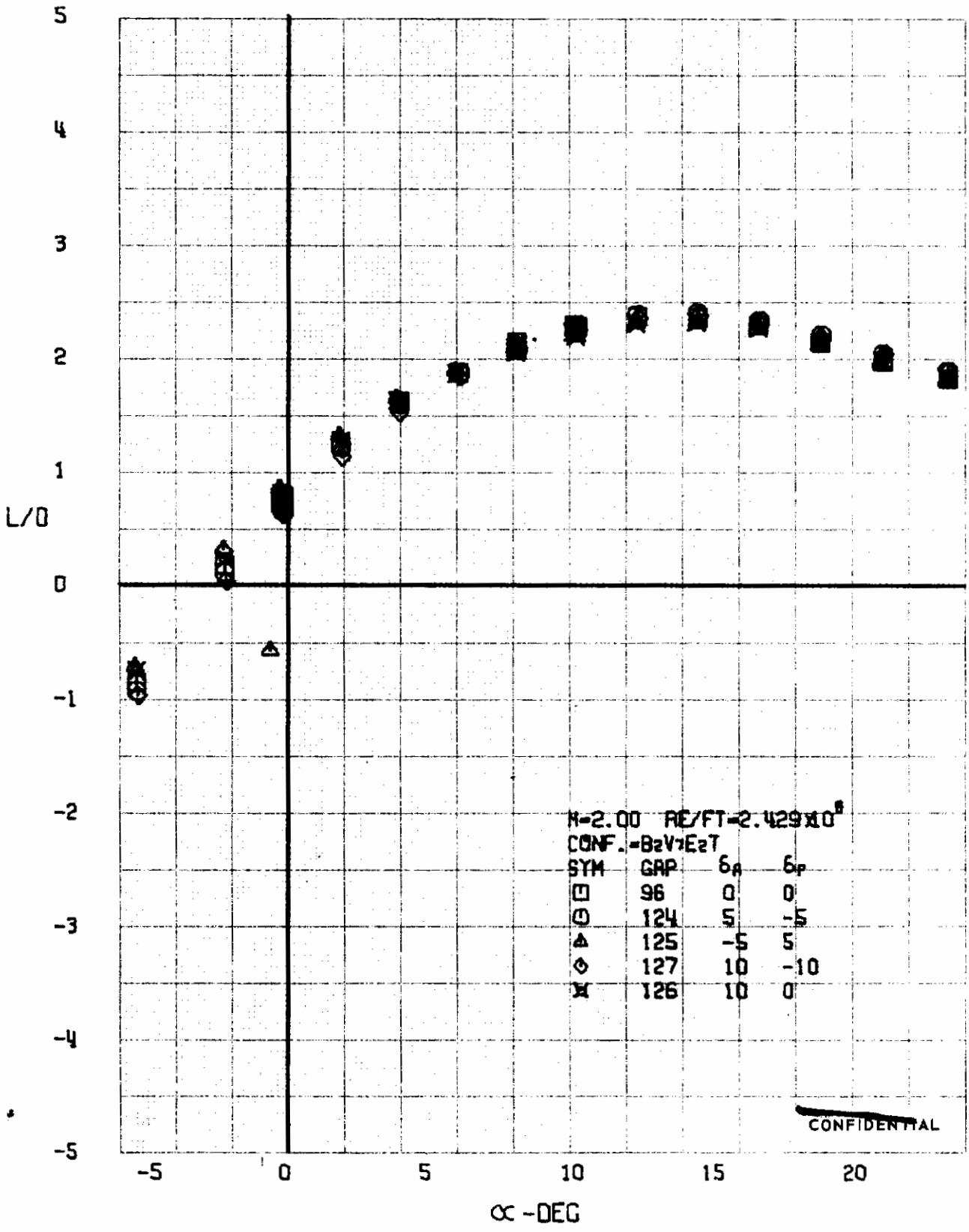

FIGURE 87 (U) AILERON EFFECTS
- LIFT-DRAG RATIO VARIATION WITH ANGLE OF ATTACK (M=2.00)

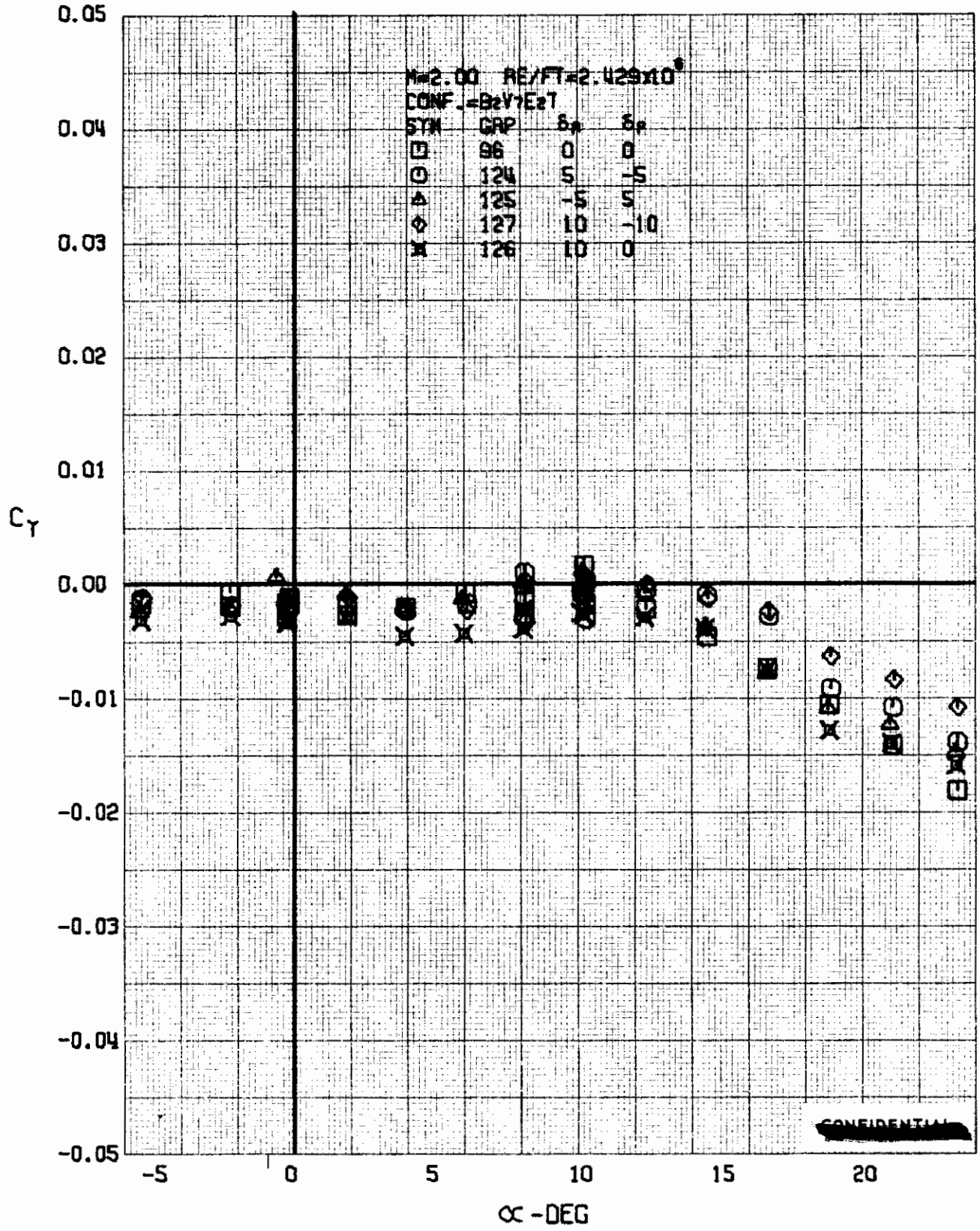

FIGURE 88 (U) AILERON EFFECTS
- SIDE FORCE COEFFICIENT VARIATION WITH ANGLE OF ATTACK (M=2.00)

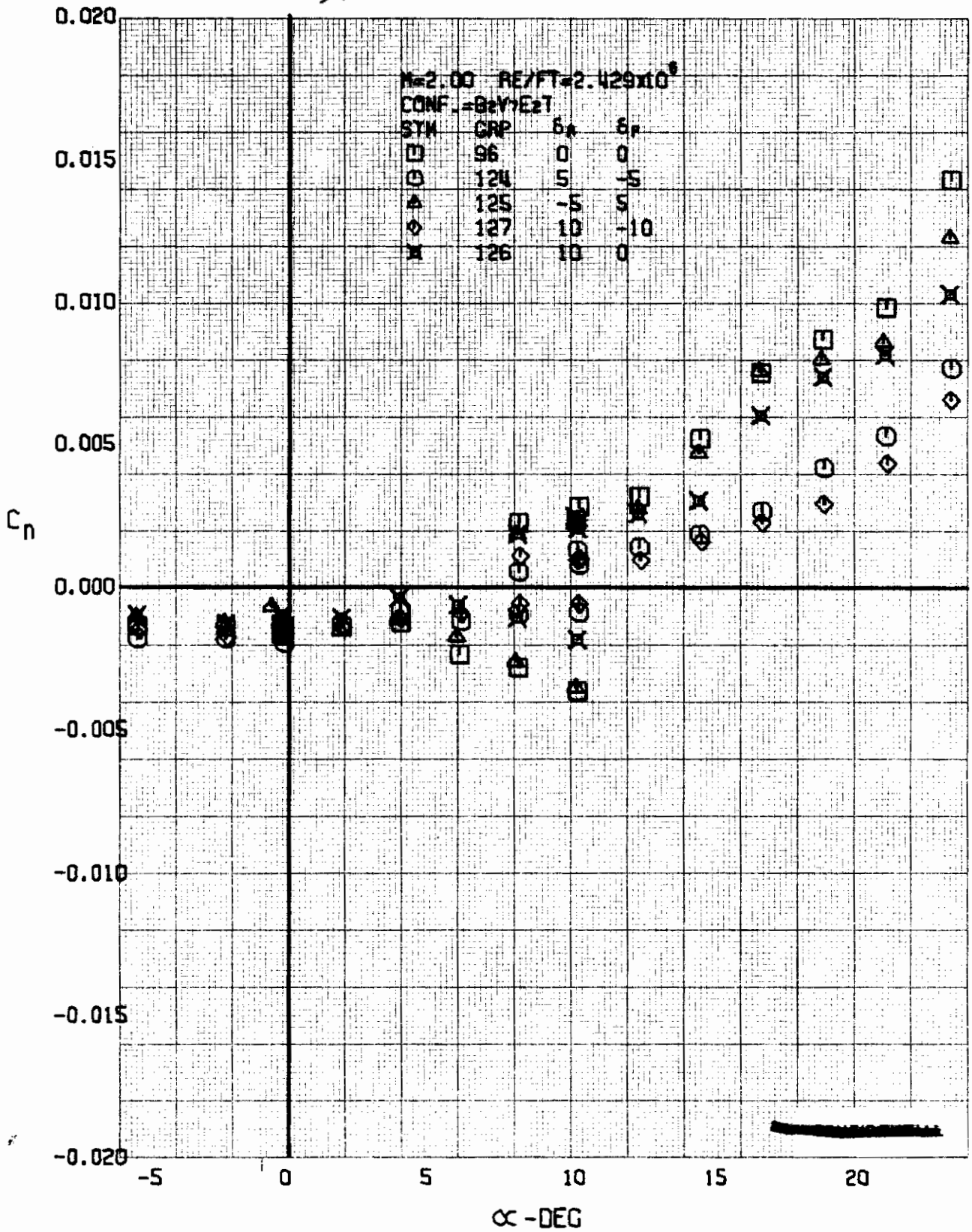

FIGURE 89 (U) AILERON EFFECTS
- YAWING MOMENT COEFFICIENT VARIATION WITH ANGLE OF ATTACK (M=2.00)

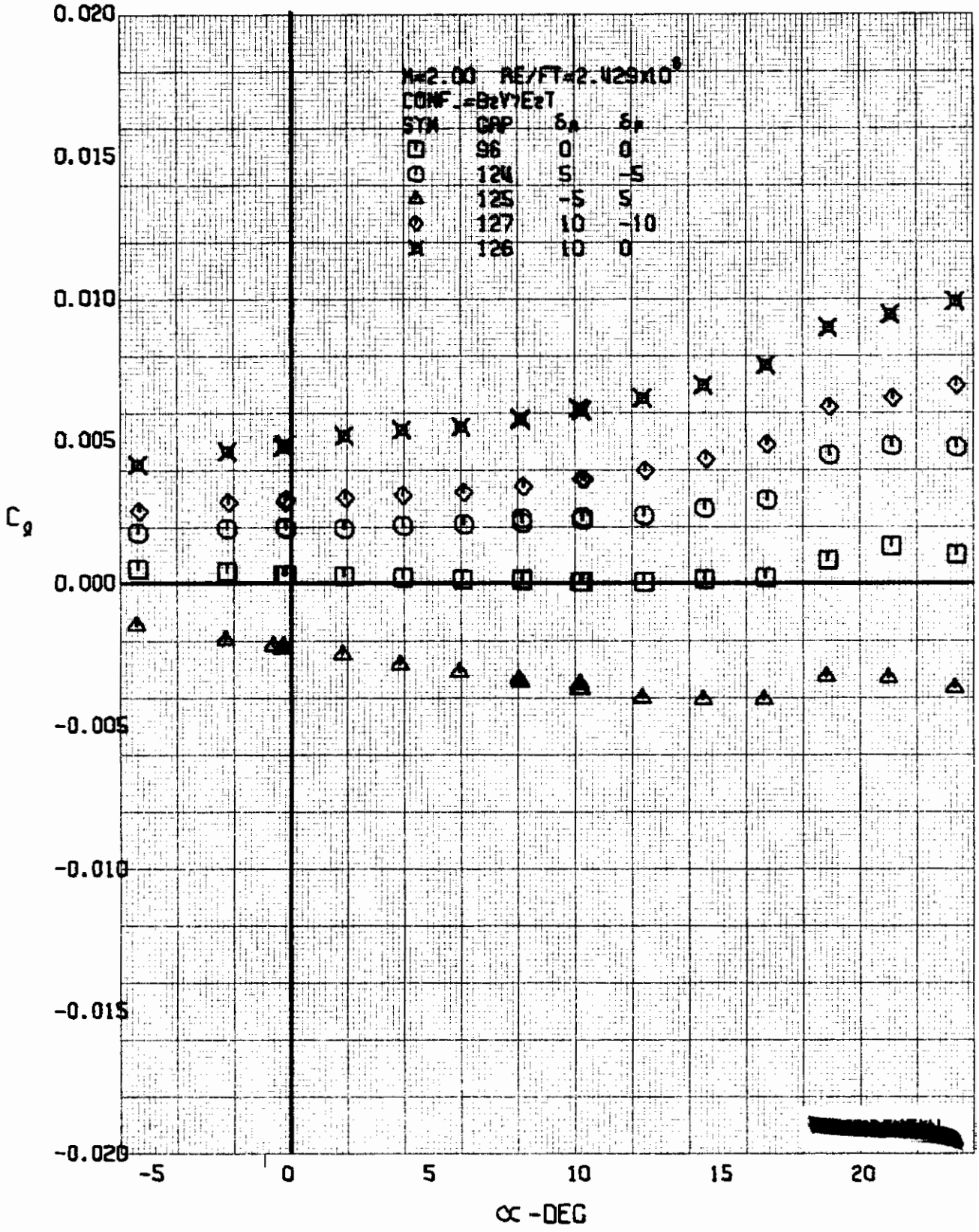

FIGURE 90 (U) AILERON EFFECTS
- ROLLING MOMENT COEFFICIENT VARIATION WITH ANGLE OF ATTACK (M=2.00)

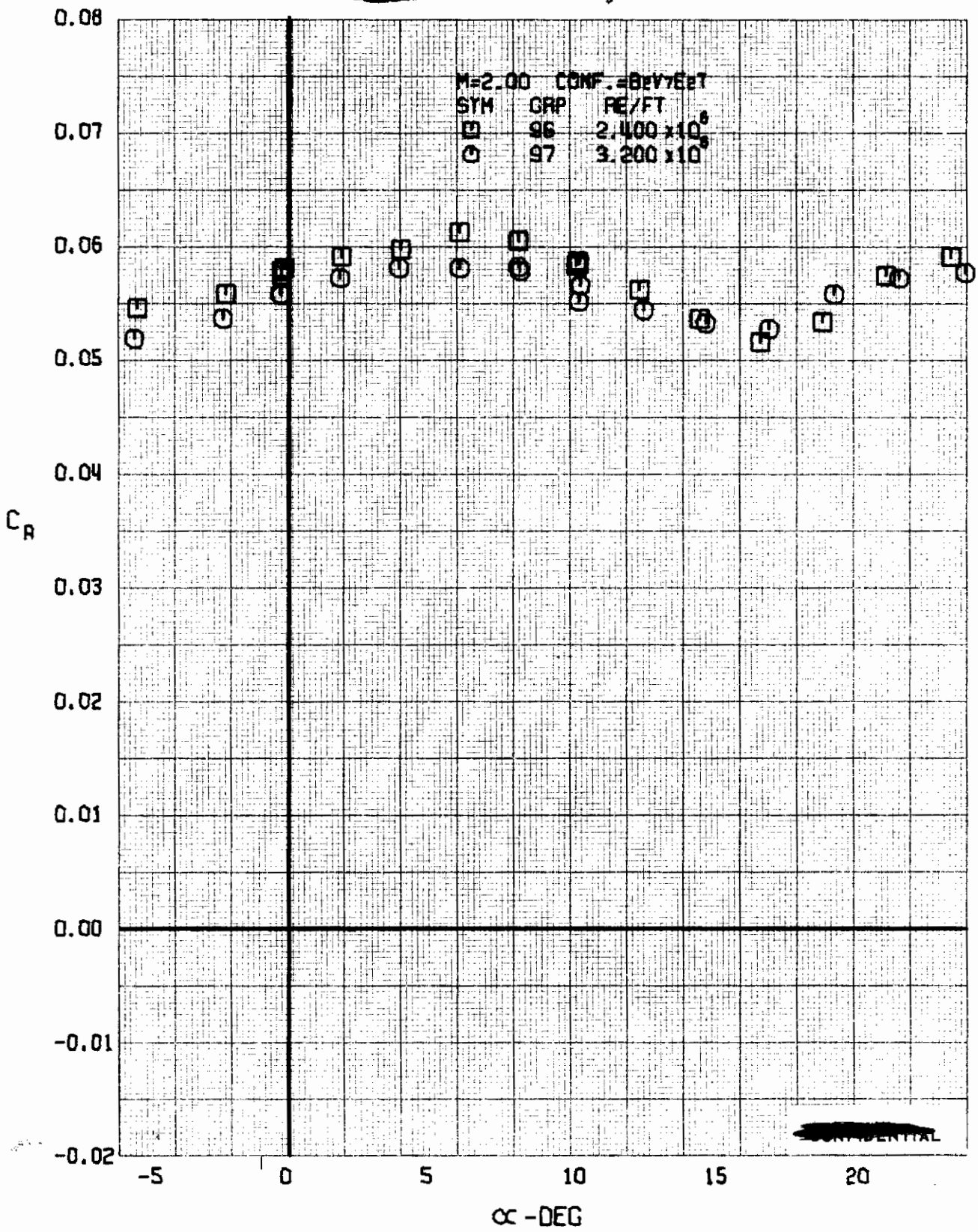

FIGURE 91 (U) REYNOLDS NUMBER EFFECTS
- AXIAL FORCE COEFFICIENT VARIATION WITH ANGLE OF ATTACK (M=2.00)

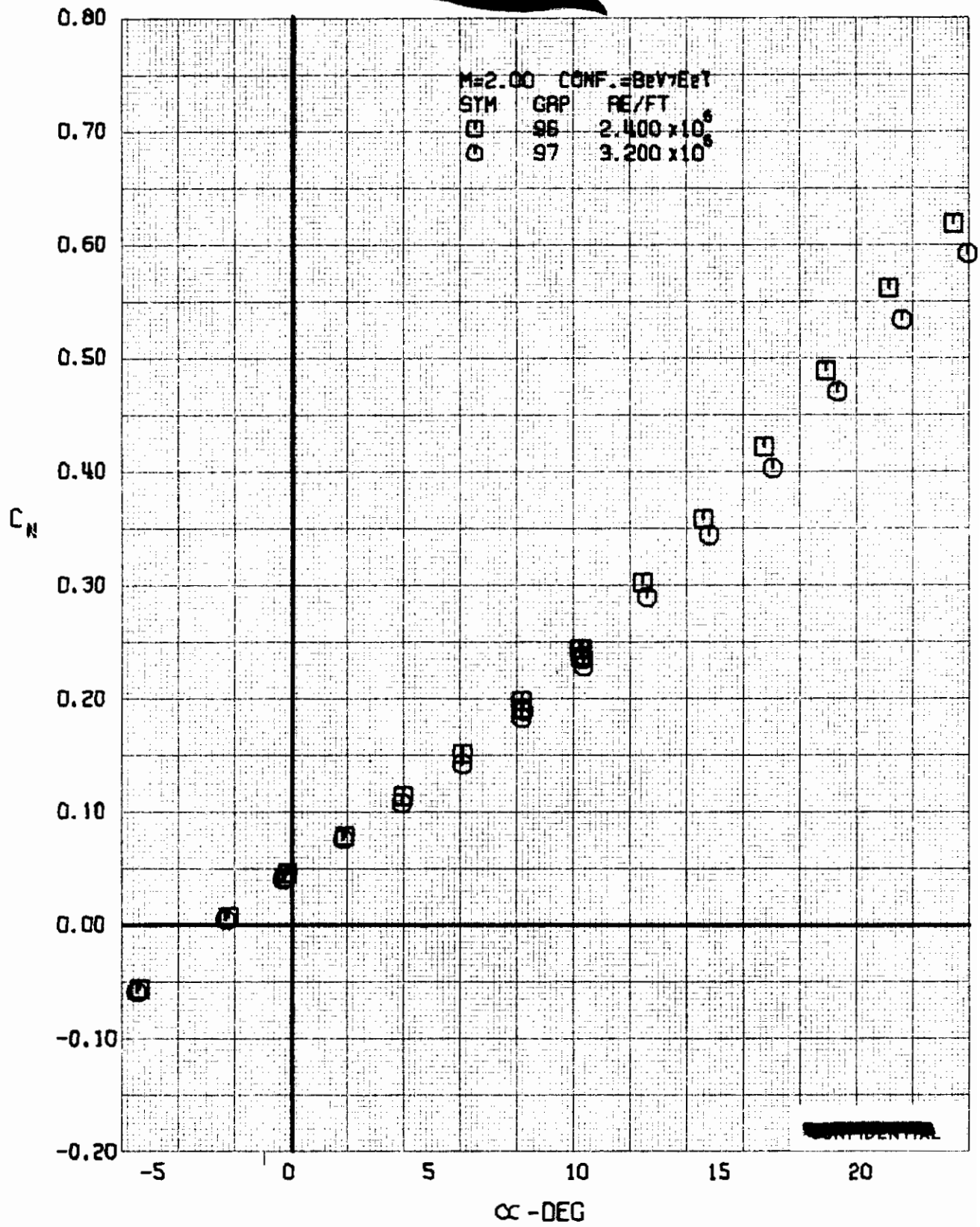

FIGURE 92 (U) REYNOLDS NUMBER EFFECTS
- NORMAL FORCE COEFFICIENT VARIATION WITH ANGLE OF ATTACK (M=2.00)

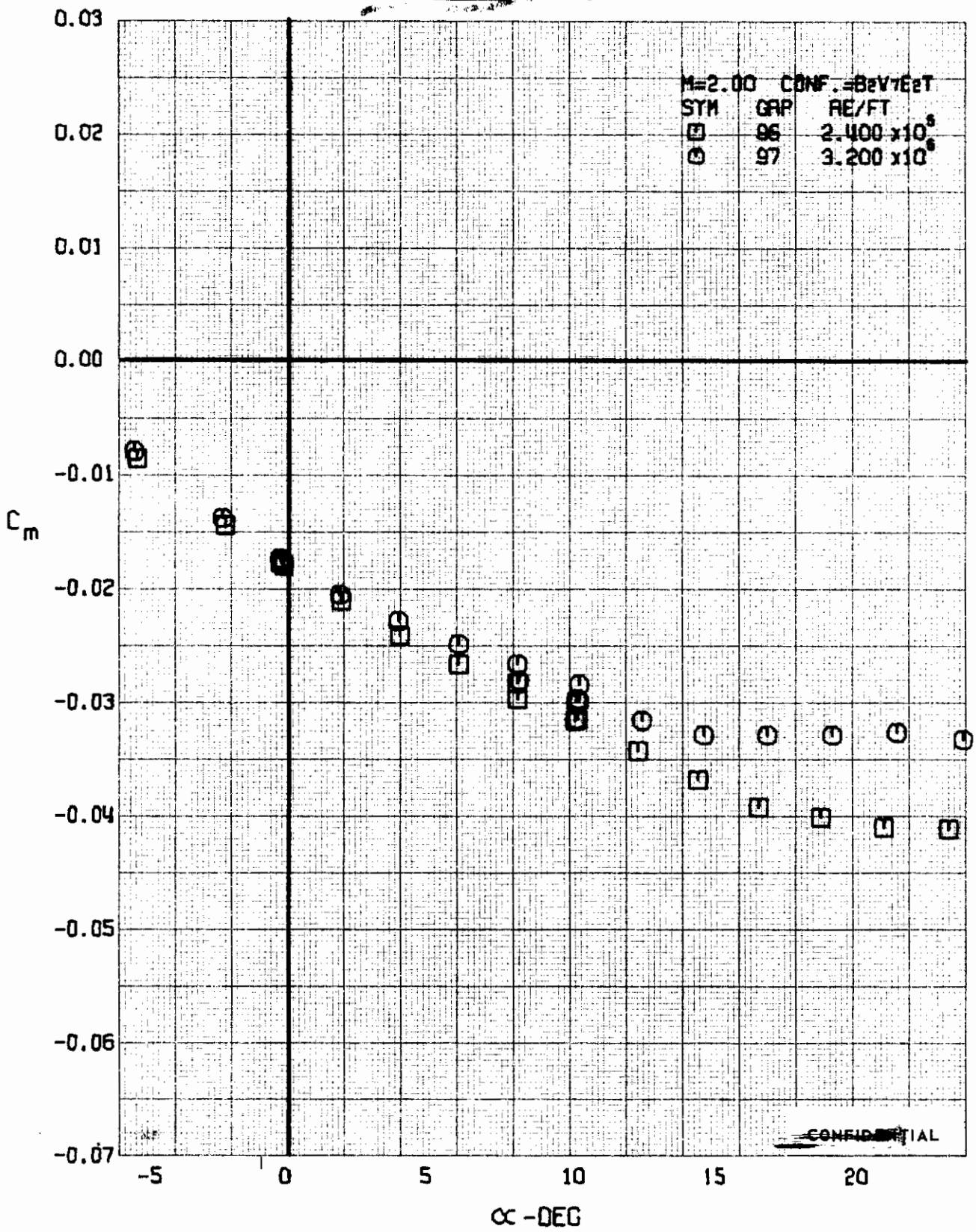

FIGURE 93 (U) REYNOLDS NUMBER EFFECTS
- PITCHING MOMENT COEFFICIENT VARIATION WITH ANGLE OF ATTACK (M=2.00)

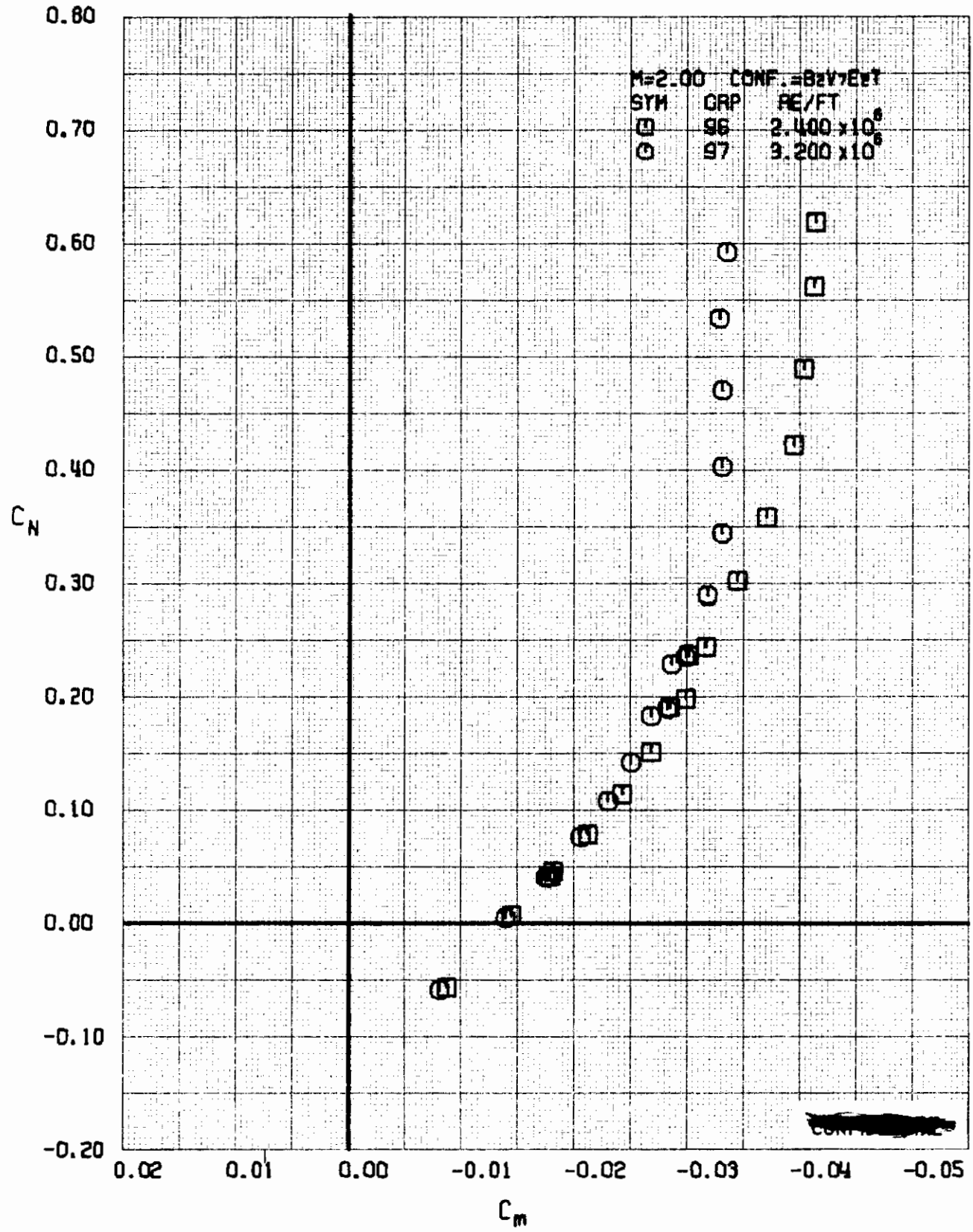

FIGURE 94 (U) REYNOLDS NUMBER EFFECTS
- LONGITUDINAL STABILITY VARIATION (M=2.00)

CONFIDENTIAL

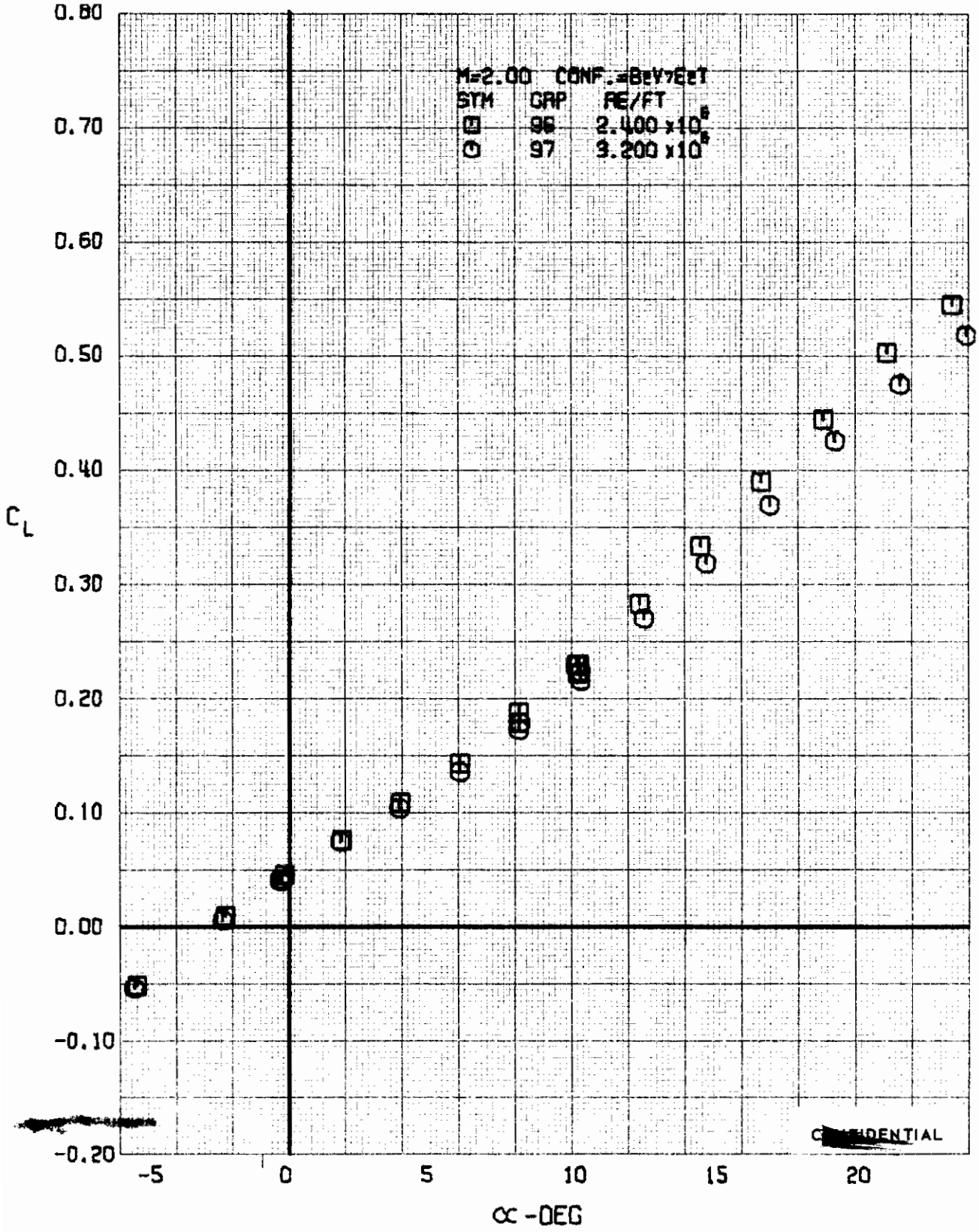

FIGURE 95 (U) REYNOLDS NUMBER EFFECTS
- LIFT COEFFICIENT VARIATION WITH ANGLE OF ATTACK (M=2.00)

CONFIDENTIAL

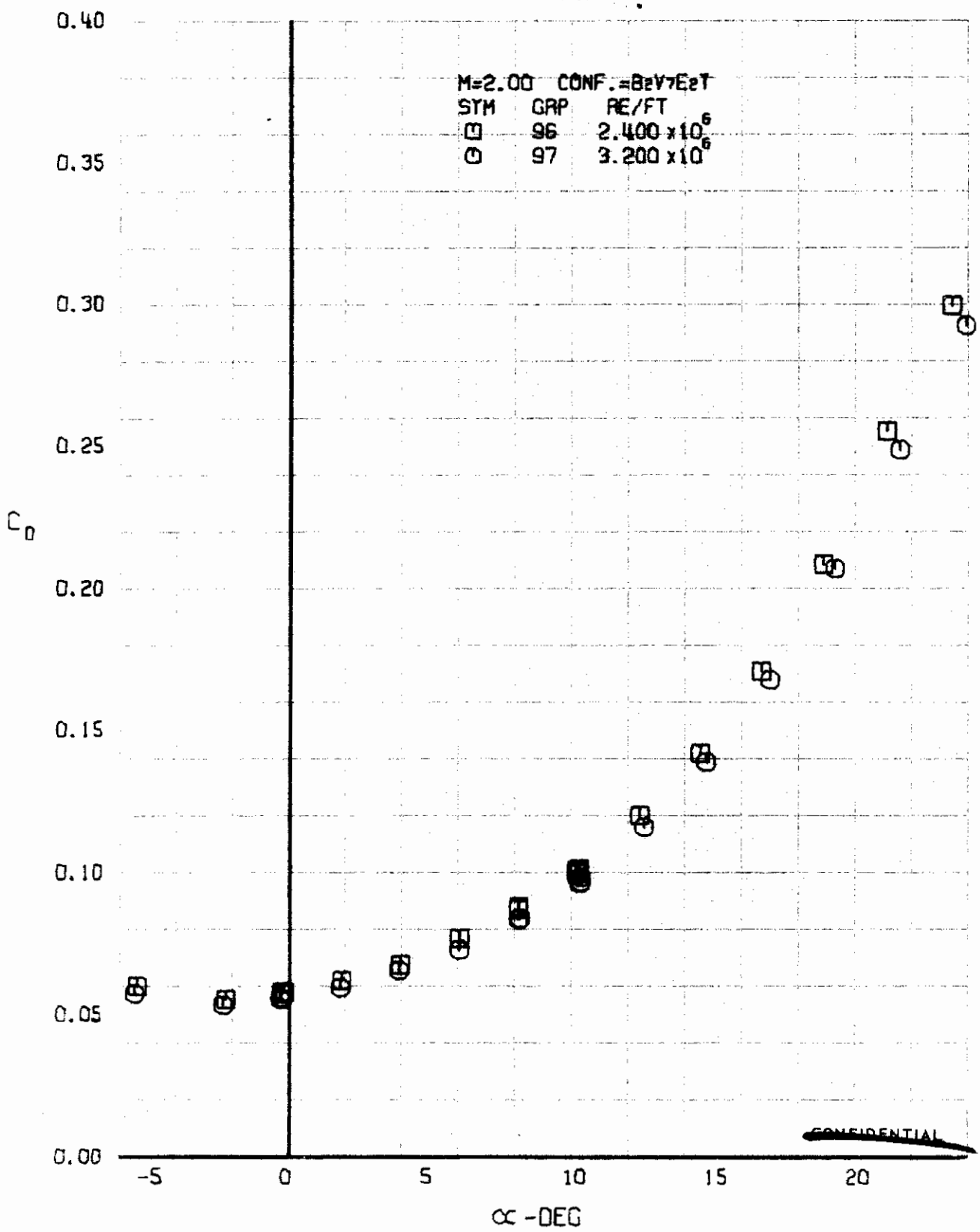

FIGURE 96 (U) REYNOLDS NUMBER EFFECTS
- DRAG COEFFICIENT VARIATION WITH ANGLE OF ATTACK (M=2.00)

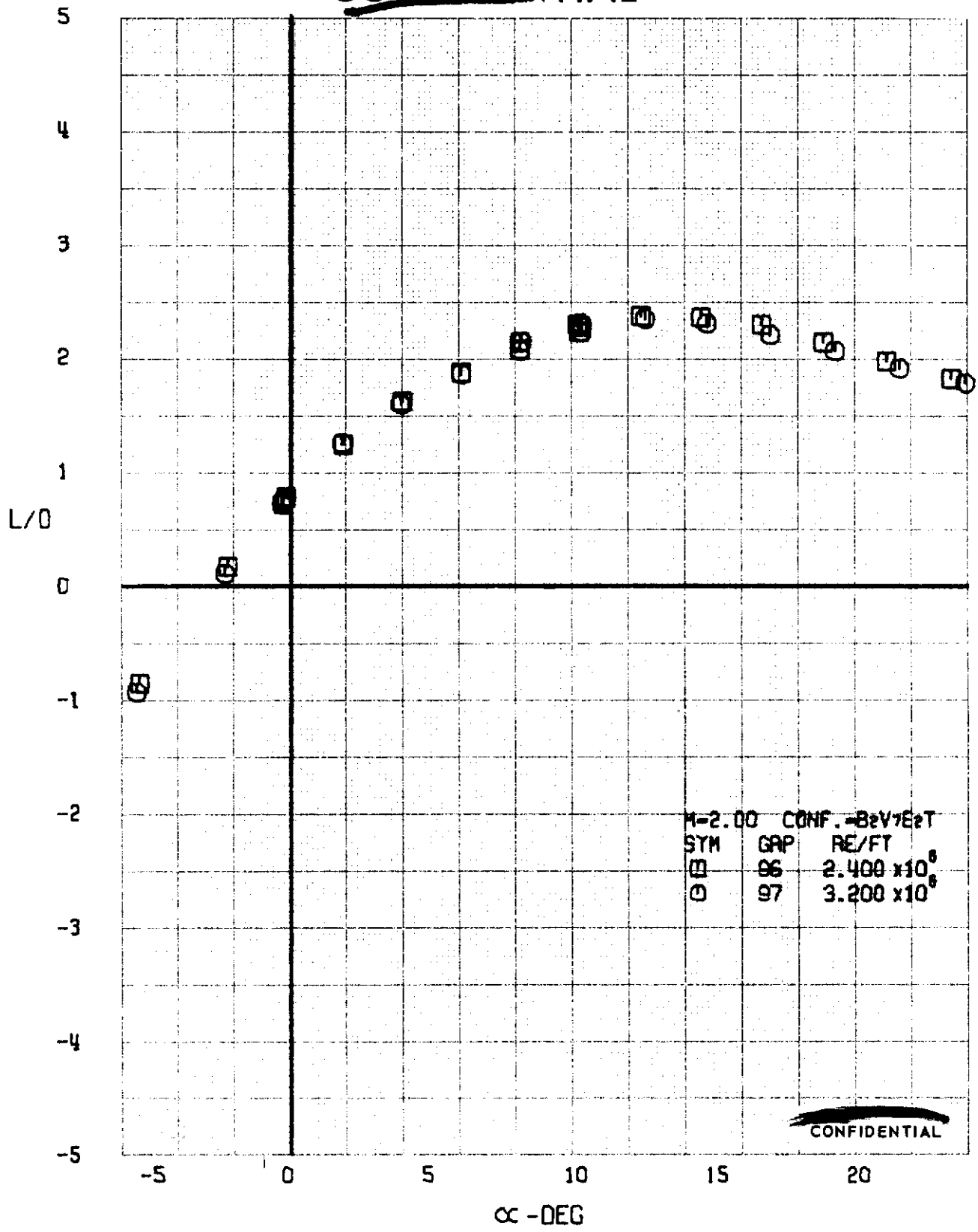

FIGURE 97 (U) REYNOLDS NUMBER EFFECTS
- LIFT-DRAG RATIO VARIATION WITH ANGLE OF ATTACK (M=2.00)

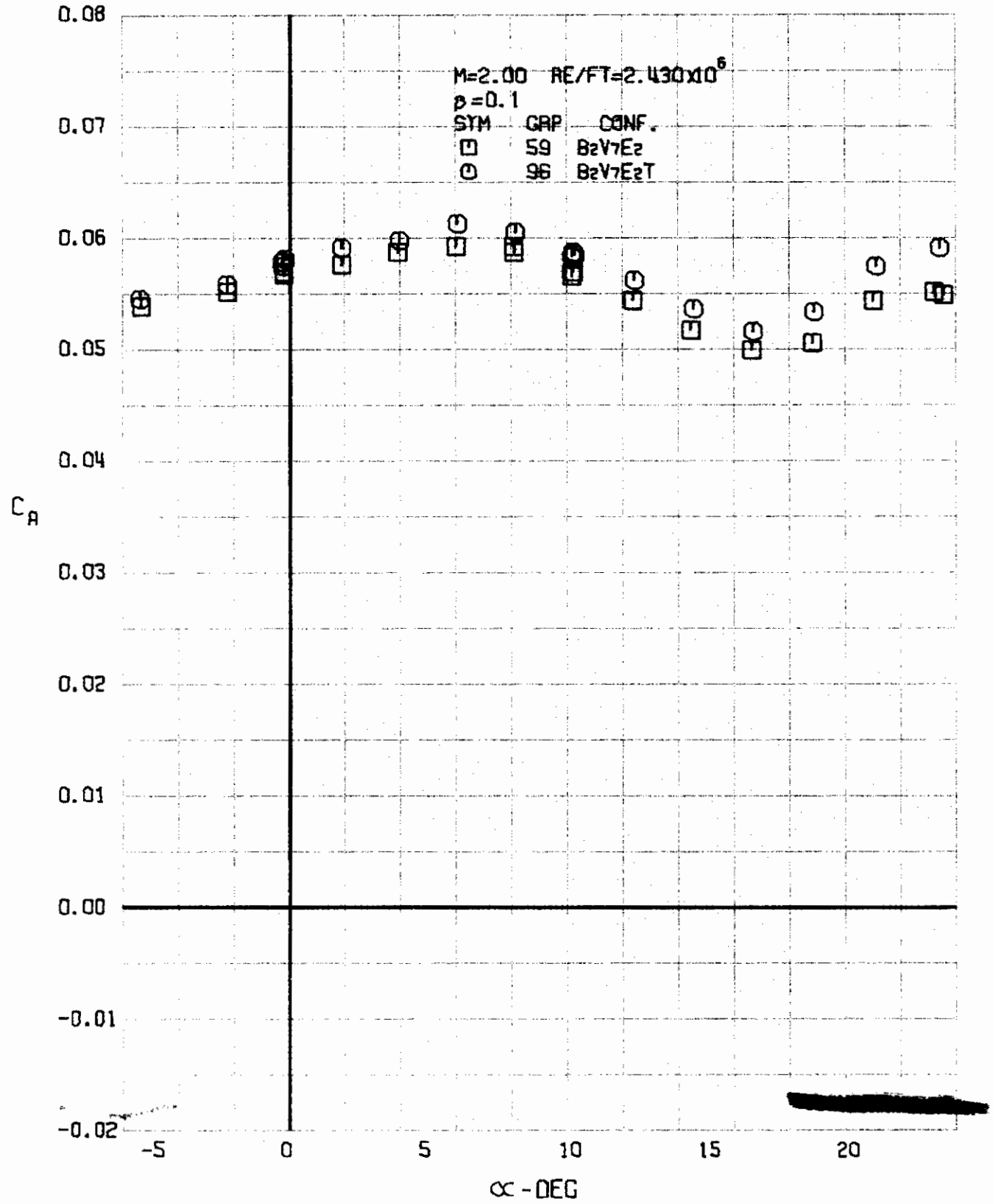

FIGURE 98 (U) FORCED TRANSITION EFFECTS
- AXIAL FORCE COEFFICIENT VARIATION WITH ANGLE OF ATTACK (M=2.00)

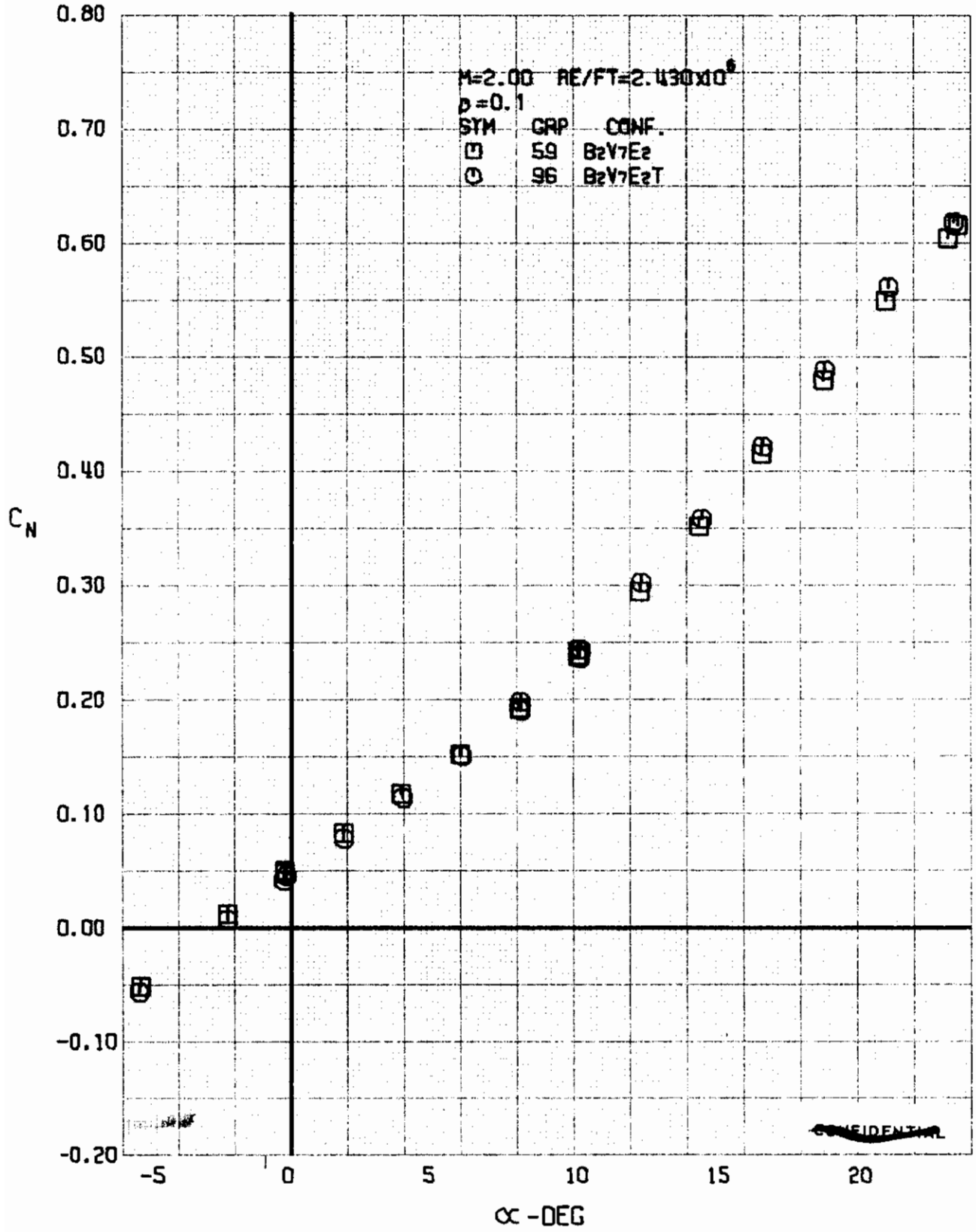

FIGURE 99 (U) FORCED TRANSITION EFFECTS
- NORMAL FORCE COEFFICIENT VARIATION WITH ANGLE OF ATTACK (M=2.00)

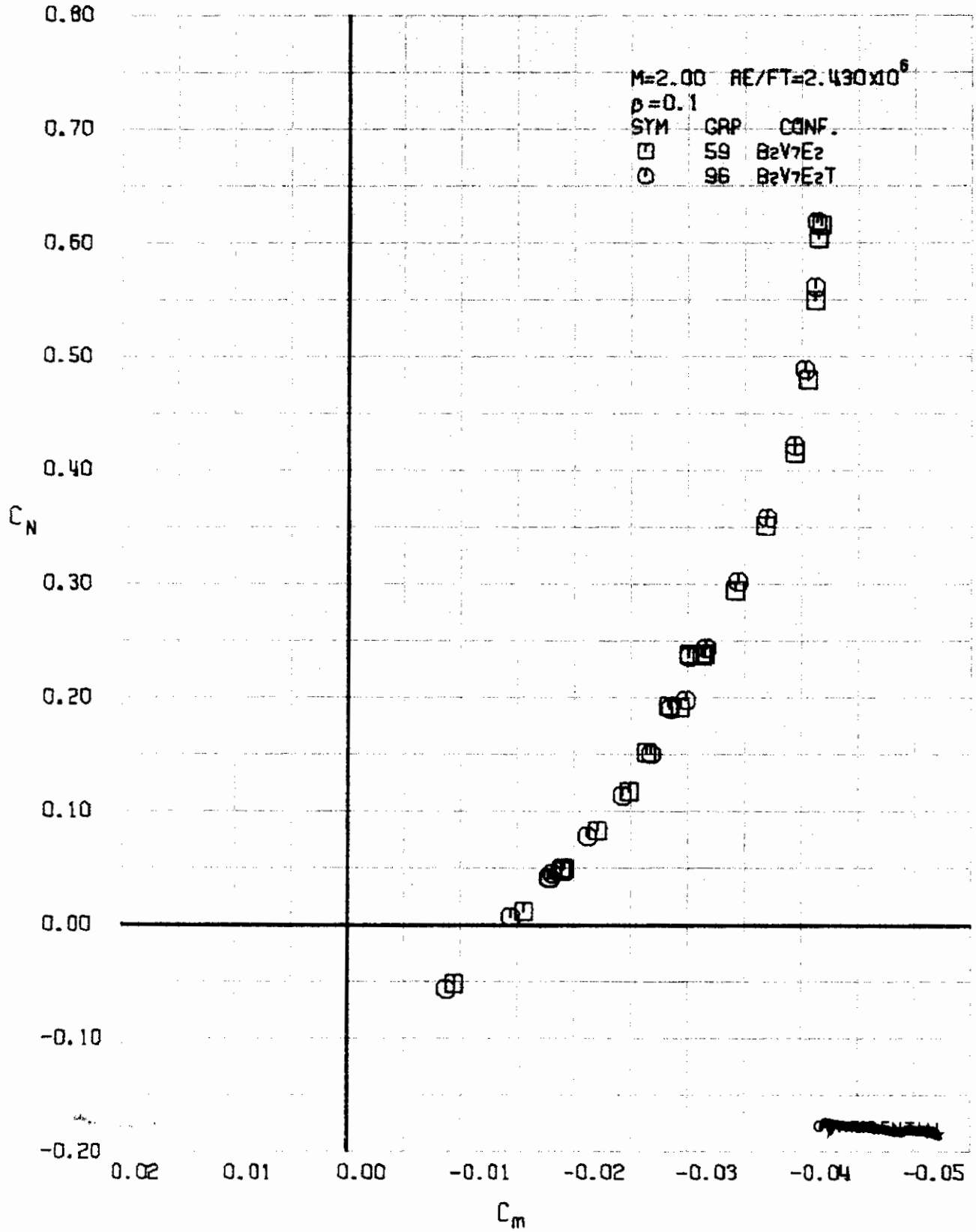

FIGURE 100 (U) FORCED TRANSITION EFFECTS
- LONGITUDINAL STABILITY VARIATION (M=2.00)

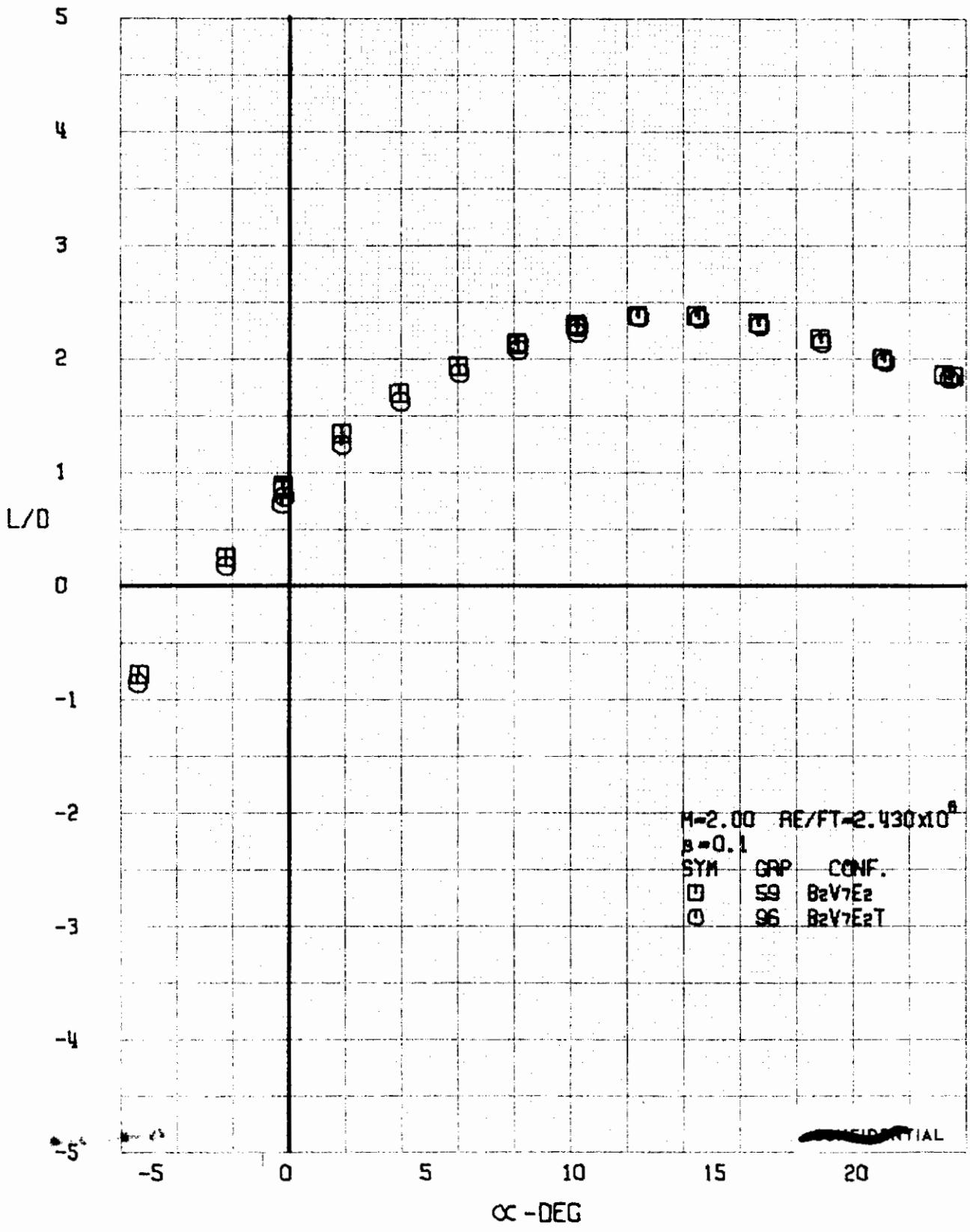

FIGURE 101 (U) FORCED TRANSITION EFFECTS
- LIFT-DRAG RATIO VARIATION WITH ANGLE OF ATTACK (M=2.00)

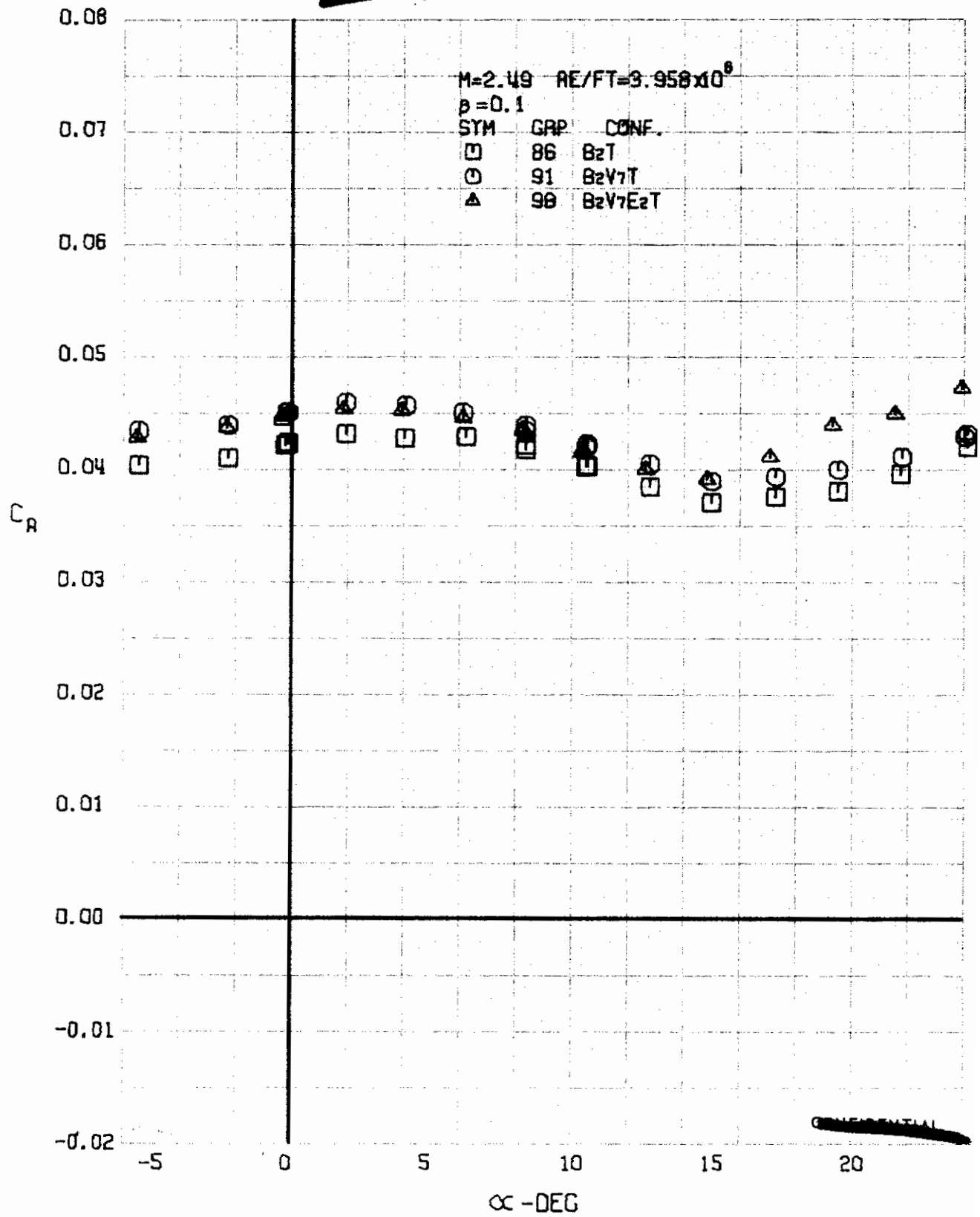

FIGURE 102 (U) CONFIGURATION BUILDUP
- AXIAL FORCE COEFFICIENT VARIATION WITH ANGLE OF ATTACK (M=2.49)

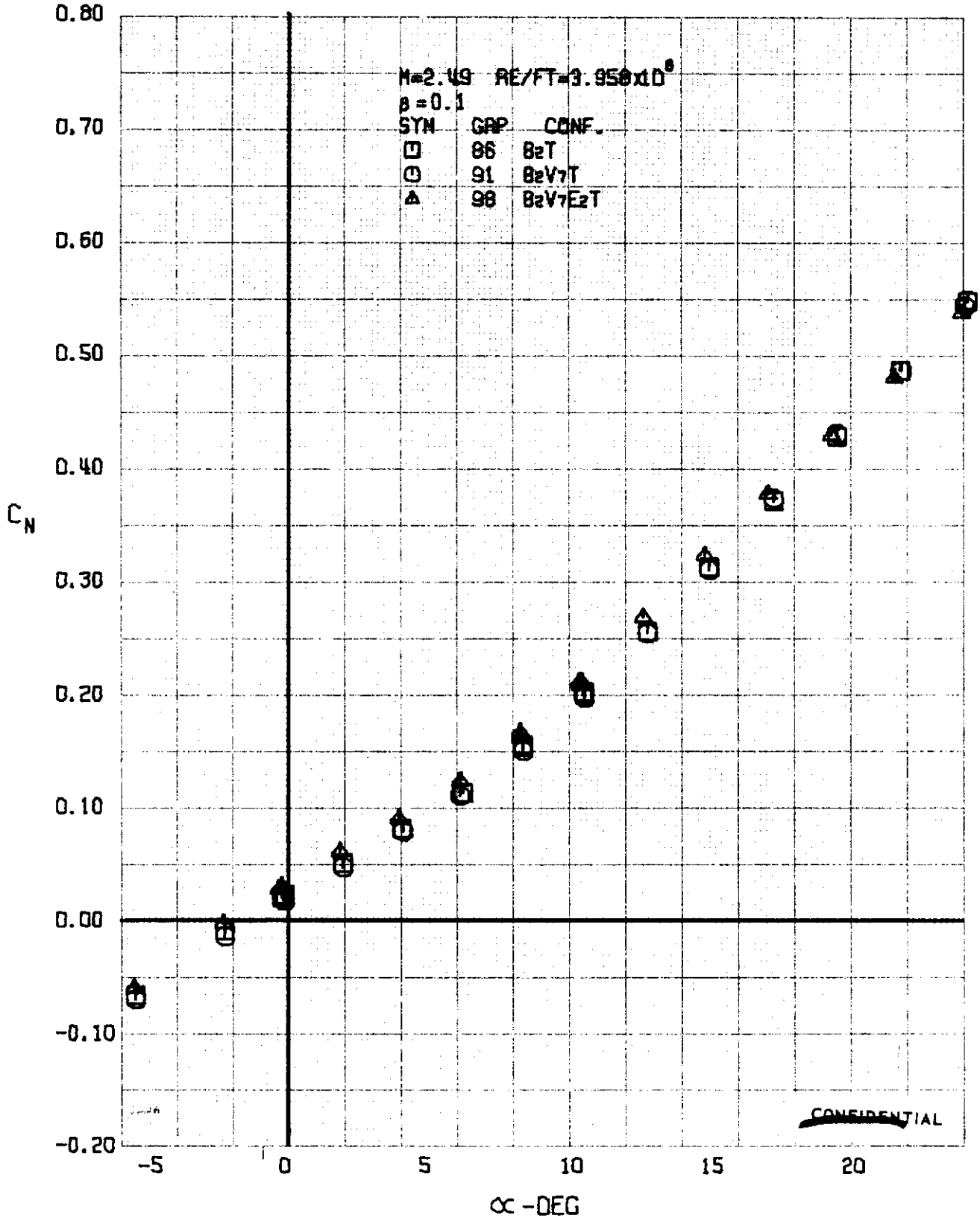

FIGURE 103 (U) CONFIGURATION BUILDUP
- NORMAL FORCE COEFFICIENT VARIATION WITH ANGLE OF ATTACK (M=2.49)

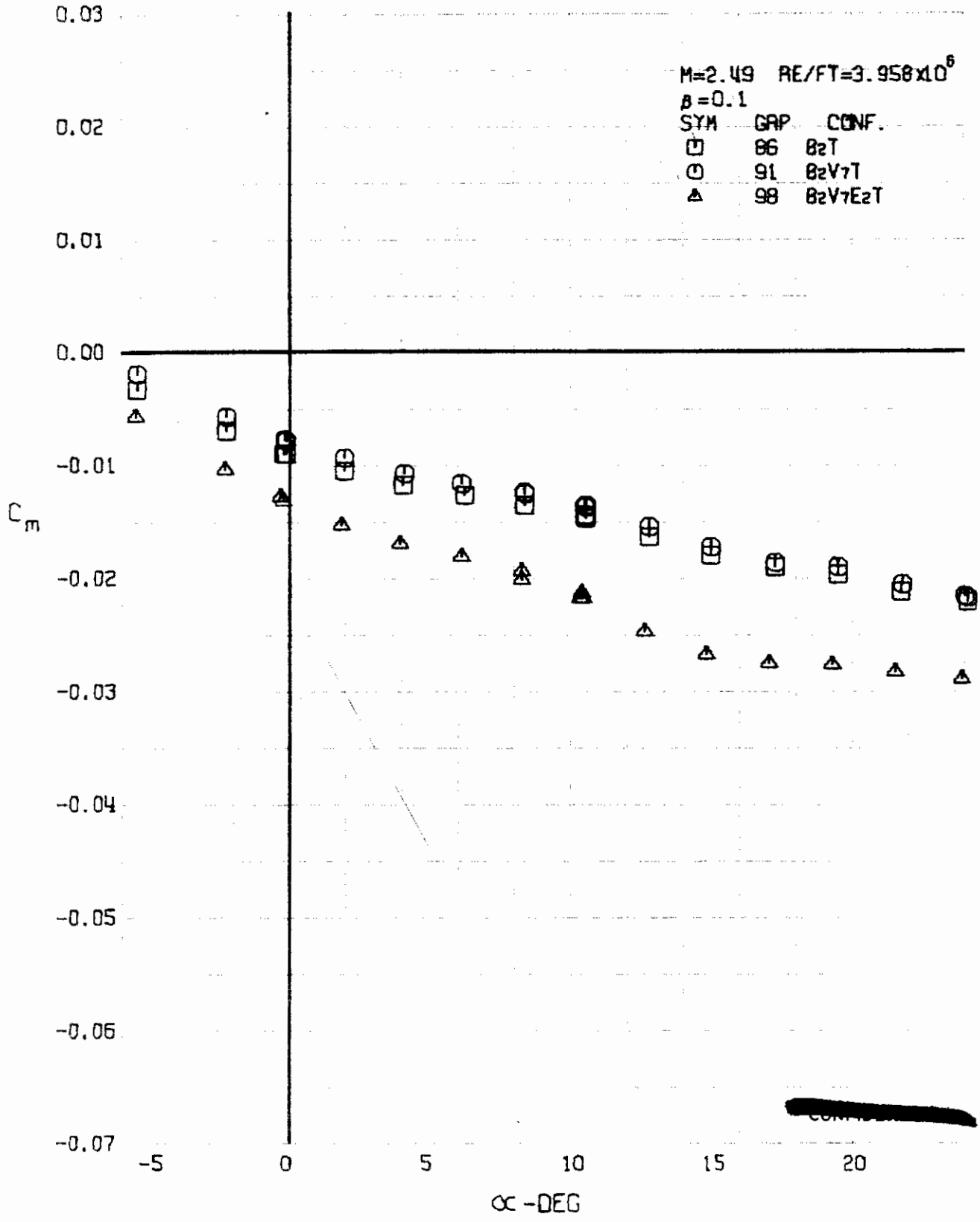

FIGURE 10. (U) CONFIGURATION BUILDUP
- PITCHING MOMENT COEFFICIENT VARIATION WITH ANGLE OF ATTACK (M=2.49)

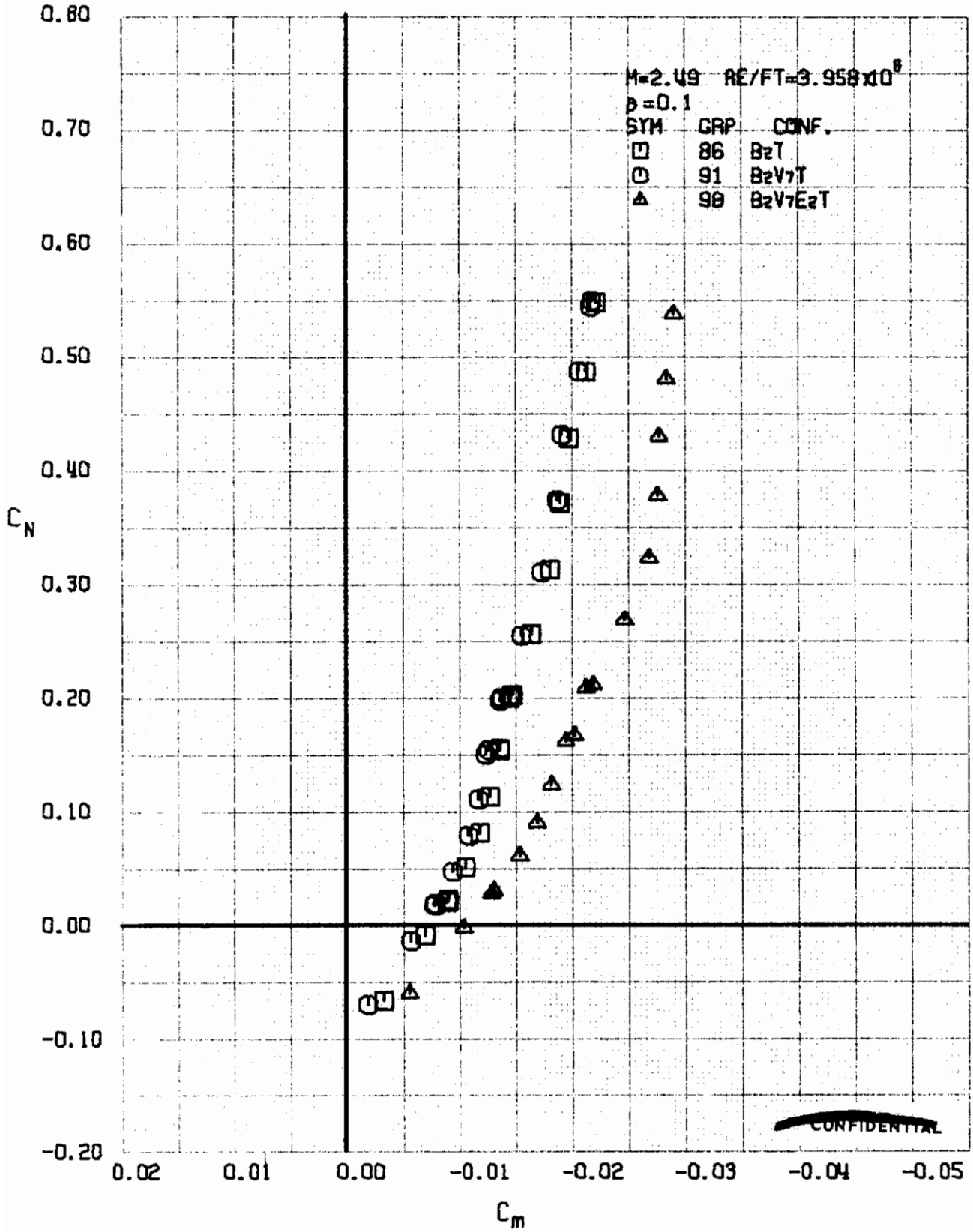

FIGURE 105 (U) CONFIGURATION BUILDUP
- LONGITUDINAL STABILITY VARIATION (M=2.49)

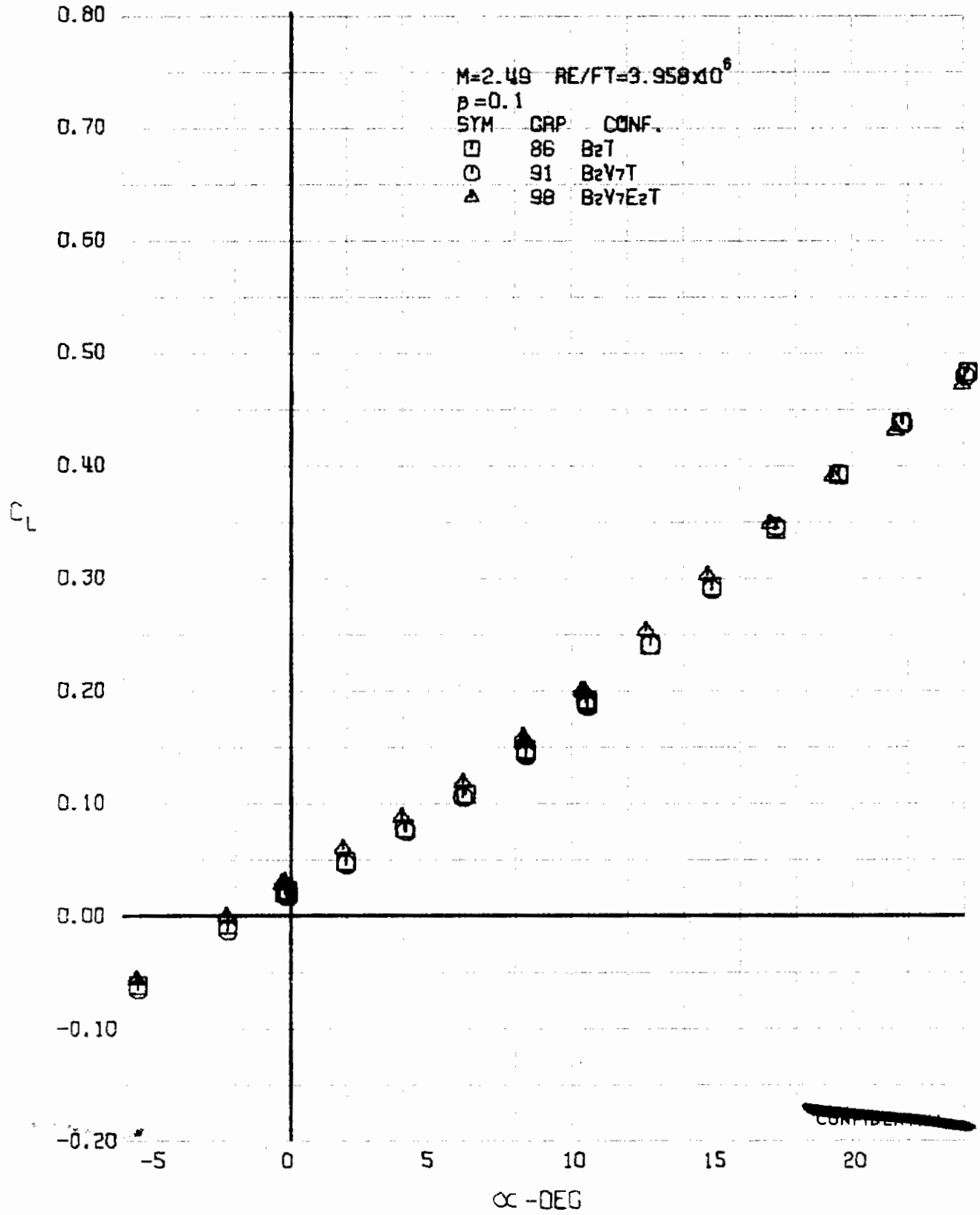

FIGURE 106 (U) CONFIGURATION BUILDUP
- LIFT COEFFICIENT VARIATION WITH ANGLE OF ATTACK (M=2.49)

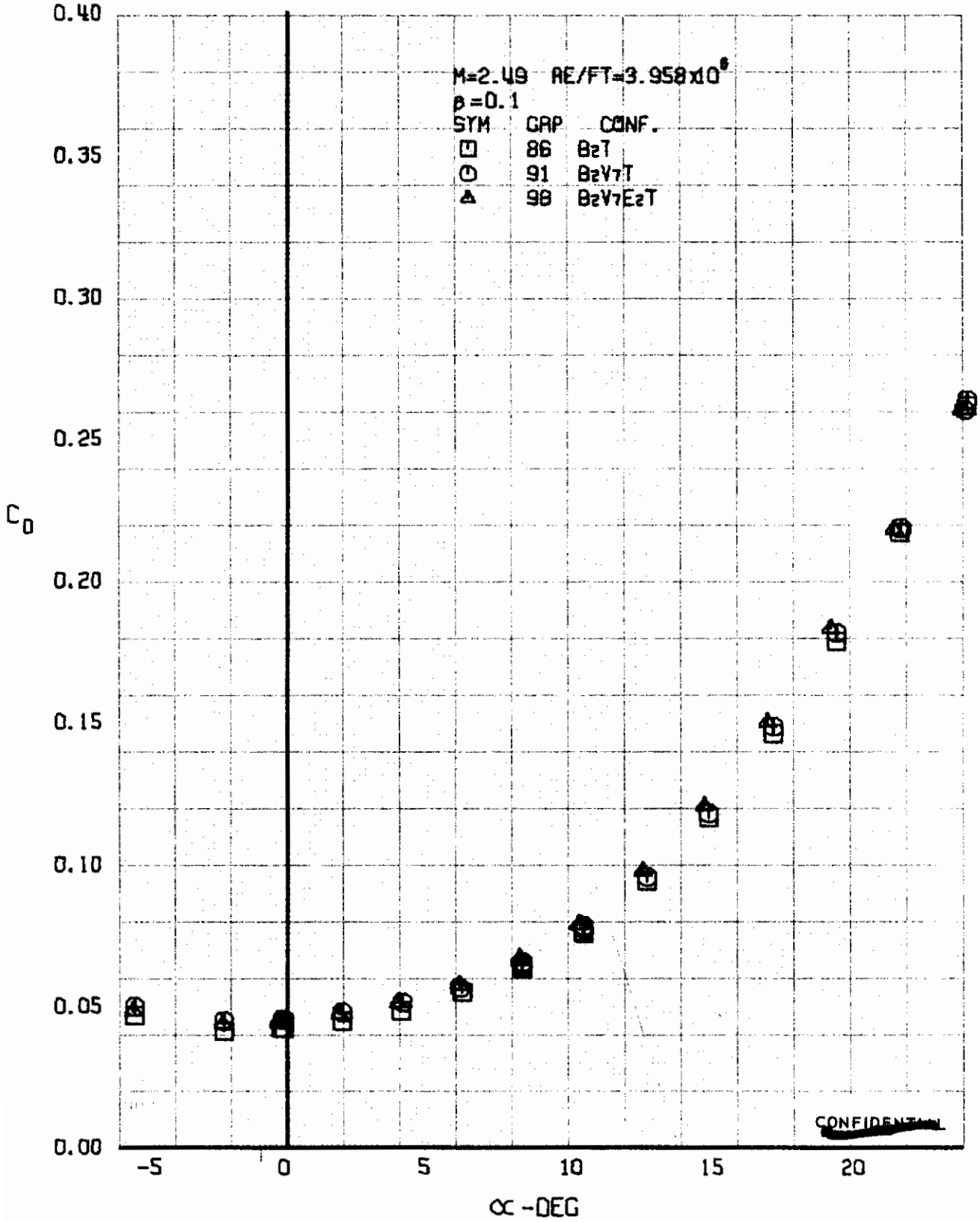

FIGURE 107 (U) CONFIGURATION BUILDUP
- DRAG COEFFICIENT VARIATION WITH ANGLE OF ATTACK (M=2.49)

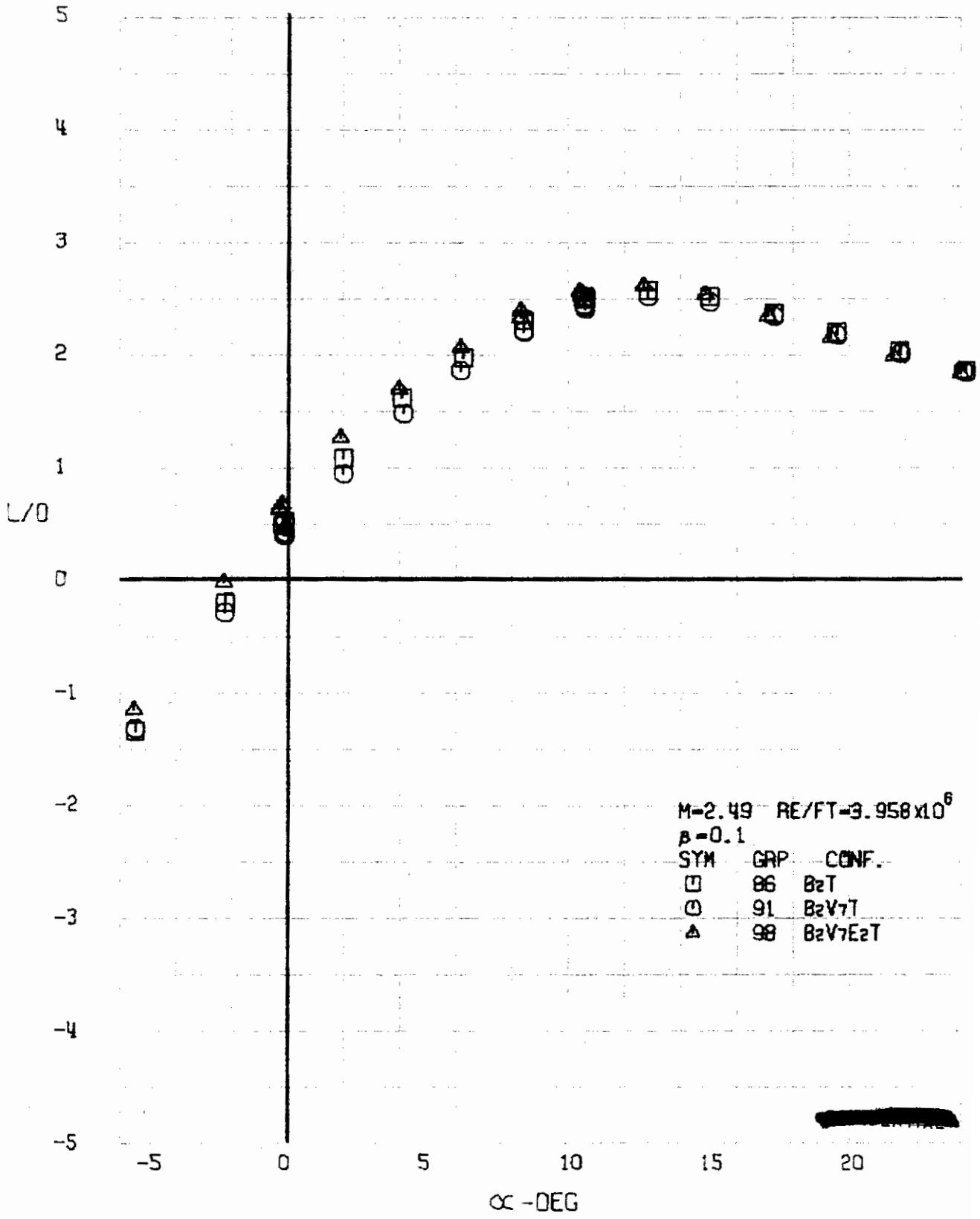

FIGURE 108 (U) CONFIGURATION BUILDUP
- LIFT-DRAG RATIO VARIATION WITH ANGLE OF ATTACK (M=2.49)

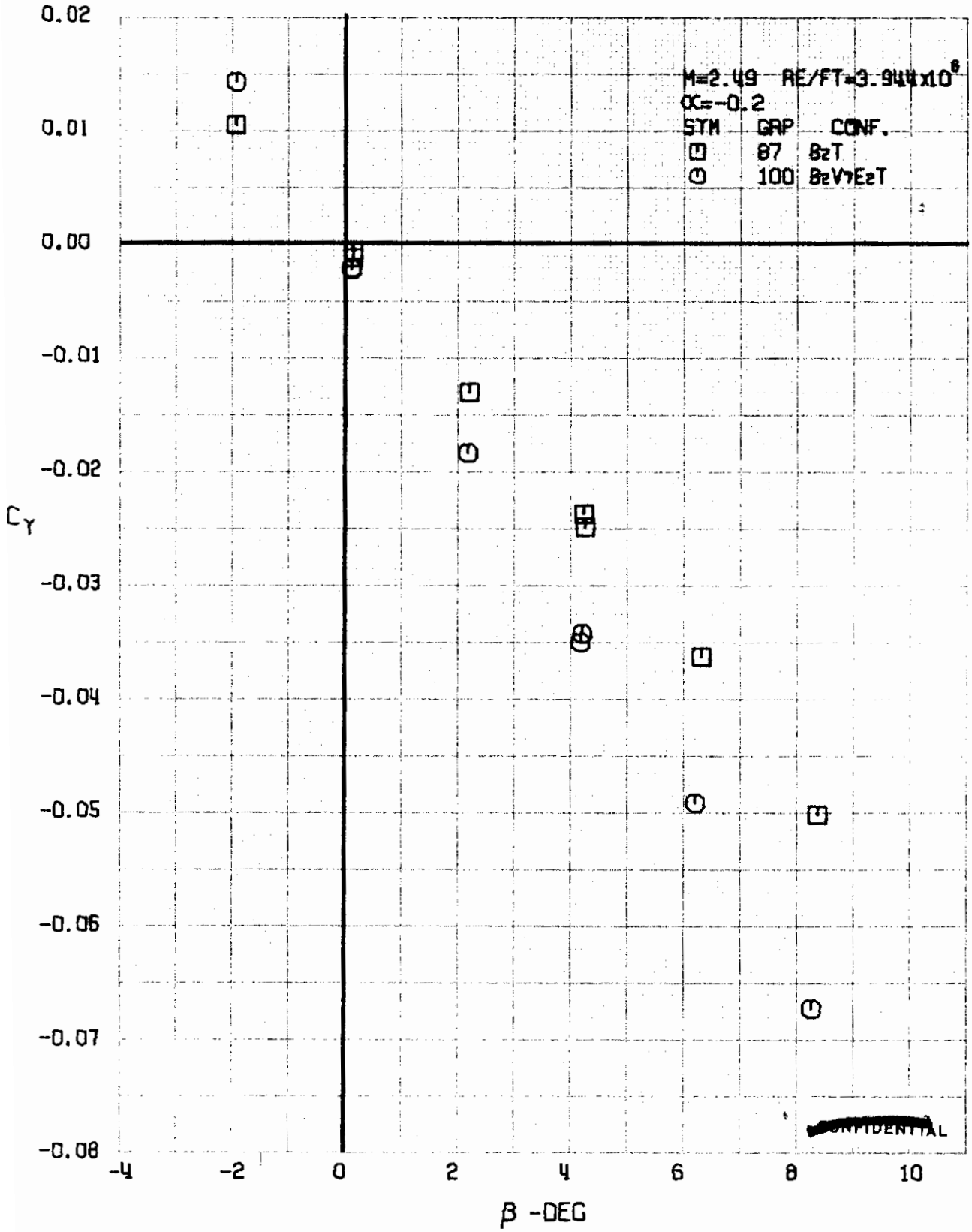

FIGURE 109 (U) CONFIGURATION BUILDUP
- SIDE FORCE COEFFICIENT VARIATION WITH ANGLE OF YAW (M=2.49)

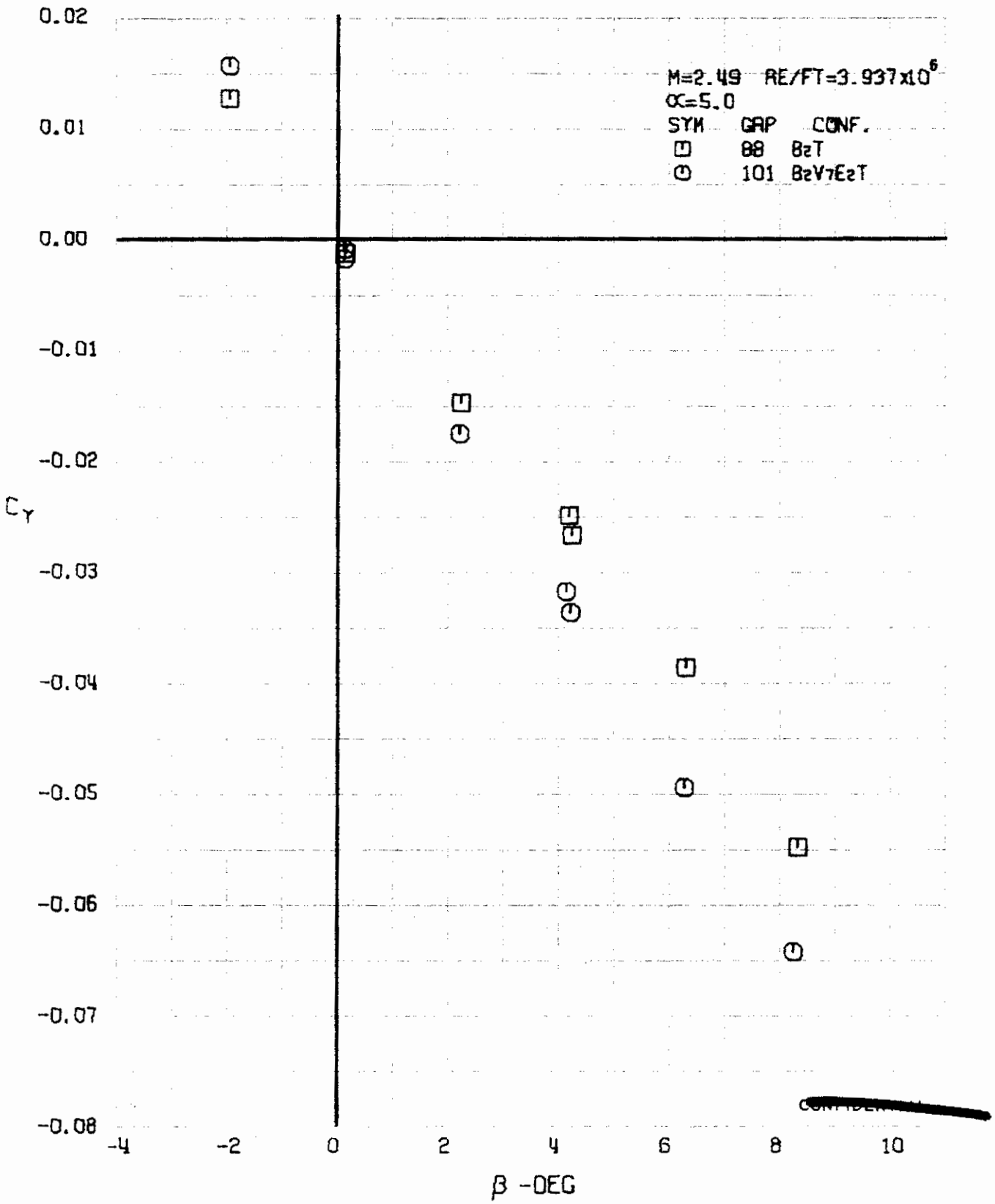

FIGURE 11C (U) CONFIGURATION BUILDUP
- SIDE FORCE COEFFICIENT VARIATION WITH ANGLE OF YAW (M=2.49)

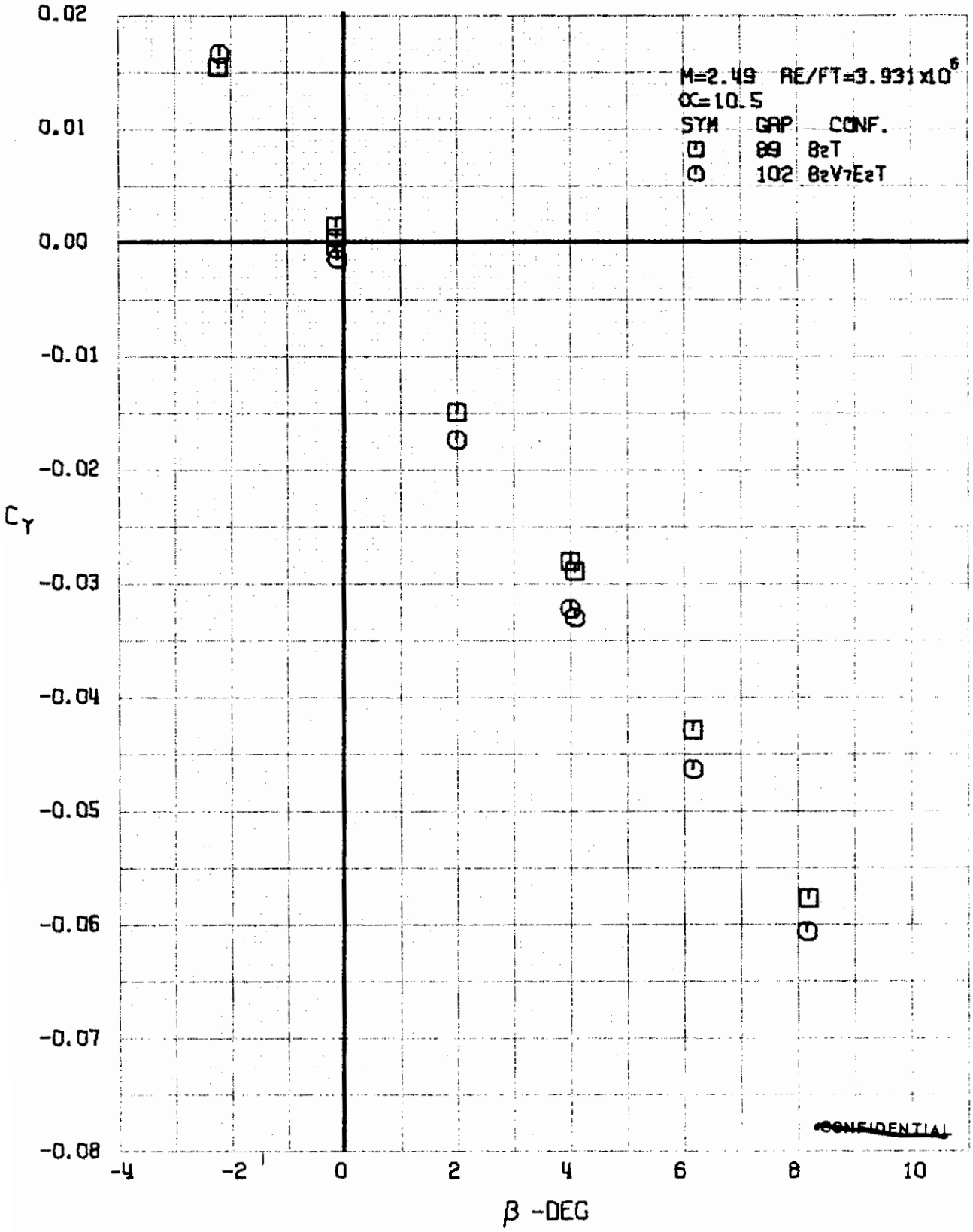

FIGURE 111 (U) CONFIGURATION BUILDUP
- SIDE FORCE COEFFICIENT VARIATION WITH ANGLE OF YAW (M=2.49)

CONFIDENTIAL

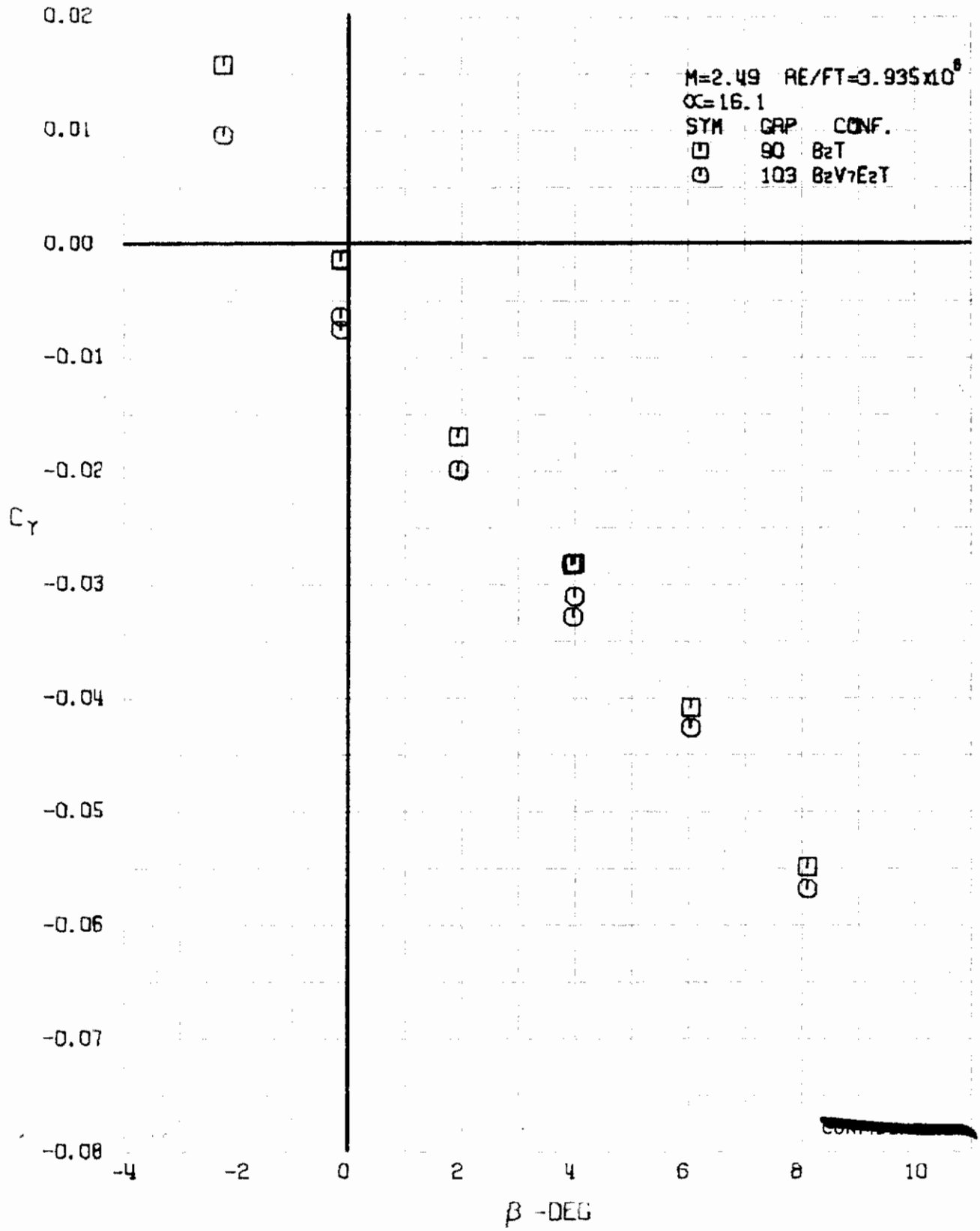

FIGURE 112 (U) CONFIGURATION BUILDUP
- SIDE FORCE COEFFICIENT VARIATION WITH ANGLE OF YAW (M=2.49)

CONFIDENTIAL

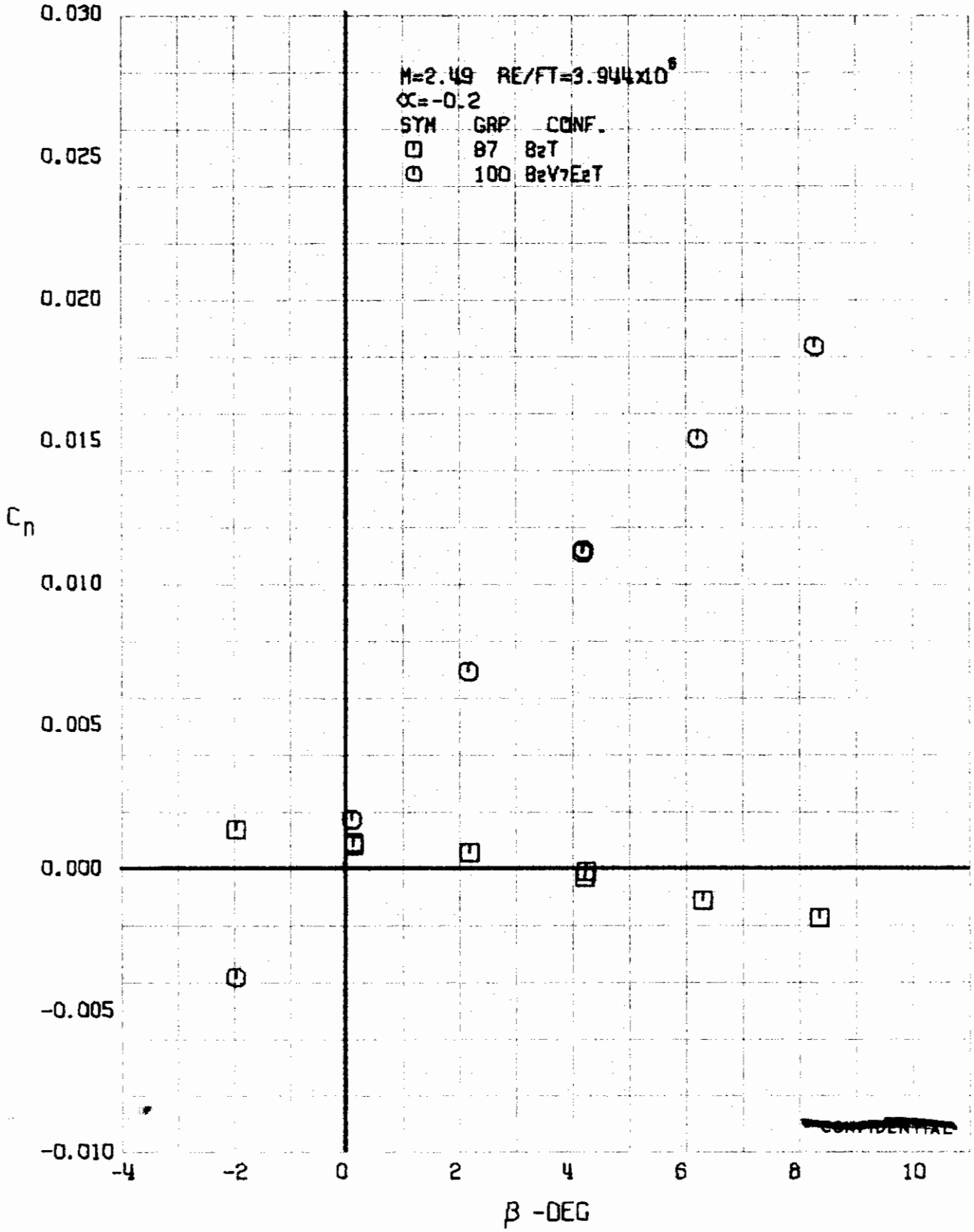

FIGURE 113 (U) CONFIGURATION BUILDUP
- YAWING MOMENT COEFFICIENT VARIATION WITH ANGLE OF YAW (M=2.49)

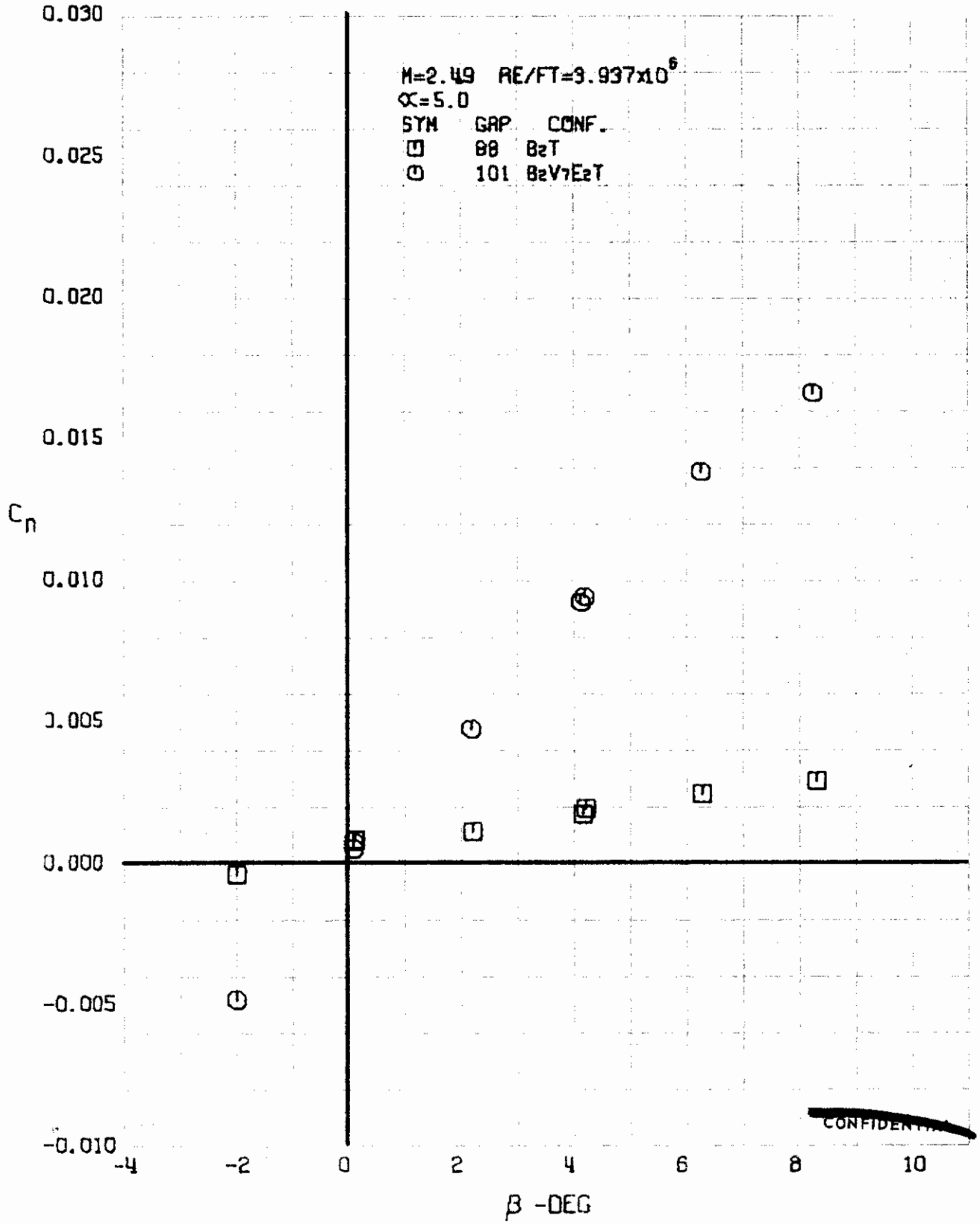

FIGURE 124 (U) CONFIGURATION BUILDUP
- YAWING MOMENT COEFFICIENT VARIATION WITH ANGLE OF YAW (M=2.49)

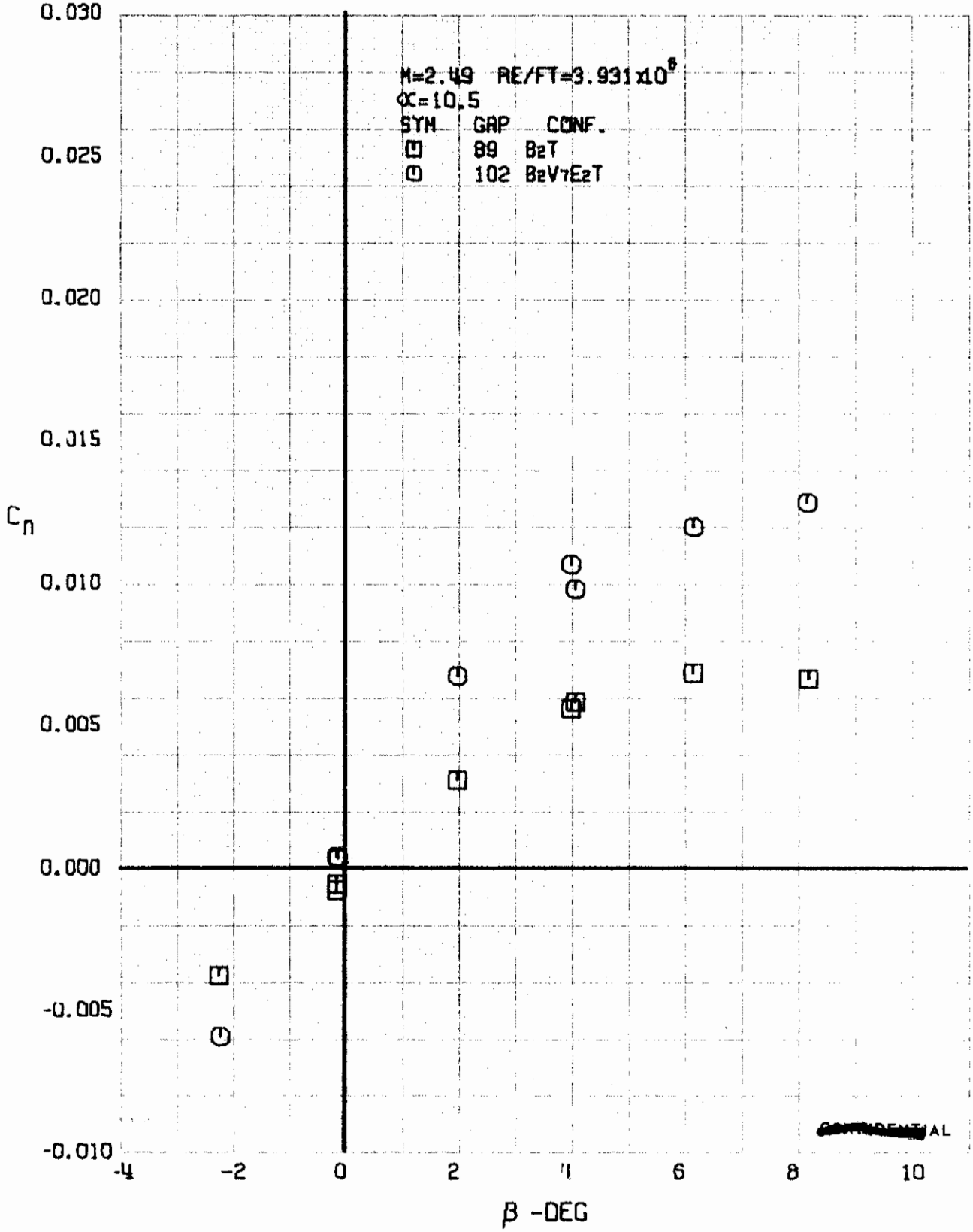

FIGURE 115 (U) CONFIGURATION BUILDUP
- YAWING MOMENT COEFFICIENT VARIATION WITH ANGLE OF YAW (M=2.49)

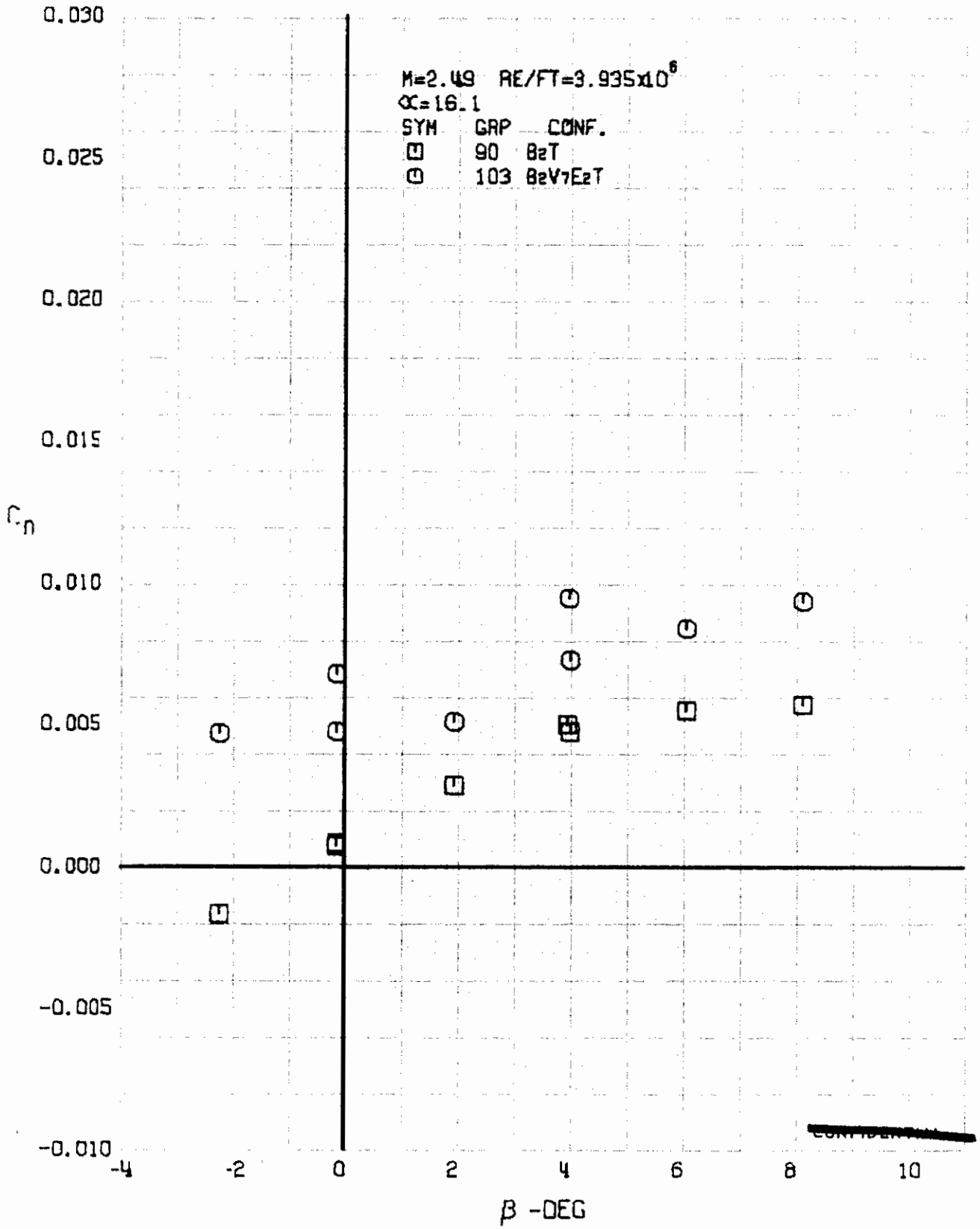

FIGURE 116 (U) CONFIGURATION BUILDUP
- YAWING MOMENT COEFFICIENT VARIATION WITH ANGLE OF YAW (M=2.49)

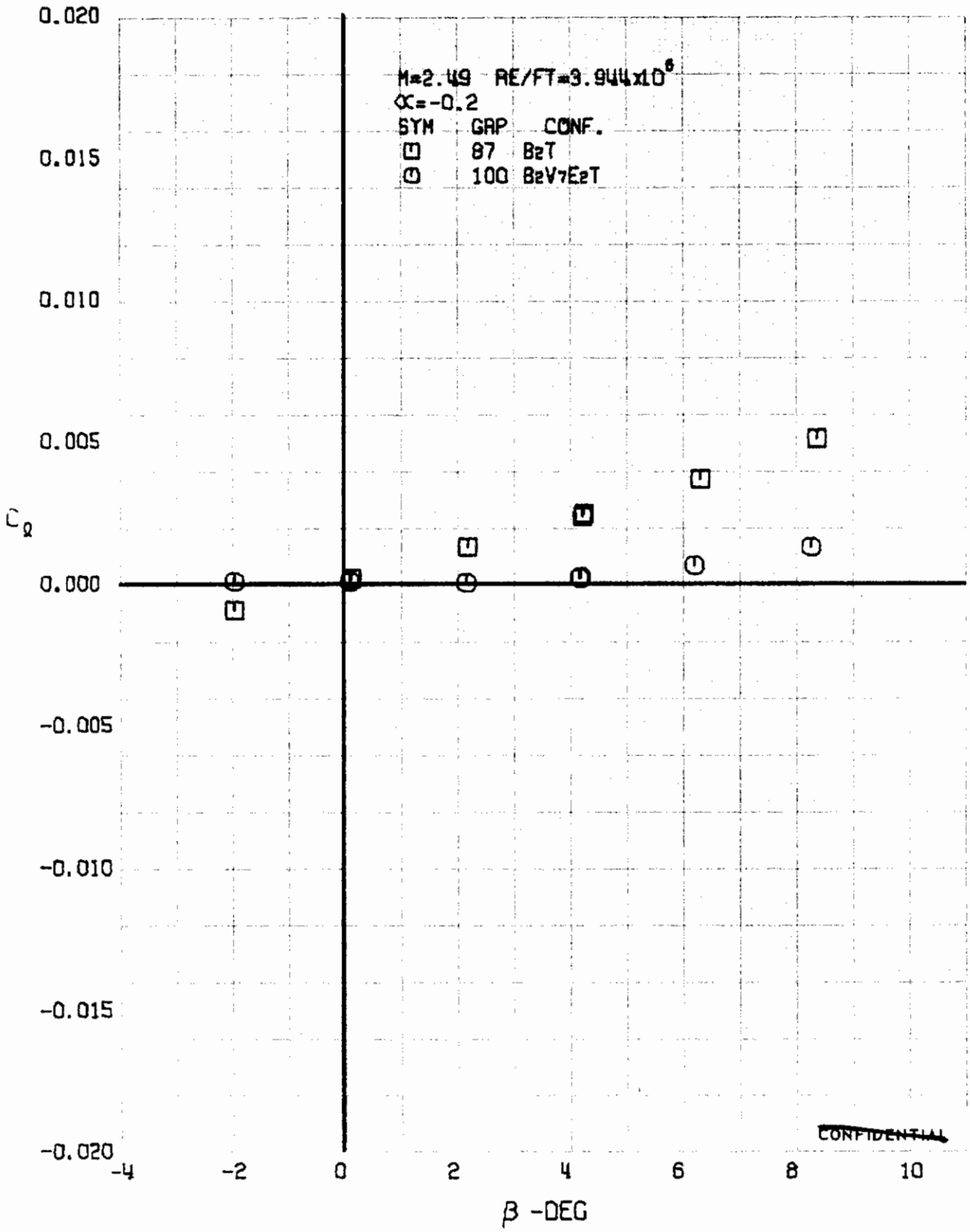

FIGURE 117 (U) CONFIGURATION BUILDUP
- ROLLING MOMENT COEFFICIENT VARIATION WITH ANGLE OF YAW (M=2.49)

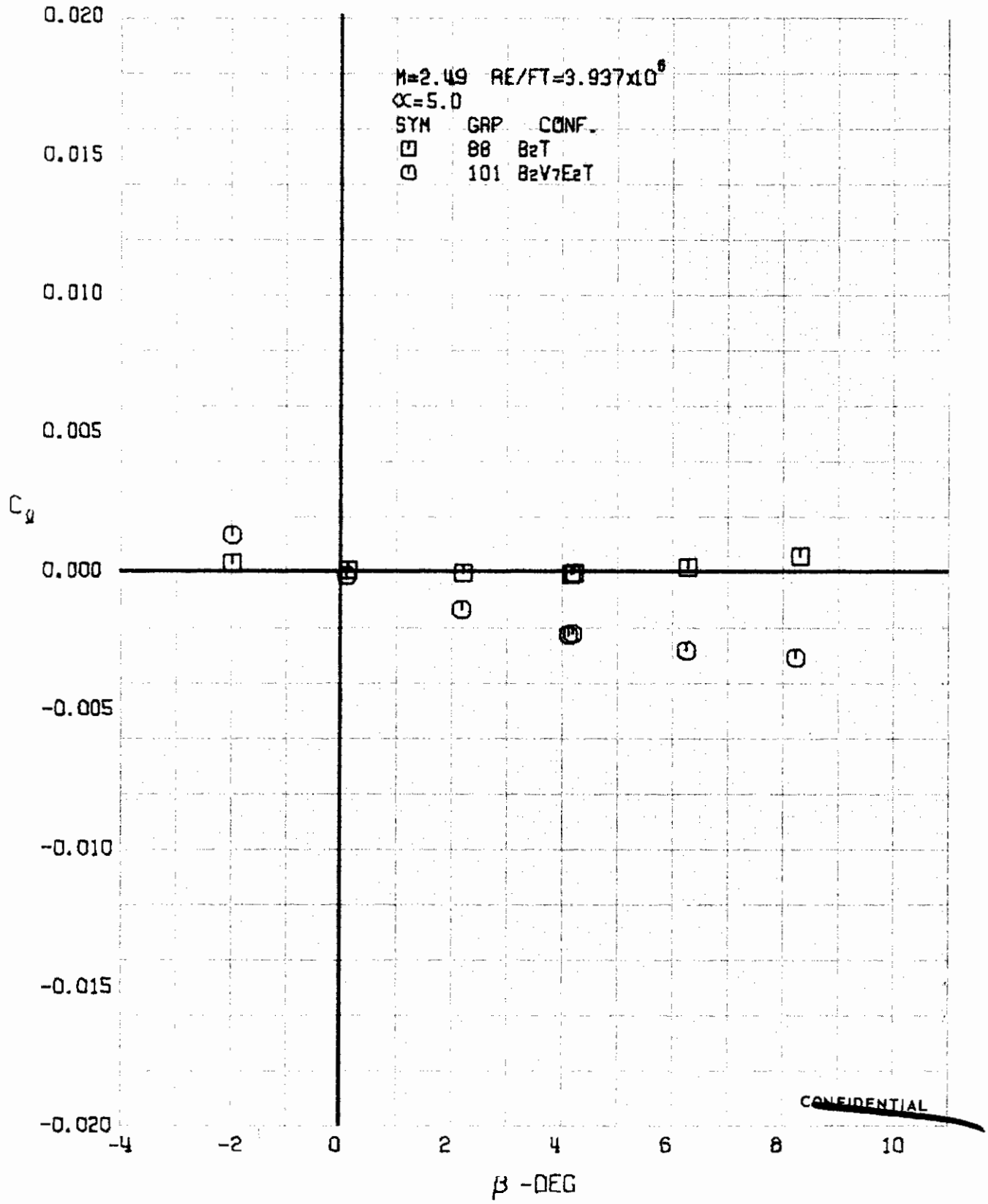

FIGURE 118 (U) CONFIGURATION BUILDUP
- ROLLING MOMENT COEFFICIENT VARIATION WITH ANGLE OF YAW (M=2.49)

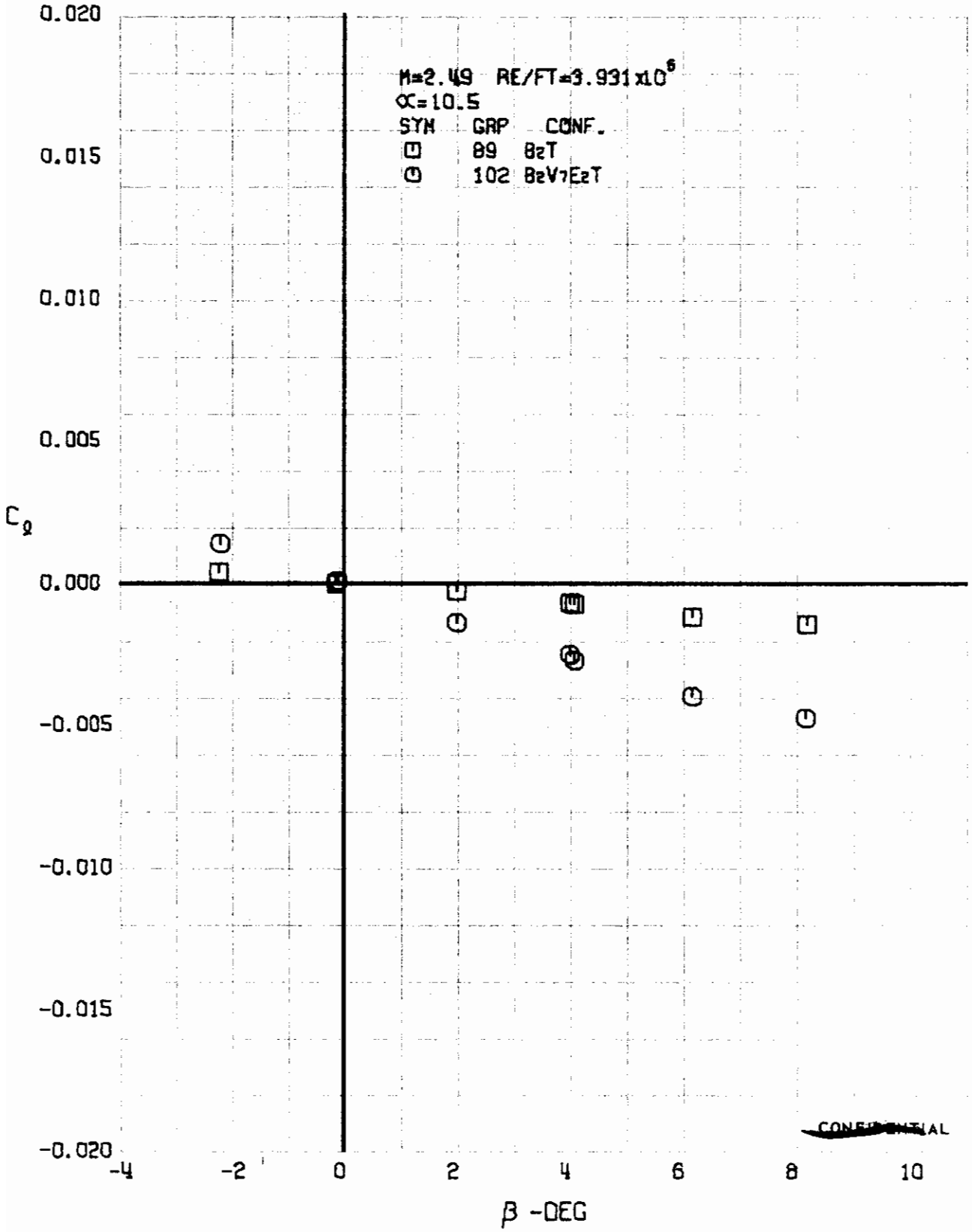

FIGURE 119 (U) CONFIGURATION BUILDUP
- ROLLING MOMENT COEFFICIENT VARIATION WITH ANGLE OF YAW (M=2.49)

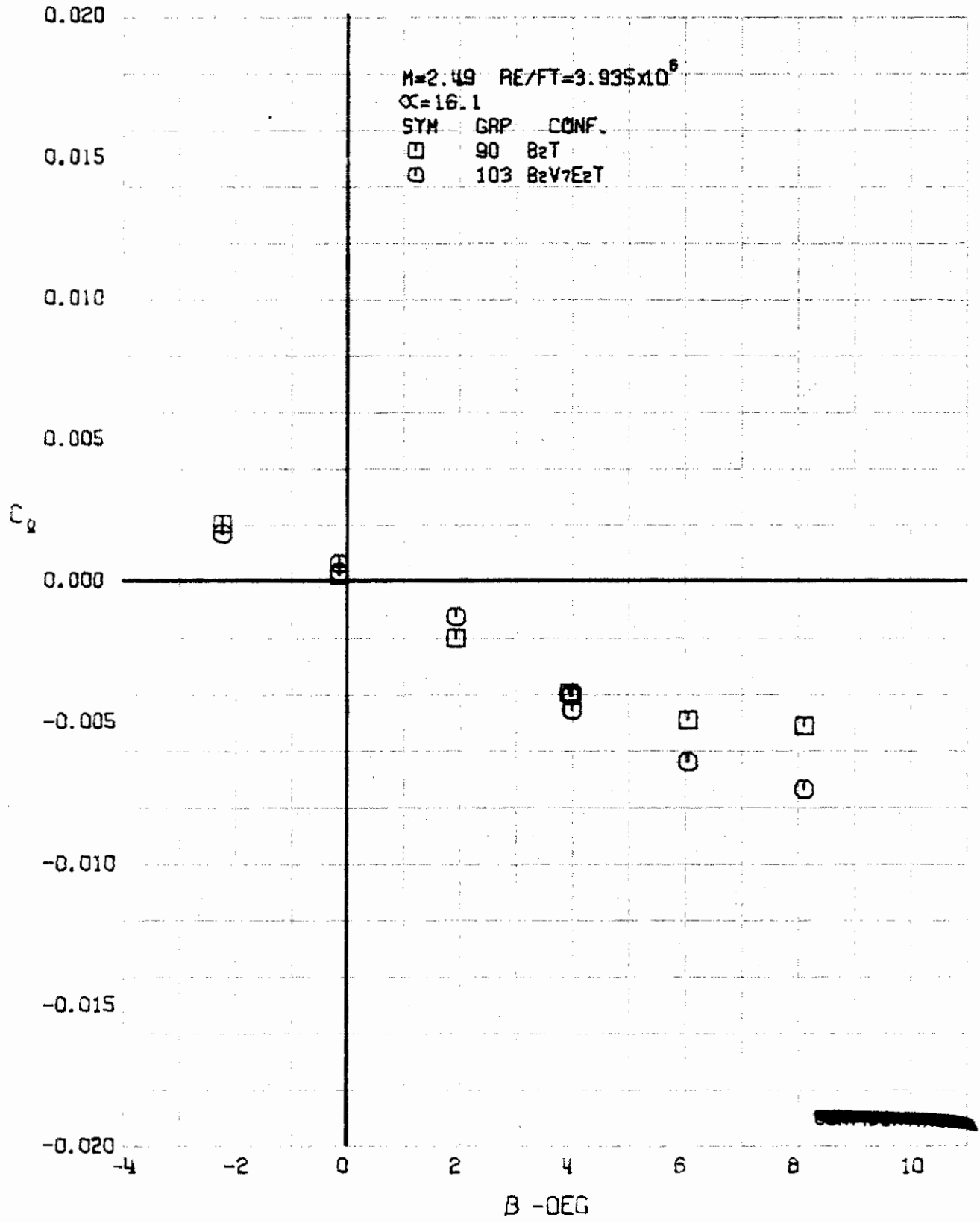

FIGURE 120 (U) CONFIGURATION BUILDUP
- ROLLING MOMENT COEFFICIENT VARIATION WITH ANGLE OF YAW (M=2.49)

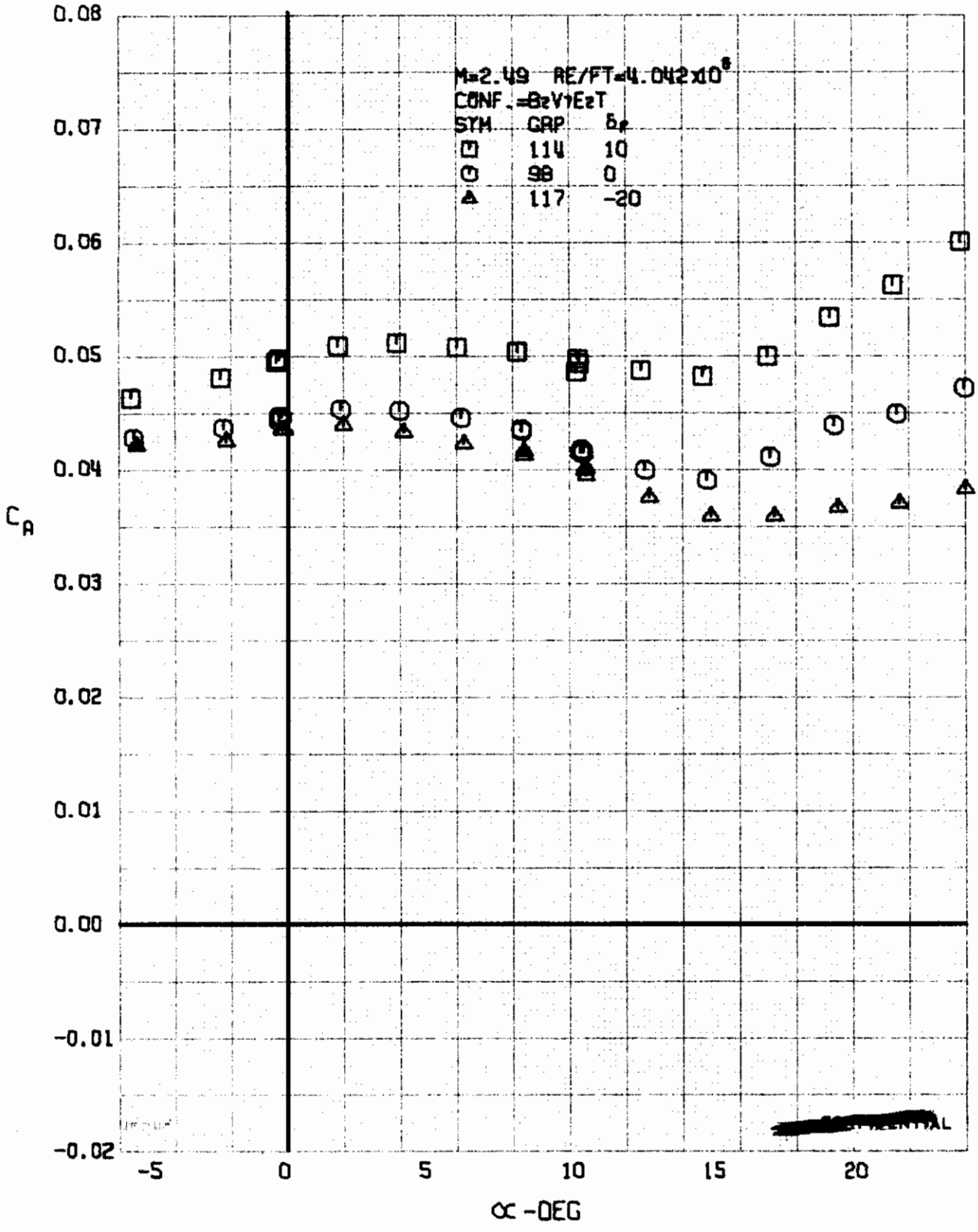

FIGURE 121 (U) ELEVON EFFECTS
- AXIAL FORCE COEFFICIENT VARIATION WITH ANGLE OF ATTACK (M=2.49)

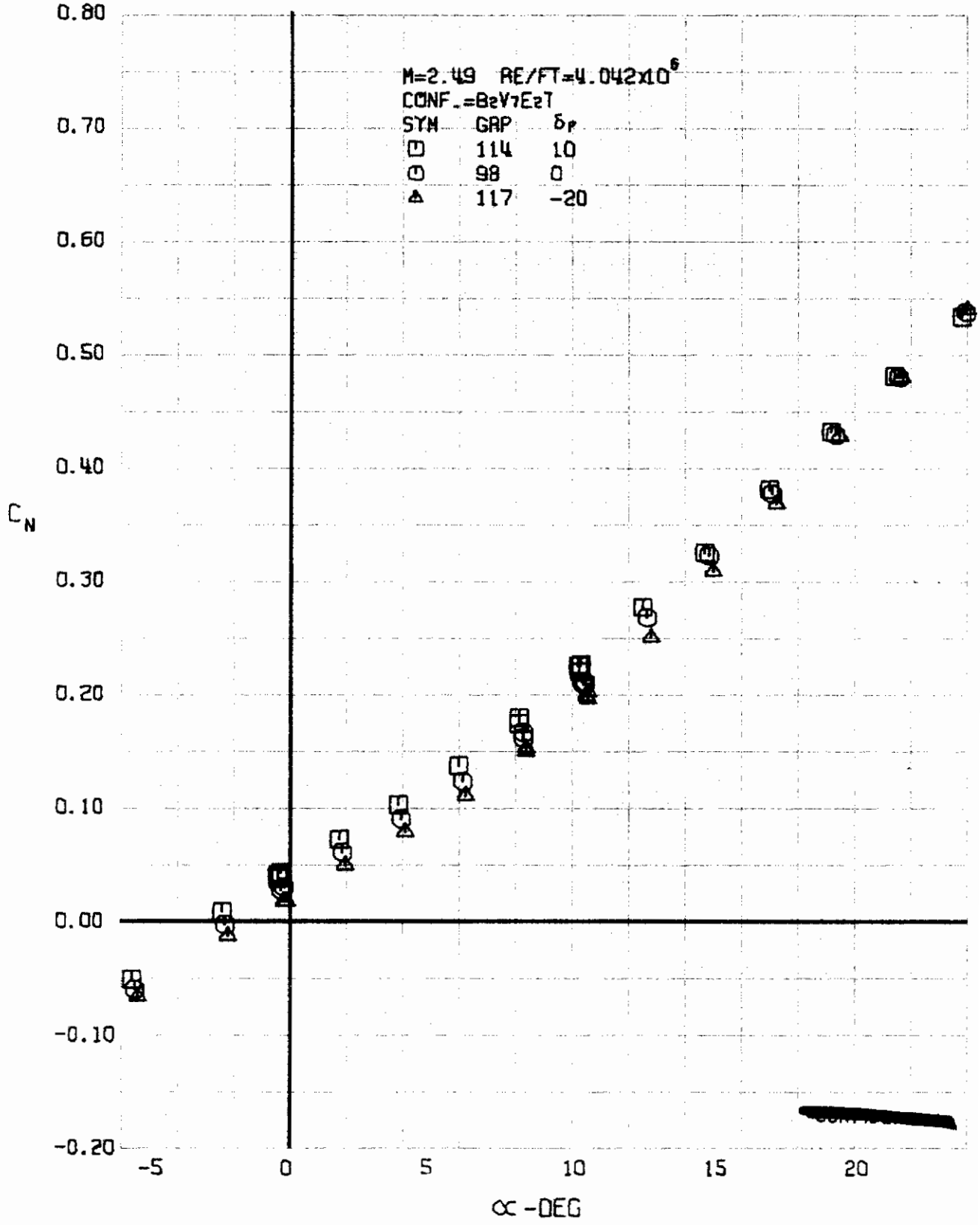

FIGURE 122 (U) ELEVON EFFECTS
- NORMAL FORCE COEFFICIENT VARIATION WITH ANGLE OF ATTACK (M=2.49)

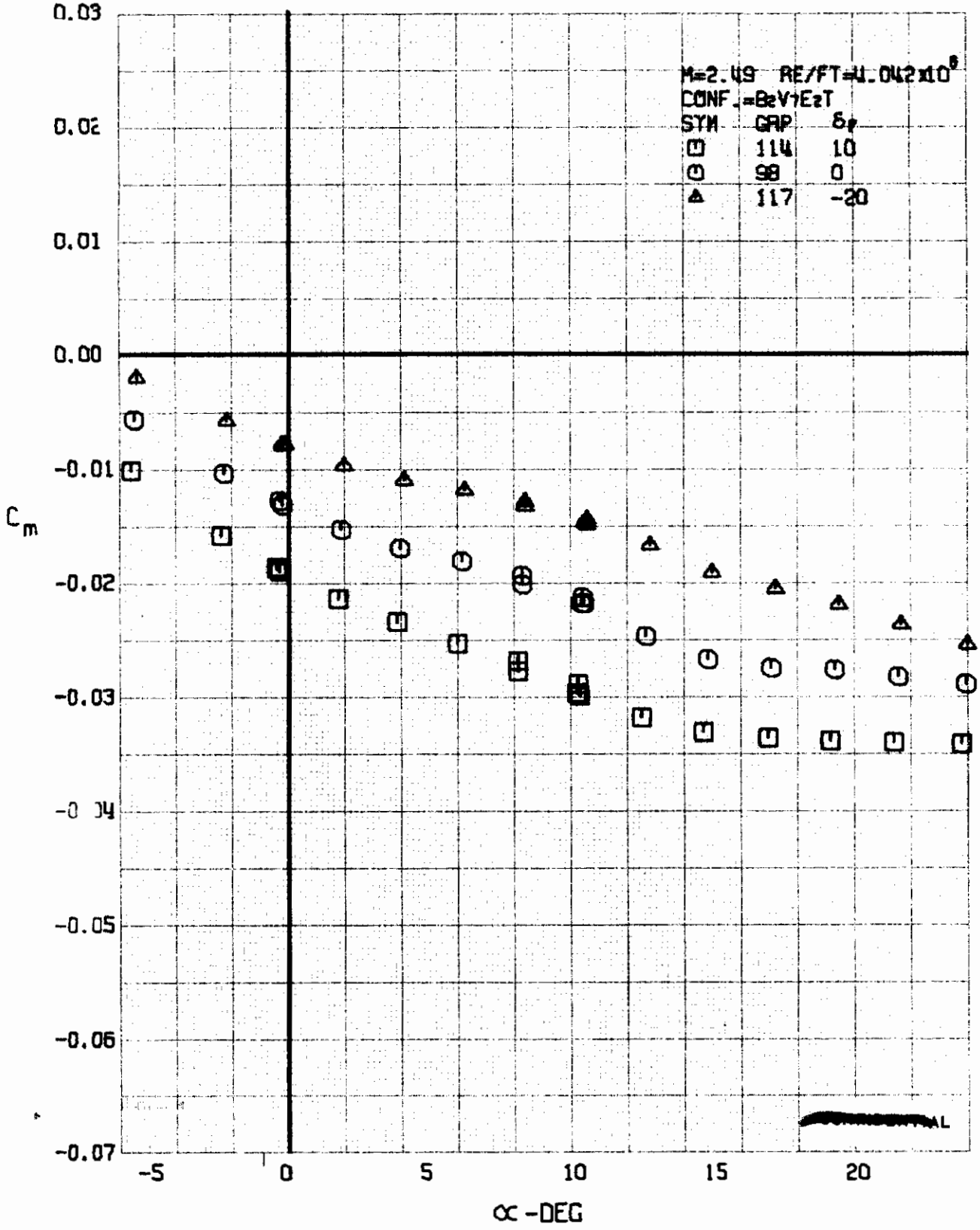

FIGURE 123 (U) ELEVON EFFECTS
- PITCHING MOMENT COEFFICIENT VARIATION WITH ANGLE OF ATTACK (M=2.49)

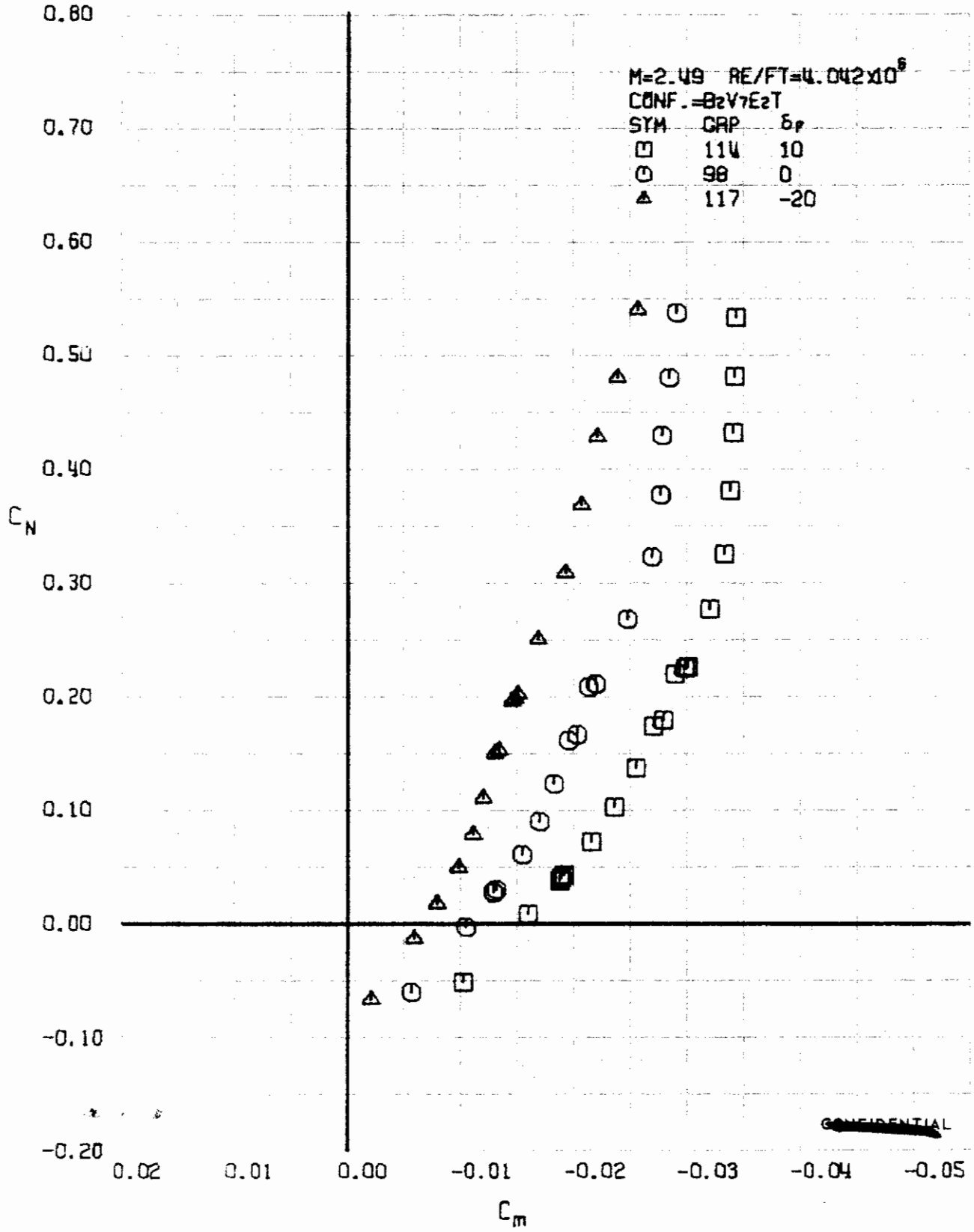

FIGURE 124 (U) ELEVON EFFECTS
- LONGITUDINAL STABILITY VARIATION (M=2.49)

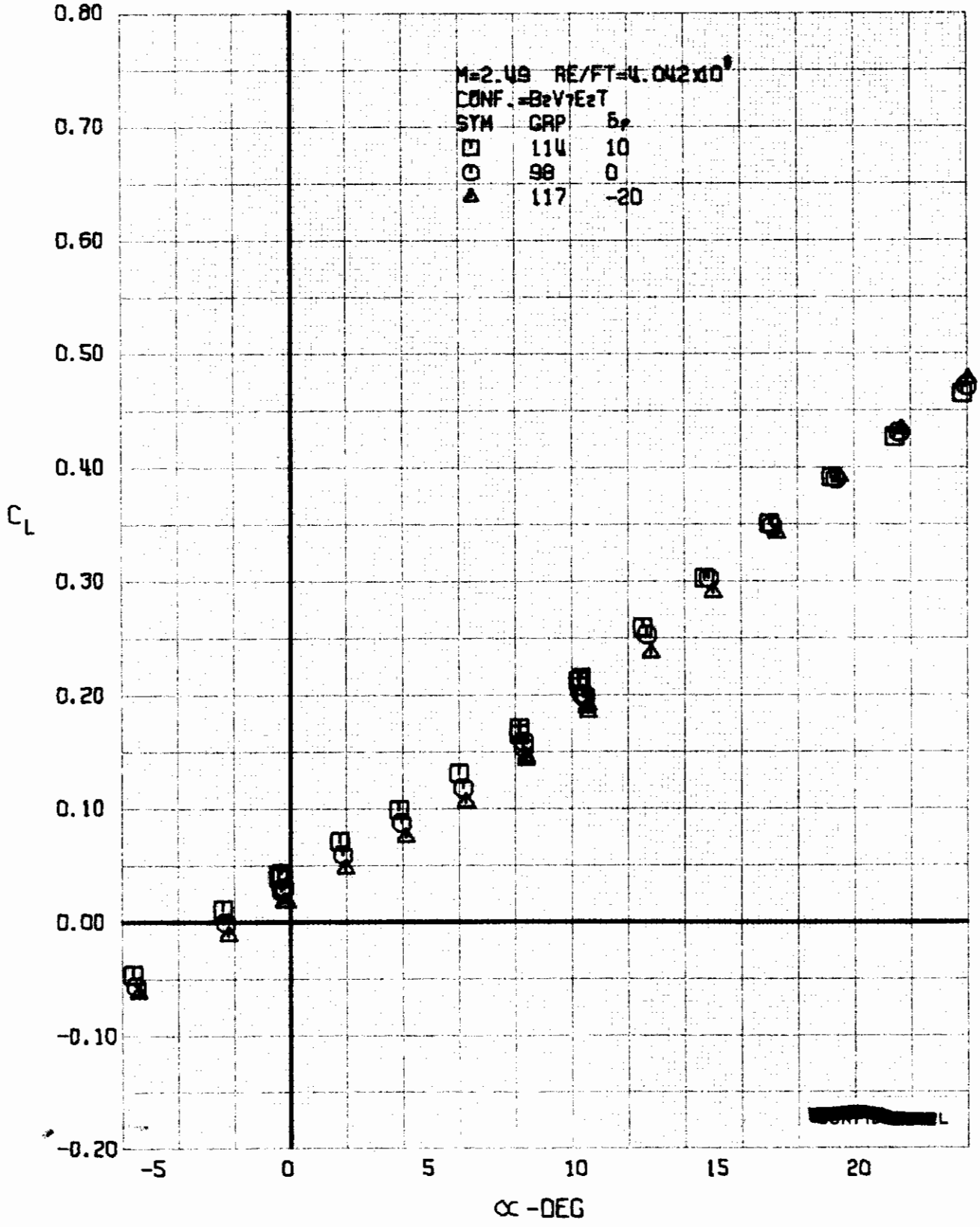

FIGURE 125 (U) ELEVON EFFECTS
- LIFT COEFFICIENT VARIATION WITH ANGLE OF ATTACK (M=2.49)

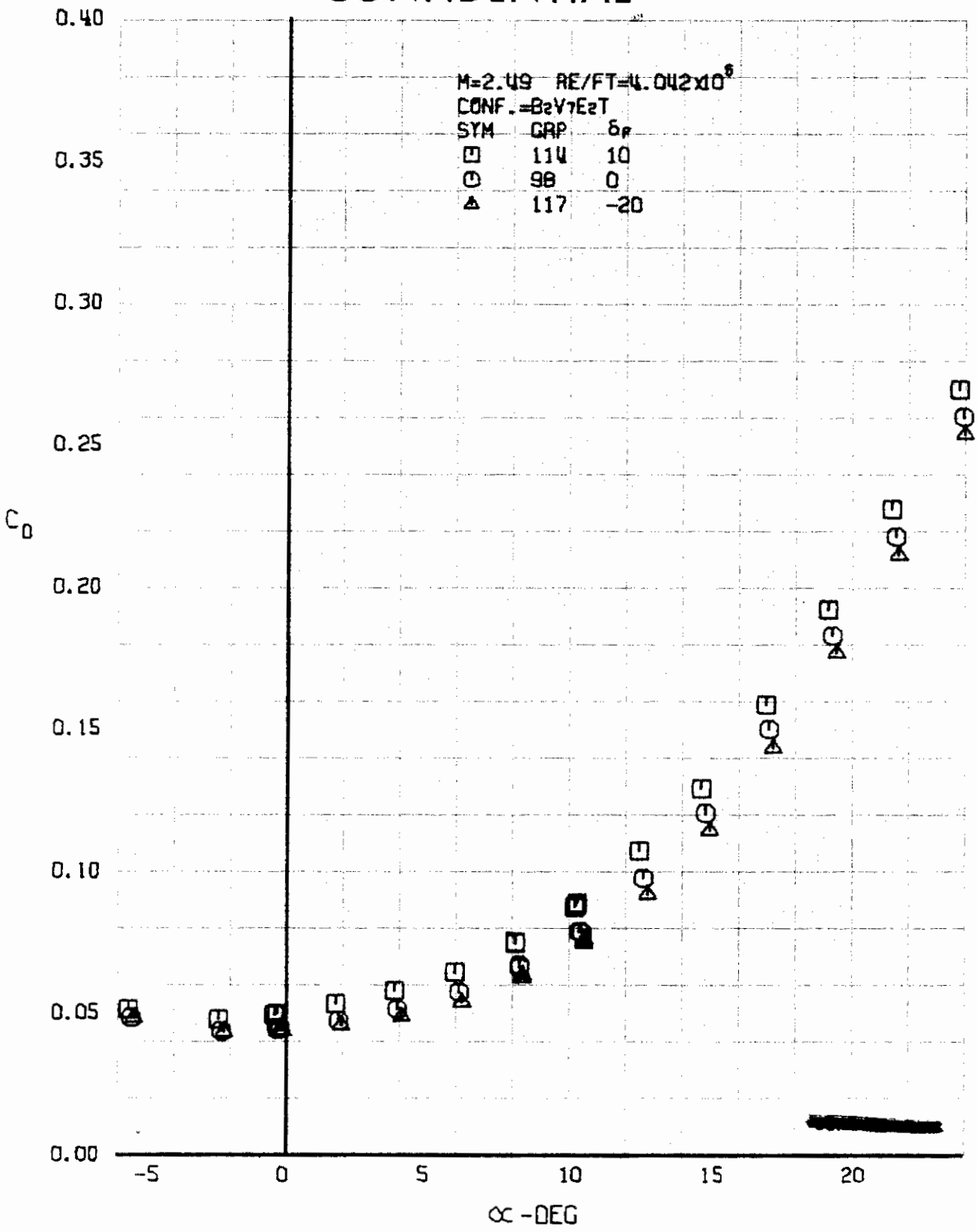

FIGURE 126 (U) ELEVON EFFECTS
- DRAG COEFFICIENT VARIATION WITH ANGLE OF ATTACK (M=2.49)

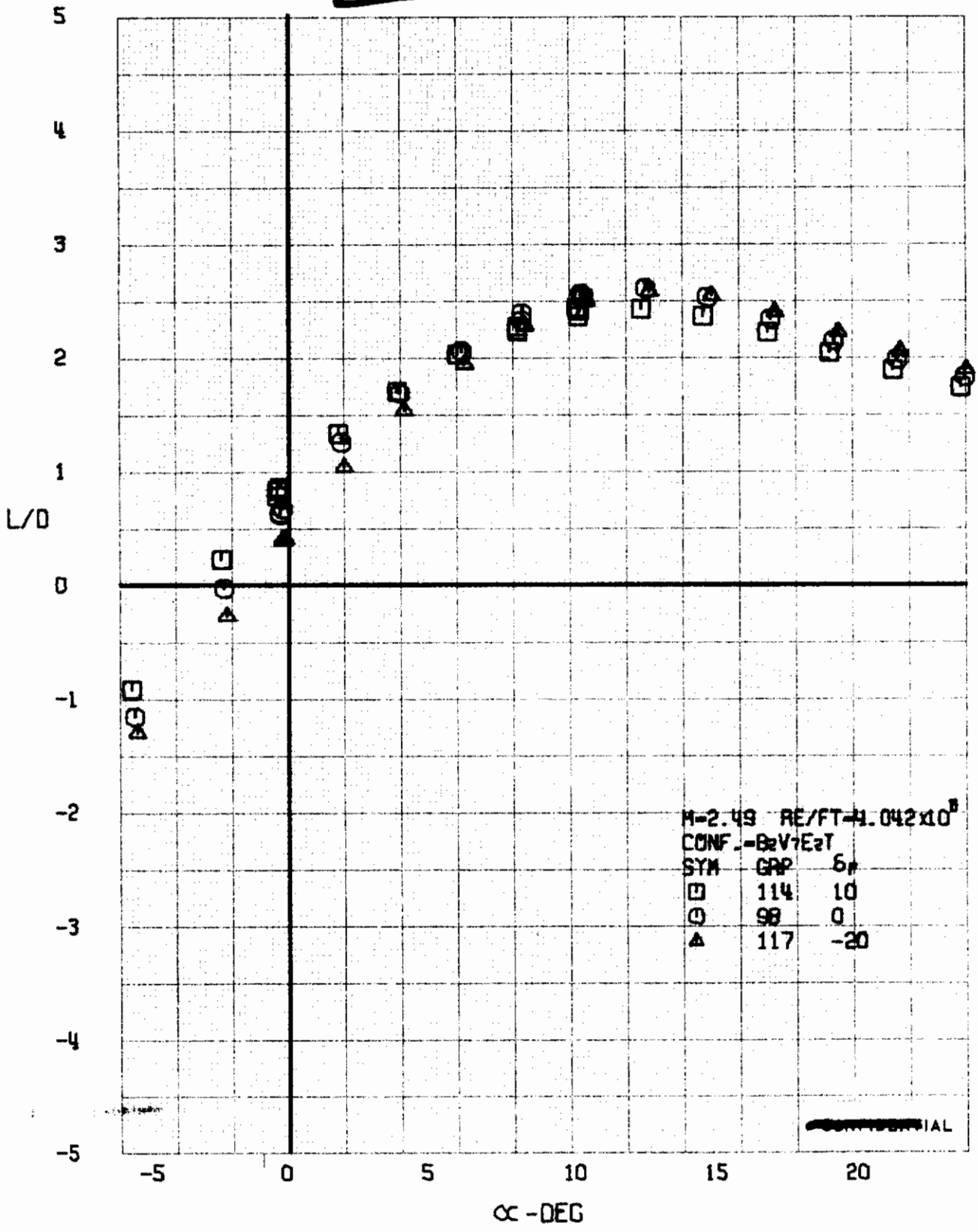

FIGURE 127 (U) ELEVON EFFECTS
- LIFT-DRAG RATIO VARIATION WITH ANGLE OF ATTACK (M=2.49)

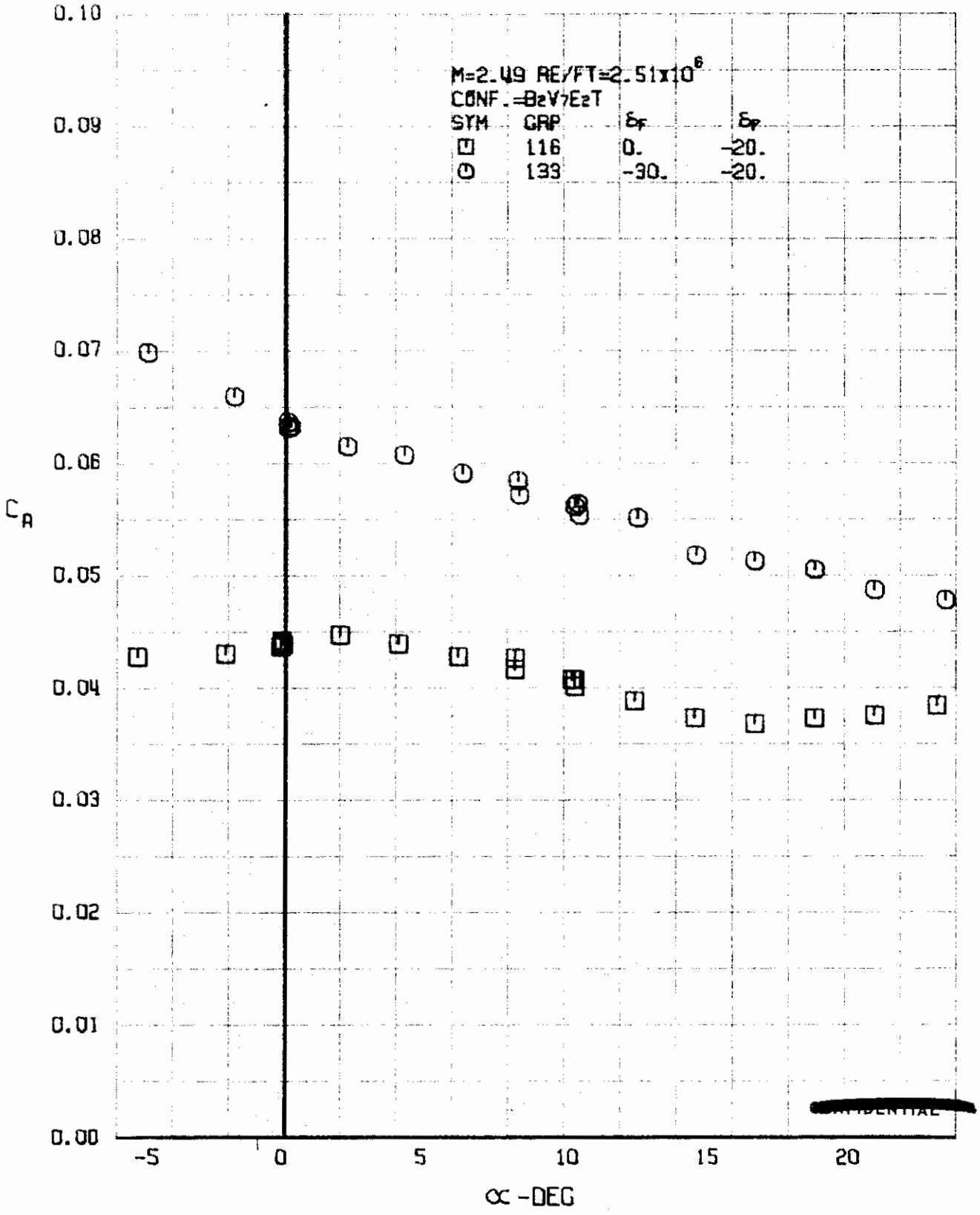

FIGURE 128 (U) FLAP EFFECTS
- AXIAL FORCE COEFFICIENT VARIATION WITH ANGLE OF ATTACK (M=2.49)

~~CONFIDENTIAL~~

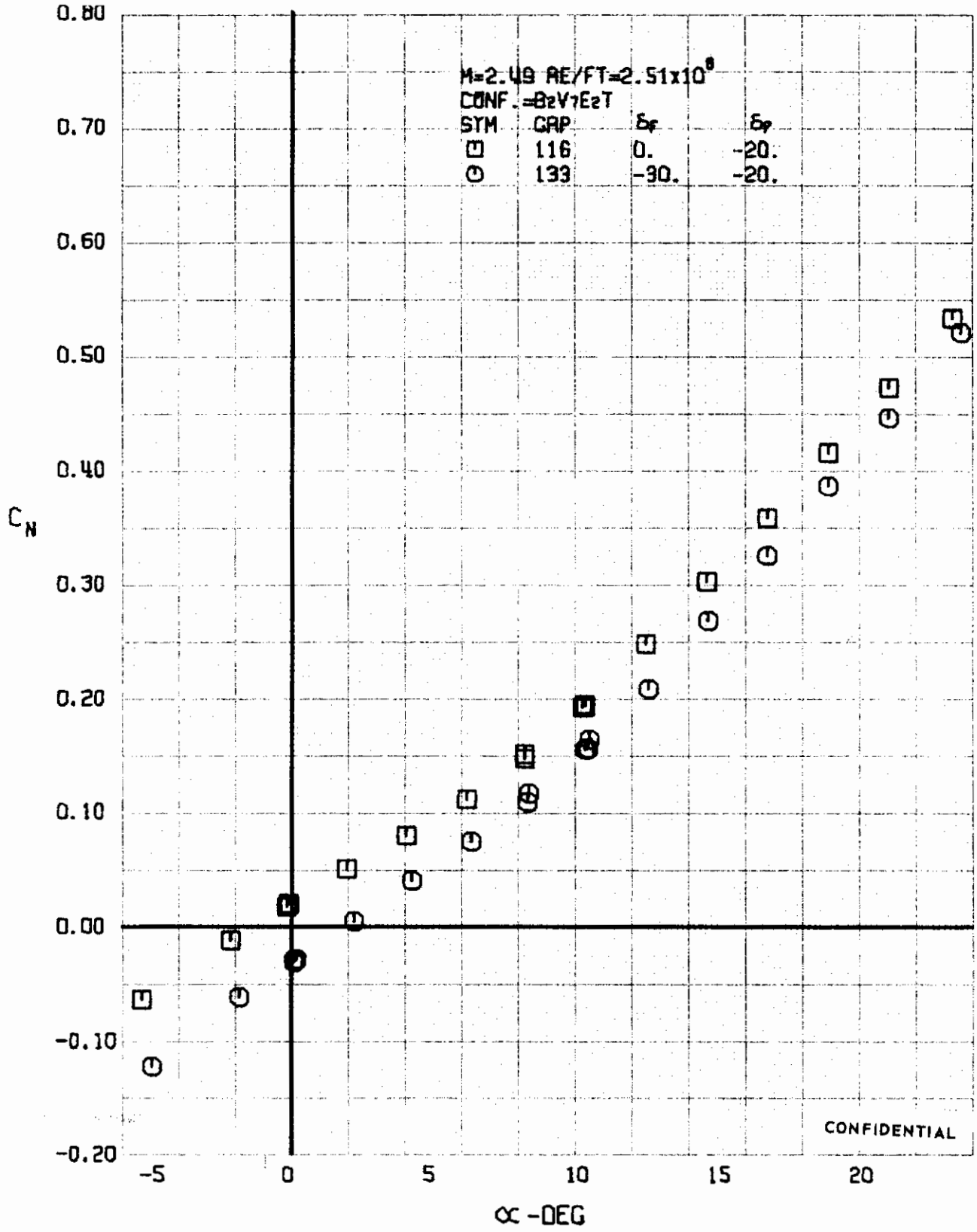

FIGURE 129 (U) FLAP EFFECTS
- NORMAL FORCE COEFFICIENT VARIATION WITH ANGLE OF ATTACK (M=2.49)

~~CONFIDENTIAL~~

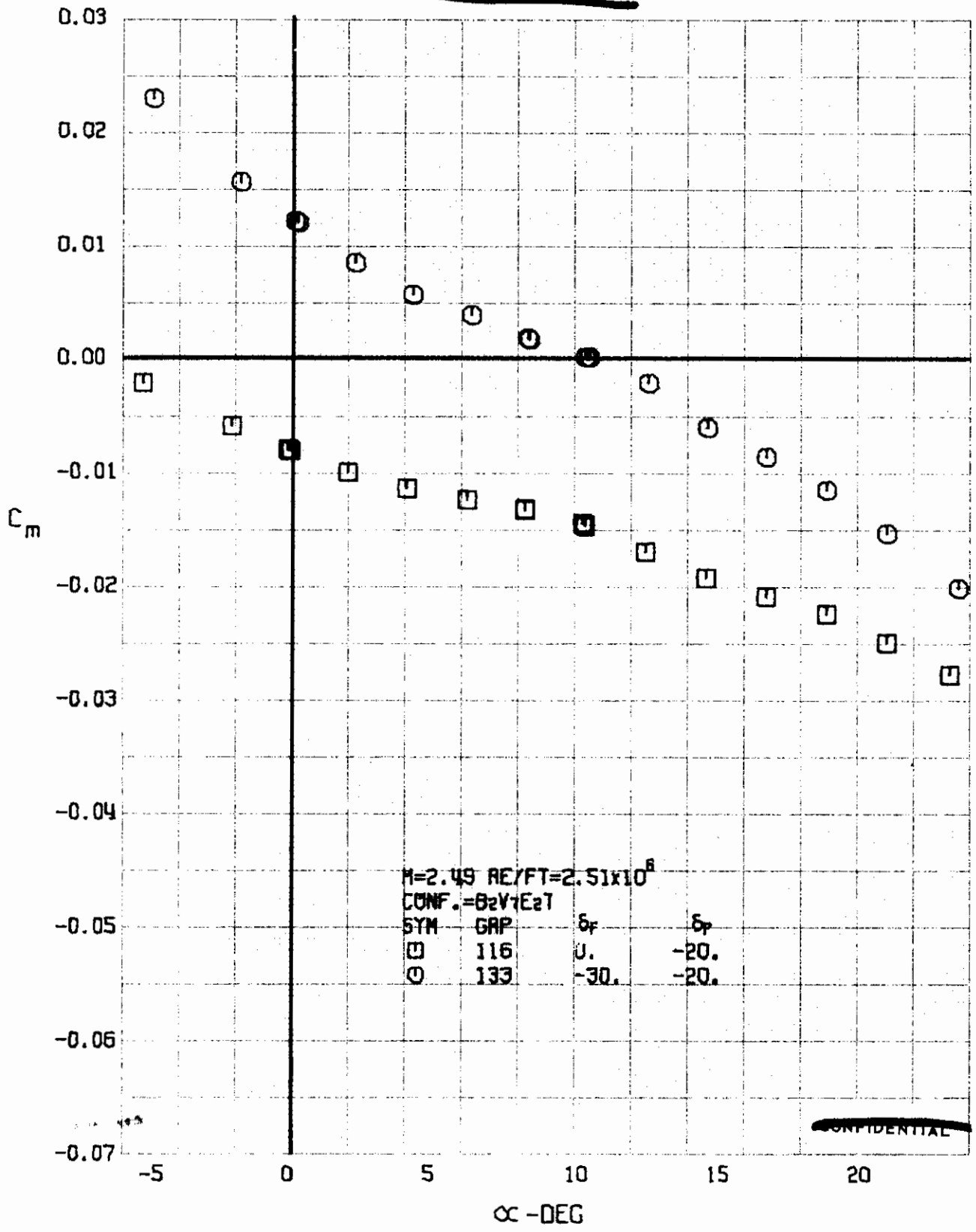

FIGURE 130 (U) FLAP EFFECTS
- PITCHING MOMENT COEFFICIENT VARIATION WITH ANGLE OF ATTACK (M=2.49)

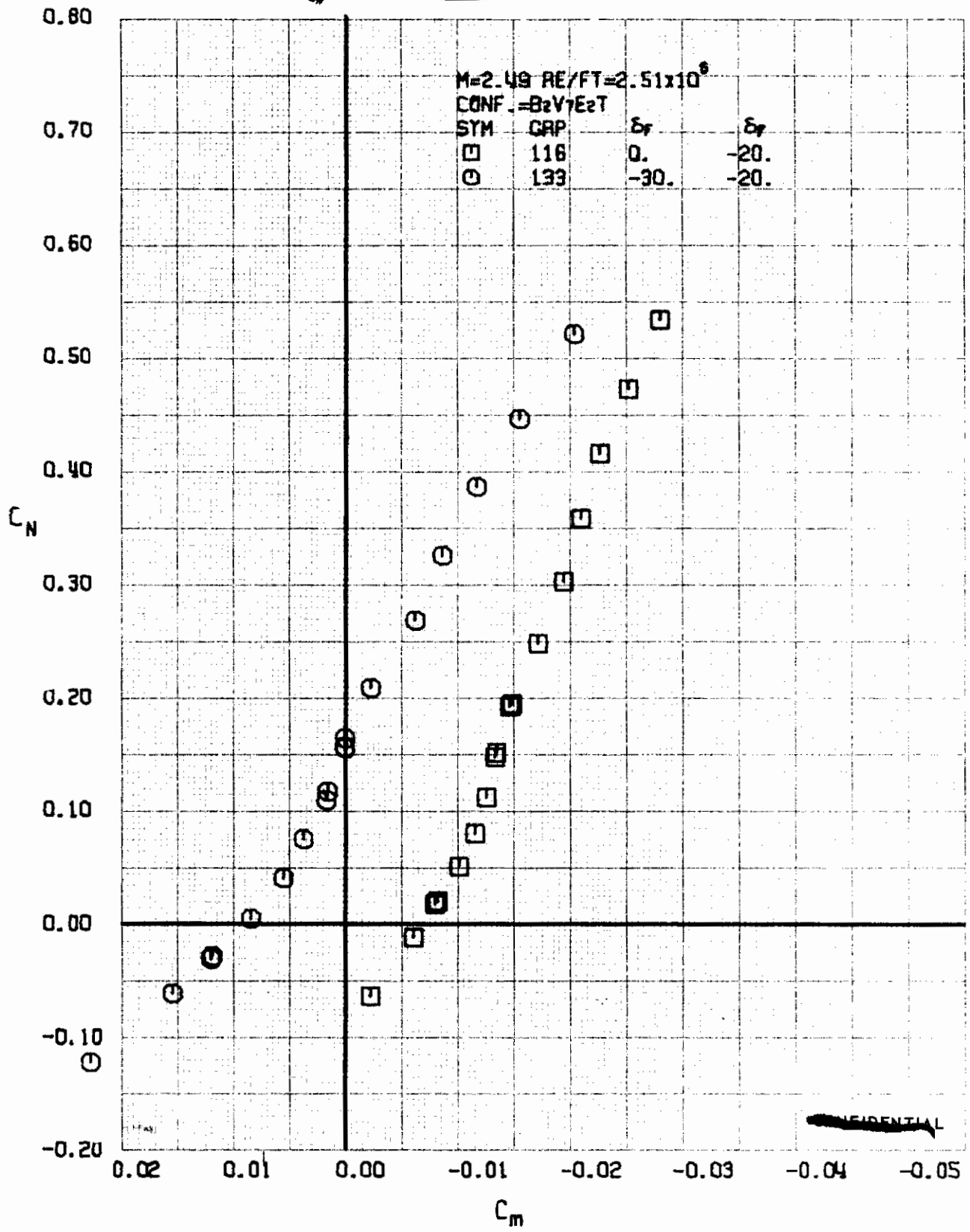

FIGURE 131 (U) FLAP EFFECTS
- LONGITUDINAL STABILITY VARIATION (M=2.49)

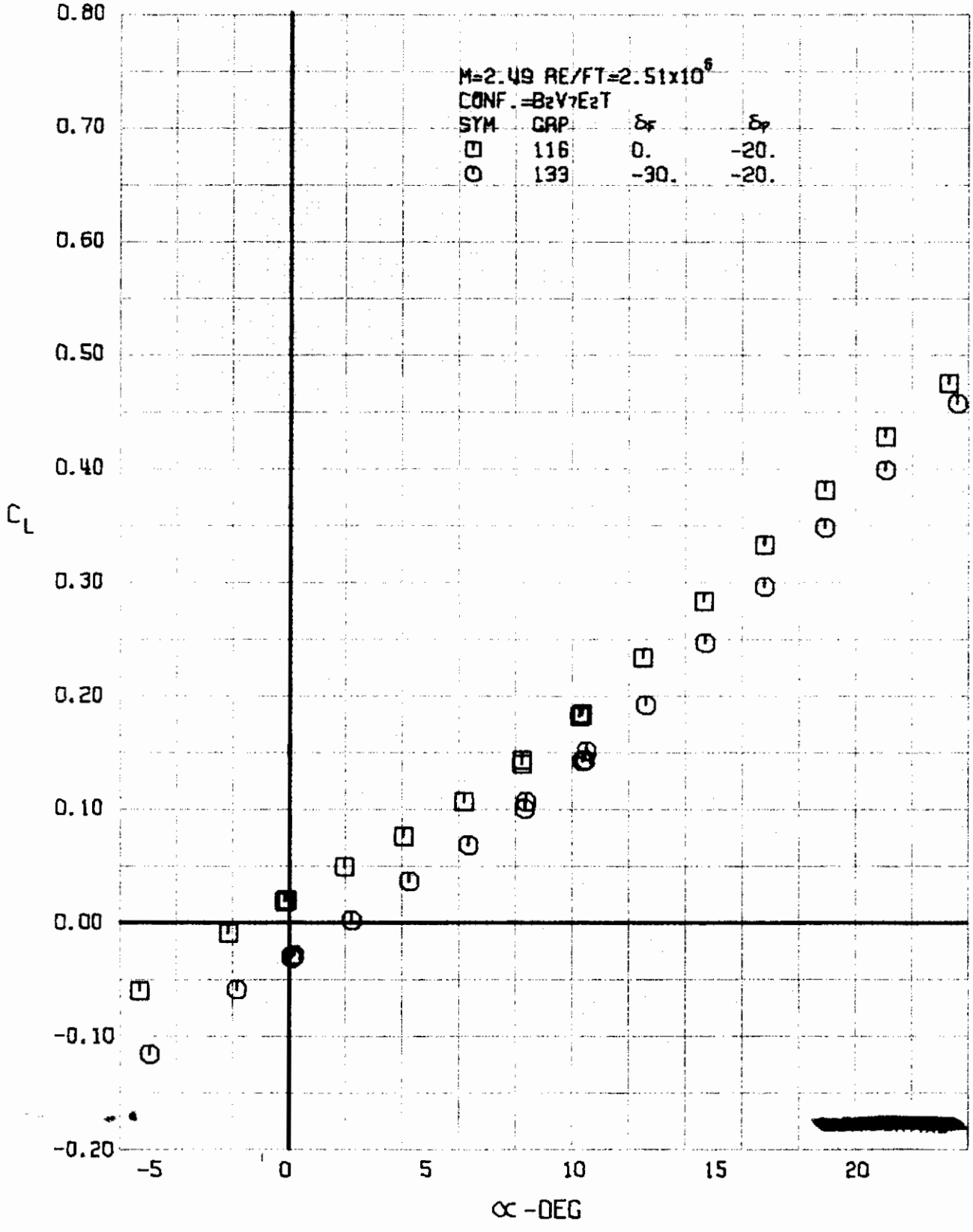

FIGURE 132 (U) FLAP EFFECTS
- LIFT COEFFICIENT VARIATION WITH ANGLE OF ATTACK (M=2.49)

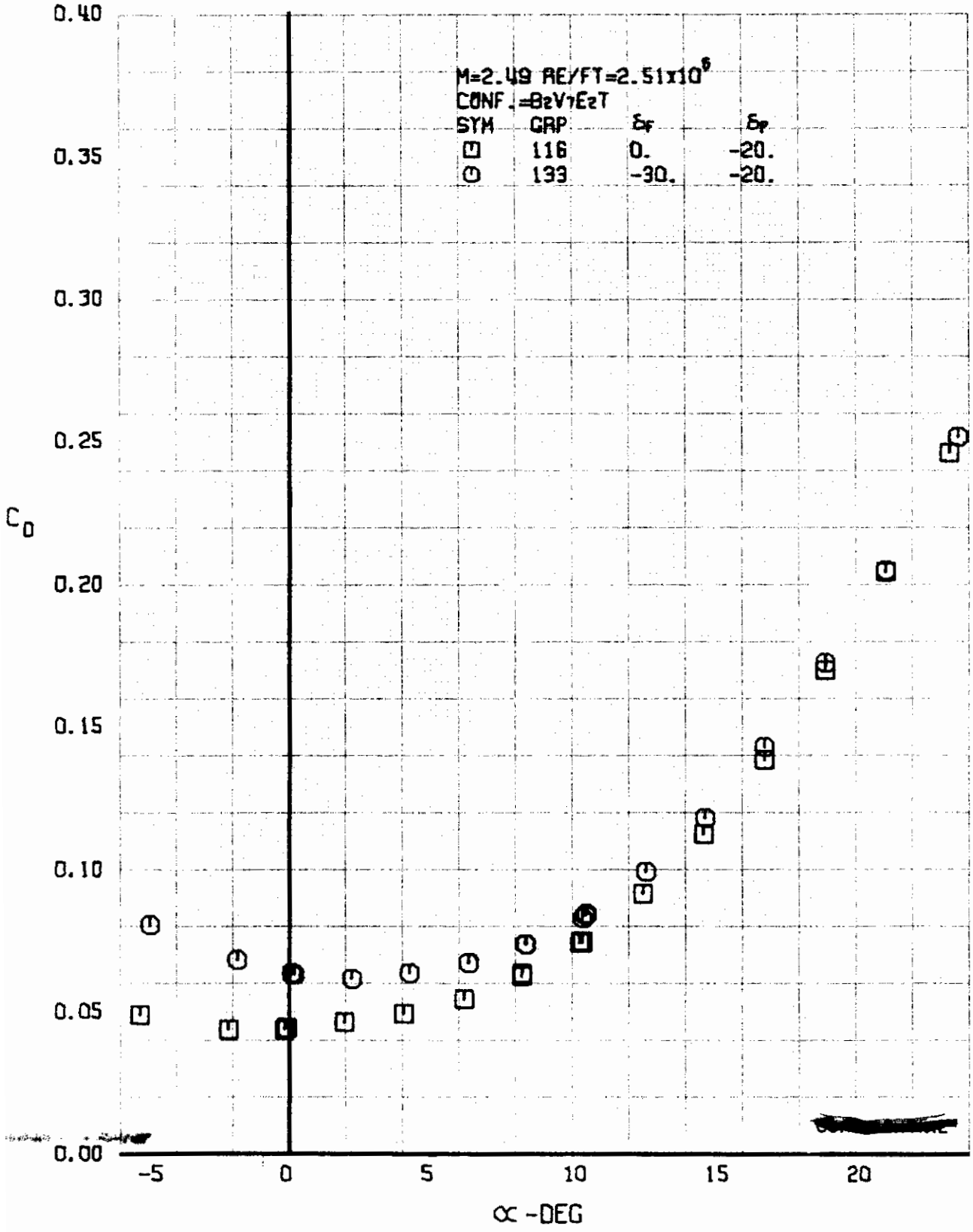

FIGURE 133 (U) FLAP EFFECTS
- DRAG COEFFICIENT VARIATION WITH ANGLE OF ATTACK (M=2.49)

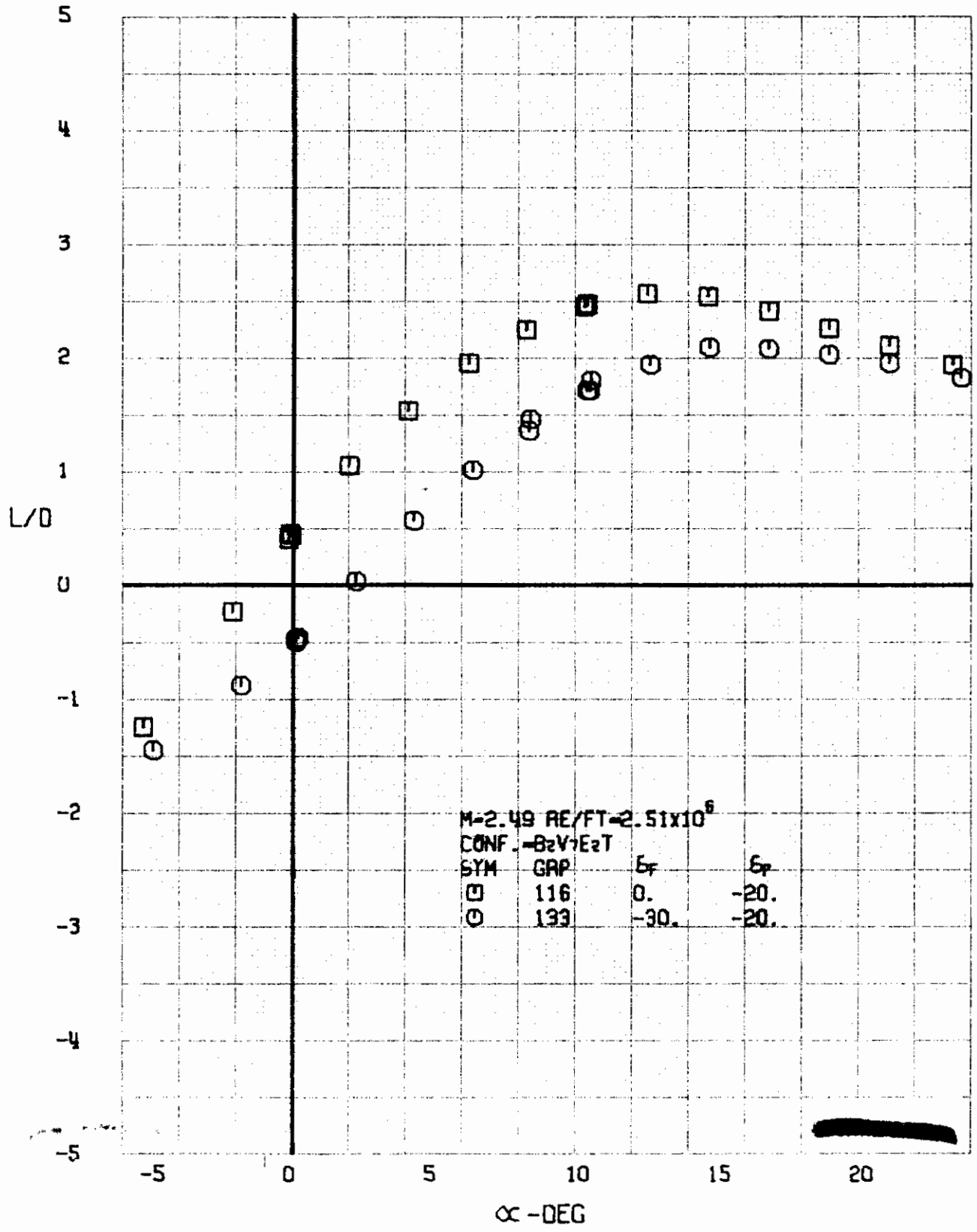

FIGURE 134 (U) FLAP EFFECTS
- LIFT-DRAG RATIO VARIATION WITH ANGLE OF ATTACK (M=2.49)

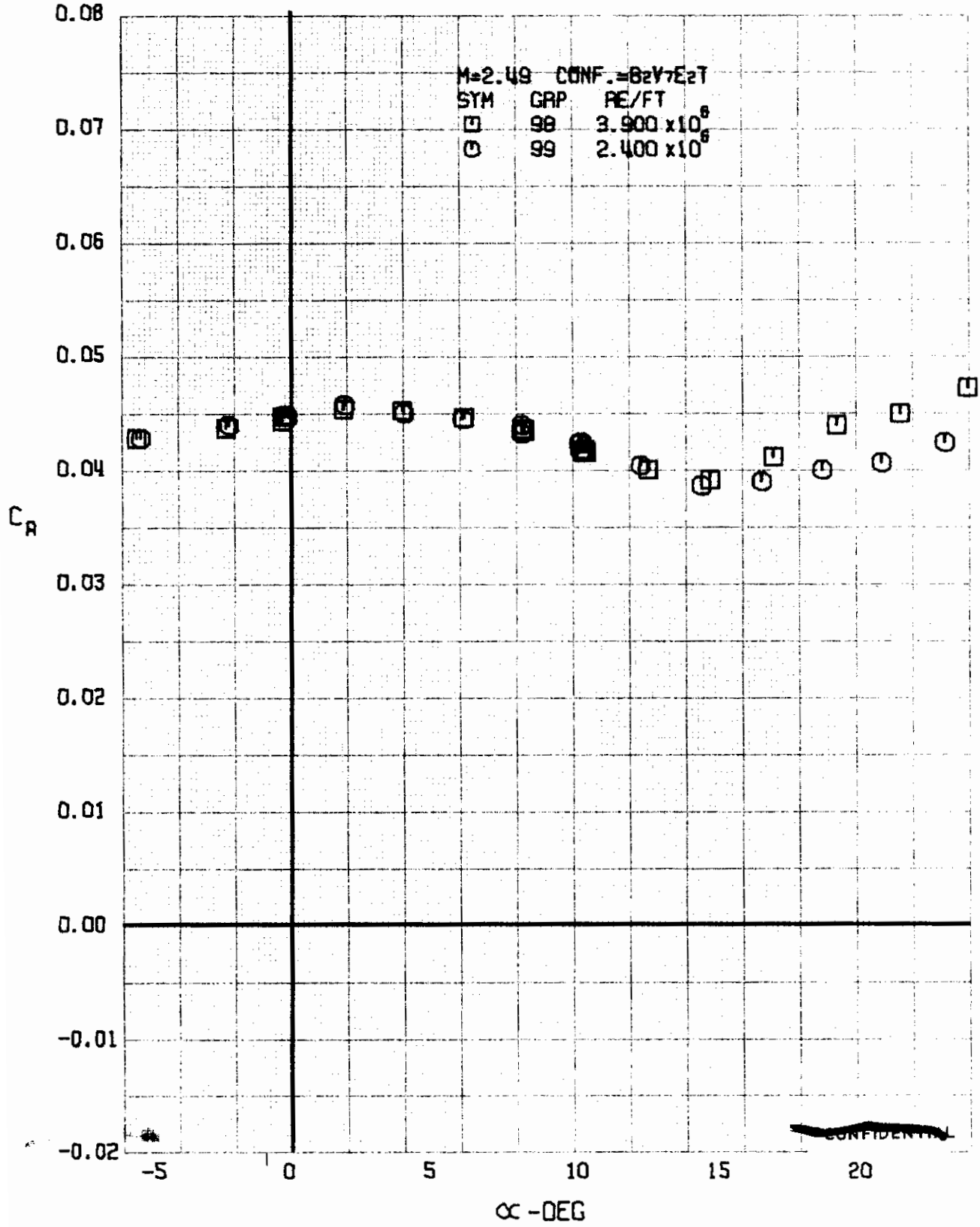

FIGURE 135 (U) REYNOLDS NUMBER EFFECTS
- AXIAL FORCE COEFFICIENT VARIATION WITH ANGLE OF ATTACK (M=2.49)

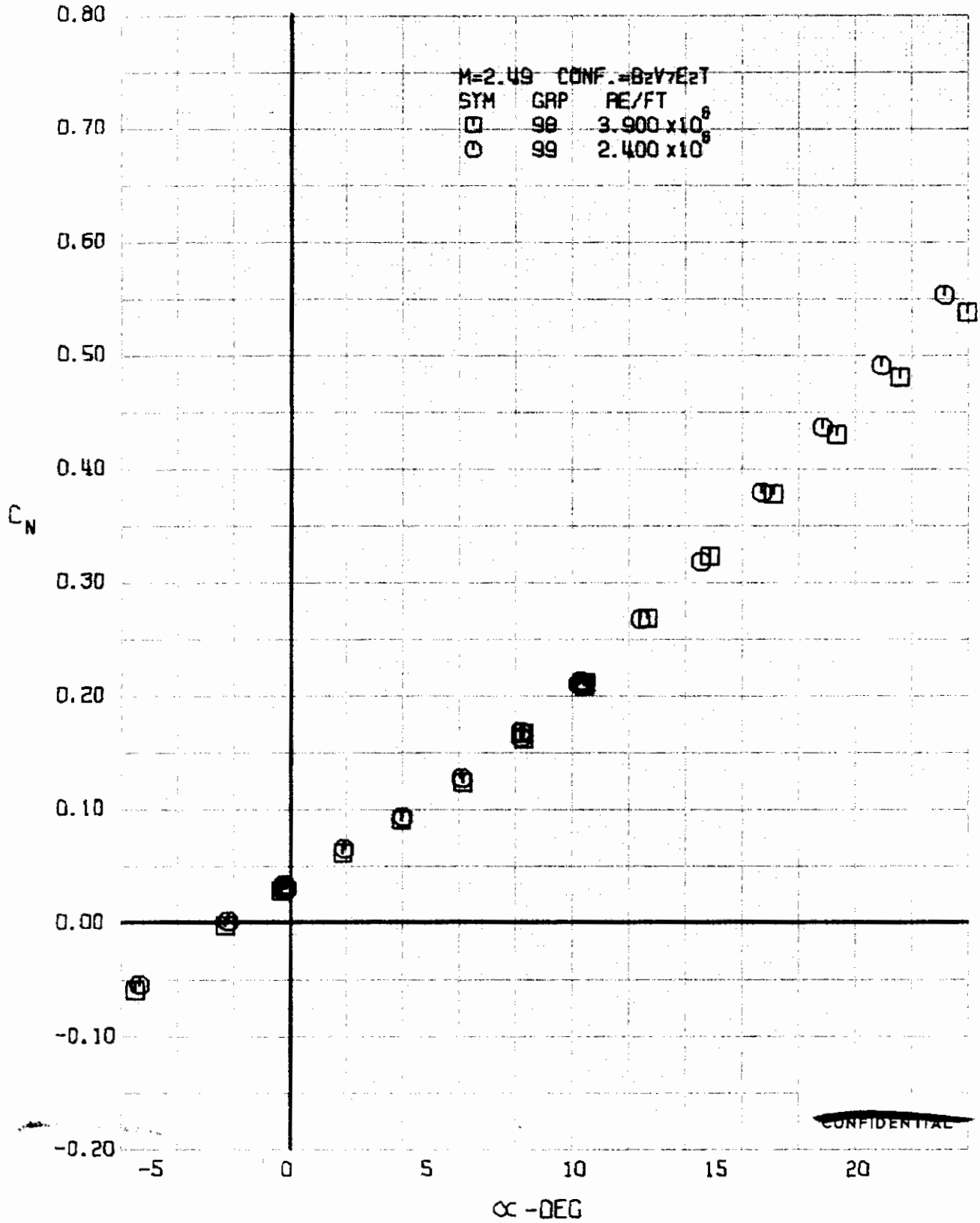

FIGURE 136 (U) REYNOLDS NUMBER EFFECTS
- NORMAL FORCE COEFFICIENT VARIATION WITH ANGLE OF ATTACK (M=2.49)

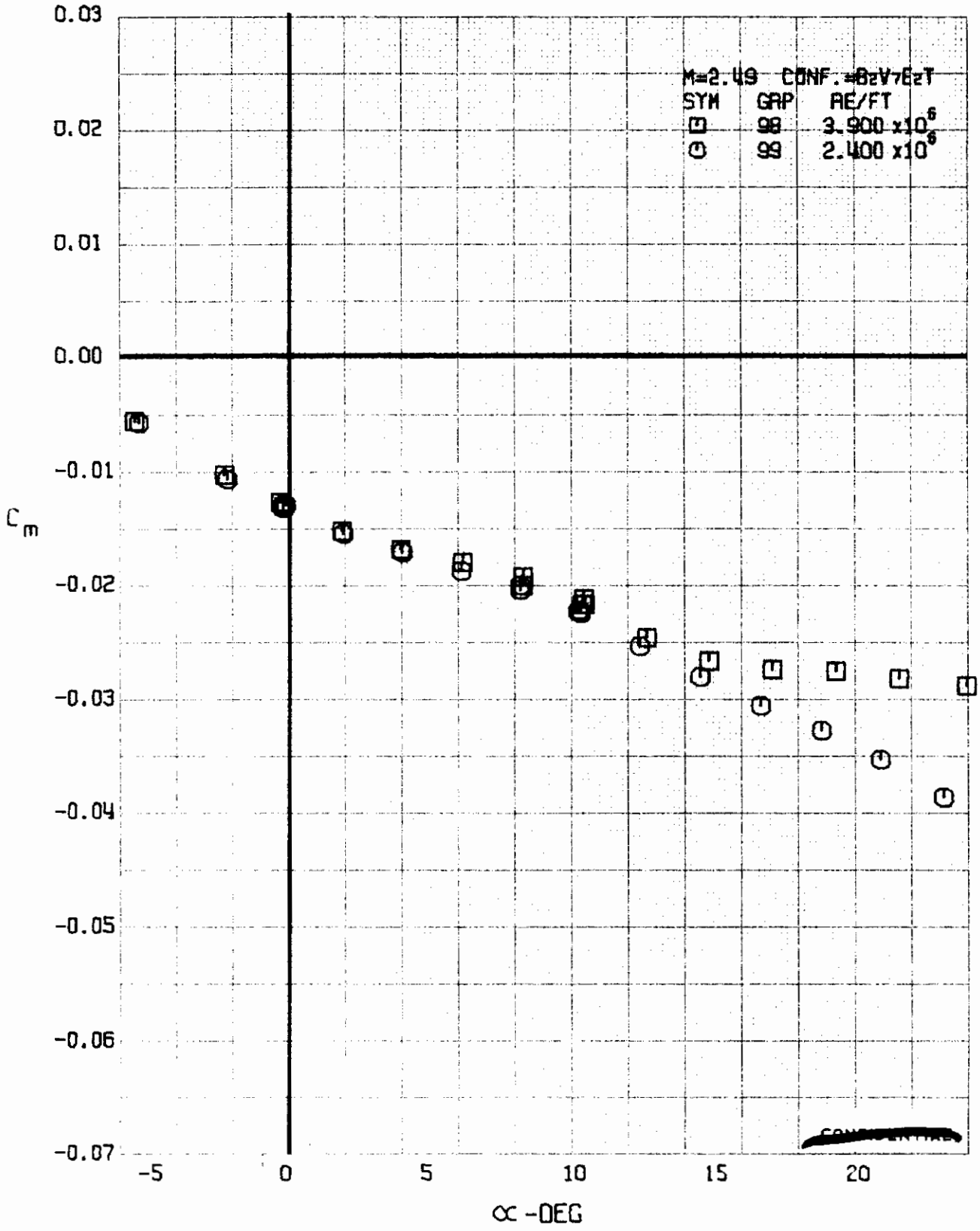

FIGURE 137 (U) REYNOLDS NUMBER EFFECTS
- PITCHING MOMENT COEFFICIENT VARIATION WITH ANGLE OF ATTACK (M=2.49)

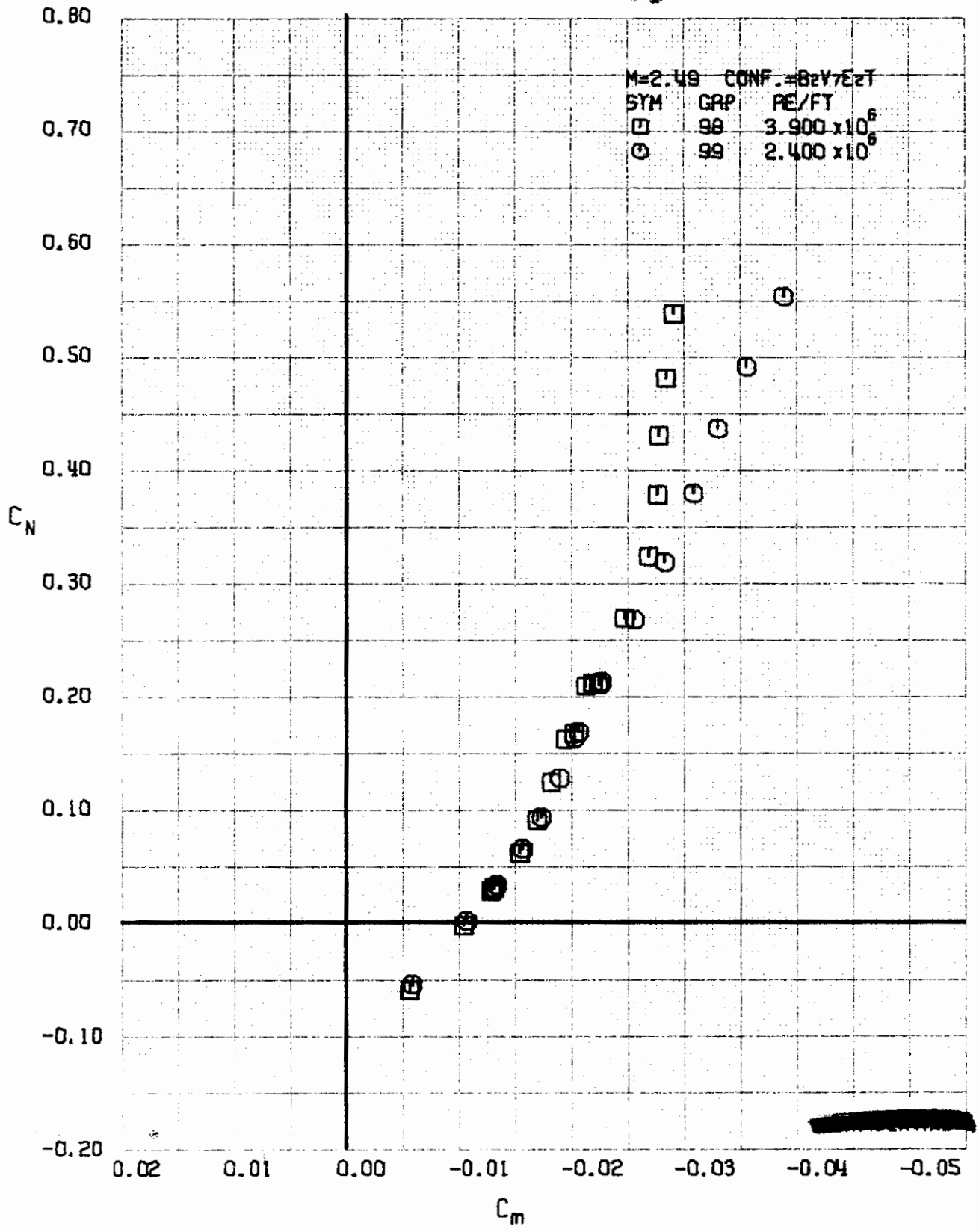

FIGURE 138 (U) REYNOLDS NUMBER EFFECTS
- LONGITUDINAL STABILITY VARIATION (M=2.49)

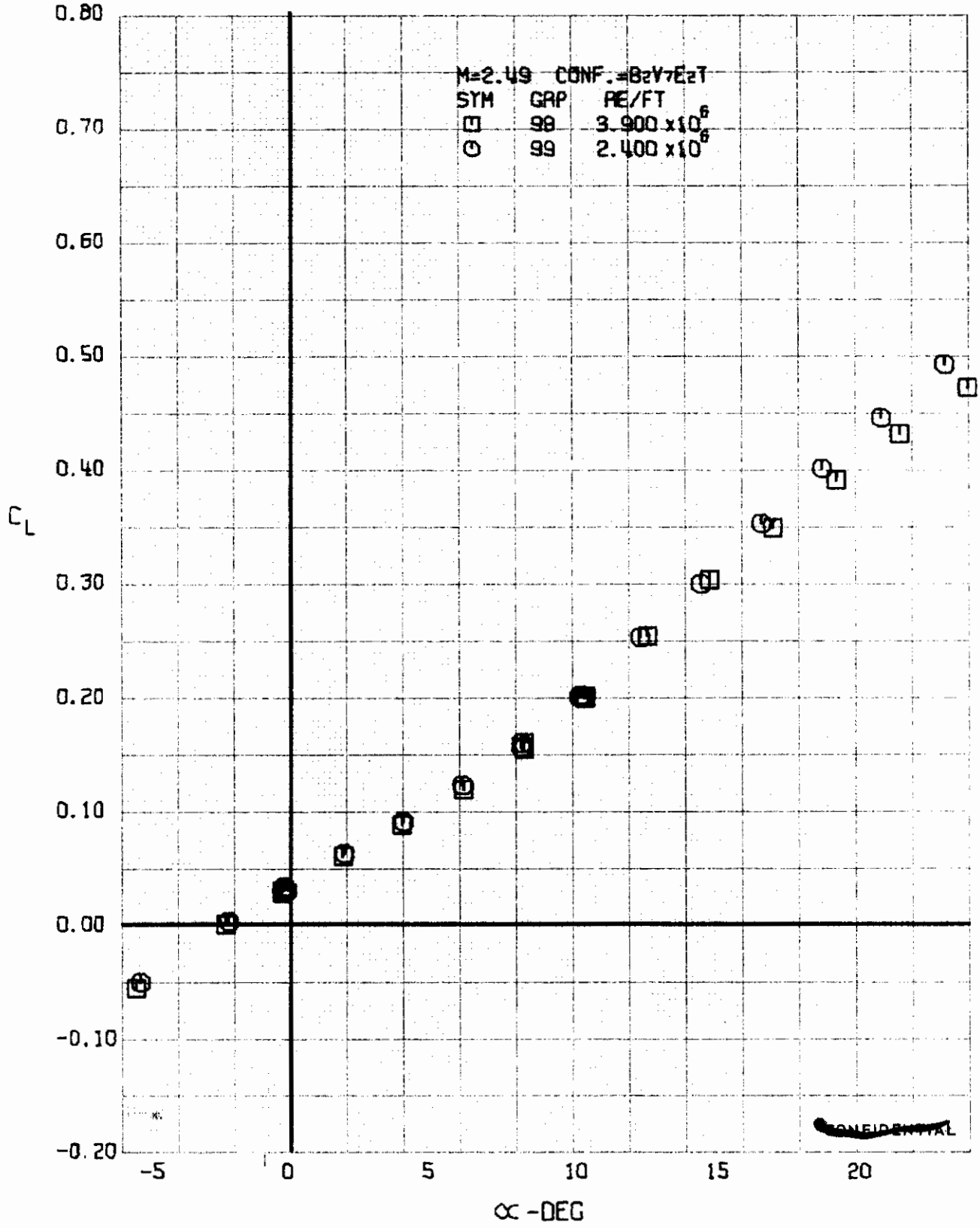

FIGURE 139 (U) REYNOLDS NUMBER EFFECTS
- LIFT COEFFICIENT VARIATION WITH ANGLE OF ATTACK (M=2.49)

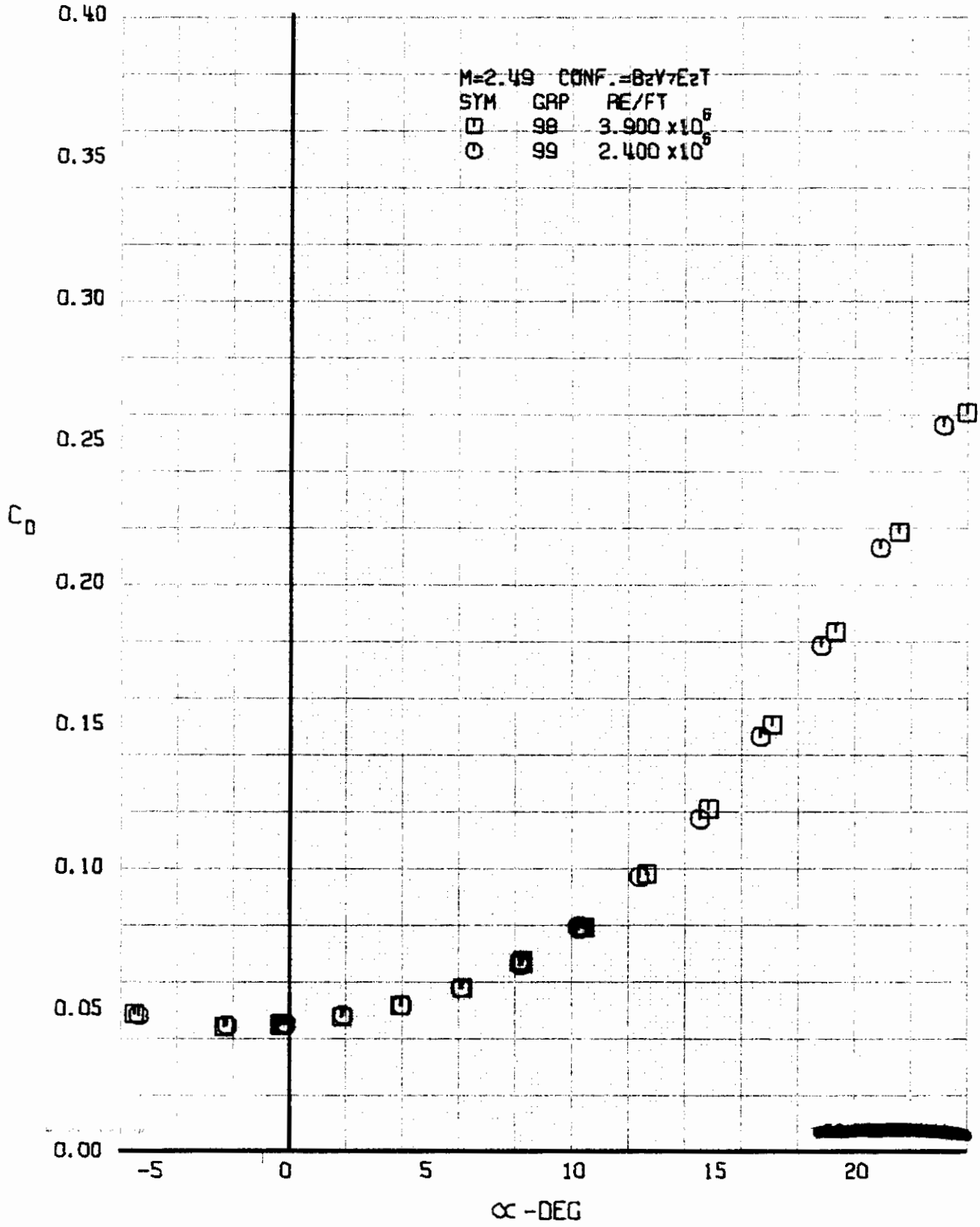

FIGURE 140 (U) REYNOLDS NUMBER EFFECTS
- DRAG COEFFICIENT VARIATION WITH ANGLE OF ATTACK (M=2.49)

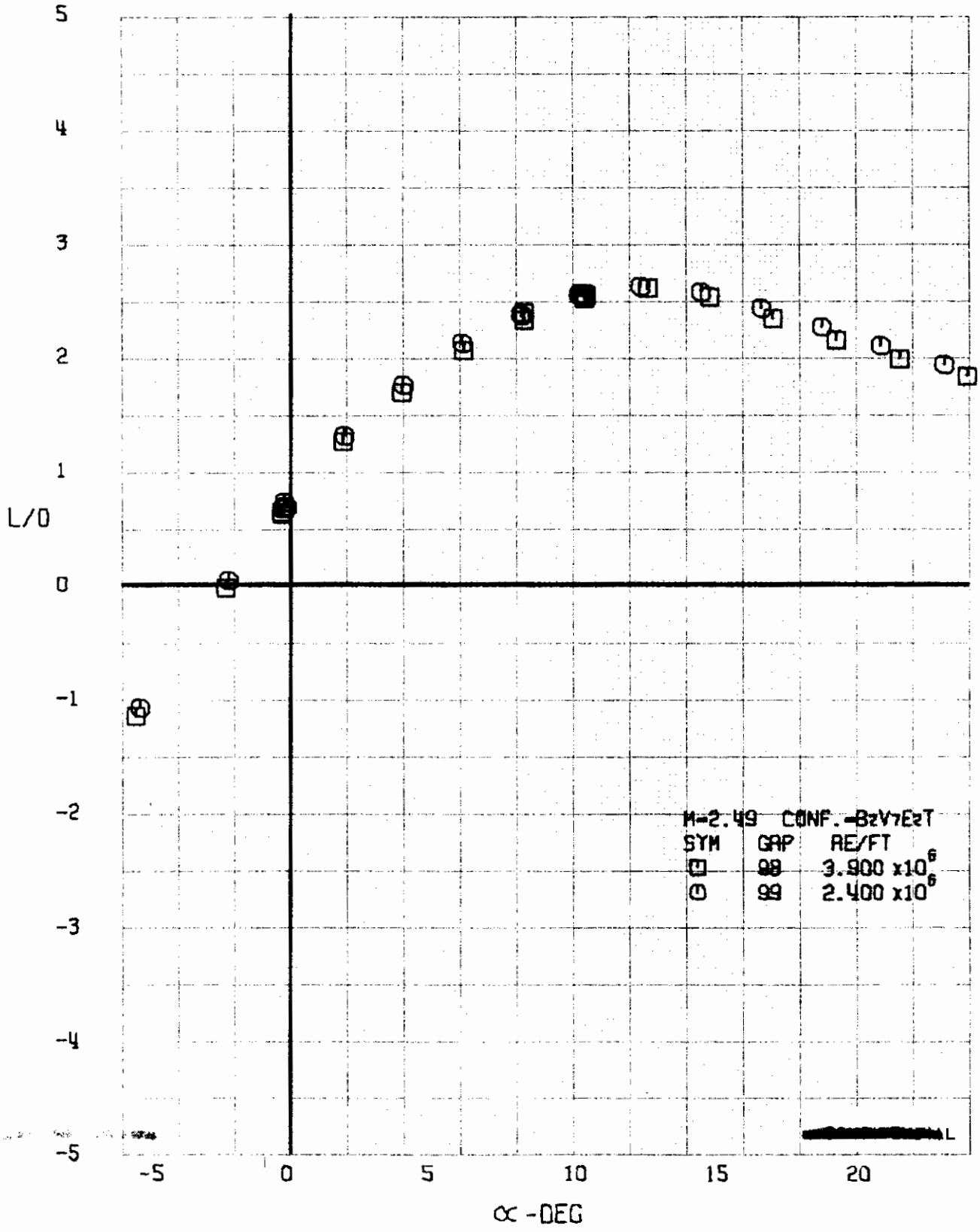

FIGURE 141 (U) REYNOLDS NUMBER EFFECTS
- LIFT-DRAG RATIO VARIATION WITH ANGLE OF ATTACK (M=2.49)

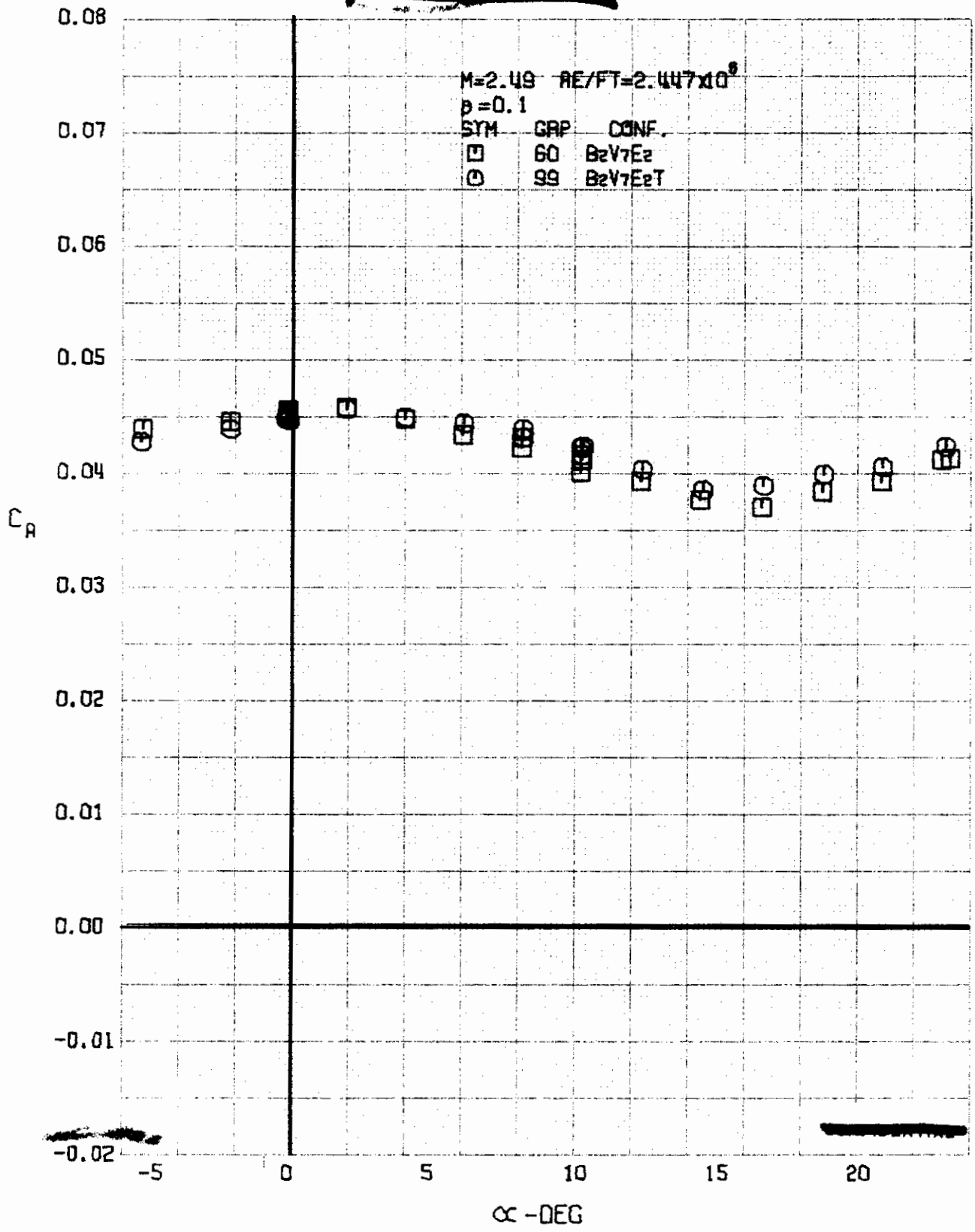

FIGURE 142 (U) FORCED TRANSITION EFFECTS
- AXIAL FORCE COEFFICIENT VARIATION WITH ANGLE OF ATTACK (M=2.49)

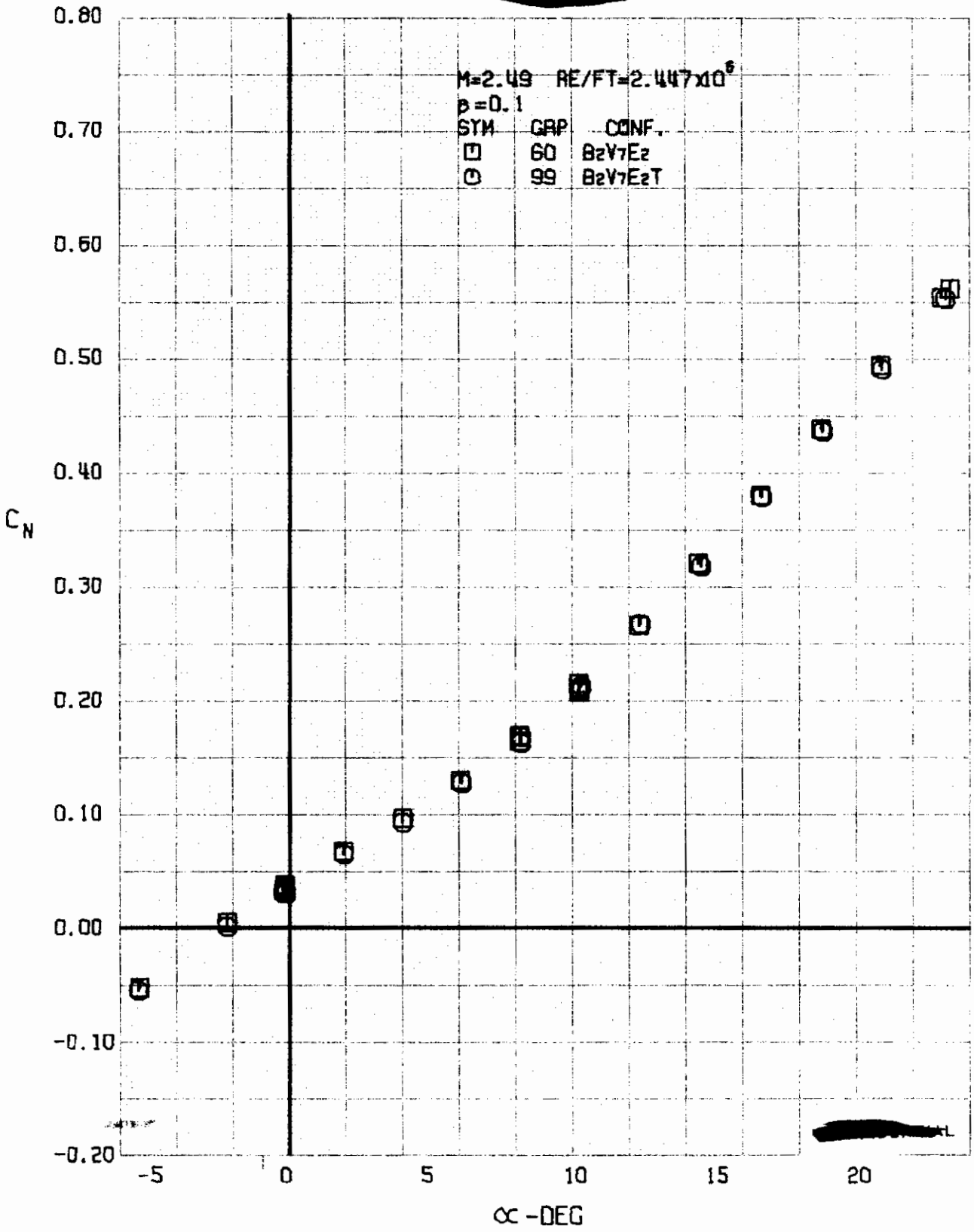

FIGURE 143 (U) FORCED TRANSITION EFFECTS
- NORMAL FORCE COEFFICIENT VARIATION WITH ANGLE OF ATTACK (M=2.49)

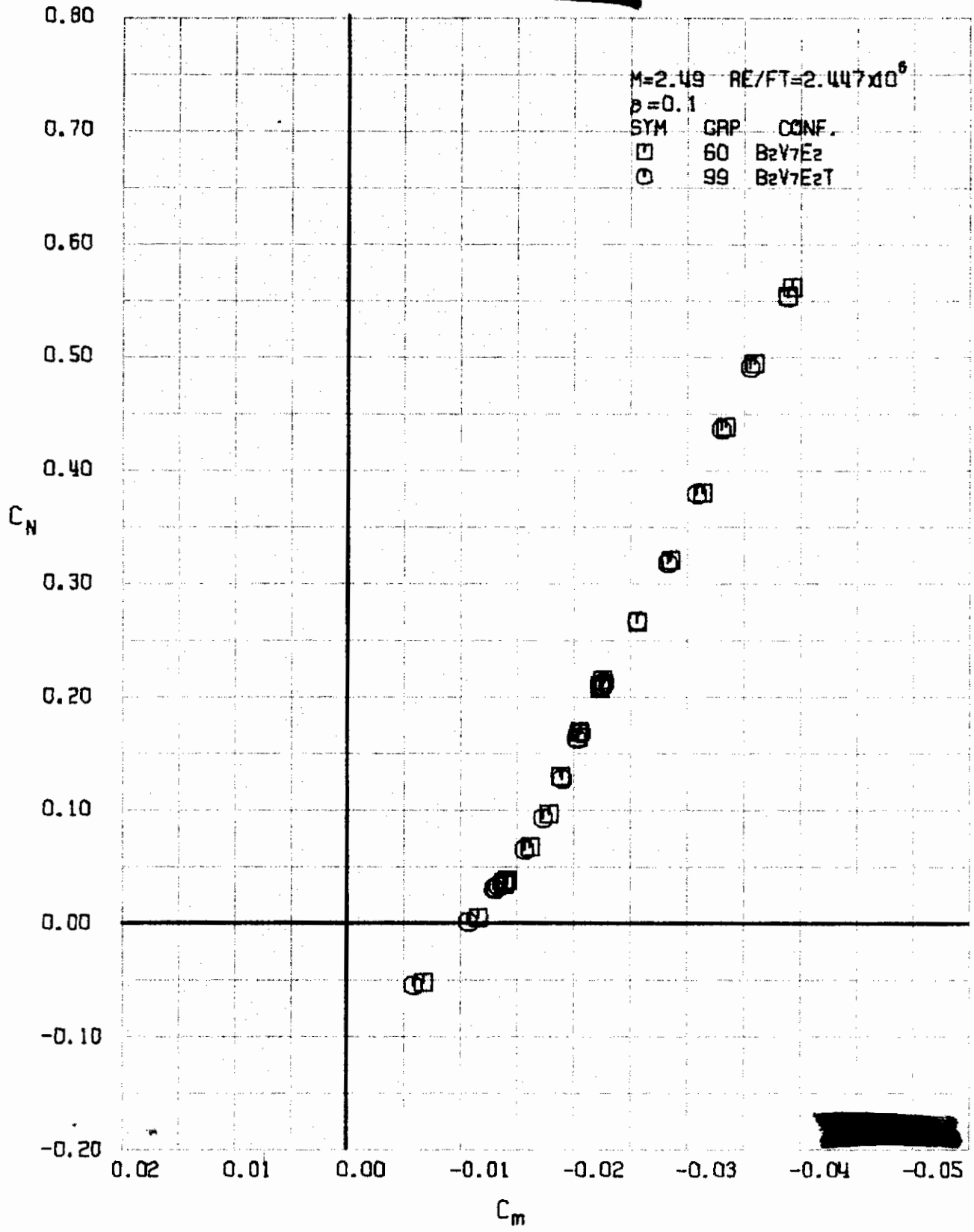

FIGURE 144 (U) FORCED TRANSITION EFFECTS
- LONGITUDINAL STABILITY VARIATION (M=2.49)

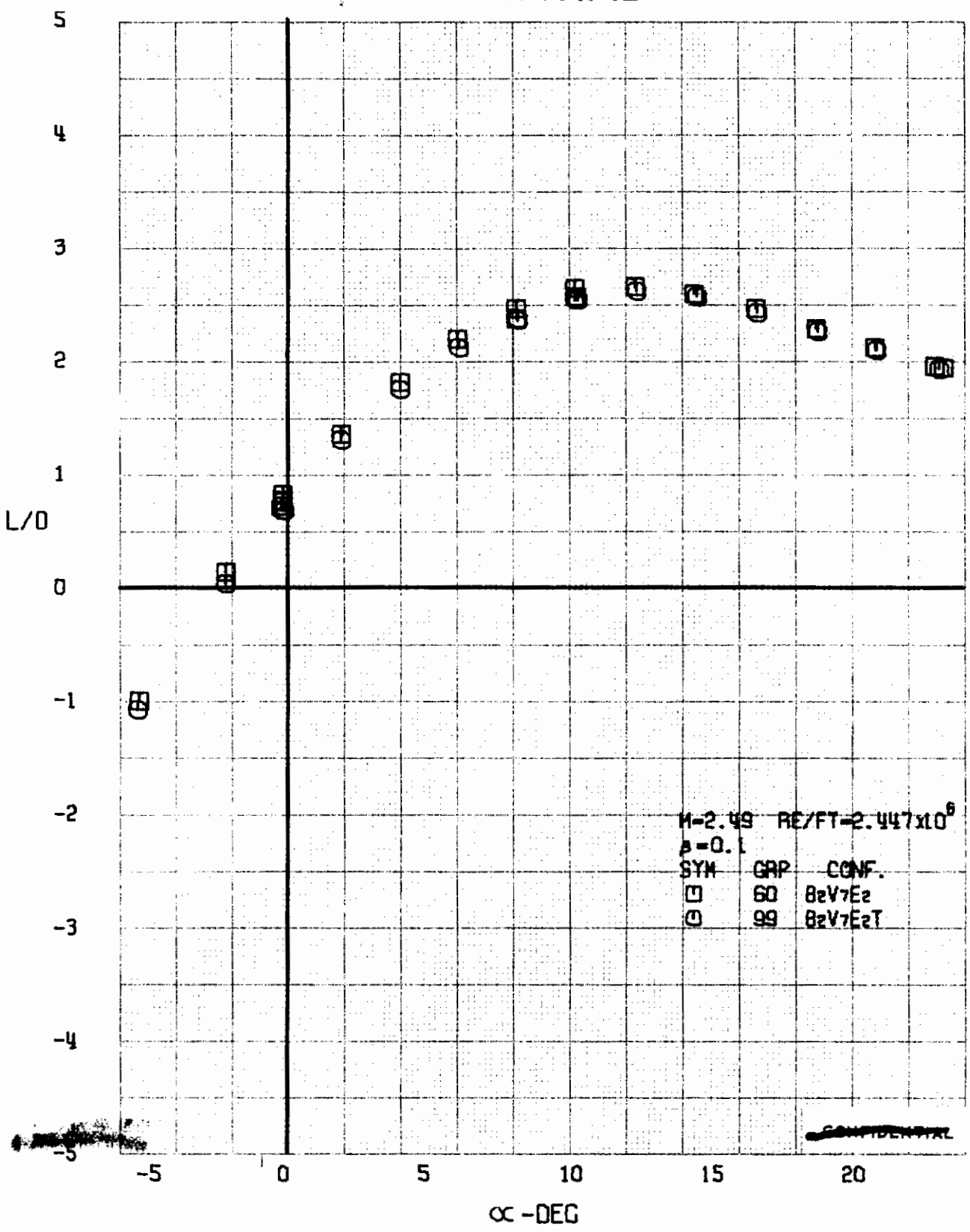

FIGURE 145 (U) FORCED TRANSITION EFFECTS
- LIFT-DRAG RATIO VARIATION WITH ANGLE OF ATTACK (M=2.49)

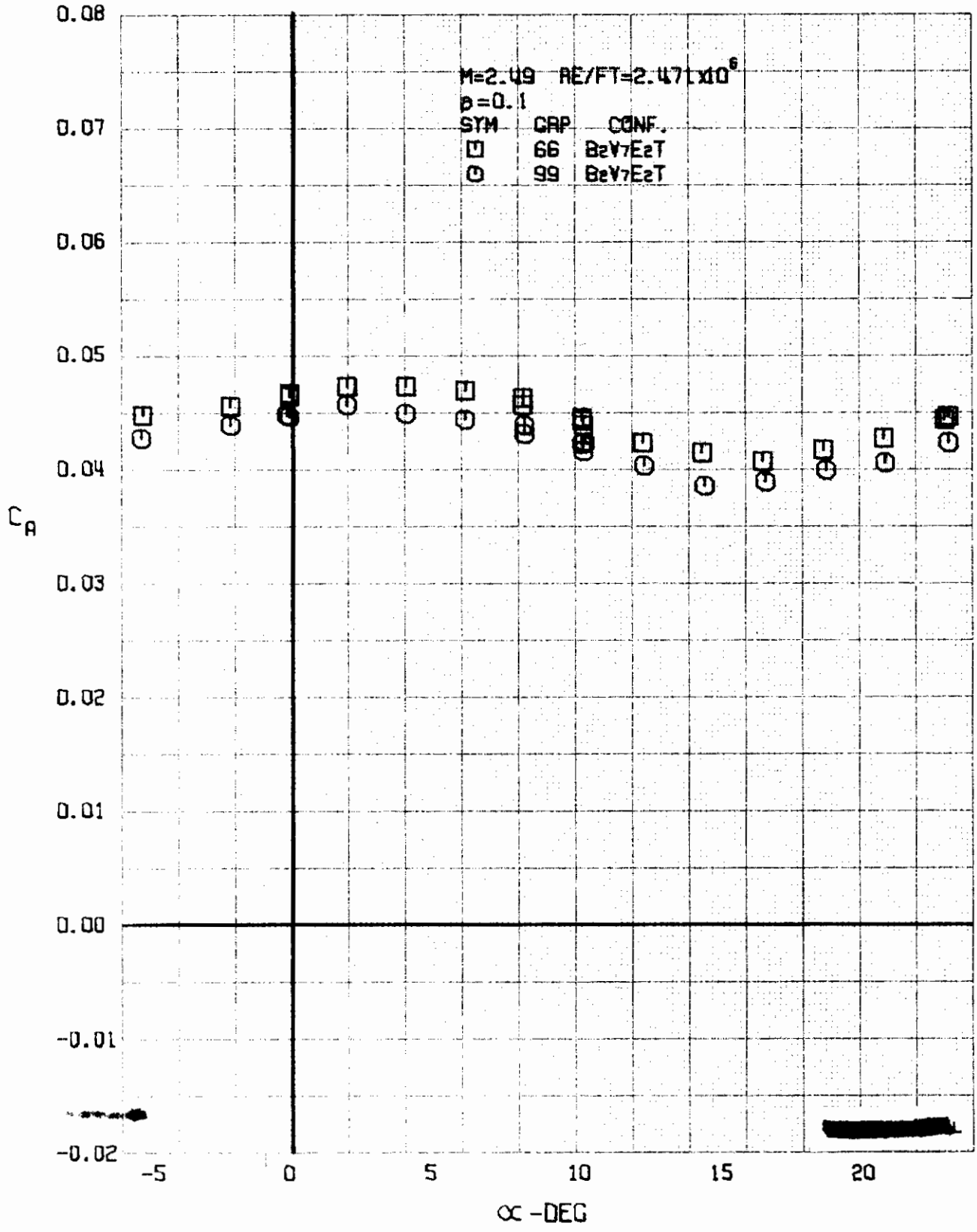

FIGURE 146 (U) REPEATABILITY
- AXIAL FORCE COEFFICIENT VARIATION WITH ANGLE OF ATTACK (M=2.49)

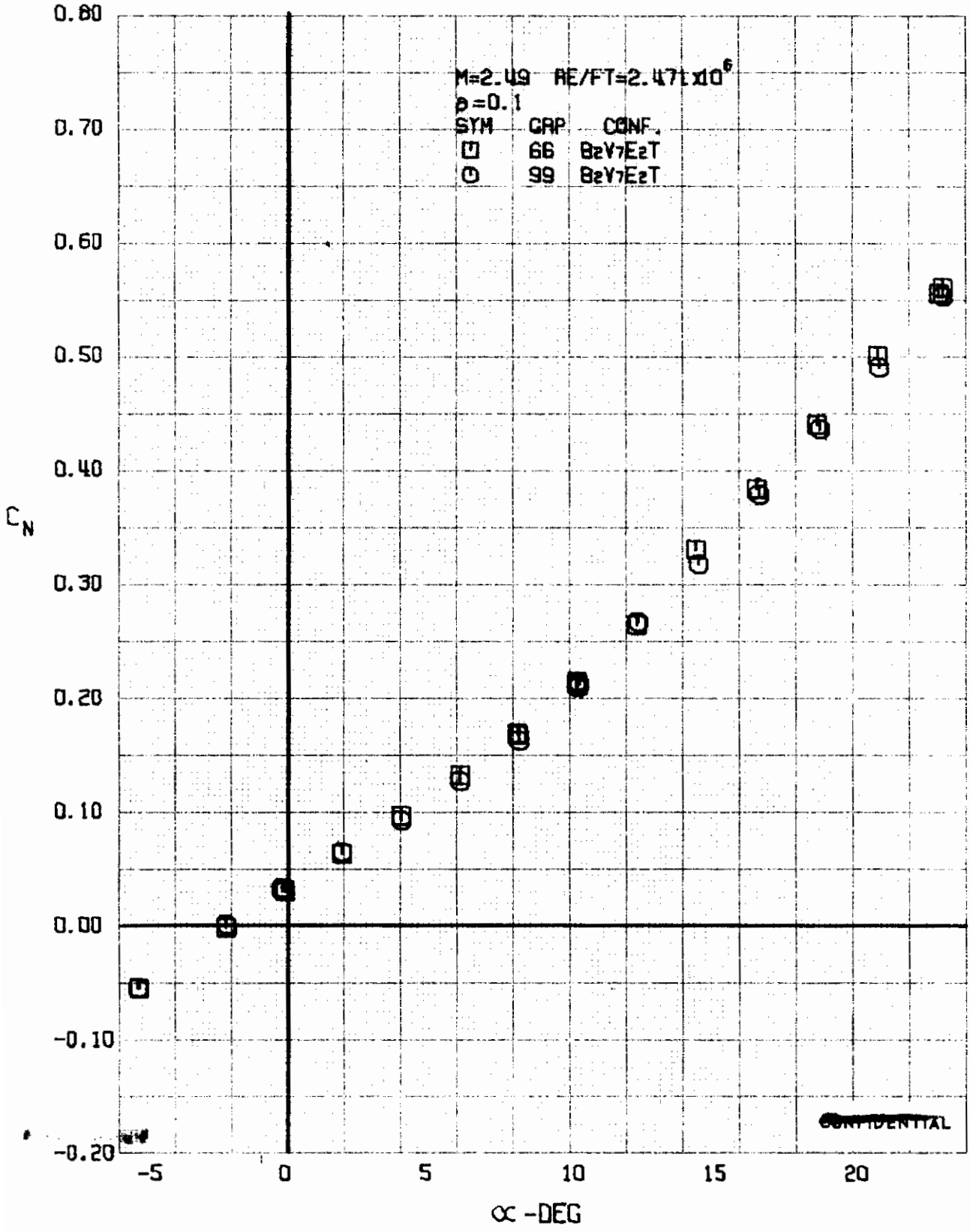

FIGURE 147 (U) REPEATABILITY
- NORMAL FORCE COEFFICIENT VARIATION WITH ANGLE OF ATTACK (M=2.49)

CONFIDENTIAL

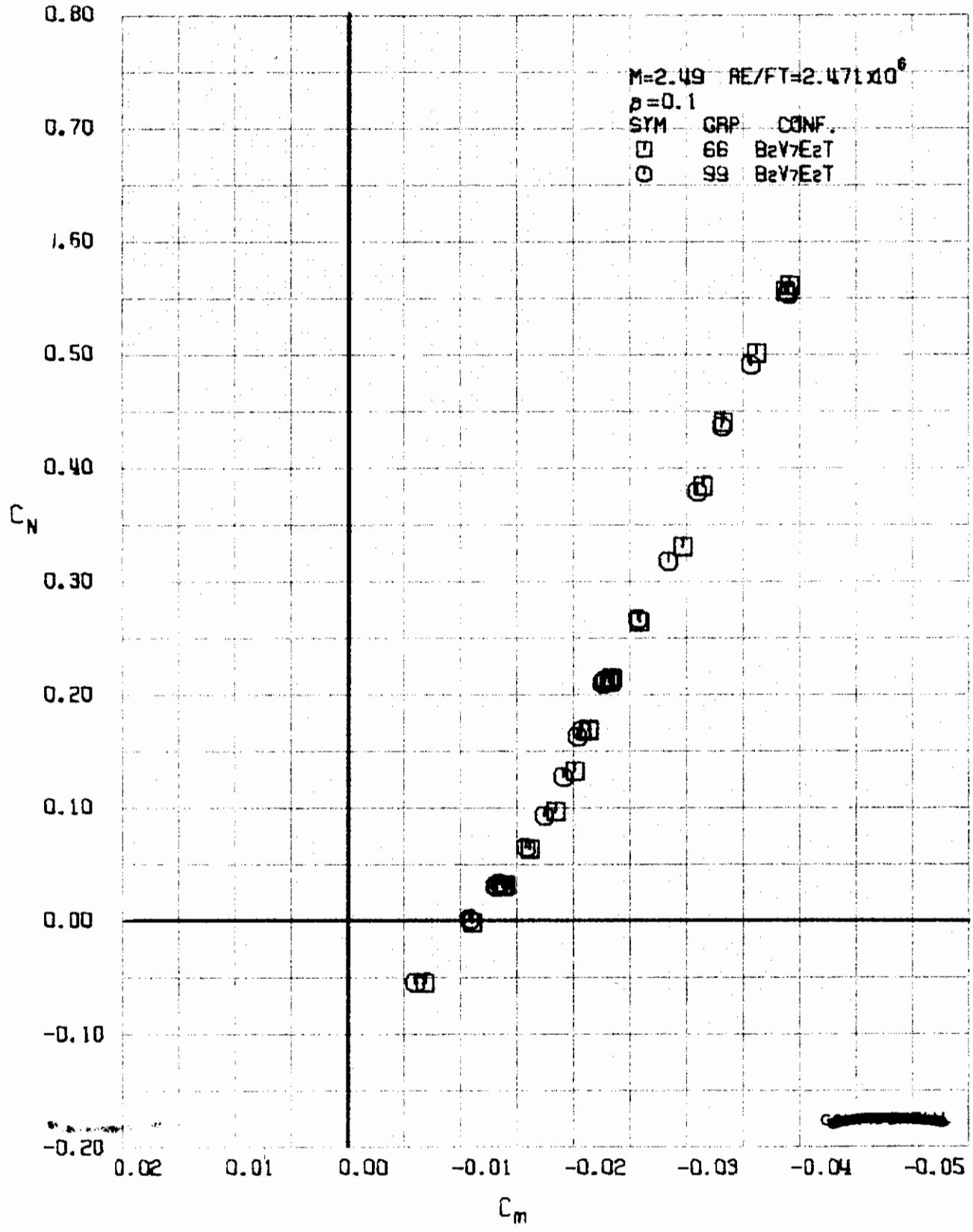

FIGURE 148 (U) REPEATABILITY
- LONGITUDINAL STABILITY VARIATION (M=2.49)

CONFIDENTIAL

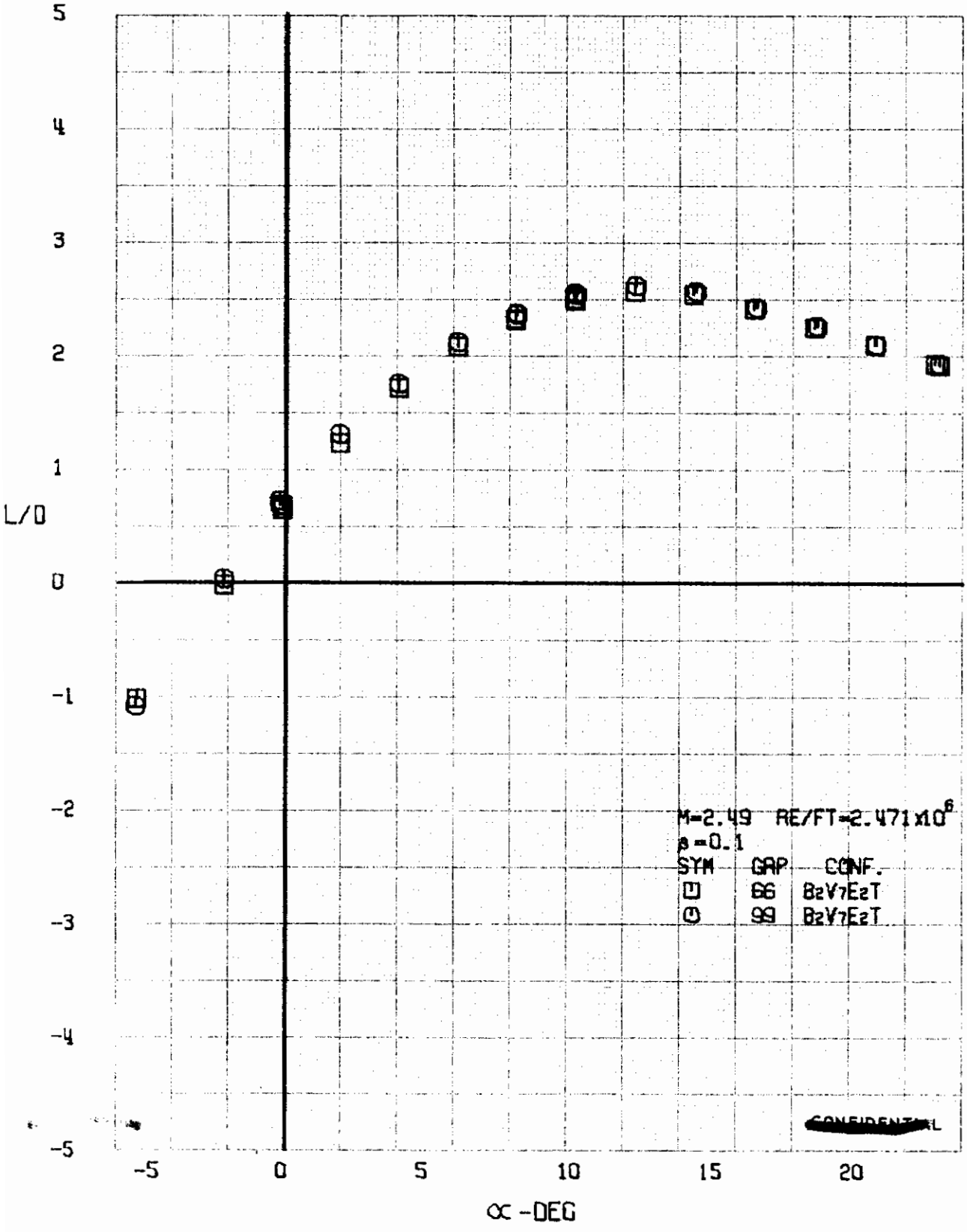

FIGURE 149 (U) REPEATABILITY
- LIFT-DRAG RATIO VARIATION WITH ANGLE OF ATTACK (M=2.49)

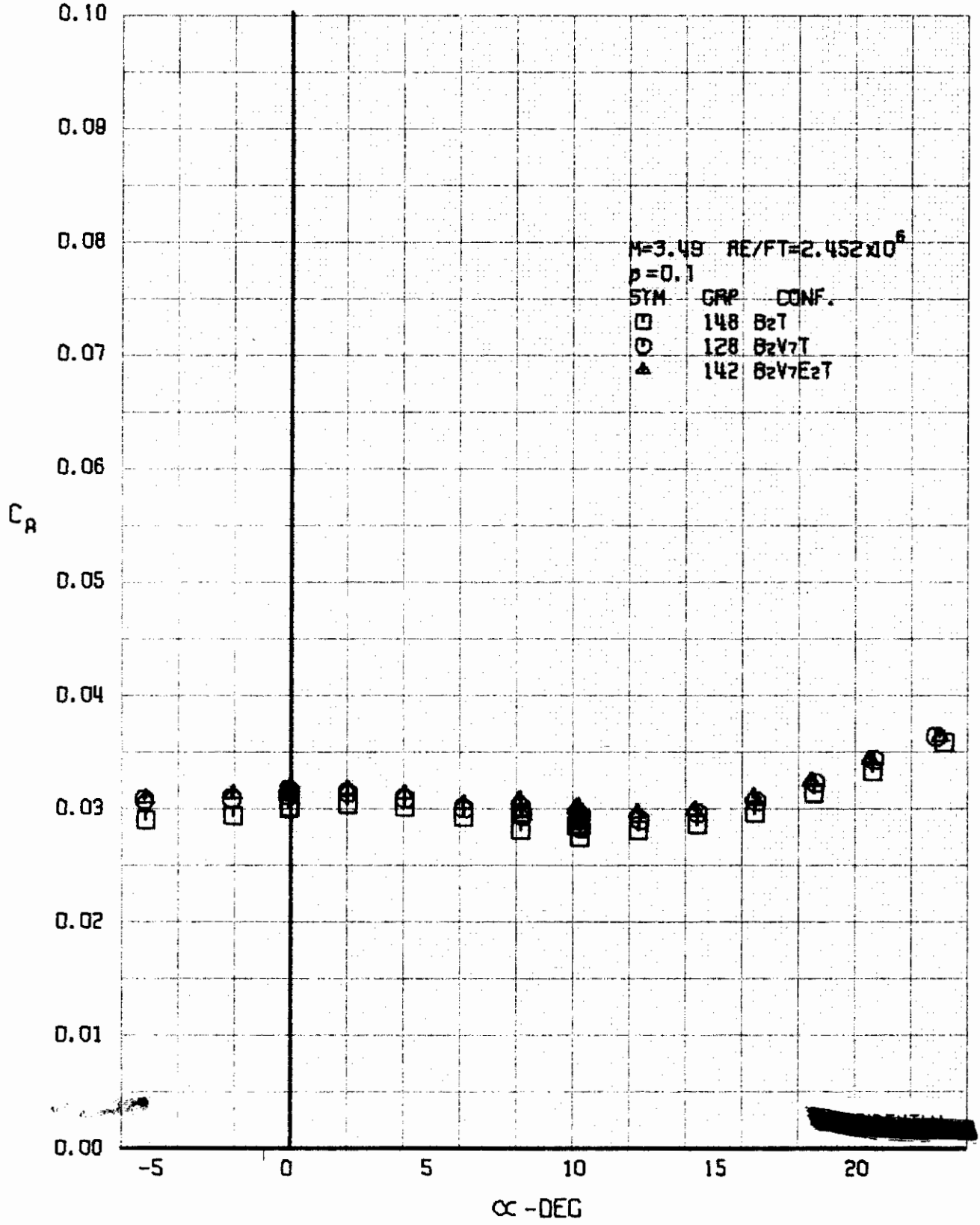

FIGURE 150 (U) CONFIGURATION BUILDUP
- AXIAL FORCE COEFFICIENT VARIATION WITH ANGLE OF ATTACK (M=3.49)

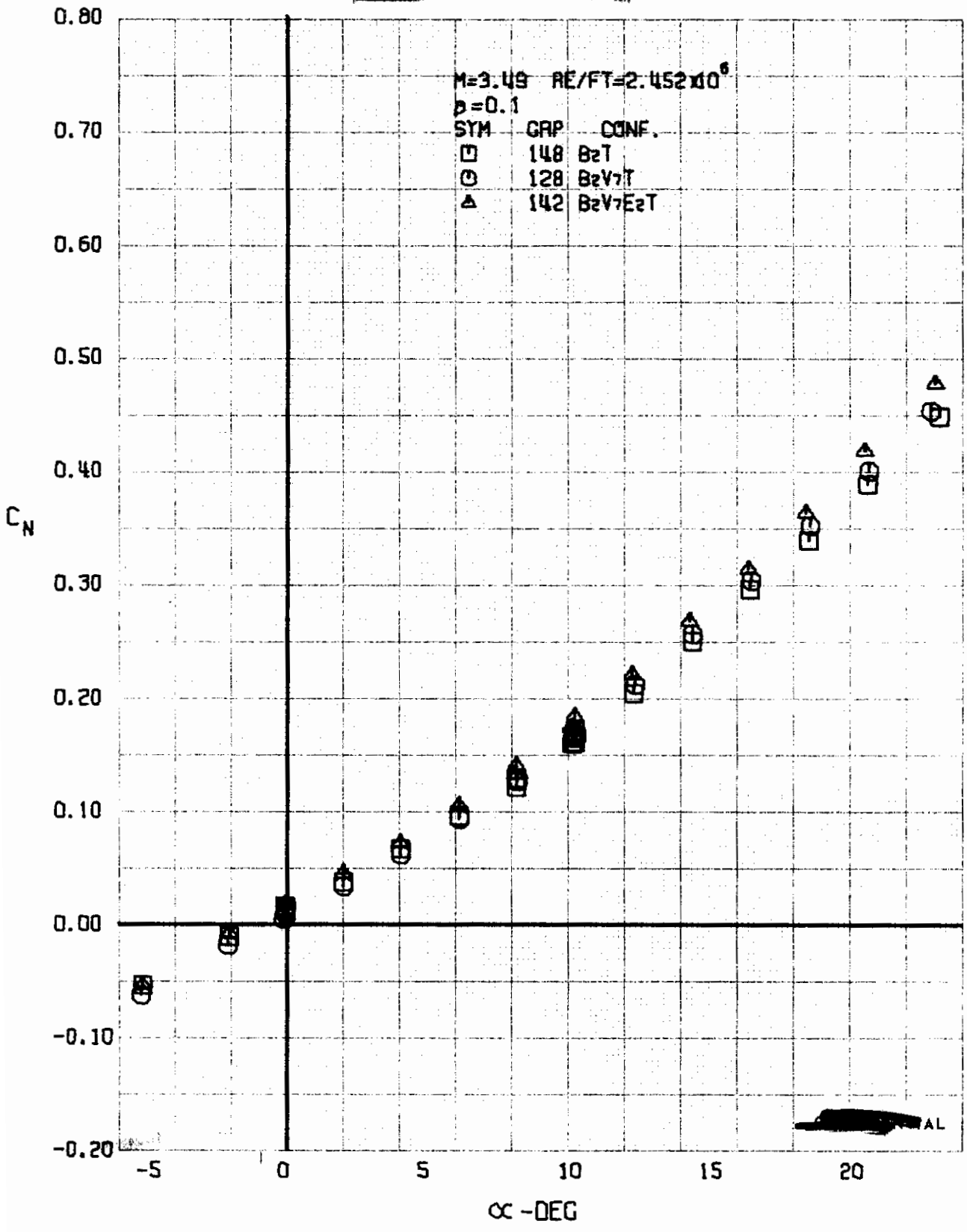

FIGURE 151 (U) CONFIGURATION BUILDUP
- NORMAL FORCE COEFFICIENT VARIATION WITH ANGLE OF ATTACK (M=3.49)

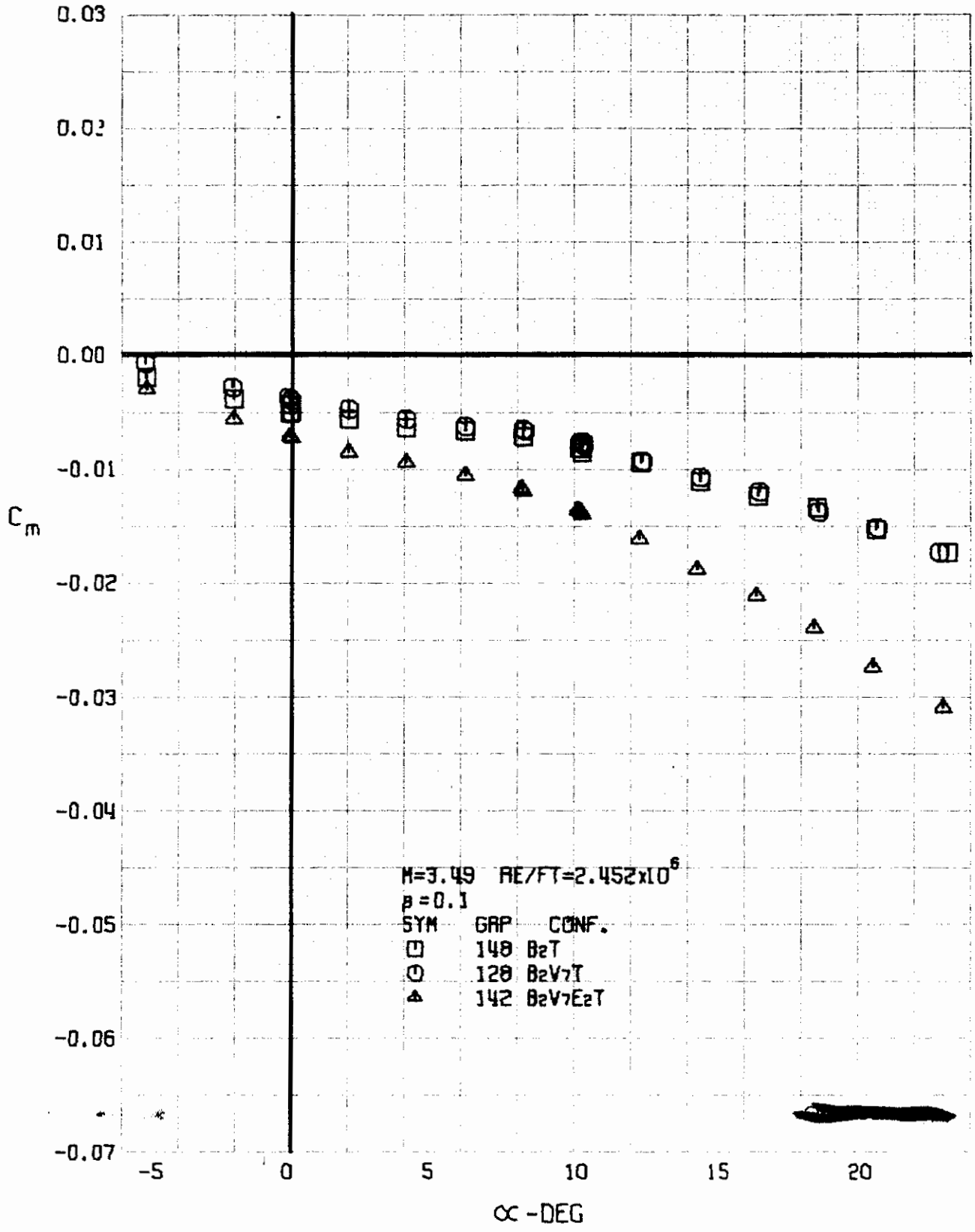

FIGURE 152 (U) CONFIGURATION BUILDUP
- PITCHING MOMENT COEFFICIENT VARIATION WITH ANGLE OF ATTACK (M=3.49)

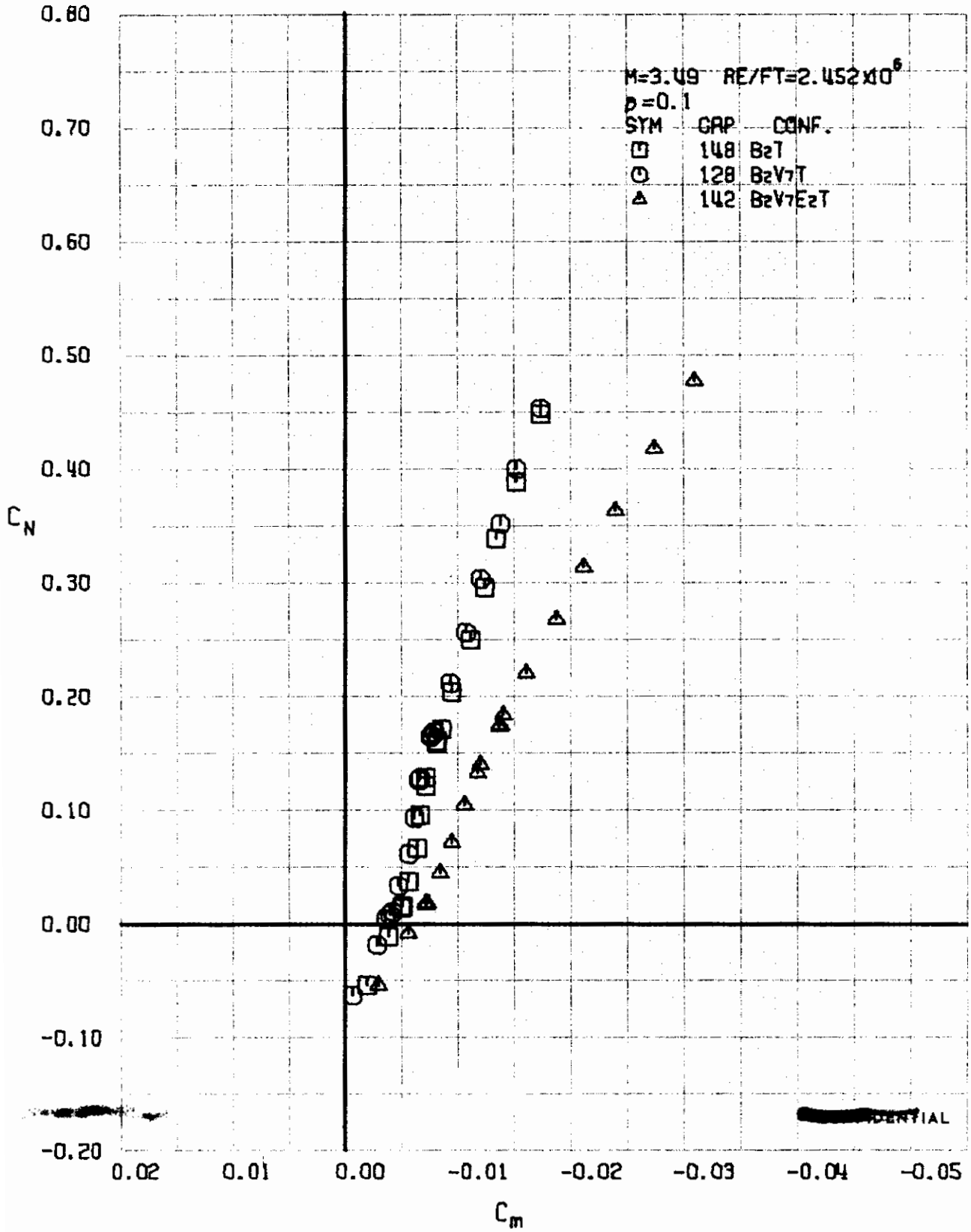

FIGURE 153 (U) CONFIGURATION BUILDUP
- LONGITUDINAL STABILITY VARIATION (M=3.49)

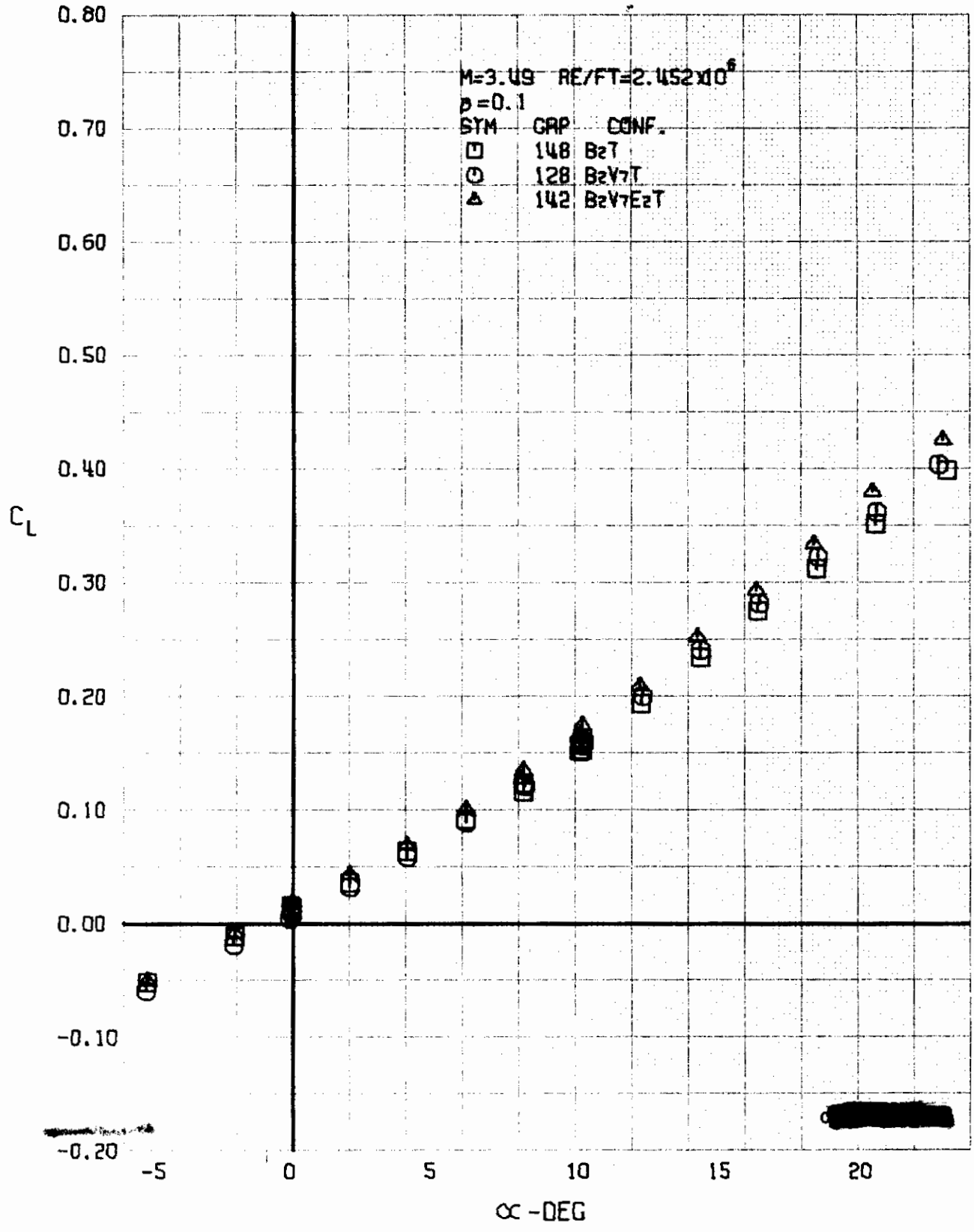

FIGURE 154 (U) CONFIGURATION BUILDUP
- LIFT COEFFICIENT VARIATION WITH ANGLE OF ATTACK (M=3.49)

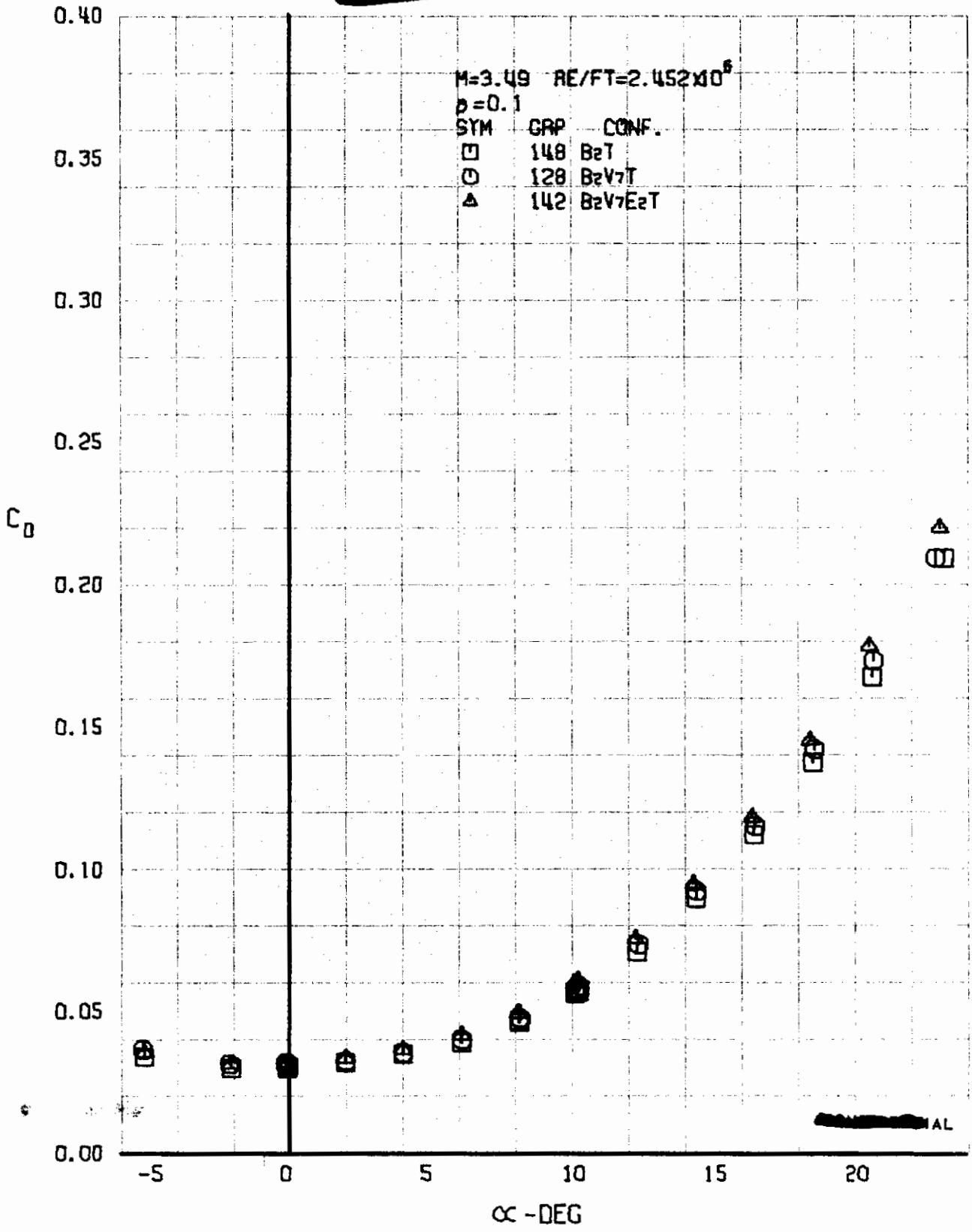

FIGURE 155 (U) CONFIGURATION BUILDUP
- DRAG COEFFICIENT VARIATION WITH ANGLE OF ATTACK (M=3.49)

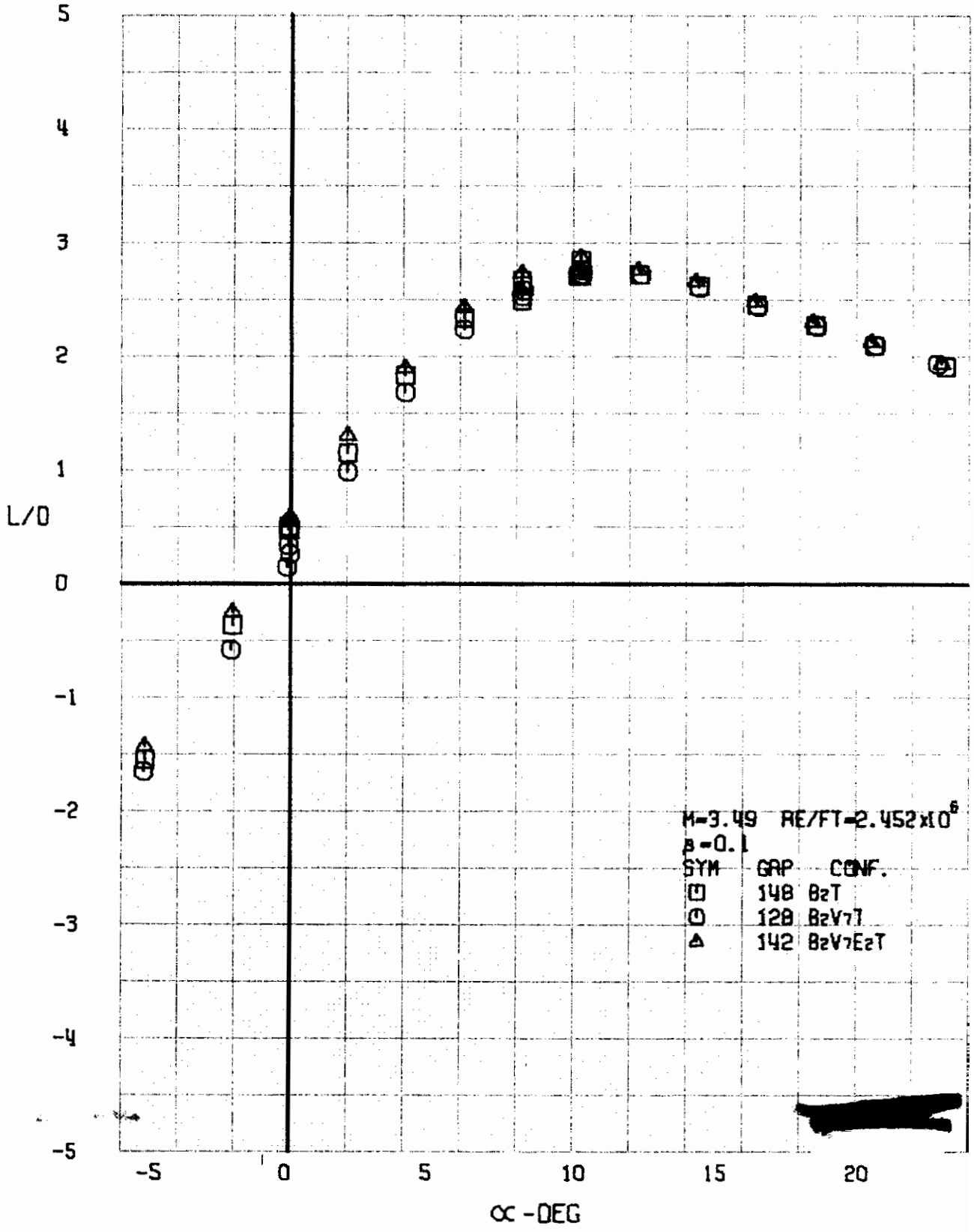

FIGURE 156 (U) CONFIGURATION BUILDUP
- LIFT-DRAG RATIO VARIATION WITH ANGLE OF ATTACK (M=3.49)

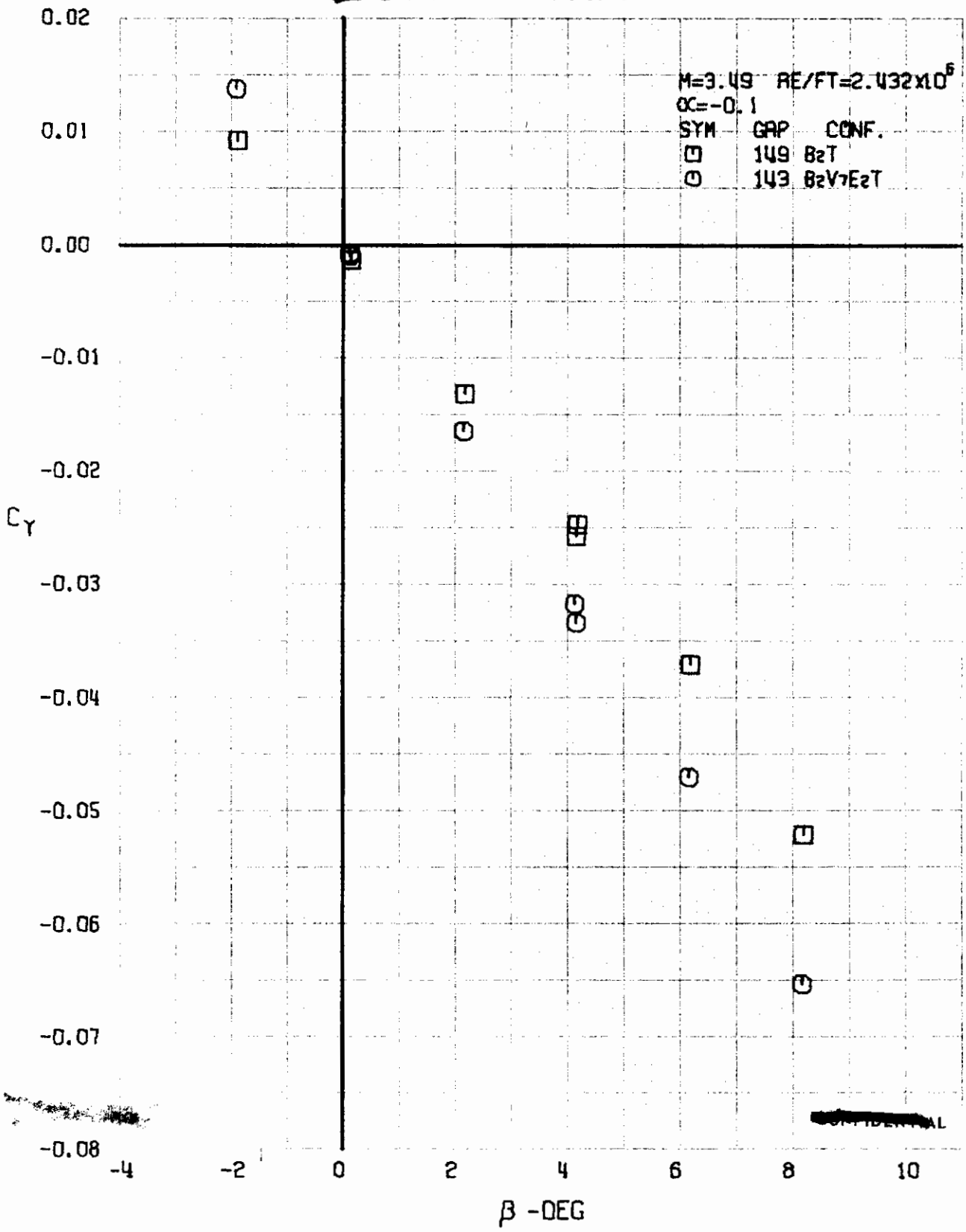

FIGURE 157 (U) CONFIGURATION BUILDUP
- SIDE FORCE COEFFICIENT VARIATION WITH ANGLE OF YAW (M=3.49)

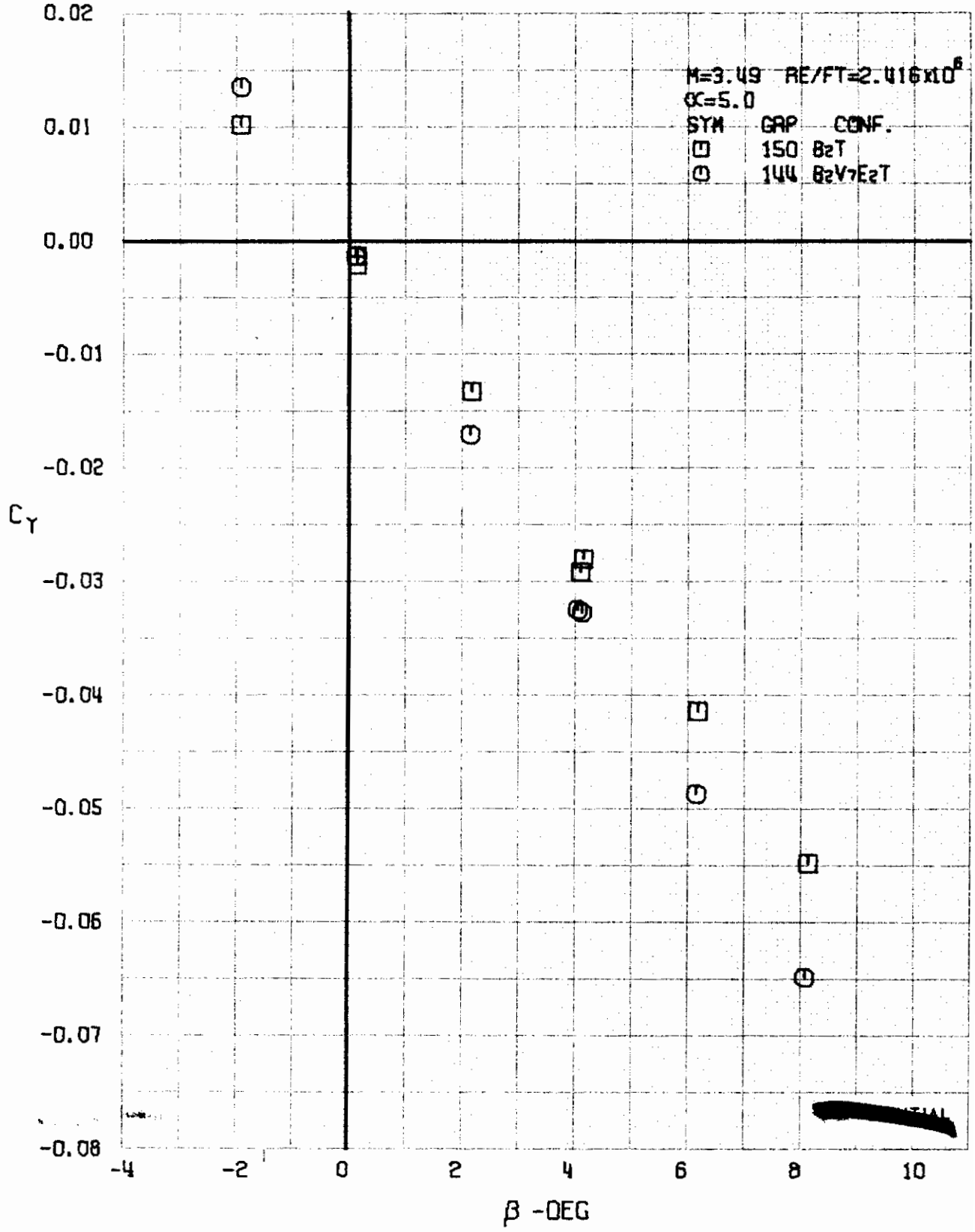

FIGURE 158 (U) CONFIGURATION BUILDUP
- SIDE FORCE COEFFICIENT VARIATION WITH ANGLE OF YAW (M=3.49)

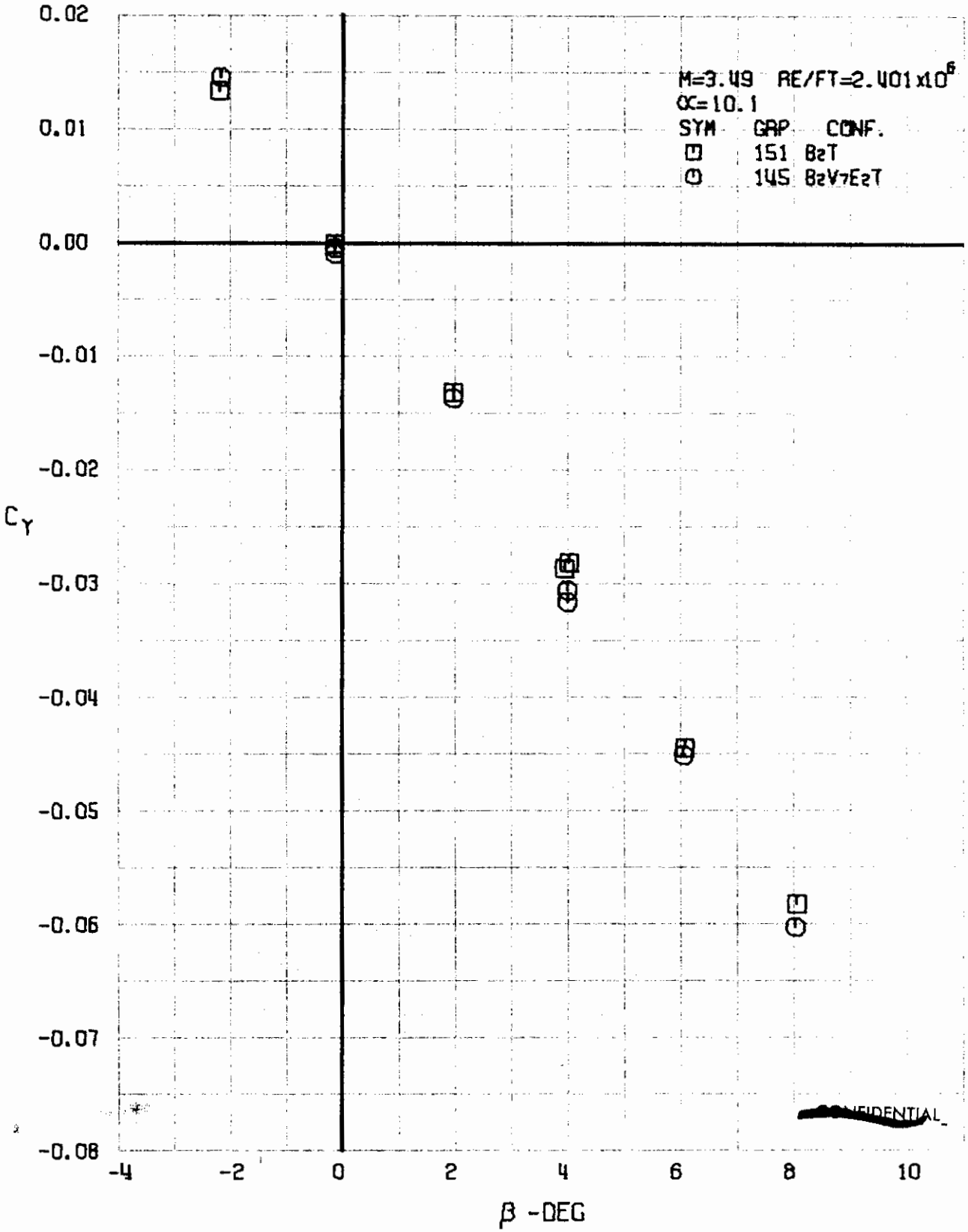

FIGURE 159 (U) CONFIGURATION BUILDUP
- SIDE FORCE COEFFICIENT VARIATION WITH ANGLE OF YAW (M=3.49)

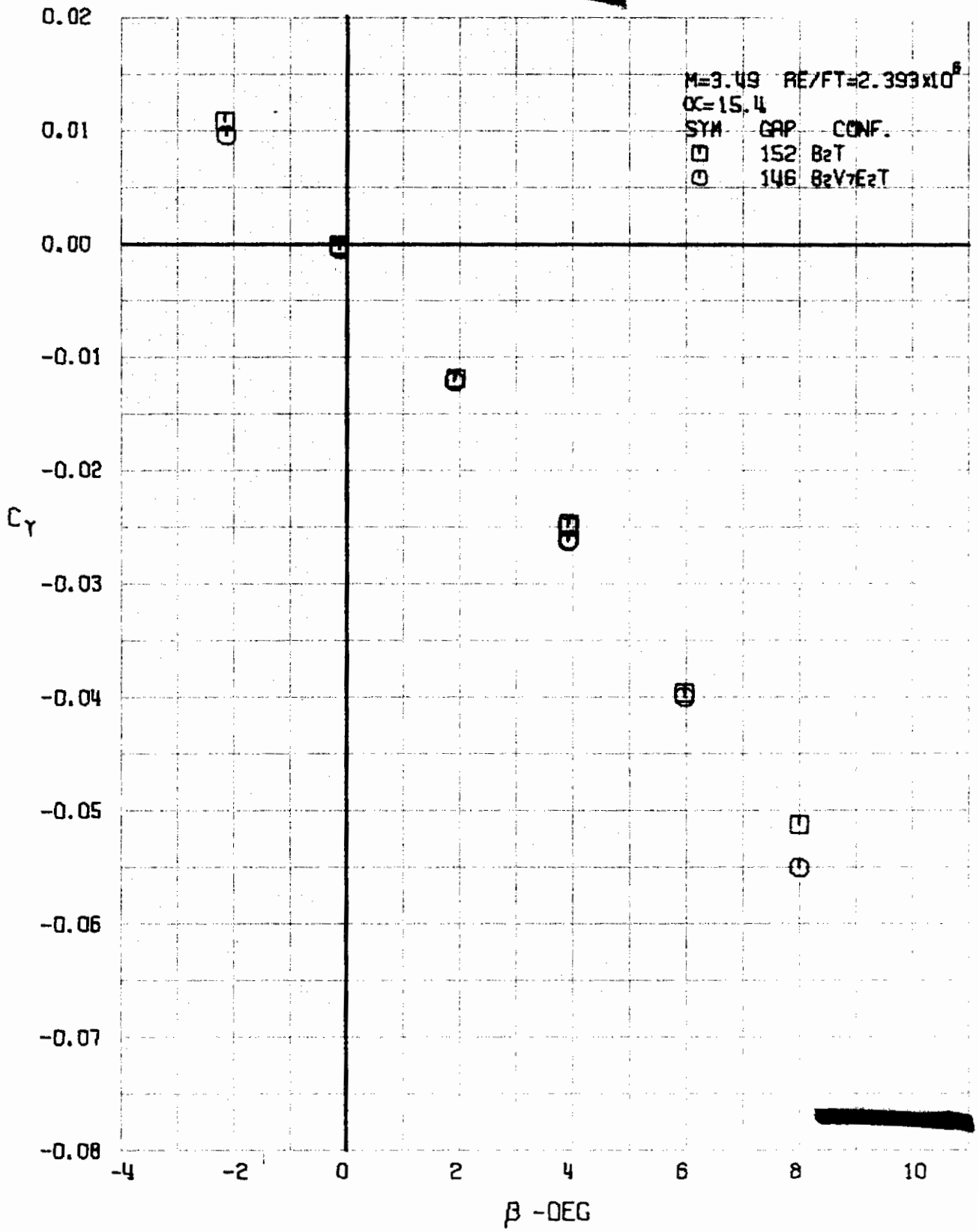

FIGURE 160 (U) CONFIGURATION BUILDUP
- SIDE FORCE COEFFICIENT VARIATION WITH ANGLE OF YAW (M=3.49)

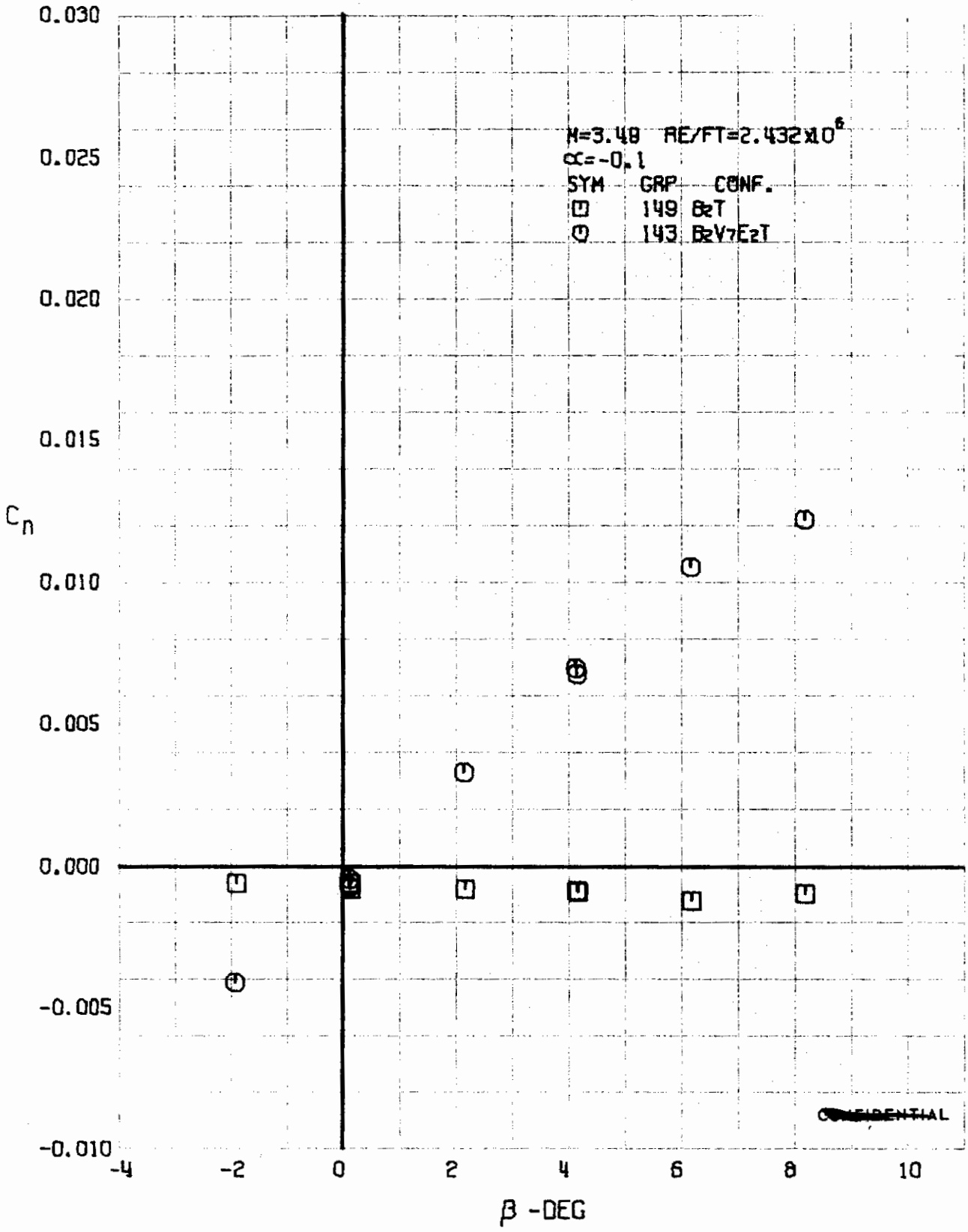

FIGURE 161 (U) CONFIGURATION BUILDUP
- YAWING MOMENT COEFFICIENT VARIATION WITH ANGLE OF YAW (M=3.49)

~~CONFIDENTIAL~~

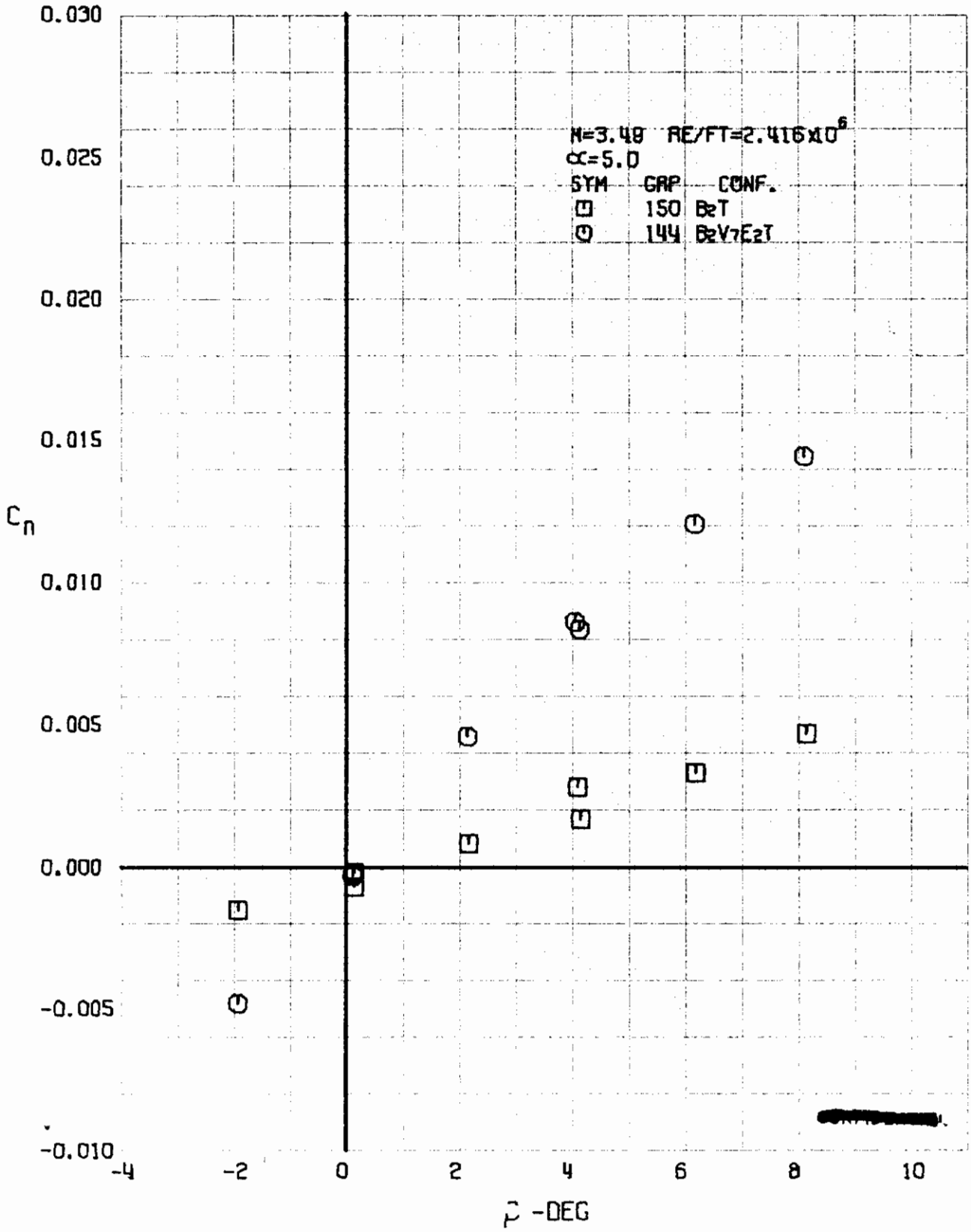

FIGURE 162 (U) CONFIGURATION BUILDUP
- YAWING MOMENT COEFFICIENT VARIATION WITH ANGLE OF YAW (M=3.49)

~~CONFIDENTIAL~~

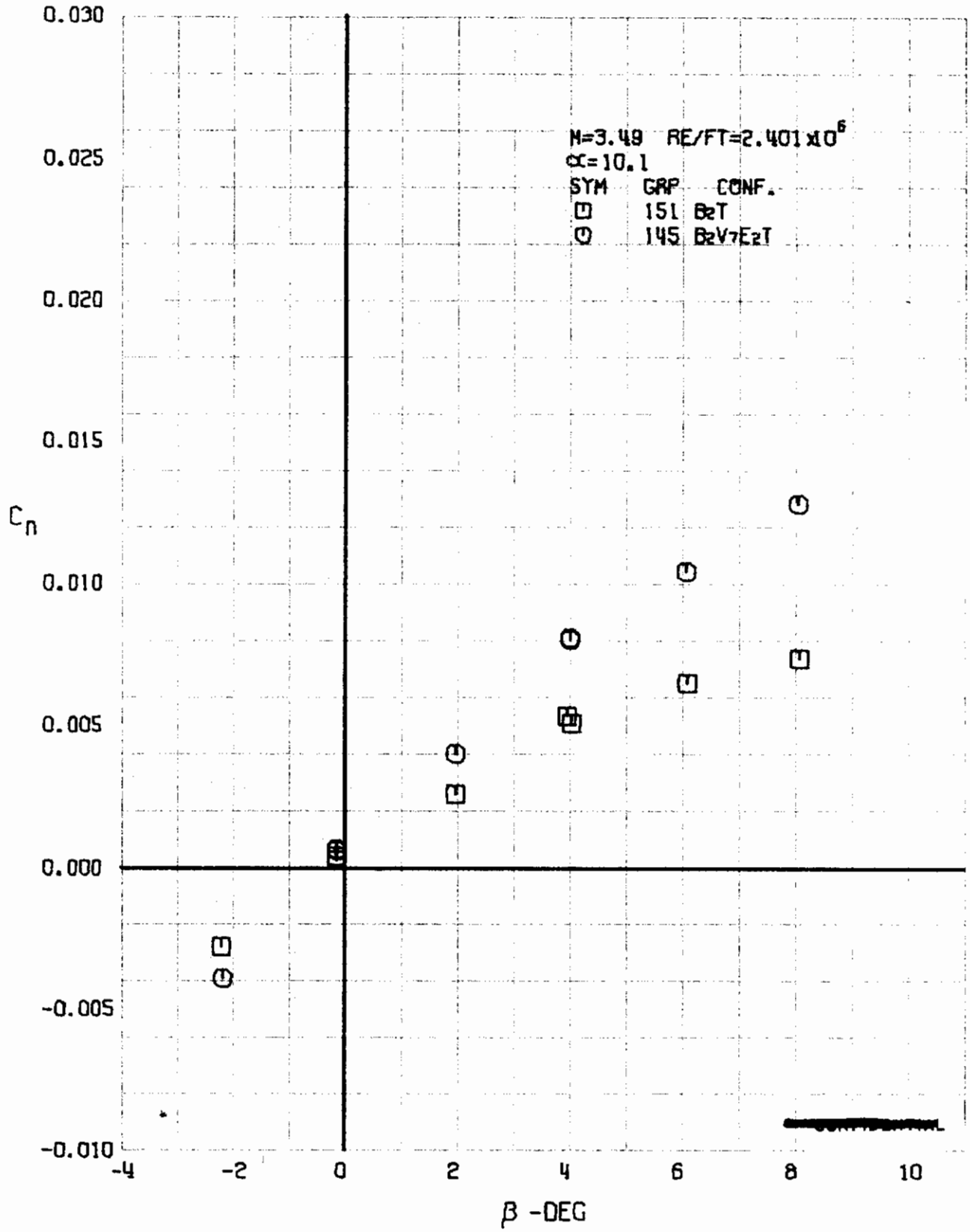

FIGURE 163 (U) CONFIGURATION BUILDUP
- YAWING MOMENT COEFFICIENT VARIATION WITH ANGLE OF YAW (M=3.49)

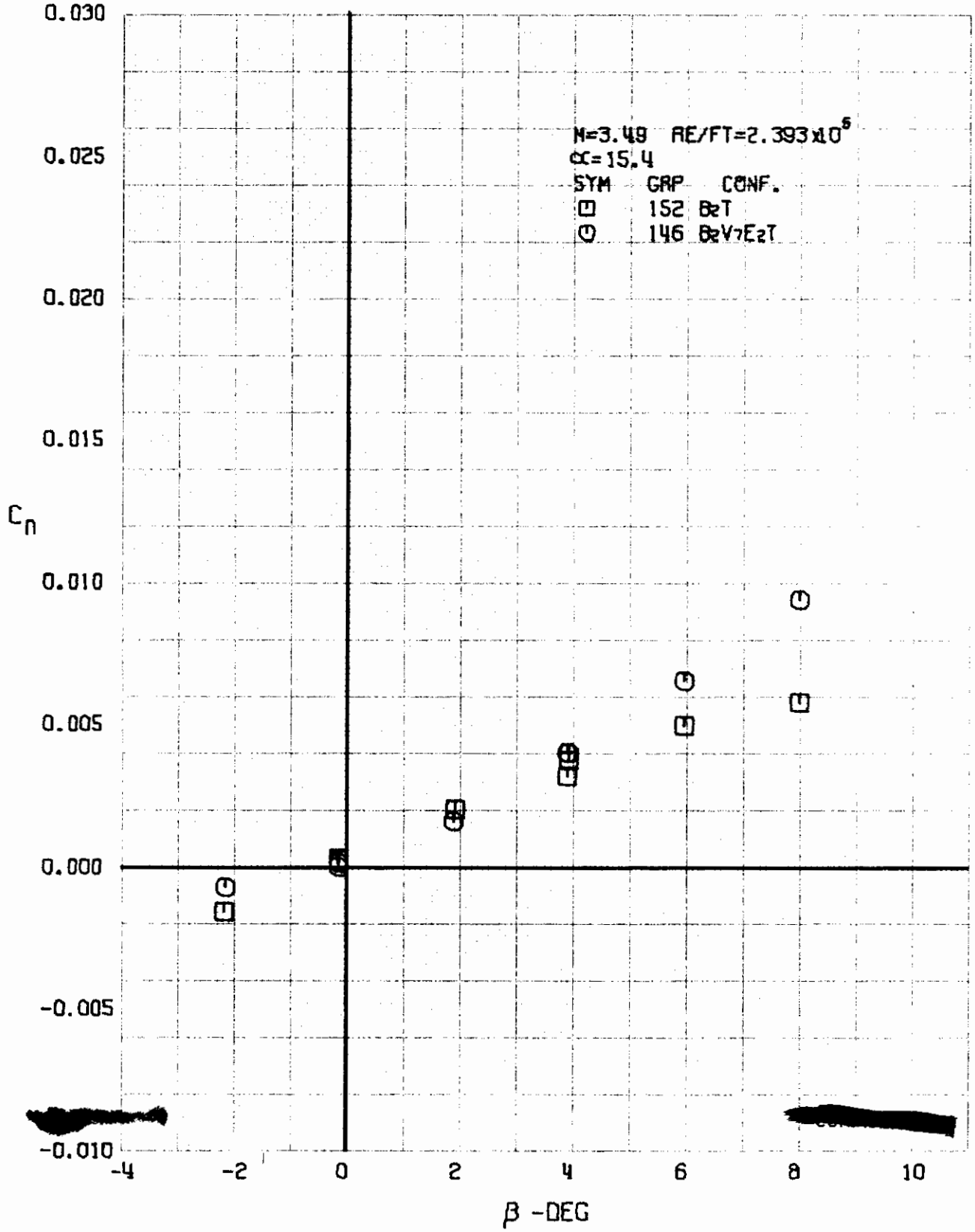

FIGURE 164 (U) CONFIGURATION BUILDUP
- YAWING MOMENT COEFFICIENT VARIATION WITH ANGLE OF YAW (M=3.49)

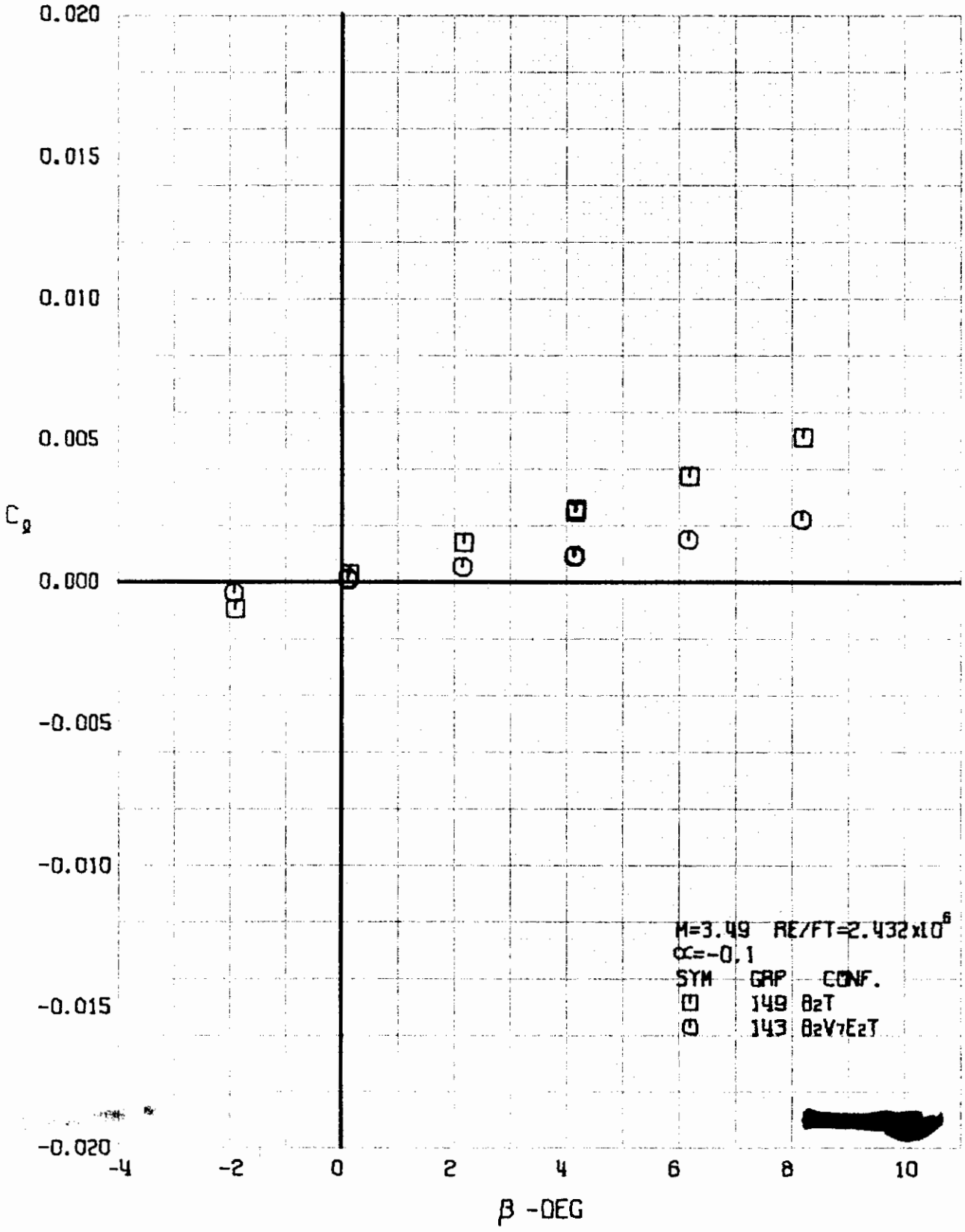

FIGURE 165 (U) CONFIGURATION BUILDUP
- ROLLING MOMENT COEFFICIENT VARIATION WITH ANGLE OF YAW (M=3.49)

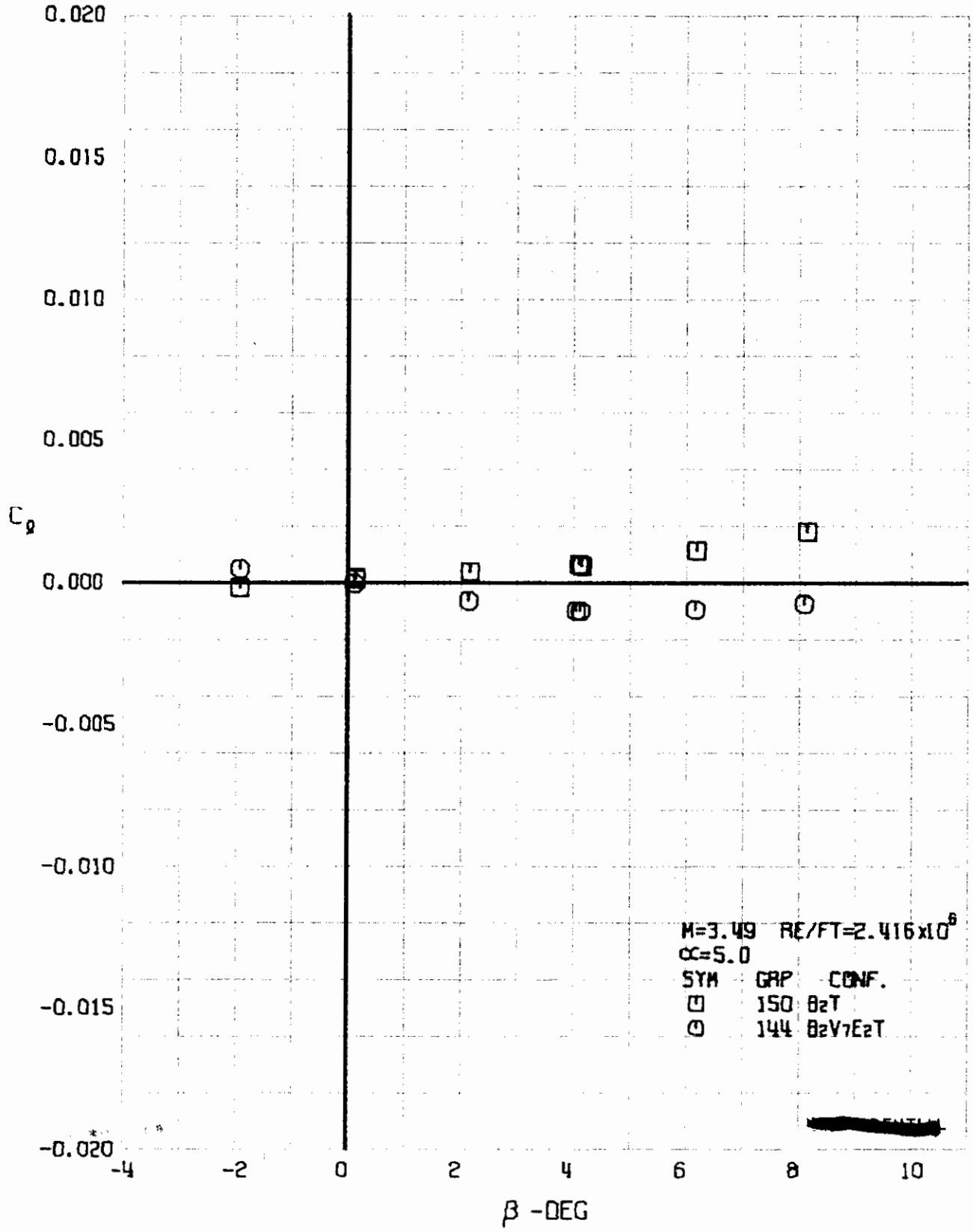

FIGURE 166 (U) CONFIGURATION BUILDUP
- ROLLING MOMENT COEFFICIENT VARIATION WITH ANGLE OF YAW (M=3.49)

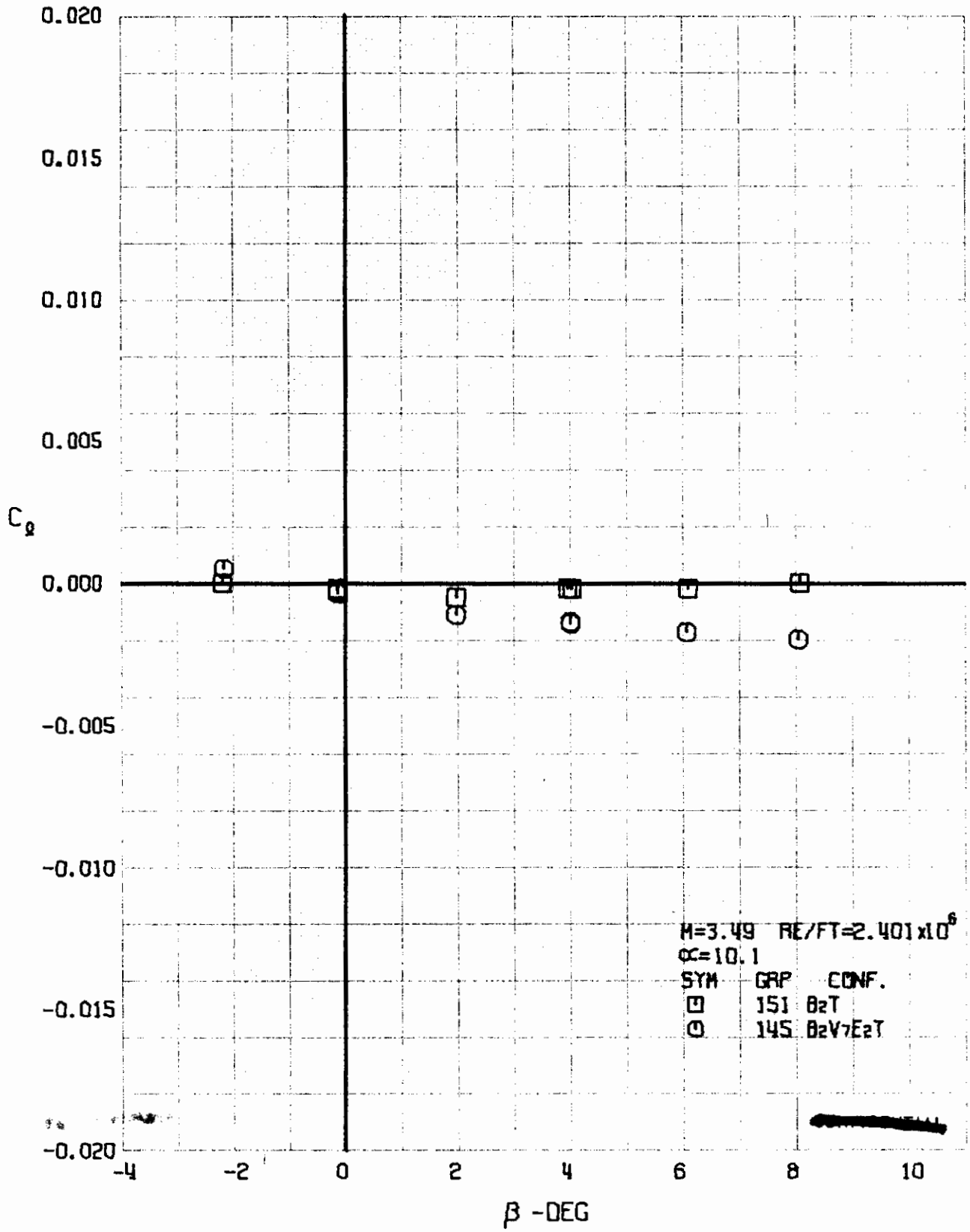

FIGURE 167 (U) CONFIGURATION BUILDUP
- ROLLING MOMENT COEFFICIENT VARIATION WITH ANGLE OF YAW (M=3.49)

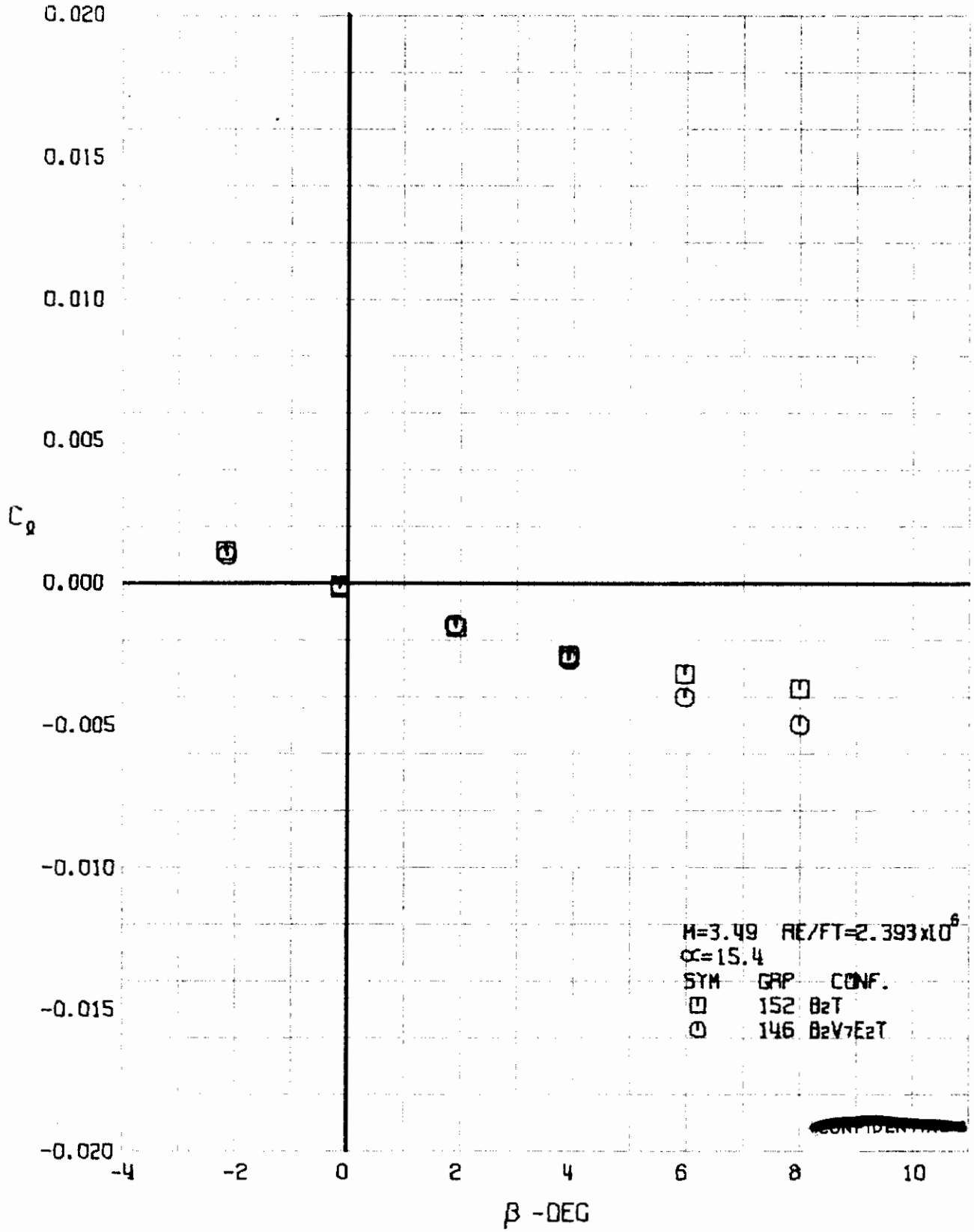

FIGURE 168 (U) CONFIGURATION BUILDUP
- ROLLING MOMENT COEFFICIENT VARIATION WITH ANGLE OF YAW (M=3.49)

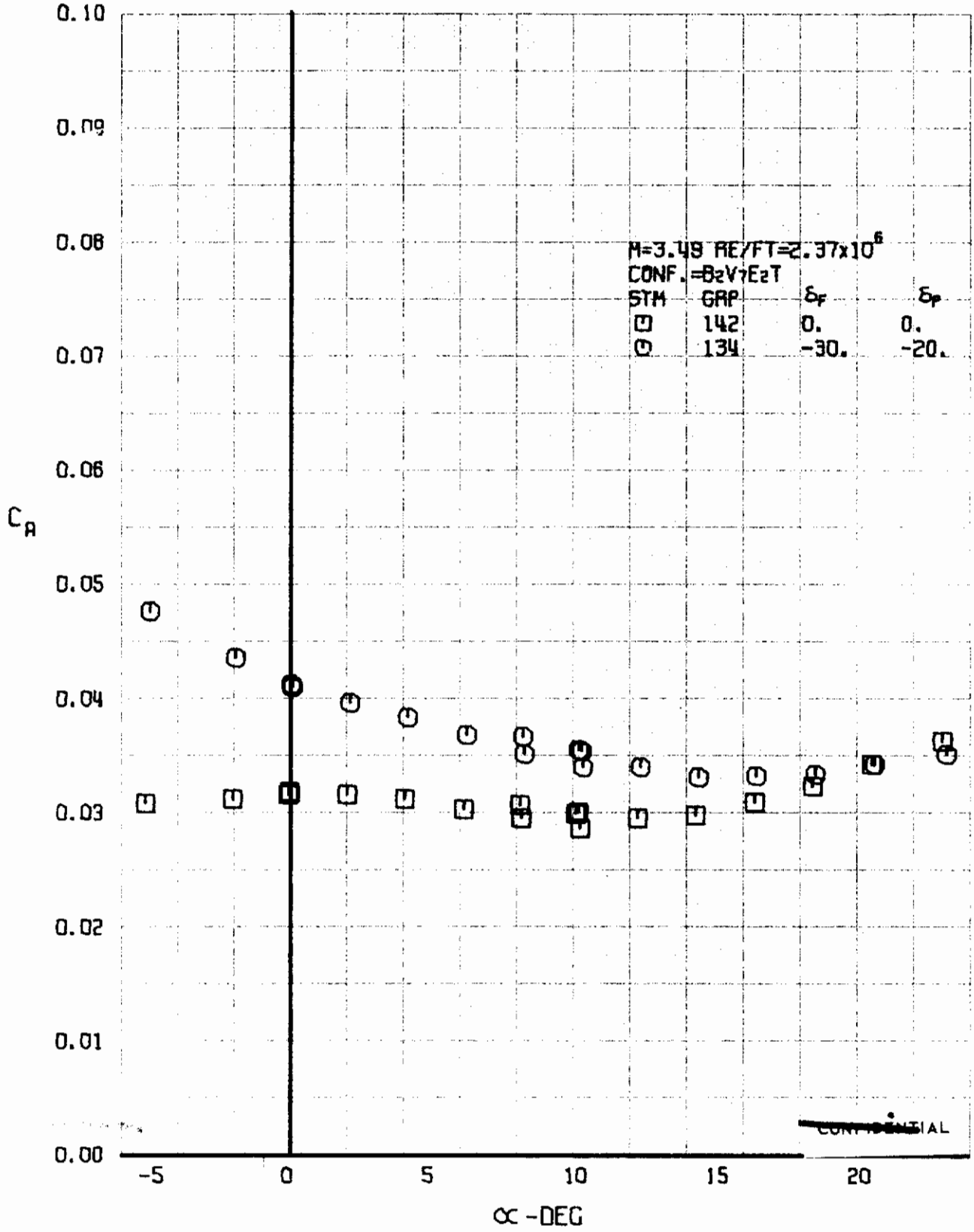

FIGURE 169 (U) COMBINED ELEVON AND FLAP EFFECTS - AXIAL FORCE COEFFICIENT VARIATION WITH ANGLE OF ATTACK (M=3.49)

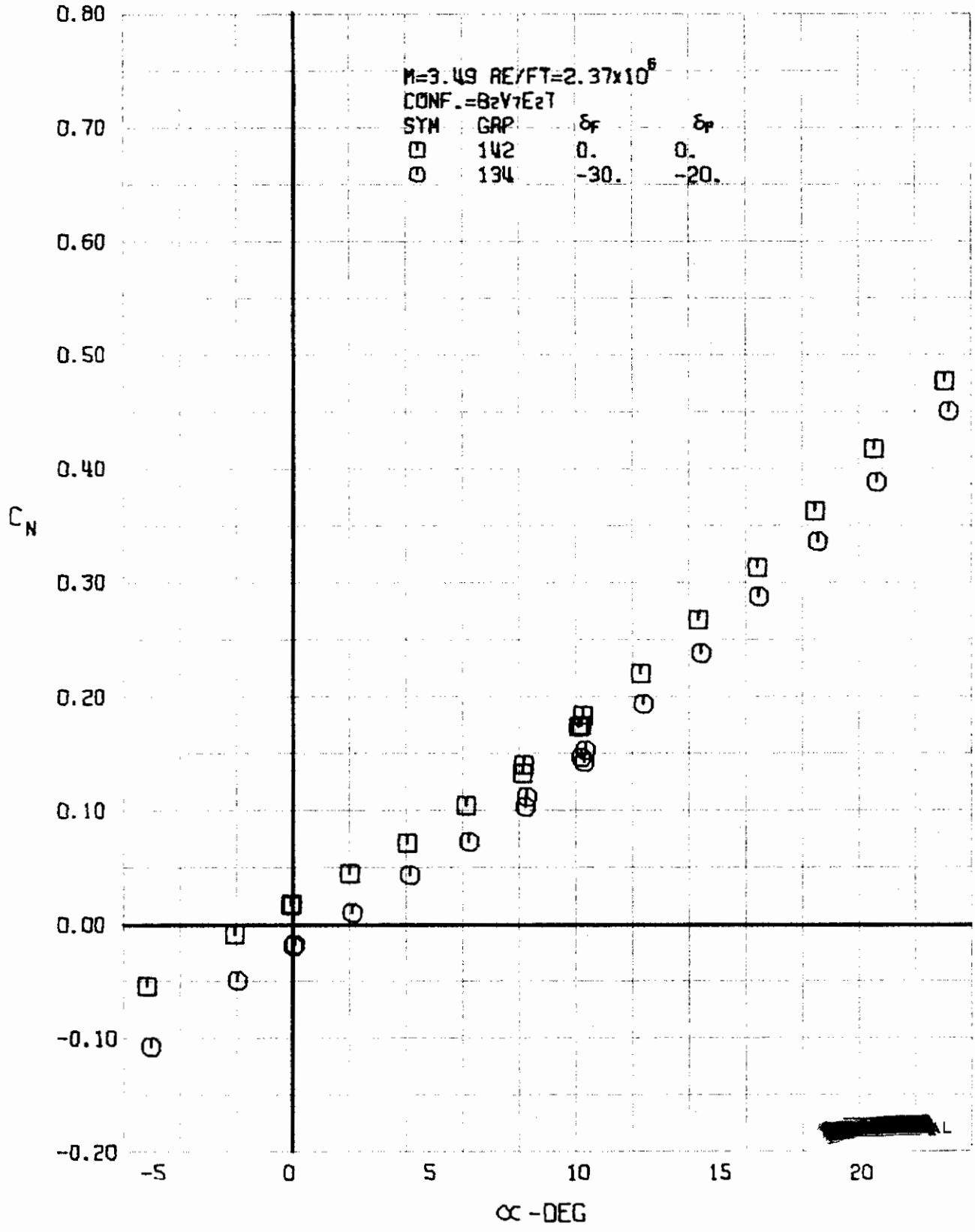

FIGURE 170 (U) COMBINED ELEVON AND FLAP EFFECTS - NORMAL FORCE COEFFICIENT VARIATION WITH ANGLE OF ATTACK (M=3.49)

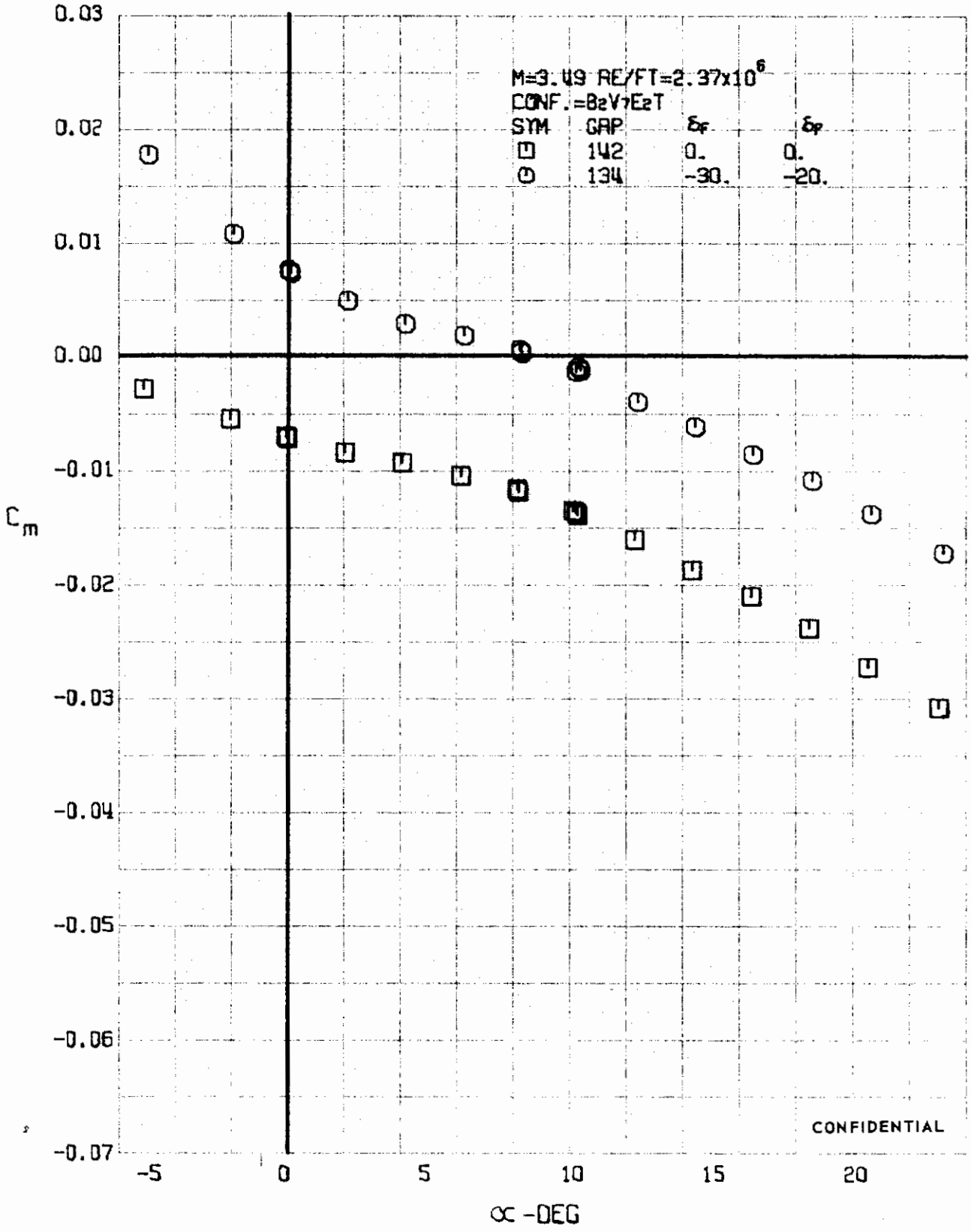

FIGURE 171 (U) COMBINED ELEVON AND FLAP EFFECTS - PITCHING MOMENT COEFFICIENT VARIATION WITH ANGLE OF ATTACK (M=3.49)

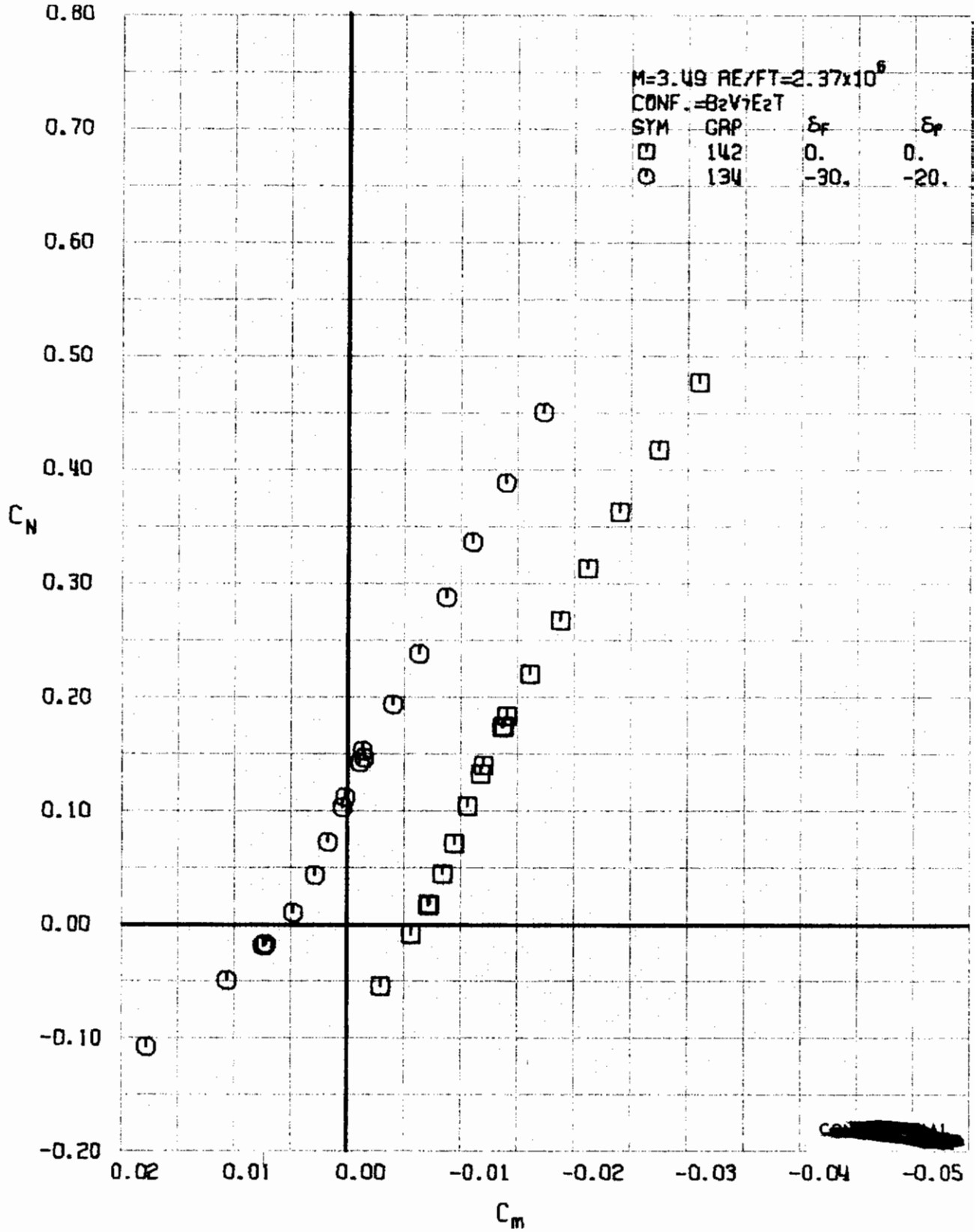

FIGURE 172 (U) COMBINED ELEVON AND FLAP EFFECTS - LONGITUDINAL STABILITY VARIATION (M=3.49)

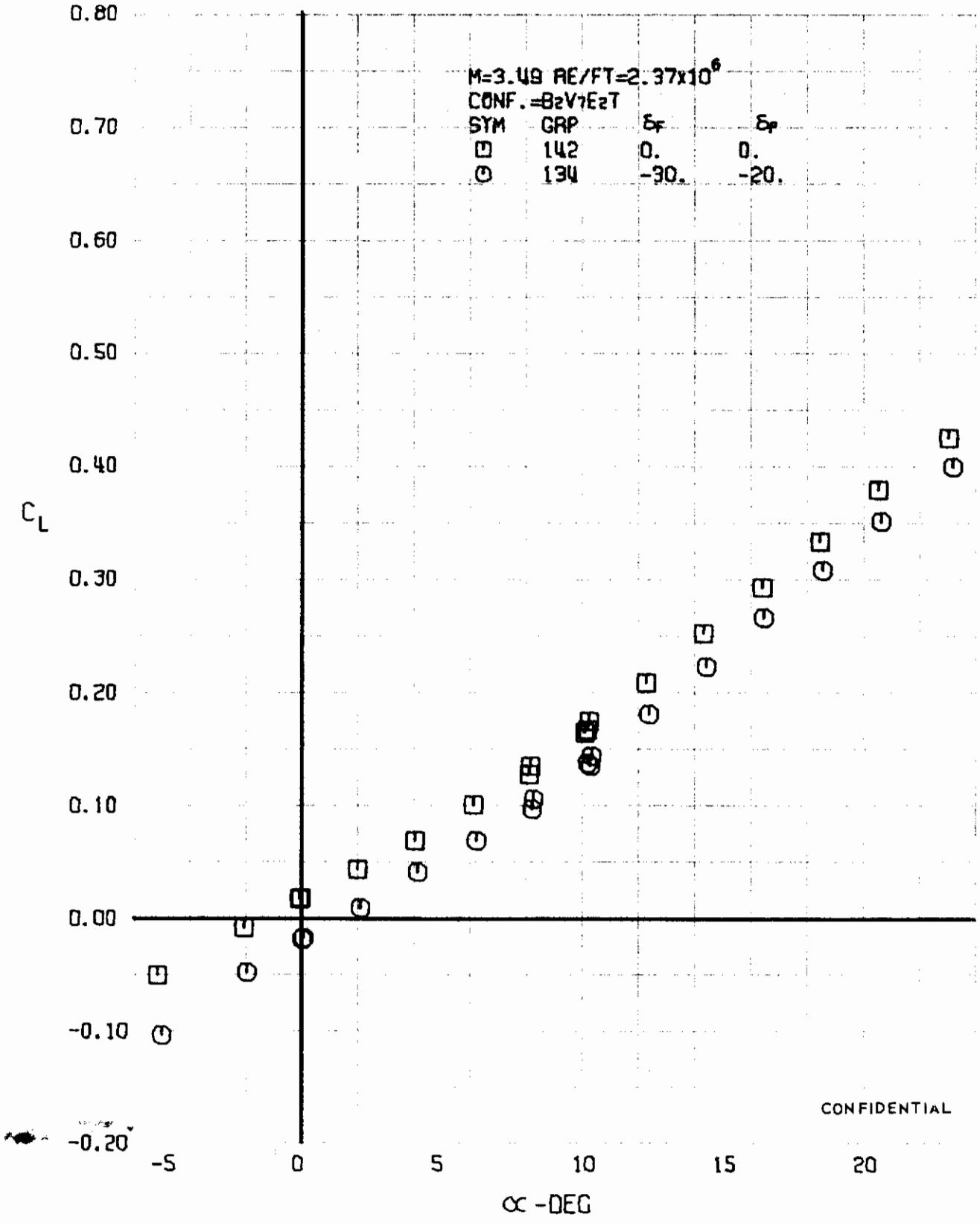

FIGURE 73 (U) COMBINED ELEVON AND FLAP EFFECTS
- LIFT COEFFICIENT VARIATION WITH ANGLE OF ATTACK (M=3.49)

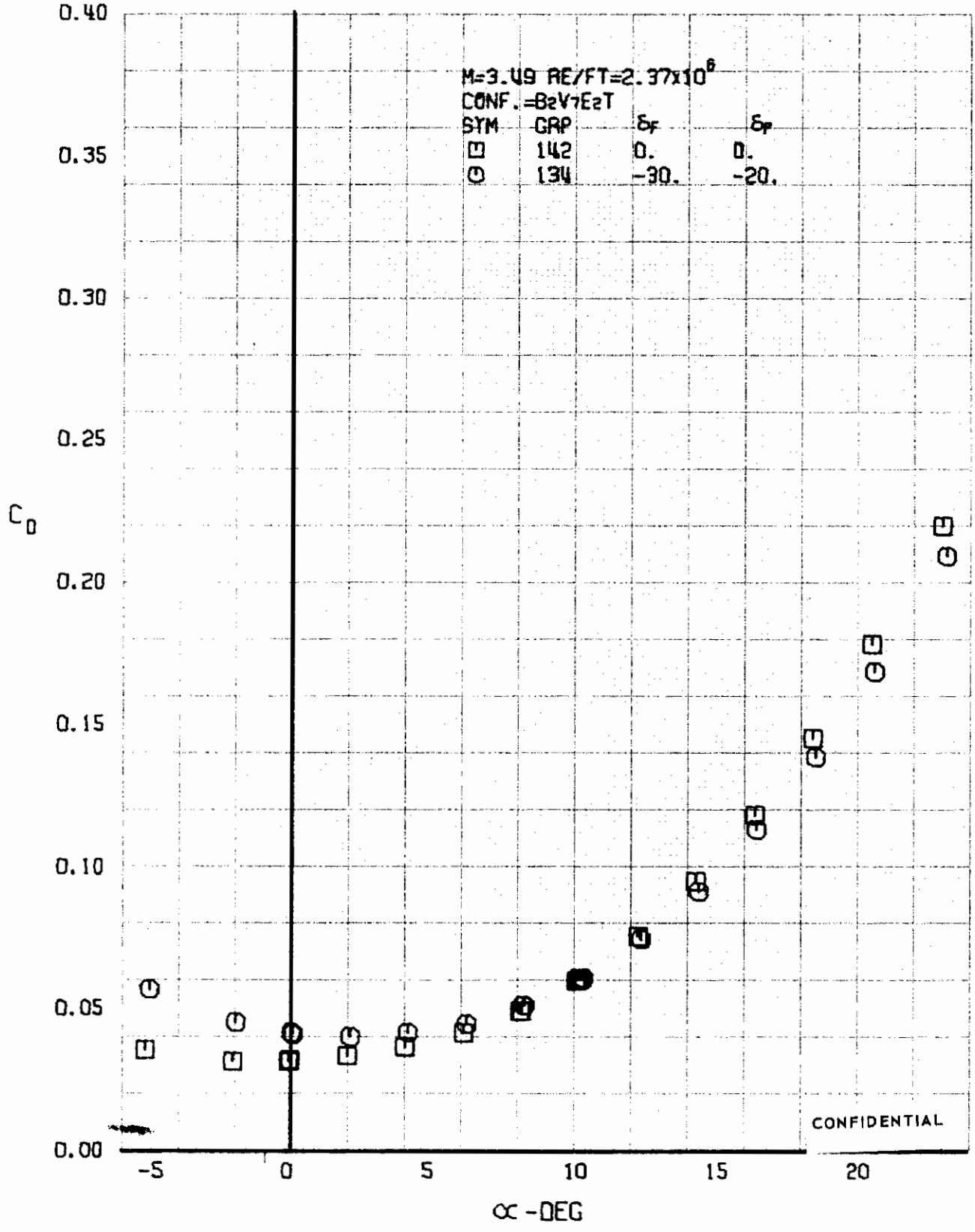

FIGURE 174 (U) COMBINED ELEVON AND FLAP EFFECTS - DRAG COEFFICIENT VARIATION WITH ANGLE OF ATTACK (M=3.49)

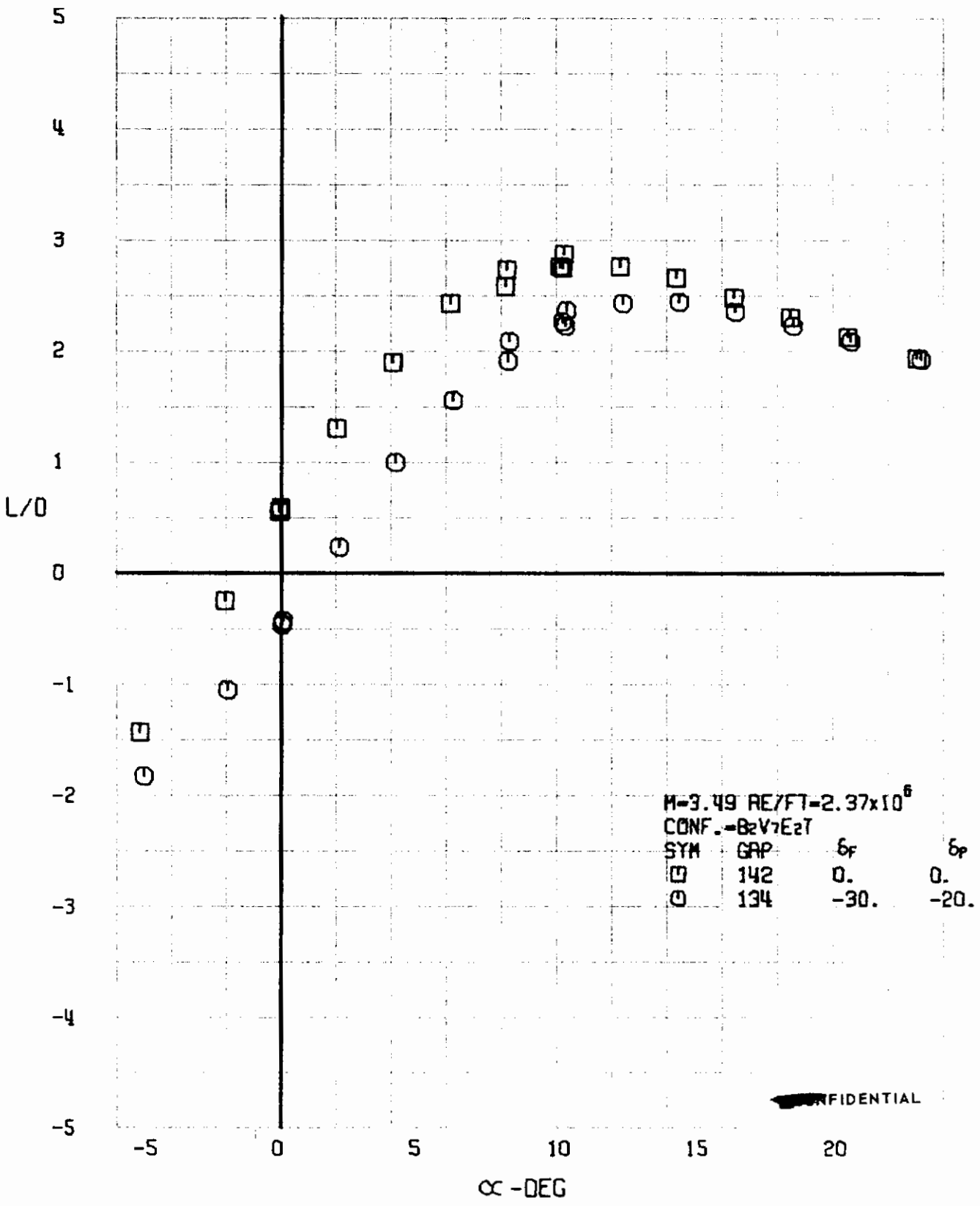

FIGURE 175 (U) COMBINED ELEVON AND FLAP EFFECTS - LIFT-DRAG RATIO VARIATION WITH ANGLE OF ATTACK (M=3.49)

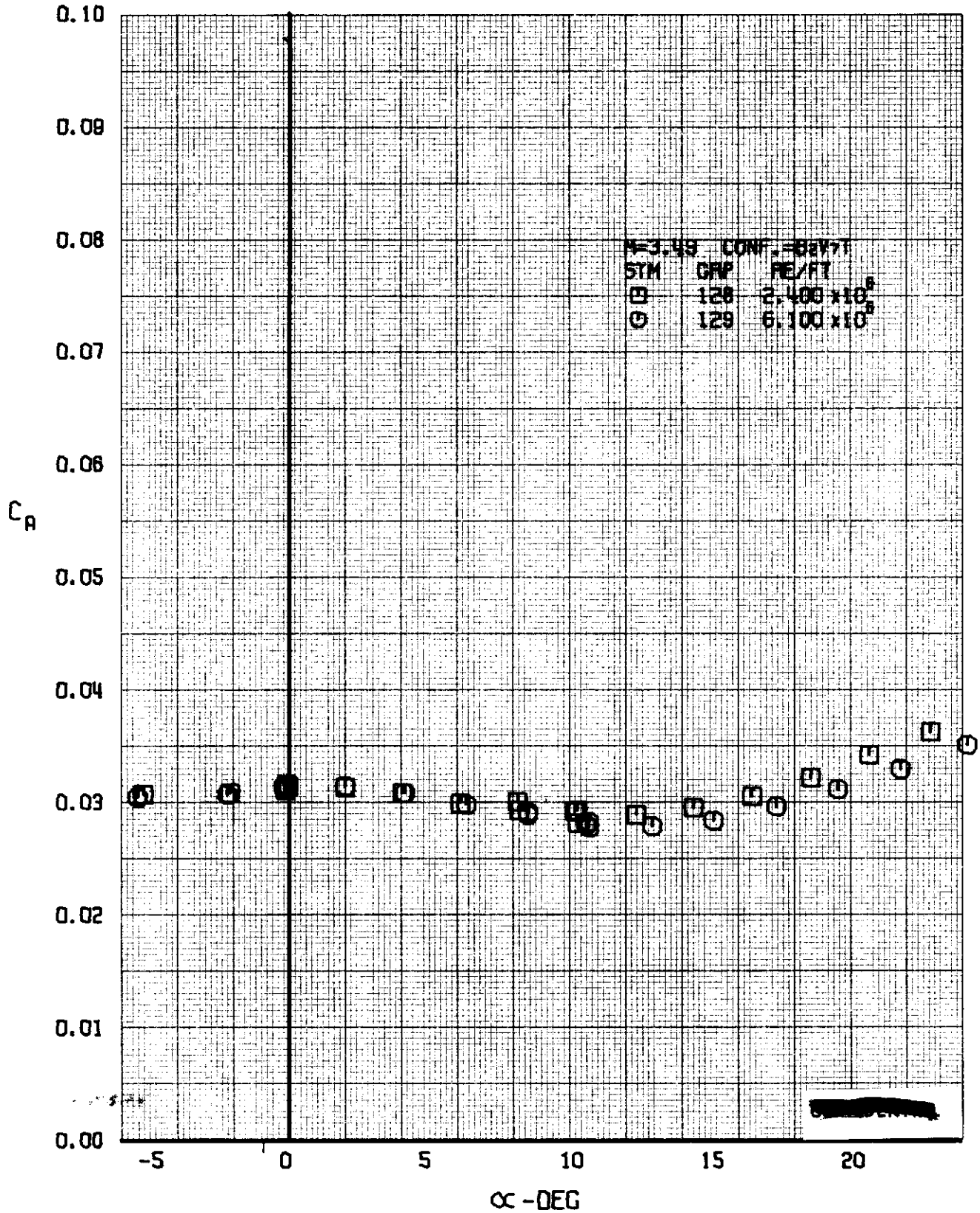

FIGURE 176 (U) REYNOLDS NUMBER EFFECTS
- AXIAL FORCE COEFFICIENT VARIATION WITH ANGLE OF ATTACK (M=3.49)

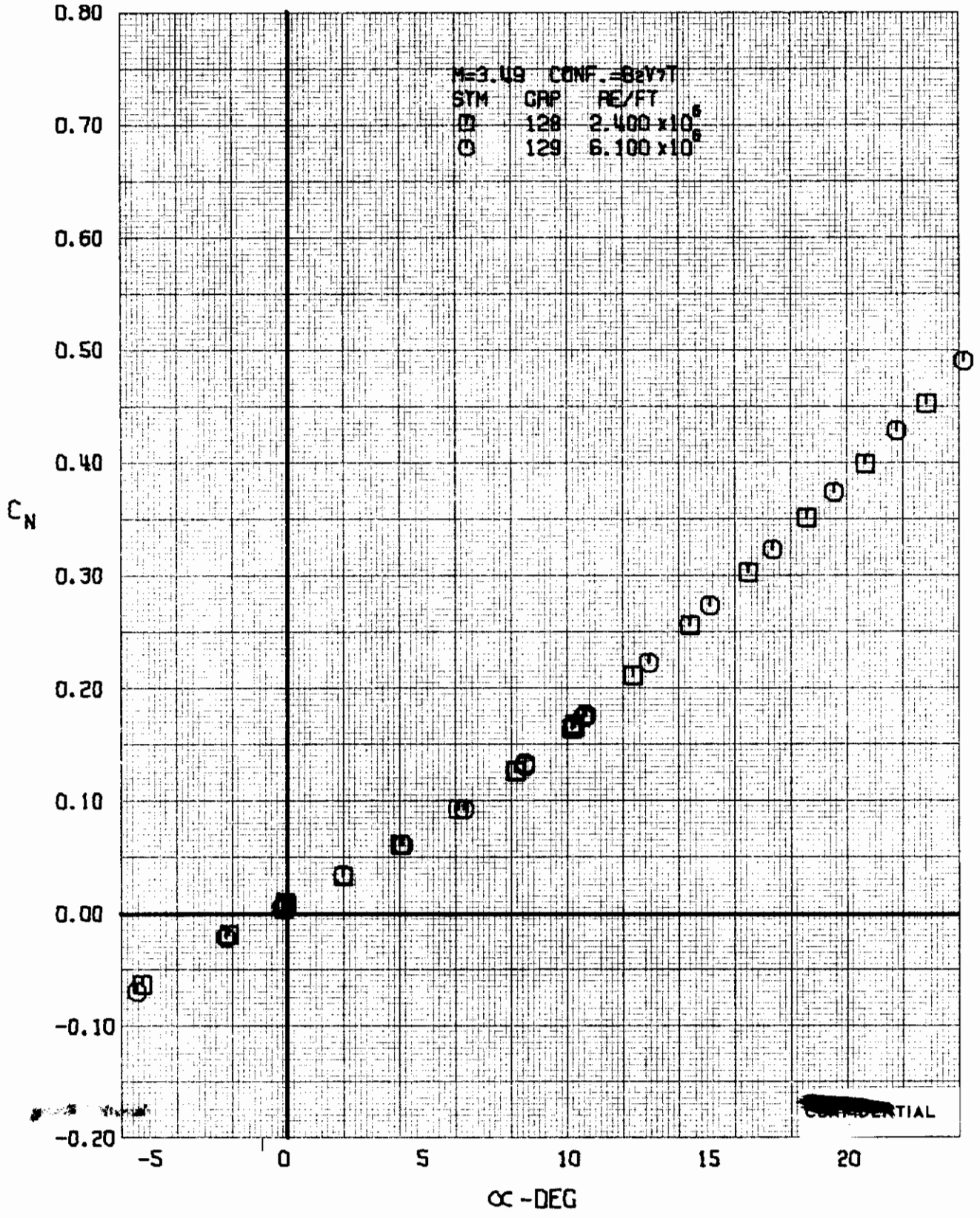

FIGURE 177 (U) REYNOLDS NUMBER EFFECTS
- NORMAL FORCE COEFFICIENT VARIATION WITH ANGLE OF ATTACK (M=3.49)

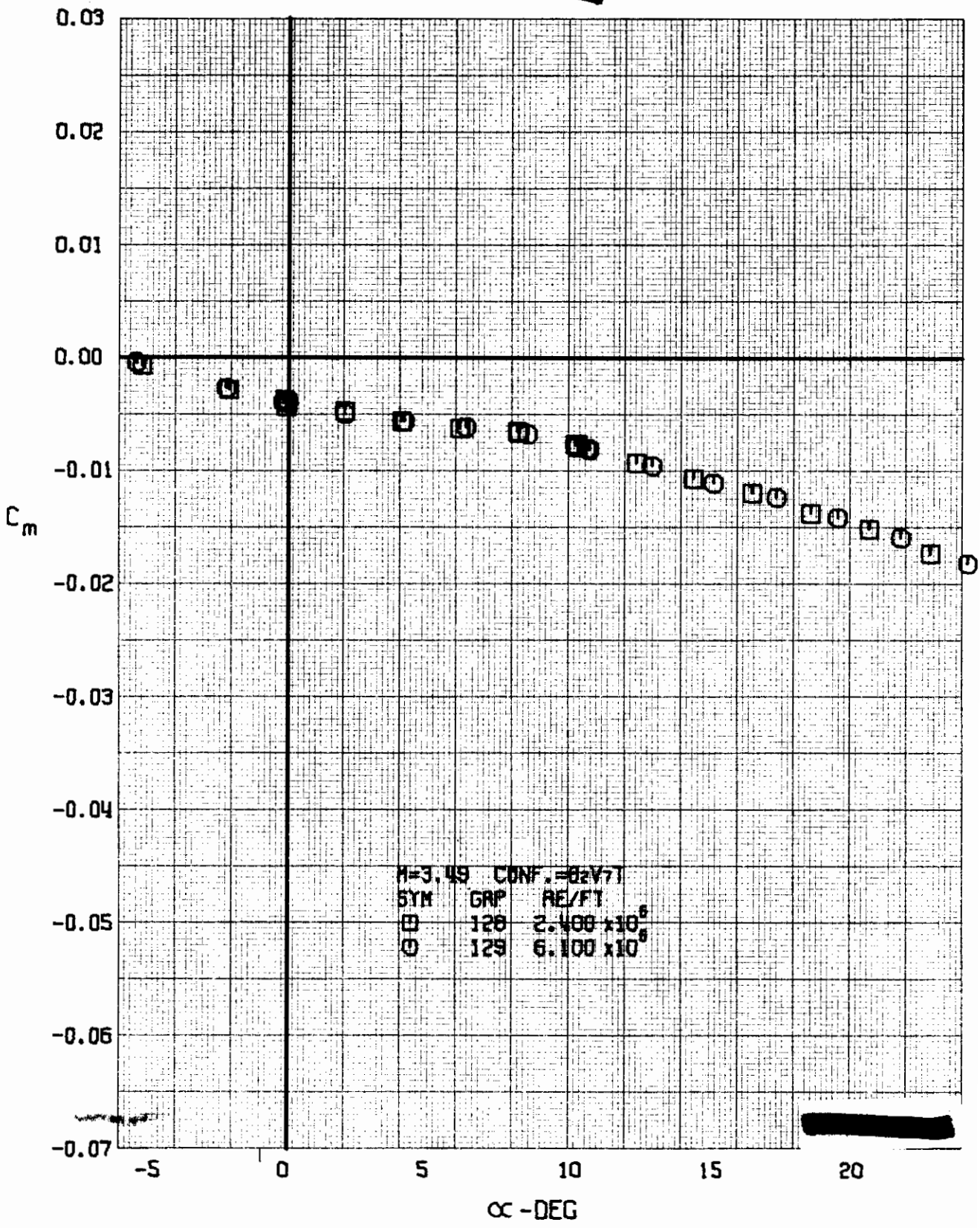

FIGURE 178 (U) REYNOLDS NUMBER EFFECTS
- PITCHING MOMENT COEFFICIENT VARIATION WITH ANGLE OF ATTACK (M=3.49)

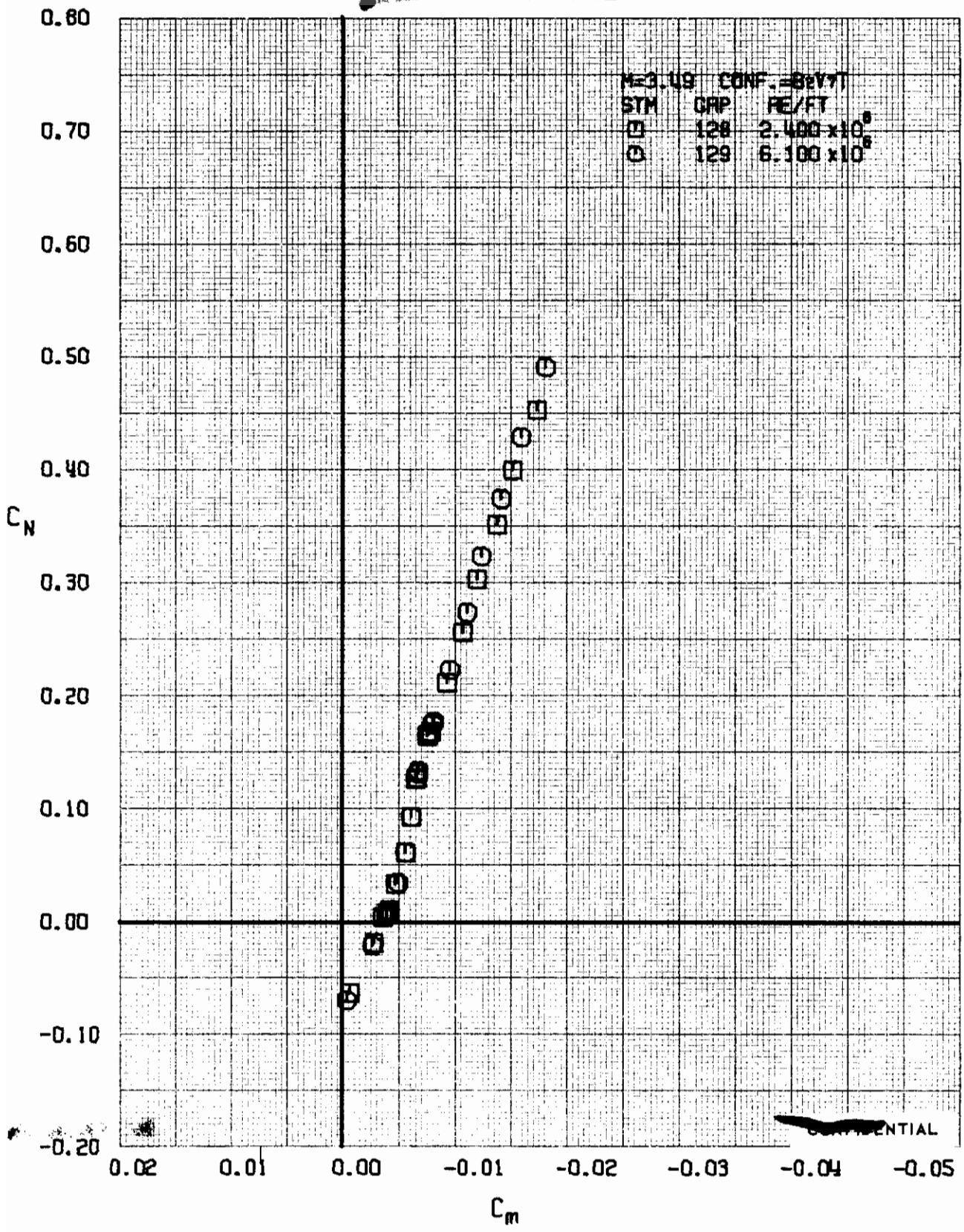

FIGURE 179 (U) REYNOLDS NUMBER EFFECTS
- LONGITUDINAL STABILITY VARIATION (M=3.49)

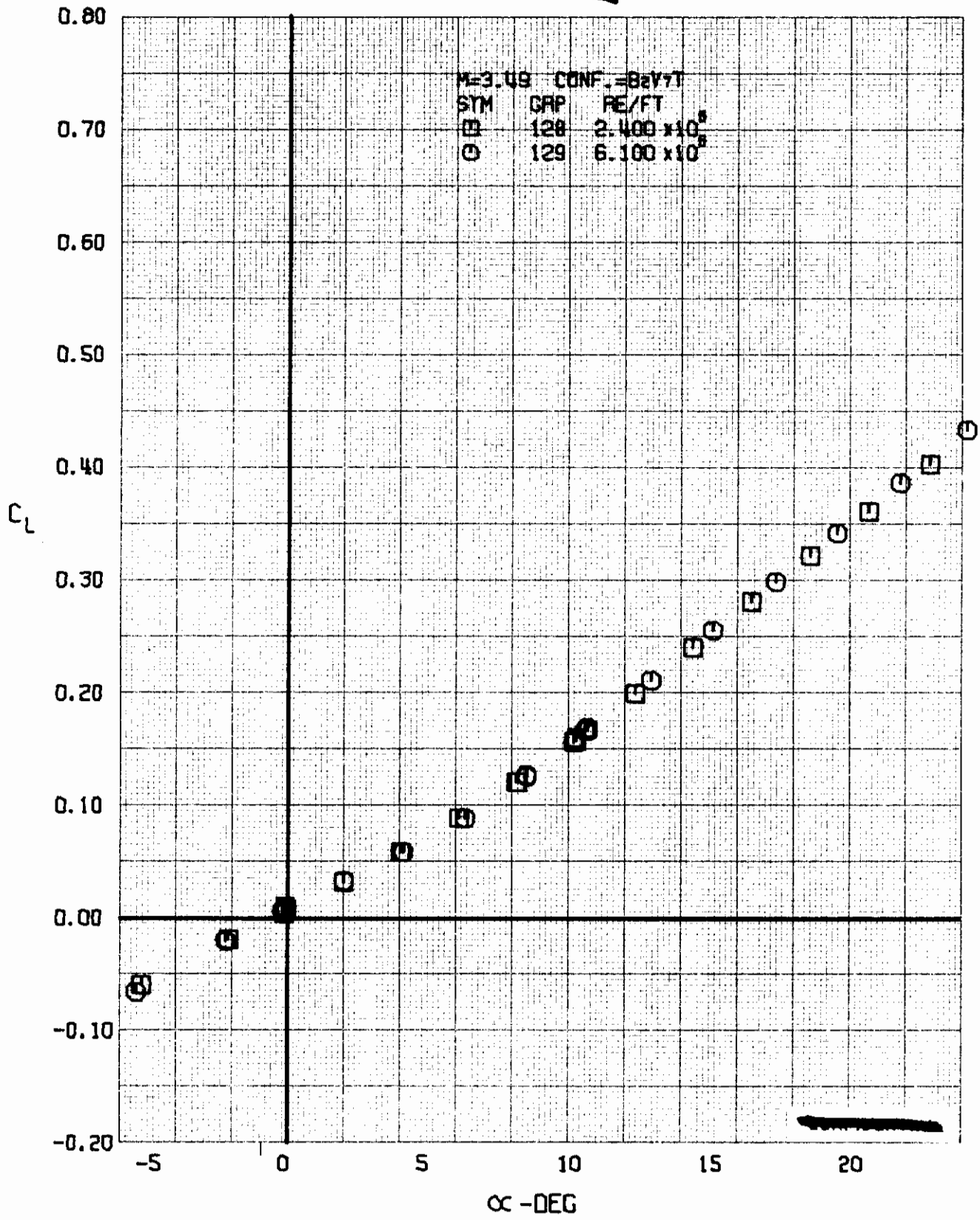

FIGURE 180 (U) REYNOLDS NUMBER EFFECTS
- LIFT COEFFICIENT VARIATION WITH ANGLE OF ATTACK (M=3.49)

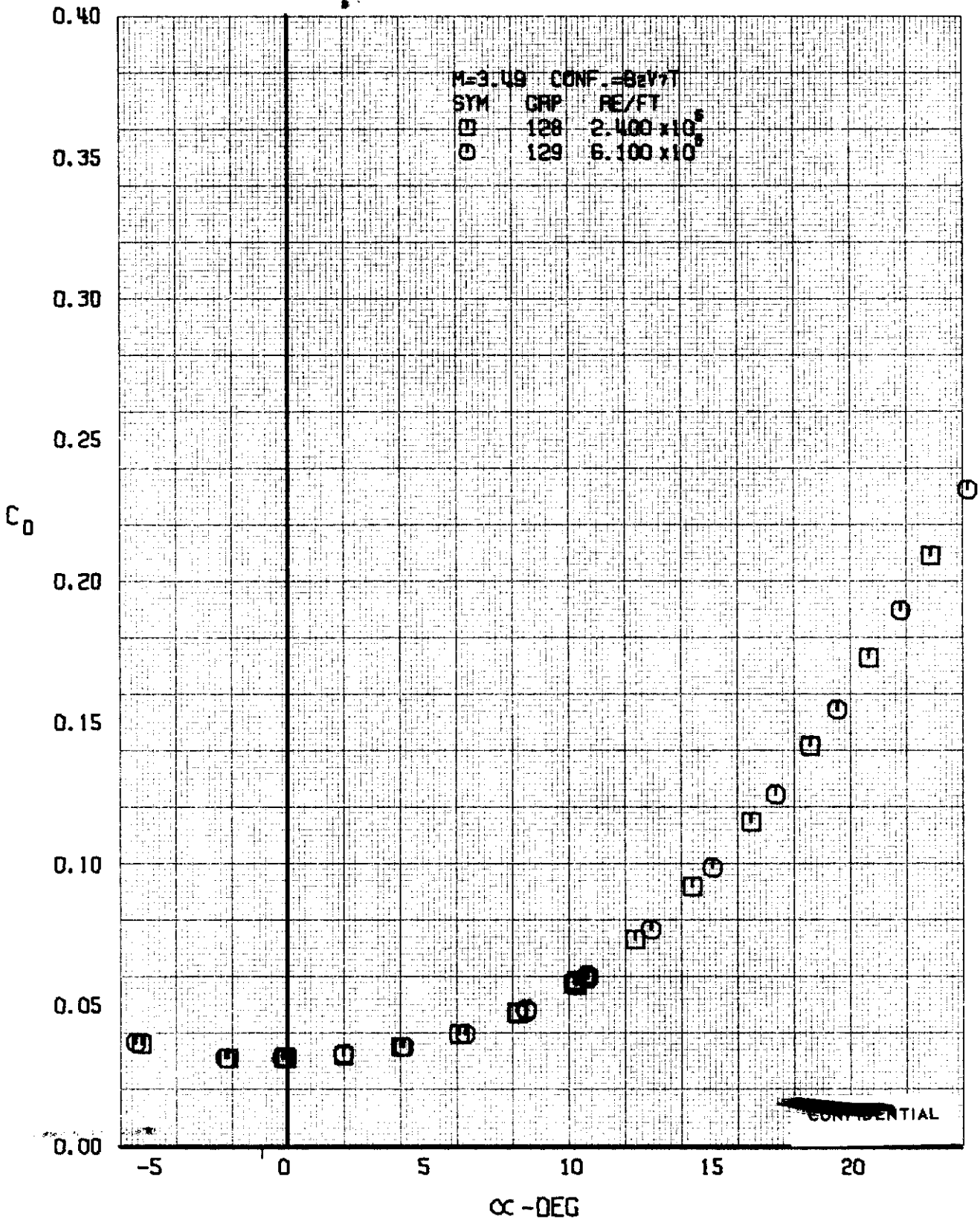

FIGURE 181 (U) REYNOLDS NUMBER EFFECTS
- DRAG COEFFICIENT VARIATION WITH ANGLE OF ATTACK (M=3.49)

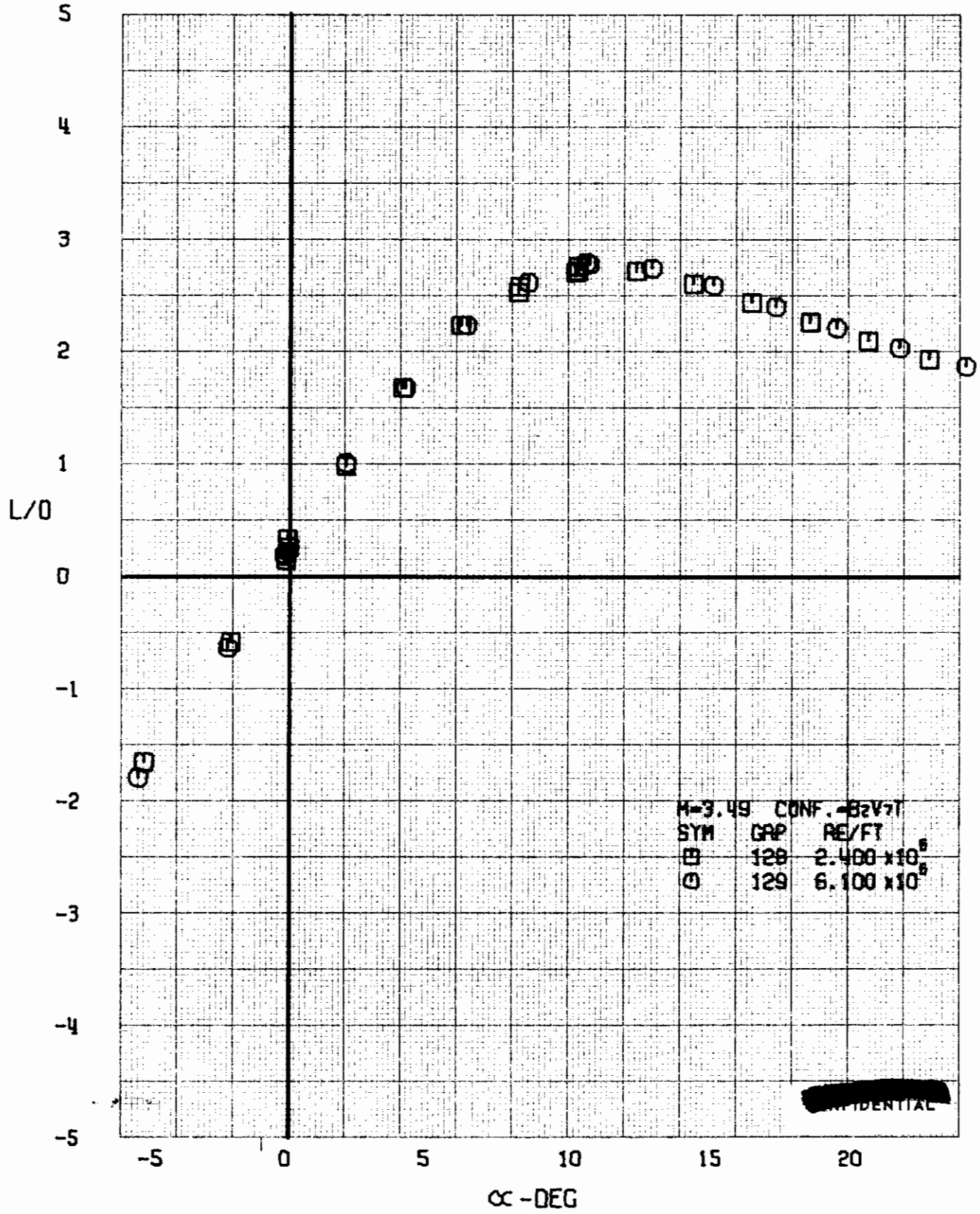

FIGURE 182 (U) REYNOLDS NUMBER EFFECTS
- LIFT-DRAG RATIO VARIATION WITH ANGLE OF ATTACK (M=3.49)

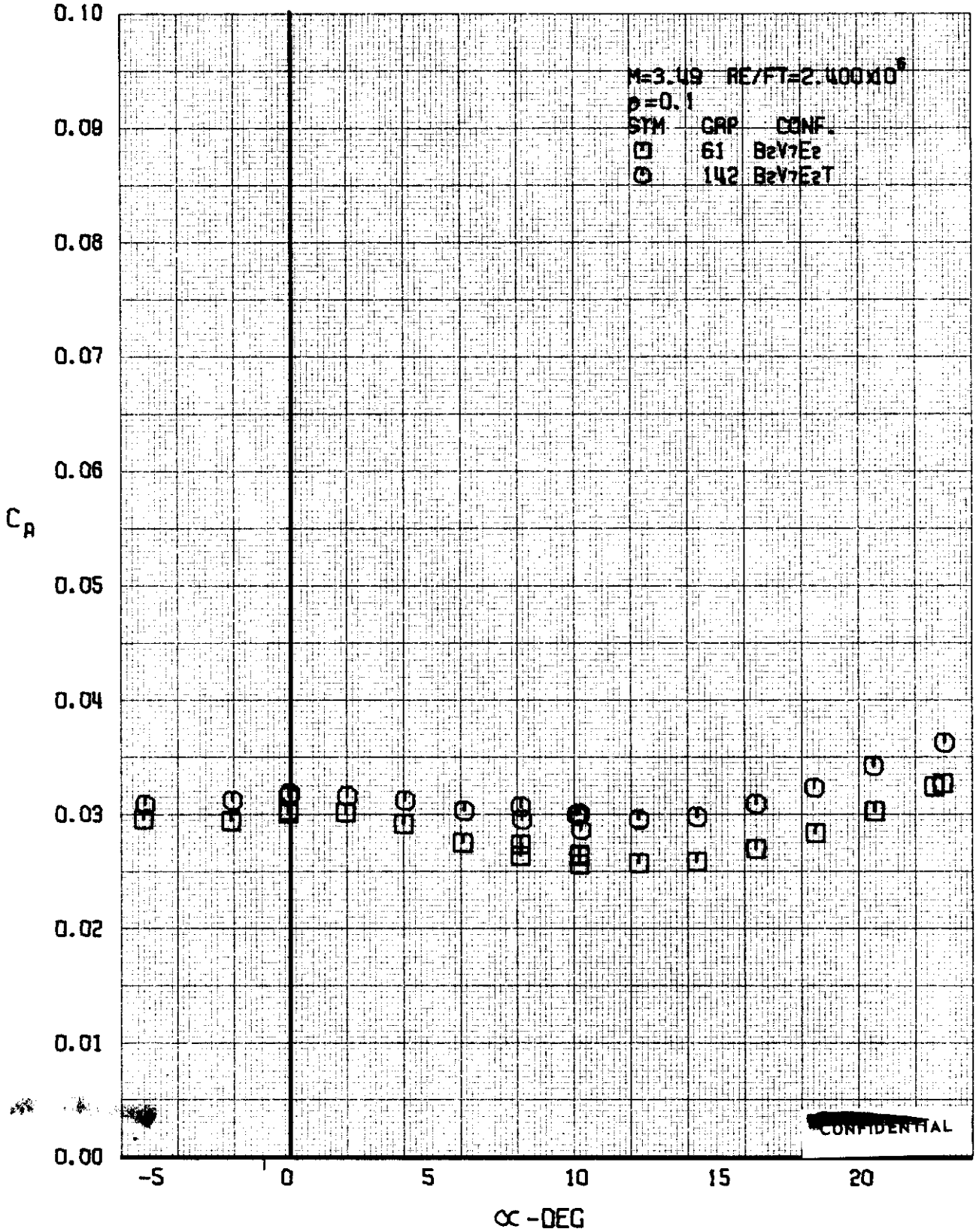

FIGURE 183 - (U) FORCED TRANSITION EFFECTS
- AXIAL FORCE COEFFICIENT VARIATION WITH ANGLE OF ATTACK (M=3.49)

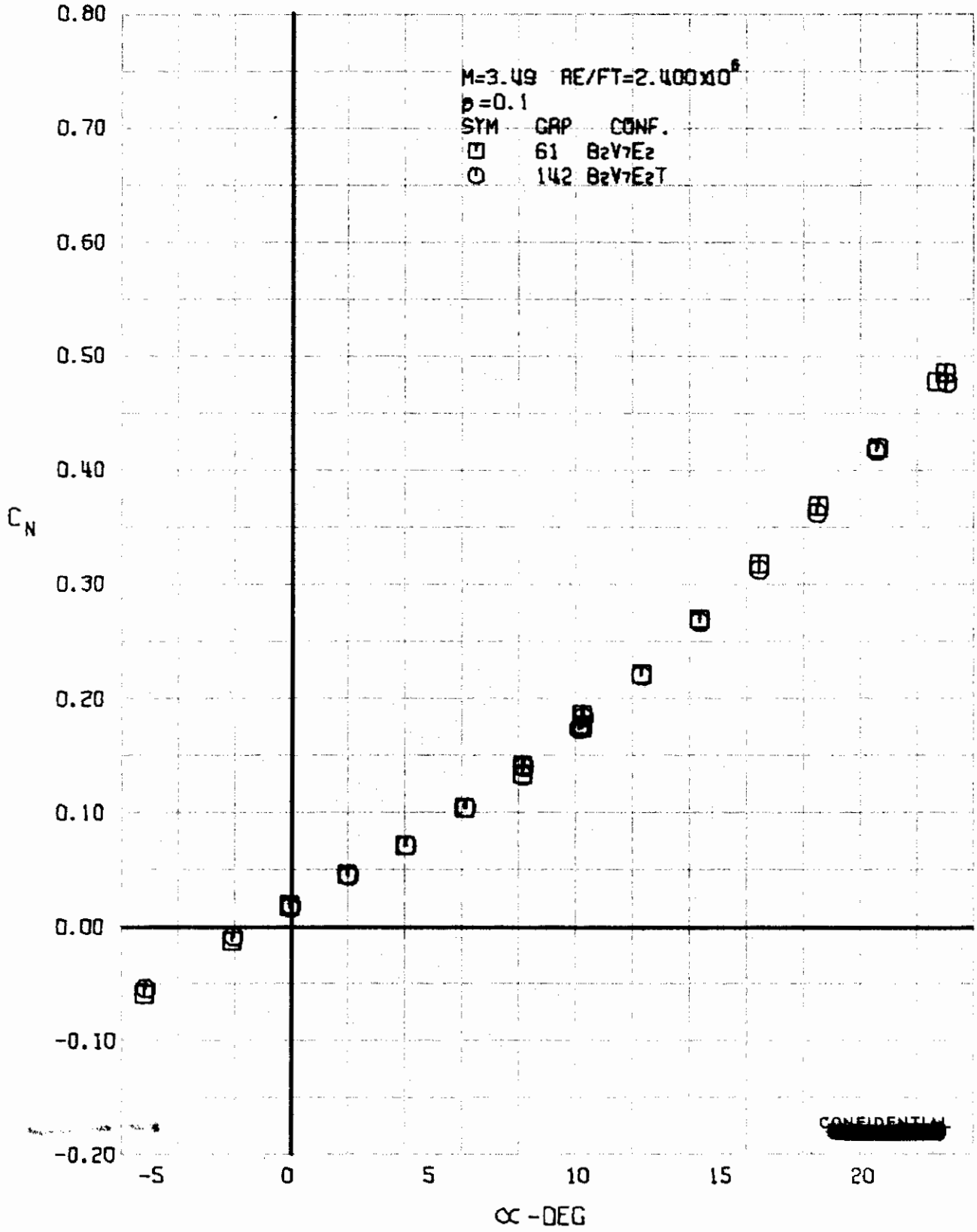

FIGURE 184 (U) FORCED TRANSITION EFFECTS
- NORMAL FORCE COEFFICIENT VARIATION WITH ANGLE OF ATTACK (M= 3.49)

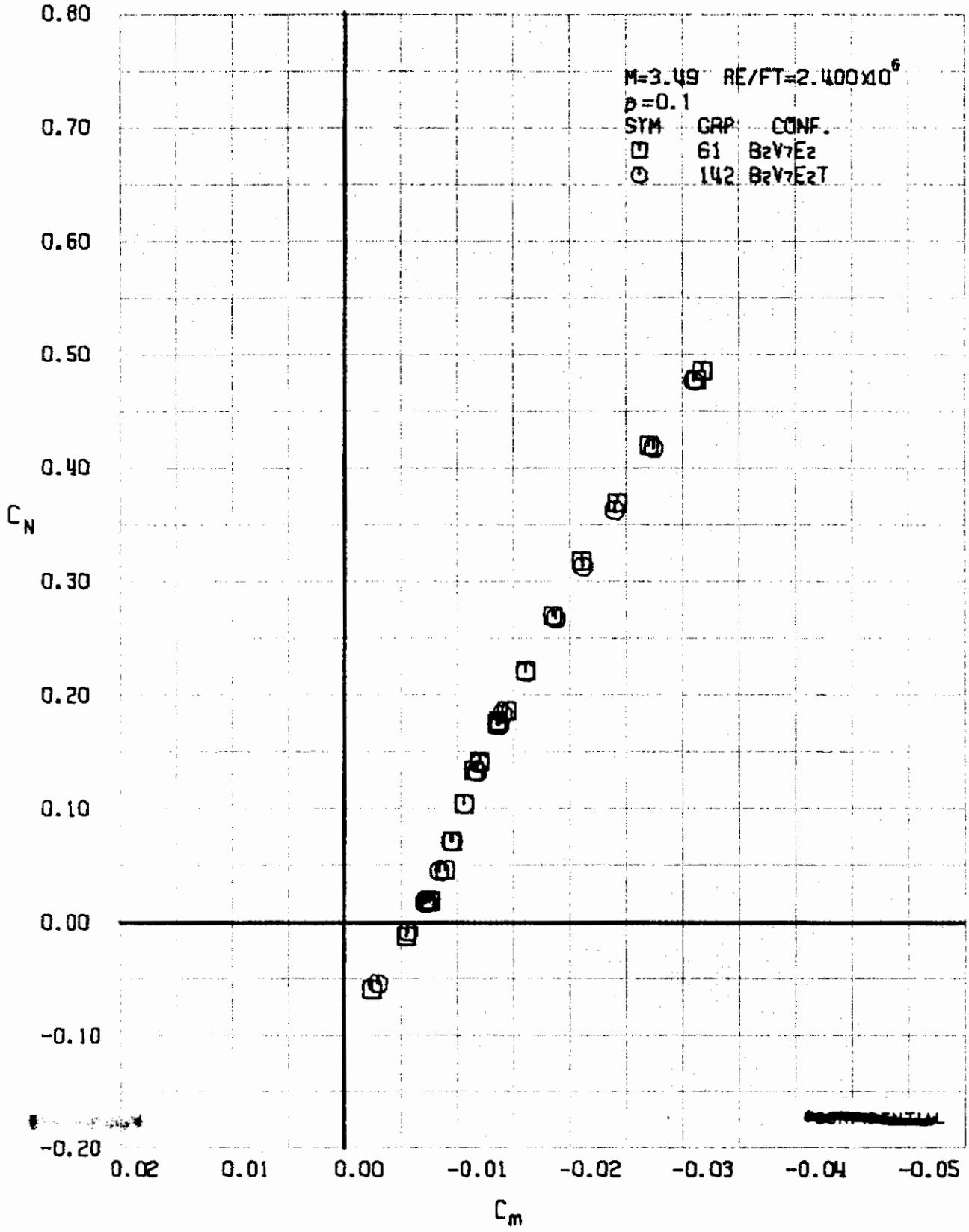

FIGURE 185 (U) ORCED TRANSITION EFFECTS
- LONGITUDINAL STABILITY VARIATION (M=3.49)

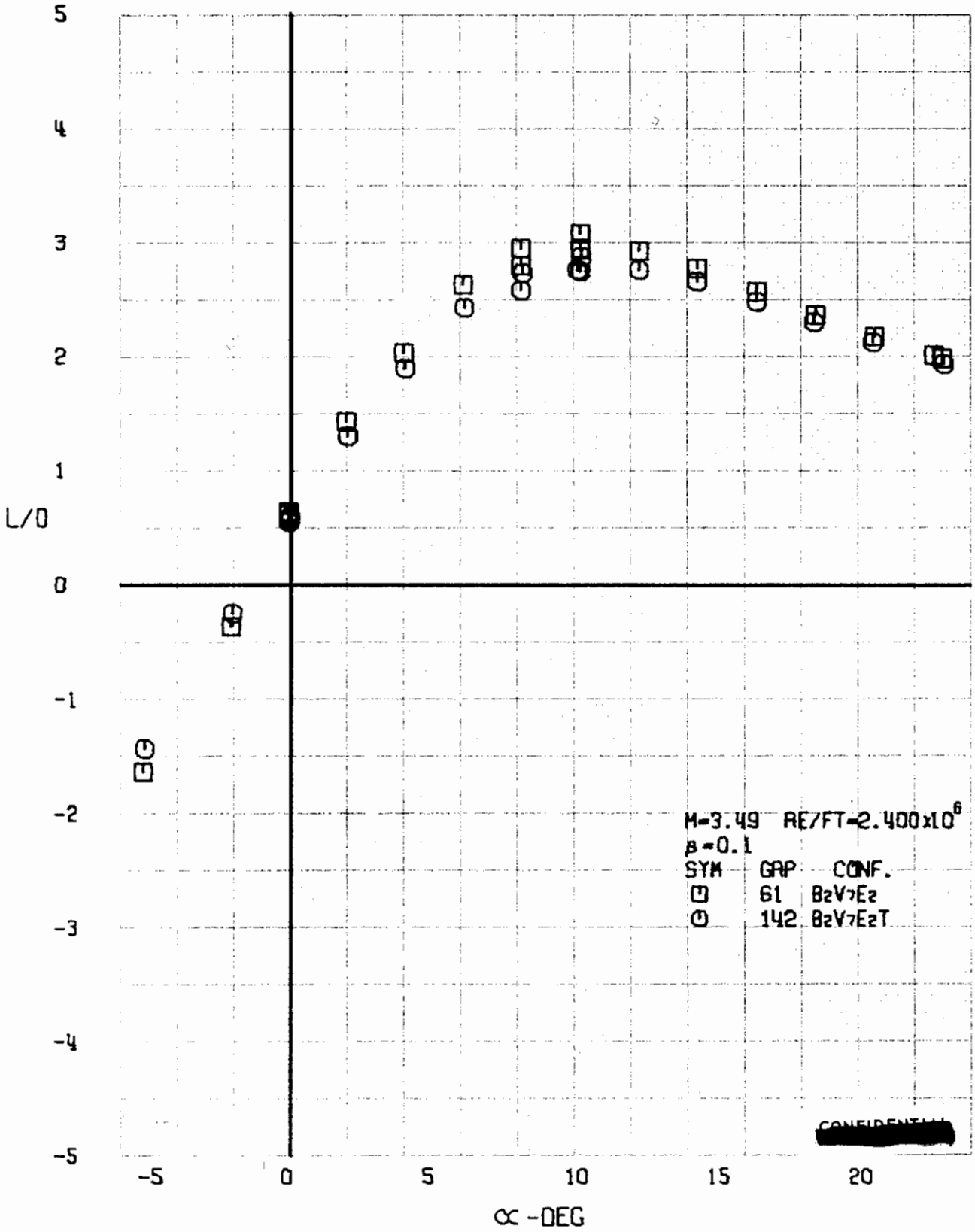

FIGURE 186 - (U) FORCED TRANSITION EFFECTS
- LIFT-DRAG RATIO VARIATION WITH ANGLE OF ATTACK (M=3.49)

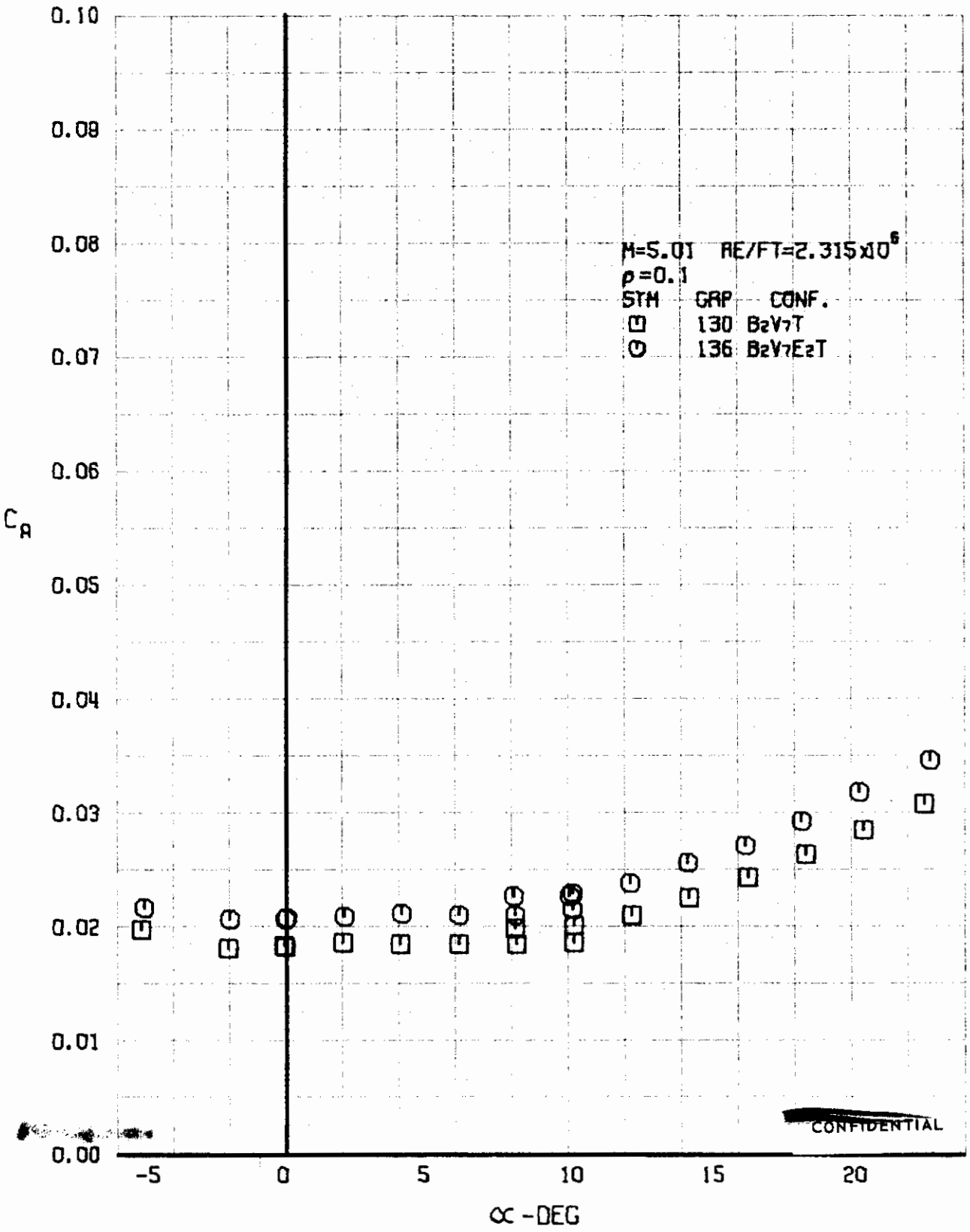

FIGURE 187 (U) CONFIGURATION BUILDUP
- AXIAL FORCE COEFFICIENT VARIATION WITH ANGLE OF ATTACK (M=5.01)

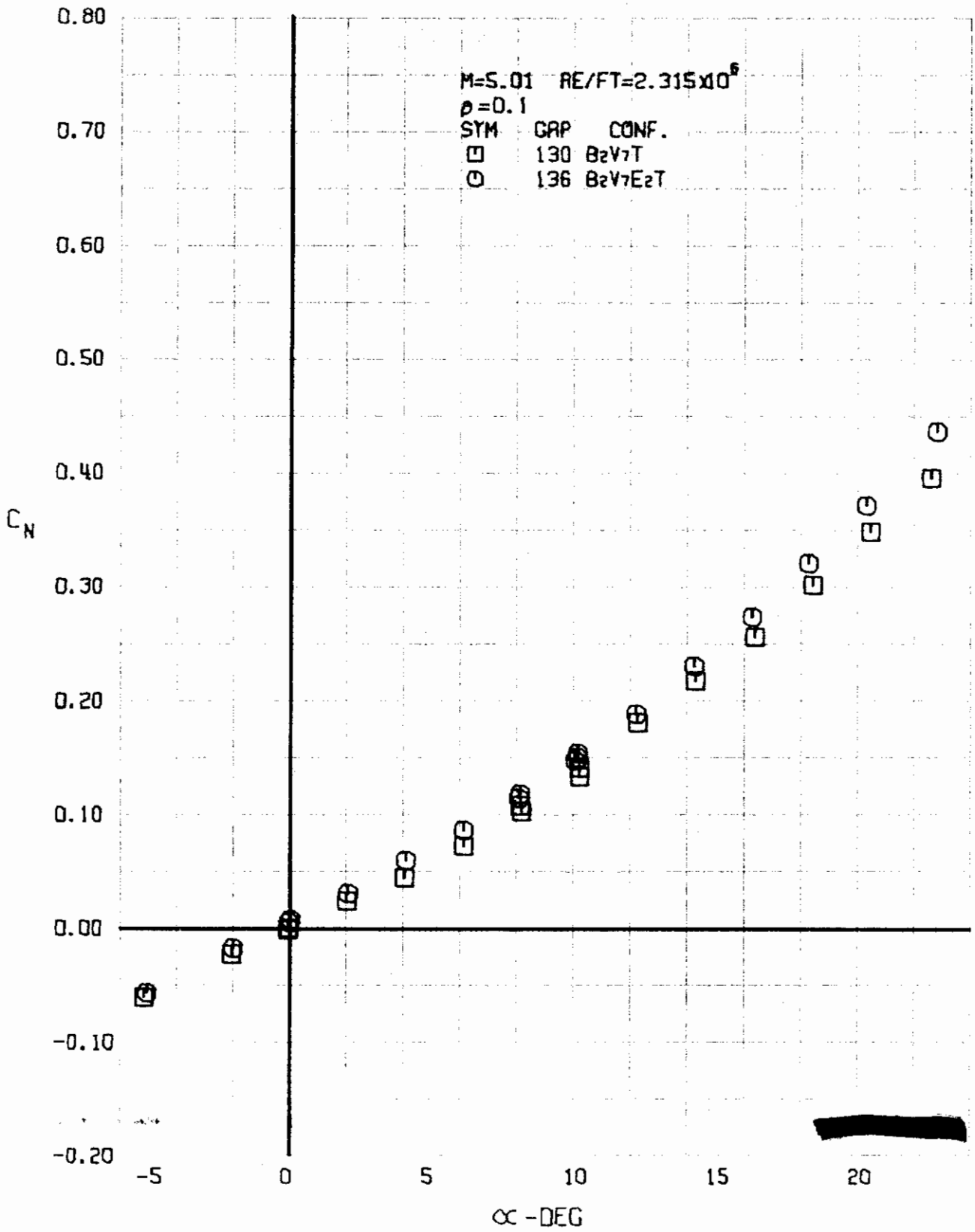

FIGURE 188 (U) CONFIGURATION BUILDUP
- NORMAL FORCE COEFFICIENT VARIATION WITH ANGLE OF ATTACK (M=5.01)

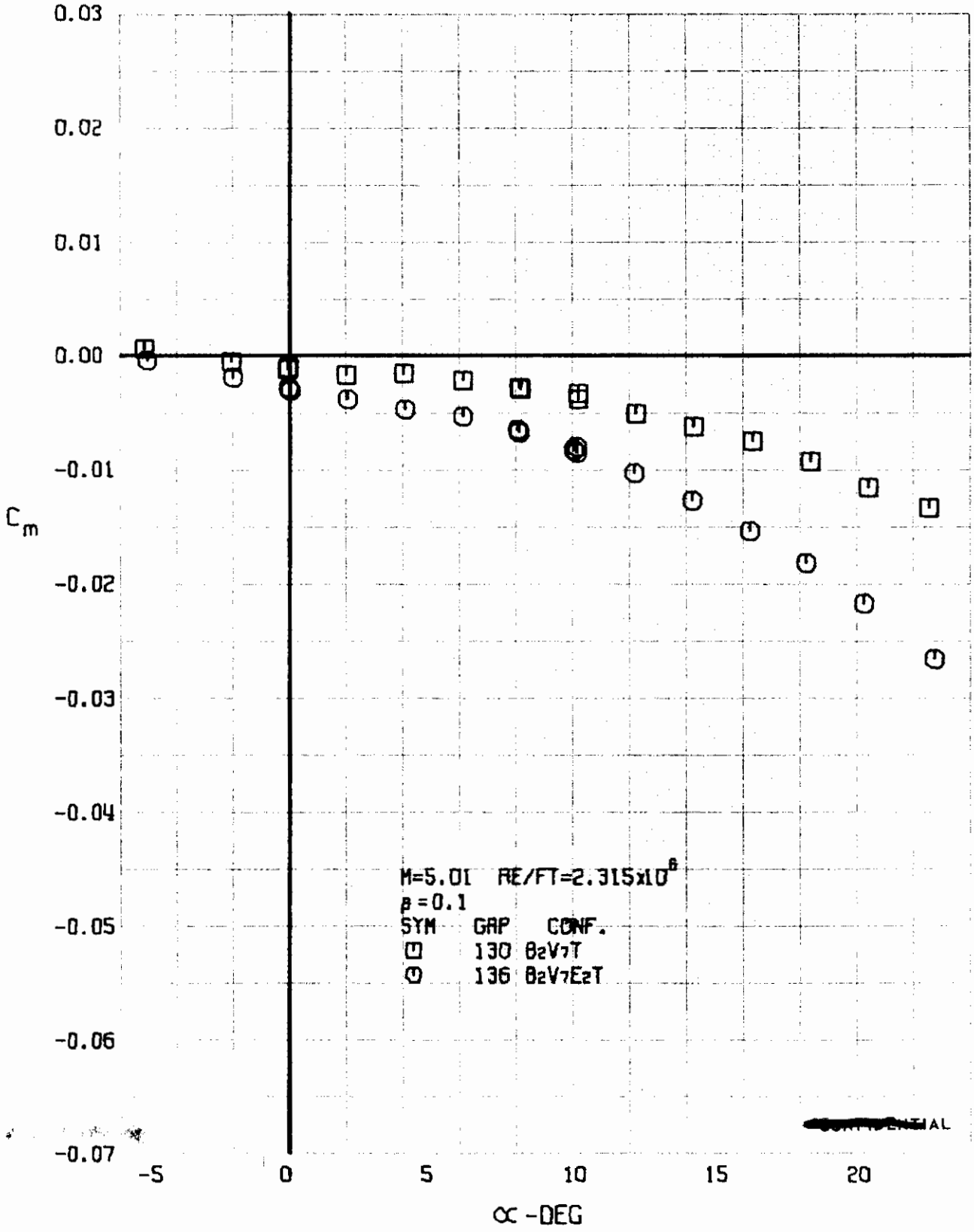

FIGURE 189 (U) CONFIGURATION BUILDUP
- PITCHING MOMENT COEFFICIENT VARIATION WITH ANGLE OF ATTACK (M=5.01)

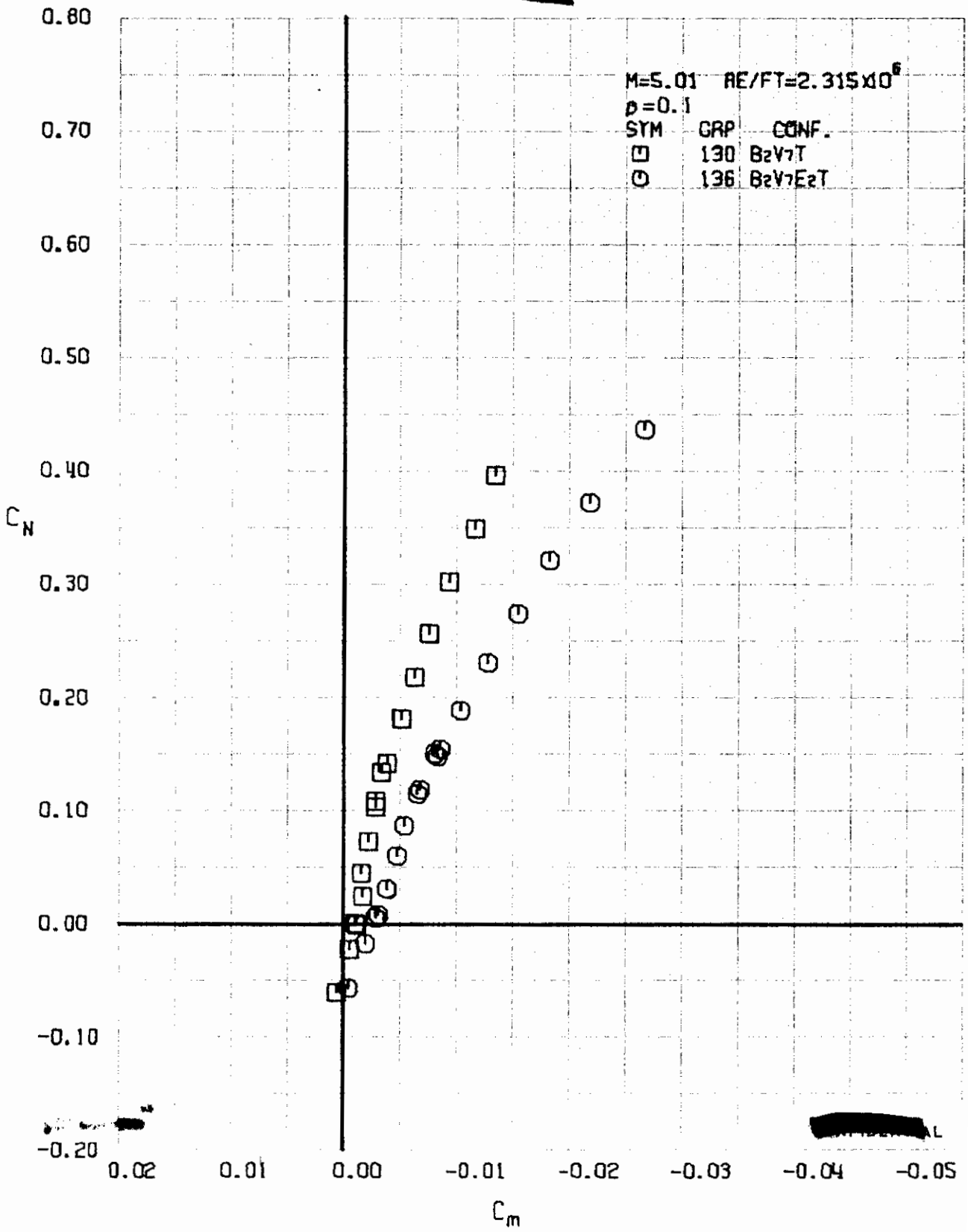

FIGURE 130 (U) CONFIGURATION BUILDUP
- LONGITUDINAL STABILITY VARIATION (M=5.01)

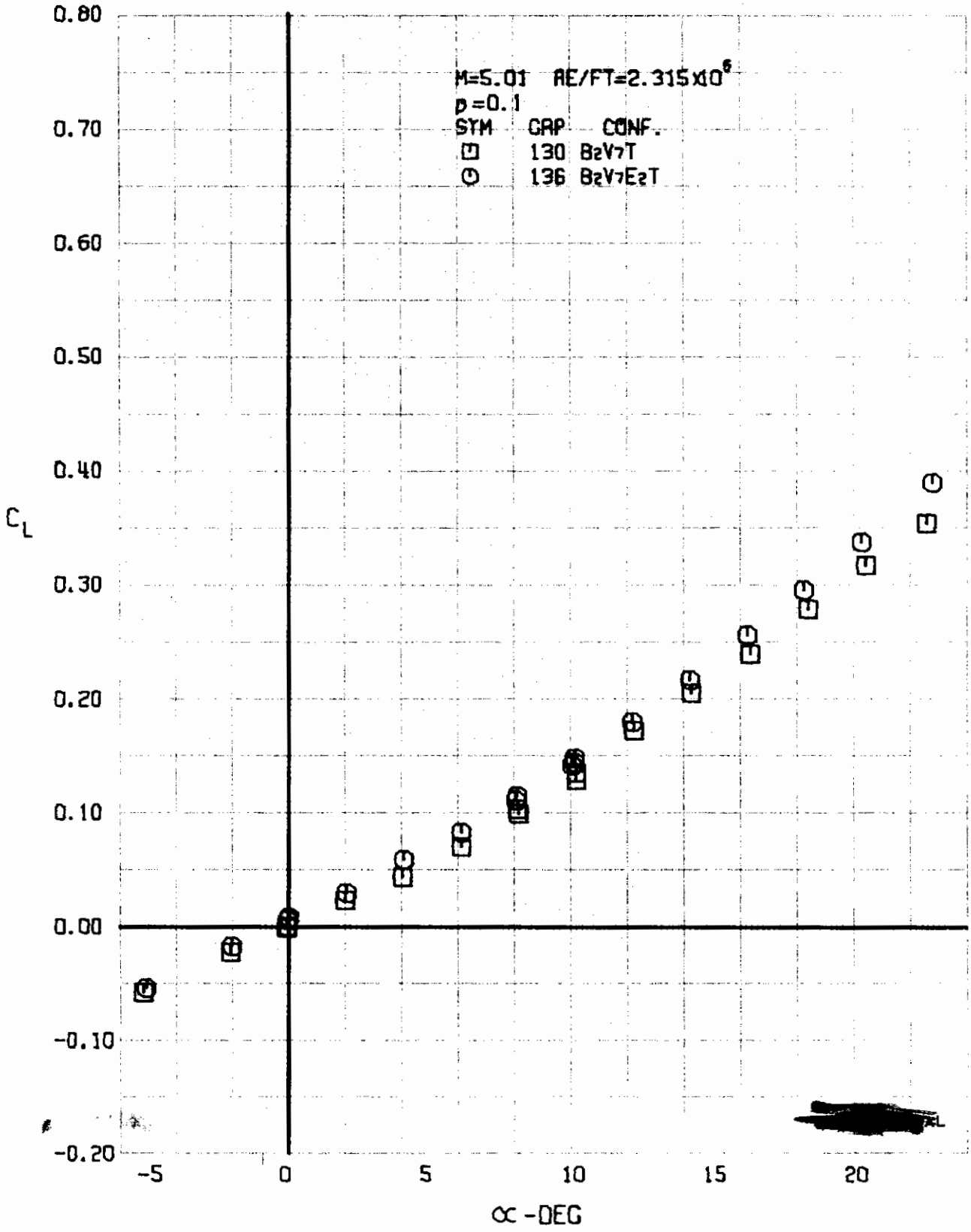

FIGURE 191 (U) CONFIGURATION BUILDUP
- LIFT COEFFICIENT VARIATION WITH ANGLE OF ATTACK (M=5.01)

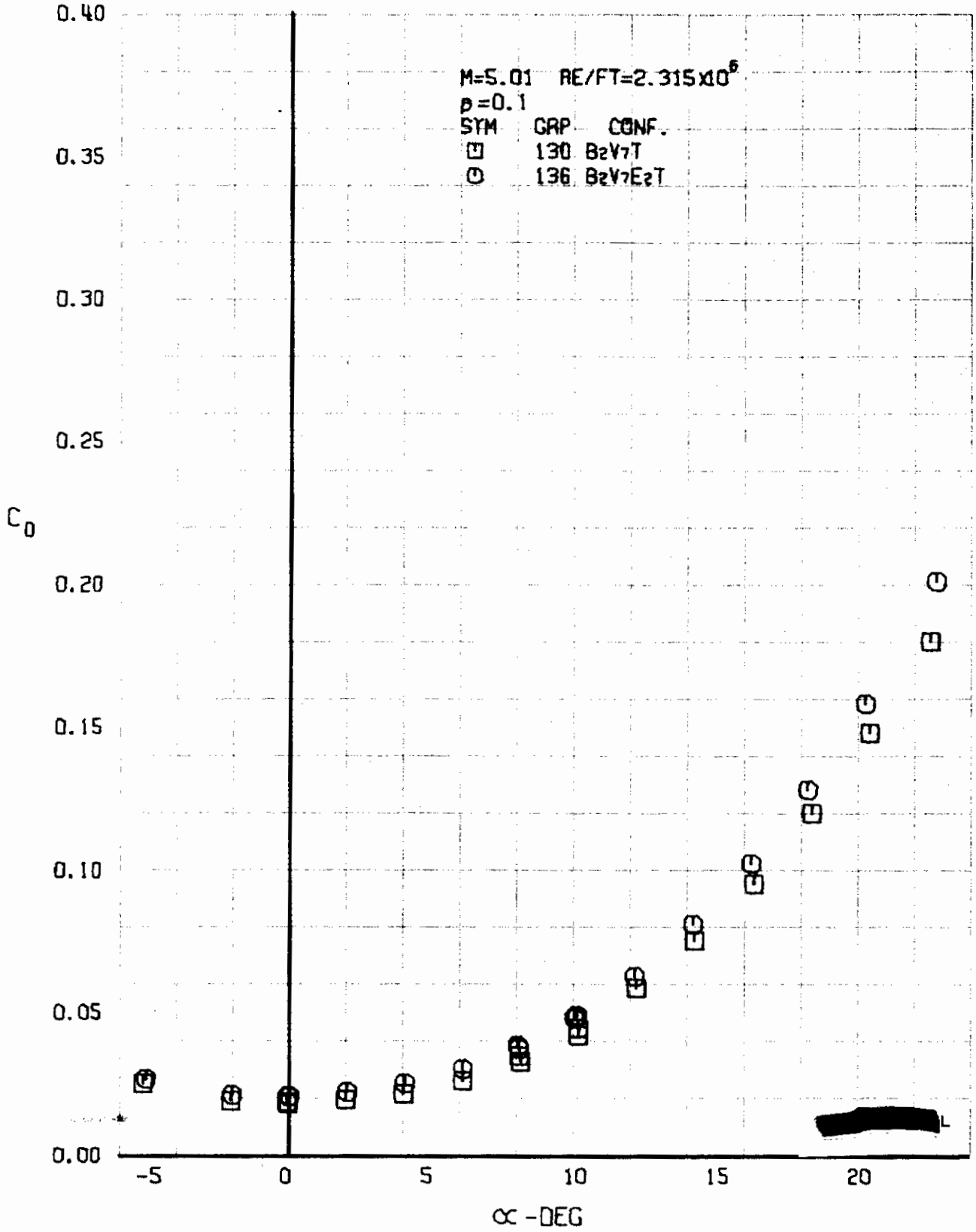

FIGURE 192 (U) CONFIGURATION BUILDUP
- DRAG COEFFICIENT VARIATION WITH ANGLE OF ATTACK (M=5.01)

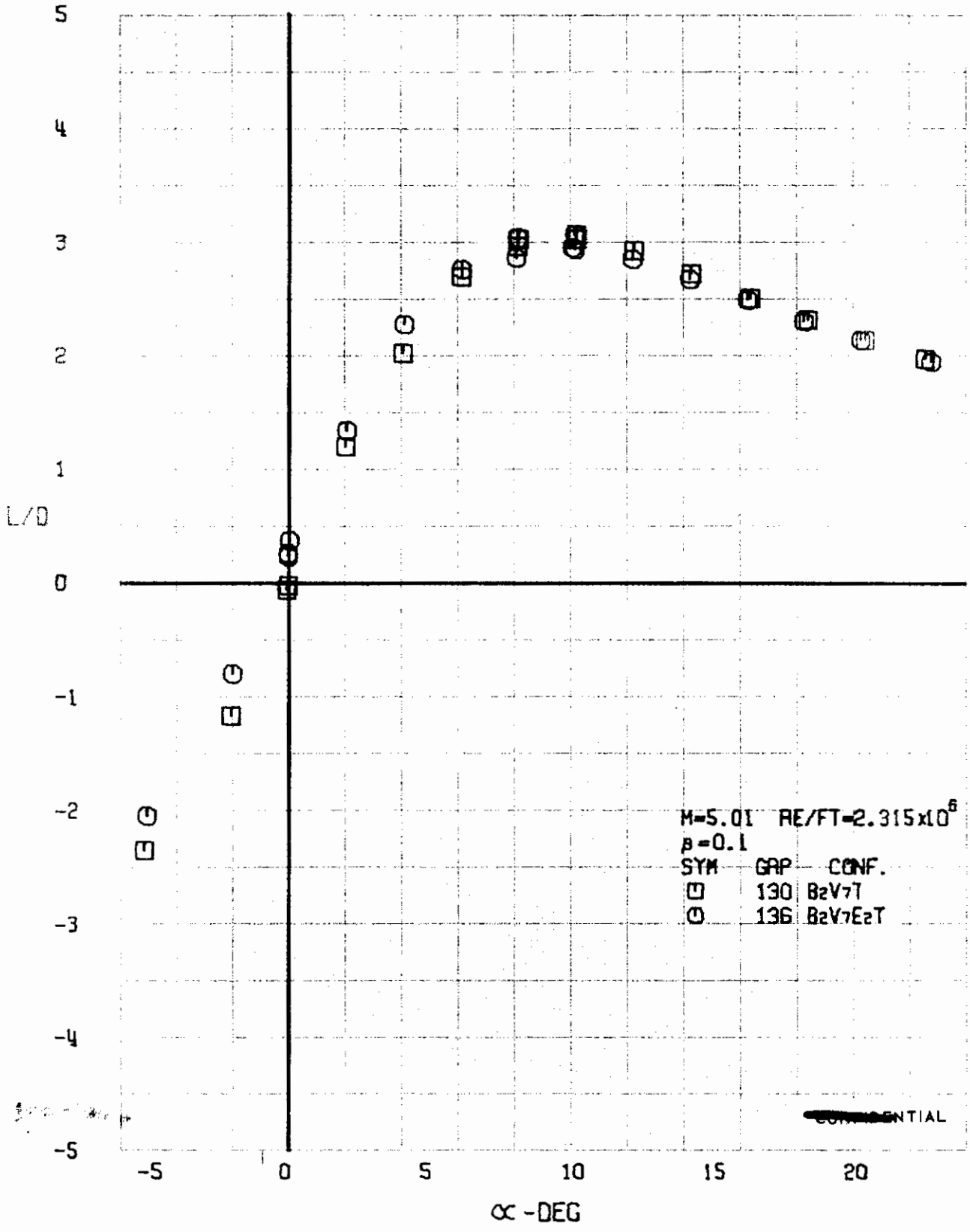

FIGURE 193 (U) CONFIGURATION BUILDUP
- LIFT-DRAG RATIO VARIATION WITH ANGLE OF ATTACK (M=5.01)

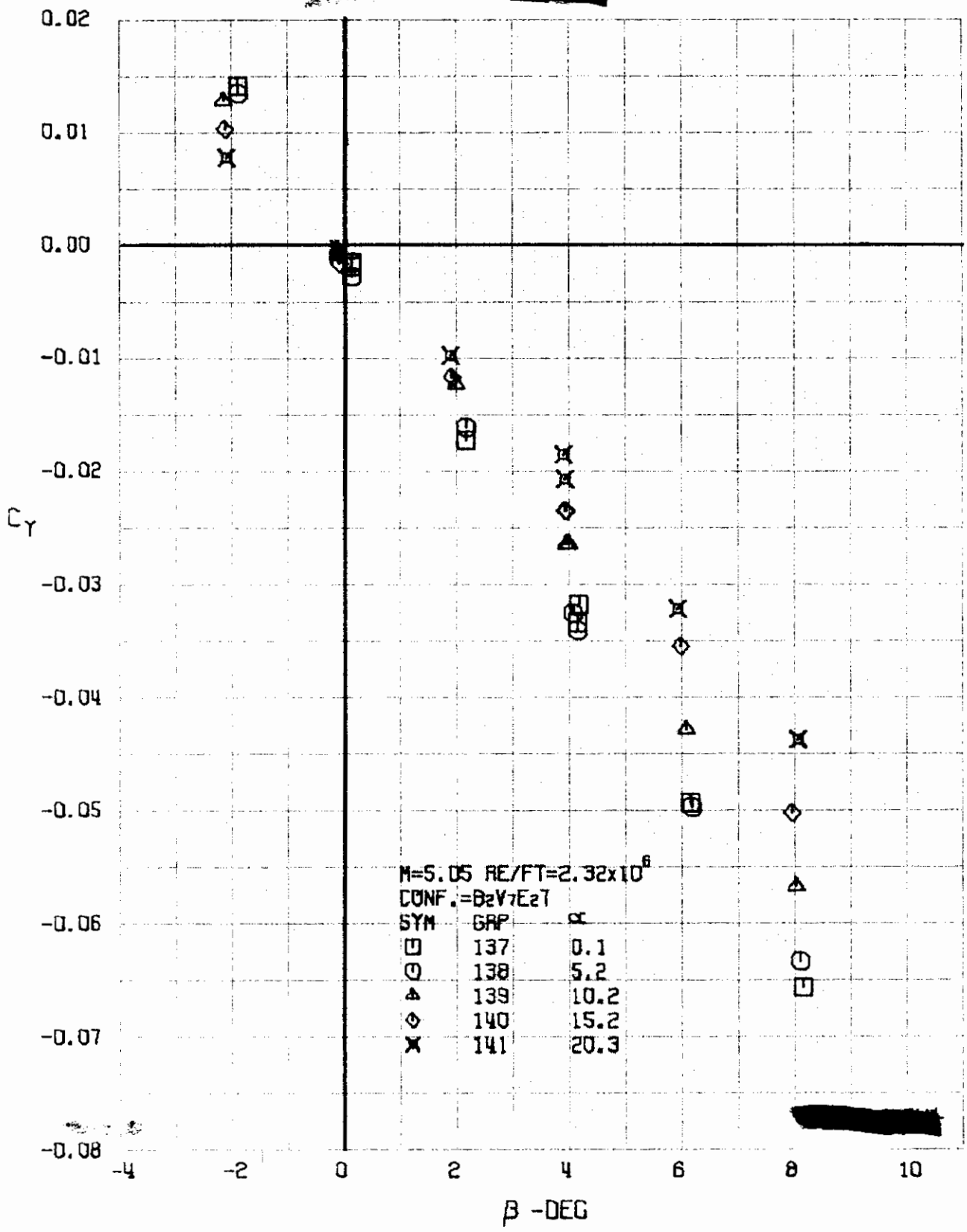

FIGURE 194 (U) COMPLETE CONFIGURATION
- SIDE FORCE COEFFICIENT VARIATION WITH ANGLE OF YAW (M=5.05)

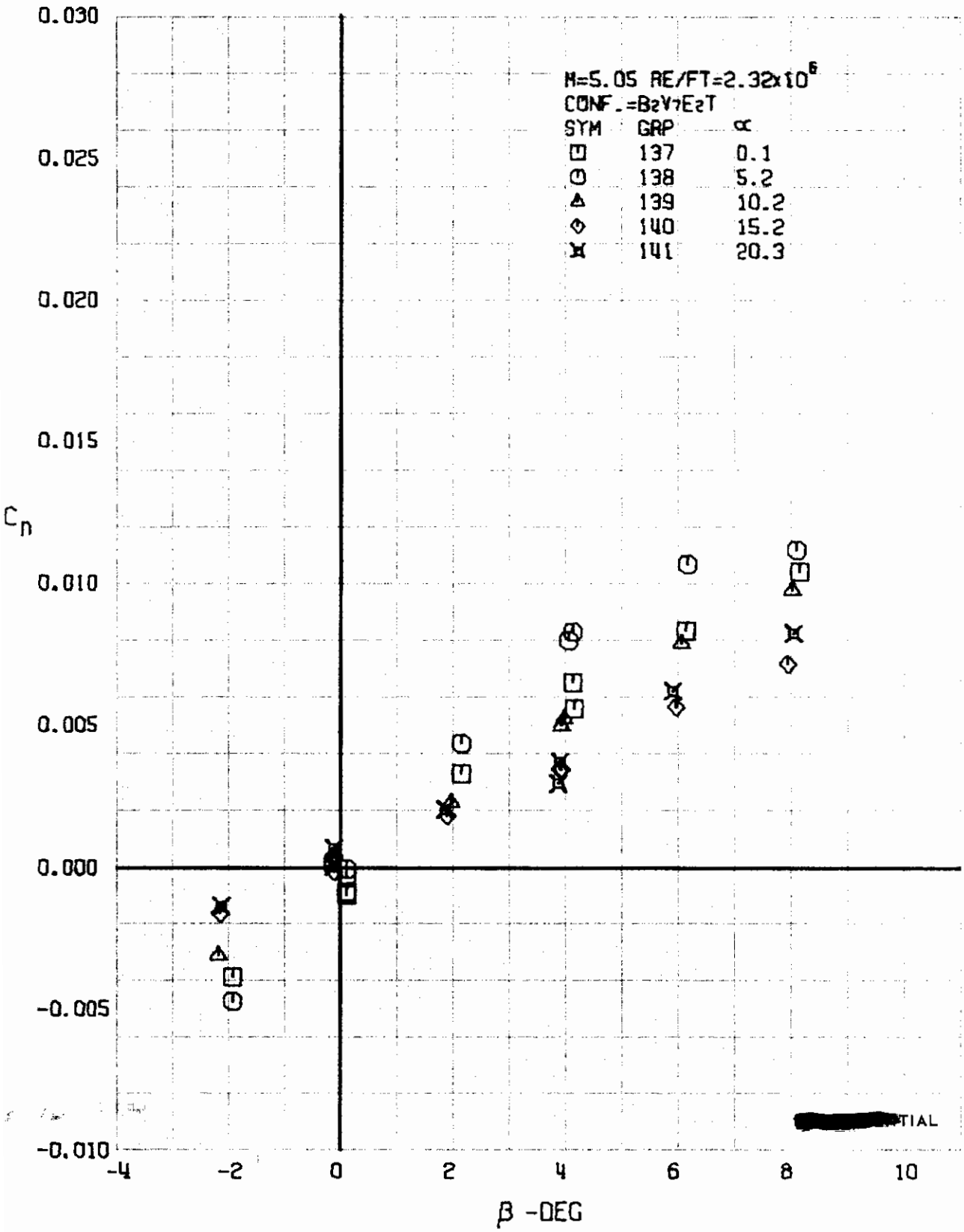

FIGURE 195 (U) COMPLETE CONFIGURATION
- YAWING MOMENT COEFFICIENT VARIATION WITH ANGLE OF YAW (M=5.05)

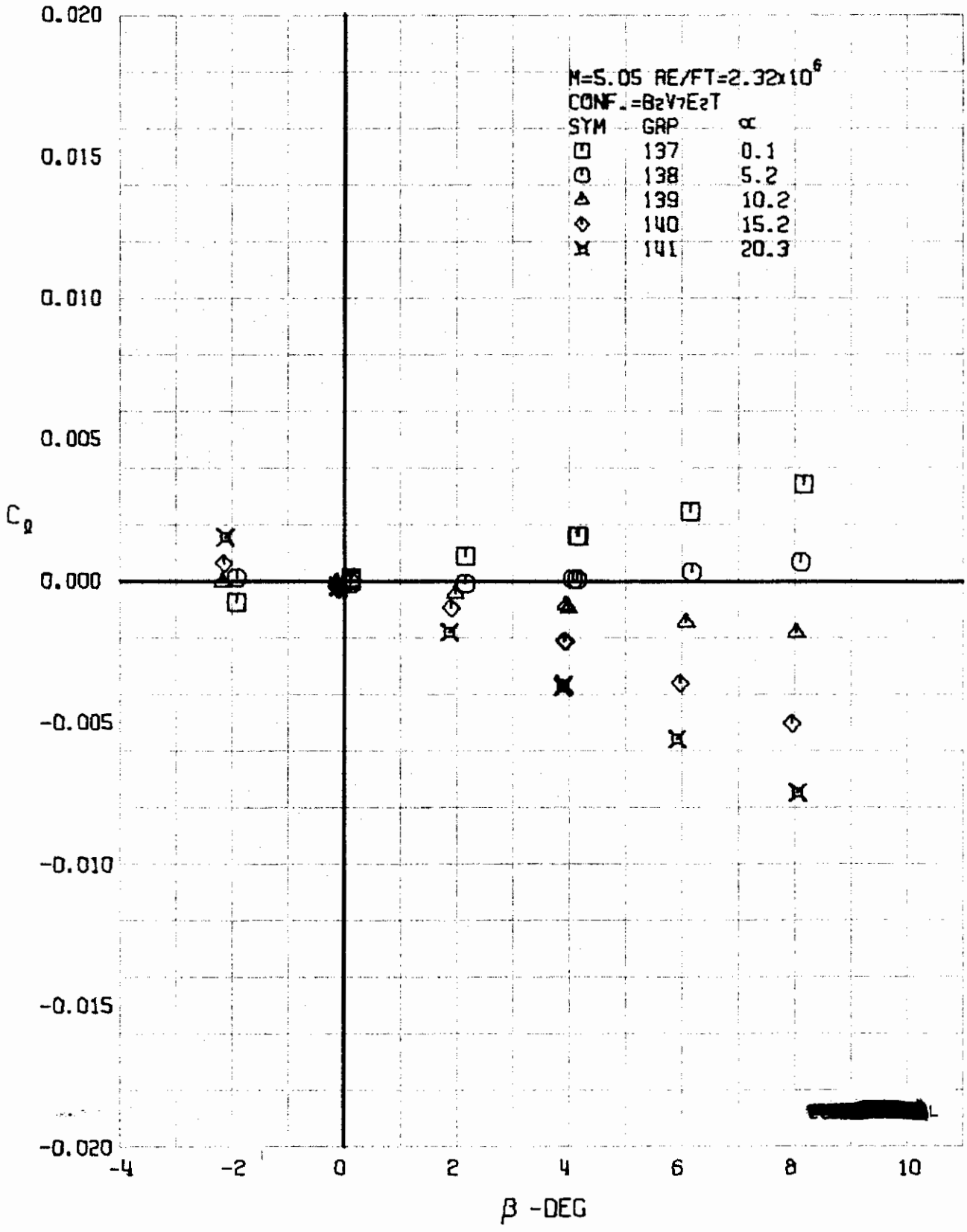

FIGURE 196 (U) COMPLETE CONFIGURATION
- ROLLING MOMENT COEFFICIENT VARIATION WITH ANGLE OF YAW (M=5.05)

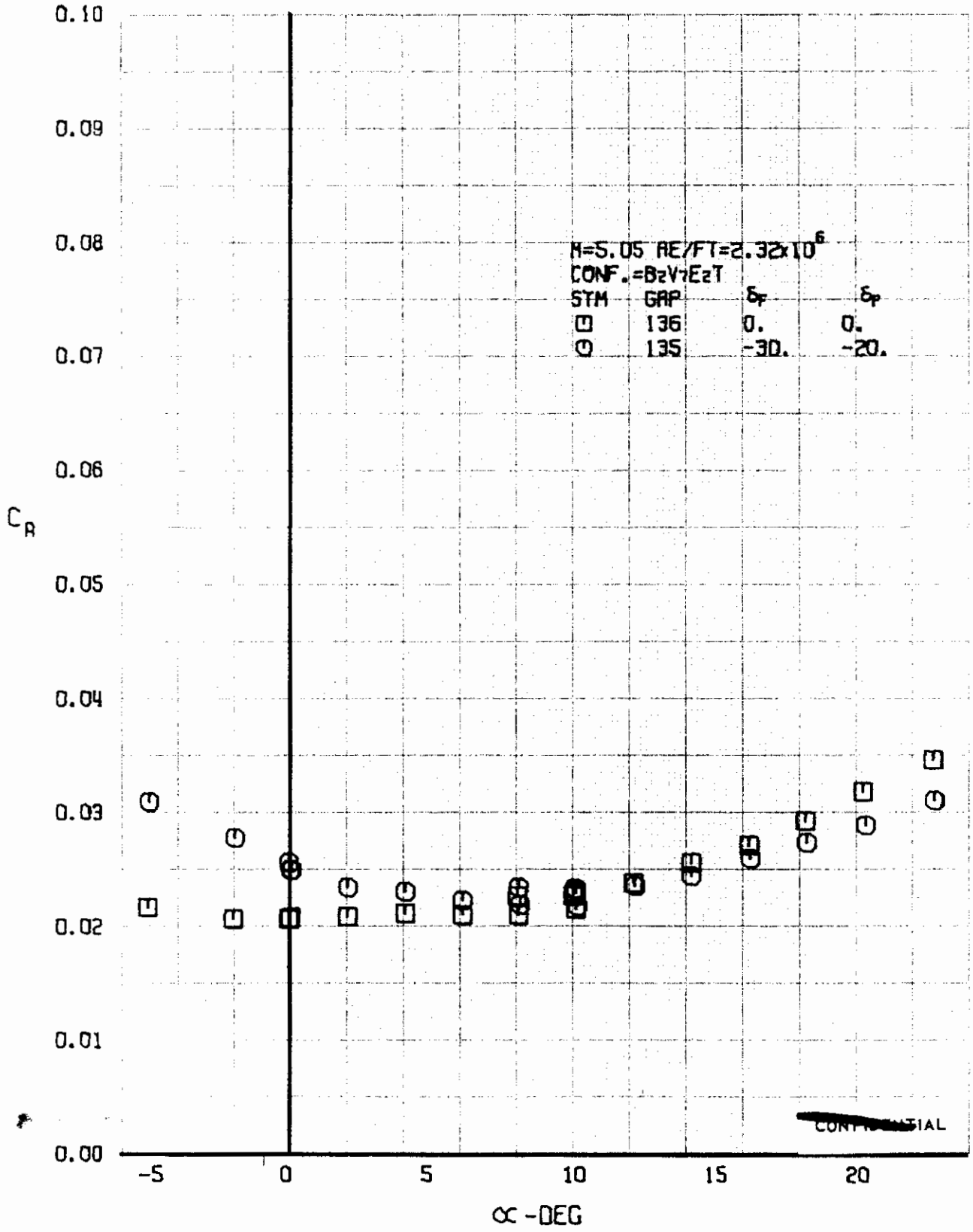

FIGURE 197 (U) COMBINED ELEVON AND FLAP EFFECTS - AXIAL FORCE COEFFICIENT VARIATION WITH ANGLE OF ATTACK (M=5.05)

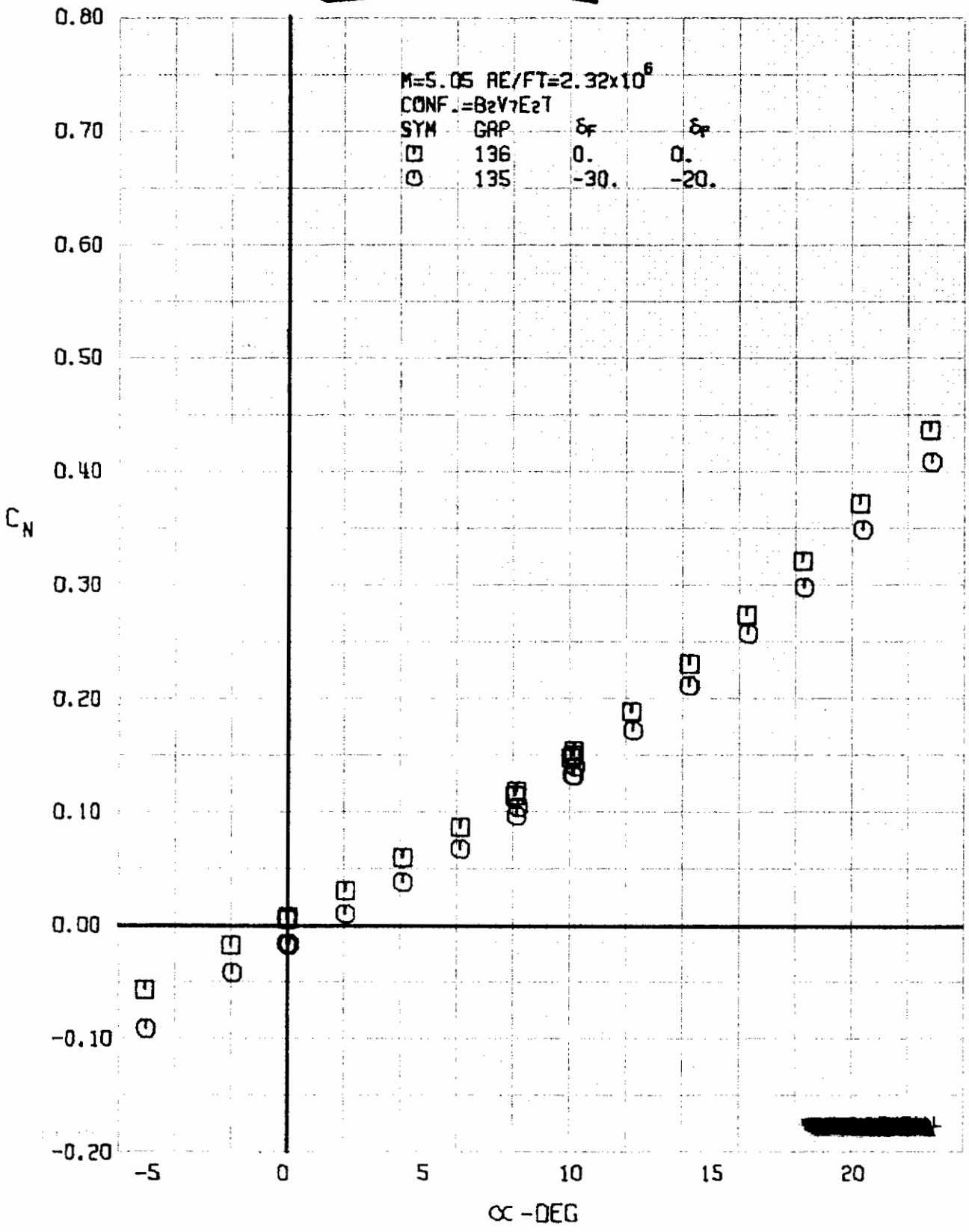

FIGURE 198 (U) COMBINED ELEVON AND FLAP EFFECTS - NORMAL FORCE COEFFICIENT VARIATION WITH ANGLE OF ATTACK (M=5.05)

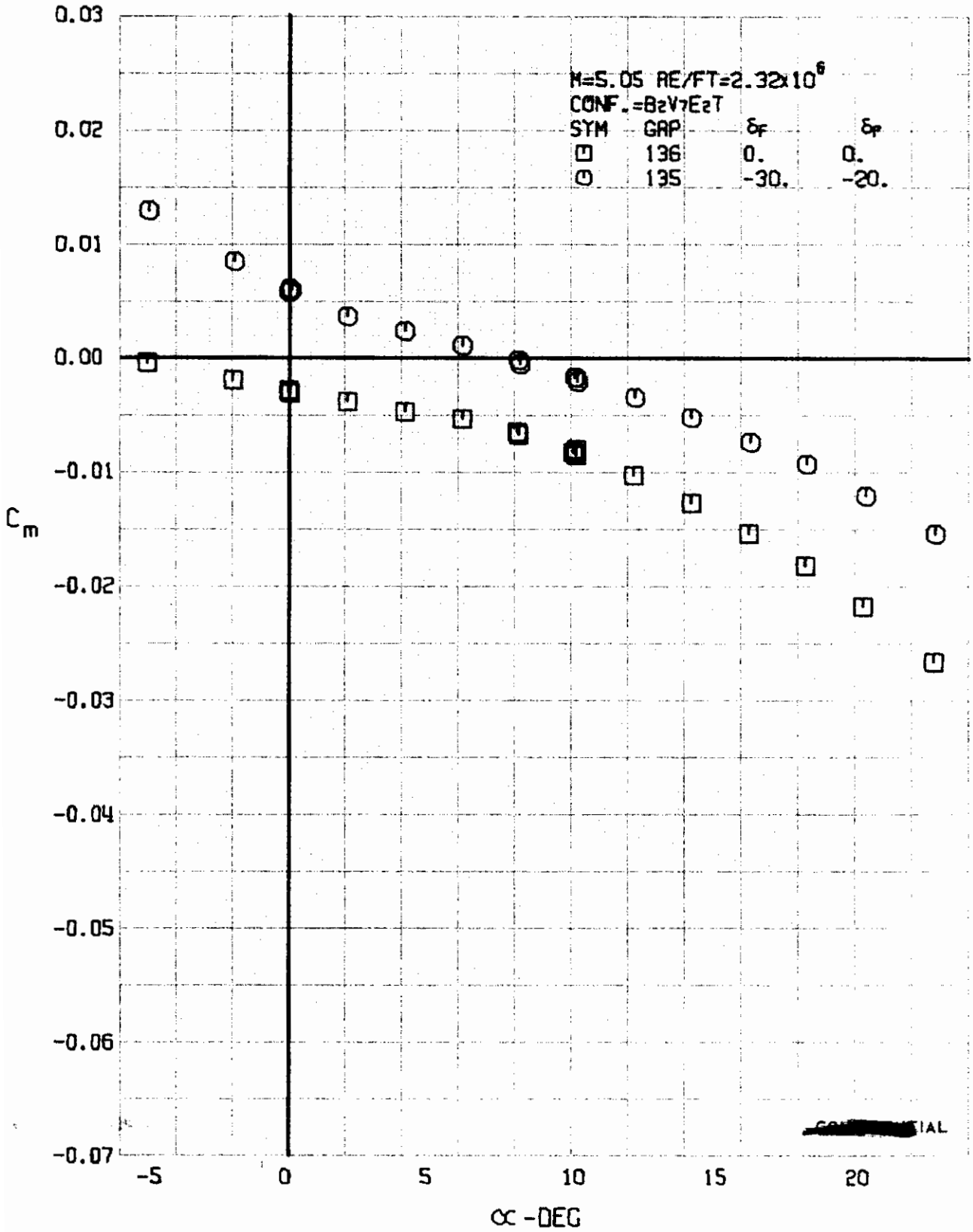

FIGURE 199 (U) COMBINED ELEVON AND FLAP EFFECTS - PITCHING MOMENT COEFFICIENT VARIATION WITH ANGLE OF ATTACK (M=5.05)

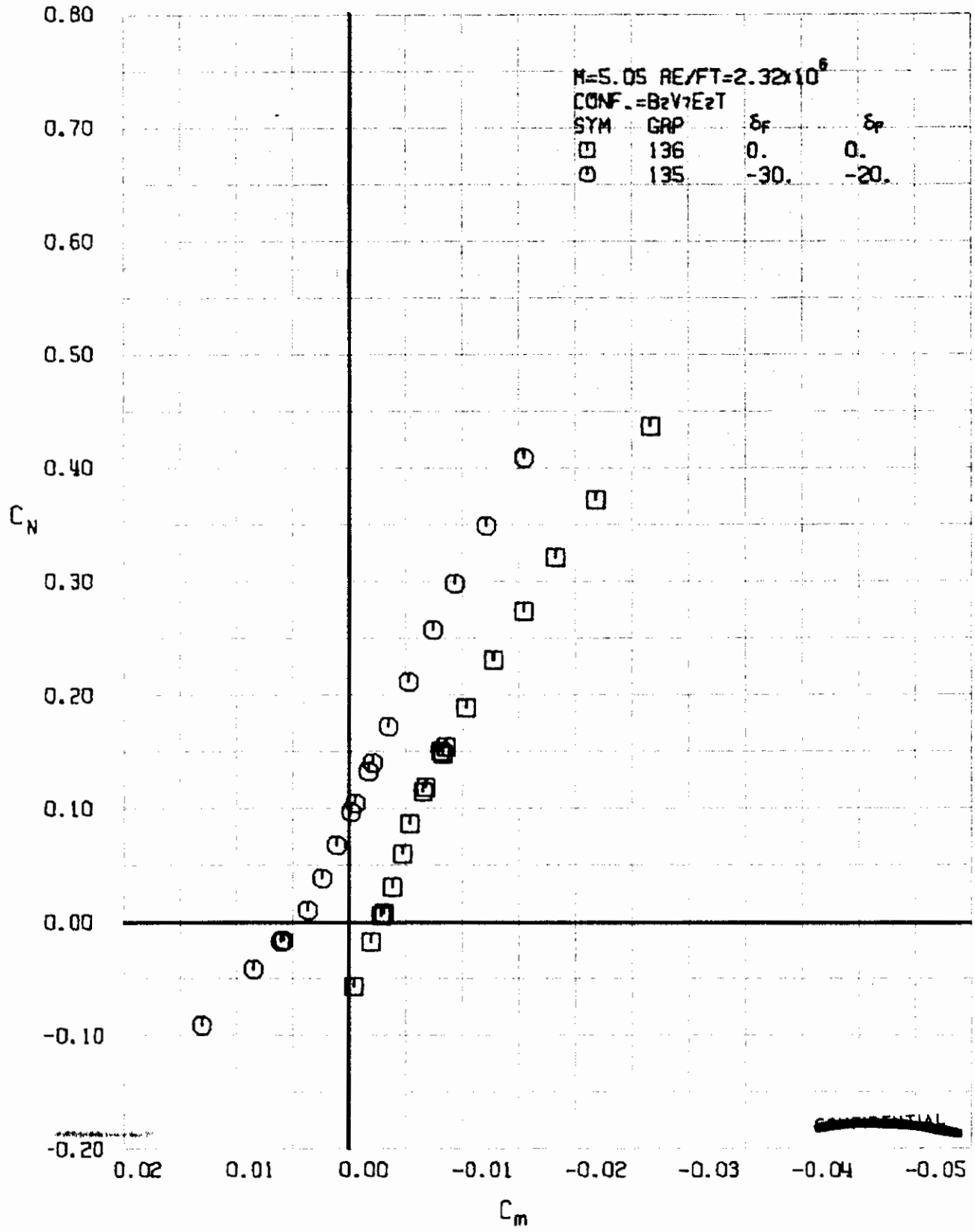

FIGURE 200 (U) COMBINED ELEVON AND FLAP EFFECTS - LONGITUDINAL STABILITY VARIATION (M=5.05)

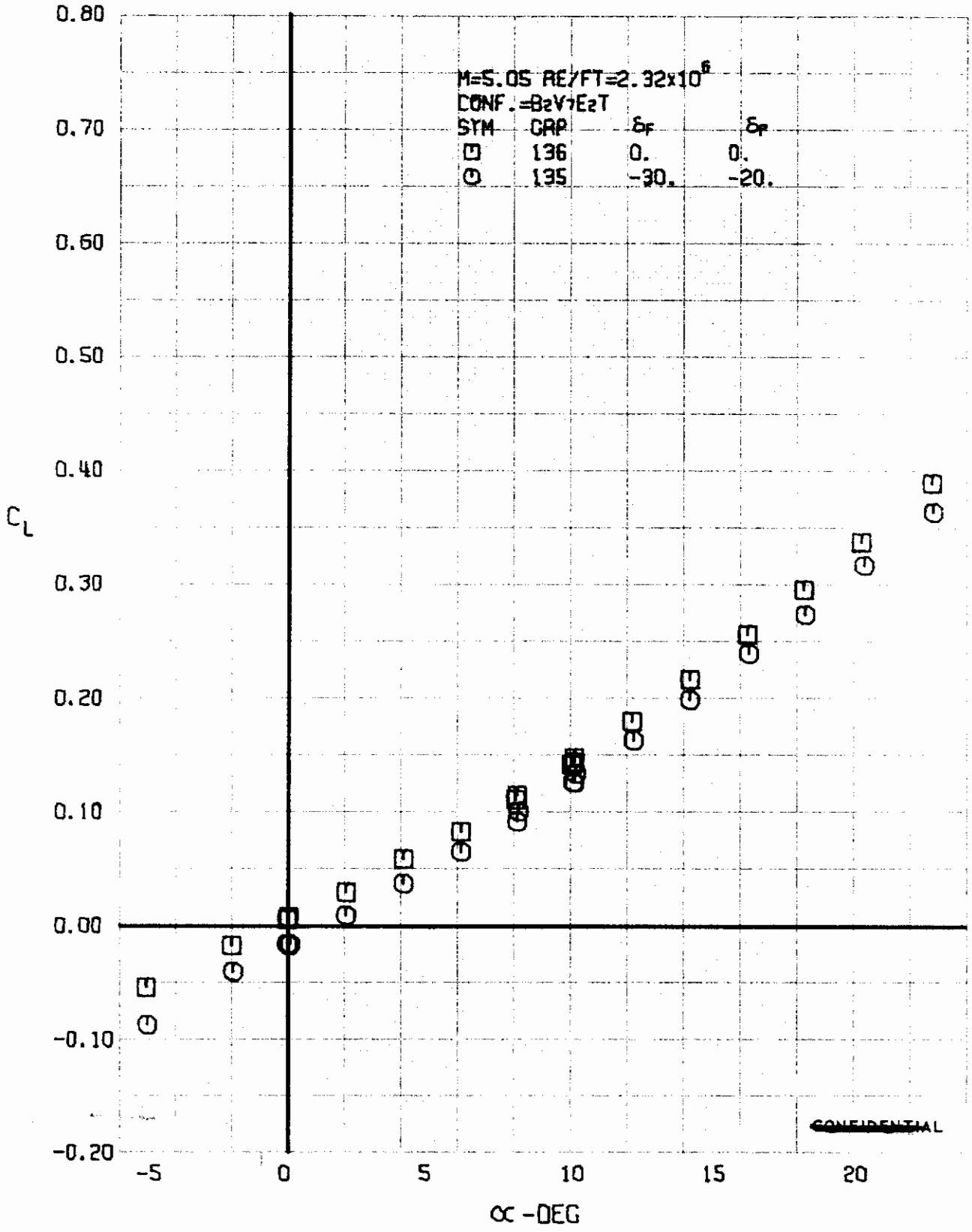

FIGURE 201 (U) COMBINED ELEVON AND FLAP EFFECTS - LIFT COEFFICIENT VARIATION WITH ANGLE OF ATTACK (M=5.05)

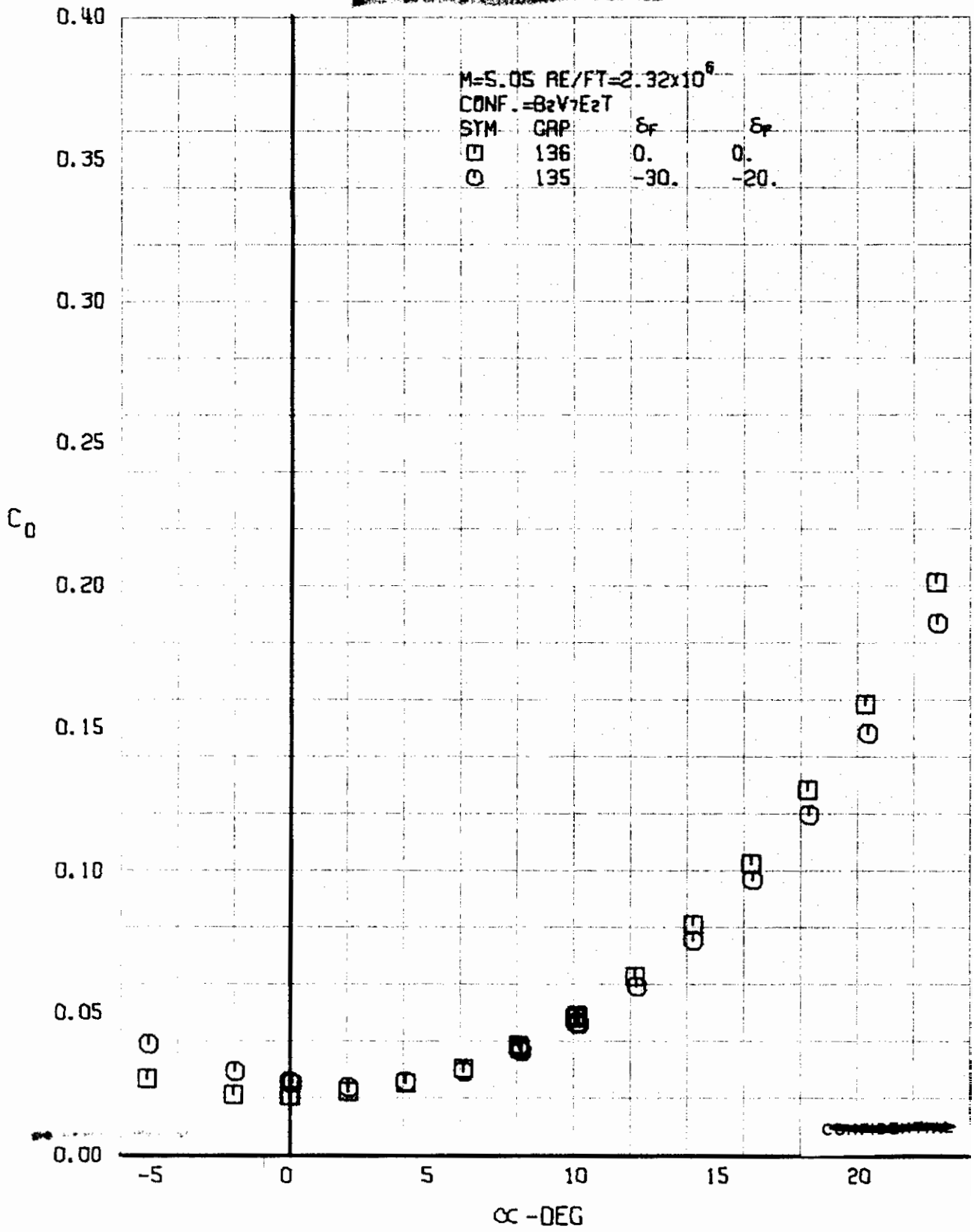

FIGURE 202 (U) COMBINED ELEVON AND FLAP EFFECTS - DRAG COEFFICIENT VARIATION WITH ANGLE OF ATTACK (M=5.05)

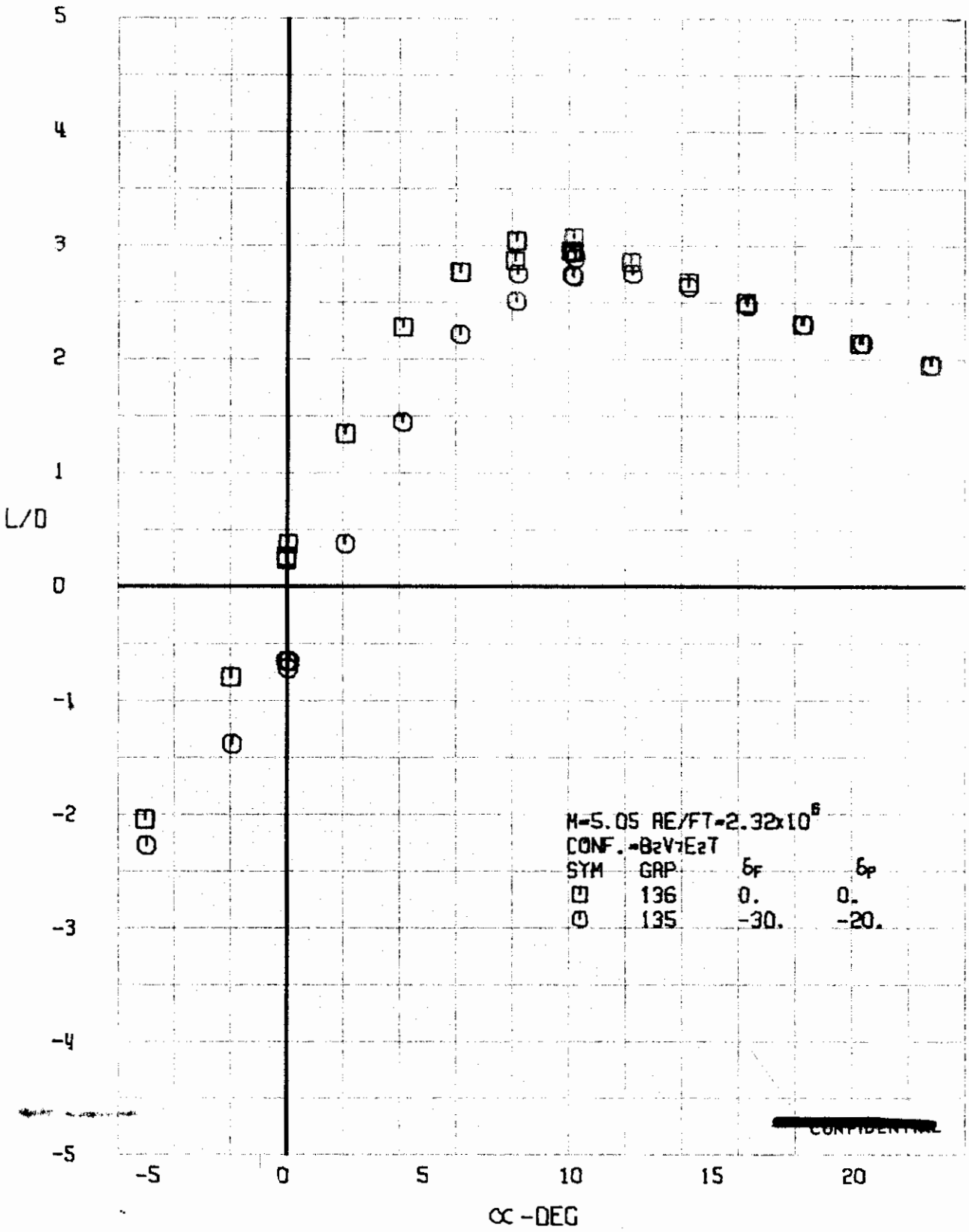

FIGURE 203 (U) COMBINED ELEVON AND FLAP EFFECTS - LIFT-DRAG RATIO VARIATION WITH ANGLE OF ATTACK (M=5.05)

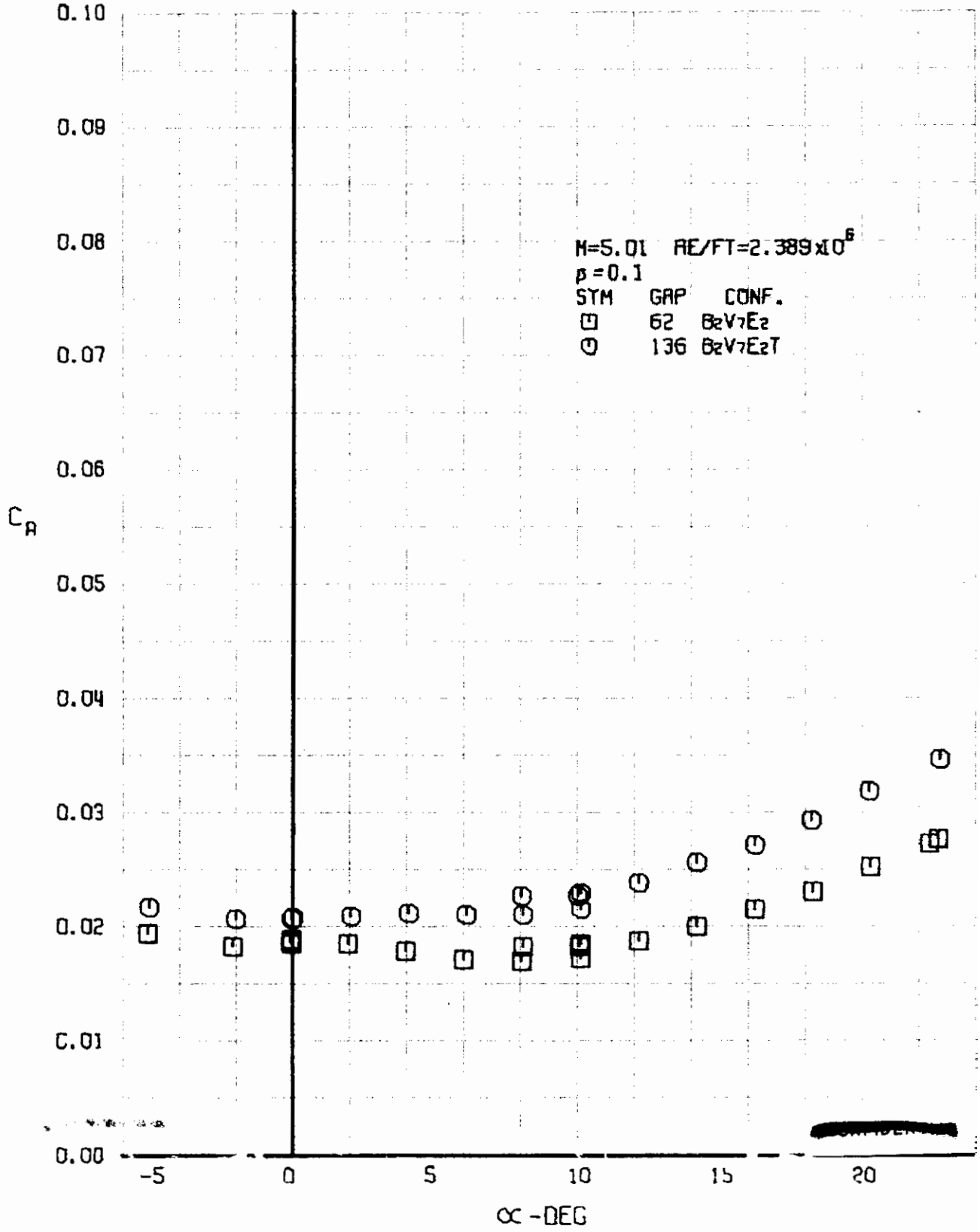

FIGURE 204 (U) FORCED TRANSITION EFFECTS
- AXIAL FORCE COEFFICIENT VARIATION WITH ANGLE OF ATTACK (M=5.01)

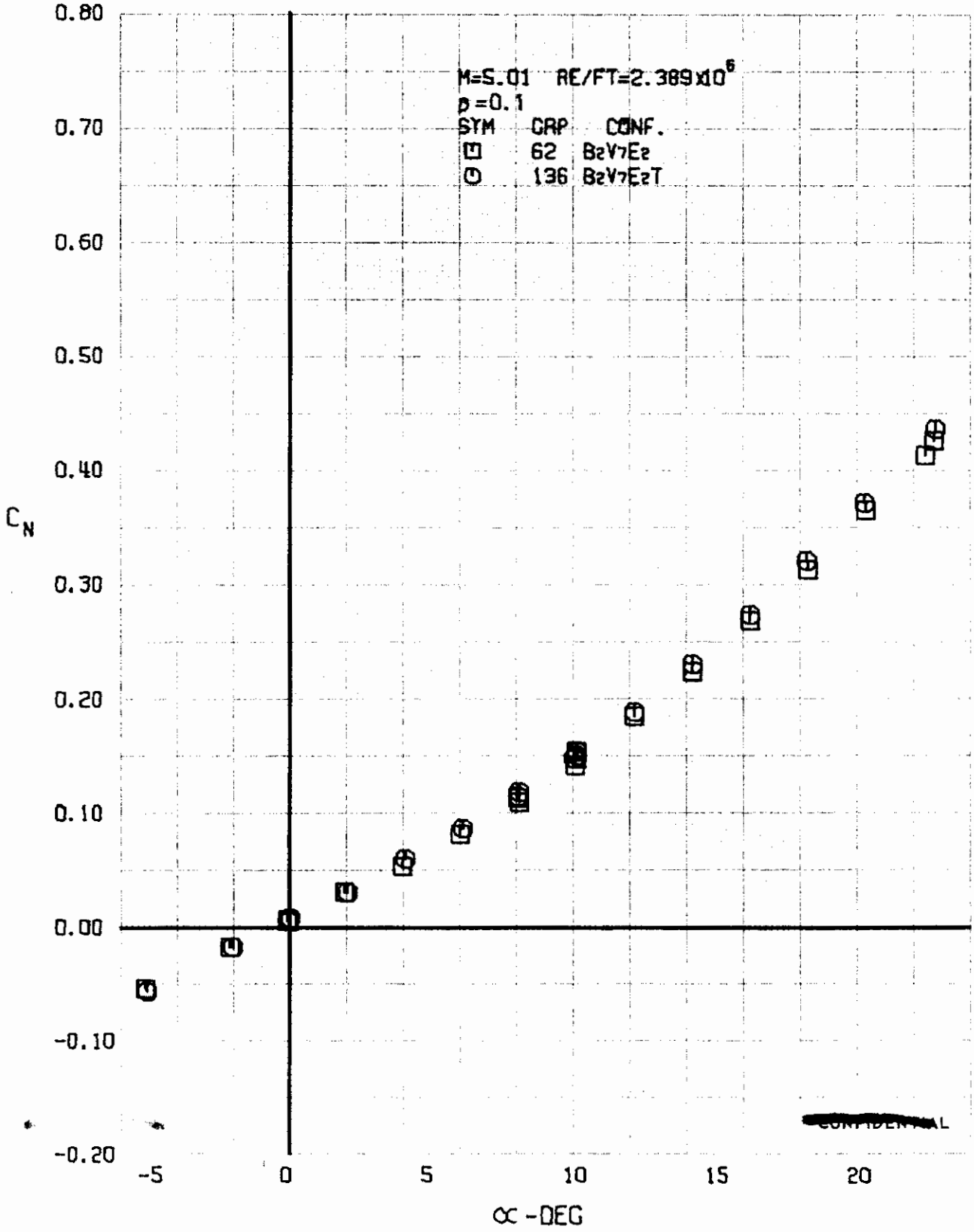

FIGURE 205 (U) FORCED TRANSITION EFFECTS
- NORMAL FORCE COEFFICIENT VARIATION WITH ANGLE OF ATTACK (M=5.01)

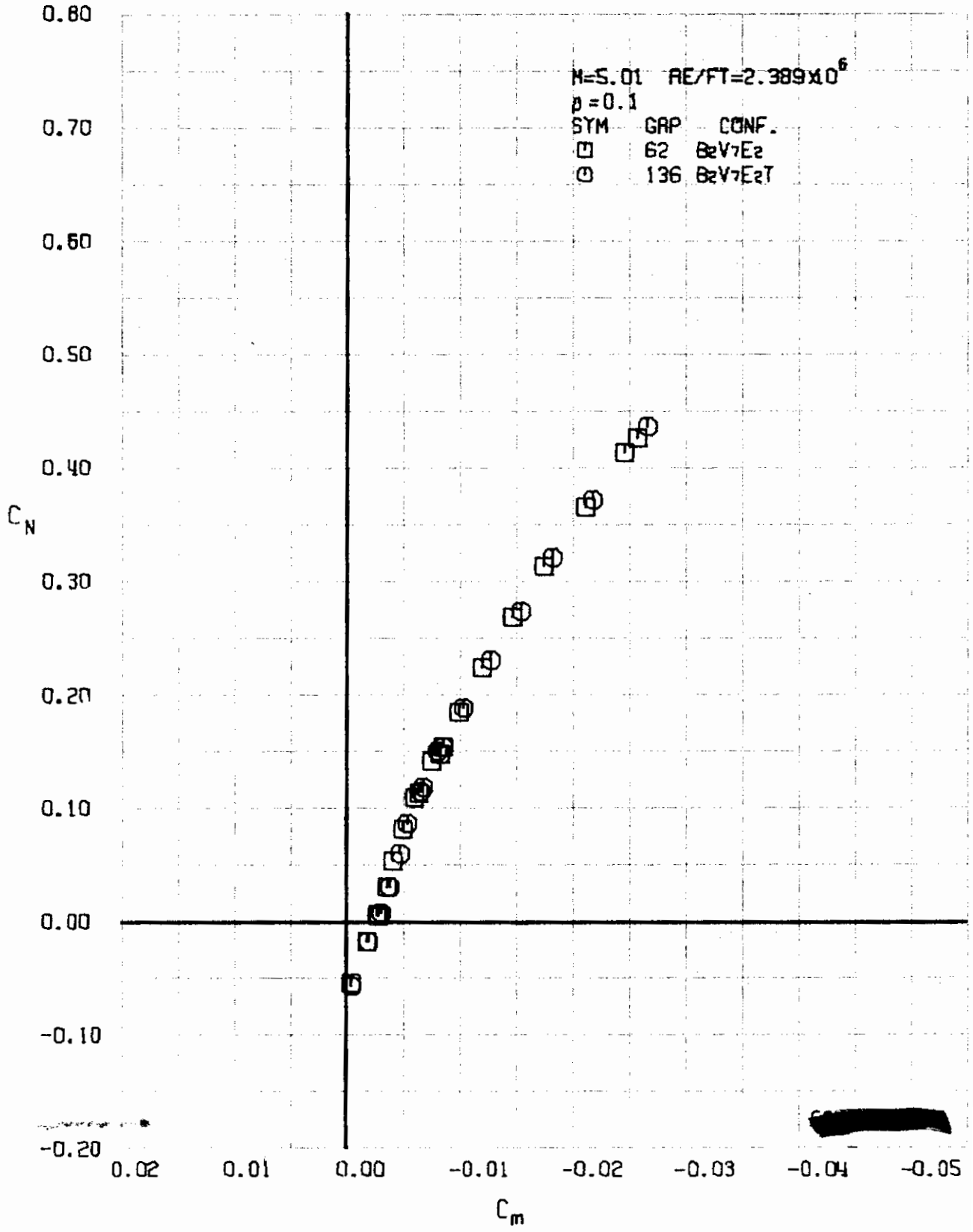

FIGURE 206 (U) FORCED TRANSITION EFFECTS
- LONGITUDINAL STABILITY VARIATION (M=5.01)

~~CONFIDENTIAL~~

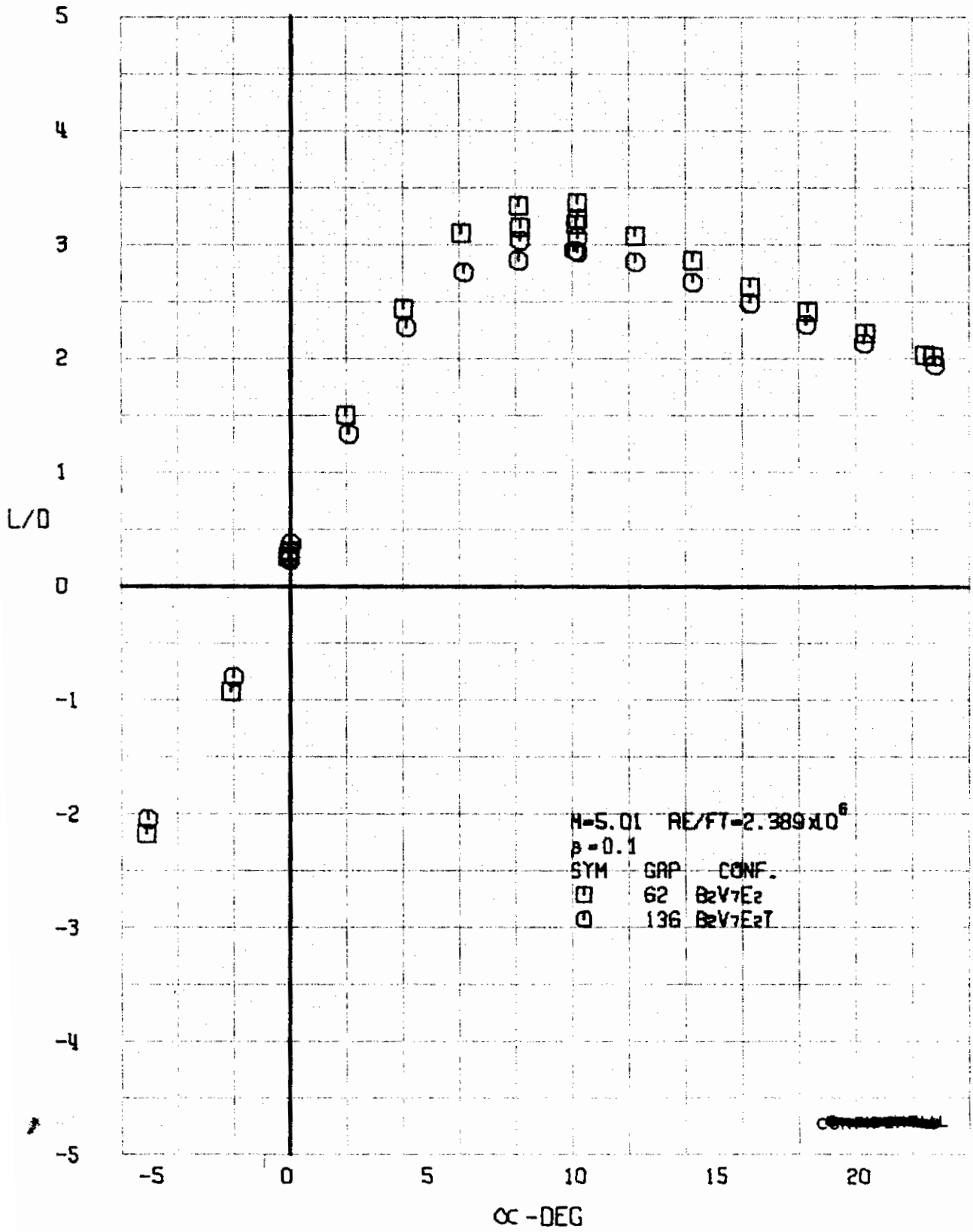

FIGURE 207 (U) FORCED TRANSITION EFFECTS
- LIFT-DRAG RATIO VARIATION WITH ANGLE OF ATTACK (M=5.01)

~~CONFIDENTIAL~~

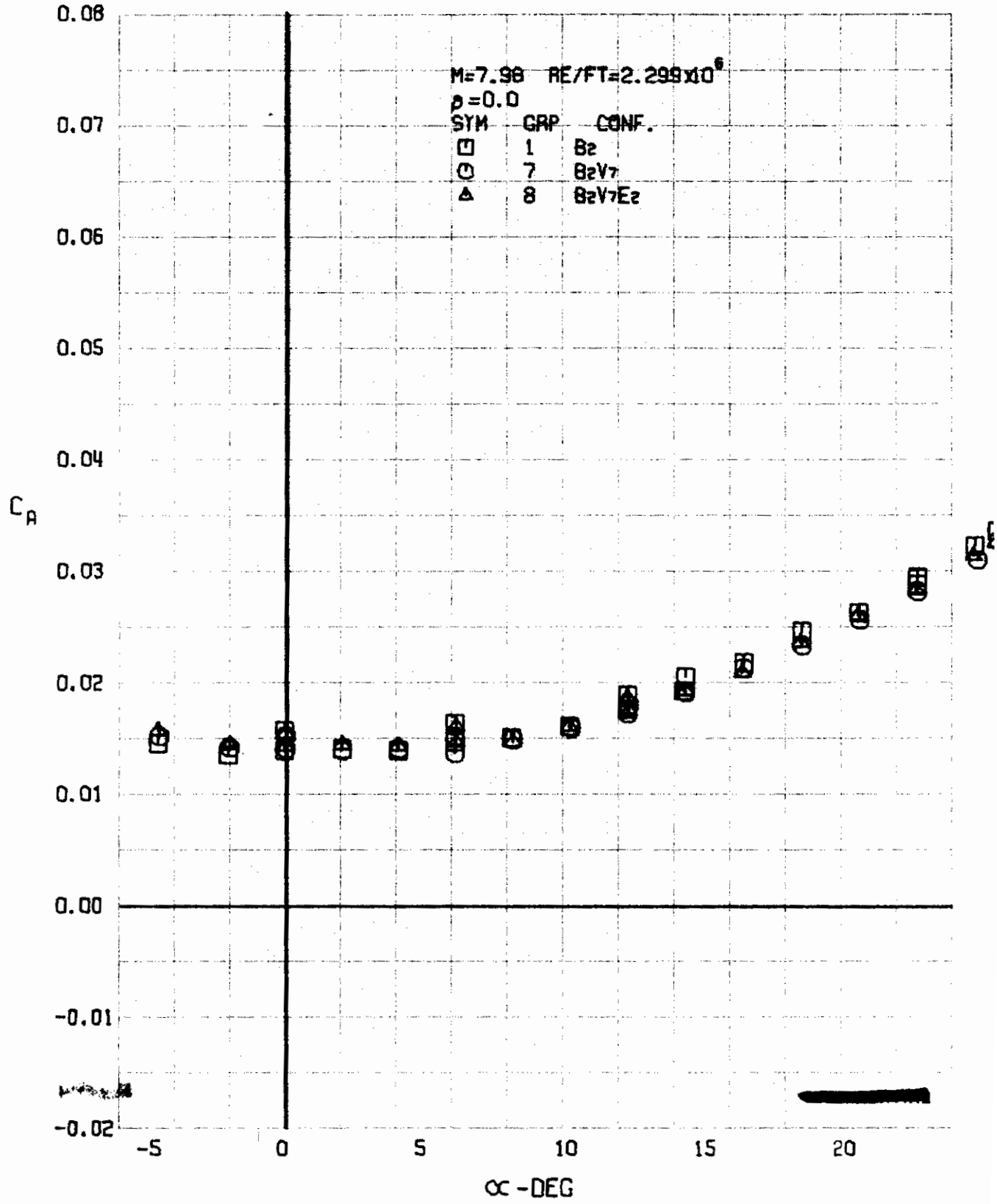

FIGURE 208 (U) CONFIGURATION BUILDUP
- AXIAL FORCE COEFFICIENT VARIATION WITH ANGLE OF ATTACK (M=7.98)

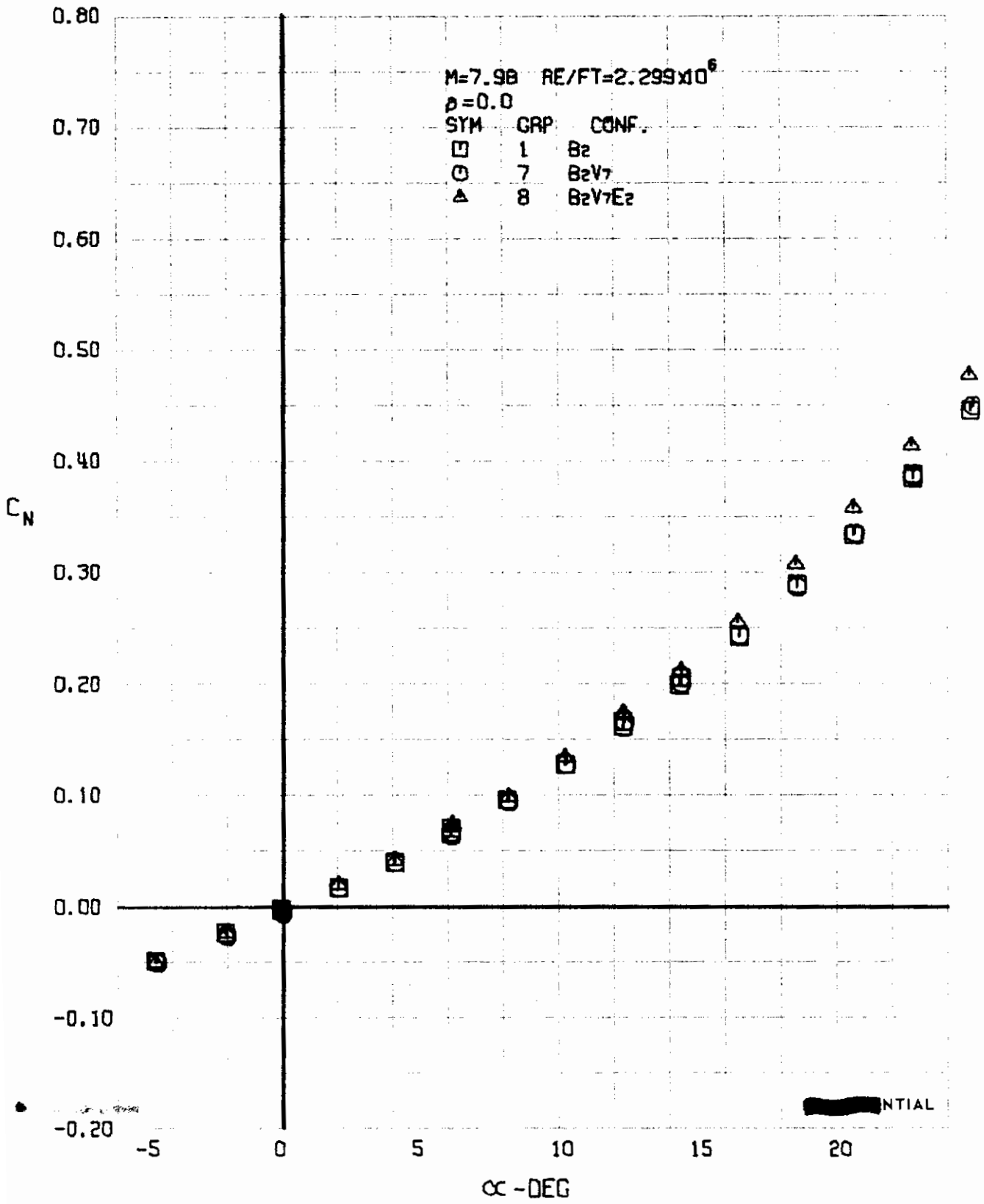

FIGURE 209 (U) CONFIGURATION BUILDUP
- NORMAL FORCE COEFFICIENT VARIATION WITH ANGLE OF ATTACK (M= 7.98)

[redacted]

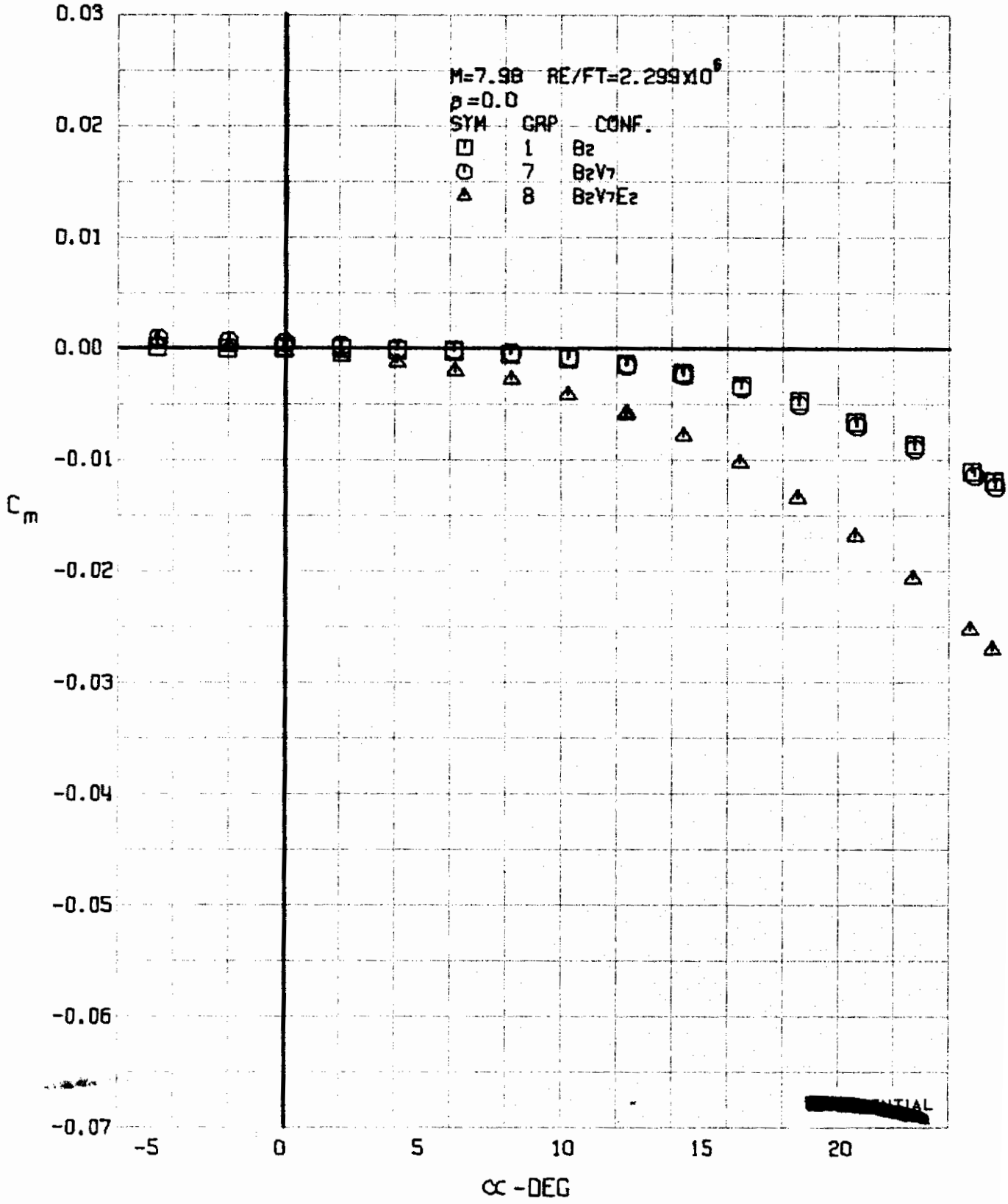

FIGURE 210 (U) CONFIGURATION BUILDUP
- PITCHING MOMENT COEFFICIENT VARIATION WITH ANGLE OF ATTACK (M=7.98)

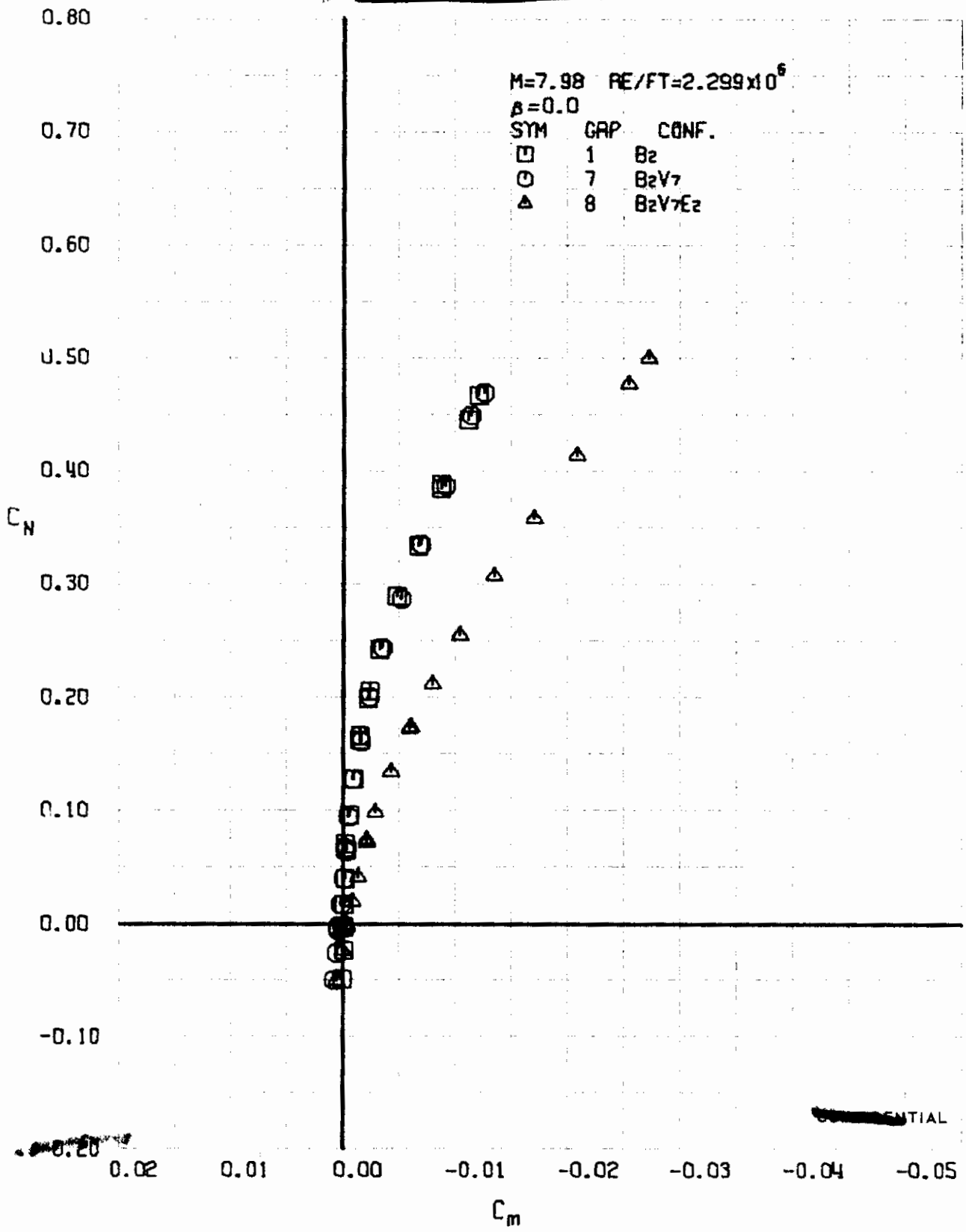

FIGURE 211 (U) CONFIGURATION BUILDUP
- LONGITUDINAL STABILITY VARIATION (M=7.98)

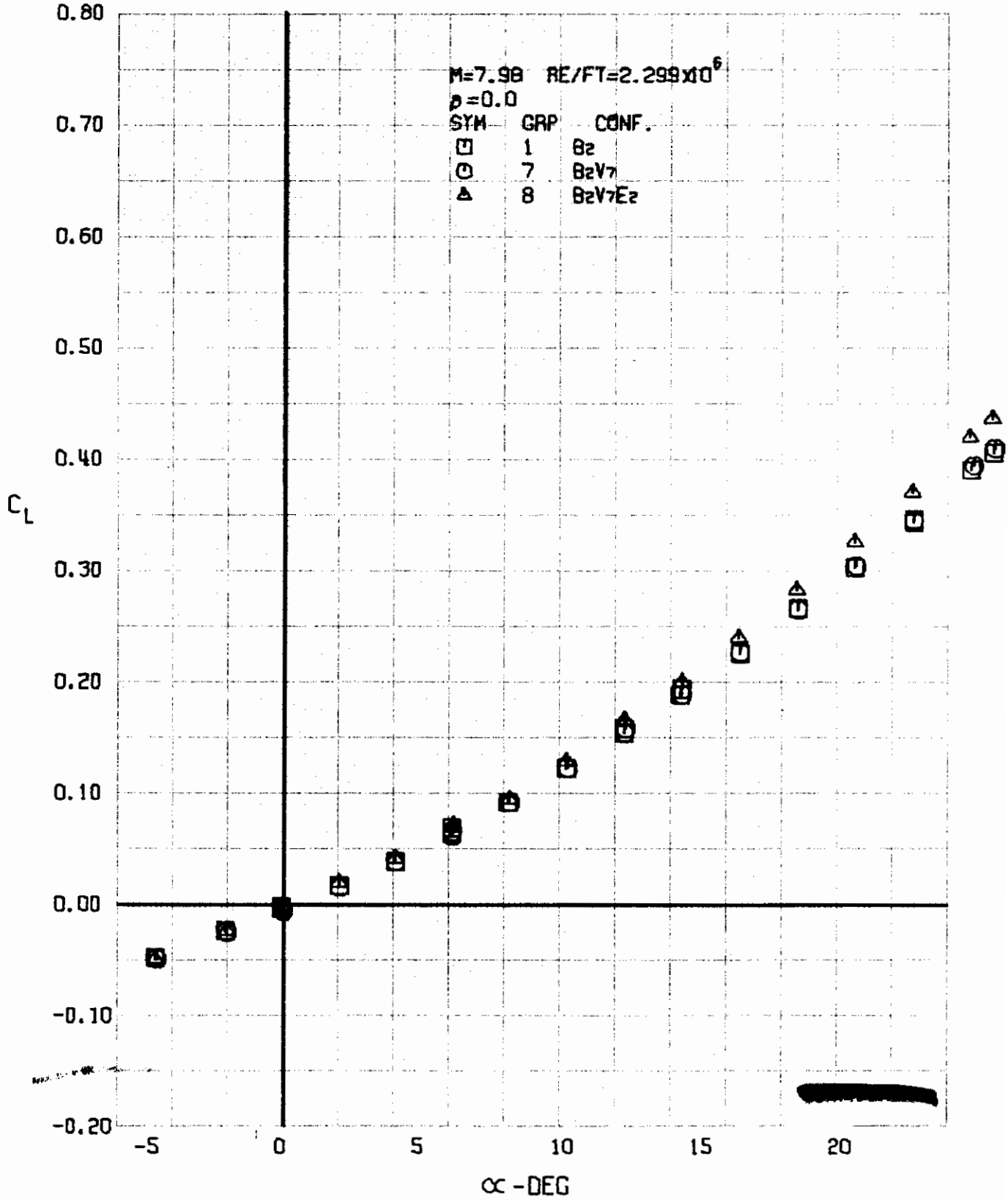

FIGURE 212 (U) CONFIGURATION BUILDUP
- LIFT COEFFICIENT VARIATION WITH ANGLE OF ATTACK (M=7.98)

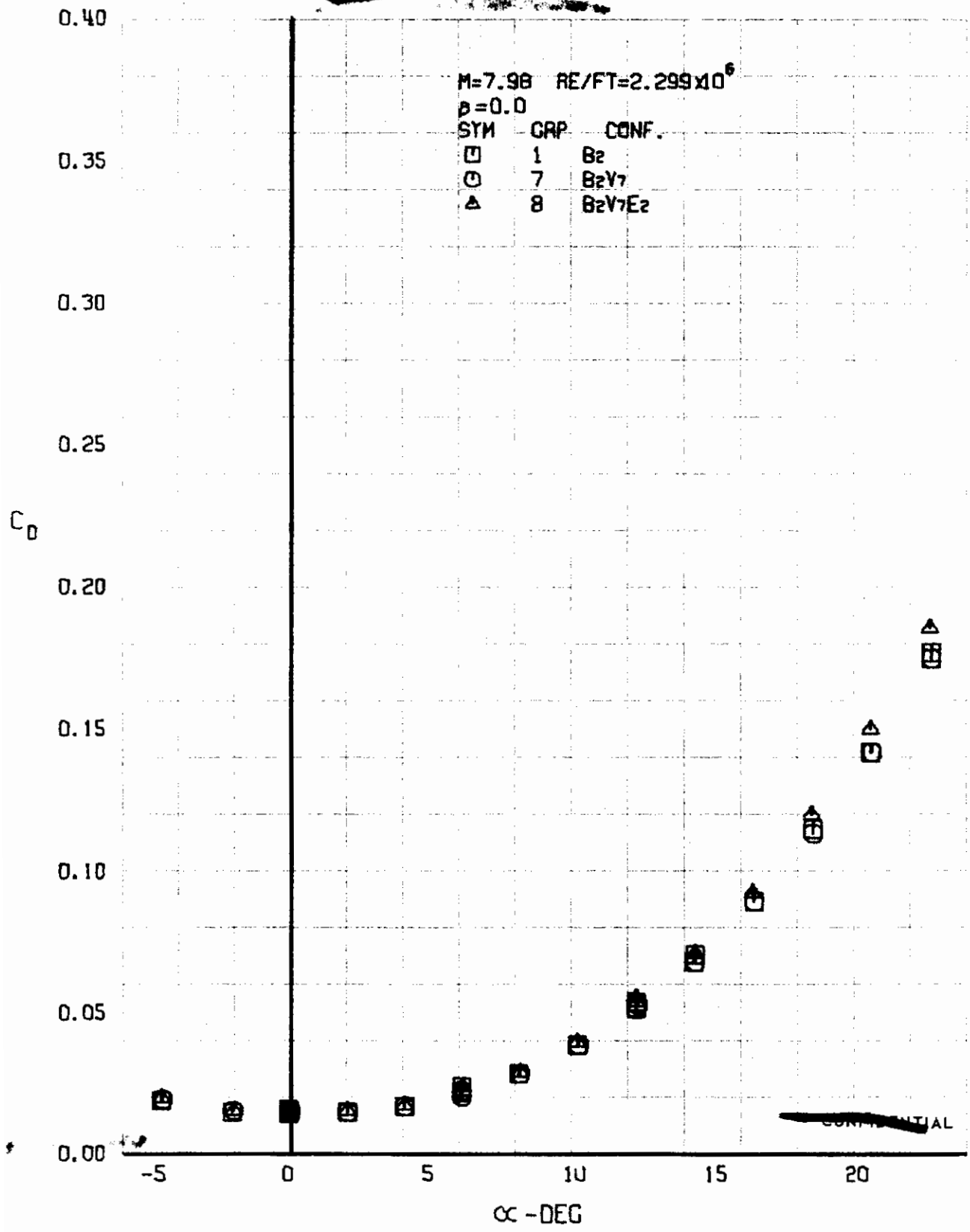

FIGURE 213 (U) CONFIGURATION BUILDUP
- DRAG COEFFICIENT VARIATION WITH ANGLE OF ATTACK (M=7.98)

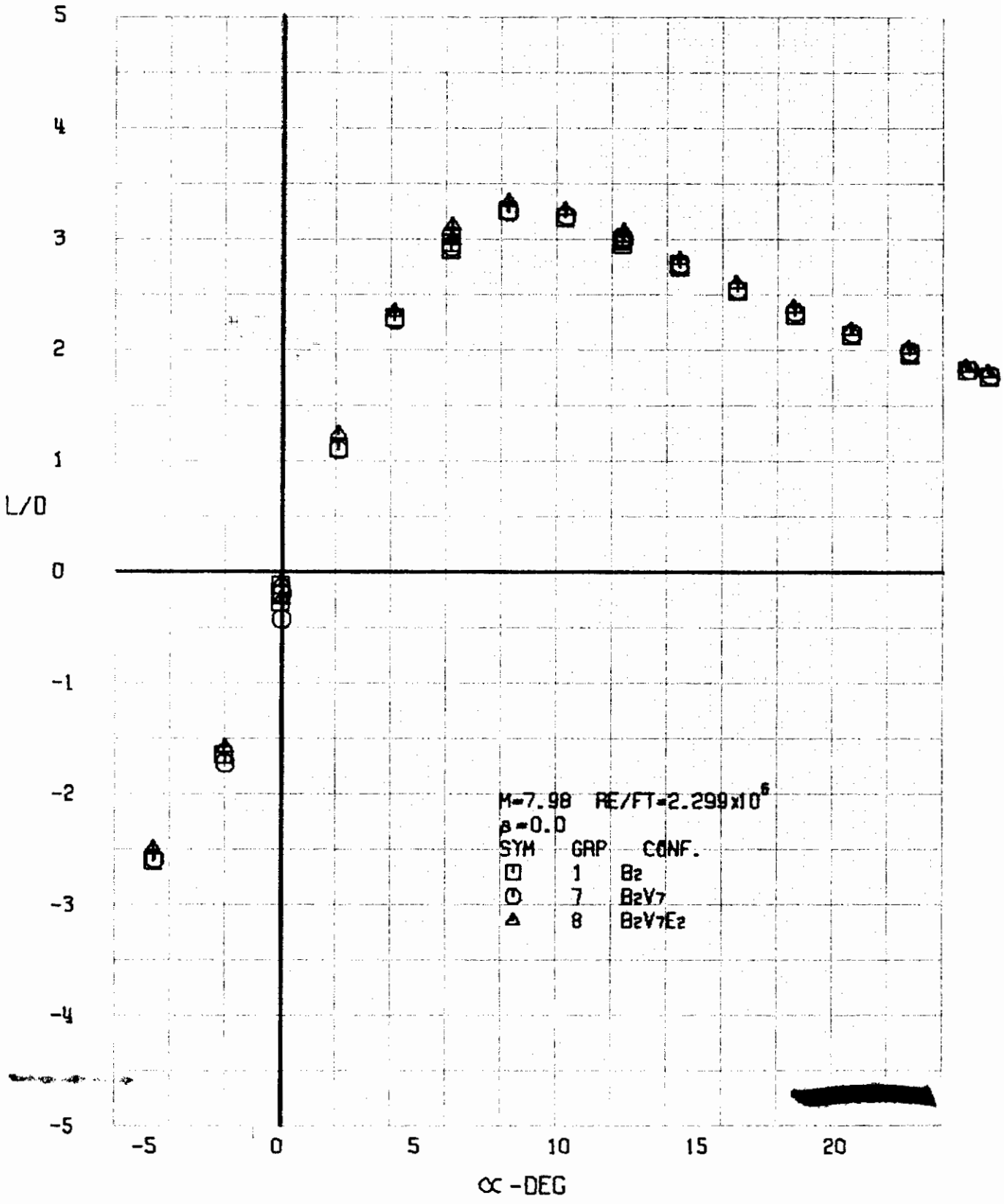

FIGURE 214 (U) CONFIGURATION BUILDUP
- LIFT-DRAG RATIO VARIATION WITH ANGLE OF ATTACK (M=7.98)

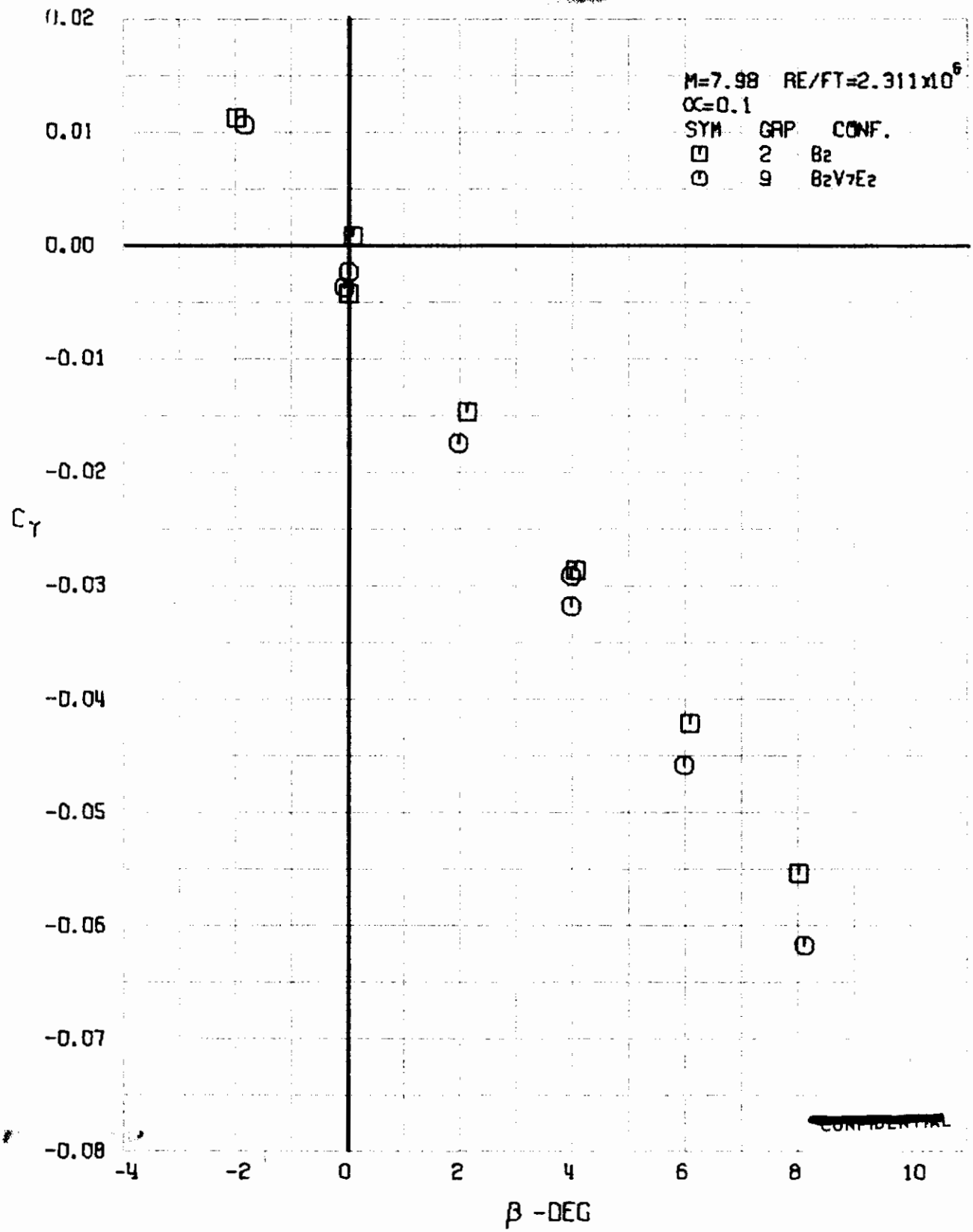

FIGURE 215 (U) CONFIGURATION BUILDUP
- SIDE FORCE COEFFICIENT VARIATION WITH ANGLE OF YAW (M=7.98)

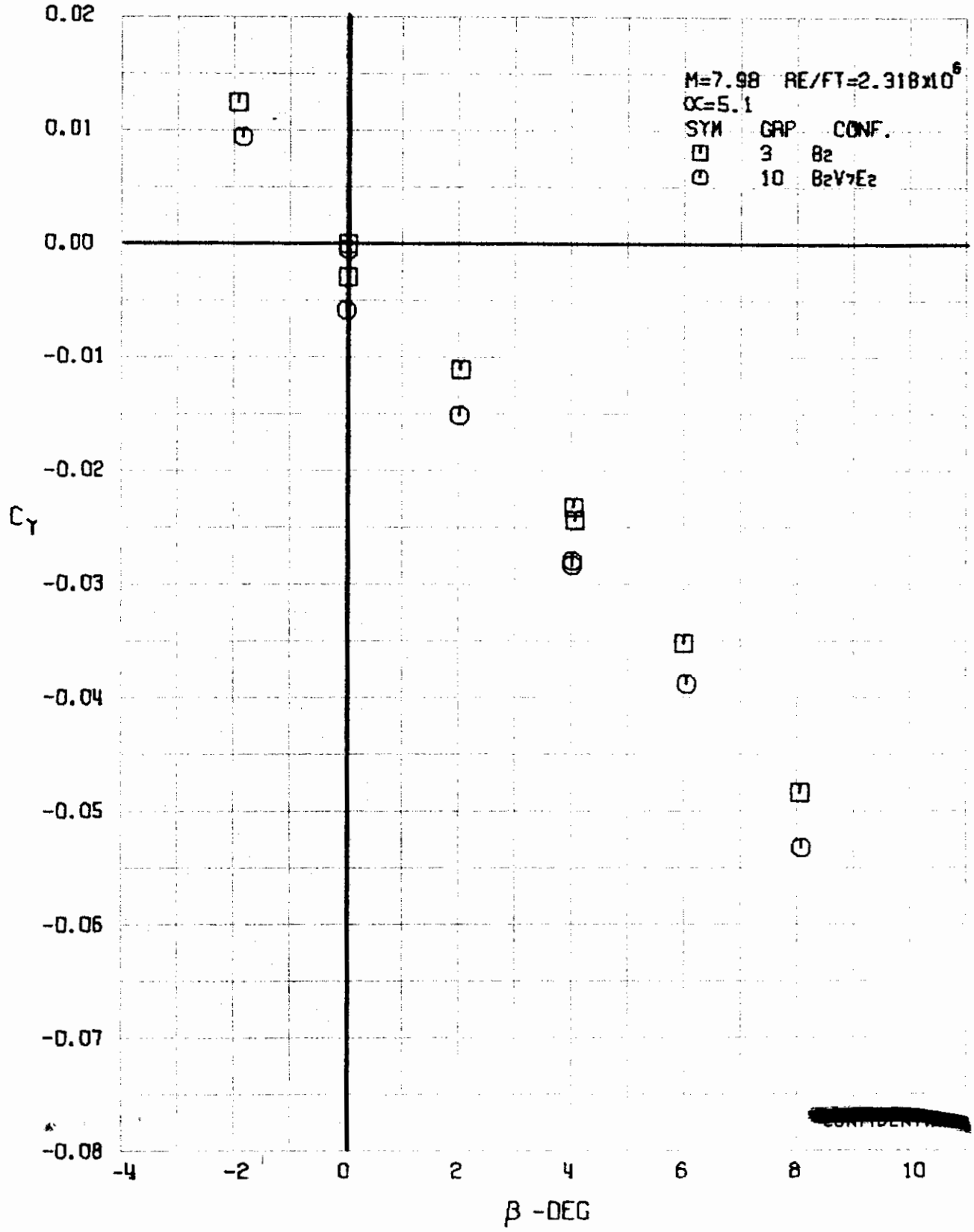

FIGURE 216 (U) CONFIGURATION BUILDUP
- SIDE FORCE COEFFICIENT VARIATION WITH ANGLE OF YAW (M=7.98)

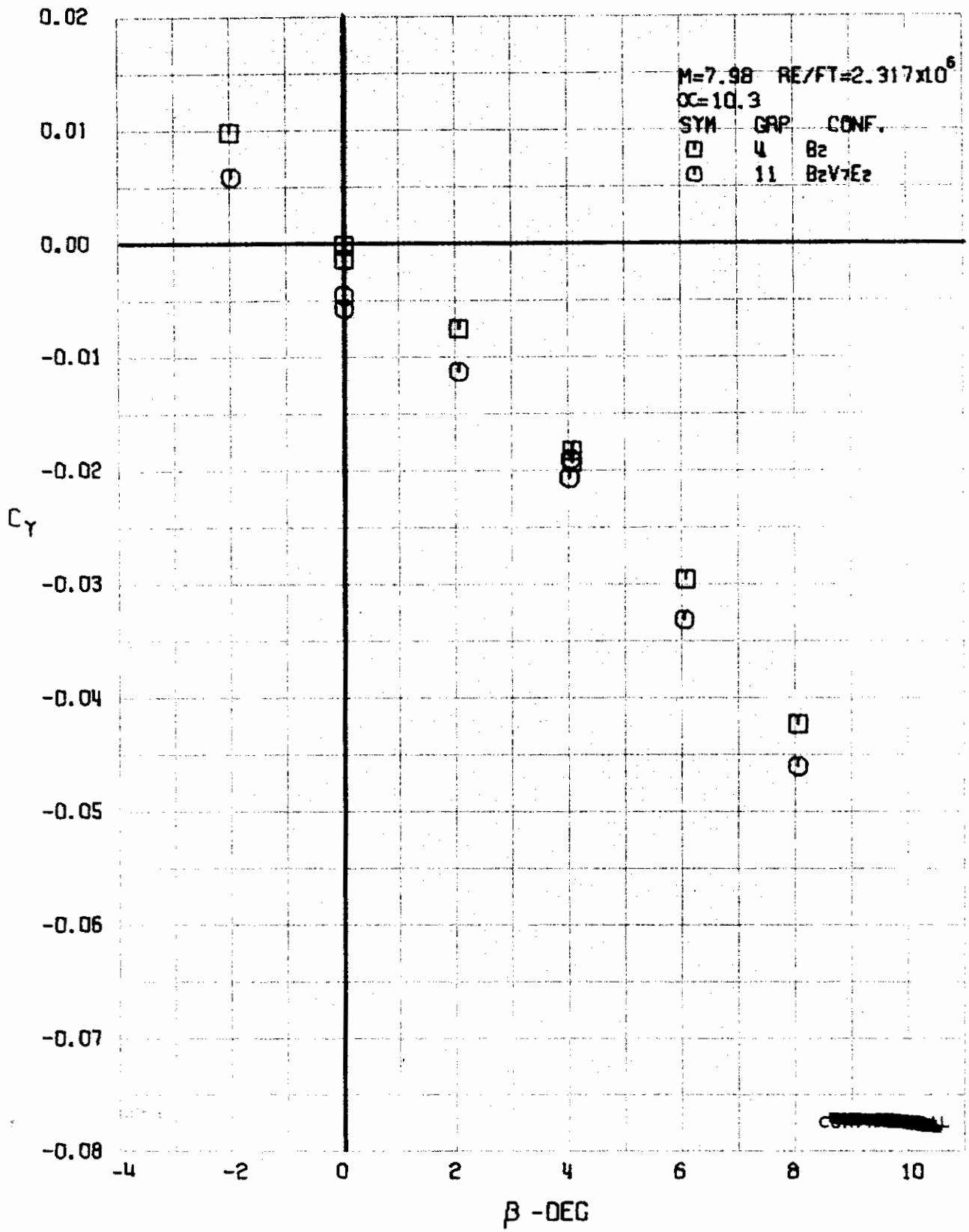

FIGURE 217 (U) CONFIGURATION BUILDUP
- SIDE FORCE COEFFICIENT VARIATION WITH ANGLE OF YAW (M=7.98)

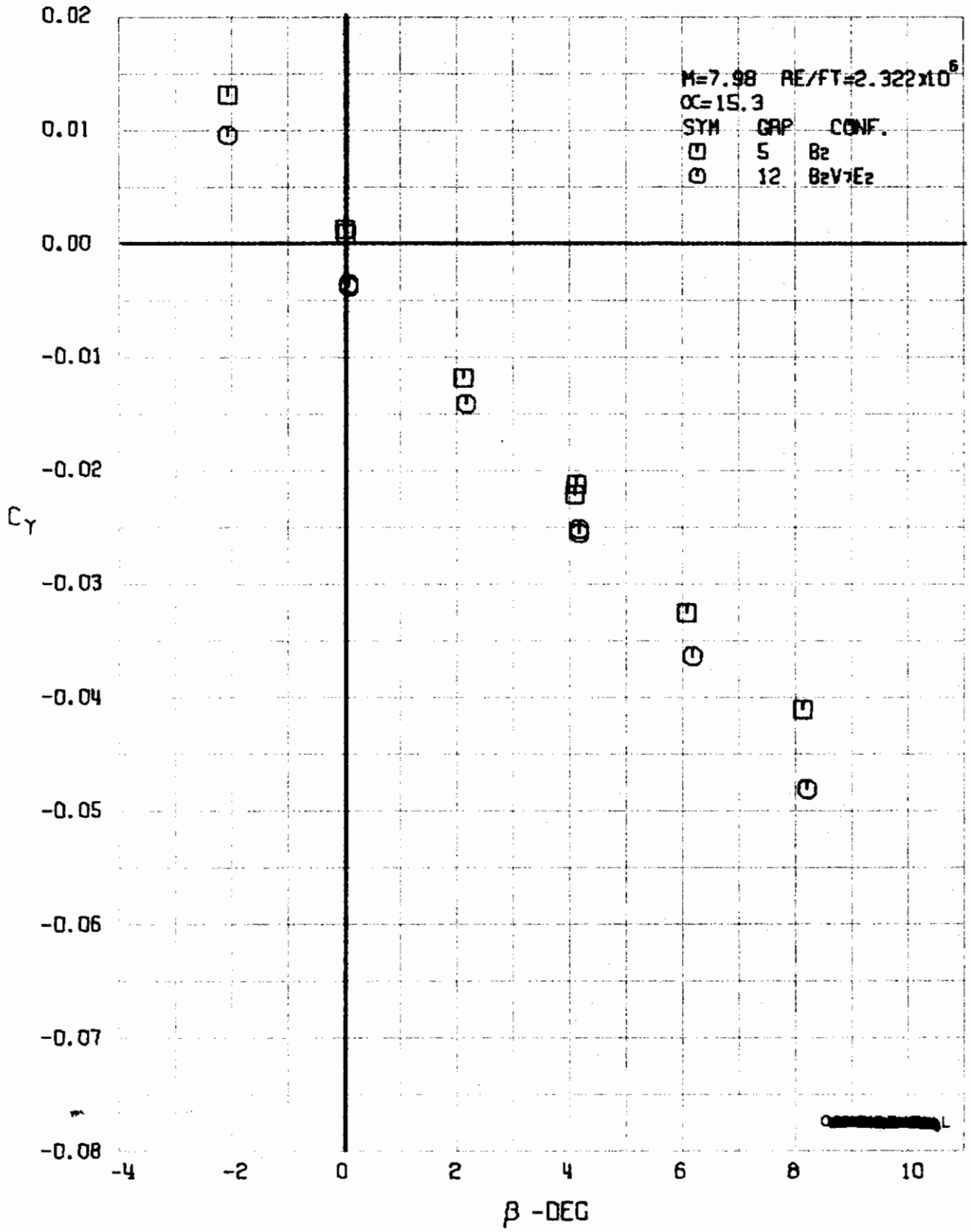

FIGURE 218 (U) CONFIGURATION BUILDUP
- SIDE FORCE COEFFICIENT VARIATION WITH ANGLE OF YAW (M=7.98)

CONFIDENTIAL

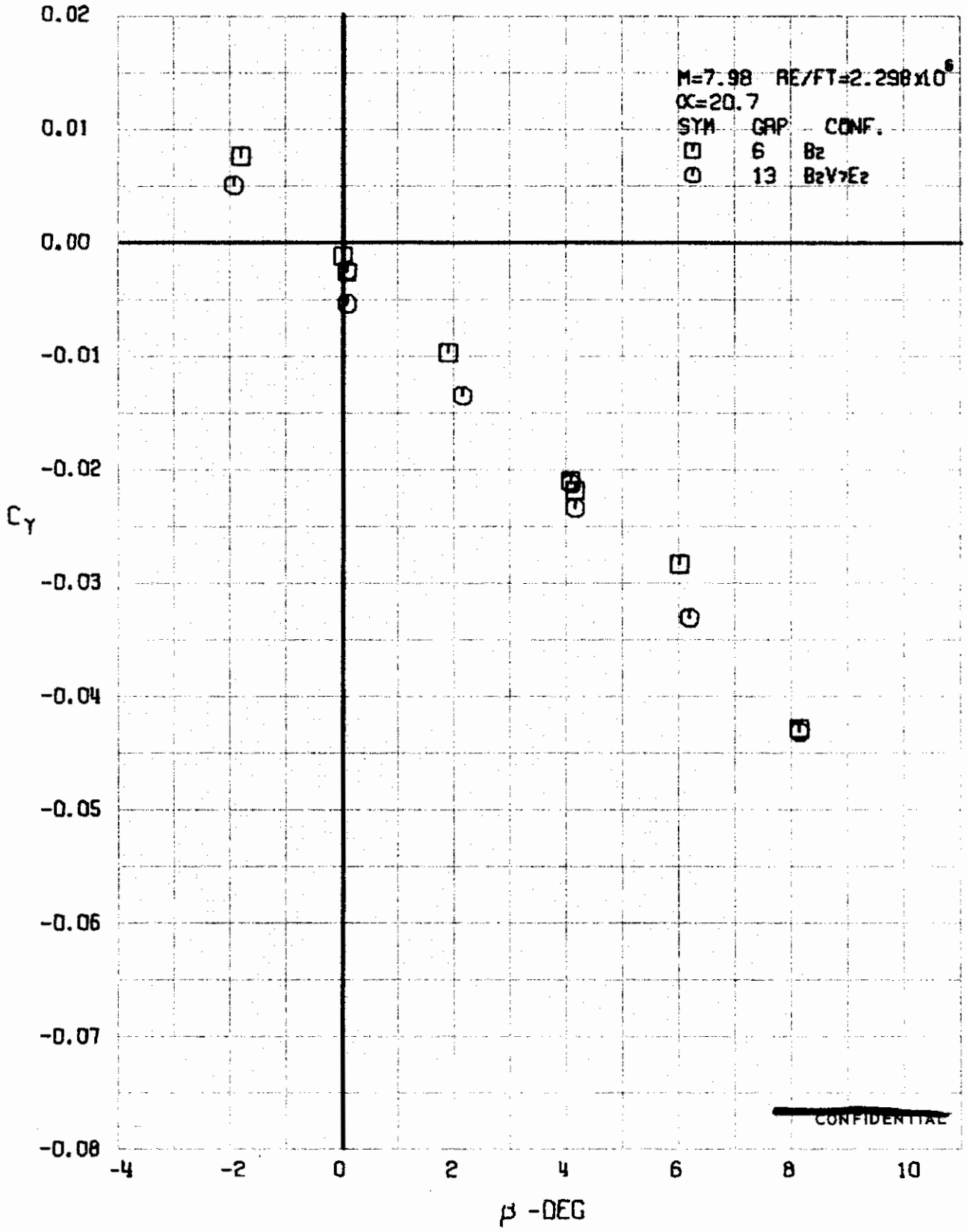

FIGURE 219 (U) CONFIGURATION BUILDUP
- SIDE FORCE COEFFICIENT VARIATION WITH ANGLE OF YAW (M=7.98)

CONFIDENTIAL

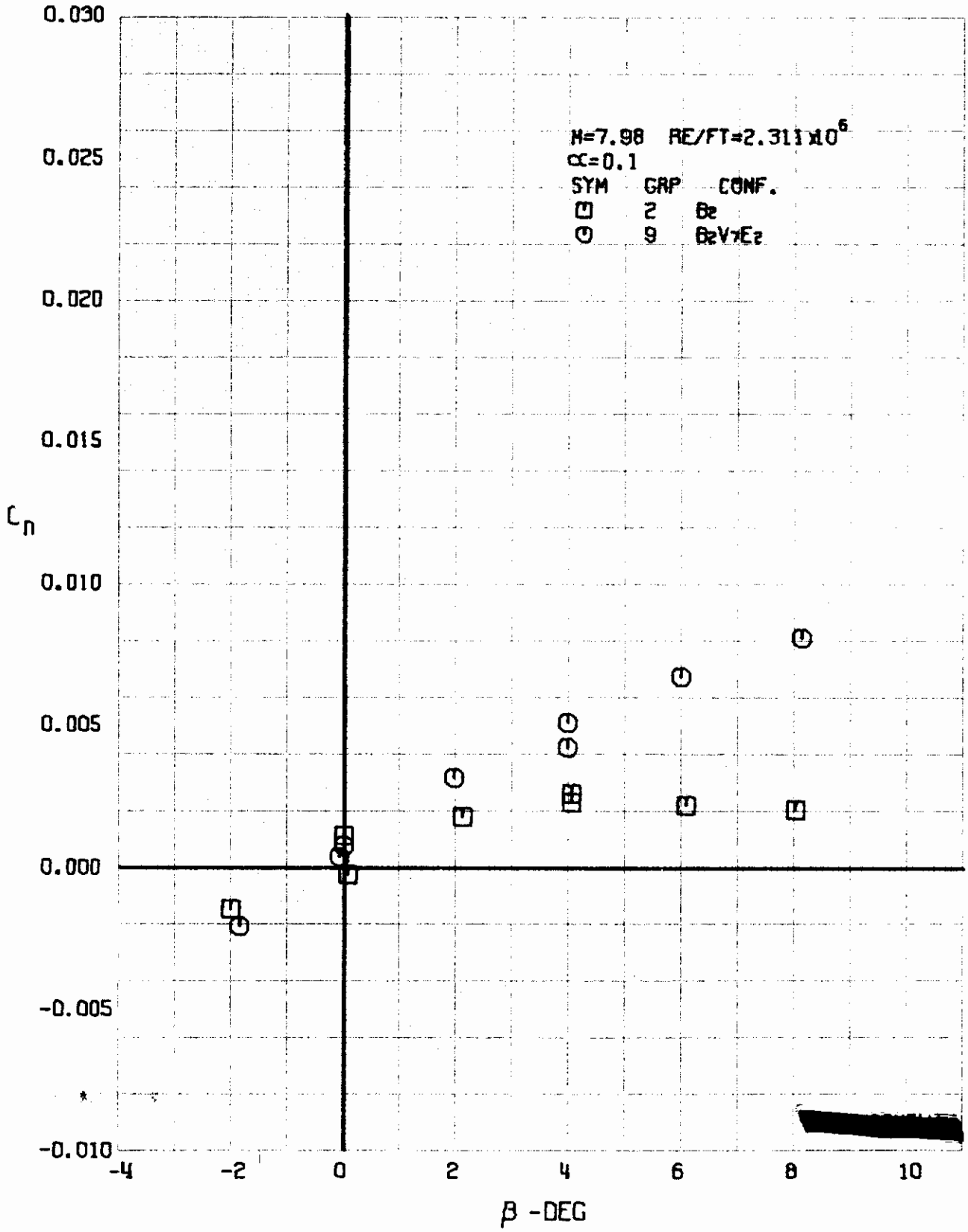

FIGURE 220 (U) CONFIGURATION BUILDUP
- YAWING MOMENT COEFFICIENT VARIATION WITH ANGLE OF YAW (M=7.98)

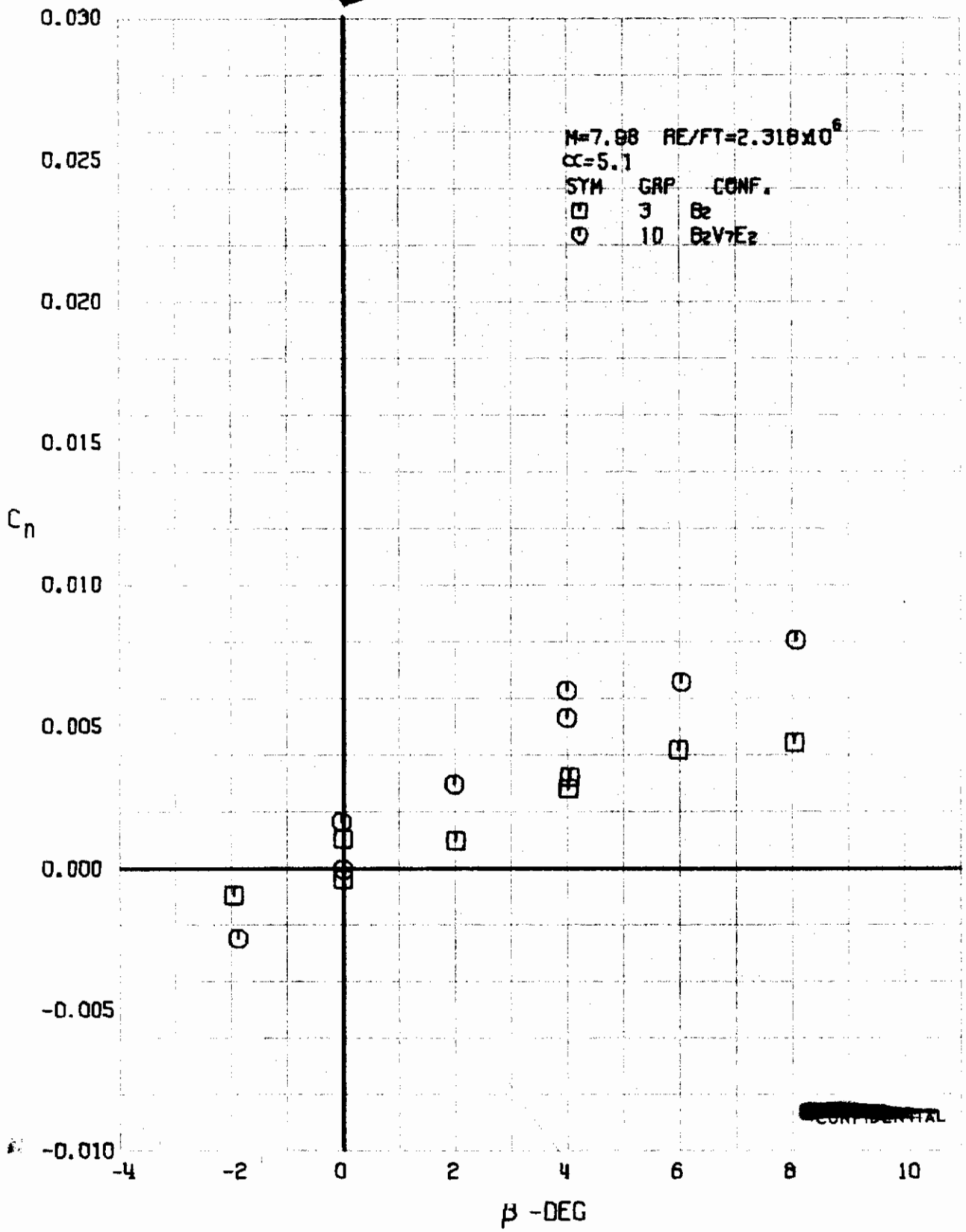

FIGURE 221 (U) CONFIGURATION BUILDUP
- YAWING MOMENT COEFFICIENT VARIATION WITH ANGLE OF YAW (M= 7.98)

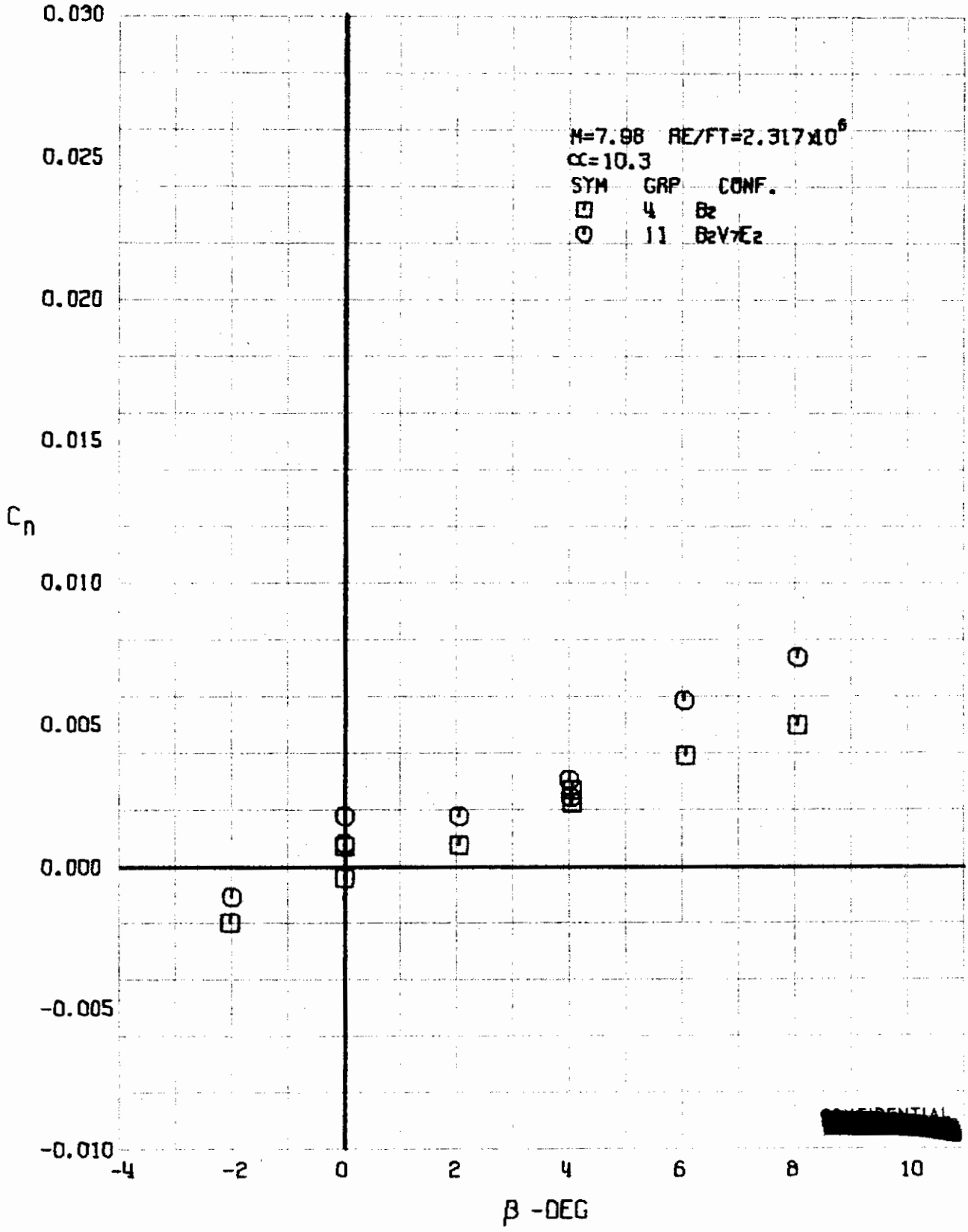

FIGURE 222 (U) CONFIGURATION BUILDUP
- YAWING MOMENT COEFFICIENT VARIATION WITH ANGLE OF YAW (M= 7.98)

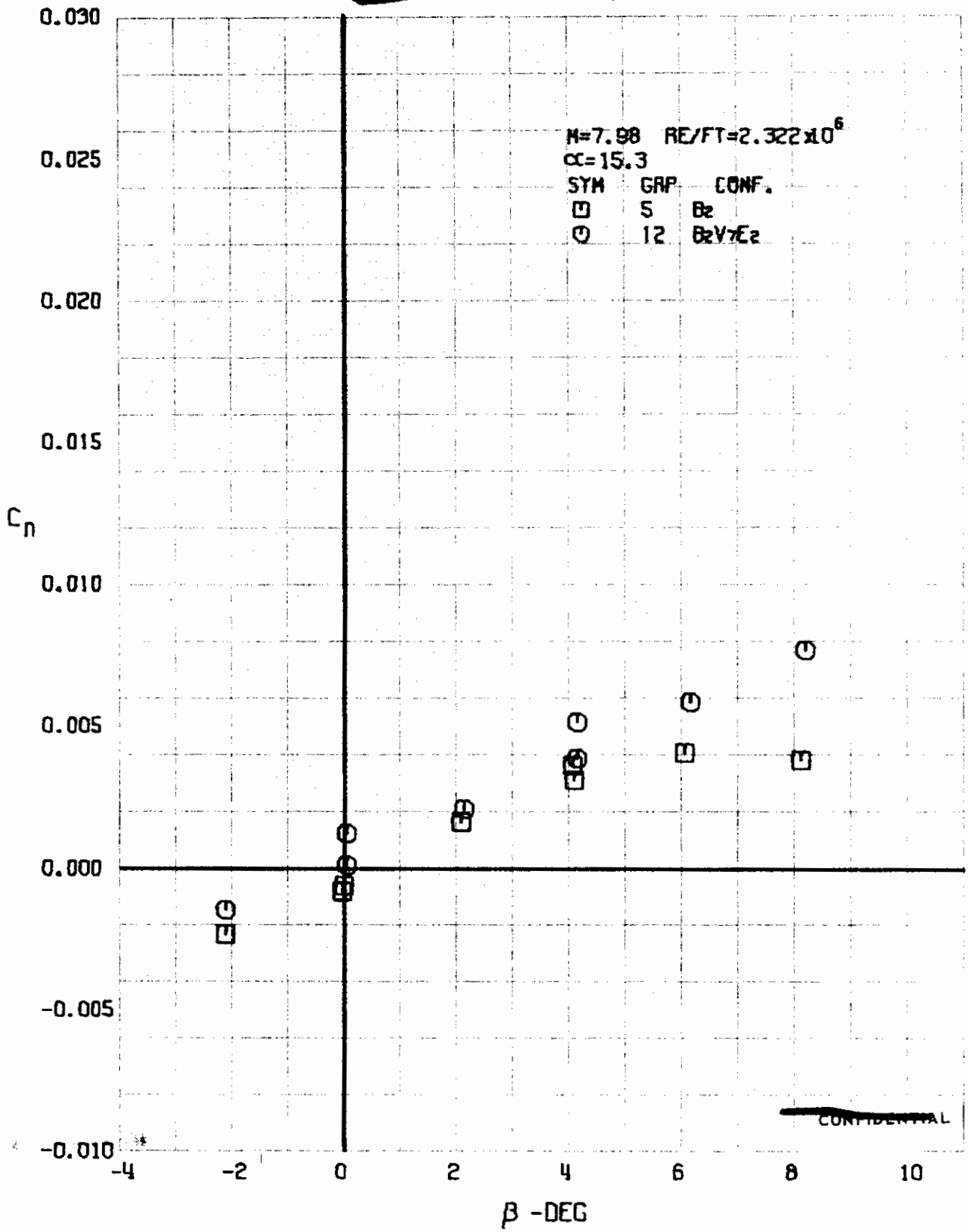

FIGURE 223 (U) CONFIGURATION BUILDUP
- YAWING MOMENT COEFFICIENT VARIATION WITH ANGLE OF YAW (M= 7.98)

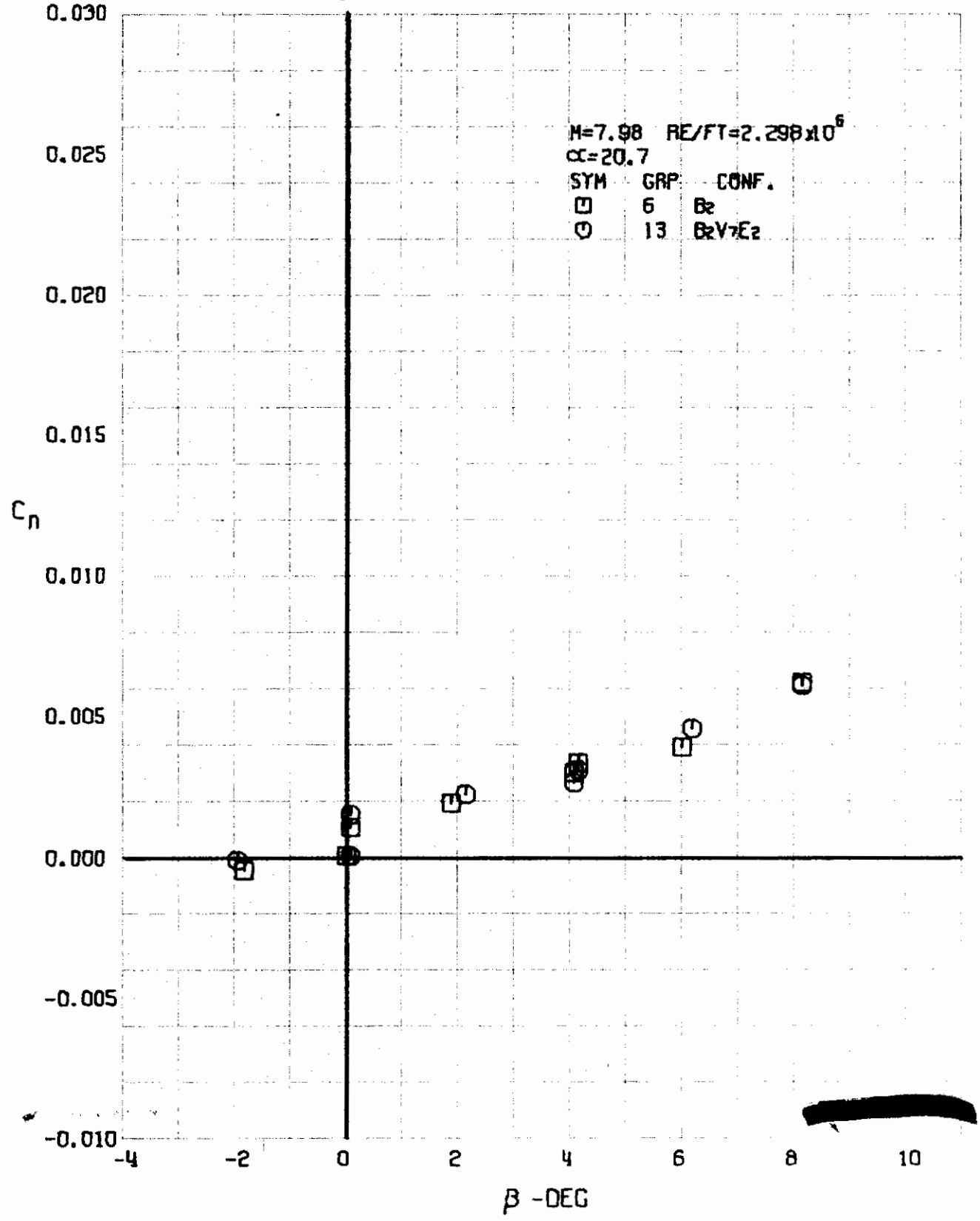

FIGURE 224 (U) CONFIGURATION BUILDUP
- YAWING MOMENT COEFFICIENT VARIATION WITH ANGLE OF YAW (M=7.98)

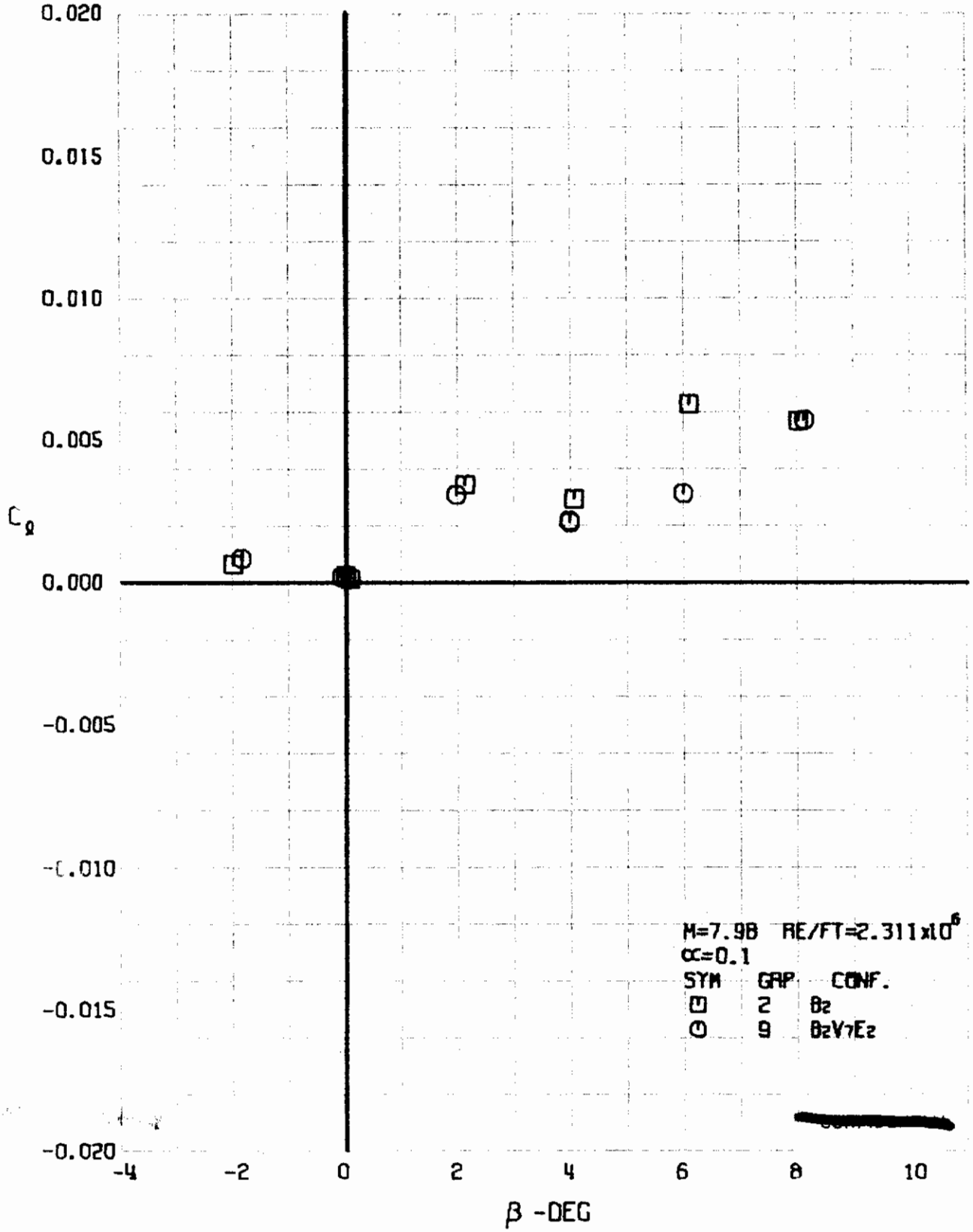

FIGURE 225 (U) CONFIGURATION BUILDUP
- ROLLING MOMENT COEFFICIENT VARIATION WITH ANGLE OF YAW (M=7.98)

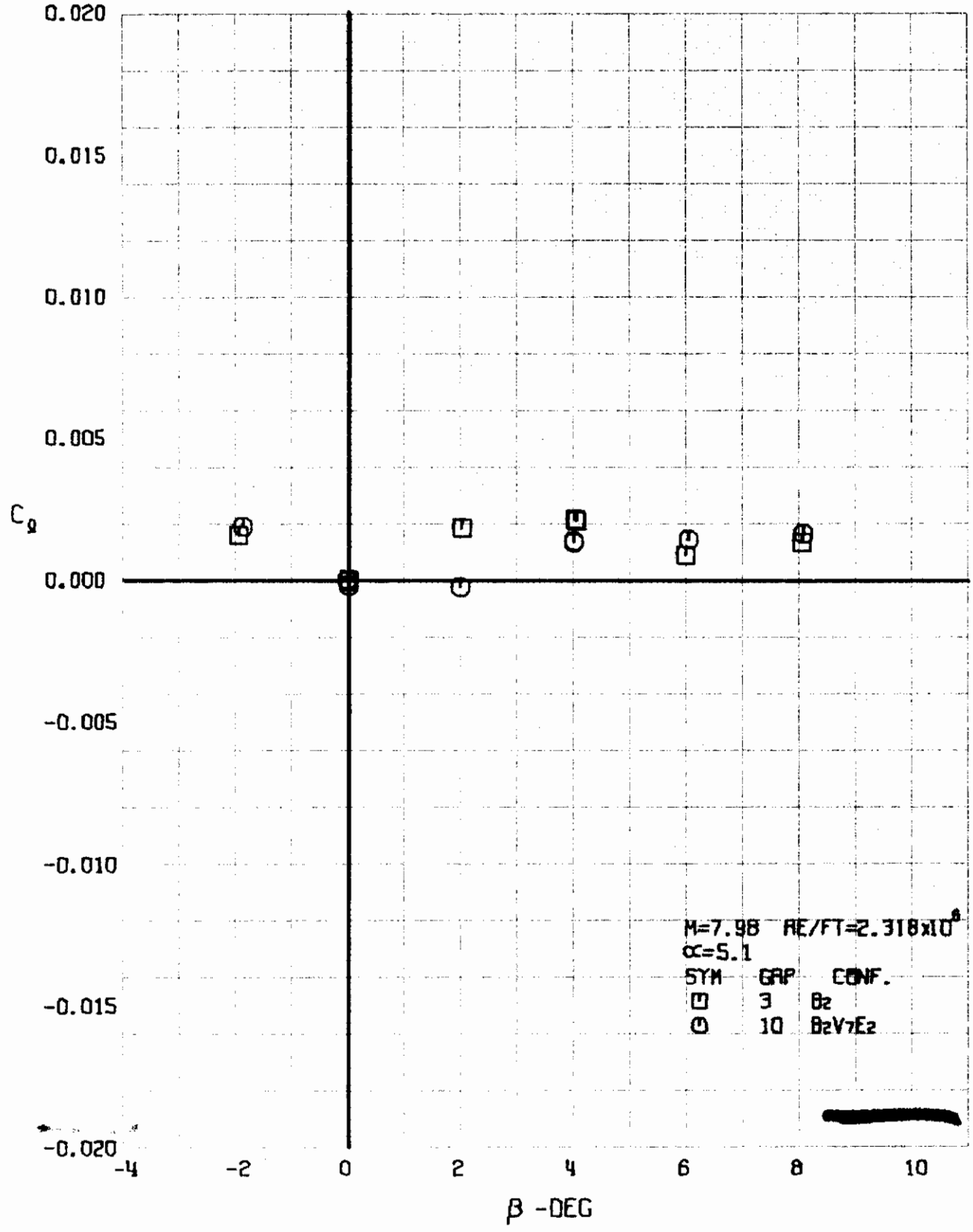

FIGURE 226 (U) CONFIGURATION BUILDUP
- ROLLING MOMENT COEFFICIENT VARIATION WITH ANGLE OF YAW (M=7.98)

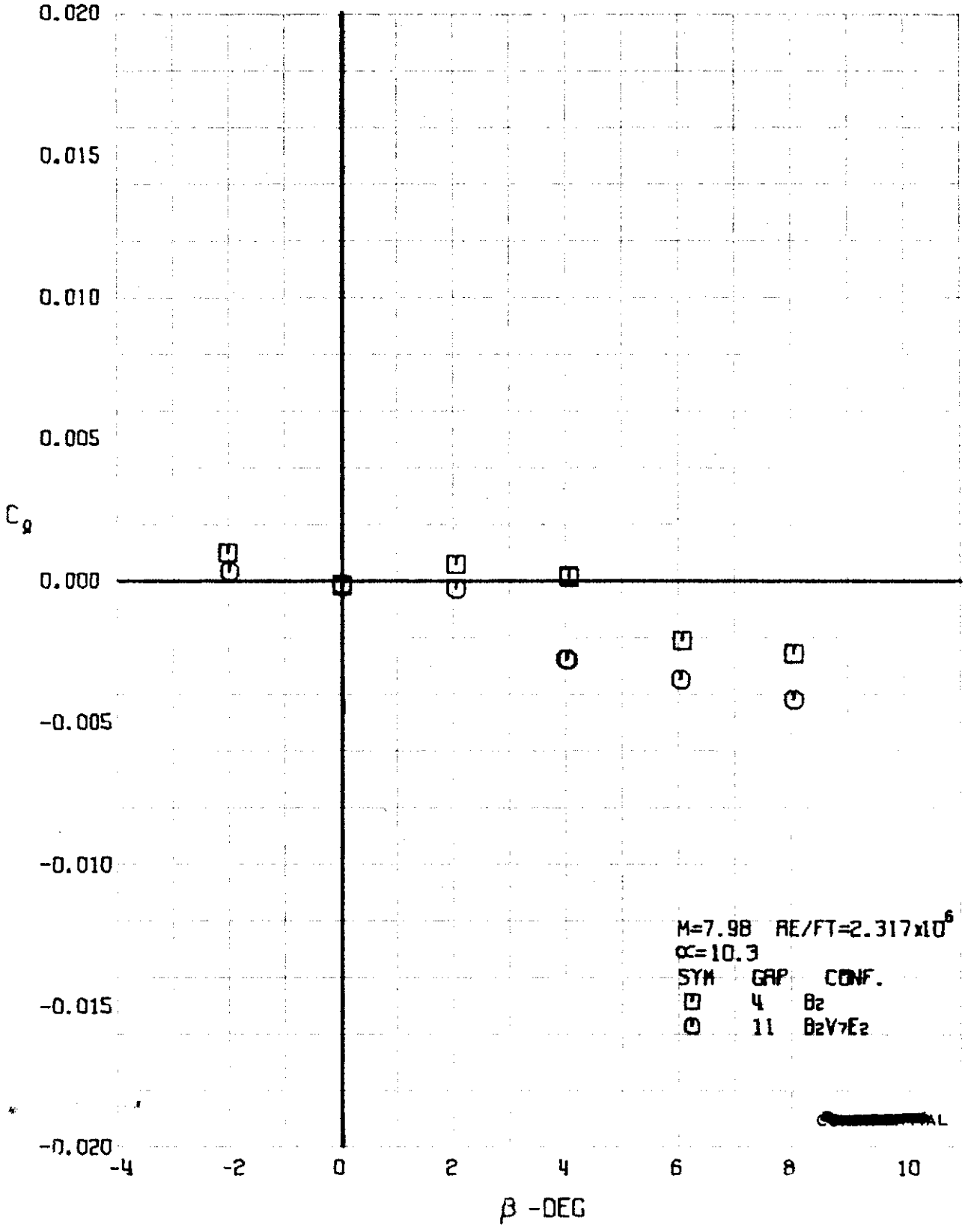

FIGURE 227 (U) CONFIGURATION BUILDUP
- ROLLING MOMENT COEFFICIENT VARIATION WITH ANGLE OF YAW (M=7.98)

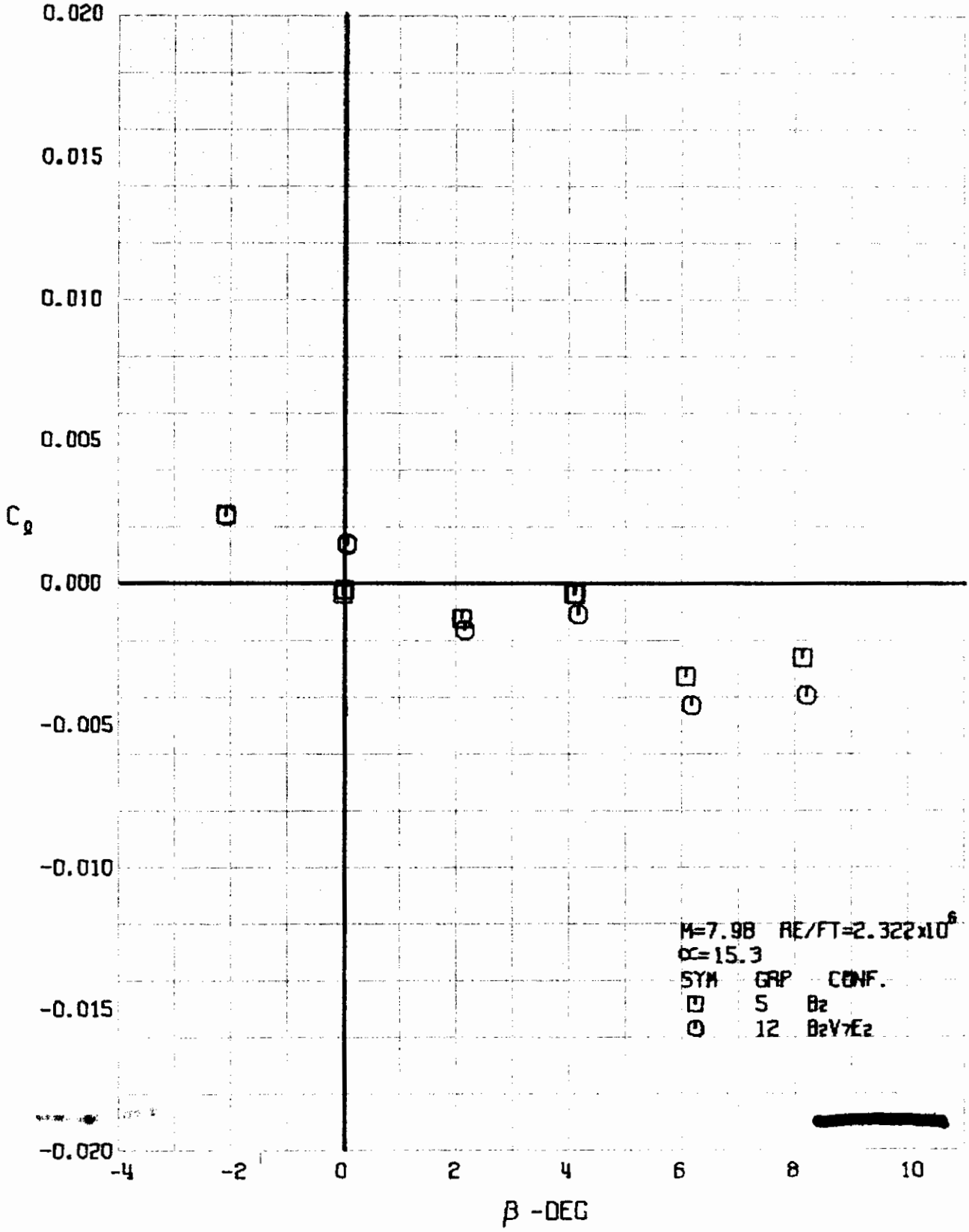

FIGURE 228 (U) CONFIGURATION BUILDUP
- ROLLING MOMENT COEFFICIENT VARIATION WITH ANGLE OF YAW (M=7.98)

[redacted]

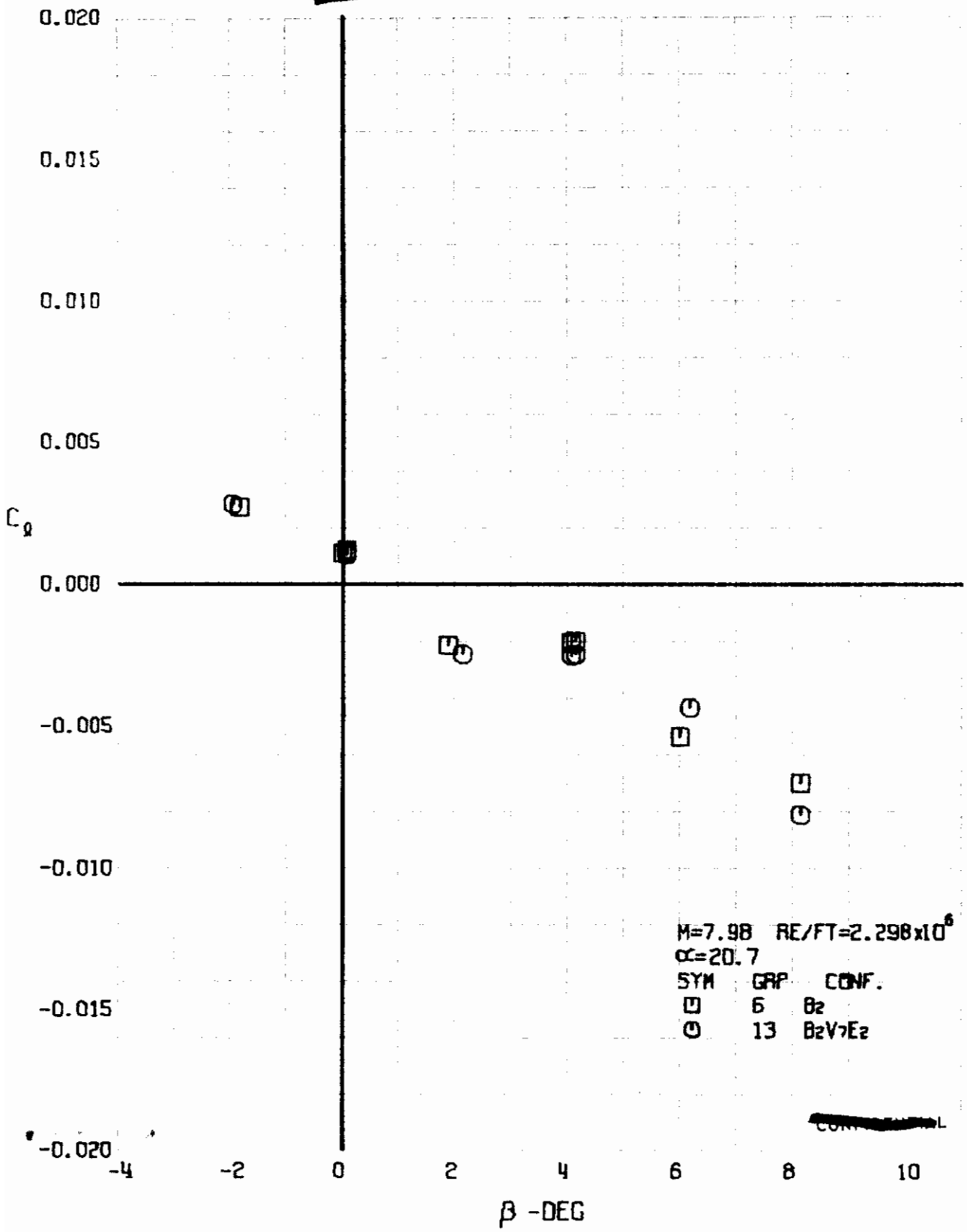

FIGURE 229 (U) CONFIGURATION BUILDUP
- ROLLING MOMENT COEFFICIENT VARIATION WITH ANGLE OF YAW (M=7.98)

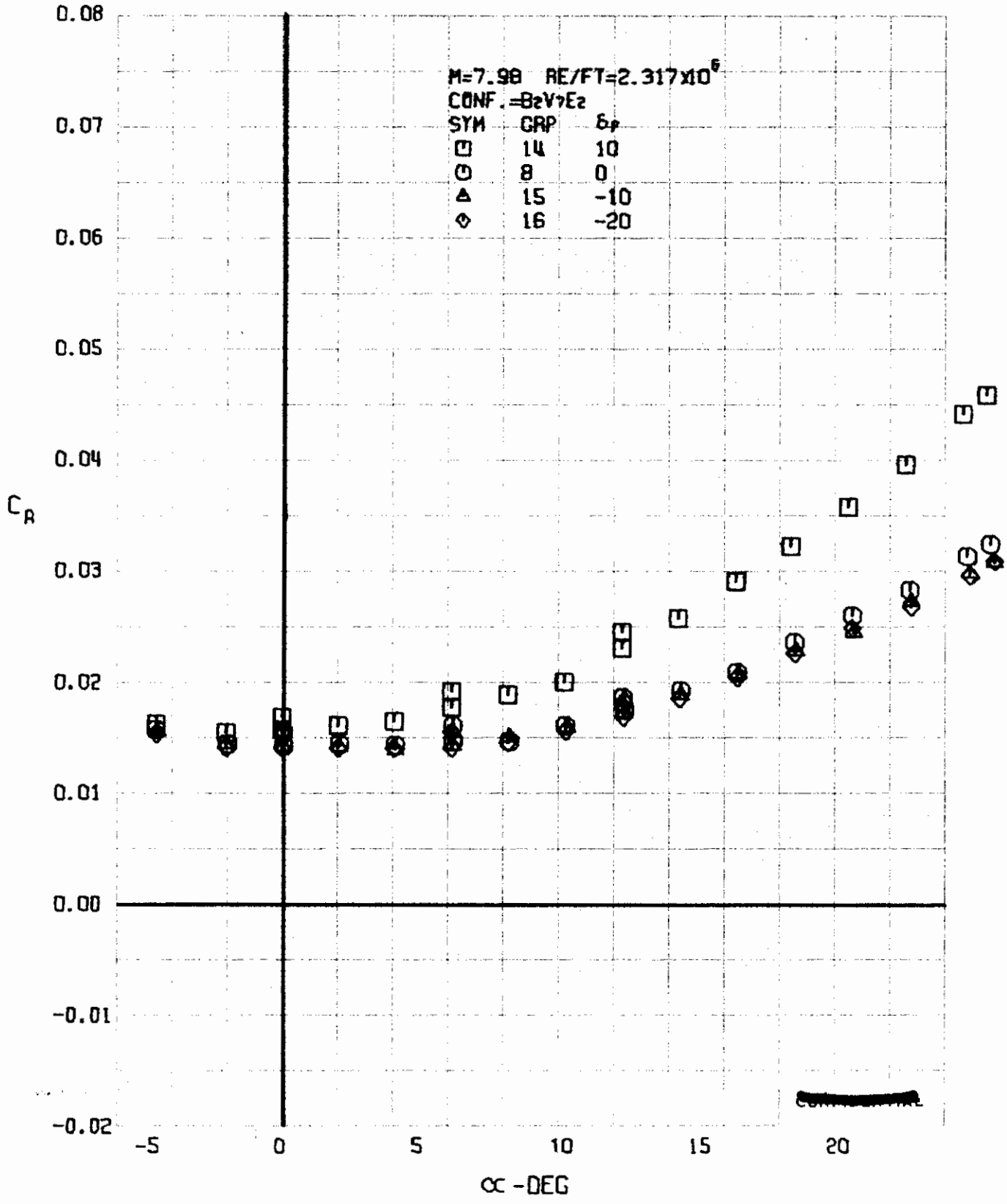

FIGURE 230 (U) ELEVON EFFECTS
- AXIAL FORCE COEFFICIENT VARIATION WITH ANGLE OF ATTACK (M=7.98)

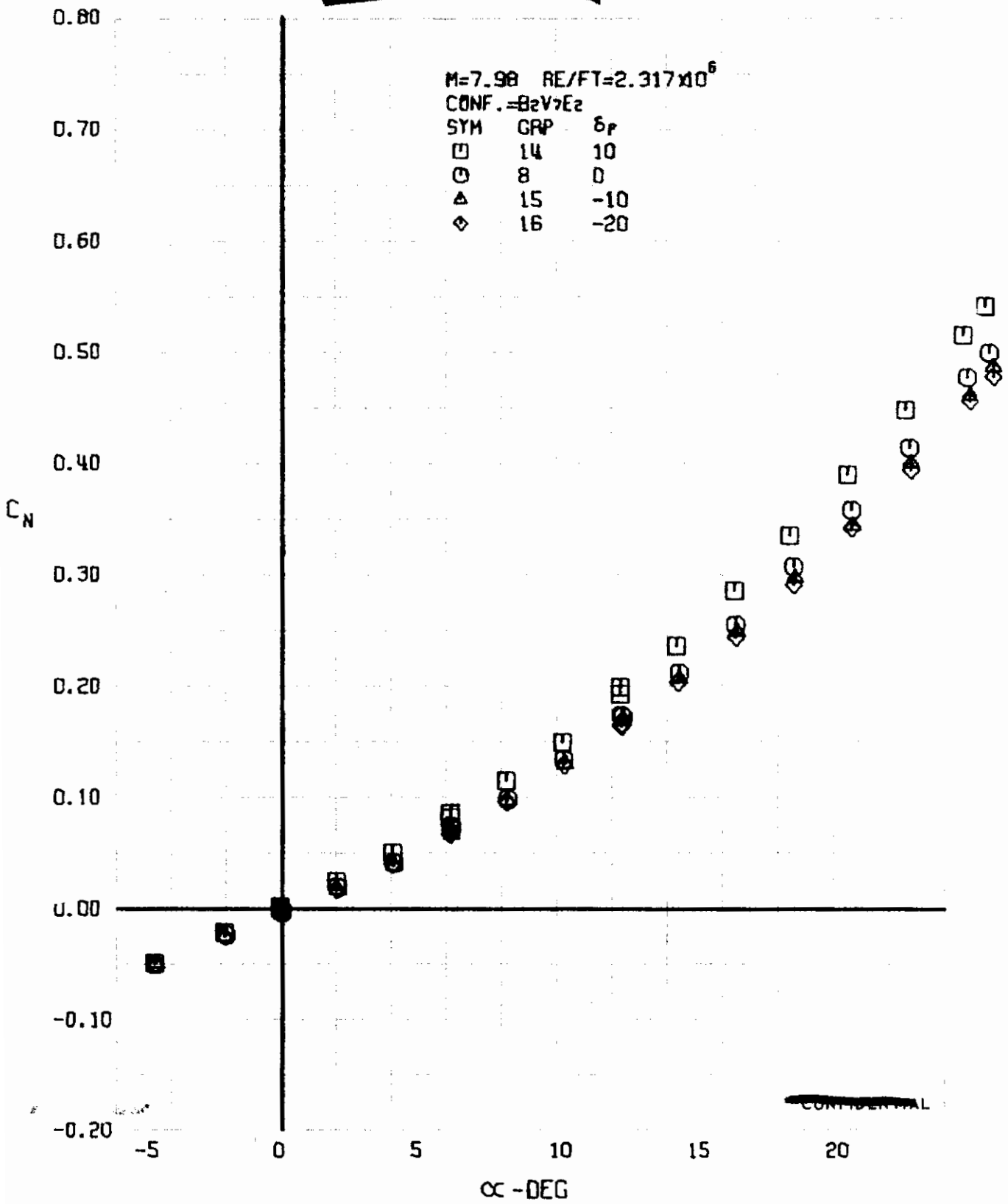

FIGURE 231 (U) ELEVON EFFECTS
- NORMAL FORCE COEFFICIENT VARIATION WITH ANGLE OF ATTACK (M= 7.98)

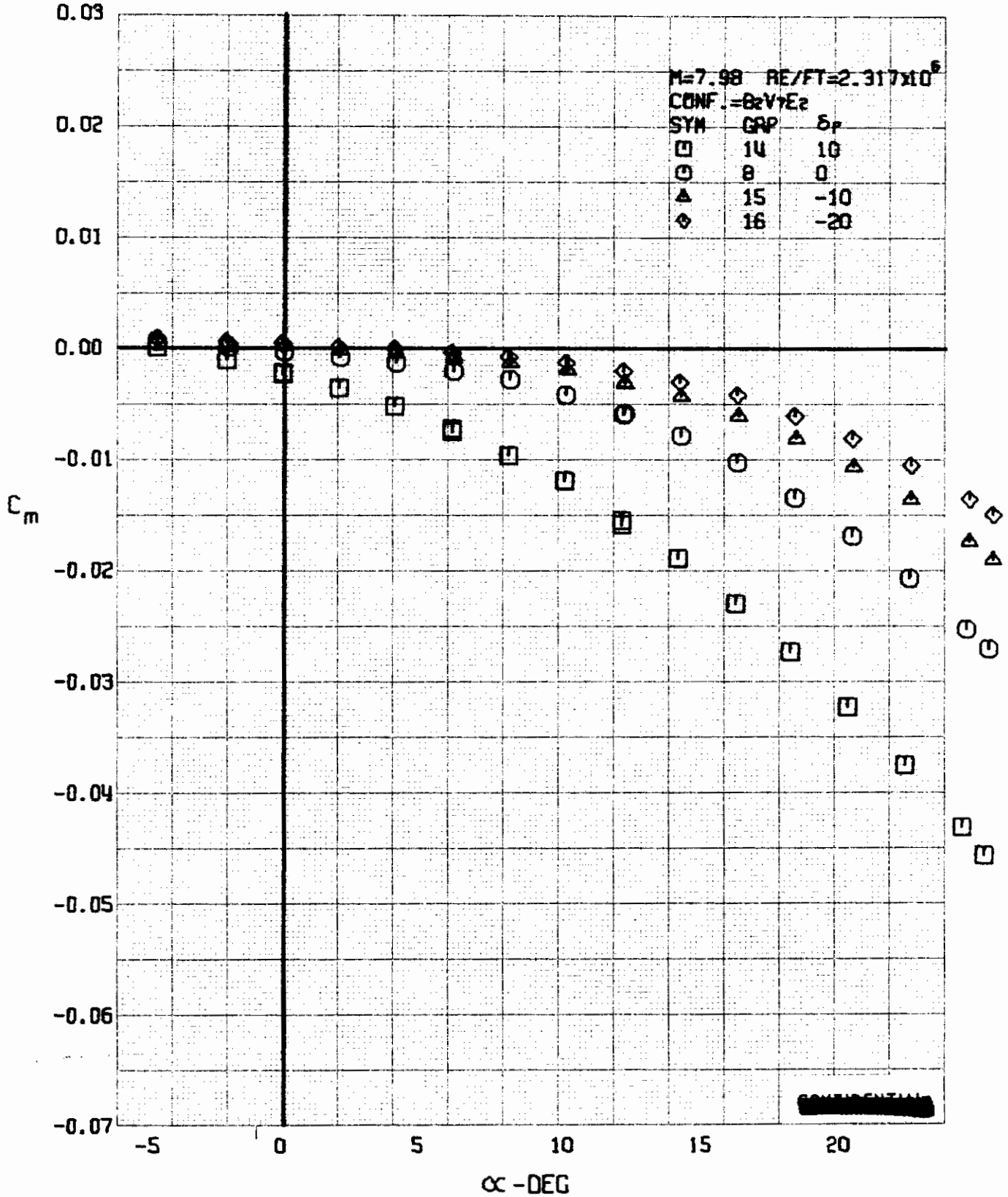

FIGURE 232 (U) ELEVON EFFECTS
- PITCHING MOMENT COEFFICIENT VARIATION WITH ANGLE OF ATTACK (M=7.98)

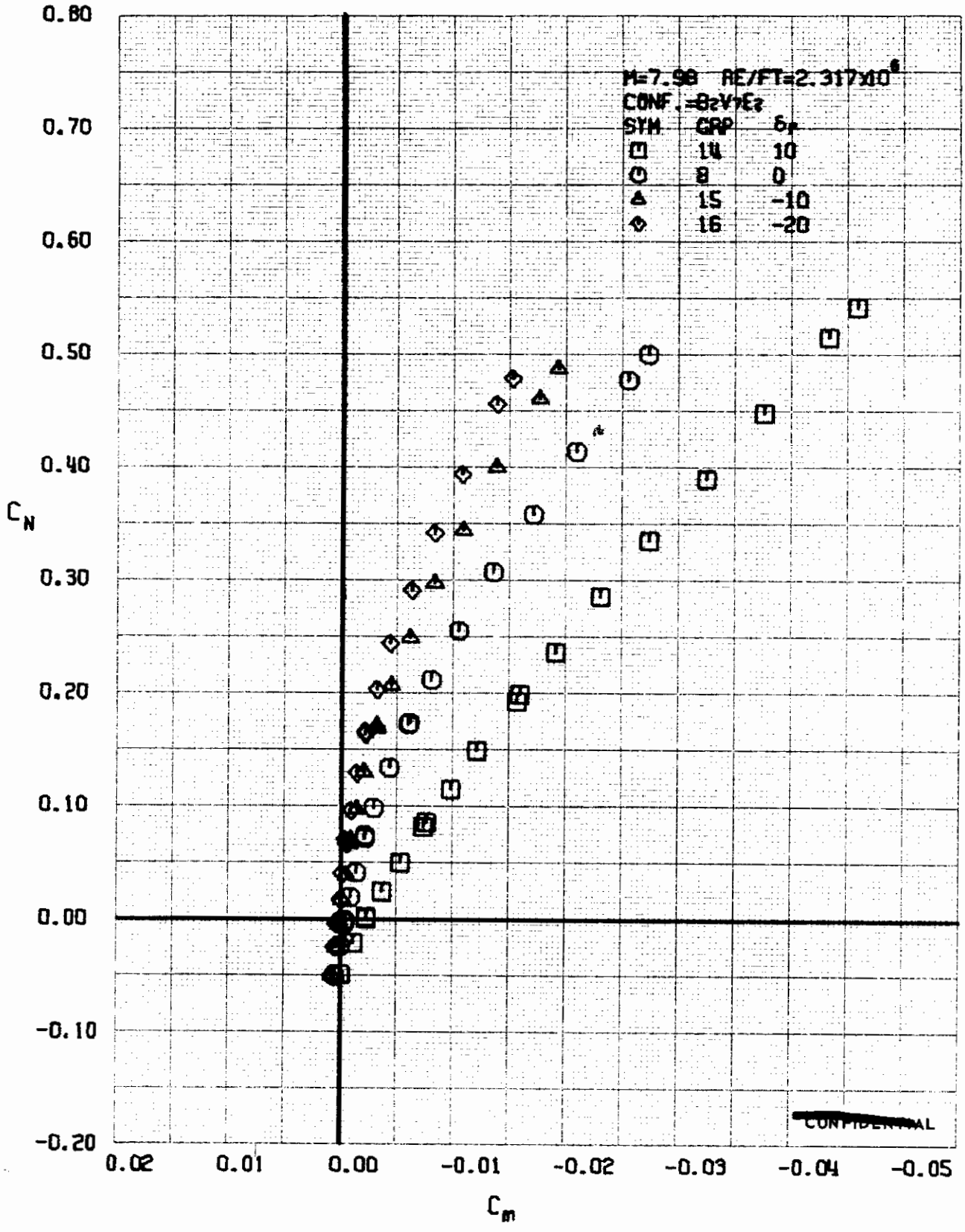

FIGURE 233 (U) ELEVON EFFECTS
- LONGITUDINAL STABILITY VARIATION (M=7.98)

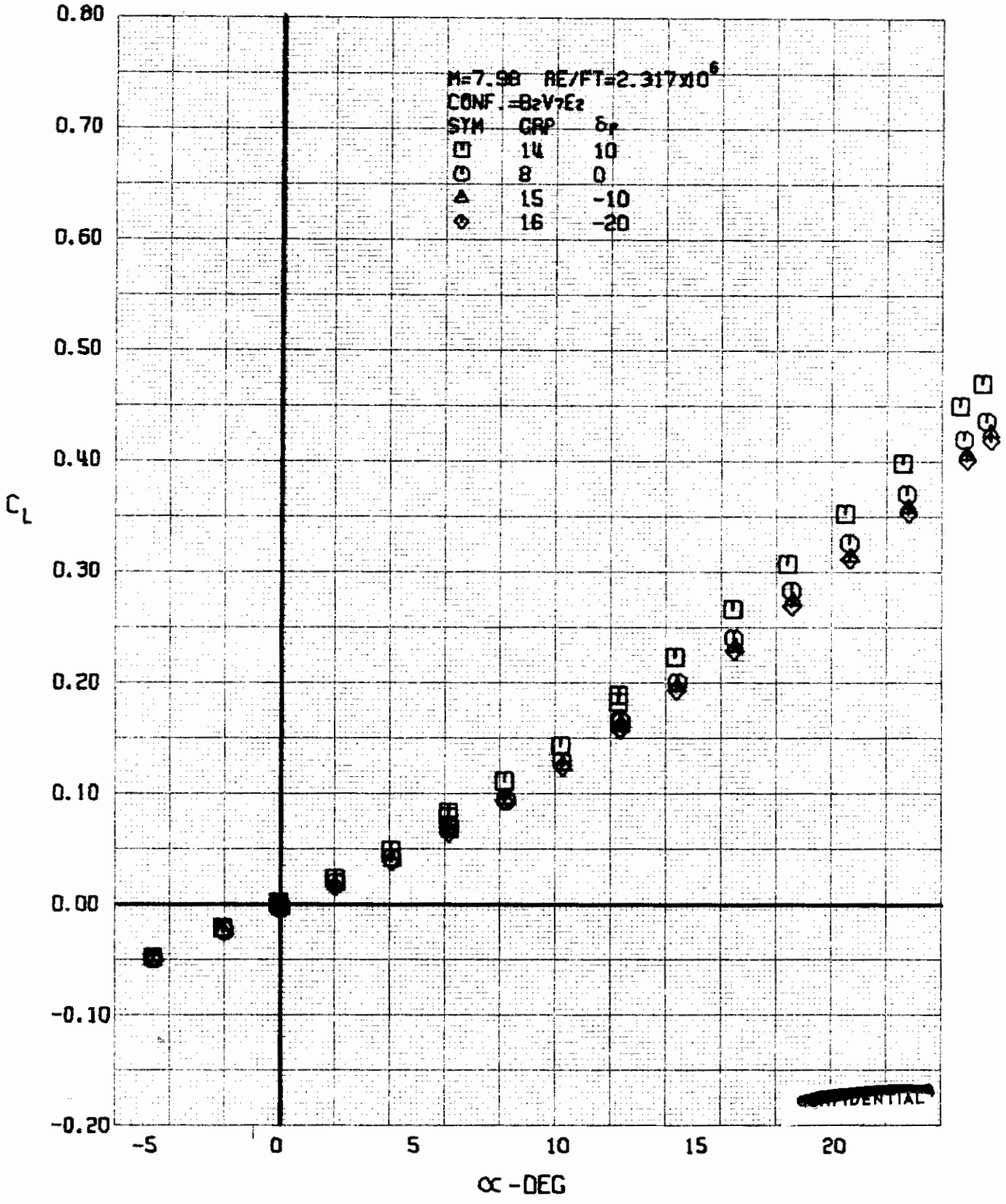

FIGURE 234 (U) ELEVON EFFECTS
- LIFT COEFFICIENT VARIATION WITH ANGLE OF ATTACK (M=7.98)

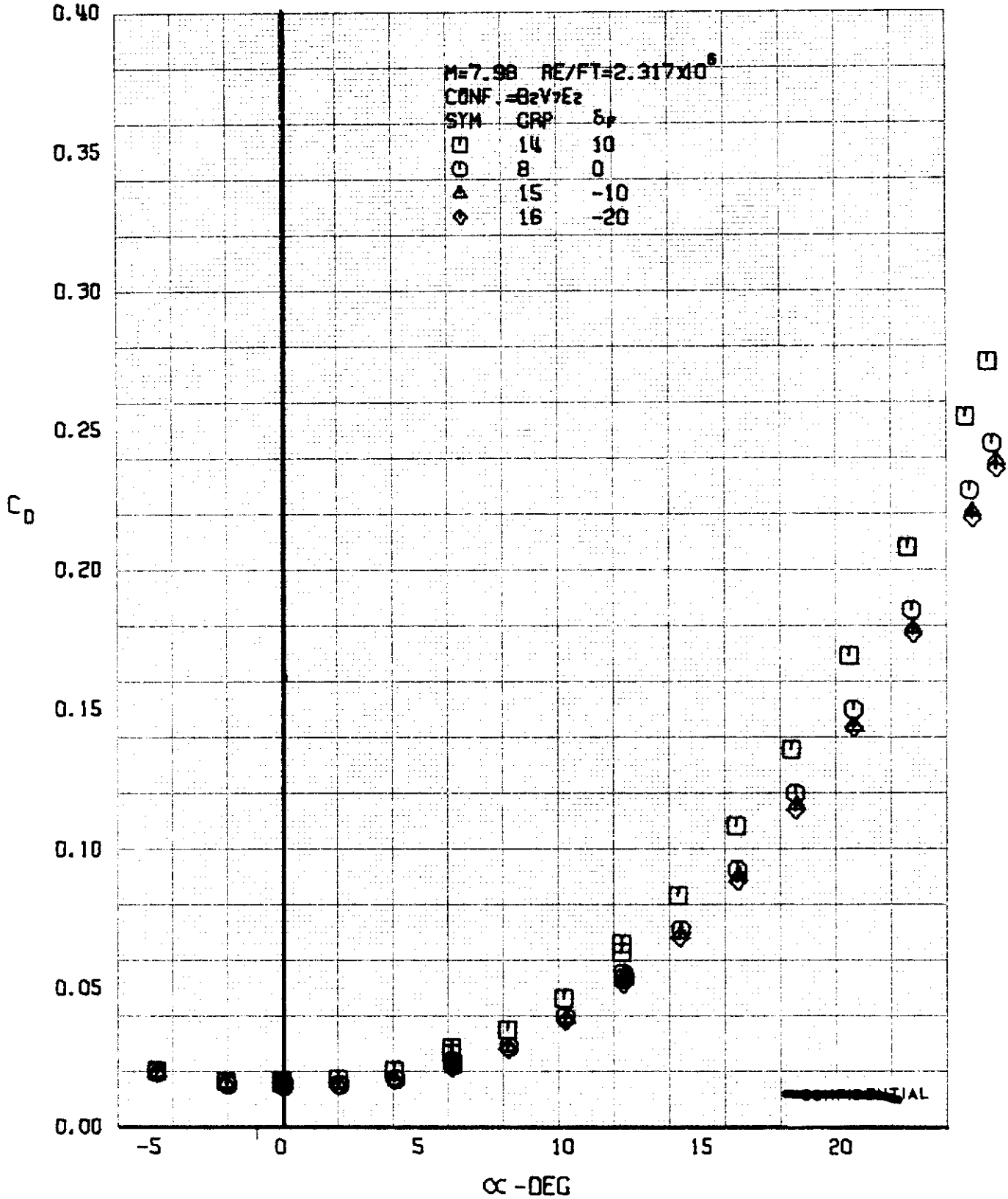

FIGURE 235 (U) ELEVON EFFECTS
- DRAG COEFFICIENT VARIATION WITH ANGLE OF ATTACK (M=7.98)

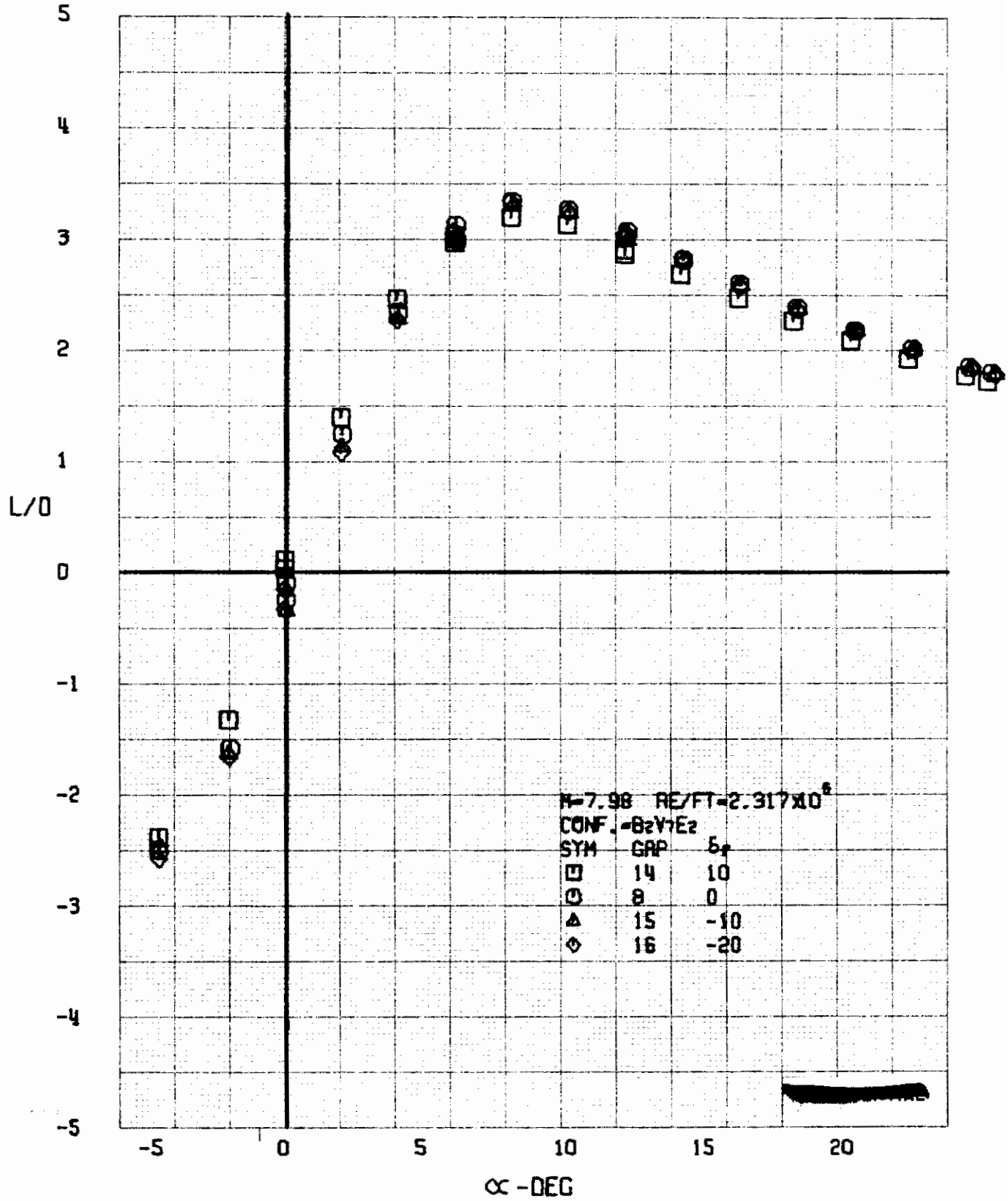

FIGURE 236 (U) ELEVON EFFECTS
- LIFT-DRAG RATIO VARIATION WITH ANGLE OF ATTACK (M=7.98)

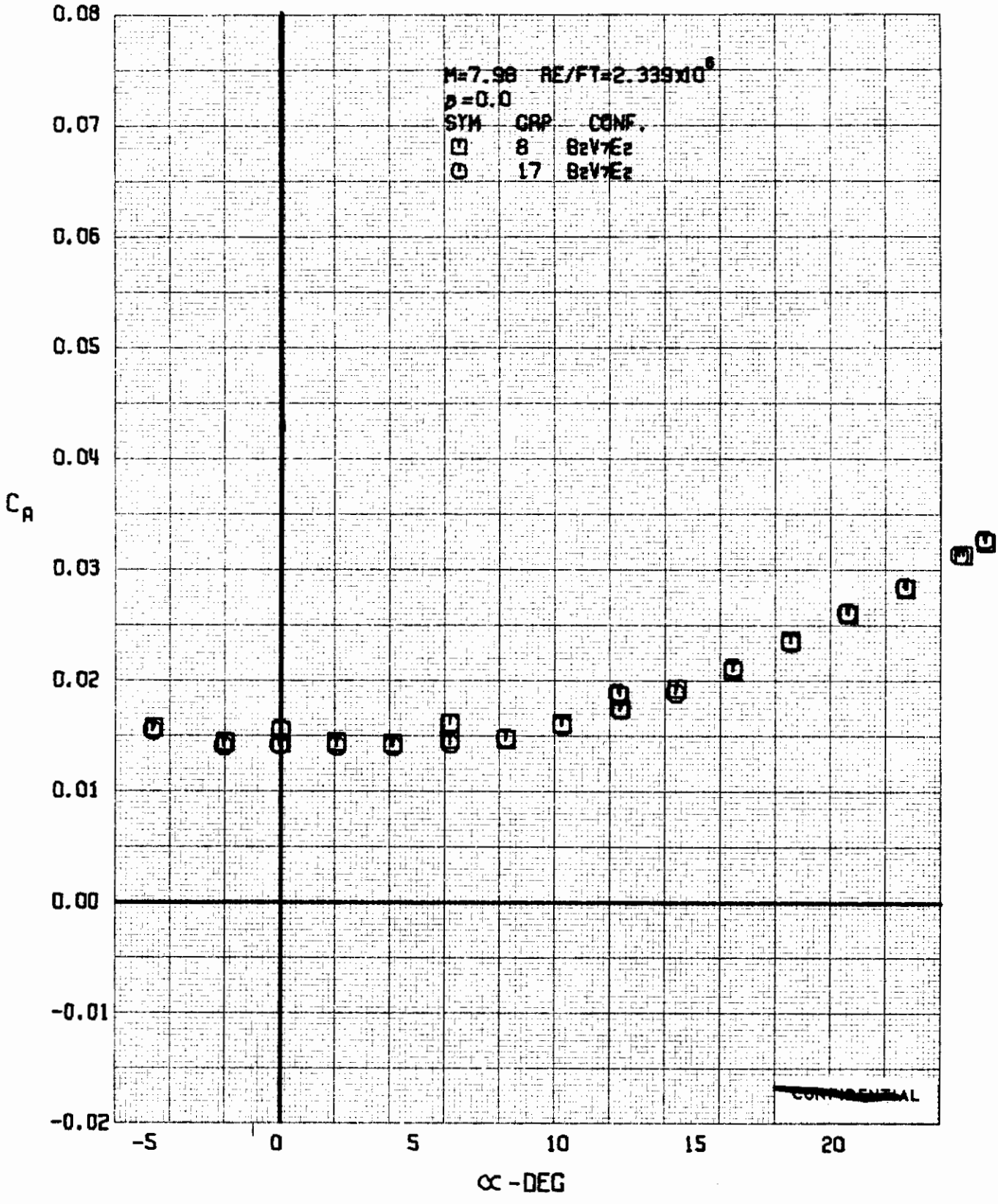

FIGURE 237 (U) REPEATABILITY
- AXIAL FORCE COEFFICIENT VARIATION WITH ANGLE OF ATTACK (M=7.98)

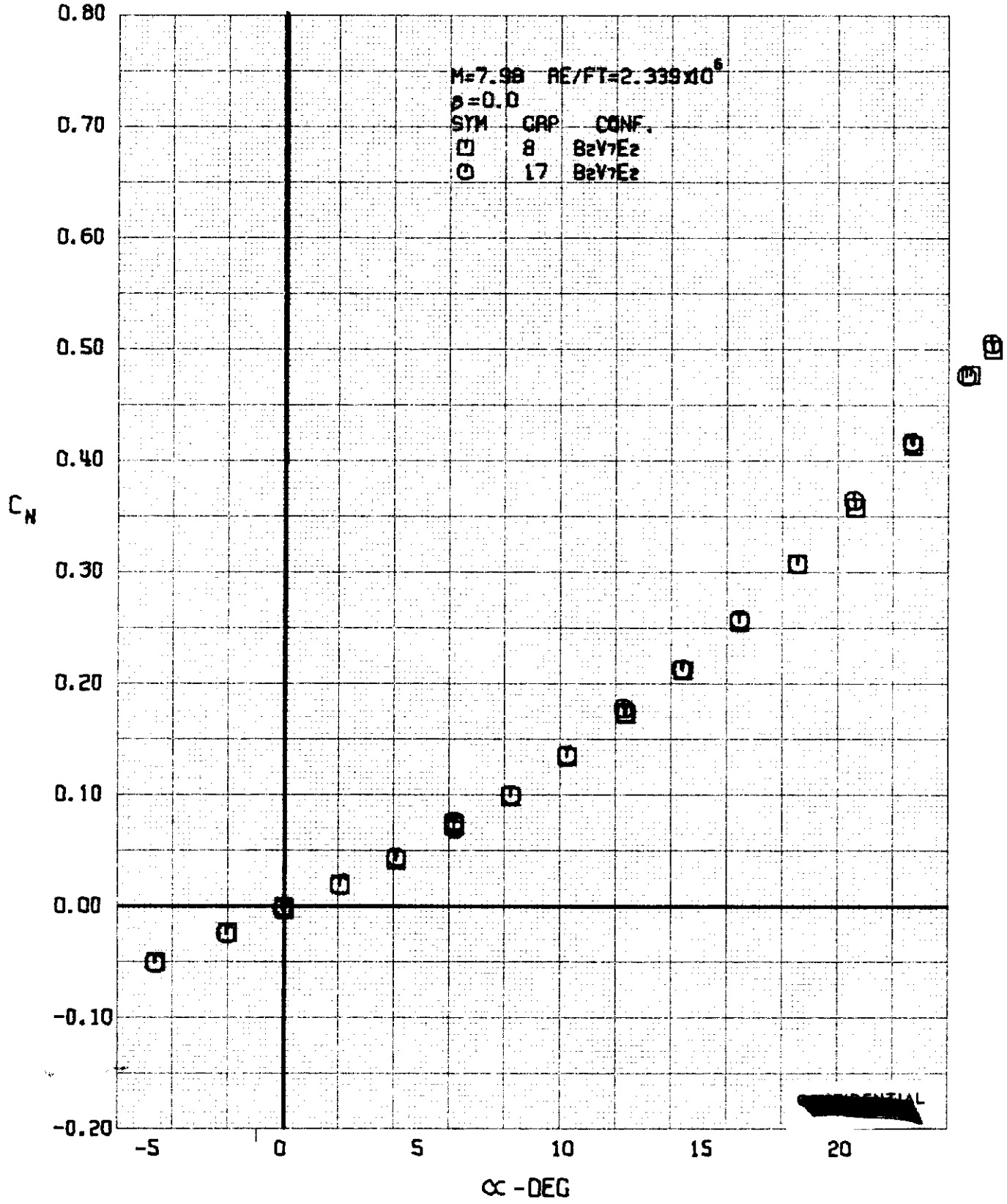

FIGURE 238 (U) REPEATABILITY
- NORMAL FORCE COEFFICIENT VARIATION WITH ANGLE OF ATTACK (M=7.98)

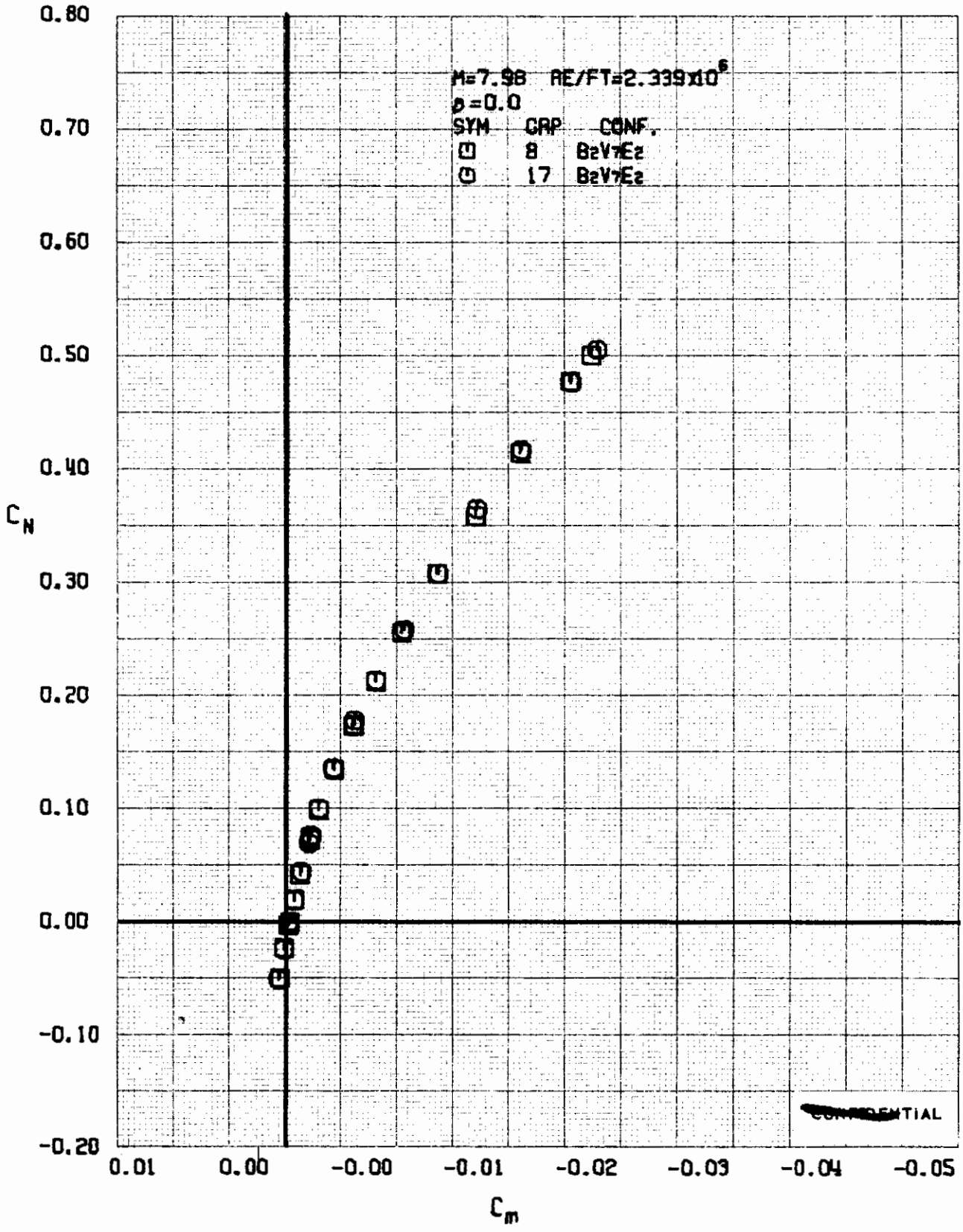

FIGURE 239 (U) REPEATABILITY
- LONGITUDINAL STABILITY VARIATION (M= 7.98)

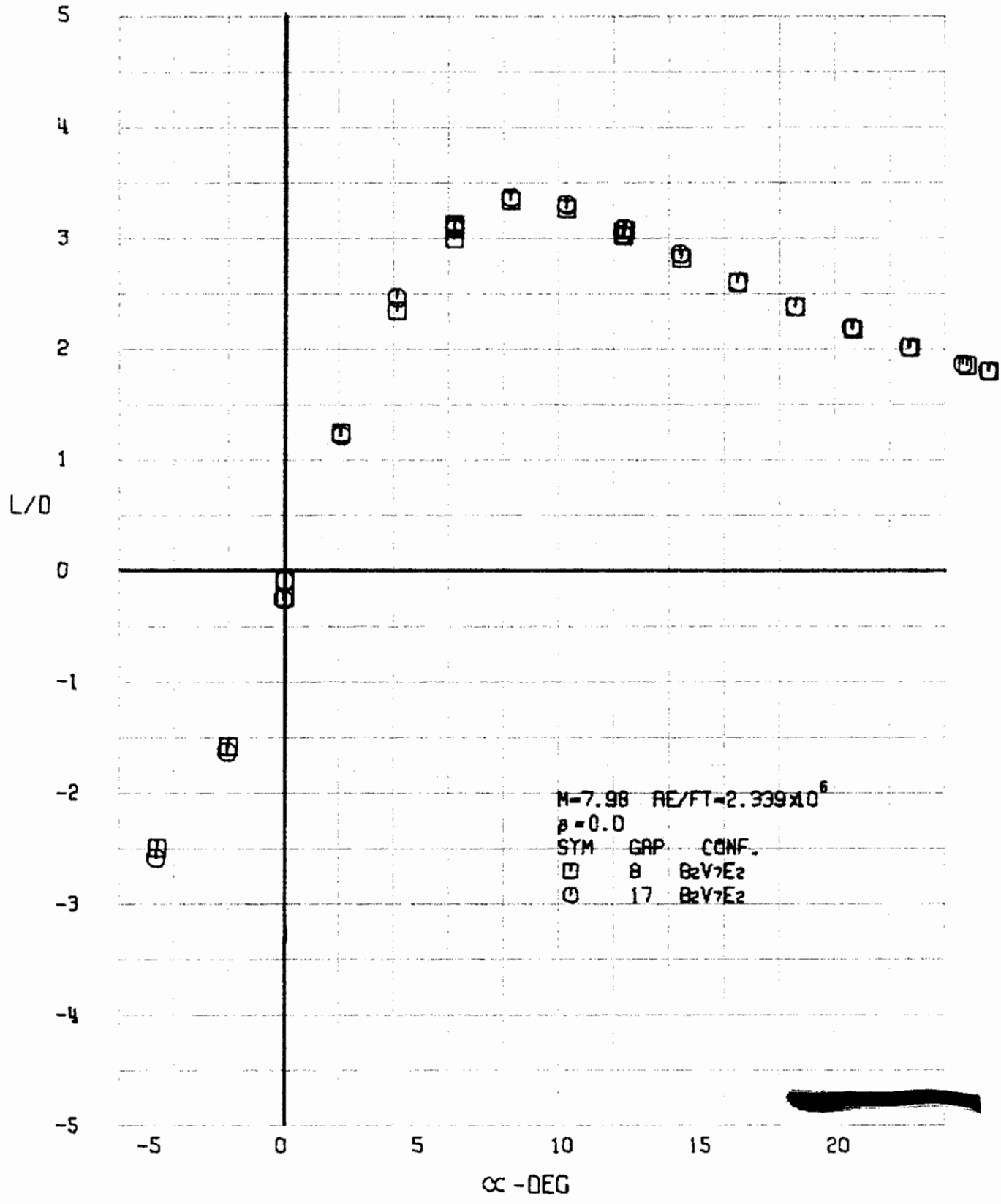

FIGURE 240 (U) REPEATABILITY
- LIFT-DRAG RATIO VARIATION WITH ANGLE OF ATTACK (M=7.98)

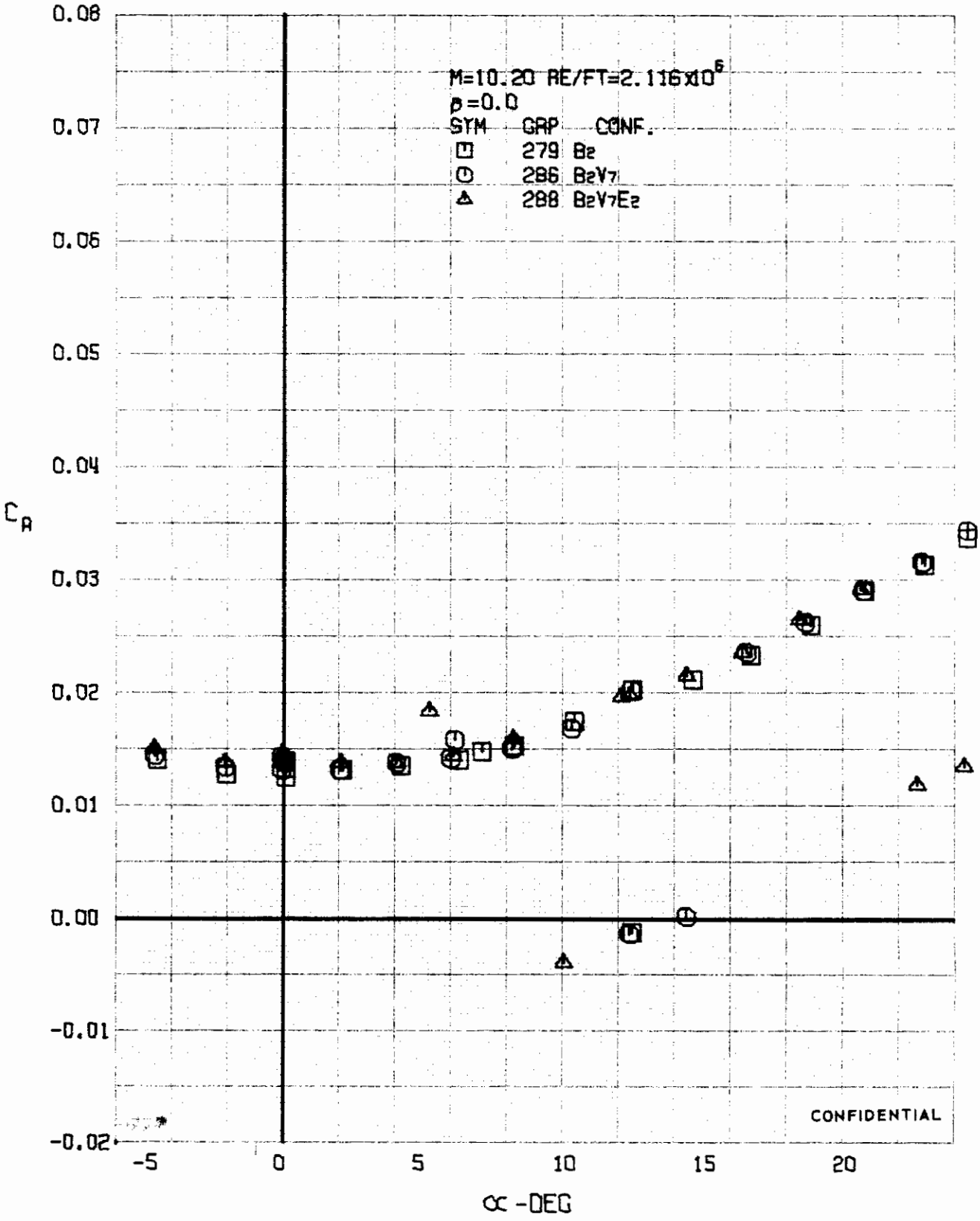

FIGURE 241 (U) CONFIGURATION BUILDUP
- AXIAL FORCE COEFFICIENT VARIATION WITH ANGLE OF ATTACK (M=10.20

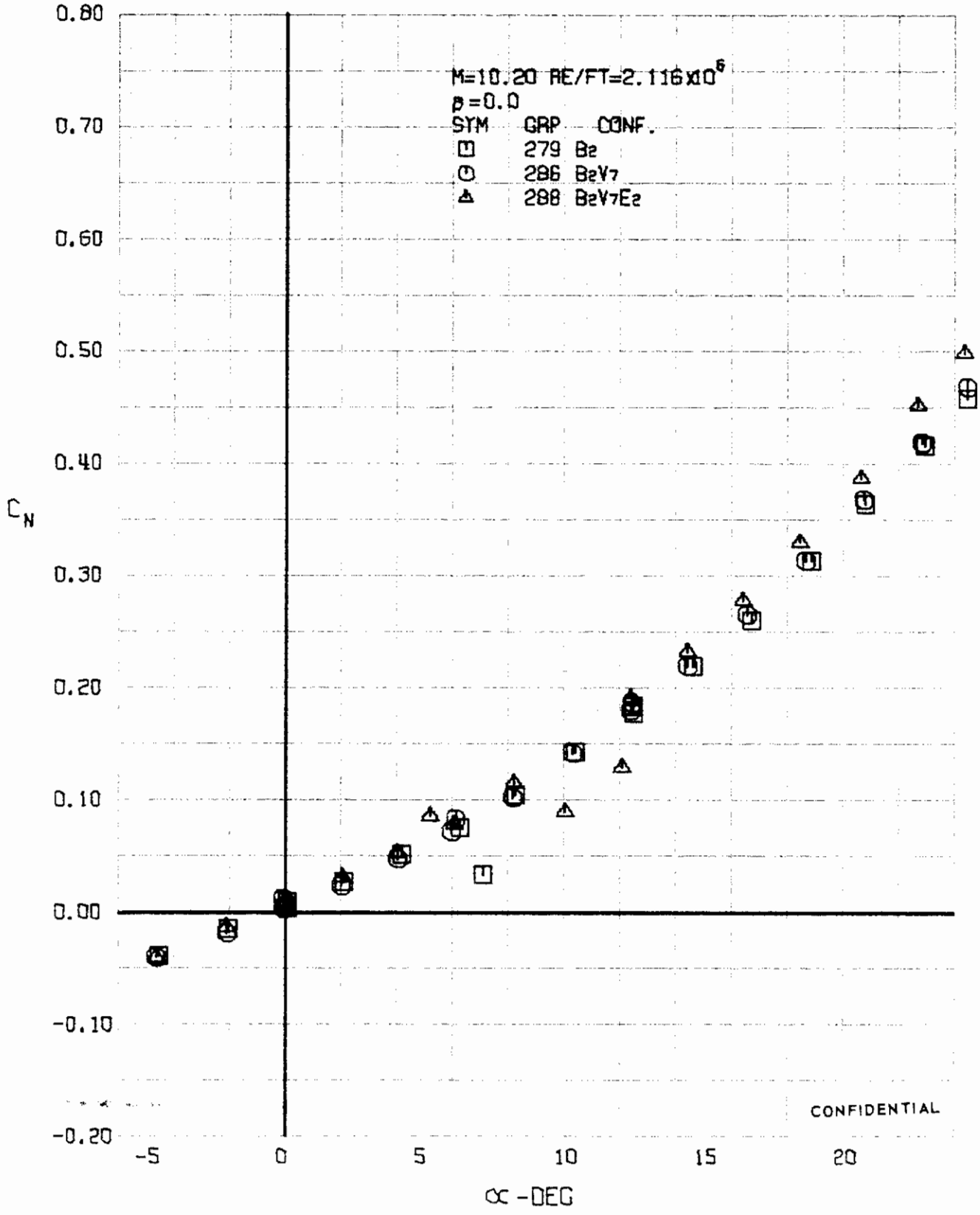

FIGURE 242 (U) CONFIGURATION BUILDUP
- NORMAL FORCE COEFFICIENT VARIATION WITH ANGLE OF ATTACK (M=10.20

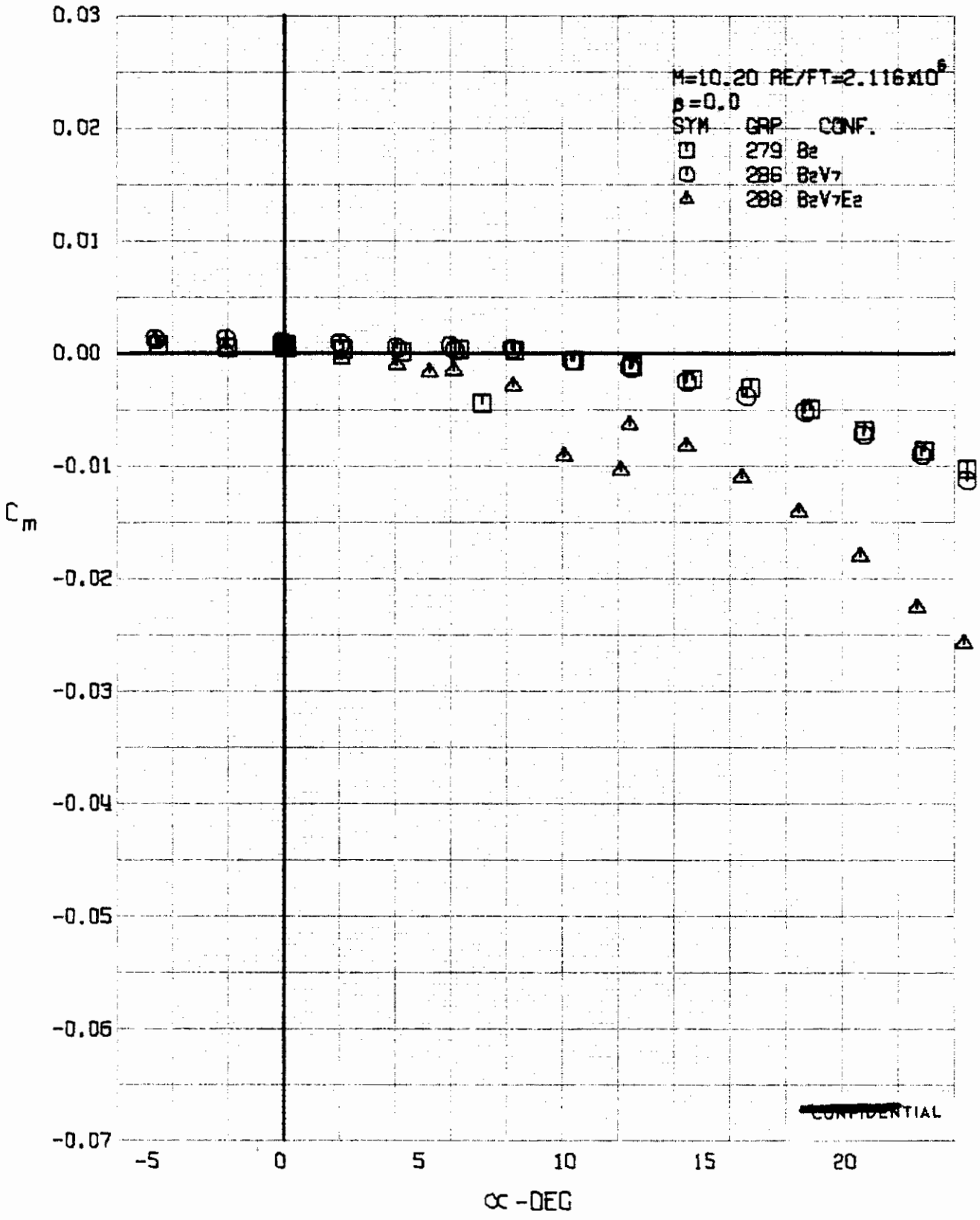

FIGURE 243 (U) CONFIGURATION BUILDUP
- PITCHING MOMENT COEFFICIENT VARIATION WITH ANGLE OF ATTACK (M=10.20

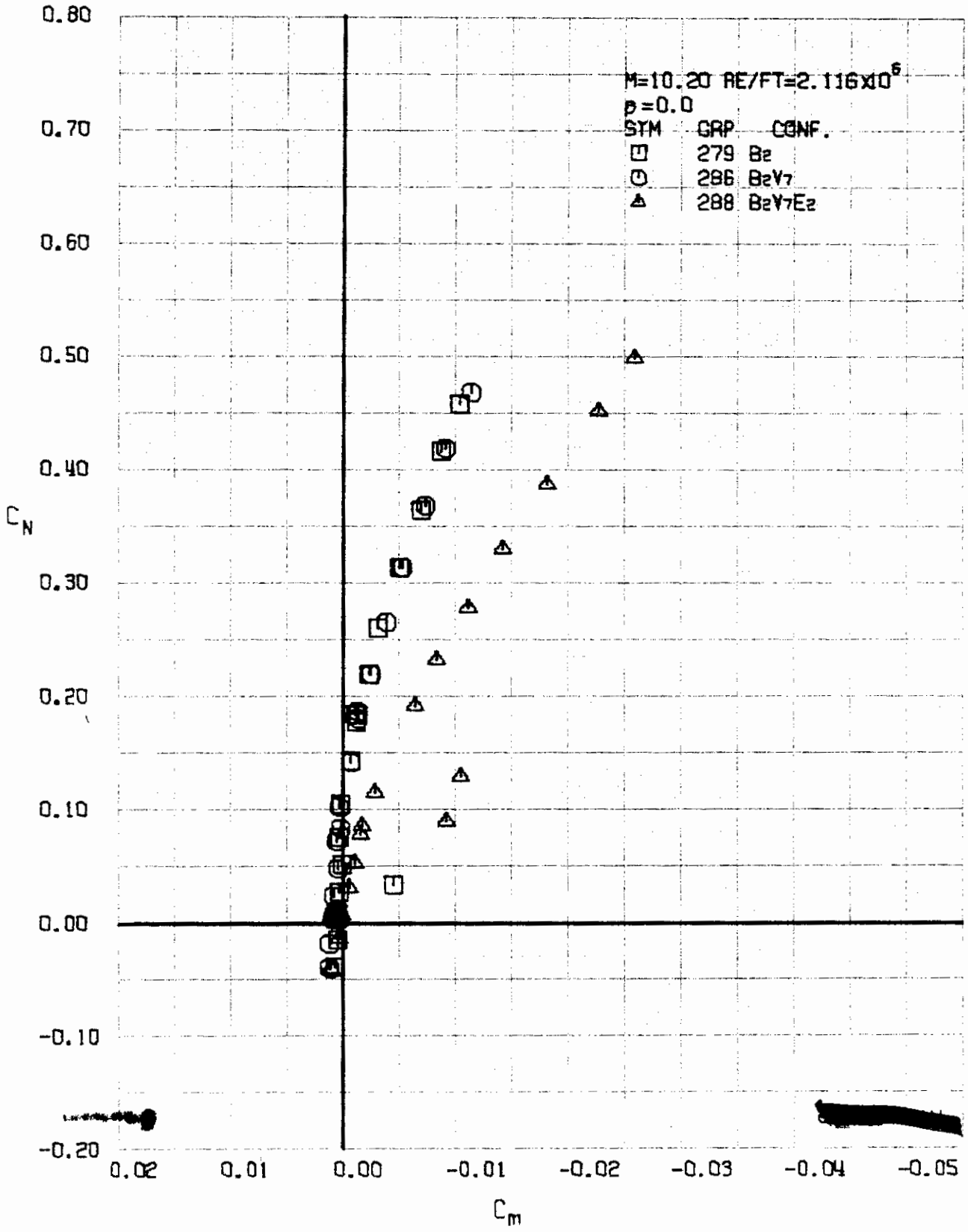

FIGURE 244 (U) CONFIGURATION BUILDUP
- LONGITUDINAL STABILITY VARIATION (M=10.20

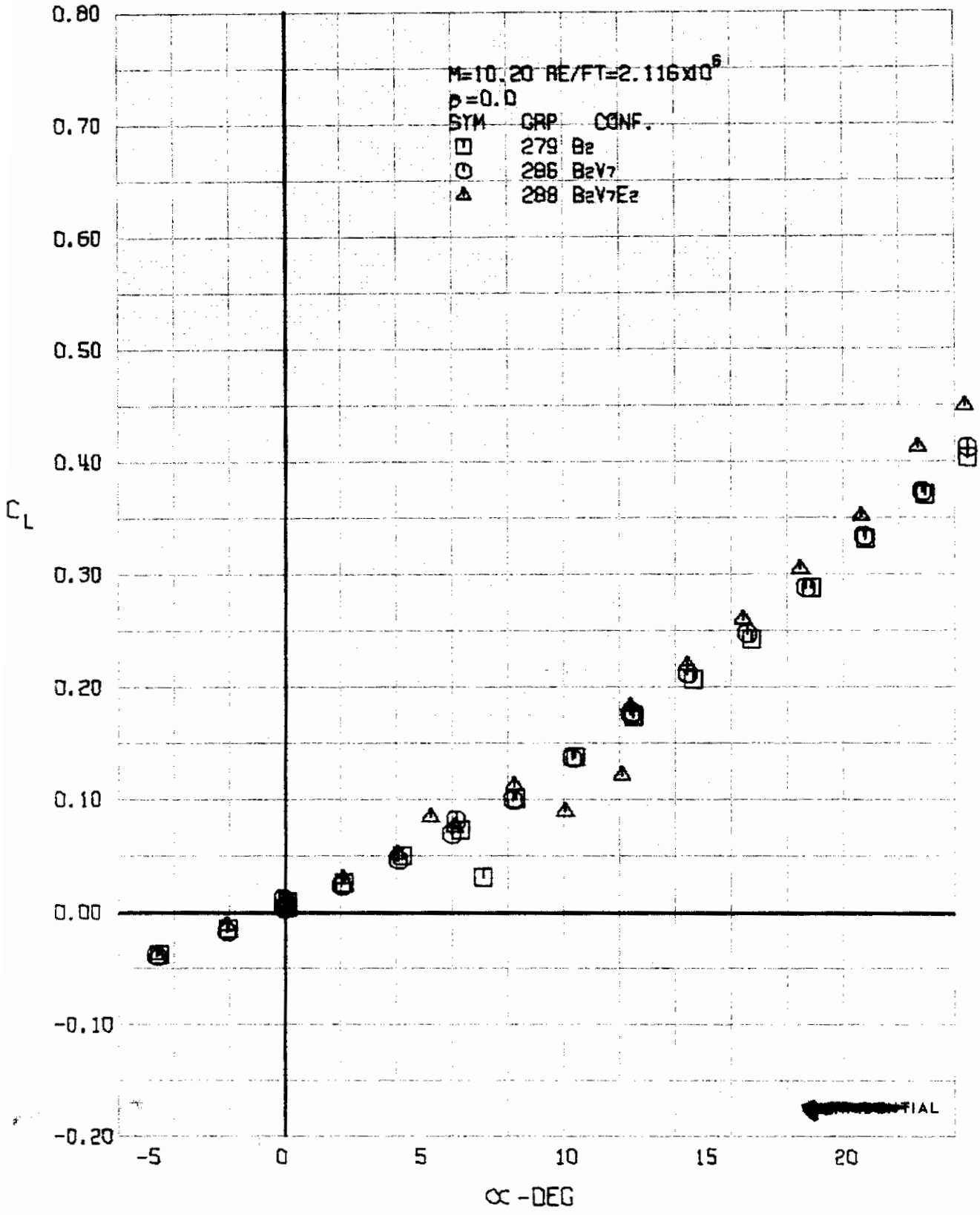

FIGURE 245 (U) CONFIGURATION BUILDUP
- LIFT COEFFICIENT VARIATION WITH ANGLE OF ATTACK (M=10.20

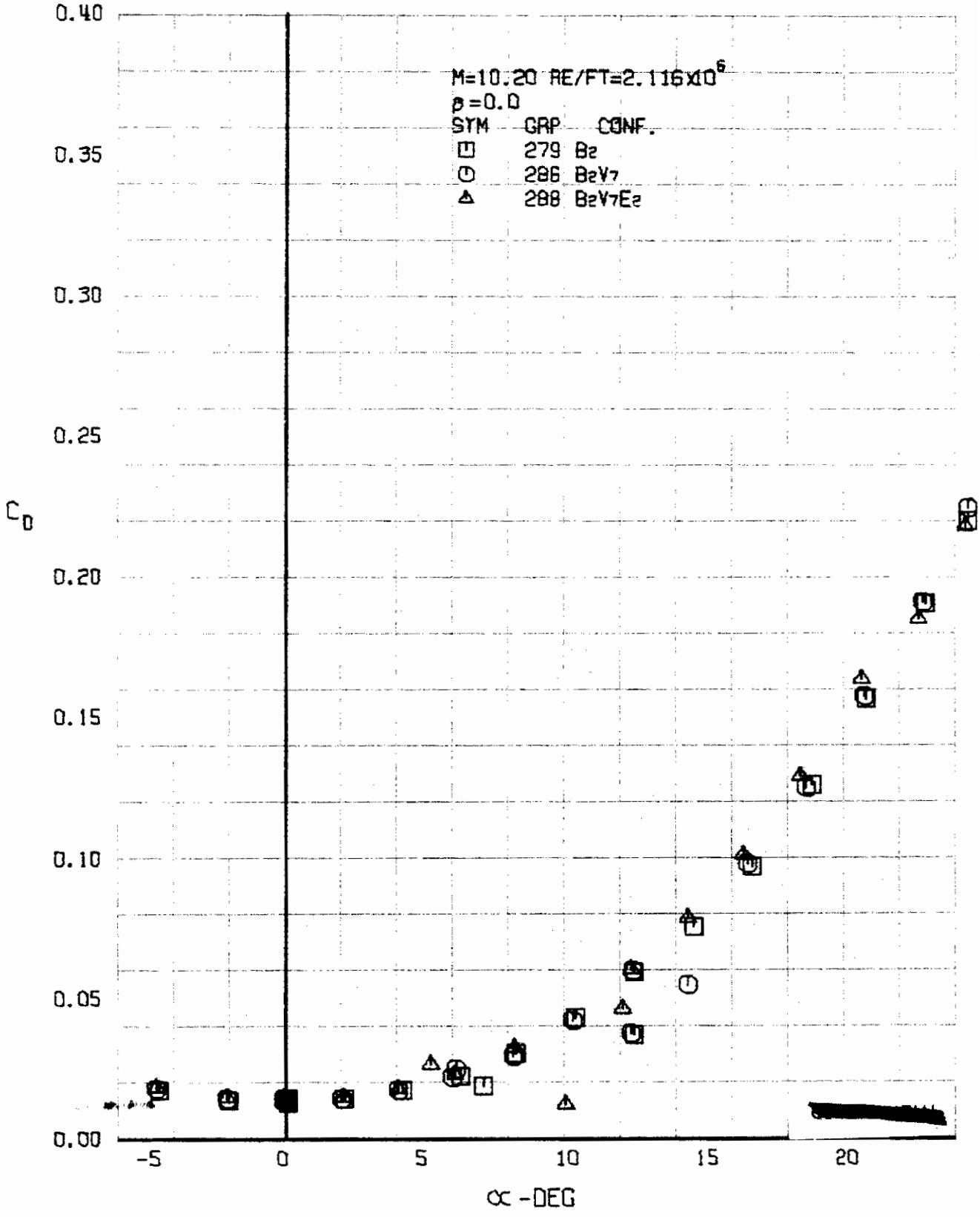

FIGURE 246 (U) CONFIGURATION BUILDUP
- DRAG COEFFICIENT VARIATION WITH ANGLE OF ATTACK (M=10.20

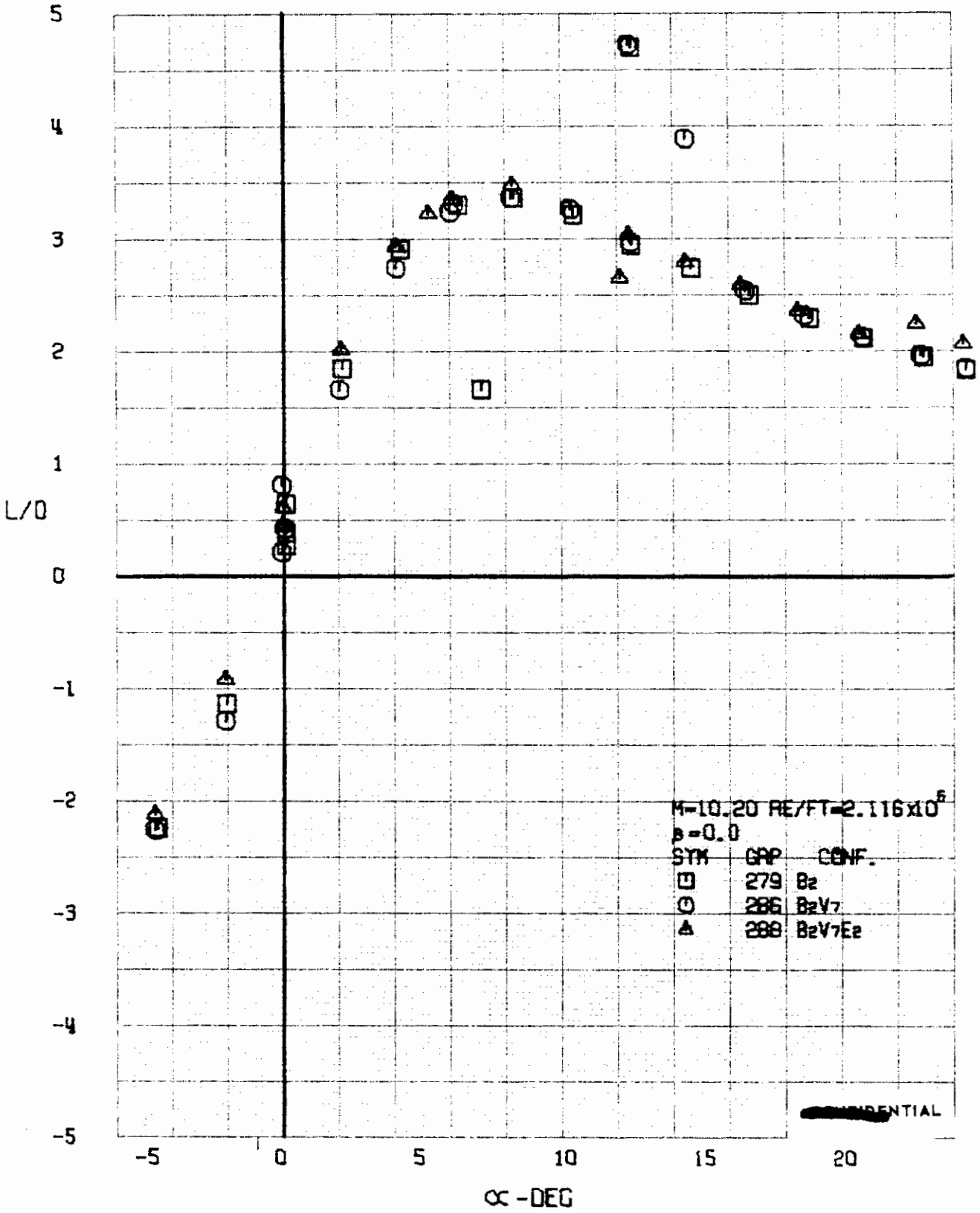

FIGURE 247 (U) CONFIGURATION BUILDUP
- LIFT-DRAG RATIO VARIATION WITH ANGLE OF ATTACK (M=10.20

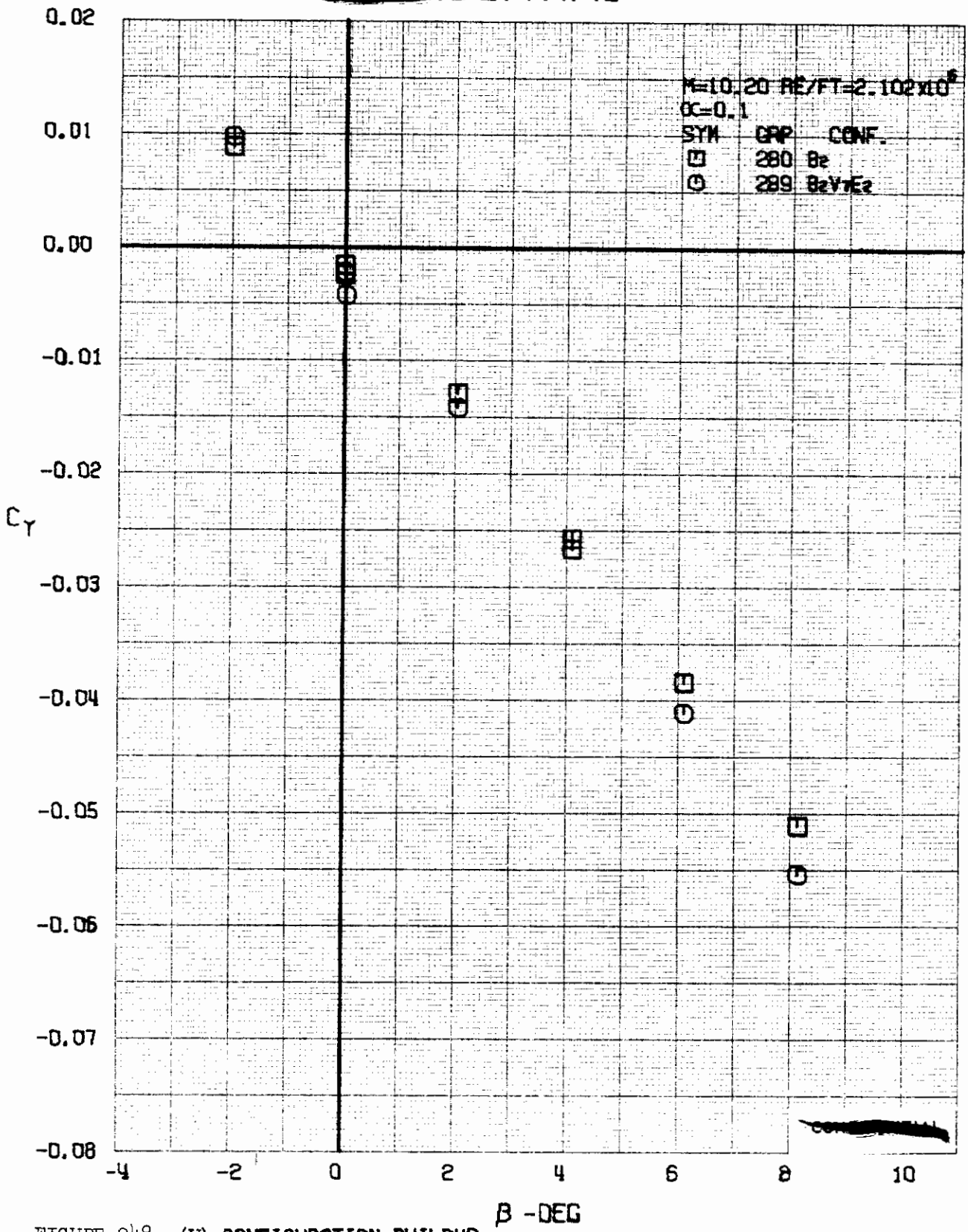

FIGURE 248 (U) CONFIGURATION BUILDUP
- SIDE FORCE COEFFICIENT VARIATION WITH ANGLE OF YAW (M=10.20

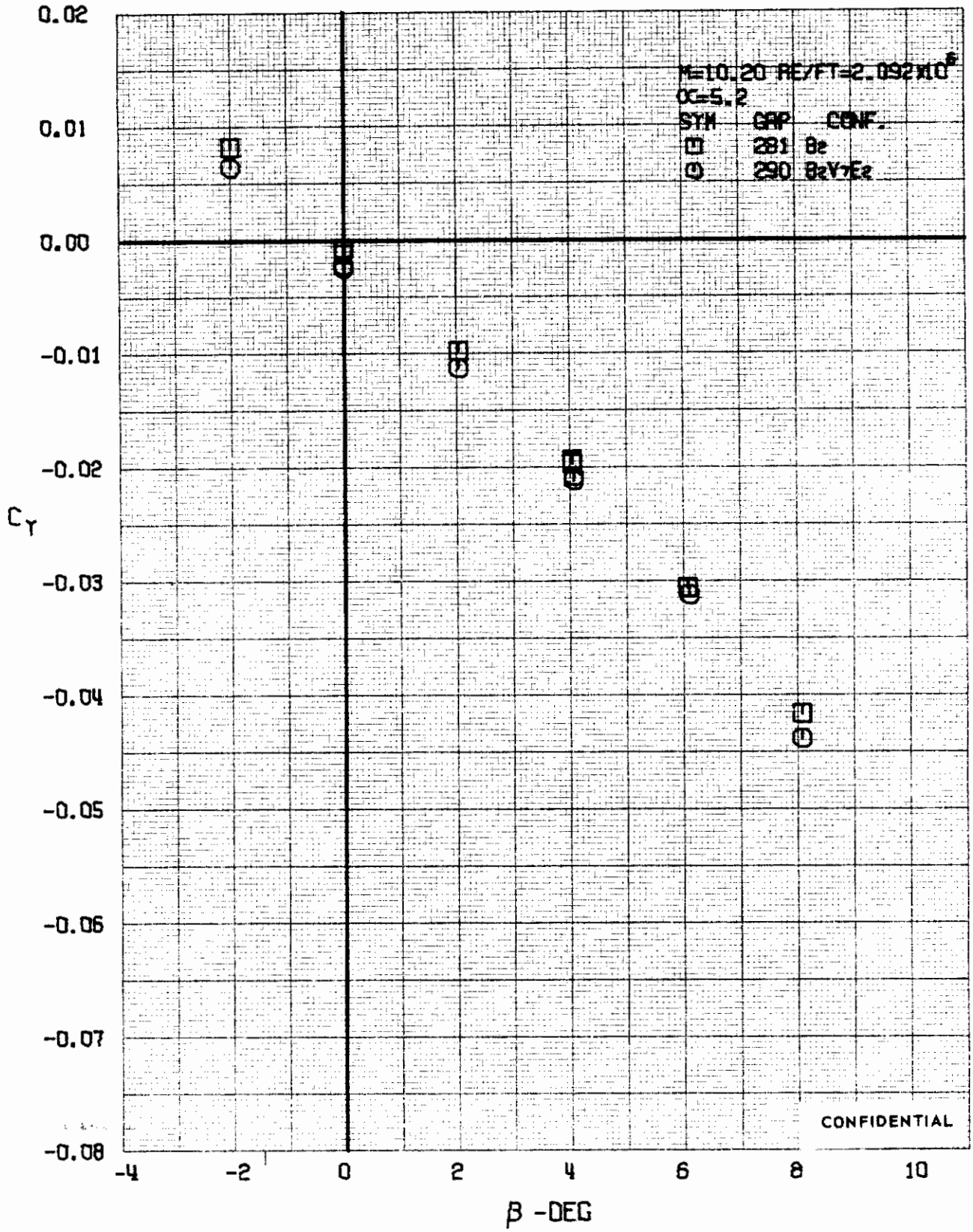

FIGURE 249 (U) CONFIGURATION BUILDUP
- SIDE FORCE COEFFICIENT VARIATION WITH ANGLE OF YAW (M=10.20

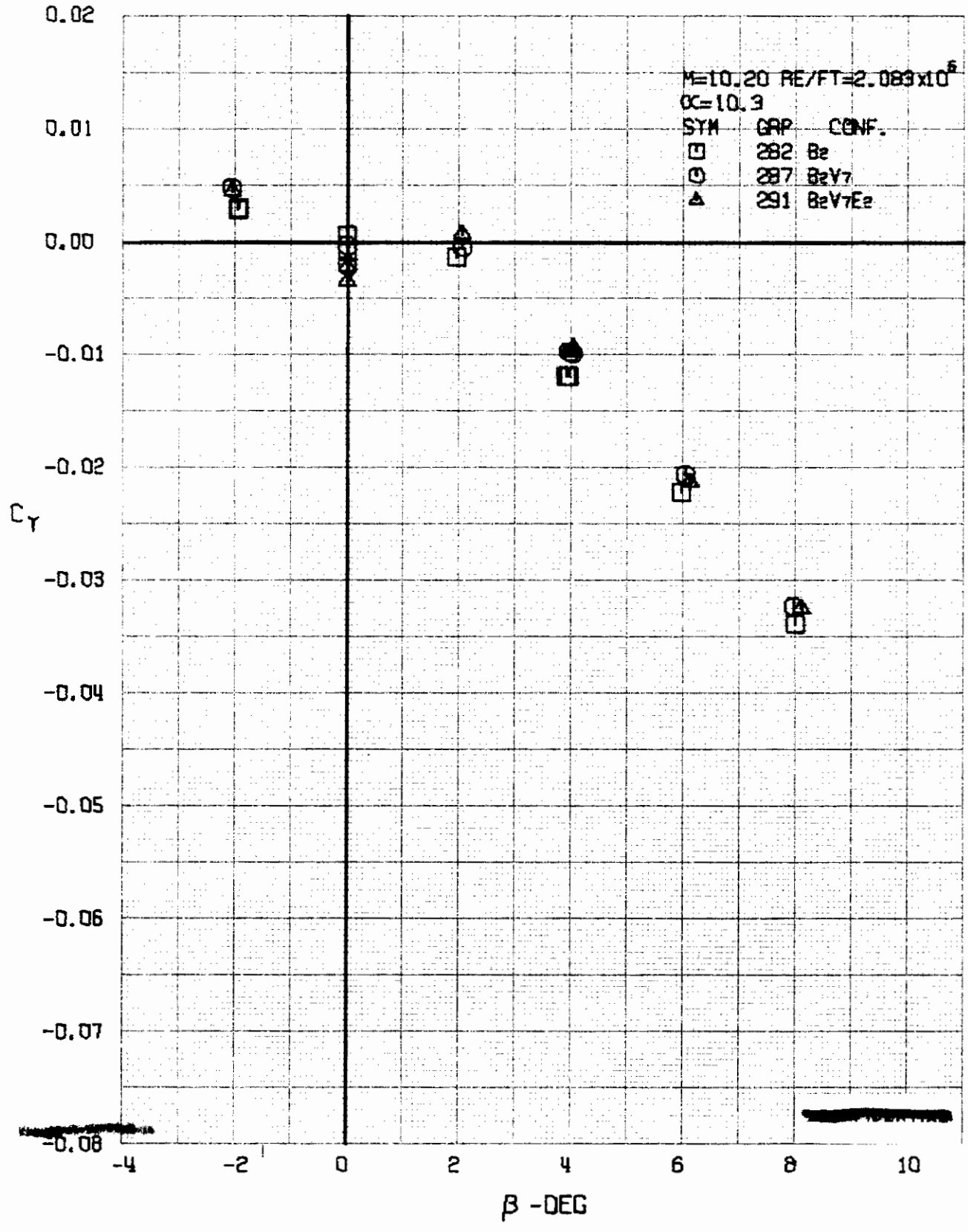

FIGURE 250 (U) CONFIGURATION BUILDUP
- SIDE FORCE COEFFICIENT VARIATION WITH ANGLE OF YAW (M=10.20

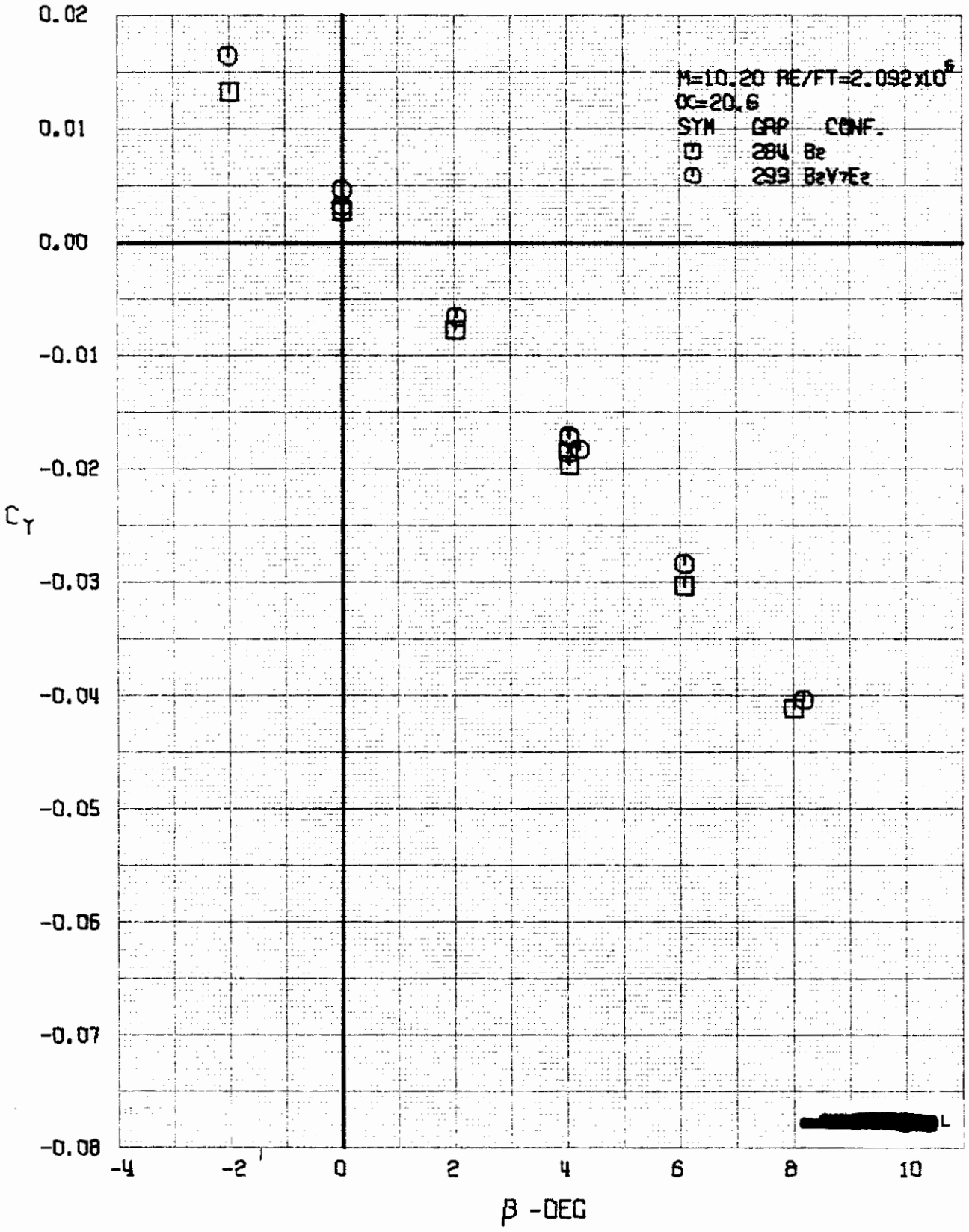

FIGURE 251 (U) CONFIGURATION BUILDUP
- SIDE FORCE COEFFICIENT VARIATION WITH ANGLE OF YAW (M= 10.20

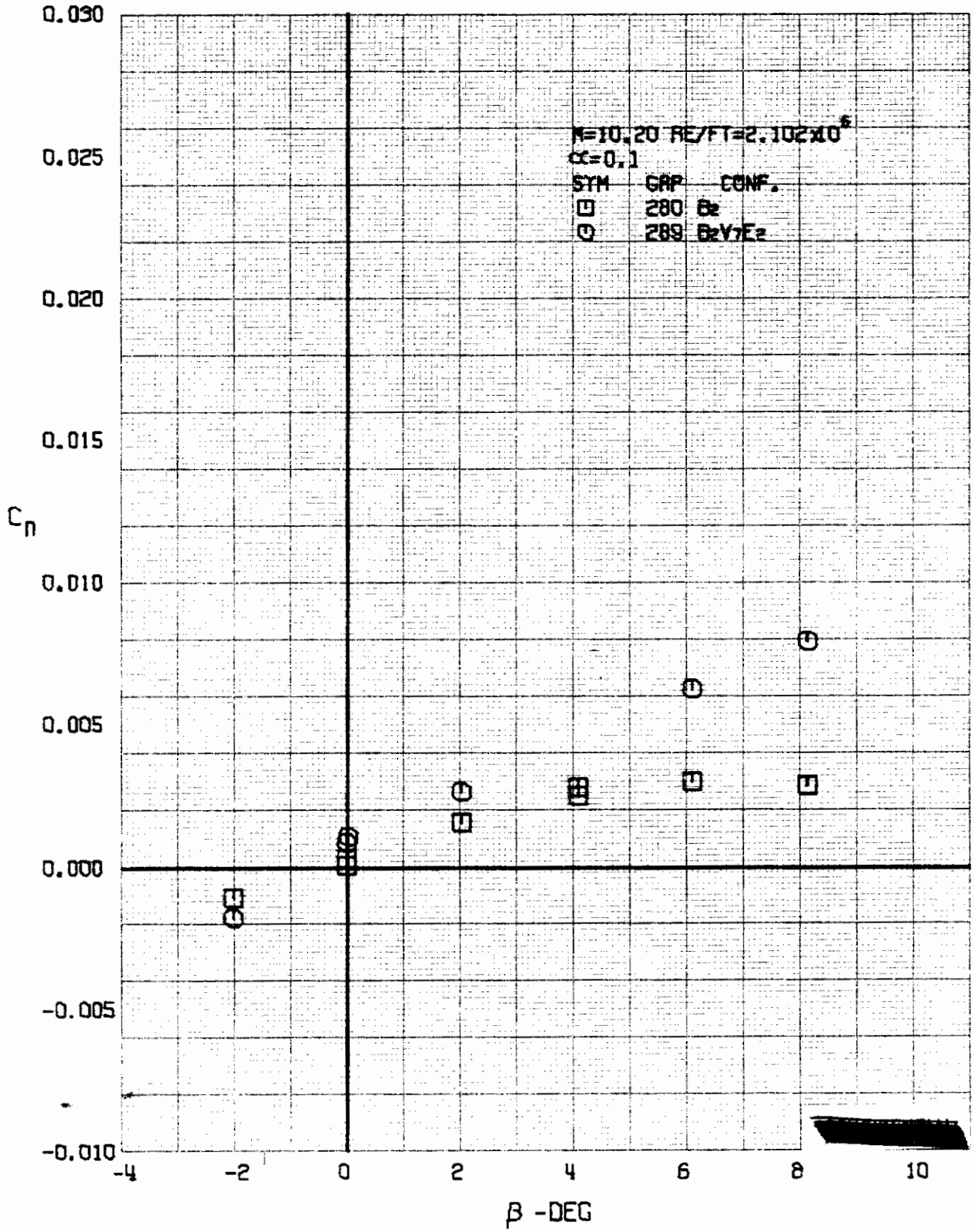

FIGURE 252 (U) CONFIGURATION BUILDUP
- YAWING MOMENT COEFFICIENT VARIATION WITH ANGLE OF YAW (M=10.20

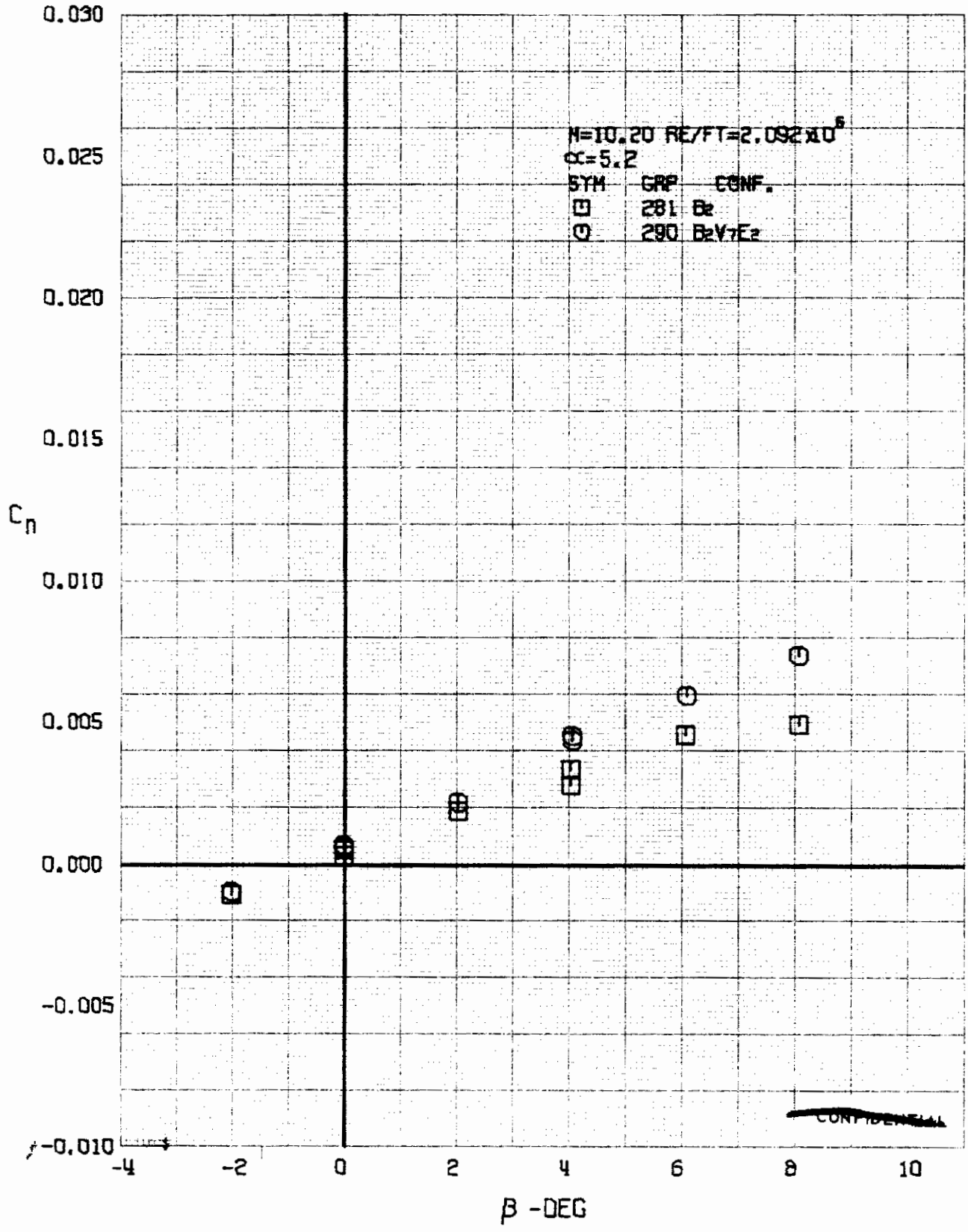

FIGURE 253 (U) CONFIGURATION BUILDUP
- YAWING MOMENT COEFFICIENT VARIATION WITH ANGLE OF YAW (M=10.20

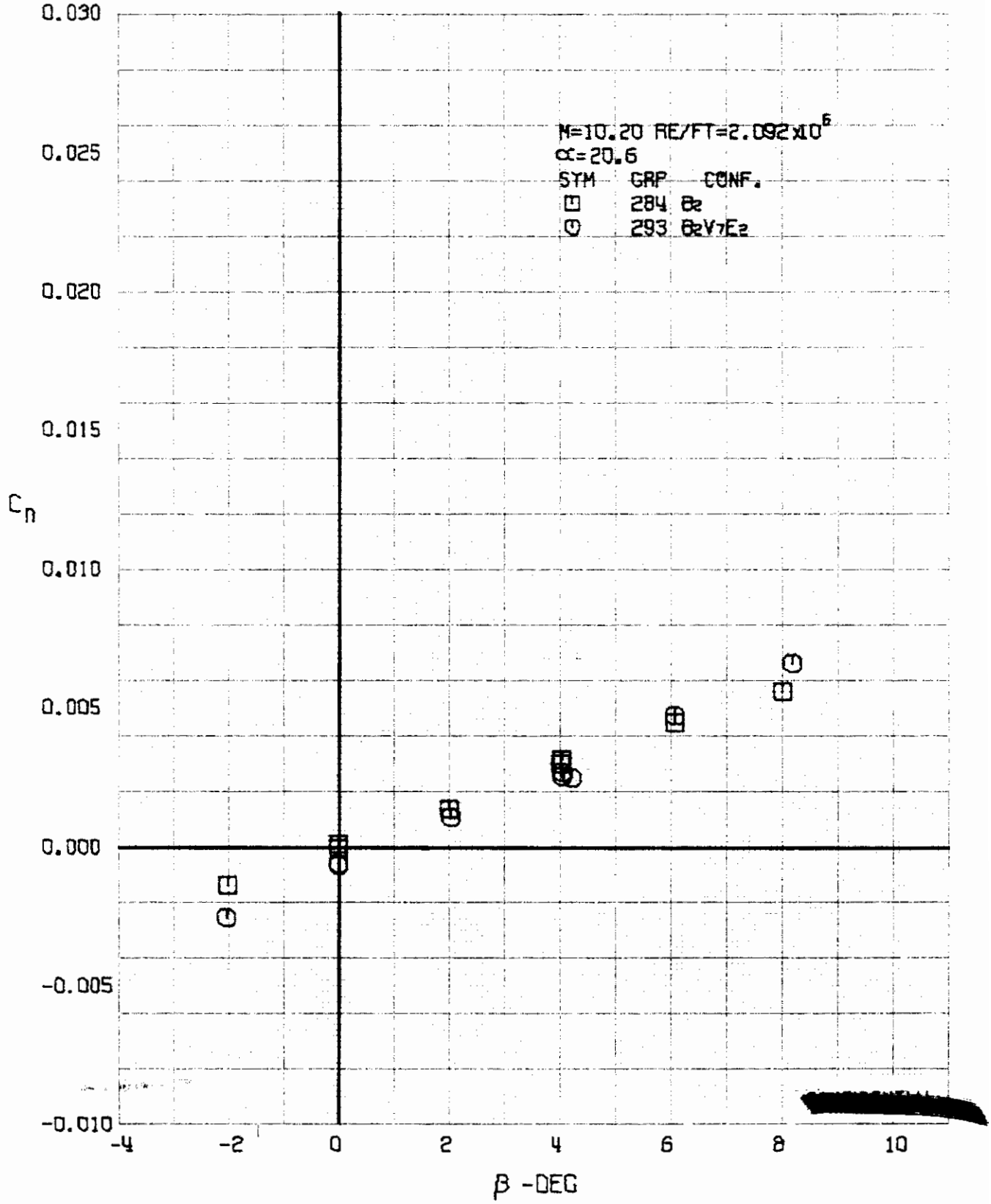

FIGURE 255 (U) CONFIGURATION BUILDUP
- YAWING MOMENT COEFFICIENT VARIATION WITH ANGLE OF YAW (M=10.20

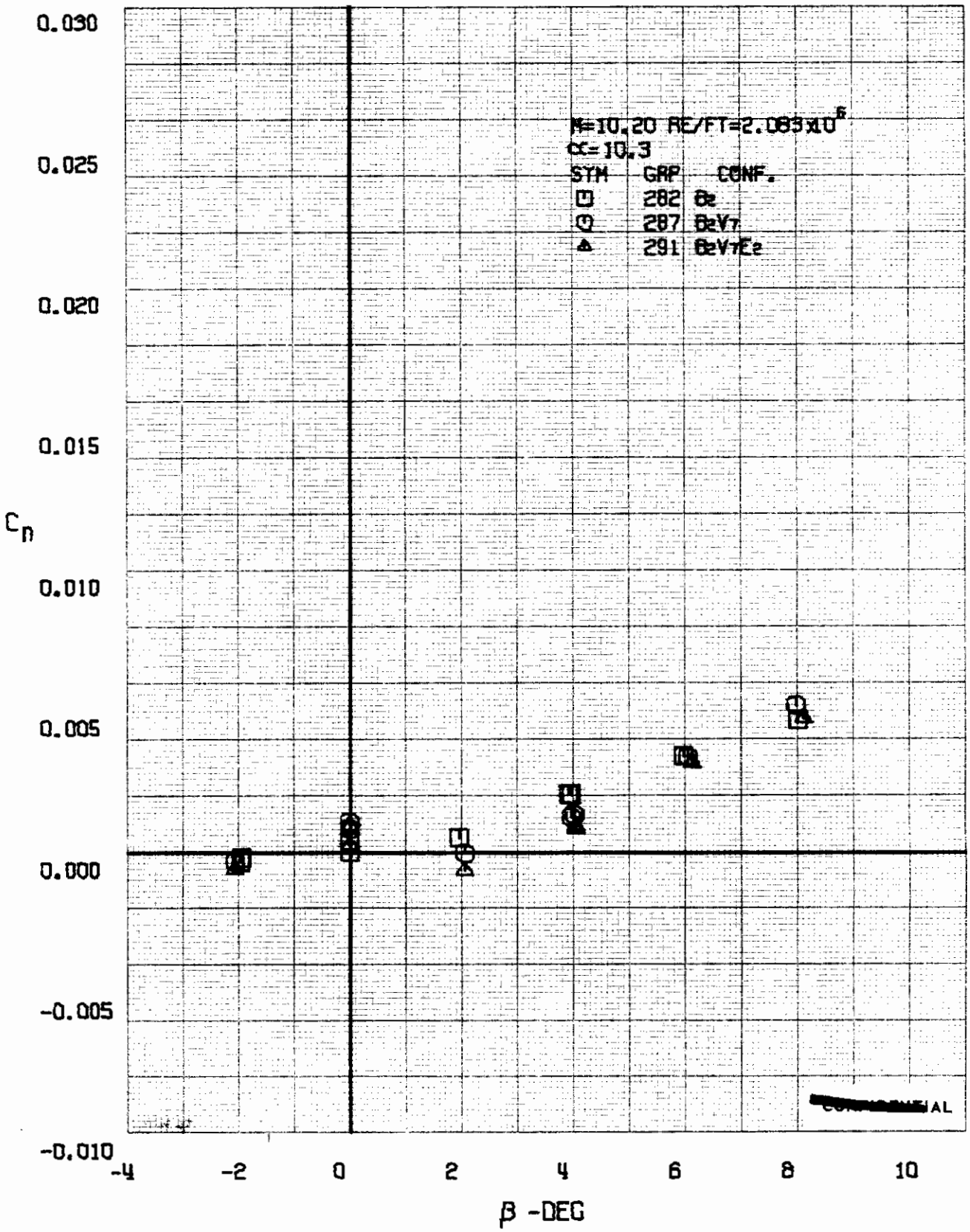

FIGURE 254 (U) CONFIGURATION BUILDUP
- YAWING MOMENT COEFFICIENT VARIATION WITH ANGLE OF YAW (M=10.20

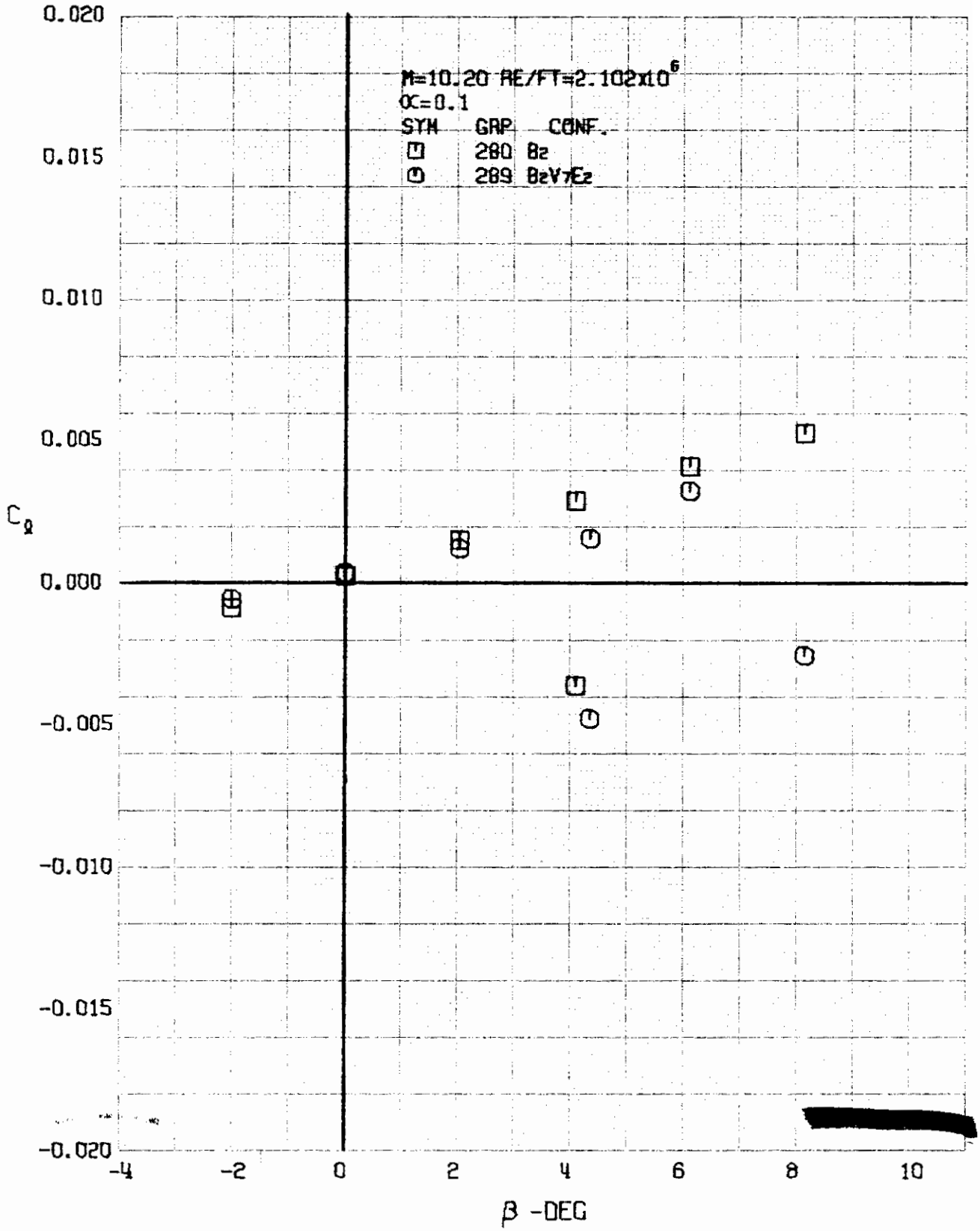

FIGURE 256 (U) CONFIGURATION BUILDUP
- ROLLING MOMENT COEFFICIENT VARIATION WITH ANGLE OF YAW (M=10.20

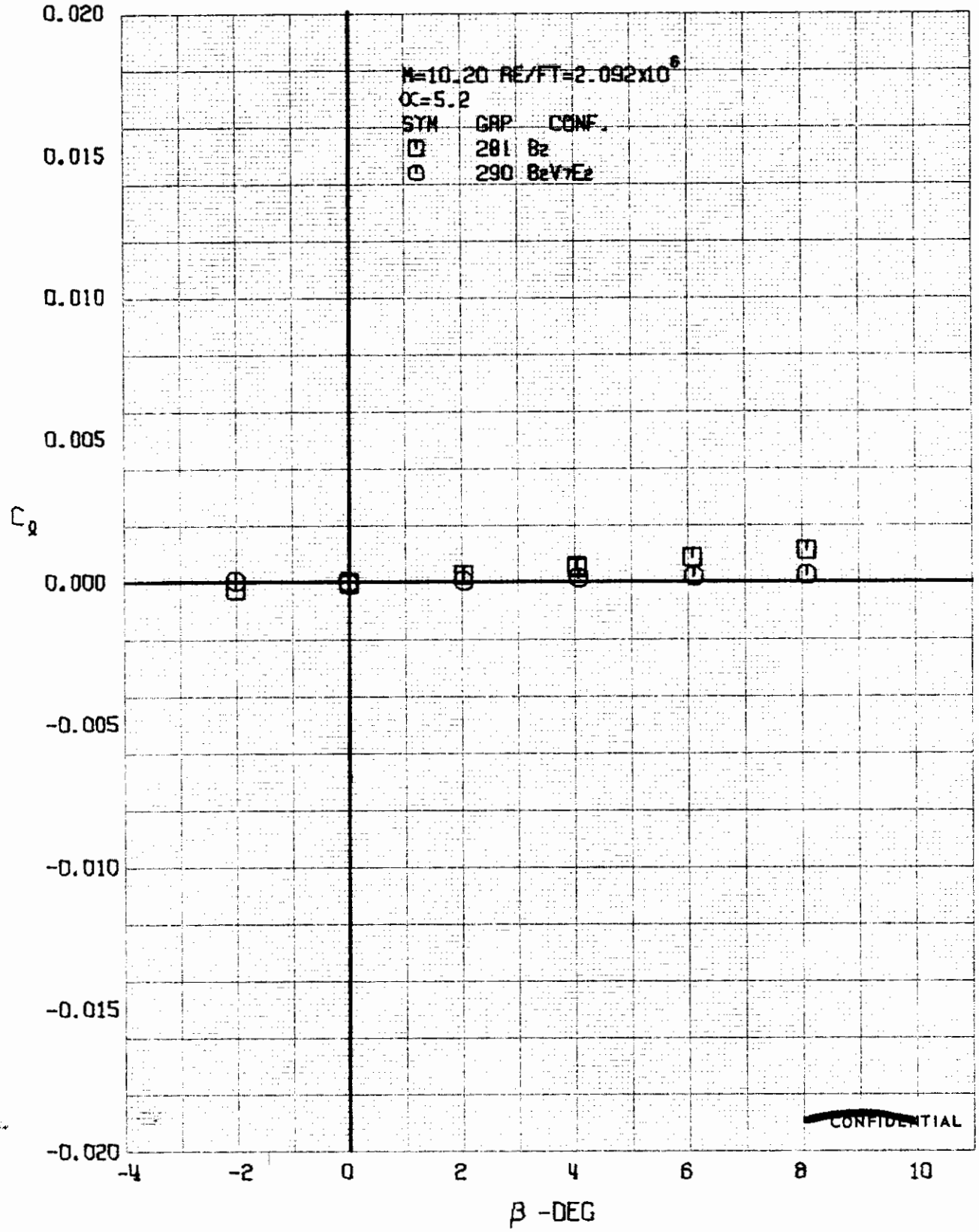

FIGURE 257 (U) CONFIGURATION BUILDUP
- ROLLING MOMENT COEFFICIENT VARIATION WITH ANGLE OF YAW (M=10.20

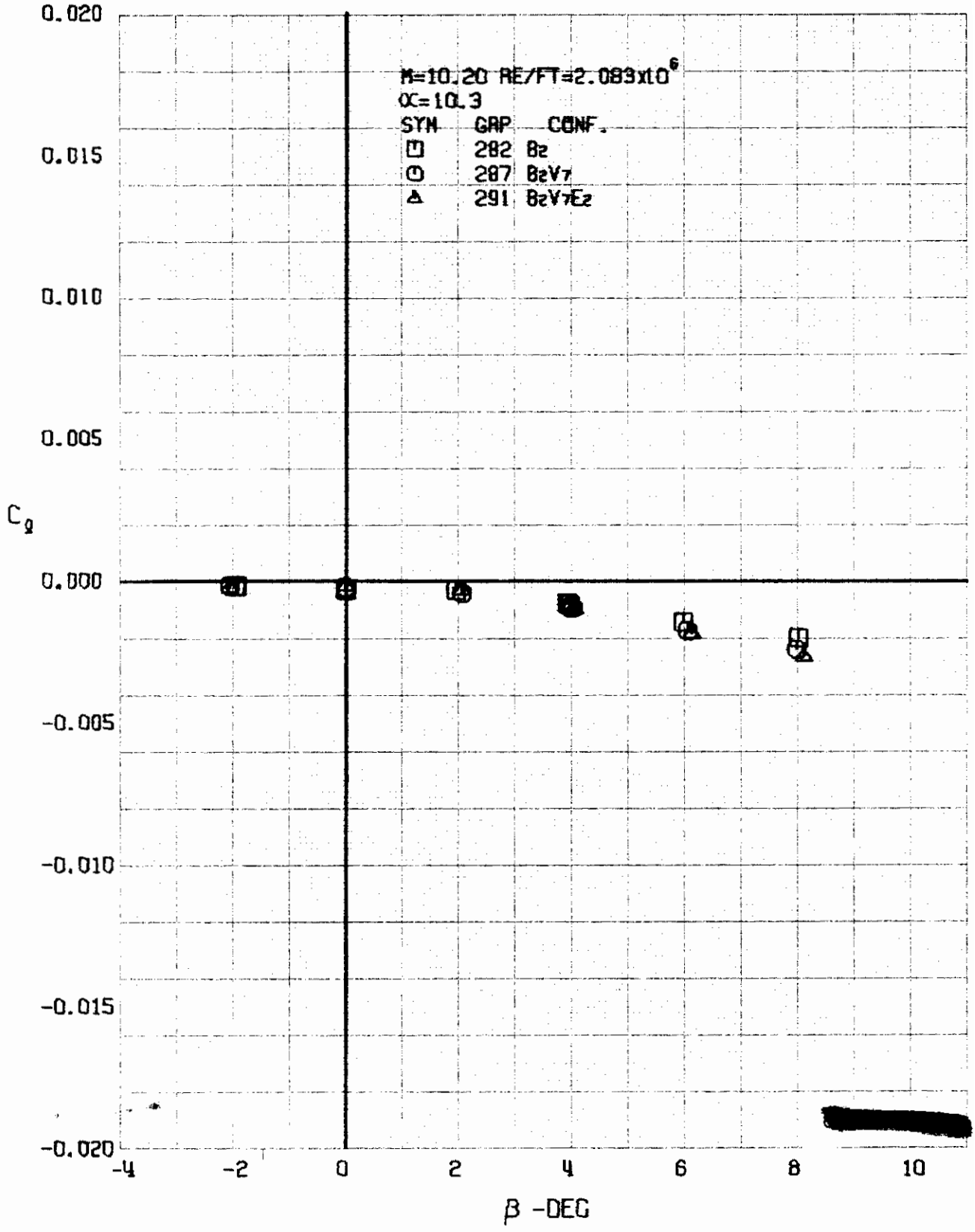

FIGURE 258 (U) CONFIGURATION BUILDUP
- ROLLING MOMENT COEFFICIENT VARIATION WITH ANGLE OF YAW (M=10.20

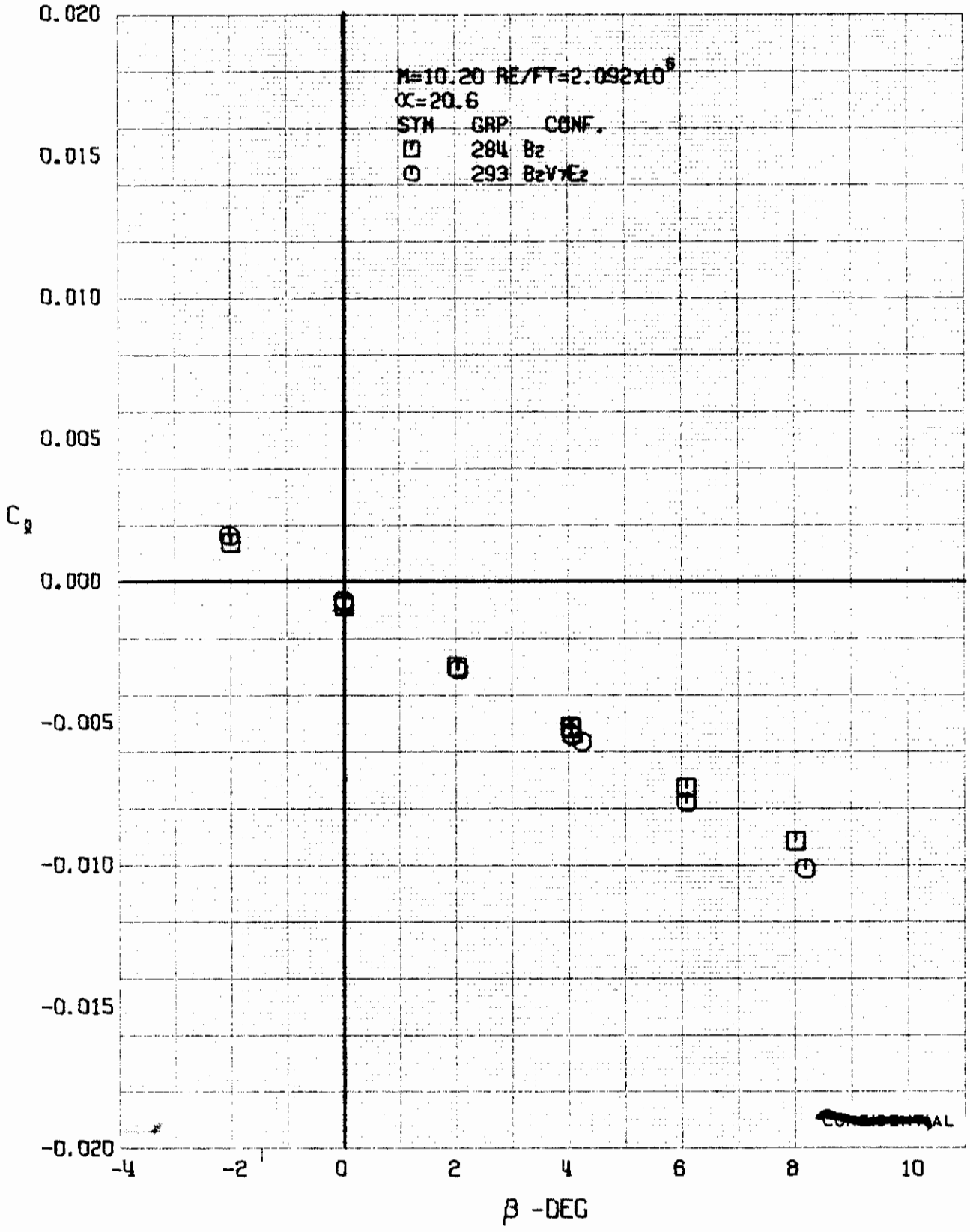

FIGURE 259 (U) CONFIGURATION BUILDUP
- ROLLING MOMENT COEFFICIENT VARIATION WITH ANGLE OF YAW (M=10.20

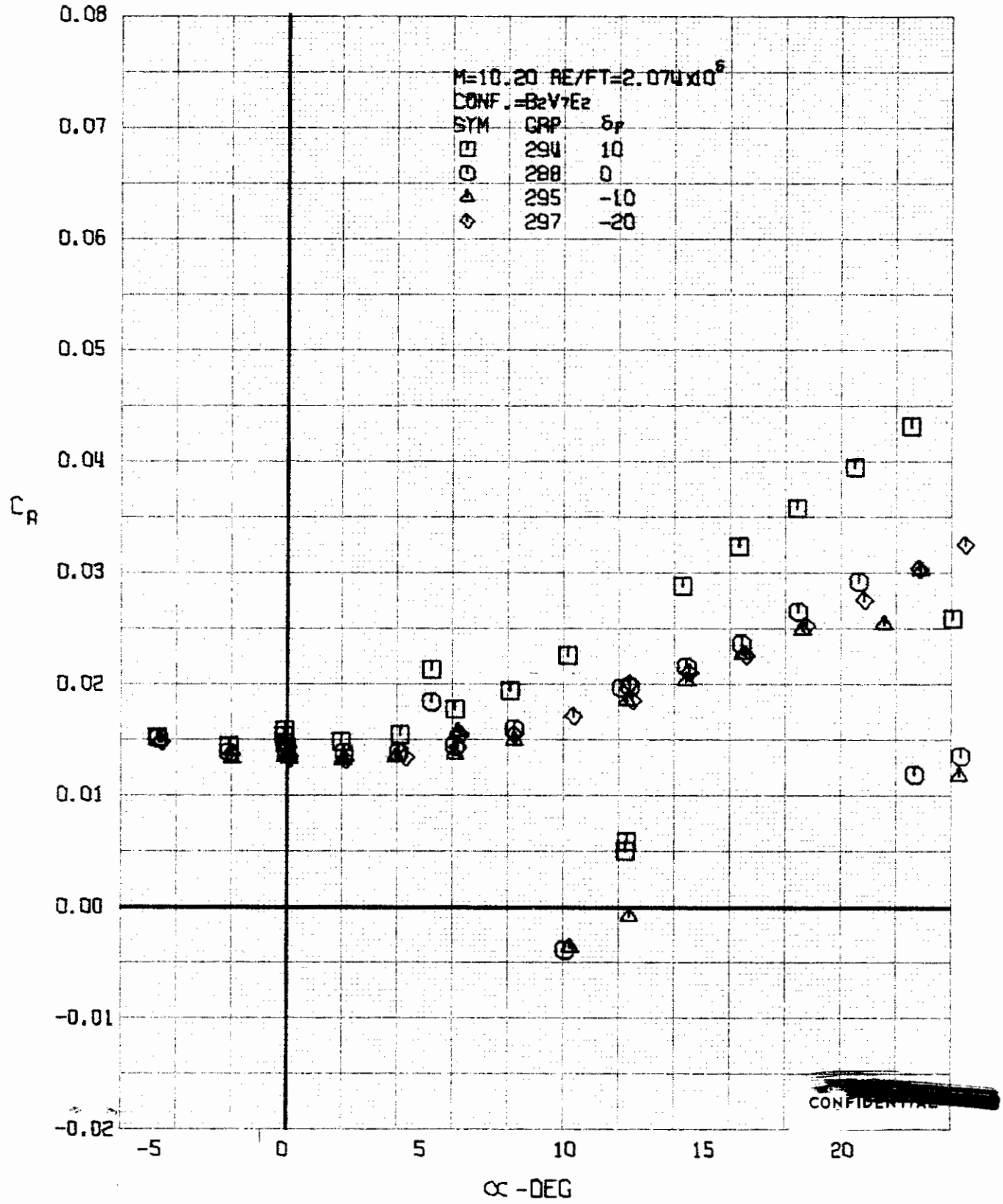

FIGURE 260 (U) ELEVON EFFECTS
- AXIAL FORCE COEFFICIENT VARIATION WITH ANGLE OF ATTACK (M=10.20

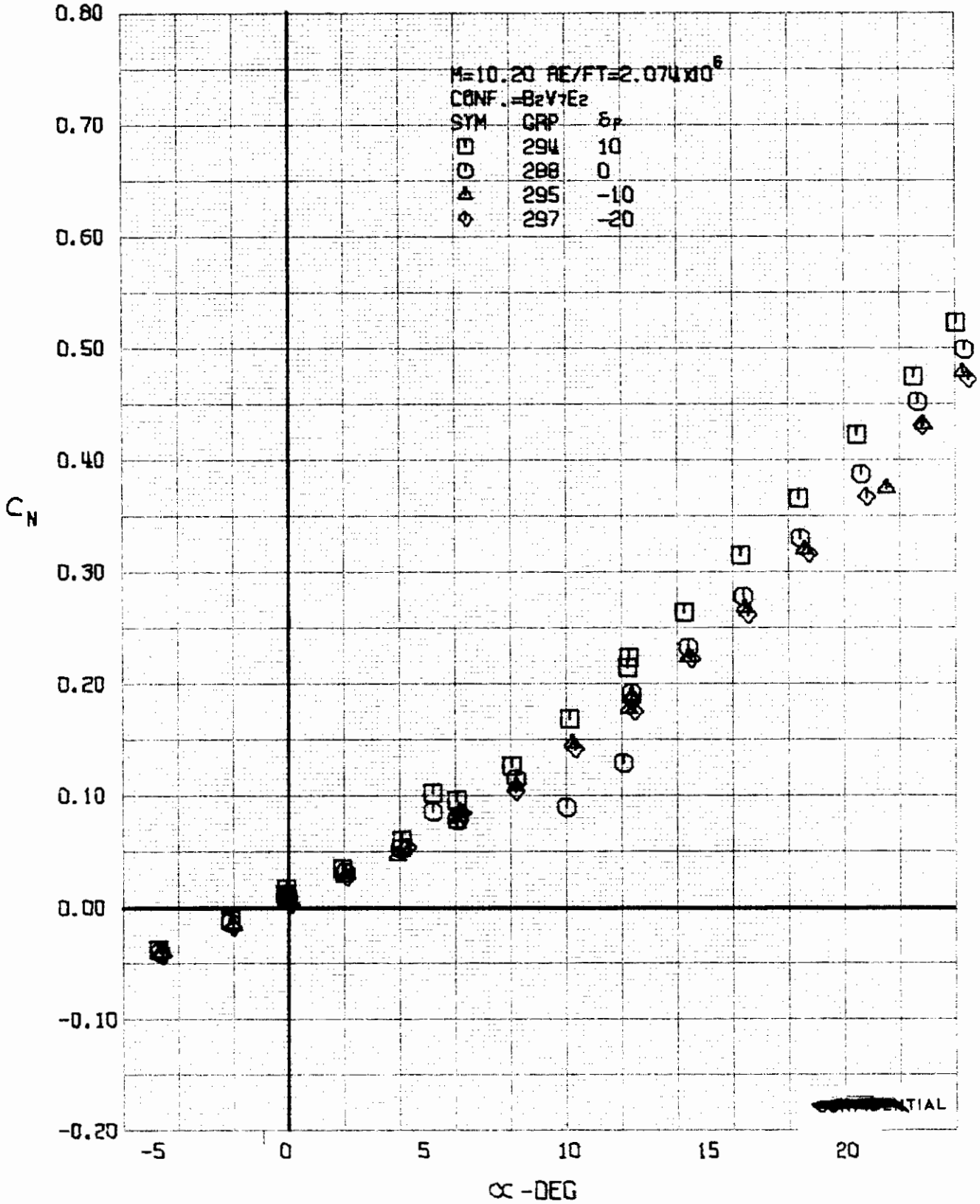

FIGURE 261 (U) ELEVON EFFECTS
- NORMAL FORCE COEFFICIENT VARIATION WITH ANGLE OF ATTACK (M=10.20

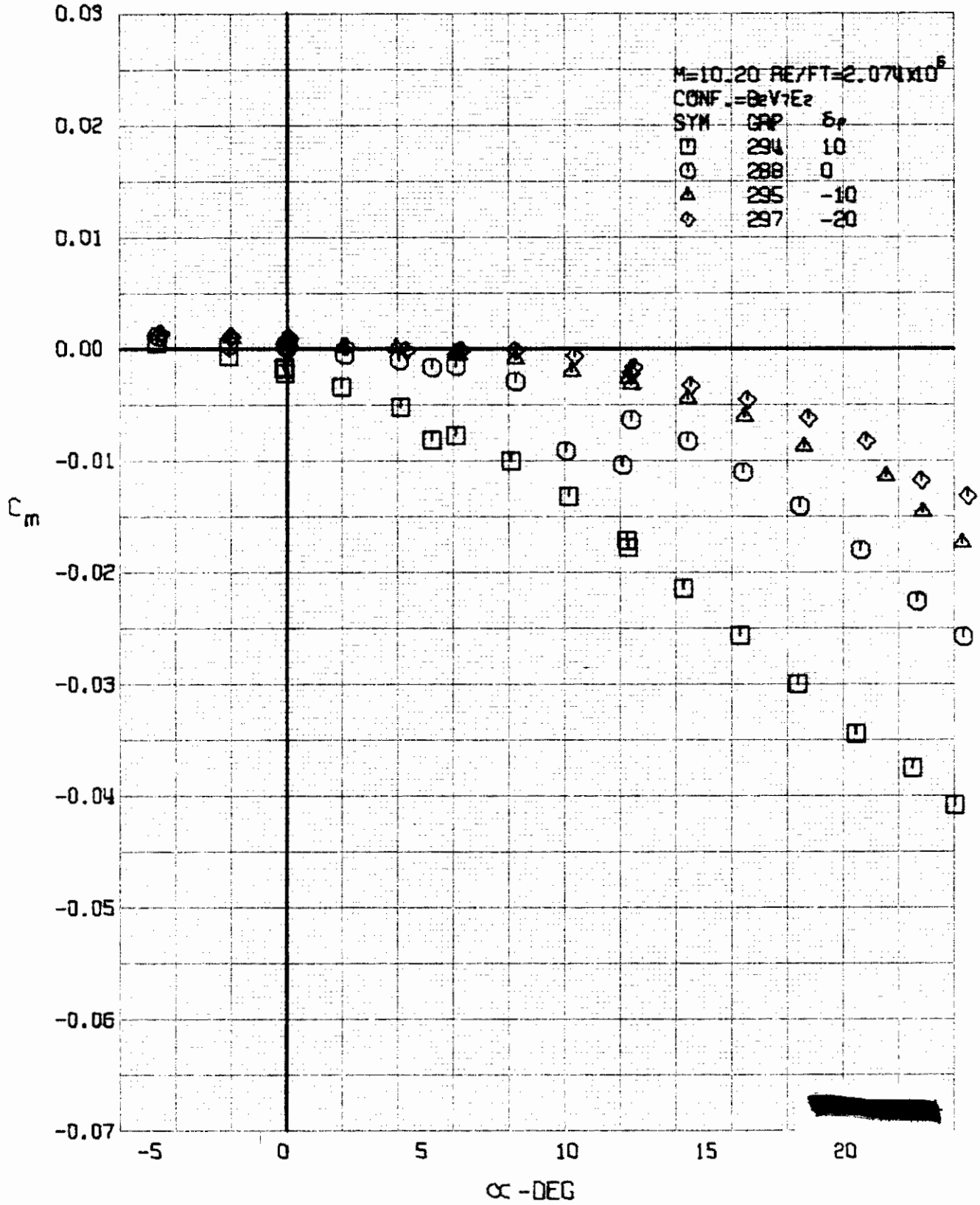

FIGURE 262 (U) ELEVON EFFECTS
- PITCHING MOMENT COEFFICIENT VARIATION WITH ANGLE OF ATTACK (M=10.20

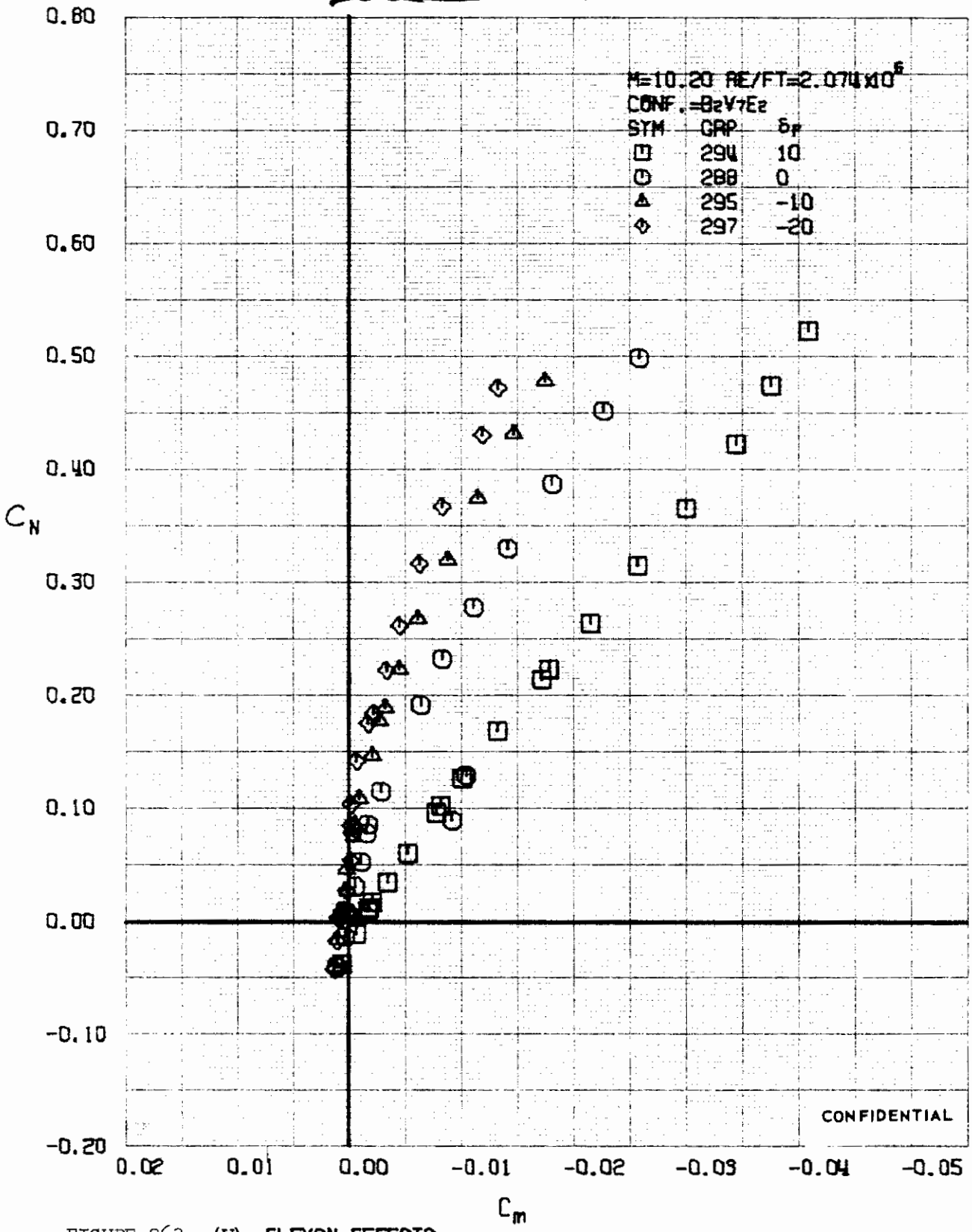

FIGURE 263 (U) ELEVON EFFECTS
- LONGITUDINAL STABILITY VARIATION (M=10.20

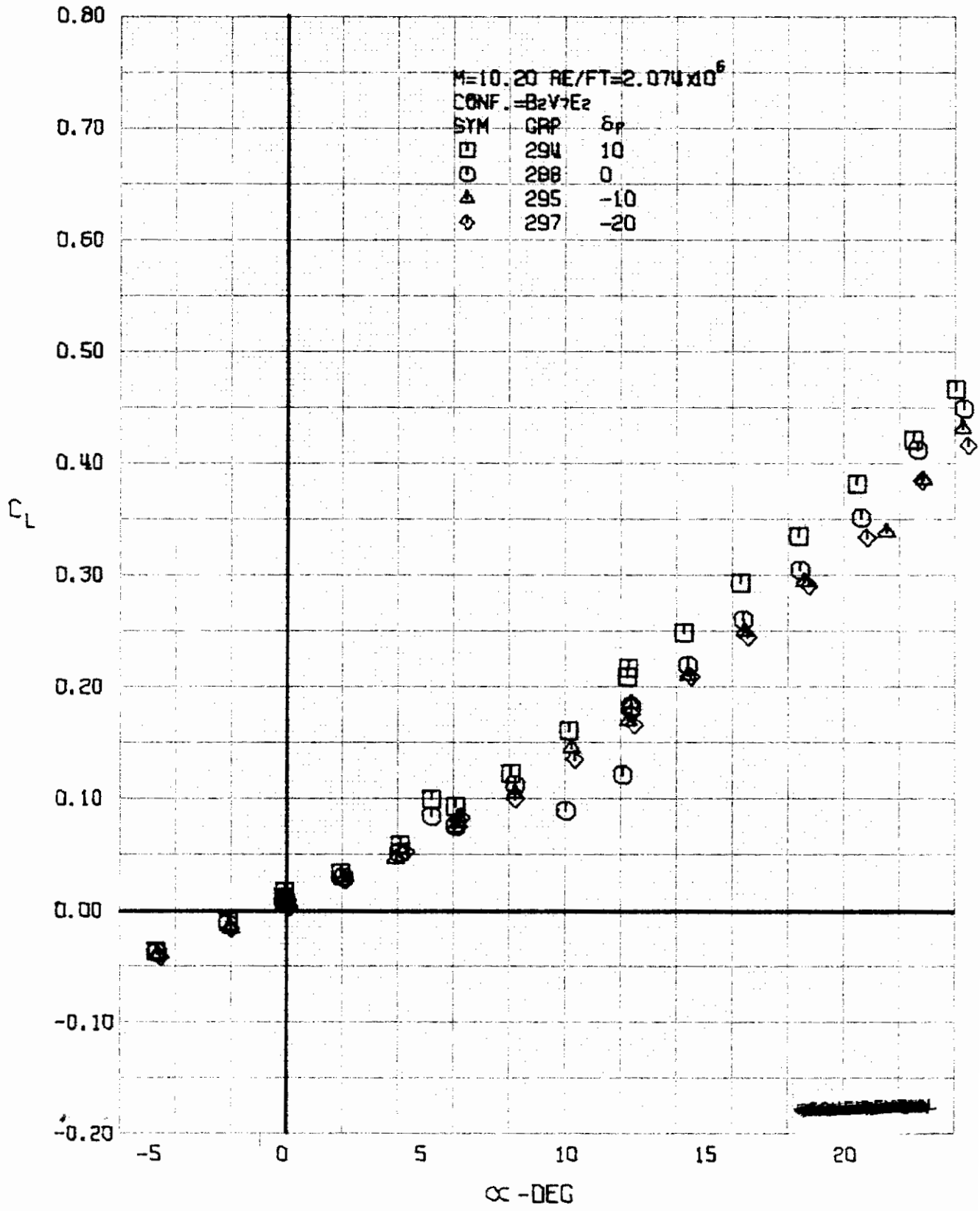

FIGURE 264 (U) ELEVON EFFECTS
- LIFT COEFFICIENT VARIATION WITH ANGLE OF ATTACK (M=10.20

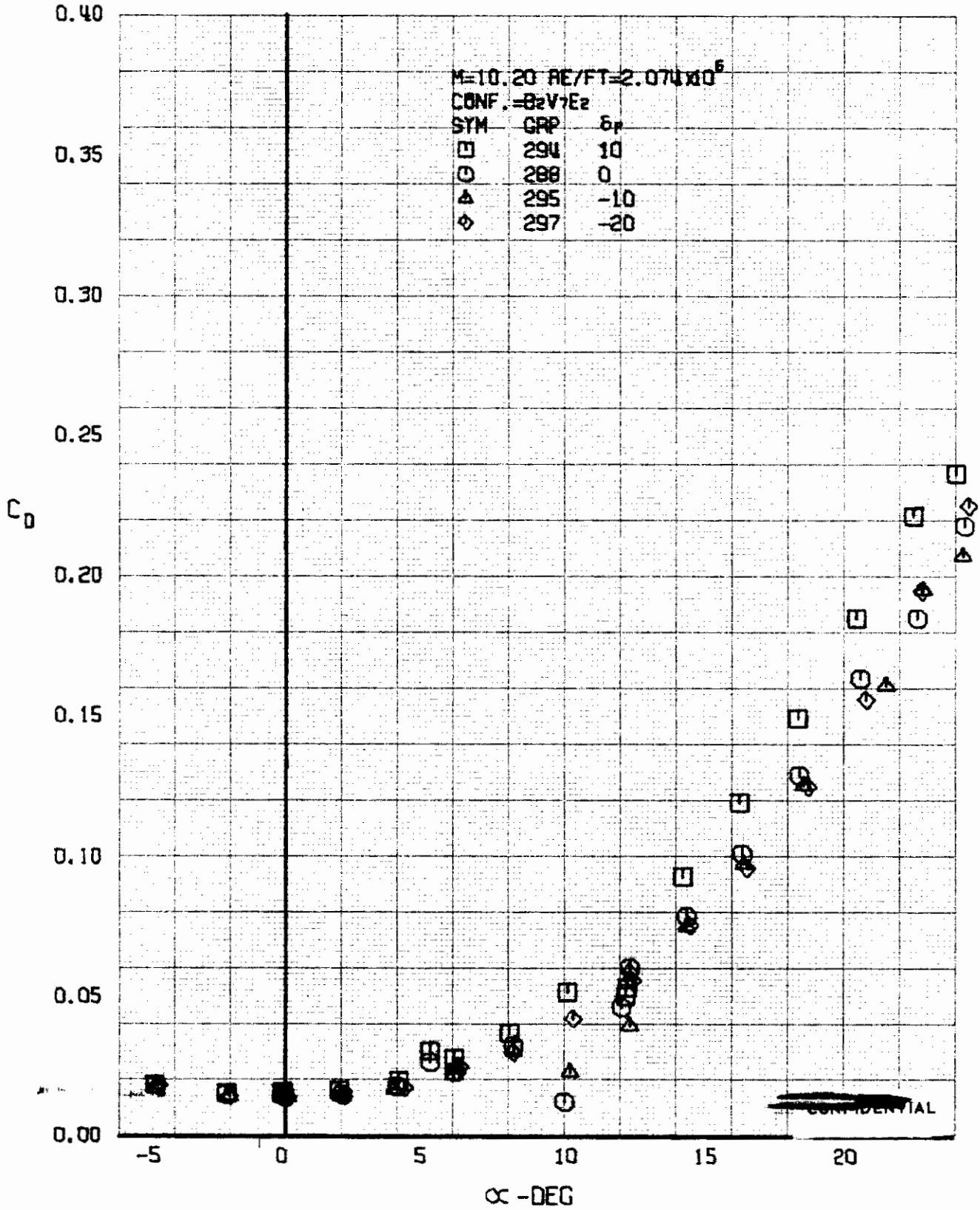

FIGURE 265 (U) ELEVON EFFECTS
- DRAG COEFFICIENT VARIATION WITH ANGLE OF ATTACK (M=10.20

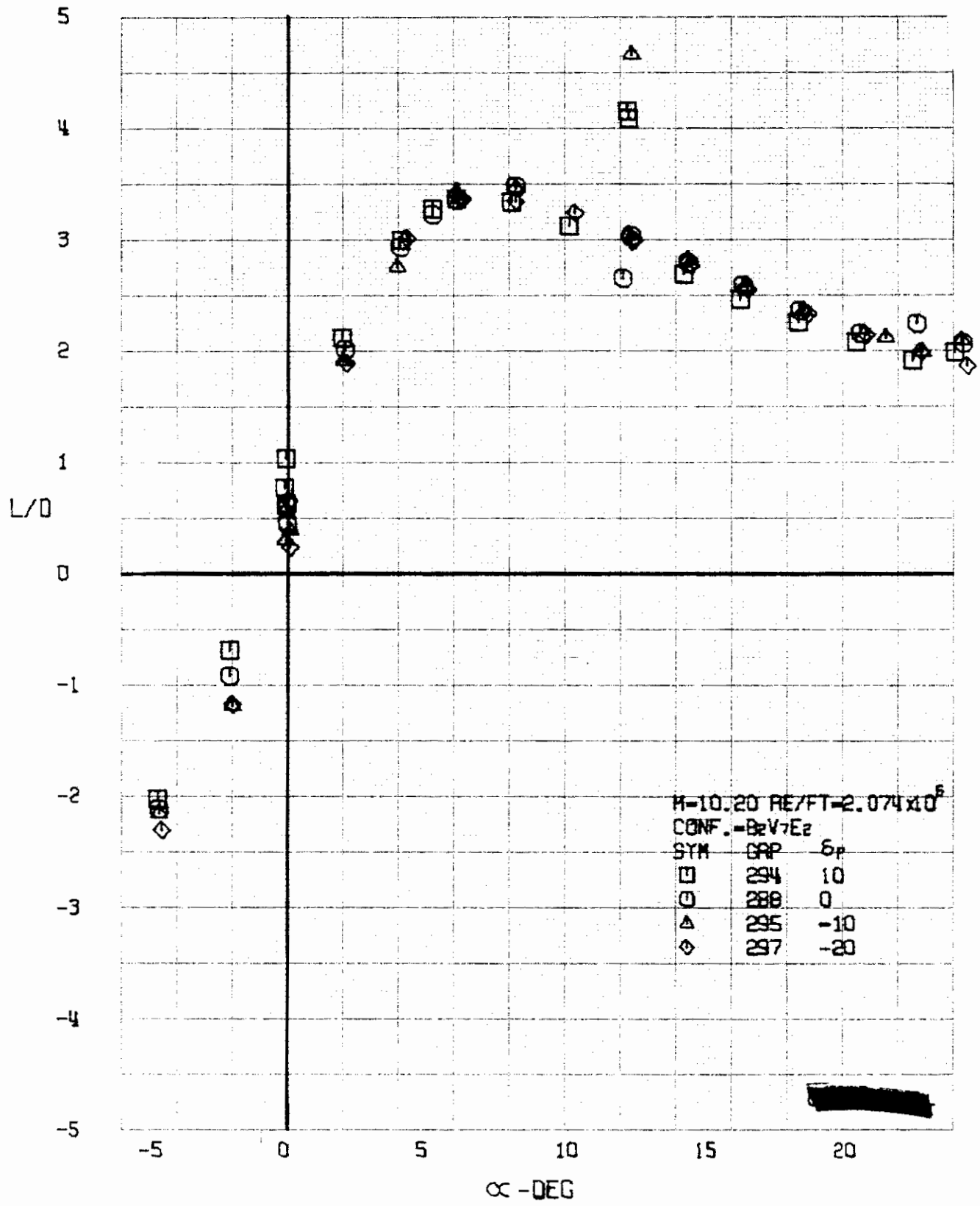

FIGURE 266 (U) ELEVON EFFECTS
- LIFT-DRAG RATIO VARIATION WITH ANGLE OF ATTACK (M=10.20

(REVERSE SIDE IS BLANK)

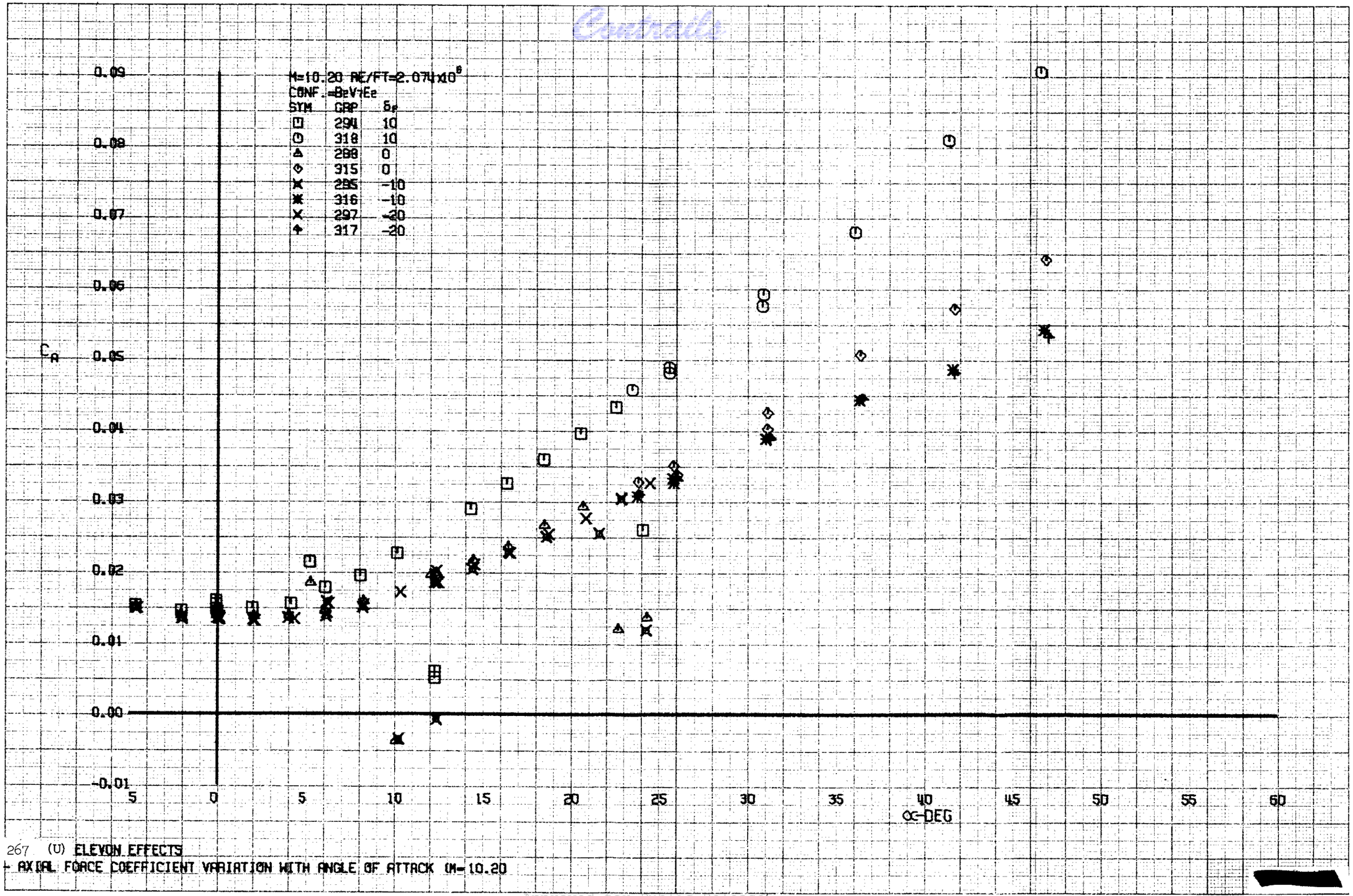

FIGURE 267 (U) ELEVON EFFECTS
- AXIAL FORCE COEFFICIENT VARIATION WITH ANGLE OF ATTACK (M=10.20

(REVERSE SIDE IS BLANK)

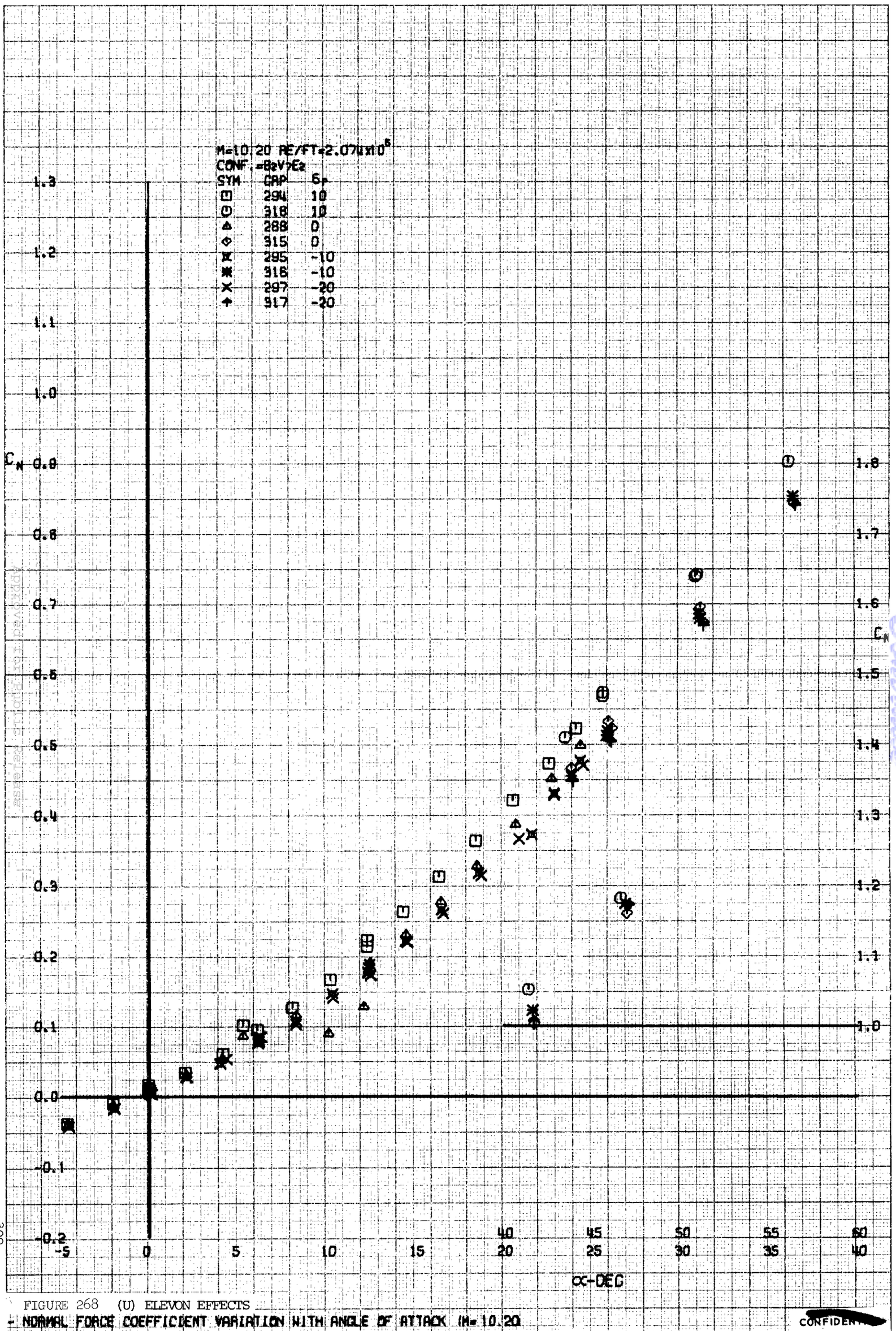

FIGURE 268 (U) ELEVON EFFECTS
- NORMAL FORCE COEFFICIENT VARIATION WITH ANGLE OF ATTACK (M= 10.20

CONFIDENTIAL

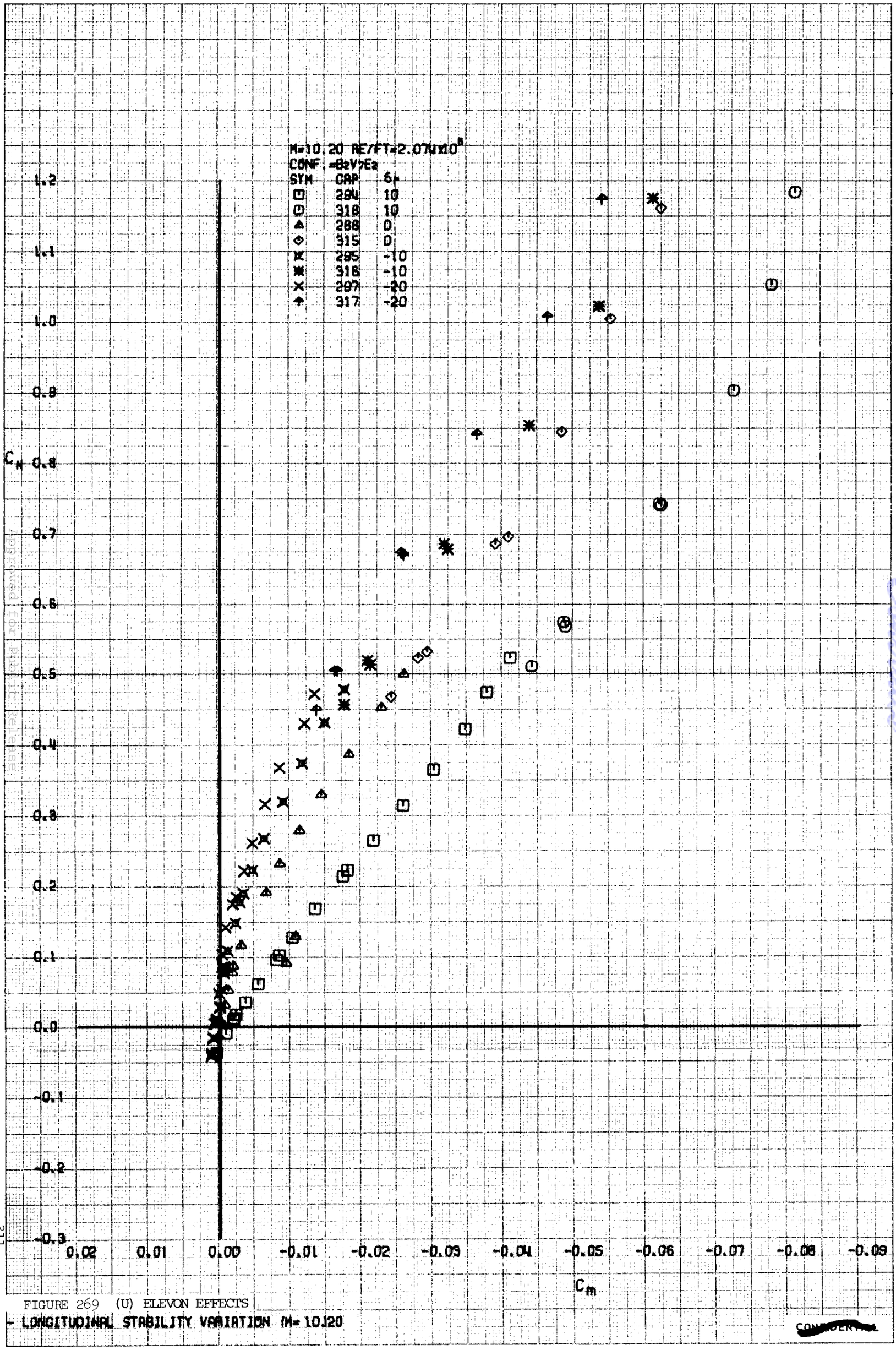

FIGURE 269 (U) ELEVON EFFECTS - LONGITUDINAL STABILITY VARIATION M= 10.20

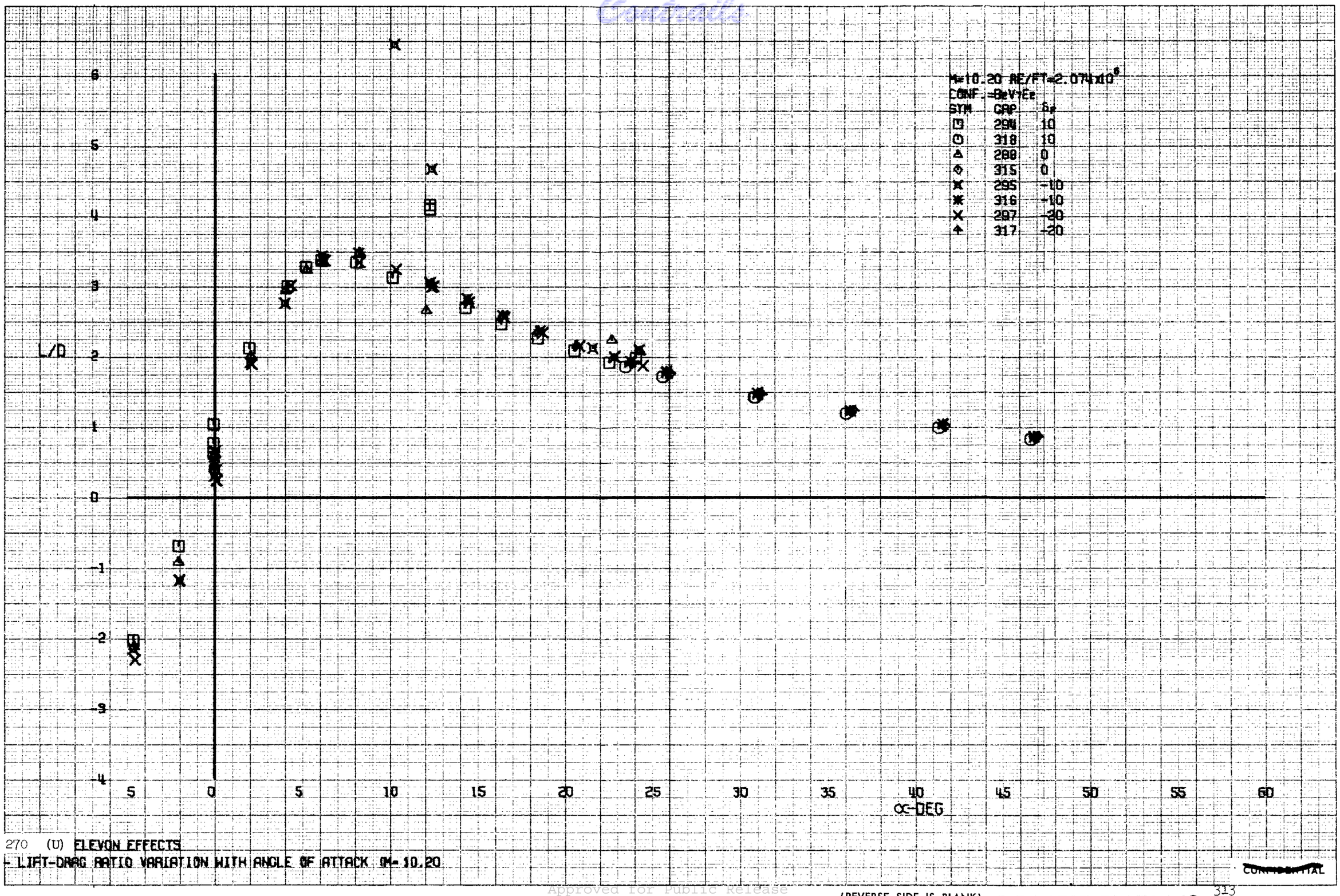

FIGURE 270 (U) ELEVON EFFECTS - LIFT-DRAG RATIO VARIATION WITH ANGLE OF ATTACK M=10.20

~~CONFIDENTIAL~~

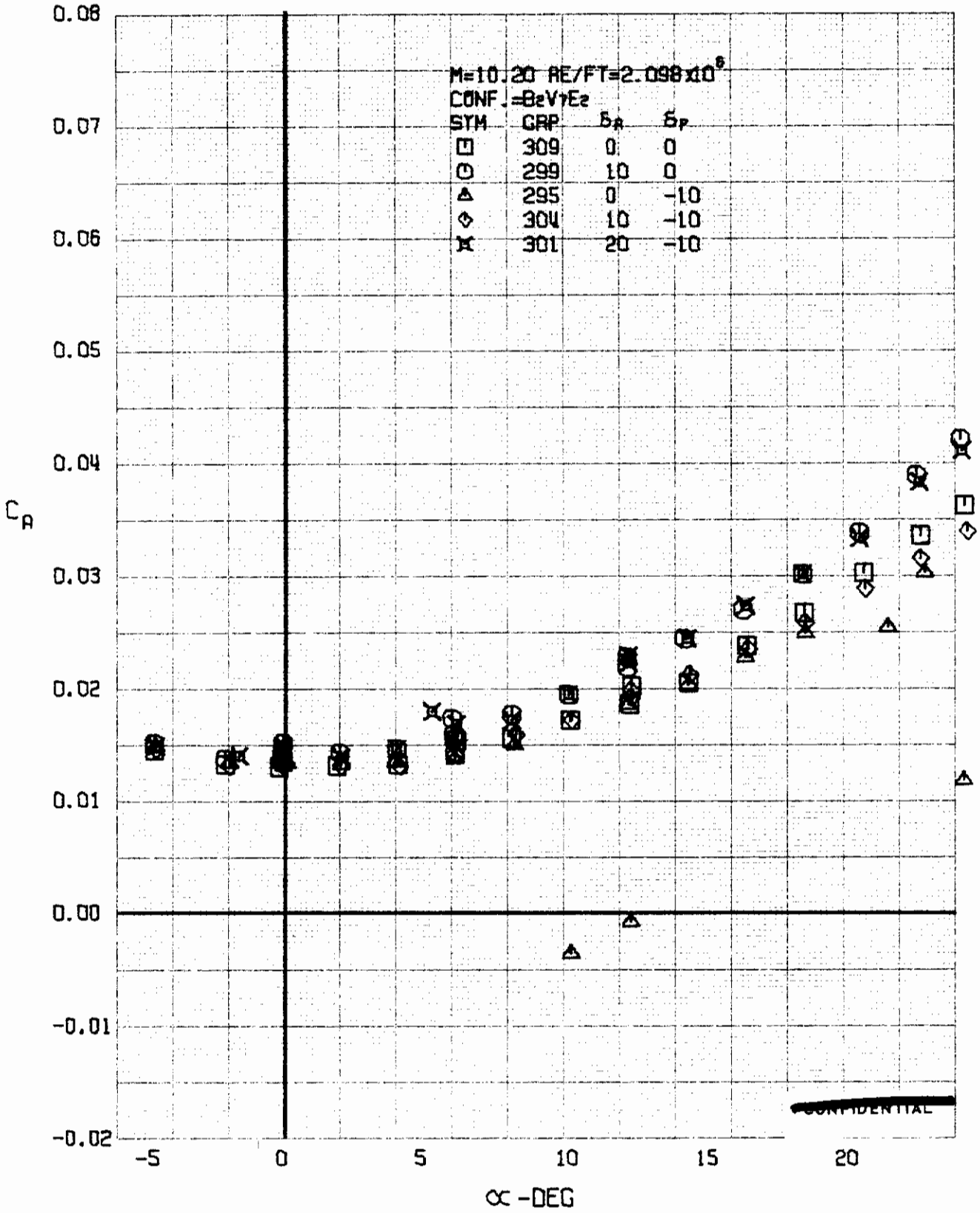

FIGURE 271 (U) AILERON EFFECTS
- AXIAL FORCE COEFFICIENT VARIATION WITH ANGLE OF ATTACK (M=10.20

~~CONFIDENTIAL~~

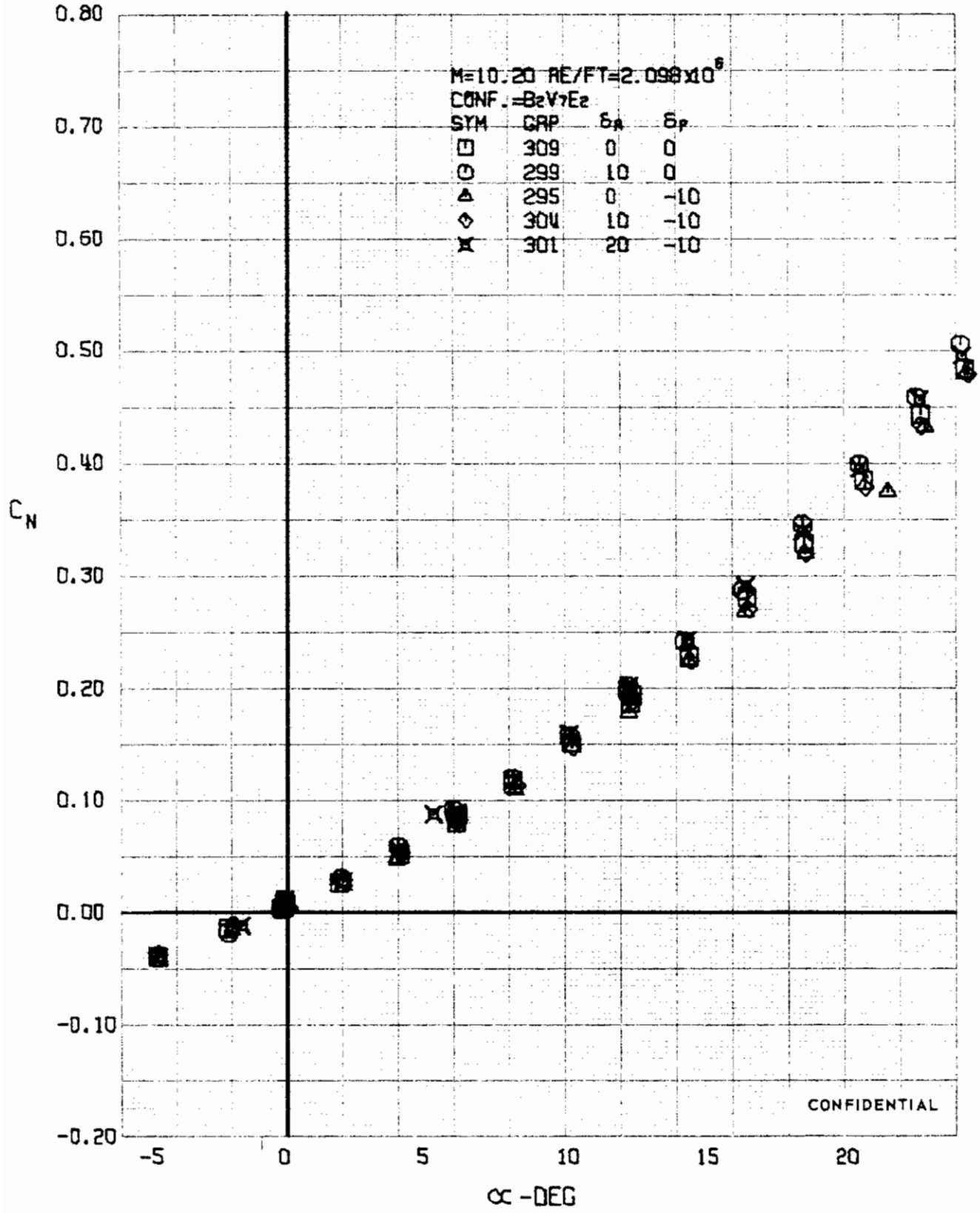

FIGURE 272 (U) AILERON EFFECTS
- NORMAL FORCE COEFFICIENT VARIATION WITH ANGLE OF ATTACK (M=10.20

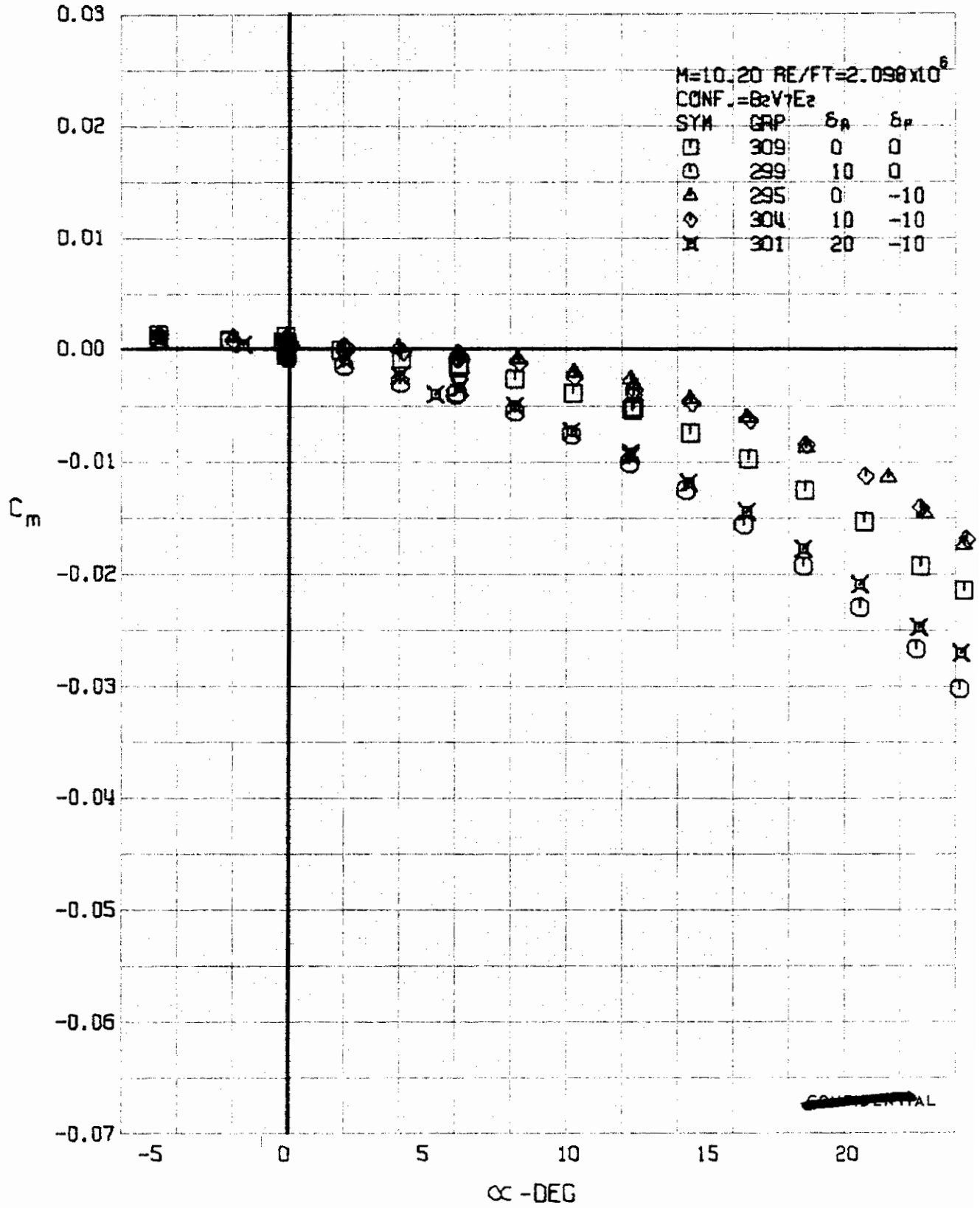

FIGURE 273 (U) AILERON EFFECTS
- PITCHING MOMENT COEFFICIENT VARIATION WITH ANGLE OF ATTACK (M=10.20

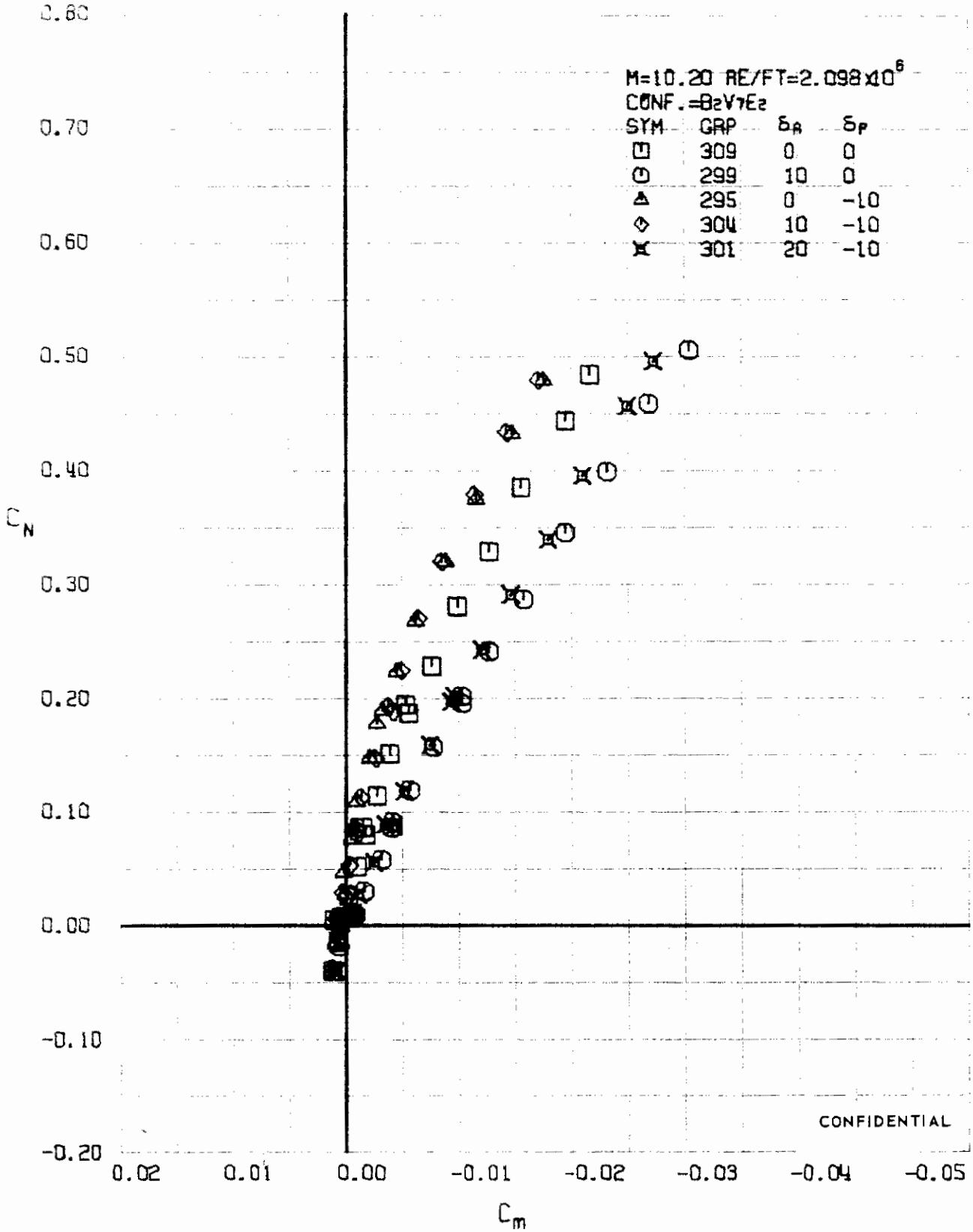

FIGURE 274 (U) AILERON EFFECTS
- LONGITUDINAL STABILITY VARIATION (M=10.20

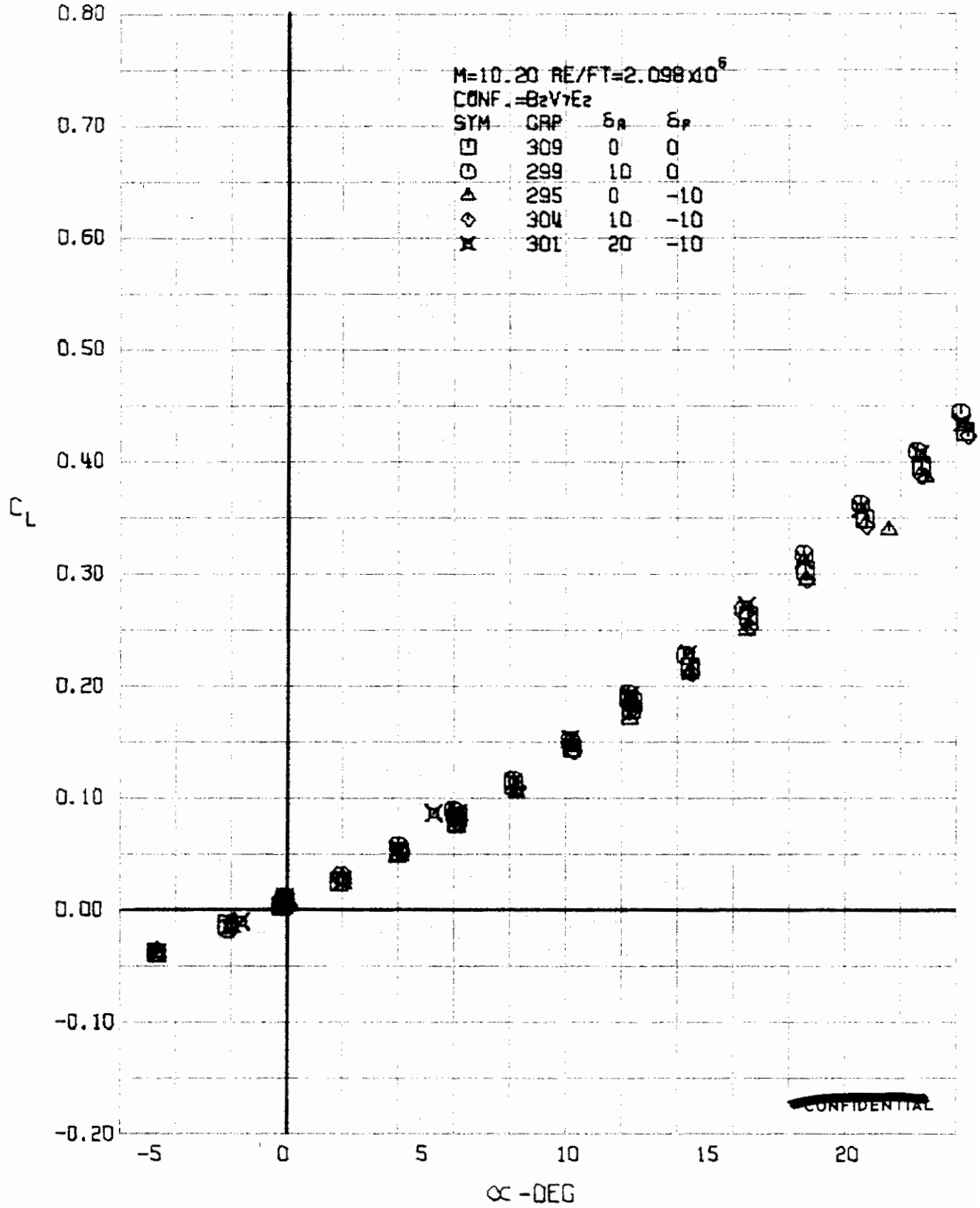

FIGURE 275 (U) AILERON EFFECTS
- LIFT COEFFICIENT VARIATION WITH ANGLE OF ATTACK (M=10.20

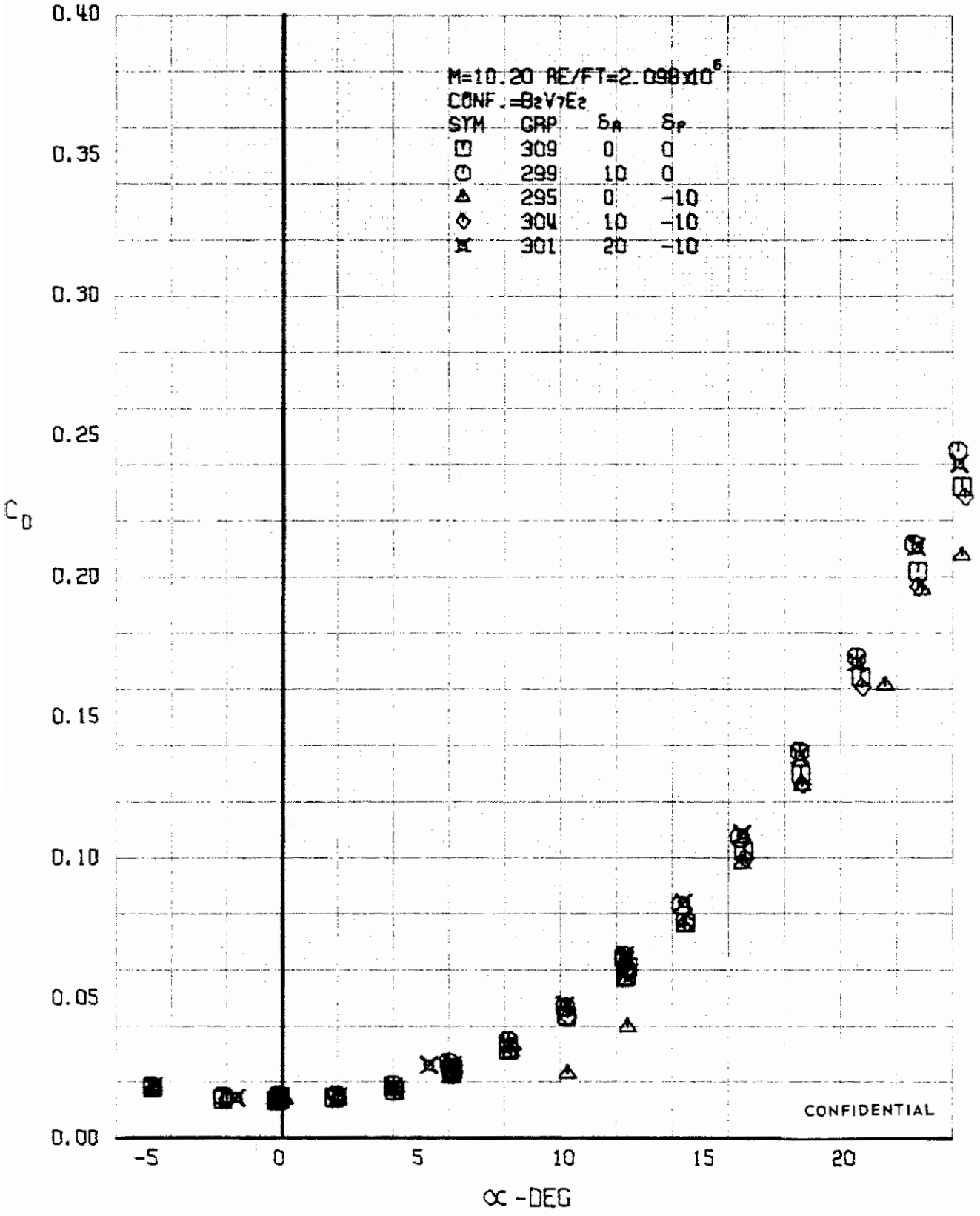

FIGURE 276 (U) AILERON EFFECTS
- DRAG COEFFICIENT VARIATION WITH ANGLE OF ATTACK (M=10.20

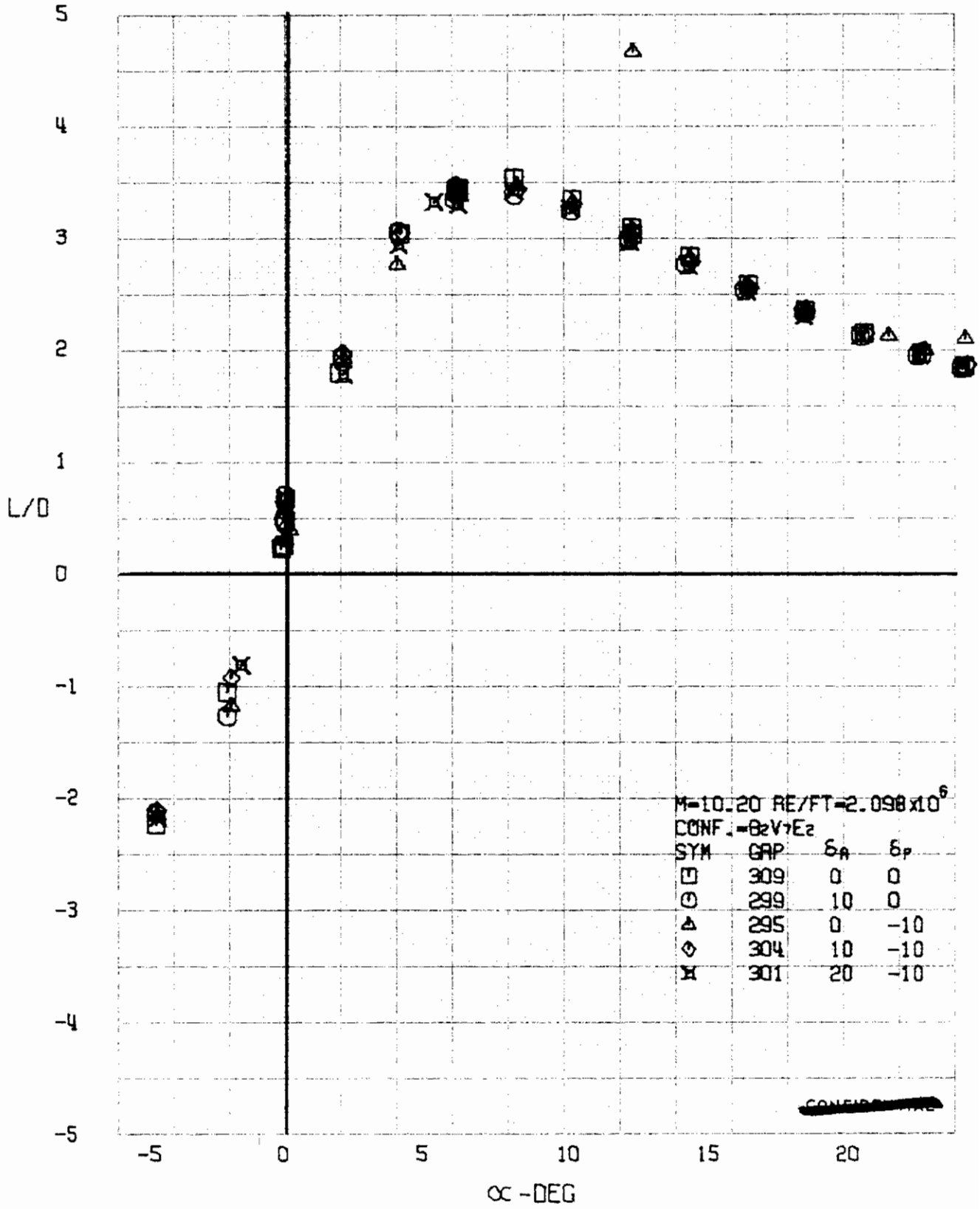

FIGURE 277 (U) AILERON EFFECTS
- LIFT-DRAG RATIO VARIATION WITH ANGLE OF ATTACK (M=10.20

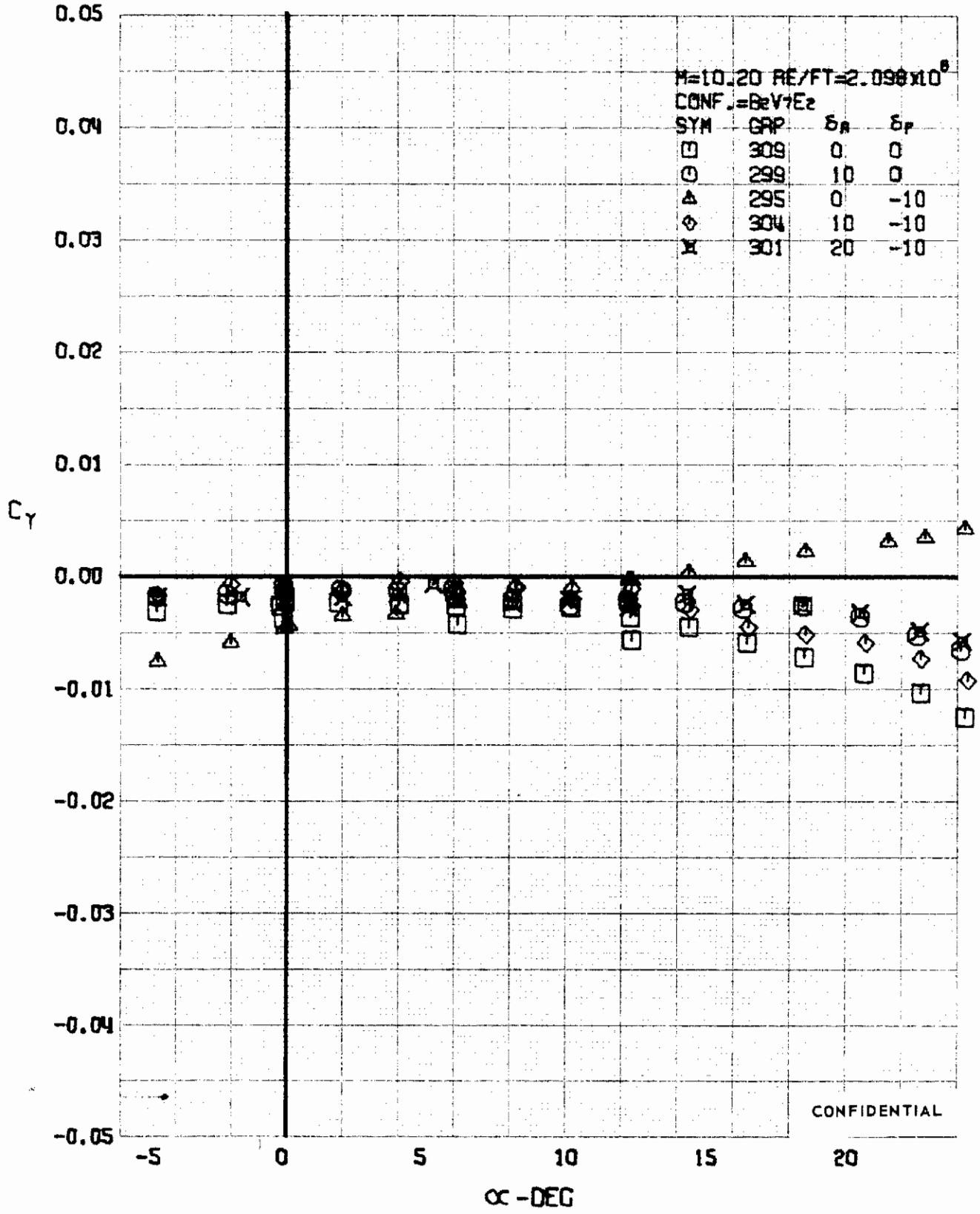

FIGURE 278 (U) AILERON EFFECTS
- SIDE FORCE COEFFICIENT VARIATION WITH ANGLE OF ATTACK (M=10.20

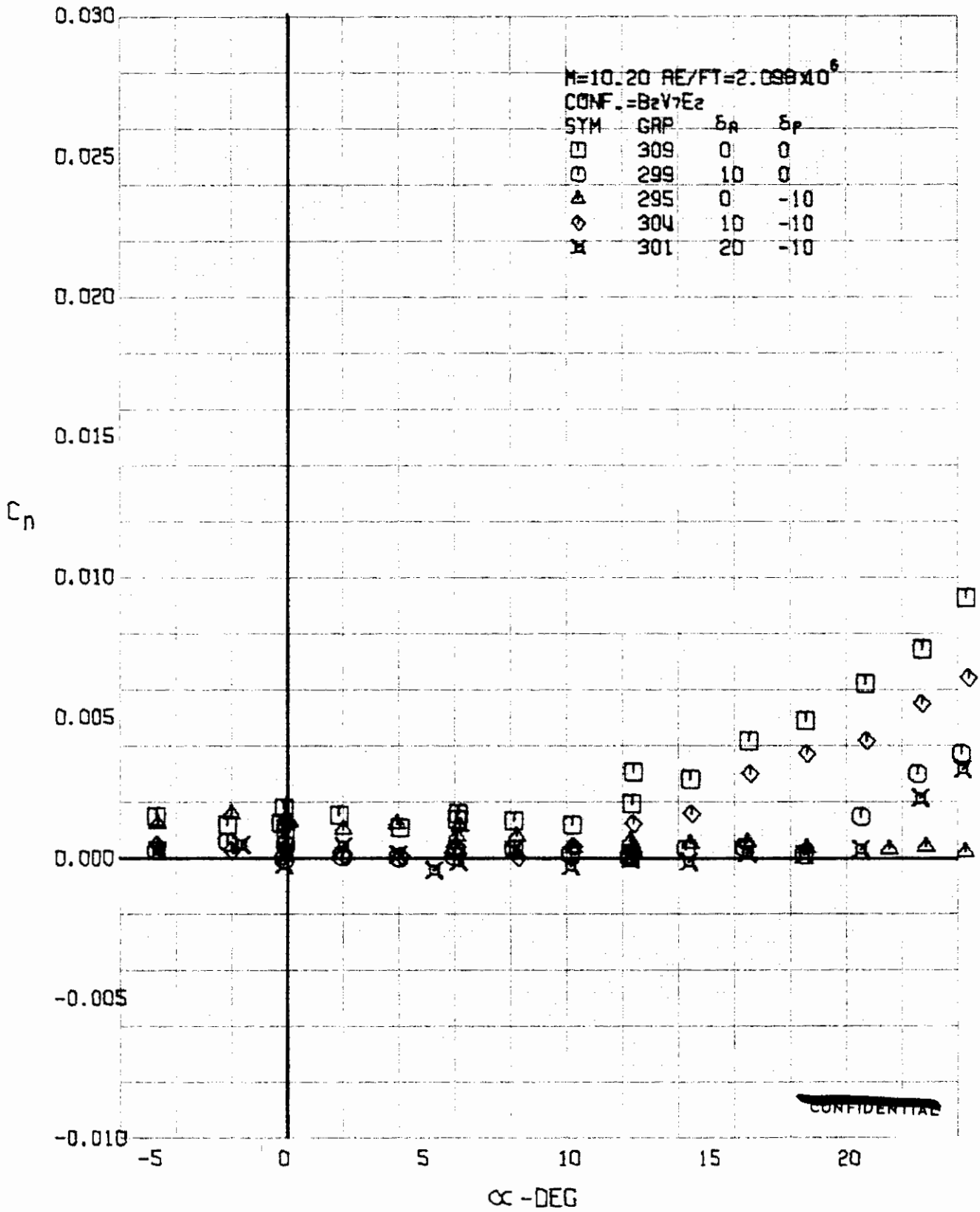

FIGURE 279 (U) AILERON EFFECTS
- YAWING MOMENT COEFFICIENT VARIATION WITH ANGLE OF ATTACK M=10.20

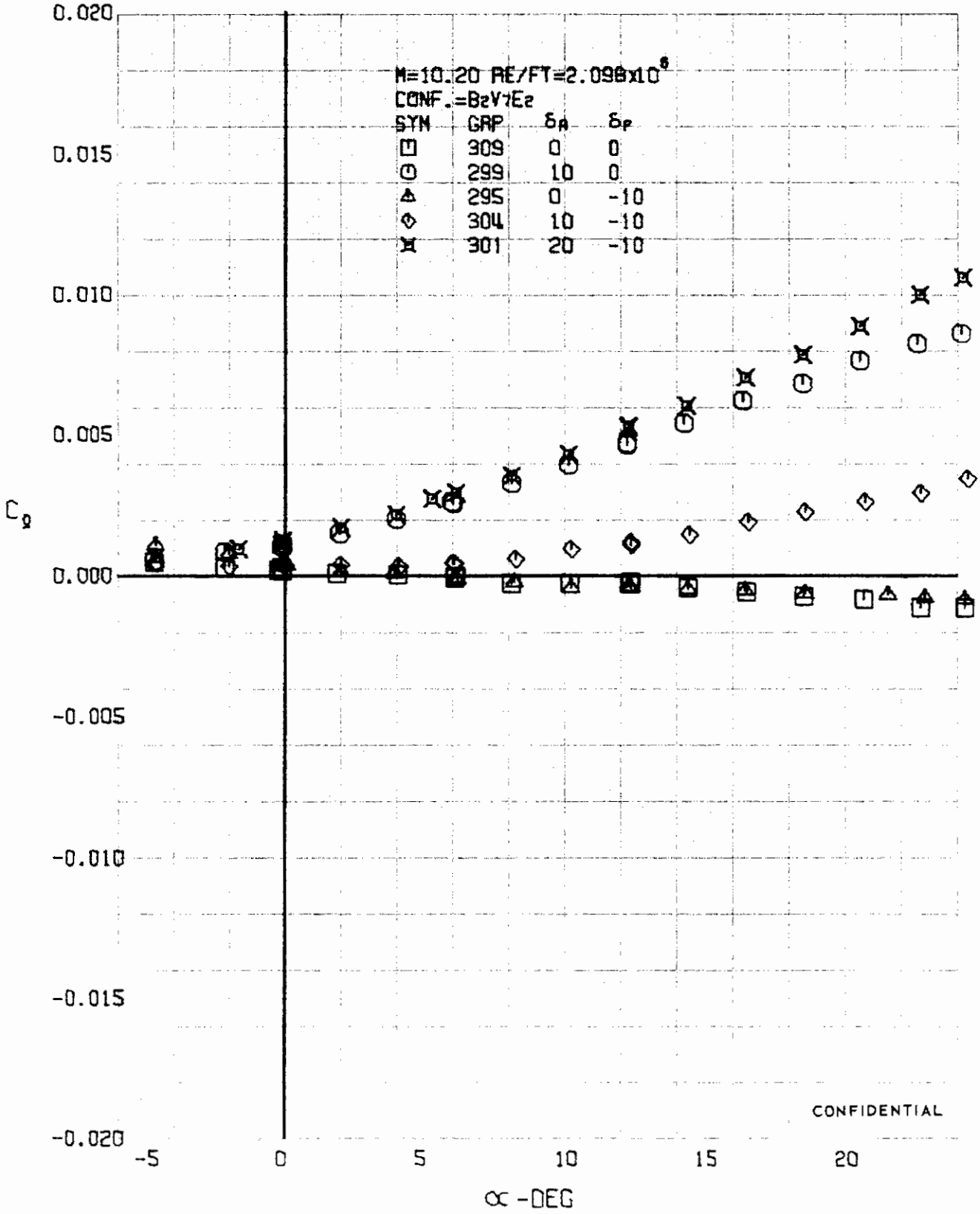

FIGURE 280 (U) AILERON EFFECTS
- ROLLING MOMENT COEFFICIENT VARIATION WITH ANGLE OF ATTACK (M=10.20

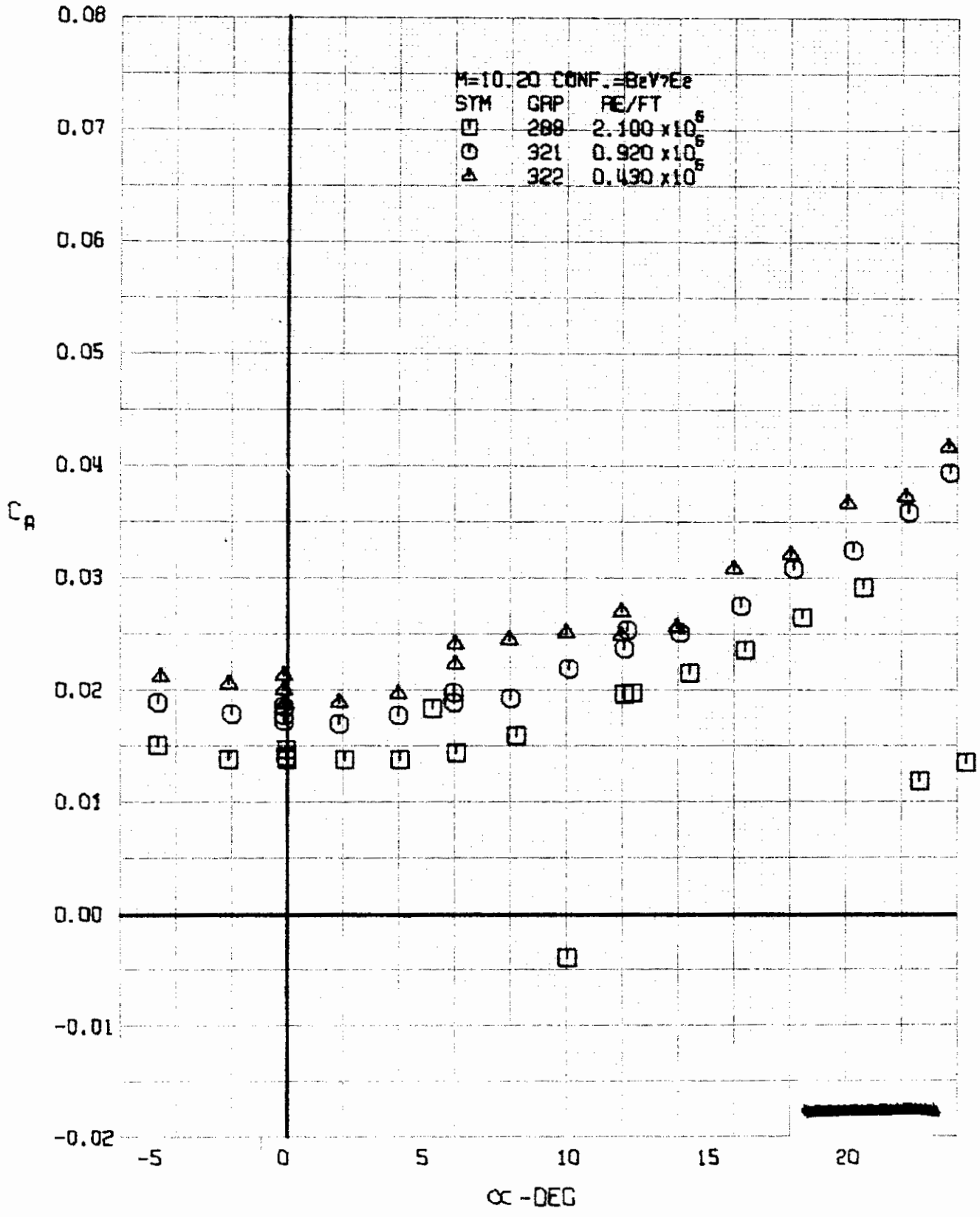

FIGURE 281 (U) REYNOLDS NUMBER EFFECTS
- AXIAL FORCE COEFFICIENT VARIATION WITH ANGLE OF ATTACK (M=10.20

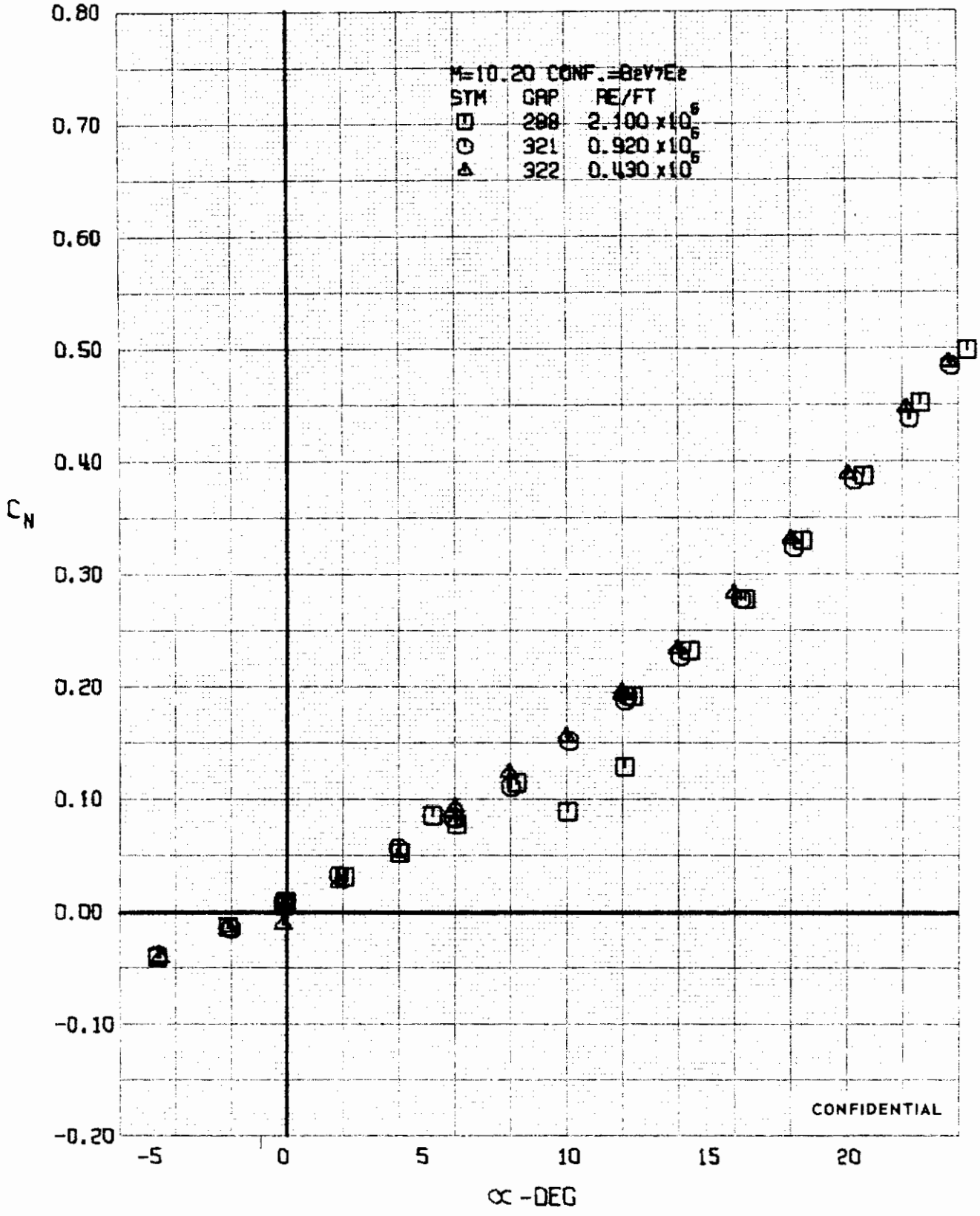

FIGURE 282 (U) REYNOLDS NUMBER EFFECTS
- NORMAL FORCE COEFFICIENT VARIATION WITH ANGLE OF ATTACK (M=10.20

CONFIDENTIAL

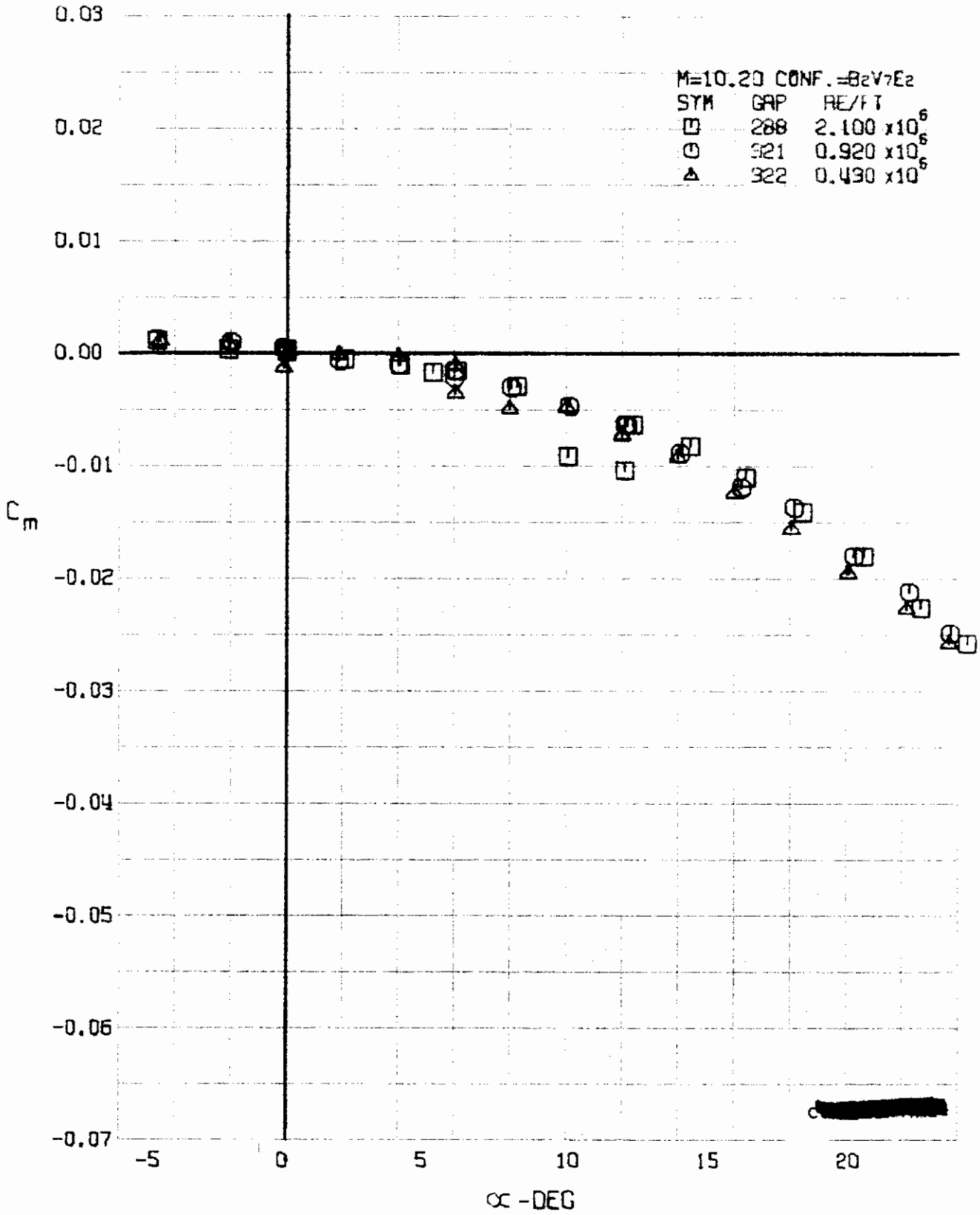

FIGURE 283 (U) REYNOLDS NUMBER EFFECTS
- PITCHING MOMENT COEFFICIENT VARIATION WITH ANGLE OF ATTACK (M=10.20

CONFIDENTIAL

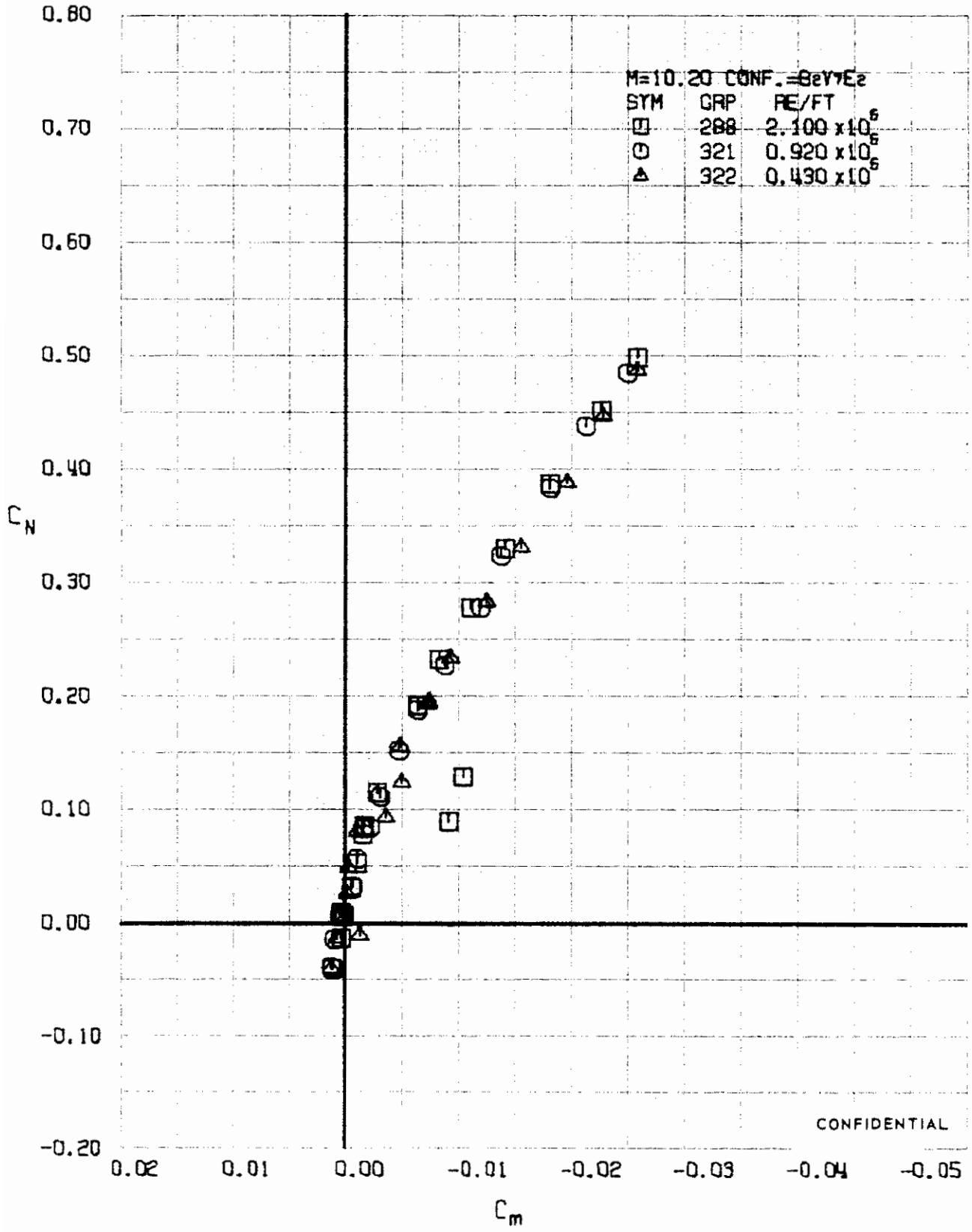

FIGURE 284 : (U) REYNOLDS NUMBER EFFECTS
- LONGITUDINAL STABILITY VARIATION (M= 10.20

CONFIDENTIAL

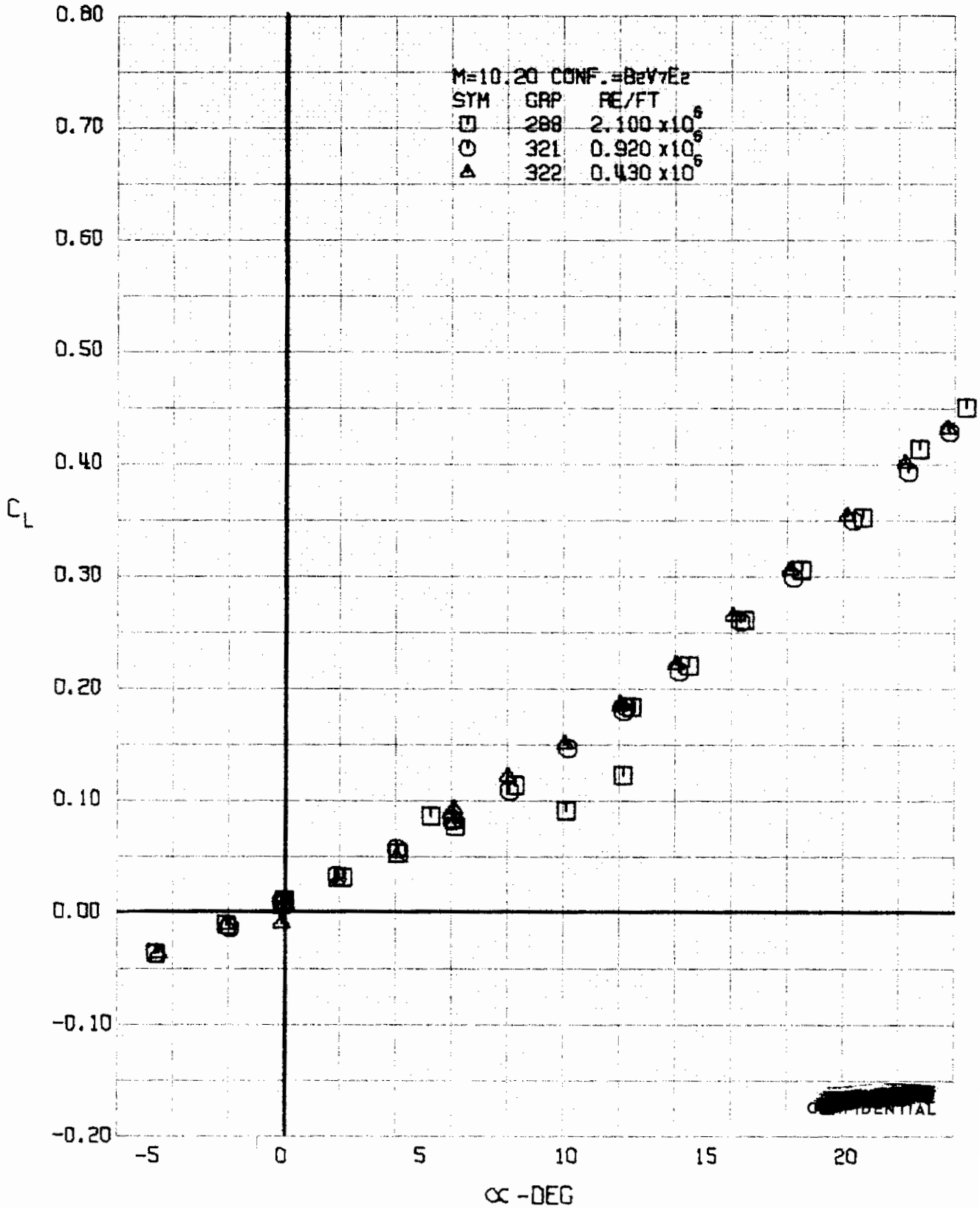

FIGURE 285 (U) REYNOLDS NUMBER EFFECTS
- LIFT COEFFICIENT VARIATION WITH ANGLE OF ATTACK (M=10.20

CONFIDENTIAL

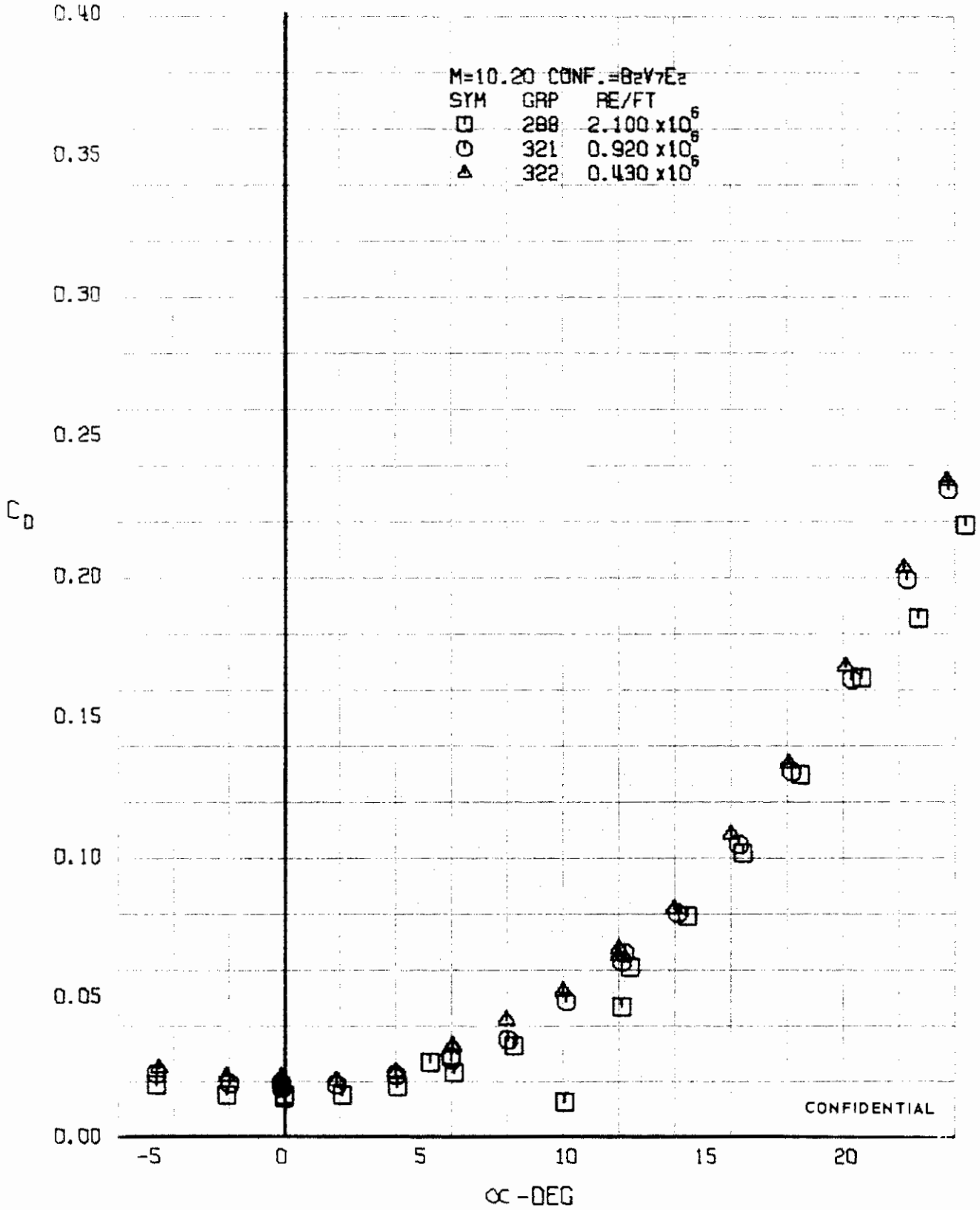

FIGURE 286 (U) REYNOLDS NUMBER EFFECTS
- DRAG COEFFICIENT VARIATION WITH ANGLE OF ATTACK (M=10.20

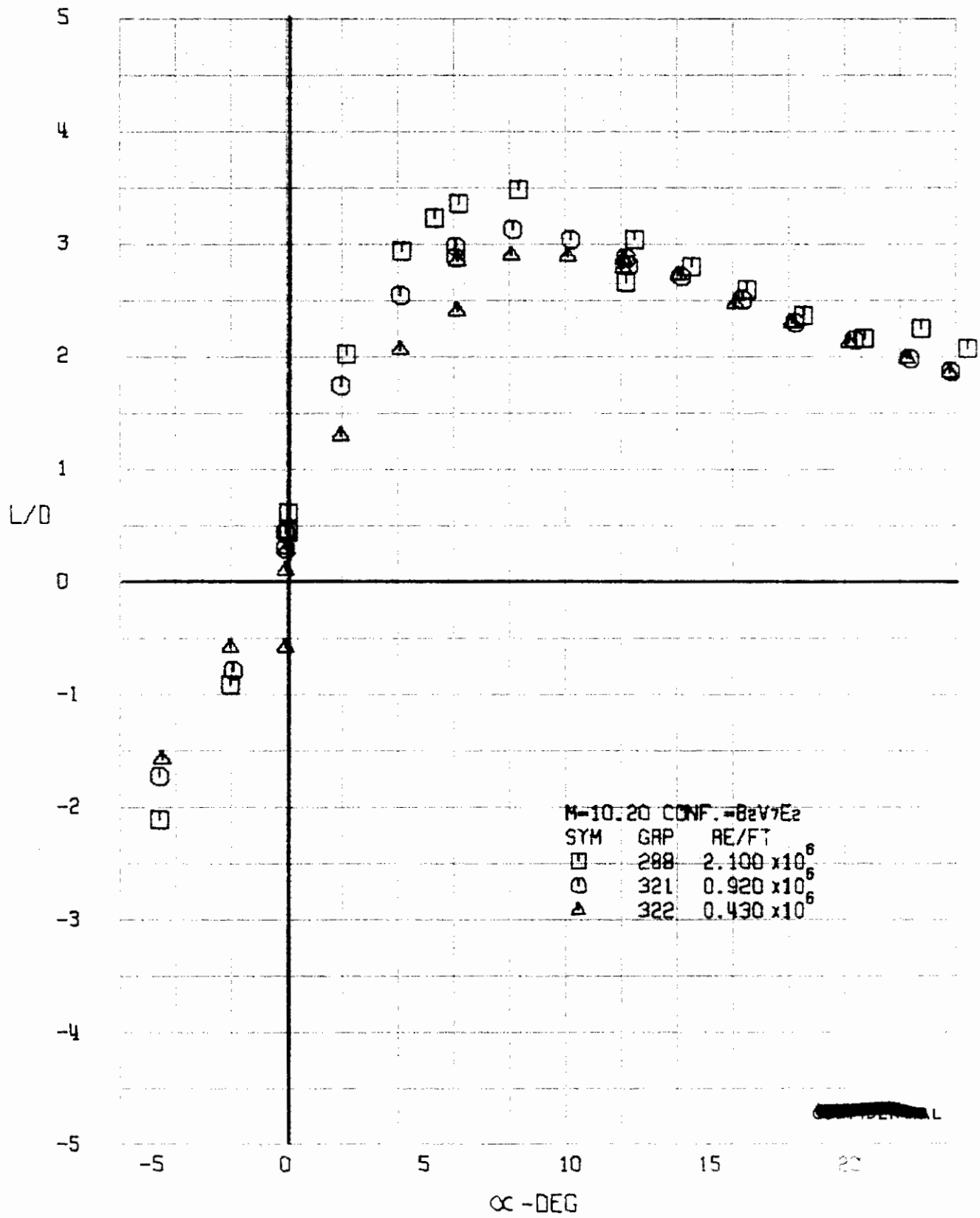

FIGURE 287 (U) REYNOLDS NUMBER EFFECTS
- LIFT-DRAG RATIO VARIATION WITH ANGLE OF ATTACK (M=10.20

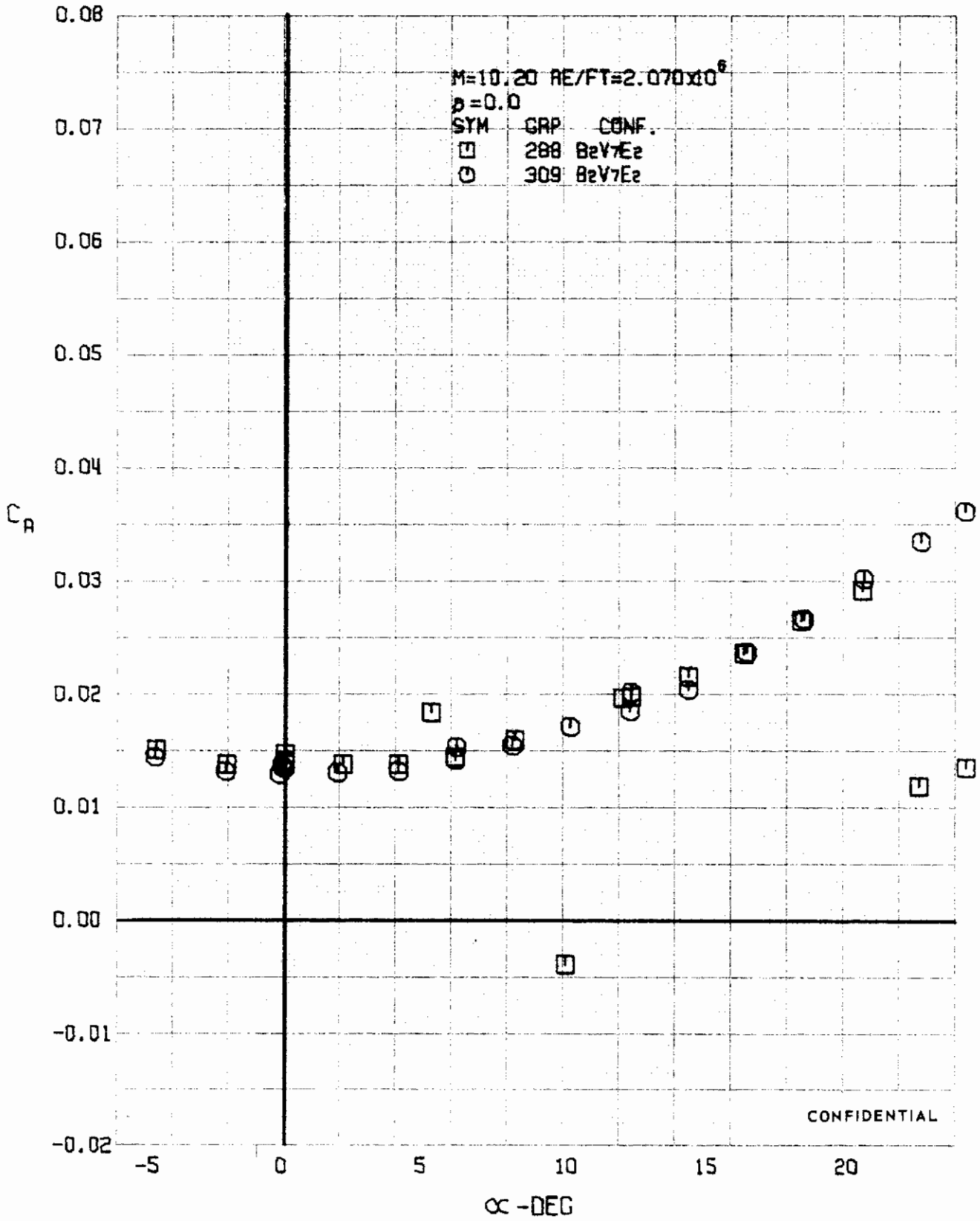

FIGURE 288 (U) REPEATABILITY
- AXIAL FORCE COEFFICIENT VARIATION WITH ANGLE OF ATTACK (M=10.20

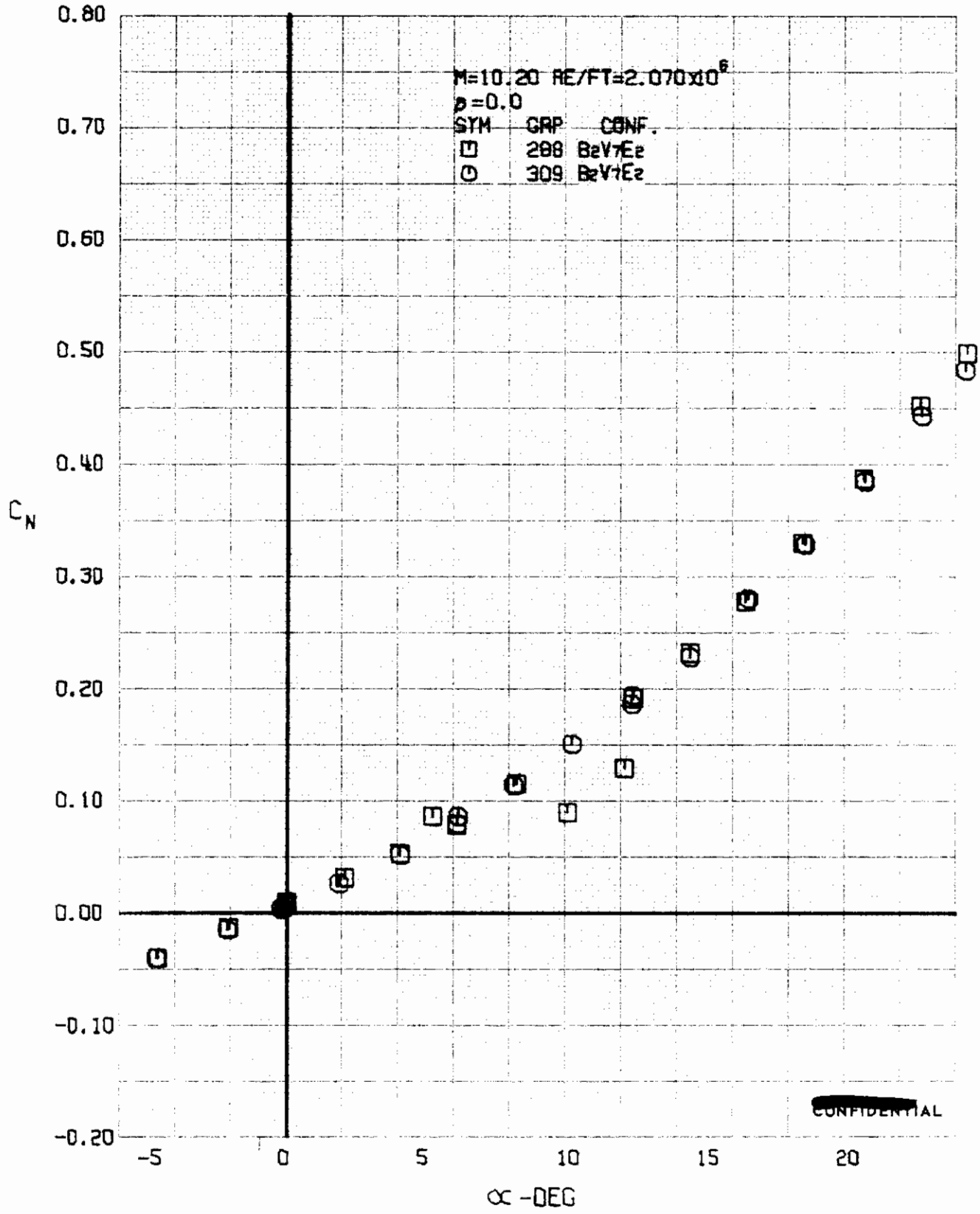

FIGURE 289 (U) REPEATABILITY
- NORMAL FORCE COEFFICIENT VARIATION WITH ANGLE OF ATTACK (M=10.20

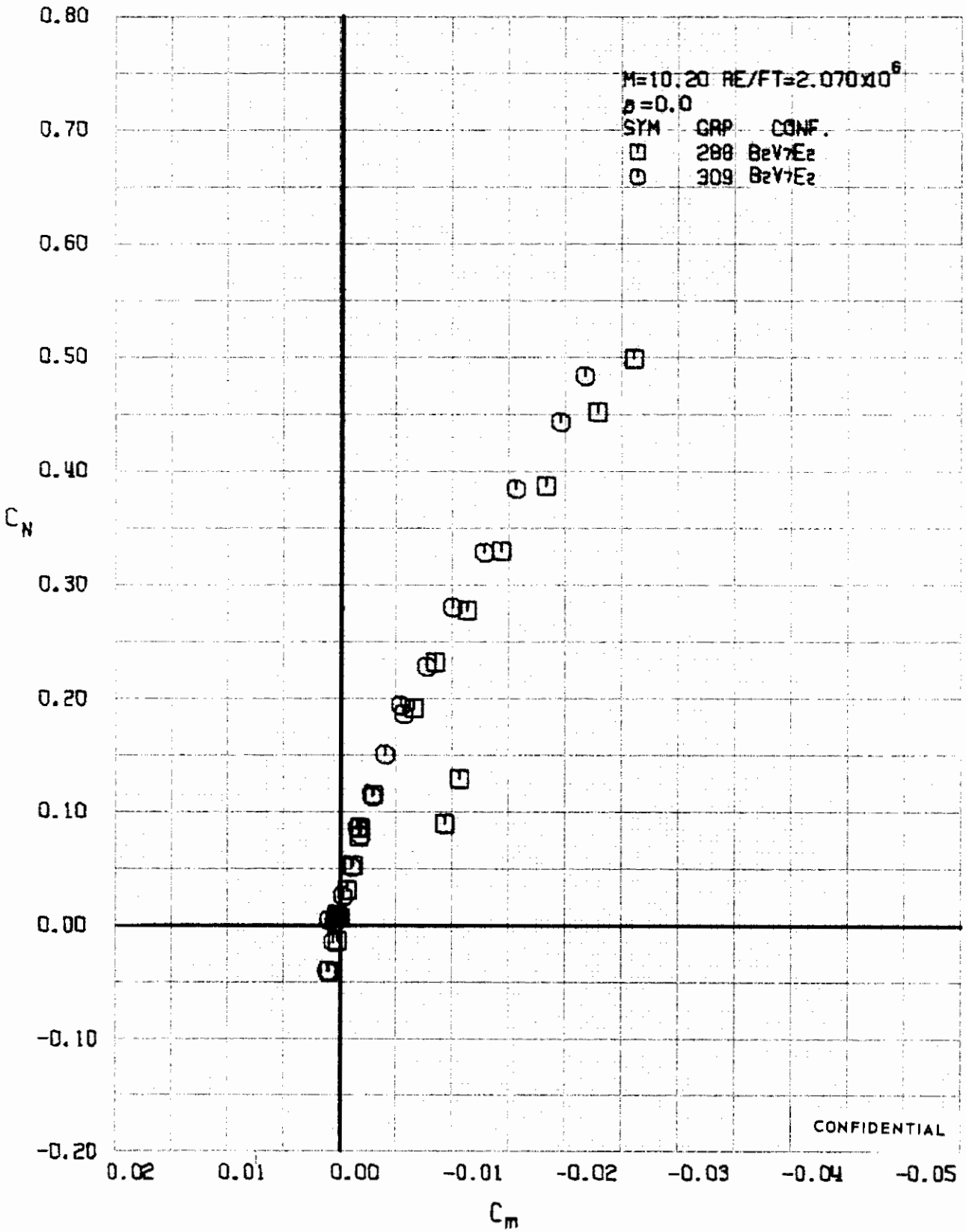

FIGURE 290 (U) REPEATABILITY
- LONGITUDINAL STABILITY VARIATION (M=10.20

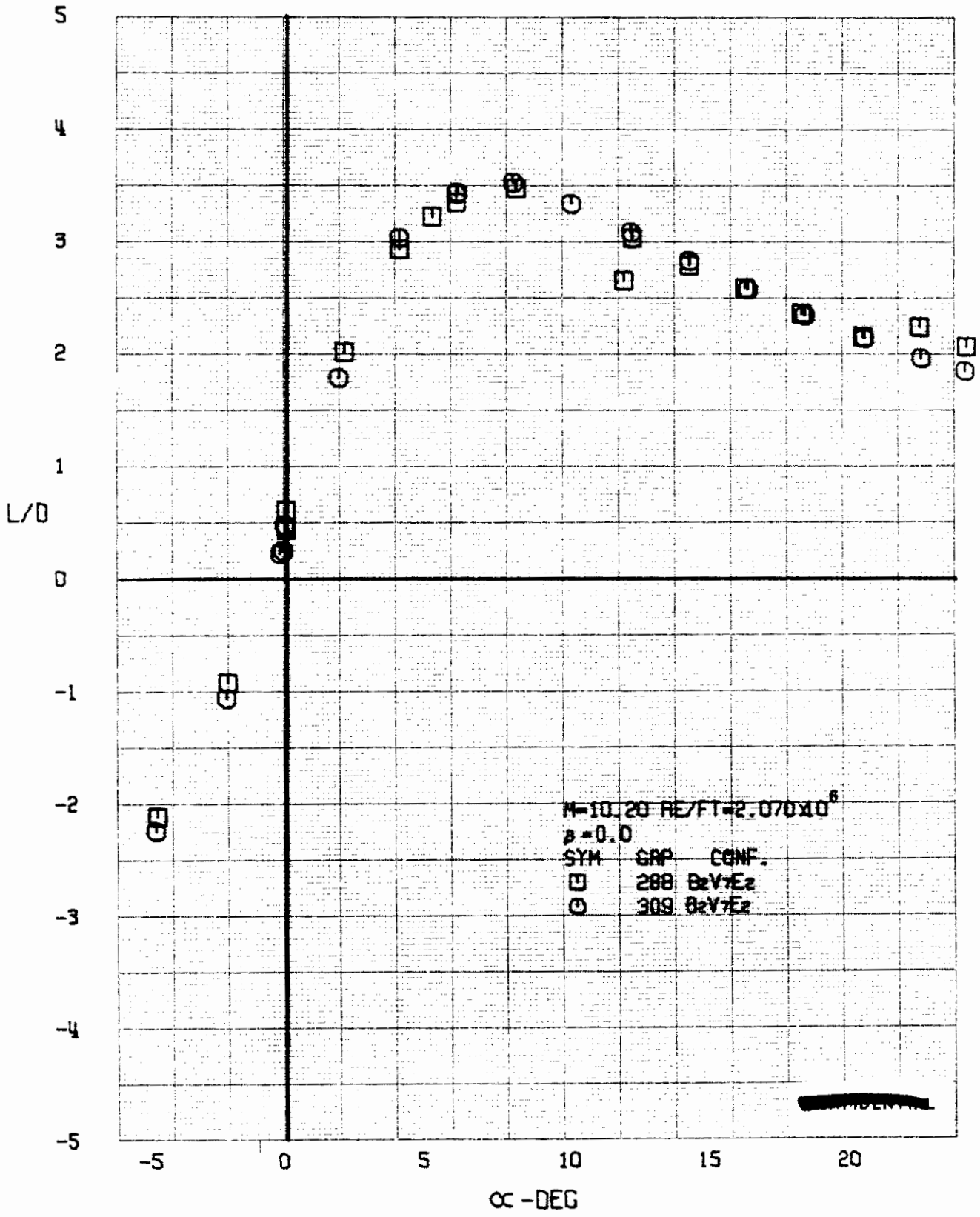

FIGURE 291 (U) REPEATABILITY
- LIFT-DRAG RATIO VARIATION WITH ANGLE OF ATTACK (M=10.20

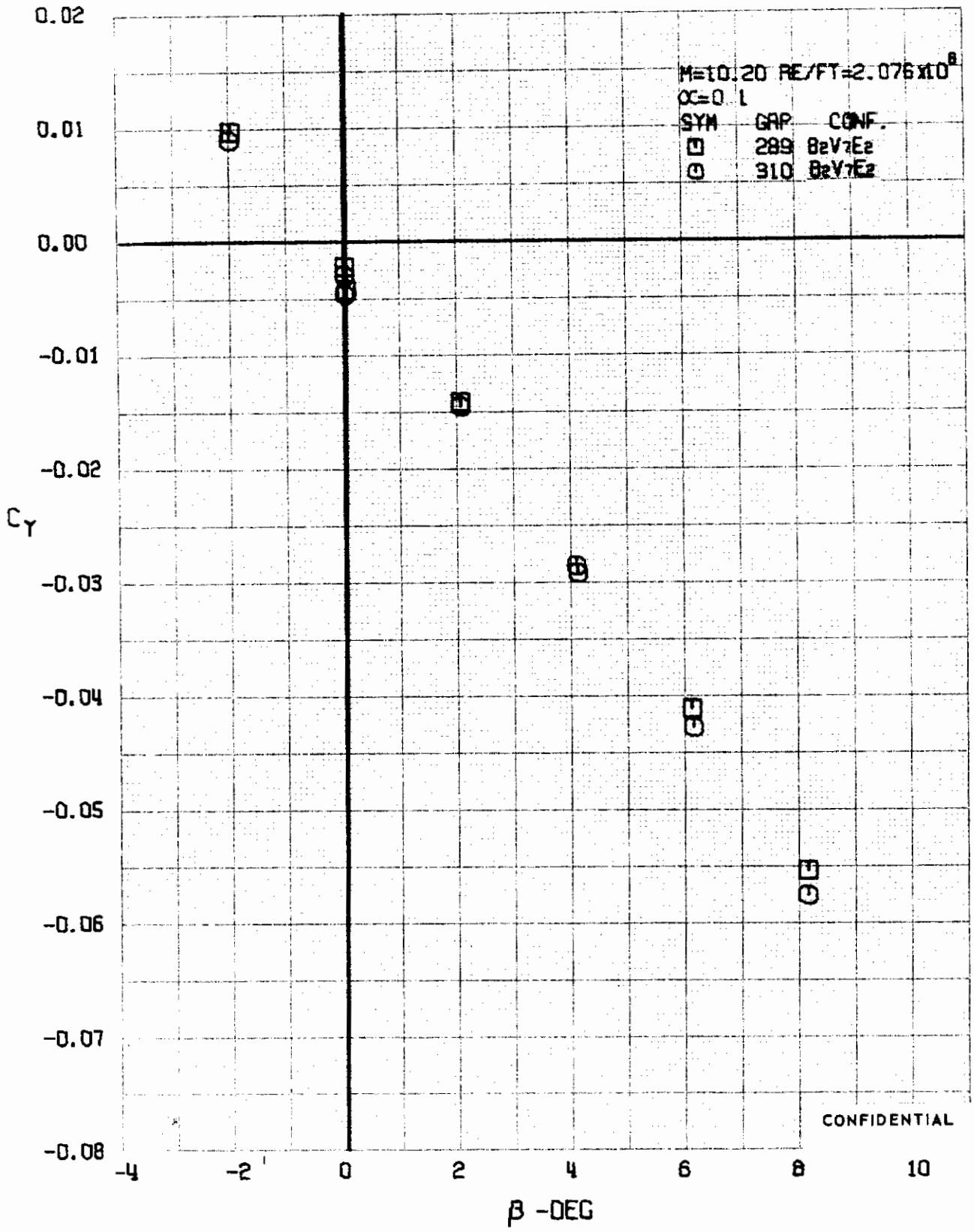

FIGURE 292 (U) REPEATABILITY
- SIDE FORCE COEFFICIENT VARIATION WITH ANGLE OF YAW (M= 10.20

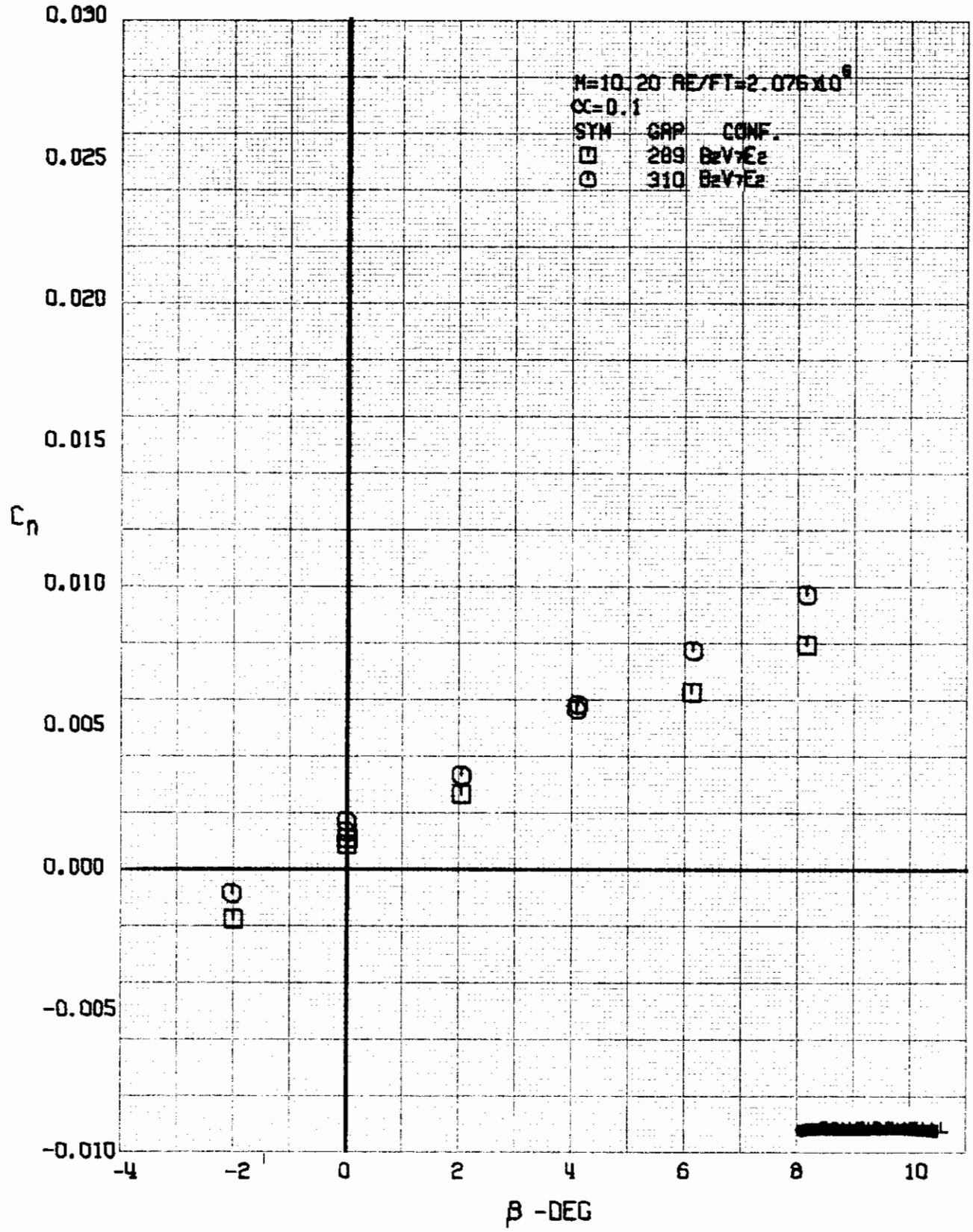

FIGURE 293 (U) REPEATABILITY
- YAWING MOMENT COEFFICIENT VARIATION WITH ANGLE OF YAW (M=10.20

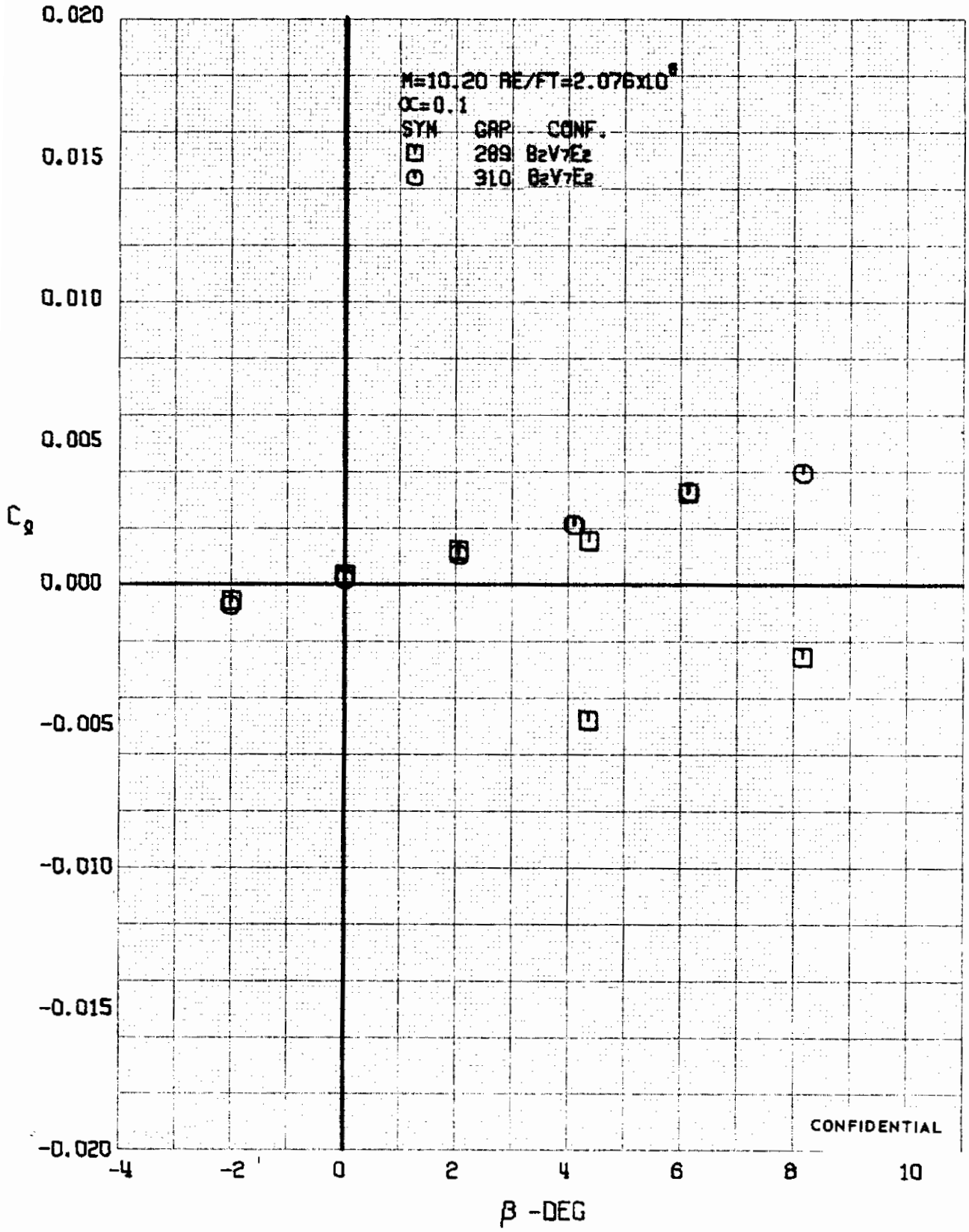

FIGURE 294 (U) REPEATABILITY
- ROLLING MOMENT COEFFICIENT VARIATION WITH ANGLE OF YAW (M=10.20

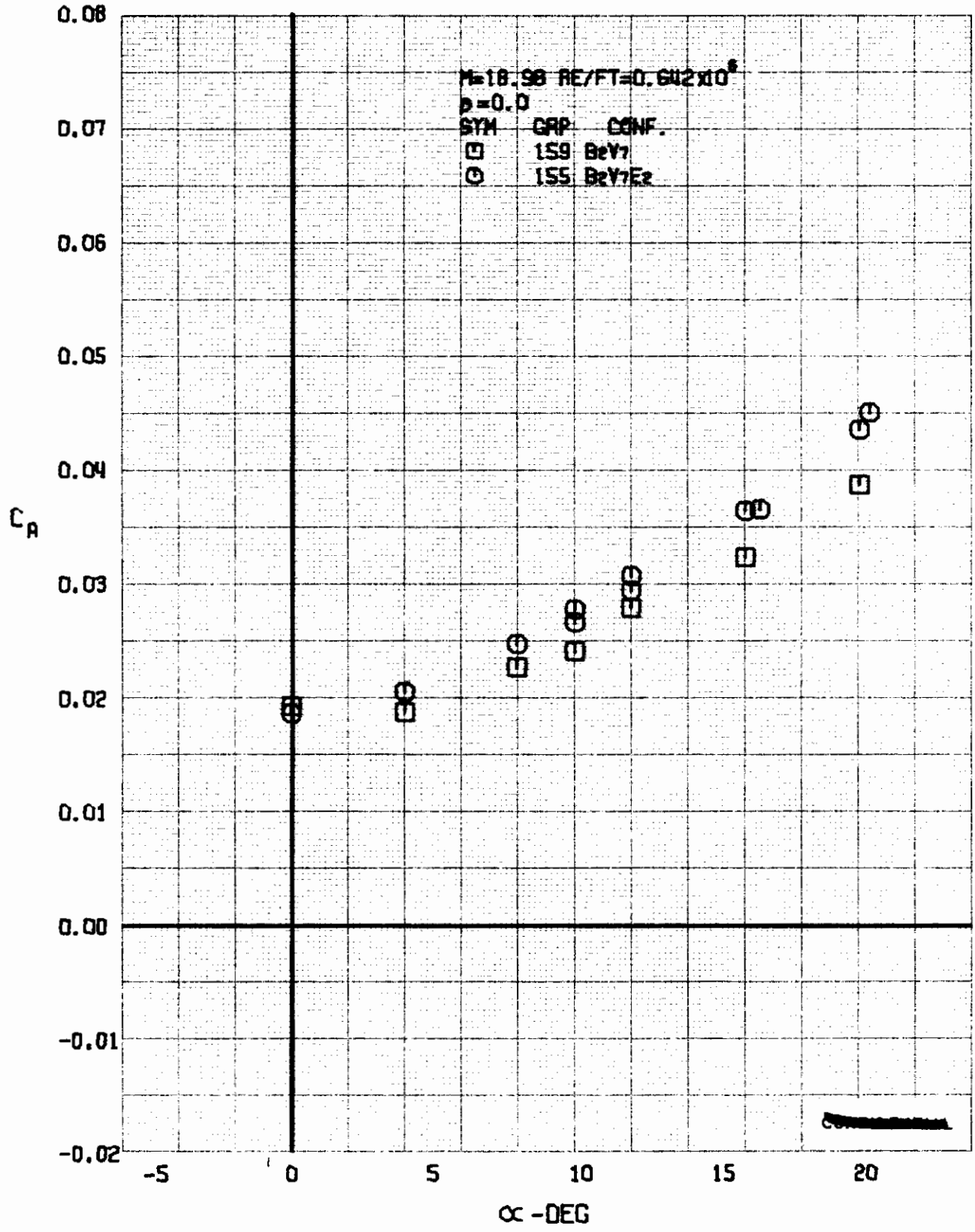

FIGURE 295 (U) CONFIGURATION BUILDUP
- AXIAL FORCE COEFFICIENT VARIATION WITH ANGLE OF ATTACK (M=18.98

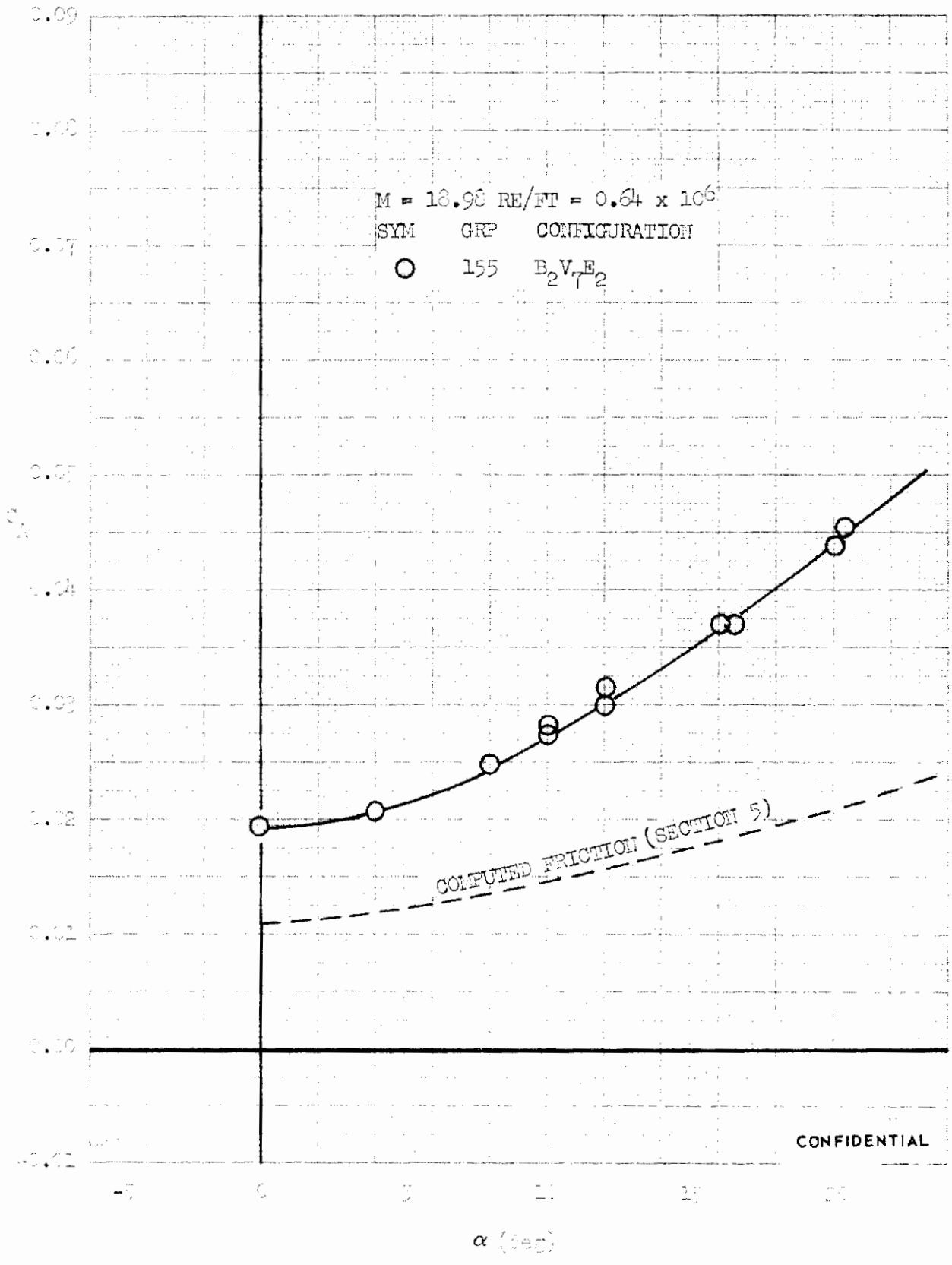

FIGURE 296 (U) AXIAL FORCE BUILDUP - AXIAL FORCE COEFFICIENT VARIATION WITH ANGLE OF ATTACK

LOCKHEED CALIFORNIA COMPANY

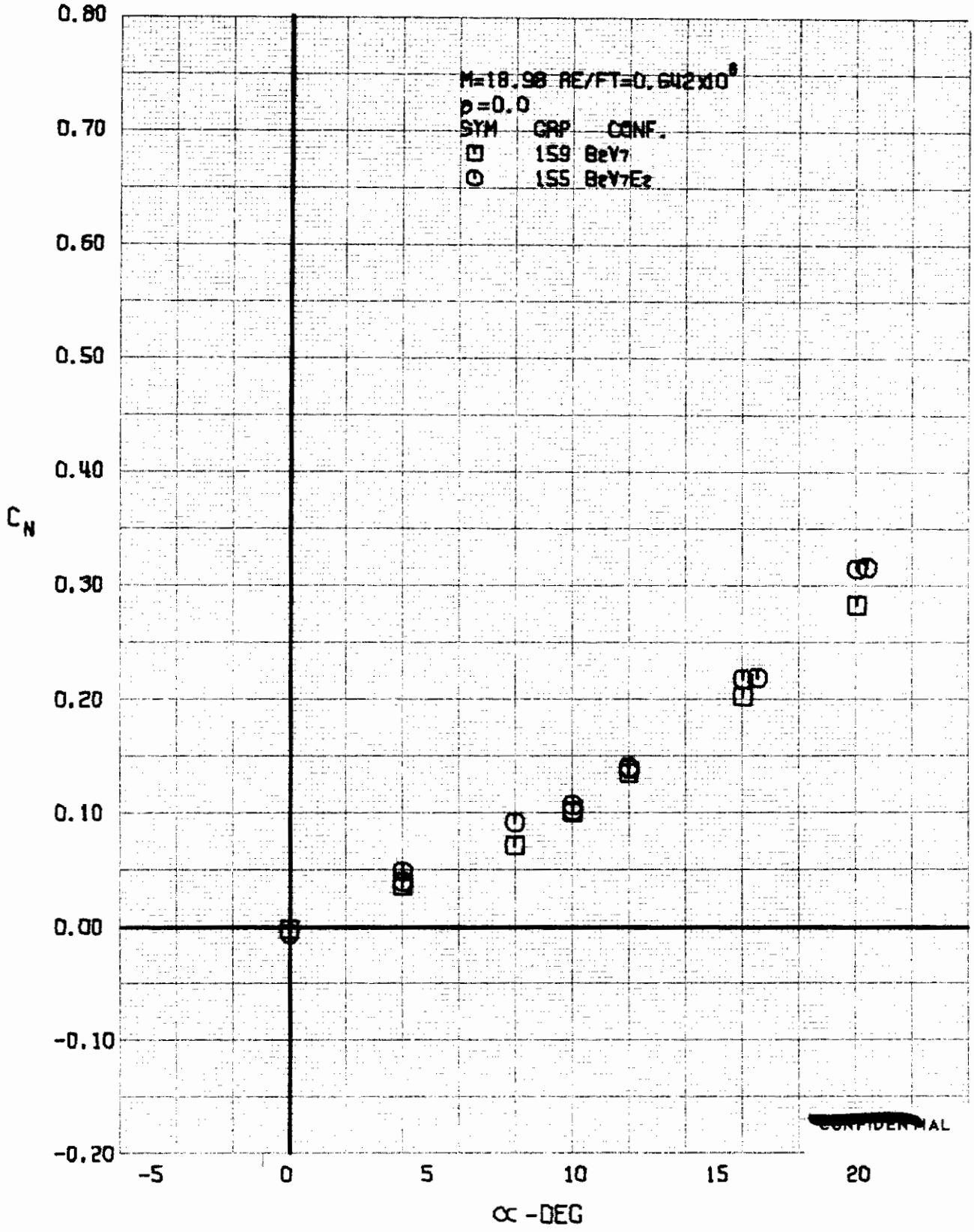

FIGURE 297 (U) CONFIGURATION BUILDUP
- NORMAL FORCE COEFFICIENT VARIATION WITH ANGLE OF ATTACK (M=18.98

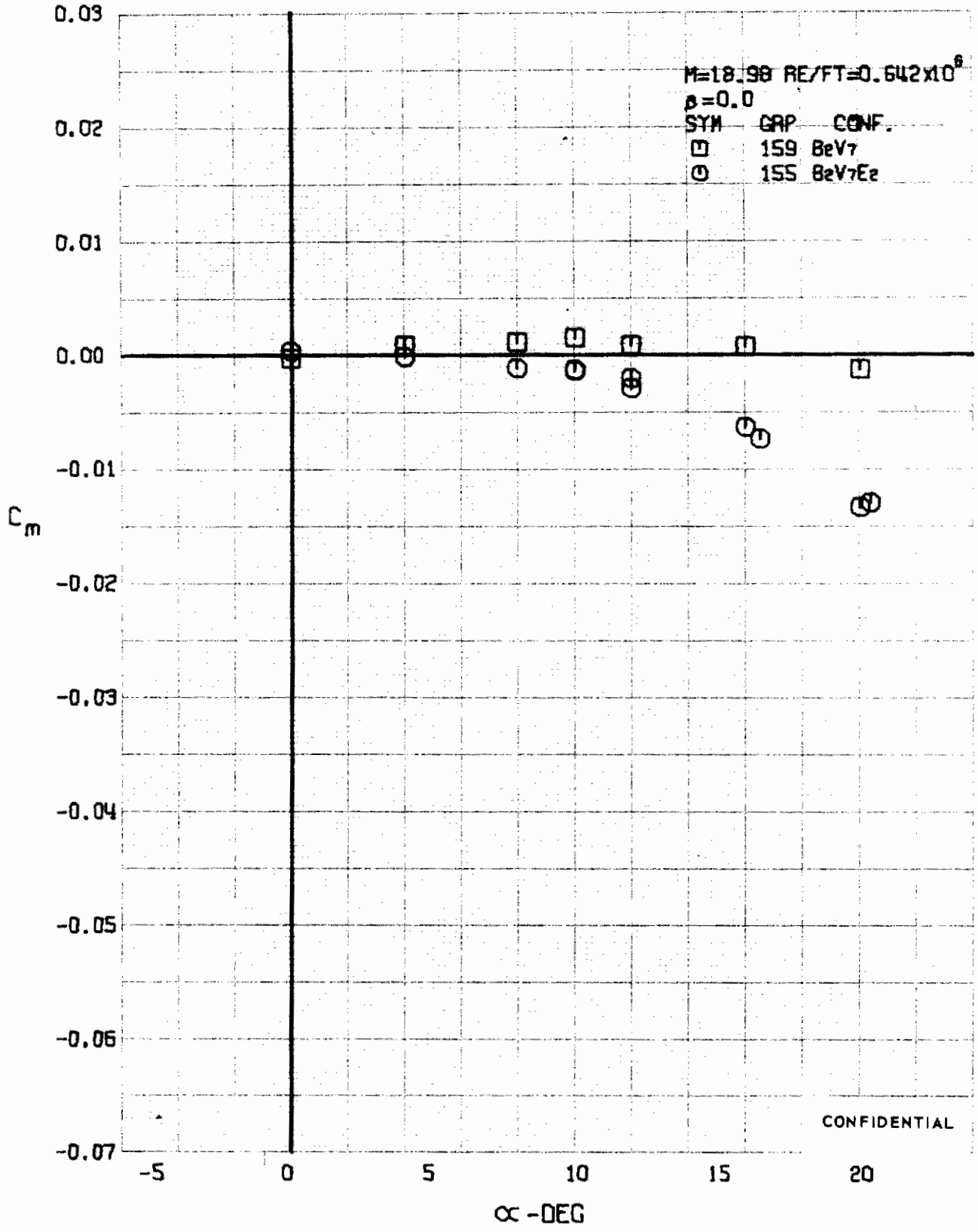

FIGURE 298 (U) CONFIGURATION BUILDUP
- PITCHING MOMENT COEFFICIENT VARIATION WITH ANGLE OF ATTACK (M= 18.98

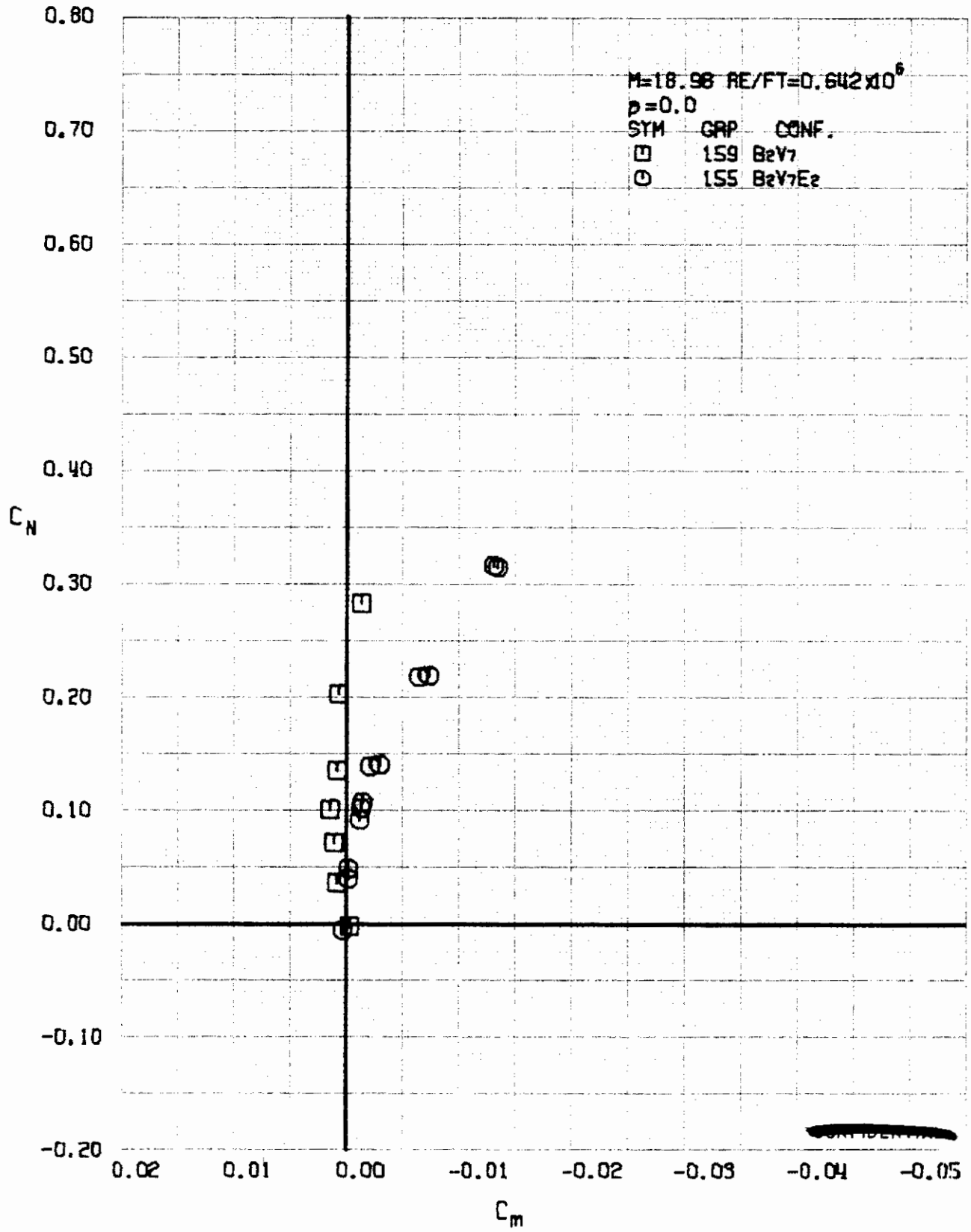

FIGURE 299 (U) CONFIGURATION BUILDUP
- LONGITUDINAL STABILITY VARIATION (M= 18.98

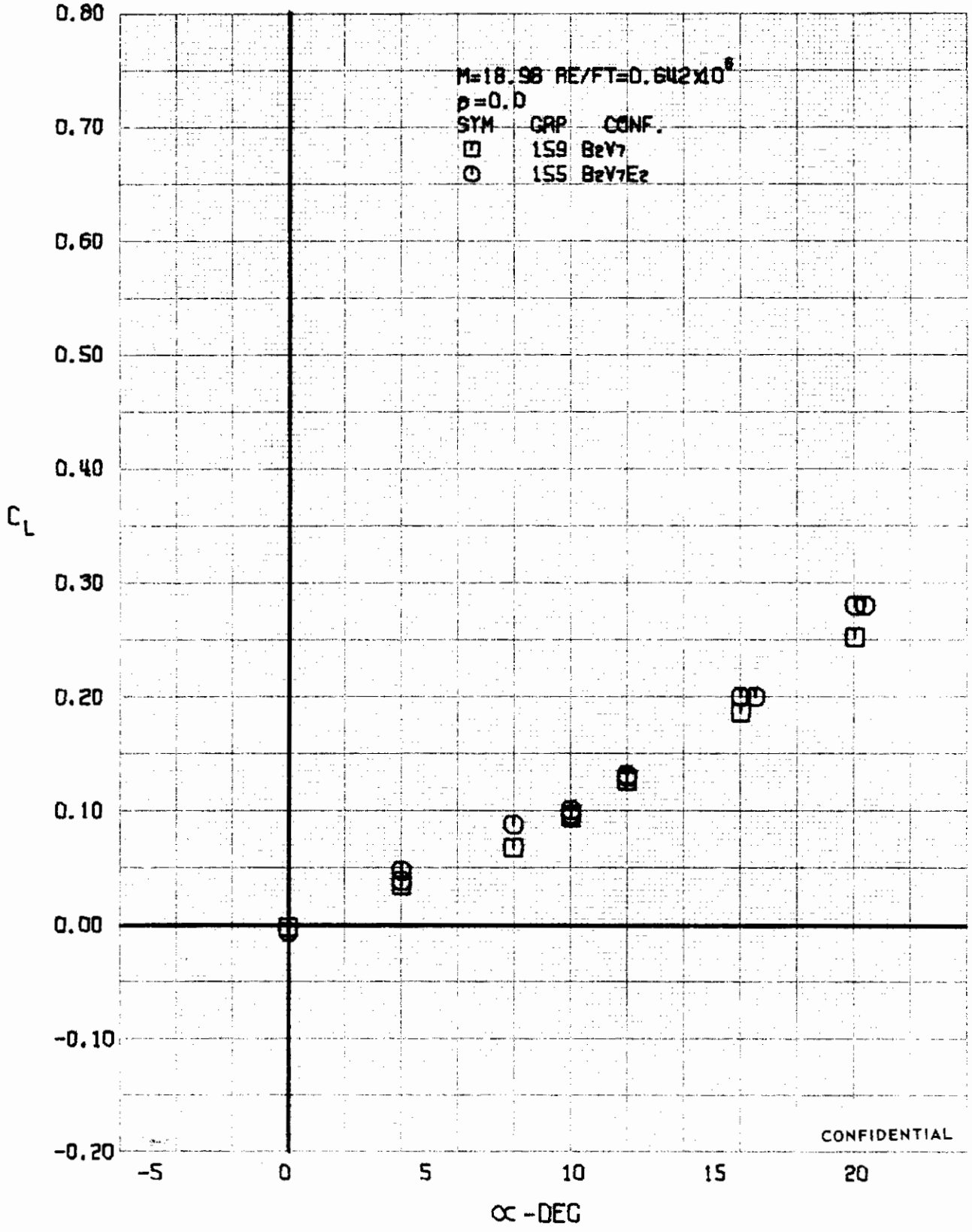

FIGURE 300 (U) CONFIGURATION BUILDUP
- LIFT COEFFICIENT VARIATION WITH ANGLE OF ATTACK (M=18.98

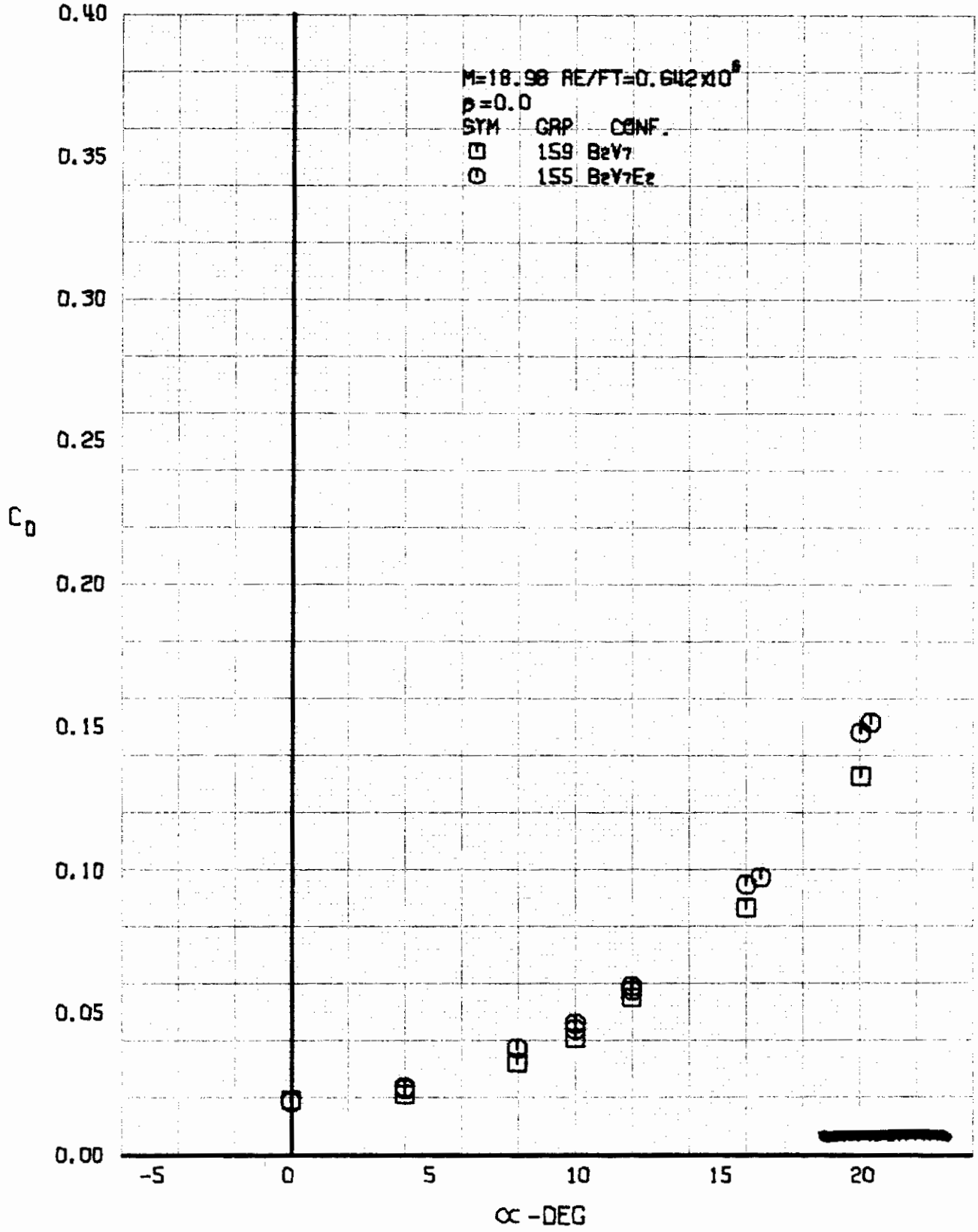

FIGURE 301 (U) CONFIGURATION BUILDUP
- DRAG COEFFICIENT VARIATION WITH ANGLE OF ATTACK (M=18.98

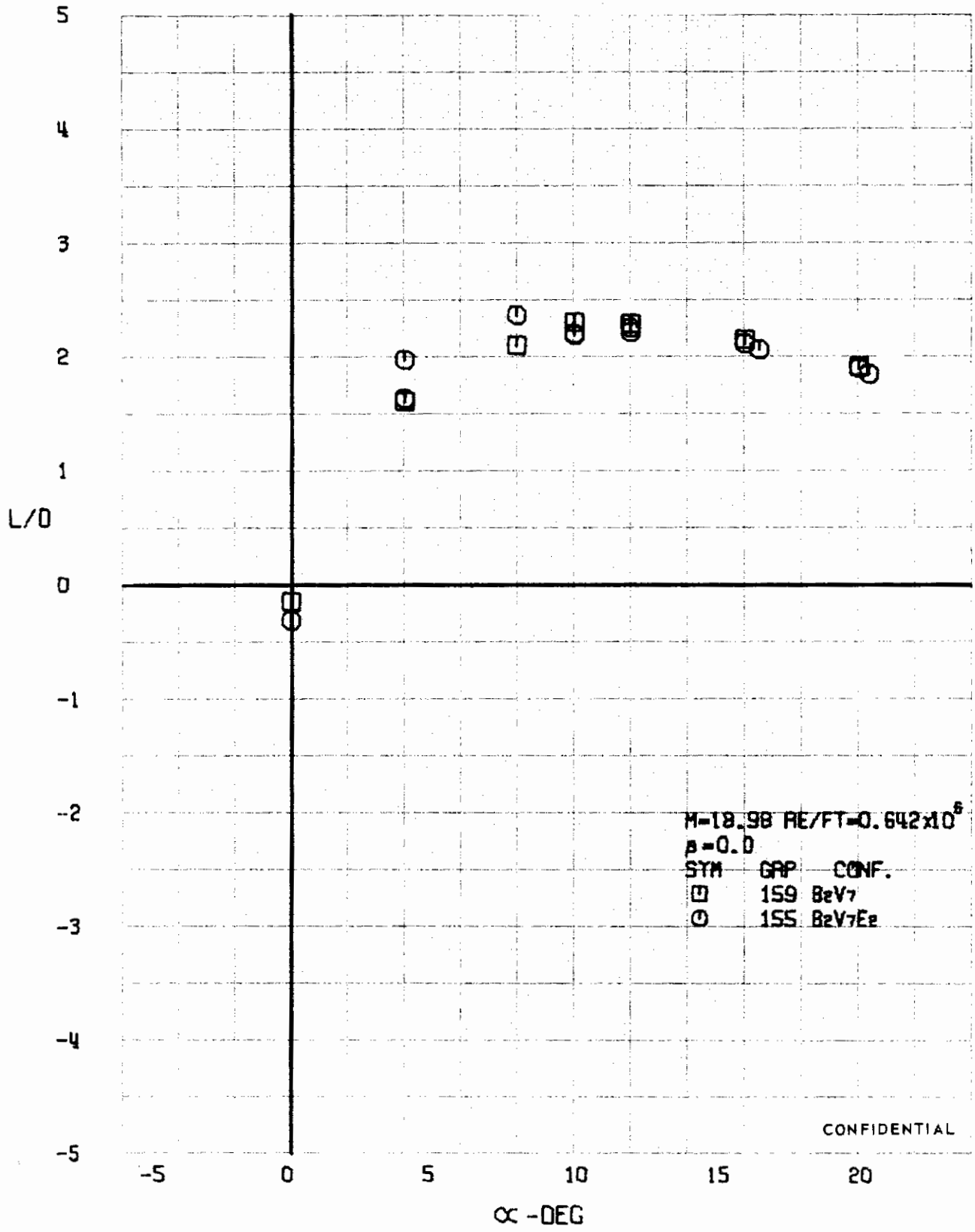

FIGURE 302 : (U) CONFIGURATION BUILDUP
- LIFT-DRAG RATIO VARIATION WITH ANGLE OF ATTACK (M= 18.98

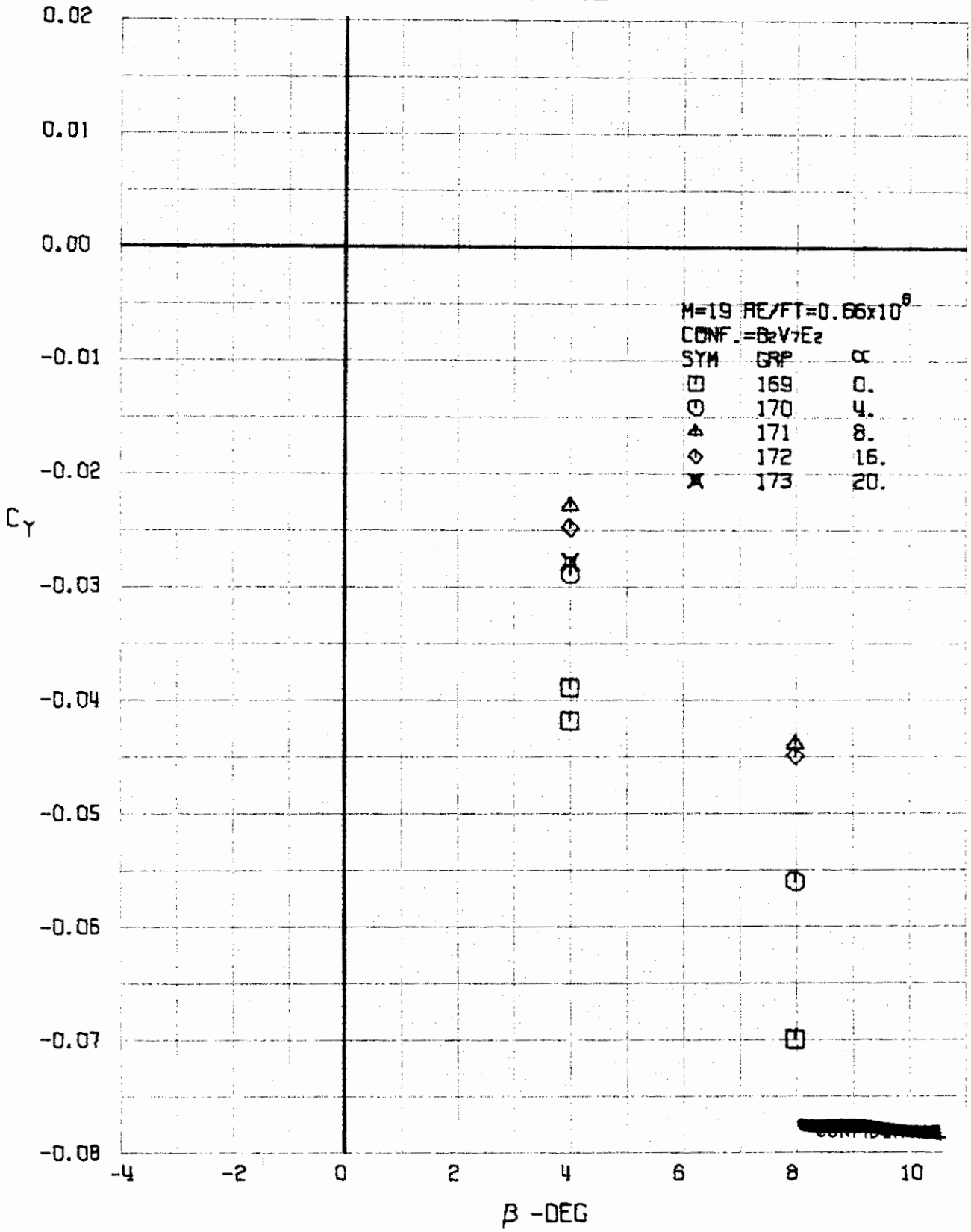

FIGURE 303 (U) COMPLETE CONFIGURATION
- SIDE FORCE COEFFICIENT VARIATION WITH ANGLE OF YAW (M=18.77)

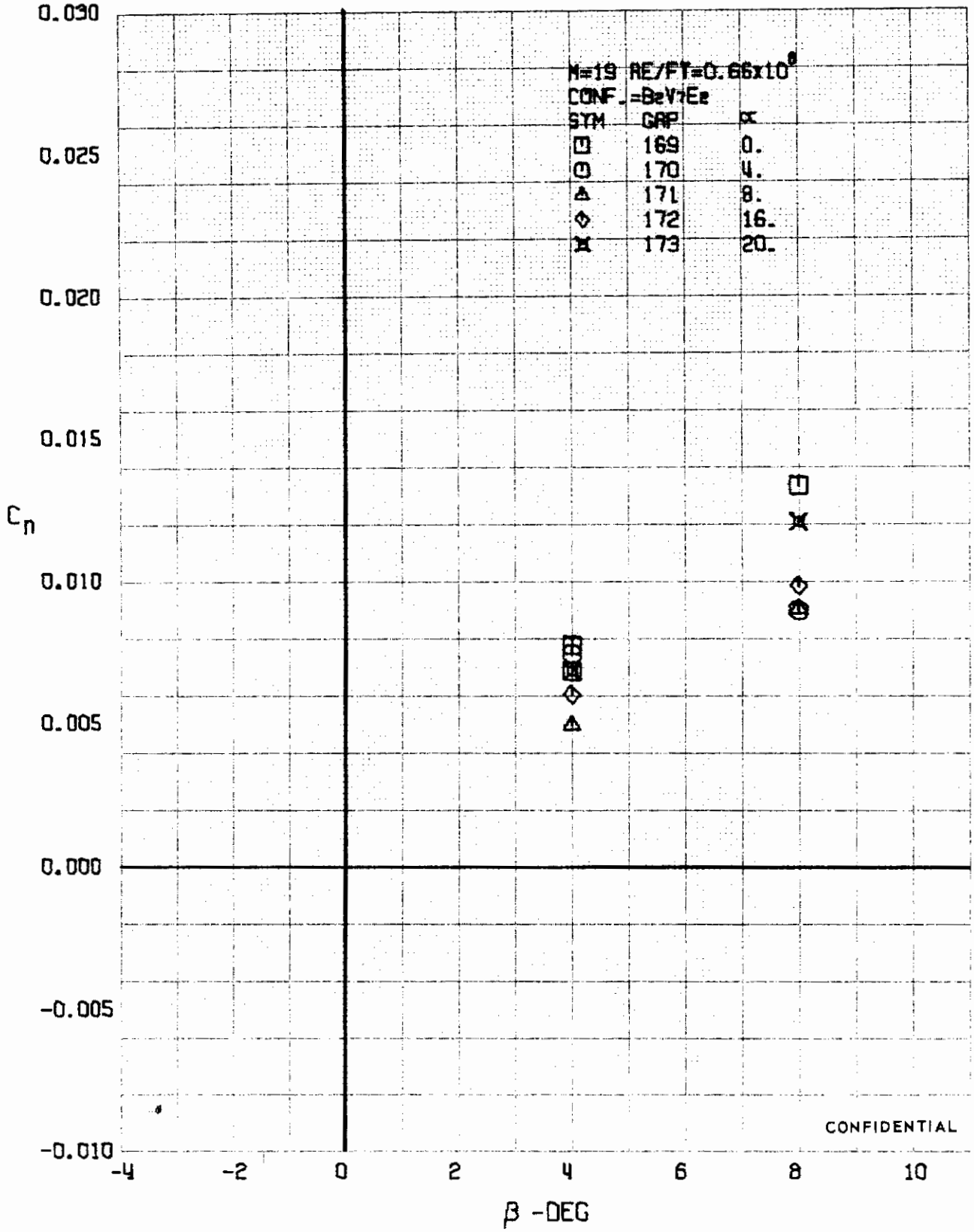

FIGURE 304 (U) COMPLETE CONFIGURATION
- YAWING MOMENT COEFFICIENT VARIATION WITH ANGLE OF YAW (M= 18.77)

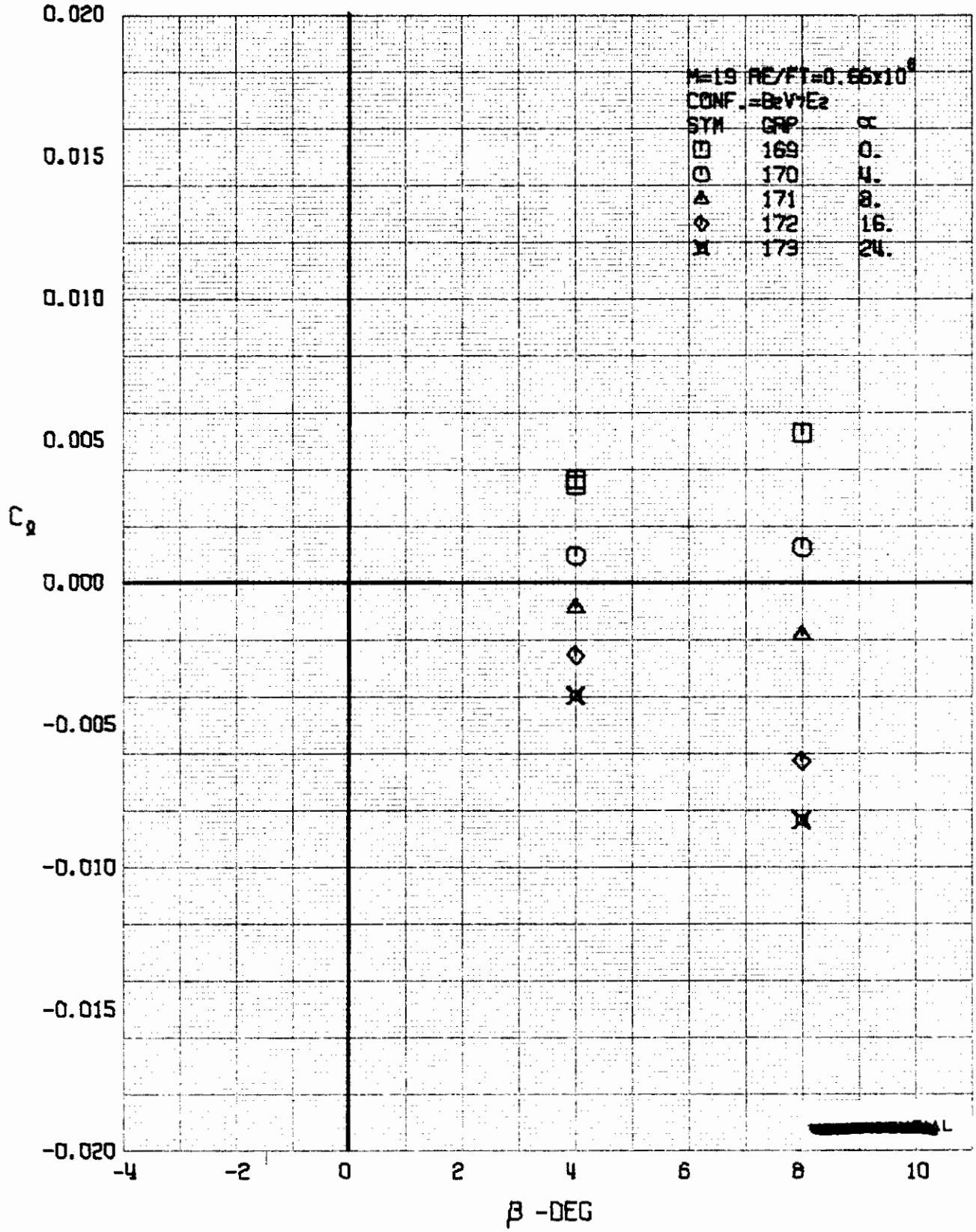

FIGURE 305 (U) COMPLETE CONFIGURATION
- ROLLING MOMENT COEFFICIENT VARIATION WITH ANGLE OF YAW (M=1.8.7)

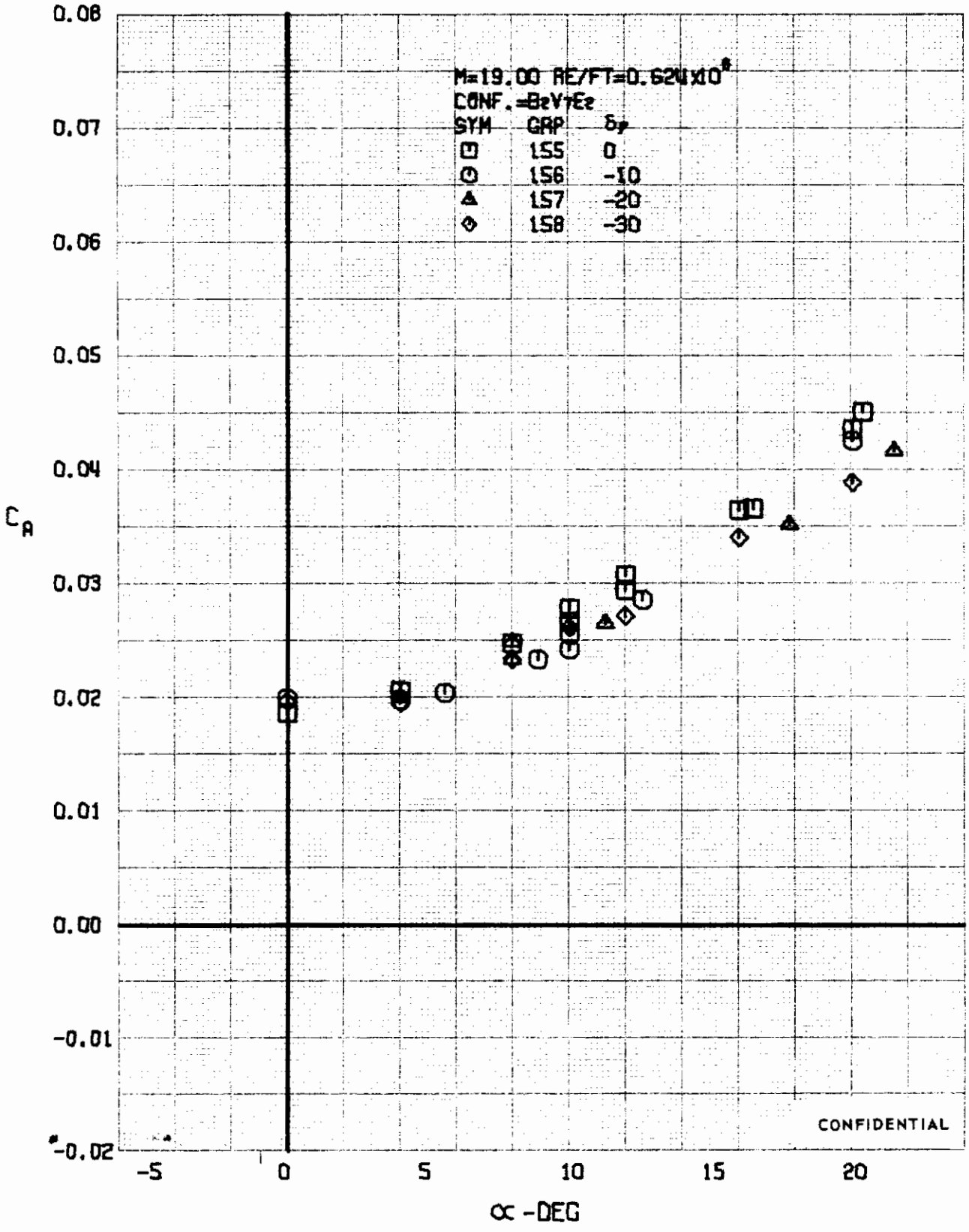

FIGURE 306 (U) ELEVON EFFECTS
- AXIAL FORCE COEFFICIENT VARIATION WITH ANGLE OF ATTACK (M=19.00

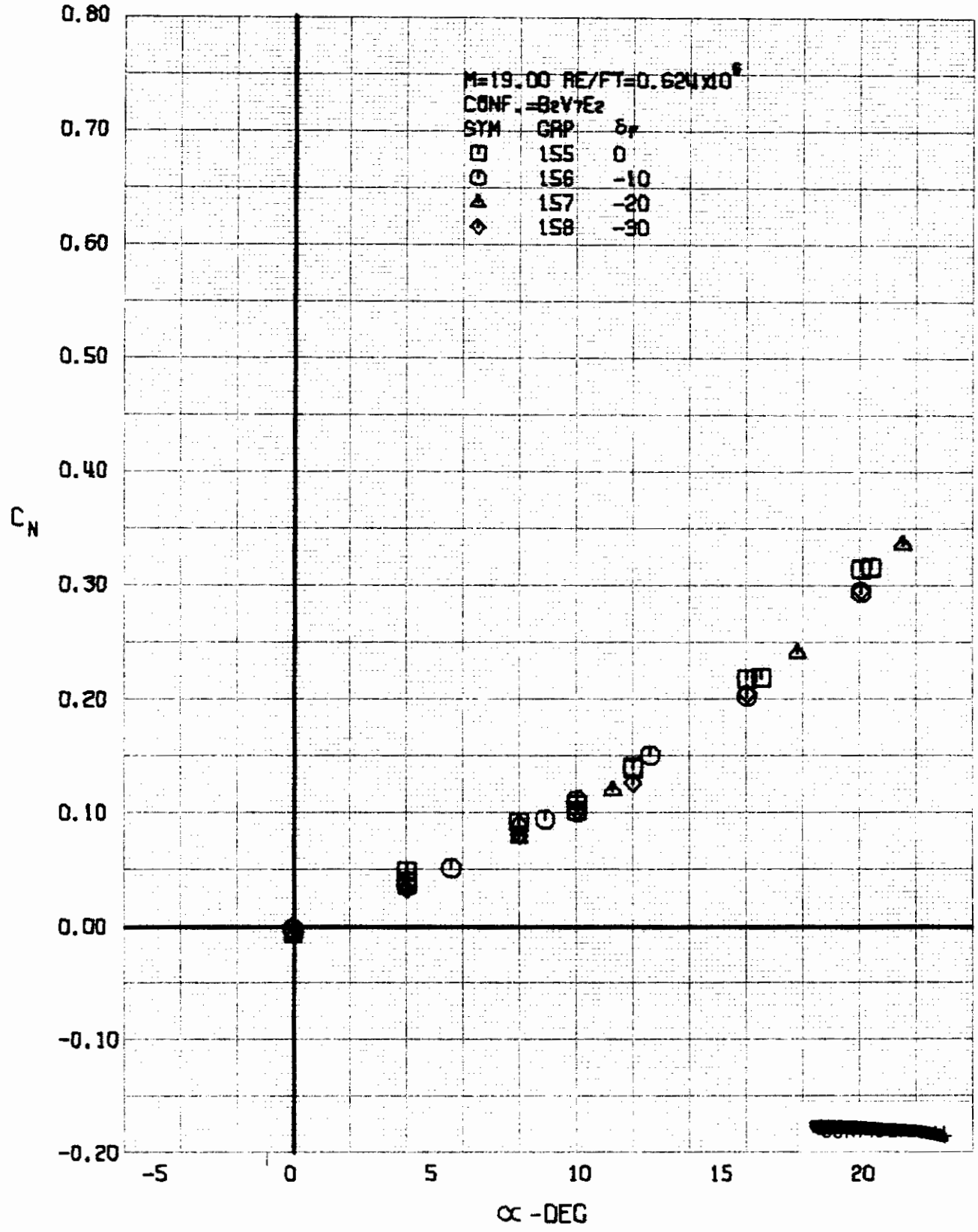

FIGURE 307 (U) ELEVON EFFECTS
- NORMAL FORCE COEFFICIENT VARIATION WITH ANGLE OF ATTACK (M= 19.00

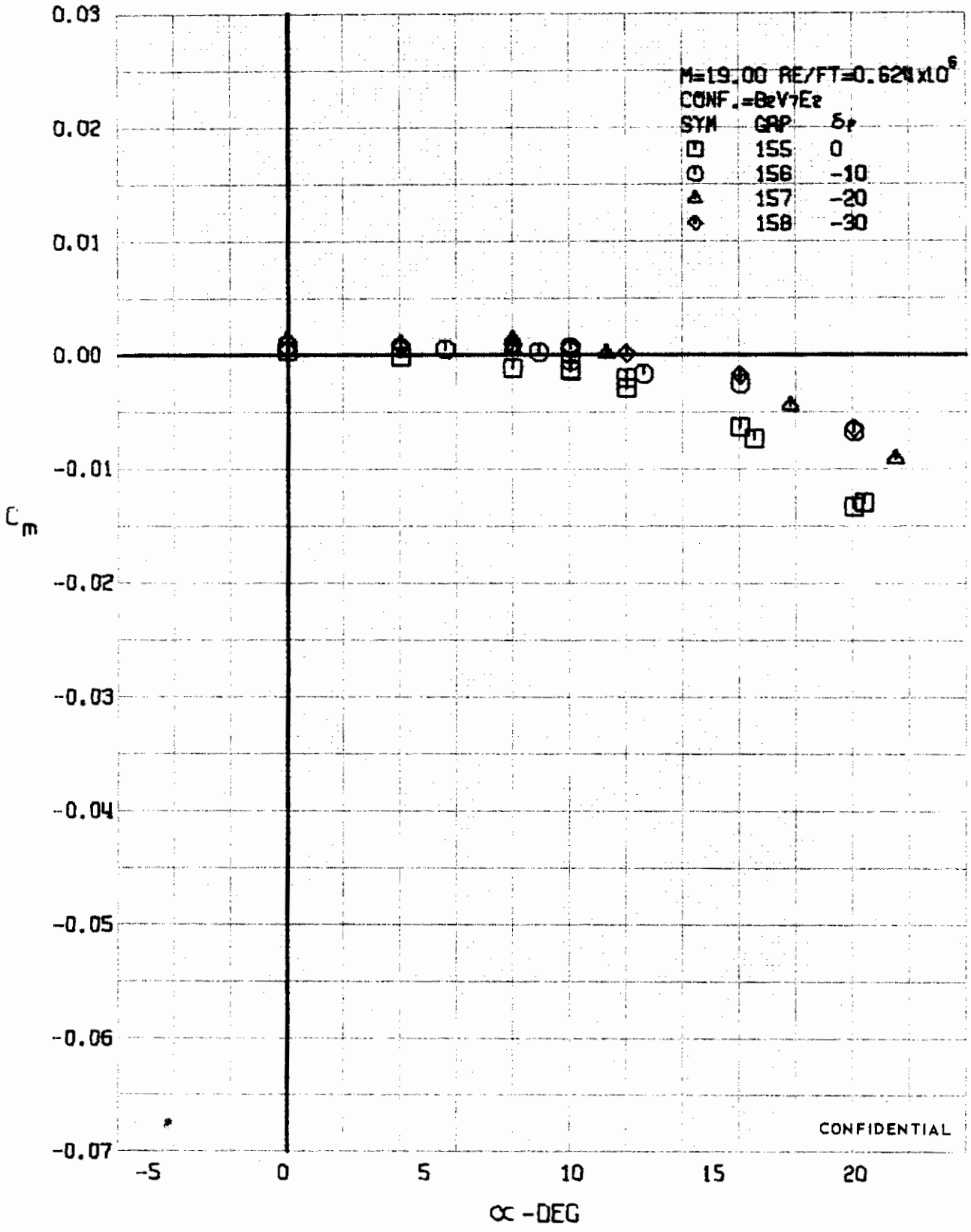

FIGURE 308 (U) ELEVON EFFECTS
- PITCHING MOMENT COEFFICIENT VARIATION WITH ANGLE OF ATTACK (M=19.00

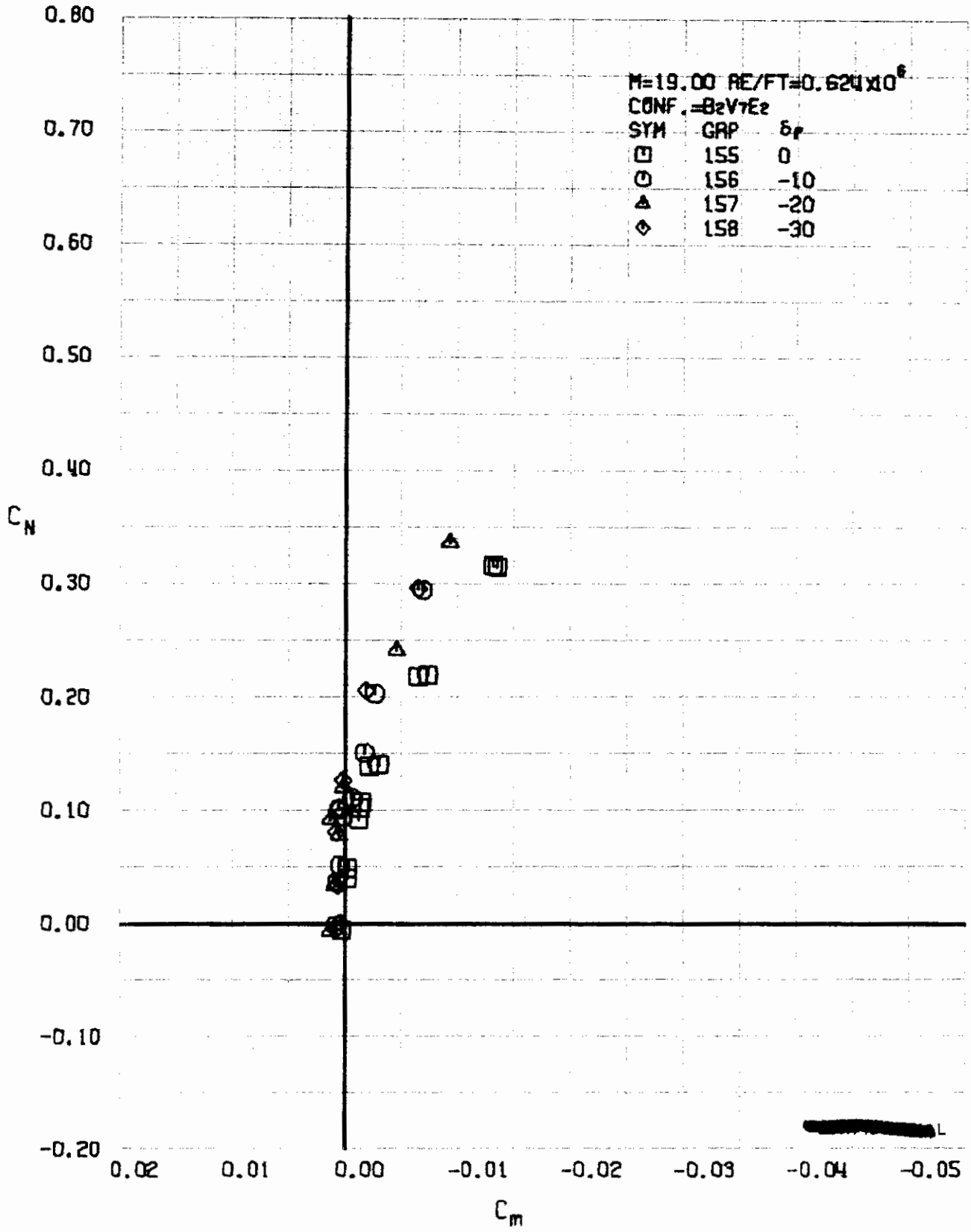

FIGURE 309 (U) ELEVON EFFECTS
- LONGITUDINAL STABILITY VARIATION (M= 19.00

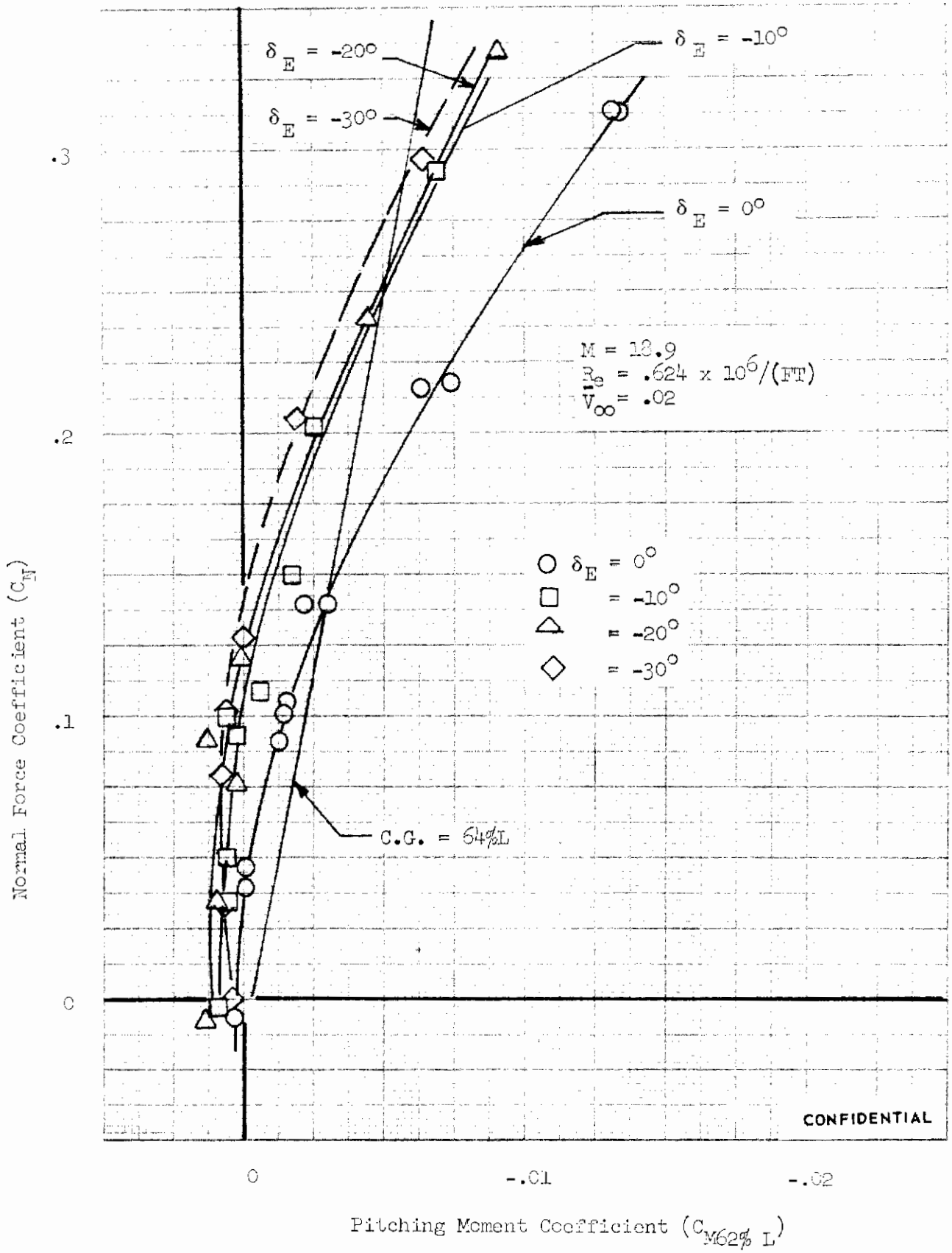

FIGURE 310 (U) FDL-5 LONGITUDINAL STABILITY (M = 18.9)

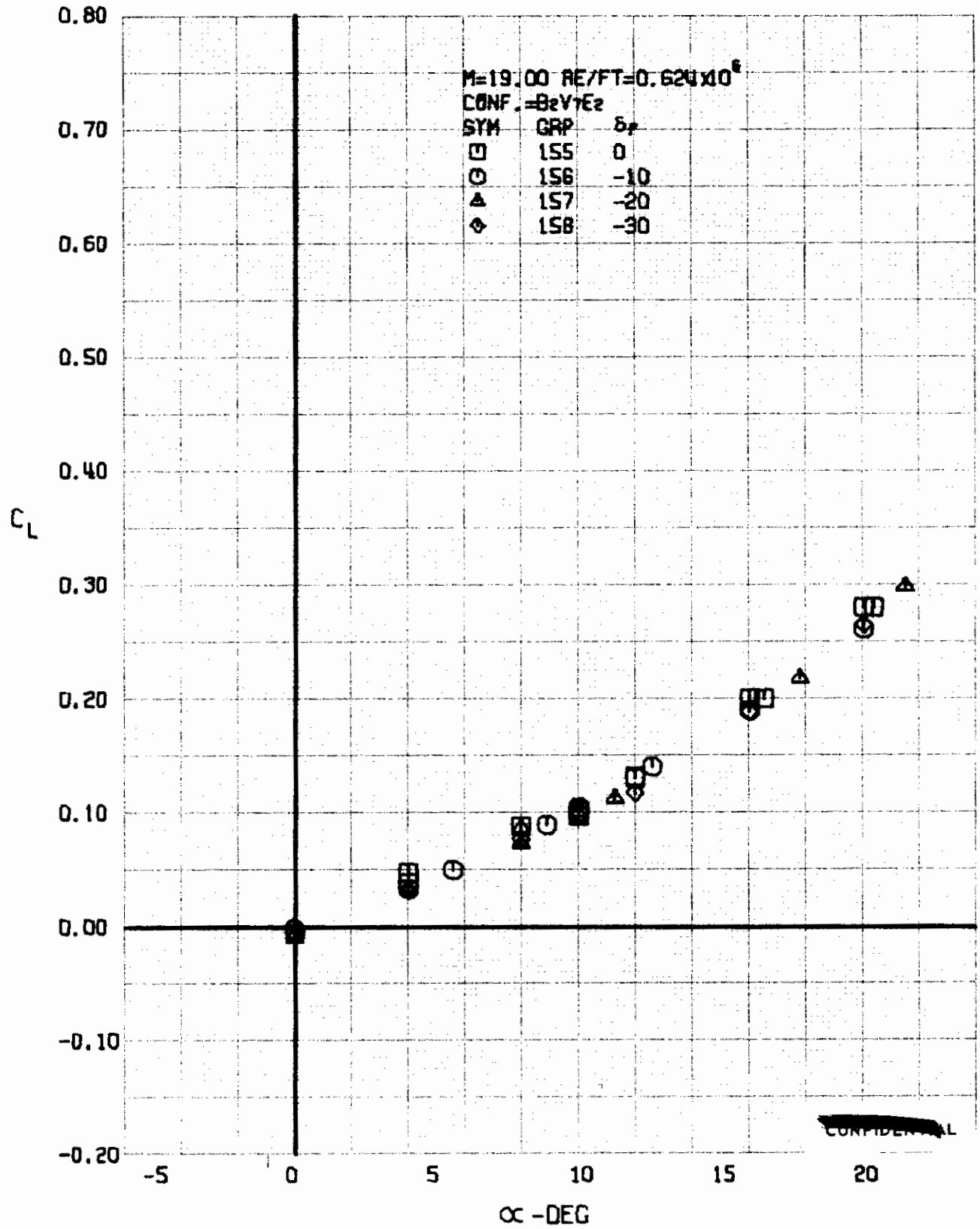

FIGURE 311 (U) ELEVON EFFECTS
- LIFT COEFFICIENT VARIATION WITH ANGLE OF ATTACK (M= 19.00

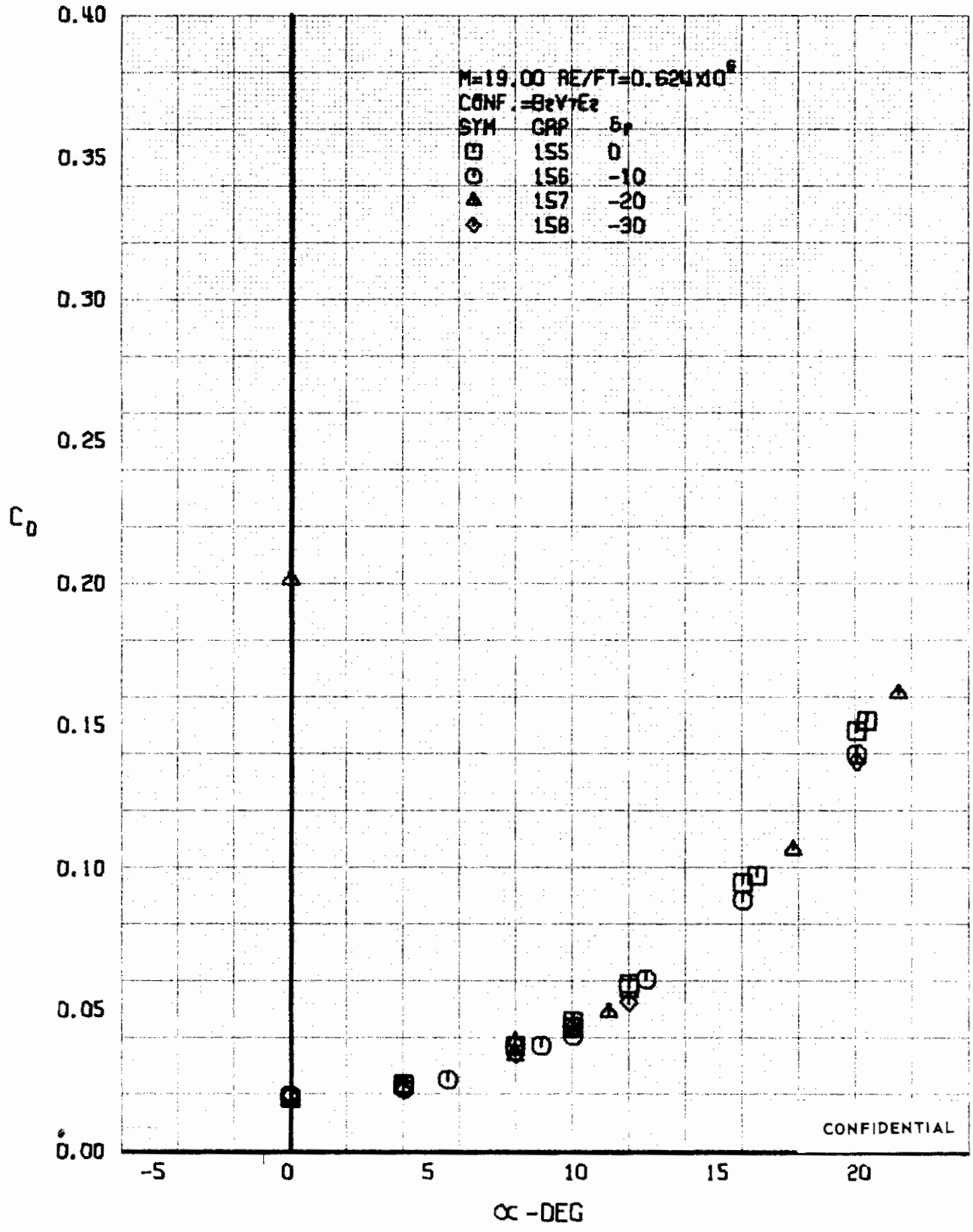

FIGURE 312 (U) ELEVON EFFECTS
- DRAG COEFFICIENT VARIATION WITH ANGLE OF ATTACK (M=19.00

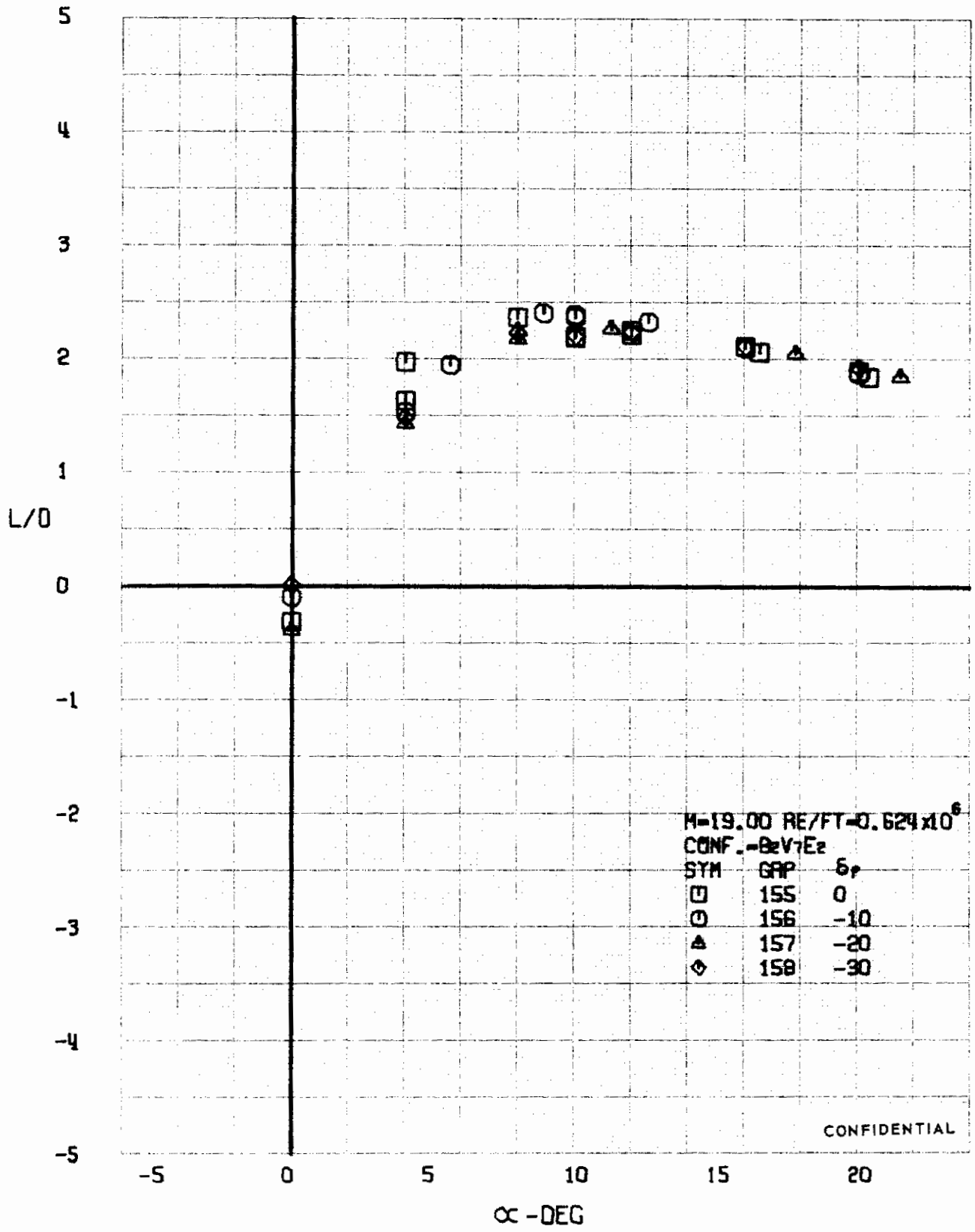

FIGURE 313 (U) **ELEVON EFFECTS**
- LIFT-DRAG RATIO VARIATION WITH ANGLE OF ATTACK (M= 19.00

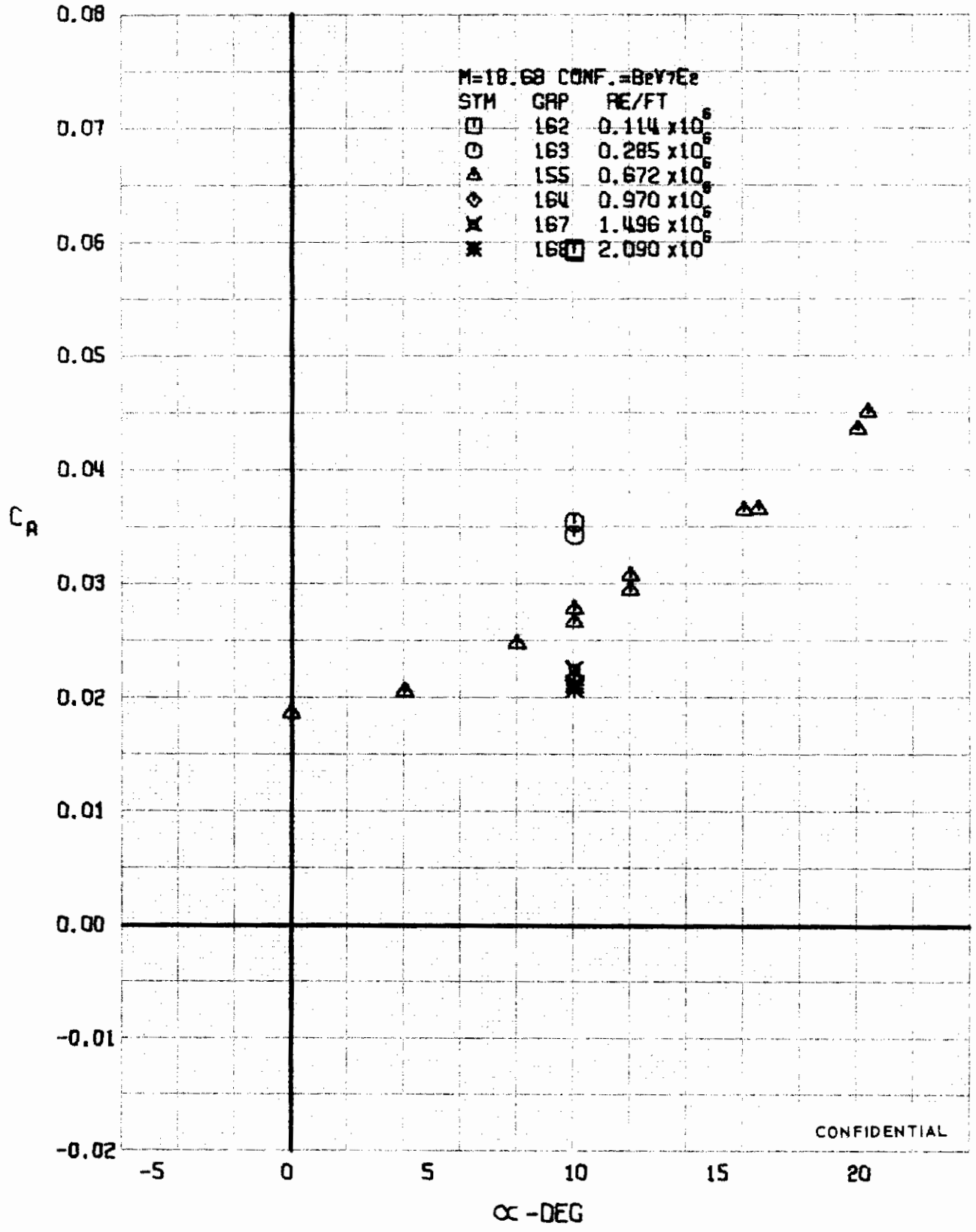

FIGURE 314 (U) REYNOLDS NUMBER EFFECTS
- AXIAL FORCE COEFFICIENT VARIATION WITH ANGLE OF ATTACK (M=18.68

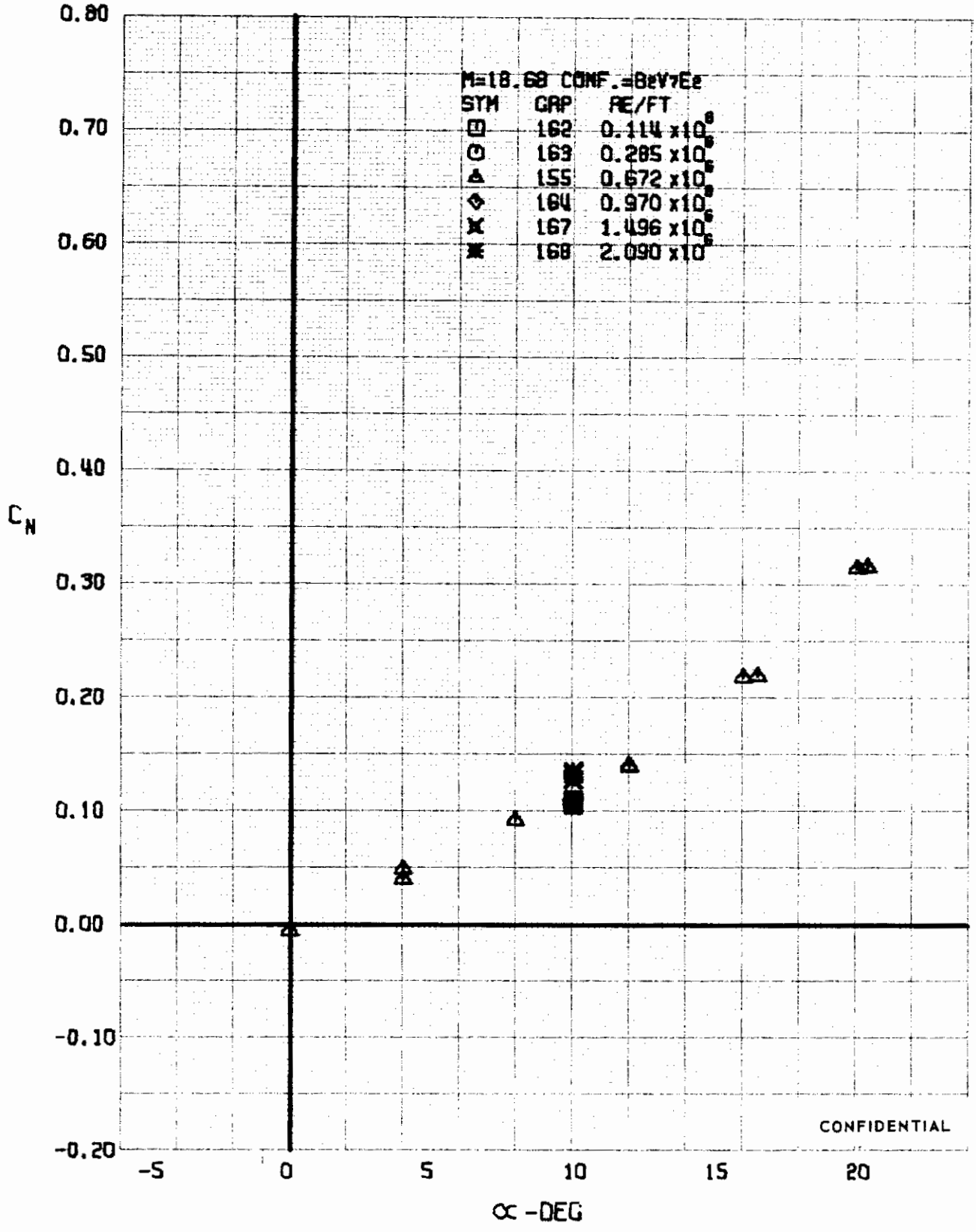

FIGURE 315 (U) REYNOLDS NUMBER EFFECTS
- NORMAL FORCE COEFFICIENT VARIATION WITH ANGLE OF ATTACK (M= 18.68

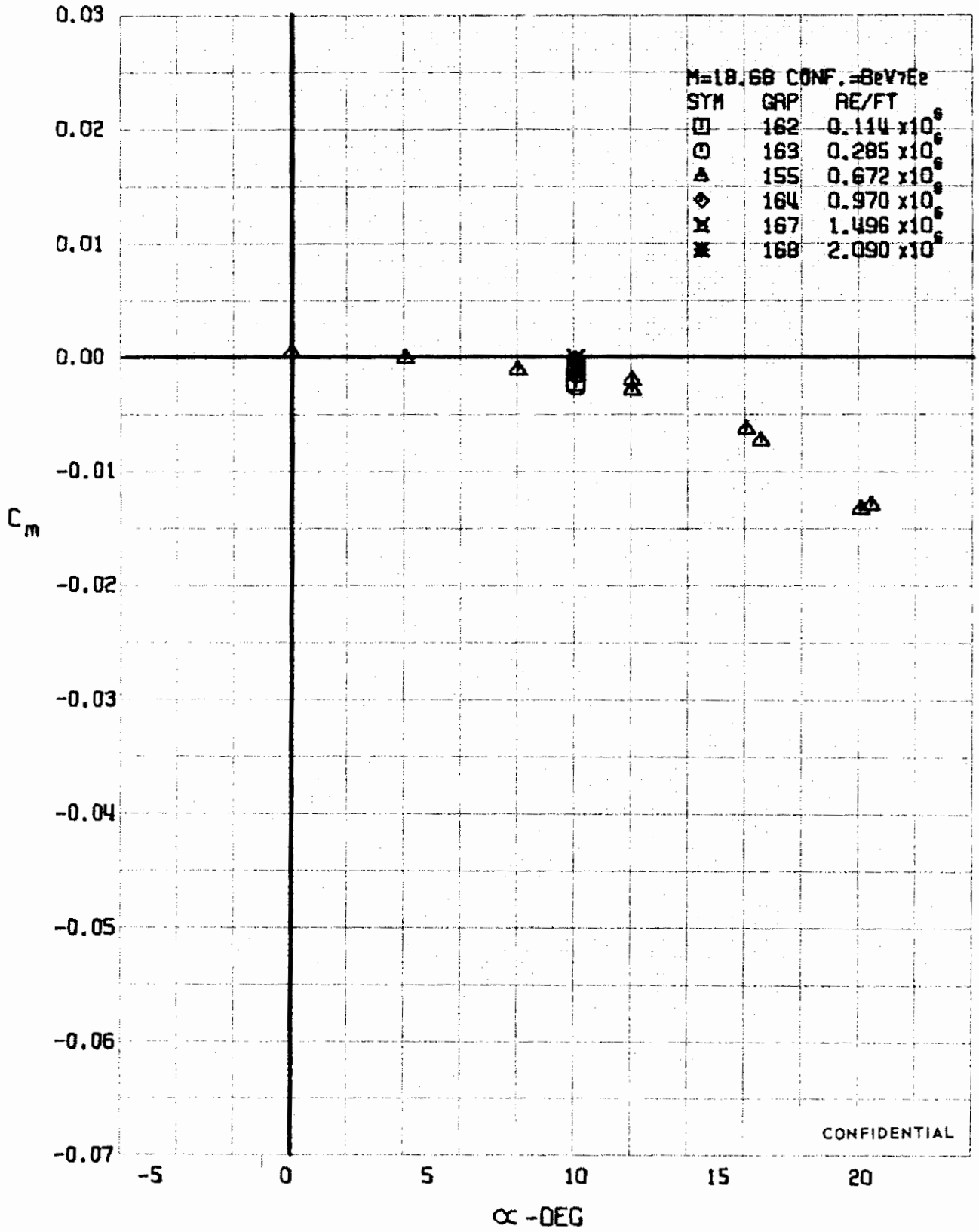

FIGURE 316 (U) REYNOLDS NUMBER EFFECTS
- PITCHING MOMENT COEFFICIENT VARIATION WITH ANGLE OF ATTACK (M= 18.68

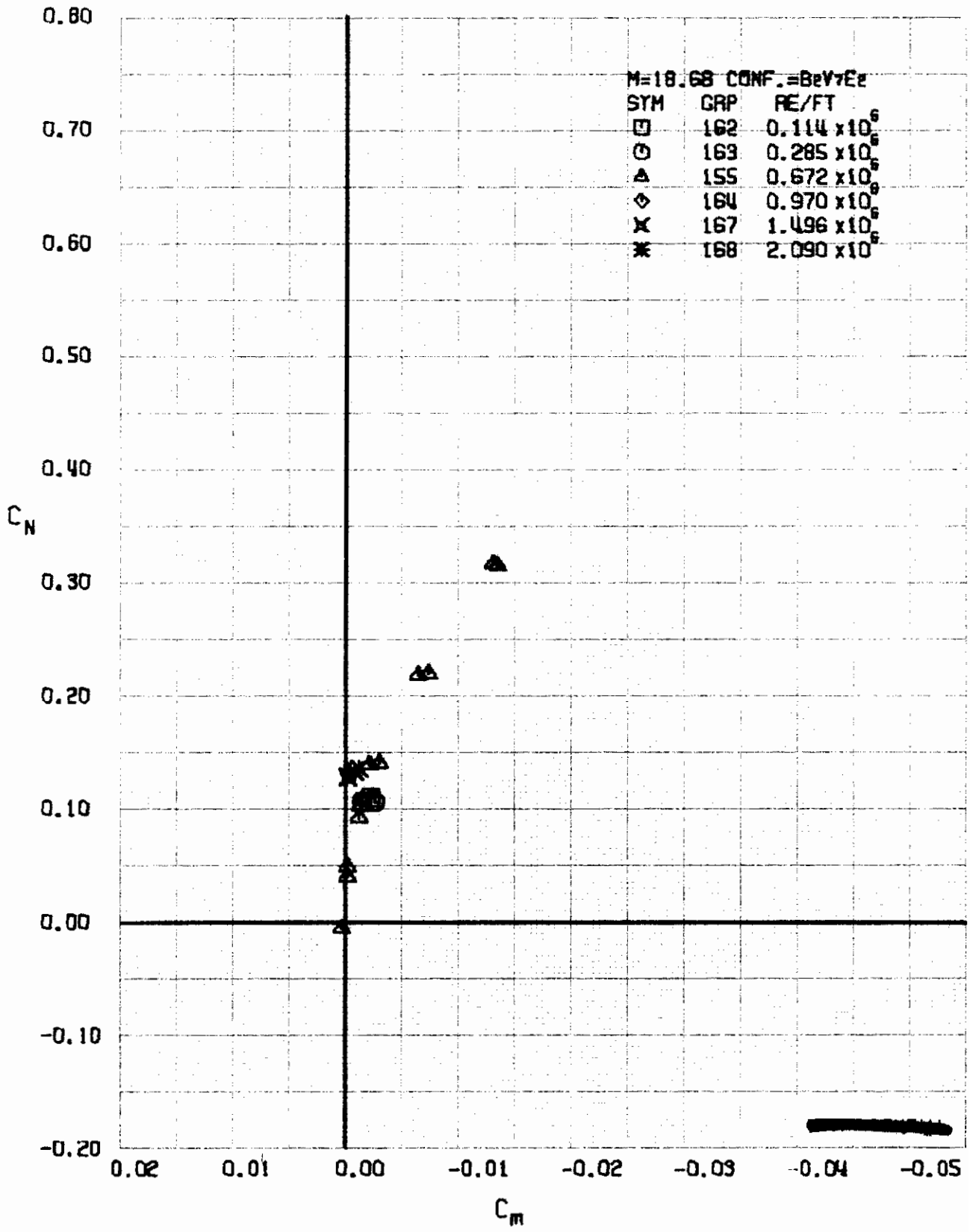

FIGURE 317 (U) REYNOLDS NUMBER EFFECTS
- LONGITUDINAL STABILITY VARIATION (M= 18.68

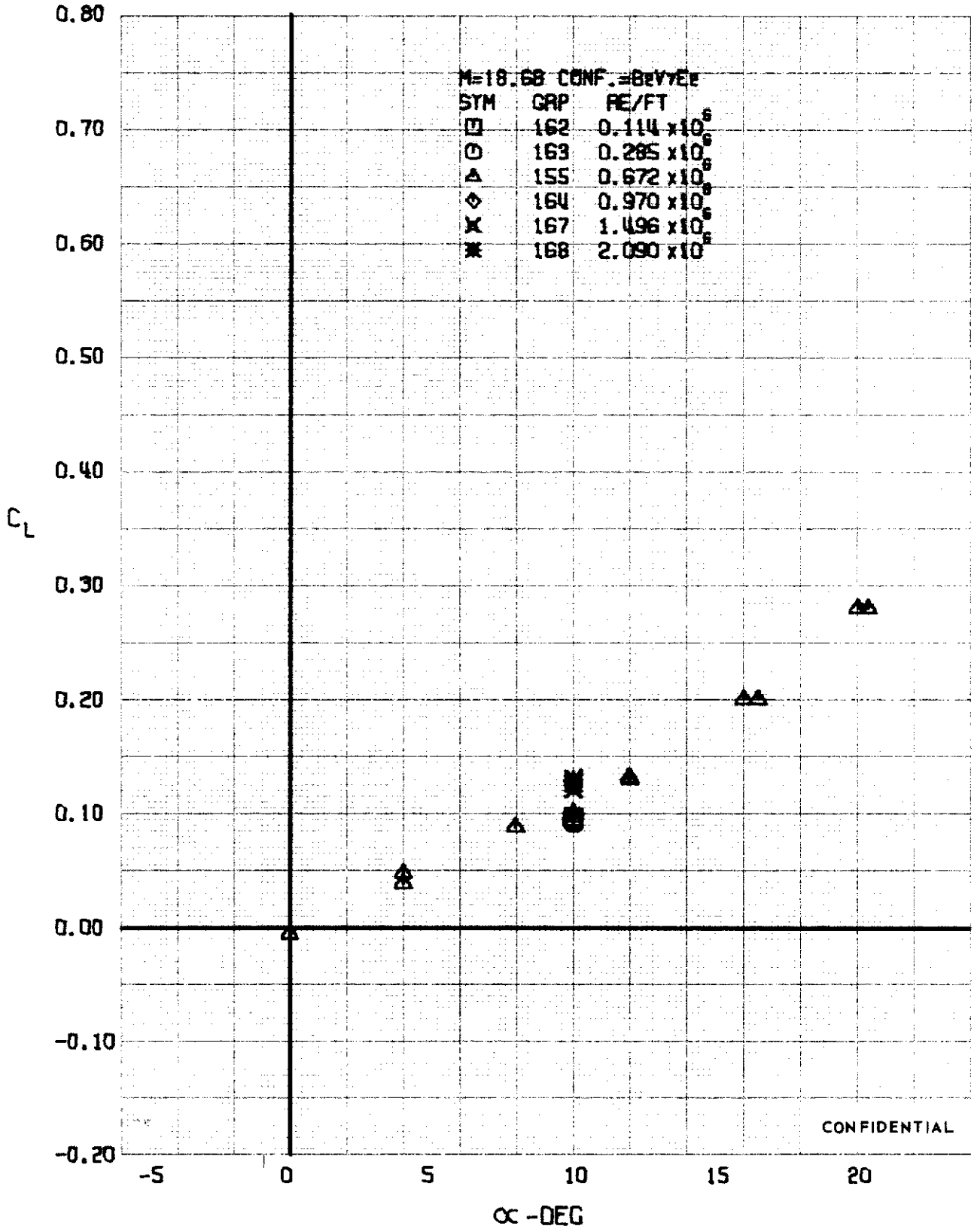

FIGURE 318 (U) REYNOLDS NUMBER EFFECTS
- LIFT COEFFICIENT VARIATION WITH ANGLE OF ATTACK (M=18.68

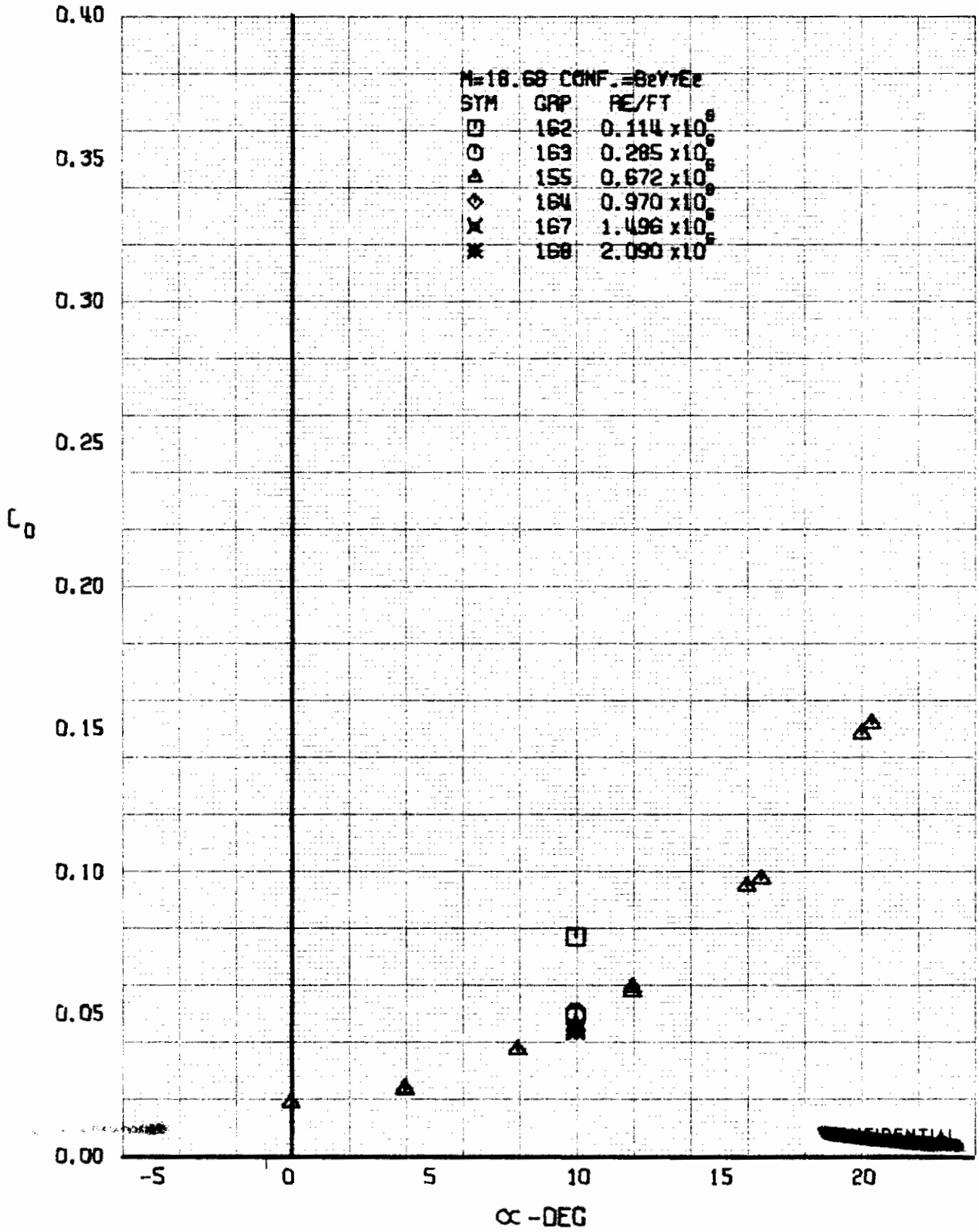

FIGURE 319 (U) REYNOLDS NUMBER EFFECTS
- DRAG COEFFICIENT VARIATION WITH ANGLE OF ATTACK (M=18.68

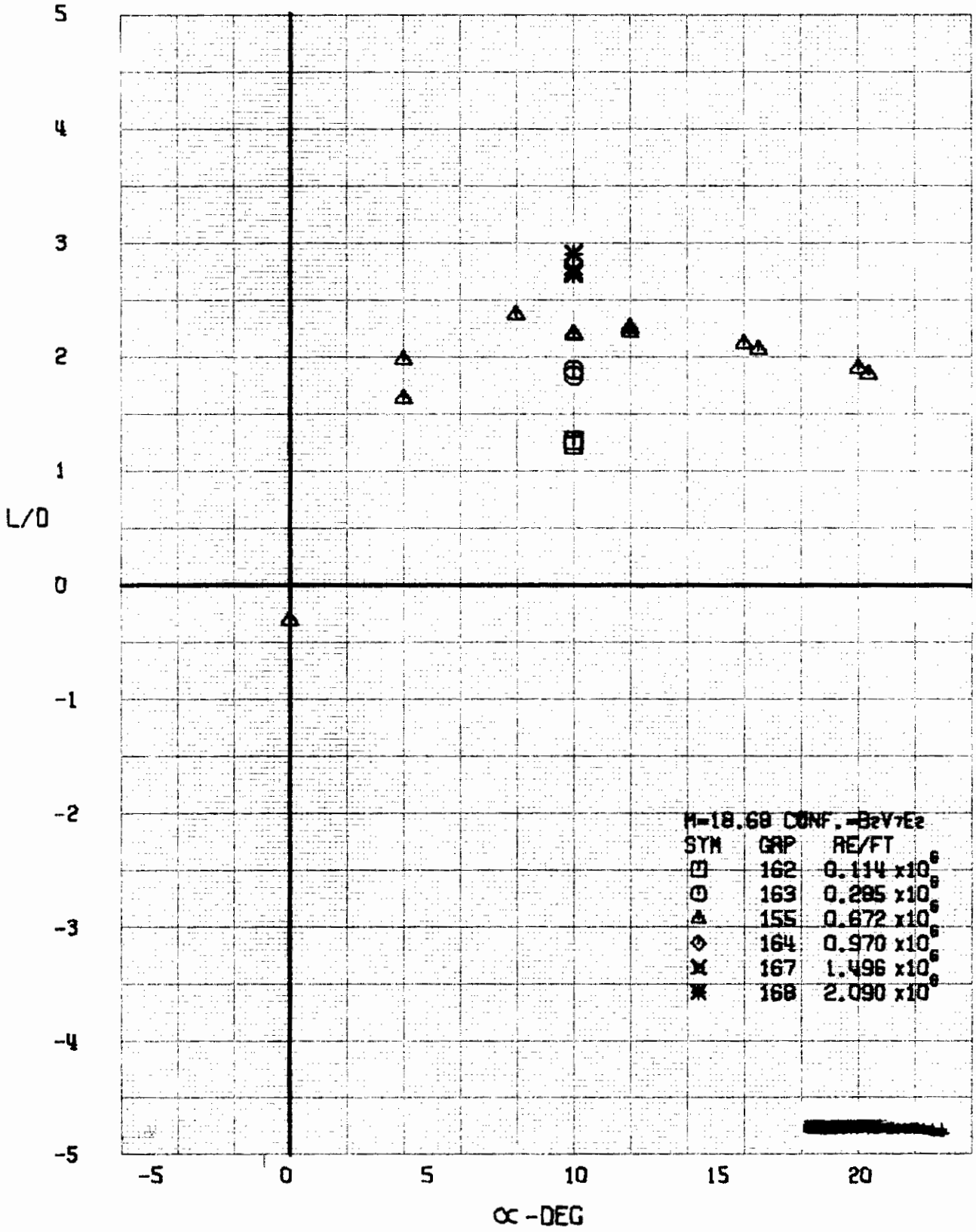

FIGURE 320 (U) REYNOLDS NUMBER EFFECTS
- LIFT-DRAG RATIO VARIATION WITH ANGLE OF ATTACK (M= 18.68

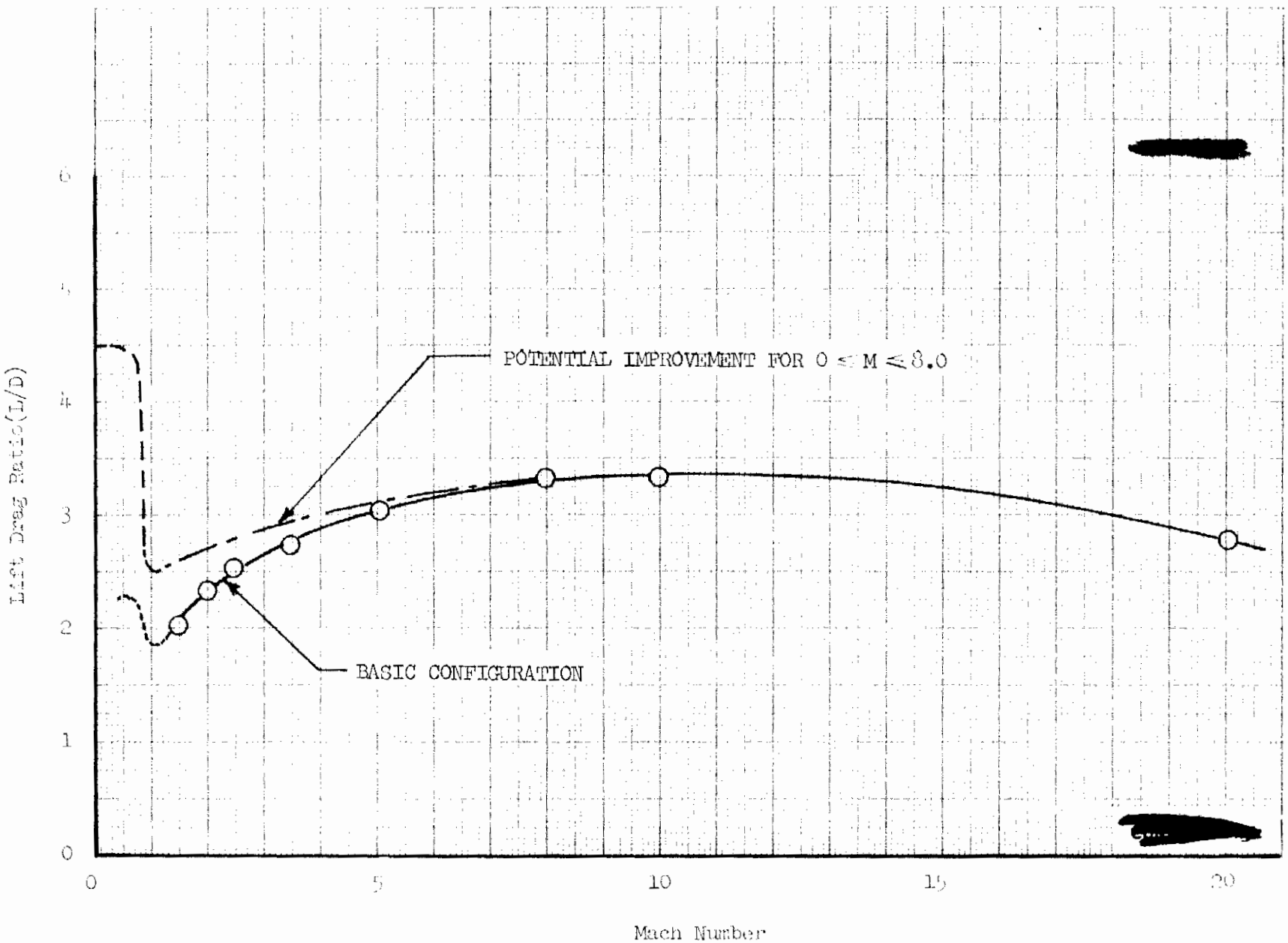

FIGURE 321 (U) FDL-5 VARIATION OF MAXIMUM L/D WITH MACH NUMBER

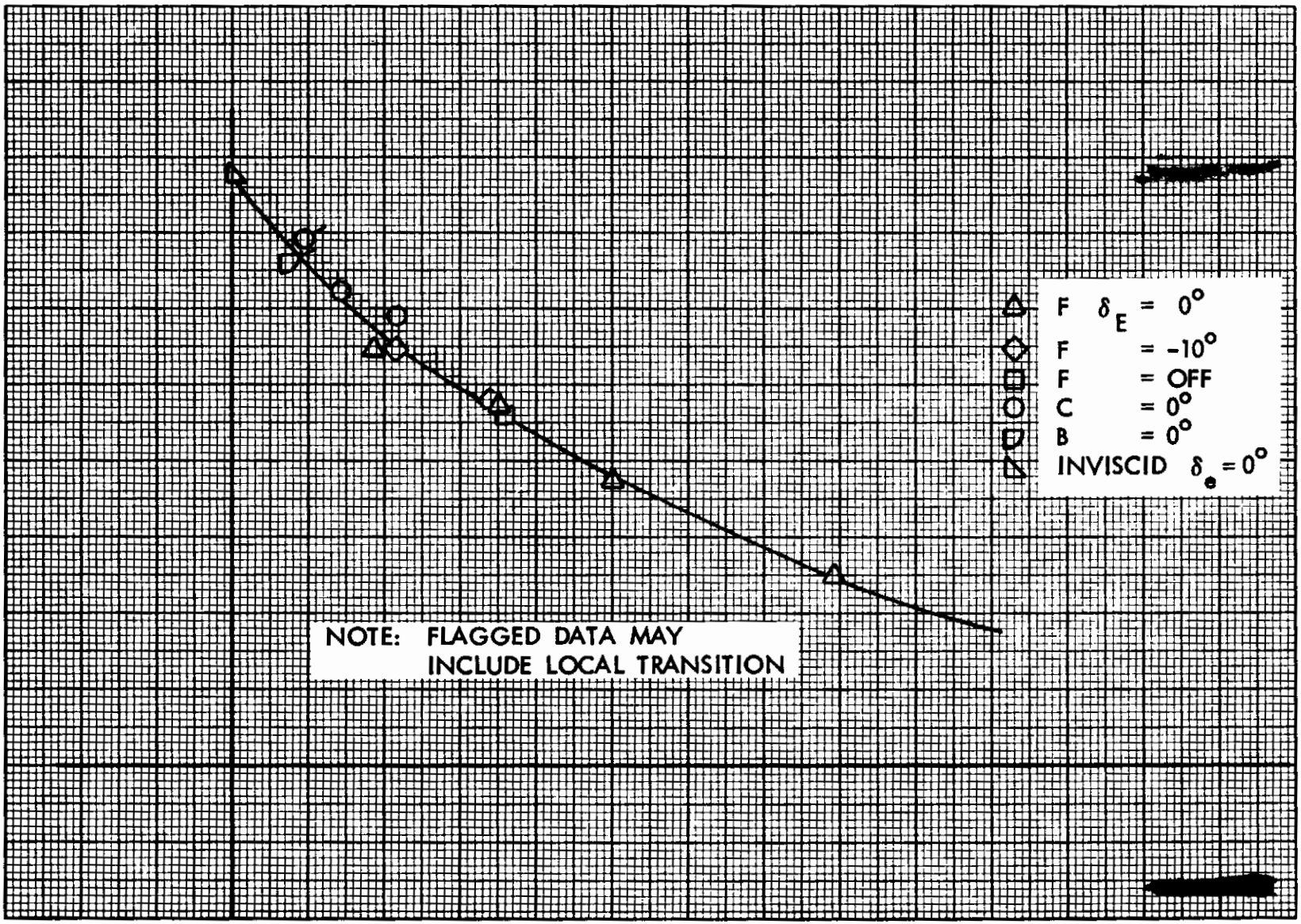

FIGURE 322 (U) VARIATION OF L/D_{MAX} WITH RAREFACTION PARAMETER

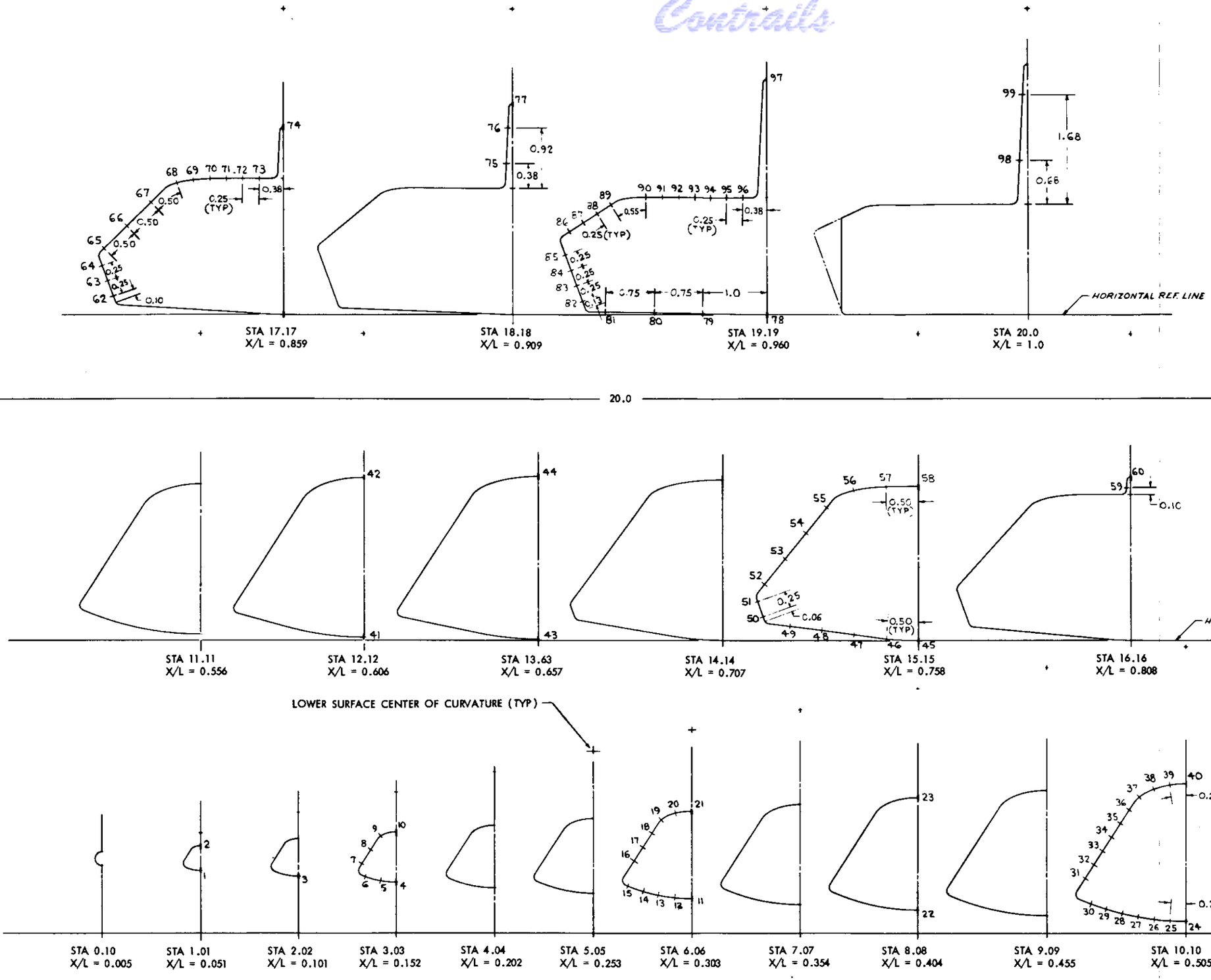

NOTE

1. ALL PRESSURE TAP LOCATIONS ARE DIMENSIONED ALONG SURFACE CONTOURS
2. DIMENSIONS AT STA 10.1 ALSO APPLY TO STA 3.03 AND 6.06
3. ALL PRESSURE TAPS ARE ON RIGHT SIDE OF MODEL
4. PRESSURE TAP LOCATIONS ON AFT LOWER COMPRESSION SURFACE ARE DIMENSIONED FROM LEADING EDGE TANGENCY POINT.

FIGURE 323 (U) PRESSURE MODEL INSTRUMENTATION LOCATIONS, TUNNELS A AND C

(REVERSE SIDE IS BLANK)

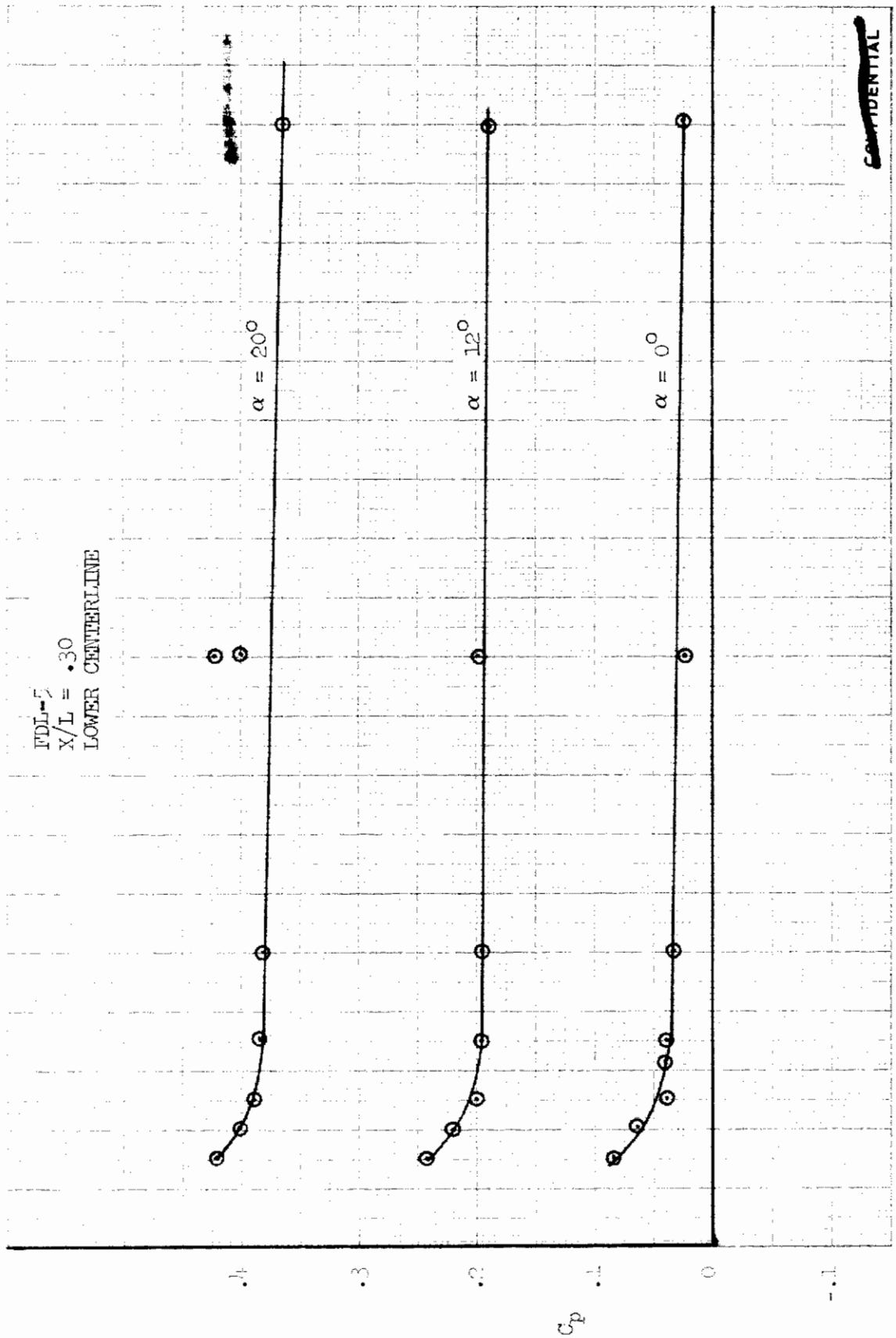

FIGURE 324a (U) VARIATION OF A LOWER SURFACE CENTERLINE PRESSURE COEFFICIENT WITH MACH NUMBER (X/L = .30)

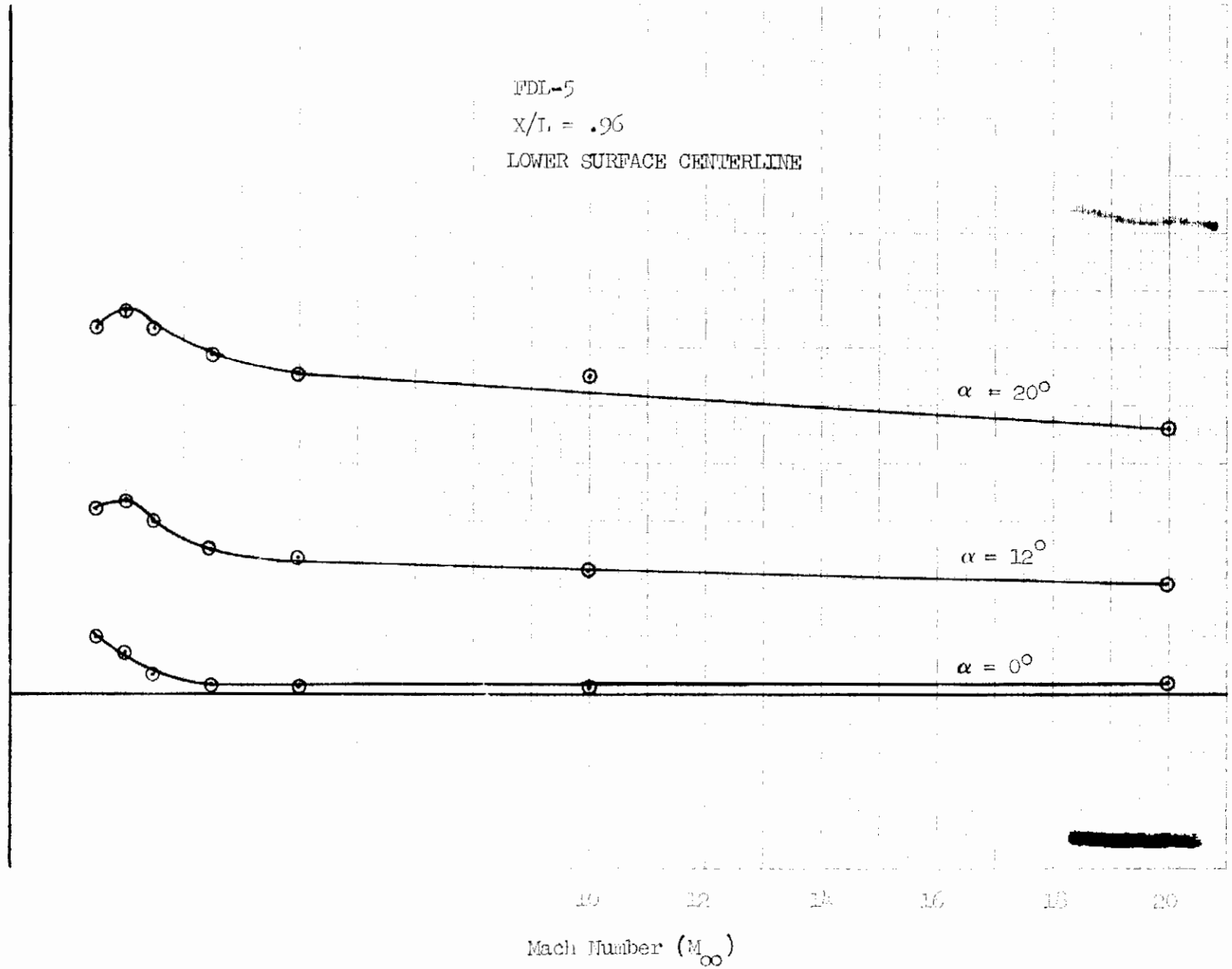

FIGURE 241 (U) VARIATION OF A LOWER SURFACE CENTERLINE PRESSURE COEFFICIENT WITH MACH NUMBER (X/L = .96)

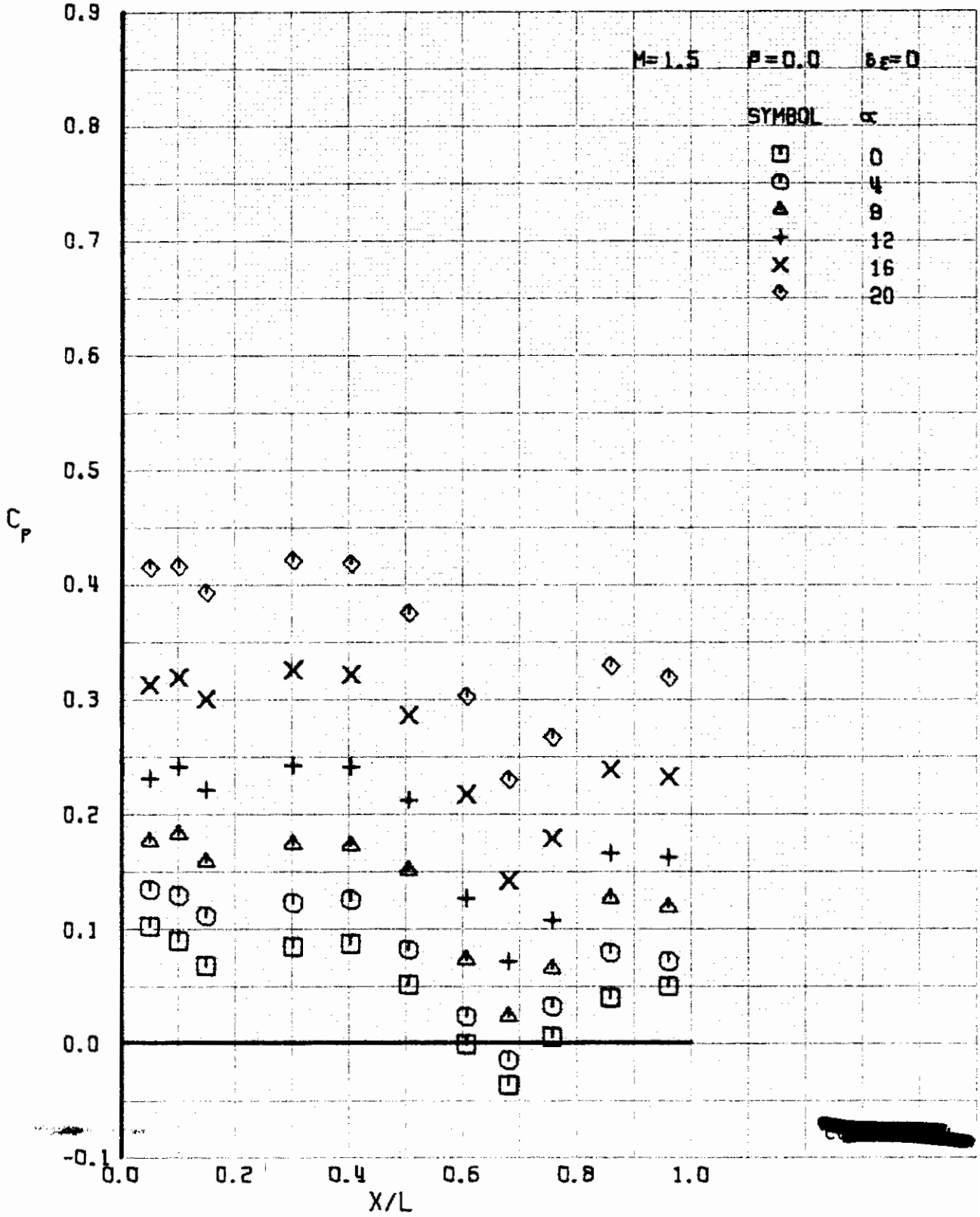

FIGURE 325 (U) LOWER SURFACE CENTERLINE PRESSURES

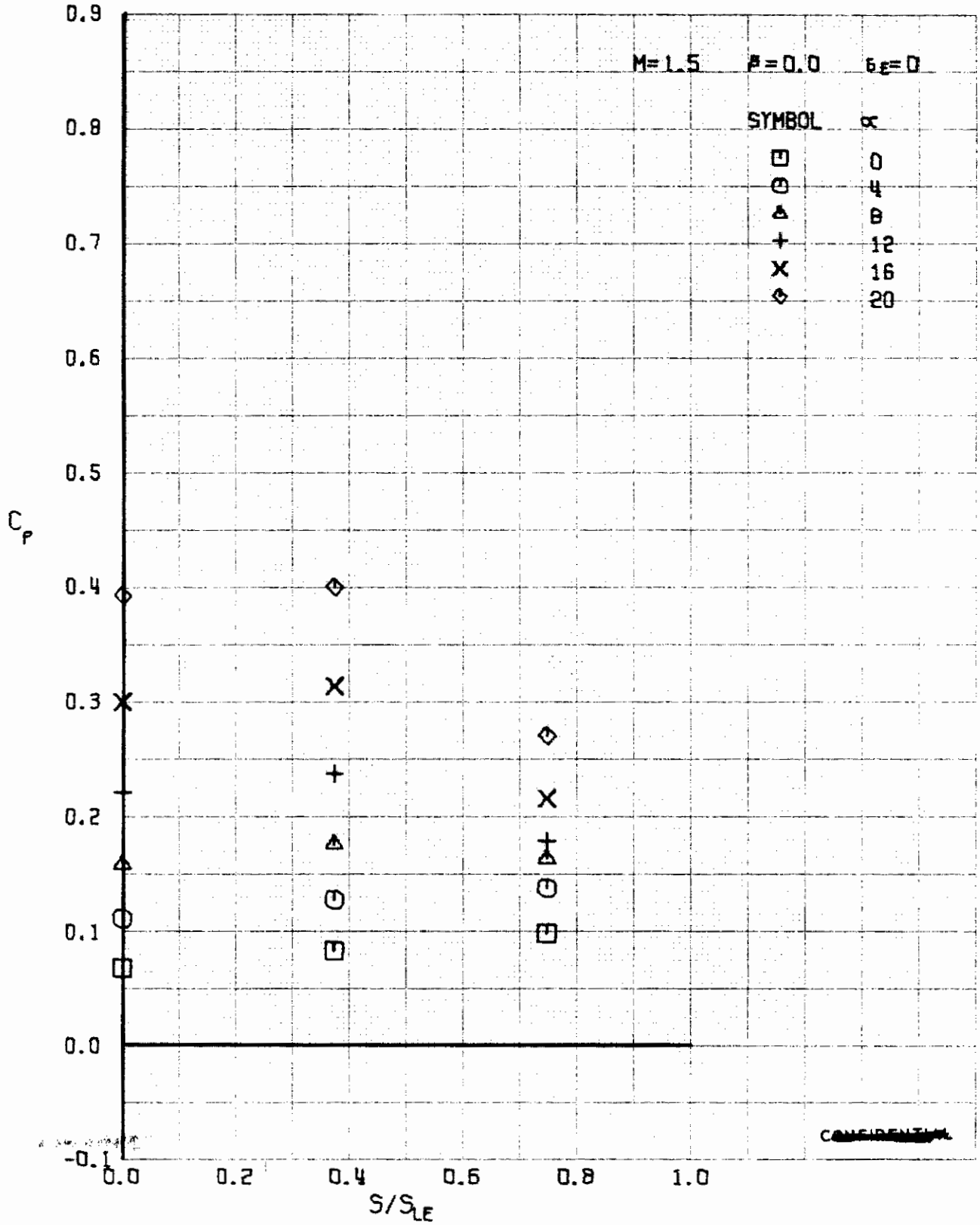

FIGURE 326 (U) LOWER SURFACE SPANWISE PRESSURES AT X/L = 0.15

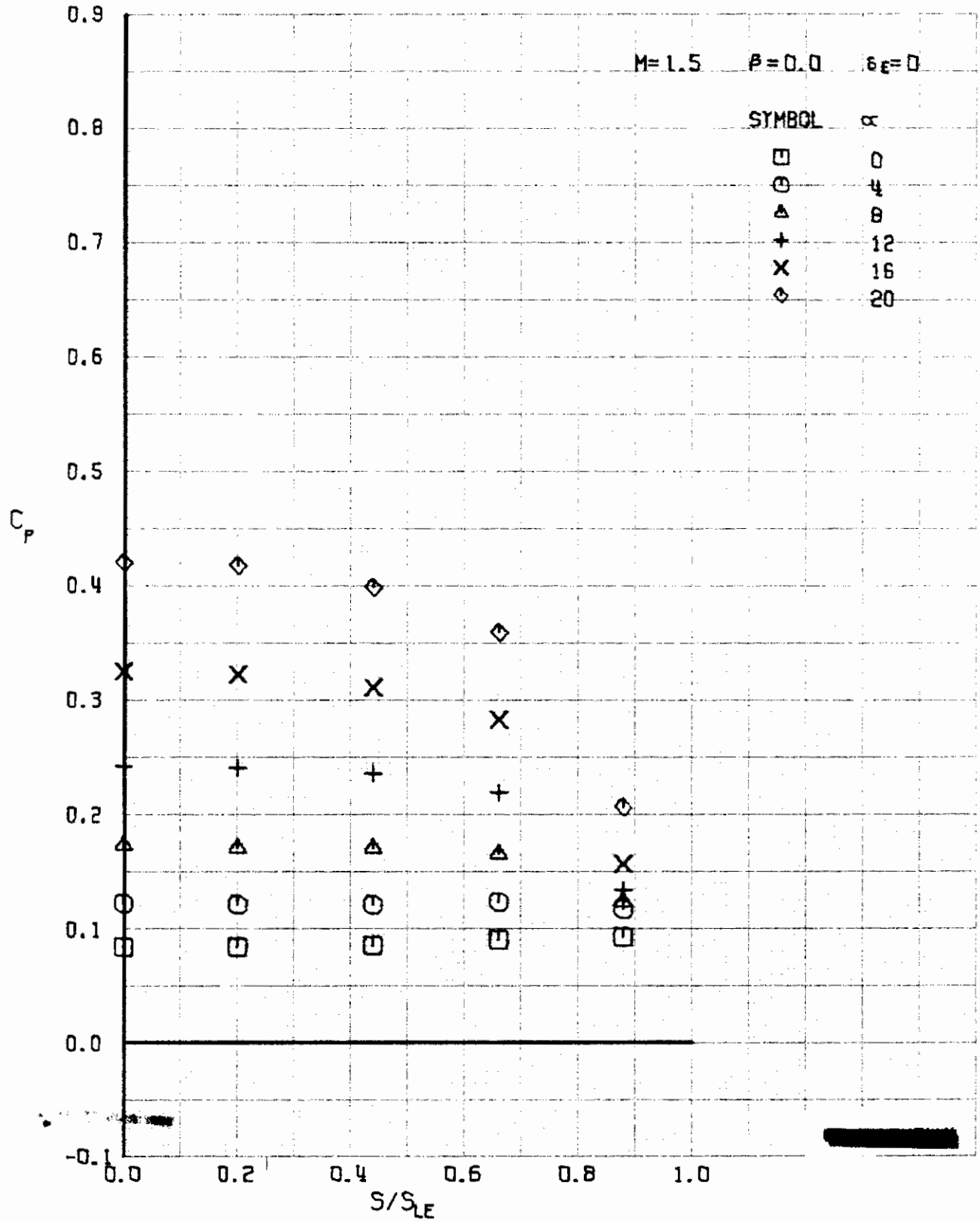

FIGURE 327 (U) LOWER SURFACE SPANWISE PRESSURES AT X/L = 0.30

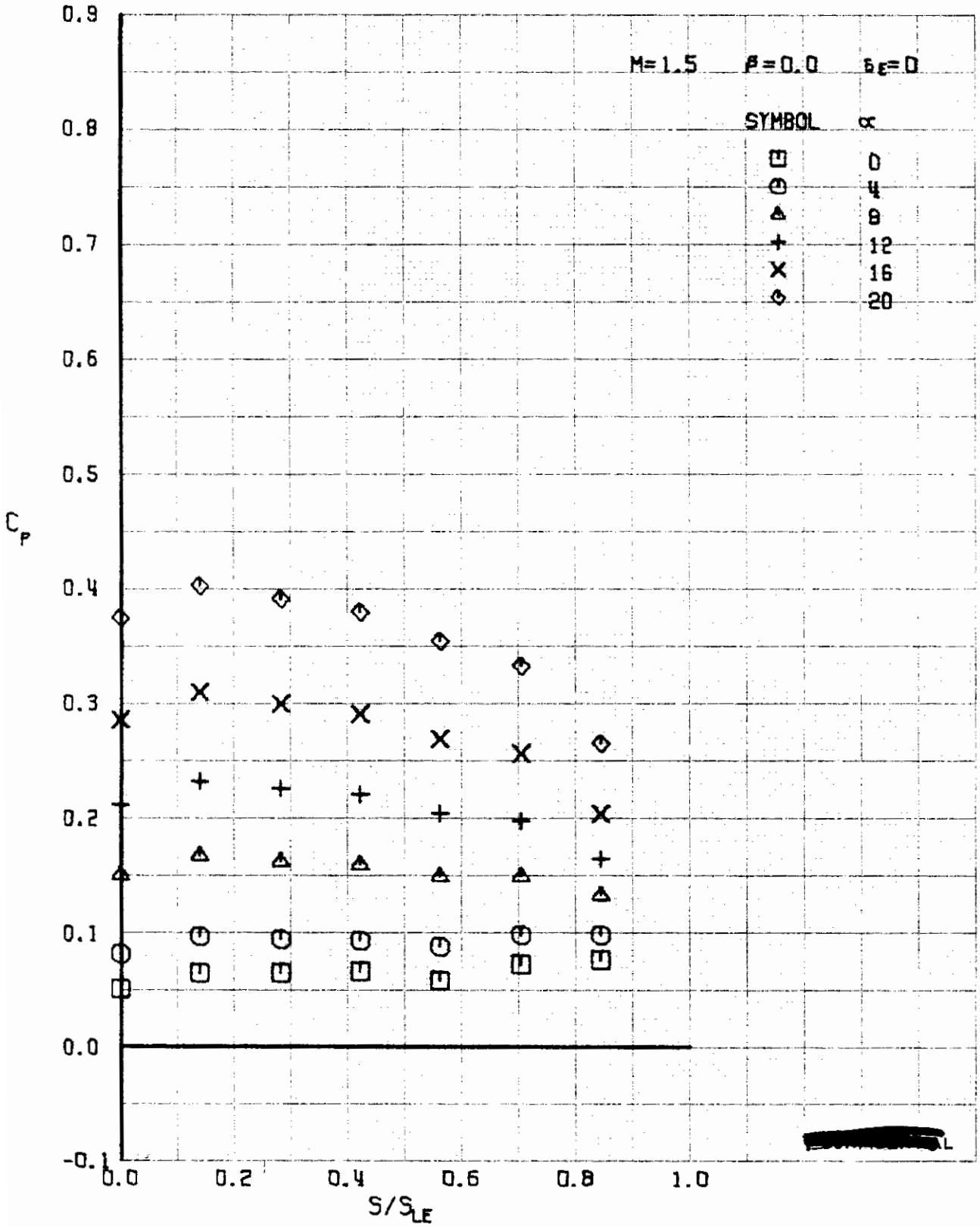

FIGURE 328 (U) LOWER SURFACE SPANWISE PRESSURES AT X/L = 0.50

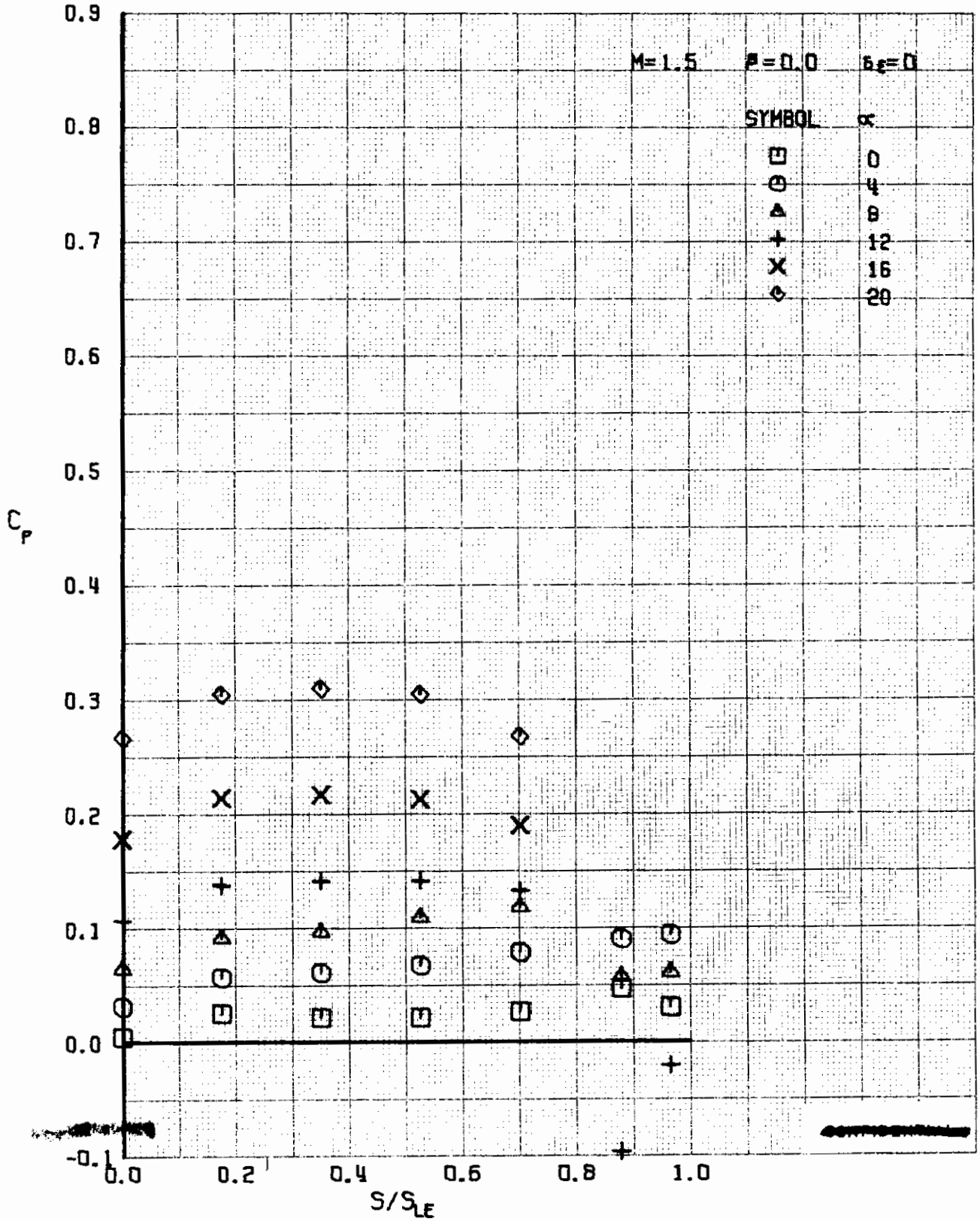

FIGURE 329 (U) LOWER SURFACE SPANWISE PRESSURES AT X/L = 0.76

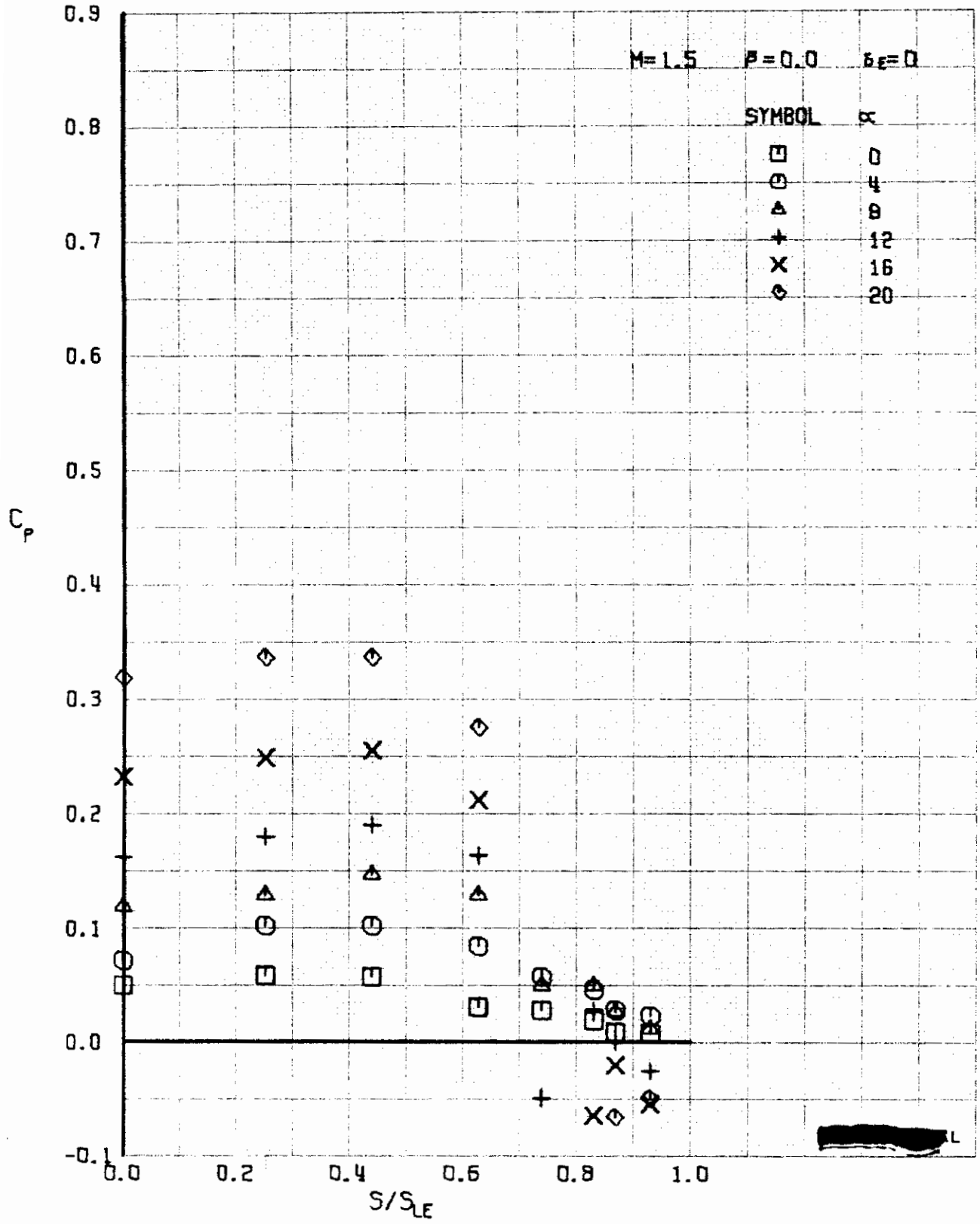

FIGURE 330 (U) LOWER SURFACE SPANWISE PRESSURES AT X/L = 0.96

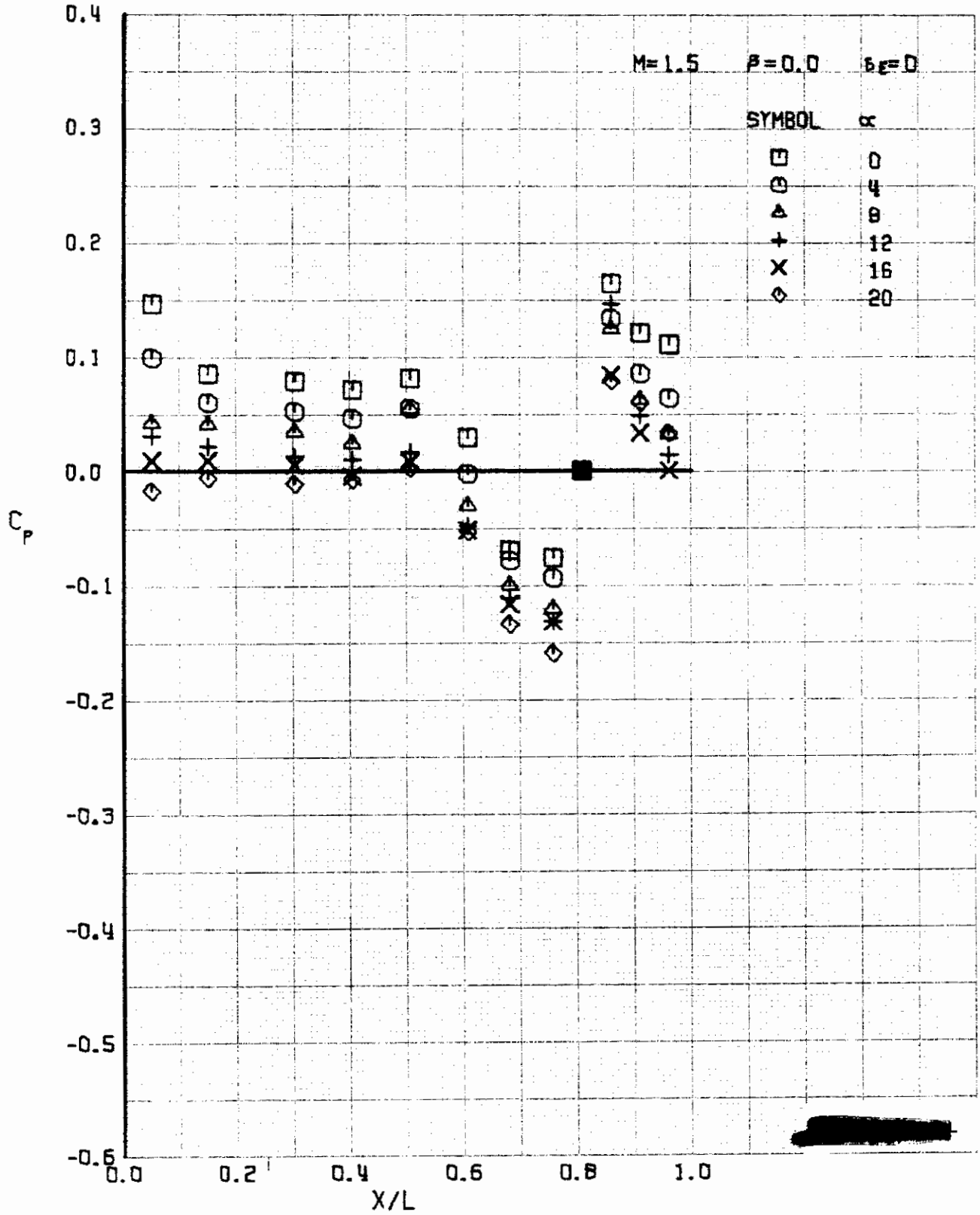

FIGURE 331 (U) UPPER SURFACE CENTERLINE PRESSURES

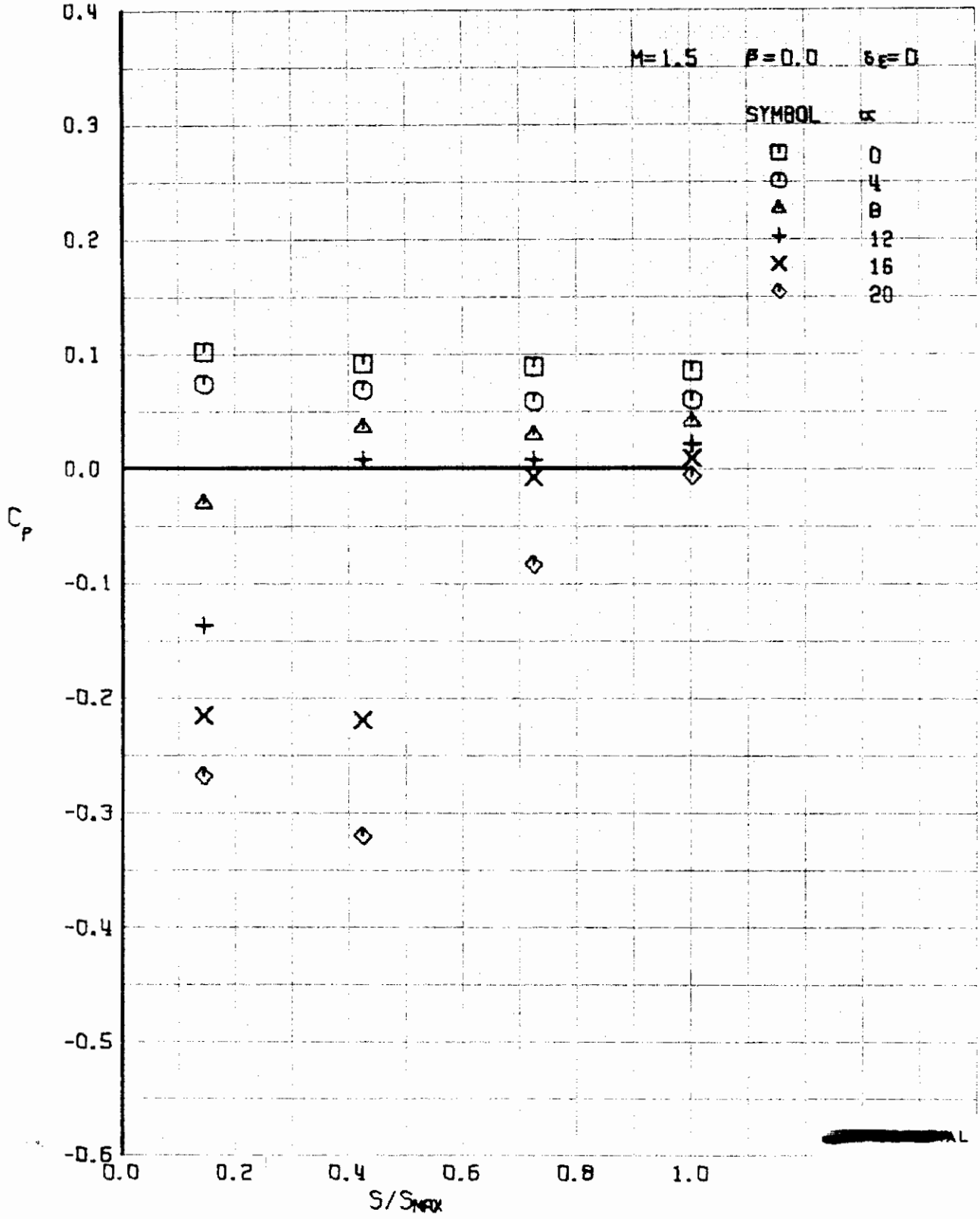

FIGURE 332 (U) UPPER SURFACE SPANWISE PRESSURES AT X/L = 0.15

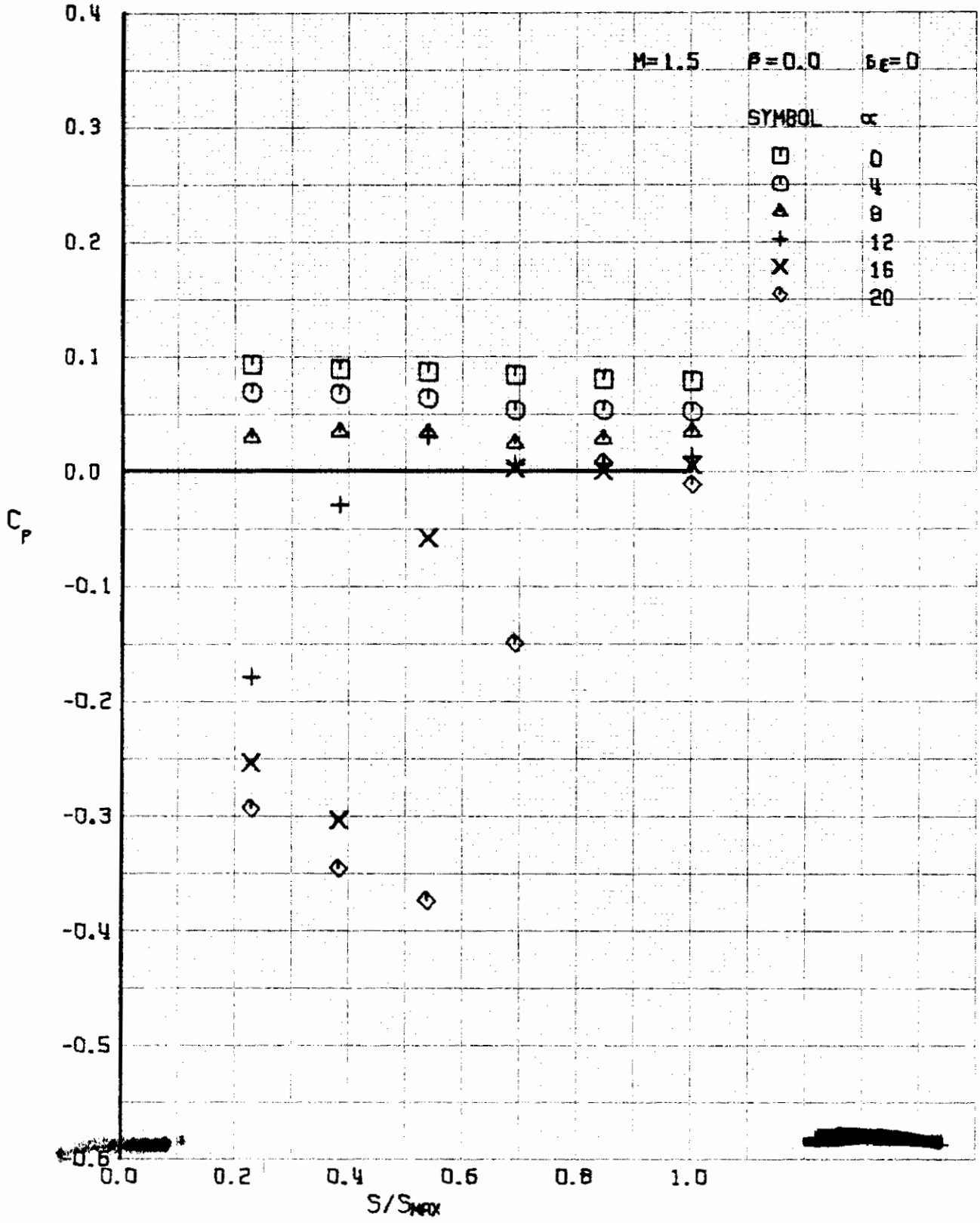

FIGURE 333 (U) UPPER SURFACE SPANWISE PRESSURES AT X/L = 0.30

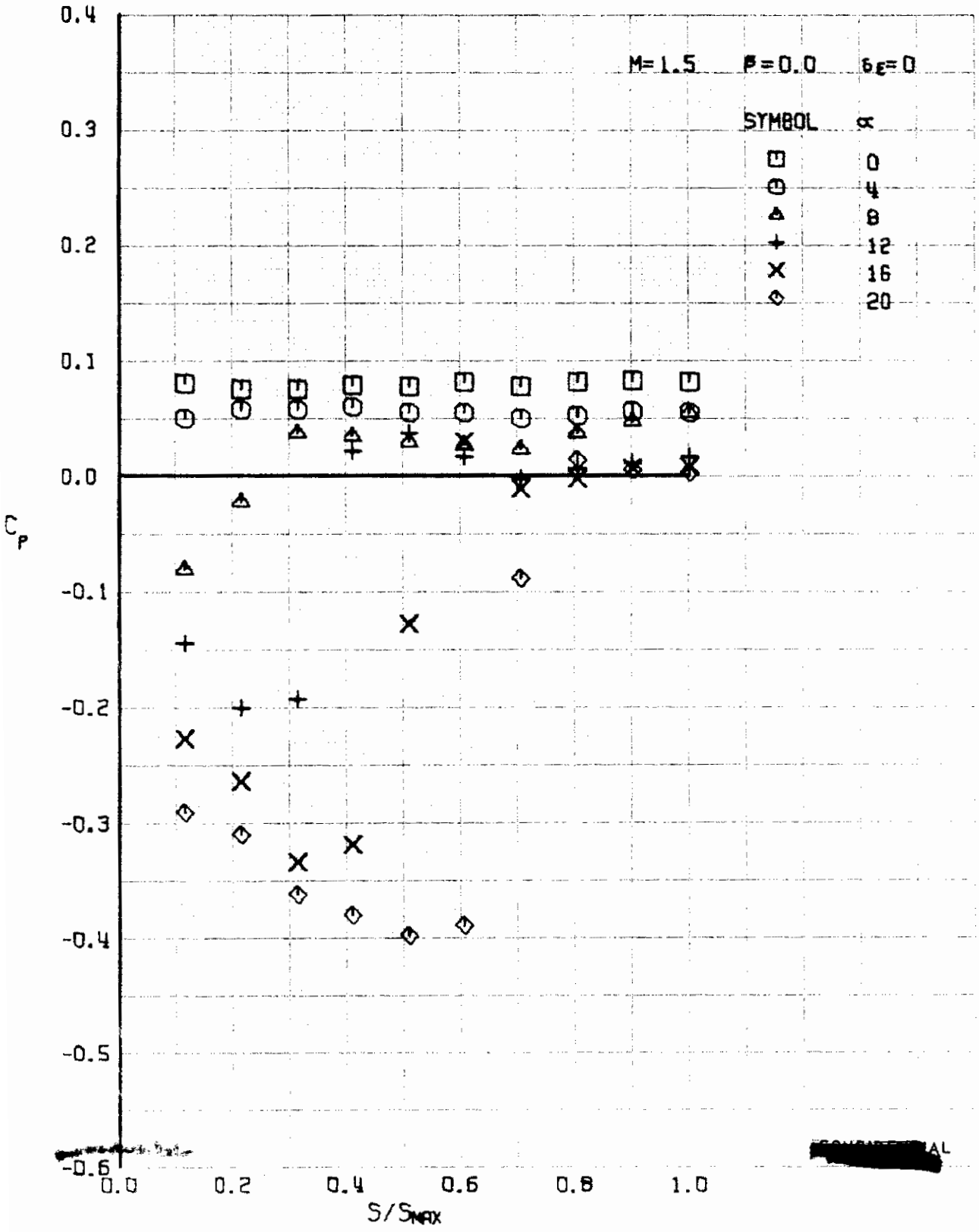

FIGURE 33⅓ (U) UPPER SURFACE SPANWISE PRESSURES AT X/L = 0.50

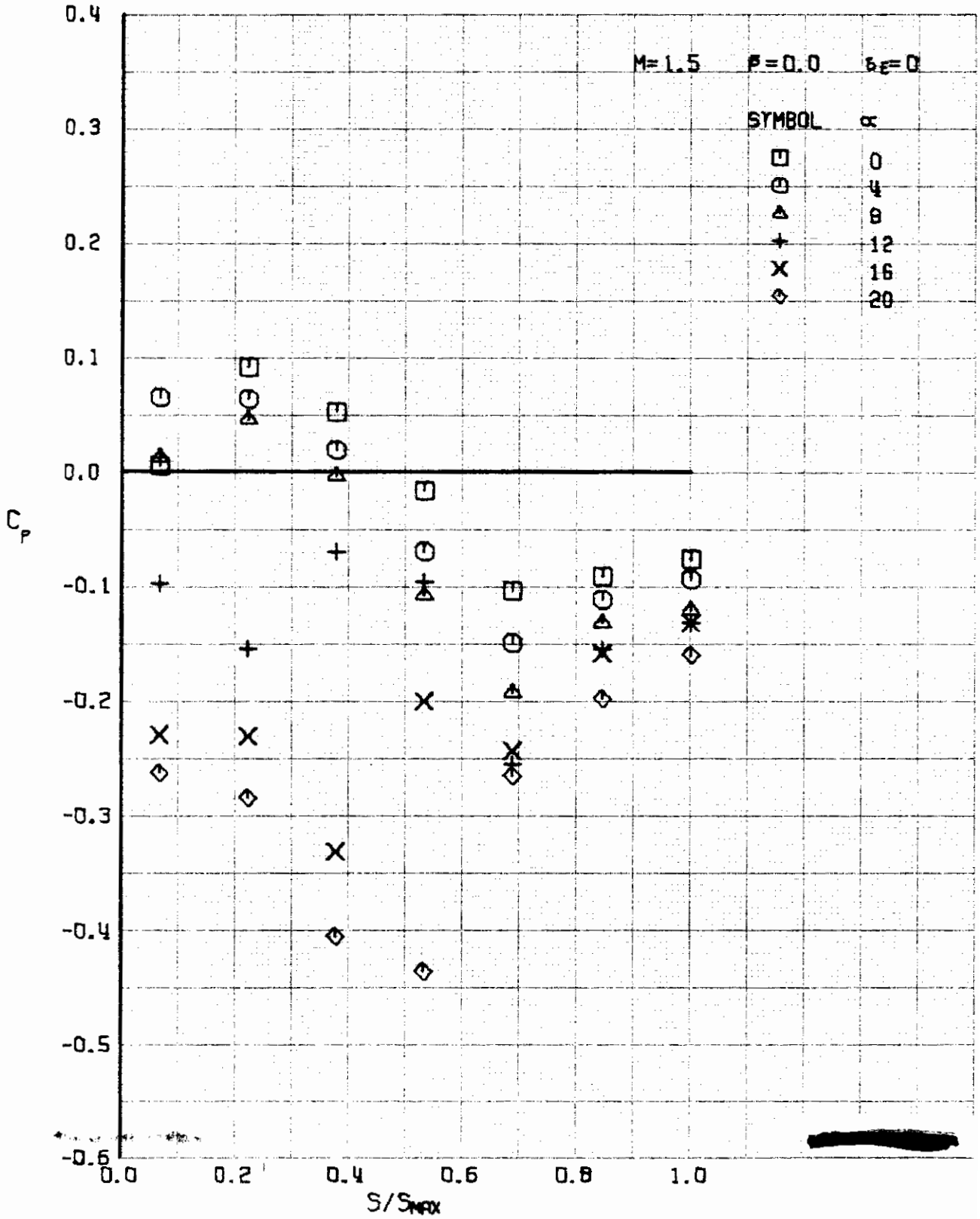

FIGURE 335 (U) UPPER SURFACE SPANWISE PRESSURES AT X/L = 0.76

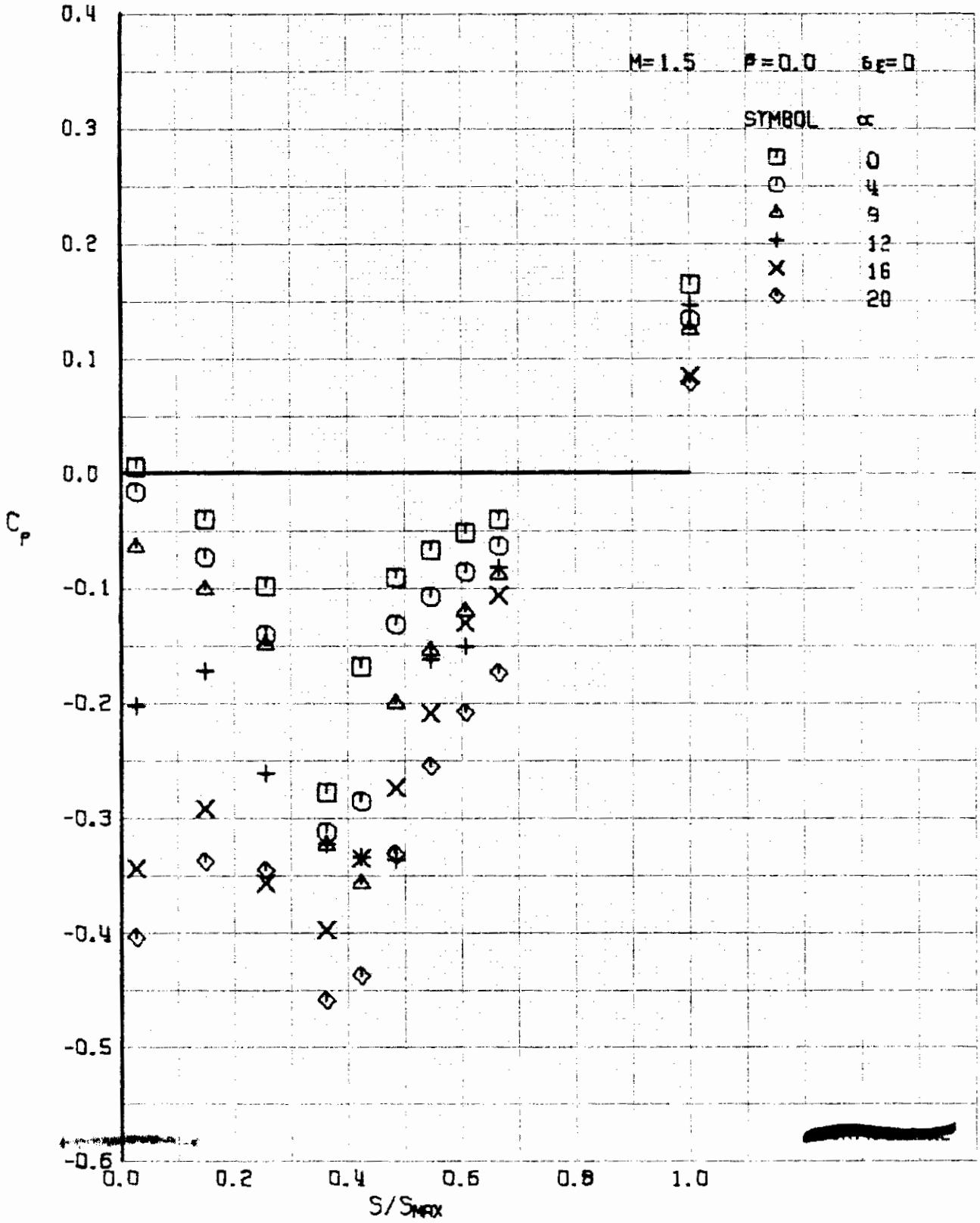

FIGURE 336 (U) UPPER SURFACE SPANWISE PRESSURES AT X/L = 0.86

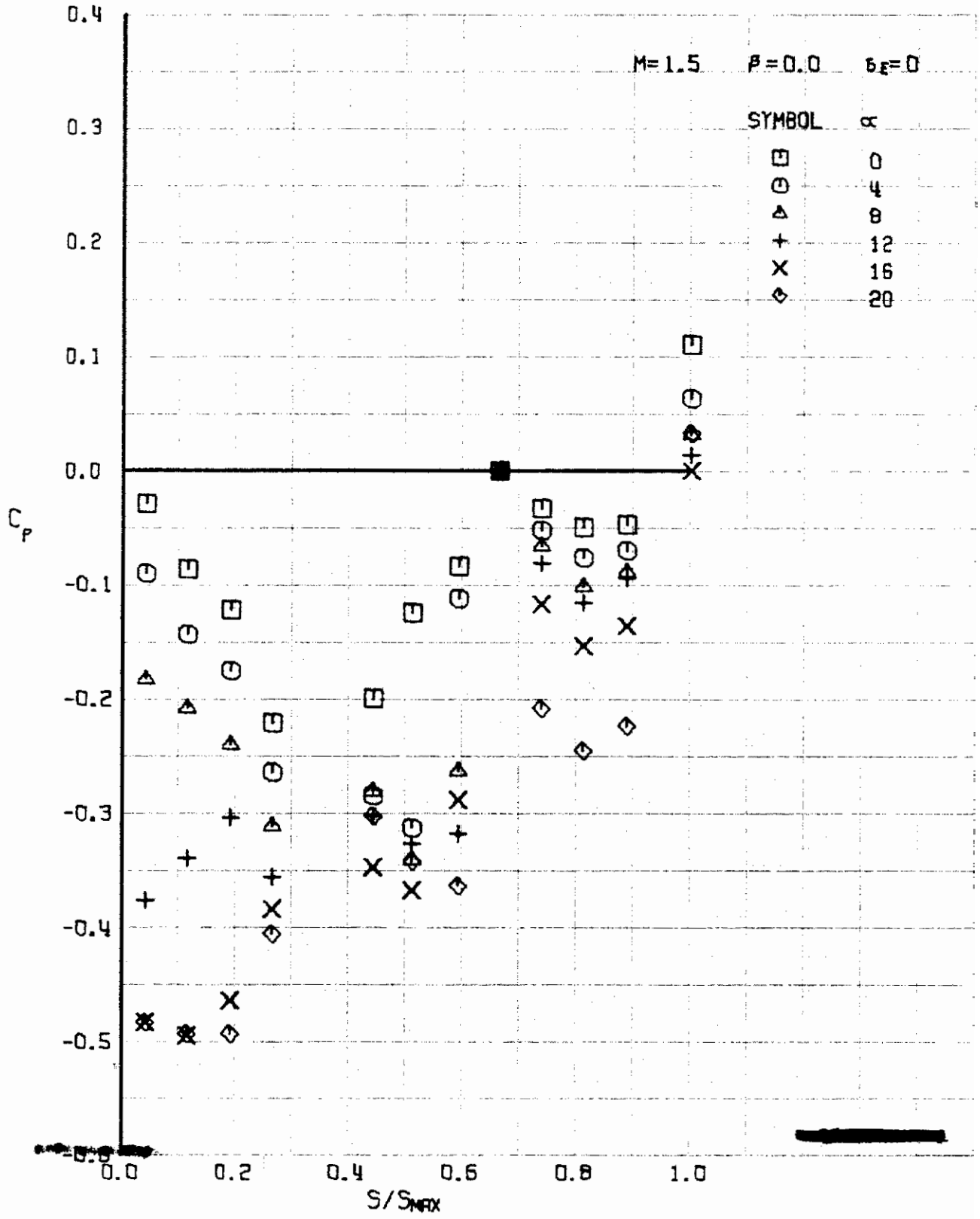

FIGURE 337 (U) UPPER SURFACE SPANWISE PRESSURES AT X/L = 0.96

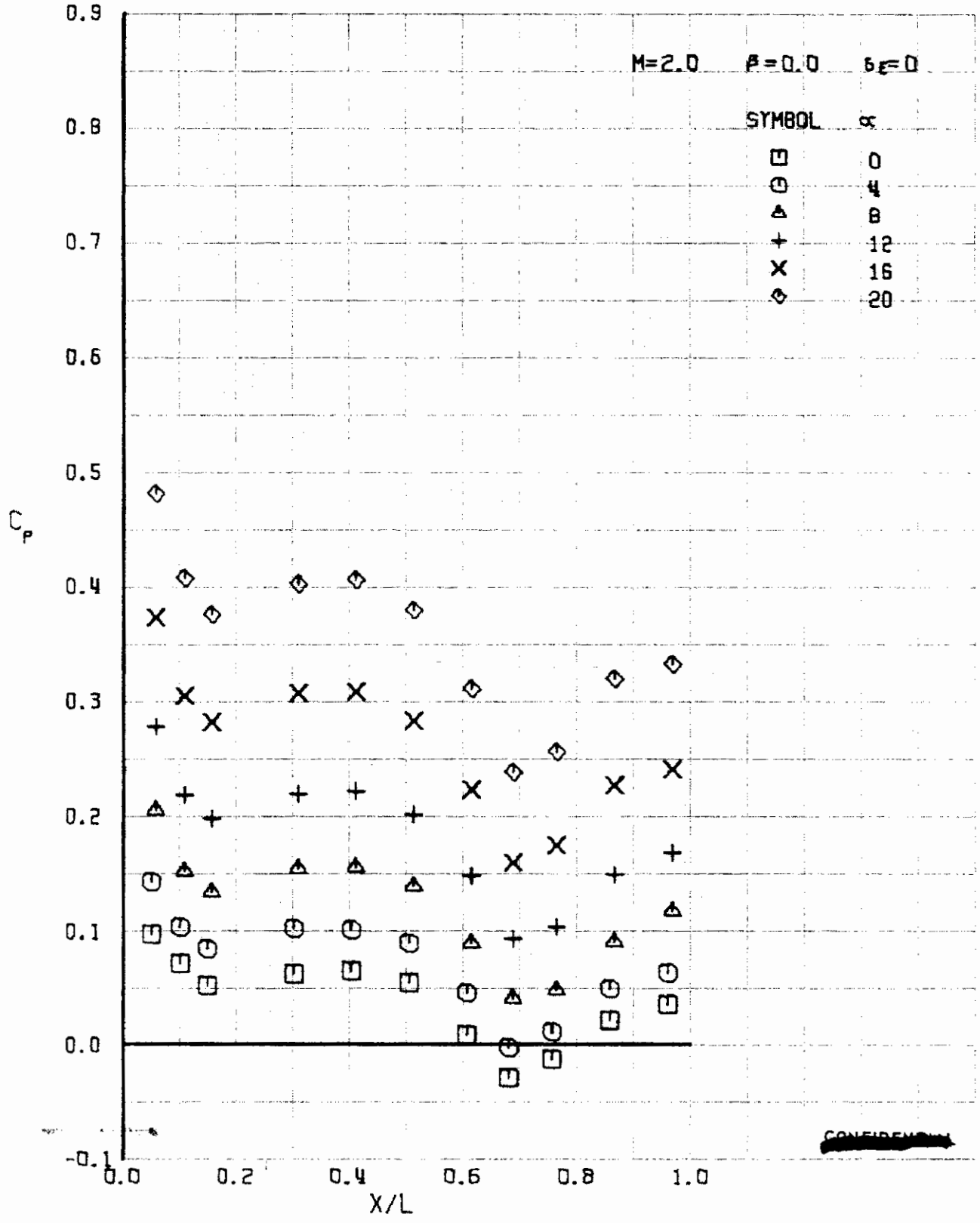

FIGURE 338 (U) LOWER SURFACE CENTERLINE PRESSURES

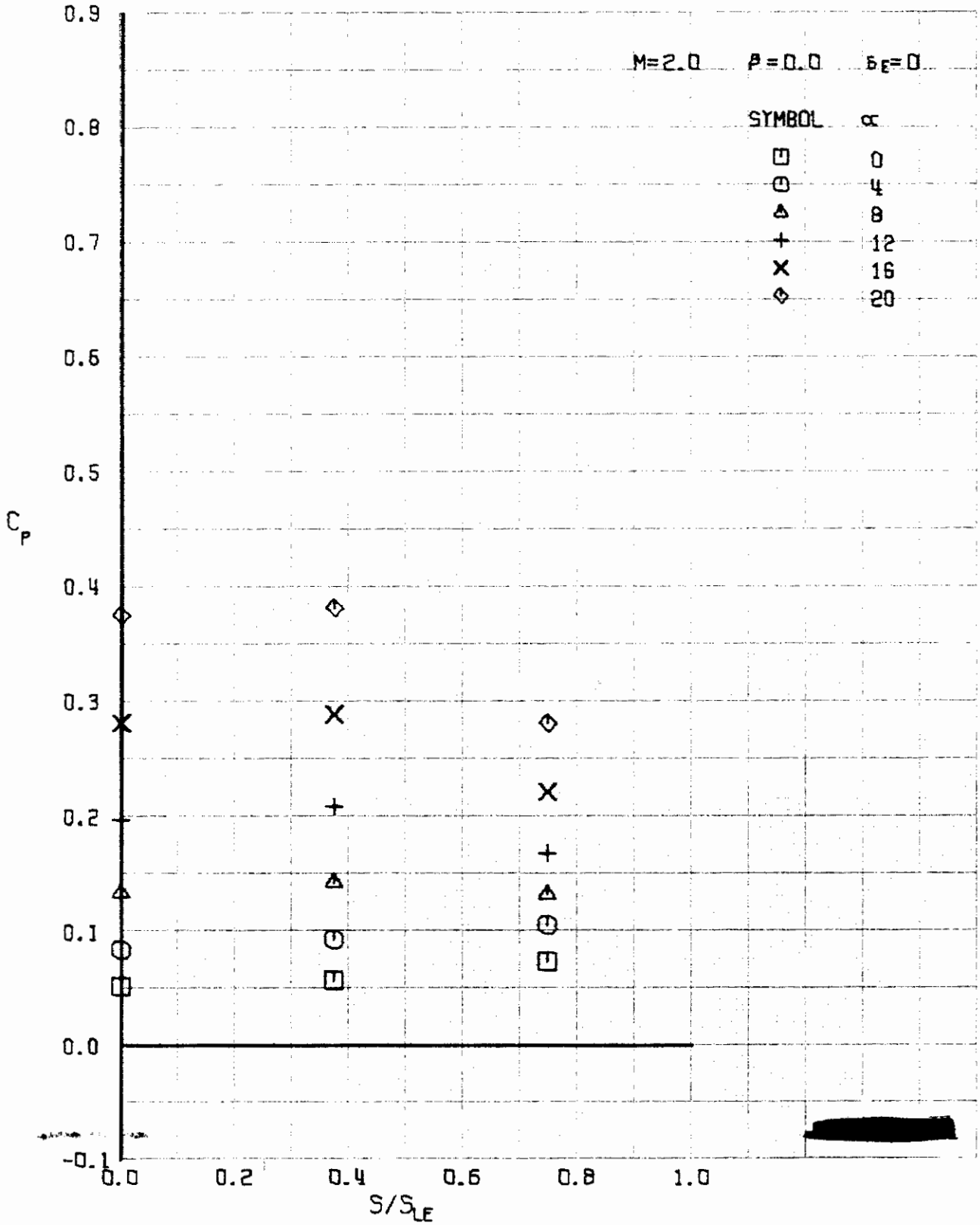

FIGURE 339 (U) LOWER SURFACE SPANWISE PRESSURES AT X/L = 0.15

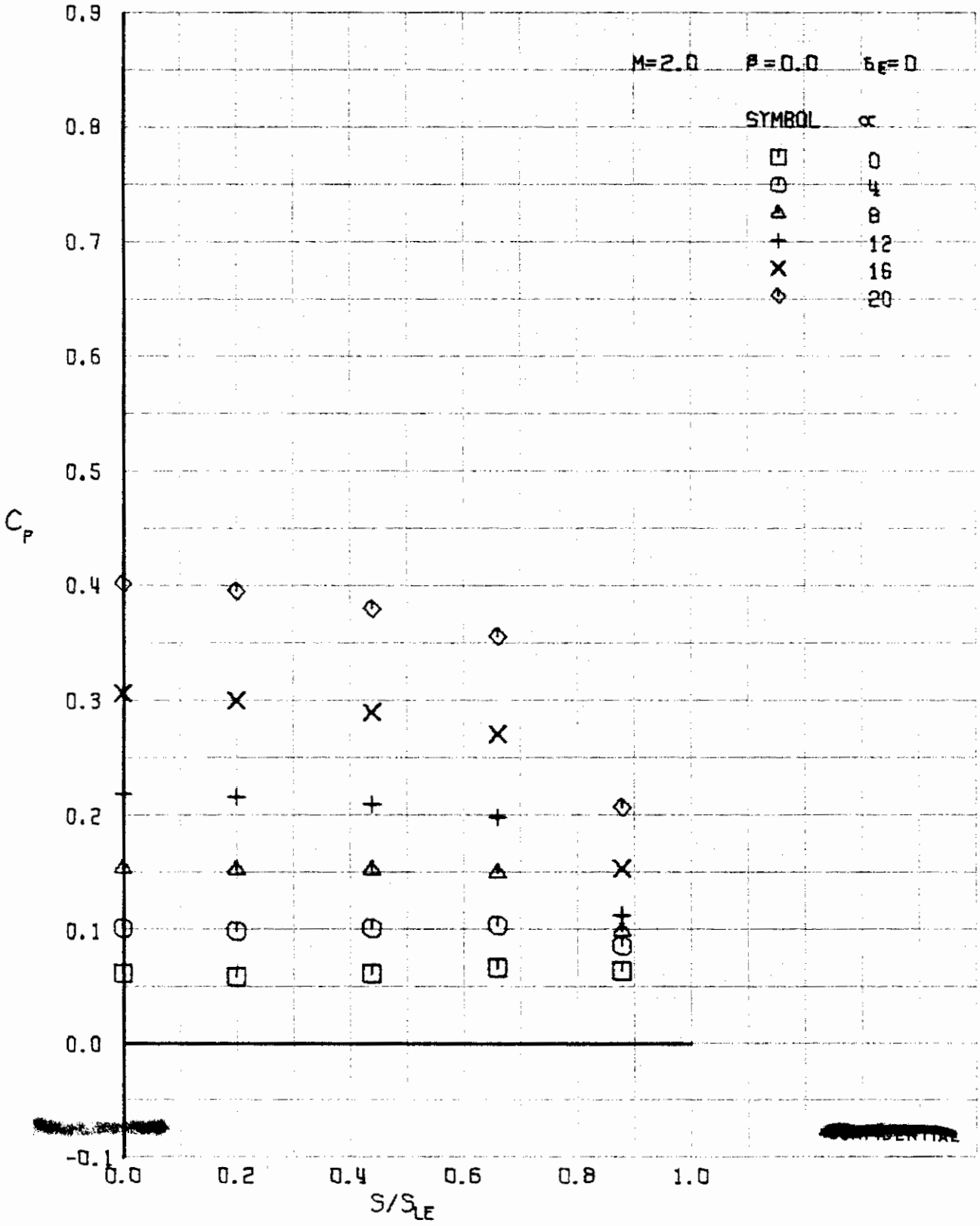

FIGURE 340 (U) LOWER SURFACE SPANWISE PRESSURES AT X/L = 0.30

CONFIDENTIAL

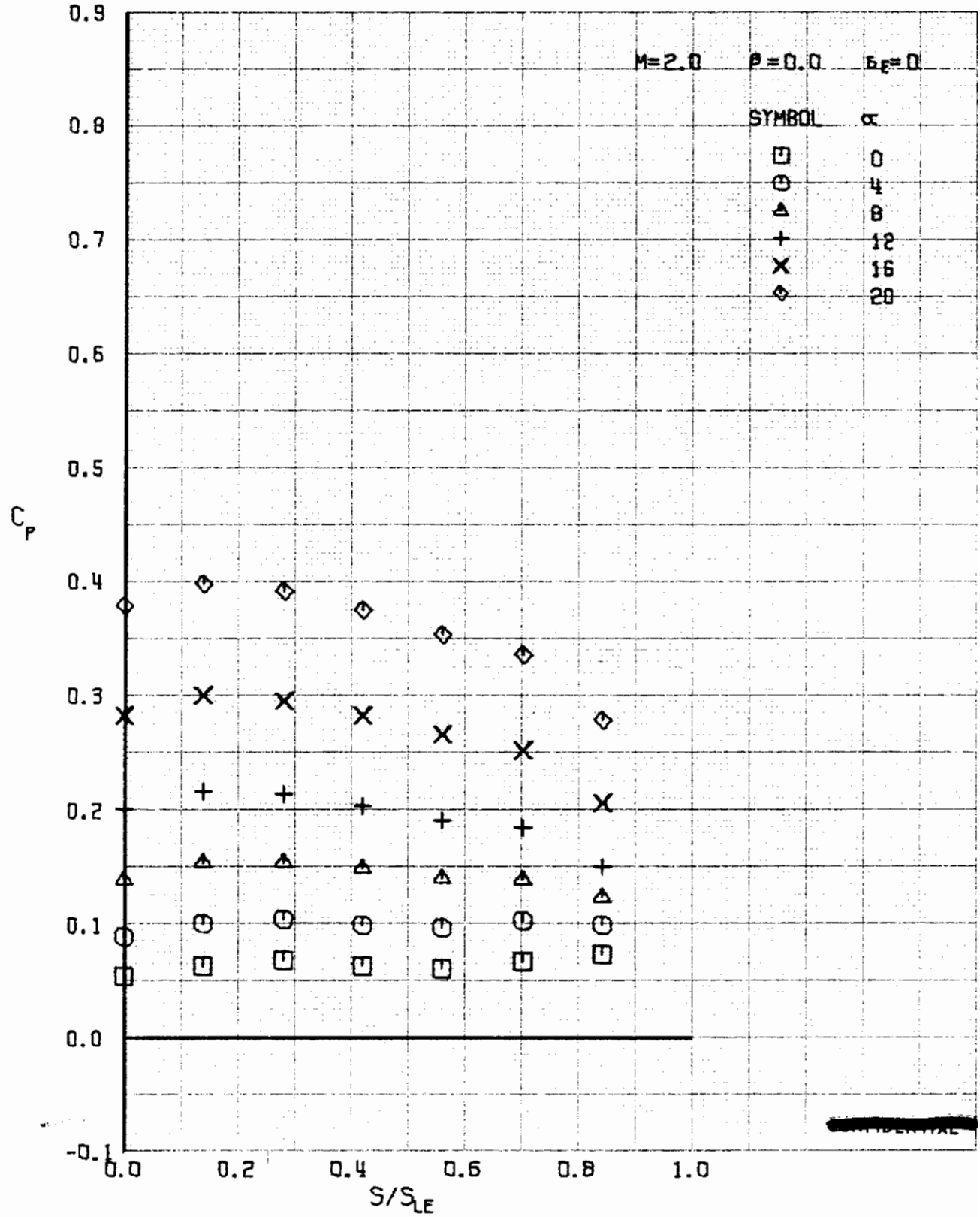

FIGURE 341 (U) LOWER SURFACE SPANWISE PRESSURES AT X/L = 0.50

CONFIDENTIAL

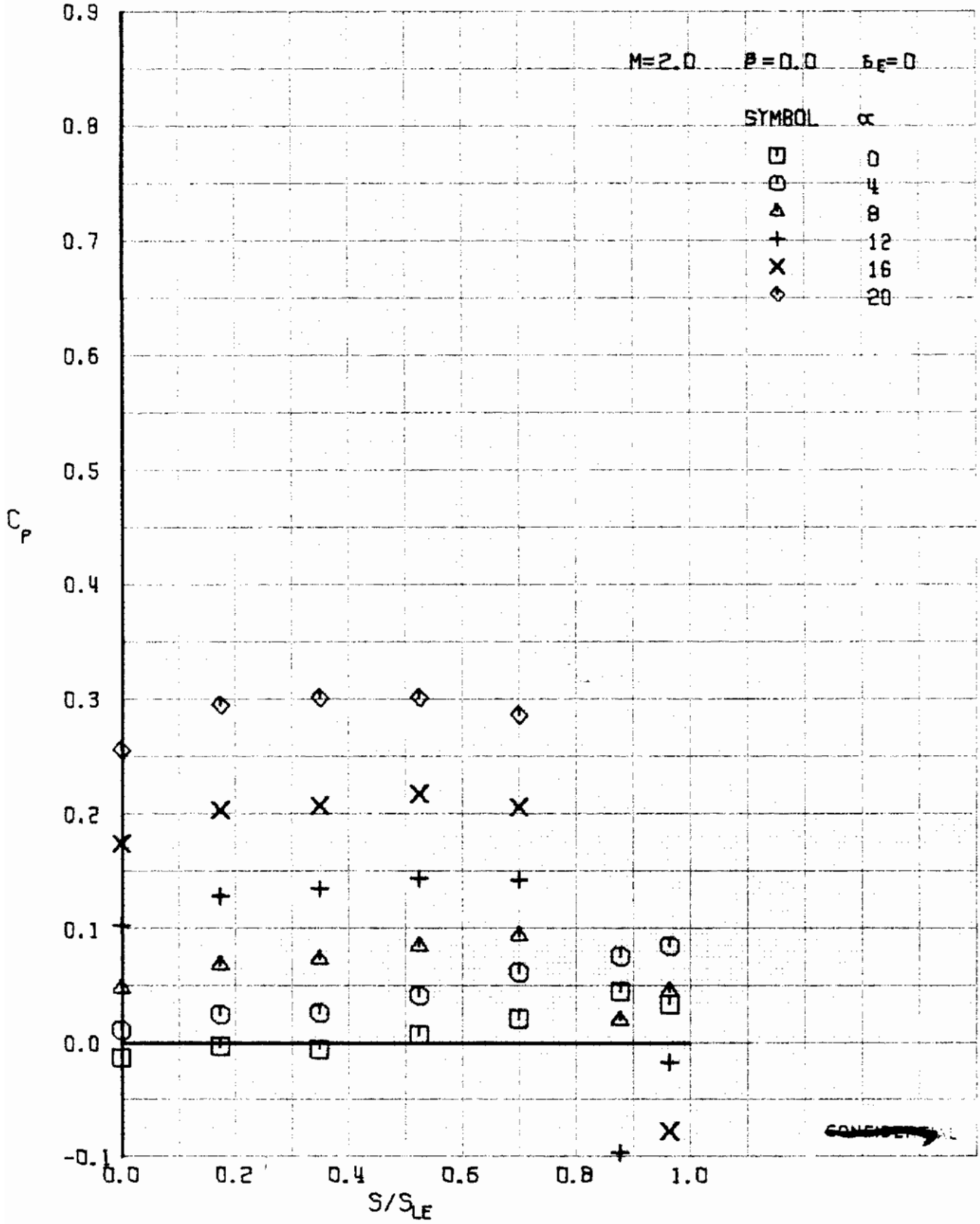

FIGURE 342 (U) LOWER SURFACE SPANWISE PRESSURES AT X/L = 0.7

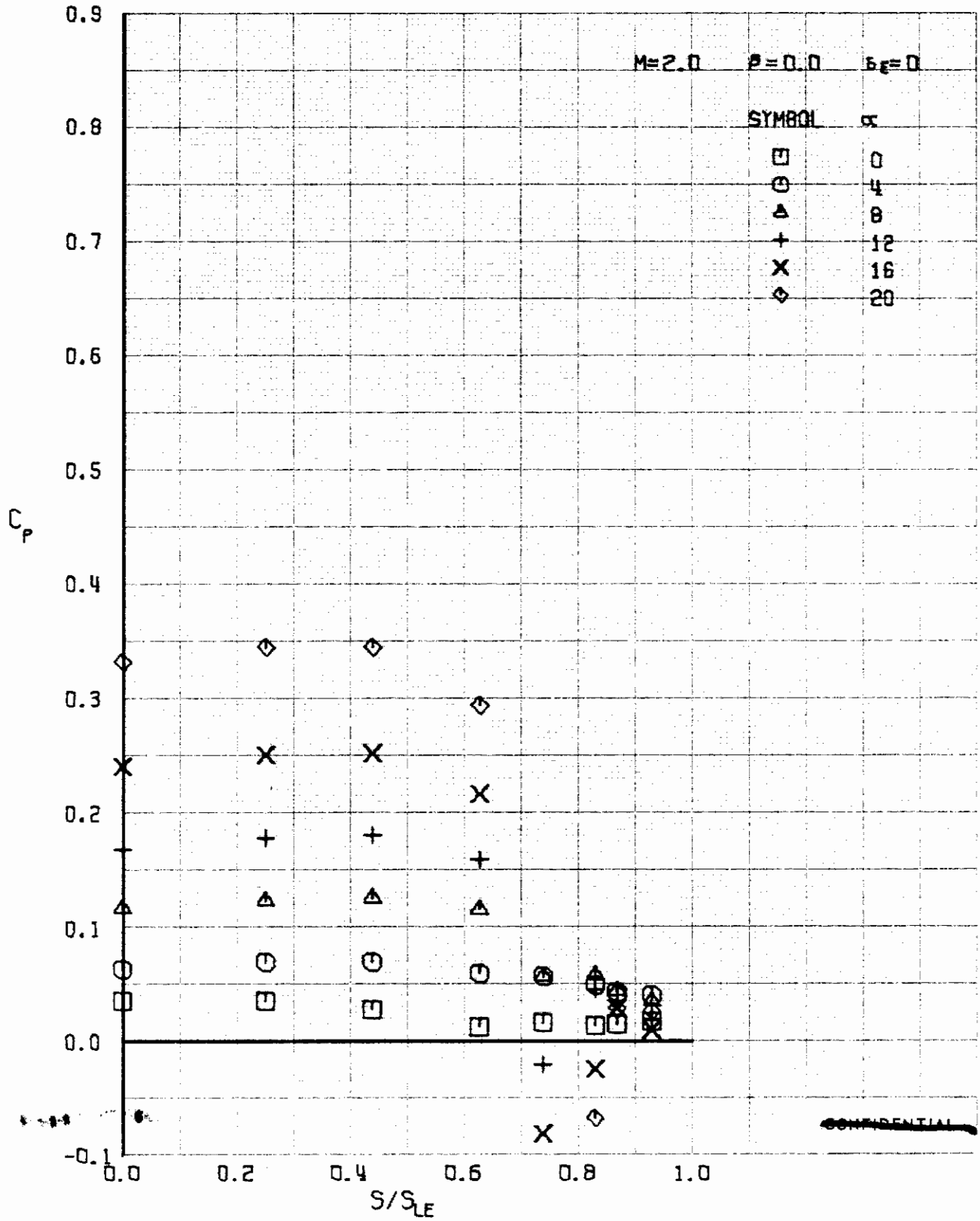

FIGURE 343 (U) LOWER SURFACE SPANWISE PRESSURES AT X/L = 0.96

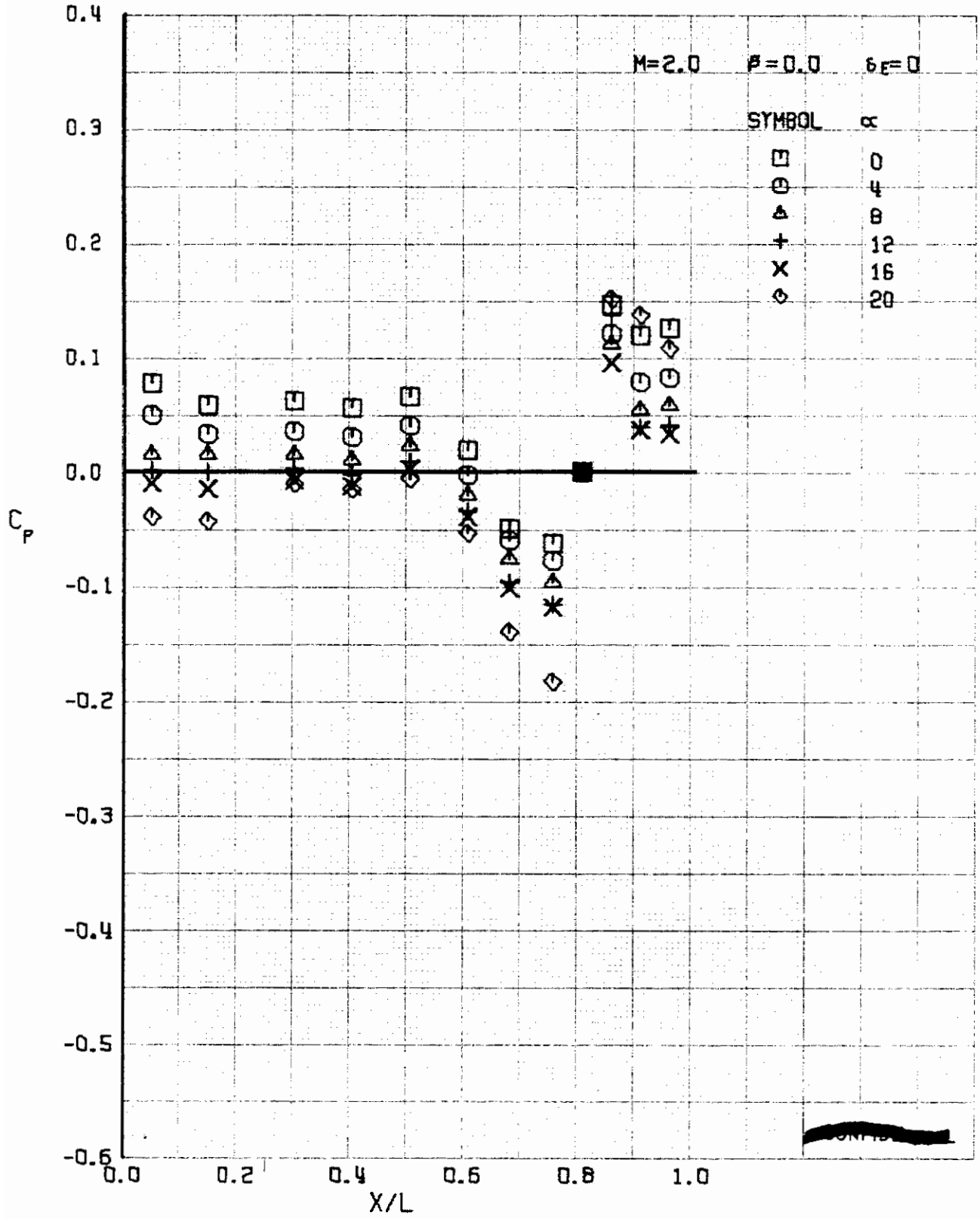

FIGURE 344 (U) UPPER SURFACE CENTERLINE PRESSURES

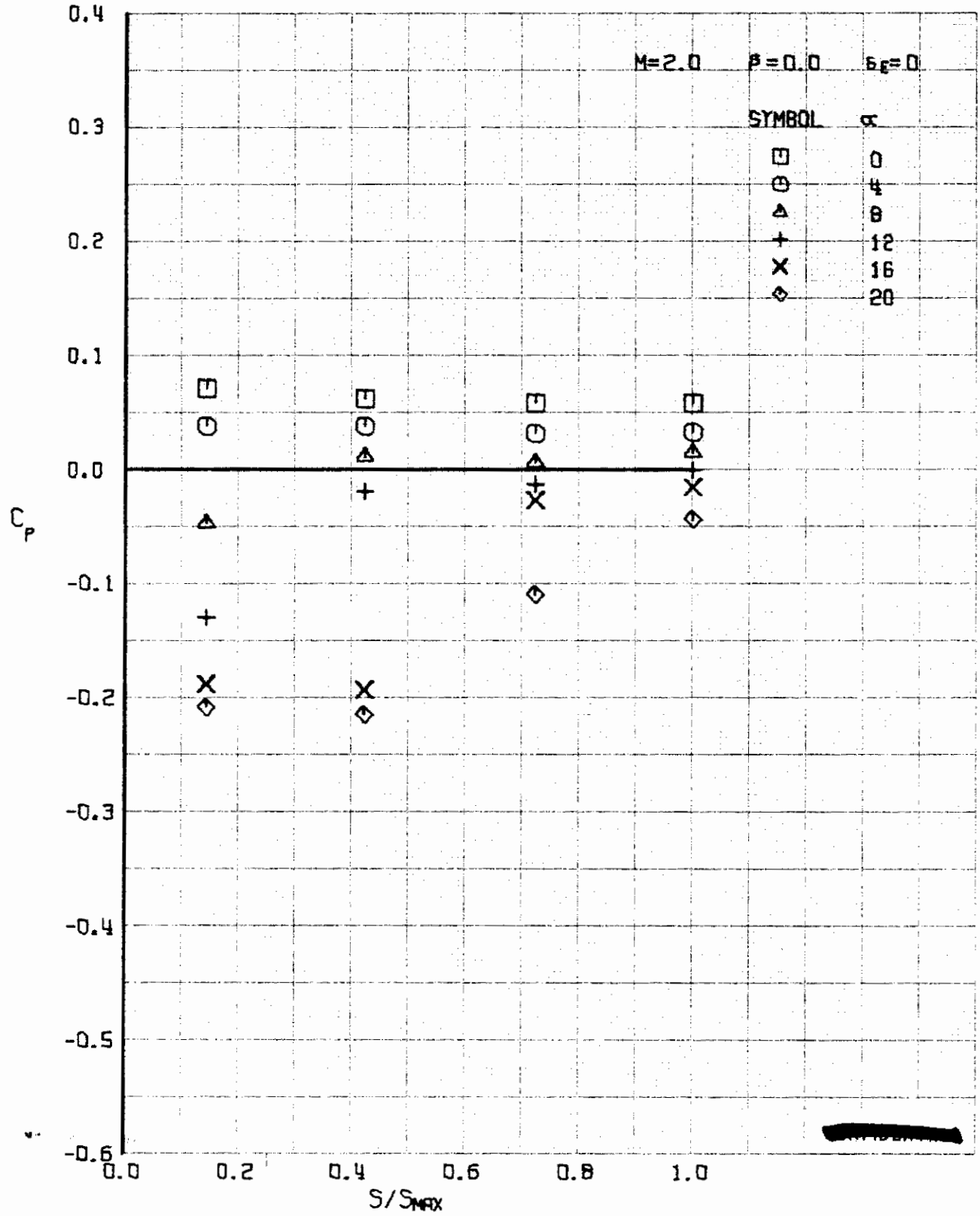

FIGURE 345 (U) UPPER SURFACE SPANWISE PRESSURES AT X/L = 0.15

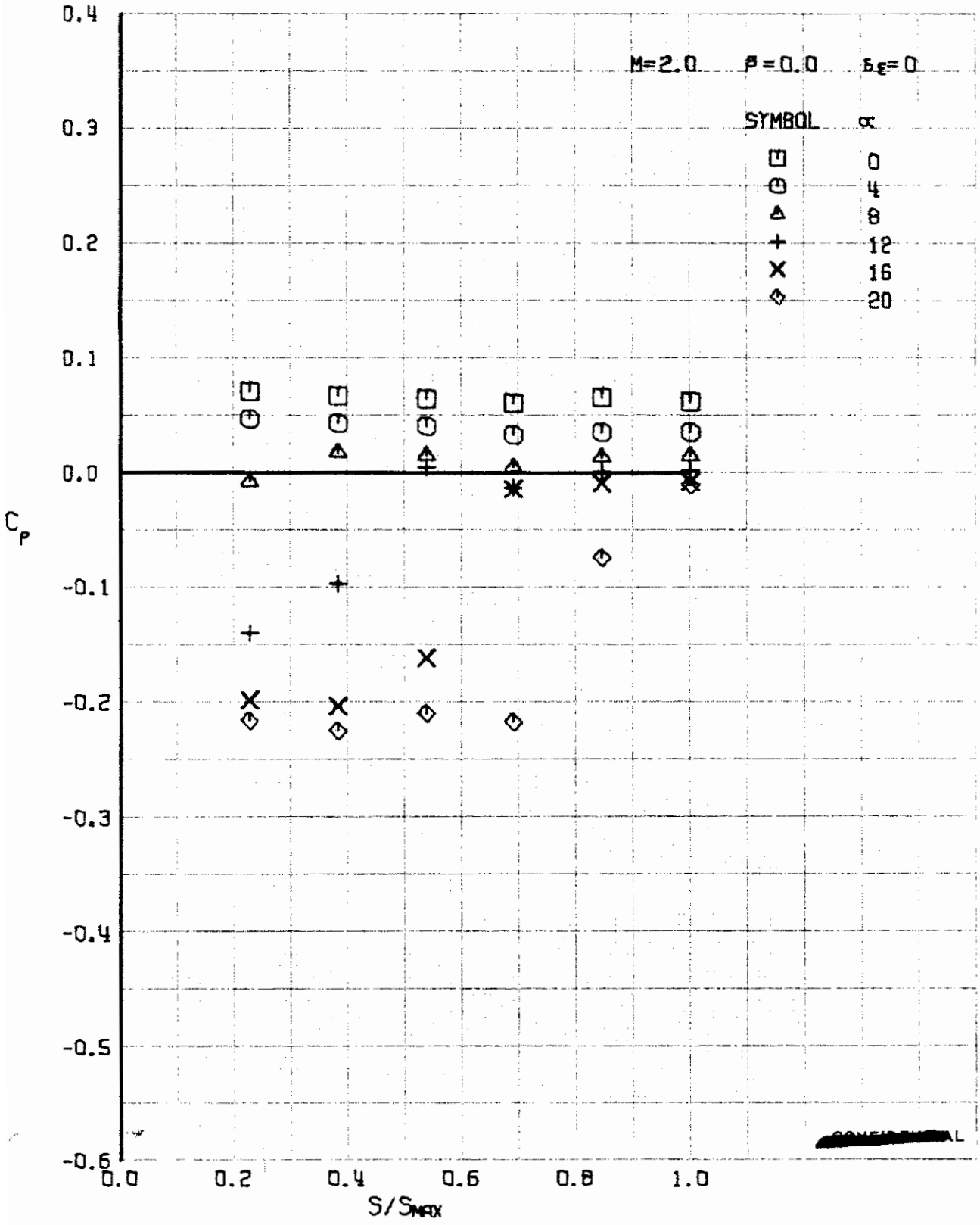

FIGURE 346 (U) UPPER SURFACE SPANWISE PRESSURES AT X/L = 0.30

CONFIDENTIAL

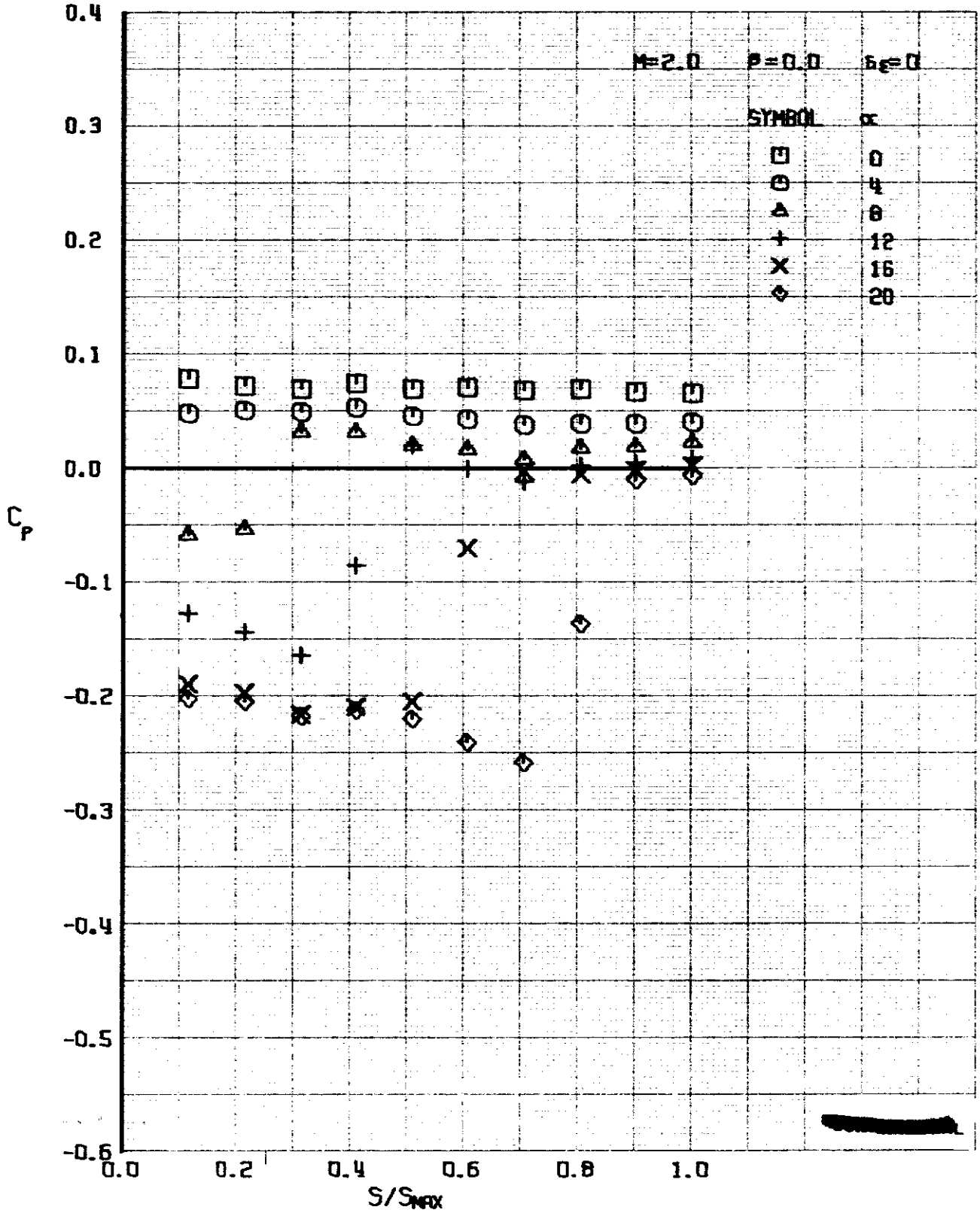

FIGURE 347 (U) UPPER SURFACE SPANWISE PRESSURES AT X/L = 0.50

CONFIDENTIAL

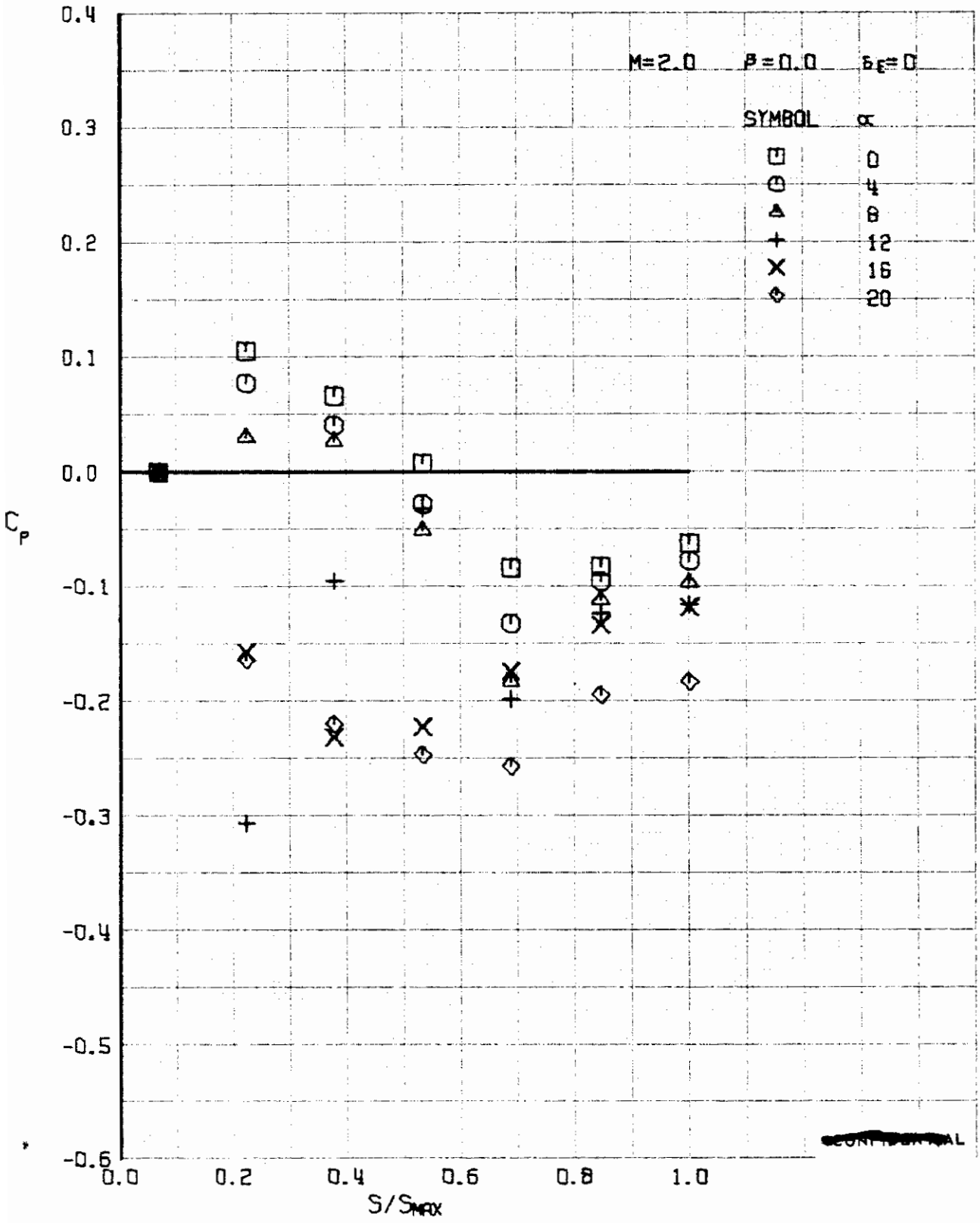

FIGURE 348 (U) UPPER SURFACE SPANWISE PRESSURES AT X/L = 0.76

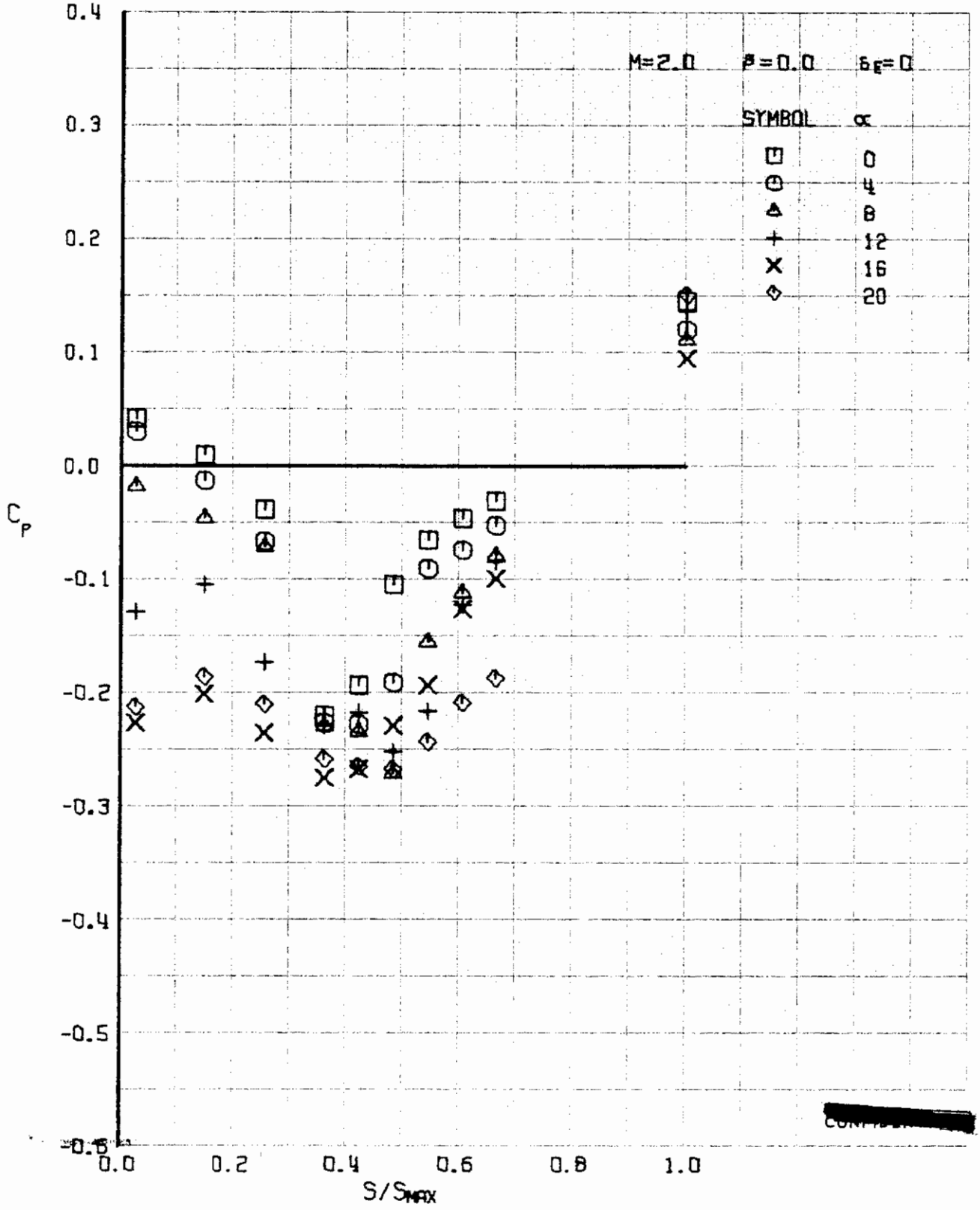

FIGURE 349 (U) UPPER SURFACE SPANWISE PRESSURES AT X/L = 0.86

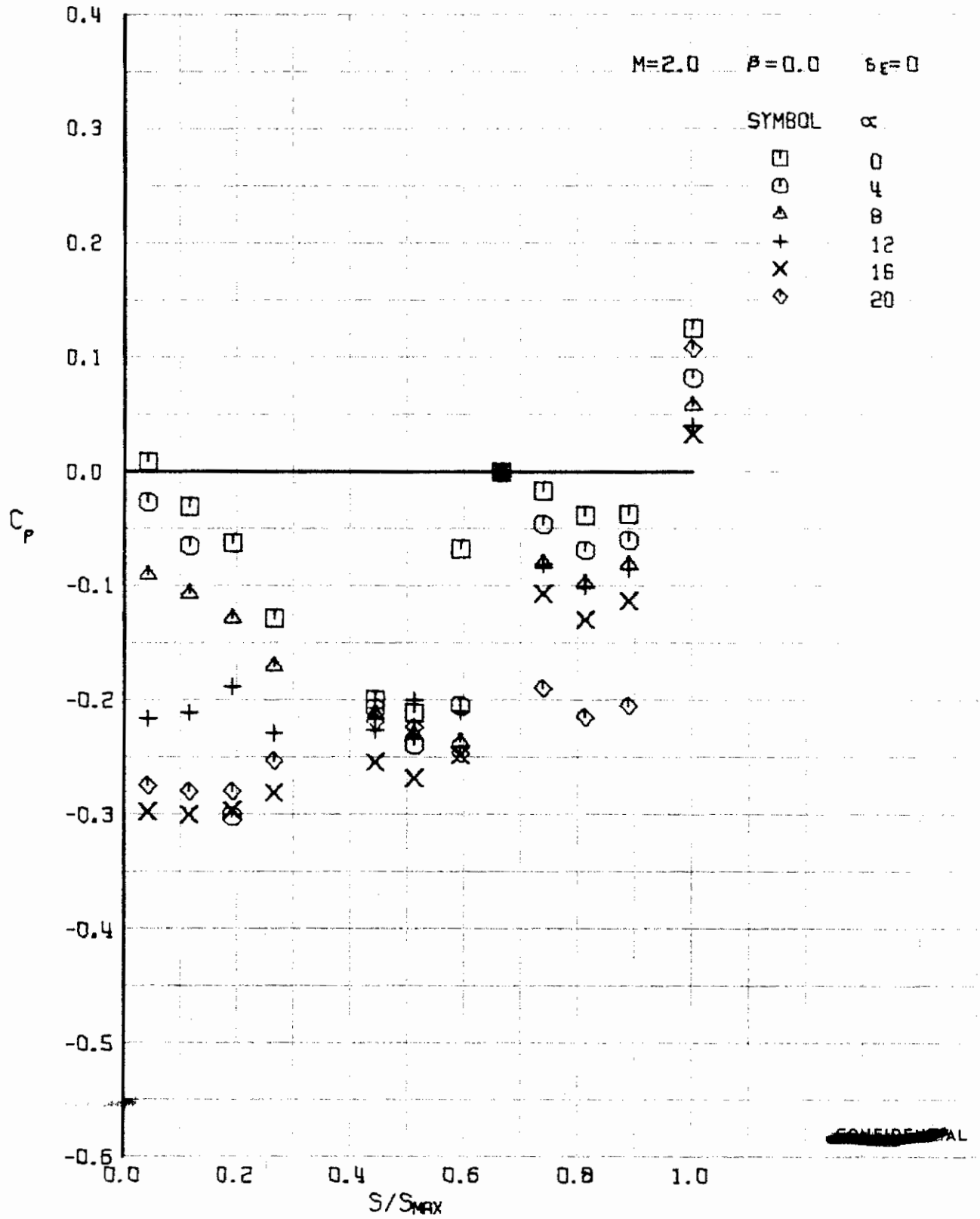

FIGURE 350 (U) UPPER SURFACE SPANWISE PRESSURES AT X/L = 0.96

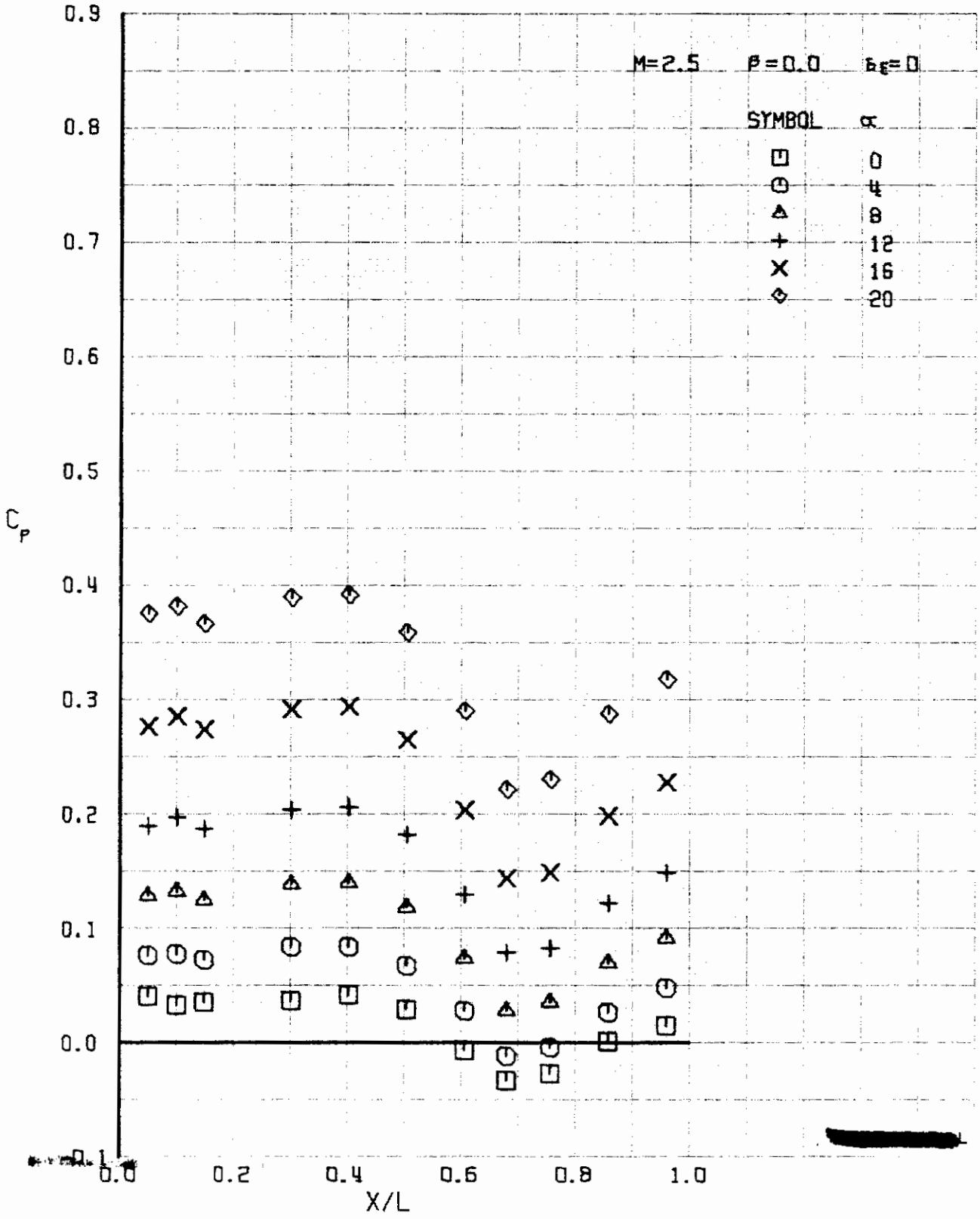

FIGURE 351 (U) LOWER SURFACE CENTERLINE PRESSURES

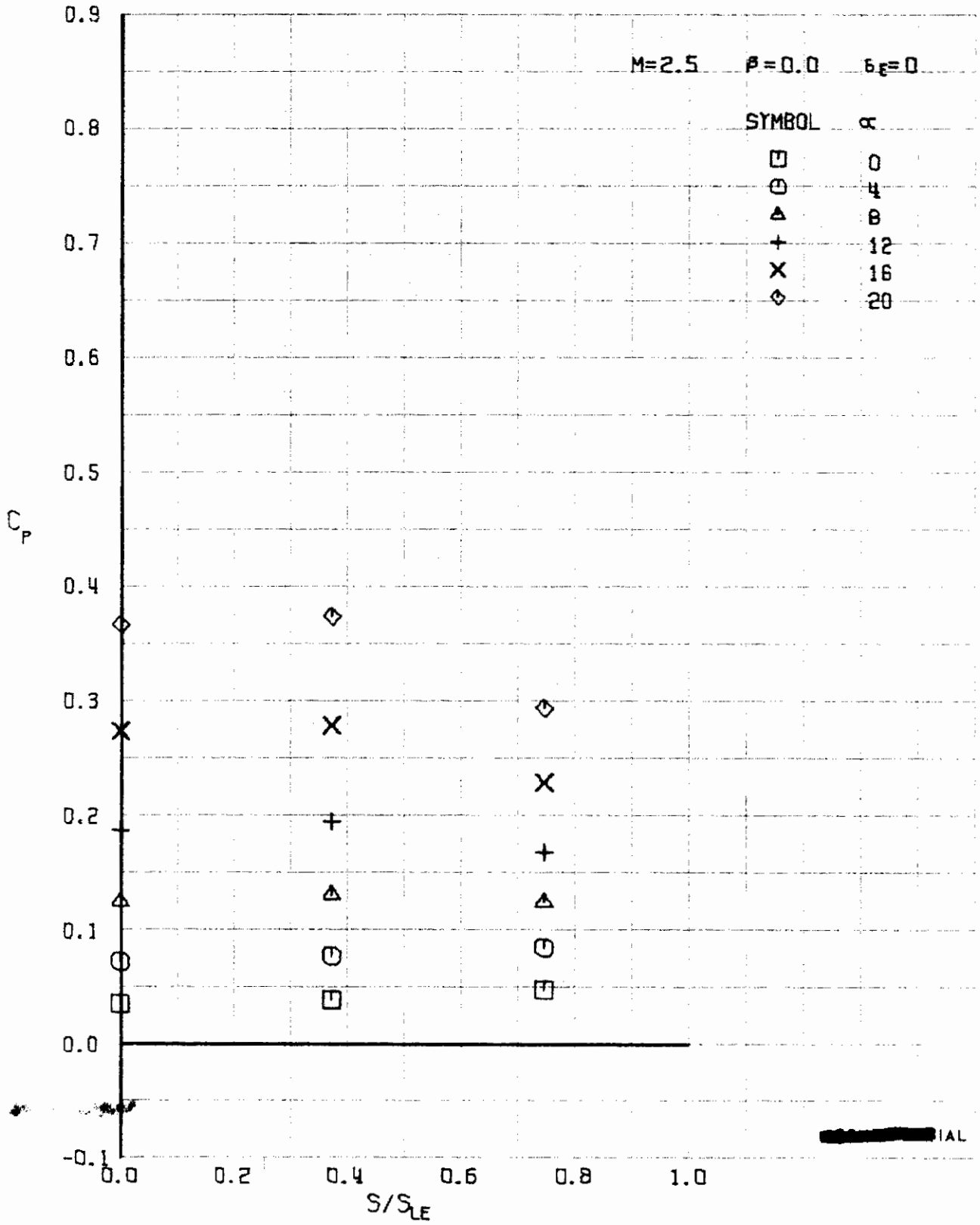

FIGURE 352 (U) LOWER SURFACE SPANWISE PRESSURES AT X/L = 0.15

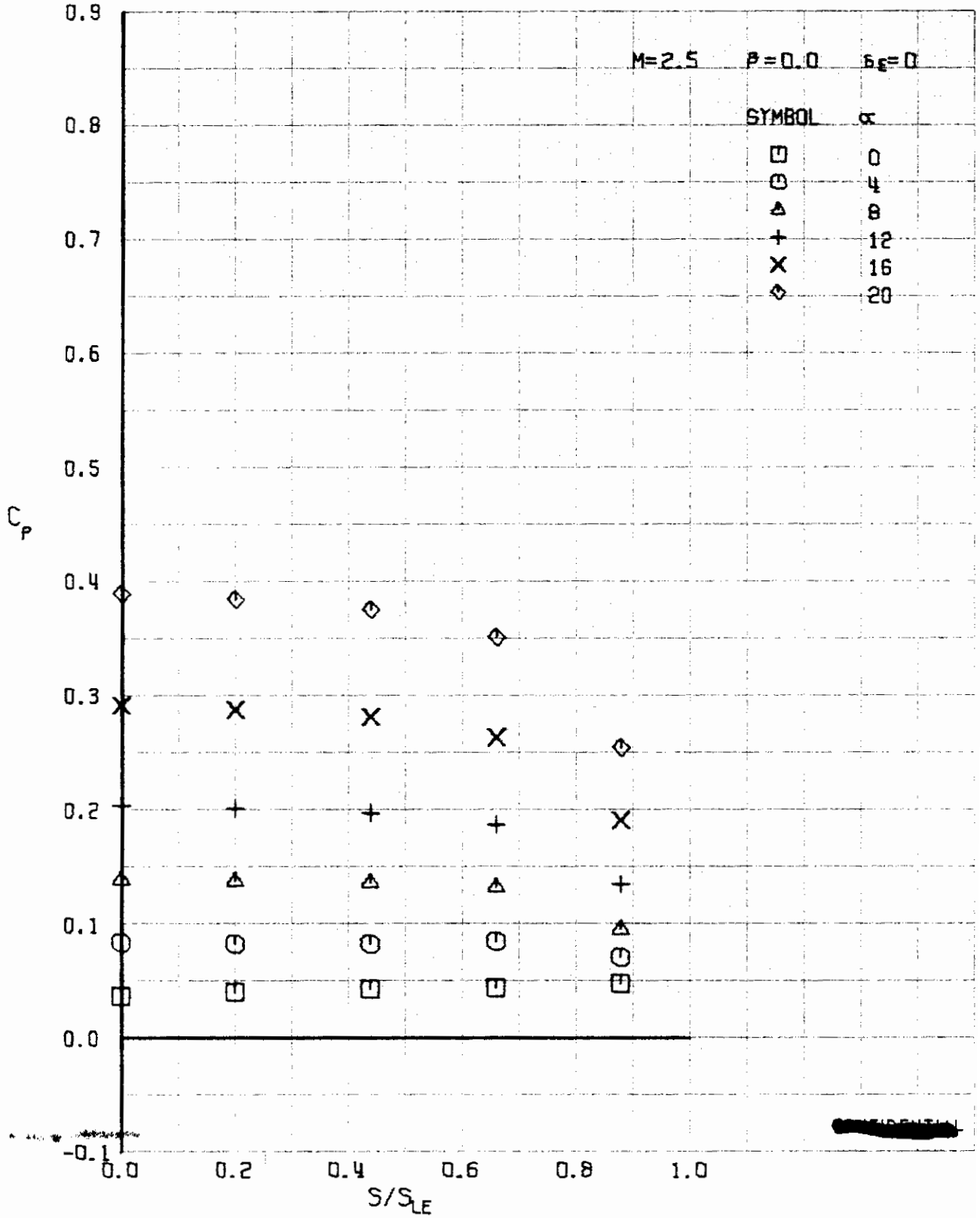

FIGURE 353 (U) LOWER SURFACE SPANWISE PRESSURES AT X/L = 0.30

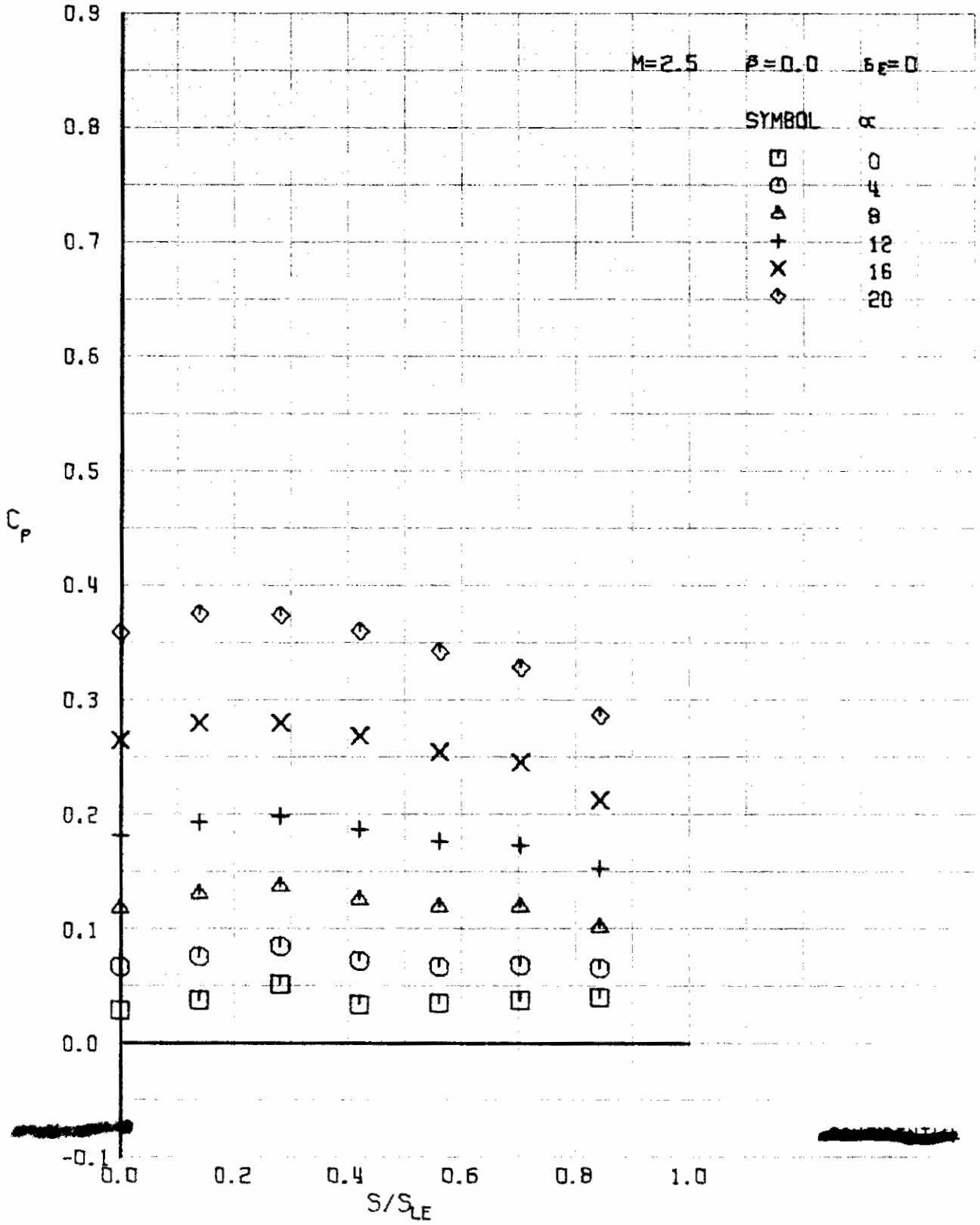

FIGURE 354 (U) LOWER SURFACE SPANWISE PRESSURES AT X/L = 0.50

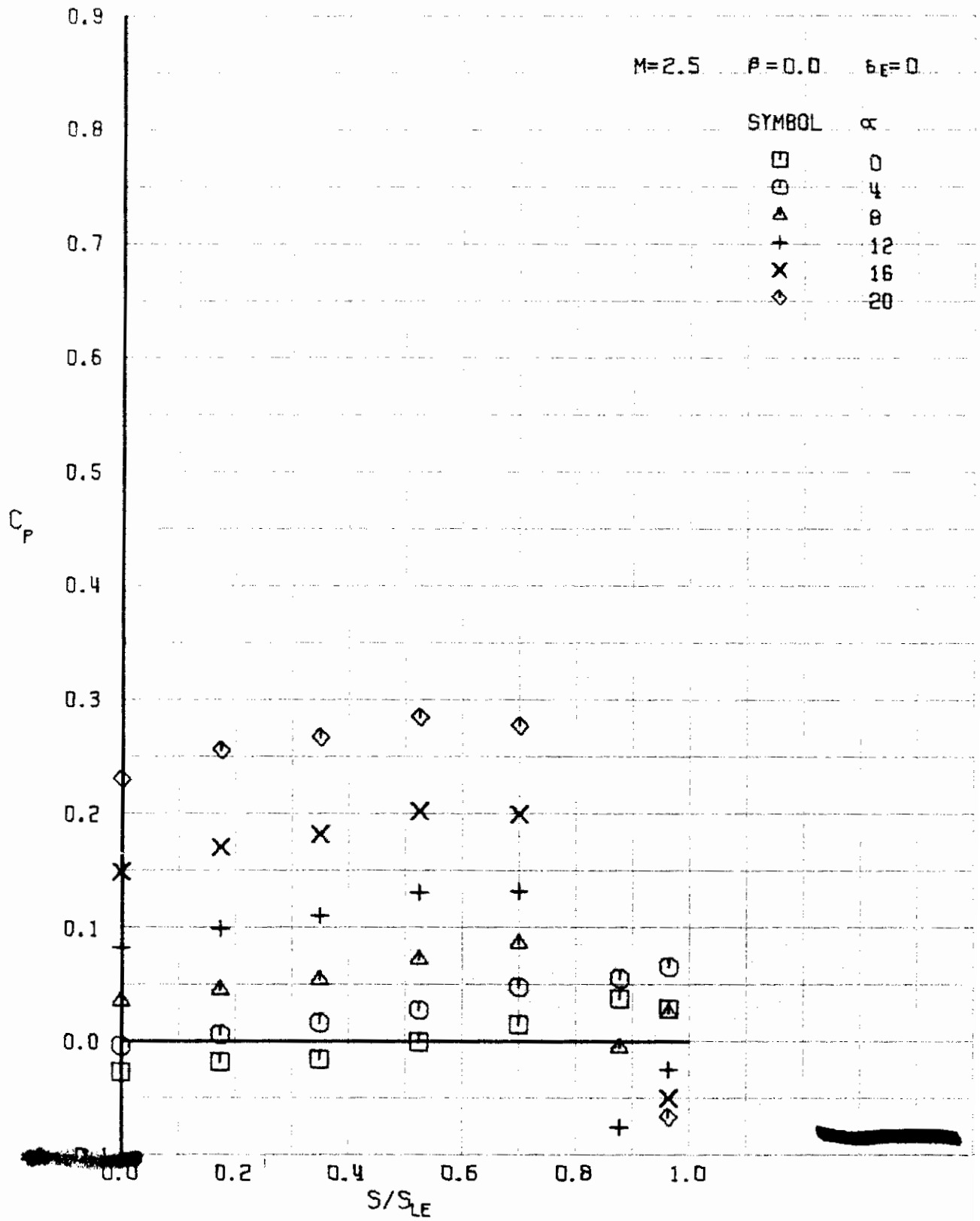

FIGURE 355 (U) LOWER SURFACE SPANWISE PRESSURES AT X/L = 0.76

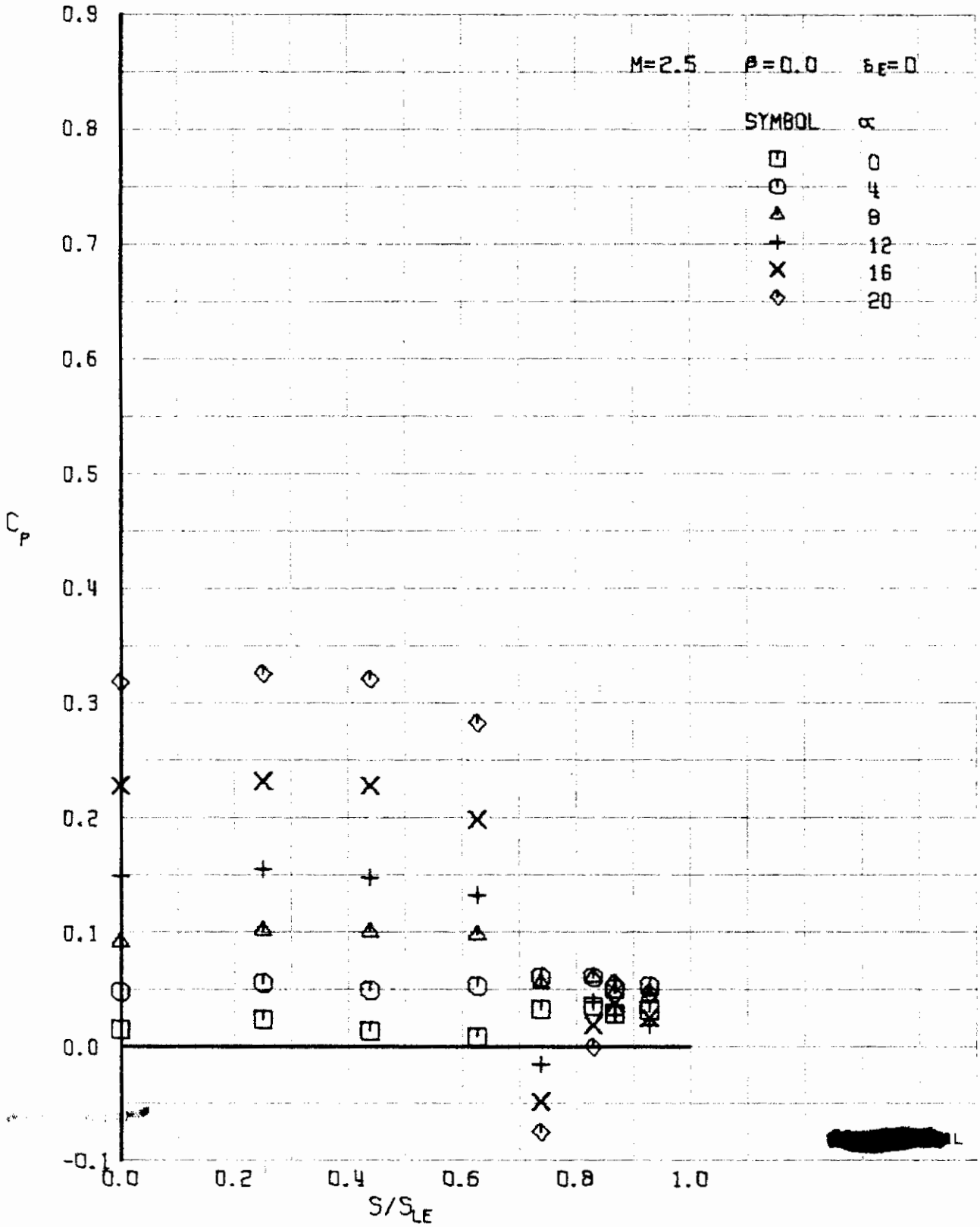

FIGURE 356 (U) LOWER SURFACE SPANWISE PRESSURES AT X/L = 0.96

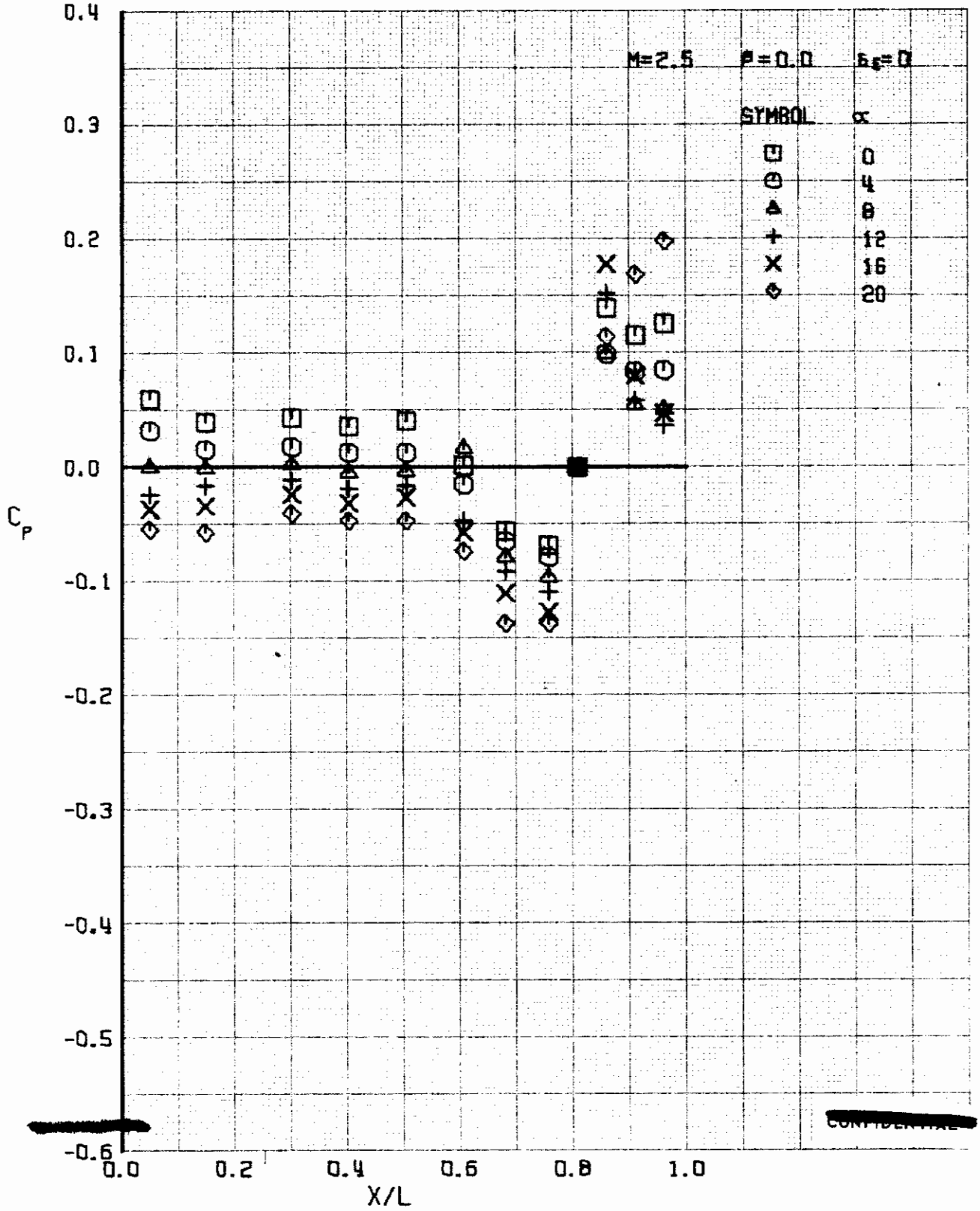

FIGURE 357 (U) UPPER SURFACE CENTERLINE PRESSURES

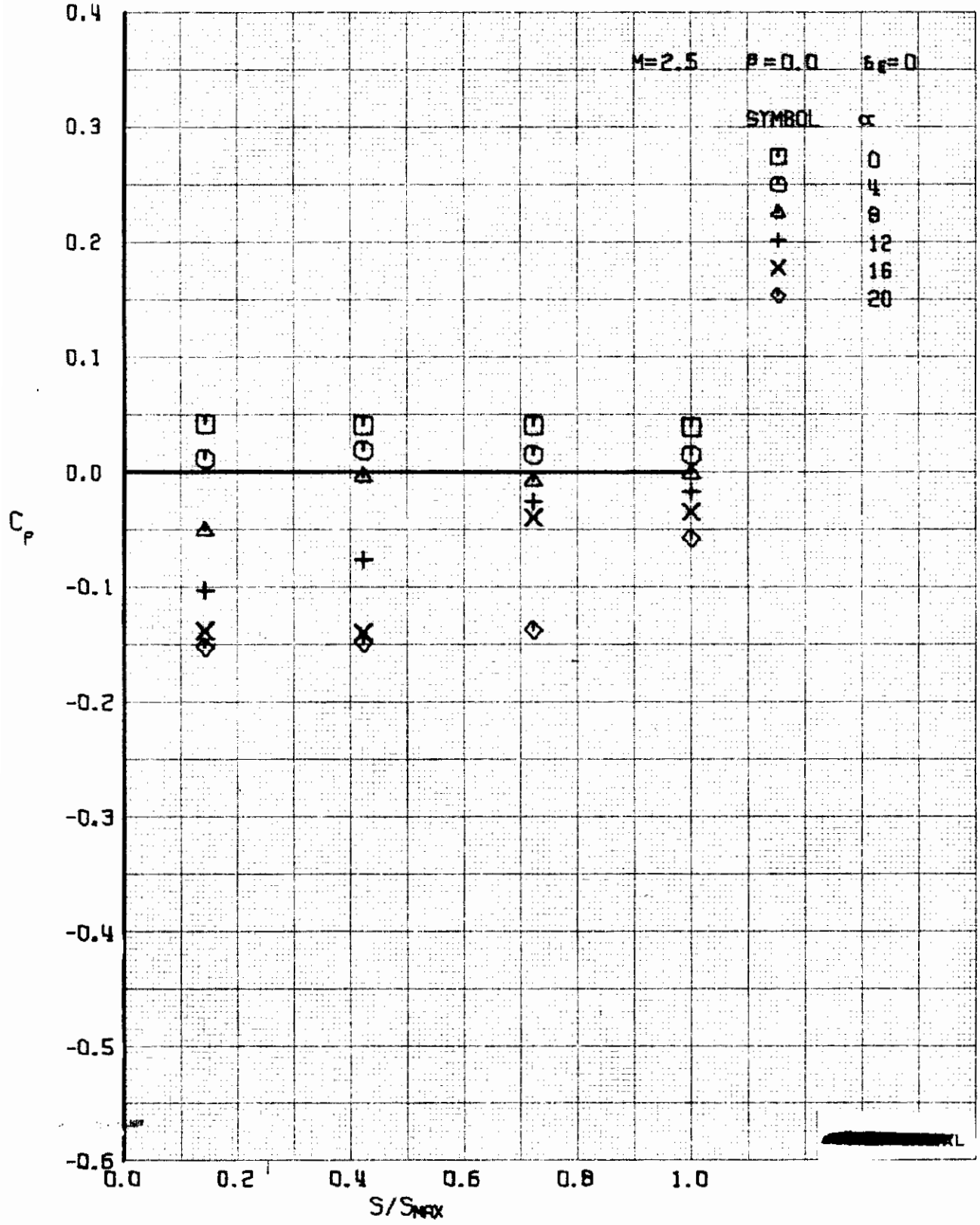

FIGURE 358 (U) UPPER SURFACE SPANWISE PRESSURES AT X/L = 0.15

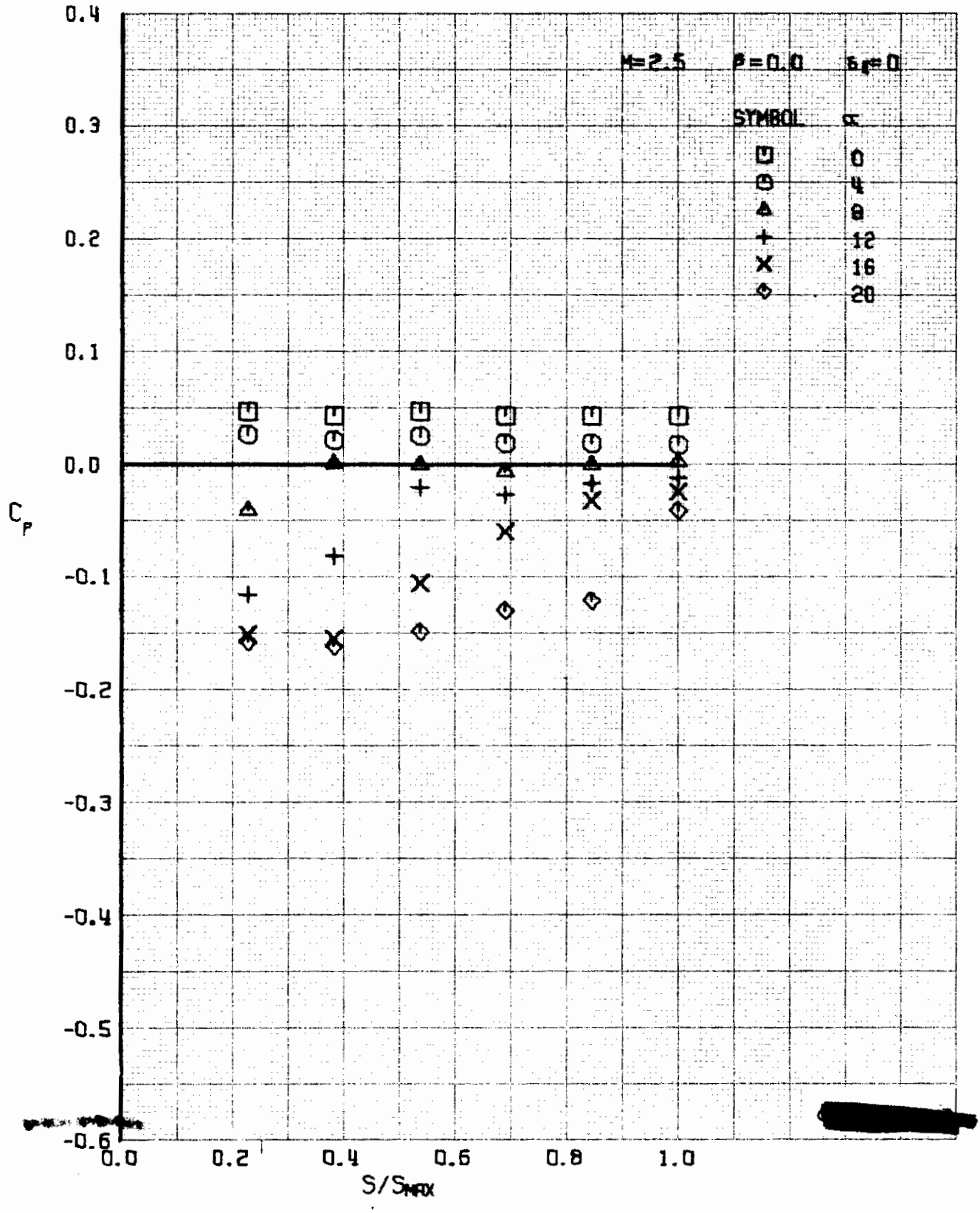

FIGURE 359 (U) UPPER SURFACE SPANWISE PRESSURES AT X/L = 0.30

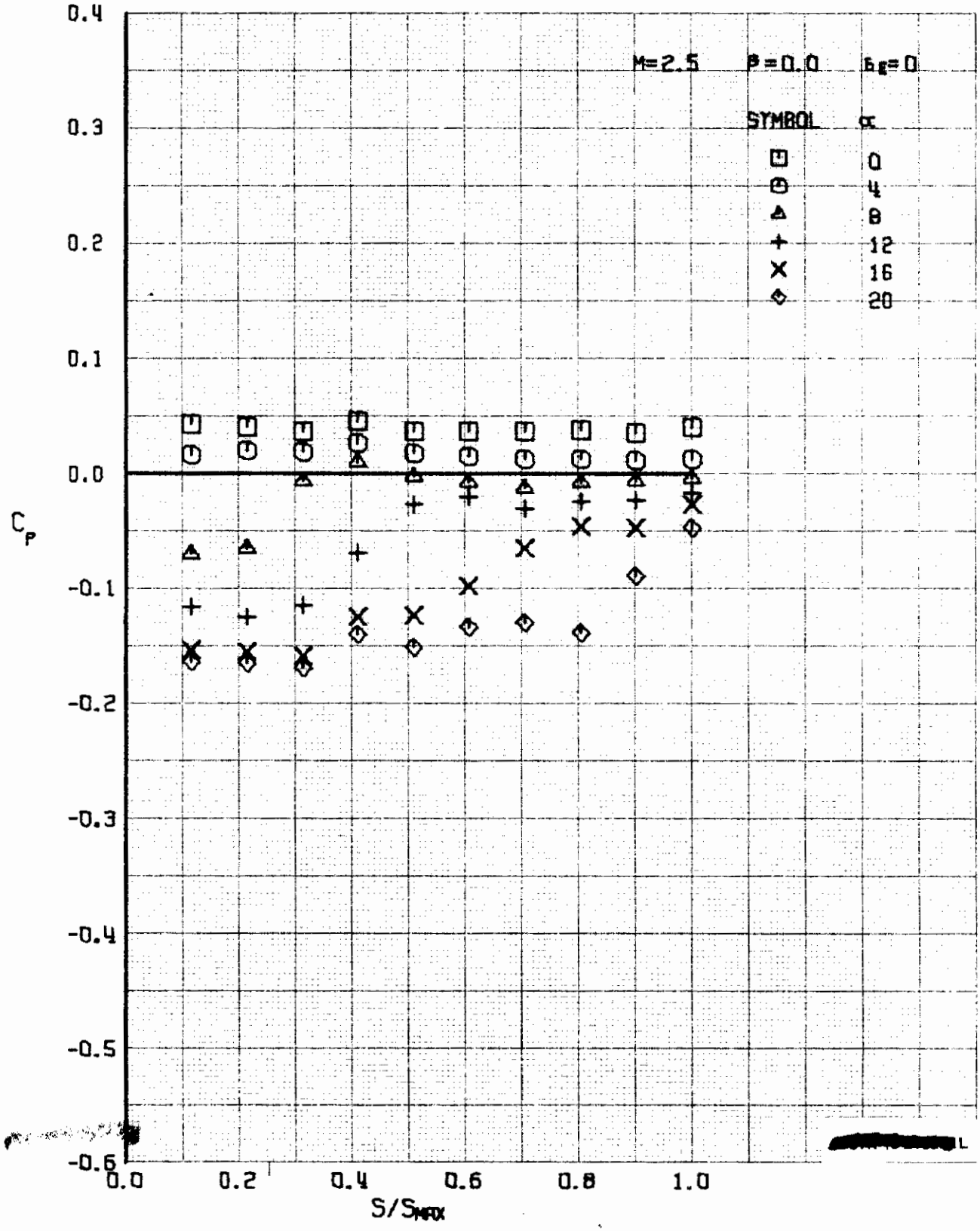

FIGURE 360 (U) UPPER SURFACE SPANWISE PRESSURES AT X/L = 0.50

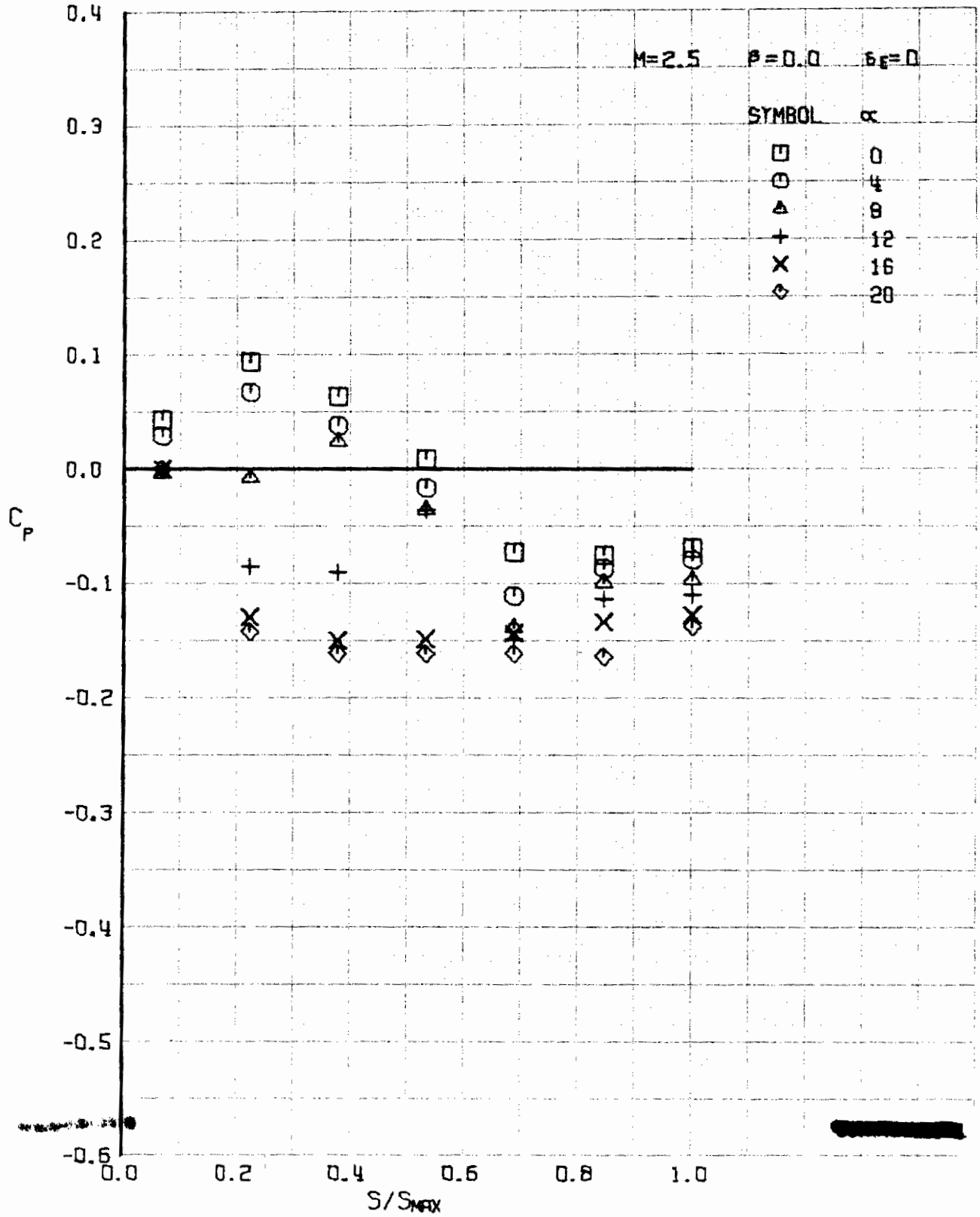

FIGURE 361 (U) UPPER SURFACE SPANWISE PRESSURES AT X/L = 0.76

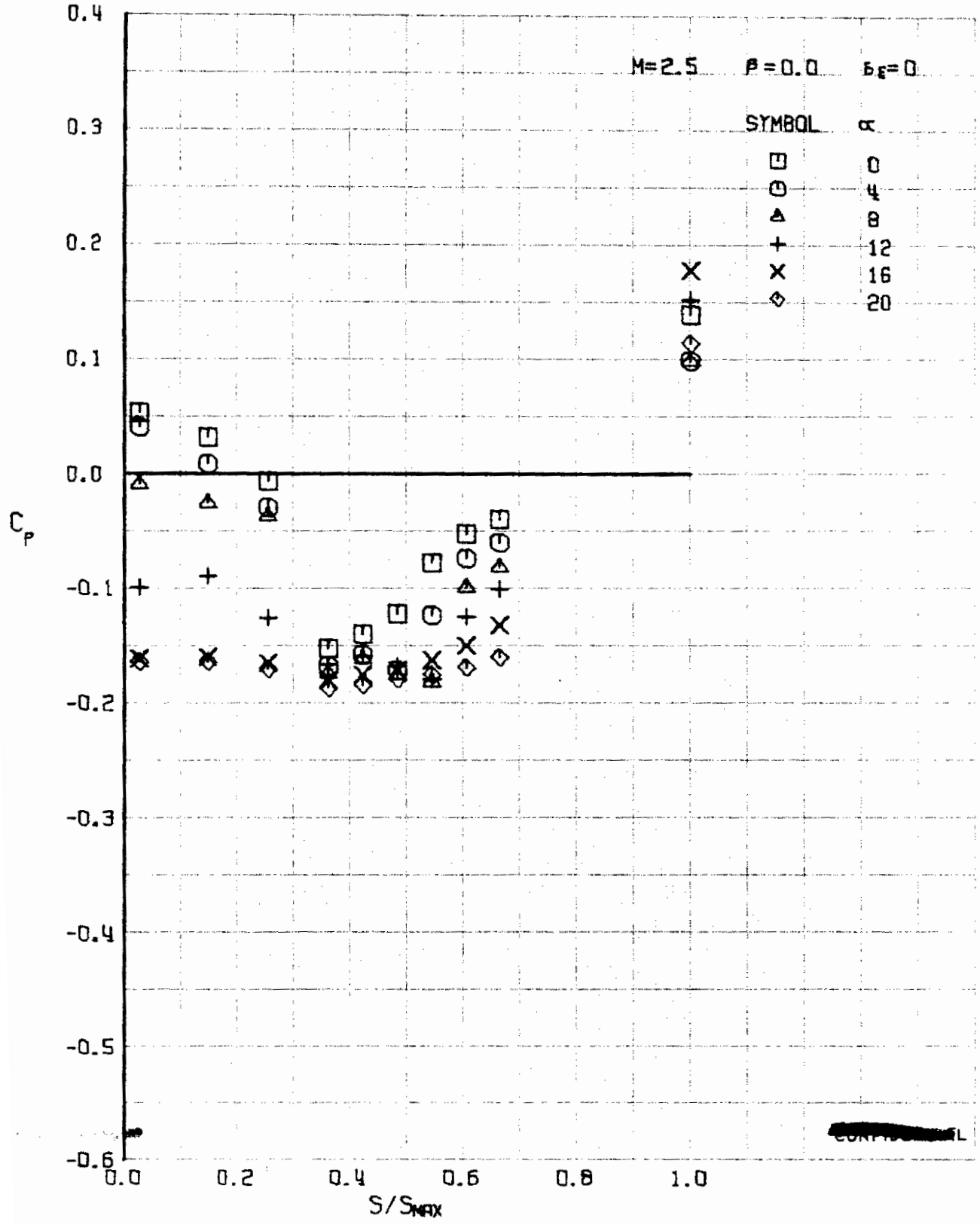

FIGURE 362 (U) UPPER SURFACE SPANWISE PRESSURES AT X/L = 0.86

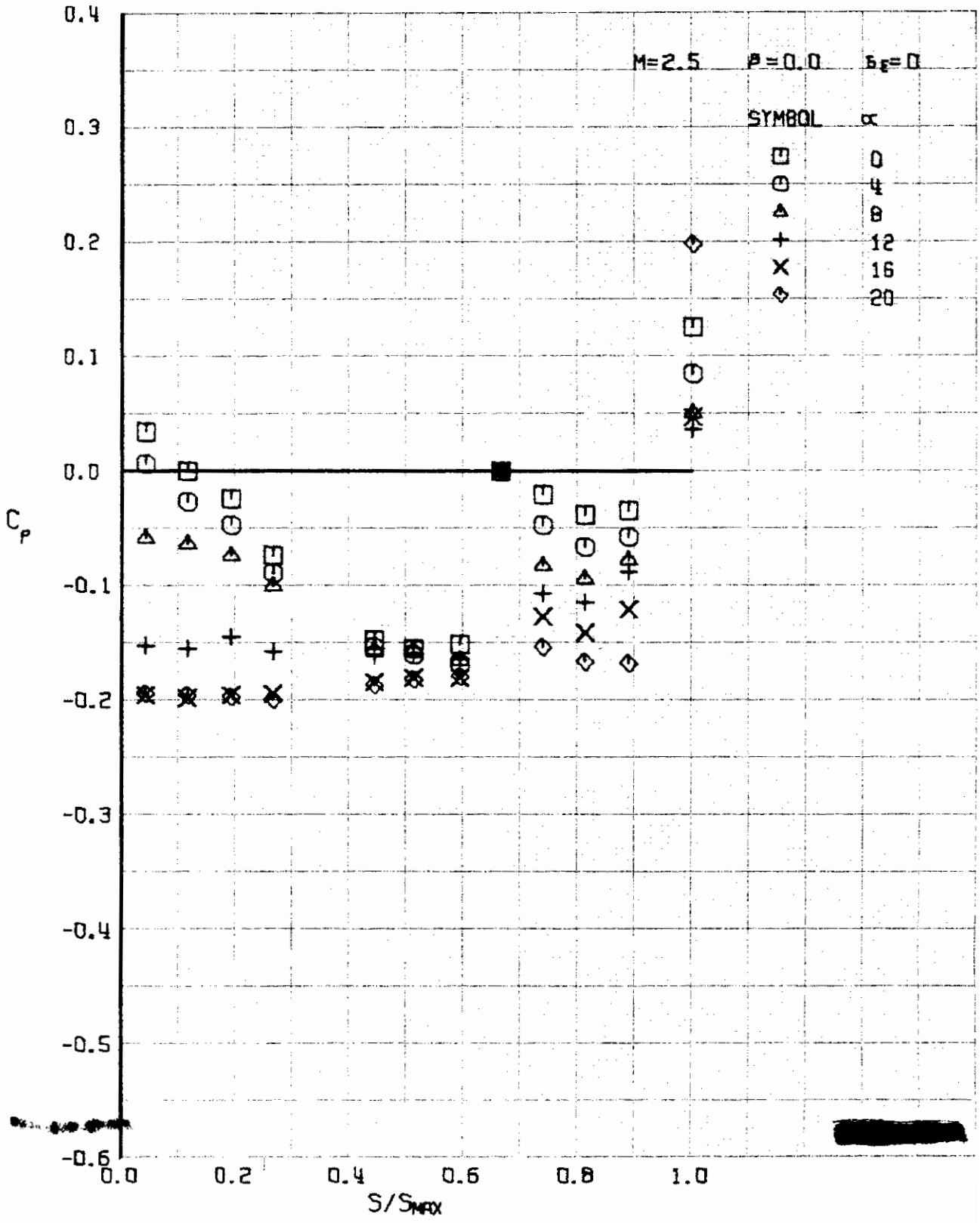

FIGURE 363 (U) UPPER SURFACE SPANWISE PRESSURES AT X/L = 0.96

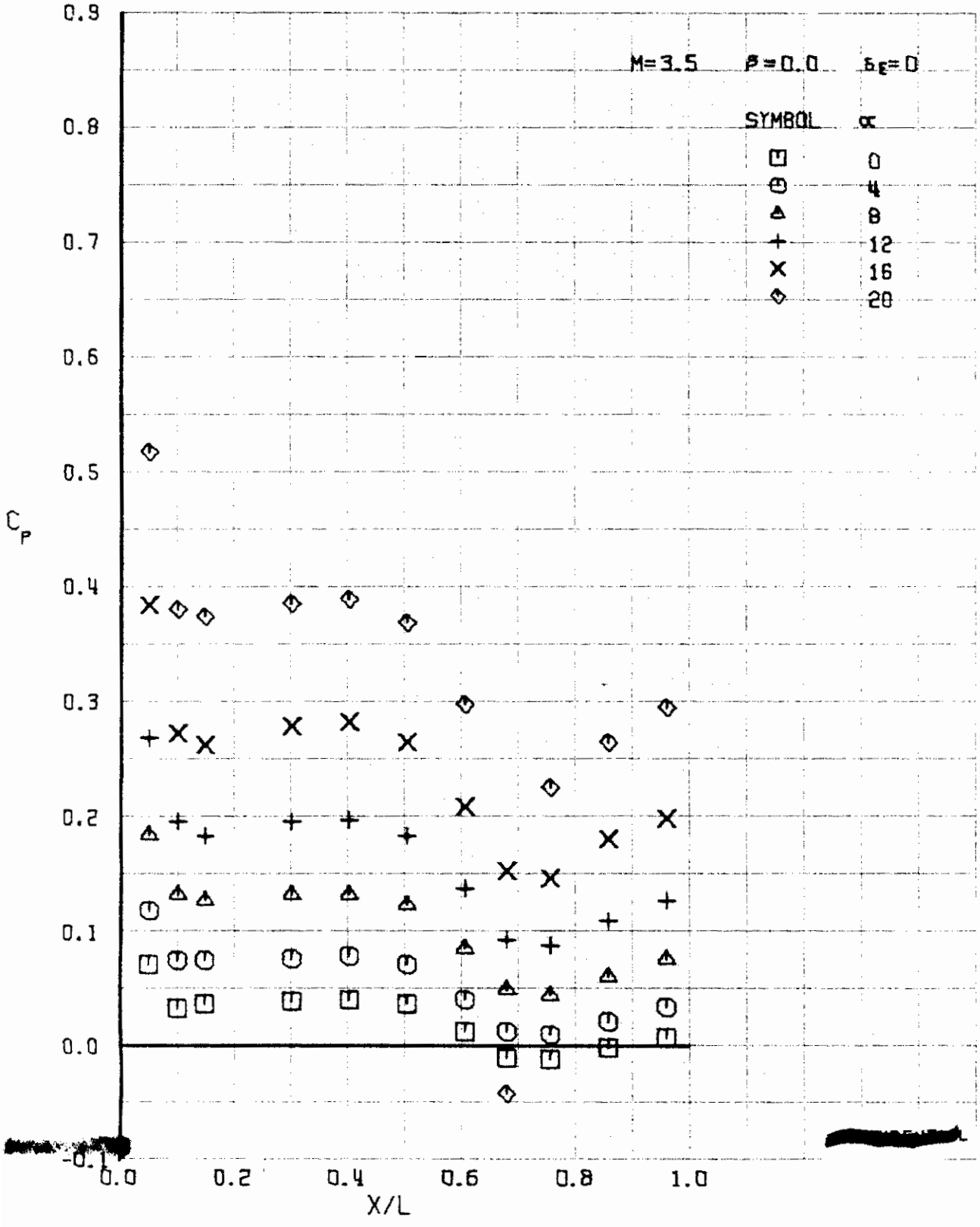

FIGURE 364 (U) LOWER SURFACE CENTERLINE PRESSURES

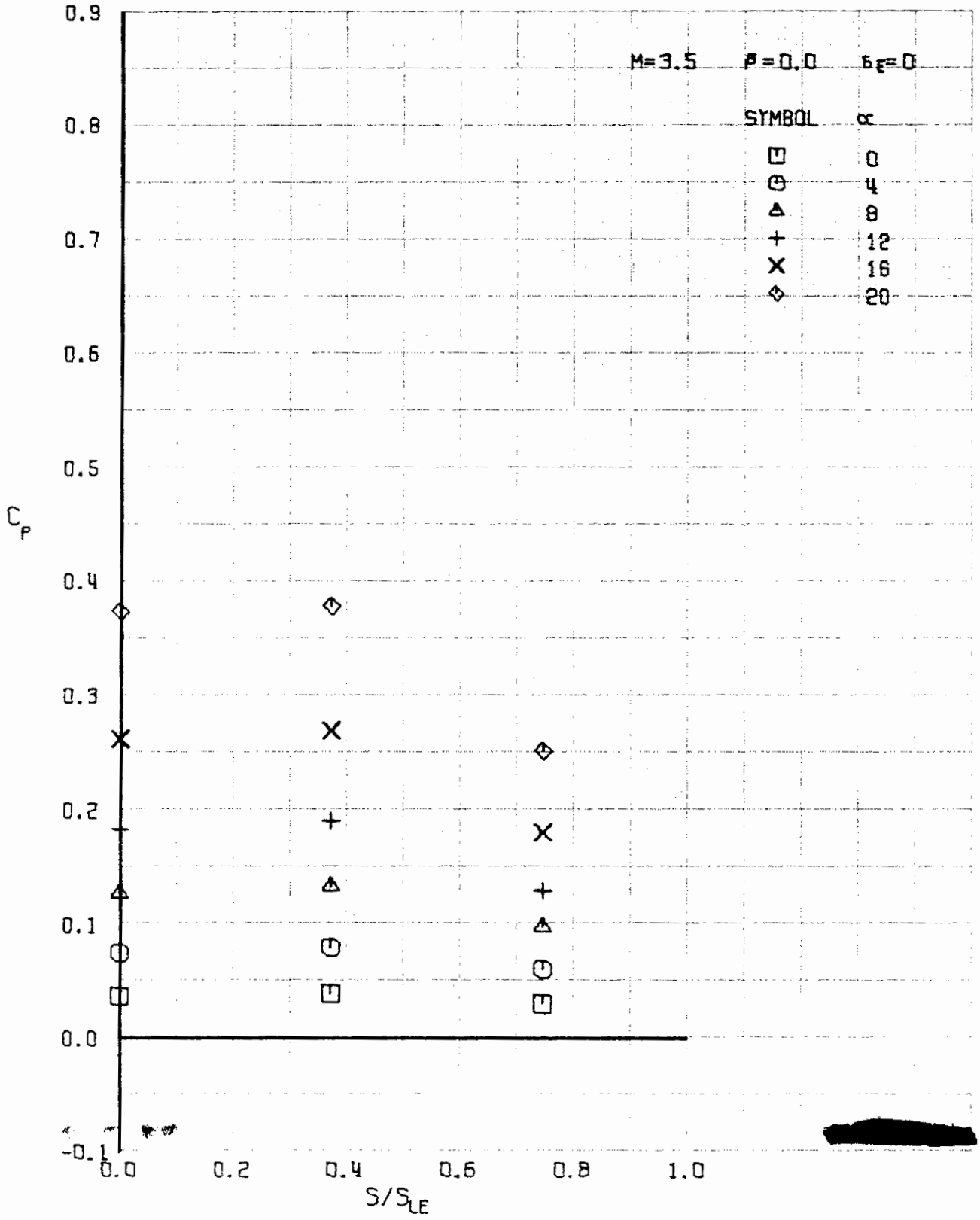

FIGURE 365 (U) LOWER SURFACE SPANWISE PRESSURES AT X/L = 0.15

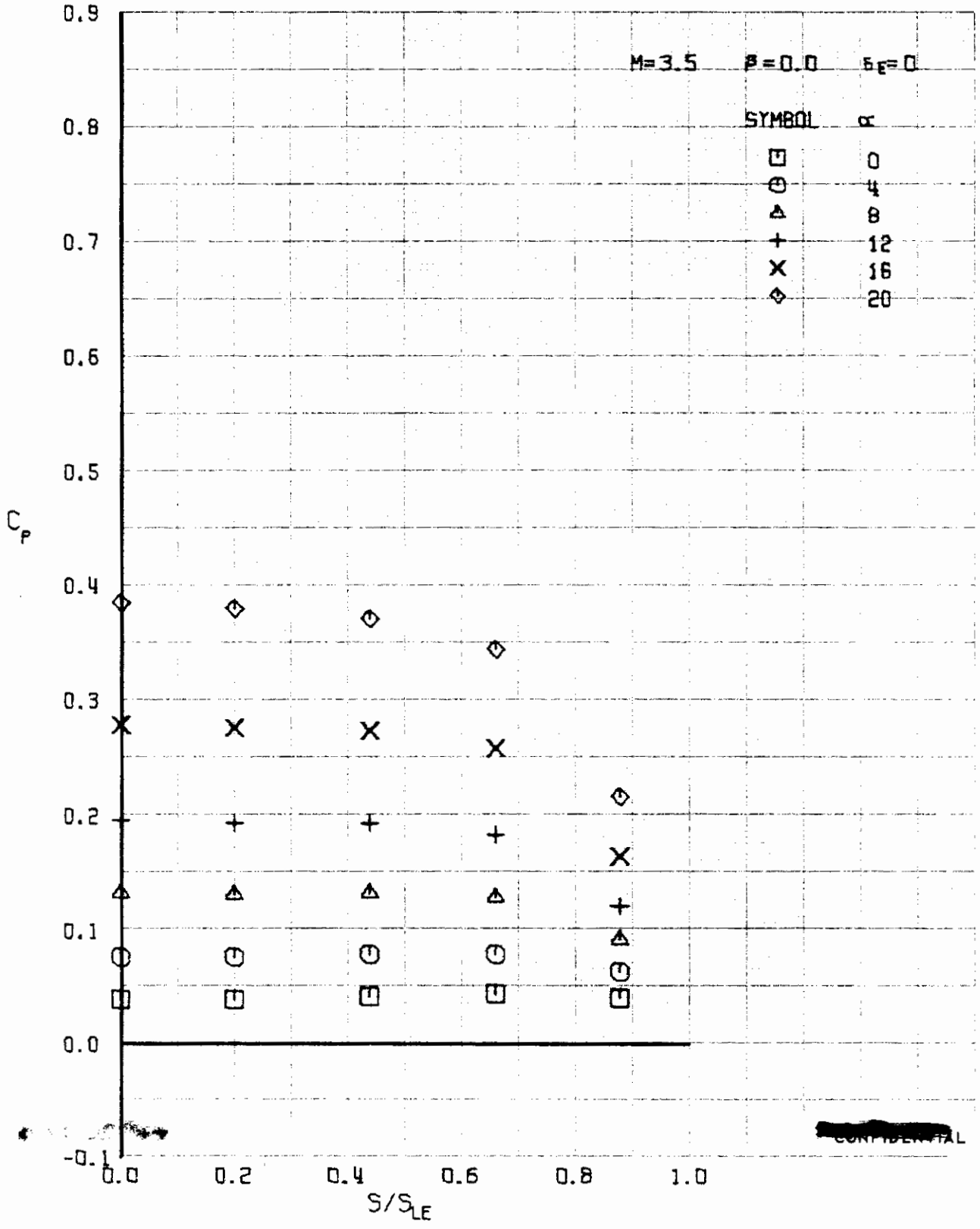

FIGURE 366 (U) LOWER SURFACE SPANWISE PRESSURES AT X/L = 0.30

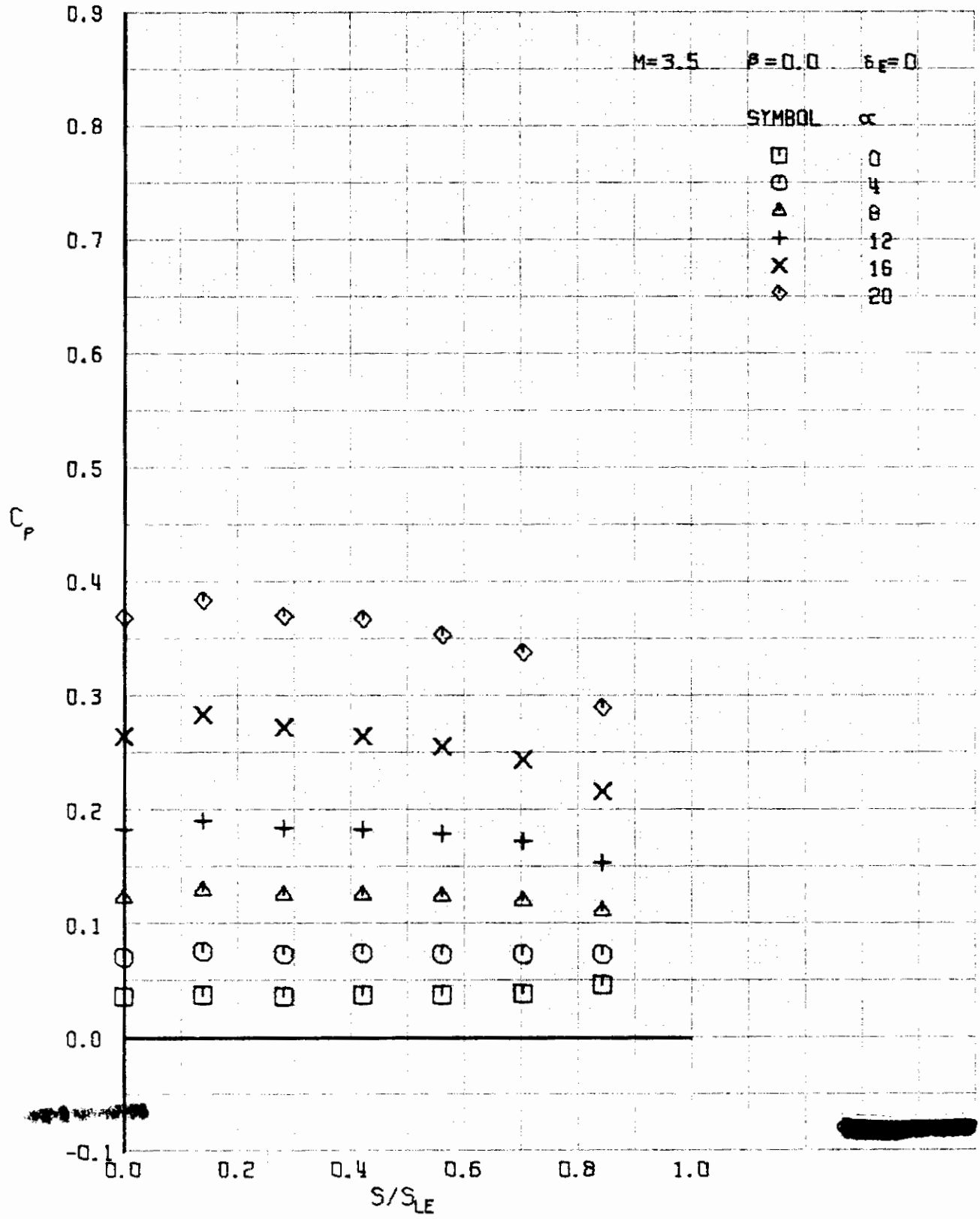

FIGURE 367 (U) LOWER SURFACE SPANWISE PRESSURES AT X/L = 0.50

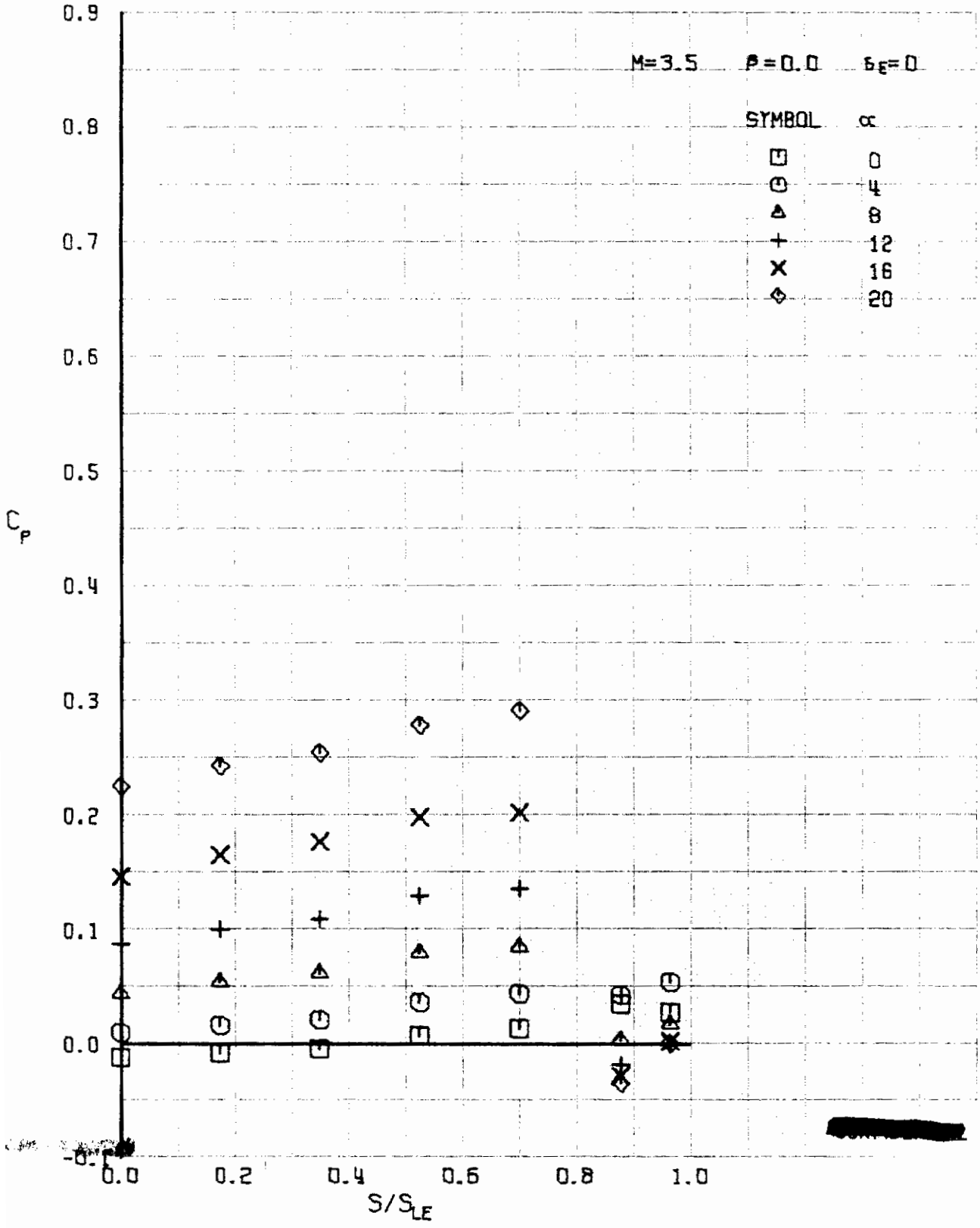

FIGURE 368 (U) LOWER SURFACE SPANWISE PRESSURES AT X/L = 0.76

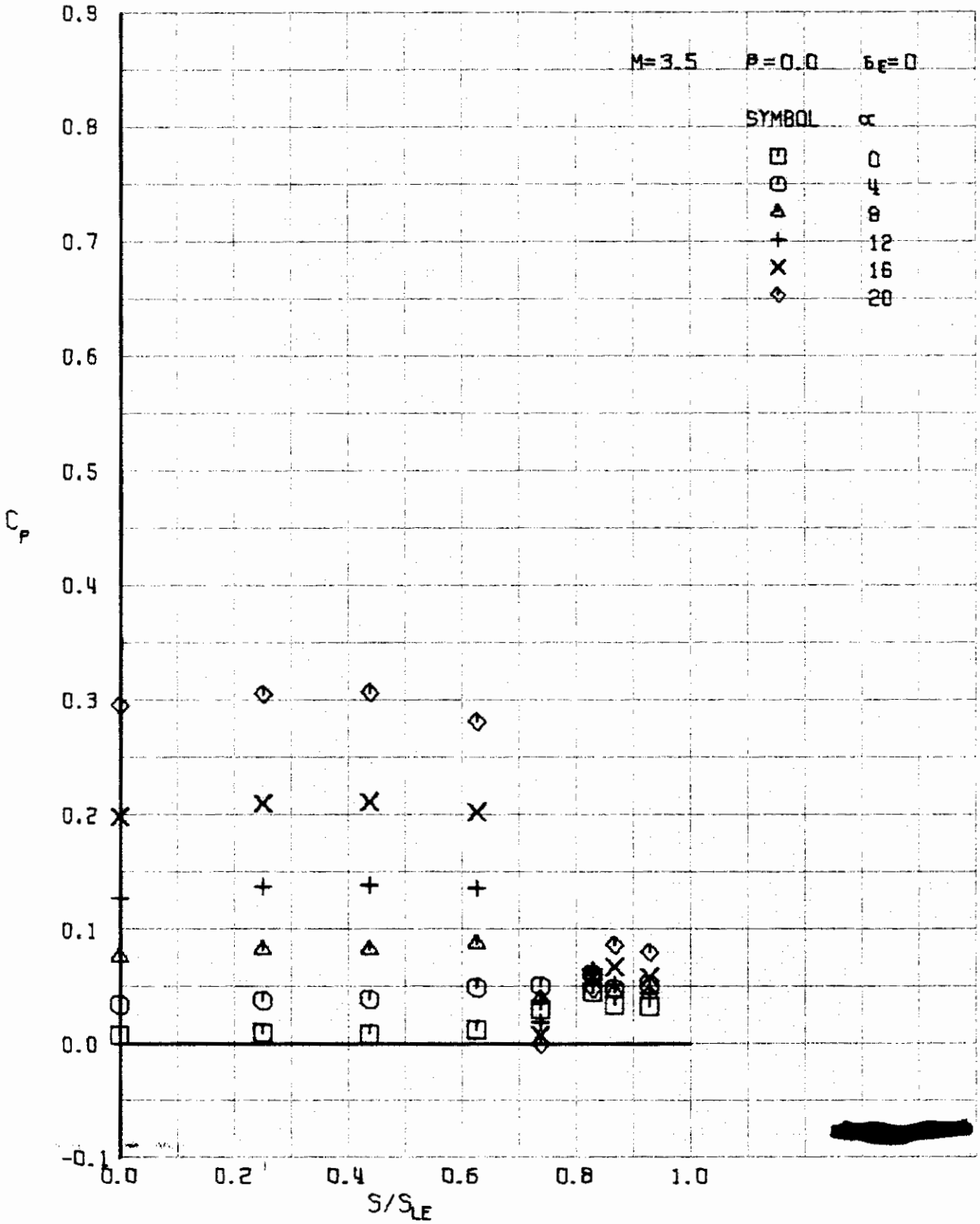

FIGURE 369 (U) LOWER SURFACE SPANWISE PRESSURES AT X/L = 0.96

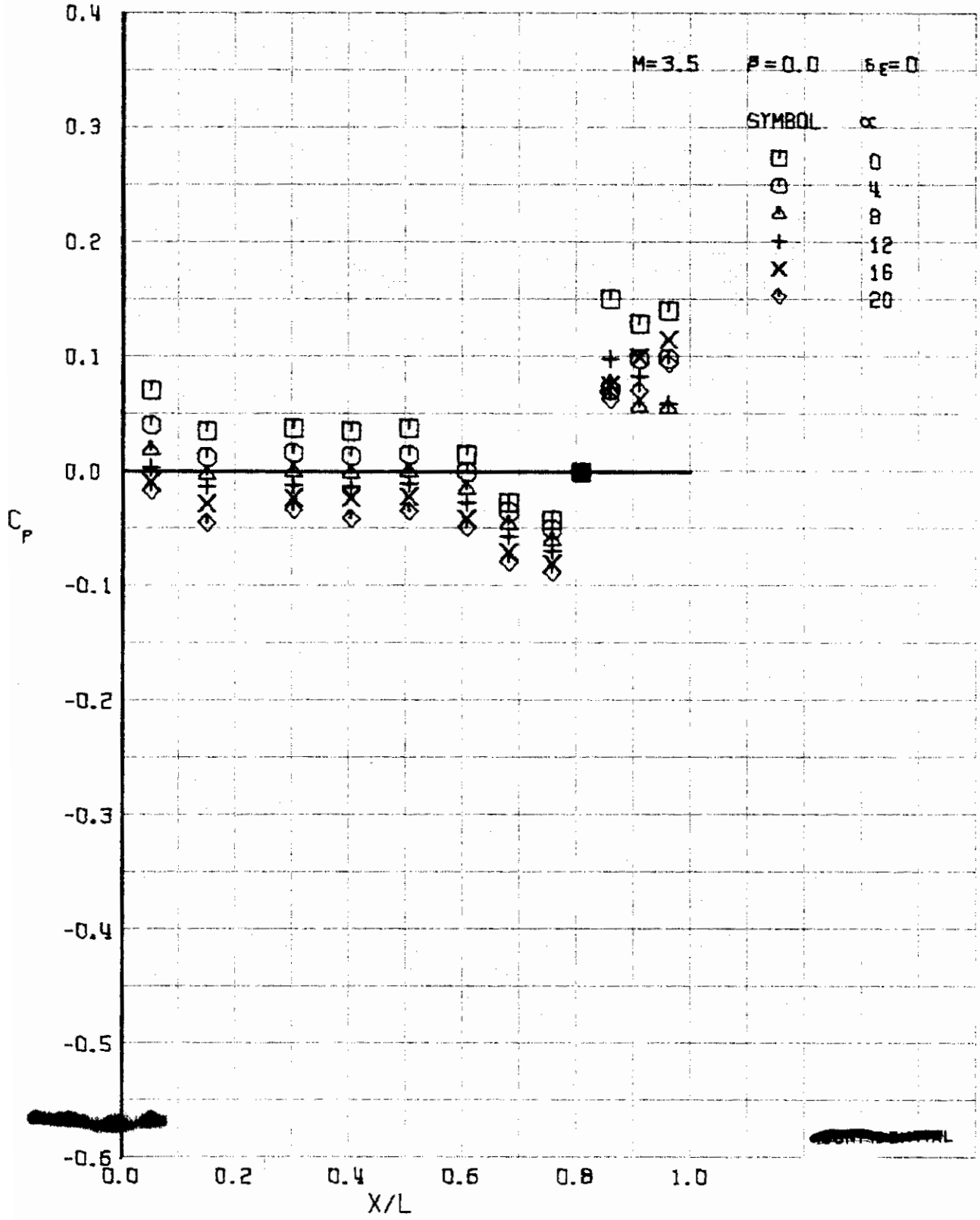

FIGURE 370 (U) UPPER SURFACE CENTERLINE PRESSURES

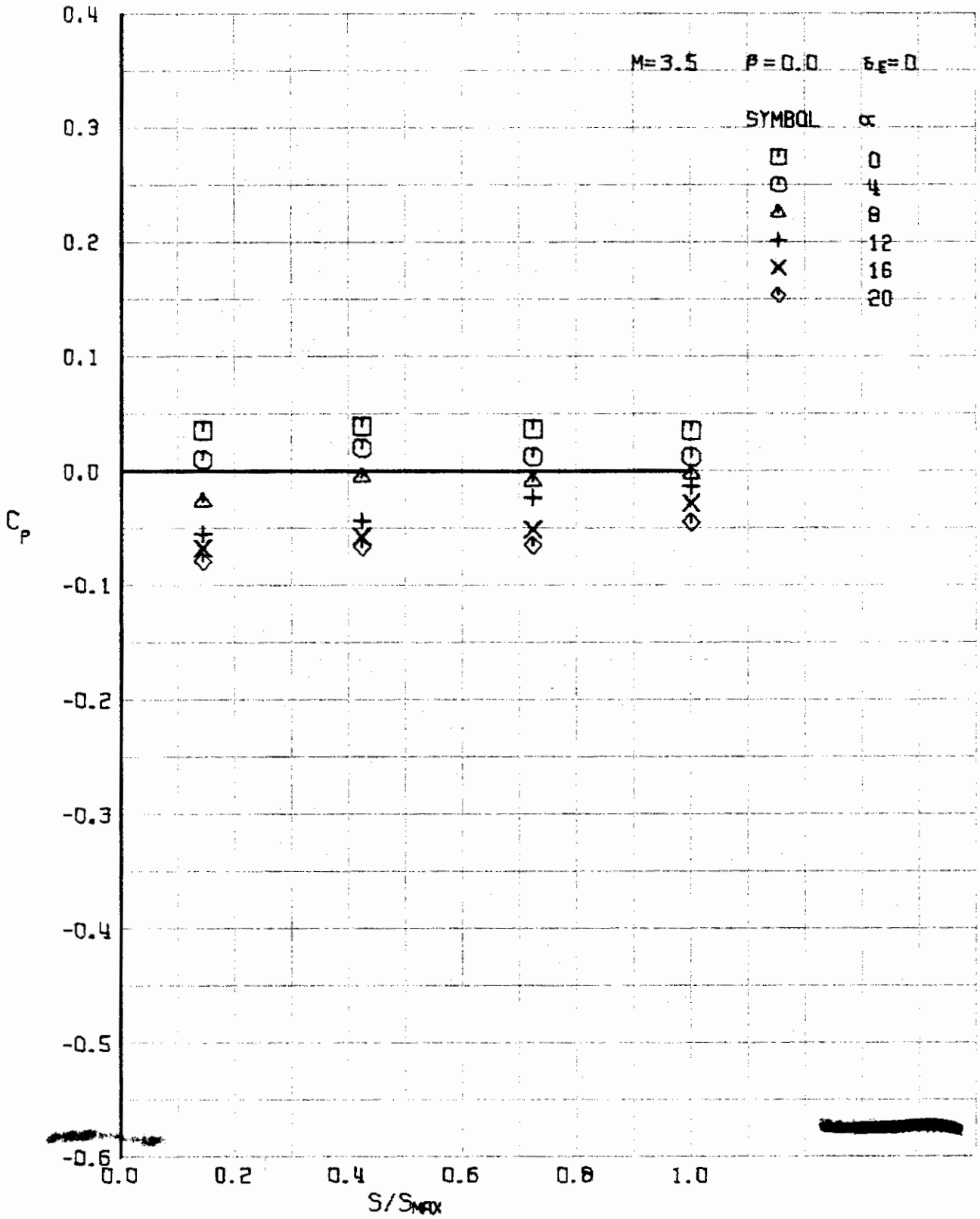

FIGURE 371 (U) UPPER SURFACE SPANWISE PRESSURES AT X/L = 0.15

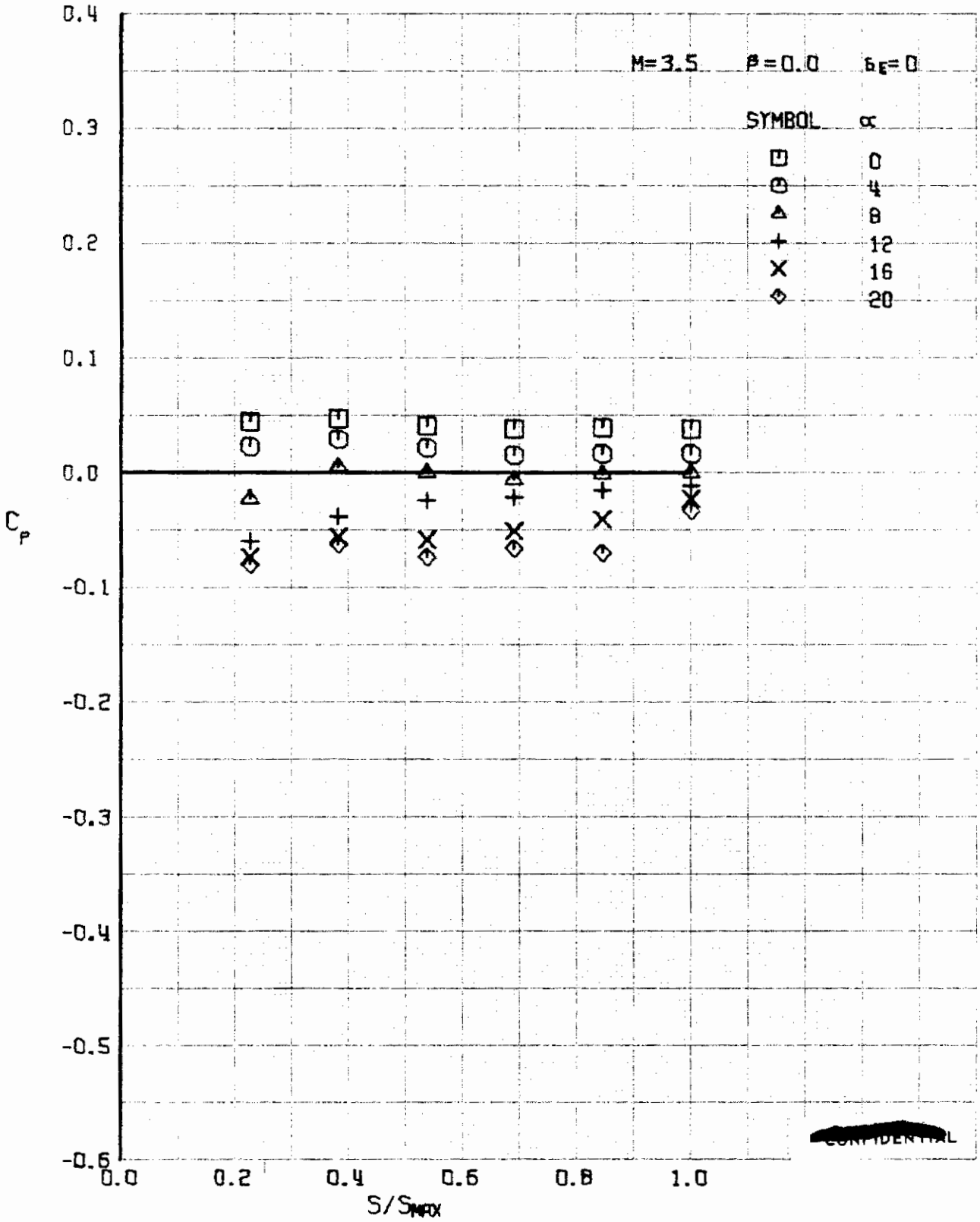

FIGURE 372 (U) UPPER SURFACE SPANWISE PRESSURES AT X/L = 0.30

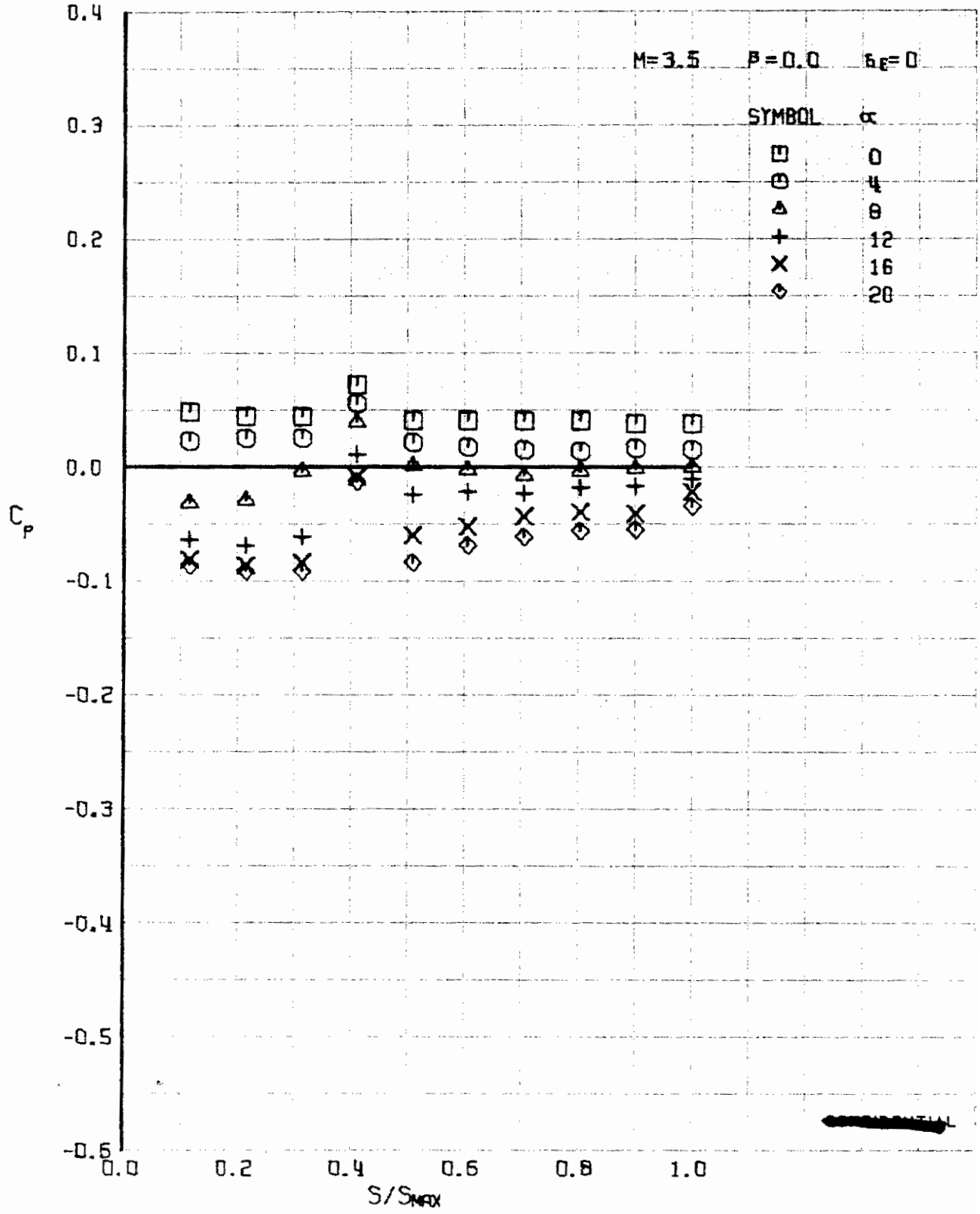

FIGURE 373 (U) UPPER SURFACE SPANWISE PRESSURES AT X/L = 0.50

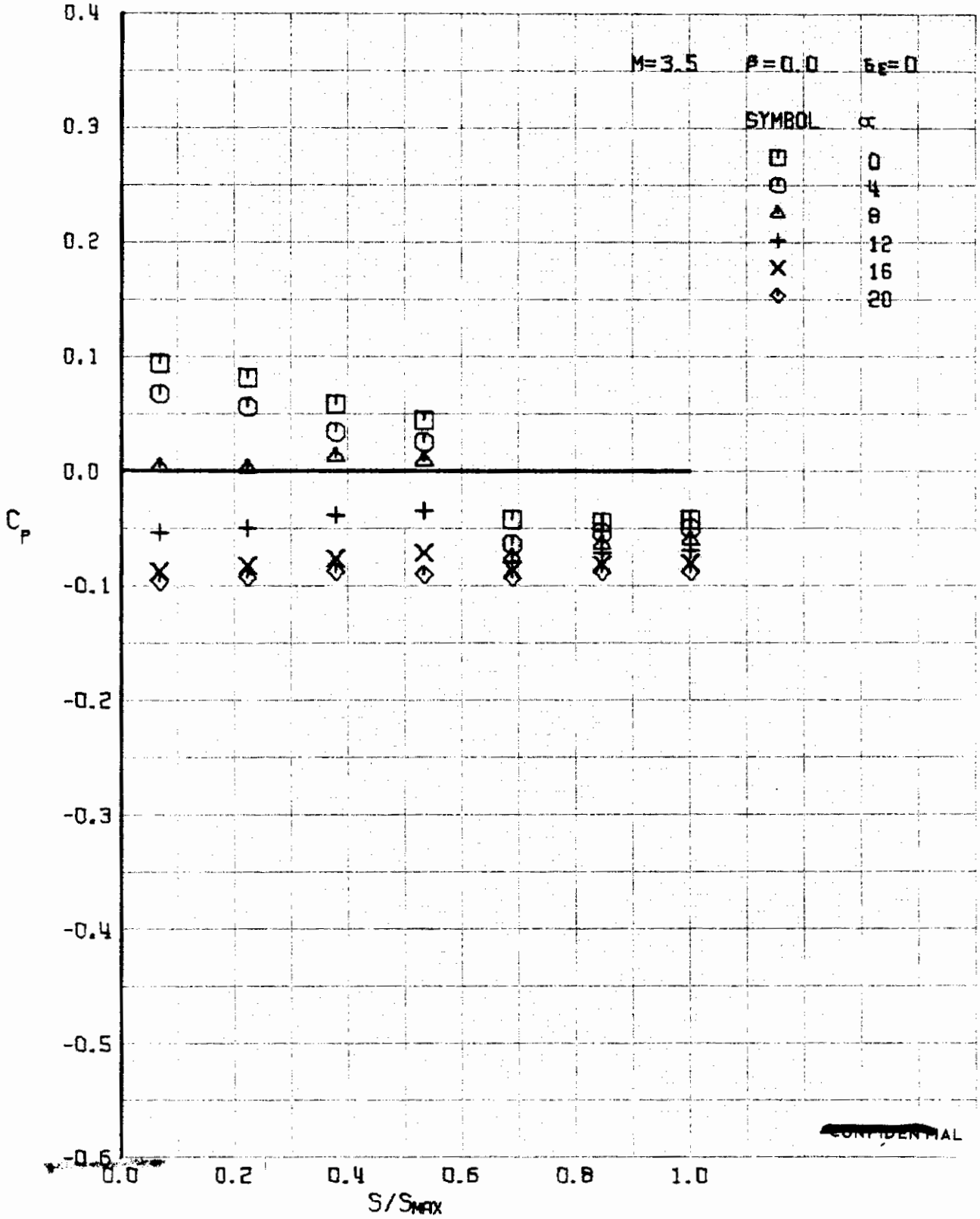

FIGURE 374 (U) UPPER SURFACE SPANWISE PRESSURES AT X/L = 0.76

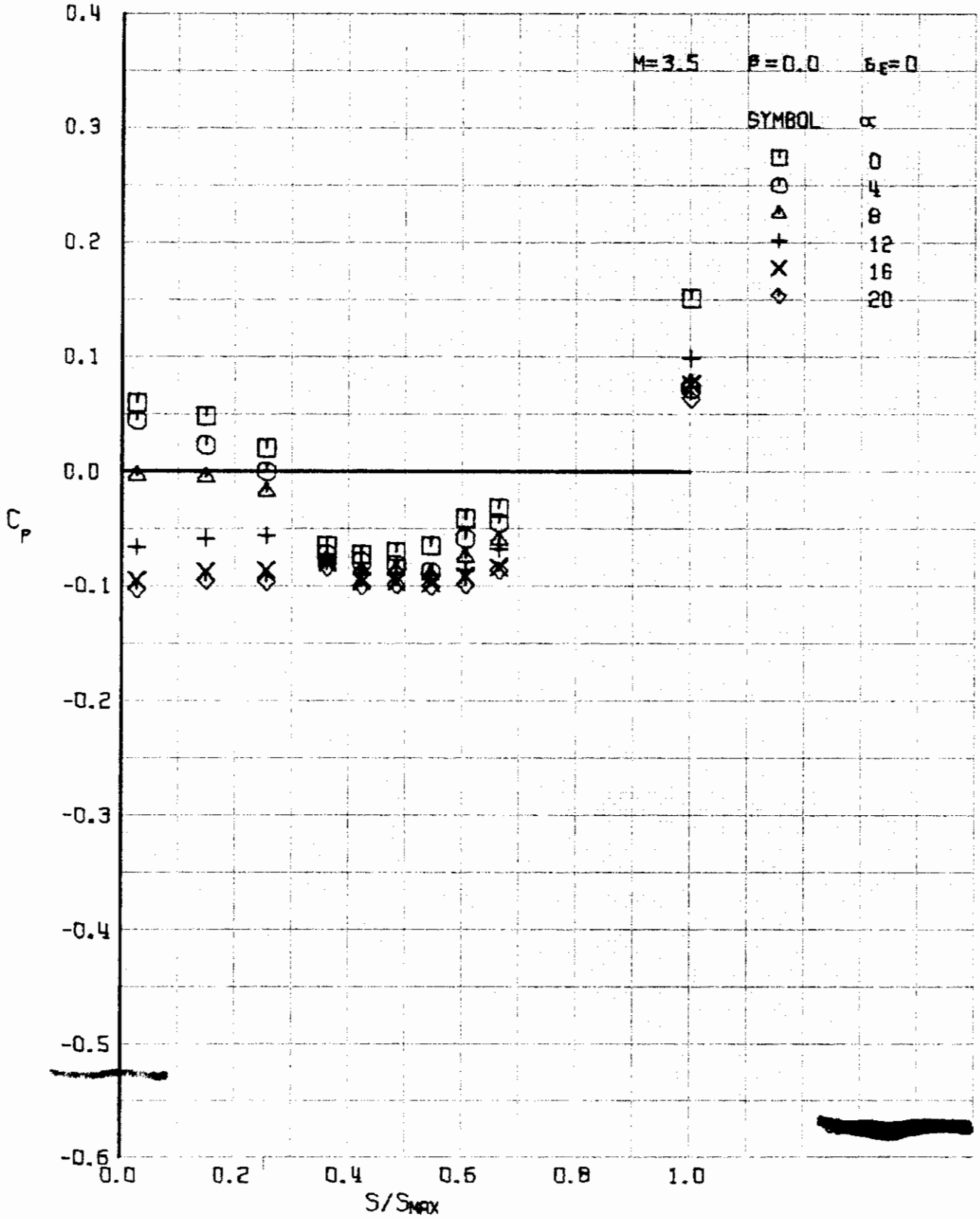

FIGURE 375 (U) UPPER SURFACE SPANWISE PRESSURES AT X/L = 0.86

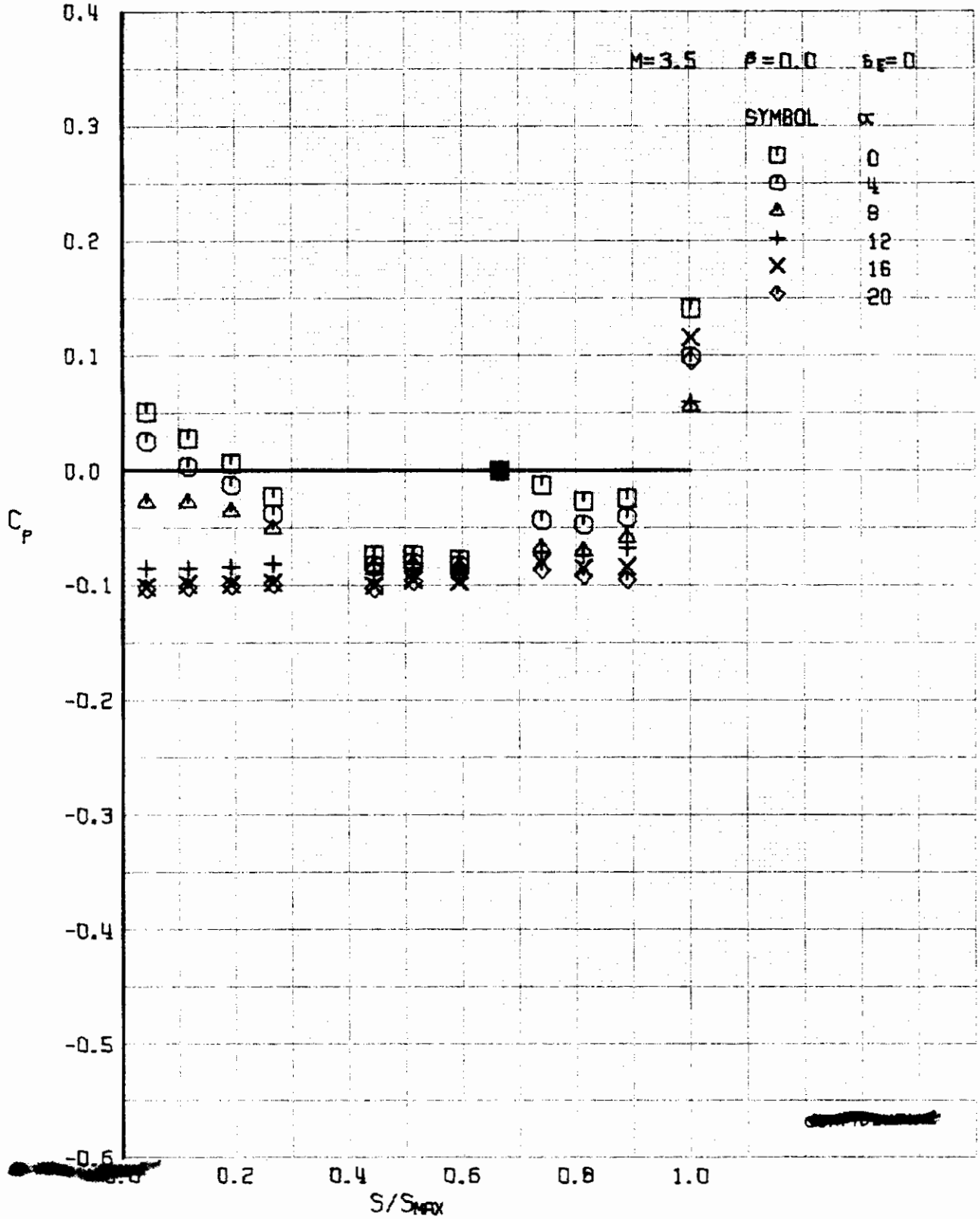

FIGURE 376 (U) UPPER SURFACE SPANWISE PRESSURES AT X/L = 0.96

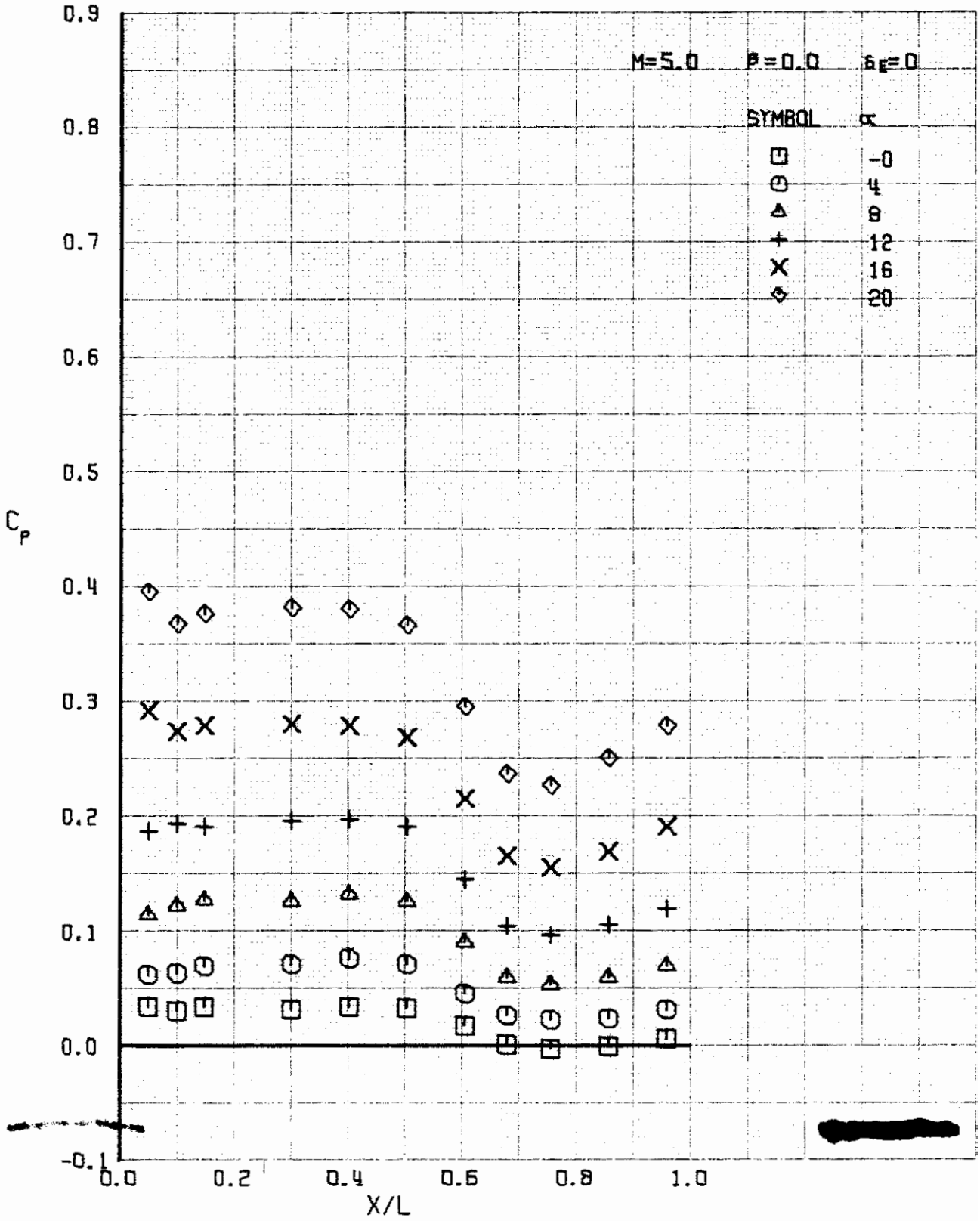

FIGURE 377 (U) LOWER SURFACE CENTERLINE PRESSURES

[redacted]

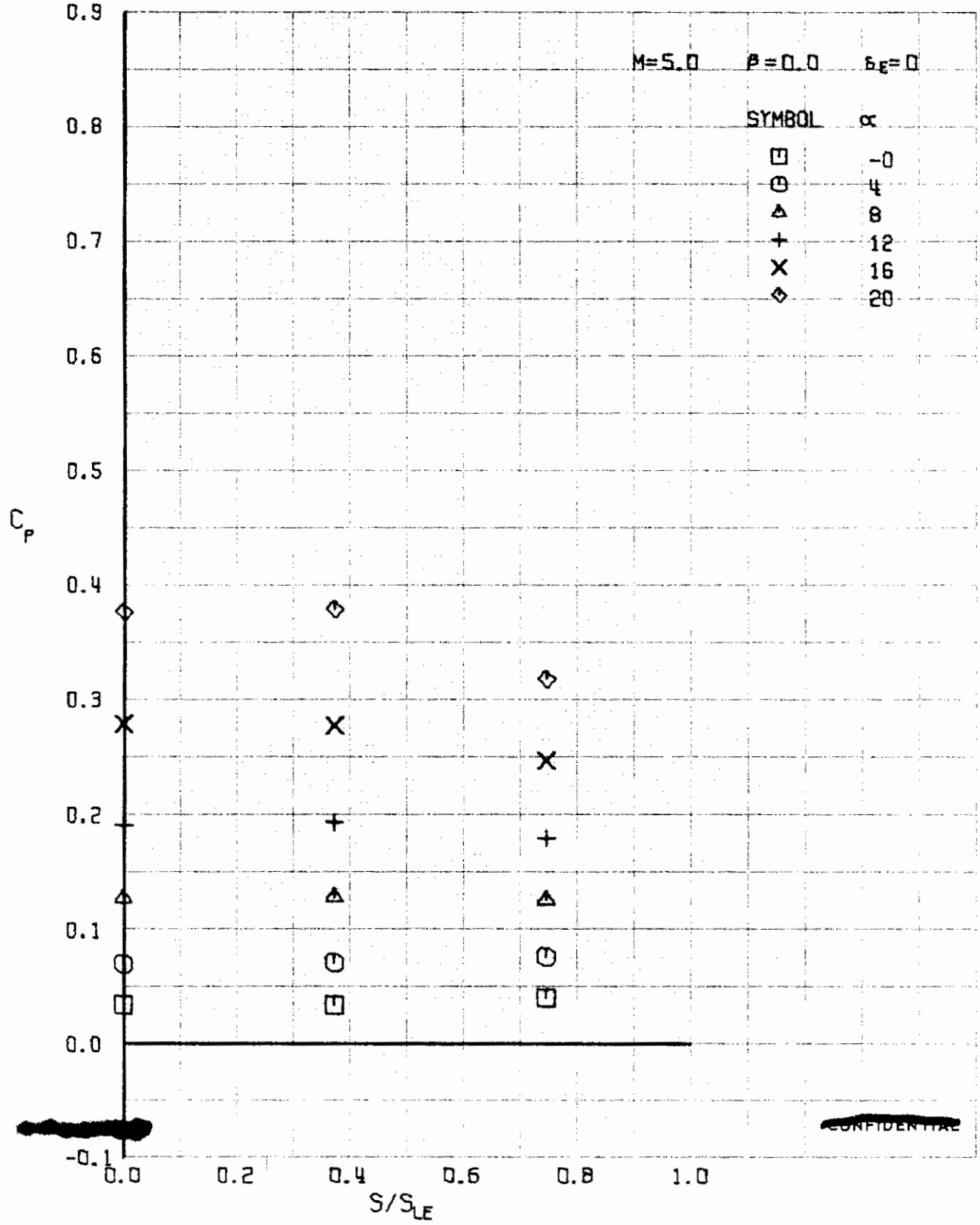

FIGURE 378 (U) LOWER SURFACE SPANWISE PRESSURES AT X/L = 0.15

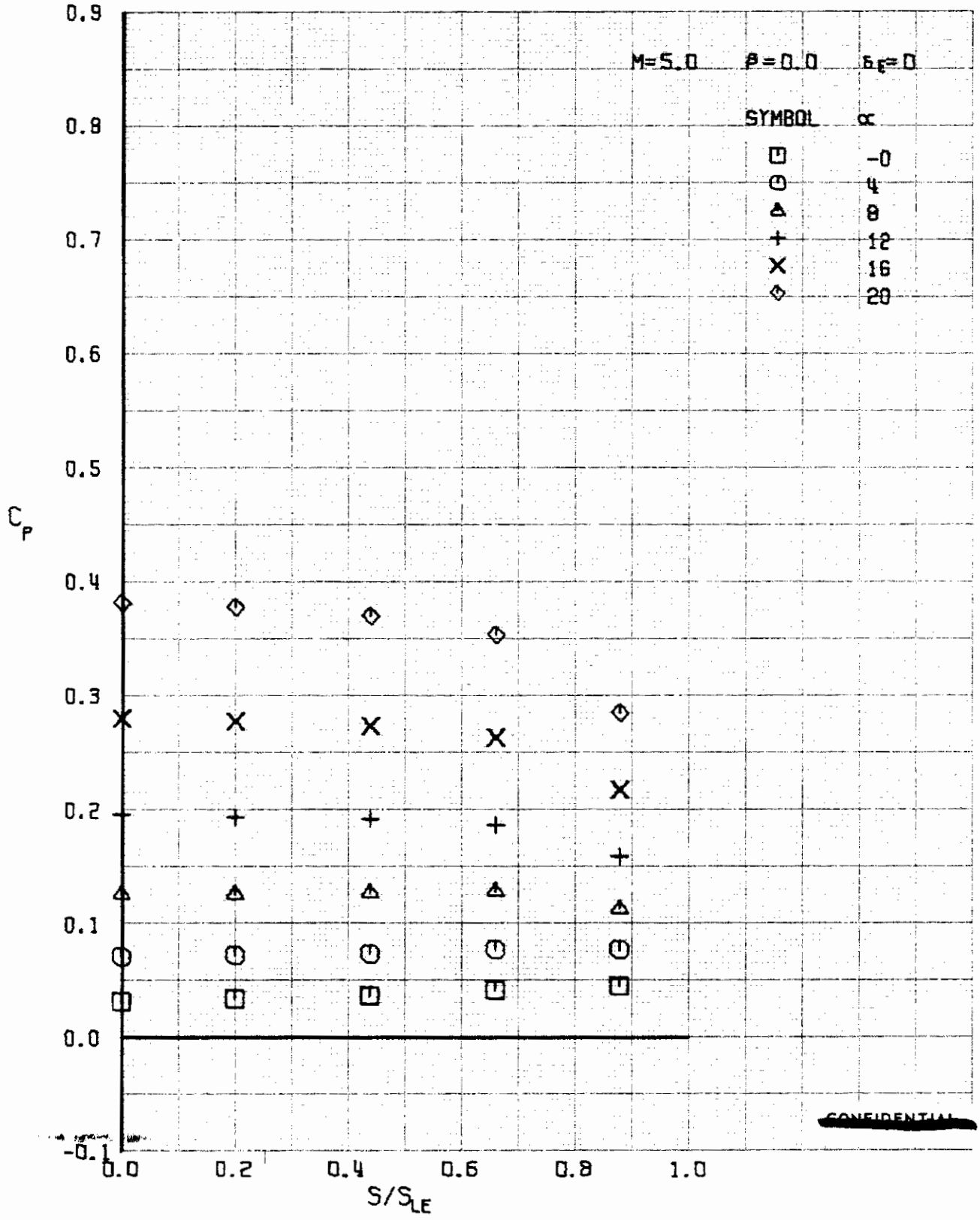

FIGURE 379 (U) LOWER SURFACE SPANWISE PRESSURES AT X/L = 0.30

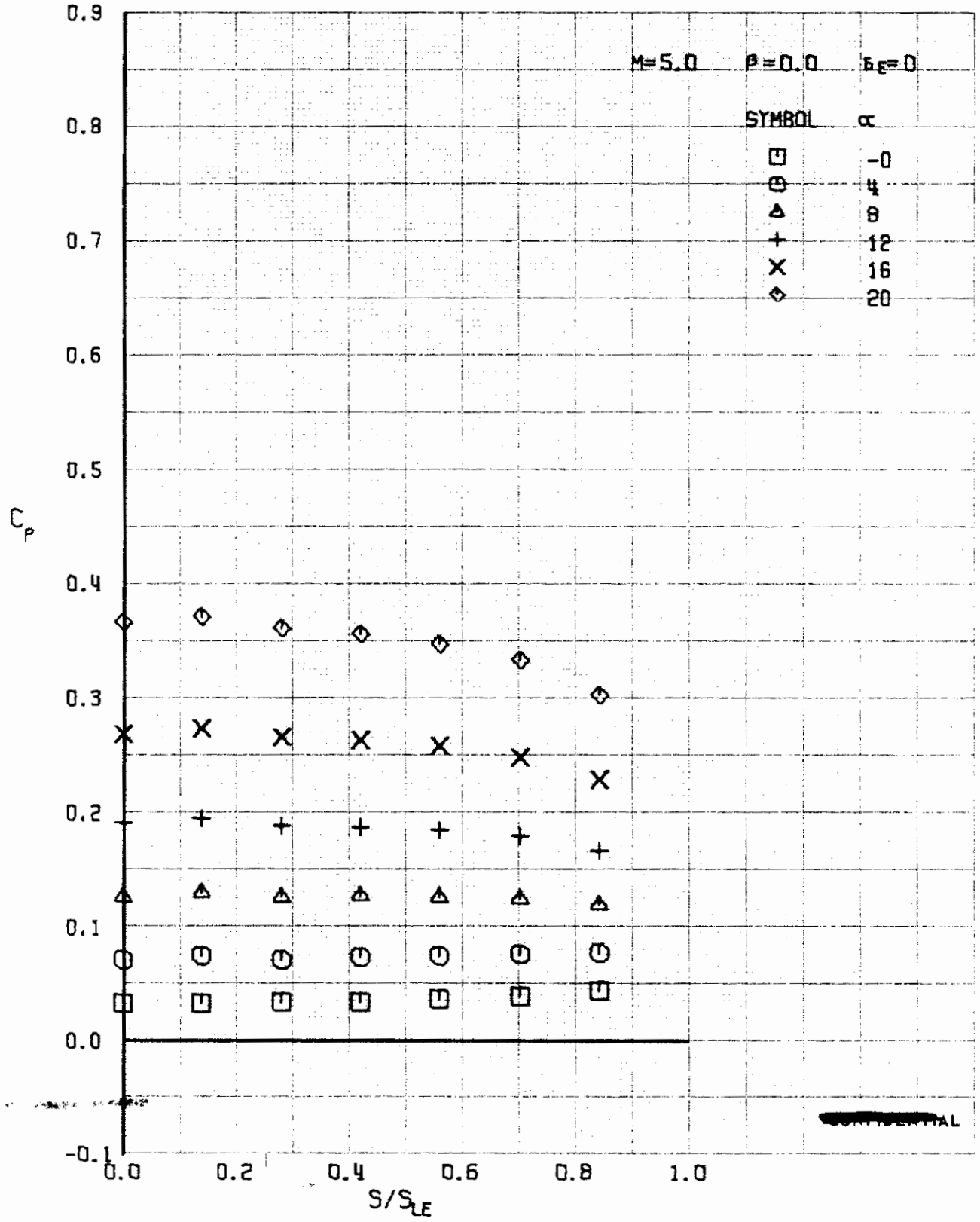

FIGURE 380 (U) LOWER SURFACE SPANWISE PRESSURES AT X/L = 0.50

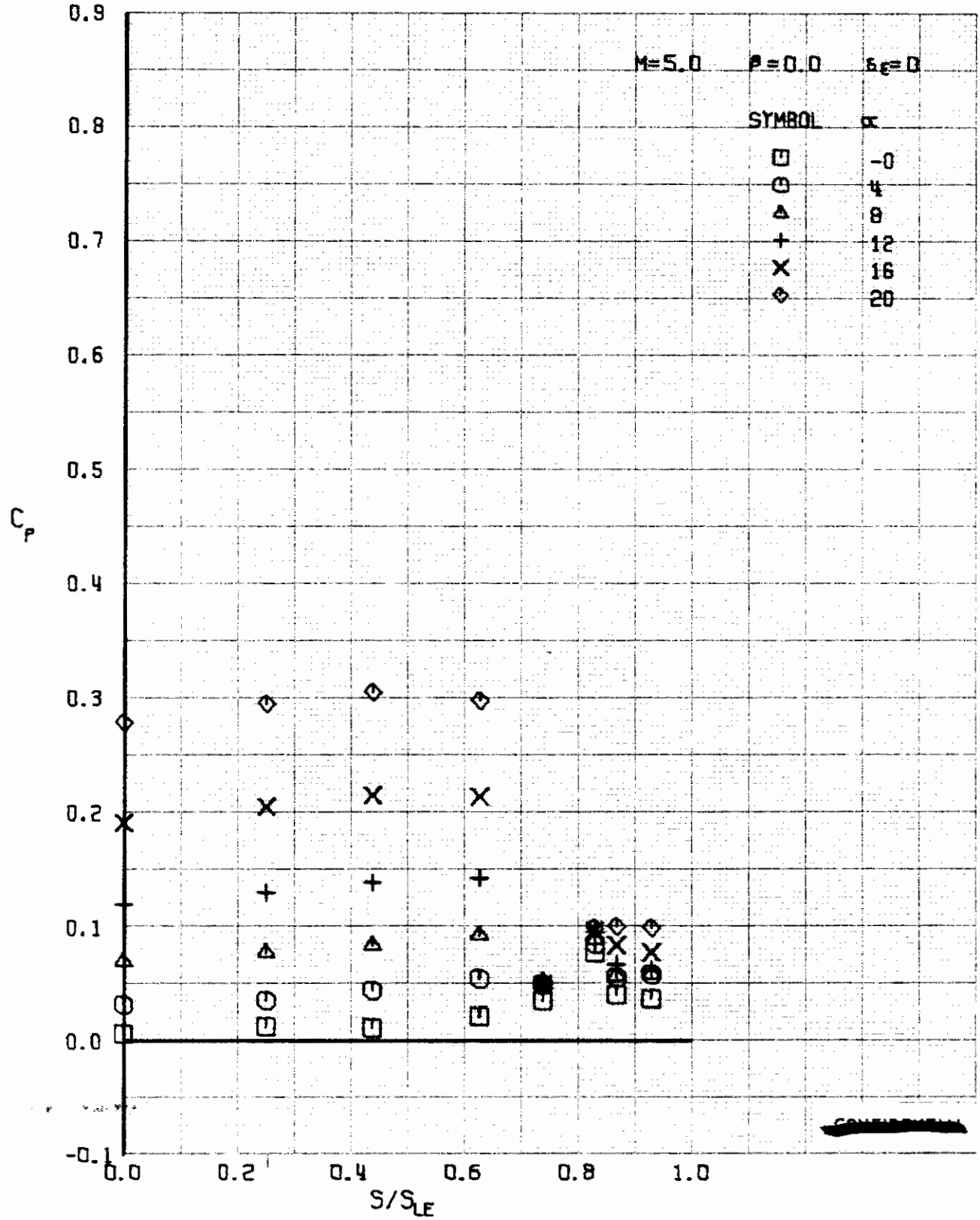

FIGURE 381 (U) LOWER SURFACE SPANWISE PRESSURES AT X/L = 0.76

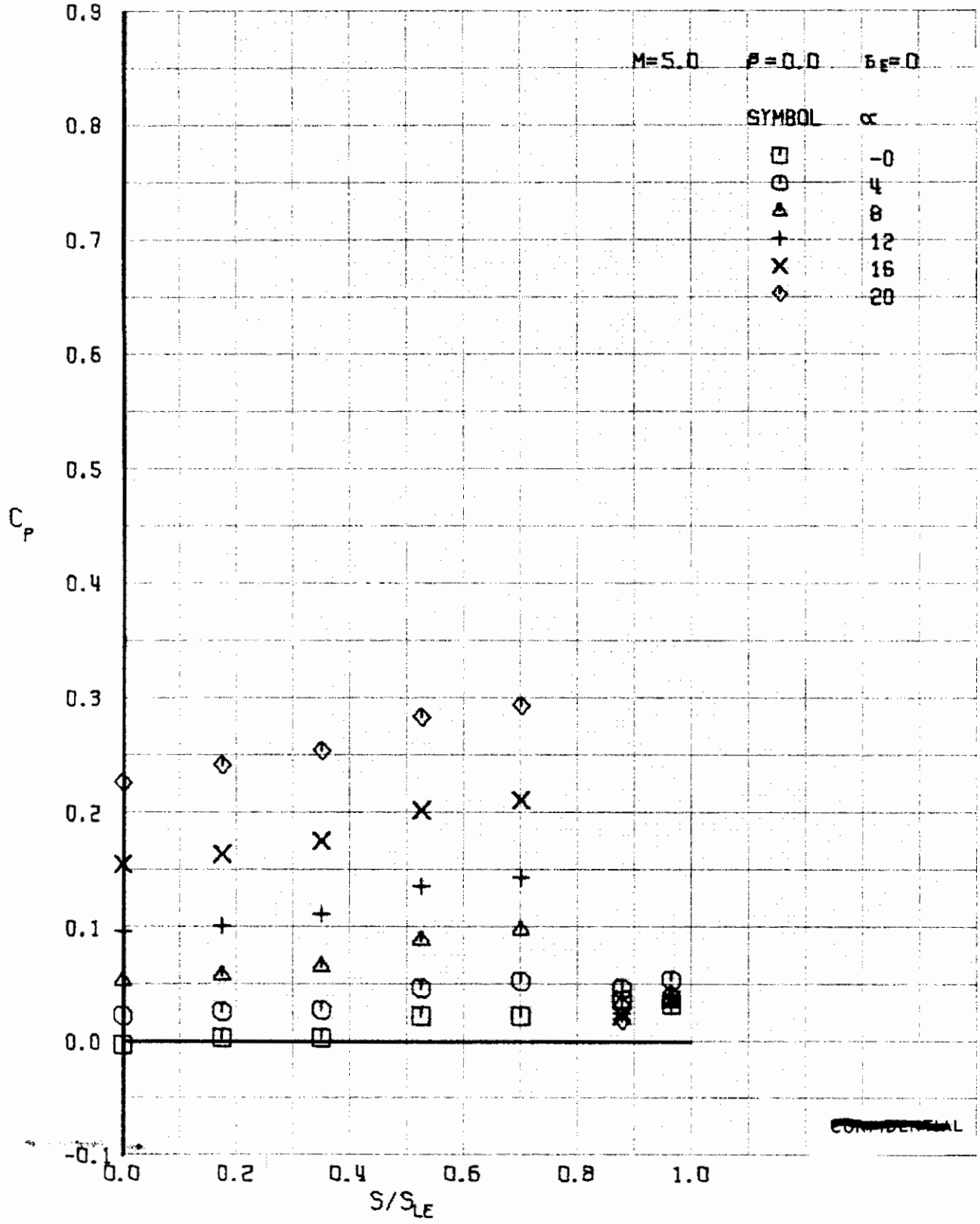

FIGURE 382 (U) LOWER SURFACE SPANWISE PRESSURES AT X/L = 0.96

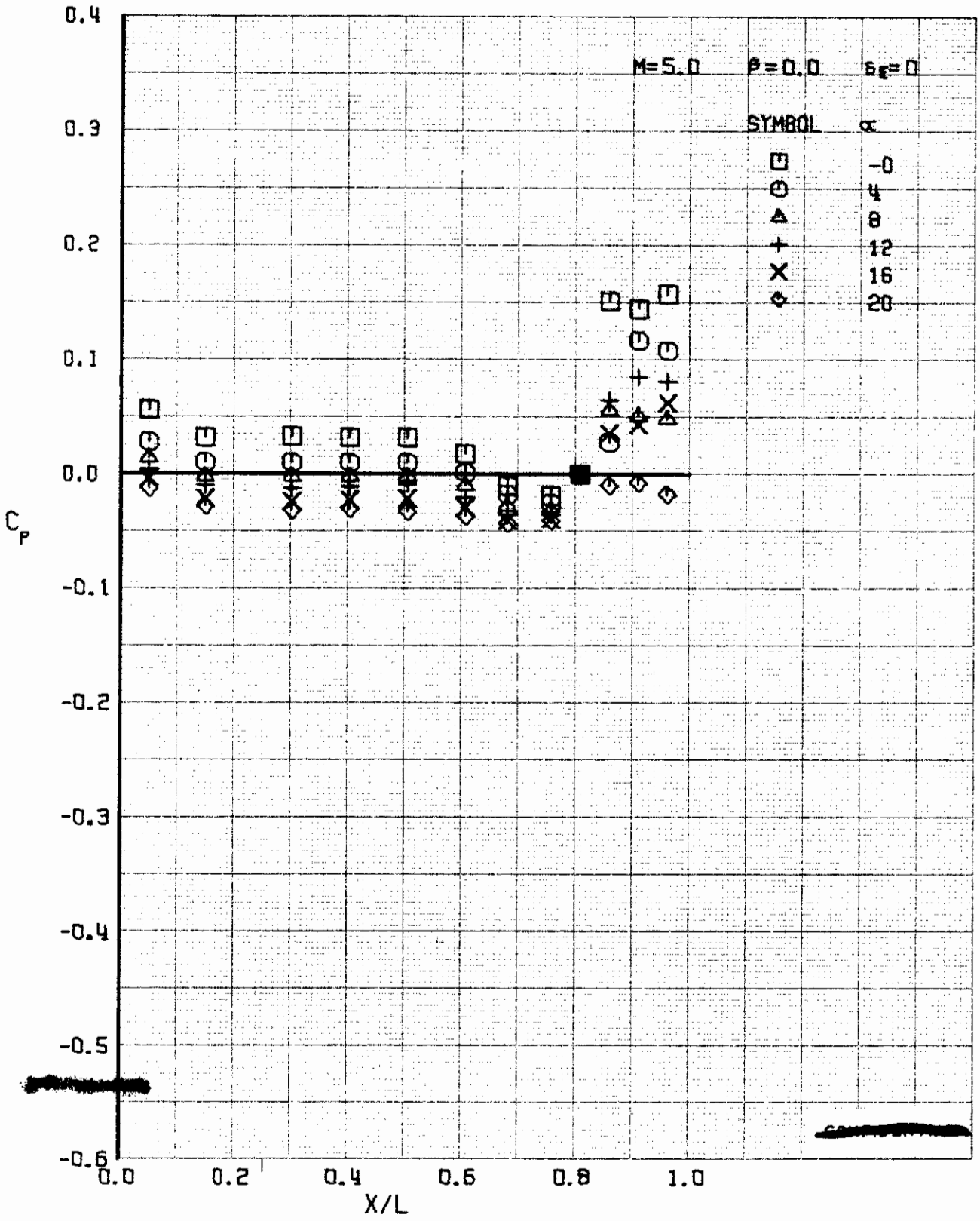

FIGURE 383 (U) UPPER SURFACE CENTERLINE PRESSURES

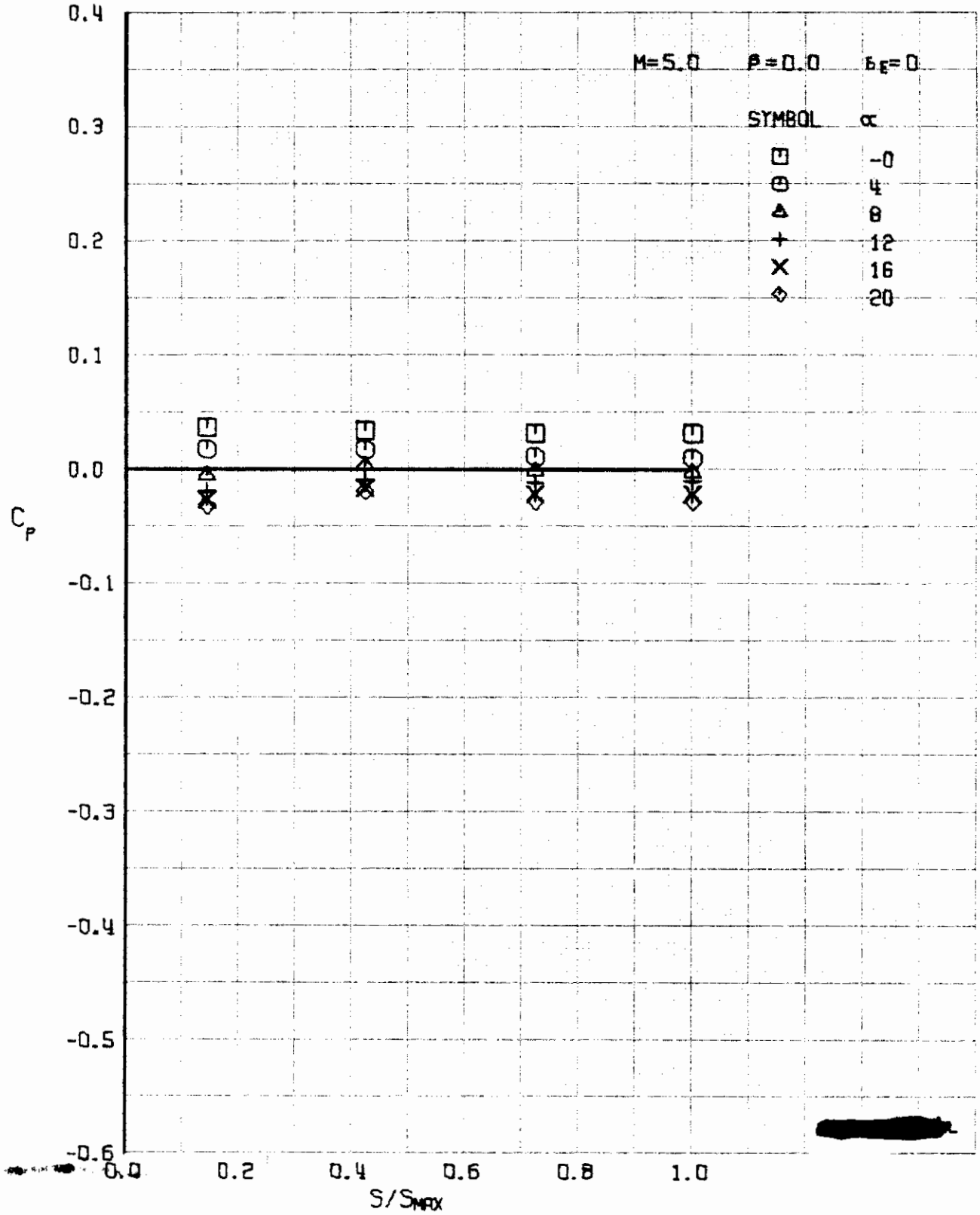

FIGURE 384 (U) UPPER SURFACE SPANWISE PRESSURES AT X/L = 0.15

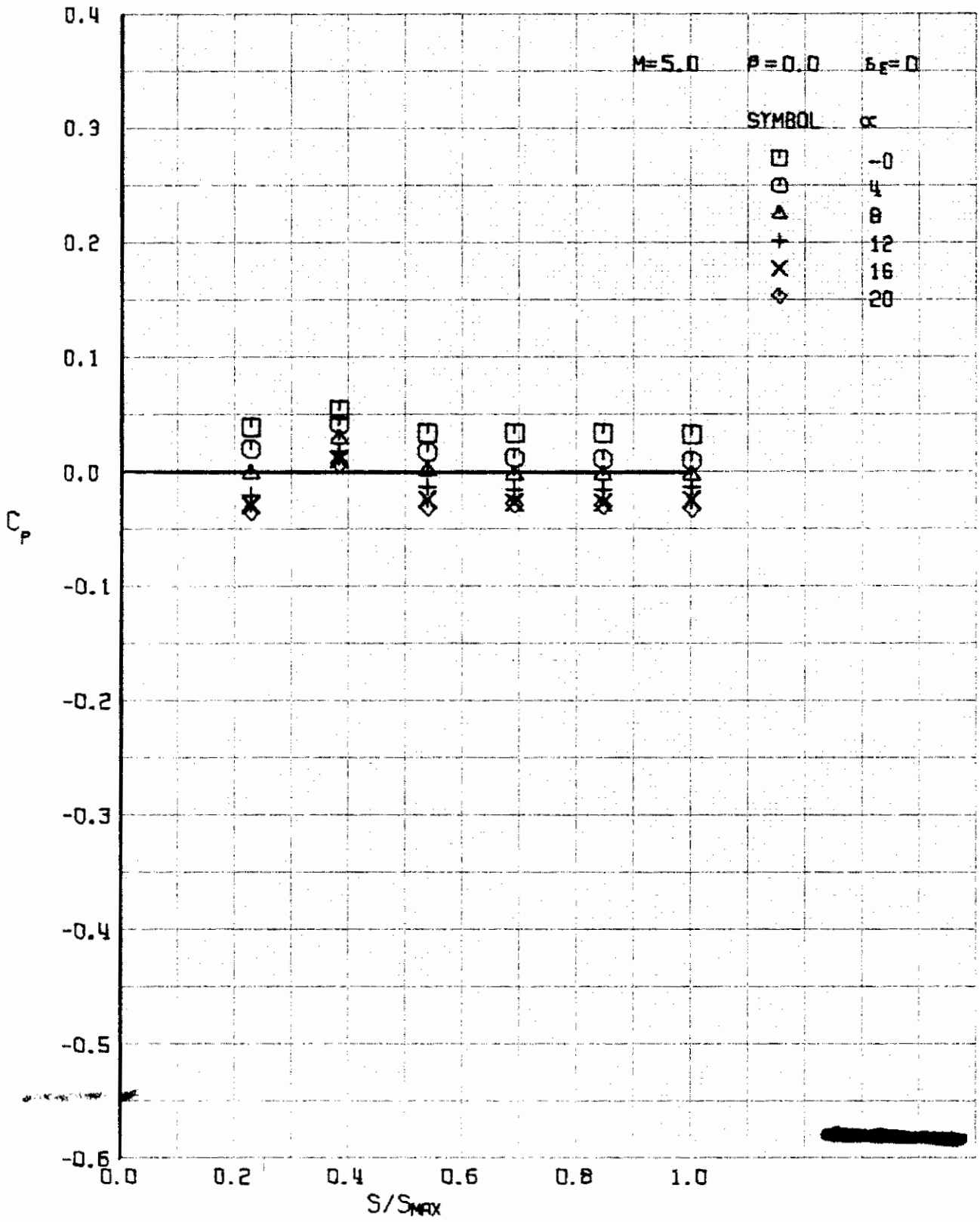

FIGURE 385 (U) UPPER SURFACE SPANWISE PRESSURES AT X/L = 0.30

[redacted]

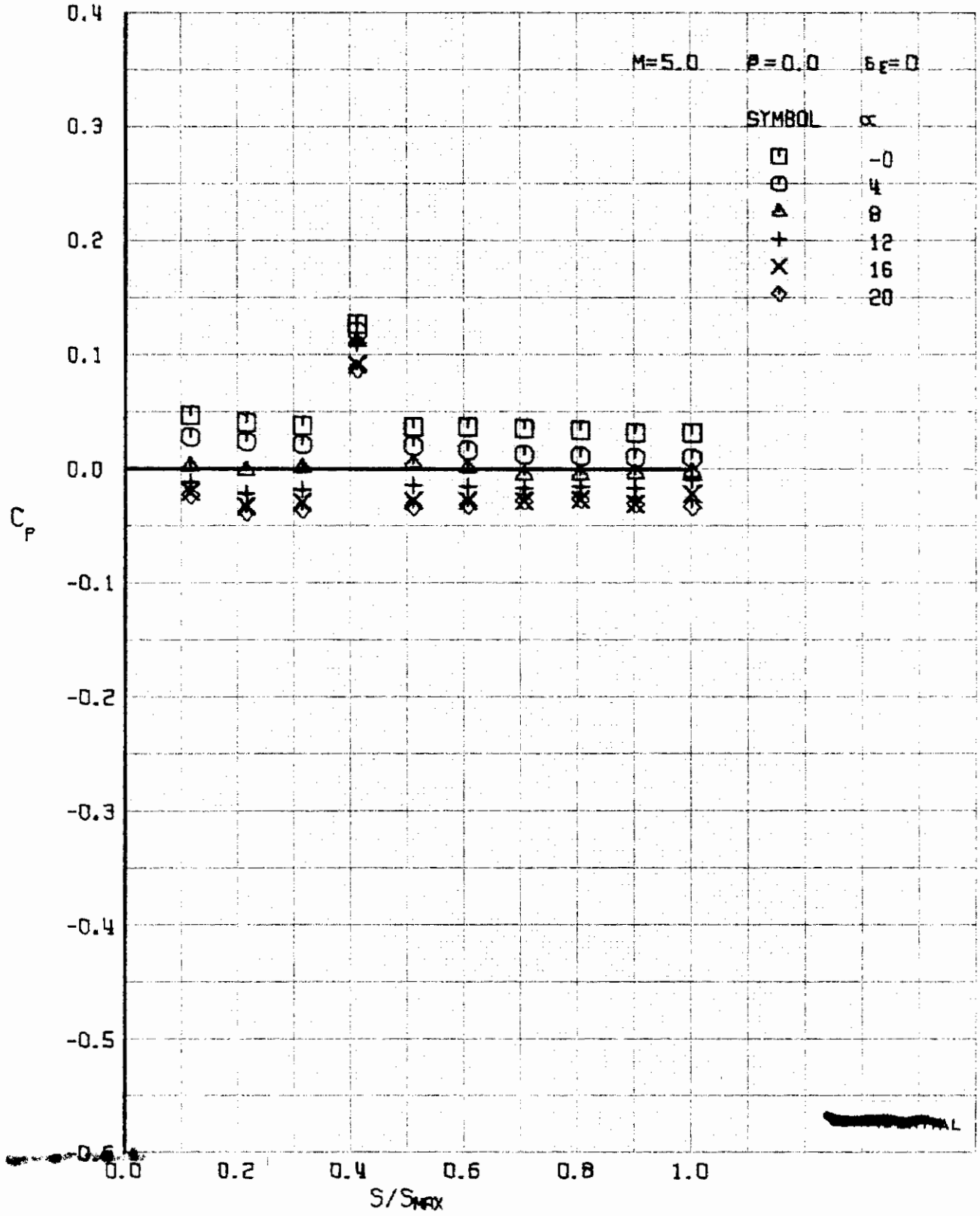

FIGURE 386 (U) UPPER SURFACE SPANWISE PRESSURES AT X/L = 0.50

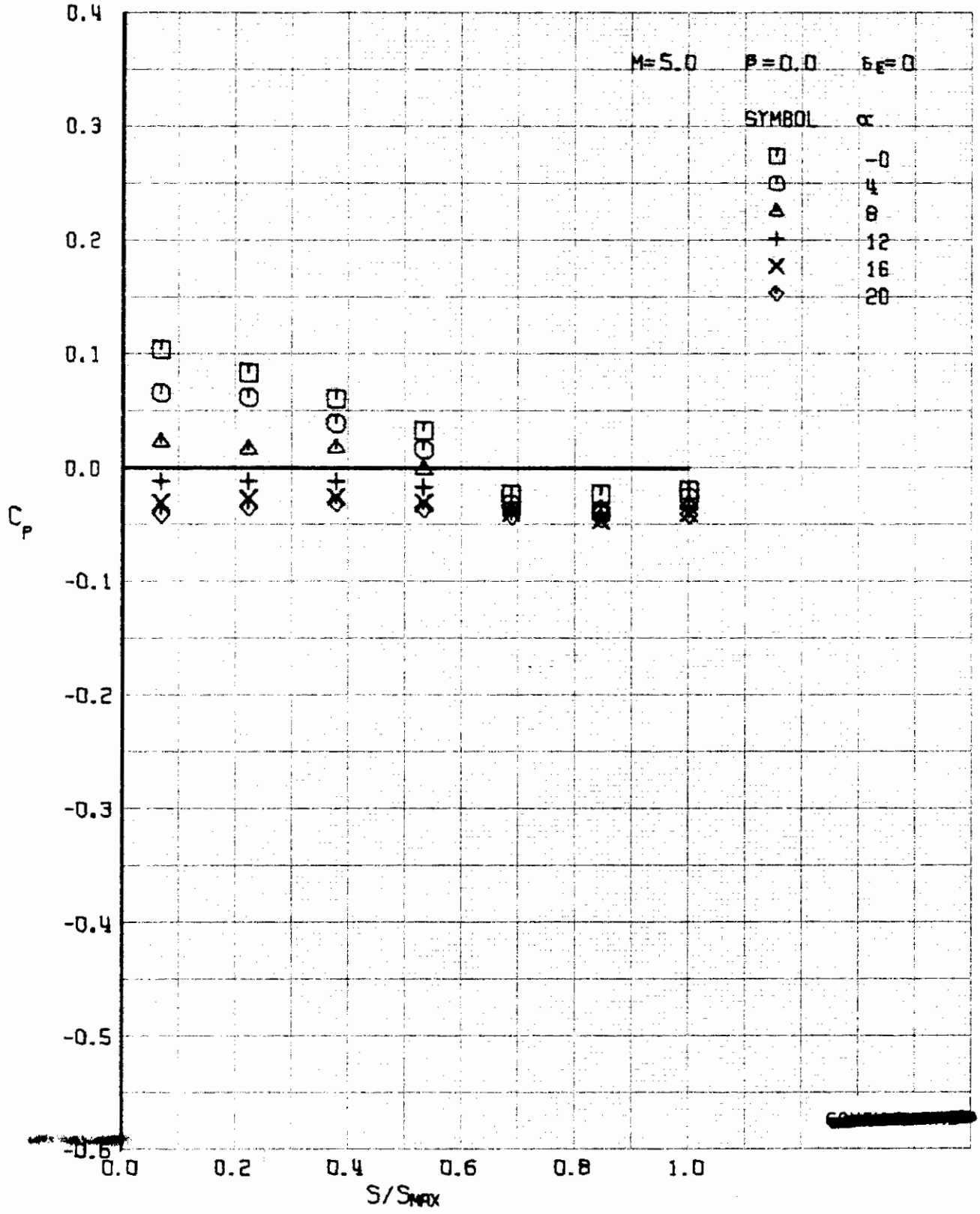

FIGURE 387 (U) UPPER SURFACE SPANWISE PRESSURES AT X/L = 0.76

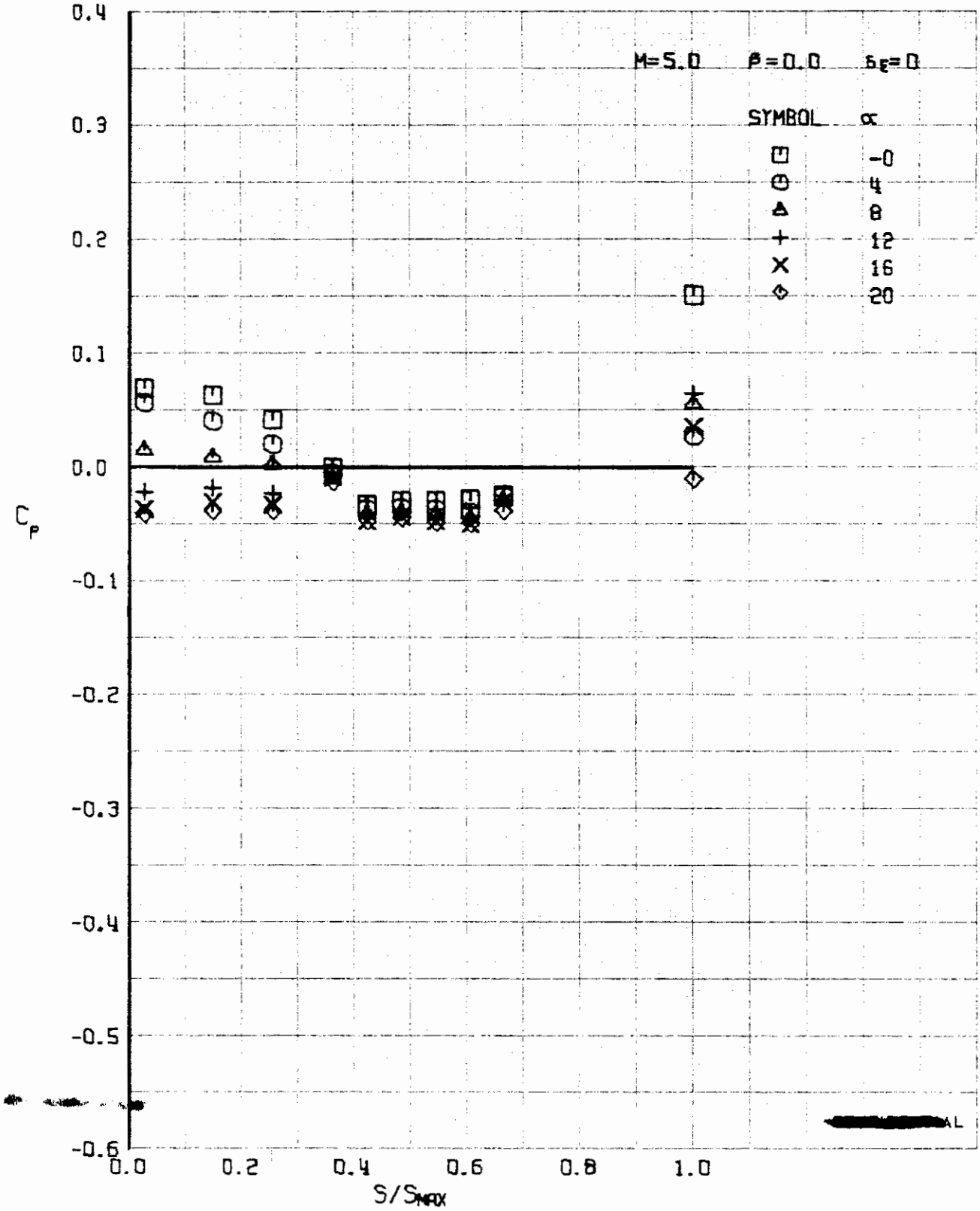

FIGURE 388 (U) UPPER SURFACE SPANWISE PRESSURES AT X/L = 0.86

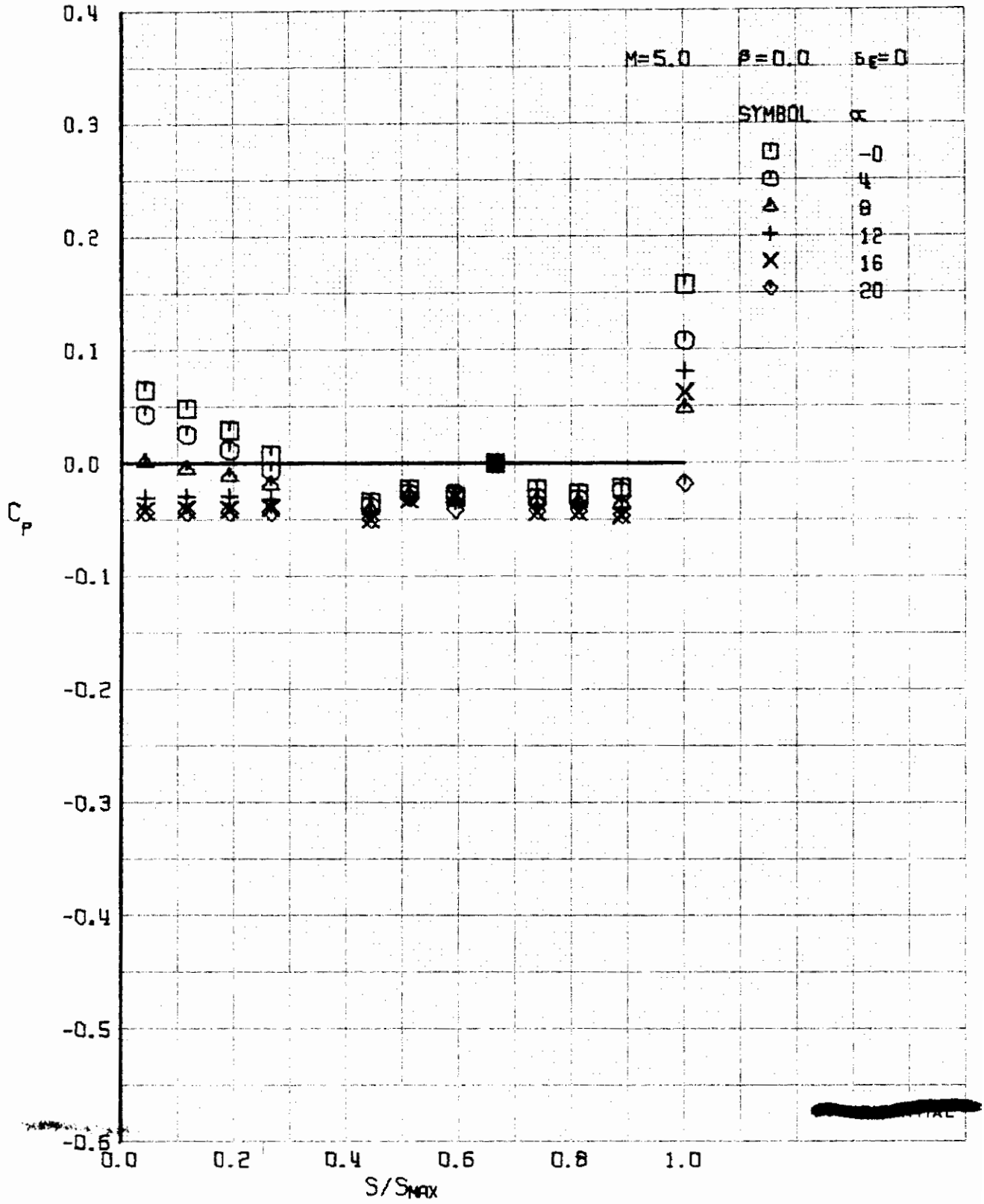

FIGURE 389 (U) UPPER SURFACE SPANWISE PRESSURES AT X/L = 0.96

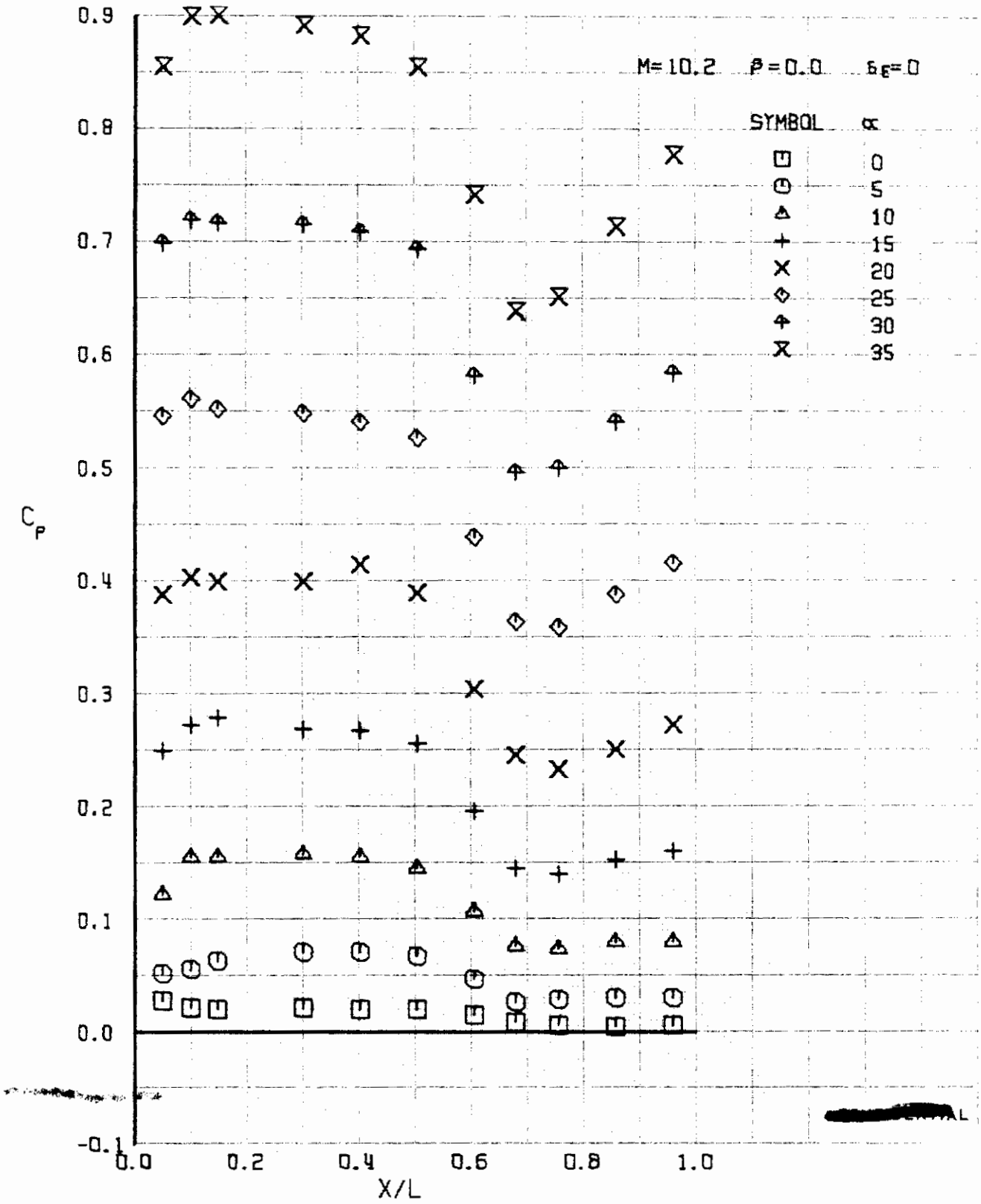

FIGURE 390 (U) LOWER SURFACE CENTERLINE PRESSURES

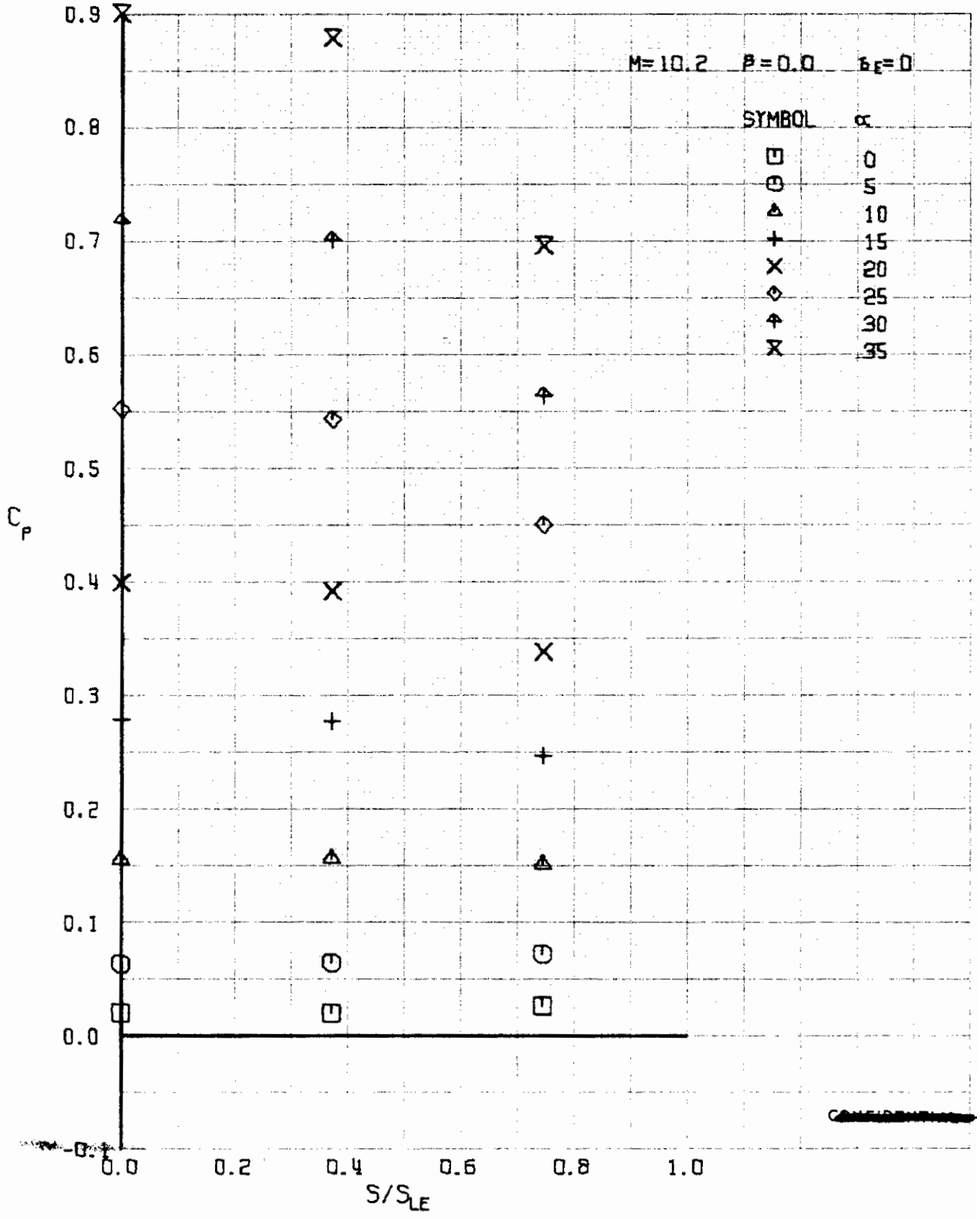

FIGURE 391 (U) LOWER SURFACE SPANWISE PRESSURES AT X/L = 0.15

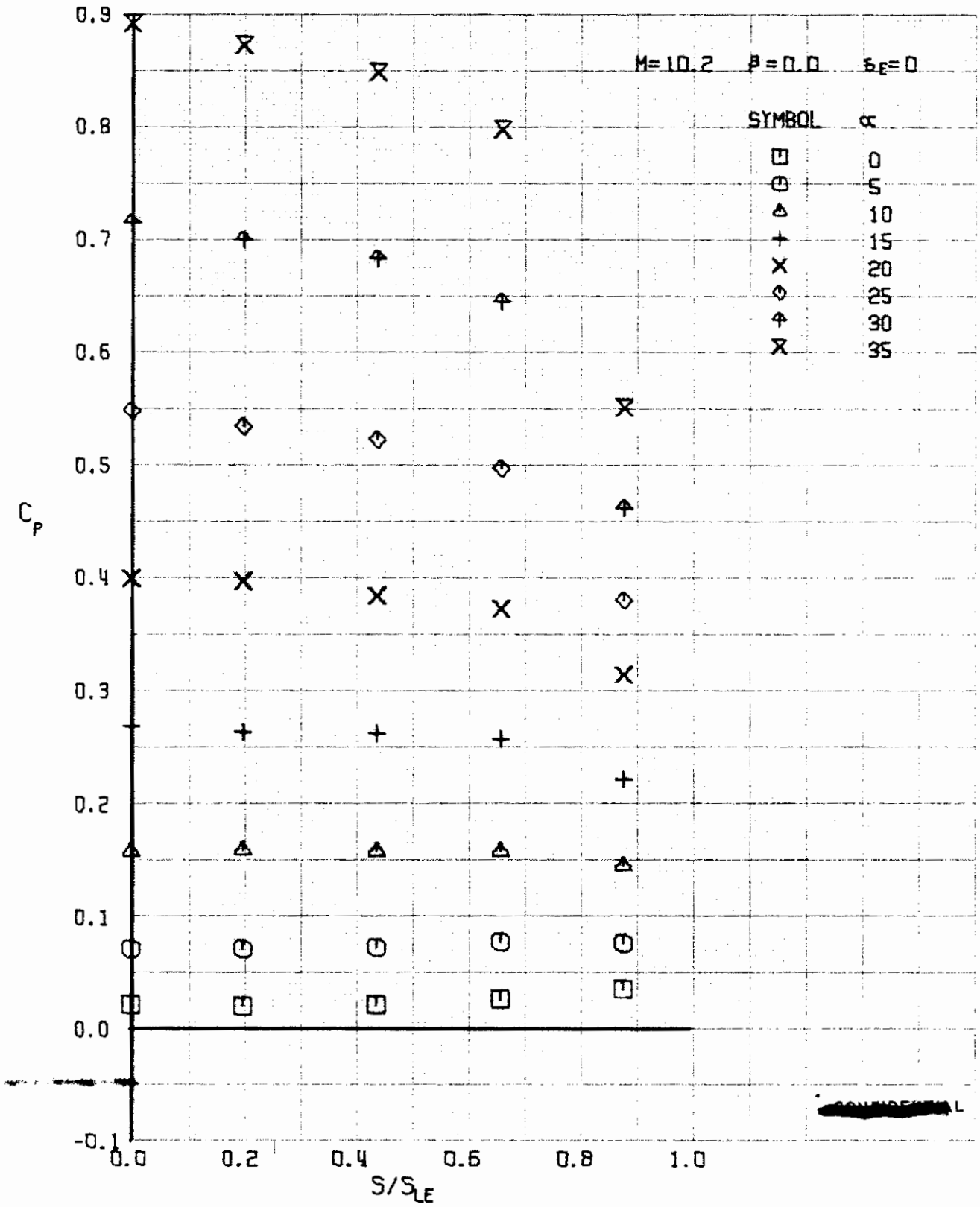

FIGURE 392 (U) LOWER SURFACE SPANWISE PRESSURES AT X/L = 0.30

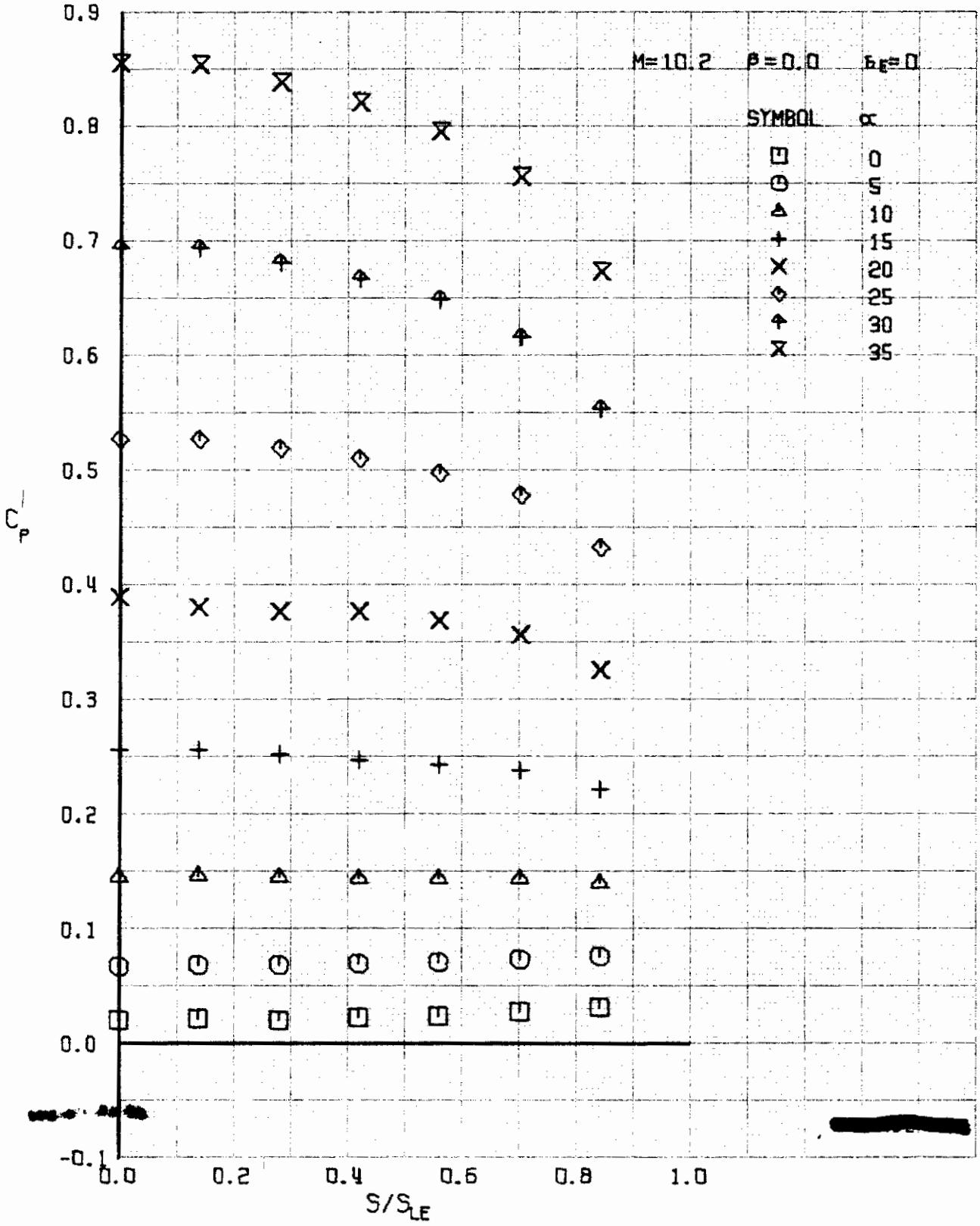

FIGURE 393 (U) LOWER SURFACE SPANWISE PRESSURES AT X/L = 0.50

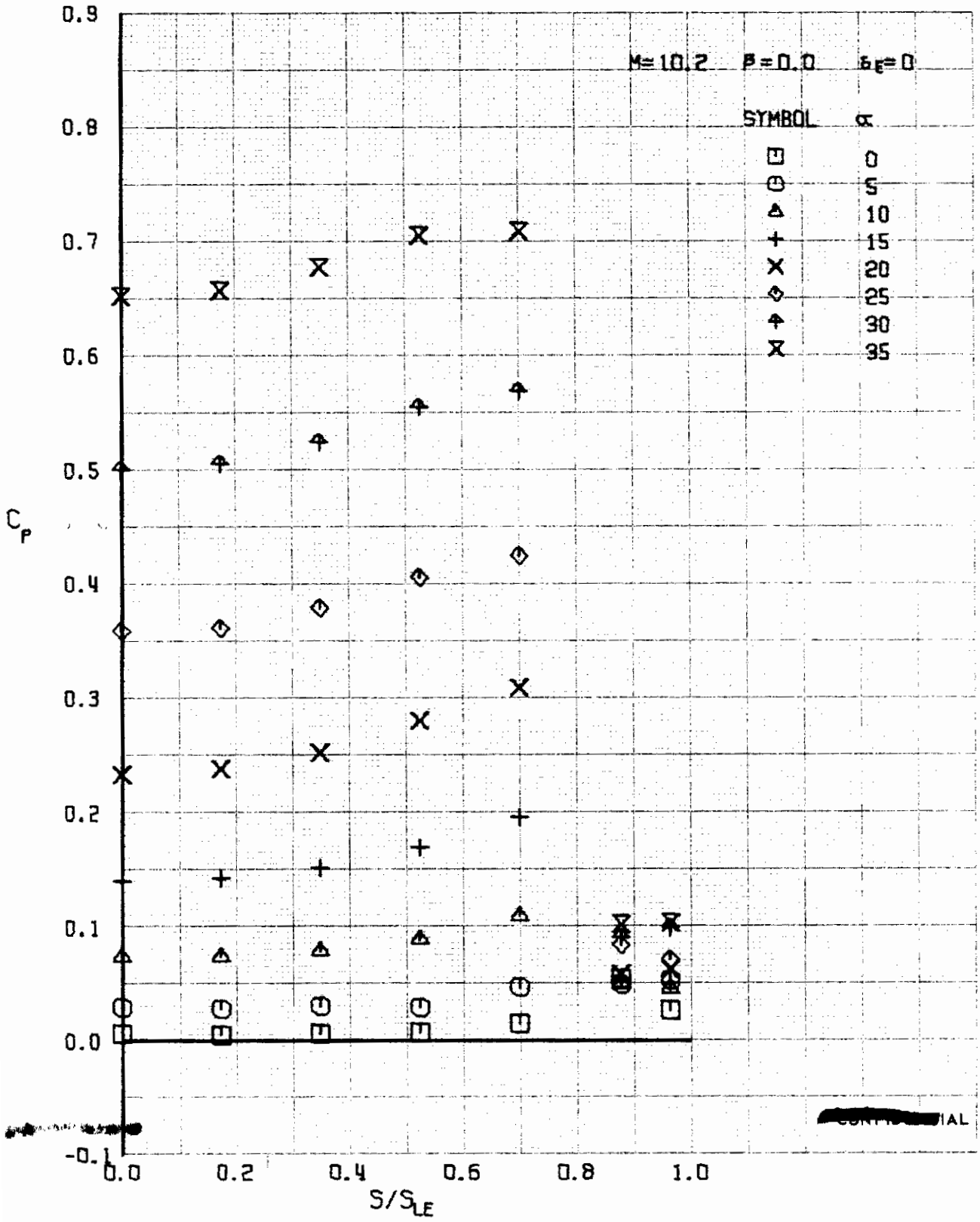

FIGURE 394 (U) LOWER SURFACE SPANWISE PRESSURES AT X/L = 0.76

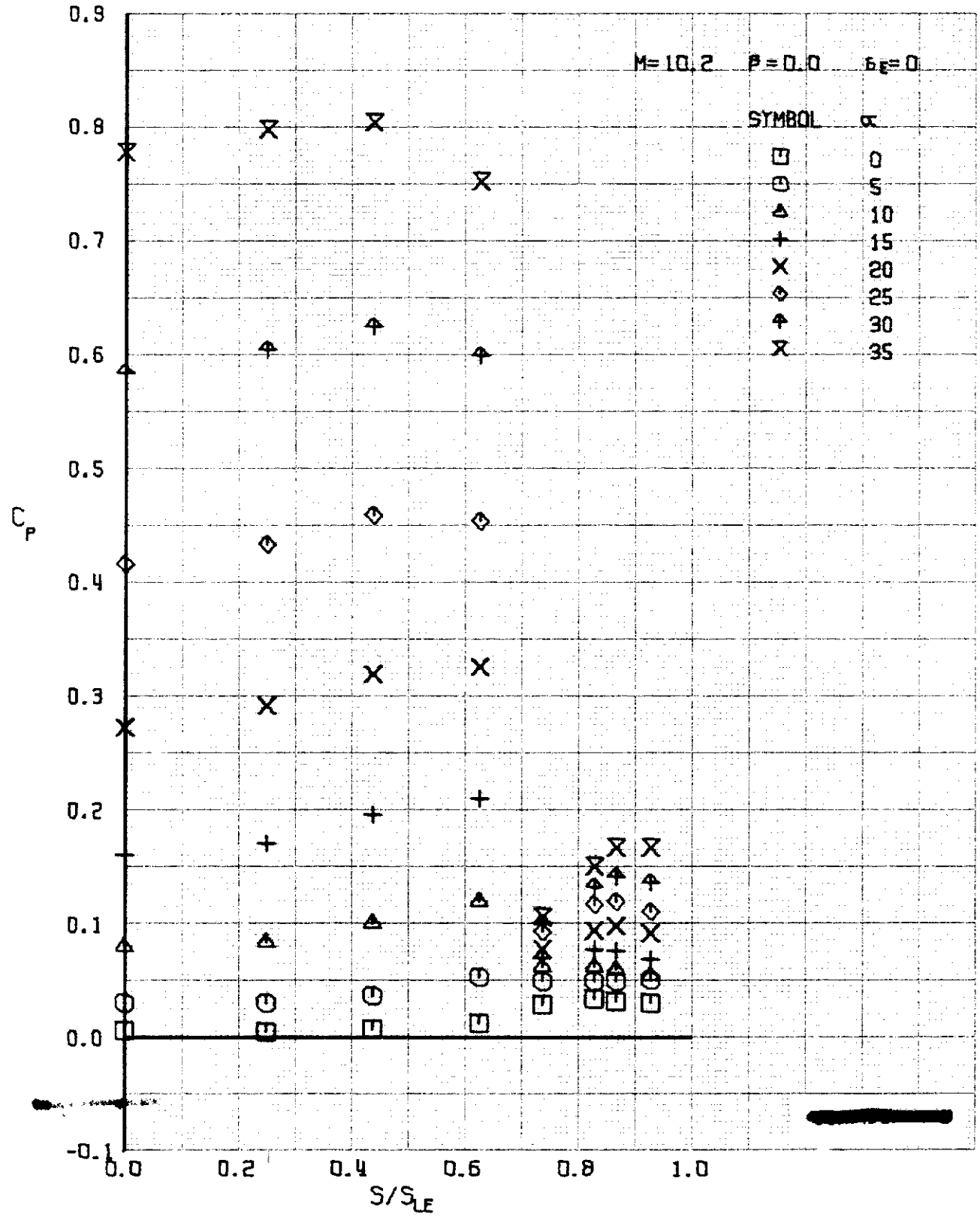

FIGURE 395 (U) LOWER SURFACE SPANWISE PRESSURES AT X/L = 0.96

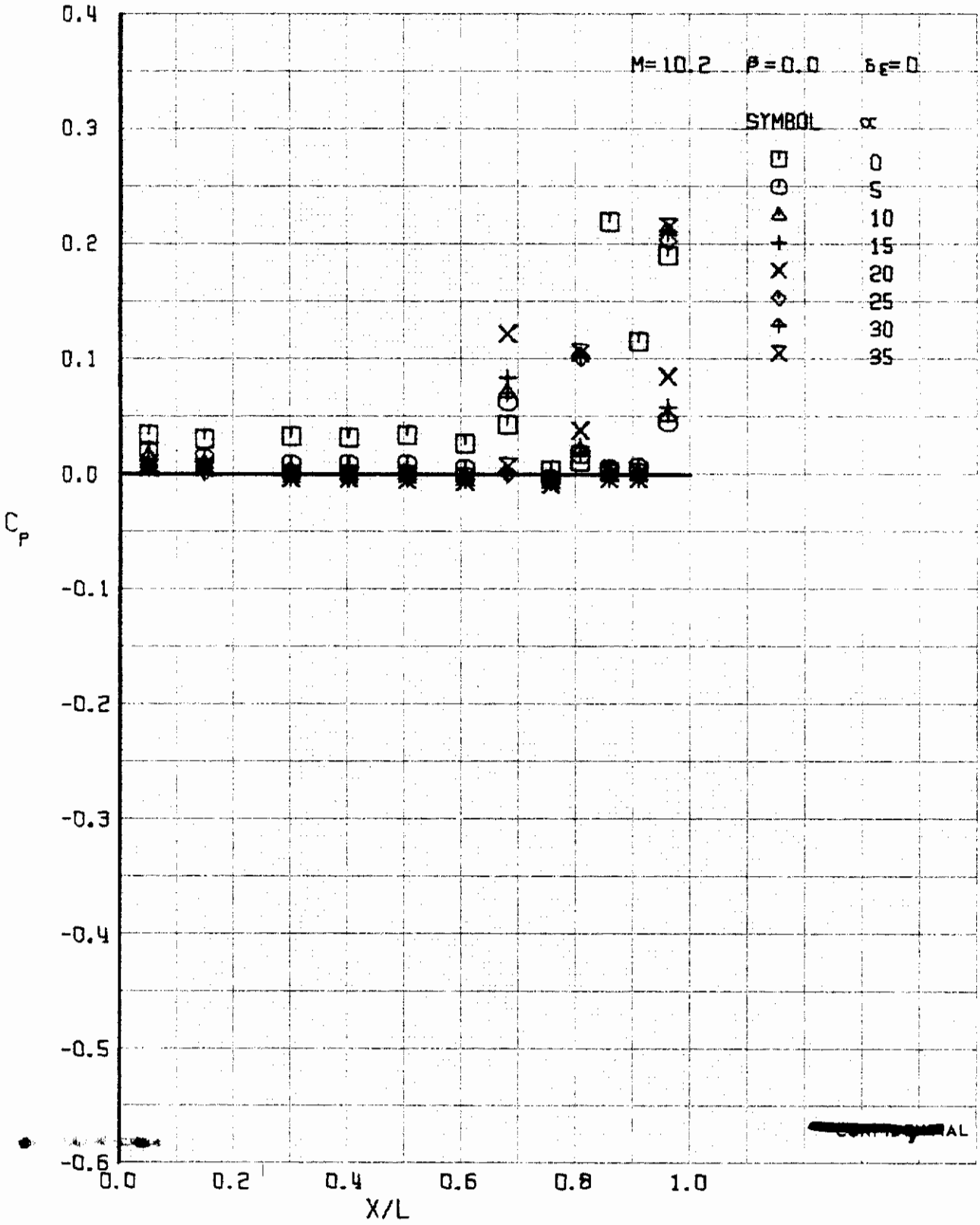

FIGURE 396 (U) UPPER SURFACE CENTERLINE PRESSURES

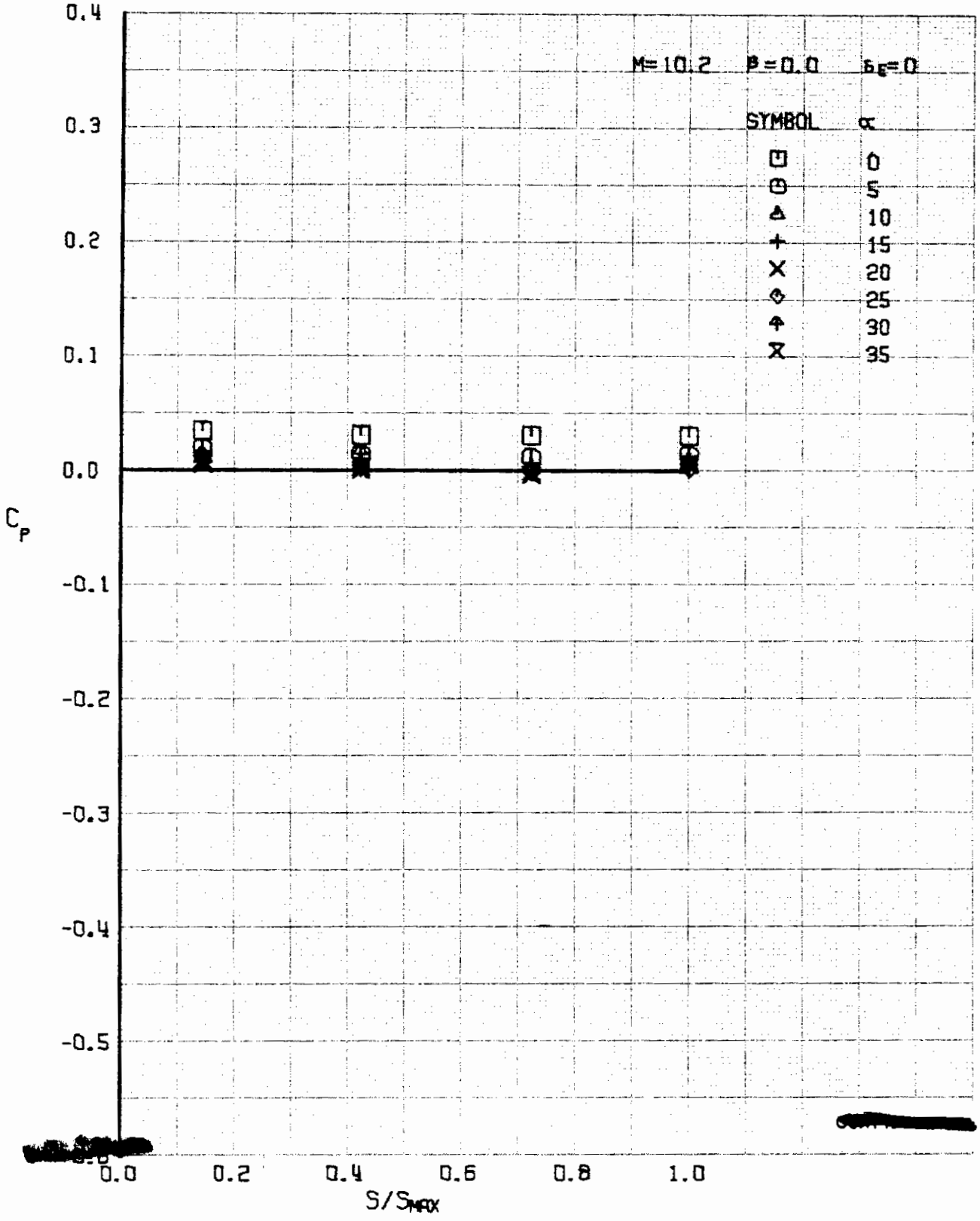

FIGURE 397 (U) UPPER SURFACE SPANWISE PRESSURES AT X/L = 0.15

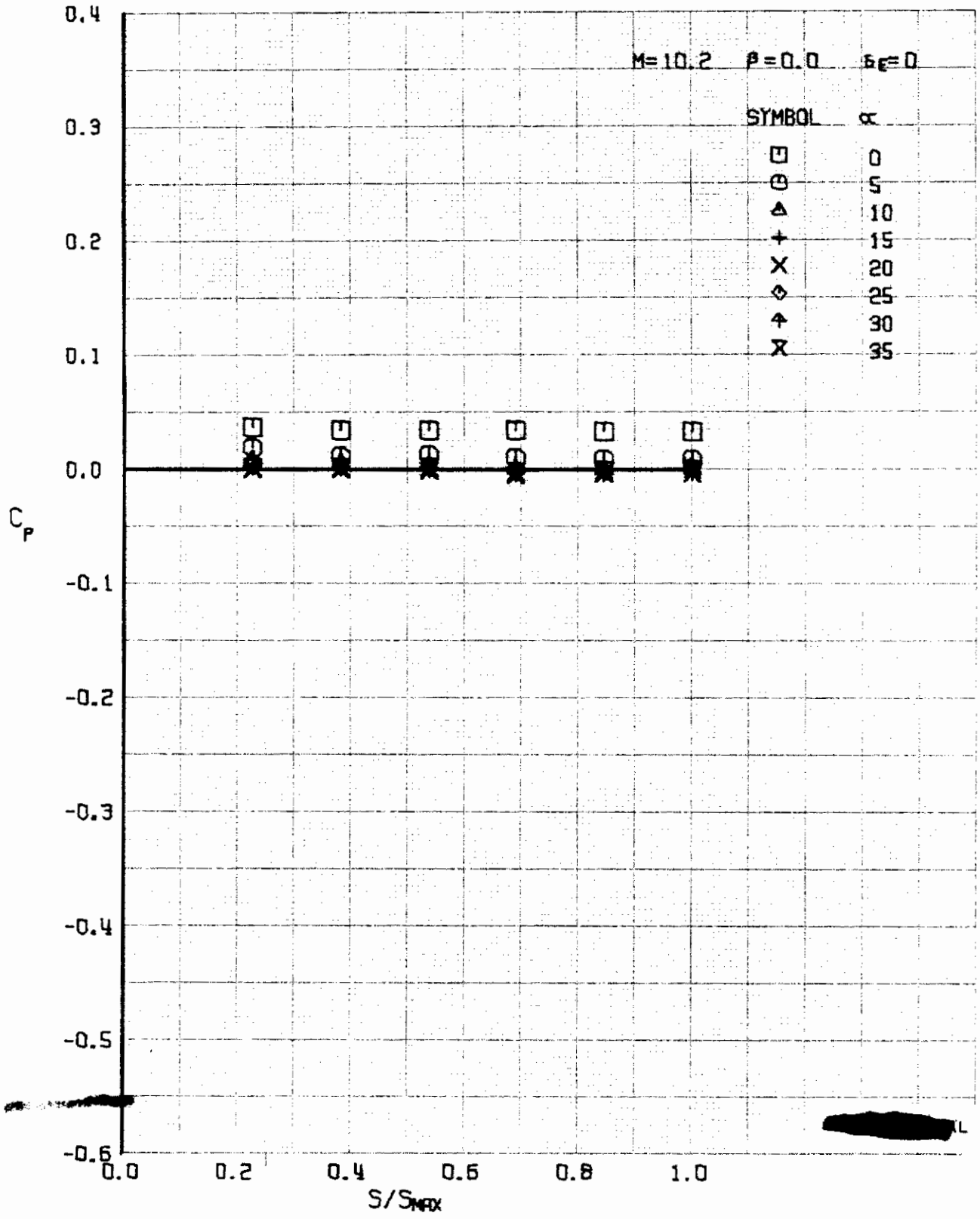

FIGURE 398 (U) UPPER SURFACE SPANWISE PRESSURES AT X/L = 0.30

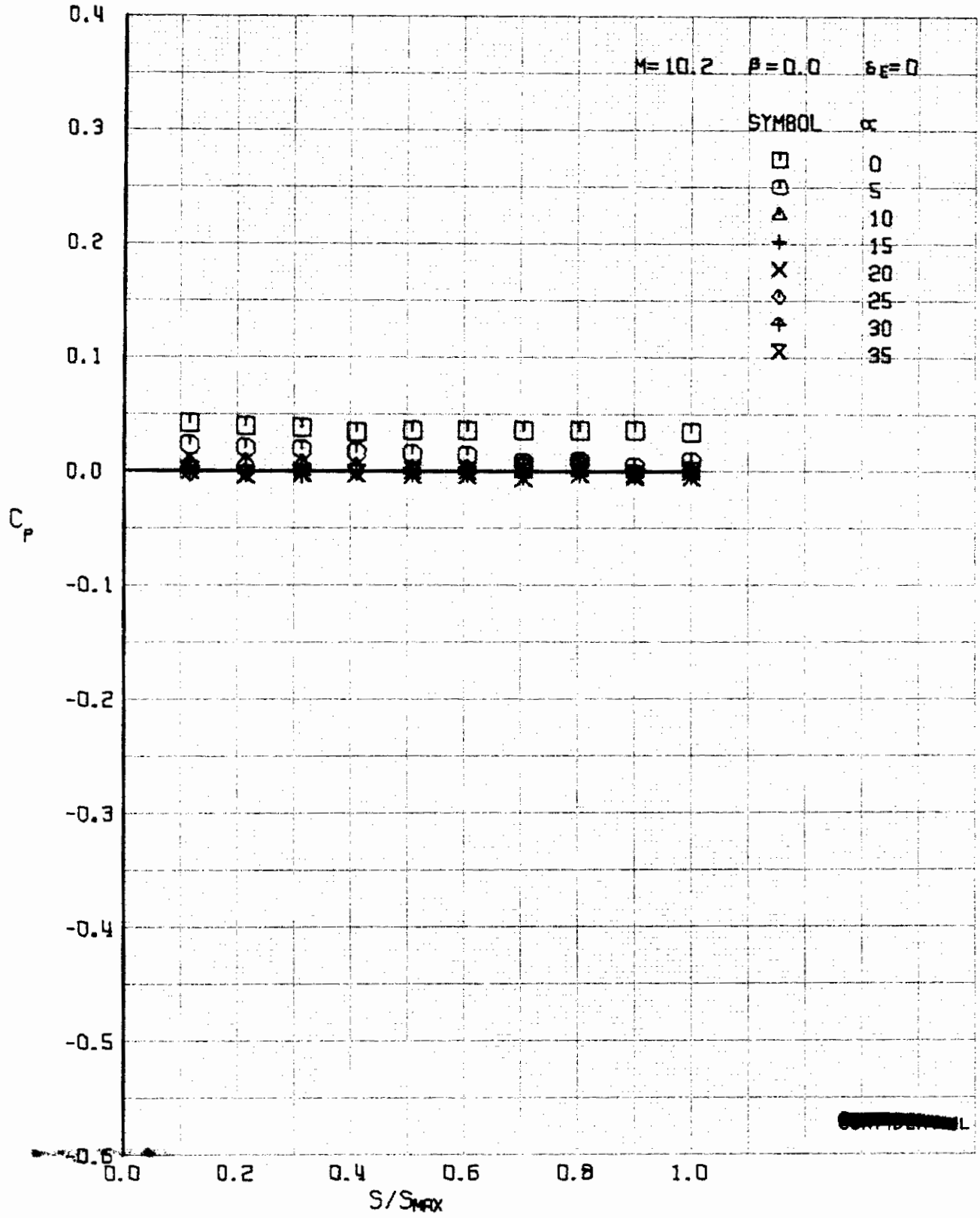

FIGURE 399 (U) UPPER SURFACE SPANWISE PRESSURES AT X/L = 0.50

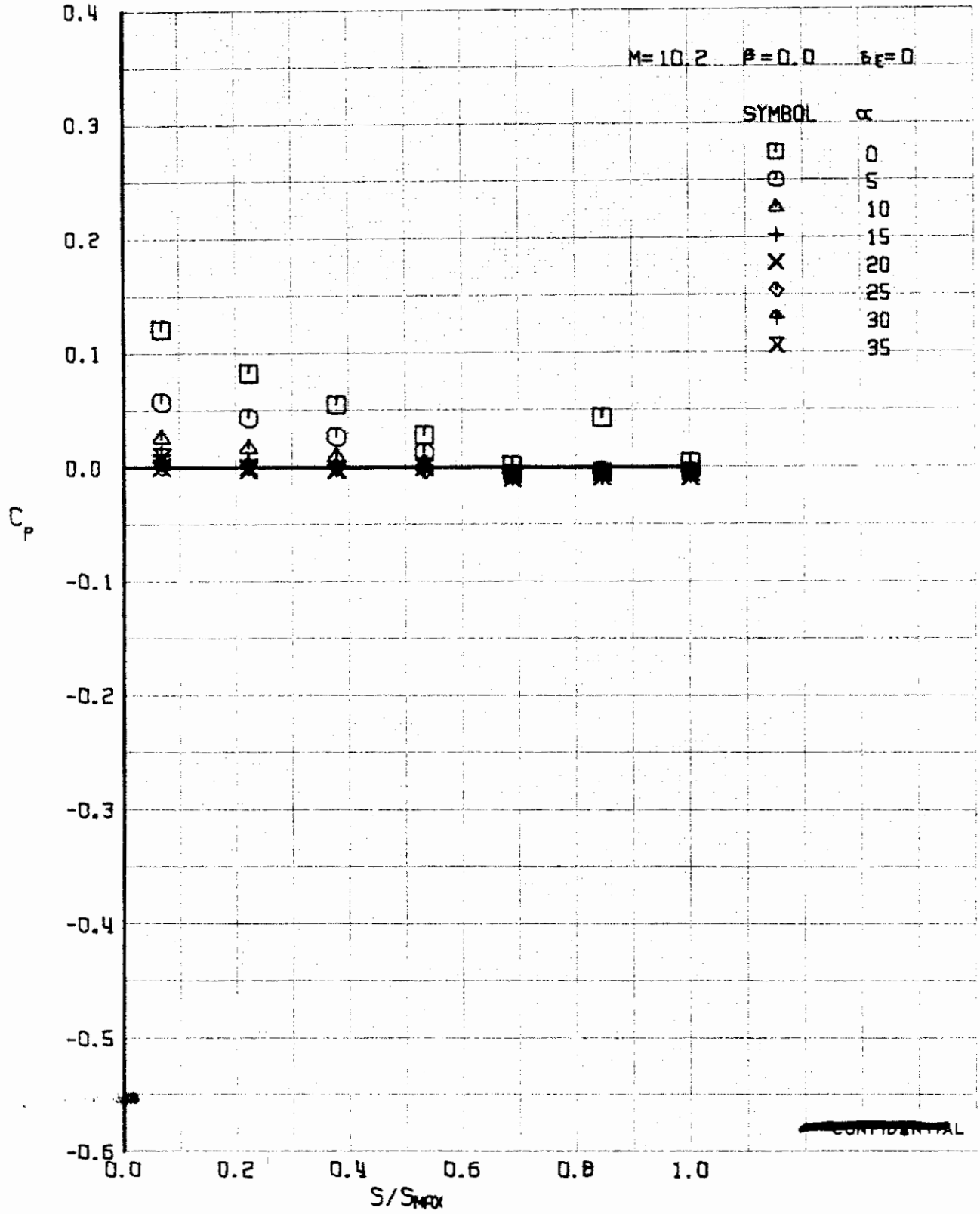

FIGURE 400 (U) UPPER SURFACE SPANWISE PRESSURES AT X/L = 0.76

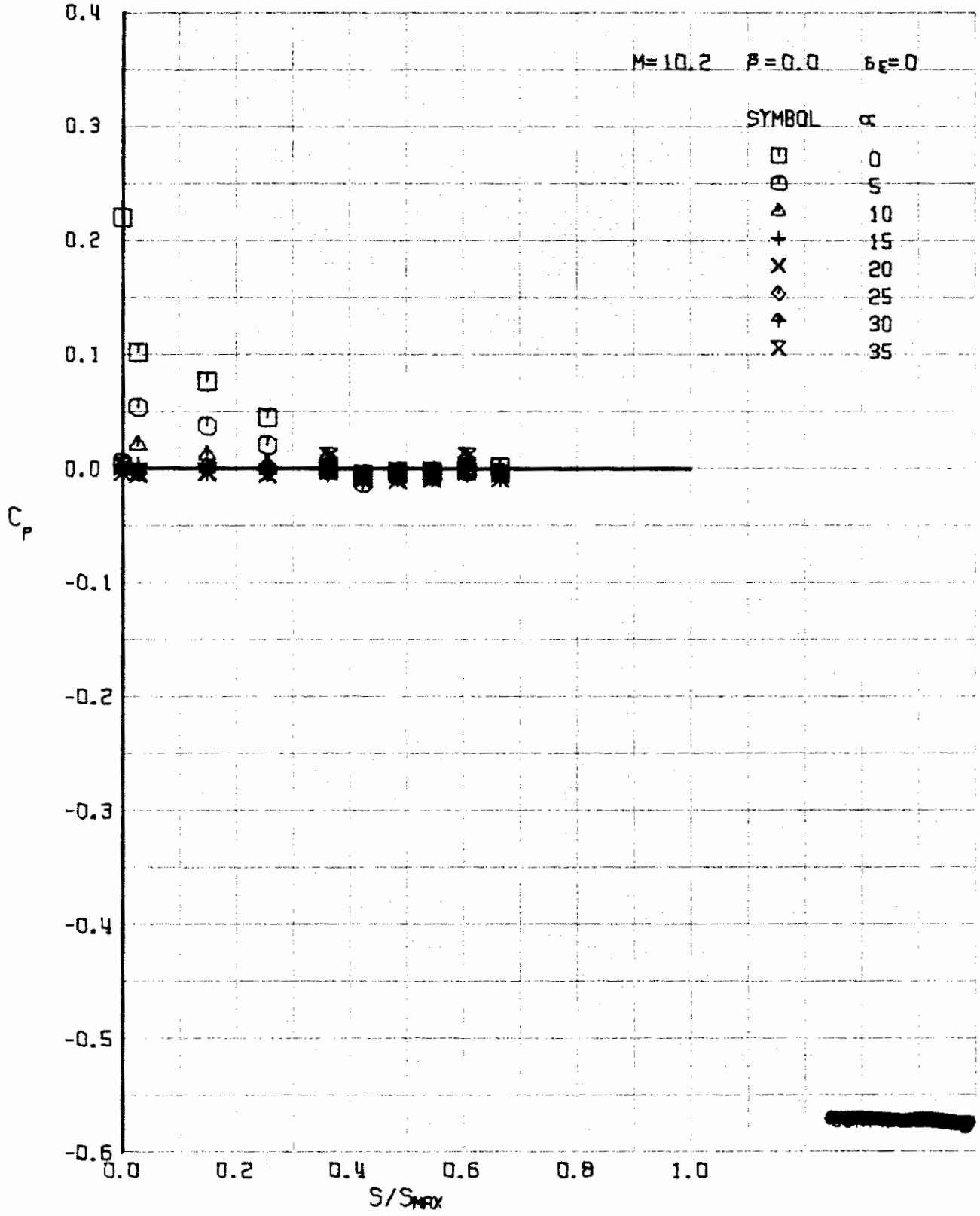

FIGURE 401 (U) UPPER SURFACE SPANWISE PRESSURES AT X/L = 0.86

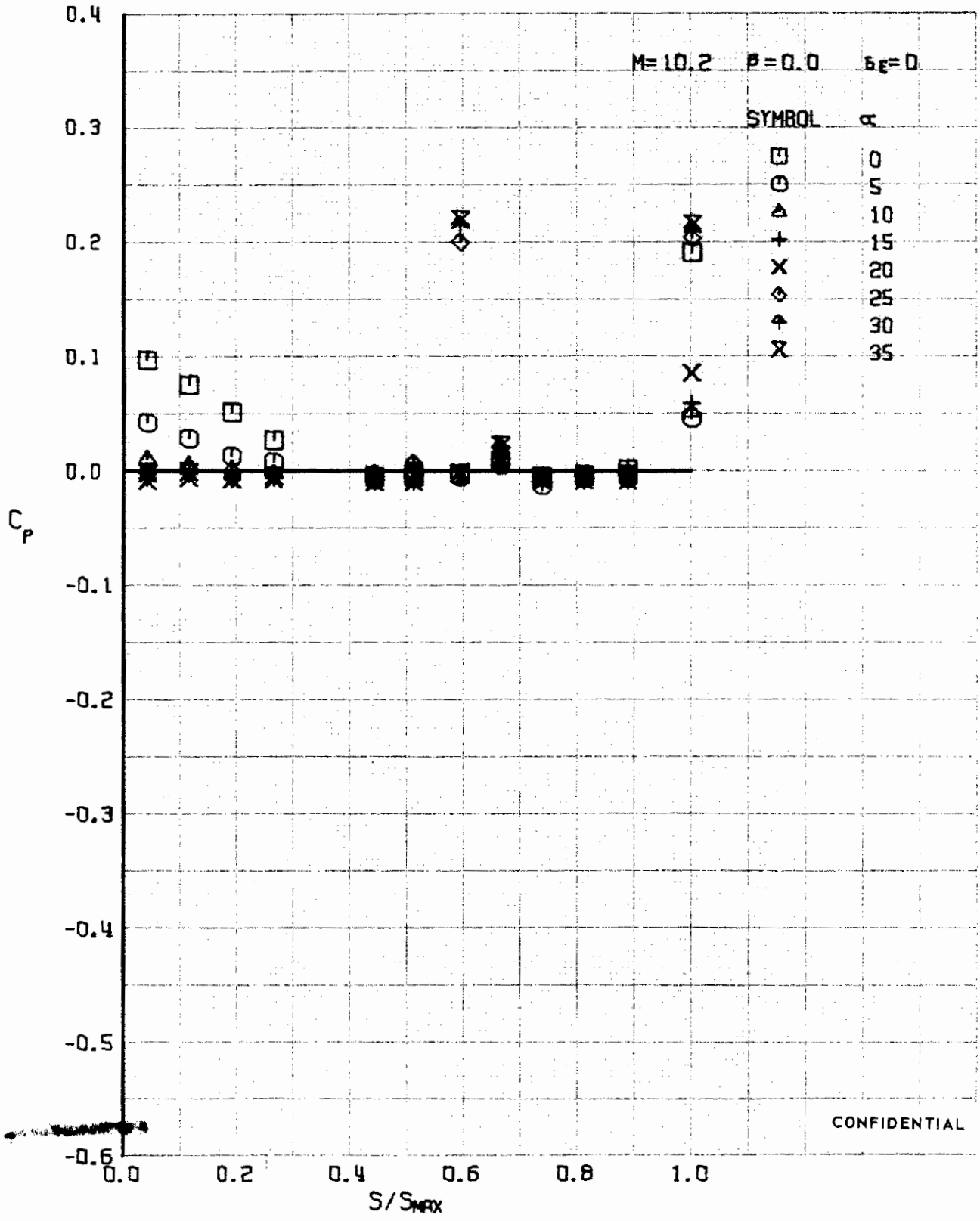

FIGURE 402 (U) UPPER SURFACE SPANWISE PRESSURES AT X/L = 0.96

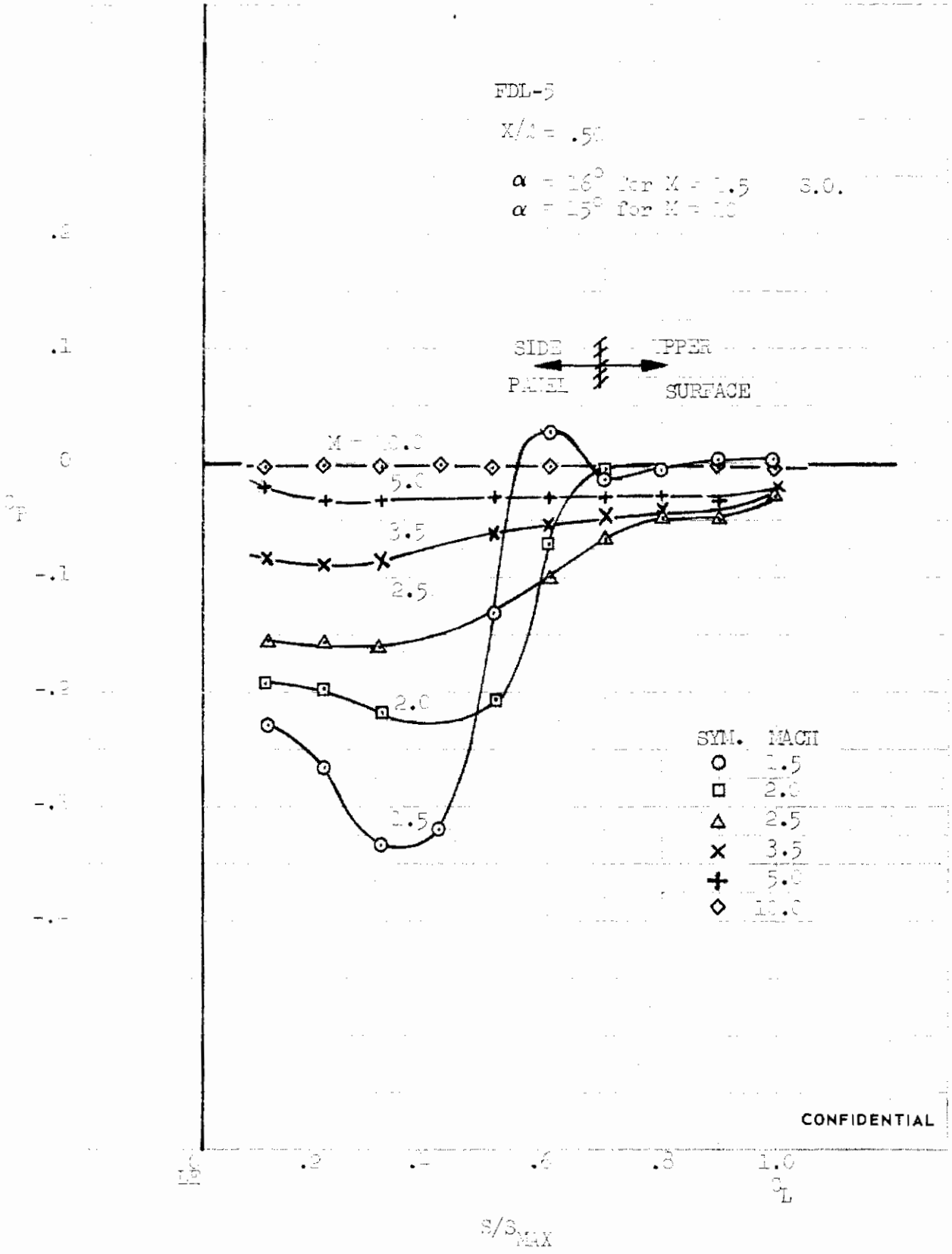

FIGURE 403 (U) VARIATION OF UPPER AFT SURFACE PRESSURE DISTRIBUTION WITH MACH NUMBER

a. X/L = 0.533

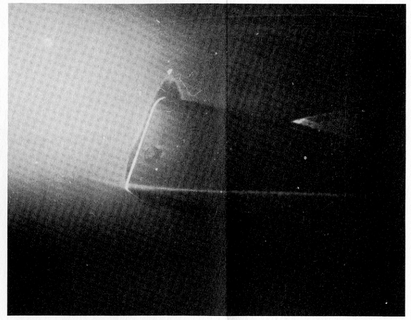

b. X/L = 0.583

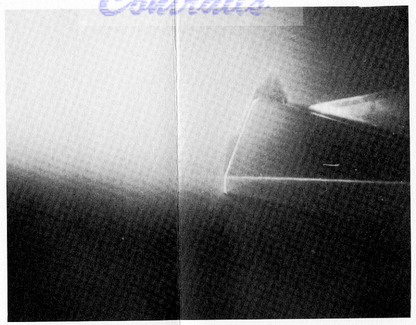

c. X/L = 0.733

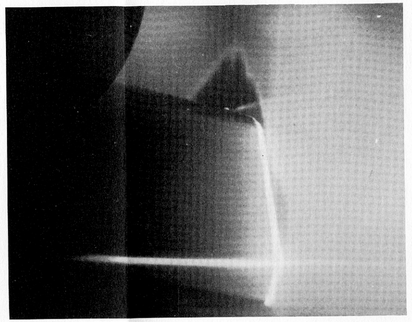

d. X/L = 0.783

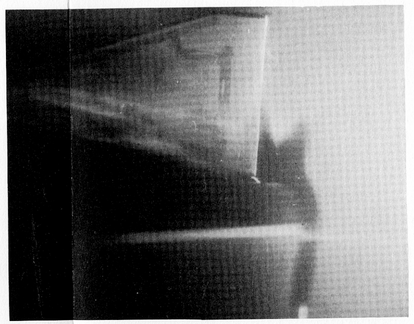

e. X/L = 1.028

FIGURE 404 (U) VAPOR SCREEN PHOTOS
M = 1.5 α = 9 degrees

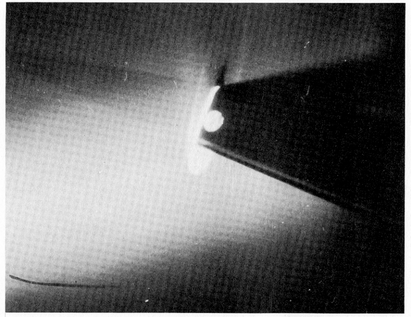

a. X/L = 0.250

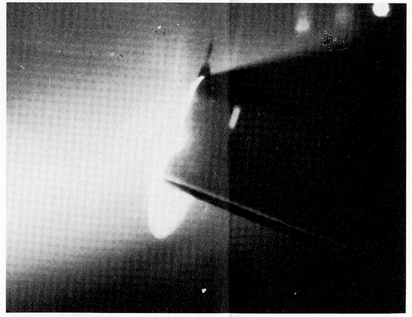

b. X/L = 0.450

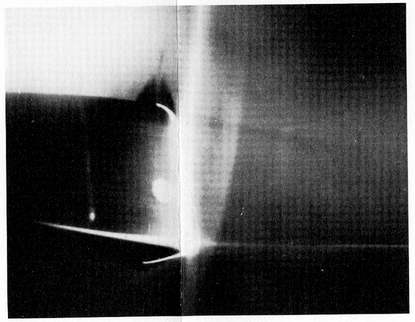

c. X/L = 0.683

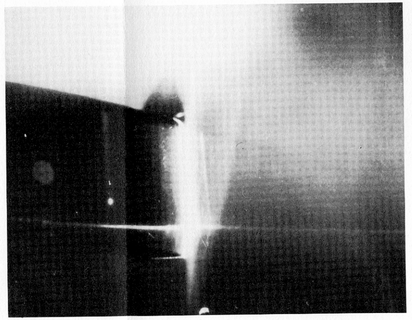

d. X/L = 0.783

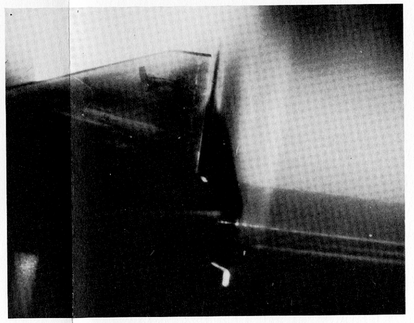

e. X/L = 1.053

FIGURE 405 (U) VAPOR SCREEN PHOTOS
M = 5.0 α = 9 degrees

(REVERSE SIDE IS BLANK)

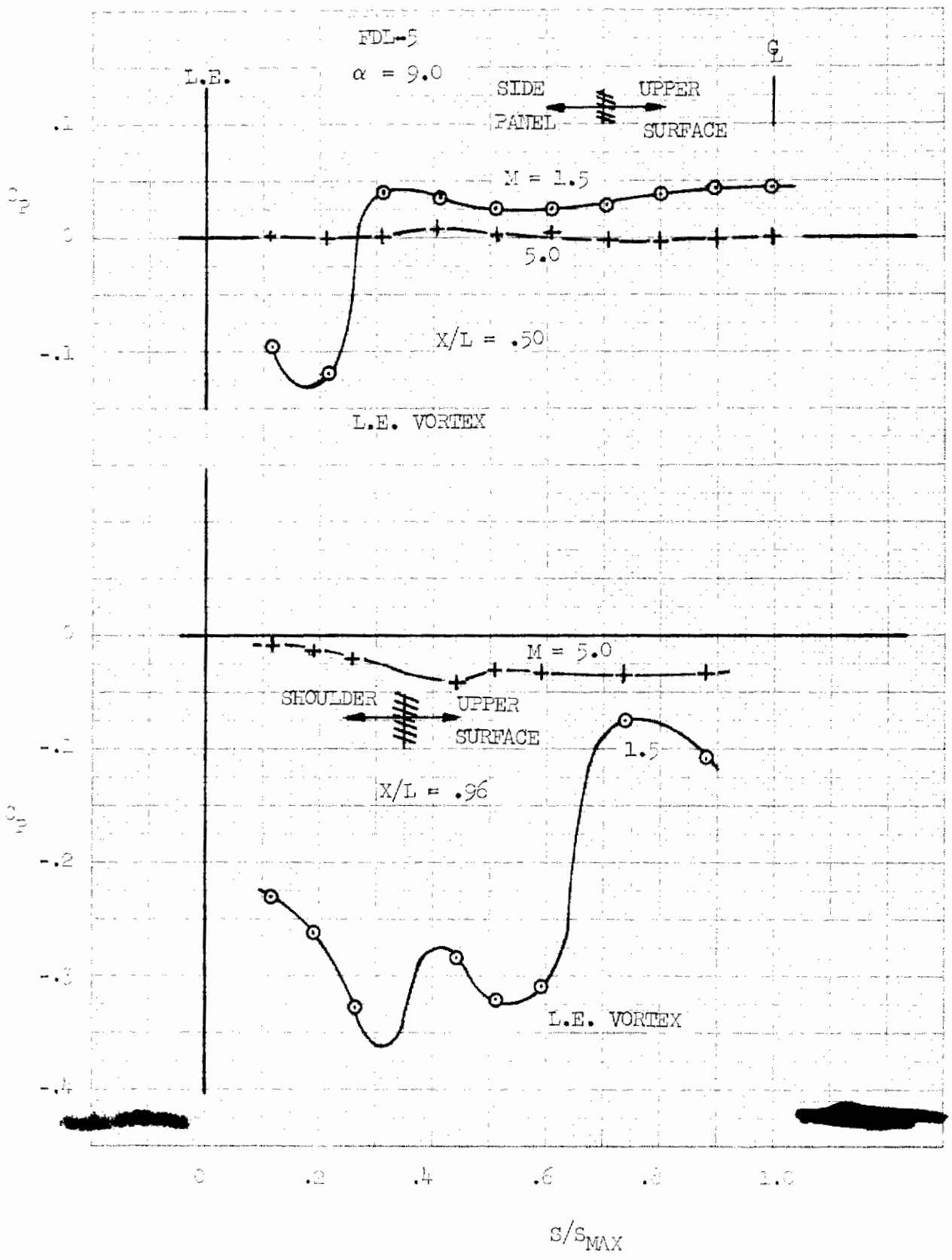

FIGURE 406 (U) CORRELATION WITH VAPOR SCREEN PHOTOS

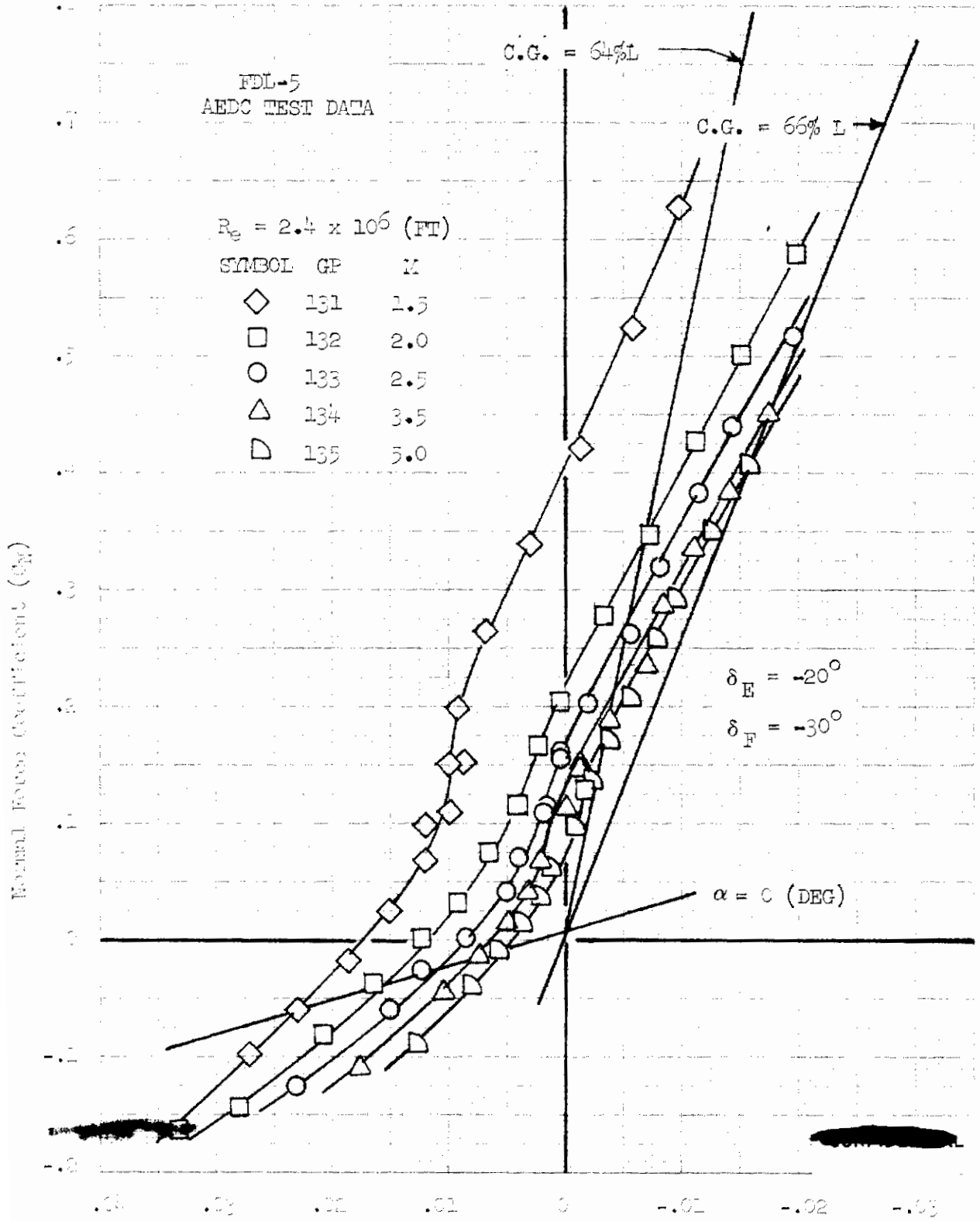

FIGURE 407 (U) FDL-5 FLAP EFFECT ON LONGITUDINAL STABILITY

α = 0 degrees

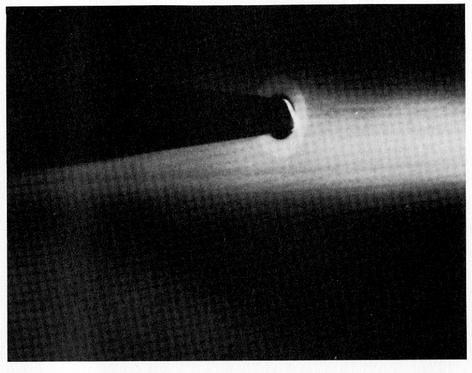

a. X/L = 0.150

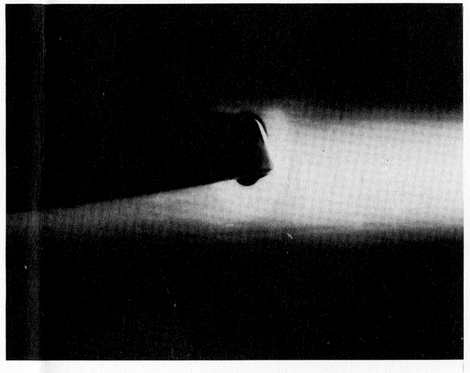

b. X/L = 0.300

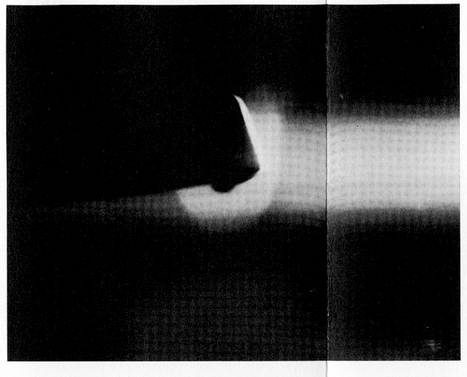

c. X/L = 0.450

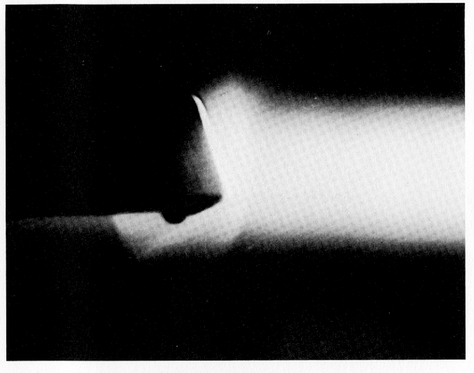

d. X/L = 0.600

α = 5 degrees

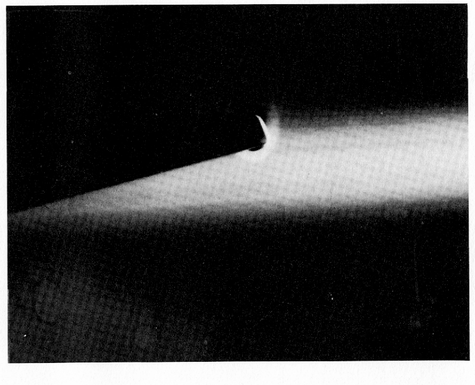

e. X/L = 0.150

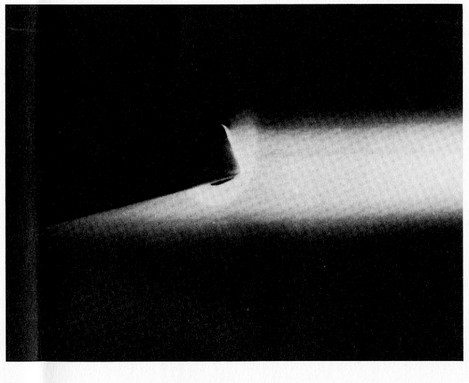

f. X/L = 0.300

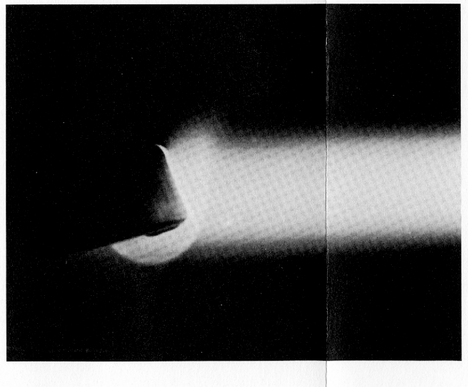

g. X/L = 0.450

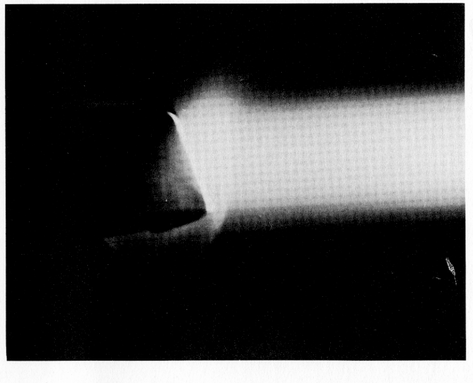

h. X/L = 0.600

FIGURE 408 VAPOR SCREEN PHOTOS
M = 8.0

(REVERSE SIDE IS BLANK)

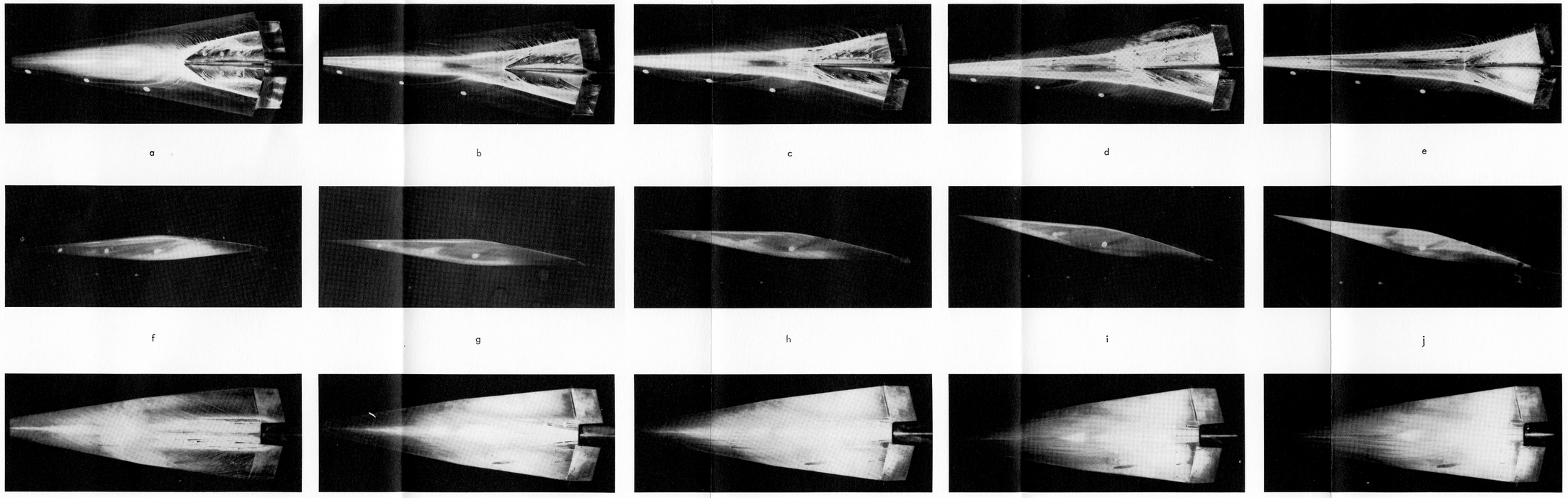

FIGURE 409 (u) OIL FLOW PHOTOS M = 10

(REVERSE SIDE IS BLANK)

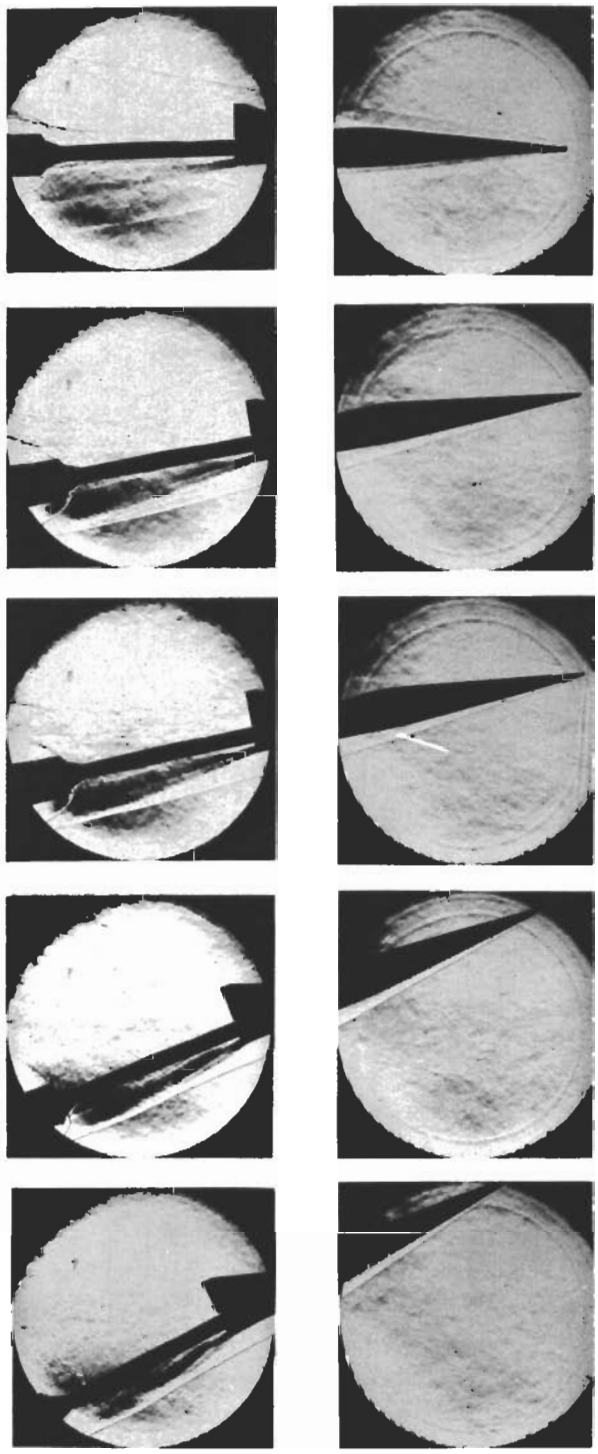

UNCLASSIFIED

FIGURE 410 (U) SCHLIEREN PHOTOGRAPHS, FORE AND AFT WINDOW PAIRS, 20-INCH FORCE MODEL, M = 8.0

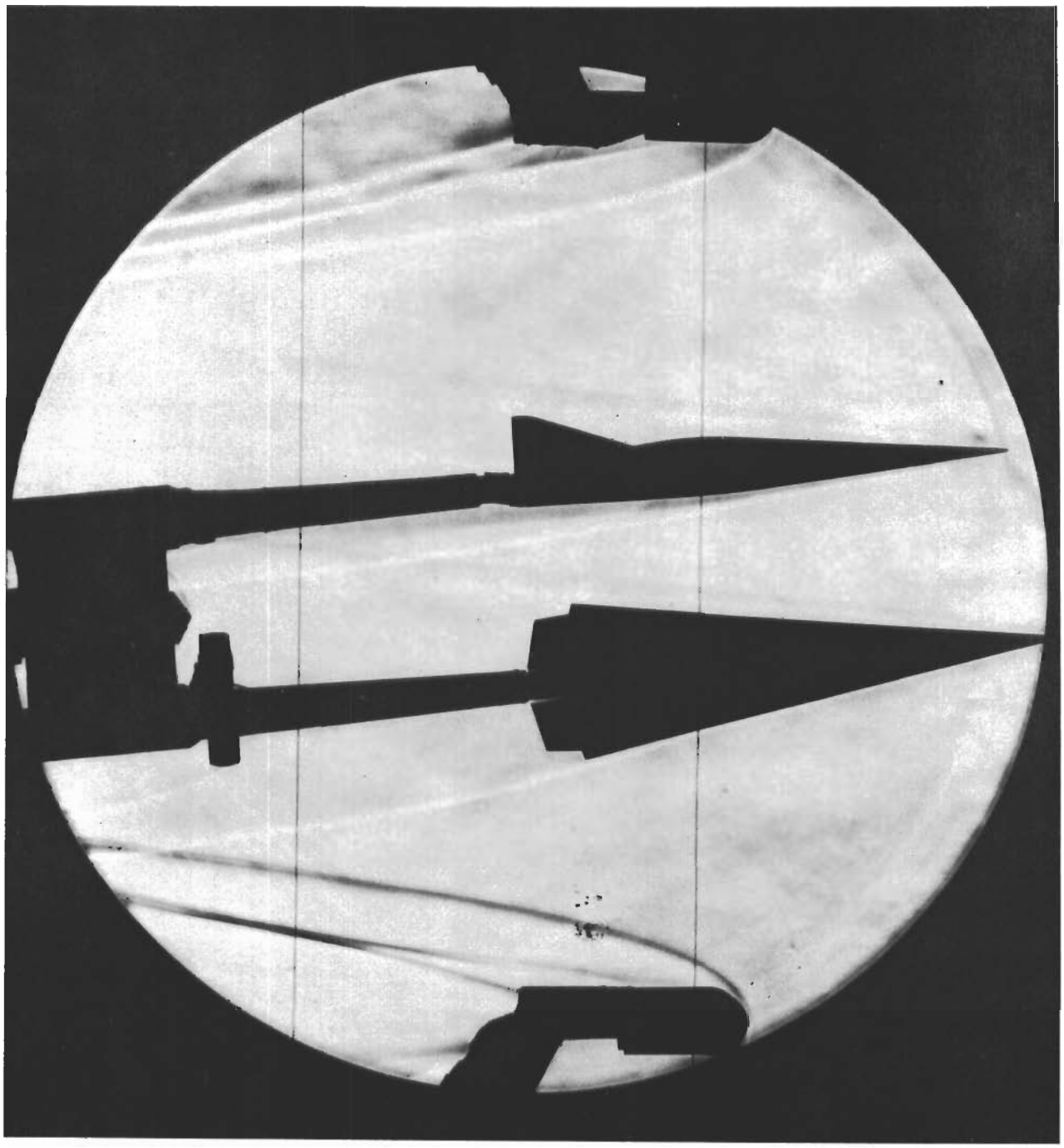

UNCLASSIFIED

FIGURE 411 (U) SCHLIEREN PHOTO, 15-INCH FIBER GLASS MODEL FDL-5
DUAL INSTALIATION, M = 18.1
Upper model: α = 4 deg β = 0 deg
Lower model: α = 0 deg β = 4 deg

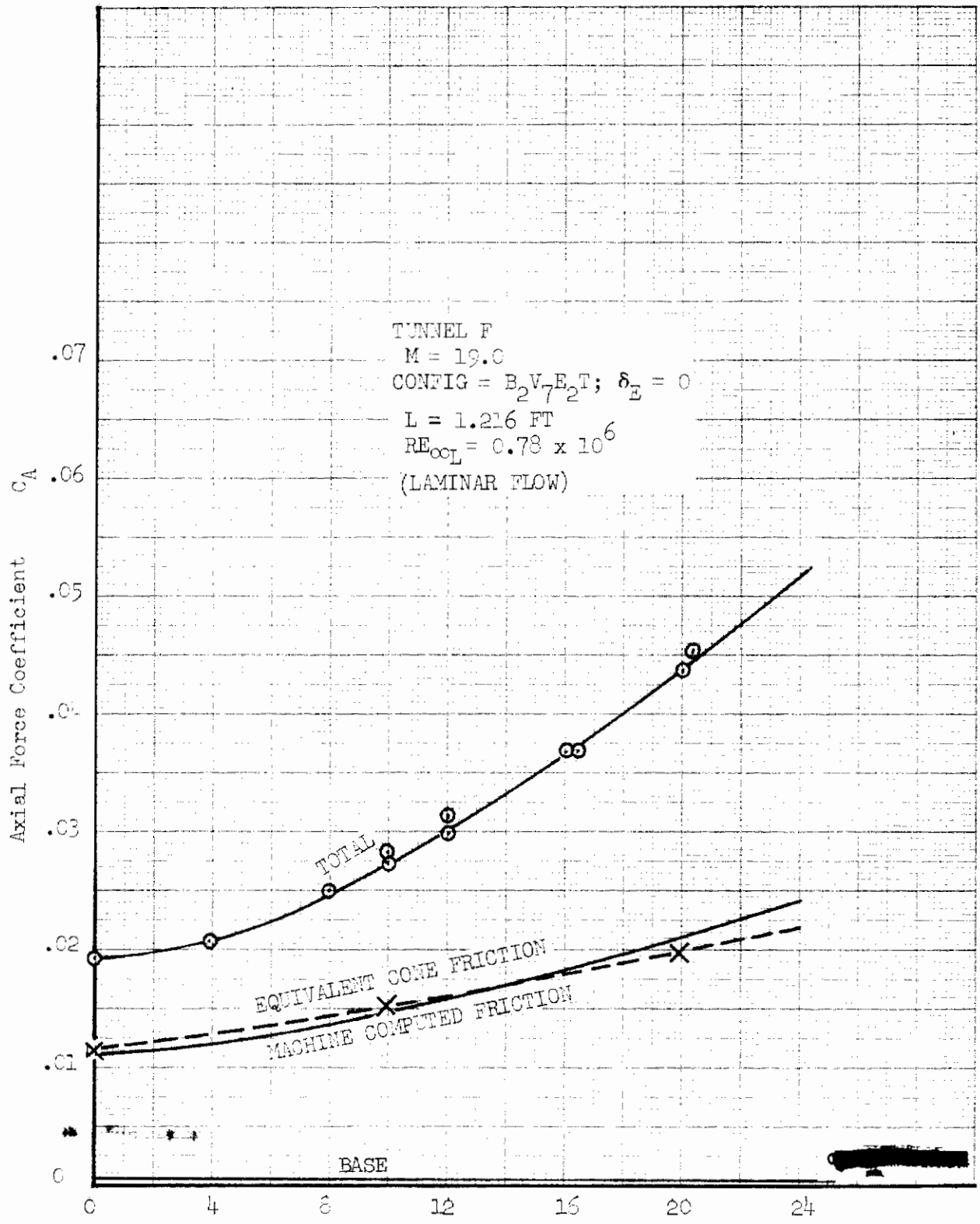

FIGURE 412 (U) AXIAL FORCE BUILDUP ON TEST MODELS SHOWING CALCULATED FRICTION CONTRIBUTIONS, M = 19.0

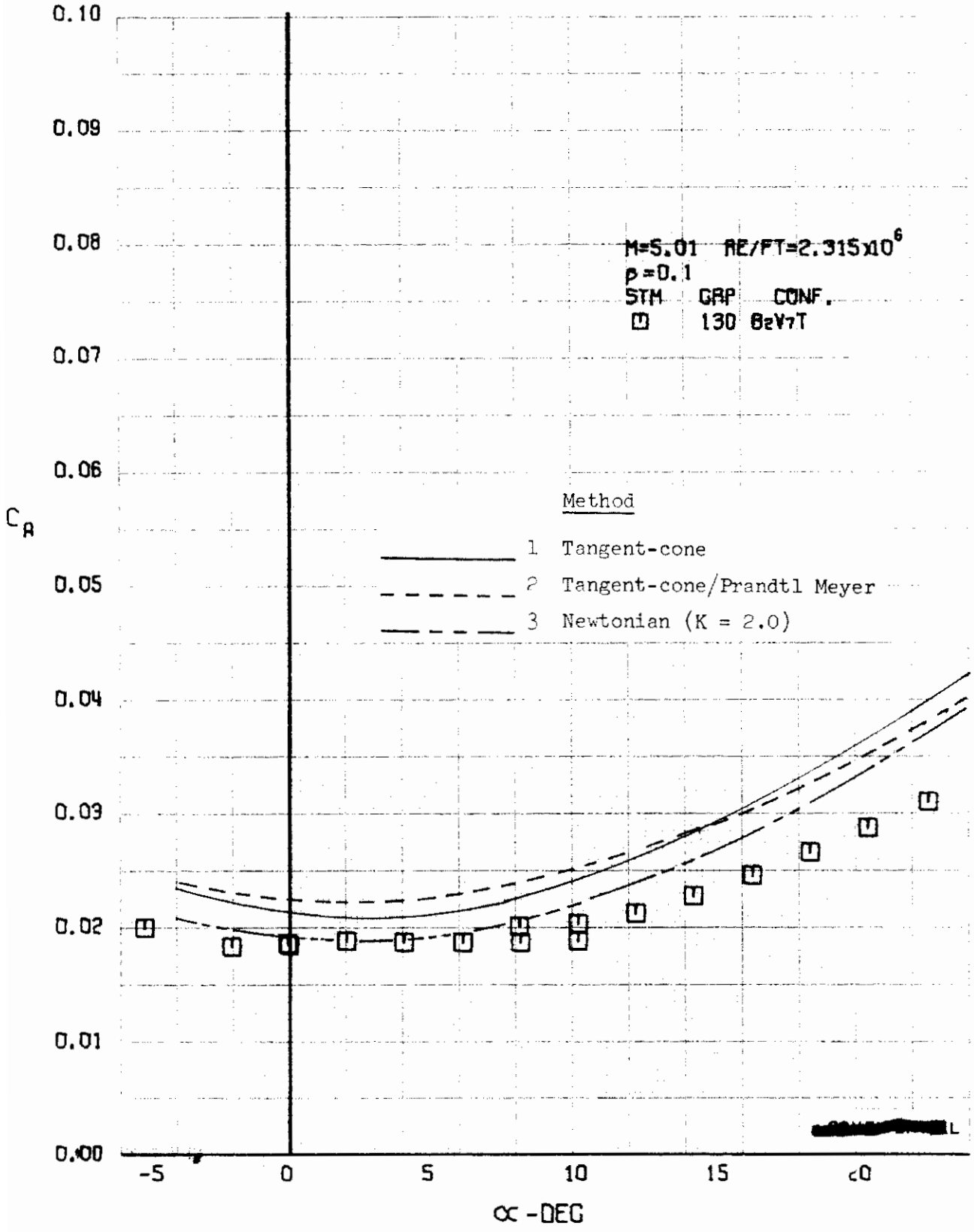

FIGURE 413 (U) COMPARISON OF ESTIMATED AND EXPERIMENTAL COEFFICIENTS - AXIAL FORCE COEFFICIENT VARIATION WITH ANGLE OF ATTACK (M=5.01)

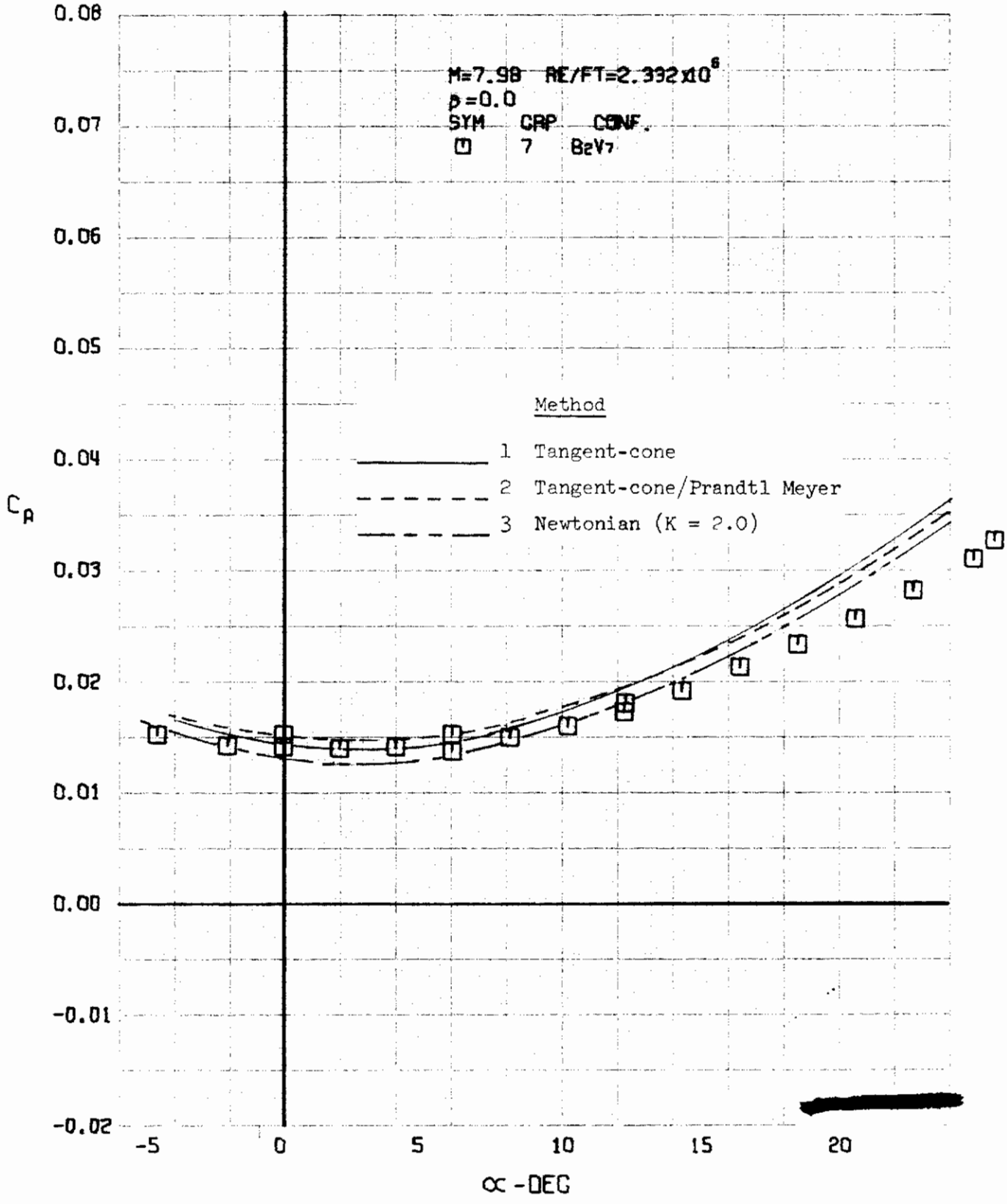

FIGURE 414 (U) COMPARISON OF ESTIMATED AND EXPERIMENTAL COEFFICIENTS - AXIAL FORCE COEFFICIENT VARIATION WITH ANGLE OF ATTACK (M=7.98)

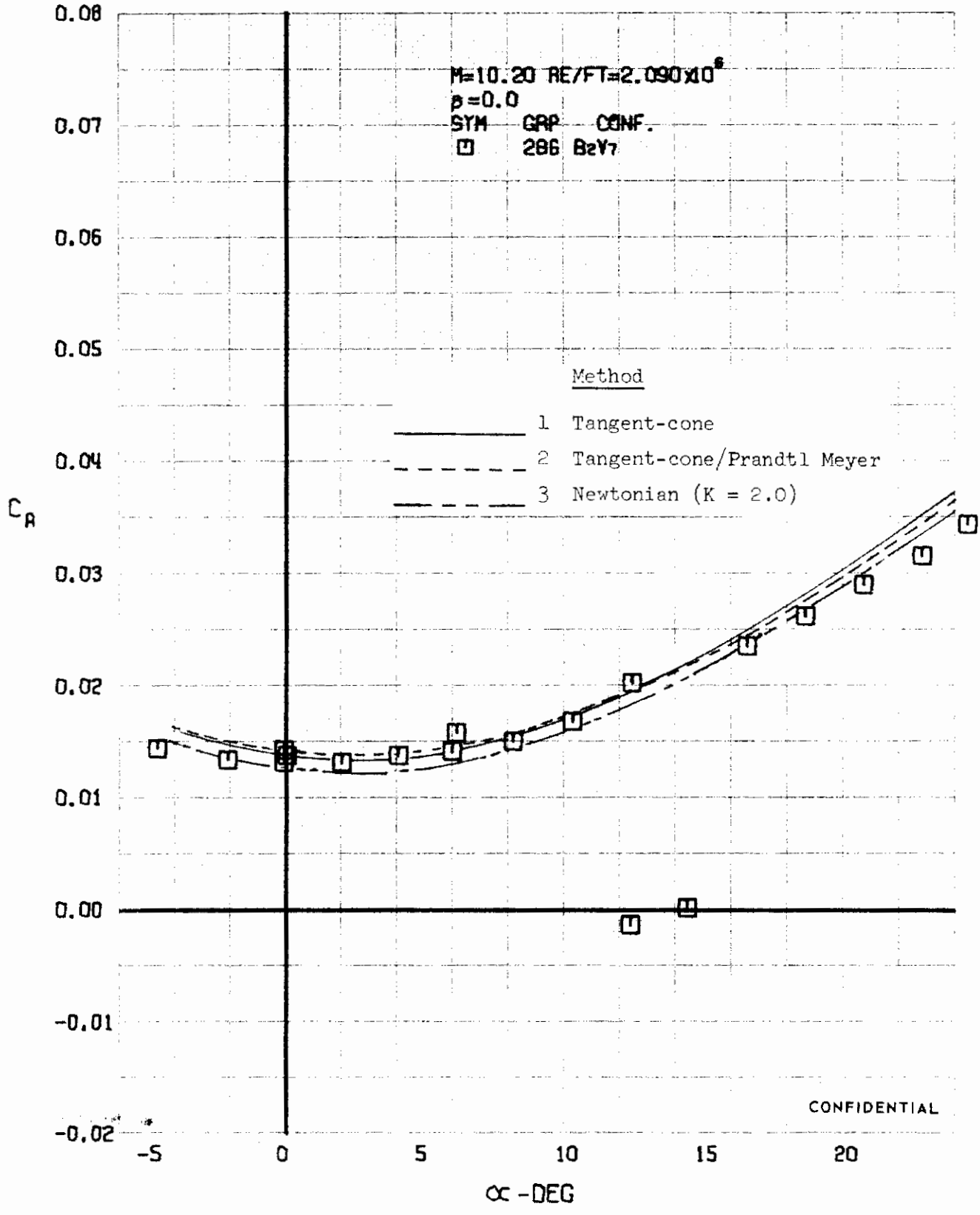

FIGURE 415 (U) COMPARISON OF ESTIMATED AND EXPERIMENTAL COEFFICIENTS - AXIAL FORCE COEFFICIENT VARIATION WITH ANGLE OF ATTACK (M=10.20

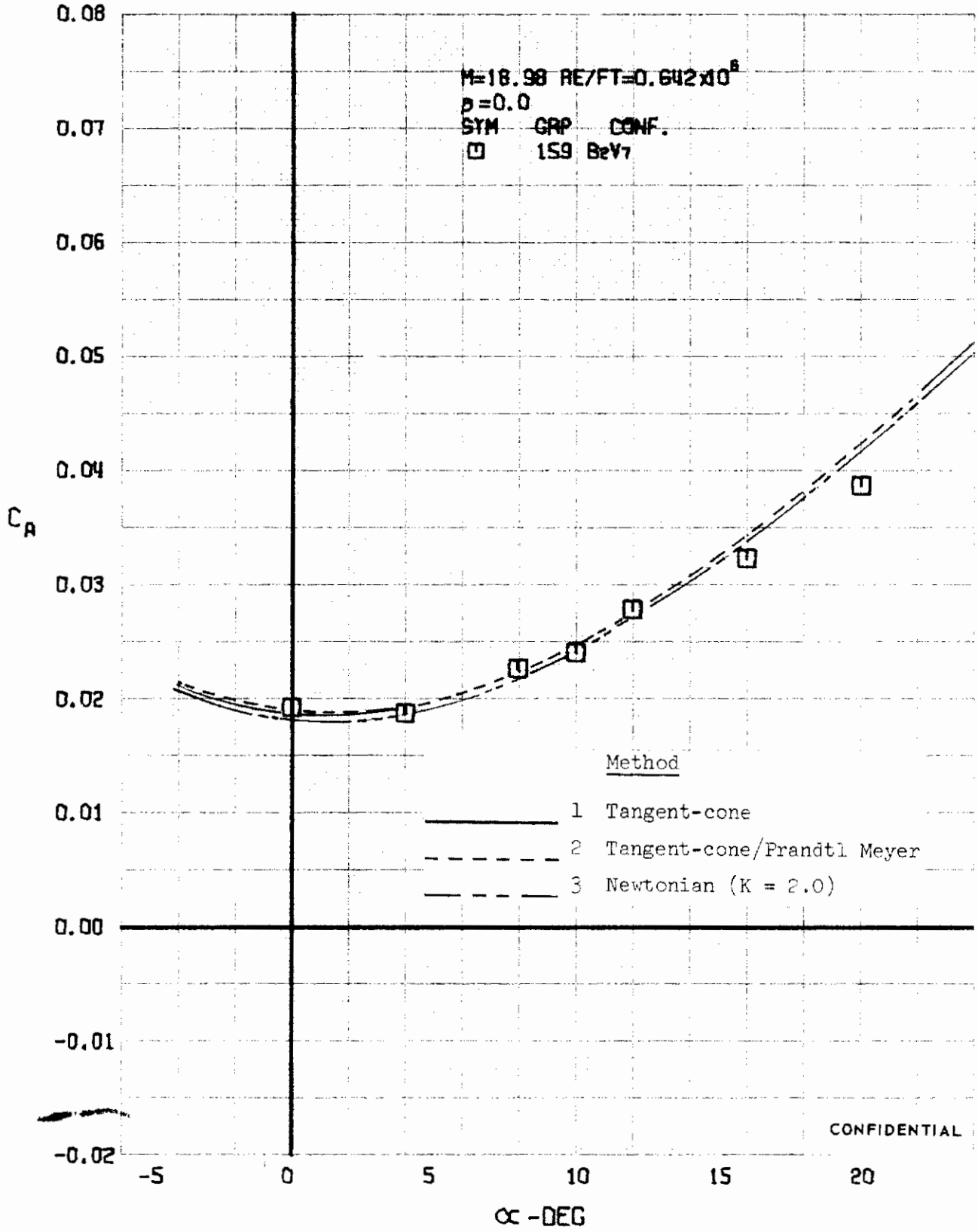

FIGURE 416 (U) COMPARISON OF ESTIMATED AND EXPERIMENTAL COEFFICIENTS - AXIAL FORCE COEFFICIENT VARIATION WITH ANGLE OF ATTACK (M=18.98

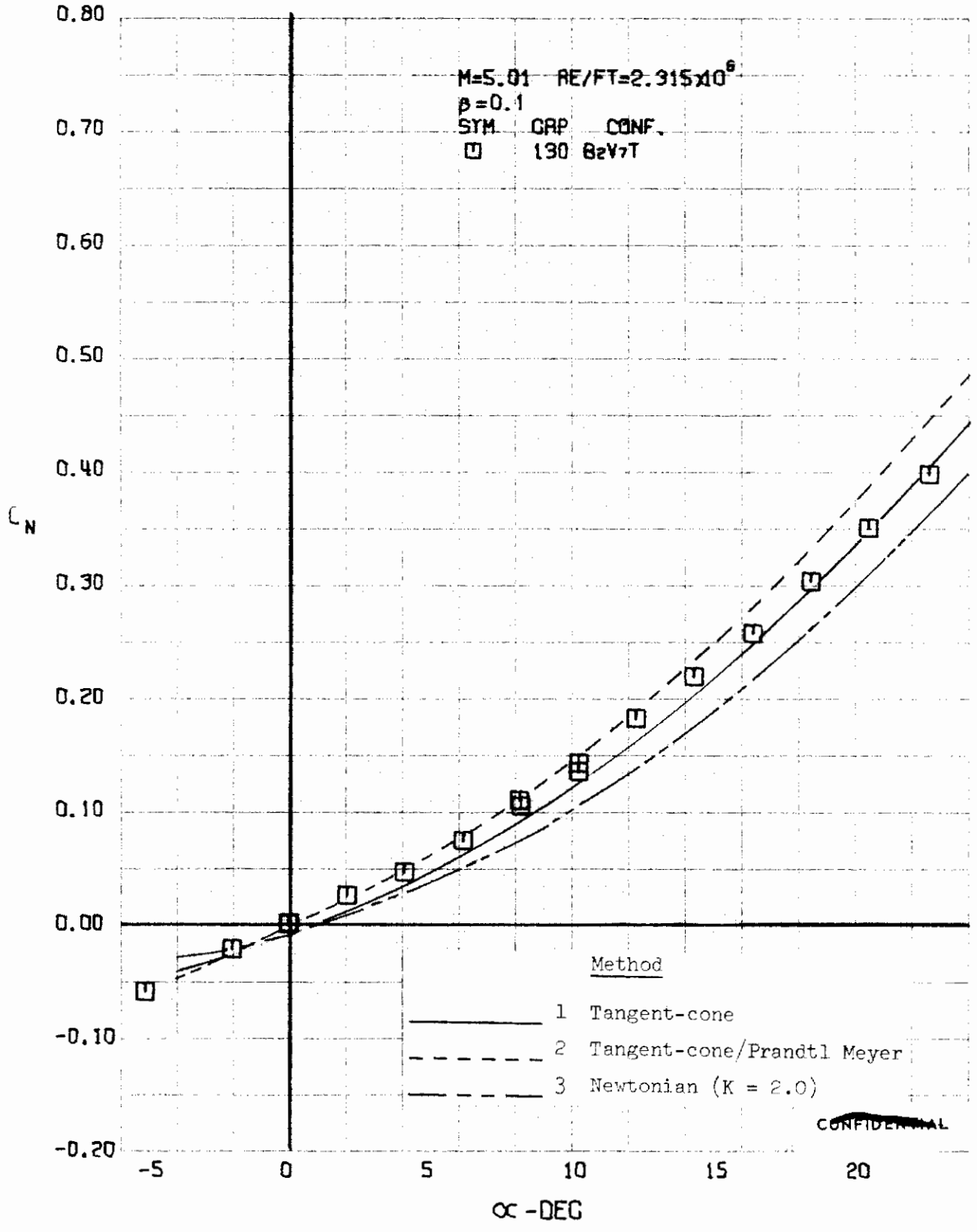

FIGURE 417 (U) COMPARISON OF ESTIMATED AND EXPERIMENTAL COEFFICIENTS - NORMAL FORCE COEFFICIENT VARIATION WITH ANGLE OF ATTACK (M=5.01)

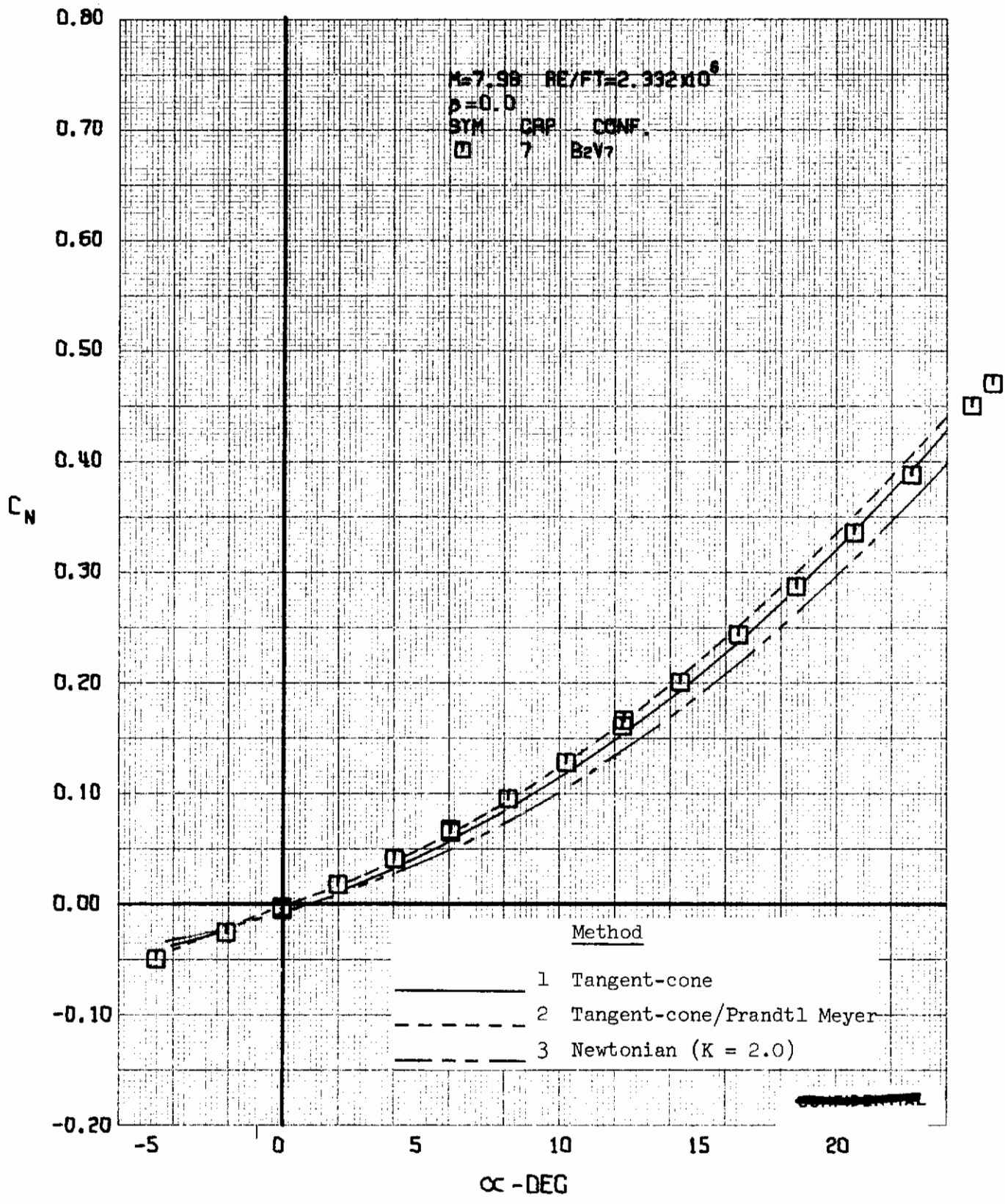

FIGURE 418 (U) COMPARISON OF ESTIMATED AND EXPERIMENTAL COEFFICIENTS - NORMAL FORCE COEFFICIENT VARIATION WITH ANGLE OF ATTACK (M= 7.98)

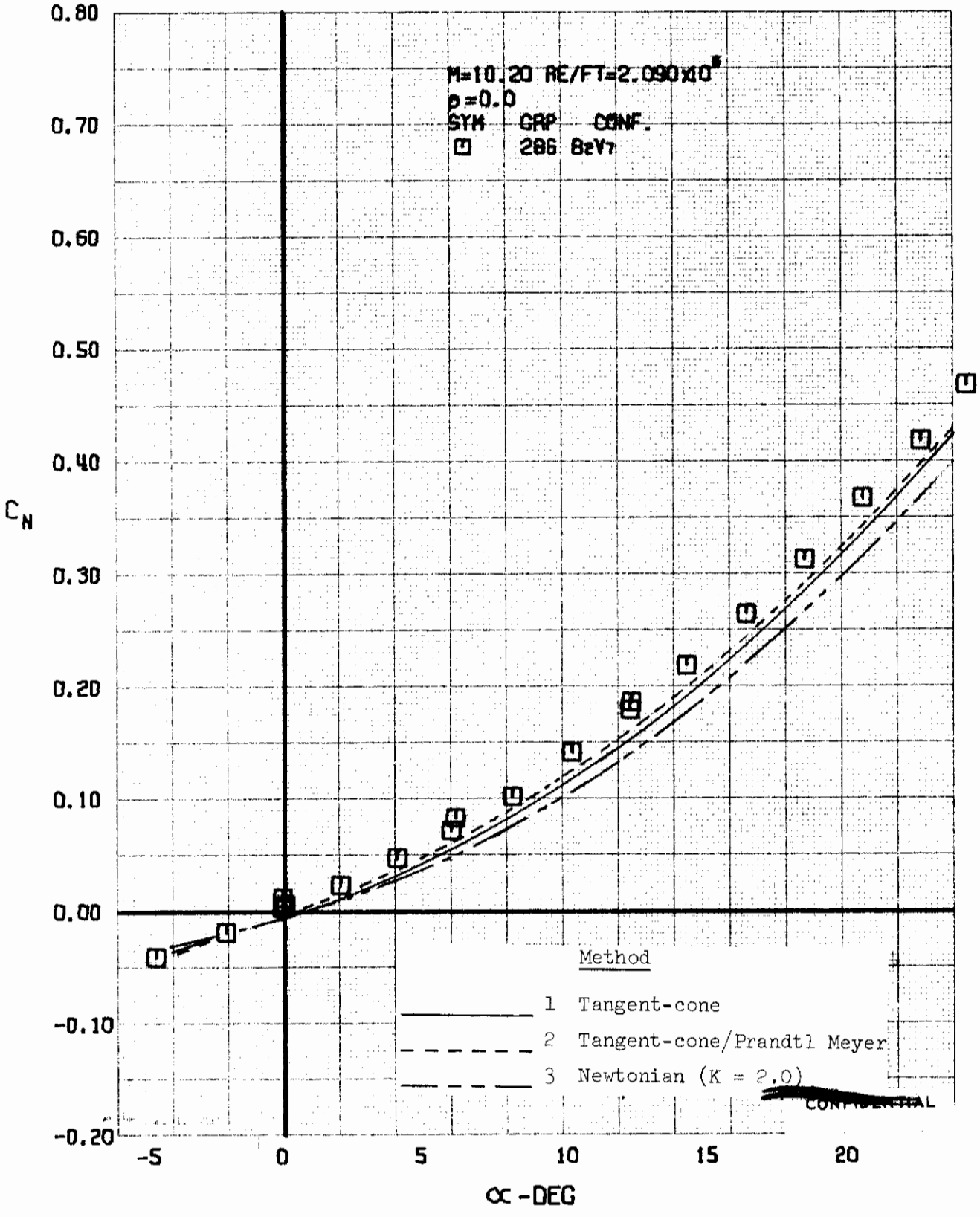

FIGURE 419 (U) COMPARISON OF ESTIMATED AND EXPERIMENTAL COEFFICIENTS - NORMAL FORCE COEFFICIENT VARIATION WITH ANGLE OF ATTACK (M= 10.20

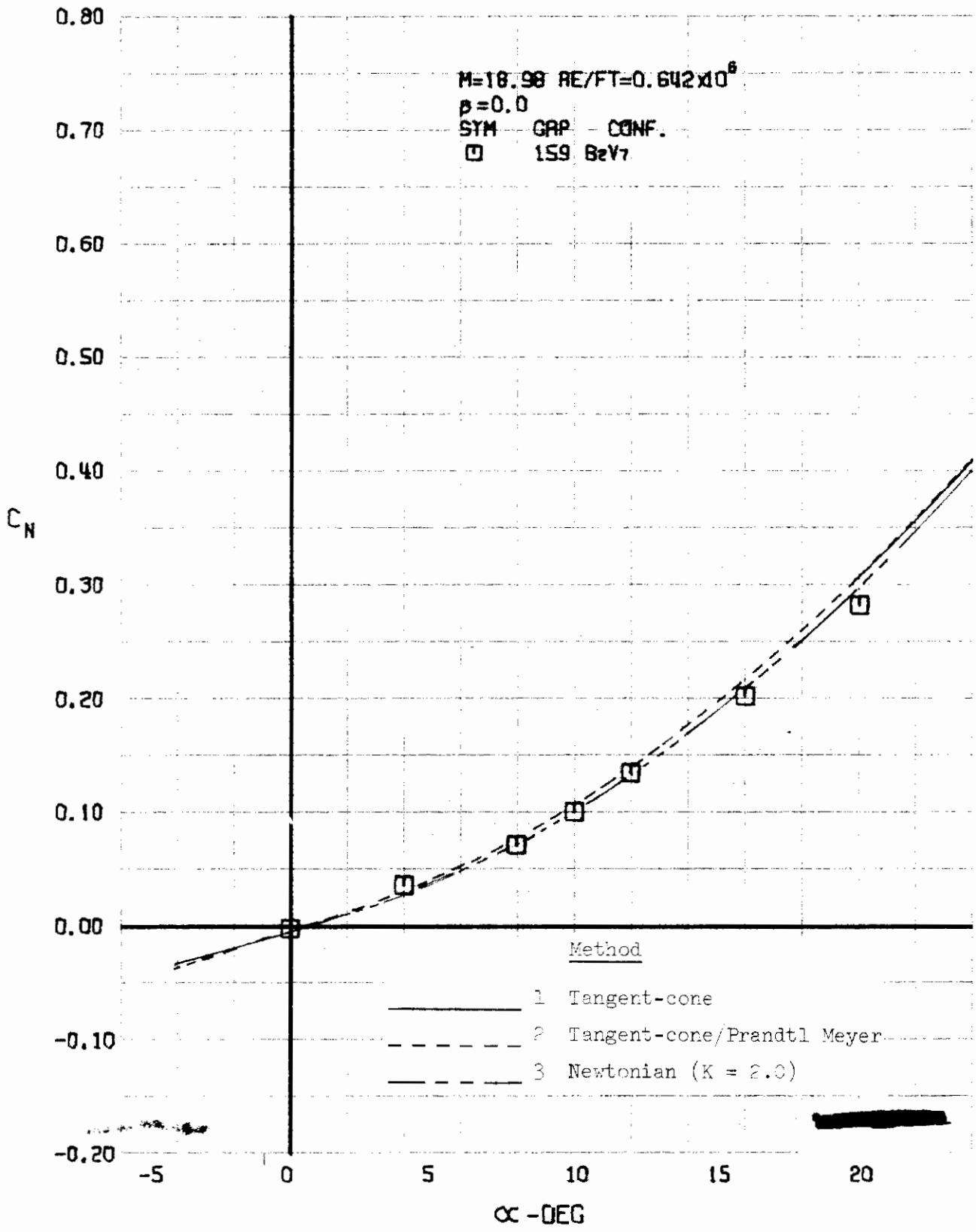

FIGURE 420 (U) COMPARISON OF ESTIMATED AND EXPERIMENTAL COEFFICIENTS - NORMAL FORCE COEFFICIENT VARIATION WITH ANGLE OF ATTACK (M=18.98

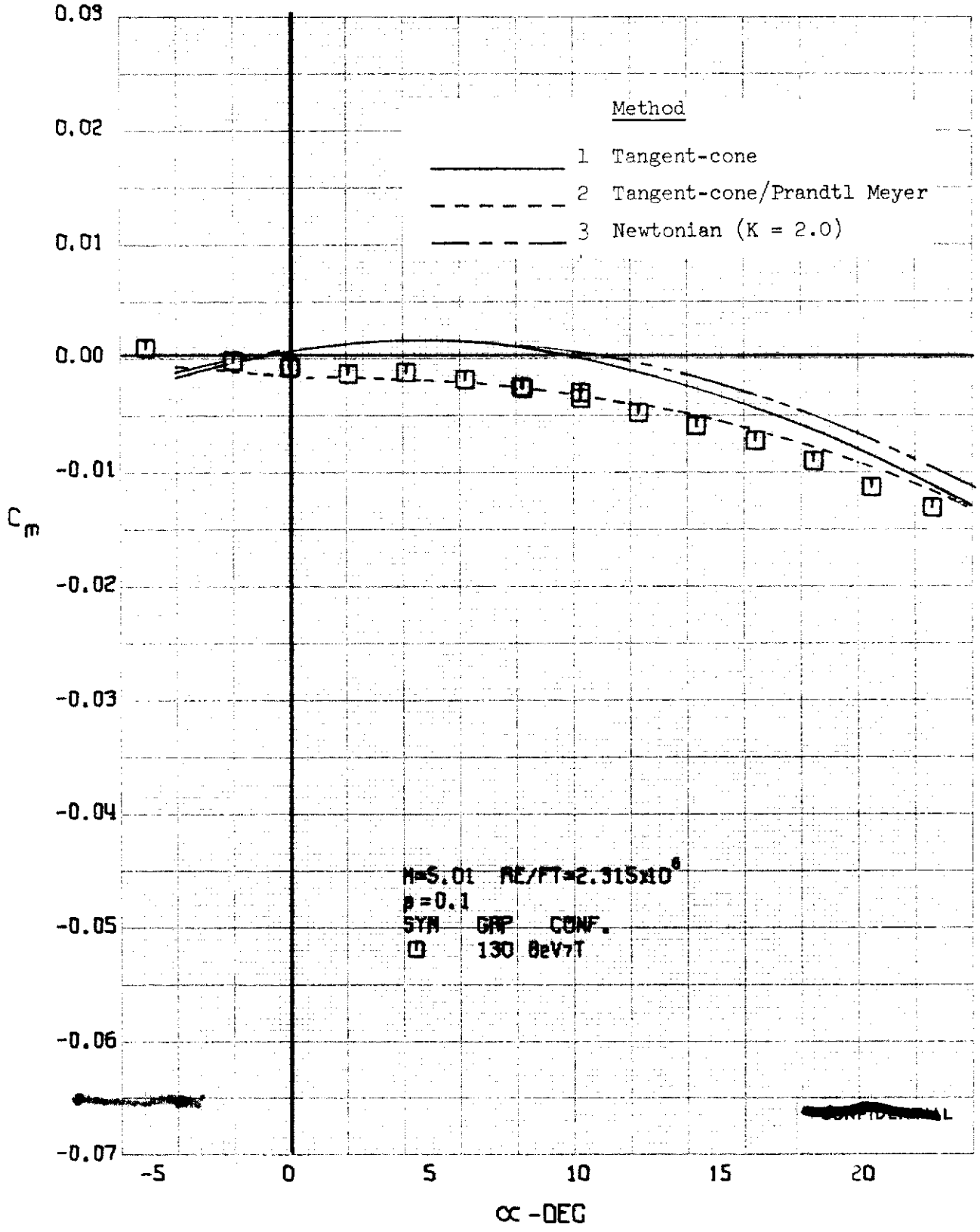

FIGURE 421 (U) COMPARISON OF ESTIMATED AND EXPERIMENTAL COEFFICIENTS PITCHING MOMENT COEFFICIENT VARIATION WITH ANGLE OF ATTACK (M=5.01)

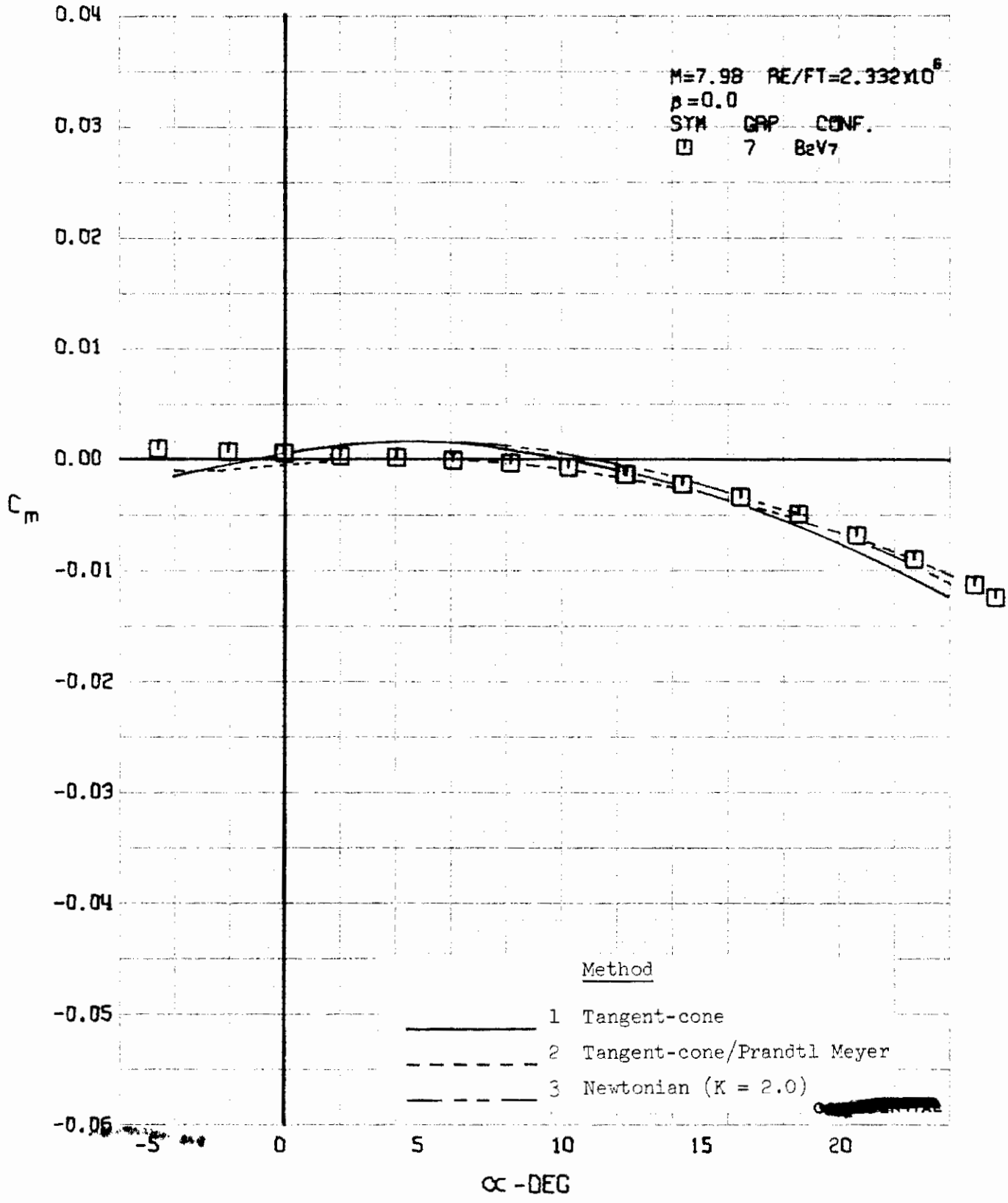

FIGURE 422 (U) COMPARISON OF ESTIMATED AND EXPERIMENTAL COEFFICIENTS - PITCHING MOMENT COEFFICIENT VARIATION WITH ANGLE OF ATTACK (M= 7.98)

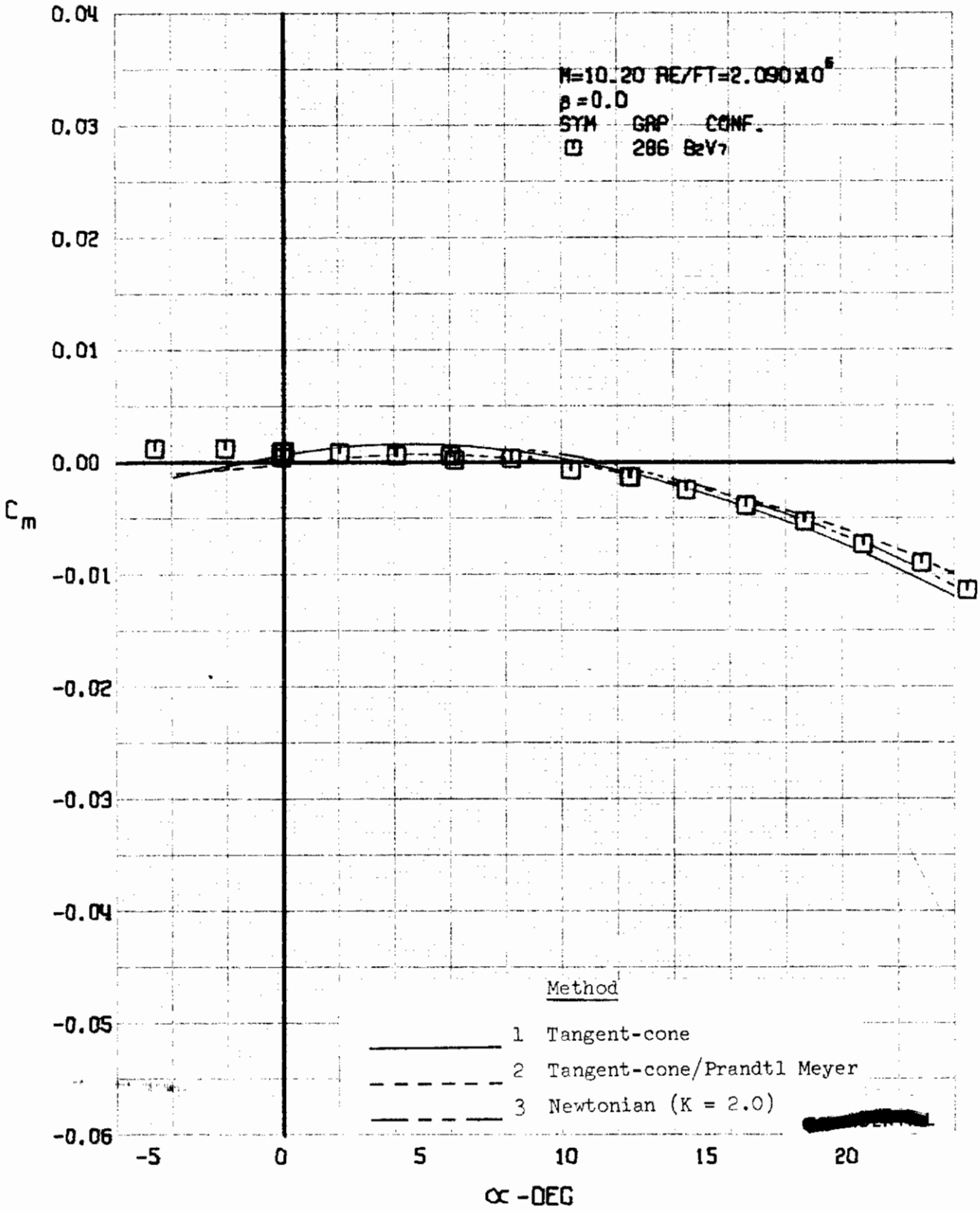

FIGURE 423 (U) COMPARISON OF ESTIMATED AND EXPERIMENTAL COEFFICIENTS - PITCHING MOMENT COEFFICIENT VARIATION WITH ANGLE OF ATTACK (M= 10.20

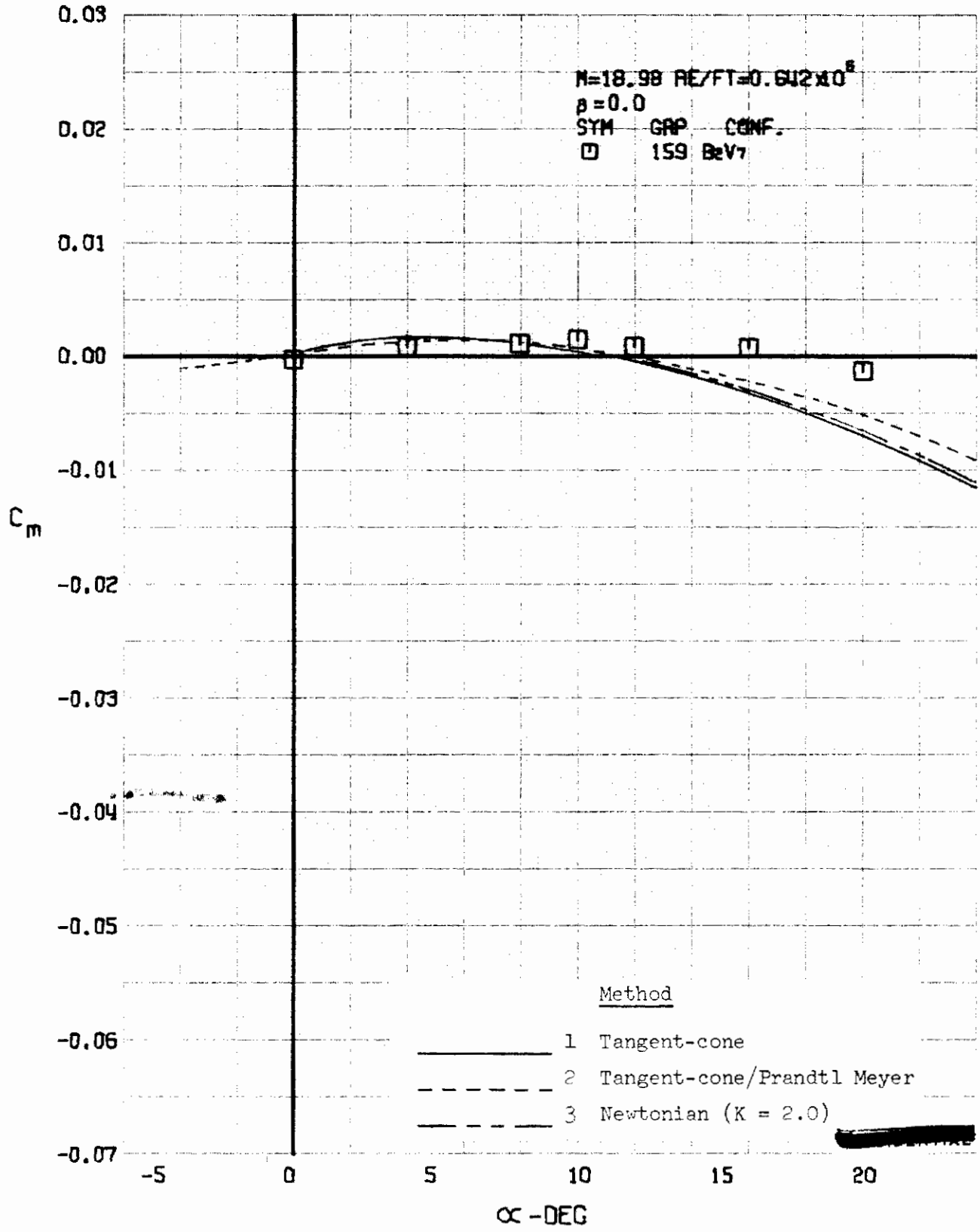

FIGURE 424 (U) COMPARISON OF ESTIMATED AND EXPERIMENTAL COEFFICIENTS - PITCHING MOMENT COEFFICIENT VARIATION WITH ANGLE OF ATTACK (M= 18.98

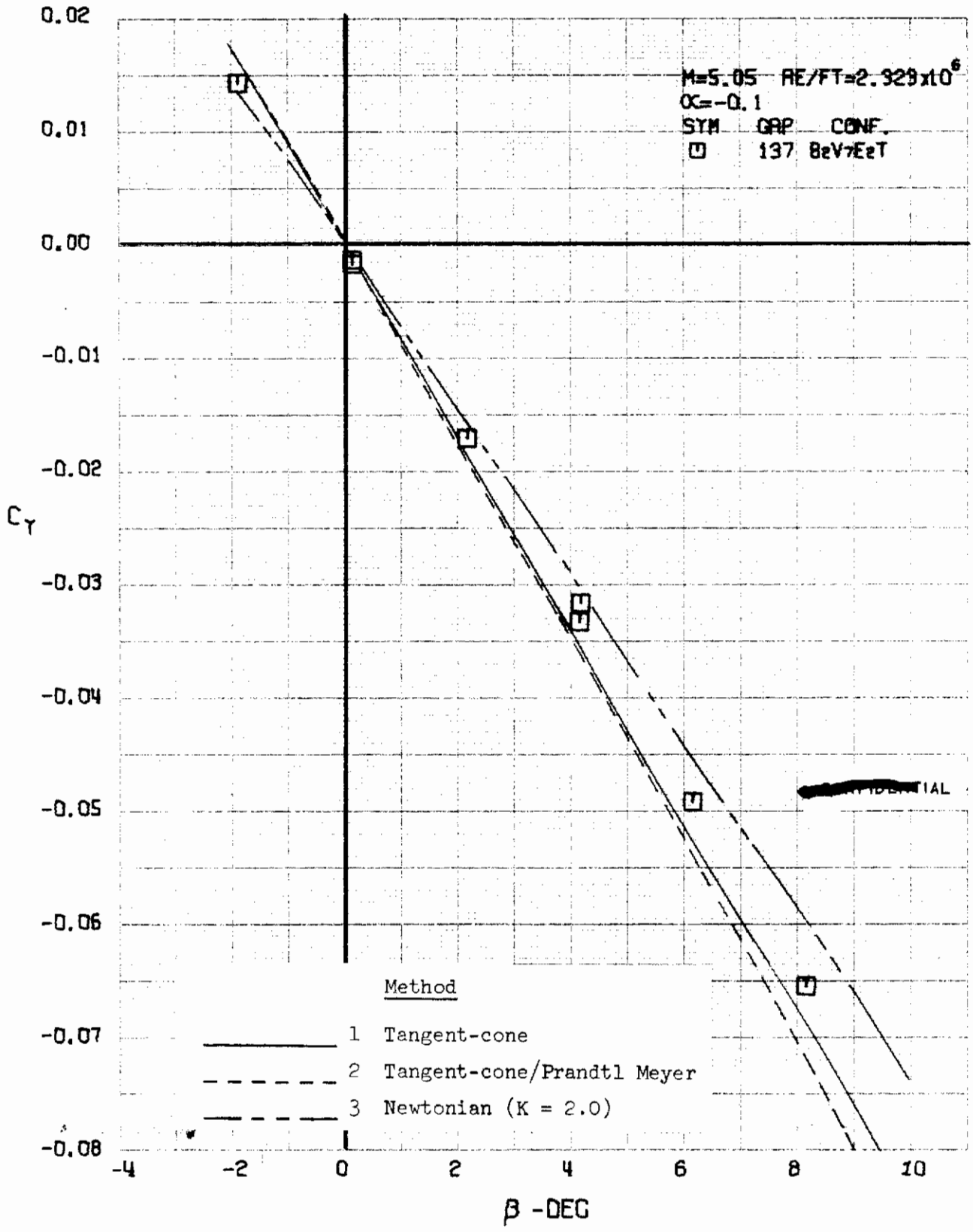

FIGURE 425 (U) COMPARISON OF ESTIMATED AND EXPERIMENTAL COEFFICIENTS - SIDE FORCE COEFFICIENT VARIATION WITH ANGLE OF YAW (M=5.05)

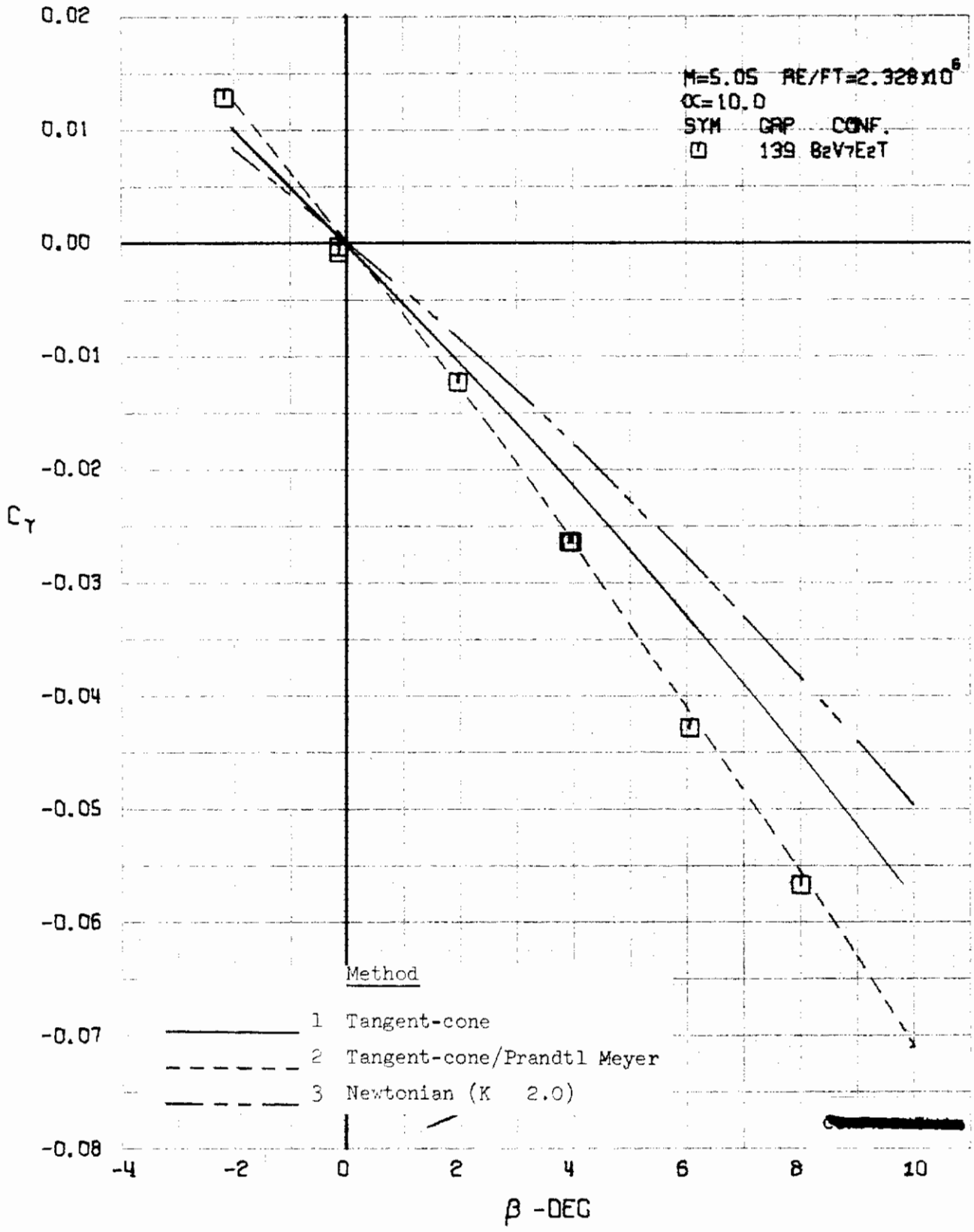

FIGURE 426 (U) COMPARISON OF ESTIMATED AND EXPERIMENTAL COEFFICIENTS - SIDE FORCE COEFFICIENT VARIATION WITH ANGLE OF YAW (M=5.05)

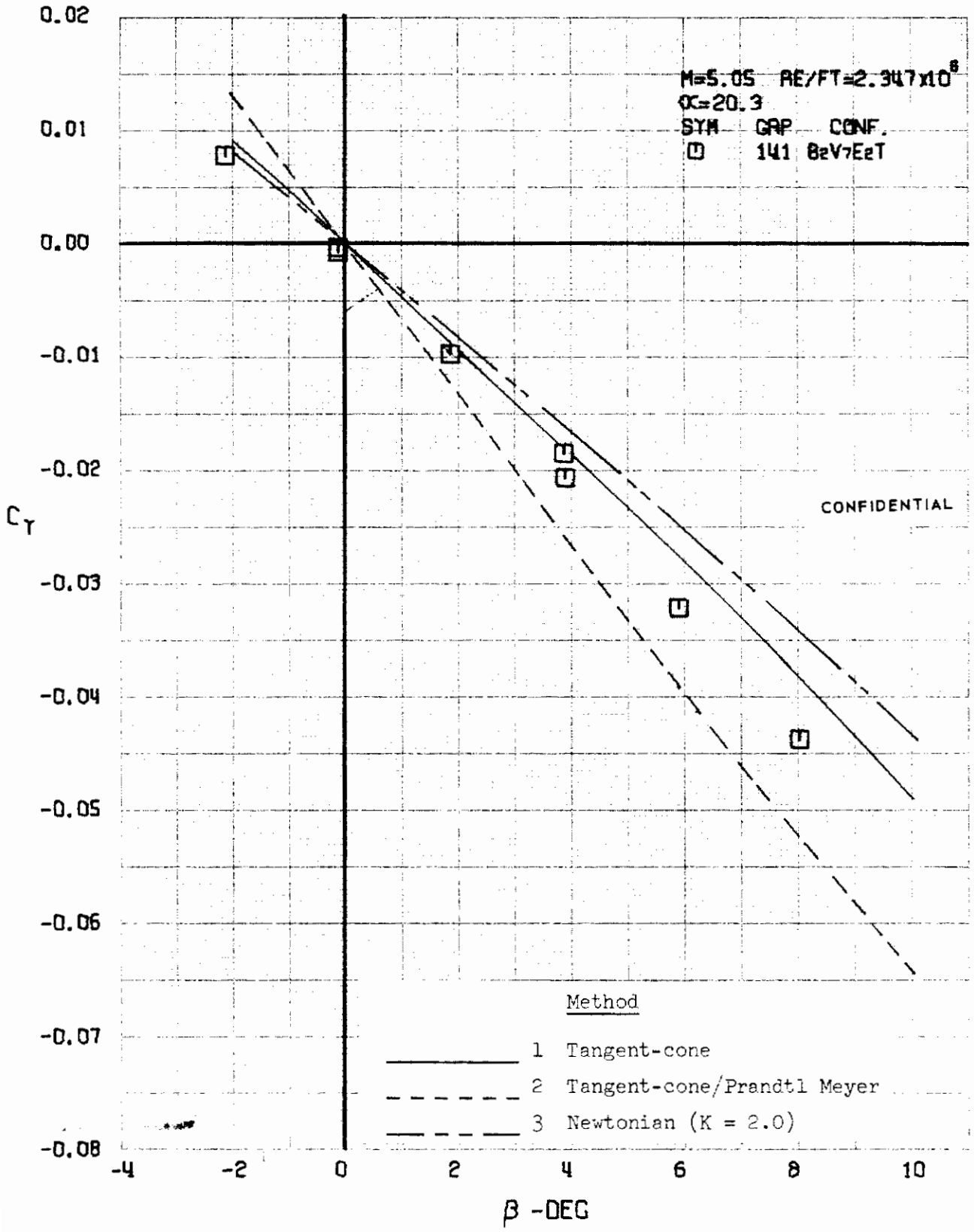

FIGURE 427 (U) COMPARISON OF ESTIMATED AND EXPERIMENTAL COEFFICIENTS - SIDE FORCE COEFFICIENT VARIATION WITH ANGLE OF YAW (M=5.05)

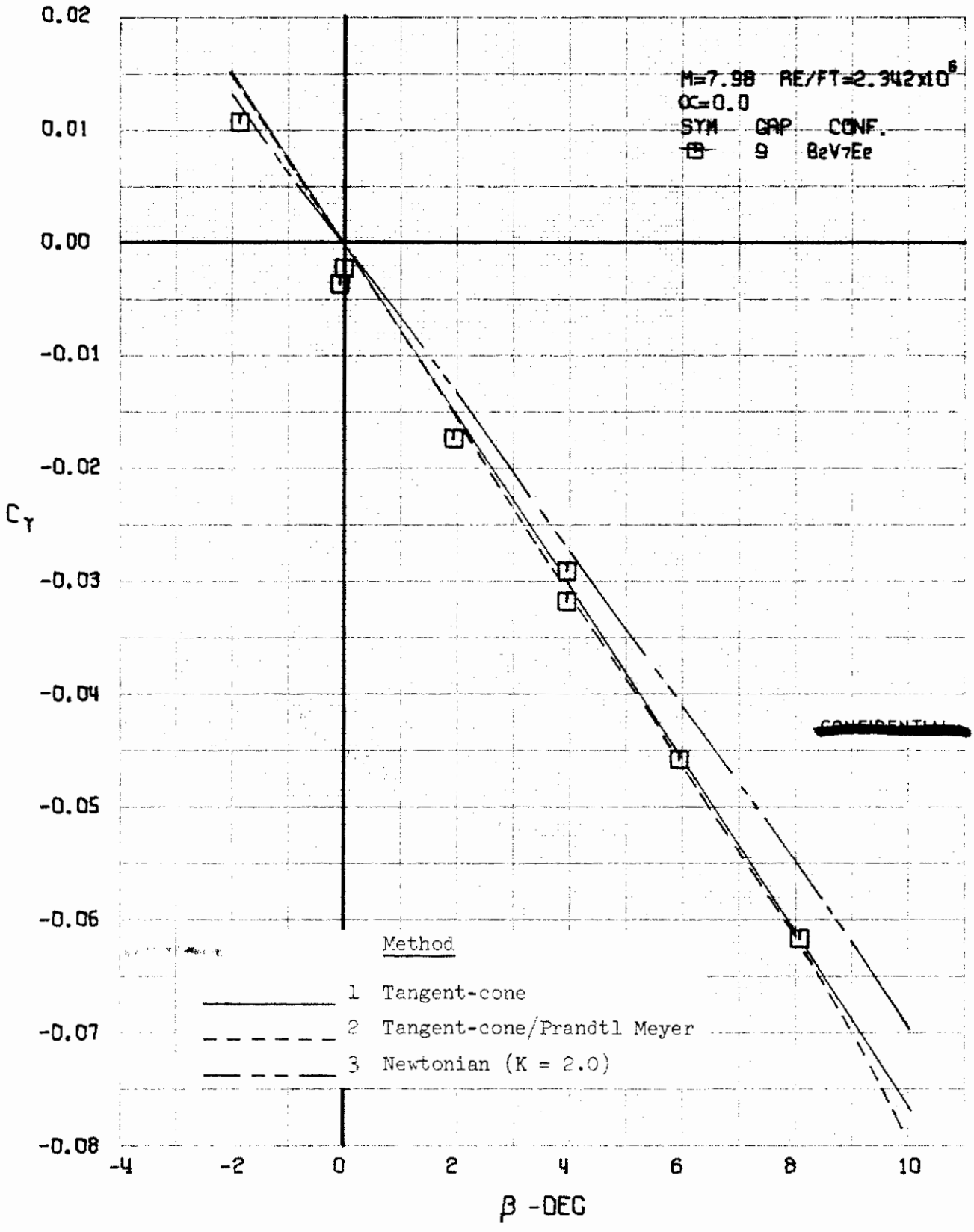

FIGURE 428 (U) COMPARISON OF ESTIMATED AND EXPERIMENTAL COEFFICIENTS - SIDE FORCE COEFFICIENT VARIATION WITH ANGLE OF YAW (M= 7.98)

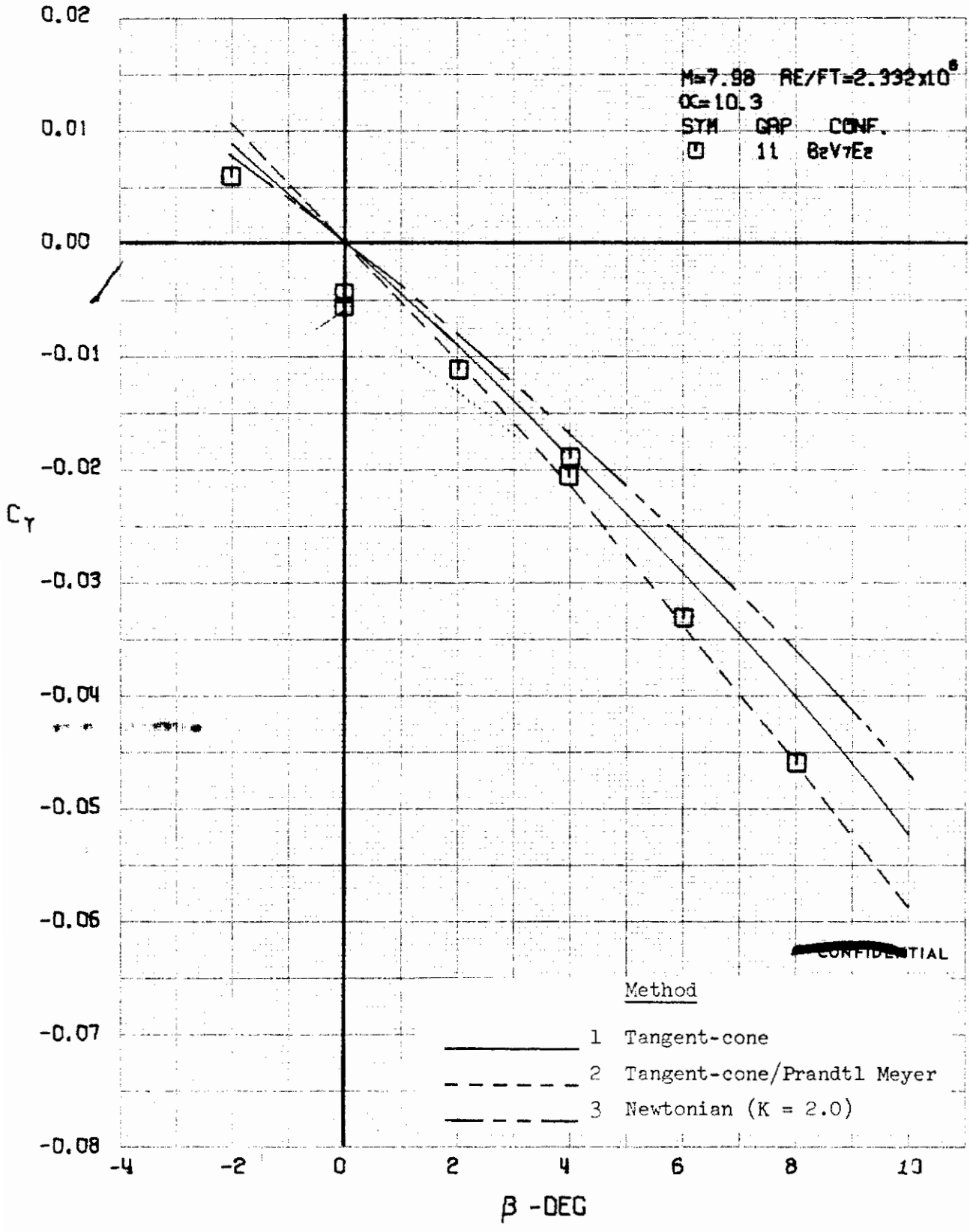

FIGURE 429 (U) COMPARISON OF ESTIMATED AND EXPERIMENTAL COEFFICIENTS - SIDE FORCE COEFFICIENT VARIATION WITH ANGLE OF YAW (M= 7.98)

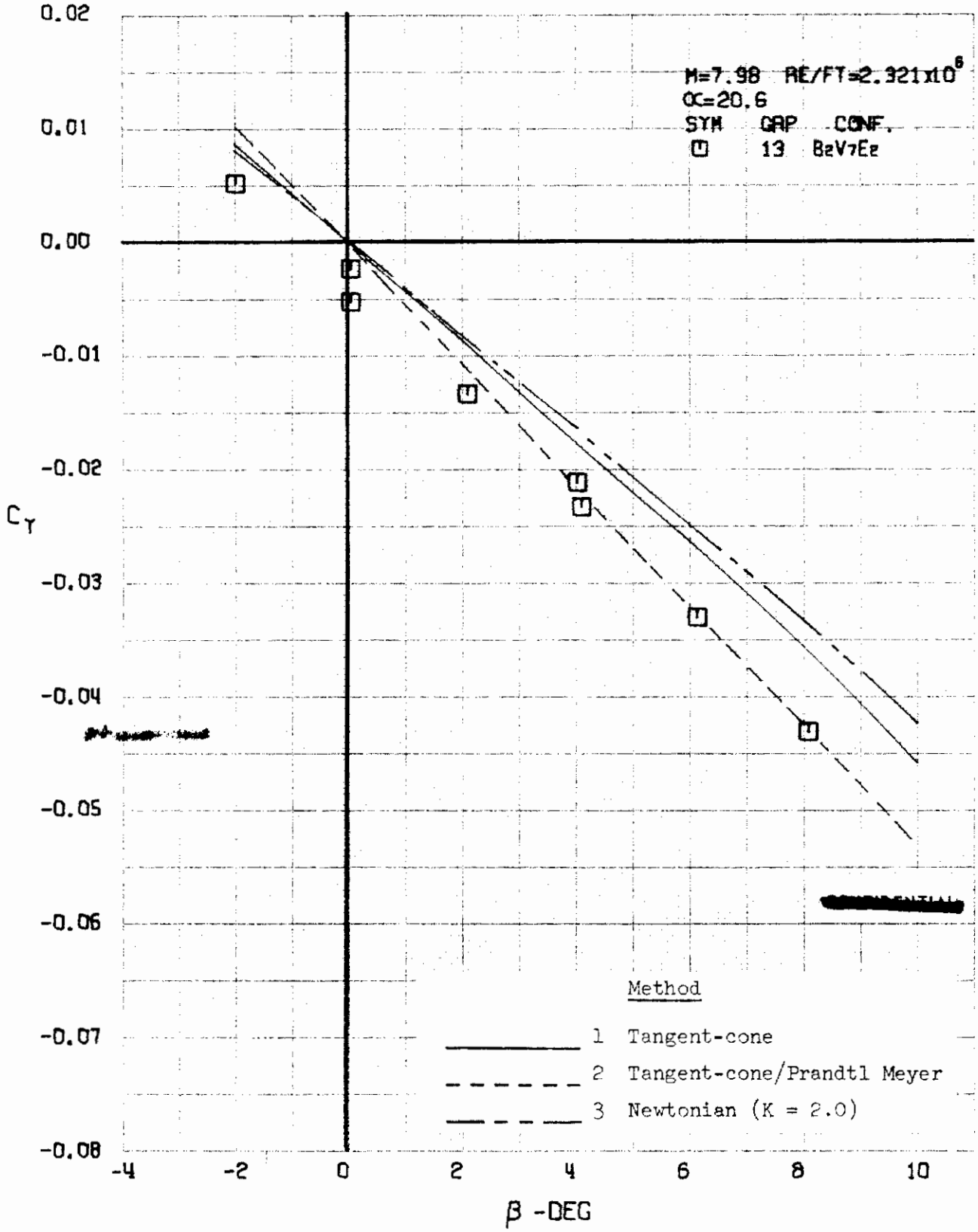

FIGURE 430 (U) COMPARISON OF ESTIMATED AND EXPERIMENTAL COEFFICIENTS - SIDE FORCE COEFFICIENT VARIATION WITH ANGLE OF YAW (M=7.98)

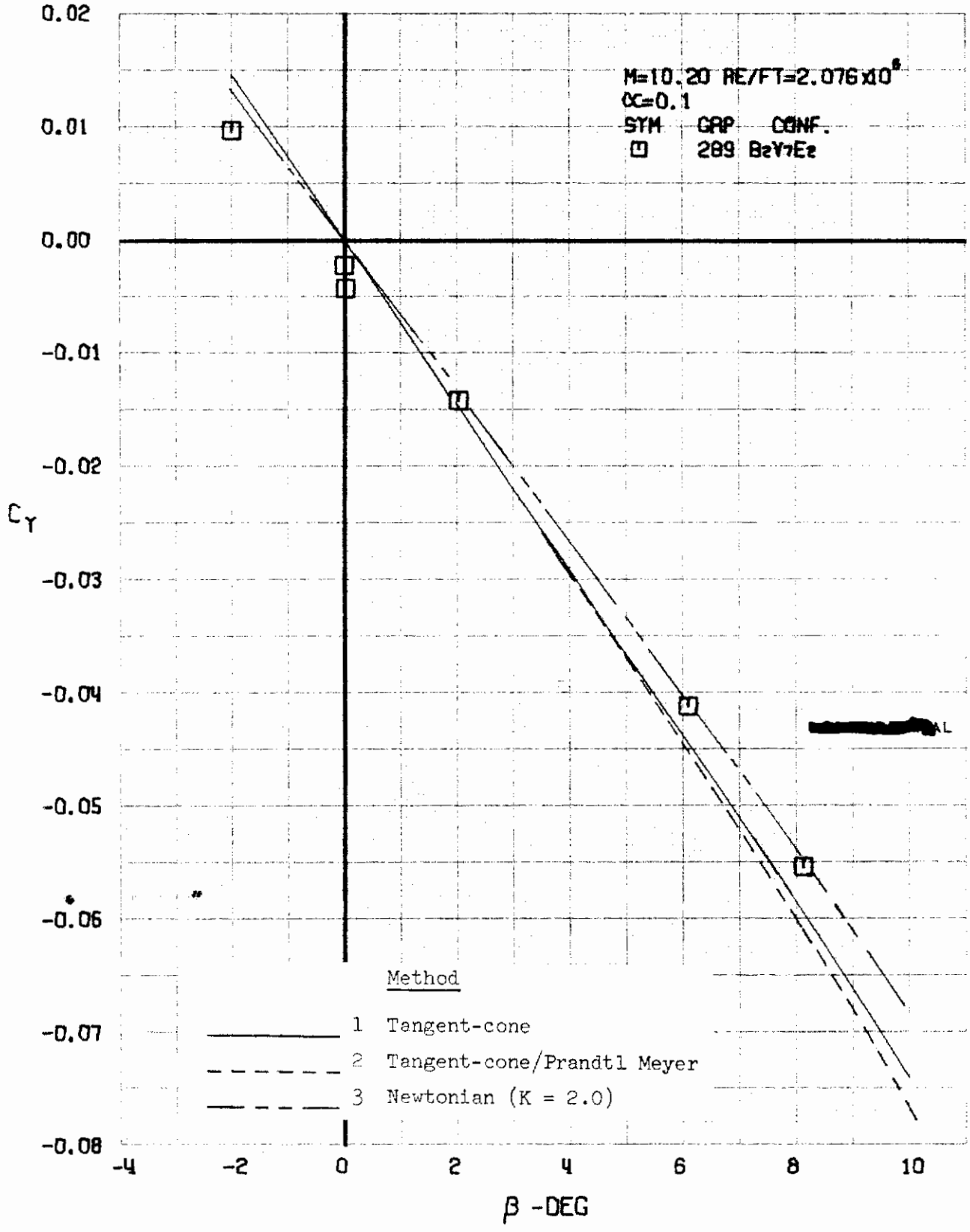

FIGURE 431 (U) COMPARISON OF ESTIMATED AND EXPERIMENTAL COEFFICIENTS - SIDE FORCE COEFFICIENT VARIATION WITH ANGLE OF YAW (M= 10.20

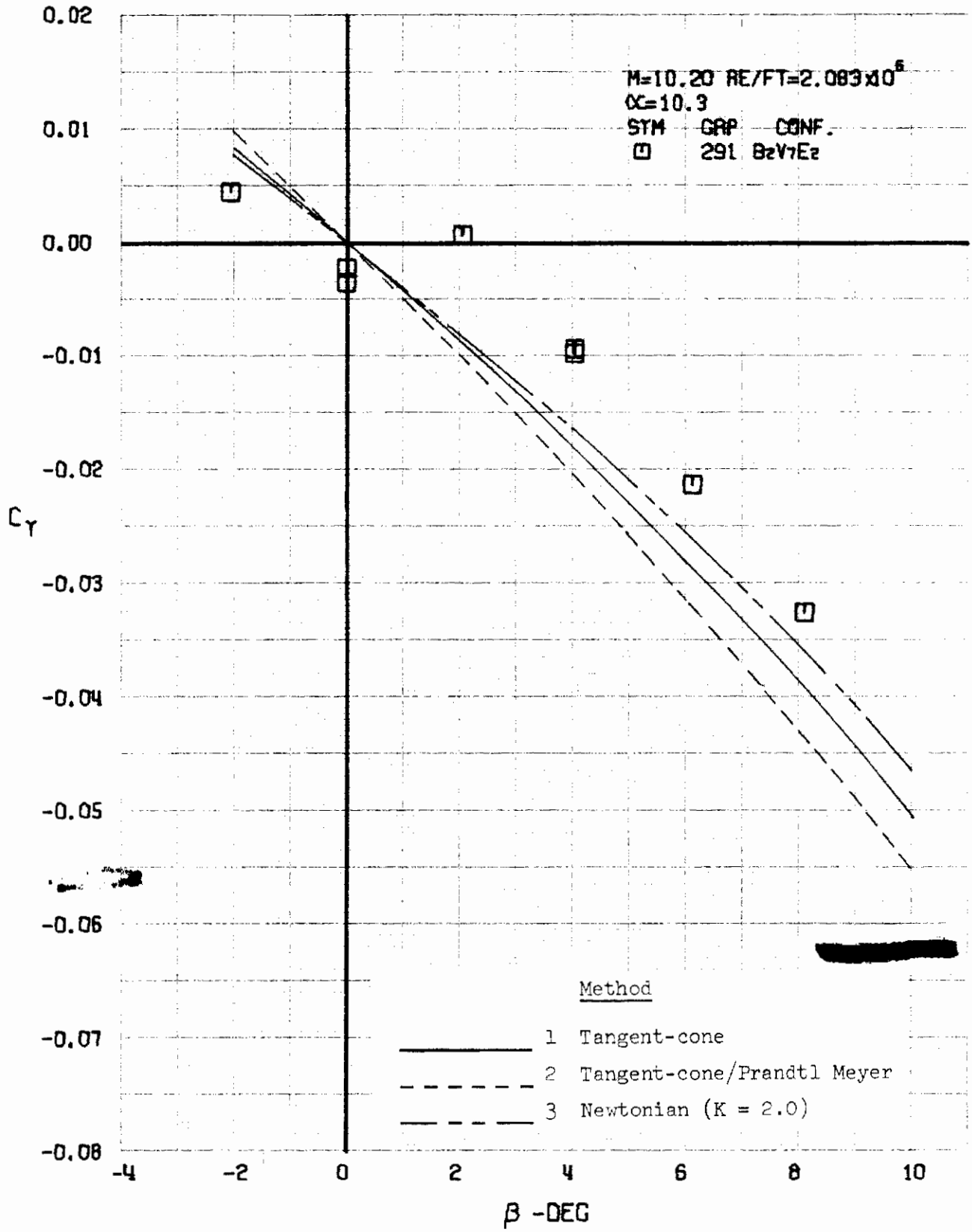

FIGURE 432 (U) COMPARISON OF ESTIMATED AND EXPERIMENTAL COEFFICIENTS - SIDE FORCE COEFFICIENT VARIATION WITH ANGLE OF YAW (M= 10.20

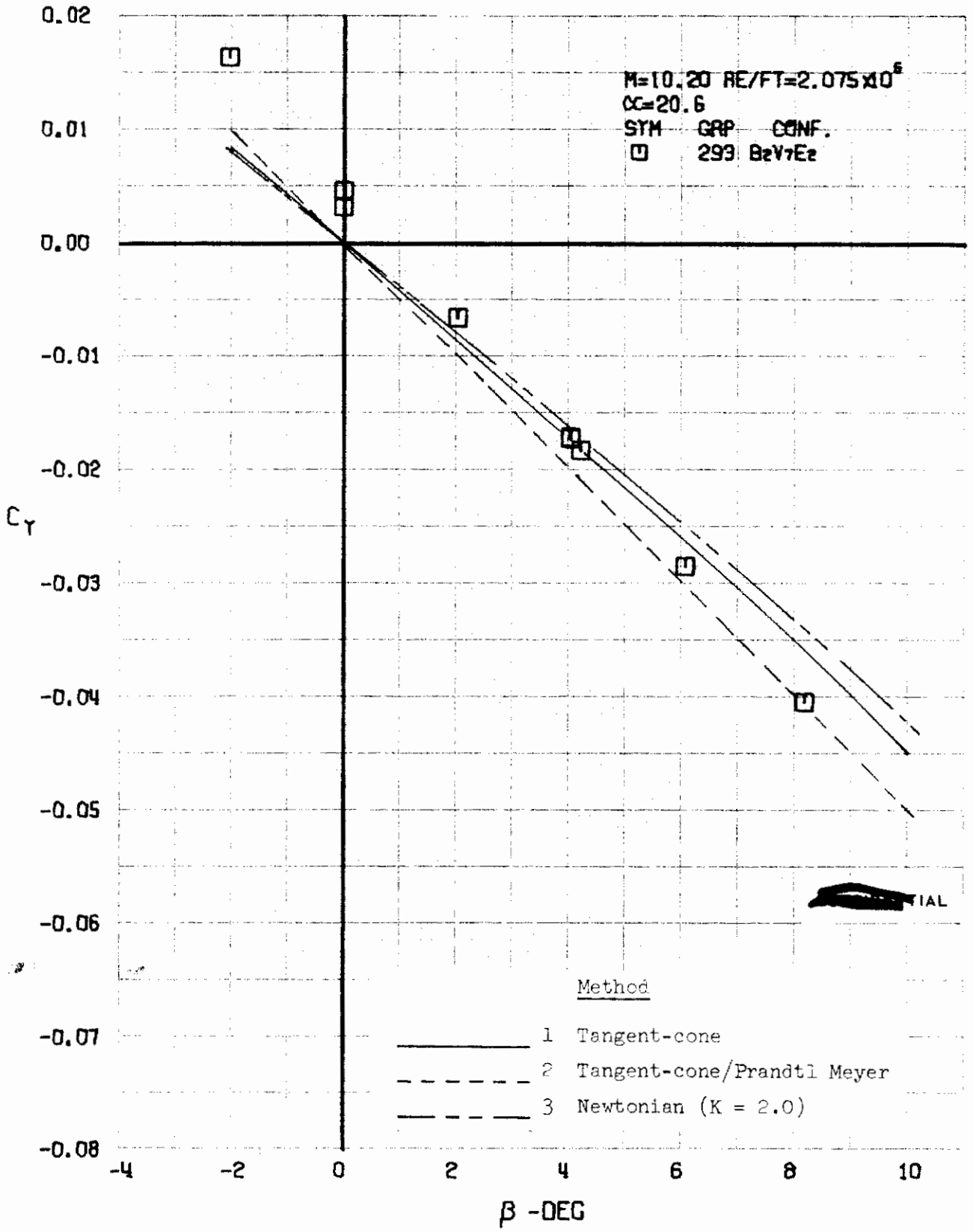

FIGURE 433 (U) COMPARISON OF ESTIMATED AND EXPERIMENTAL COEFFICIENTS - SIDE FORCE COEFFICIENT VARIATION WITH ANGLE OF YAW (M= 10.20

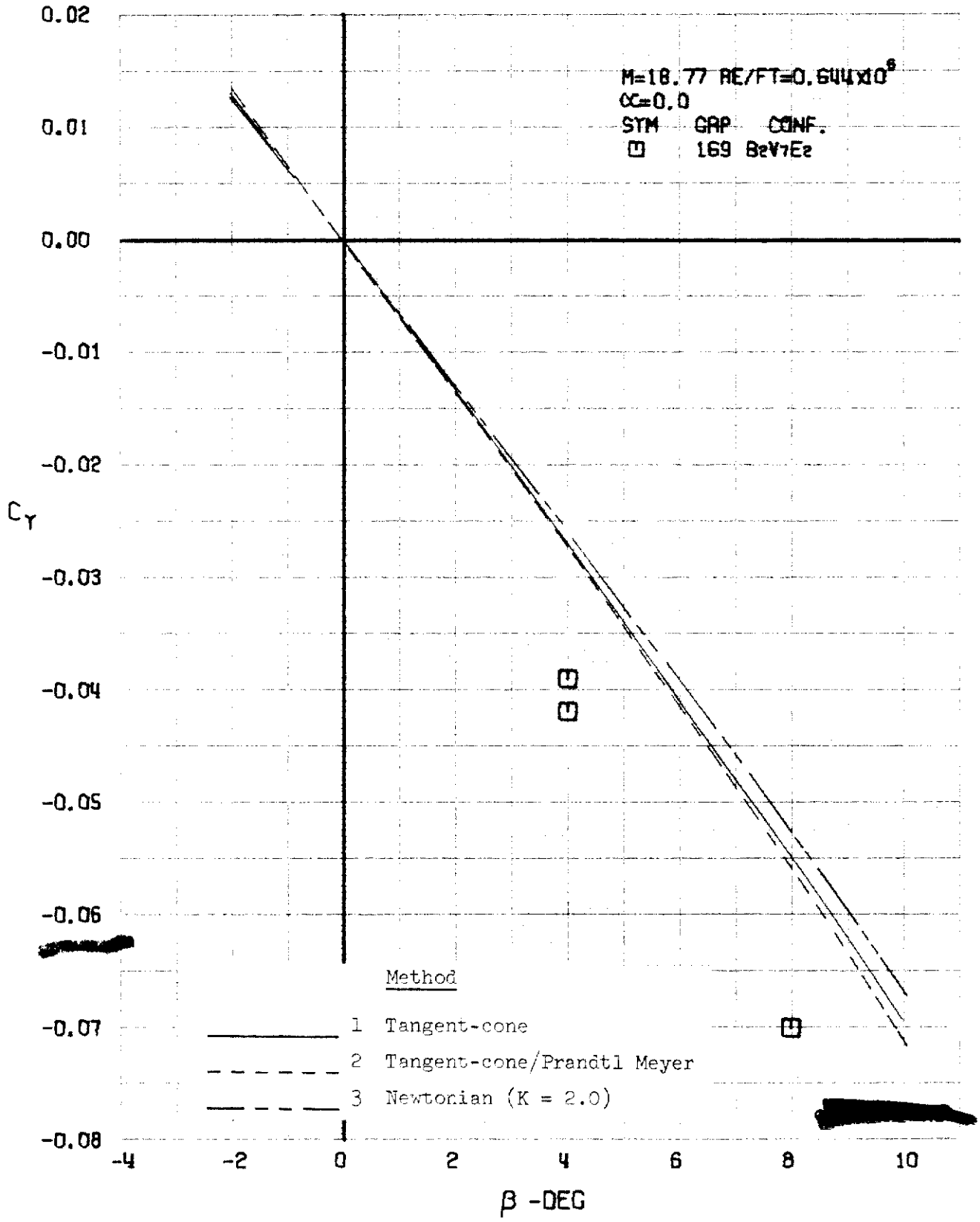

FIGURE 434 (U) COMPARISON OF ESTIMATED AND EXPERIMENTAL COEFFICIENTS - SIDE FORCE COEFFICIENT VARIATION WITH ANGLE OF YAW (M= 18.77

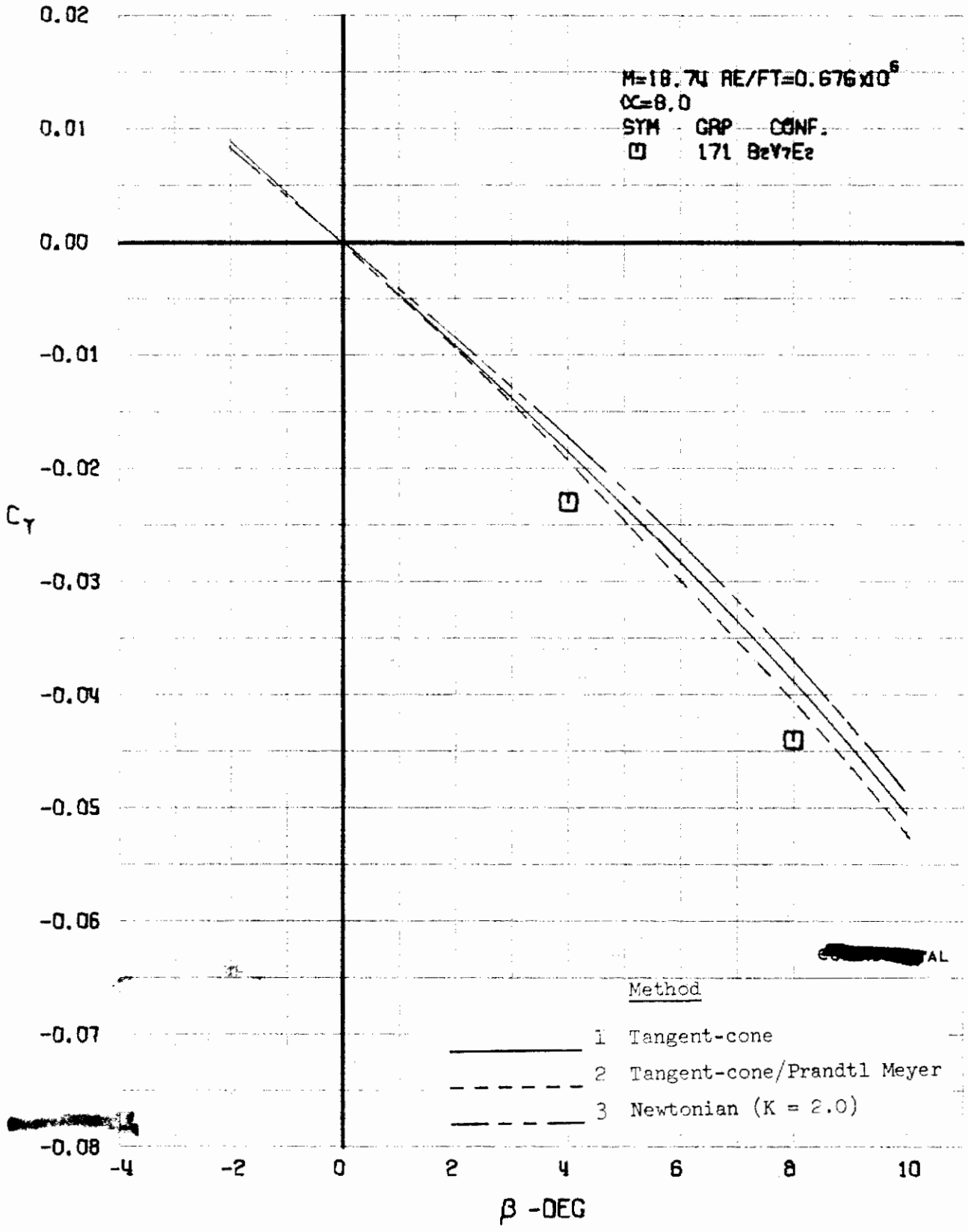

FIGURE 435 (U) COMPARISON OF ESTIMATED AND EXPERIMENTAL COEFFICIENTS - SIDE FORCE COEFFICIENT VARIATION WITH ANGLE OF YAW (M= 18.74

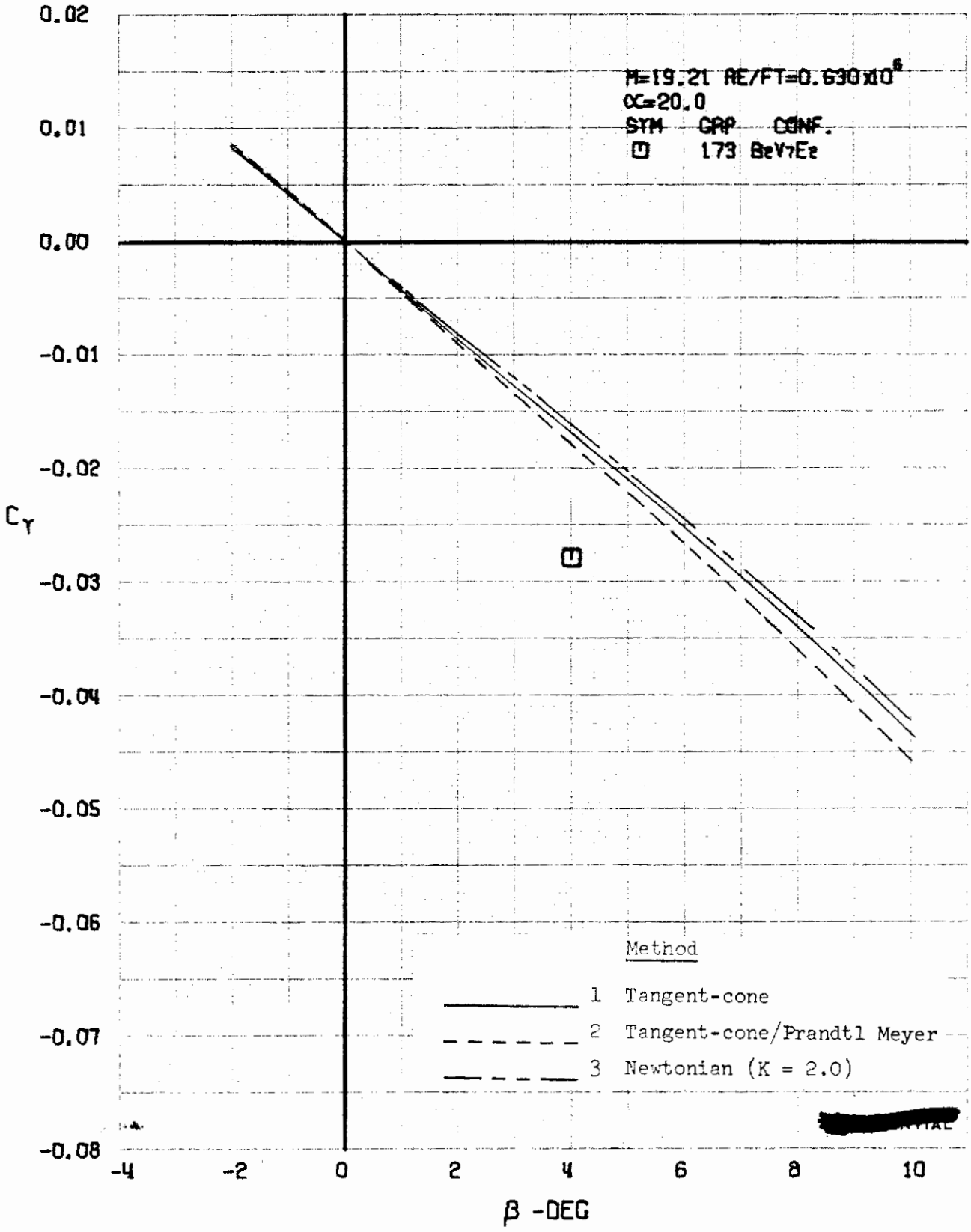

FIGURE 436 (U) COMPARISON OF ESTIMATED AND EXPERIMENTAL COEFFICIENTS - SIDE FORCE COEFFICIENT VARIATION WITH ANGLE OF YAW (M= 19.21

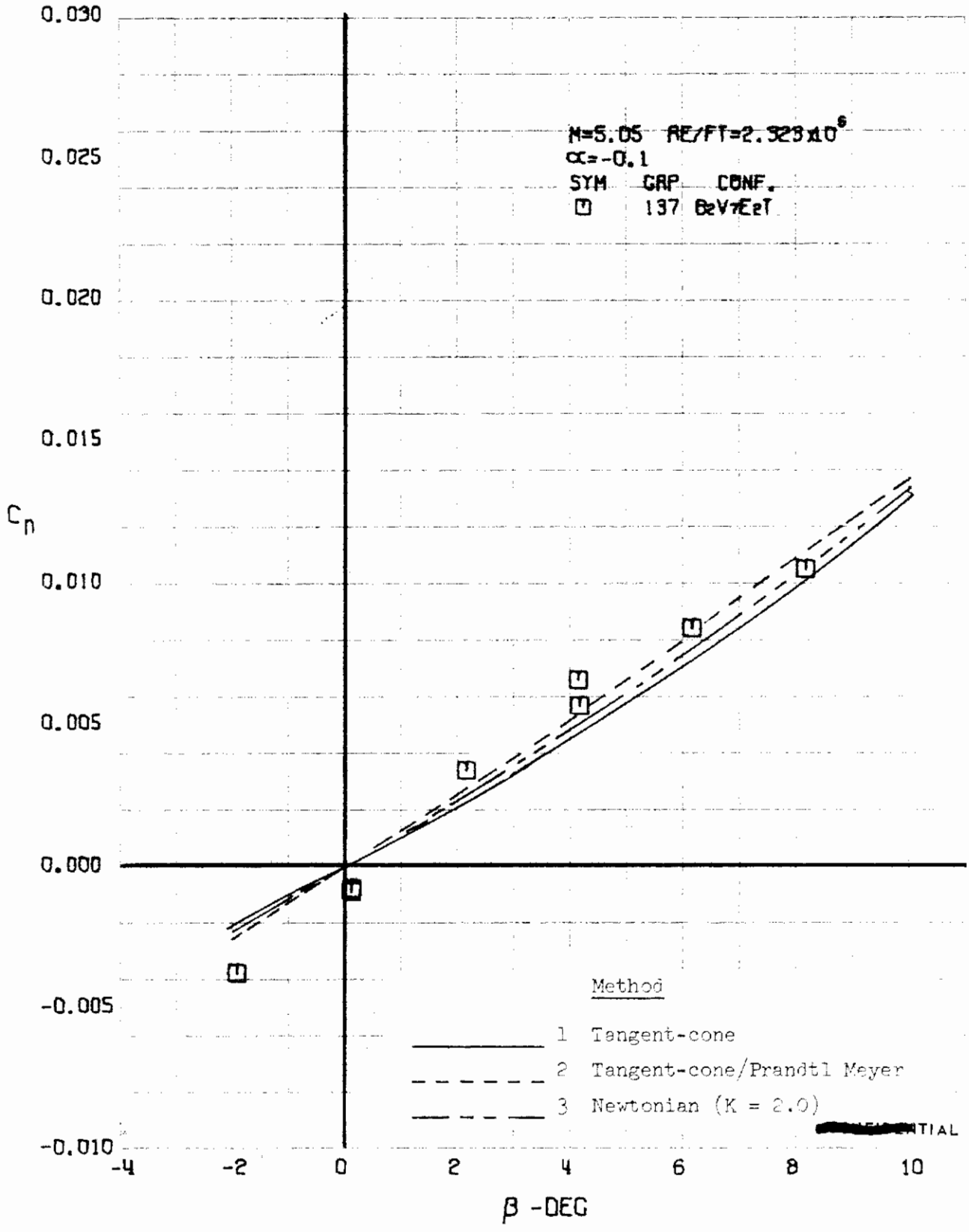

FIGURE 437 (U) COMPARISON OF ESTIMATED AND EXPERIMENTAL COEFFICIENTS - YAWING MOMENT COEFFICIENT VARIATION WITH ANGLE OF YAW (M=5.05)

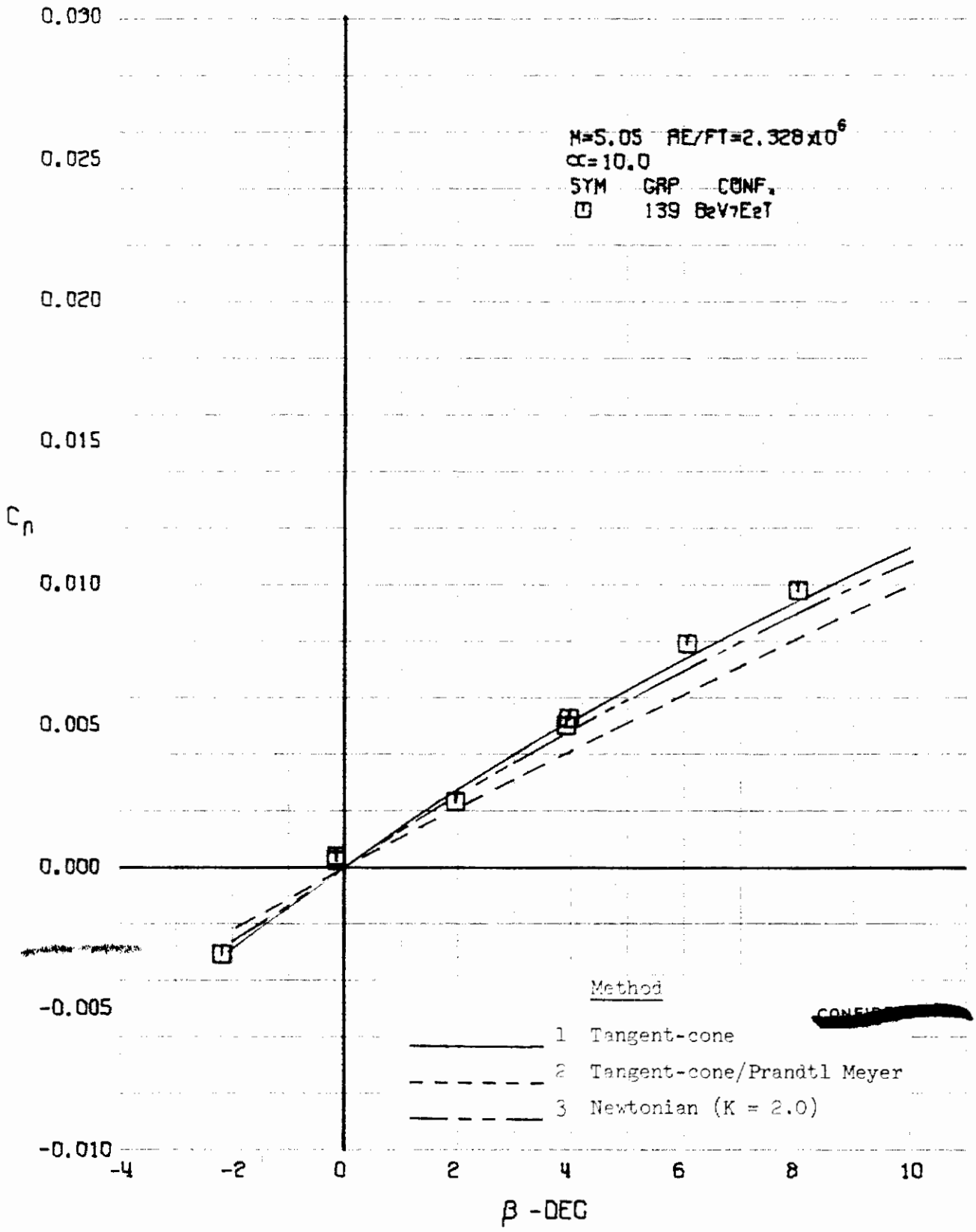

FIGURE 438 (U) COMPARISON OF ESTIMATED AND EXPERIMENTAL COEFFICIENTS - YAWING MOMENT COEFFICIENT VARIATION WITH ANGLE OF YAW (M=5.05)

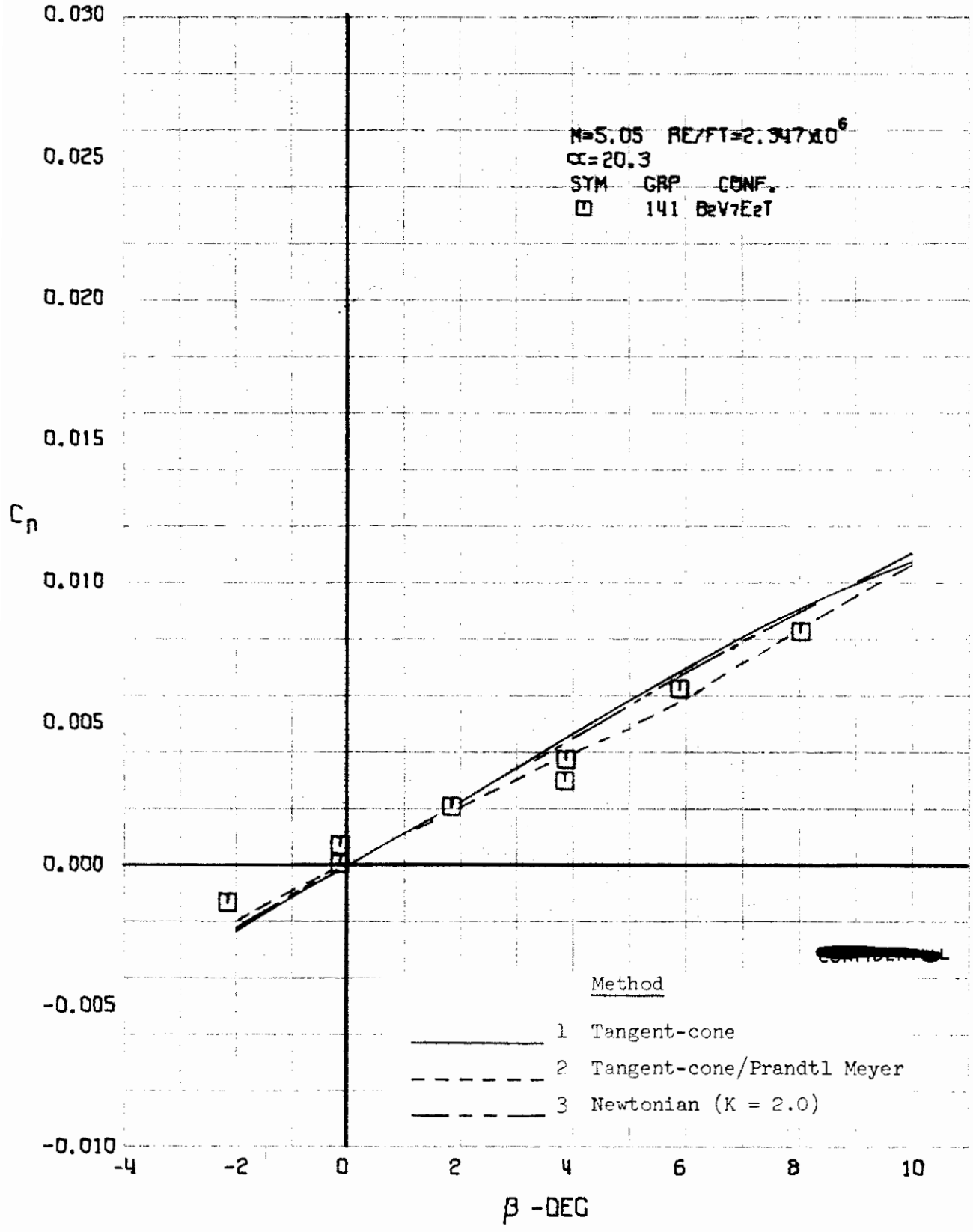

FIGURE 439 (U) COMPARISON OF ESTIMATED AND EXPERIMENTAL COEFFICIENTS - YAWING MOMENT COEFFICIENT VARIATION WITH ANGLE OF YAW (M=5.05)

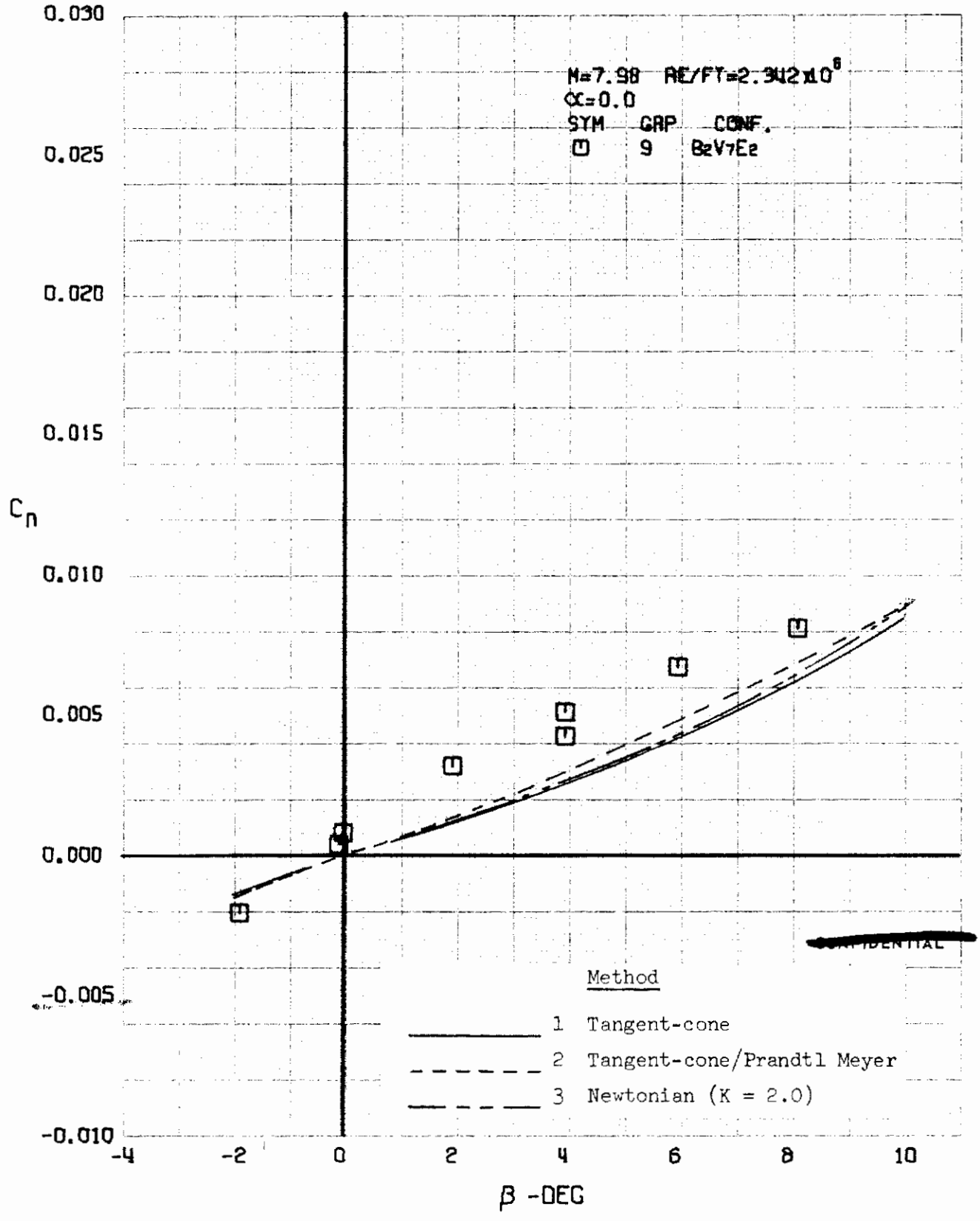

FIGURE 440 (U) COMPARISON OF ESTIMATED AND EXPERIMENTAL COEFFICIENTS - YAWING MOMENT COEFFICIENT VARIATION WITH ANGLE OF YAW (M= 7.98)

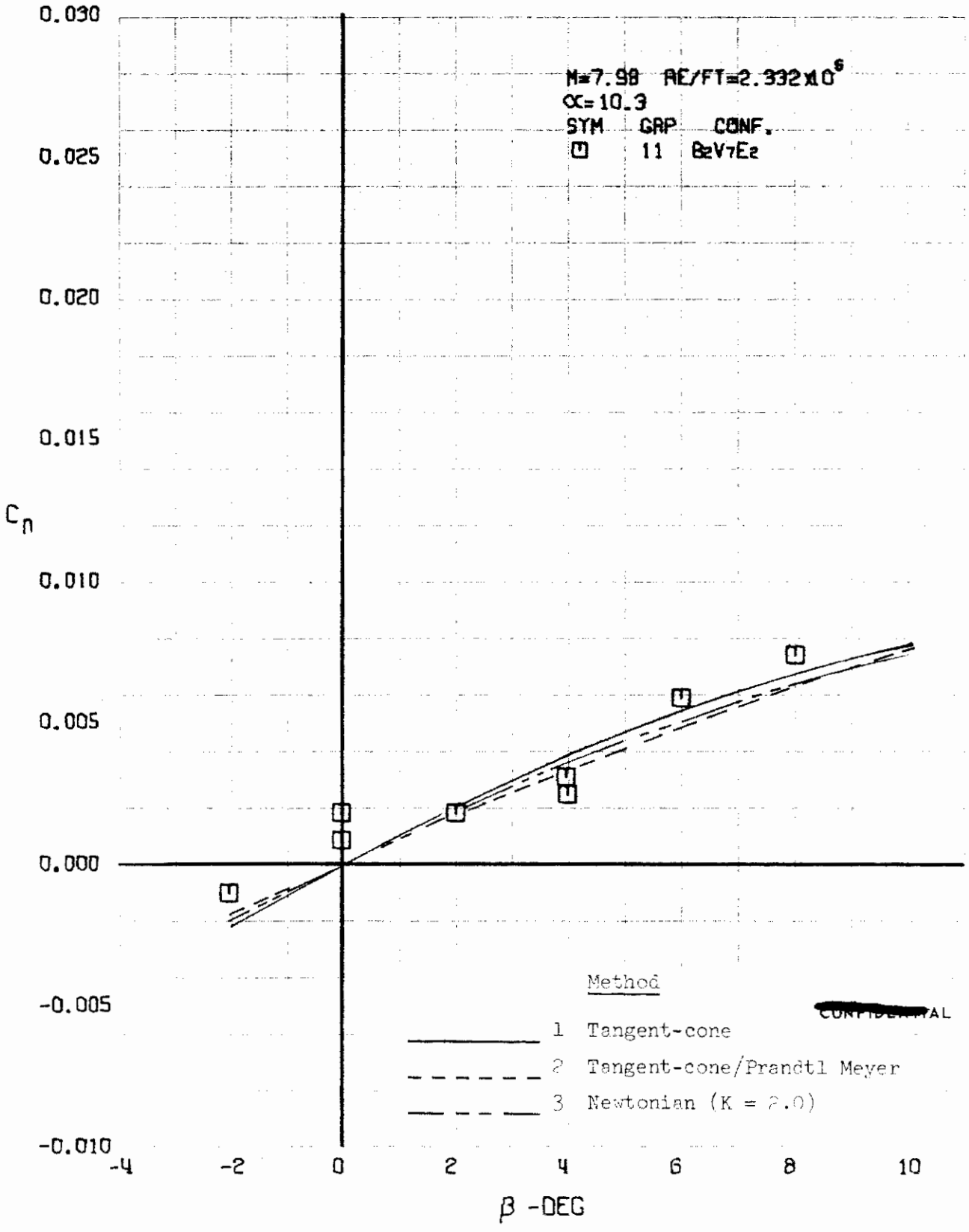

FIGURE 441 (U) COMPARISON OF ESTIMATED AND EXPERIMENTAL COEFFICIENTS - YAWING MOMENT COEFFICIENT VARIATION WITH ANGLE OF YAW (M= 7.98)

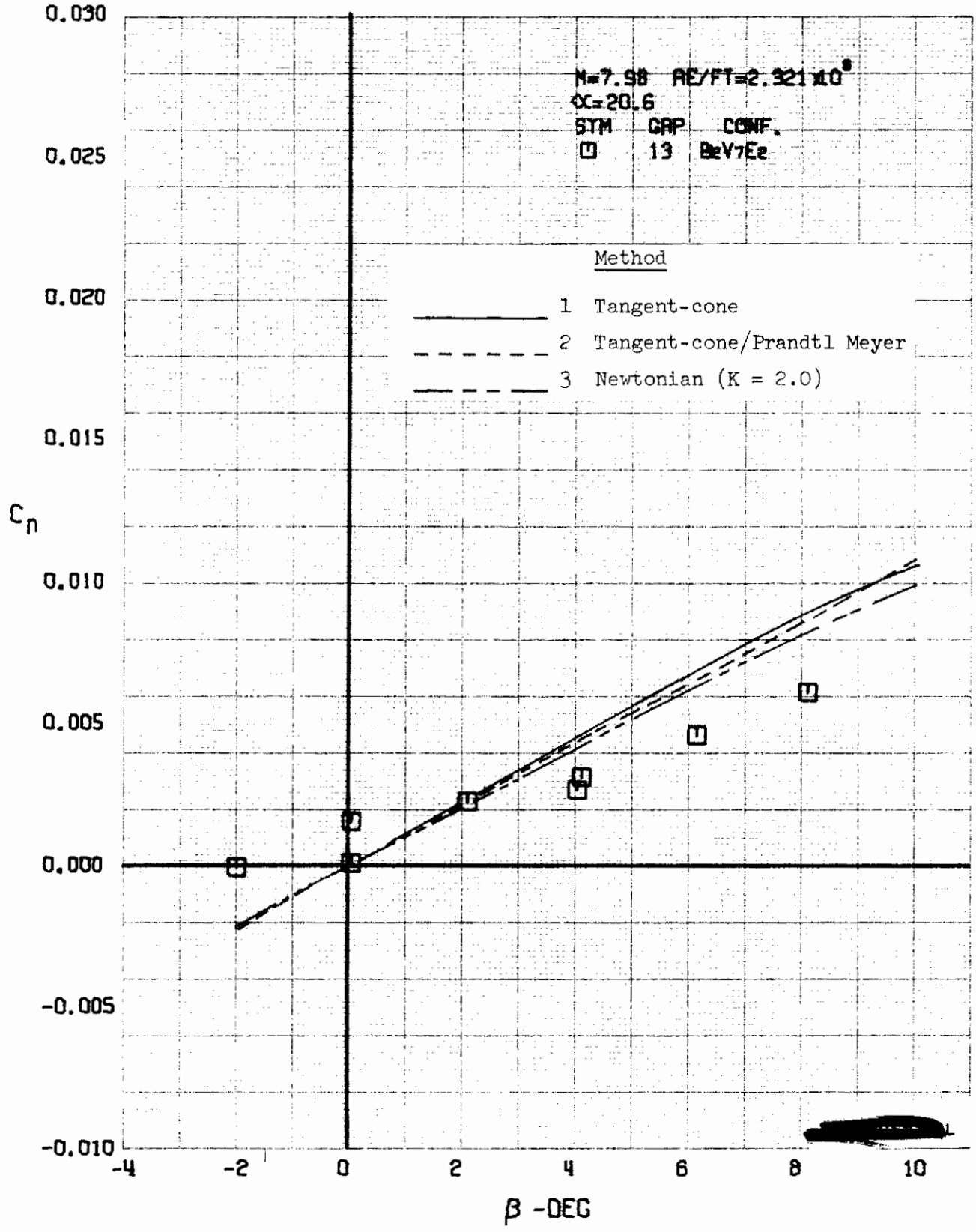

FIGURE 442 (U) COMPARISON OF ESTIMATED AND EXPERIMENTAL COEFFICIENTS - YAWING MOMENT COEFFICIENT VARIATION WITH ANGLE OF YAW (M= 7.98)

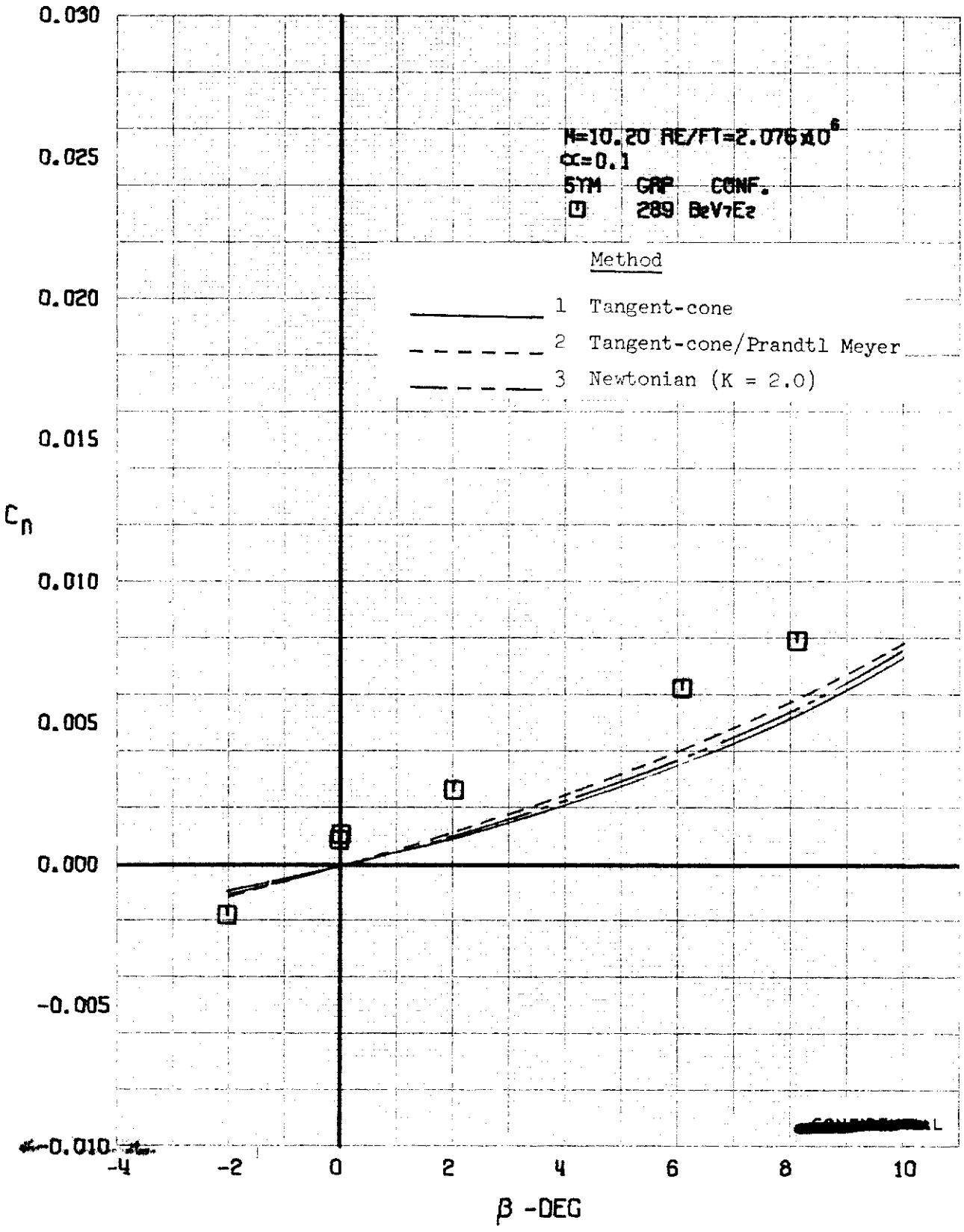

FIGURE 443 (U) COMPARISON OF ESTIMATED AND EXPERIMENTAL COEFFICIENTS - YAWING MOMENT COEFFICIENT VARIATION WITH ANGLE OF YAW (M= 10.20

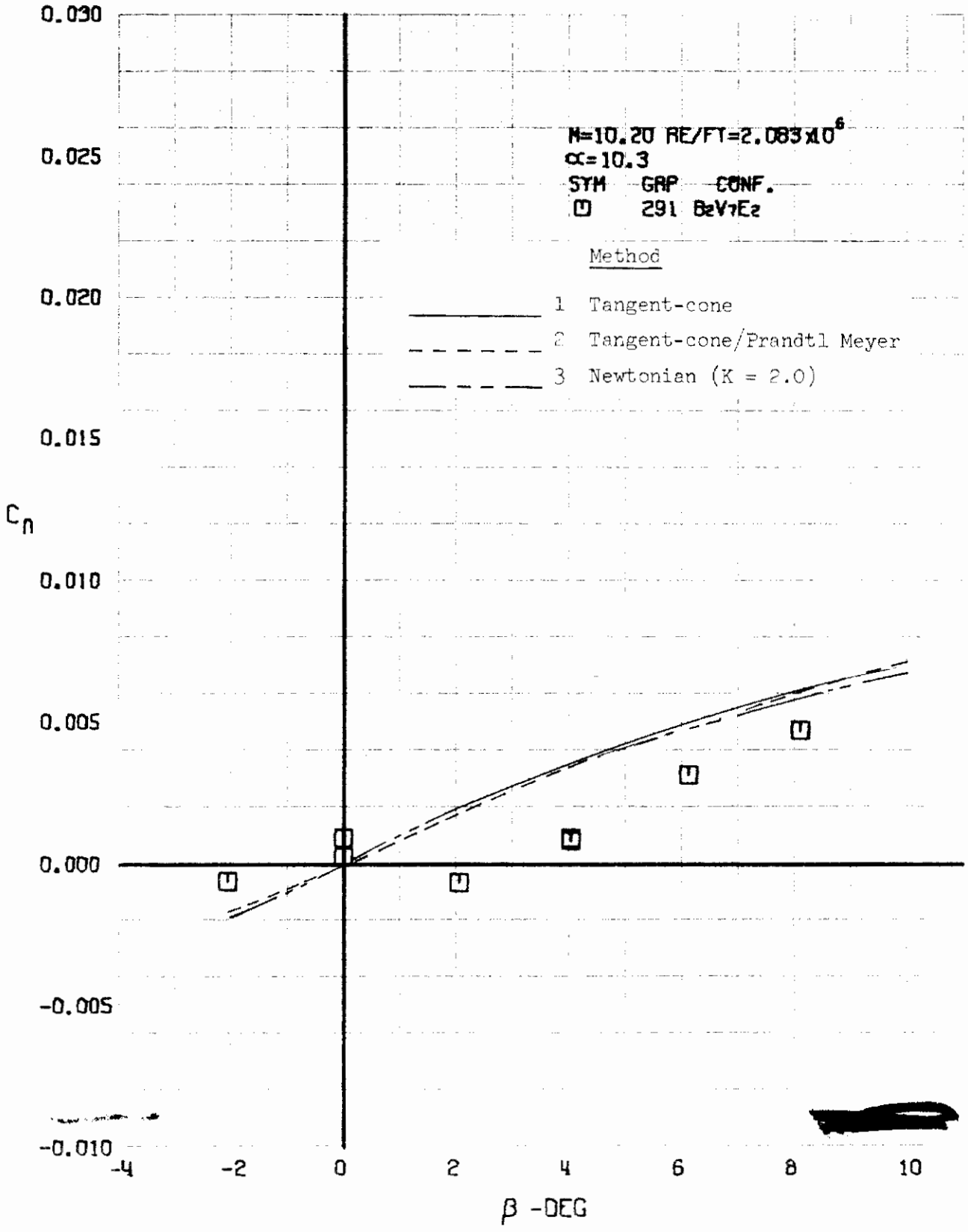

FIGURE 444 (U) COMPARISON OF ESTIMATED AND EXPERIMENTAL COEFFICIENTS - YAWING MOMENT COEFFICIENT VARIATION WITH ANGLE OF YAW (M=10.20

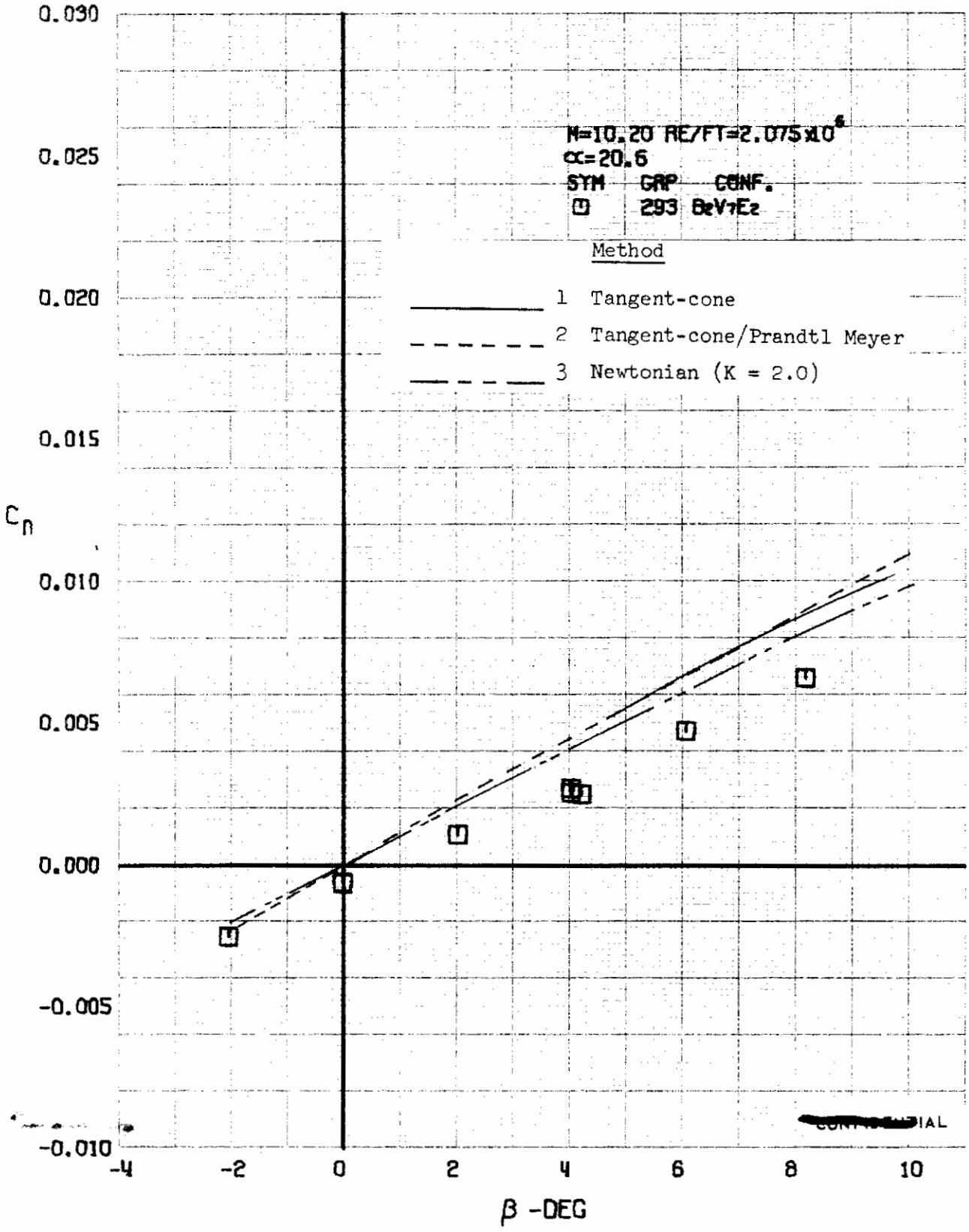

FIGURE 445 (U) COMPARISON OF ESTIMATED AND EXPERIMENTAL COEFFICIENTS - YAWING MOMENT COEFFICIENT VARIATION WITH ANGLE OF YAW (M= 10.20

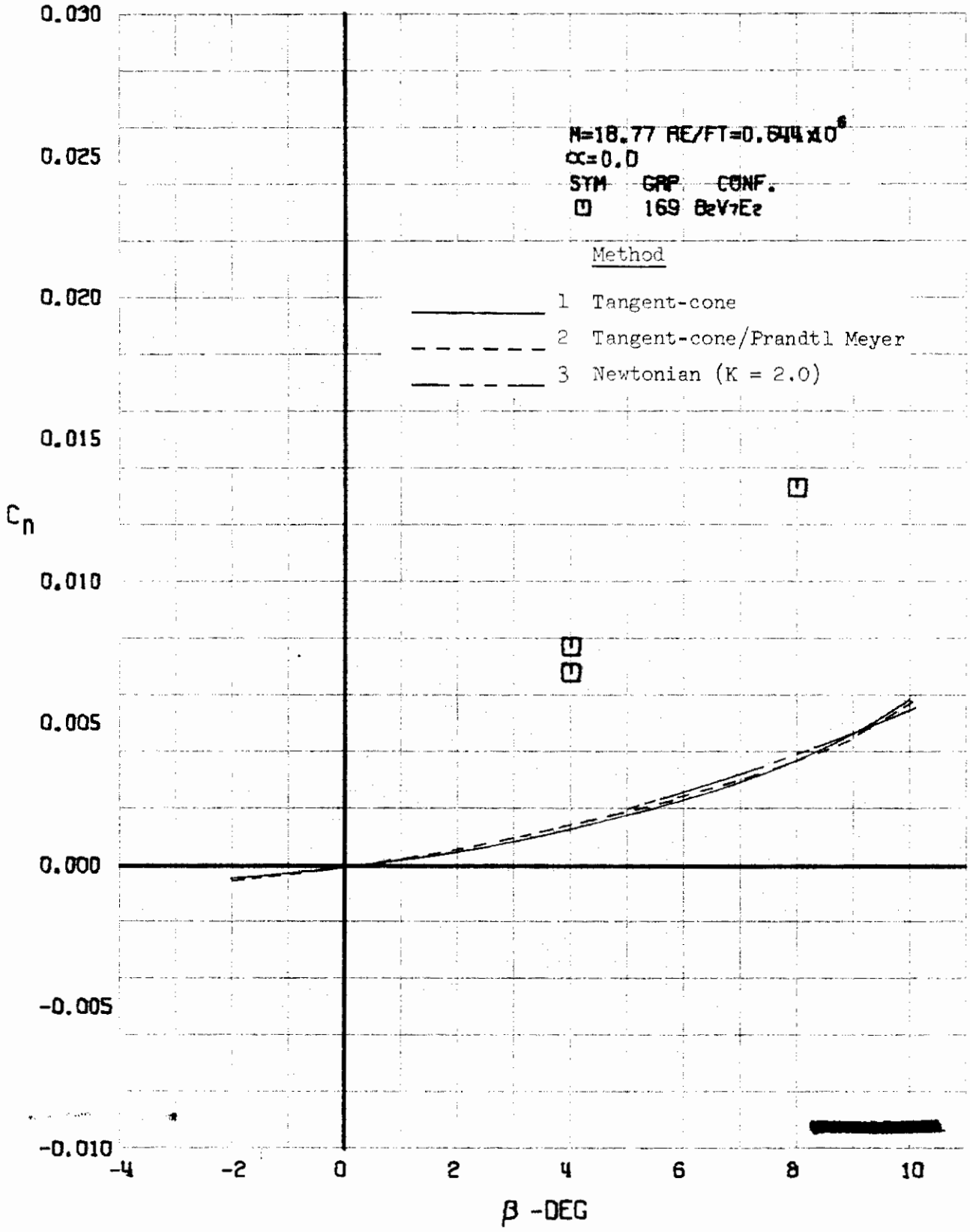

FIGURE 446 (U) COMPARISON OF ESTIMATED AND EXPERIMENTAL COEFFICIENTS - YAWING MOMENT COEFFICIENT VARIATION WITH ANGLE OF YAW (M=18.77)

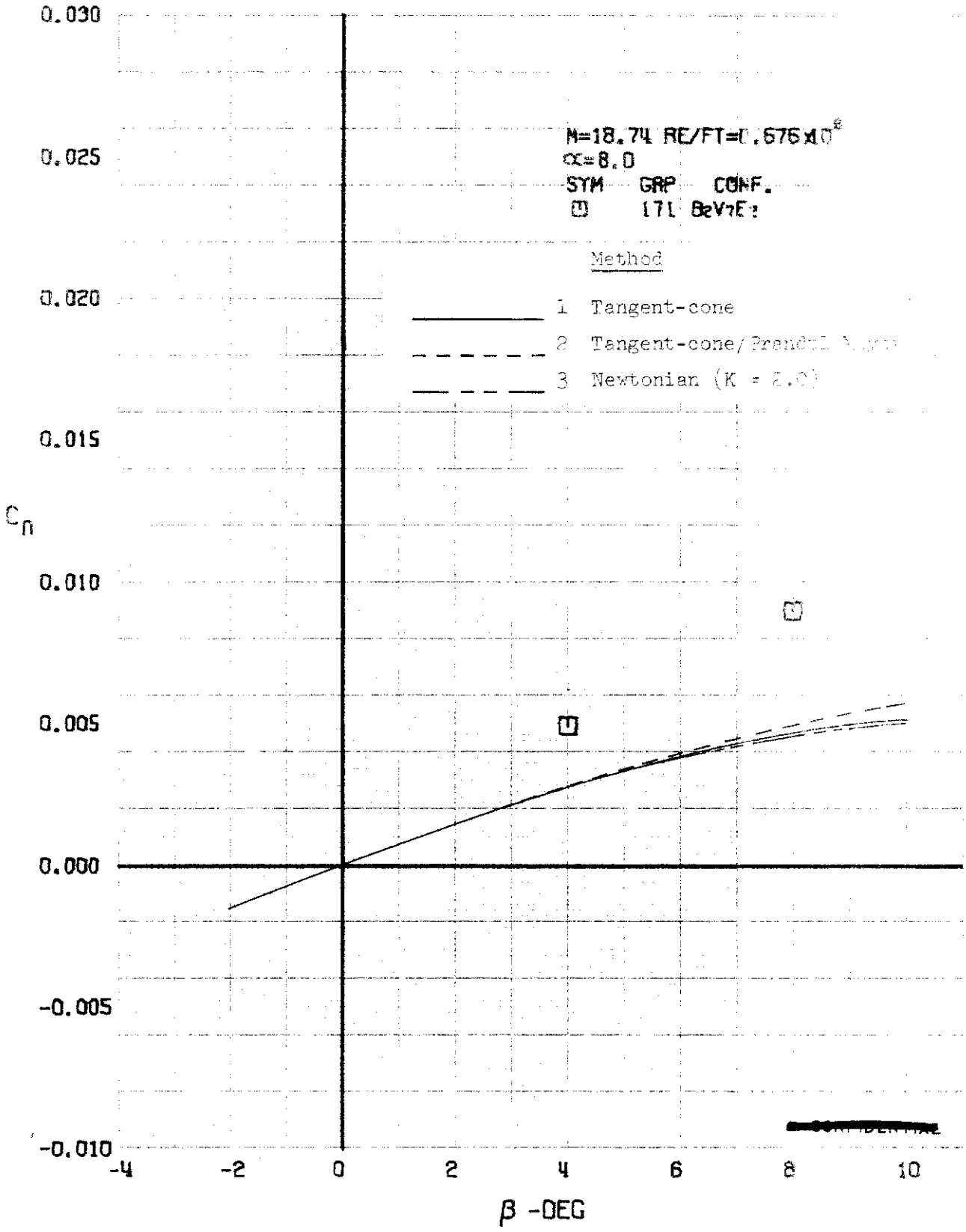

FIGURE 447 (U) COMPARISON OF ESTIMATED AND EXPERIMENTAL COEFFICIENTS - YAWING MOMENT COEFFICIENT VARIATION WITH ANGLE OF YAW (M= 18.74

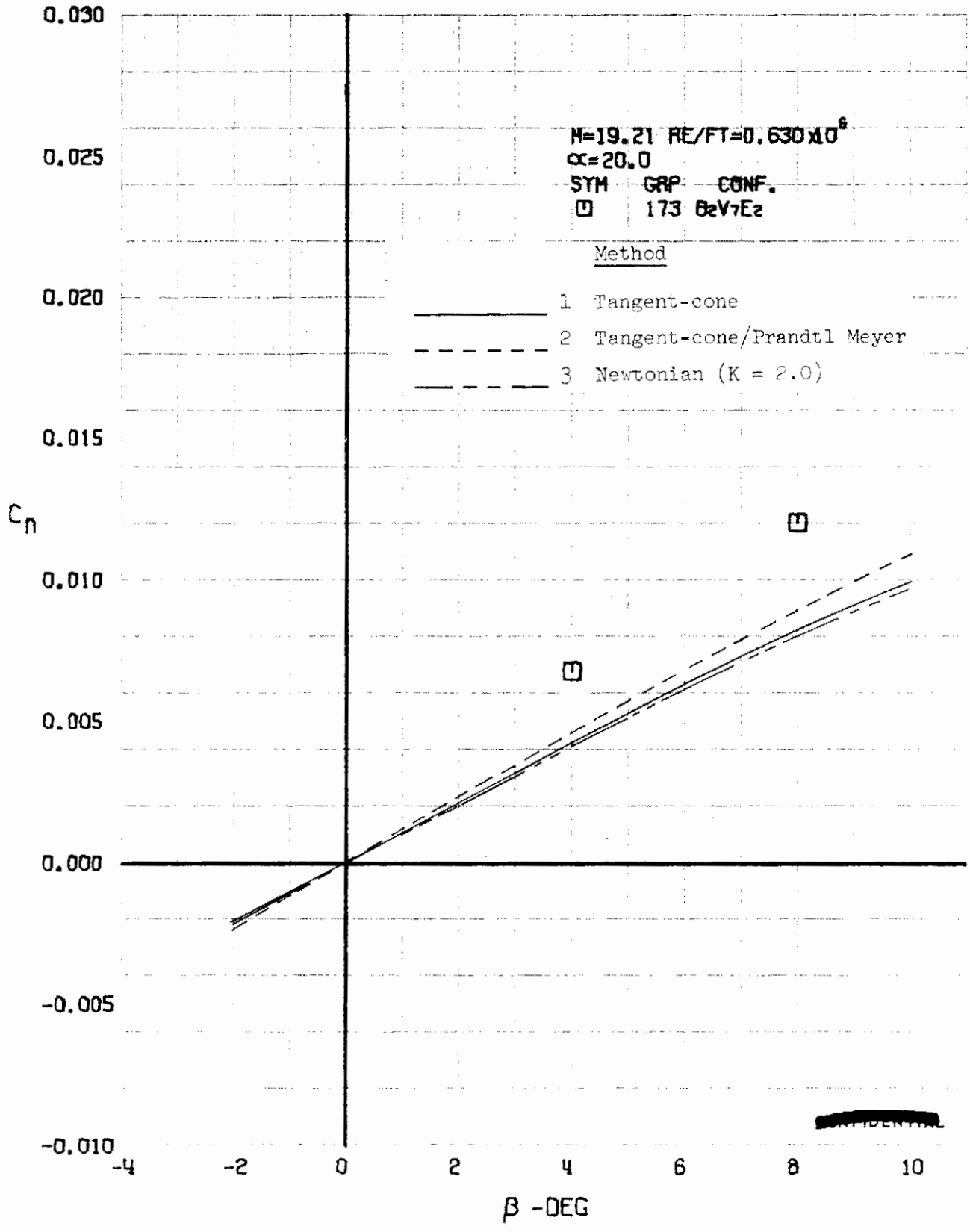

FIGURE 448 (U) COMPARISON OF ESTIMATED AND EXPERIMENTAL COEFFICIENTS - YAWING MOMENT COEFFICIENT VARIATION WITH ANGLE OF YAW (M=19.21)

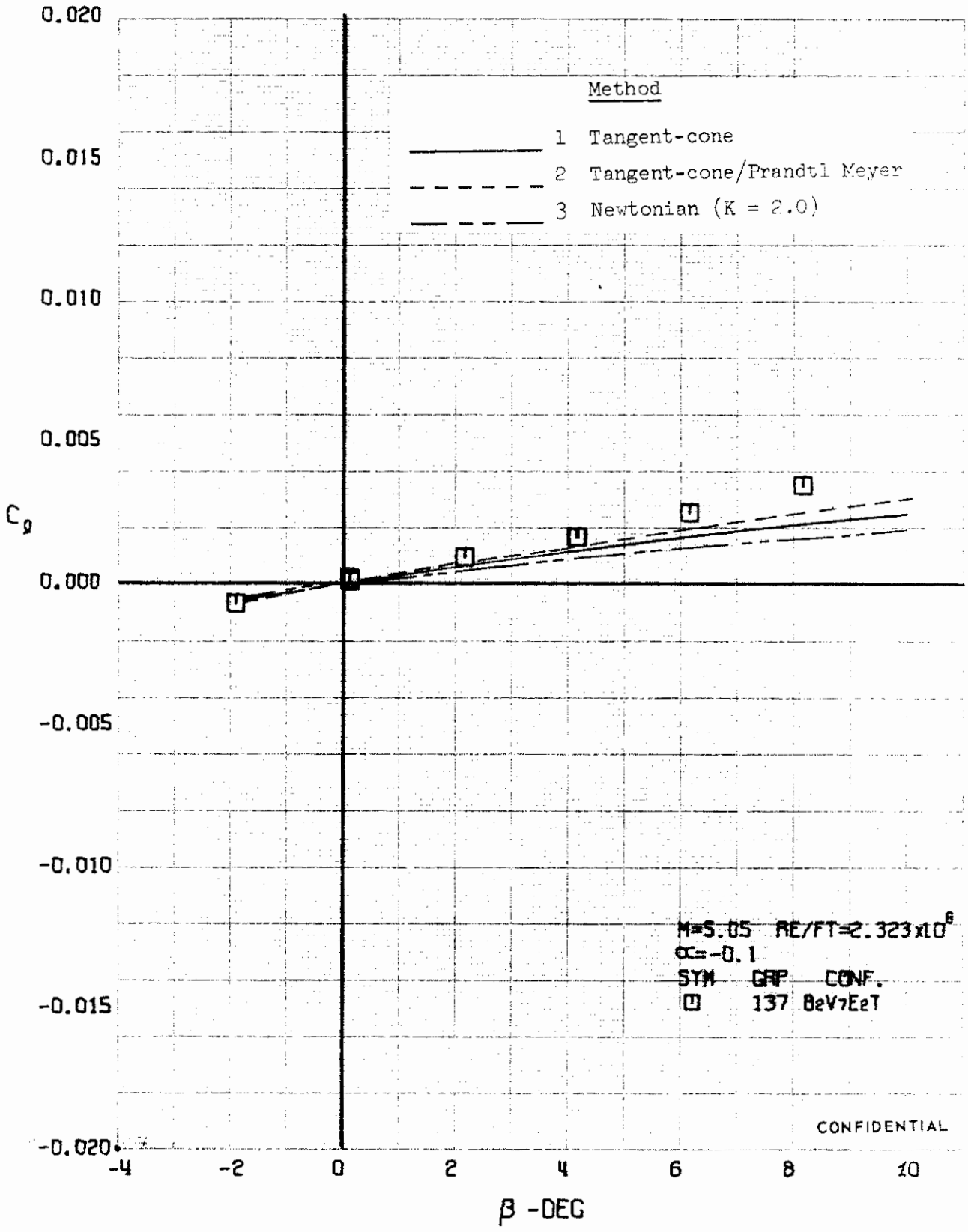

FIGURE 449 (U) COMPARISON OF ESTIMATED AND EXPERIMENTAL COEFFICIENTS - ROLLING MOMENT COEFFICIENT VARIATION WITH ANGLE OF YAW (M=5.05)

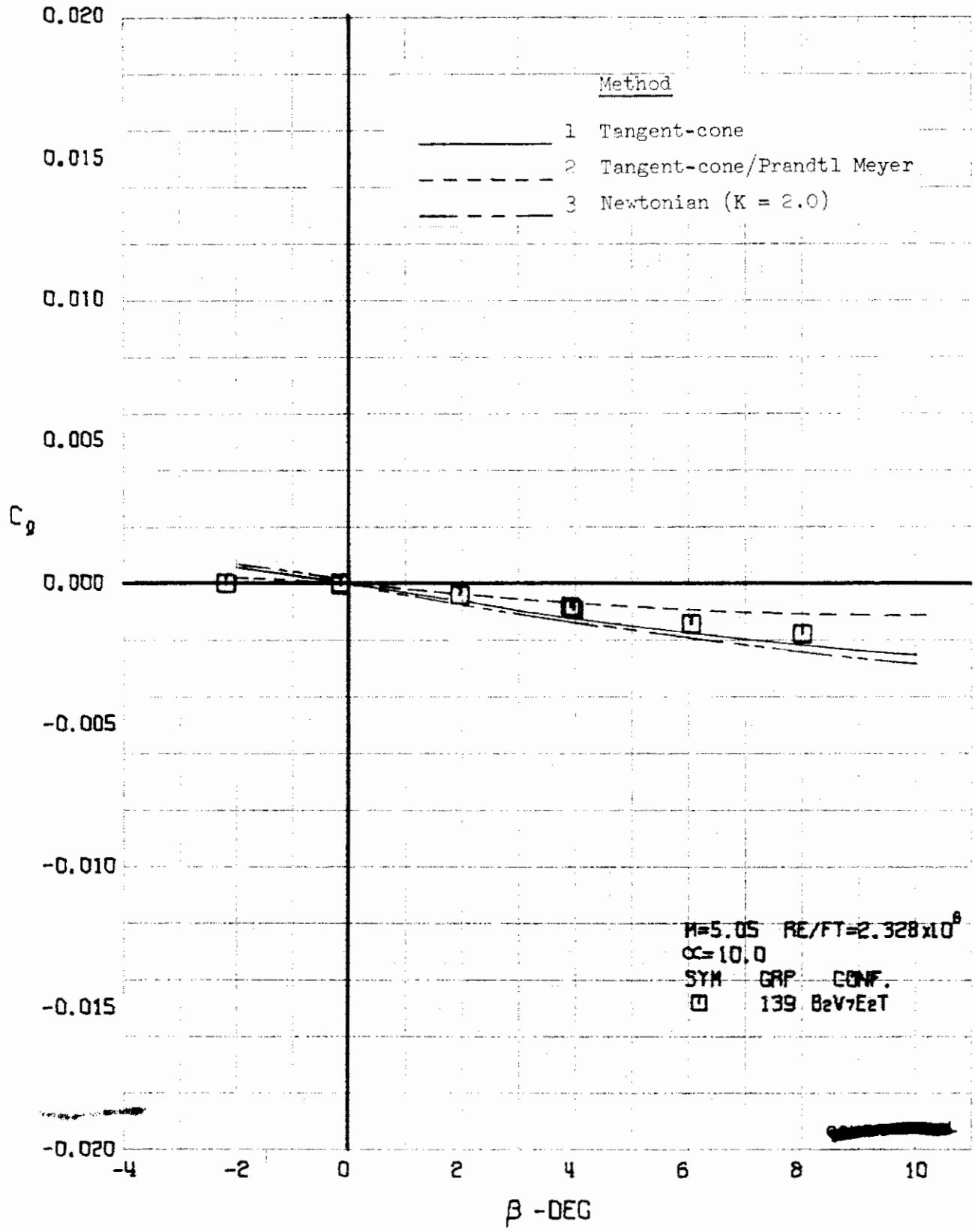

FIGURE 450 (U) COMPARISON OF ESTIMATED AND EXPERIMENTAL COEFFICIENTS - ROLLING MOMENT COEFFICIENT VARIATION WITH ANGLE OF YAW (M=5.05)

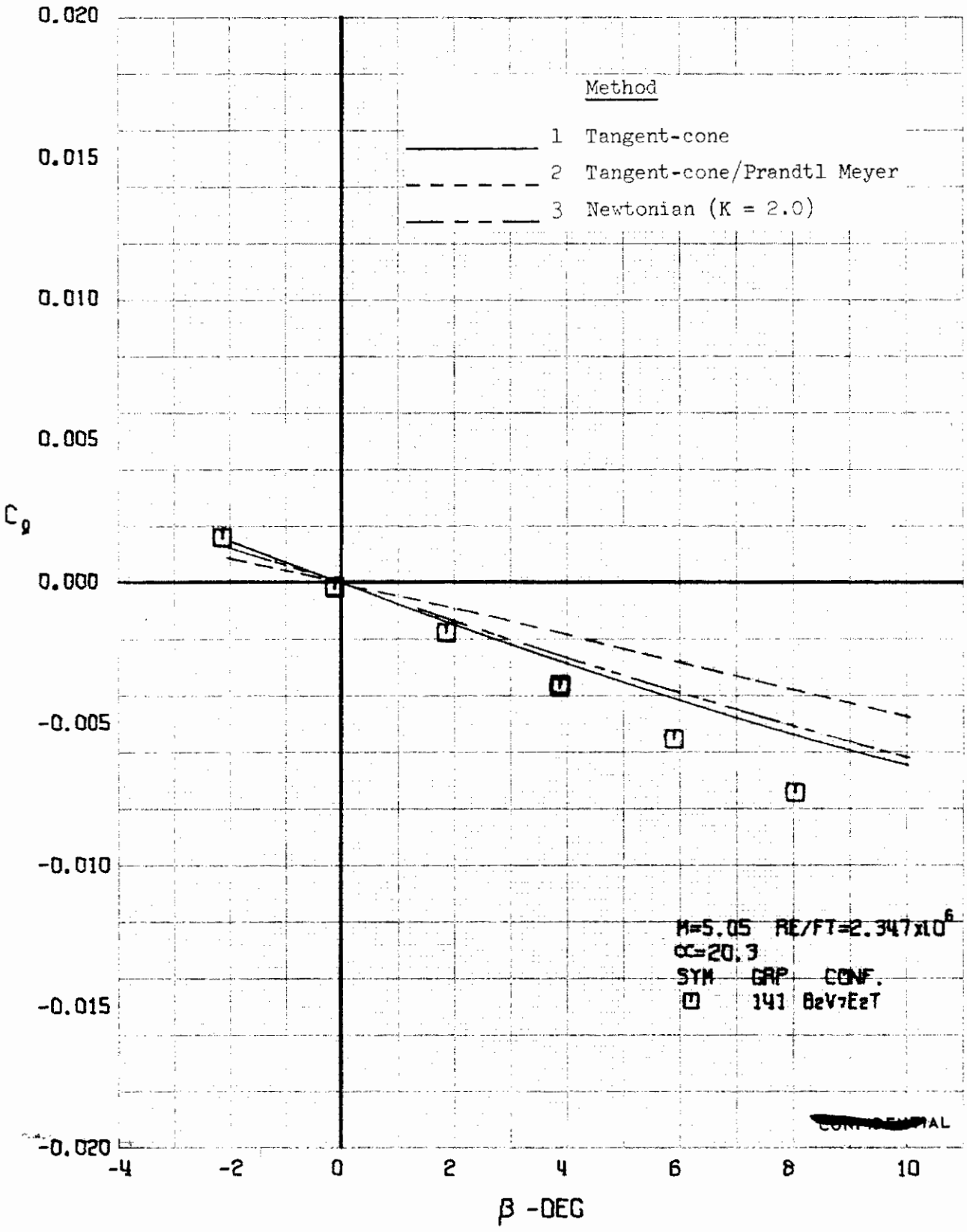

FIGURE 451 (U) COMPARISON OF ESTIMATED AND EXPERIMENTAL COEFFICIENTS - ROLLING MOMENT COEFFICIENT VARIATION WITH ANGLE OF YAW (M=5.05)

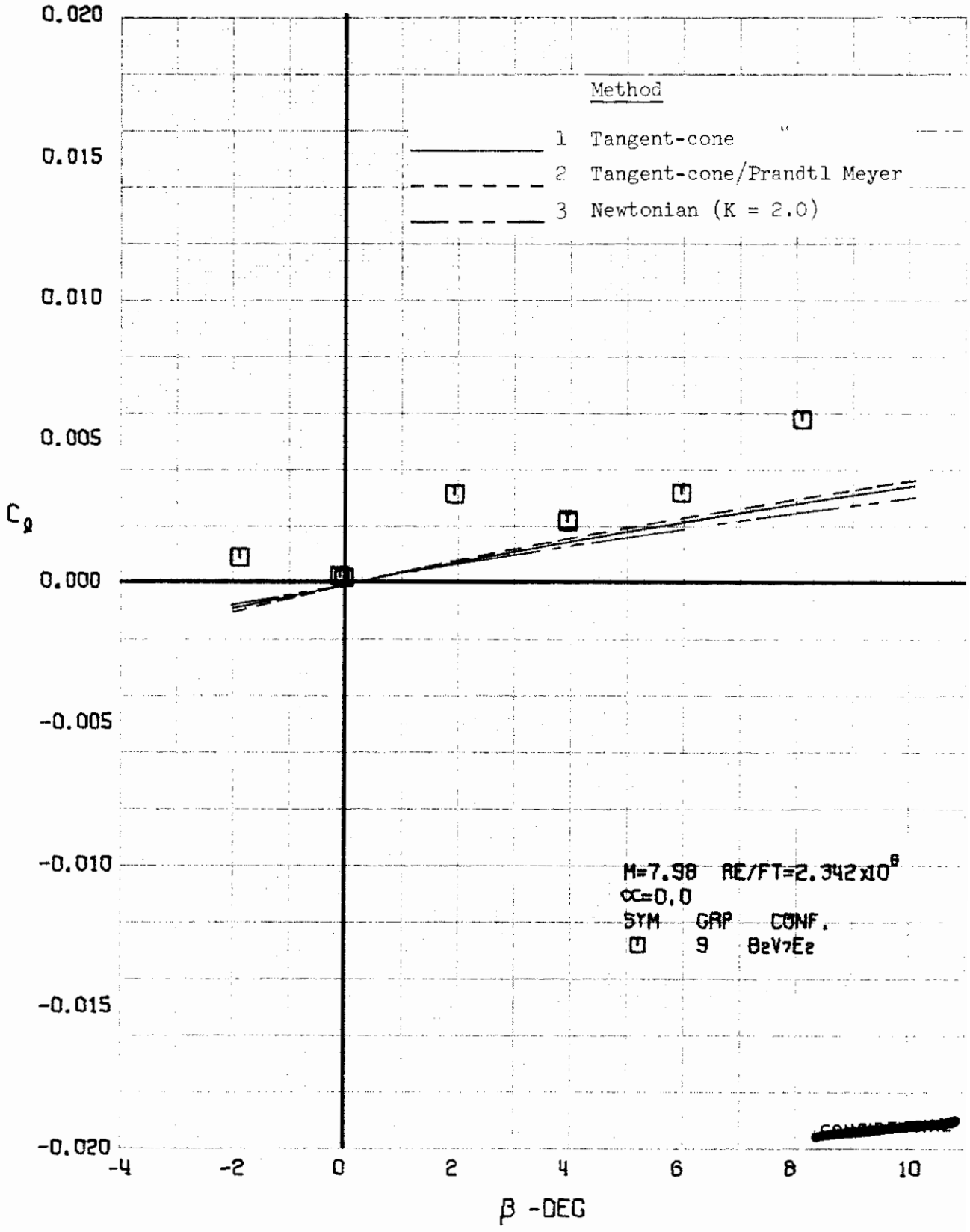

FIGURE 452 (U) COMPARISON OF ESTIMATED AND EXPERIMENTAL COEFFICIENTS - ROLLING MOMENT COEFFICIENT VARIATION WITH ANGLE OF YAW (M=7.98)

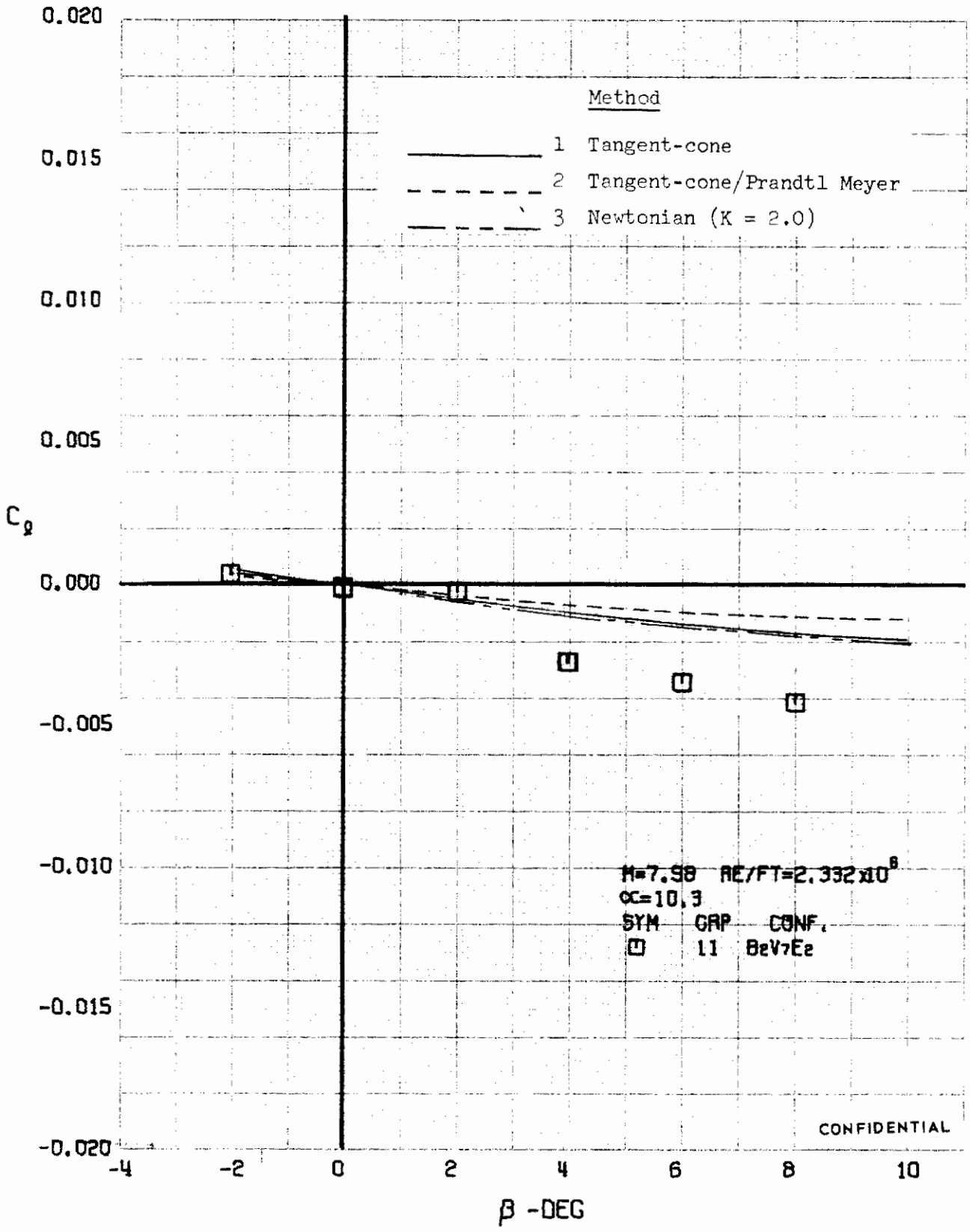

FIGURE 453 (U) COMPARISON OF ESTIMATED AND EXPERIMENTAL COEFFICIENTS - ROLLING MOMENT COEFFICIENT VARIATION WITH ANGLE OF YAW (M=7.98)

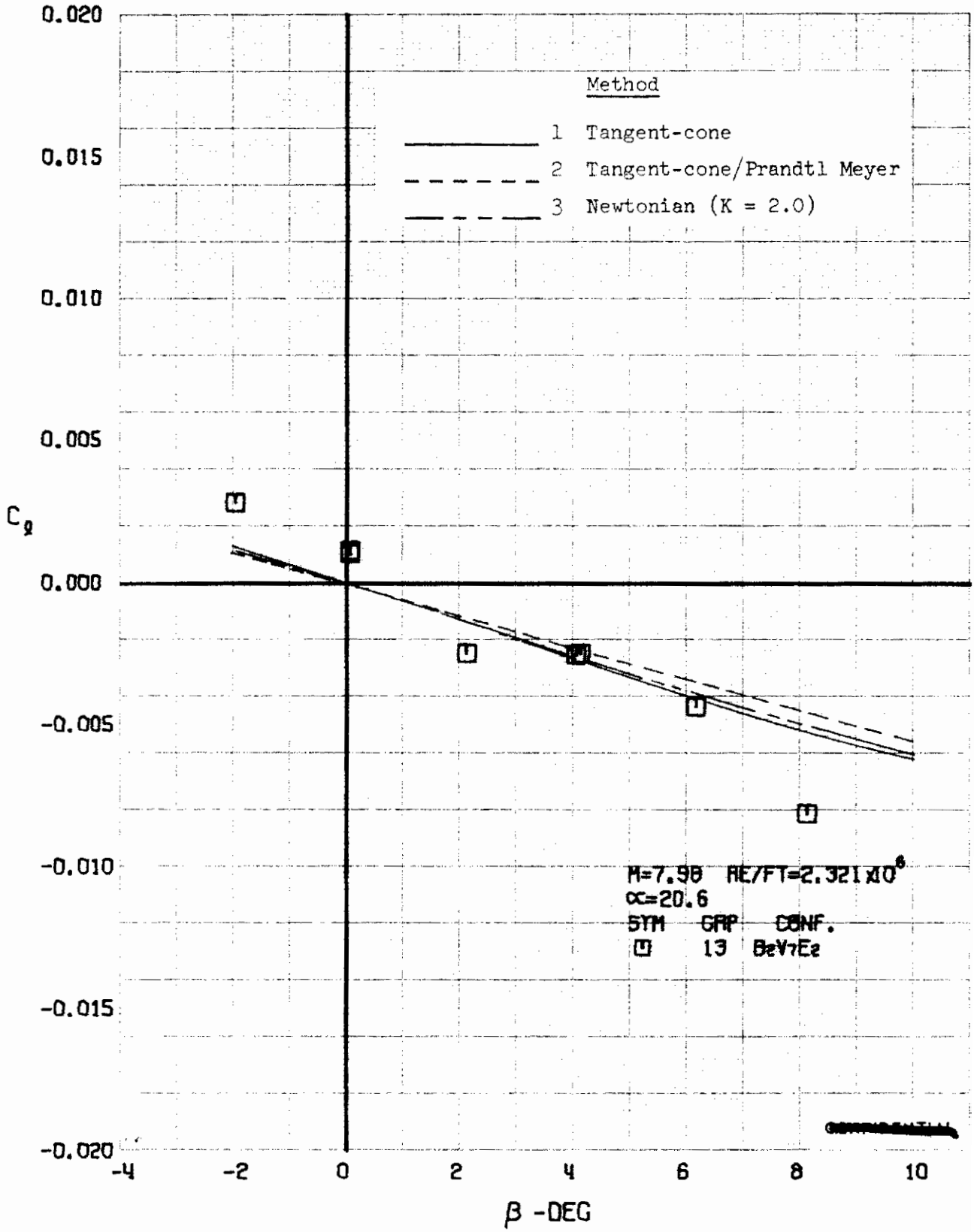

FIGURE 454 (U) COMPARISON OF ESTIMATED AND EXPERIMENTAL COEFFICIENTS - ROLLING MOMENT COEFFICIENT VARIATION WITH ANGLE OF YAW (M=7.98)

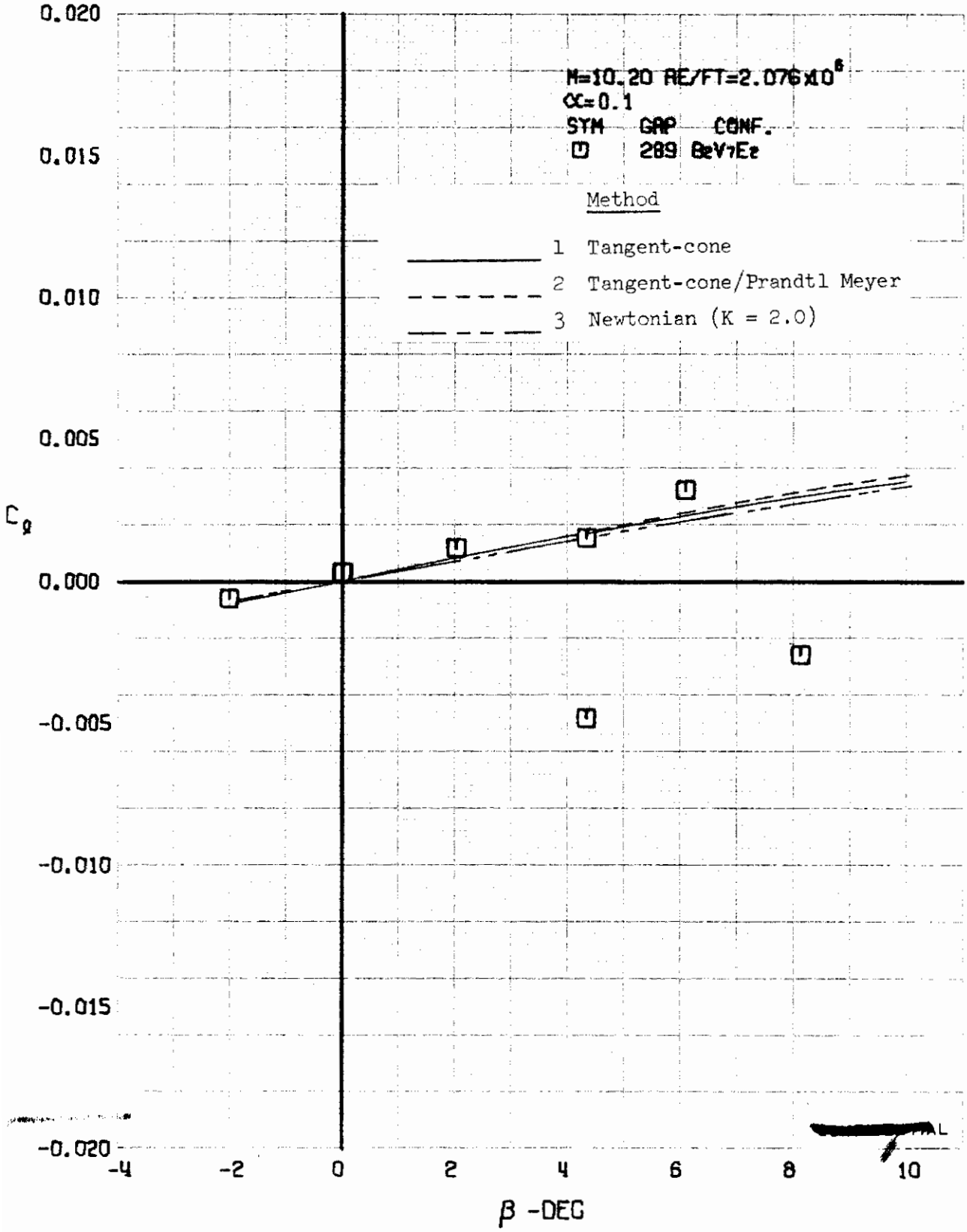

FIGURE 455 (U) COMPARISON OF ESTIMATED AND EXPERIMENTAL COEFFICIENTS - ROLLING MOMENT COEFFICIENT VARIATION WITH ANGLE OF YAW (M=10.20

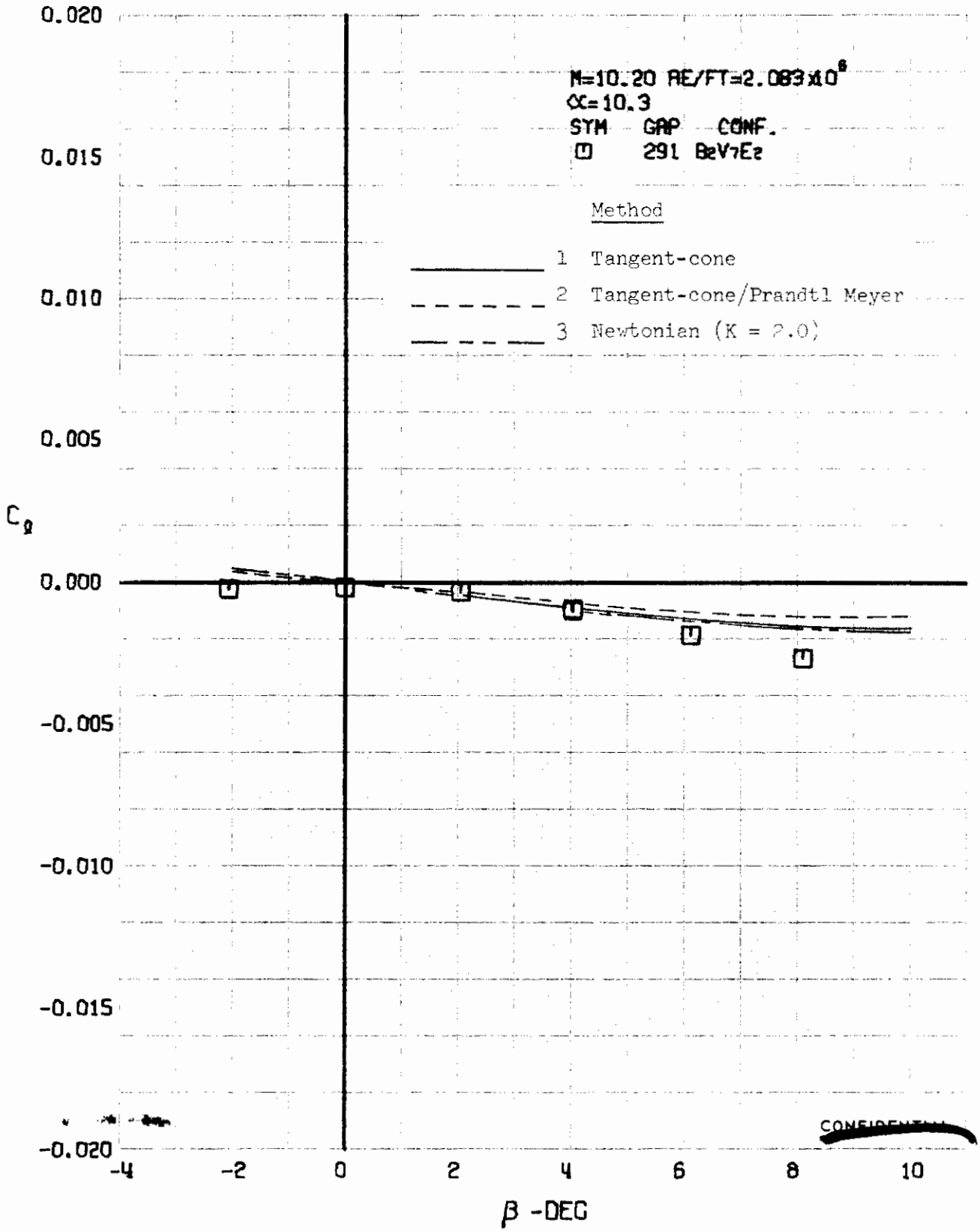

FIGURE 456 (U) COMPARISON OF ESTIMATED AND EXPERIMENTAL COEFFICIENTS - ROLLING MOMENT COEFFICIENT VARIATION WITH ANGLE OF YAW (M=10.20

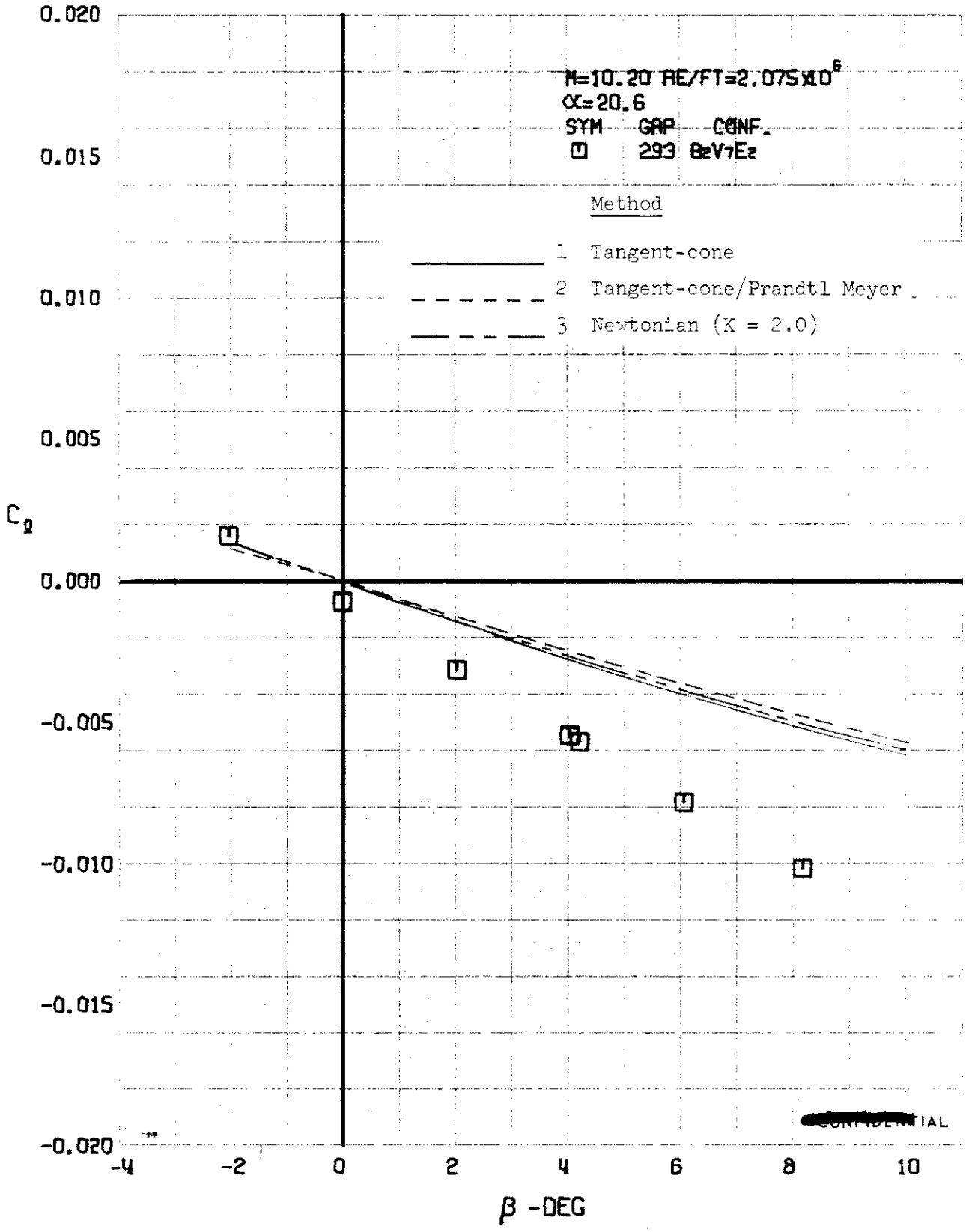

FIGURE 457 (U) COMPARISON OF ESTIMATED AND EXPERIMENTAL COEFFICIENTS - ROLLING MOMENT COEFFICIENT VARIATION WITH ANGLE OF YAW (M=10.20

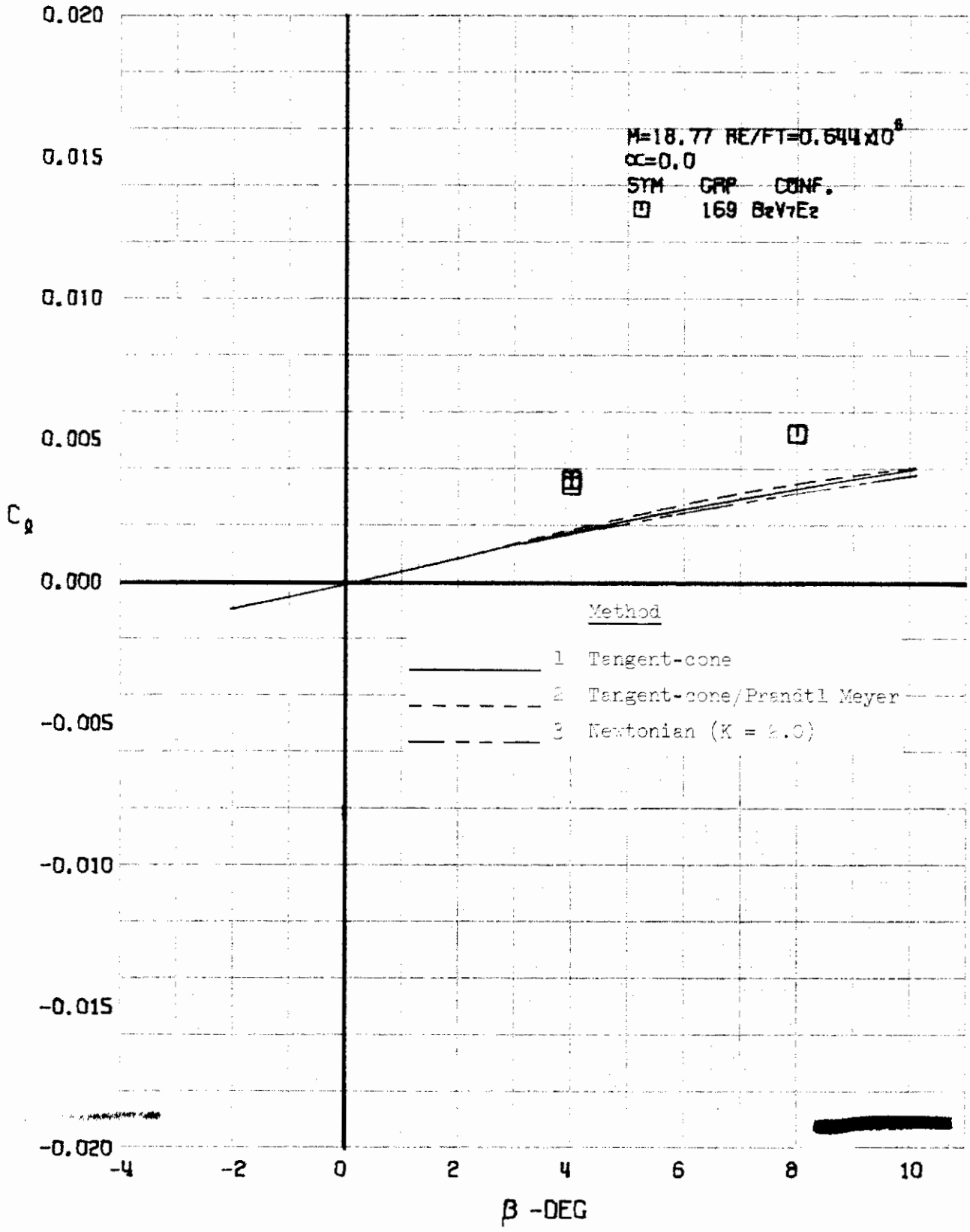

FIGURE 458 (U) COMPARISON OF ESTIMATED AND EXPERIMENTAL COEFFICIENTS - ROLLING MOMENT COEFFICIENT VARIATION WITH ANGLE OF YAW (M=18.77

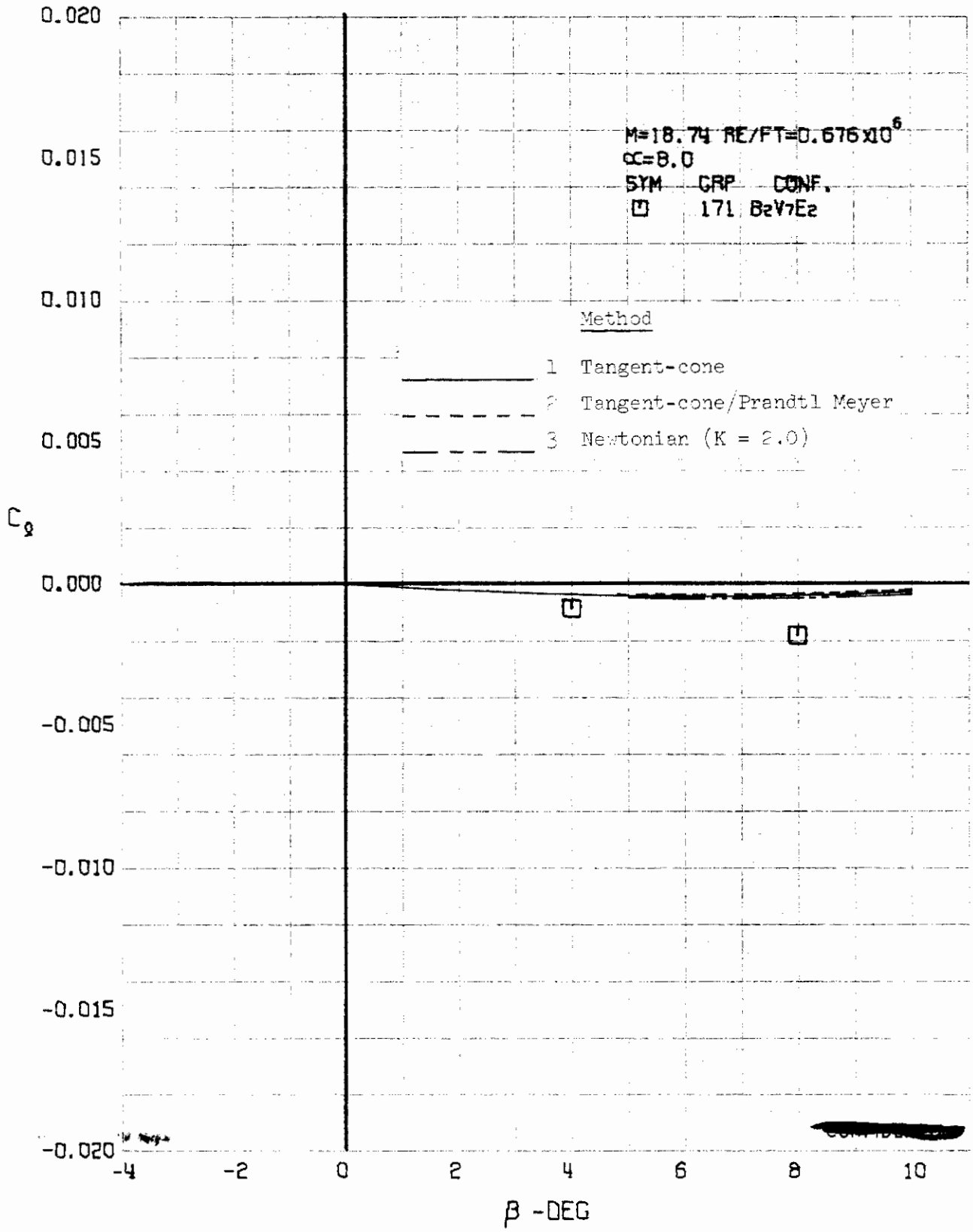

FIGURE 4-59 (U) COMPARISON OF ESTIMATED AND EXPERIMENTAL COEFFICIENTS ROLLING MOMENT COEFFICIENT VARIATION WITH ANGLE OF YAW (M= 18.74

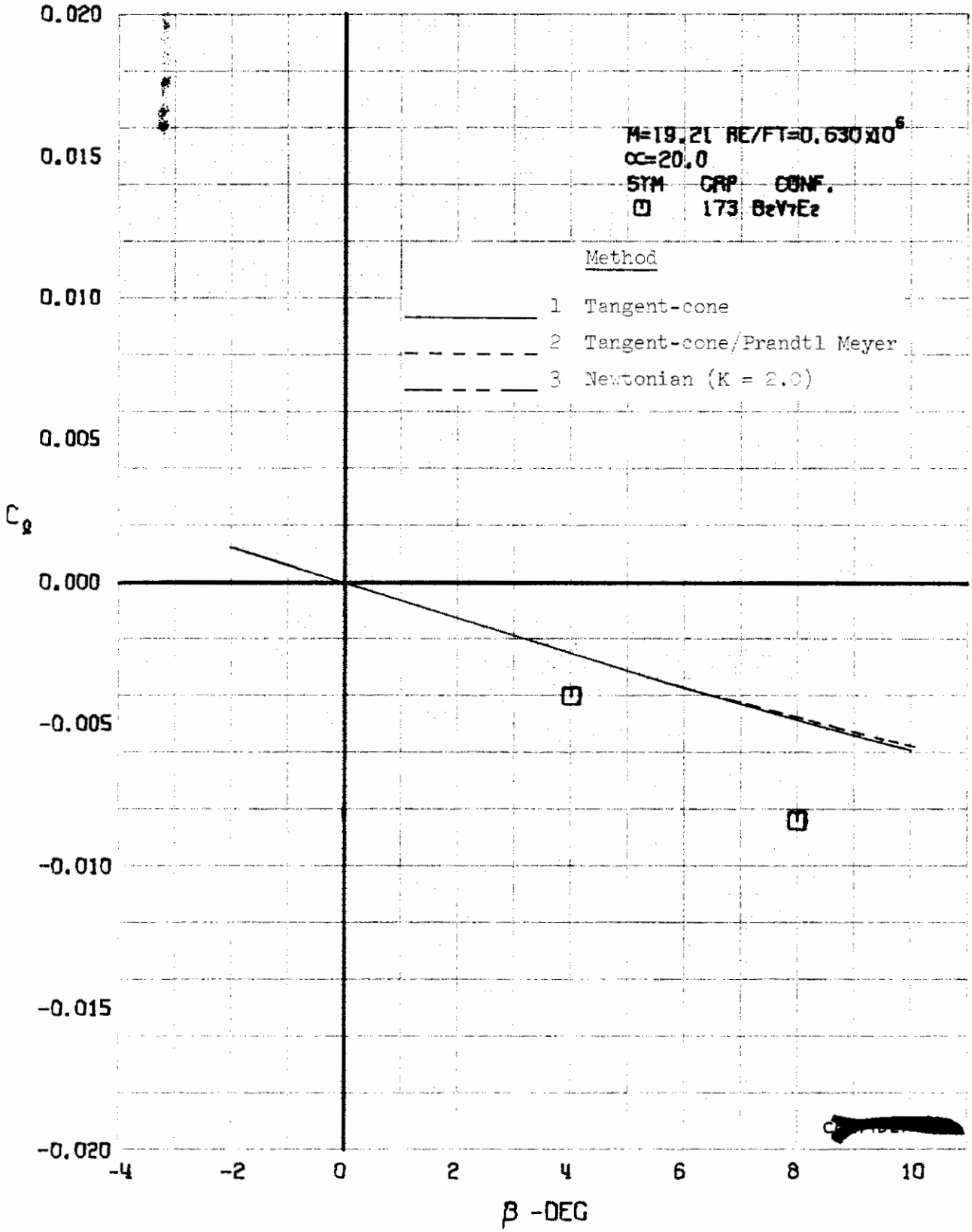

FIGURE 460 (U) COMPARISON OF ESTIMATED AND EXPERIMENTAL COEFFICIENTS - ROLLING MOMENT COEFFICIENT VARIATION WITH ANGLE OF YAW (M=19.21

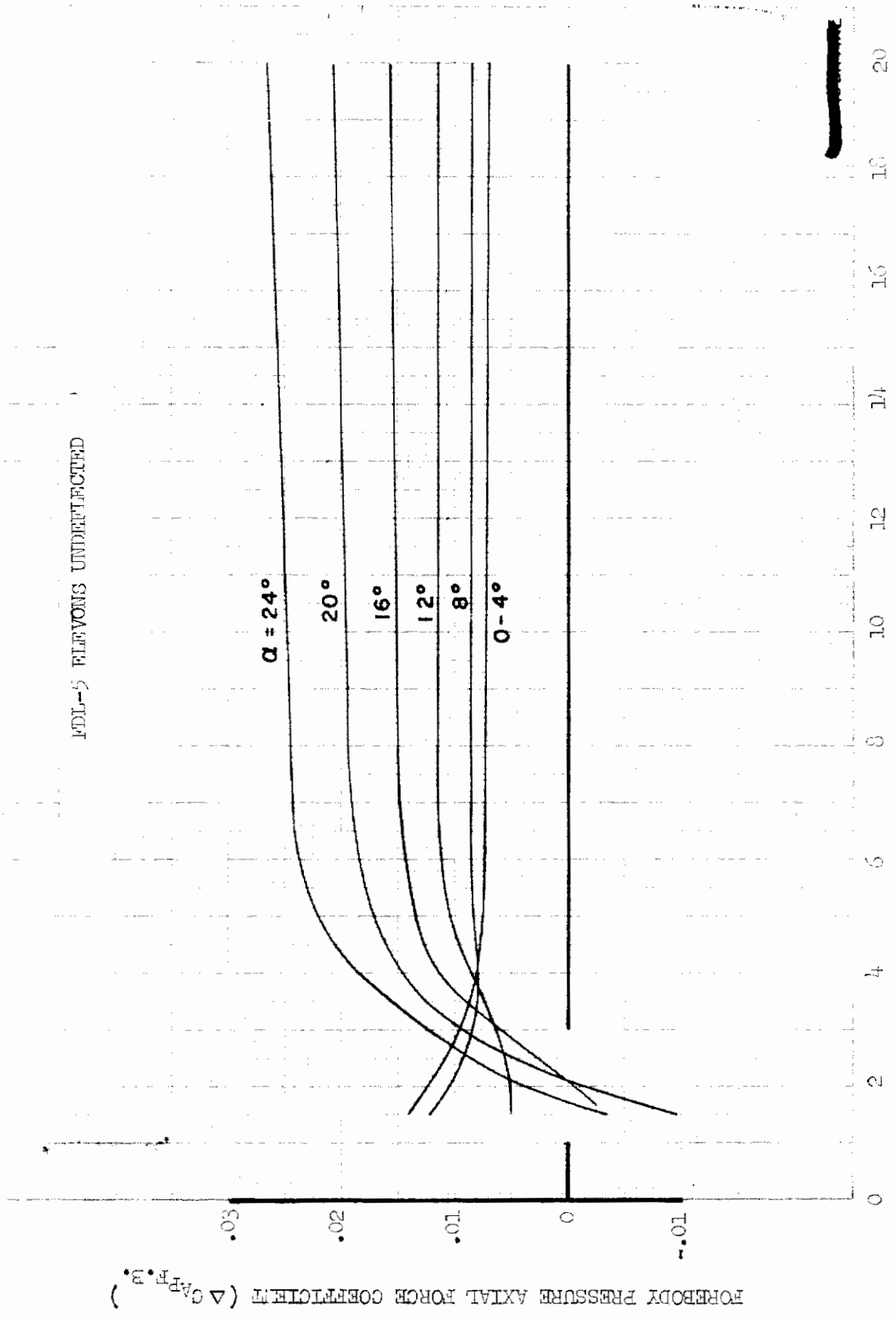

FIGURE 461 (U) FDL-5 FOREBODY PRESSURE AXIAL FORCE VARIATION WITH MACH NUMBER

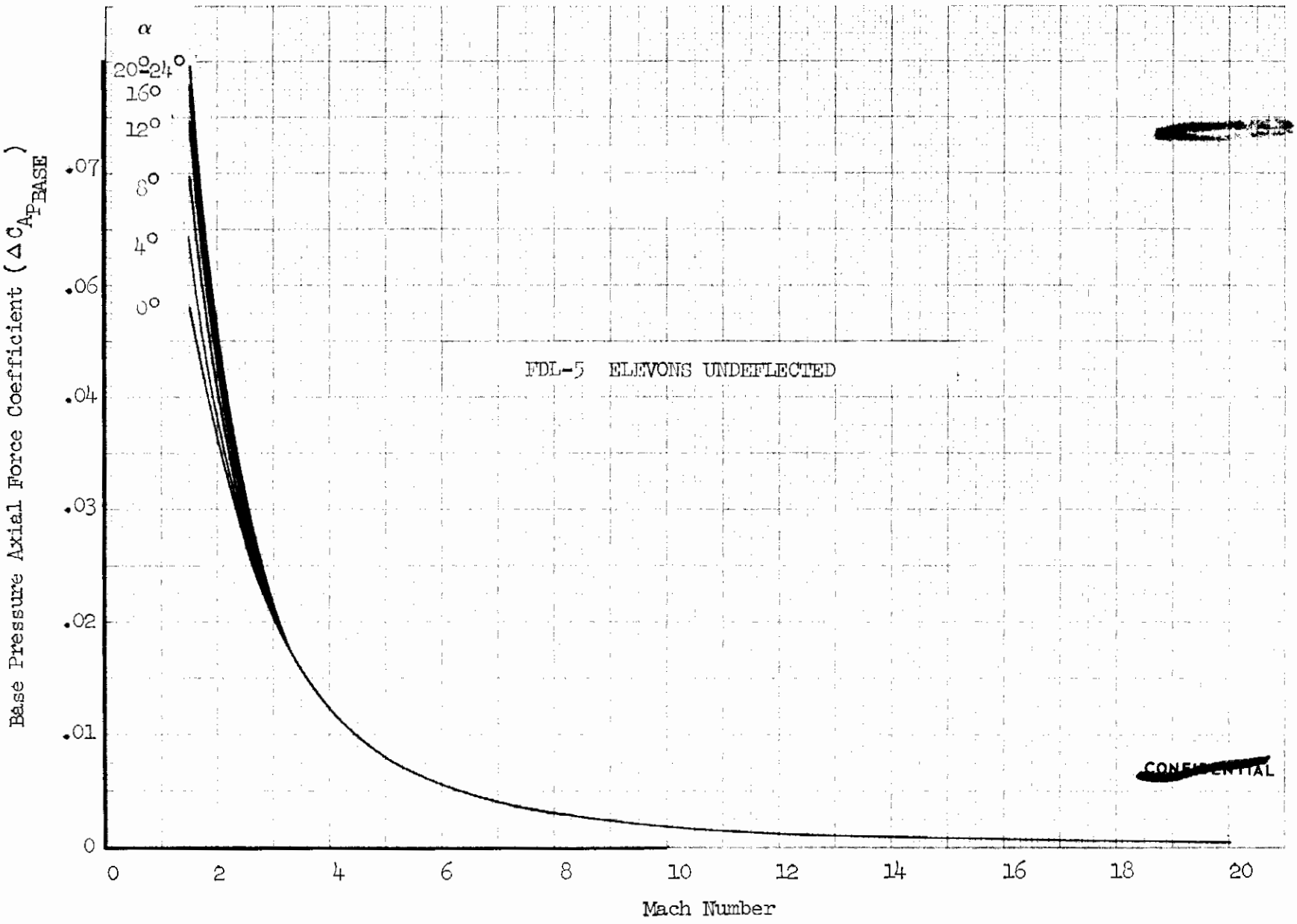

FIGURE 462 (U) FDL-5 BASE PRESSURE AXIAL FORCE VARIATION WITH MACH NUMBER

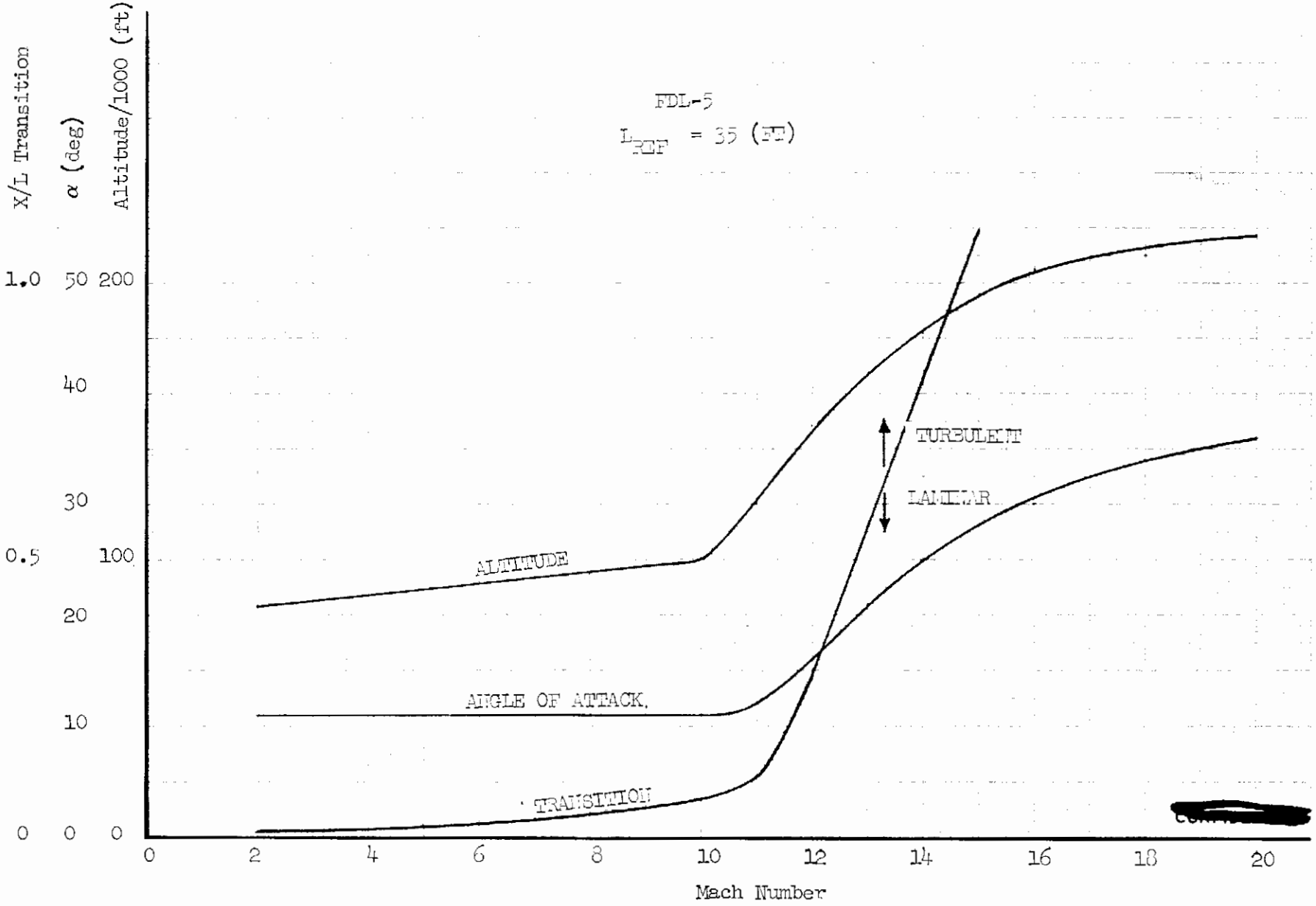

FIGURE 463 (U) FDL-5 HIGH ALTITUDE REFERENCE TRAJECTORY

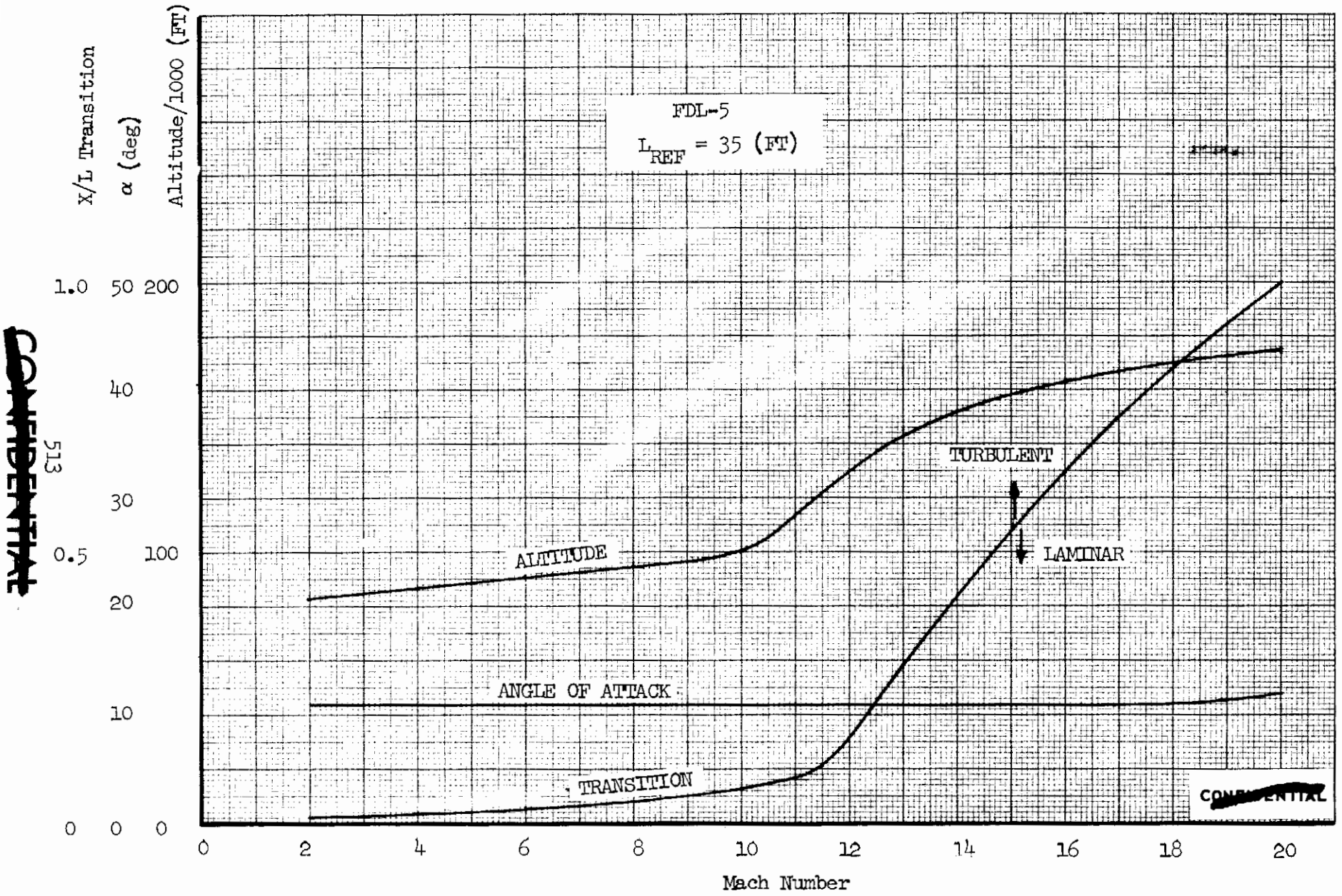

FIGURE 464 (U) FDL-5 LOW ALTITUDE REFERENCE TRAJECTORY

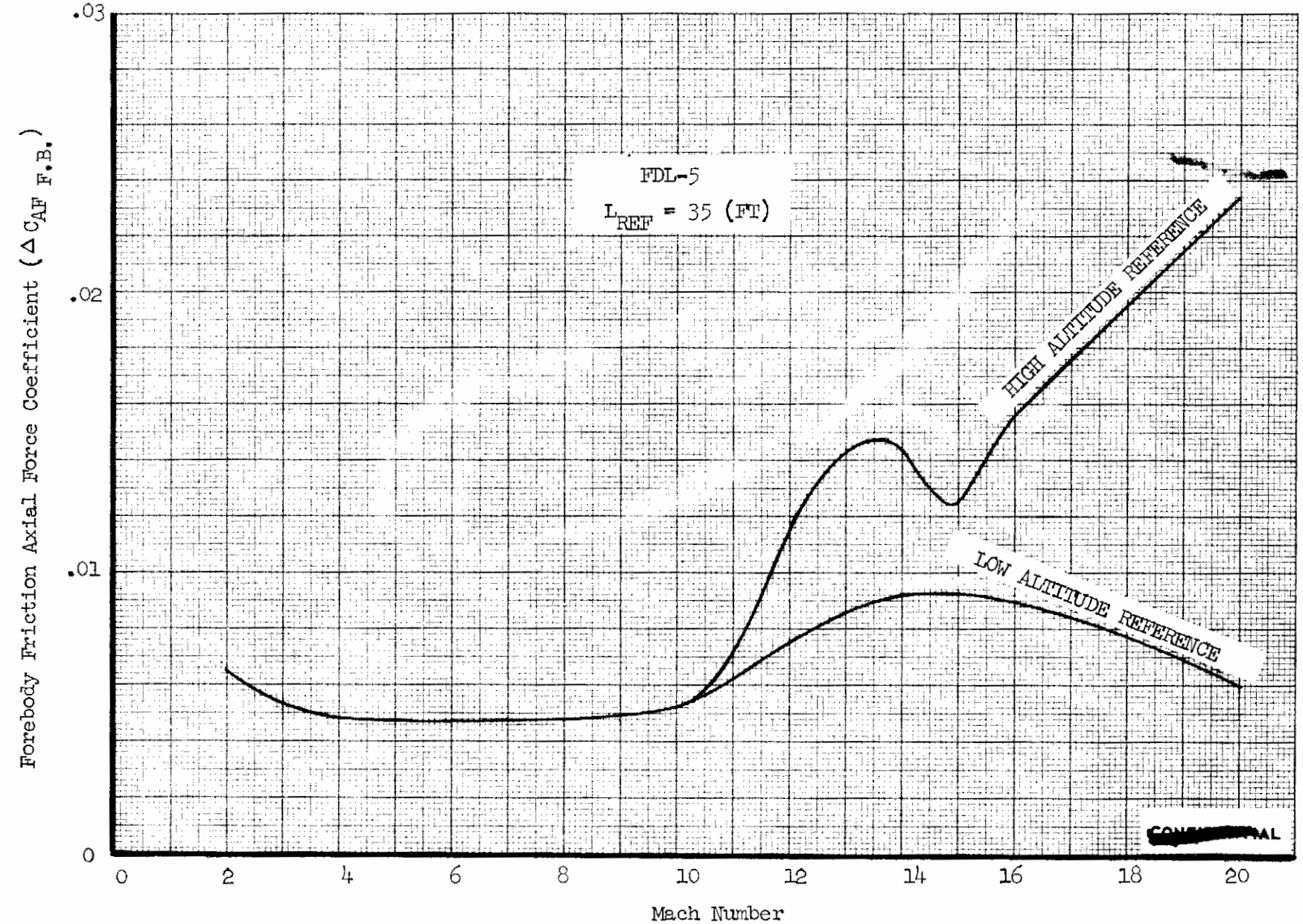

FIGURE 465 (U) FRICTION AXIAL FORCE VARIATION WITH MACH NUMBER FOR HIGH AND LOW ALTITUDE REFERENCE TRAJECTORIES

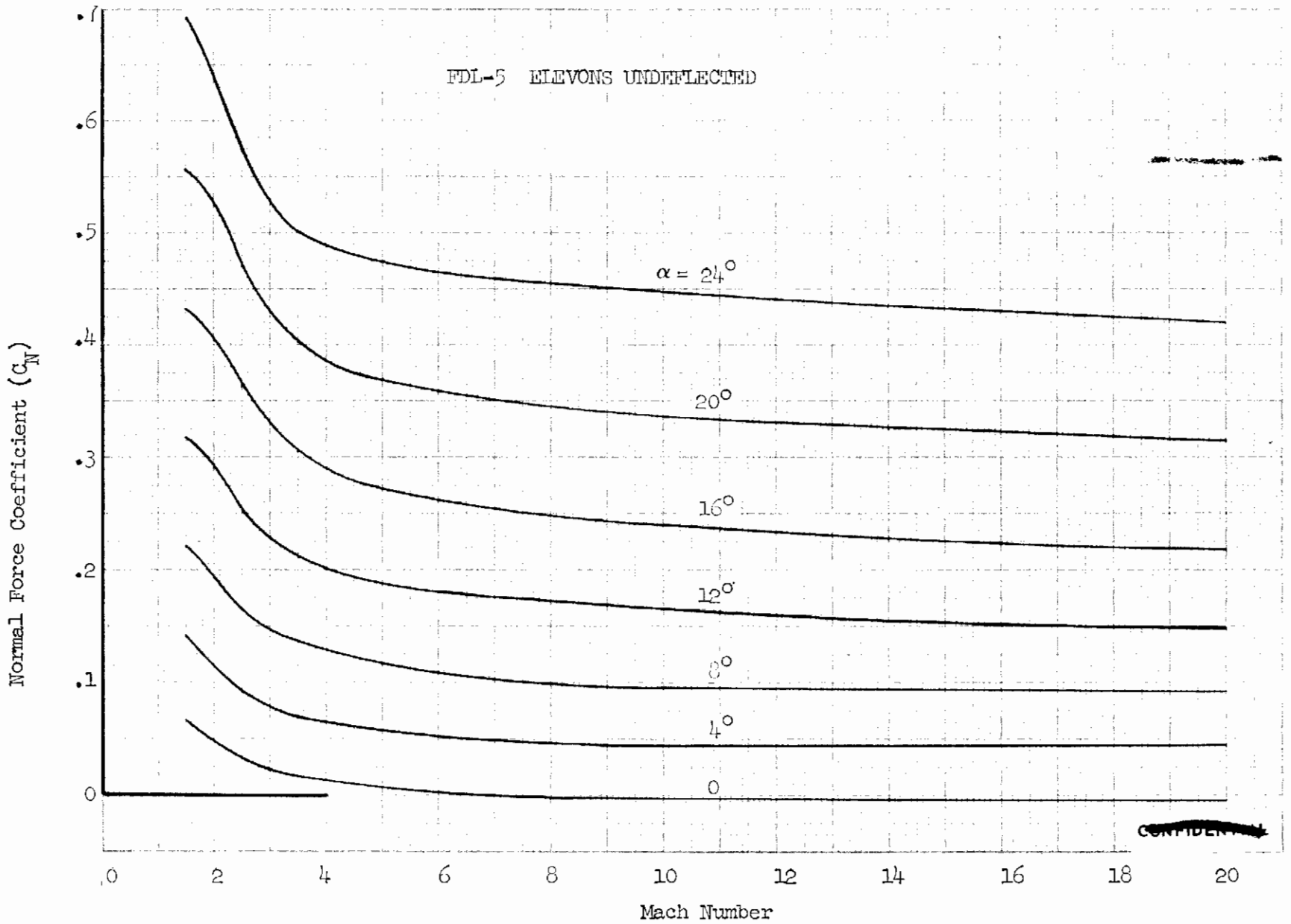

FIGURE 466 (U) NORMAL FORCE VARIATION WITH MACH NUMBER

CONFIDENTIAL

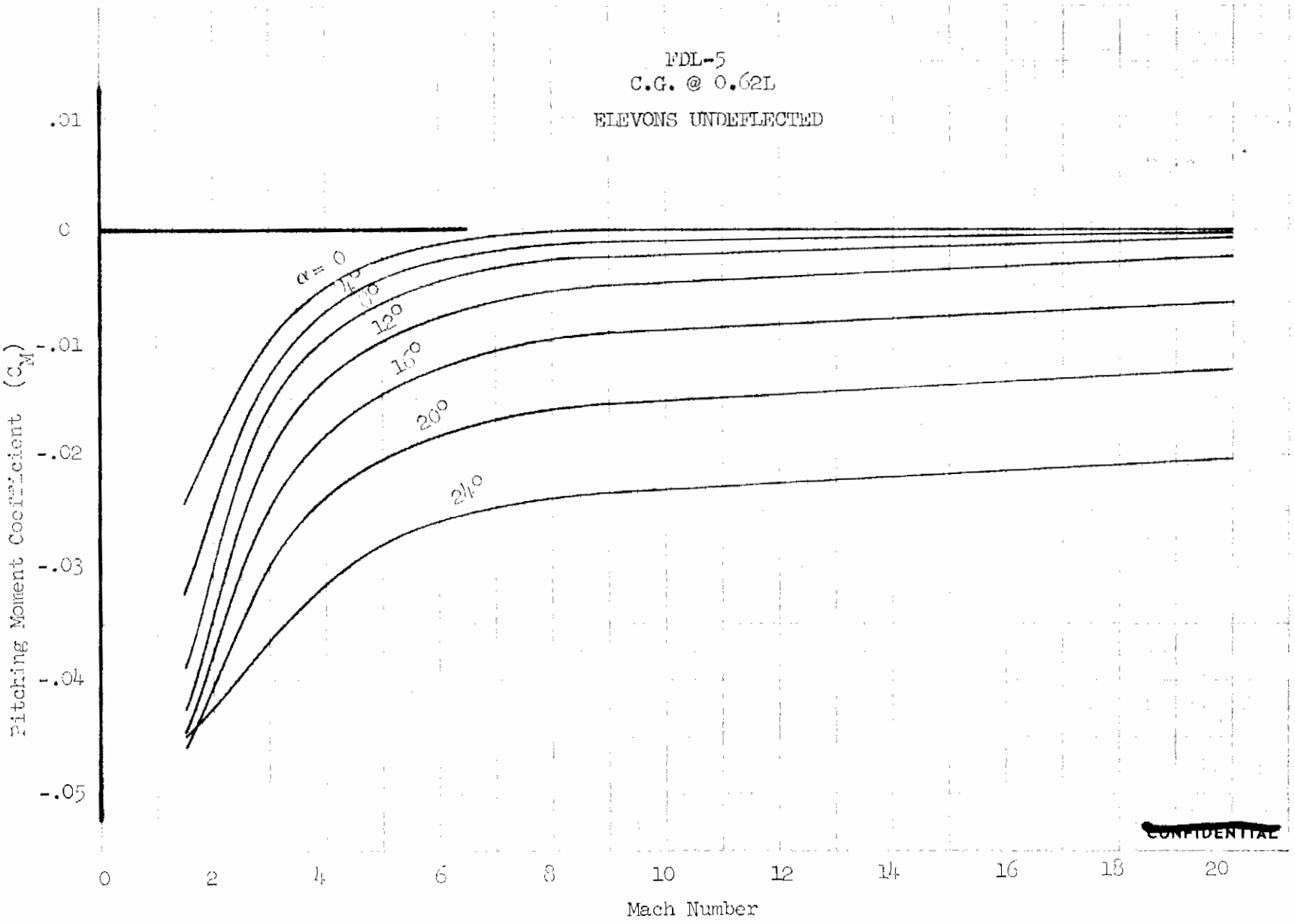

FIGURE 467 (U) FDL-5 PITCHING MOMENT VARIATION WITH MACH NUMBER

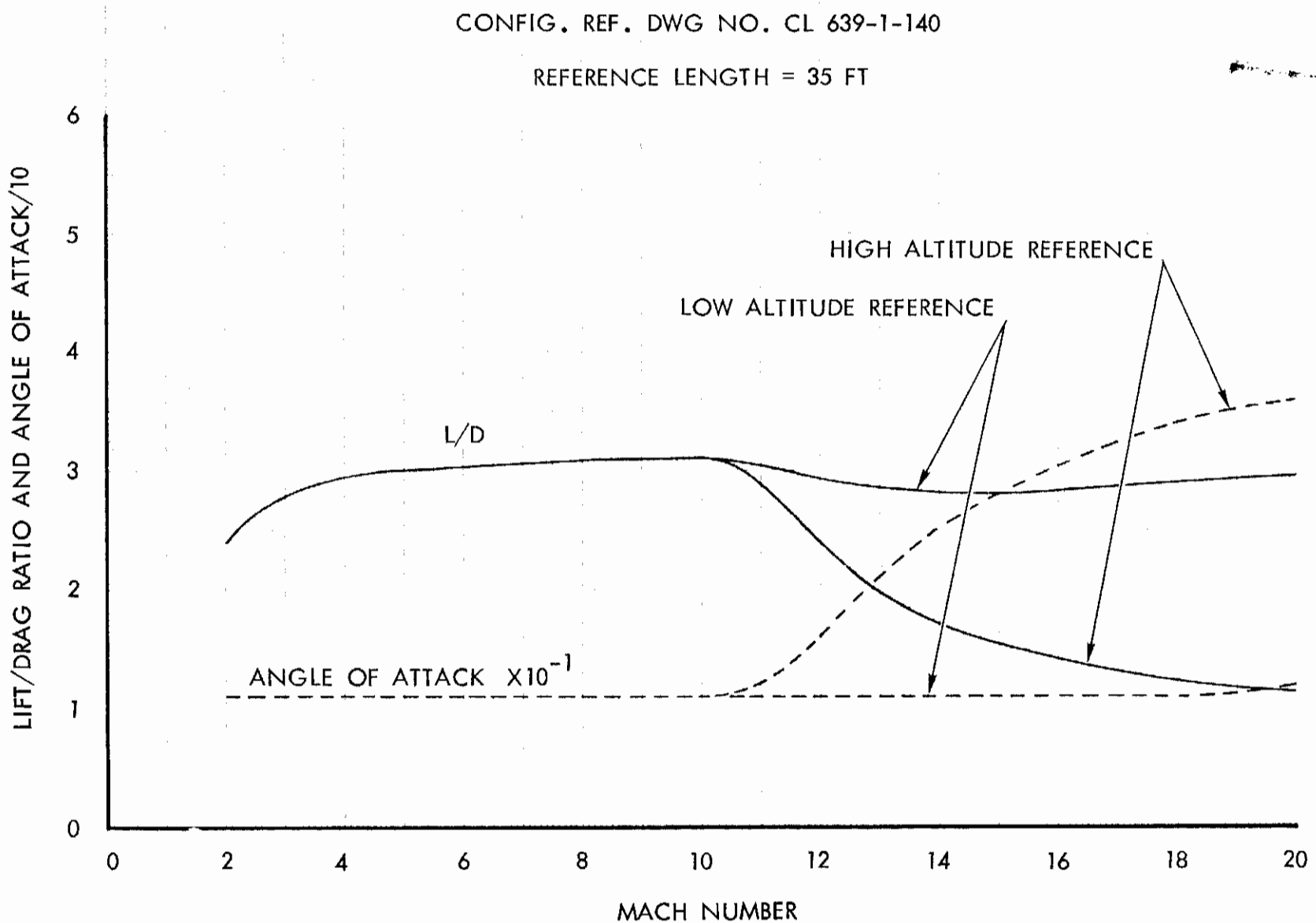

FIGURE 468 (U) L/D AND ANGLE OF ATTACK HISTORIES FOR HIGH AND LOW ALTITUDE REFERENCE TRAJECTORIES

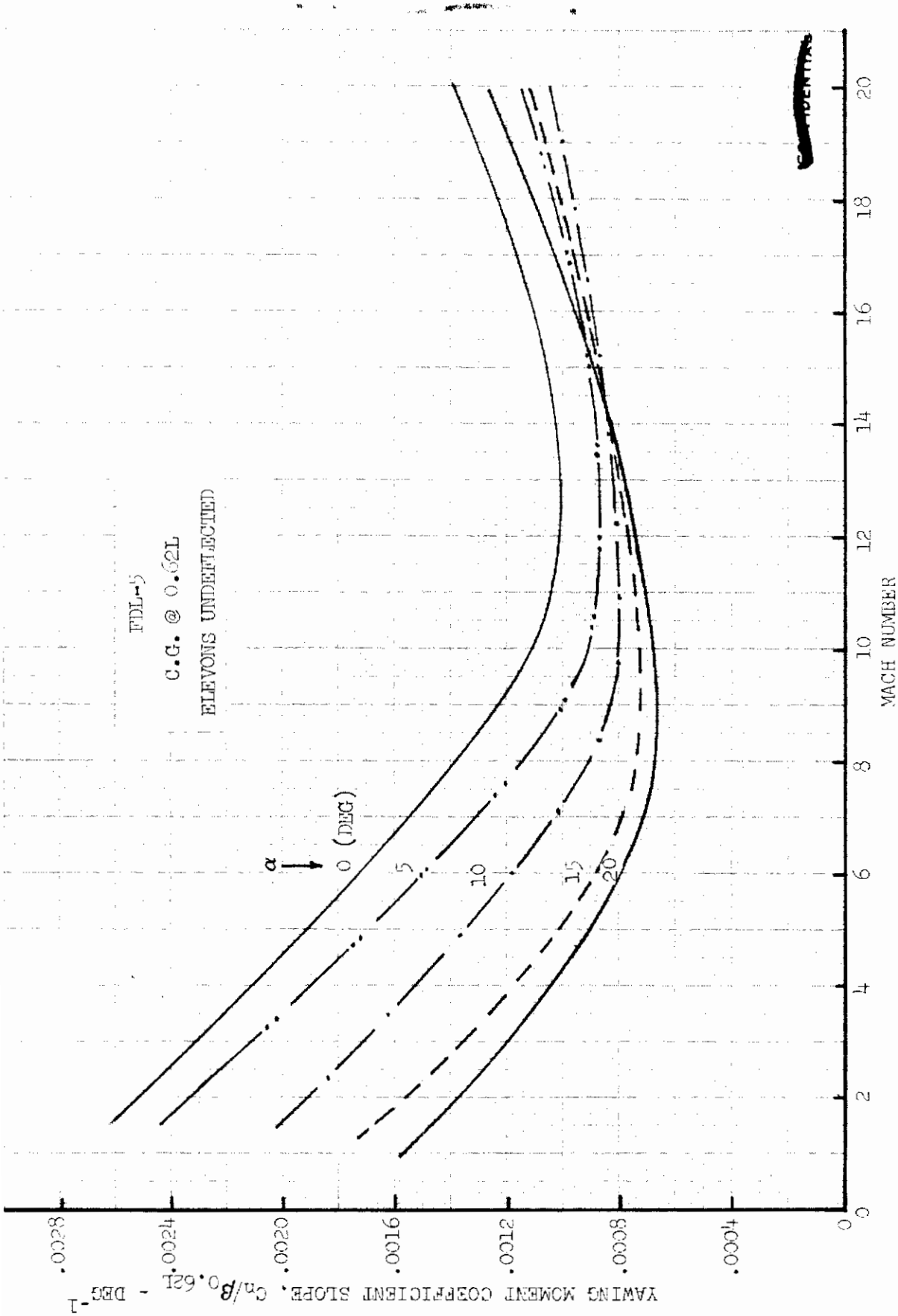

FIGURE 469 (U) FDL-5 YAWING MOMENT COEFFICIENT SLOPE VARIATION WITH MACH NUMBER

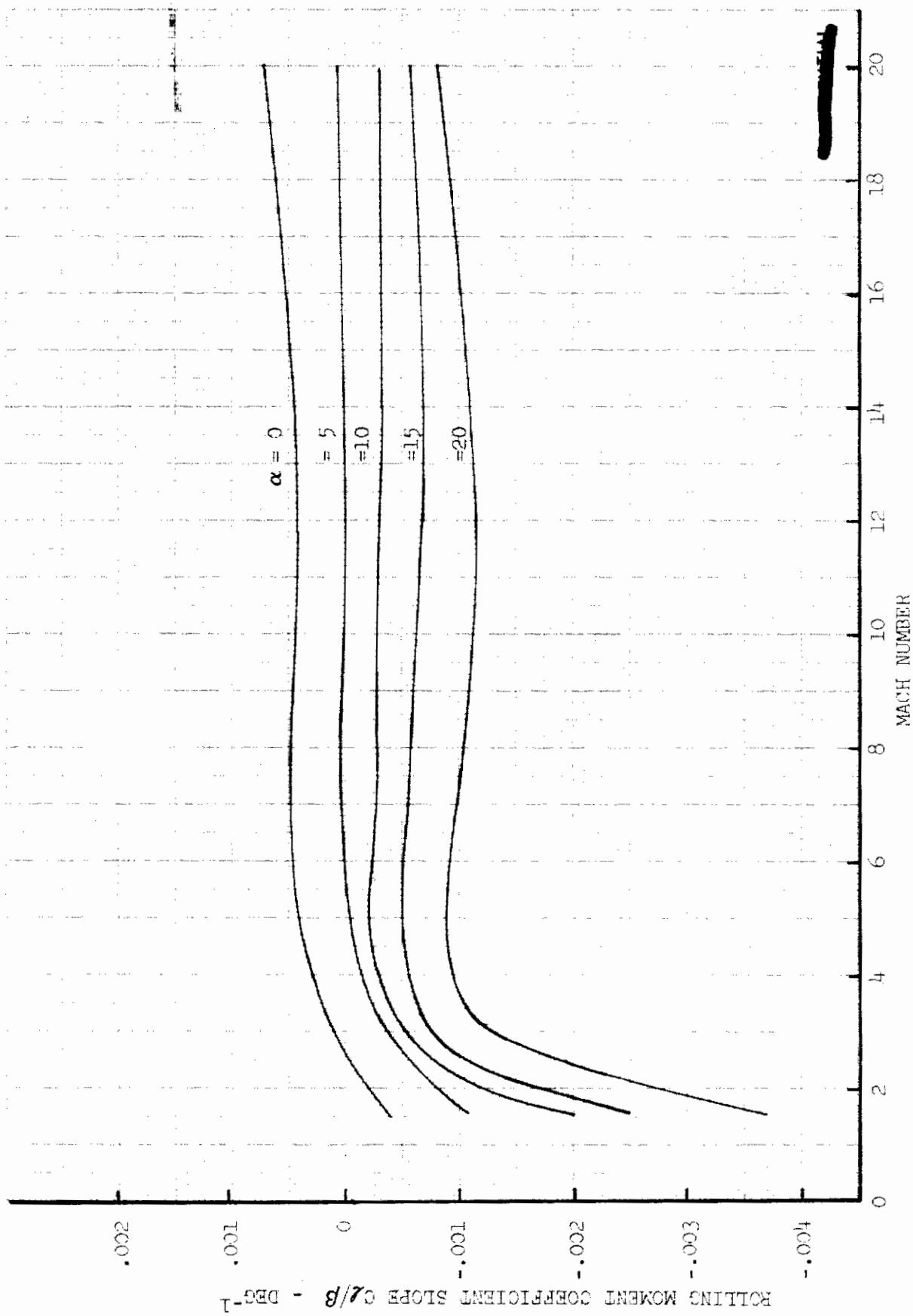

FIGURE 470 (U) FDL-5 ROLLING MOMENT COEFFICIENT SLOPE VARIATION WITH MACH NUMBER

FIGURE 474 (U) ELEVON EFFECTIVENESS - NORMAL FORCE INCREMENT VARIATION WITH MACH NUMBER (δ_E = + 10°)

FIGURE 472 (U) ELEVON EFFECTIVENESS - NORMAL FORCE INCREMENT VARIATION WITH MACH NUMBER (δ_R = -10°)

FIGURE 473 (U) ELEVON EFFECTIVENESS - NORMAL FORCE INCREMENT VARIATION WITH MACH NUMBER ($\delta_E = -20^\circ$)

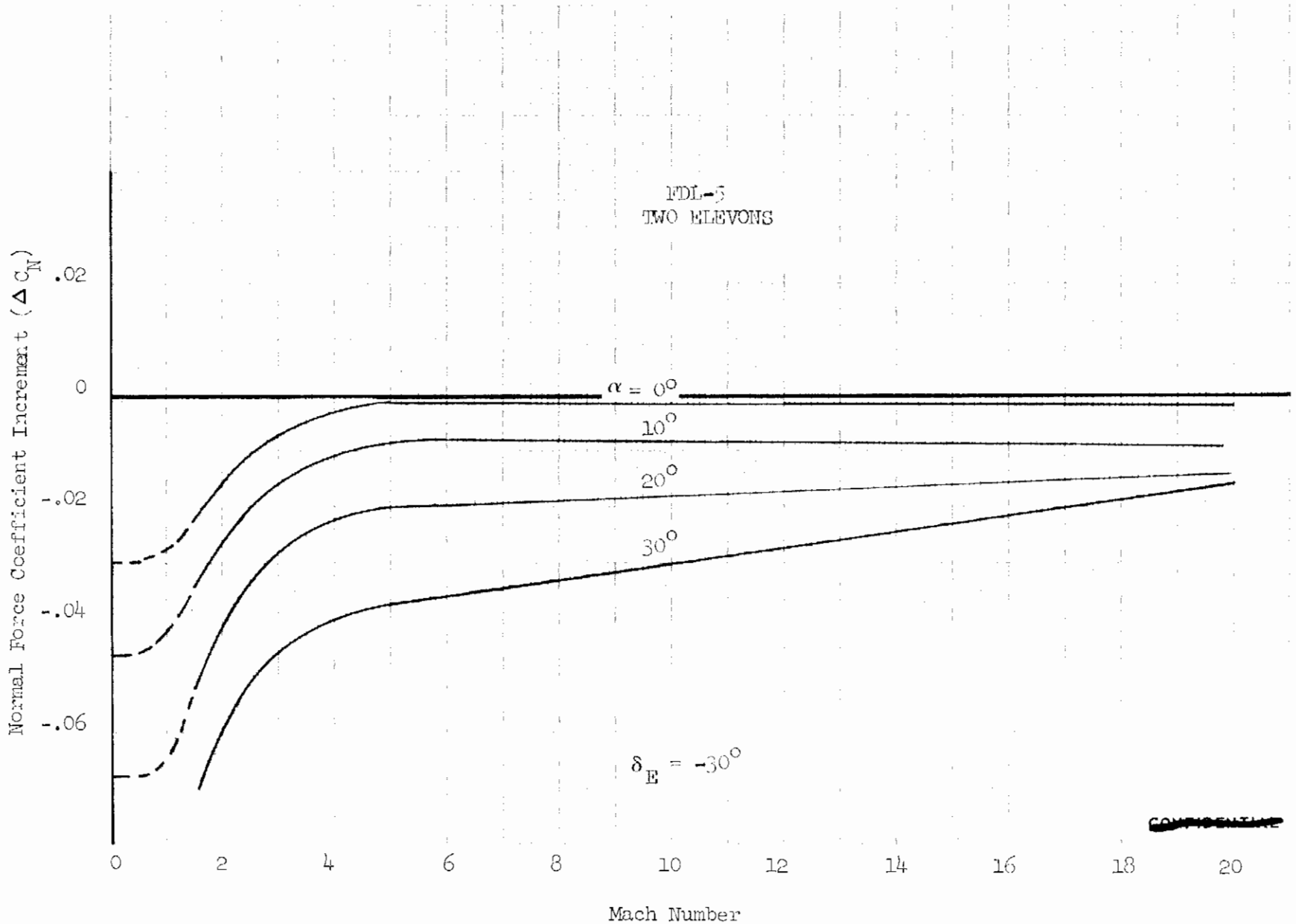

FIGURE 474 (U) ELEVON EFFECTIVENESS - NORMAL FORCE INCREMENT VARIATION WITH MACH NUMBER ($\delta_E = -30^\circ$)

CONFIDENTIAL

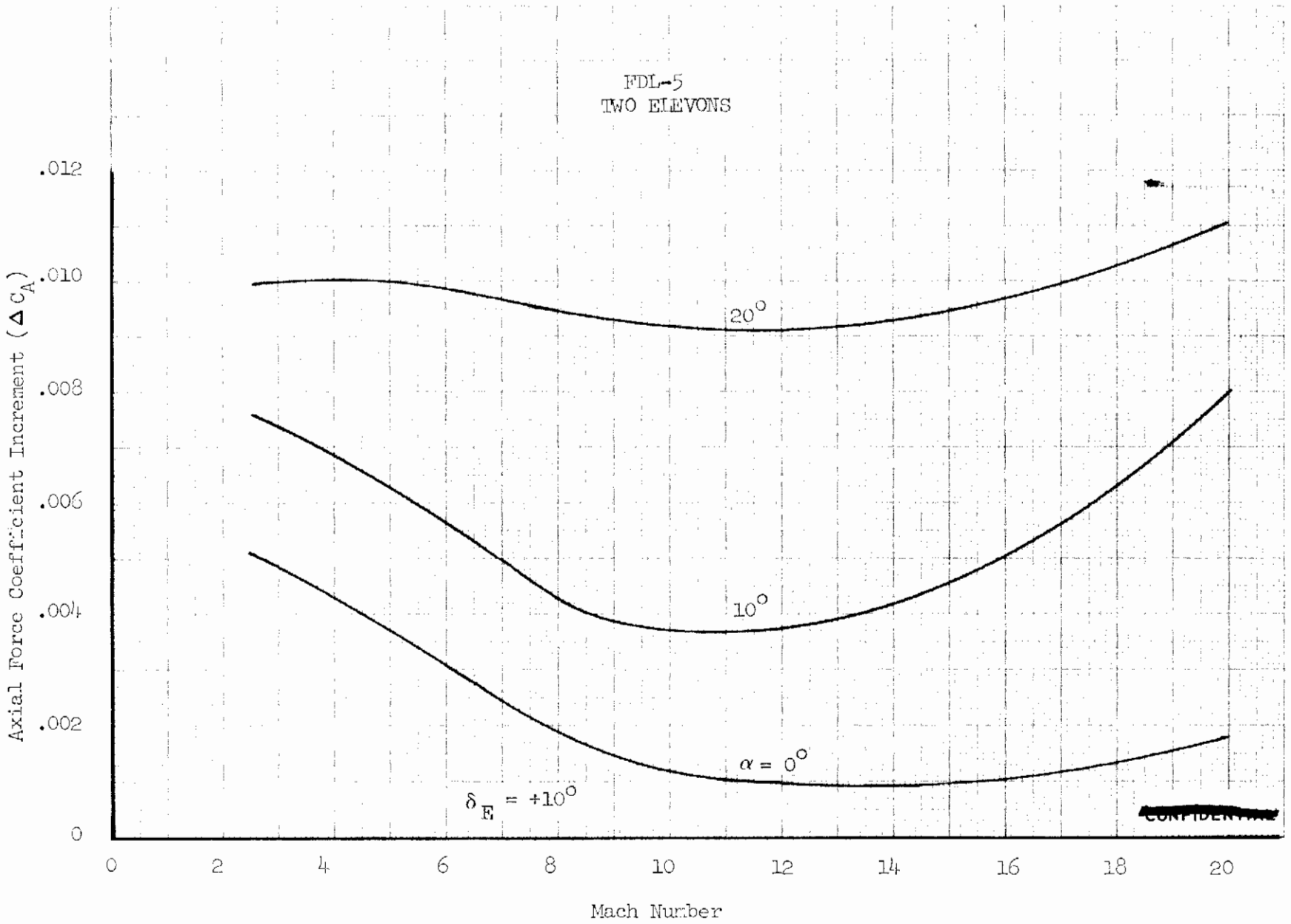

FIGURE 475 (U) ELEVON EFFECTIVENESS - AXIAL FORCE INCREMENT VARIATION WITH MACH NUMBER (δ_E = + 10°)

FIGURE 476 (U) ELEVON EFFECTIVENESS - AXIAL FORCE INCREMENT VARIATION WITH MACH NUMBER
(δ_E = -10°)

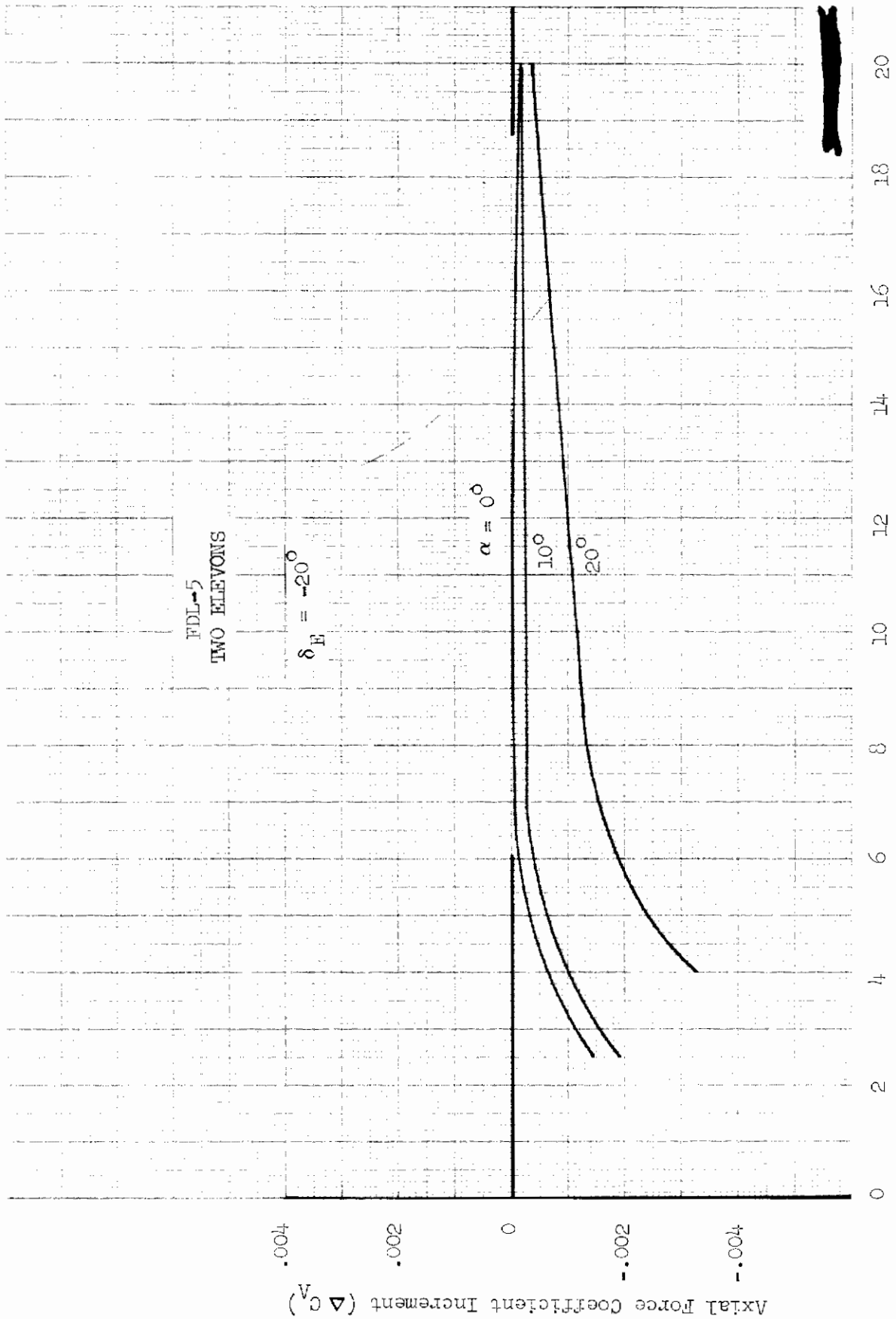

FIGURE 477 (U) ELEVON EFFECTIVENESS - AXIAL FORCE INCREMENT VARIATION WITH MACH NUMBER ($\delta_E = -20^\circ$)

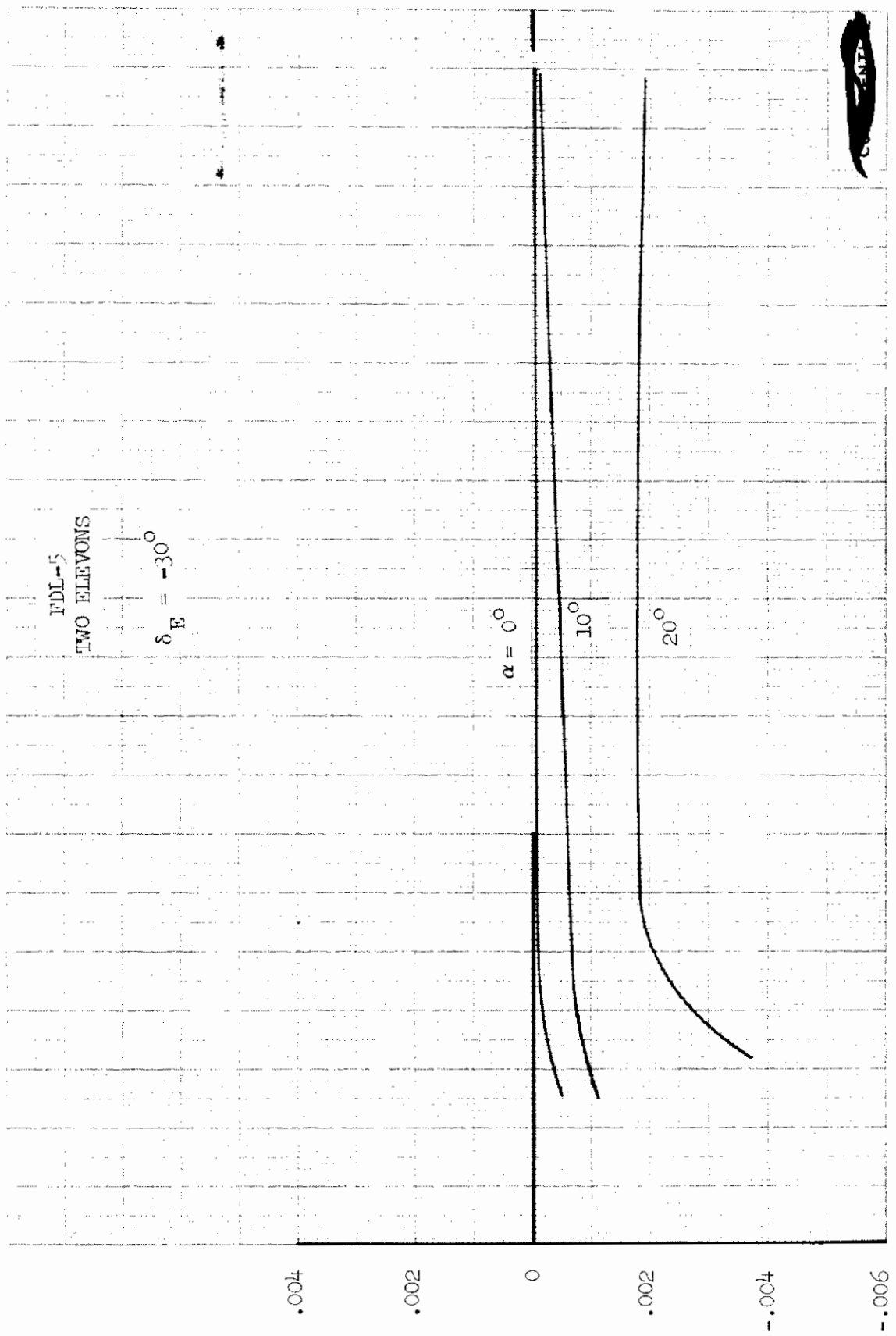

FIGURE 478 (U) ELEVON EFFECTIVENESS - AXIAL FORCE INCREMENT VARIATION WITH MACH NUMBER ($\delta_E = -30^\circ$)

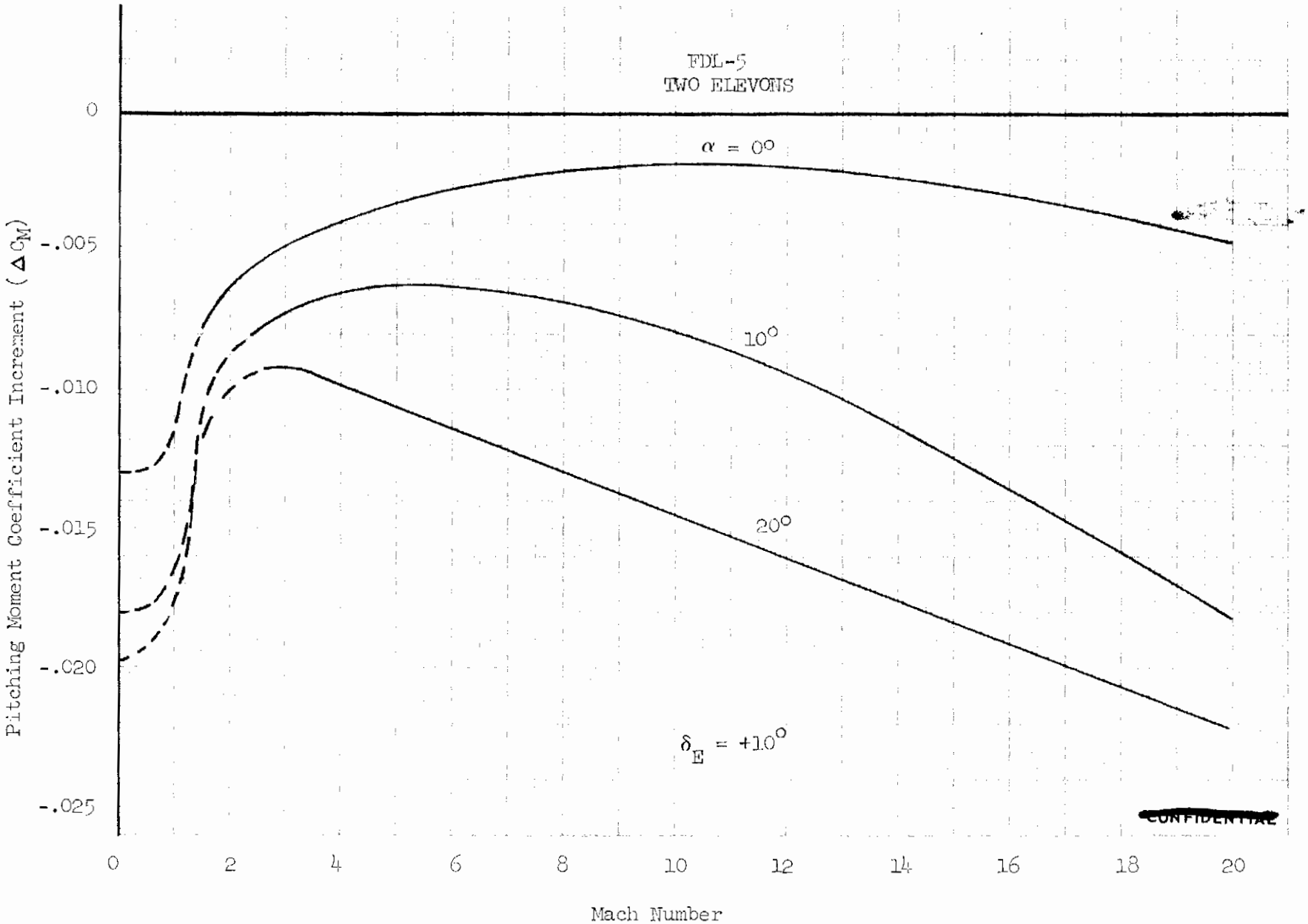

FIGURE 479 (U) ELEVON EFFECTIVENESS - PITCHING MOMENT INCREMENT VARIATION WITH MACH NUMBER (δ_E = +10°)

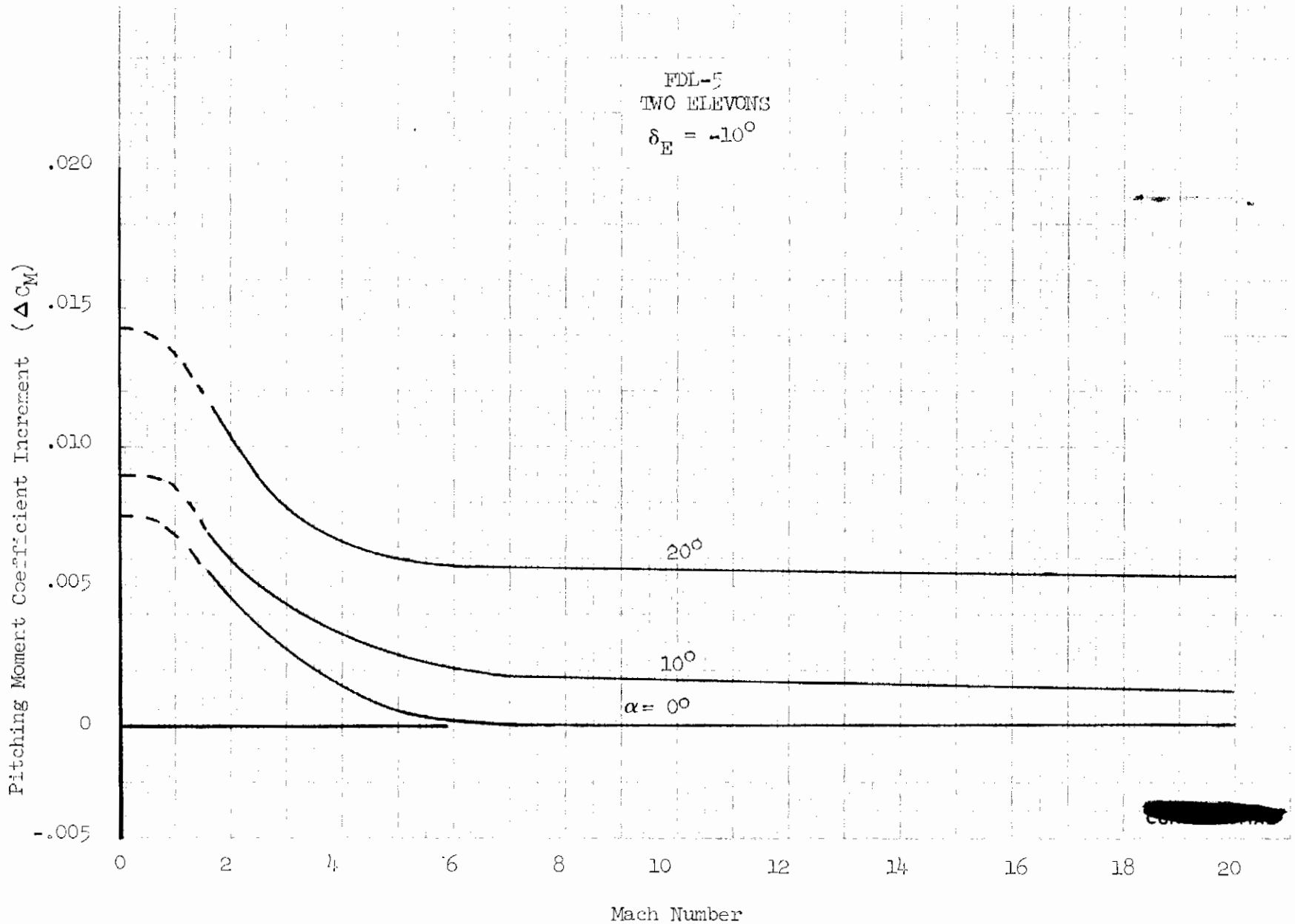

FIGURE 480 (U) ELEVON EFFECTIVENESS - PITCHING MOMENT INCREMENT VARIATION WITH MACH NUMBER (δ_E = -10°)

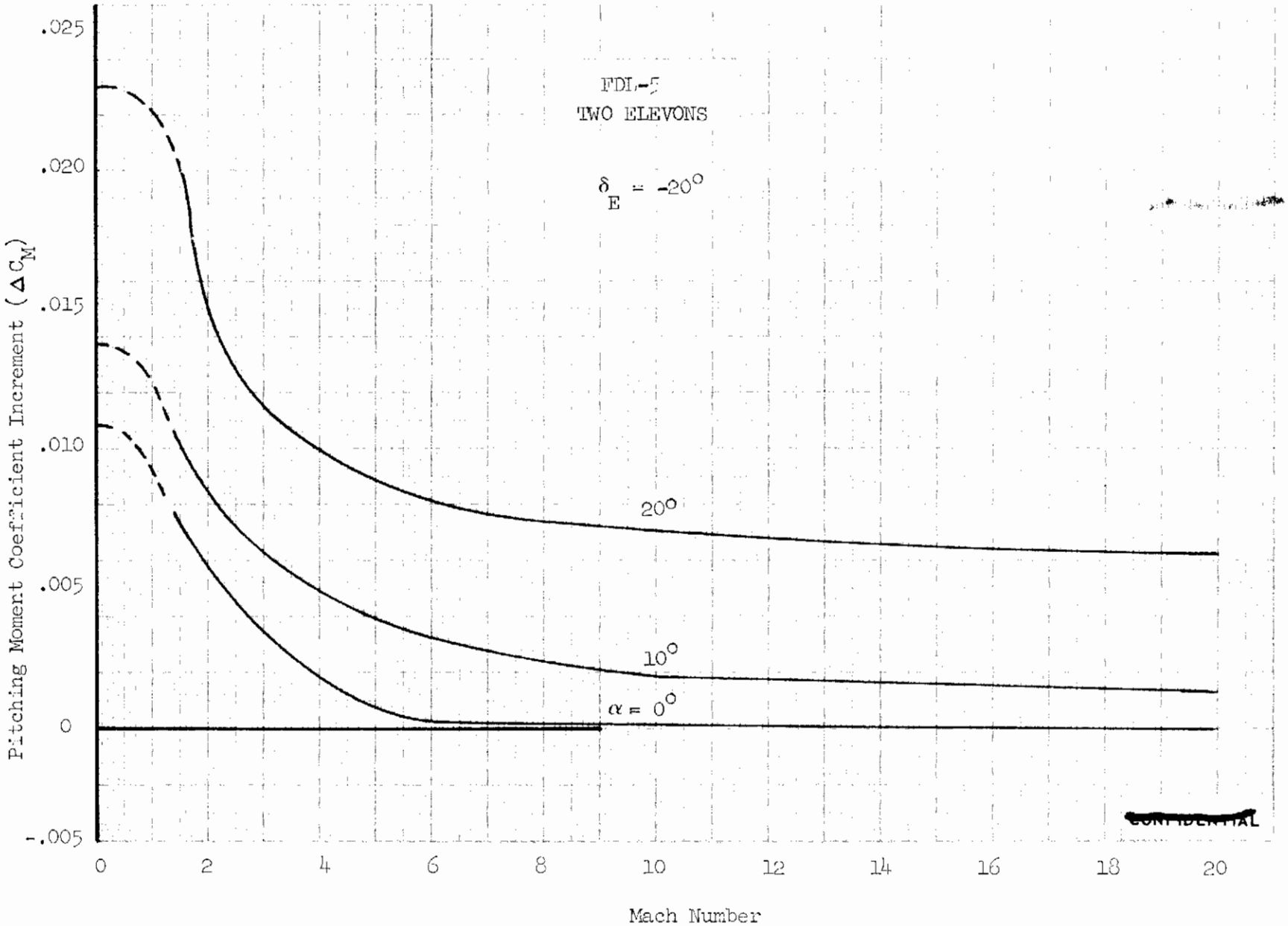

FIGURE 481 (U) ELEVON EFFECTIVENESS - PITCHING MOMENT INCREMENT VARIATION WITH MACH NUMBER ($\delta_E = -20^\circ$)

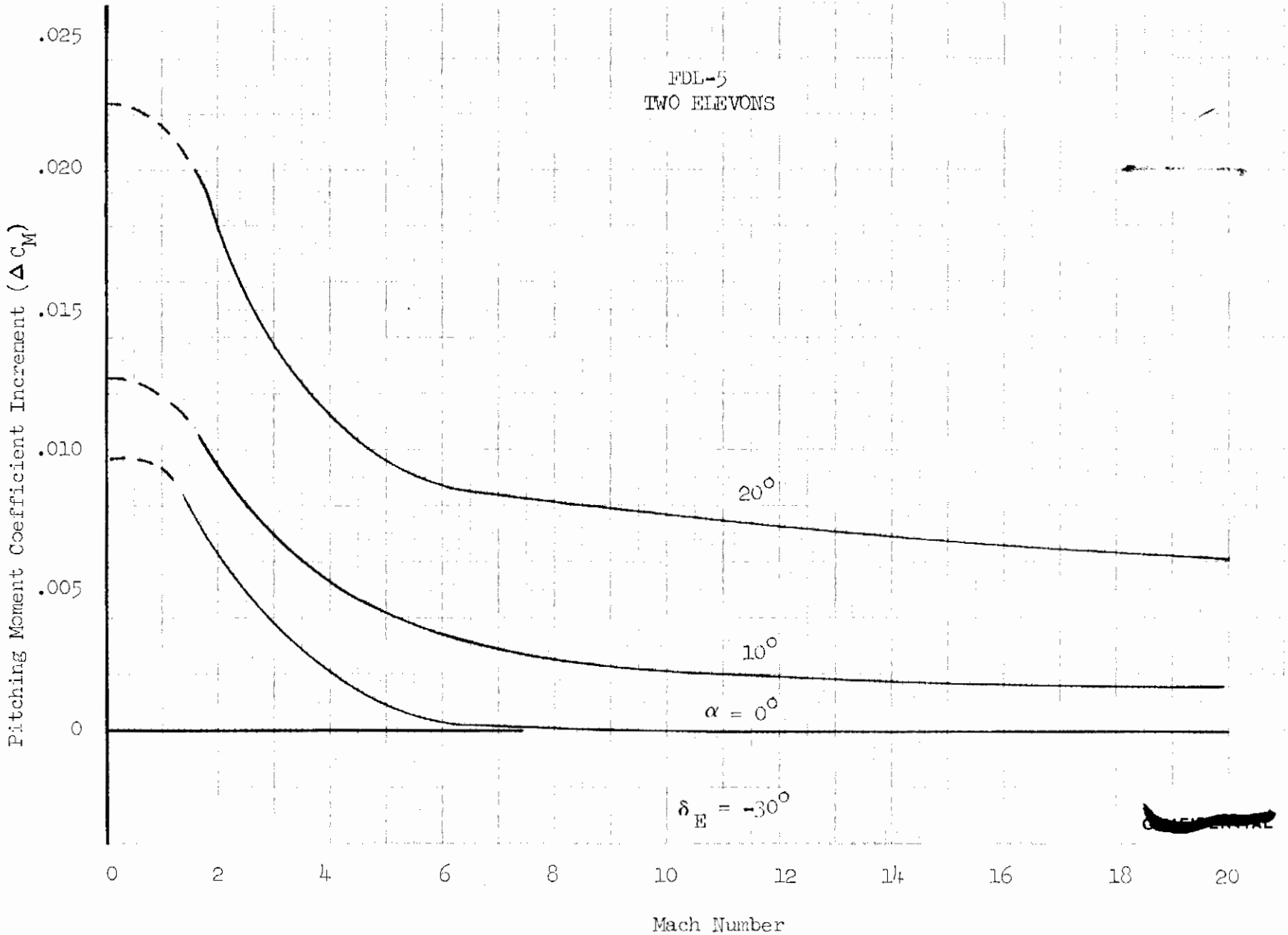

FIGURE 482 (U) ELEVON EFFECTIVENESS - PITCHING MOMENT INCREMENT VARIATION WITH MACH NUMBER (δ_E = -30°)

FIGURE 483 (U) ELEVON HINGE MOMENT VARIATION WITH MACH NUMBER (δ_E = +10°)

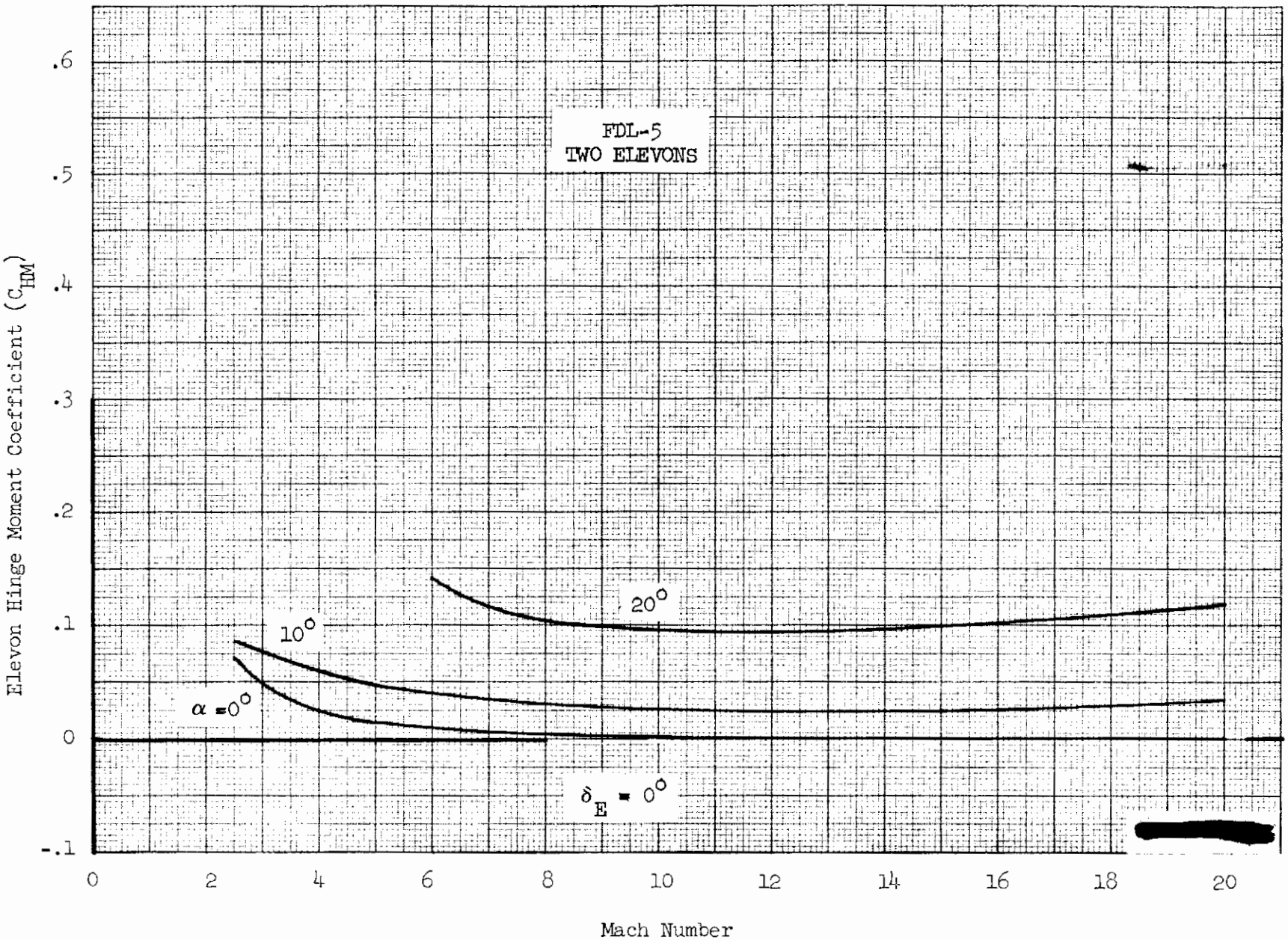

FIGURE 484 (U) ELEVON HINGE MOMENT VARIATION WITH MACH NUMBER ($\delta_E = 0^\circ$)

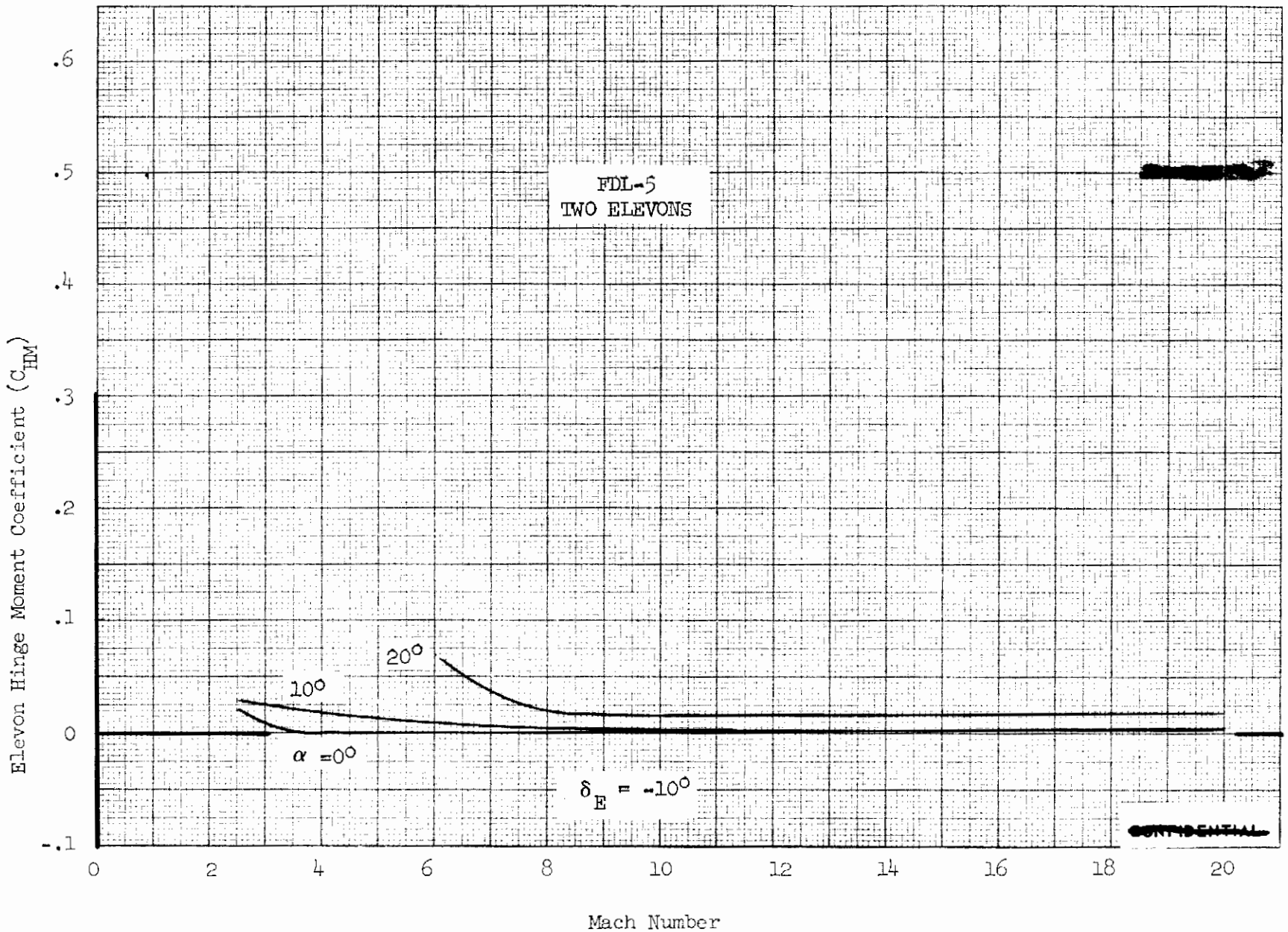

FIGURE 485 (U) ELEVON HINGE MOMENT VARIATION WITH MACH NUMBER (δ_E = -10°)

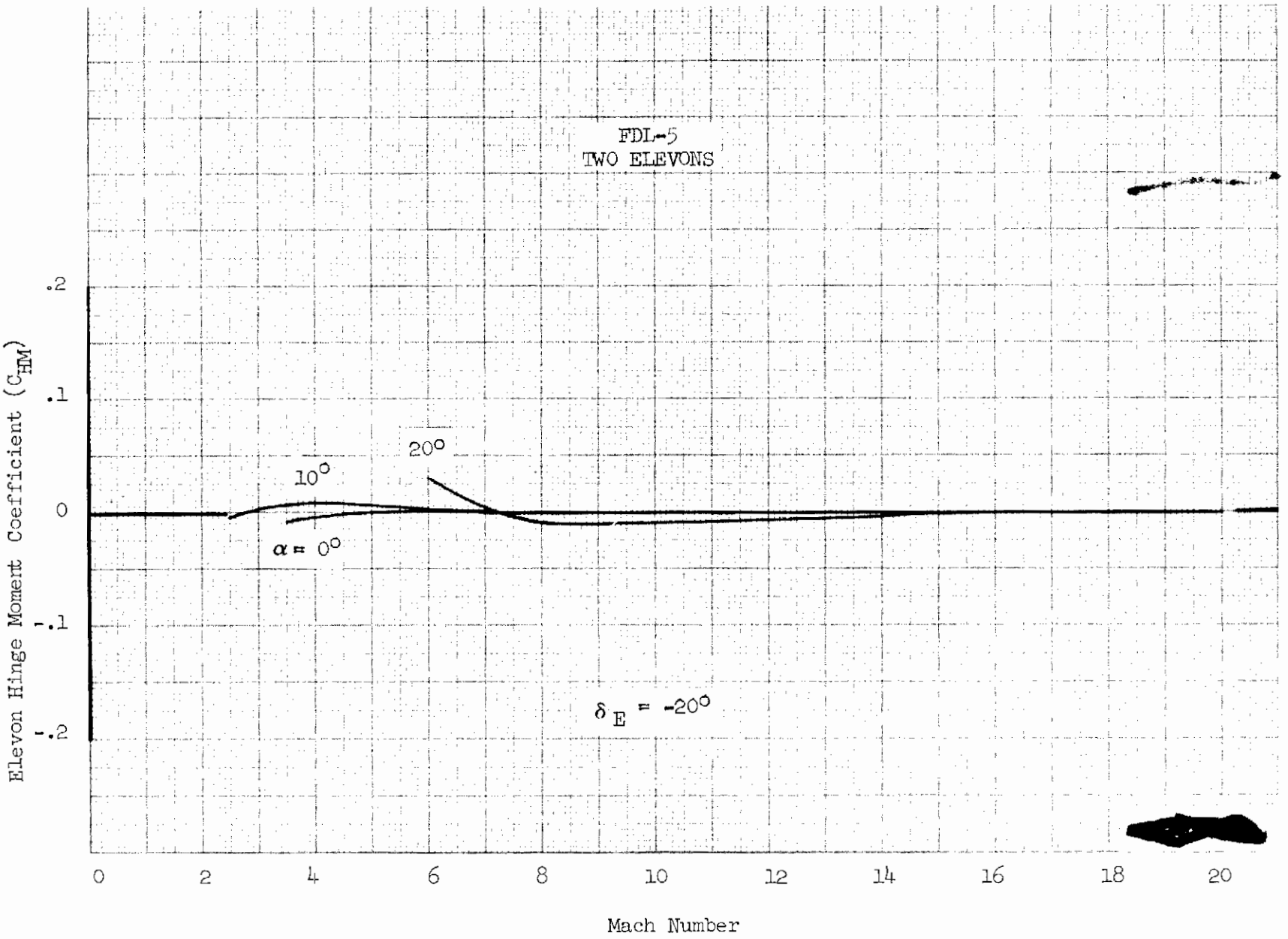

FIGURE 486 (U) ELEVON HINGE MOMENT VARIATION WITH MACH NUMBER (δ_E = -20°)

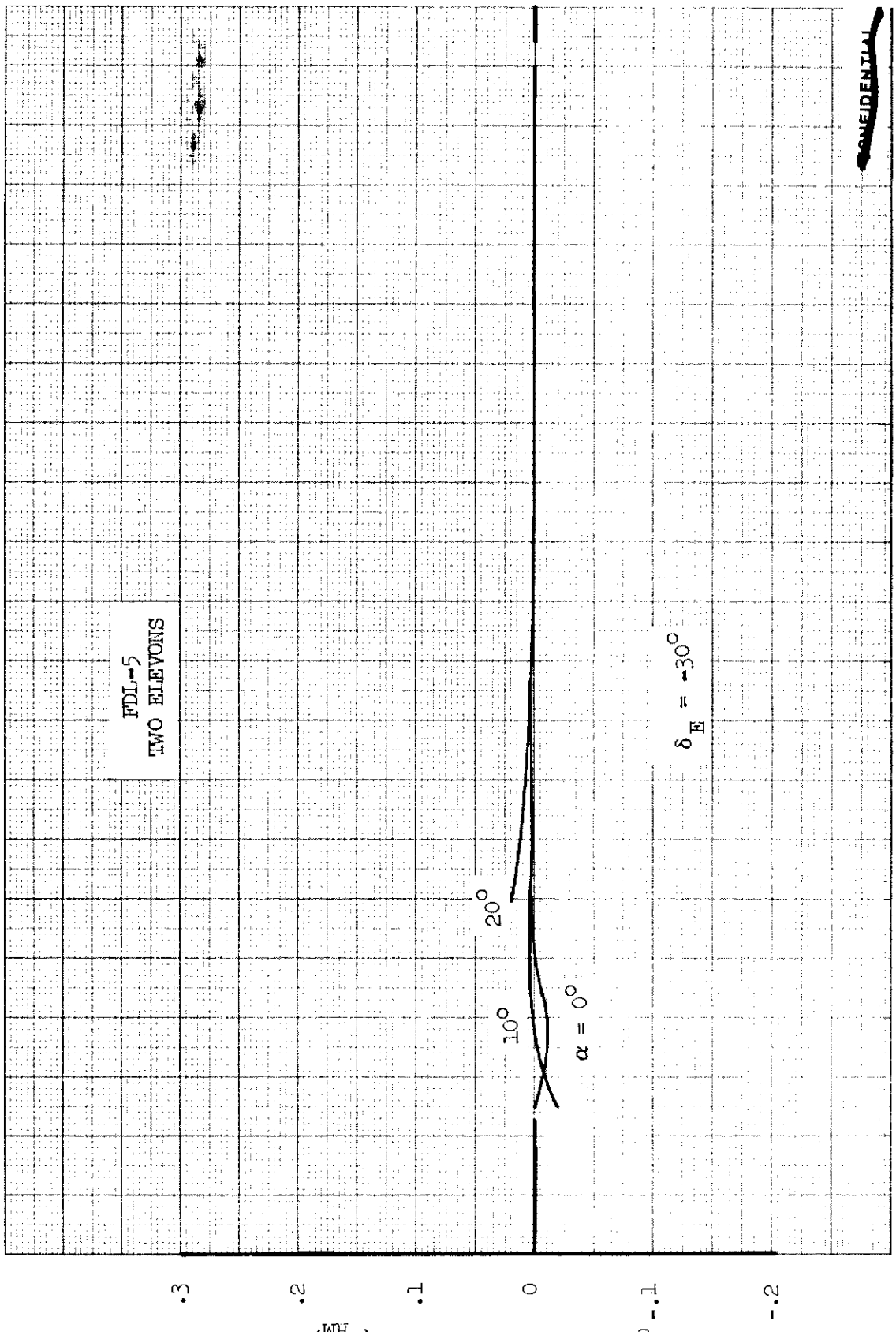

FIGURE 487 (U) ELEVON HINGE MOMENT VARIATION WITH MACH NUMBER ($\delta_E = -30^\circ$)

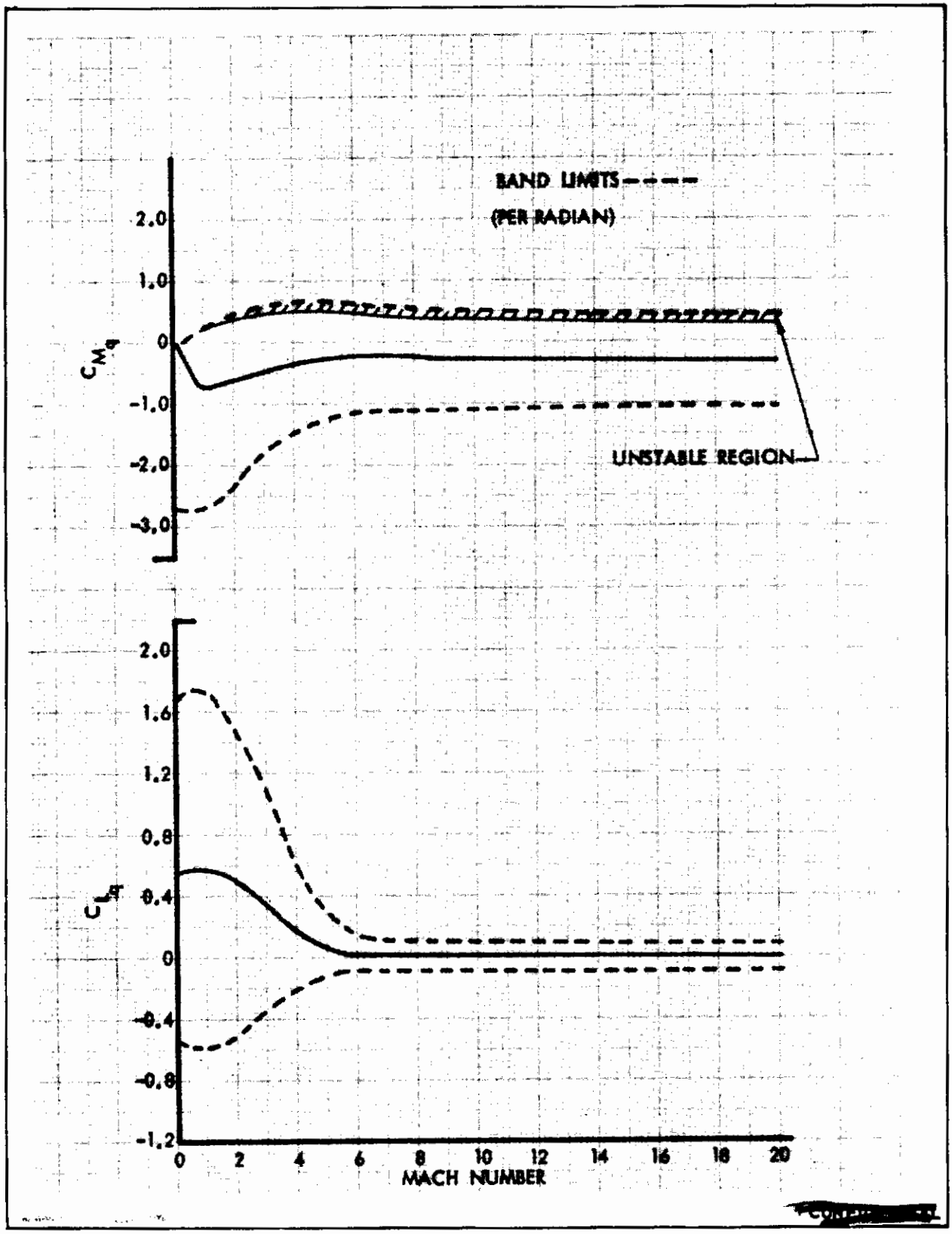

FIGURE 488 (U) VARIATION OF q DERIVATIVES WITH MACH NUMBER

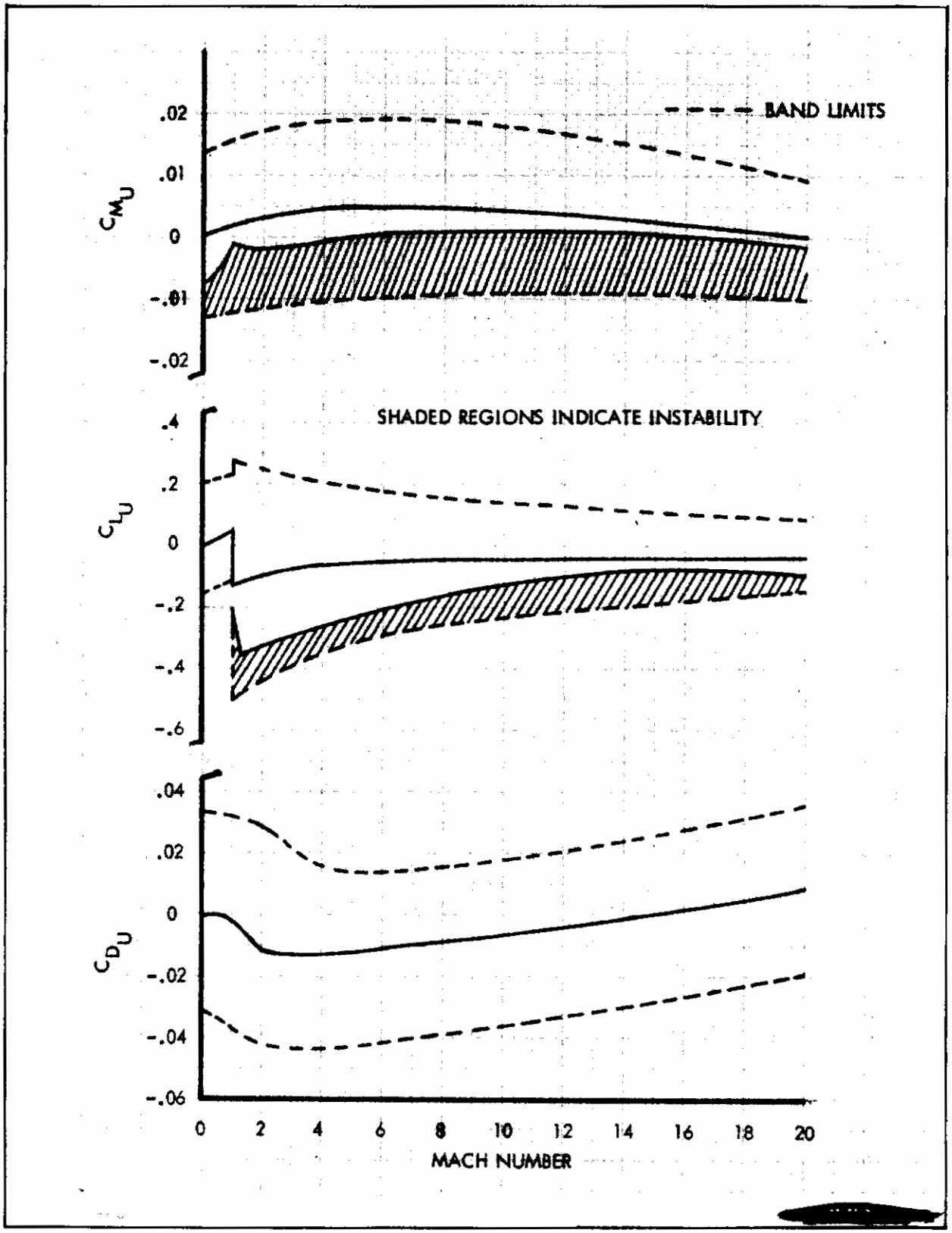

FIGURE 489 (U) VARIATION OF U DERIVATIVES WITH MACH NUMBER

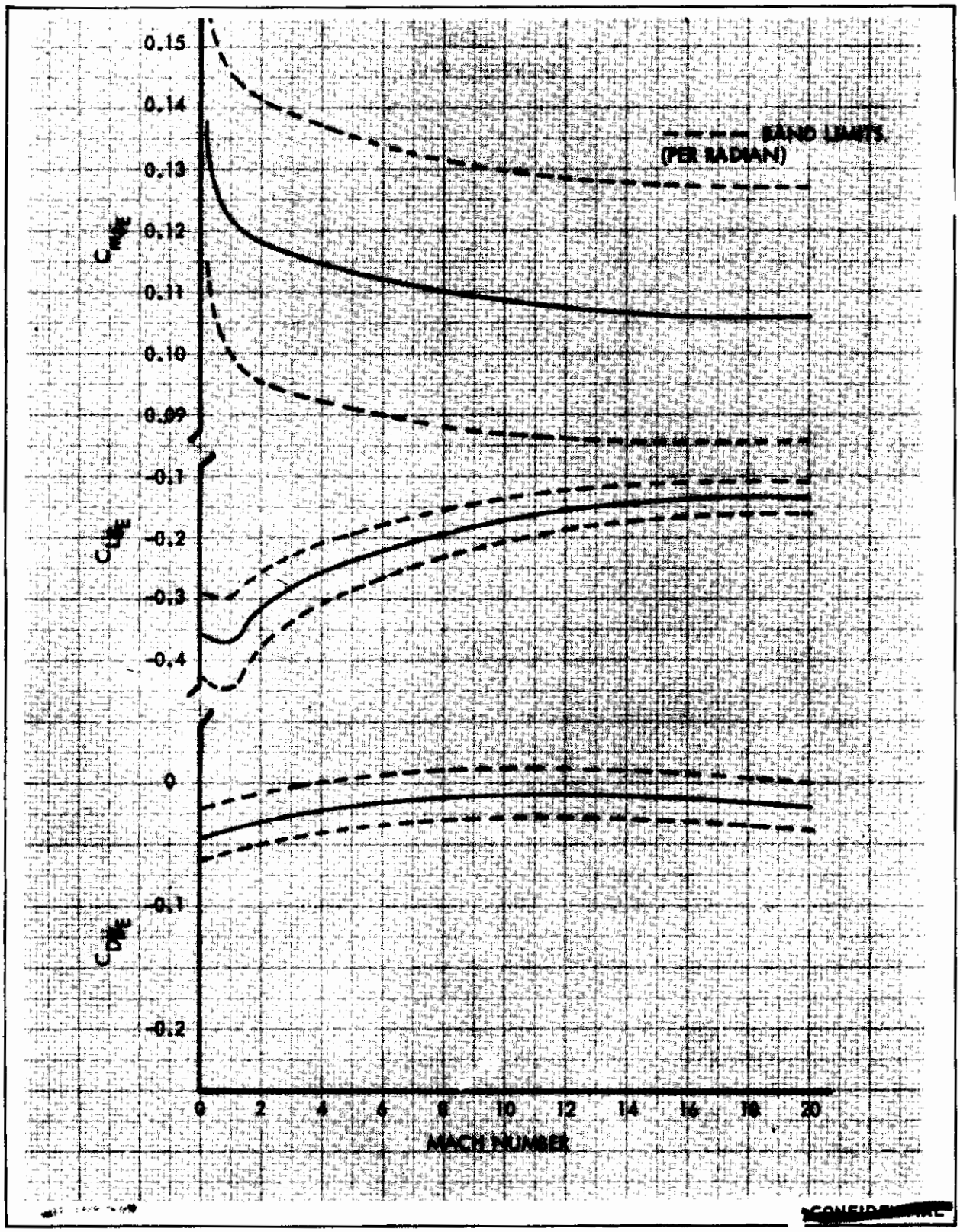

FIGURE 490 (U) VARIATION OF δ_E DERIVATIVES WITH MACH NUMBER

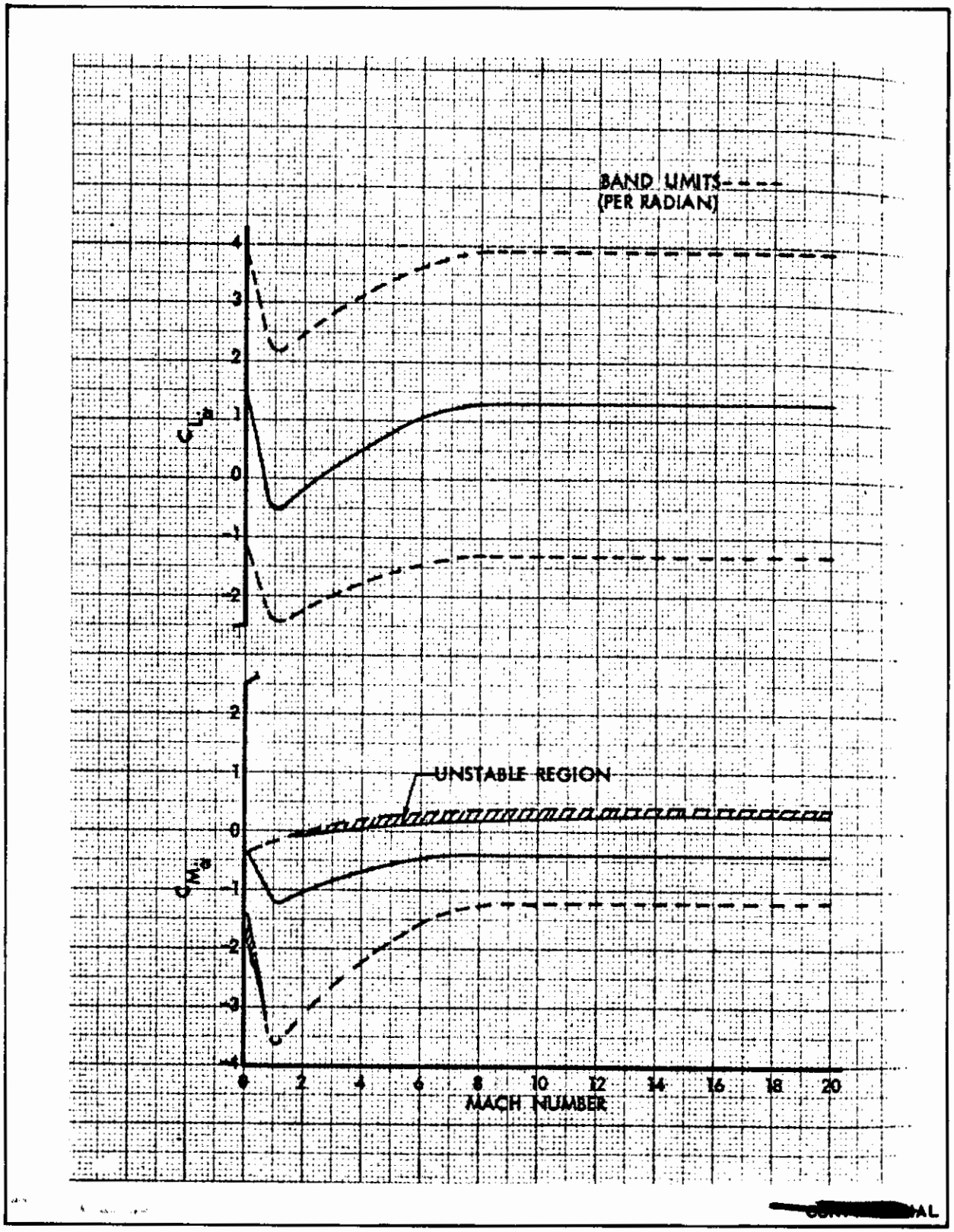

FIGURE 491 (U) VARIATION OF ∞ DERIVATIVES WITH MACH NUMBER

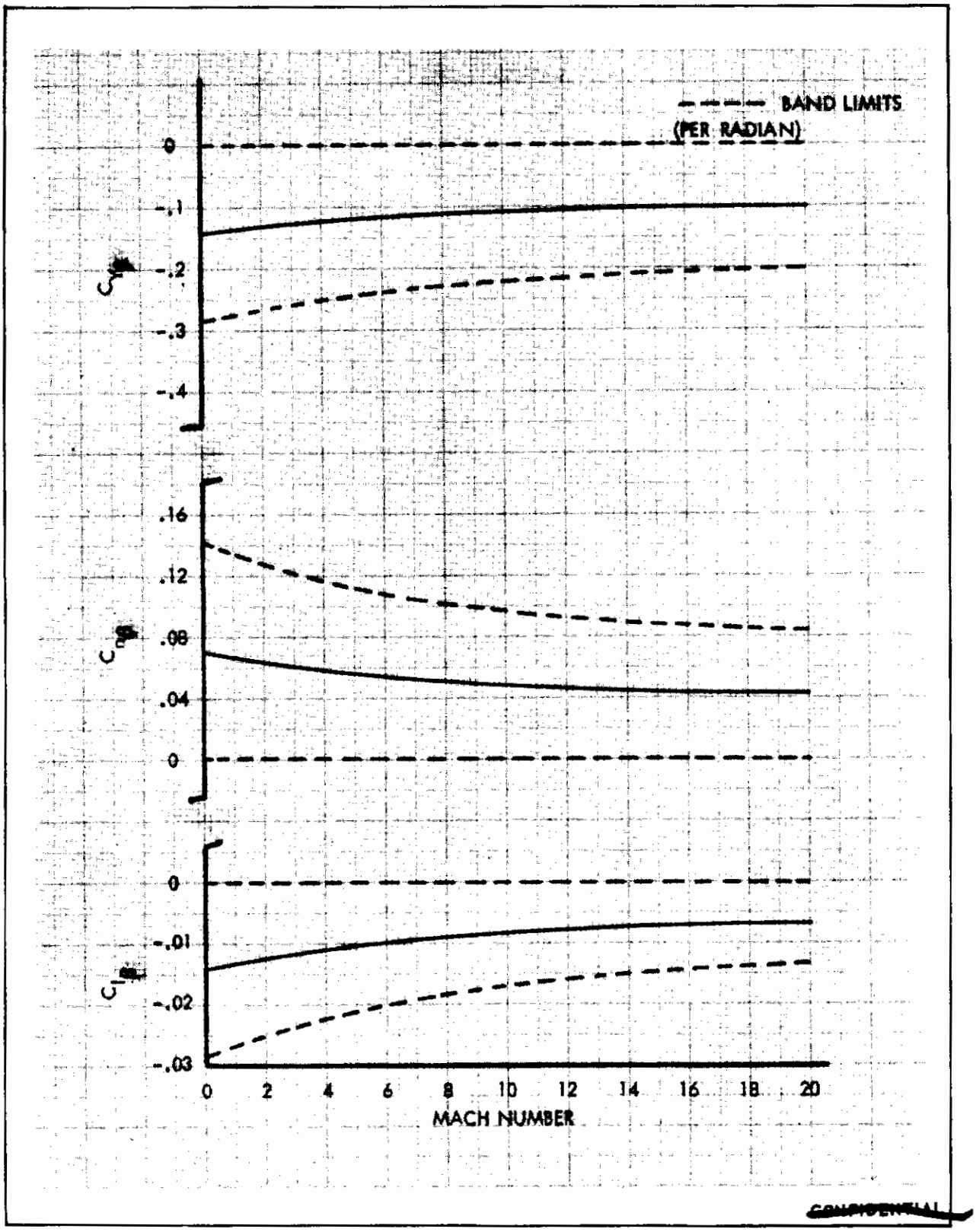

FIGURE 492 (U) VARIATION OF β DERIVATIVES WITH MACH NUMBER

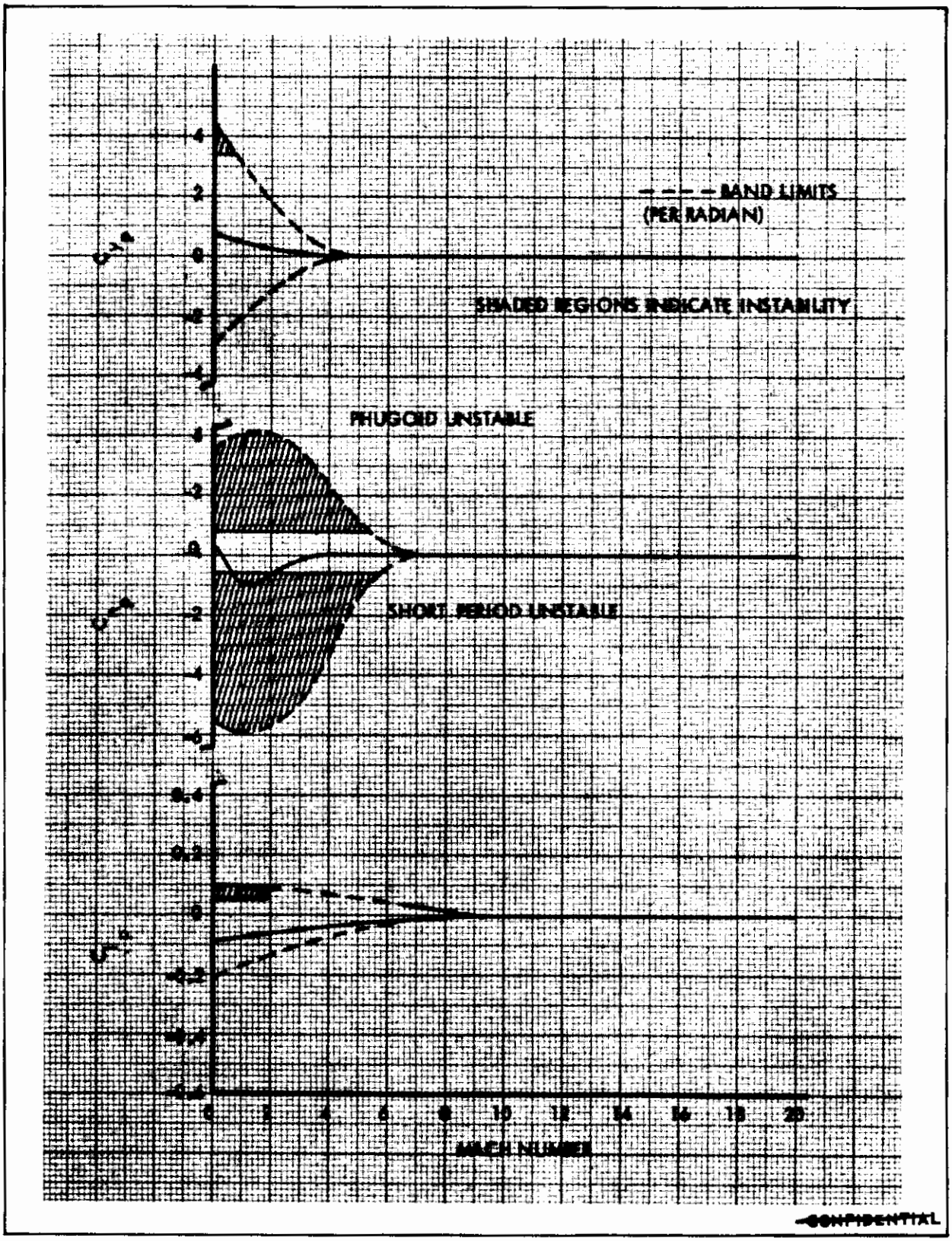

FIGURE 493 (U) VARIATION OF ρ DERIVATIVES WITH MACH NUMBER

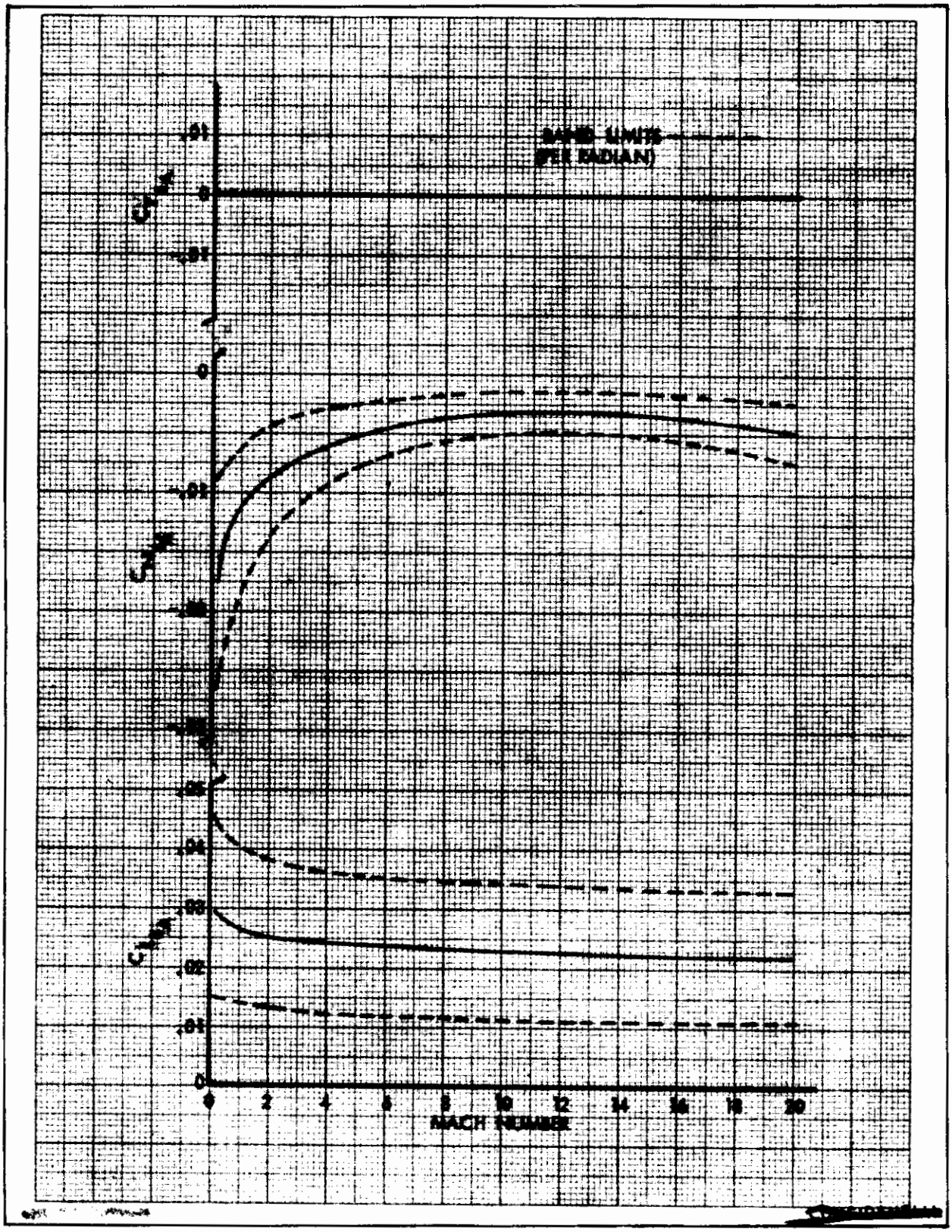

FIGURE 494 (U) VARIATION OF δA DERIVATIVES WITH MACH NUMBER

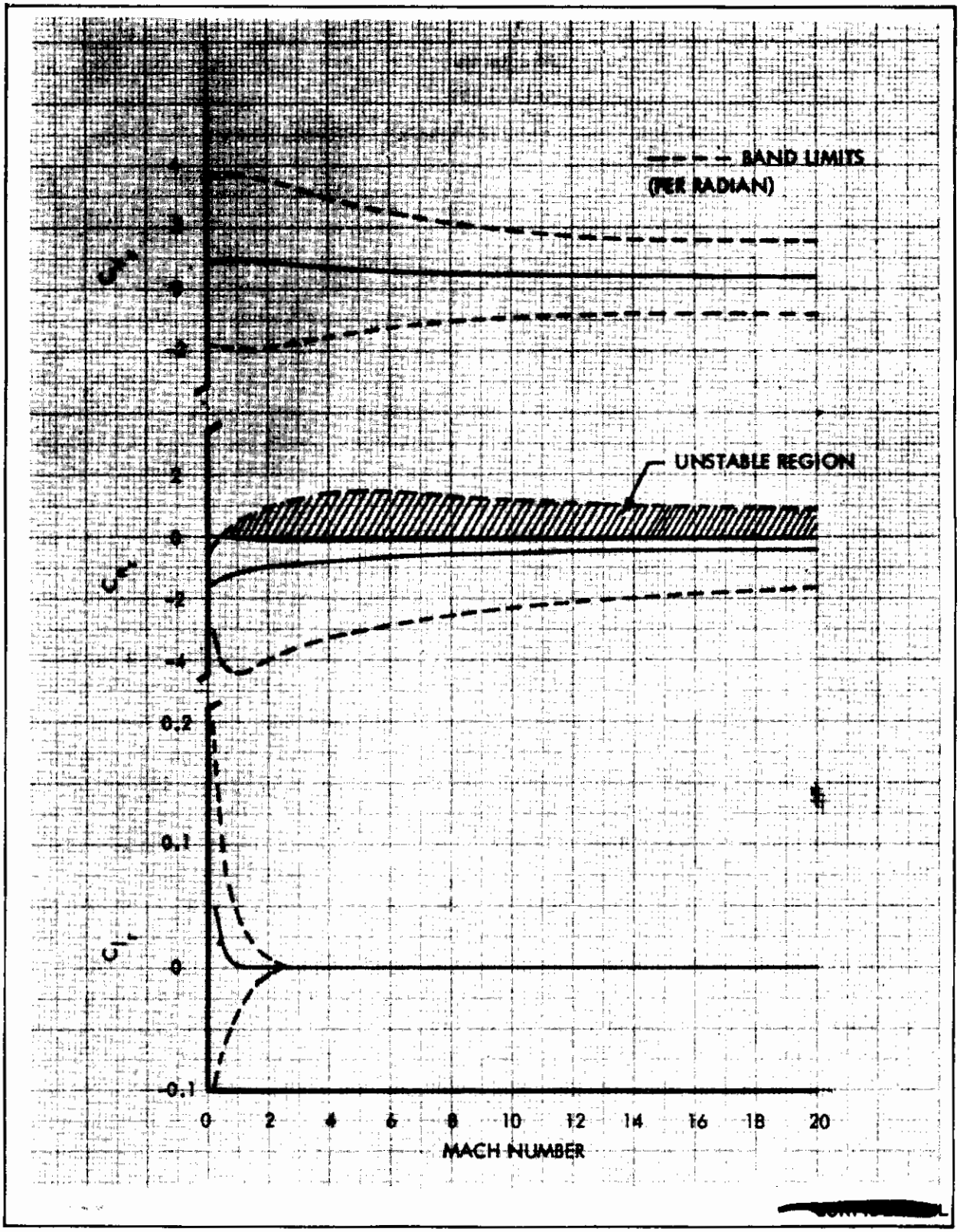

FIGURE 495 (U) VARIATION OF r DERIVATIVES WITH MACH NUMBER

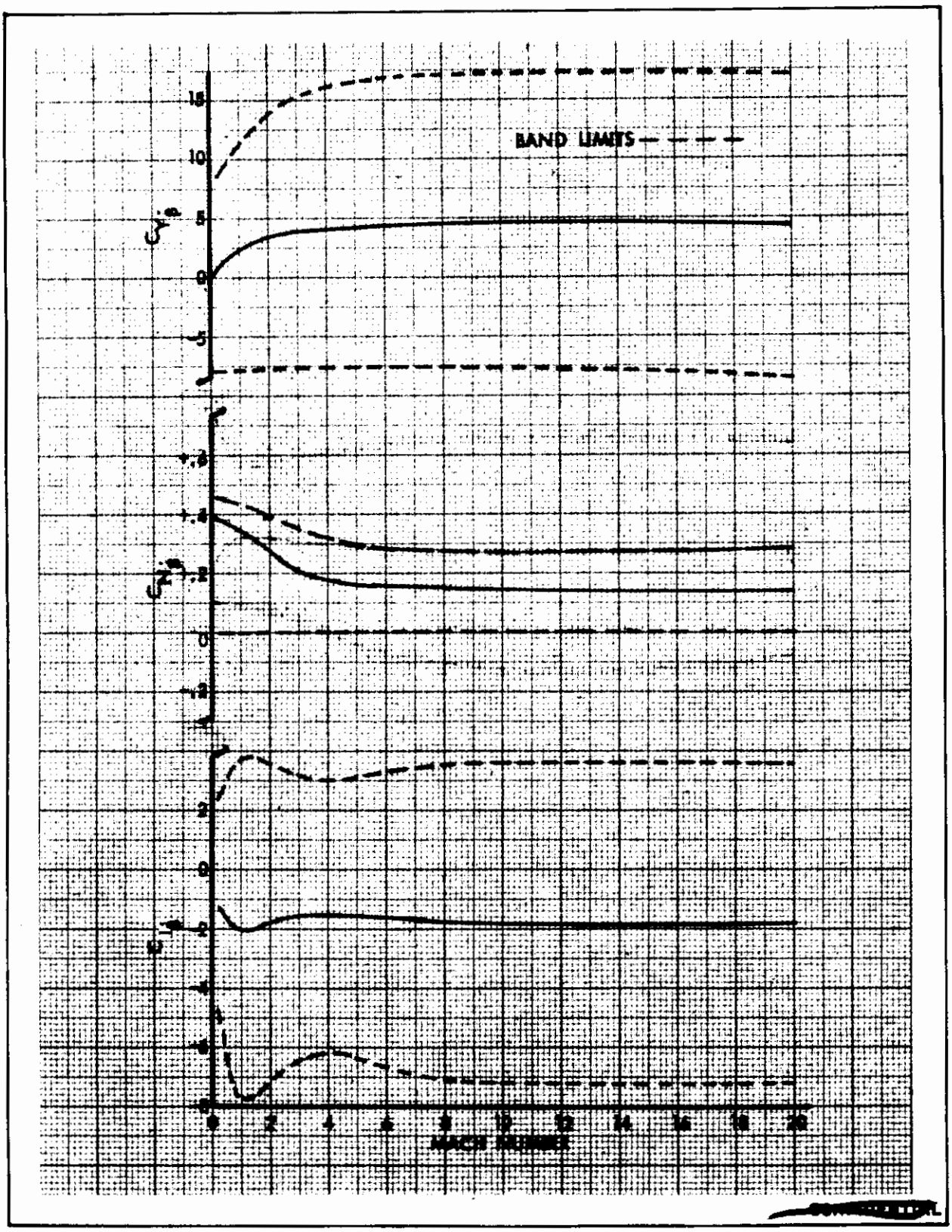

FIGURE 496 (U) VARIATION OF β DERIVATIVES WITH MACH NUMBER

(REVERSE SIDE IS BLANK)

DOCUMENT CONTROL DATA - R&D

(Security classification of title, body of abstract and indexing annotation must be entered when the overall report is classified)

1. ORIGINATING ACTIVITY *(Corporate author)*
Lockheed Aircraft Corporation
Burbank, California

2a. REPORT SECURITY CLASSIFICATION
CONFIDENTIAL

2b. GROUP
4

3. REPORT TITLE
PRELIMINARY DESIGN AND EXPERIMENTAL INVESTIGATION OF THE FDL-5A UNMANNED HIGH L/D SPACECRAFT
PART III, Aerodynamics

4. DESCRIPTIVE NOTES *(Type of report and inclusive dates)*
Final Report (1 July 1966 through 31 March 1968)

5. AUTHOR(S) *(Last name, first name, initial)*
C. F. Ehrlich, J. J. Rising, R. S. Peyton, and C. M. Onspaugh

6. REPORT DATE	7a. TOTAL NO. OF PAGES	7b. NO. OF REFS
March 1968	536	17

8a. CONTRACT OR GRANT NO.
Contract No. AF 33(615)-5241

b. PROJECT NO.
1366

c.

d.

9a. ORIGINATOR'S REPORT NUMBER(S)
LR 21204 (PART III)
LAC/619517

9b. OTHER REPORT NO(S) *(Any other numbers that may be assigned this report)*
AFFDL-TR-68-24- Part III

10. AVAILABILITY/LIMITATION NOTICES
This report is subject to special export controls and each transmittal to foreign governments or foreign nationals may be made only with prior approval of the Air Force Flight Dynamics Laboratory (FDMS), Wright-Patterson Air Force Base, Ohio 45433

11. SUPPLEMENTARY NOTES

12. SPONSORING MILITARY ACTIVITY
Air Force Flight Dynamics
Air Force Systems Command
Wright-Patterson Air Force Base, Ohio 45433

13. ABSTRACT

The aerodynamic wind tunnel test program for the FDL-5 configuration is described in this Part III. The description includes the models, test facilities, data reduction and presentation, and the test schedules. A complete presentation of the aerodynamic test data is provided. The data include six component force and moment data, pressure data, and photographic data for the Mach number range between 1.5 to 20. Correlations between the data and appropriate theories are presented. The overall aerodynamic characteristics of the FDL-5 configuration are defined.

DD FORM 1 JAN 64 1473

14. KEY WORDS	LINK A		LINK B		LINK C	
	ROLE	WT	ROLE	WT	ROLE	WT
* Aerodynamic Wind Tunnel Test Program						
* FDL-5 Configuration						
* High L/D Entry Vehicles						

INSTRUCTIONS

1. ORIGINATING ACTIVITY: Enter the name and address of the contractor, subcontractor, grantee, Department of Defense activity or other organization *(corporate author)* issuing the report.

2a. REPORT SECURITY CLASSIFICATION: Enter the overall security classification of the report. Indicate whether "Restricted Data" is included. Marking is to be in accordance with appropriate security regulations.

2b. GROUP: Automatic downgrading is specified in DoD Directive 5200.10 and Armed Forces Industrial Manual. Enter the group number. Also, when applicable, show that optional markings have been used for Group 3 and Group 4 as authorized.

3. REPORT TITLE: Enter the complete report title in all capital letters. Titles in all cases should be unclassified. If a meaningful title cannot be selected without classification, show title classification in all capitals in parenthesis immediately following the title.

4. DESCRIPTIVE NOTES: If appropriate, enter the type of report, e.g., interim, progress, summary, annual, or final. Give the inclusive dates when a specific reporting period is covered.

5. AUTHOR(S): Enter the name(s) of author(s) as shown on or in the report. Enter last name, first name, middle initial. If military, show rank and branch of service. The name of the principal author is an absolute minimum requirement.

6. REPORT DATE: Enter the date of the report as day, month, year; or month, year. If more than one date appears on the report, use date of publication.

7a. TOTAL NUMBER OF PAGES: The total page count should follow normal pagination procedures, i.e., enter the number of pages containing information.

7b. NUMBER OF REFERENCES: Enter the total number of references cited in the report.

8a. CONTRACT OR GRANT NUMBER: If appropriate, enter the applicable number of the contract or grant under which the report was written.

8b, 8c, & 8d. PROJECT NUMBER: Enter the appropriate military department identification, such as project number, subproject number, system numbers, task number, etc.

9a. ORIGINATOR'S REPORT NUMBER(S): Enter the official report number by which the document will be identified and controlled by the originating activity. This number must be unique to this report.

9b OTHER REPORT NUMBER(S): If the report has been assigned any other report numbers *(either by the originator or by the sponsor)*, also enter this number(s).

10. AVAILABILITY/LIMITATION NOTICES: Enter any limitations on further dissemination of the report, other than those imposed by security classification, using standard statements such as:

(1) "Qualified requesters may obtain copies of this report from DDC."

(2) "Foreign announcement and dissemination of this report by DDC is not authorized."

(3) "U. S. Government agencies may obtain copies of this report directly from DDC. Other qualified DDC users shall request through _____."

(4) "U. S. military agencies may obtain copies of this report directly from DDC. Other qualified users shall request through _____."

(5) "All distribution of this report is controlled. Qualified DDC users shall request through _____."

If the report has been furnished to the Office of Technical Services, Department of Commerce, for sale to the public, indicate this fact and enter the price, if known.

11. SUPPLEMENTARY NOTES: Use for additional explanatory notes.

12. SPONSORING MILITARY ACTIVITY: Enter the name of the departmental project office or laboratory sponsoring *(paying for)* the research and development. Include address.

13. ABSTRACT: Enter an abstract giving a brief and factual summary of the document indicative of the report, even though it may also appear elsewhere in the body of the technical report. If additional space is required, a continuation sheet shall be attached.

It is highly desirable that the abstract of classified reports be unclassified. Each paragraph of the abstract shall end with an indication of the military security classification of the information in the paragraph, represented as *(TS), (S), (C), or (U)*.

There is no limitation on the length of the abstract. However, the suggested length is from 150 to 225 words.

14. KEY WORDS: Key words are technically meaningful terms or short phrases that characterize a report and may be used as index entries for cataloging the report. Key words must be selected so that no security classification is required. Identifiers, such as equipment model designation, trade name, military project code name, geographic location, may be used as key words but will be followed by an indication of technical context. The assignment of links, rules, and weights is optional.